NATURAL AND ARTIFICIAL ORBITS AROUND THE MARTIAN MOON PHOBOS

by

MATTIA ZAMARO

A Thesis Submitted in Partial Fulfilment of the Requirements for the Degree of Doctor of Philosophy

to the
Department of Mechanical and Aerospace Engineering
University of Strathclyde

October 2015

ACADEMIC YEAR 2014/2015

Declaration

This thesis is the result of the author's original research. It has been composed by the author and has not been previously submitted for examination which has led to the award of a degree.

The copyright of this thesis belongs to the author under the terms of the United Kingdom Copyright Acts as qualified by University of Strathclyde Regulation 3.50. Due acknowledgement must always be made of the use of any material contained in, or derived from, this thesis.

The author: Mattia Zamaro

Date: 05/10/2015

Acknowledgments

In view of this important achievement for me, I would like to take the opportunity to thank all the people who helped me along the way.
My first dedication is to my parents and relatives, who have always supported me with patience and care.
I would like to thank anyone who encouraged me to bring out the best in myself, from professors in schools to coaches in sports, nevertheless clearly all my friends, school and university mates, who have always reminded me how they have confidence in my possibilities and capabilities, and have actively supported me in my studies.
Most of all, I would like to acknowledge my supervisor, Dr James Biggs, who believed in me from the beginning, by selecting me for this fellowship, and gave me the opportunity to carry out this research. Moreover, he has been always interested and willing to listen to me during this period. Finally, I would like to thank the researchers of the AstroNet-II training network, in particular the coordinator Prof Gerard Gómez, who made this a wonderful experience.

Abstract

One of the paramount stepping stones towards the long-term goal of undertaking human missions to Mars is the exploration of the Martian moons. In particular, Phobos is becoming an appealing destination for future scientific missions of NASA and ESA. Phobos is a tiny celestial body that orbits around Mars at low altitude. The unique combination of these two characteristics yields the sphere of influence of the moon to be very close to its surface. Therefore, orbital dynamics around Phobos are particularly complex, because many strong perturbations are involved. The classical models of the Keplerian two-body problem, and the circular three-body problem are not accurate enough to describe the motion of a spacecraft in the vicinity of Phobos.

In this thesis, the description of the relative orbital dynamics in proximity of this moon is extended to a more accurate nonlinear model. This is undertaken by the inclusion of the perturbations due to the orbital eccentricity and the inhomogeneous gravity field of Phobos.

Subsequently, several classes of non-Keplerian orbits are identified, using the analytical and numerical methodologies of dynamical systems theory. These techniques exploit the improved description of the natural dynamics, enabled by the extended model, to provide low-cost guidance trajectories, that minimize the fuel consumption and extend the mission range. In addition, the potential of exploiting artificial orbits with low-thrust is investigated.

The performance and requirements of these orbits are assessed, and a number of potential mission applications near Phobos are proposed. These low-cost operations include close-range observation, communication, passive radiation shielding, and orbital pit-stops for human spaceflight. These results could be exploited in upcoming missions targeting the exploration of this Martian moon. Furthermore, the new model can provide evidence to support the accretion theory of Phobos' origin, and to explain the formation of the craters and grooves on Phobos.

Keywords

Phobos - Mars manned mission - inhomogeneous gravity - artificial equilibria - Libration Point orbits - Invariant Manifolds - Quasi-Satellite orbits - radiation shielding - Phobos origin - Phobos morphology - Dynamical Systems Theory - numerical continuation

Contents

List of Figures

List of Tables

Nomenclature

List of Symbols

a	acceleration $[m/s^2]$
	semi-major axis $[m]$
a_n	Fourier expansion cosine coefficient
b	semi-minor axis $[m]$
b_n	Fourier expansion sine coefficient
c	specific Jacobi constant $[J/kg]$
c_i	optical coefficient: specular (sr) and diffusive (dr) reflectance, absorbance (a), transmittance (t), emission (e) [-]
c_n	Fourier expansion complex coefficient
c_{light}	speed of light: $2.998m/s$
d	distance $[m]$
e	eccentricity [-]
	error state vector
	Floquet mode's eigenvector
	specific total energy $[J/kg]$
	vector of the basis
f	generic function
	specific gravitational force $[m/s^2]$
	vectorfield of the continuous dynamical system
g	intensity of gravitational field $[m/s^2]$
	metric matrix
	Poincaré map's surface of section's constraint function
h	altitude $[m]$
	specific Hamiltonian function $[J/kg]$
i	inclination $[rad]$
l	length $[m]$
	mean longitude $[rad]$
	normalized arclength [-]
	specific Lagrangian function $[J/kg]$
m	mass $[kg]$

	multiplier
	natural modes vector
	order of the spherical harmonic
n	counter number
	degree of the spherical harmonic
	Fourier expansion frequency coefficient
	mean motion $[rad/s]$
	neutron [-]
	normal versor
	spin rate
	versor direction [-]
p	orbital parameter or semi-latus rectum $[m]$
	pressure $[Pa]$
	proton
	specific momenta $[m/s]$
q	heat flux $[W/m^2]$
	relative position vector of the 3BP $[m]$
r	distance from a reference point $[m]$
	frequency ratio of the torus [-]
	radius $[m]$
r_H	Hill's radius $[m]$
r_{P2}^{P1}	distance of P2 from P1 points
s	archlength
	distance $[m]$
	stable state
t	specific kinetic energy $[J/kg]$
	time $[s]$
u	argument of latitude $[rad]$
	input vector
	specific gravitational potential $[J/kg]$
u_{eff}	specific effective/augmented potential of the 3BP $[J/kg]$
v	eigenvector
	velocity $[m/s]$
w	width of a closed curve
x	position first component $[m]$
	state vector of the dynamical system
	variables of the DC
y	position second component $[m]$
z	difference of state vector from EP
	performance vector
	position third component $[m]$

A	area
	linear state matrix
A_n	Fourier expansion magnitude coefficient
$A_i(\alpha)$	attitude matrix, related to rotation of angle α along the i=1,2,3 axis
A_{F2}^{F1}	attitude matrix, related to rotation from F1 to F2 frames
AU	Astronomical Unit, Earth-Sun mean distance: $1.49597870691 \cdot 10^{11} m$
Az	Azimuth angle $[rad]$
$Ab.D.$	Absorbed Dose [Gy]
$Am.D.Eq.$	Ambient Dose Equivalent [Sv]
B	linear state-input matrix
C	circular Equinoctial orbital parameter [-]
	curve
	linear output-state matrix
$C_{n,m}$	spherical harmonics series expansion first coefficient [-]
D	linear output-input matrix
E	eccentric anomaly $[rad]$
$Ef.D.$	Effective Dose [Sv]
$Eq.D.$	Equivalent Dose [Sv]
F	generic frame
	generic function
	objective function of the DC
G	Cavendish gravitational constant: $6.67259 \cdot 10^{-11} m^3/s^2 kg$
GM	gravitational parameter $[m^3/s^2]$
H	Hessian matrix
	hyperbolic anomaly $[rad]$
I	identity matrix
	inertial frame
J	cost functional
	Jacobian matrix
$J_{n,m}$	spherical harmonics series expansion coefficient magnitude [-]
K	controller gain matrix
	eccentric longitude $[rad]$
	ratio y/x planar amplitudes of the orbit input of the lp algorithm
L	length of a curve
	light function [-]
	true longitude $[rad]$
	unit of length of the 3BP $[m]$
L_i	Lagrangian/Libration point of the 3BP (i=1,2,3,4,5)
$L_{\odot\oplus}$	light function of radiating body $\odot$ and shadowing body $\oplus$ [-]
$L_{\oplus}$	light function of the Sun and the shadowing body $\oplus$ [-]
M	generic matrix

	mask function [-]
	mean anomaly $[rad]$
	monodromy matrix
	total mass of the 3BP system $[kg]$
	truncated order
N	direction of line of nodes
	integer number
	linear state-input weight matrix
	body's Node of reference
	surface normal versor
	truncated degree
NP	body's North Pole
O	occulting function [-]
$O_{\oplus}$	occulting function of occulting body $\oplus$ [-]
OE	orbital elements
P	generic point
	map function of the discrete dynamical system
	matrix $[\omega\wedge]^2$
	parabolic anomaly $[rad]$
	period of a generic function
	projector matrix: along parallel ($\backslash\backslash$) or orthogonal ($\perp$) space of a vector v
	linear sensitivity matrix
P_{1-2}	planar Equinoctial orbital parameters [-]
P_n	Legendre polynomial
P_n^m	associated Legendre polynomial
PM	body's Prime Meridian
Q	linear state weight matrix
Q_{1-2}	equatorial Equinoctial orbital parameters [-]
R	linear input weight matrix
	mean radius $[m]$
S	circular Equinoctial orbital parameter [-]
	shadow function [-]
	surface
$S_{n,m}$	spherical harmonics series expansion second coefficient [-]
T	period $[s]$
	transformation of coordinates
TOF	Time Of Flight [s]
U	(right/by rows) eigenversors matrix
	generic set
V	(left/by columns) eigenversors matrix
W	invariant manifold set

	matrix $[\omega\wedge]$
$W^{u/s,\pm}$	invariant manifold (unstable/stable positive/negative branch)
X	position-velocity variables
	variables of the DC
α	alpha particle
	generic angle $[rad]$
	Floquet mode's component
	planar x-amplitude of the orbit input of the lp algorithm
	pitch angle $[rad]$
	right-ascension $[rad]$
β	Sun angle $[rad]$
	vertical amplitude of the orbit input of the lp algorithm
δ	declination $[rad]$
	variational term
	yaw angle $[rad]$
δ_{ij}	Kronecker's delta
ϵ	elevation angle $[rad]$
	threshold [-]
ϕ	flow of the dynamical system
	latitude $[rad]$
φ	phase $[rad]$
	1st Euler angle $[rad]$
γ	adimensional Hill's radius of the secondary in the 3BP [-]
	Ares Constellation Point (Earth's vernal equinox)
γ_i	adimensional distance of L_i from the secondary body
θ	generic parametrization variable of the invariant curve
	spin axis' tilt with respect to orbital plane $[rad]$
	2nd Euler angle $[rad]$
θ_n	Fourier expansion phase coefficient
ϑ	co-latitude $[rad]$
	polar anomaly coordinate $[rad]$
λ	argument of true latitude $[rad]$
	eigenvalue
	lightness number [-]
$\lambda_{n,m}$	spherical harmonics series expansion coefficient anomaly $[rad]$
μ	mass parameter of the 3BP [-]
ν	flow of the dynamical system in the phase-space
	true anomaly $[rad]$
π	Floquet mode's projector
ϖ	longitude of pericenter $[rad]$
ρ	density $[kg/m^3]$

	relative position $[m]$
	rotation number of the invariant curve's parametrization variable $[rad]$
σ	numerical continuation parameter
ψ	azimuthal anomaly coordinate $[rad]$
	longitude $[rad]$
	3rd Euler angle $[rad]$
τ	time-return to a map
ω	argument of pericenter $[rad]$
ω_{F2}^{F1}	angular velocity, related to rotation from F1 to F2 frames $[rad/s]$
Δ	variation term
Δv	maneuver specific impulse $[m/s]$
Γ	Christoffels' symbols 3D matrix
	Poincaré map's surface of section
Φ	state transition matrix of the dynamical system
Λ	eigenvalues matrix
Π	monodromy matrix of a discretized invariant curve of a map
Ω	right-ascension of ascending node $[rad]$
	solid angle $[sr]$
∇	gradient vector

List of Superscripts

$\bullet$	time-derivative
$\wedge$	versor
c	central branch
	control action
d	disturbance (orbital perturbation: p)
s	stable branch
u	unstable branch
C	corrected value
F	value through Fourier series approximation
P	predicted value
T	target value
$+$	positive branch
$-$	negative branch
$-$	central body centered normalized
	mean (integral) value
	normalized variable
$\sim$	EP centered normalized
	force-constrained variable

List of Subscripts

In order of writing:

body	1	Mars
	2	Phobos
	E	Earth
	M	Planetary moon
	P	Planet
	S	Sun
	c	chief
	d	deputy
	$\odot$	Radiating body
		Sun
	$\oplus$	Central Body
	$'$	Anti-Body position
state	L	Lagrangian
	H	Hamiltonian
final condition	f	
initial condition	0	
state-derivative	/	
reference system	frame ID	
component	due to related frame	
P	planar	
T	target	
V	vertical	
OE	M	mean
	O	osculating

List of Coordinate Reference Systems

A reference frame in cartesian coordinates (x, y, z) is generally identified by a cluster of three symbols, representing respectively: the origin point, the x-y plane, and the point the x-axis's direction points towards.
Additional short nomenclature for particular coordinate frames is stated below.

ID	Symbols	Axes	Definition
BCI_b	$bE_E\gamma$	x, y, z	Body-Centered Inertial frame of body b: Body barycenter - Earth Equator plane - Earth Vernal Equinox
BCE_b	bE_bN_b	x, y, z	Body-Centered Equatorial frame of body b: Body barycenter - Body Equator plane - Body Node (on Earth Equator plane)
BCBF_b	bE_bPM_b	x, y, z	Body-Centered Body-Fixed frame of body b: Body barycenter - Body Equator plane - Body Prime Meridian
H_b	$bO_bR_b^0$	r, θ (or t), h	Hill's frame of body b: Body barycenter - Body orbital plane - Body direction from central body at origin 0
PI_b	-	x, y, z	Principal of Inertia frame of body b
ECI	$EE_E\gamma$	x, y, z	Earth-Centered Inertial frame
MCE	ME_MN_M	x, y, z	Mars Areocentric frame
ECEF	EE_EPM_E	x, y, z	Earth-Centered Earth-Fixed frame
Se	$SO_E\gamma$	x, y, z	Heliocentric frame
Ee	$EO_E\gamma$	x, y, z	Earth Ecliptic frame
3B	$B_{12}O_2R_2^1$	x, y, z	Adimensional Relative/Rotating/Synodic frame of the 3BP
R	-	x, y, z	Rotating frame (ω_R directed along z)
TSE	-	r, ϑ, ψ	Topographical frame: Top-South-East

List of Abbreviations

2BP	Two-Body Problem
2BP-R	Two-Body Problem in a Rotating frame
3BP	Three-Body Problem
3BP-R	Three-Body Problem in a Rotating frame
4BP	Four-Body Problem
AEP	Artificial Equilibrium Point
AFF	Artificial Formation Flying
AIM	Artificial Invariant Manifold
ALPO	Artificial Libration Point Orbit
AOCS	Attitude and Orbital Control System
ARE	Algebraic Riccati Equation
BCM	Bicircular Model
CA	Constant Acceleration

CCD	Charge-Coupled Device
CCM	Concentric Circular Model
CR3BP	Circular Restricted Three-Body Problem
CR3BPH	Hill's approximation of the Circular Restricted Three-Body Problem
CR3BP-CA	Circular Restricted Three-Body Problem with Constant Acceleration
CR3BP-GH	Circular Restricted Three-Body Problem with Gravity Harmonics
CR3BP-J_2	Circular Restricted Three-Body Problem with J_2 perturbation
CR3BP-$J_{2,2}$	Circular Restricted Three-Body Problem with $J_{2,2}$ perturbation
DC	Differential Corrector
DOF	Degree of Freedom
DST	Dynamical systems Theory
PCR3BP	Planar Circular Restricted Three-Body Problem
E3BP	Elliptic Three-Body Problem
ER3BP	Elliptic Restricted Three-Body Problem
ER3BP-GH	Elliptic Restricted Three-Body Problem with Gravity Harmonics
EDL	Entry-Descent-Landing
EP	Equilibrium Point
FEEP	Field-Emission Electric Propulsion
FF	Formation Flying
FFT	Fast Fourier Transform
FLI	Fast Lyapunov Indicator
FOV	Field of View
FTLE	Finite-Time Lyapunov Exponent
GCR	Galactic Cosmic Ray
GEO	Geostationary Earth Orbit
GH	Gravity Harmonic
GNC	Guidance, Navigation and Control
HJB	Hamilton-Jacobi-Bellman equation
IH	Infinite-Horizon
IM	Invariant Manifold
IR	Infrared
KAM	Kolmogorov-Arnold-Moser
LEO	Low Earth Orbit
LMS	Least Mean Square
LP	Libration Point
lp	Lindstedt-Poincaré
LQR	Linear Quadratic Regulator
MLE	Maximum Lyapunov Exponent
MLI	Multi-Layer Insulation
MRP	Mars Radiation Pressure
nBP	n-Body Problem

NC	Numerical Continuation
NEO	Near-Earth Object
NK	Non-Keplerian
NL	Nonlinear
OCT	Optimal Control Theory
ODE	Ordinary Differential Equation
OE	Orbital Element
PID	Proportional-Integral-Derivative
P-R2BP	Perturbed Restricted Two-Body Problem
P-R3BP	Perturbed Restricted Three-Body Problem
PO	Periodic Orbit
PRP	Phobos Radiation Pressure
PSI	Pseudo-Inverse
QPO	Quasi-Periodic Orbit
QSO	Quasi-Satellite Orbit
R2BP	Restricted Two-Body Problem
R3BP	Restricted Three-Body Problem
R4BP	Restricted Four-Body Problem
RnBP	Restricted n-Body Problem
SDC	State-Dependent Coefficient
SDRE	State-Dependent Riccati Equation
SEPE	Solar Energetic Particle Event
SH	Shape Harmonic
SK	Station-Keeping
SOI	Sphere of Influence
SRP	Solar Radiation Pressure
SS	Solar System
SS	Sun-Synchronous
STM	State Transition Matrix
SVD	Singular Value Decomposition
TI	Time-Invariant
TV	Time-Variant
UV	Ultraviolet
VDCO	Vertical-Displaced Circular Orbit

Chapter 1

Introduction

1.1 Scientific Interest in the Martian Moons

Phobos and Deimos are the two natural satellites of Mars, and they were discovered in 1877 by the American astronomer Asaph Hall. Since their discovery, the two moons of Mars have become increasingly interesting astronomical objects to investigate throughout the last century. In particular, the **origin** of the Martian moons is still a controversial topic with no unified agreement [1, 2, 3]. The mainstream theory is based on the common irregular shape and tiny size of both moons, that resemble two asteroids. For this reason, Phobos and Deimos could well be native to the Main Asteroid Belt, which were sling-shot by Jupiter and then captured by Mars [4, 5], or even be the inactive nuclei of captured comets [6]. A second explanation follows the theory of planetesimals widely accepted to explain the formation of most of the major bodies of the Solar System. In this case, the two Martian moons originated by coalescence of material in the primordial Solar System. In particular, Phobos and Deimos could well be remnants of the same birth cloud that created Mars, thus composed by proto-Mars material [2]. This hypothesis represents an in-situ formation, in contrast to the capture origin, and is supported by the common orbital characteristics, such as low eccentricity, inclination and altitude, of both moons. A last and novel theory was instead proposed recently, which represents a second-generation in-situ formation [2, 7, 8]. This speculates that a previous small body either broke up in orbit or impacted Mars, and the orbiting debris or ejecta from the Red Planet created a ring of dust around Mars, that eventually built up to create Phobos and Deimos, as the only survivors. This is known as accretion theory, and could describe together both the current orbits and dimensions of the Martian moons. In particular the impact theory is supported by the fact that the angular momentum of Mars is incoherent with its current mass and spin rate.

However, the solution to the puzzle of the origin of these moons is further complicated by their mysterious *composition*, which has only been inferred from infrared spectral analysis. The surface's composition of both moons is still not completely understood and appears also unique, if compared to the majority of similar bodies in the Solar

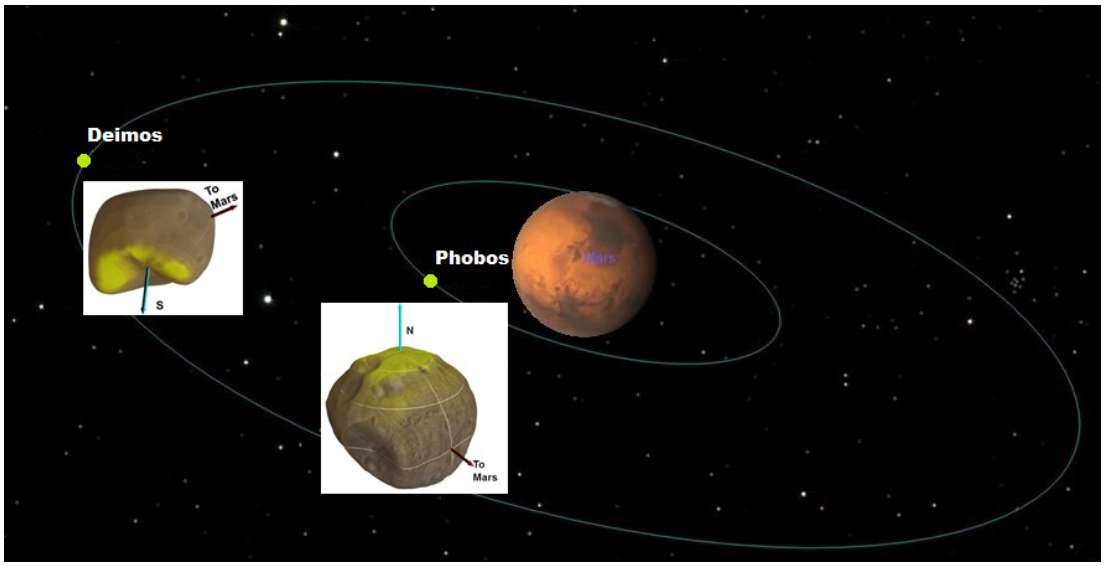

Figure 1.1: **The Martian system.**

System. New research outcomes shift over the years between C, D and T types of the Tholen spectral classification, since chemical markers of other types are detected [4, 5, 2]. This fosters the debate between different hypotheses for the moons' origin. In particular, rich carbonaceous chondrite's spectra is the most common within the Main Asteroid Belt, and would support a capture origin, while the presence of Martian phyllosilicates would support an in-situ formation. The combination of these observations with the measured gravity and size of the moons shows an uncommon low bulk density and high porosity of these moons [2]. This suggests that the Martian moons could hide a considerable amount of iced water, as well as having a hollow internal structure with a significant portion of voids. The latter is highly inconsistent with an asteroid capture. For all these reasons, the accretion theory from Mars ejecta is currently considered the most probable hypothesis to explain the origin of Phobos. In this sense, the altitude of Phobos is also within the Roche's radius for deformable bodies [2, 7], while the capture scenario is more consistent for Deimos. Hence, Phobos would be a natural Martian "time capsule", and it is speculated that its rocks could provide evidence of alien life present on the Red Planet in the past [9].

A second anomaly of scientific interest is the current orbit of Phobos. Recent observations from spacecraft sent to Mars found significant discrepancies between predicted orbit models and the current position of the moon. Such behavior remains unclear, and could be due to a coupling between forced libration motion and inhomogeneous gravity field [10, 11], or by relativistic effects on the navigation measurements [12].

Another related area of scientific interest is the future evolution of Phobos. The closest moon of Mars is also astrodynamically interesting due to the low altitude of its orbit around Mars. As a practical comparison, the height of Phobos is lower than that required for Mars-synchronous rotation: Phobos rises from the West more than

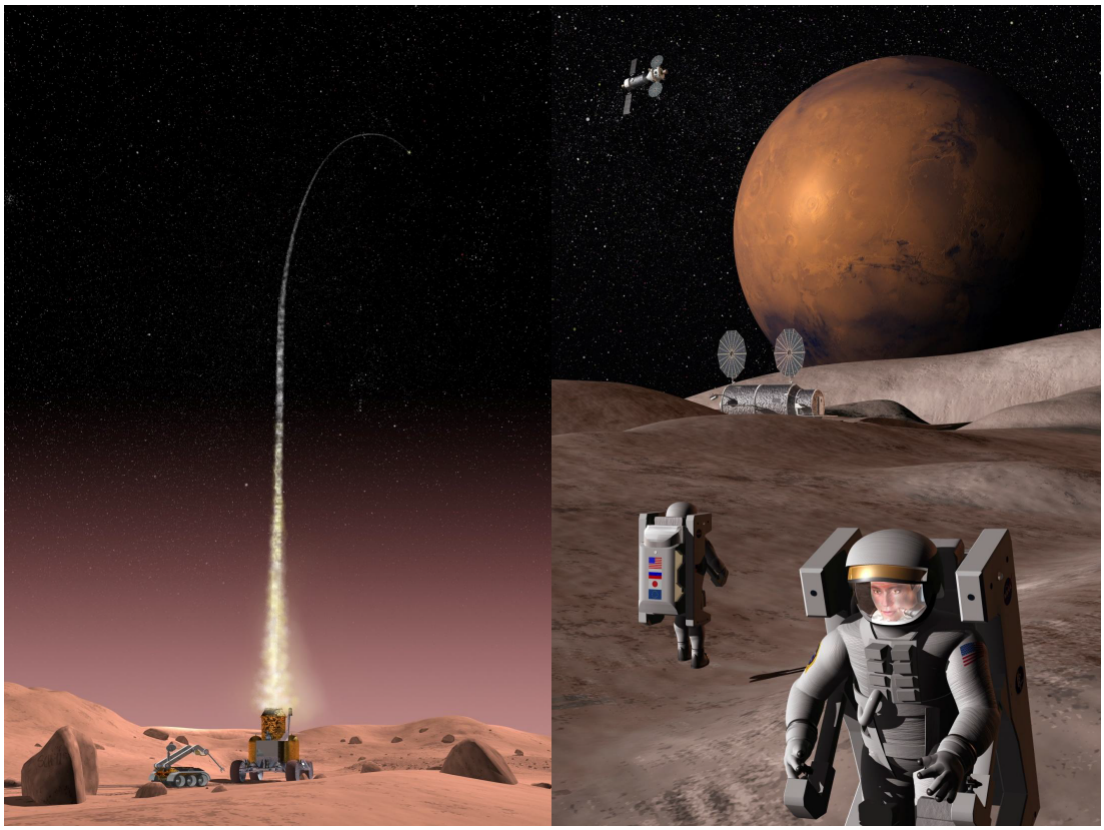

Figure 1.2: **Concept of the Lockheed Martin Red Rocks mission** [19].

three times a day as seen from Mars' surface near the Equator, whereas near the Poles Phobos is never seen, since it is always under the horizon. As a result of this proximity, its altitude is currently decreasing due to the pull of Mars [13]. Two possible scenarios have been proposed for the evolution of Phobos. In the first case, the moon would eventually crash into Mars. In the second case, the tidal interaction with Mars would break it up into a planetary ring [13], once Phobos falls within the Roche's radius for rigid bodies.

A final anomaly of scientific interest is given by the peculiar orography of the surface of Phobos. First of all, it is marked by several big craters. In particular, the largest of them, named *Stickney* after Hall's wife's maiden name, is located on the face of the moon pointing towards Mars and heavily characterizes the shape of Phobos. Second of all, the surface of Phobos is marked by a dense texture of *grooves*. The origin of these unique features is another mystery of this celestial body, and is currently speculated to have occurred through flows of debris orbiting or ejected from Mars [14, 15, 16], as well as rings of dust or clouds of fine-grained regolith existing on Phobos [17, 18].

1.2 Rationales and Current Plans for Space Missions to Phobos

Section 1.1 presented the outline of the scientific interests in undertaking a space mission to the moons of Mars. In particular, it emerged that there is still a lack of understanding of the main physical characteristics of both Phobos and Deimos. Thus, more data needs to be acquired regarding the superficial and internal composition, the inhomogeneous gravity field and shape, and the actual orbit around Mars of these moons. This information will allow scientists to solve the current enigma surrounding their origin, which would provide insight into the Solar System's origin itself, as well as provide an answer to the other mysteries of Phobos and Deimos outlined in section 1.1.

In addition to purely scientific goals, the Martian moons have been proposed as attractive destinations for space exploration since the early '80s [20, 21]. The American Viking program (1975) and Soviet Phobos-2 spacecraft (1988) were the first missions to successfully provide images of the two moons. Starting from this period, a "PhD mission" to Phobos and Deimos was first conceived in [21] to be an ideal candidate for landing a spacecraft as a precursor to a robotic or crewed exploration on Mars. Unmanned missions to the Martian moons could exploit them as stable platforms, where instruments are placed for gravity waves astronomy, radio astronomy, astrometry, and the study of asteroids and comets. Also, a Mars-pointing ground station [22, 21] equipped with telescopes and antennas will permit multiple and fast access for observation and communication with the Red Planet without orbital maintenance. Manned missions to the Mars-facing side of Phobos and Deimos can then use these instruments to remotely control robotic scouts dispatched on Mars [22, 21] (see Fig.1.2). Indeed, landing and take-off of equipment or crewed spacecraft is much cheaper on the moons than on the planet itself. This represents the main advantage always presented when promoting a space mission to the moons of Mars [23, 1]. The interplanetary Δv to leave/arrive in the planet's orbit is lower than leave/arrive at its surface, and the low gravity and absence of atmosphere of such small bodies additionally lower the impact and escape velocity[1]. The latter aspects increase the safety and make feasible also the use of low-cost electromagnetic propulsion. This allows also multiple rovers to be dispatched with the same mission cost, as well as to reduce the risks connected to an interplanetary return trip of the samples back to Earth. All these advantages would likely enable a human expedition to Mars sooner than if we did not undertake a mission to Phobos first [22]. In addition, the Martian moons can also provide attractive in-situ resources that could be exploited by human missions for refueling and life sustainability, like iced water (as recalled from section 1.1) and basic chemical elements from rocks mining. In particular, landing on Phobos and Deimos and establishing an

[1]The microgravity environment of Phobos is characterized by a Keplerian escape velocity at its mean surface of only $11m/s$, which means a human being (or a rover) could auto-inject itself out of the body with a very small force.

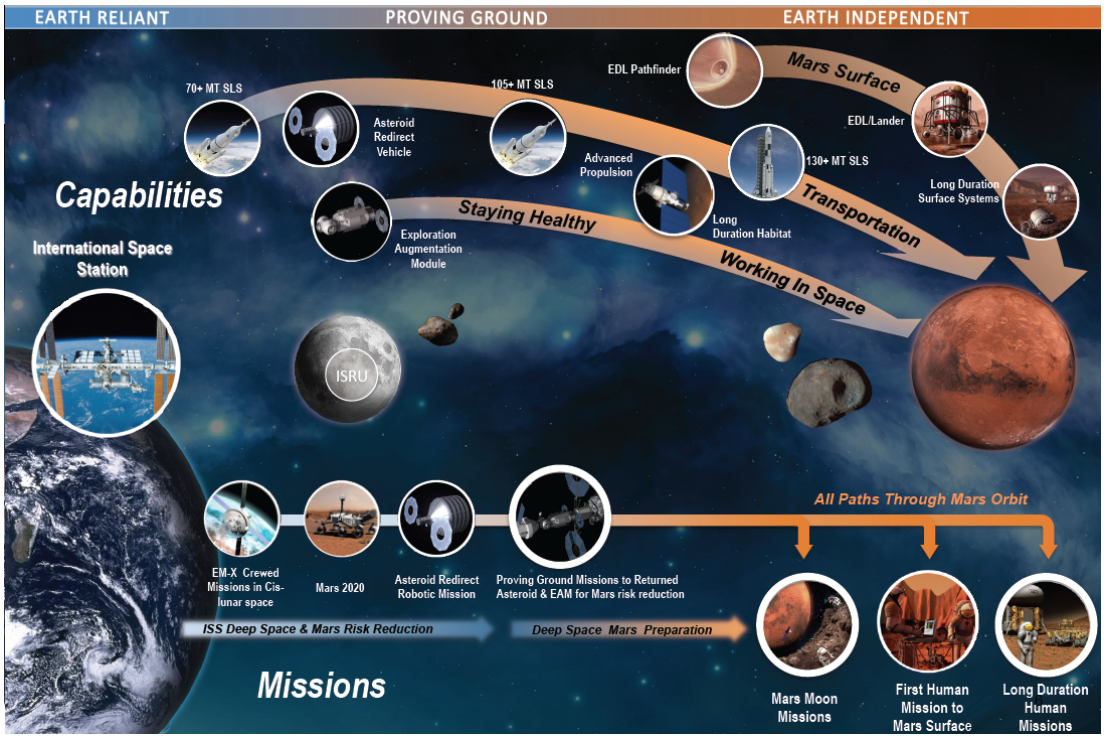

Figure 1.3: **Concept of the NASA roadmap for the human space exploration beyond LEO** [23].

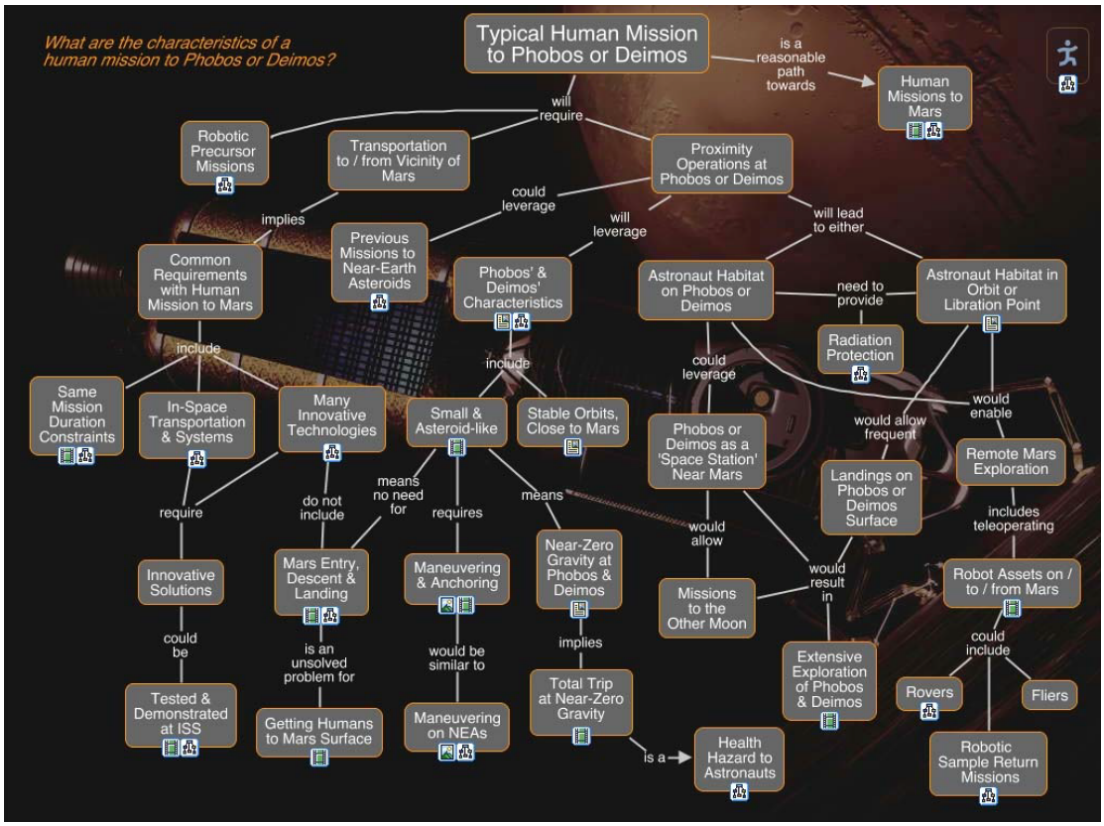

Figure 1.4: **What are the characteristic of a human mission to Phobos and Deimos?** [24]

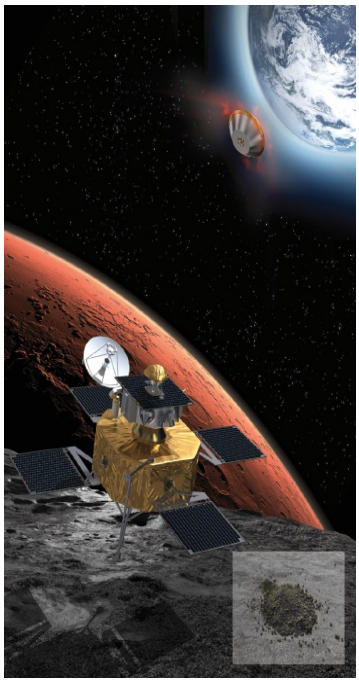

Figure 1.5: **Concept of the ESA Phootprint sample-and-return mission** [26].

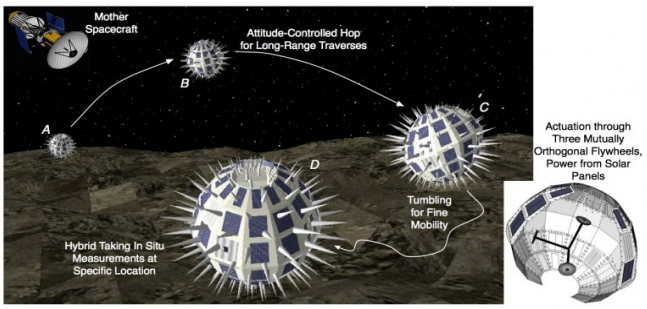

Figure 1.6: **Concept of the NASA Phobos Surveyor mission and its robotic hedgehogs** [27].

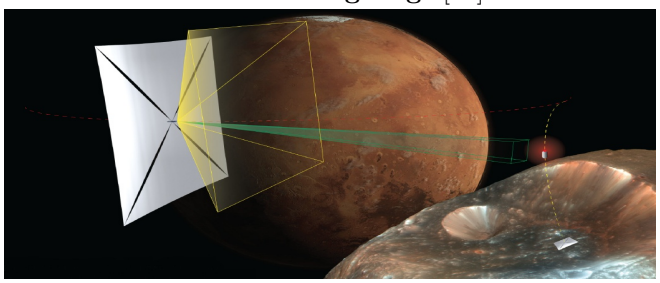

Figure 1.7: **Concept of the NASA Innovative Advanced Concepts for a Phobos sample-and-return mission with two interplanetary CubeSats, a Solar Sail, and a tether** [28].

outpost inside a crater or a cave, would provide natural protection to massively reduce the impact of life-threatening radiation from the cosmic rays [19]. A human detachment in Stickney would be passively sheltered from about 90% of cosmic radiation [25].

In summary, the development of space missions to the Martian moons, as a pathway to the scientific and human exploration of Mars, is motivated by several rationales with *economic*, *operational*, *contingency*, and *exploitation* potential. Therefore, *the Martian moons' exploration has become a* **key milestone** *to the long term goal of a human mission to Mars* in the current roadmap of NASA [29], see Fig.1.3 and Fig.1.4. In particular **Phobos**, the inner-most and largest moon of the two, has received most of the attention in terms of mission concepts. Phobos is a ready-made space station, that can become the strategic cornerstone of a human colonization of Mars [30, 22]. In 2010, ESA Mars Express flew-by Phobos at only $67km$ altitude, and $3km/s$ relative speed, providing updated physical data that boosted the scientific research of Phobos. In 2012, the famous landing of the NASA Curiosity rover has provided a platform for the daily observation of Phobos, in addition to the pre-existing flotilla on the Red Planet. Dedicated space missions to land on Phobos have been designed in the past, but all have failed (the Soviet Phobos-1 and Phobos-2, and the Russian Phobos-Grunt). During its Ministerial Council Meeting of November 2012 [31], ESA confirmed post-2018 mission concepts: the Mars Robotic Exploration Programme [26, 32] would include a mission, named Phootprint, to return back to Earth a sample from Phobos [33, 34], see Fig.1.5. The return to Earth is a paramount ambition required by the

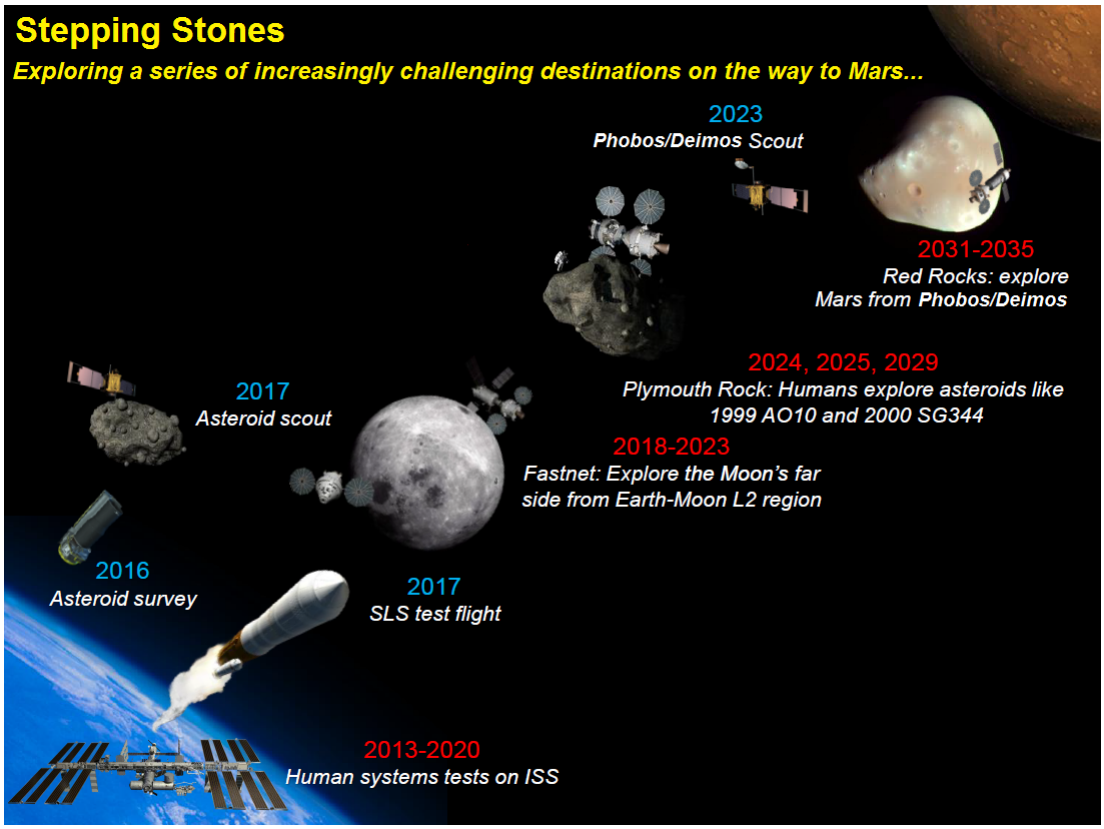

Figure 1.8: **Concept of the envisioned Lockheed Martin Stepping Stones program** [19].

wide scientific research on Phobos outlined in section 1.1, because it makes it possible to analyze the internal composition of the moon in detail in an advanced laboratory facility [35]. The related results would enable to plan the in-situ resources utilization at Phobos. Another sample-and-return mission to this moon is currently proposed by NASA Innovative Advanced Concepts team, that will use two CubeSats propelled by a solar sail and joined by a tether mechanism [36, 28], see Fig.1.7. In addition Lockheed Martin has envisioned a systematic program, named "Stepping Stones", to plan the technology development of the future human space exploration beyond LEO, in the aftermath of the "Flexible Path" plan advocated by the 2009 Augustine Commission [19]. Fig.1.8 presents these increasingly challenging building blocks, that will incrementally develop and demonstrate the capabilities required for the human exploration of the Red Planet. In this framework, *the Martian moons are a logical step between NEOs and Mars, with the advantages given by both destinations.* Also the Human Spaceflight Architecture team [37, 24, 38] and the Small Bodies Assessment group [39] of NASA are in an advanced stage of their assessment, and have recently published viable designs of human space mission to Phobos, see Fig.1.9-1.10. In this sense, the SETI and NASA proposed "Phobos and Deimos & Mars Environment" (PADME) mission is competing for the Discovery program funding [40], and it will address the scientific unknowns of the two Martian moons in rapid time and at low-cost. At the beginning of 2013,

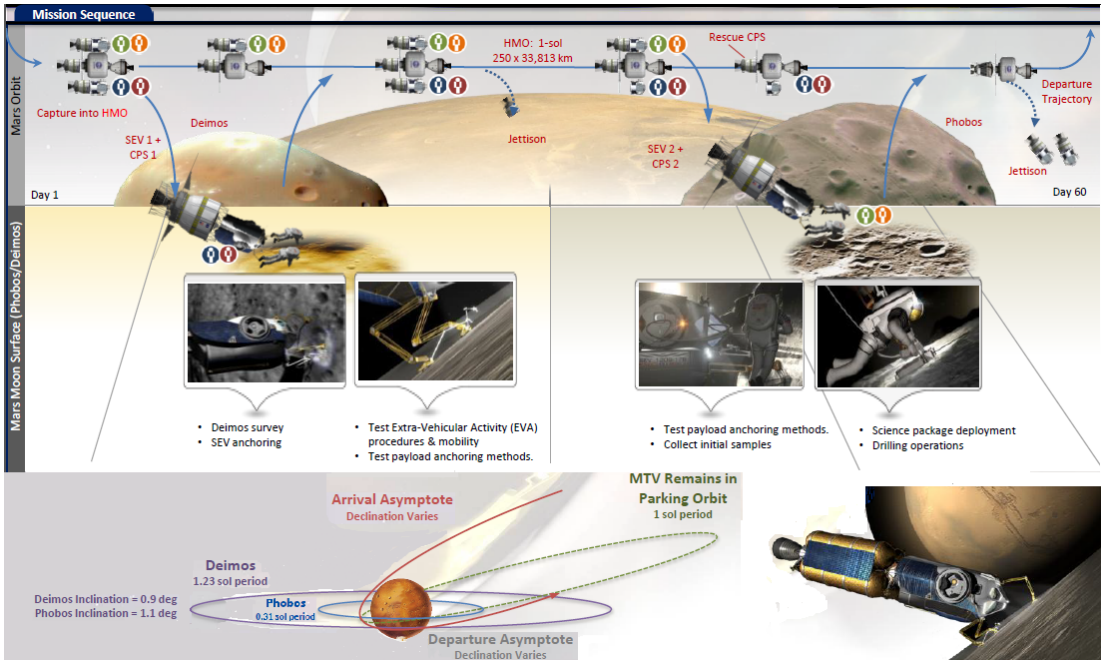

Figure 1.9: **Concept of the NASA strategy for a human mission to Phobos and Deimos** [24].

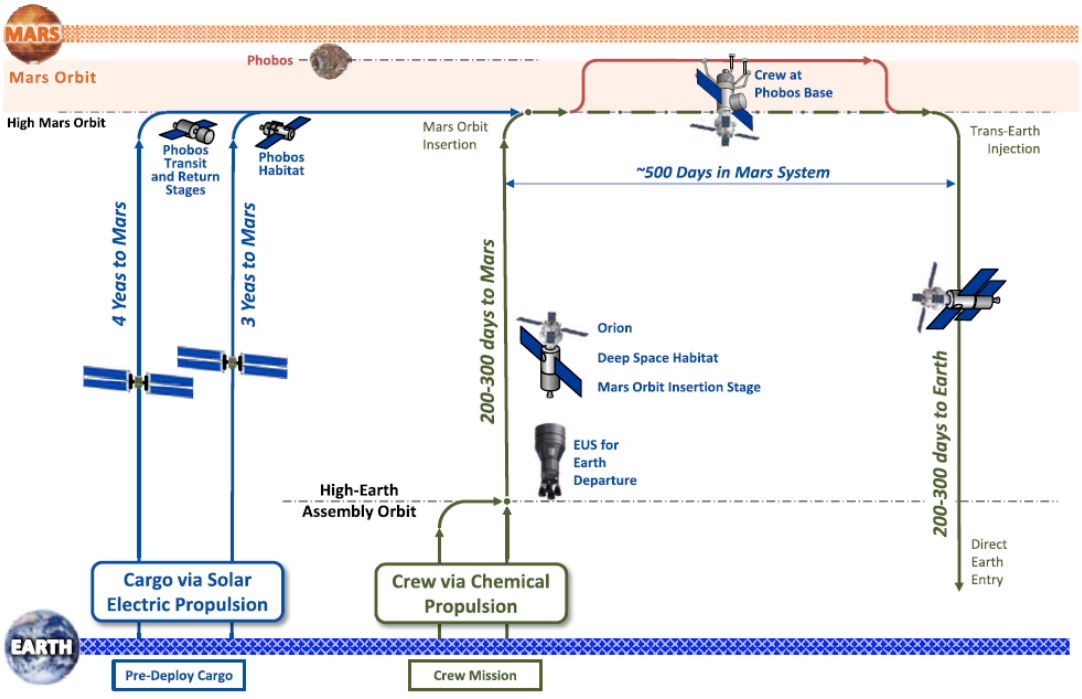

Figure 1.10: **Concept of the NASA strategy for a human mission to Phobos** [38].

with the development of a new rover platform for the exploration of minor bodies, consisting of robotic hedgehogs (see Fig.1.6), NASA is also taking into consideration a mission (named Phobos Surveyor) to Phobos as a test-bed for this new technology [41, 42, 27, 43, 44]. Phobos was also the target for the space mission design during the 2013 Caltech Space Challenge [45, 46], and of two dedicated conferences [47].

1.3 Objectives of the Research

This research takes inspiration from the increasing interest in developing future space missions to the moons of Mars. Due to the current mission concepts outlined in section 1.2, this work focuses on Mars' closest and largest moon Phobos. In particular, space missions to this moon are motivated by the wide array of scientific and engineering attractions presented in sections 1.1-1.2. The high-level objective of this work is to identify new mission opportunities around Phobos, that could effectively be used in planned or future space missions. Since this research belongs to the field of astrodynamics, these opportunities are identified by the possible orbits that a spacecraft could use to fly around Phobos. These orbits could be natural or artificial. In the latter case, the spacecraft makes use of a primary propulsion system to yield a trajectory that is not possible naturally[2].

A spacecraft's orbit is identified by different attributes. The first feature considered is the shape, position, and profile over time of the orbit: the orbits of interest in this thesis could be a stationary point, a periodic or quasi-periodic orbit, or a transfer trajectory between two states. Each of these reference motions constitutes an *invariant object*. The second feature is the *dynamical model* where the object is computed: this is given by the reference frame and the mechanical equations of translational motion, which constitute a dynamical system. The third feature is the *method* used to compute the invariant object as a solution of the dynamical system. The fourth feature is given by the *performances* of the dynamical object. For a spacecraft's orbit, they can be very diverse: line-of-sight and coverage of the area of a celestial body or of the sky, environmental conditions encountered, fuel consumption of an artificial orbit and control action required for maintaining a natural orbit. The fifth and summarizing feature is represented by the range of *applications* that the orbit can provide in the framework of a space mission to Phobos.

This thesis addresses all described features with the aim of analyzing all the possible kinds of natural orbits around Phobos. In particular, the first driver is to reduce the propellant consumption for station-keeping in proximity of Phobos, extending the mission lifetime by exploiting the natural dynamics. This requires the use of advanced techniques of **dynamical systems theory** to compute the solutions of highly nonlinear systems that represent the orbital dynamics of spacecraft in the vicinity of Phobos.

[2]Secondary propulsion is almost always needed to contrast the disturbances and maintain the spacecraft along the reference orbit.

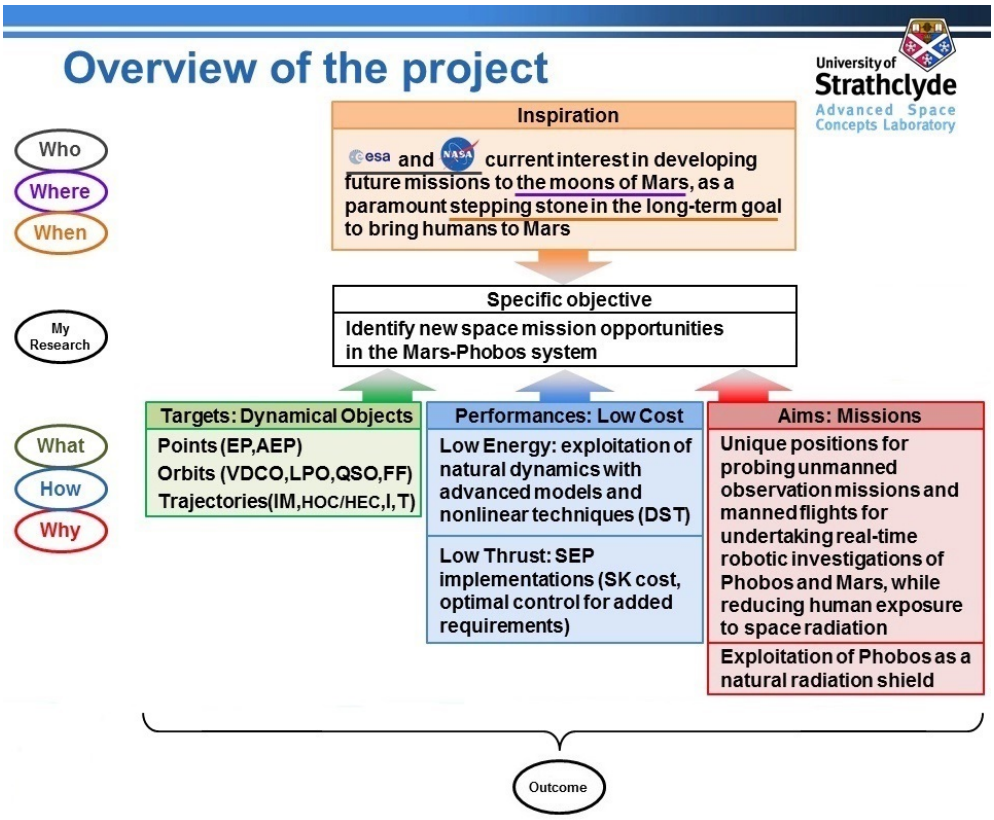

Figure 1.11: **Overview of the project.**

The objectives of this thesis can be summarized as follows:

- To derive an appropriate model of the relative orbital dynamics around Phobos.
- To consider all the classes of natural orbits around Phobos.
- To compute the reference signal of these natural orbits using advanced analytical or numerical techniques of dynamical systems theory, applying these methods in a new case.
- To investigate the potential of using low-thrust propulsion, deriving the artificial equivalent of these orbits with a constant acceleration law.
- To derive the performances of these orbits for space missions.
- To investigate the possibility of exploiting Phobos as a passive shield from space radiation.
- To assess the performances of these orbits against the possible requirements of each mission segment.
- To propose possible applications of these orbits in feasible space mission scenarios at Phobos.

1.4 Contributions of the Thesis

The study carried out has made the following contributions.

An improved model of the relative dynamics around Phobos is derived and proposed for the computation of orbits in the neighborhood of the moon[3]. The proposed model is an extension of the classical ER3BP to include the highly-inhomogeneous gravity field of Phobos, which is modeled through a spherical harmonics series expansion, known as gravity harmonics. The inclusion of high-order gravity harmonics, as well as tetrahedron models, has been considered in the past [48, 49] in the framework of a perturbed R2BP for computation of orbits in the vicinity of asteroids. The third-body perturbation (which in case of Phobos is due to Mars) and the eccentricity perturbation are instead significant actions for the case of Phobos, and the relative dynamics in its proximity cannot neglect any of these forces. The proposed dynamical model is named Mars-Phobos ER3BP-GH, and the Phobos' gravity harmonics are stated up to fourth degree and order.

In the past few decades, dynamical systems tools developed for the CR3BP have provided an in-depth understanding of the spacecraft's motion in this model of the orbital dynamics [50]. The Libration Point Orbits have been computed extensively, using semi-analytical methods (such as Lindstedt-Poincaré series expansions [50, 51]) and numerical techniques (such as numerical continuation [50, 52]), for the Sun-Earth and Earth-Moon systems, where the approximation of the natural dynamics using the CR3BP is an accurate one. The study of the invariant motions of these systems has proved invaluable for real space missions, such as ISEE-3/ICE (1978), WIND (1994), SOHO (1995), ACE (1997) and Genesis (2001), where they have been exploited as energy-efficient trajectories to minimize the spacecraft's fuel consumption during station-keeping and orbital transfers. Following this, the concept of dynamical substitute of these invariant objects was introduced in [53] to compute the equivalent of the Libration Point Orbits in the ER3BP [54] and in slightly perturbed dynamics, for example considering the effect of only the J_2 zonal harmonic [55, 56], the solar radiation pressure [49] and the fourth-body perturbations of the major Solar System's bodies [53]. In [57] a multiple shooting method is used in a high-fidelity perturbation model to correct the classical Libration Point Orbits of the Mars-Phobos CR3BP. The resulting solutions are not appropriate dynamical substitutes nor their performance analysis suitable to be optimized in the mission design loop. In this research, the dynamical substitutes of the Libration Point Orbits are computed in an ER3BP-GH, where the perturbation of gravity harmonics up to fourth degree and order is significant on the CR3BP, using the methodology of numerical continuation.

In this thesis, the modeling of the relative orbital dynamics around Phobos is ex-

[3]The neighborhood is identified by the region of space straddle the boundary of the Hill's sphere of influence of Phobos. The width of this shell could be considered to be approximately one Phobos' mean radius. Therefore the neighborhood of Phobos is accounted to span from its inhomogeneous surface to an altitude of about $10km$ over it, along every direction.

tended to include the low-thrust continuous propulsion. To investigate the potential of using this technology, a constant acceleration profile is considered as the orbital control law [58]. In this research, the artificial equivalents of the Libration Point Orbits [59] about Phobos are computed using numerical continuation of the new solutions found previously.

The growing interest in undertaking a successful mission to Phobos has fostered in recent years the need to probe suitable orbits about it [57]. Early analysis focused on simple hovering station-keeping (artificial equilibrium points [60]) and exploitation of stable Quasi-Satellite Orbits [61, 62], and these orbits have been applied in the design of past missions. In particular, the stability analysis of artificial equilibrium points has been conducted only in the planar CR3BP [63]. In this research, the stability analysis of the artificial equilibrium points in the spatial CR3BP is presented, and applied in the Mars-Phobos, the Sun-Earth, and the Earth-Moon systems. Besides, the concept of artificial equilibria is further generalized from the synchronous case to any rotational velocity. In particular, the case of synchronous type-III highly non-keplerian orbits of [64] is investigated for the case of Phobos, and the fuel consumption and stability analysis of these vertical-displaced circular orbits in the R2BP and CR3BP are presented in this thesis.

The Quasi-Satellite Orbits have recently gained attention as suitable orbits for future space missions. In particular, these orbits are very useful for orbiting around small planetary satellites [65], like the Martian moons. Quasi-Satellite Orbits would represent the main orbital mission segments around Phobos in the ESA Phootprint mission, and preliminary studies have already been made [66]. The main focus is the modeling and the subsequent stability analysis of these orbits. In particular, the mechanism of stability of Quasi-Satellite Orbits has already been discovered using linearization in the ER3BP [62] and perturbed R2BP [67], and simulation studies have been carried out in high-fidelity models in terms of the relative state around Phobos [61]. In this research the stability region of the Quasi-Satellite Orbits around Phobos is identified by high-fidelity simulations in terms of the osculating Keplerian orbital elements of the spacecraft around Mars.

The physical environment around Phobos is investigated. The lighting conditions for a spacecraft in the vicinity of Phobos are analyzed with detail in a Sun-Mars-Phobos R4BP. The surface coverage and occulting conditions of Phobos are analyzed using a high-order shape harmonics series expansion for the moon's surface. In this thesis, the outcomes are used to conduct the performance analysis of the classes of orbits around Phobos. In particular, the invariant manifolds of the natural and artificial Libration Point Orbits are applied as landing and take-off trajectories for a spacecraft to and from the moon's inhomogeneous surface. This is a unique feature of the Mars-Phobos CR3BP, because the natural trajectories, at low energy, to transfer between the spheres of influence of the two primaries in the Sun-Earth and Earth-Moon systems fly widely far from the bodies [68]. In addition, the Libration Point Orbits are shown to provide

a useful station-keeping strategy for *passive radiation shielding* from the cosmic rays, without landing on the moon's surface.

In this thesis, the maintenance and operational performances of all the classes of orbits around Phobos are assessed against the desired requirements of the orbital segments of a space mission around Phobos. Following this, possible applications are proposed for planned and future space missions to Phobos.

The several astrodynamical mysteries of Phobos were outlined in section 1.1. In this context, the extension of the model of the orbital dynamics to consider the gravity harmonics of Phobos, and the computation of the natural Libration Point Orbits and their invariant manifolds in this system, are also hypothesized to be responsible for the natural transportation of debris and dust around Phobos. In this thesis, further evidence is shown to support the theory of accretion for the origin of Phobos [7], and possible explanation is addressed to explain the formation of the craters and grooves of the moon [17, 14].

1.4.1 Publications of the Research

The computation of the dynamical substitutes of the Libration Point Orbits in an ER3BP-GH has produced the following publications.

- M. Zamaro and J. Biggs (2014) Dynamical systems techniques for designing Libration Point Orbits in proximity of highly-inhomogeneous planetary satellites: Application to the Mars-Phobos elliptic three-body problem with additional gravity harmonics. In *10th International Conference on Mathematical Problems in Engineering, Aerospace and Sciences*, International Congress on Nonlinear Problems in Aviation and Aeronautics (ICNPAA 2014), 2014-07-15 - 2014-07-18, Narvik. AIP Conference Proceedings, 1637, pp. 1228-1240 [`http://dx.doi.org/10.1063/1.4904697`].

- M. Zamaro and J. Biggs (2015) Natural motion around the Martian moon Phobos: The dynamical substitutes of the libration point orbits in an elliptic three-body problem with gravity harmonics. Celestial Mechanics and Dynamical Astronomy, 122(3): 263-302 [`http://dx.doi.org/10.1007/s10569-015-9619-2`].

The identification and assessment of the natural and artificial orbits around Phobos have produced the following publications.

- M. Zamaro and J. Biggs (2014) Identification of new orbits to enable future mission opportunities for the human exploration of the Martian moon Phobos. In *65th International Astronautical Congress* (IAC 2014), 2014-09-29 - 2014-10-03, Toronto. [`http://strathprints.strath.ac.uk/49981`].

- M. Zamaro and J. Biggs (2014) Identification of new orbits to enable future mission opportunities for the human exploration of the Martian moon Phobos. Accepted for publication in Acta Astronautica on 04/09/2015.

1.5 Structure of the Thesis

The thesis is organized as follows.

Chapter 2. Introduces the reader to the physical environment connected to the orbital dynamics and constraints of a spacecraft in the vicinity of Phobos. The relative dynamics are described in the framework of the Mars-Phobos CR3BP, and the analysis of the orbital perturbation is carried out in this model. Furthermore, lighting and occulting conditions are identified in the Phobos' neighborhood.

Chapter 3. Following the preliminary results, a new model of the relative orbital dynamics is derived. This is obtained extending the classical CR3BP to an ER3BP with an inhomogeneous gravity field of the second massive body, described through a gravity harmonics series expansion (ER3BP-GH).

Chapter 4. The Libration Point Orbits in the CR3BP are used as initial guesses in numerical continuation schemes that allow the computation of their dynamical substitutes in the new, more realistic, ER3BP-GH. The resulting natural periodic and quasi-periodic Libration Point Orbits, and their invariant manifolds, in the Mars-Phobos ER3BP-GH are presented, together with their related applications and performances.

Chapter 5. The inclusion of continuous thrust is considered with a constant acceleration profile. This allows the derivation of artificial equilibria using solar electric propulsion, such as artificial equilibrium points and vertical-displaced circular orbits, and orbiting around the formers, realizing artificial Libration Point Orbits. Moreover, the implementation of artificial Martian Formation Flying in Phobos' orbit is investigated.

Chapter 6. The dynamical modeling and the stability analysis of the Quasi-Satellite Orbits around Phobos is carried out.

Chapter 7. Provides a summary of the different solutions focusing on their potential applications in space missions to Phobos, and it concludes the thesis suggesting their potential usefulness in a real-world mission scenario. The thesis concludes by addressing areas of future research.

Appendix A. Collects complementary equations of motion of the elliptic three-body problem in alternative coordinates used in section 3.4.

Appendix B. Introduces the reader to the analytical and numerical methodologies of dynamical systems theory to identify and compute periodic and quasi-periodic solutions. These prerequisite concepts and techniques are used in chapter 4-5-6.

Appendix C. Introduces the reader to the fundamentals of Optimal Control Theory, and its application to the CR3BP.

Appendix D. Collects complementary graphs used in chapter 4 and section 5.4.

Appendix E. Collects complementary graphs used in chapter 6.

Appendix F. The Libration Point Orbits around Deimos are computed.

Chapter 2

Analysis of the Orbital Dynamics and Physical Environment around Phobos

In this chapter the preliminary analysis of a space mission to Phobos is conducted. The physical characteristics of Phobos and its orbit are introduced in section 2.1. Then, the basic design aspects of the orbital mechanics and the physical environment of a spacecraft in orbit around Phobos are presented. Section 2.2 introduces the equations of motion of the relative orbital dynamics, section 2.3 presents the model of the CR3BP and the main results obtained when the Mars-Phobos-spacecraft system is considered as a special case. In this framework, a related analysis of the orbital perturbations is conducted in section 2.4. This analysis identifies the main perturbations around the moon, which will form the basis of an extended, more accurate, model of a spacecraft's motion in the vicinity of Phobos in chapter 3. The second part of this chapter is dedicated to the analysis of the physical environment in the vicinity of Phobos: sections 2.5-2.6-2.5 present the radiation, lighting and occulting conditions.

2.1 Physical and Astrodynamical Characteristics

The immediately noticeable characteristics of Phobos are its small size (even smaller than some asteroids) and its irregular shape. In particular in Fig.2.1-2.2 we see that its surface is marked by a dense texture of grooves and by several big craters, where Stickney is by far the largest crater. As illustrated in Fig.1.1, we see that Phobos has an almost circular and equatorial orbit around Mars, with a low altitude above it. In addition, this natural satellite rotates with a synchronous period and almost zero-tilt with respect to its orbital motion. The combination of all these orbital characteristics implies that Phobos is *tidally-locked*. This means that the attitude of the moon is fixed with respect to the central planet, in this case Mars. As a result, the Stickney crater is located on the side of the moon permanently pointing towards Mars. Table 2.1 presents

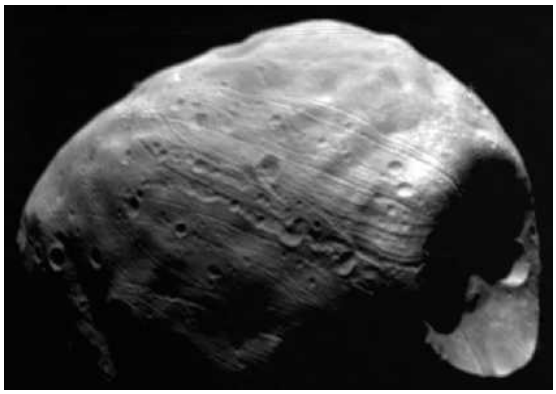

Figure 2.1: **Phobos.** The image was taken by Viking 1. The large crater on the right is Stickney. Several chains of grooves are visible [Wikipedia].

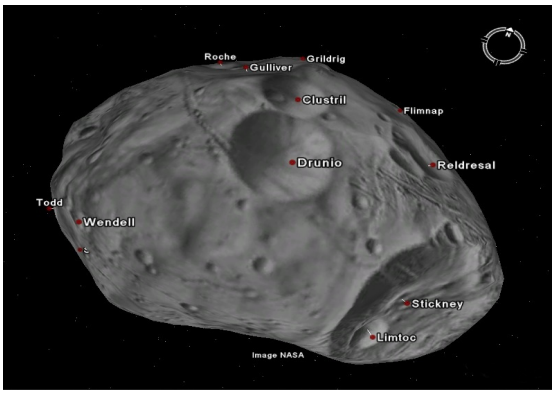

Figure 2.2: **Rendering map of the craters of Phobos.** Leading side of the moon [Google Earth].

a summary of the physical and orbital parameters of Mars and Phobos that have been used in the analysis of the orbits undertaken in this thesis. Characteristics of the other Martian moon Deimos are shown together by comparison, and they are very similar to the ones of Phobos.

In accordance with the nomenclature defined at the beginning of this thesis, recall below how four classes of reference frames (in cartesian coordinates) for a given body are defined.

- A body-centered body-fixed frame (BCBF) has its origin in the body's barycenter and its attitude is fixed with respect to the body's geometry, with vertical z-axis aligned along the body's spin axis, and x-axis pointing towards the body's Prime Meridian intersection on the equatorial plane.

- A Hill's frame (H) has its origin in the body's barycenter and rotates with fixed attitude with respect to its osculating orbit around a central body, with vertical z-axis perpendicular to the orbital plane, and radial x-axis pointing outwards from the barycenter of the two bodies.

- A body-centered equatorial frame (BCE) is the same of the BCBF frame, apart from the x-axis which points towards the body's Node of reference[1].

None of the reference frames defined above is inertial.

- A body-centered inertial frame (BCI) has its origin in the body's barycenter, with vertical z-axis aligned along the Earth's spin axis, and x-axis pointing towards the Earth's vernal equinox γ.

Due to millennial movements, a frozen approximation of the orientation of Earth's spin axis and γ is made for a given time span, which is defined as epoch. The current inertial

[1]The direction of the body's Node of reference corresponds to the cross-product between Earth's and body's spin axes [70].

Table 2.1: **Physical and astrodynamical properties of Mars and its two moons Phobos and Deimos.** The full values used are retrieved from the following sources. Ephemerides: NASA JPL at 25th July 2012 00.00CT (ICRF/J2000.0). Sun mass = $1.9891 \cdot 10^{30} kg$. Satellites' axial tilt is reported at date: mean values at epoch are: 1.08° (Phobos) and 1.77° (Deimos) [69].

Property	Mars	Phobos	Deimos
$m\ [kg]$	$6.4185 \cdot 10^{23}$	$1.0659 \cdot 10^{16}$	$1.4762 \cdot 10^{15}$
R mean sphere $[m]$	$3.3899 \cdot 10^{6}$	$11.1 \cdot 10^{3}$	$6.2 \cdot 10^{3}$
R mean ellipsoid $[m]$	-	$[13.1 \times 11.1 \times 9.3] \cdot 10^{3}$	$[7.8 \times 6.0 \times 5.1] \cdot 10^{3}$
Axial tilt θ [°]	25.19	0.30	0.32
Rotation sidereal T	$24.62h$	Revolution T	Revolution T
Revolution T	$687d$	$7.65h$	$30.31h$
Albedo c_r	0.20	0.07	0.07
Orbital Elements	$SO_E\gamma$	ME_MN_M	ME_MN_M
$a\ [AU]$	1.5237	$6.2696 \cdot 10^{-5}$	$1.5682 \cdot 10^{-4}$
$e\ [-]$	0.0934	0.0156	0.0002
i [°]	1.8488	1.0668	1.7515
Ω [°]	49.5258	329.2279	301.9019
ω [°]	286.5159	253.6956	22.4286
ν [°]	253.4836	17.1688	159.8874

axes used in astrodynamics refer to their mean position at 12UTC on 1st January 2000, and the related epoch is known as J2000.0.

In summary, an orbit around a central body is defined with respect to its BCE frame, whose axes are referred to the BCI at J2000.0. Thus, the motion around an orbiting body could be defined in two ways: relative to the shape of such secondary body in its BCBF frame, or relative to the motion of such satellite in its Hill's frame around the primary body. In the first case, the secondary is fixed in position and attitude, while the primary moves and spins. In the second case, both bodies are in fixed positions, and they generally both spin.

2.2 Relative Orbital Dynamics

The general equations of motion of the relative orbital dynamics, that will be used to describe the different kinds of orbits presented in this thesis, are stated in Eq.2.1,

$$\ddot{\mathbf{q}} = -\mathbf{a_A} + \mathbf{a_G} + \mathbf{a_P} + \mathbf{a_C} + \mathbf{a_D} \tag{2.1}$$

where $\mathbf{q}$ is the position of the spacecraft in the chosen coordinate frame. The first term $\mathbf{a_A}$ is the apparent acceleration of the general relative frame of reference, and is presented in Eq.2.2.

$$\mathbf{a_A} = \mathbf{a_{A,T}} + \boldsymbol{\omega} \wedge \boldsymbol{\omega} \wedge \mathbf{q} + \dot{\boldsymbol{\omega}} \wedge \mathbf{q} + 2\boldsymbol{\omega} \wedge \dot{\mathbf{q}} \tag{2.2}$$

The total apparent acceleration is a function of the frame's translational acceleration $\mathbf{a_{A,T}}$ and angular velocity $\boldsymbol{\omega}$ with respect to an inertial reference. The rotational terms in Eq.2.2 are known respectively as: centripetal, Euler, and Coriolis accelerations. Recall that in Eq.2.1, the resulting force (per unit of mass) acts opposite to the apparent acceleration: such action is called an apparent force and does not originate from any physical action, but only from the fact that the reference system is not inertial. Therefore, the apparent force is the term that characterizes the equations of motion of relative dynamics.

The second term in Eq.2.1 is the distinguishing force in orbital mechanics. $\mathbf{a_G}$ is the sum of the gravity accelerations of the celestial bodies of interest. From Newton's law of Universal Gravitation, a point-mass $\oplus$, with mass $m_\oplus$ and positioned in $\mathbf{q}_\oplus$, produces an attractive force per unit of mass

$$\mathbf{a_{G,\oplus}} = -\frac{Gm_\oplus}{||\mathbf{q}-\mathbf{q}_\oplus||^3}(\mathbf{q}-\mathbf{q}_\oplus) \tag{2.3}$$

on a body positioned in $\mathbf{q}$, where G is the gravitational constant. In particular, the gravity force could be expressed as the gradient $\mathbf{a_{G,\oplus}} = \nabla u_{G,\oplus} = u_{G,\oplus/\mathbf{q}}$ of the gravitational potential $u_{G,\oplus} = Gm_\oplus/||\mathbf{q}-\mathbf{q}_\oplus||$, which is conservative if the point-mass is fixed in the reference frame. Eq.2.3 still works if $\oplus$ is a spherical and homogeneous body, when used outside of its bulk. Eq.2.3 is also valid for a body of any shape and inertial properties, because the gravity field tends to the one of a point-mass as long as the distance from the barycenter increases, which is the usual approximation used in orbital mechanics.

The third term $\mathbf{a_P}$ in Eq.2.1 indicates the thrusting acceleration of the propulsion system of the spacecraft required for artificial orbits, while for natural orbits $\mathbf{a_P} = \mathbf{0}$.

The first three terms in Eq.2.1 constitute the model of the dynamics where the reference signal of the orbit over time $\mathbf{q}(t)$ is solved. This is the scope of the guidance system in the mission. This motion will be perturbed in the real world by the disturbance $\mathbf{a_D}$, consisting of the forces not considered in the model, and by the perturbations on the initial condition $\mathbf{q_0}$, due to the inaccuracies of the navigation system. To track the guidance law, such perturbations need to be counteracted by the station-keeping action $\mathbf{a_C}$ of the orbital control system of the spacecraft. The control law can be either planned in feedforward or performed in feedback.

2.3 Analysis of the Dynamics in the Mars-Phobos CR3BP

The study of the Mars-Phobos system is conducted with the R3BP model [50], which is to consider the gravitational effect of the third body (the spacecraft in our case) negligible with respect to the two massive bodies, or primaries. Throughout the thesis, Mars is indicated as the primary body (1), and Phobos as the secondary (2). In this section, due to the small eccentricity of the orbit of Phobos around Mars (see Table 2.1,

which is very similar to the common Sun-Earth case), the preliminary analysis of the dynamics of the spacecraft is carried out in the CR3BP [50], which is to approximate the motion of the two primaries to trace two Keplerian circular orbits around their center of mass.

2.3.1 Introduction to the CR3BP

The analysis of the CR3BP began in the eighteenth century (1747: d'Alembert, Clairaut; 1887: Poincaré; 1912: Sundman), and since then a lot of research has been undertaken in mathematics to better understand this particular non-integrable problem. Currently, space mission design often takes into consideration these results to exploit low-energy trajectories that require less fuel consumption than the ones obtained through a multiple patched-conics approach [50], which is to approximate the global 3B dynamics as the sum of multiple 2BPs inside each sphere of influence of the two primary bodies. This has also become necessary with the widespread use of electric propulsion in modern spacecraft, since the crossing of the fictitious sphere of influence is not suitable any longer to be approximated as instantaneous [50].

The study of the dynamical behavior in the proximity of the Lagrangian or Libration collinear point L_1 and L_2 inspired the definition of Halo [71, 72] and Lissajous orbits. The first missions to exploit these results were the well-known ISEE-3/ICE (1978), WIND (1994), SOHO (1995) and ACE (1997). Due to their practical significance, two particular cases of 3BPs have been studied in detail: the Sun-Earth system, which was used to design the aforementioned missions, and the Earth-Moon system, used for the ARTEMIS mission (2010). In particular, a lot of speculation was made at the beginning to use these libration points to establish space hubs or gateway stations for the future exploration of the Solar System. Nowadays, the use of dynamical system theory has provided better understanding of the 3BP dynamics: the invariant manifolds of periodic orbits around the collinear Libration points, or Conley-McGehee tubes [73, 74, 75, 50], are used to derive high efficient transfer trajectories.

In this thesis, the procedures of the 3BP will be extended to the the Mars-Phobos system, to derive low-energy orbits which could potentially be exploited by upcoming space missions to this Martian moon.

2.3.2 The Mars-Phobos CR3BP

The CR3BP is expressed in non-dimensional units, setting the unit of mass to be the total mass of the system, and the unit of length L to be the semi-major axis of the orbit of the two primaries. In addition the time is set to correspond to the mean anomaly of their orbit. The only parameter of the normalized time-invariant CR3BP is the mass ratio μ, the normalized mass of the second body. Thus, the value of μ universally characterizes the solution of the CR3BP.

Throughout the thesis, comparisons of parameters of all the general pairs of primaries

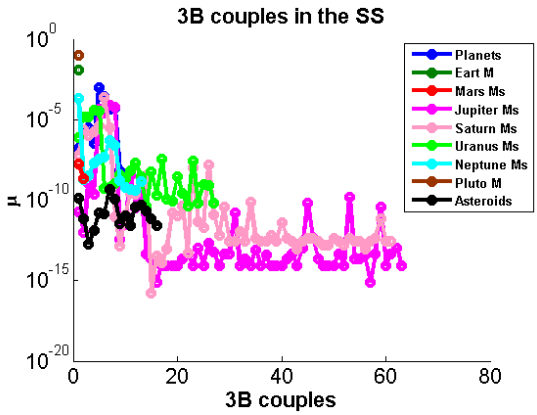

Figure 2.3: **Mass parameter of the 3B couples in the Solar System.** Major moons and asteroids are considered.

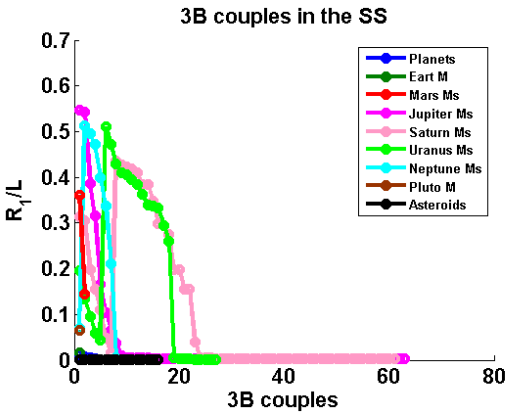

Figure 2.4: **Length unit of the 3B couples in the Solar System.** Semi-major axis of the orbit relative to the primary's mean size. Major moons and asteroids are considered.

of the Solar System will be discussed. These parameters are computed using mean physical values for: all the 1D cases of Sun-planet (including Pluto), all the 2D cases of planet-satellite, and a 1D array of significant cases of Sun-asteroid. The parameter in study will be plotted with different colored 1D functions, identified by the same primary body. Thus, the integer abscissa represents the varying secondary body. In particular, the order of the secondaries is generally given by the increasing distance from the primary, apart from the first positions which are allocated with the most significant moons or asteroids. This because the objective is to look to the general behavior of the parameter in the existing cases of the Solar System, and if a specific couple is relevant it will be recalled explicitly.

It is immediately apparent that two characteristics of the Mars-Phobos system differ it from the classical cases of 3BPs studied so far in the literature. These two aspects will be repeatedly recalled in this thesis. First of all, the mass parameter for the case of the Mars-Phobos couple is

$$\mu = 1.66059511088139 \cdot 10^{-8}$$

As we see in Fig.2.3, **the mass parameter of the system is very small**, if compared to other cases of Sun-planet or planet-satellite couples of primaries studied in the Solar System. However, this is also true for the case of the small planets, Deimos, and some moons of the large outer planets, like Jupiter and Saturn. In particular, the mass parameter of a Sun-asteroid R3BP is far lower than the Mars-Phobos μ. Second of all, **the length unit of the system is very small** too, since the Mars' mean radius R_1 has the same order of magnitude as L. In particular, the altitude of Phobos' orbit is less than twice the radius of Mars

$$R_1/L = 36\%$$

This is an uncommon condition for all the general pairs of primaries of the Solar System, as we see in Fig.2.4. In contrast to the mass parameter, this consideration does not modify the results obtained with the normalized CR3BP, but this acts as the length

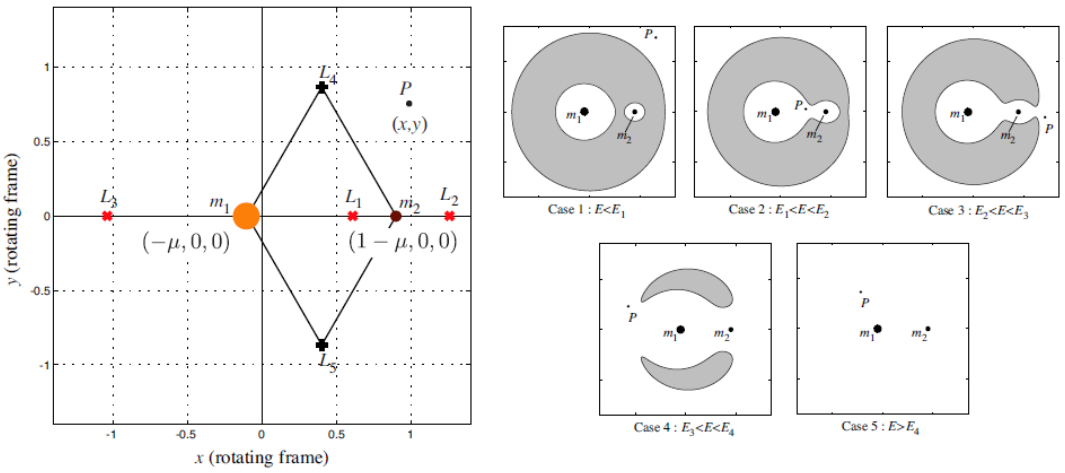

Figure 2.5: **The Three-Body Problem.** At left, relative reference frame, positions of the bodies and the equilibrium points. At right, realms of possible motion as a function of the energy of the system [50].

and time scaling factor of the problem when computing the absolute outcomes for the practical engineering applications in the design of a space mission to Phobos. From this preliminary comparison of two physical parameters, it is possible to expect significant constraints on the trajectory design, but also to consider innovative solutions that are not usual in the other cases of 3BPs in the Solar System.

2.3.3 Equations of Motion

The motion of the spacecraft in the CR3BP is expressed in a rotating reference frame, that will be referred to as 3B frame. This synodic frame corresponds to the Hill's frame of the circular orbit of the secondary, except for the origin, which is the barycenter of the system. The configuration of the system is shown in Fig.2.5.

In the normalized 3B frame, define the vector of the relative position $\mathbf{q}$ of the spacecraft and its relative velocity $\dot{\mathbf{q}}$. The normalized positions of the two massive bodies and their normalized masses are then straightforward. It is useful to define also the distance $\mathbf{r}$ of the spacecraft from the two bodies.

$$\mathbf{q} = \begin{bmatrix} x \\ y \\ z \end{bmatrix} \ , \ \dot{\mathbf{q}} = \begin{bmatrix} \dot{x} \\ \dot{y} \\ \dot{z} \end{bmatrix} \tag{2.4}$$

$$m_1 = 1 - \mu \ , \ m_2 = \mu \tag{2.5}$$

$$\mathbf{q_1} = \begin{bmatrix} x_1 \\ y_1 \\ z_1 \end{bmatrix} = \begin{bmatrix} -\mu \\ 0 \\ 0 \end{bmatrix} \ , \ \mathbf{q_2} = \begin{bmatrix} x_2 \\ y_2 \\ z_2 \end{bmatrix} = \begin{bmatrix} 1-\mu \\ 0 \\ 0 \end{bmatrix} \tag{2.6}$$

$$\mathbf{r_1} = \mathbf{q} - \mathbf{q_1} = \begin{bmatrix} x+\mu \\ y \\ z \end{bmatrix} \ , \ \mathbf{r_2} = \mathbf{q} - \mathbf{q_2} = \begin{bmatrix} x+\mu-1 \\ y \\ z \end{bmatrix} \tag{2.7}$$

$$\|\mathbf{r_1}\| = \sqrt{(x+\mu)^2 + y^2 + z^2}\ ,\ \|\mathbf{r_2}\| = \sqrt{(x+\mu-1)^2 + y^2 + z^2} \tag{2.8}$$

The 3B frame in the CR3BP is not inertial, but rotates uniformly with the orbital angular velocity of the two primaries. Therefore the equations of motion are expressed with the relative dynamics of Eq.2.1. The frame's normalized constant angular velocity is

$$\boldsymbol{\omega} = \begin{bmatrix} \omega_x \\ \omega_y \\ \omega_z \end{bmatrix} = \begin{bmatrix} 0 \\ 0 \\ 1 \end{bmatrix} \tag{2.9}$$

and the apparent acceleration is the sum of the centripetal and Coriolis terms. The notation is simplified by defining the skew-symmetric matrix $\mathbf{W} \in \mathbb{R}^{3\times3} : \mathbf{W}\cdot(\cdot) = \hat{\mathbf{z}}\wedge(\cdot)$ and the related square matrix $\mathbf{P} = \mathbf{W}^2$ (note that $-\mathbf{P}$ is a planar projector).

$$\mathbf{a_A} = \boldsymbol{\omega} \wedge \boldsymbol{\omega} \wedge \mathbf{q} + 2\boldsymbol{\omega} \wedge \dot{\mathbf{q}} = \mathbf{P}\mathbf{q} + 2\mathbf{W}\dot{\mathbf{q}} \tag{2.10}$$

Recall that the inertial position is simply obtained re-scaling and counter-rotating the relative position by an appropriate time-variant attitude matrix, where the angle corresponds to the normalized time. The inertial velocity is obtained in the same way, after adding the drag term $\boldsymbol{\omega} \wedge \mathbf{q} = \mathbf{W}\mathbf{q}$.

The gravitational force $\mathbf{a_G}$, and the related potential u, is the sum of the effects of the two bodies, which are fixed in the 3B frame. An added constant term in the potential is historically used for some mathematical manipulations [76, 50], but it does not affect the results.

$$u = u_{G,1} + u_{G,2} + \frac{1}{2}m_1m_2 = \frac{m_1}{\|\mathbf{r_1}\|} + \frac{m_2}{\|\mathbf{r_2}\|} + \frac{1}{2}m_1m_2 \tag{2.11}$$

$$\mathbf{a_G} = \mathbf{a_{G,1}} + \mathbf{a_{G,2}} = -\frac{m_1}{\|\mathbf{r_1}\|^3}\mathbf{r_1} - \frac{m_2}{\|\mathbf{r}_2\|^3}\mathbf{r_2} = u_{/\mathbf{q}} \tag{2.12}$$

Finally, the equations of motion can be stated in the Lagrangian state-model form, where $\mathbf{x}$ is the resulting state of the vectorfield $\mathbf{f}$ of the dynamical system reduced to a first-order ODE. The common expressions $\mathbf{I_n}$, $\mathbf{0_n}$, $\mathbf{0_{nxm}}$ are used to indicate respectively an identity, square and rectangular null matrix of dimensions n and m. Eq.2.13 yields the CR3BP highlighting the linear part, constituted by the apparent force, and the nonlinear part constituted by the gravitational force.

$$\mathbf{x} = \begin{bmatrix} \mathbf{q} \\ \dot{\mathbf{q}} \end{bmatrix}\ ,\ \dot{\mathbf{x}} = \mathbf{f_{CR3BP}}(\mathbf{x}) = \mathbf{A}\mathbf{x} + \begin{bmatrix} \mathbf{0_{3x1}} \\ u_{/\mathbf{q}}(\mathbf{q}) \end{bmatrix}\ ,\ \mathbf{A} = \begin{bmatrix} \mathbf{0_3} & \mathbf{I_3} \\ -\mathbf{P} & -2\mathbf{W} \end{bmatrix} \tag{2.13}$$

The CR3BP defined above is a non-integrable time-invariant Hamiltonian system. Therefore, it is possible to demonstrate in Eq.2.14-2.15 by calculating the energy integral of the system [50], that these dynamical equations have an integral of motion called the Jacobi integral c. This can be related to the mechanical energy per unit of

mass e of the system, which in these relative dynamics is the sum of the relative kinetic energy, the drag kinetic energy and the gravitational potential energy. The last two terms can be combined, to define an effective or augmented potential of the CR3BP, providing an inertial-like description of the dynamical equations, that resembles the two classical components of the mechanical energy. This is shown in Eq.2.16 with the usual definition of the Lagrangian function per unit of mass.

$$\frac{d}{dt}\left\{\frac{1}{2}\dot{\mathbf{q}}^T\dot{\mathbf{q}}+\frac{1}{2}\mathbf{q}^T\mathbf{P}\mathbf{q}\right\}=\frac{d}{dt}u\Rightarrow t_R-t_D=u-\frac{c}{2} \tag{2.14}$$

$$e=t_R-t_D-u=t_R(\dot{\mathbf{q}})-u_{eff}(\mathbf{q})=-c/2 \tag{2.15}$$

$$l=t+u=\frac{1}{2}\dot{\mathbf{q}}^T\dot{\mathbf{q}}+\dot{\mathbf{q}}^T\mathbf{W}\mathbf{q}-\frac{1}{2}\mathbf{q}^T\mathbf{P}\mathbf{q}+u=t_R(\dot{\mathbf{q}})+t_C(\dot{\mathbf{q}},\mathbf{q})+u_{eff}(\mathbf{q}) \tag{2.16}$$

It can be useful to describe the system with the Hamiltonian approach. The Hamiltonian state vector is obtained substituting the relative velocity vector with the related position-conjugated momenta $\mathbf{p}$, which corresponds to the inertial velocity (in the relative frame's components).

$$\mathbf{p}=l_{/\dot{\mathbf{q}}}=\dot{\mathbf{q}}+\mathbf{W}\mathbf{q}\Rightarrow\left\{\begin{array}{l}\mathbf{x_H}=\mathbf{T_H^L}\mathbf{x_L}\\ \mathbf{x_L}=\mathbf{T_L^H}\mathbf{x_H}\end{array}\right.,\mathbf{T_H^L}=\begin{bmatrix}\mathbf{I_3}&\mathbf{0_3}\\ \mathbf{W}&\mathbf{I_3}\end{bmatrix},\mathbf{T_L^H}=\begin{bmatrix}\mathbf{I_3}&\mathbf{0_3}\\ -\mathbf{W}&\mathbf{I_3}\end{bmatrix} \tag{2.17}$$

Eq.2.17 defines the direct and inverse Legendre transformation $\mathbf{T}$ between Lagrangian and Hamiltonian state vectors $\mathbf{x_L}$ and $\mathbf{x_H}$, for the CR3BP. Finally, the equations of motion and the energy of the dynamical system can be stated in the Hamiltonian form.

$$\mathbf{x}=\begin{bmatrix}\mathbf{q}\\ \mathbf{p}\end{bmatrix},\dot{\mathbf{x}}=\mathbf{f_{CR3BP}}(\mathbf{x})=\mathbf{A}\mathbf{x}+\begin{bmatrix}\mathbf{0_{3x1}}\\ u_{/\mathbf{q}}(\mathbf{q})\end{bmatrix},\mathbf{A}=\begin{bmatrix}-\mathbf{W}&\mathbf{I_3}\\ \mathbf{0_3}&-\mathbf{W}\end{bmatrix} \tag{2.18}$$

$$h=\frac{1}{2}\mathbf{p}^T\mathbf{p}-\mathbf{p}^T\mathbf{W}\mathbf{q}-u=e \tag{2.19}$$

2.3.4 Hill's Surfaces and Regions of Influence

The Hill's surfaces, or zero-velocity surfaces, are the iso-surfaces in the position domain of the Jacobi integral with null velocity. For a given initial condition $\mathbf{x_0}$, the related Hill's surface defines the boundary of the 3D position-space where the natural motion is constrained. This means that with the given energy, regions of space outside the surfaces are not naturally reachable. This is shown in Fig.2.5 for the planar CR3BP: in this case, the projections of the Hill's surfaces onto the coordinated planes are called the Hill's curves. Increasing the energy (which is, decreasing the Jacobi integral) the

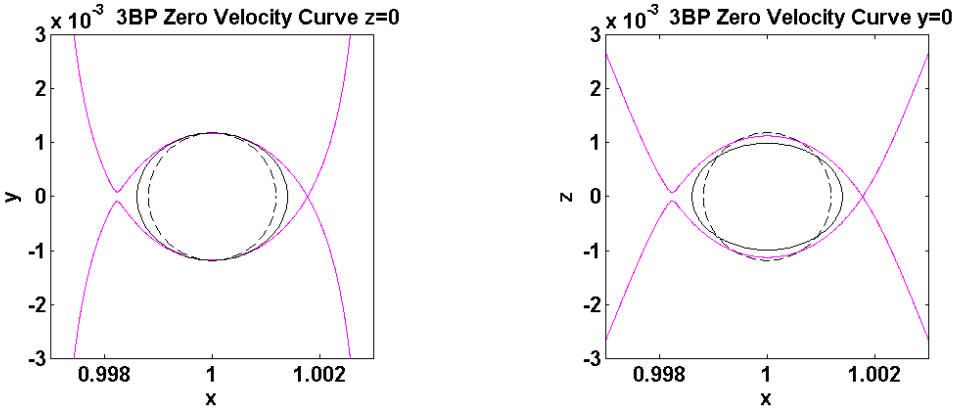

Figure 2.6: **Hill's surfaces in the neighborhood of Phobos for L_2 energy.** On the left, x-y projection; on the right, x-z projection. Mean ellipsoid (plain line) and mean radius approximation (dashed line) for Phobos.

white region in Fig.2.5 of accessible space grows, starting from two inner realms, one around each massive body, and from an exterior realm around both of them. First the two inner realms merge, meaning that natural transfers between the two massive bodies can occur. Afterwards, the new single inner realm merges with the exterior one: first on the secondary's side, then on the primary's side, and finally all the 3D space becomes naturally accessible.

The Hill's sphere of influence is the region around each massive body where the dynamics are dominated by its own gravity field: placing a point at zero relative velocity inside the SOI would result in an attraction towards the respective body. This means that the Hill's SOI is the maximum size of the two inner realms at low energy, before inner transfers are enabled. In the framework of the CR3BP, the secondary's Hill's SOI normalized radius is defined as

$$r_{H,2} = \sqrt[3]{\frac{\mu}{3}} \tag{2.20}$$

For Phobos, this radius is 0.17% of the distance from Mars, which is an altitude over the moon's mean sphere of only $5.5km$. This means that the physical space that can be used to orbit around Phobos is very close to the body at low energy, and considering the fact that Phobos is very irregular in its shape, **the maximum altitude of the Hill's SOI boundary is of only 3.5km**, as shown in Fig.2.6 using the moon's mean ellipsoid. Therefore **it is impossible to naturally orbit around Phobos with a Keplerian motion** due to only the gravitational attraction of the moon, because this can occur only at energies and distances lower than the ones of the Hill's SOI.

As μ and L decrease in the CR3BP, the SOI shrinks close to the surface of the secondary body. Thus, the two peculiarities of the Mars-Phobos couple previously highlighted are responsible for the reduction of the exploitable realm of attraction of the moon. This result significantly affects the three-body dynamics in the vicinity of the moon, and will be referred throughout this thesis as the *collapsing effect of the SOI*. In particular let now compare this outcome with all the other couples of primaries of the

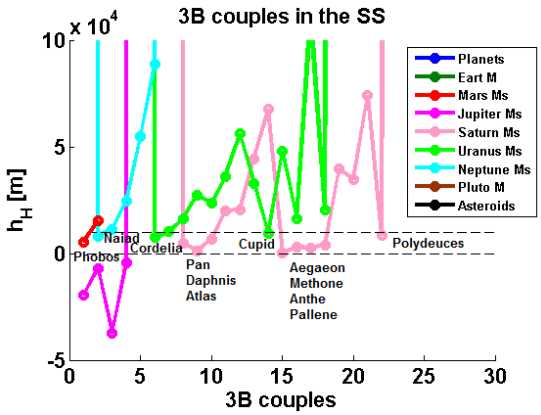

Figure 2.7: **Absolute altitude of the secondary's realm of the 3B couples in the Solar System.** Major moons and asteroids are considered. Moons between 0 and $10km$ are labeled.

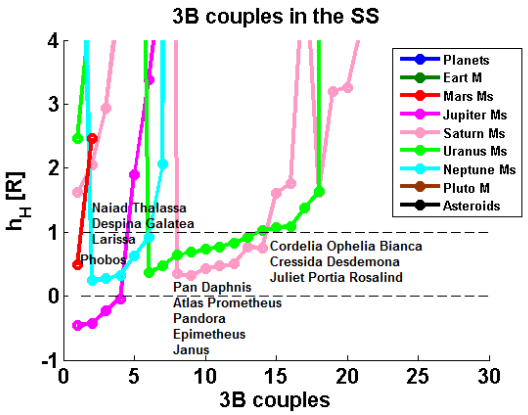

Figure 2.8: **Relative altitude of the secondary's realm of the 3B couples in the Solar System.** Normalization by the secondary's mean size. Major moons and asteroids are considered. Moons between 0 and 1 radius are labeled.

Solar System. The Hill's radius of the second massive body is evaluated with Eq.2.20, and the related altitude h_H of the Hill's SOI over the secondary's radius is derived. In Fig.2.7 this is presented in its absolute value, and in Fig.2.8 with a relative measure, normalizing the altitude by the secondary's radius. Thus, two maximum thresholds are considered: $10km$ for practical mission operation constraints, and 1 radius to define an outer boundary such that, within this altitude, perturbations due to the secondary body significantly influence the motion. Within these two absolute and relative thresholds, in addition to Mars-Phobos, only five other couples of primaries in all the Solar System fall inside, and therefore are characterized by the same collapsing effect. In particular, the other Martian moon Deimos is out of these limits. They are all cases of planetary satellites[2]: three moons of Saturn (Pan, Daphnis, Atlas), one of Uranus (Cordelia), and one of Neptune (Naiad), while four inner moons of Jupiter have their Hill's SOI inside their bulk. Orbital dynamics in proximity of these bodies are therefore very complex: no Keplerian solutions (where the central body is the secondary) nor classical LPOs of the CR3BP exist because the natural motion is highly influenced by the perturbations of the secondary body, since these moons are all highly inhomogeneous. It is worth noting that despite the small μ yielding a small normalized radius of the SOI, the collapsing effect is not encountered in the case of a Sun-asteroid couple because L is too large[3]. For example, considering a distance of $1AU$, even with a hypothetical small bulk density of $1,000kg/m^3$, using Eq.2.21 the relative altitude of the SOI of a body orbiting around the Sun is more than 100 times its mean sphere's radius. This means that for a practically small Hill's SOI (altitude of $10km$), the related body at $1AU$ should be smaller than $200m$.

[2]In addition, apart to be far from a spherical shape, all of their five orbits are also synchronous, zero-tilted, circular and equatorial - apart for Naiad which is 4° inclined from Neptune's equator.

[3]The collapsing effect can occur in the case of binary asteroids.

$$\frac{h_{H,2}}{R_2} = \frac{r_{H,2}}{R_2} - 1 = \frac{\sqrt[3]{\frac{\mu}{3}}a}{R_2} - 1 \simeq \sqrt[3]{\frac{4\pi}{9}\frac{\bar{\rho}_2}{m_1}}a - 1 \tag{2.21}$$

2.3.5 Global Orbit Structure

2.3.5.1 Equilibrium Points

The next step in the preliminary analysis of the CR3BP is the computation of the stationary points of the effective potential function, which is to determine the five equilibrium points of the 3B dynamics in the rotating frame, for the Mars-Phobos' μ. These EPs are made by three collinear points (1767: Euler) named L_1, L_2, and L_3, along the primaries' conjunction direction, and by two equilateral points (1772: Lagrange) named L_4 and L_5, equidistant from the two bodies. The first two EPs are close to the secondary, L_1 in inferior (also called cis) and L_2 in superior (also called trans) conjunction as seen from the primary, while L_3 is in opposition. The two equilateral EPs have elongation of 60° from both bodies. These five EPs are called Lagrangian or Libration points, and can be seen in Fig.2.5. In particular, as they are stationary points of the effective potential, the EPs are the critical points of the Hill's surfaces. This means that their energies are the levels that mark the evolution of the realms of accessible motion in the CR3BP, as discussed in section 2.3.4. For example, a spacecraft with energy higher or lower than the energy of L_1 is or is not able to naturally transfer between the two massive bodies. Therefore, the collinear couple L_{1-2} is very important in mission design: their distance from the secondary is a practical indicator of its SOI's size.

The problem is to solve the system of equations deriving from equating to zero the gradient of the effective potential. From the equations of motion, this means to find the positions were the gravity force is counteracted by the centrifugal force.

$$u_{eff} = u - \frac{1}{2}\mathbf{q}^T\mathbf{P}\mathbf{q} \tag{2.22}$$

$$u_{eff/\mathbf{q}} = u_{/\mathbf{q}} - \mathbf{P}\mathbf{q} = \mathbf{a_G} - \mathbf{P}\mathbf{q} = \mathbf{0} \tag{2.23}$$

L_4 and L_5 are independent from the mass parameter, so they are derived once and for all substituting $\|\mathbf{r_1}\| = \|\mathbf{r_2}\| = 1$ in Eq.2.23, after a change of variables (and for the case $z = 0$ and $y \neq 0$), and proving that the equation is satisfied. These symmetric points, that are the vertices of the two planar equilateral triangles with the massive bodies at the other two vertices, are related to the Jacobi constant $c = 3$, which is again universal: for upper energies, there are no more Hill's surfaces, which is all the 3D space is accessible.

L_1, L_2, and L_3 are instead calculated for a given μ as the solution of Eq.2.23 with the simplification of $y = z = 0$. The three cases are expressed each one with an

Table 2.2: **Location of the Equilibrium Points of the Mars-Phobos CR3BP.** Mean radius approximation for the massive bodies. Position is the distance' magnitude from Phobos' center. Altitude of L_{1-2} is over Phobos' mean radius, altitude of L_3 and L_{4-5} is over Mars' mean radius. The Phobos Hill's radius is $1.7689 \cdot 10^{-3} L = 16.591 km$.

Point	Position / Altitude	Jacobi Constant
L_1	$1.7679 \cdot 10^{-3} L = 16.582 km$ / $5.482 km$	3.0000281237 ($\Delta c\ L_1/L_2 = 10^{-8}$)
L_2	$1.7700 \cdot 10^{-3} L = 16.601 km$ / $5.501 km$	3.0000281015 ($\Delta c\ L_{1,2}/L_3 = 10^{-5}$)
L_3	$1.9999...L$ / $64\% L = 1.7 R_1$	3.0000000332 ($\Delta c\ L_3/L_{4-5} = 10^{-8}$)
L_{4-5}	L / $64\% L = 1.7 R_1$	3 ($\Delta c\ L_{1,2}/L_{4-5} = 10^{-5}$)

appropriate equation (called the Euler quintic equation) where the only variable s is the most suitable positive distance from the closer of the two massive bodies.

$$\begin{cases} 0 < s = x_2 - x_{L_1} < 1 \\ s = x_{L_2} - x_2 > 0 \\ s = x_1 - x_{L_3} > 0 \end{cases} \Rightarrow \begin{cases} s^5 + (\mu - 3)s^4 + (-2\mu + 3)s^3 - \mu s^2 + 2\mu s - \mu = 0 \\ s^5 - (\mu - 3)s^4 + (-2\mu + 3)s^3 - \mu s^2 - 2\mu s - \mu = 0 \\ s^5 + (\mu + 2)s^4 + (2\mu + 1)s^3 + (\mu - 1)s^2 + (2\mu - 2)s + \mu - 1 = 0 \end{cases} \tag{2.24}$$

These 5th order polynomial equations are solved with Newton's method using as initial guess the related Hill's SOI's radius. It is interesting to observe the limit root of these equations as the mass parameter tends to zero (recall that the Mars-Phobos μ is indeed very small). L_1 and L_2 tend to reach the secondary body's Hill's radius (the first always interiorly, the second always exteriorly). Thus, the Hill's radius of Eq.2.20 is a first-order approximation of the SOI's size, whose actual shape given by the Hill's surfaces is oblate, as shown in Fig.2.6. In contrast L_3 tends to the symmetric position to the secondary body about the primary (always interiorly).

Table 2.2 summarizes the locations of the EPs for the Mars-Phobos system. It is evident how close are L_1 and L_2 to Phobos: as they differ of only $\pm 10m$ from the Hill's radius, the conclusion recalls the one made in section 2.3.4. Since the major axis of Phobos is along the x-axis of the 3B frame, the altitude of L_{1-2} falls down to only $3.5km$, while the minimum altitude of the SOI on the z-axis is just $1km$, see Fig.2.6. As presented in Table 2.2, the related energies are also very close to each other, and already close to the one of the equilateral EPs. This is a physical indication of the microgravity environment along the orbit of a small body. In this scenario, the forbidden realm could be overcome with a suitable low-thrust propulsion system. In particular, considering also their distance, transfers between Phobos' SOI and the equilateral EPs could be exploited at low-cost.

2.3.5.2 Linearized Stability Analysis

In the past few decades the LPs have been intensively studied, and all the missions named in section 2.3.1 have dealt with trajectories in their neighborhood. Such Li-

bration Point Orbits have started to be studied through the linearized model in the vicinity of these stationary points. The related Jacobian matrix is the linear part of Eq.2.13, plus the linearization of the nonlinear term evaluated at the EP, which is the symmetric Hessian matrix $\mathbf{H}u = u_{/\mathbf{qq}}$ of the 3B gravitational potential.

$$\mathbf{x} = \mathbf{x_{EP}} + \delta\mathbf{x} \Rightarrow \delta\dot{\mathbf{x}} = \mathbf{J}(\mathbf{x_{EP}})\delta\mathbf{x} \tag{2.25}$$

$$\mathbf{J}(\mathbf{x}) = \mathbf{A} + \begin{bmatrix} \mathbf{0_3} & \mathbf{0_3} \\ u_{/\mathbf{qq}}(\mathbf{q}) & \mathbf{0_3} \end{bmatrix} \tag{2.26}$$

$$u_{/\mathbf{qq}}(\mathbf{q}) = -g(\mathbf{q})\mathbf{I_3} + 3g_1(\mathbf{q})\mathbf{r_1}\mathbf{r_1}^T + 3g_2(\mathbf{q})\mathbf{r_2}\mathbf{r_2}^T \Leftarrow \begin{cases} g(\mathbf{q}) = \frac{m_1}{\|\mathbf{r_1}\|^3} + \frac{m_2}{\|\mathbf{r_2}\|^3} \\ g_1(\mathbf{q}) = \frac{m_1}{\|\mathbf{r_1}\|^5} \\ g_2(\mathbf{q}) = \frac{m_2}{\|\mathbf{r_2}\|^5} \end{cases} \tag{2.27}$$

For the case of the collinear and equilateral LPs, the Hessian matrix can be stated in Eq.2.28, where $g(s)$ refers to $g(\mathbf{q})$ of Eq.2.27 evaluated at the LP position identified by the solution s of the quintic equation.

$$\begin{cases} u_{/\mathbf{qq}}(L_{1-2-3}) = g(s) \begin{bmatrix} 2 & 0 & 0 \\ 0 & -1 & 0 \\ 0 & 0 & -1 \end{bmatrix} \\ u_{/\mathbf{qq}}(L_{4-5}) = \begin{bmatrix} -1/4 & \pm(1-2\mu)\sqrt{33}/4 & 0 \\ \pm(1-2\mu)\sqrt{33}/4 & 5/4 & 0 \\ 0 & 0 & -1 \end{bmatrix} \end{cases} \tag{2.28}$$

Now it is straightforward to calculate the eigenvalues of the linearized system in the neighborhood of the LPs. The six eigenvalues occur in three opposite couples:

$$\begin{cases} \lambda(L_{1-2-3}) = \begin{cases} \pm i\sqrt{g} = \pm i\upsilon \\ \pm\sqrt{(g/2-1) + \sqrt{9g^2/4 - 2g}} = \pm\lambda \\ \pm\sqrt{(g/2-1) - \sqrt{9g^2/4 - 2g}} = \pm i\nu \end{cases} \\ \lambda(L_{4-5}) = \begin{cases} \pm i \\ \pm\sqrt{-1/2 + \sqrt{1/4 - 27m_1m_2/4}} \\ \pm\sqrt{-1/2 - \sqrt{1/4 - 27m_1m_2/4}} \end{cases} \end{cases} \tag{2.29}$$

For the equilateral LPs, one finds the condition for linear stability, for which all the eigenvalues are imaginary:

$$m_1m_2 = \mu(1-\mu) < 1/27 \Rightarrow \mu < 3.85\% \tag{2.30}$$

This condition is realized with the mass parameter of the Mars-Phobos system, which

is the Mars-Phobos L_{4-5} are linearly dynamical stable.

For the collinear LPs, their stability character is universal for every value of μ. The linearized system is stable in the relative out-of-plane direction, whereas on the orbital plane the 4D phase-space solution is characterized by a center $\times$ saddle behavior, which is unstable. In particular, the unstable eigenvalue is large enough to made the CR3BP known as a flagship model for the chaos dynamics. This means that the motion in the vicinity of L_{1-2} is strongly dependent from the initial conditions. In this sense, a lot of mathematical effort has been undertaken in the last fifty years to study the behavior in the region of L_{1-2}. Generalizing, every 4th order Hamiltonian system of the case center $\times$ saddle has two integrals of motion, one describing a hyperbola on the plane of two eigenvectors, and one describing a circle on the plane of the remaining two eigenvectors. In addition, Moser's theorem proves that the behavior of the linearized system in the neighborhood of the LPs of the CR3BP is valid also in the real nonlinear system [77].

Translating this in the 3B dynamics, this means that two additional reference integrals of motion exist in the planar region of L_{1-2}. They define the surplus of energy that the trajectory has with respect to the related LP, and their single values allow to distinguish four classes of orbits in that region. The presence of the center manifold provides a Lyapunov periodic orbit around the EP: this is an ellipse in the linearized system, with the major axis along the y direction, and in a μ-dependent ratio with the minor axis, whereas in the real system the orbit is distorted to a bean/tadpole shape. Then, their is a manifold of asymptotic orbits that arrive (time-forward) or leave (time-backward) the Lyapunov orbit. Finally, there are transit and non-transit orbits across the Lyapunov orbit. Their name is related to the fact that they are or not able to cross the EP's region along the x-axis: this means that they allow to transfer or not across the realms around both primaries. The term invariant manifold refers to the regions of the phase-space spanned by the asymptotic orbit of a LPO. The invariant manifolds are separatrices of motion: *the trajectories at a given Jacobi integral must be inside the tube given by the invariant manifold of the iso-energetic LPO to perform a natural transit between the two realms, which face each other as a bottleneck through the equilibrium point.*

In summary, in this section it is proved that the boundaries of the Hill's SOI for Phobos at the energy of L_{1-2} are very close to its surface, ranging from $1km$ to $3.5km$. These values are too small to use Keplerian orbits in a Phobos-centered R2B dynamics working assumption, but also the classical LPOs around L_{1-2}, exploited in depth by space mission in the Sun-Earth and Earth-Moon CR3BPs, will be highly affected by practical (distance from Phobos' surface) and physical (perturbations of Phobos) constraints. The computation of the LPOs and their invariant manifolds in the Mars-Phobos CR3BP, and their extension in a refined model of the orbital dynamics, will be undertaken in chapter 4.

2.3.6 Hill's Approximation of the CR3BP

In the case of a R3BP where the two primaries' masses are very unequal, some approximations could be made. Outside the realm of influence of the secondary, the dynamics should be analyzed as a classical R2BP around the primary. Inside the secondary's realm instead, the suggestion is to use an approximation of the CR3BP dynamics, which is known as Hill's approximation. This is motivated by the fact that, since the Hill's SOI's radius decreases with the mass parameter, staying inside of this realm automatically means that the normalized distances from the secondary are numerically small. Thus, the limit of the equations of motion of the CR3BP of Eq.2.13 for μ tending to zero is carried out. It is worth to note that this does not mean to consider the mass parameter to be zero. In this ultimate case, the full gravity of the secondary would be neglected in its vicinity, downgrading the R3BP to the relative dynamics with respect to a massless point orbiting the primary with a R2B motion (circular in this case). This is the case of Formation Flying, rendez-vous and docking maneuvers of two spacecraft[4].

Instead, the Hill's approximation of the CR3BP leads to a linearization of the gravity of the primary, because inside the collapsed SOI its variation tends to zero. The procedure requires to first carry out a coordinates transformation, expressing the CR3BP in the Hill's frame of the secondary. Also, a different and more convenient length unit is required for this framework, which is to use the Hill's radius of Eq.2.20, that is commonly referred as the factor γ. Thus, the positions of interest in the Hill's approximation of the CR3BP are practically bounded by the unit sphere. The new normalized variables are now denoted with an upper bar in the following equations.

$$\mathbf{q} = \begin{bmatrix} x=\gamma\bar{x}+(1-\mu) \\ y=\gamma\bar{y} \\ z=\gamma\bar{z} \end{bmatrix} = \gamma\bar{\mathbf{q}} + \begin{bmatrix} 1-\mu \\ 0 \\ 0 \end{bmatrix} \tag{2.31}$$

After such transformation, Eq.2.13 is taken with its limit as $\mu \to 0$, resulting in the dynamical equations of the CR3BPH in Lagrangian (Eq.2.34) and Hamiltonian (Eq.2.36) state-model form. In particular, μ disappears from the equations of motion, and the CR3BPH does not depend on any parameter, therefore its normalized solution is universal.

$$u_{/\bar{\mathbf{q}}} = -\frac{1}{\gamma^3}\frac{1-\mu}{\left(\sqrt[2]{\left(\bar{x}+\frac{1}{\gamma}\right)^2+\bar{y}^2+\bar{z}^2}\right)^3}\left(\bar{\mathbf{q}}+\begin{bmatrix}\frac{1}{\gamma}\\0\\0\end{bmatrix}\right) - \frac{1}{\gamma^3}\frac{\mu}{\left(\sqrt[2]{\bar{x}^2+\bar{y}^2+\bar{z}^2}\right)^3}\bar{\mathbf{q}} \tag{2.32}$$

$$\lim_{\mu\to 0} u_{/\bar{\mathbf{q}}} = -\bar{\mathbf{q}} + \begin{bmatrix}3\bar{x}\\0\\0\end{bmatrix} - \begin{bmatrix}1\\0\\0\end{bmatrix} - \frac{3}{\|\bar{\mathbf{q}}\|^3}\bar{\mathbf{q}} = -\mathbf{A_{H1}}\bar{\mathbf{q}} - \begin{bmatrix}1\\0\\0\end{bmatrix} - \frac{3}{\|\bar{\mathbf{q}}\|^3}\bar{\mathbf{q}}\ ,\ \mathbf{A_{H1}} = \begin{bmatrix}-2&0&0\\0&1&0\\0&0&1\end{bmatrix} \tag{2.33}$$

[4] In particular, the Hill's approximation of these equations leads to their linearization.

$$\mathbf{x} = \begin{bmatrix} \bar{\mathbf{q}} \\ \dot{\bar{\mathbf{q}}} \end{bmatrix}, \dot{\mathbf{x}} = \mathbf{A}\mathbf{x} + \begin{bmatrix} \mathbf{0_{3x1}} \\ -\frac{3}{\|\bar{\mathbf{q}}\|^3}\bar{\mathbf{q}} \end{bmatrix}, \mathbf{A} = \begin{bmatrix} \mathbf{0_3} & \mathbf{I_3} \\ -\mathbf{P} - \mathbf{A_{H1}} & -2\mathbf{W} \end{bmatrix} = \begin{bmatrix} \mathbf{0_3} & \mathbf{I_3} \\ \begin{bmatrix} 3 & 0 & 0 \\ 0 & 0 & 0 \\ 0 & 0 & -1 \end{bmatrix} & -2\mathbf{W} \end{bmatrix} \tag{2.34}$$

$$u_{eff} = u - \frac{1}{2}\bar{\mathbf{q}}^T\mathbf{P}\bar{\mathbf{q}} = -\frac{1}{2}\bar{\mathbf{q}}^T\mathbf{A_{H1}}\bar{\mathbf{q}} + \frac{3}{\|\bar{\mathbf{q}}\|} - \frac{1}{2}\bar{\mathbf{q}}^T\mathbf{P}\bar{\mathbf{q}} = \frac{3}{\|\bar{\mathbf{q}}\|} - \frac{1}{2}\bar{\mathbf{q}}^T\left(\mathbf{P} + \mathbf{A_{H1}}\right)\bar{\mathbf{q}} \tag{2.35}$$

$$\mathbf{x} = \begin{bmatrix} \bar{\mathbf{q}} \\ \bar{\mathbf{p}} \end{bmatrix}, \dot{\mathbf{x}} = \mathbf{A}\mathbf{x} + \begin{bmatrix} -\frac{1}{\gamma}\mathbf{W}\begin{bmatrix} 1-\mu \\ 0 \\ 0 \end{bmatrix} \\ -\frac{3}{\|\bar{\mathbf{q}}\|^3}\bar{\mathbf{q}} \end{bmatrix}, \mathbf{A} = \begin{bmatrix} -\mathbf{W} & \mathbf{I_3} \\ -\mathbf{A_{H1}} & -\mathbf{W} \end{bmatrix} \tag{2.36}$$

The CR3BPH has only two equilibrium points L_{1-2}, in the exact normalized positions of ± 1 along the x-axis, as expected since the limit of the original quintic equation was already observed in section 2.3.5.1. Thus, the error introduced by the Hill's approximation on the static properties inside the SOI of Phobos is only $10m$, which is a relative error of 0.1%. Also the eigenvalues of L_{1-2} have the same relative error, and are still associated to a saddle × center × center manifold structure.

$$u_{/\bar{\mathbf{q}}\bar{\mathbf{q}}}(L_{1-2}) = -\mathbf{A_{H1}} + \begin{bmatrix} 6 & 0 & 0 \\ 0 & -3 & 0 \\ 0 & 0 & -3 \end{bmatrix} = \begin{bmatrix} 8 & 0 & 0 \\ 0 & -4 & 0 \\ 0 & 0 & -4 \end{bmatrix} \tag{2.37}$$

$$\lambda(L_{1-2}) = \begin{cases} \pm i\sqrt{4} = \pm i\upsilon \\ \pm\sqrt{1+\sqrt{28}} = \pm\lambda \\ \pm\sqrt{1-\sqrt{28}} = \pm i\nu \end{cases} \tag{2.38}$$

In conclusion, the CR3BPH is a simplified version of the CR3BP with useful properties for mathematical analysis, such as symmetry and universality (it does not depend on any parameter). It is a good approximation for computing the static properties of the Mars-Phobos system, but the high instability in the L_{1-2} regions of the CR3BP is quite sensitive also to these fine approximations when propagating the orbits in the full dynamics. Therefore, the dynamical analysis of the invariant objects in the vicinity of Phobos in this thesis will be conducted without making use of the Hill's approximation.

2.4 Orbital Perturbations

An analysis is undertaken to quantify approximately the errors that occur in the Mars-Phobos system when it is approximated with the CR3BP of Eq.2.13. In this case, the Keplerian circular orbit of Phobos is also approximated as equatorial.

2.4.1 Physical Perturbations

The main physical orbital perturbations are distinguished by gravitational and non-gravitational forces.

In the first class, there is the net term that when added to the basic Newtonian point-mass force provides the true gravity pull of a general non-spherical and non-uniform body. In astrodynamics this term is usually modeled with a spherical harmonics series expansion known as gravity harmonics. For a first analysis, the dominant term for both Mars' and Phobos' gravity fields is considered, which is known as J_2 and is related to the oblateness of the body. As a reference, Mars' further harmonics start from a $J_{2,2}$ effect at Phobos which is the 19% of the one of J_2, but then their effect decreases rapidly with the degree and order. In contrast, Phobos' gravity field is highly inhomogeneous, and many additional harmonics are relevant to model it inside the SOI, starting from a $J_{2,2}$ effect which is the 84% of the one of J_2 at the boundary of the SOI. Eq.2.39 provides the formula for the J_2 gravity acceleration in a BCBF frame.

$$\mathbf{a}_G^{J_2}(\mathbf{r}_{BCBF}) = -\frac{GM_\oplus {R_\oplus}^2}{\|\mathbf{r}\|^5} J_{2,\oplus} \frac{3}{2} \begin{bmatrix} r_x \left(1 - 5\left[\frac{r_z}{\|\mathbf{r}\|}\right]^2\right) \\ r_y \left(1 - 5\left[\frac{r_z}{\|\mathbf{r}\|}\right]^2\right) \\ r_z \left(3 - 5\left[\frac{r_z}{\|\mathbf{r}\|}\right]^2\right) \end{bmatrix} \tag{2.39}$$

Additionally, the effect of the gravity harmonics on the apparent rotational acceleration of the 3B frame must also be taken into account. For J_2, this turns in an increase of the centrifugal force, because the mean motion is scaled by a factor $\sqrt{1 + \frac{3}{2} J_2 (R/L)^2}$.

The second type of gravitational perturbation is the basic gravitational term of additional bodies. In the R2BP this is known as third body perturbation, and its effect is the sum of the gravity of the additional attractor and its apparent force, as shown in Eq.2.40.

$$\mathbf{a}_{TB}\left(\mathbf{r}_2^1, \mathbf{r}_3^1, m_2, m_3\right) = -\frac{GM_{23}}{\left\|\mathbf{r}_2^1 - \mathbf{r}_3^1\right\|^3}\left(\mathbf{r}_2^1 - \mathbf{r}_3^1\right) - \frac{GM_3}{\left\|\mathbf{r}_3^1\right\|^3}\mathbf{r}_3^1 \tag{2.40}$$

In the framework of the 3BP the disturbance of an additional body is referred to as fourth body perturbation, and Eq.2.40 could be adapted using as first body the barycenter and mass of the primaries, as second body the spacecraft, and as third body the additional attractor. For Mars-Phobos, further attractors considered are the Sun, Jupiter, the Earth, and Deimos. For a basic analysis, Eq.2.40 is applied pair

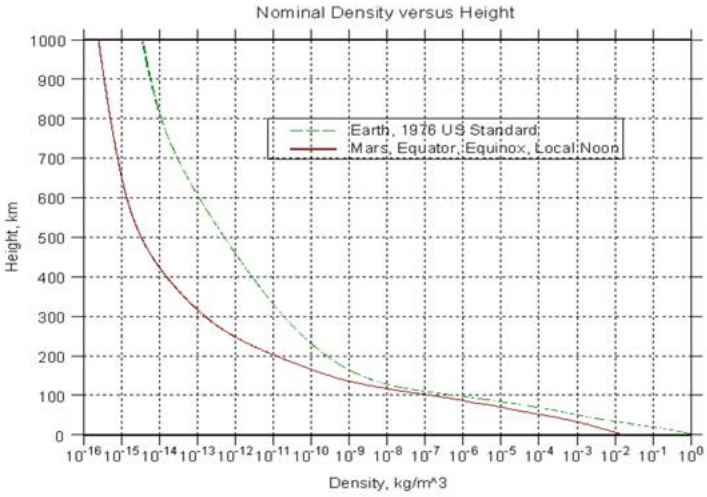

Figure 2.9: **Mars Global Reference Atmospheric Model.** Density profile compared with the one of the Earth [AGI].

by pair considering the perturbing body at its closest conjunction configuration with Phobos, and assuming coplanar orbits. For the case of Deimos, due to the short time scale and proximity of its orbit, the range between closest conjunction and farthest opposition is considered.

In the second class, there are the pressure disturbances of the atmospheric drag and the electromagnetic radiation. Phobos does not have an atmosphere, and the atmosphere of Mars is thinner than that of the Earth as a reference (actually their density profile is more irregular, see Fig.2.9), and the orbiting velocities around Mars are smaller than the ones of the Earth at the same altitude, therefore the effect at Phobos' altitude is negligible. Instead the radiation pressure analysis could be interesting also for additional implementations (solar sails). The primary source of radiation pressure (always considered in light here) is the one coming from the Sun (SRP), which has its major emission in the UV field with a mean heat flux value q of $1371 W/m^2$ at $1 AU$ (the Solar constant). Additional sources are obviously the other bodies, with IR major emission, and their reflection of the Sun incoming one, which is measured by the body's albedo coefficient (weighted by the spherical reflection factor of view; see Table 2.1). Here the radiation pressures of Mars (MRP) and Phobos (PRP) are considered. For Mars, mean IR flux at its surface is considered $110 W/m^2$, whereas mean value for Phobos is $130 W/m^2$. The local radiation pressure definition of Eq.2.41 should be integrated onto each illuminated surface of the spacecraft, considering its optical properties (along the incoming spectral distribution), summarized by its specular and diffusive reflectance coefficients[5]. Classical spacecraft's values used here are: both 40% for MLI surfaces, and both 10% for solar arrays. Also the emissivity of the spacecraft could be considered, but its effect as an orbital perturbation for a spacecraft is negligible. Finally,

[5] Assuming as usual the spacecraft's surfaces to be matt, the absorbance coefficient is then uniquely defined.

Eq.2.42 shows the perturbing acceleration, which depends also from the area-to-mass ratio of the spacecraft: here, a classical global value used is 0.01.

$$p_{RP}\left(\mathbf{r}^{\odot}\right)=\frac{q\left(\mathbf{r}^{\odot}\right)}{c_{light}}=\frac{1}{c_{light}}q_{ref}\left(\frac{d_{ref}}{\left\|\mathbf{r}^{\odot}\right\|}\right)^{2} \tag{2.41}$$

$$\mathbf{a}_{RP}\left(\mathbf{r}^{\odot}\right)=\frac{1}{m}\int p_{RP}\left(\mathbf{r}^{\odot}\right)\left[\left(1-c_{rs}\right)\hat{\mathbf{r}}_{\odot}^{dA}+2\left(c_{rs}\left(\hat{\mathbf{r}}_{\odot}^{dA}\hat{\mathbf{N}}_{dA}\right)+\frac{1}{3}c_{rd}\right)\hat{\mathbf{N}}_{dA}\right]\left(\hat{\mathbf{r}}_{\odot}^{dA}\hat{\mathbf{N}}_{dA}\right)dA \tag{2.42}$$

It is important to stress that the analysis of radiation pressure undertaken here is considered for a conventional spacecraft, whereas large solar sails are designed to actually use the SRP as a natural thrust source (with large area-to-mass ratio and enhanced optical reflectivity properties). Besides, a common problem in astrodynamics nowadays is the study of the natural motion of dust particles around Solar System's small bodies. In this case, the SRP becomes a relevant force per unit of mass (even larger than what a solar sail could deliver) because the area-to-mass ratio increases as far as the dust grain's size decreases. This could be simply shown assuming a reliable spherical and uniform model for a grain: the ratio between lighted area and total mass is indeed inversely proportional to the grain's radius.

$$\left(A/m\right)_{dust}=\frac{\pi r_{grain}^{2}}{\rho_{grain}\frac{4}{3}\pi r_{grain}^{3}}=\frac{3}{4\rho_{grain}r_{grain}} \tag{2.43}$$

Therefore, dust orbital dynamics is driven by both gravity of the Solar System's bodies of interest, and SRP. This coupling is referred to in the literature as the photo-gravitational problem.

2.4.2 Modeling Perturbations

In addition to the physical forces, artificial disturbances come from the approximation of the dynamics and the motion of the bodies in the model itself. The inclination of Phobos' orbit is small (about 1°) and acts only when considering the perturbations of other bodies, thus is not significant to be analyzed. In the Mars-Phobos CR3BP, the effect of the eccentricity (about 1.5%) of the actual Mars-Phobos orbit must be investigated. Following this value, a static indicator is straightforwardly derived. The LPs in reality are not fixed in the 3B frame, but oscillate with an amplitude of $260m$, realized when Phobos' phase is at perimars and apomars. This is definitely significant due to the low altitude ($3.5km$) of L_{1-2} over Phobos (it is 7% of this distance), and the already mentioned instability at these LPs.

To derive a related physical acceleration value, the procedure used is to compute the difference between the acceleration field of the CR3BP and the one of the elliptic model of the Mars-Phobos system. Since the ER3BP depends also on the phase of Phobos around Mars, the maximum value of such difference along Phobos' elliptic

orbit is considered. To derive an analytical formula of the eccentricity perturbation in the CR3BP to be valid for a general orbit, different choices arise to define how the user wants the trajectory to be preserved in the new dynamics. This because the orbit of the primaries is not the same. Since the interest in this thesis is to model the motion in close proximity of Phobos, the reference used is to maintain the same relative state with respect to the secondary.

First of all, the equations of motion of the ER3BP are presented in Eq.2.44 in the same 3B frame, where the distance between the two massive bodies l is not fixed anymore but it depends on the true anomaly of Phobos around Mars. Therefore the position of both primaries from their barycenter is variable and pulsating. In addition, the frame rotates now with a variable angular velocity and acceleration. Thus, Eq.2.44 could be derived from Eq.2.1-2.2.

$$\begin{aligned}\ddot{\mathbf{q}} = &- \frac{Gm_2}{\left\|\mathbf{q} - l(\nu)\begin{bmatrix}1-\mu\\0\\0\end{bmatrix}\right\|^3}\left(\mathbf{q} - l(\nu)\begin{bmatrix}1-\mu\\0\\0\end{bmatrix}\right) - \frac{Gm_1}{\left\|\mathbf{q} - l(\nu)\begin{bmatrix}-\mu\\0\\0\end{bmatrix}\right\|^3}\left(\mathbf{q} - l(\nu)\begin{bmatrix}-\mu\\0\\0\end{bmatrix}\right) + \\ &- \omega_z(\nu)^2\mathbf{P}\mathbf{q} - \dot{\omega}_z(\nu)\mathbf{W}\mathbf{q} - 2\omega_z(\nu)\mathbf{W}\dot{\mathbf{q}}\end{aligned} \tag{2.44}$$

$$l(\nu) = \frac{p}{1 + e\cos\nu} = a\frac{1 - e^2}{1 + e\cos\nu} \tag{2.45}$$

$$\omega_z(\nu) = \sqrt{\frac{GM}{p^3}}(1 + e\cos\nu)^2 = n\frac{(1 + e\cos\nu)^2}{(1 - e^2)^{3/2}} = \frac{v_\theta}{l} \tag{2.46}$$

$$\dot{\omega}_z(\nu) = -2\frac{GM}{p^3}(1 + e\cos\nu)^3 e\sin\nu = -2n^2\frac{(1 + e\cos\nu)^3}{(1 - e^2)^3}e\sin\nu = -2\omega_z\frac{v_r}{l} \tag{2.47}$$

In the relative motion's approach mentioned before, to compute the eccentricity perturbation the ER3BP must be expressed in a coordinate system centered on Phobos, which is Phobos' Hill's frame of its elliptic orbit. In this frame, Phobos is fixed whereas Mars and the system's barycenter pulsate. This translation follows the Keplerian motion in Eq.2.45 of Mars and Phobos orbits around the barycenter, expressed now in the Hill's rotating coordinates. Therefore positions and velocities are transformed from Eq.2.44 accordingly, and a new term appears in the dynamics, since the apparent translational acceleration in Eq.2.2 of the origin is now not null.

$$\begin{aligned}\ddot{\mathbf{q}} = &-\frac{Gm_2}{\|\mathbf{r}\|^3}\mathbf{q} - \frac{Gm_1}{\left\|\mathbf{q} - l(\nu)\begin{bmatrix}-1\\0\\0\end{bmatrix}\right\|^3}\left(\mathbf{q} - l(\nu)\begin{bmatrix}-1\\0\\0\end{bmatrix}\right) + \\ &- \omega_z(\nu)^2\mathbf{P}\left(\mathbf{q} - l(\nu)\begin{bmatrix}-(1-\mu)\\0\\0\end{bmatrix}\right) - \dot{\omega}_z(\nu)\mathbf{W}\left(\mathbf{q} - l(\nu)\begin{bmatrix}-(1-\mu)\\0\\0\end{bmatrix}\right) + \\ &- 2\omega_z(\nu)\mathbf{W}\left(\dot{\mathbf{q}} - \dot{l}(\nu)\begin{bmatrix}-(1-\mu)\\0\\0\end{bmatrix}\right) - \left(-\ddot{l}(\nu)\begin{bmatrix}-(1-\mu)\\0\\0\end{bmatrix}\right)\end{aligned} \tag{2.48}$$

$$\begin{cases}\dot{l}(\nu) = p\frac{e\sin\nu}{(1+e\cos\nu)^2}\omega_z(\nu) = an\frac{e\sin\nu}{(1-e^2)^{1/2}} \\ \ddot{l}(\nu) = an\frac{e\cos\nu}{(1-e^2)^{1/2}}\omega_z(\nu) = an^2\frac{(1+e\cos\nu)^2}{(1-e^2)^2}e\cos\nu = l(\nu)\frac{e\cos\nu}{1+e\cos\nu}\omega_z^2(\nu)\end{cases} \tag{2.49}$$

The four added terms represent the four usual acceleration terms of the Keplerian motion in a polar coordinate frame (radial, centripetal, transversal and Coriolis), and their sum is therefore equal to the gravity of Mars at Phobos (which is only radial). Eq.2.50 presents the ER3BP in the Hill's frame of the secondary, before any normalization.

$$\begin{aligned}\ddot{\mathbf{q}} = &-\frac{Gm_2}{\|\mathbf{q}\|^3}\mathbf{r} - \frac{Gm_1}{\left\|\mathbf{q} - l(\nu)\begin{bmatrix}-1\\0\\0\end{bmatrix}\right\|^3}\left(\mathbf{q} - l(\nu)\begin{bmatrix}-1\\0\\0\end{bmatrix}\right) + \\ &- \omega_z(\nu)^2\mathbf{P}\mathbf{q} - \dot{\omega}_z(\nu)\mathbf{W}\mathbf{q} - 2\omega_z(\nu)\mathbf{W}\dot{\mathbf{q}} - \left(\frac{GM}{l(\nu)^2}\begin{bmatrix}-(1-\mu)\\0\\0\end{bmatrix}\right)\end{aligned} \tag{2.50}$$

The special case of the CR3BP in the Hill's frame is retrieved assuming zero eccentricity.

$$\ddot{\mathbf{q}} = -\frac{Gm_2}{\|\mathbf{q}\|^3}\mathbf{r} - \frac{Gm_1}{\left\|\mathbf{q} - a\begin{bmatrix}-1\\0\\0\end{bmatrix}\right\|^3}\left(\mathbf{q} - a\begin{bmatrix}-1\\0\\0\end{bmatrix}\right) - n^2\mathbf{P}\mathbf{q} - 2n\mathbf{W}\dot{\mathbf{q}} - \left(\frac{GM}{a^2}\begin{bmatrix}-(1-\mu)\\0\\0\end{bmatrix}\right) \tag{2.51}$$

In conclusion, the eccentricity perturbation, at a fixed true anomaly, is the difference of the relative acceleration field between Eq.2.50 and Eq.2.51. Its opposite is the action that an appropriate control system would demand to the actuators in order to maintain a target trajectory expressed in the relative state from Phobos and computed in the circular case, when the real environment corresponds instead to the elliptic case.

$$\begin{aligned}\mathbf{a}_{ECC}(\mathbf{r},\dot{\mathbf{r}}) &= \ddot{\mathbf{r}}_{CR3BP}(\mathbf{r},\dot{\mathbf{r}}) - \ddot{\mathbf{r}}_{ER3BP}(\mathbf{r},\dot{\mathbf{r}}) \\ &= \ddot{\mathbf{r}}_{CR3BP}^{G2,G1,A_{ROT}}(\mathbf{r},\dot{\mathbf{r}}) - \ddot{\mathbf{r}}_{ER3BP}^{G2,G1,A_{ROT}}(\mathbf{r},\dot{\mathbf{r}}) + \ddot{\mathbf{r}}_{CR3BP}^{A_{TRANSL}}(\mathbf{r}) - \ddot{\mathbf{r}}_{ER3BP}^{A_{TRANSL}}(\mathbf{r}) \\ &= \left(\ddot{\mathbf{r}}_{CR3BP}^{G2,G1,A_{ROT}}(\mathbf{r},\dot{\mathbf{r}}) - \ddot{\mathbf{r}}_{ER3BP}^{G2,G1,A_{ROT}}(\mathbf{r},\dot{\mathbf{r}})\right) - \left(\ddot{\mathbf{r}}_{CR3BP}^{G1}\left(\begin{bmatrix}0\\0\\0\end{bmatrix}\right) - \ddot{\mathbf{r}}_{ER3BP}^{G1}\left(\begin{bmatrix}0\\0\\0\end{bmatrix}\right)\right)\end{aligned} \tag{2.52}$$

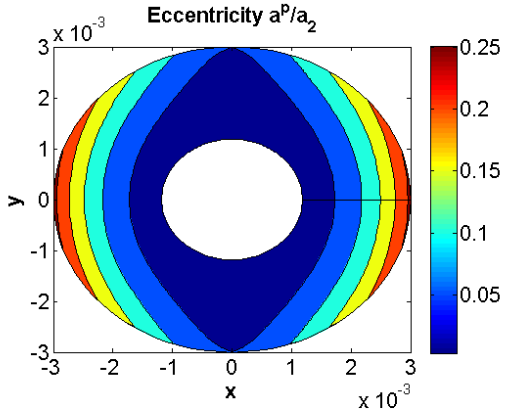

Figure 2.10: **Differential eccentricity perturbation.** The maximum magnitude a^P of the eccentricity perturbation of Eq.2.52 is shown as a ratio a^P/a_2 with respect to the magnitude a_2 of Phobos' Keplerian gravity term in the point. Phobos realm.

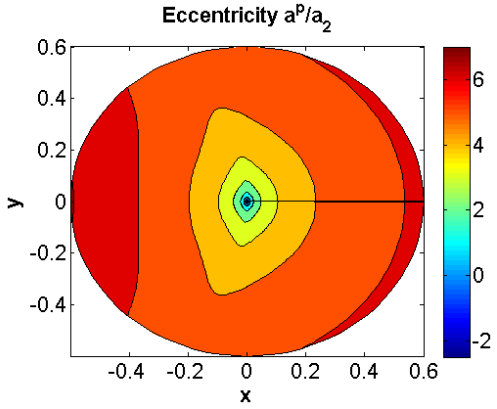

Figure 2.11: **Differential eccentricity perturbation.** The maximum magnitude a^P of the eccentricity perturbation of Eq.2.52 is shown as a ratio a^P/a_2 (in logarithmic scale) with respect to the magnitude a_2 of Phobos' Keplerian gravity term in the point.

The Eq.2.52 of the eccentricity perturbation has been rearranged in a different way, separating from the two relative accelerations the related couple of apparent translational terms, associated to the relative motion of the frame's center. This is to show that the second couple could be calculated from the gravity of the primary at Phobos in the two dynamics.

Fig.2.10-2.11 present the outcomes of the eccentricity perturbation in the Mars-Phobos CR3BP for maintenance of a fixed relative position with respect to Phobos' Hill's frame. Analysis is undertaken in the orbital plane, since an out-of-plane component would simply increase the planar value. In particular, Fig.2.10 focuses on Phobos' SOI, proving that the disturbance increases with the distance from Phobos, and accounts for a magnitude about the 6% of the Phobos' gravity at the SOI's boundary, with the maximum effect always at perimars for points along the x-axis, and in quadrature for points along the y-axis. This relative error is in accordance with the static value of the L_{1-2} location. The relative value is also the same if compared with the Sun-Earth scenario, where as mentioned the eccentricity is similar: it is already known that this is enough to destabilize the motion of the LPOs without appropriate station-keeping. The great and unexpected difference is that despite Phobos is minuscule if compared to the Earth, due to the collapsing of the SOI, Phobos' gravity at its SOI's boundary is 14 times the Earth's gravity at its SOI's boundary, for a value of $2.6mm/s^2$. Therefore, the eccentricity perturbation of Phobos is even larger in absolute value than that of the Earth and would require a significant amount of thrust ($0.02N - 0.2N$ for a $100kg - 1,000kg$ spacecraft) but in particular of fuel ($13m/s$ per day) to be counteracted.

2.4.3 Differential Perturbations Analysis

An important point to consider in conducting the orbital perturbations analysis is that the objective is to model the motion in close proximity to Phobos. Therefore the aim is to investigate the effect of the perturbations in the CR3BP affecting the relative motion with respect to Phobos. This is the same observation made in section 2.4.2 to derive the formula for the eccentricity perturbation. Therefore, evaluating the physical perturbations of section 2.4.1 with the given formulas is not sufficient, because all the disturbances not due to Phobos affect the motion of the moon itself. In order to *maintain the same relative state with respect to the secondary*, a full relative motion approach must be considered. This is close to the Formation Flying dynamics, where Phobos could be considered the "chief spacecraft" that the actual spacecraft follows in proximity like the "deputy". In this framework, it is well-known that the relative dynamics of the deputy spacecraft is affected by the differential perturbations between the chief and itself. This means that Mars' GHs, the 4Bs disturbance, SRP, and MRP should be considered as a difference from their same value computed at Phobos' center of mass. The eccentricity perturbation derived in Eq.2.52 already embeds this difference. Thus, in the framework of relative dynamics, these perturbations are all highly lowered in proximity of the moon, where they tend to zero, and increases with the distance from the secondary. In the case of Phobos, SRP and MRP are not significantly altered because the orbit of Phobos itself is not significantly altered too by them (the area-to-mass ratio of a celestial body is smaller than the one of a spacecraft). On the contrary, the effect is significant for the Mars J_2 perturbation, because Phobos' orbit around Mars is not Keplerian, but more closely follows a classical low-altitude J_2 perturbed orbit. This could be proved just looking at the ephemerides of Phobos for some revolutions: the mean orbital elements' variations, or more easily the secular variations of the osculating ones, are close to the classical predictions provided by the central body's oblateness effect.

A second point to consider is the reference trajectory where the disturbances must be evaluated. Since this analysis is undertaken to derive a basic reference for the orbital perturbations on the Mars-Phobos CR3BP, it will be applied for the simple case of fixed relative points. Also, since the interest is in the dynamics near Phobos, due to the small size of its SOI, all the perturbations are nearly isotropic, and the only variable for this simple analysis is the radial distance from Phobos along the Mars-Phobos direction (apart from the eccentricity, which has been evaluated along all three directions).

Outcomes of the differential analysis are presented in Fig.2.12-2.13, where the magnitude of the perturbations a^P is shown as a ratio a^P/a_2 with respect to the magnitude a_2 of Phobos' Keplerian gravity term in the point, and they correspond to the graph of the perturbations a^P produced in [78]. Inside the Phobos' SOI, all the fourth body effects and PRP are definitely far lower than Phobos' and Mars' first zonal harmonics. Mars' J_2 and the Sun's gravity differential perturbations become significant as Phobos'

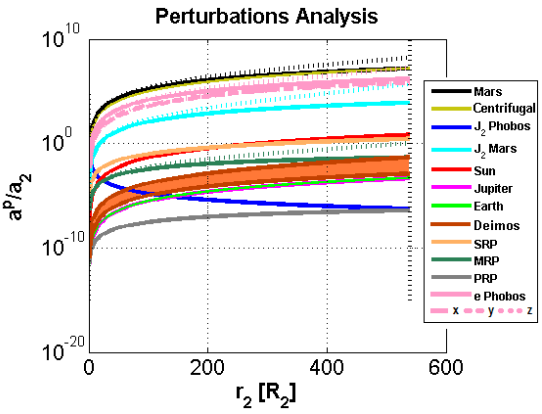

Figure 2.12: **Differential perturbations analysis.** In case of double lines for the same perturbation, plain one is for outward distance, dotted one for inward distance from Phobos towards Mars. Final distance value is Phobos' altitude over Mars.

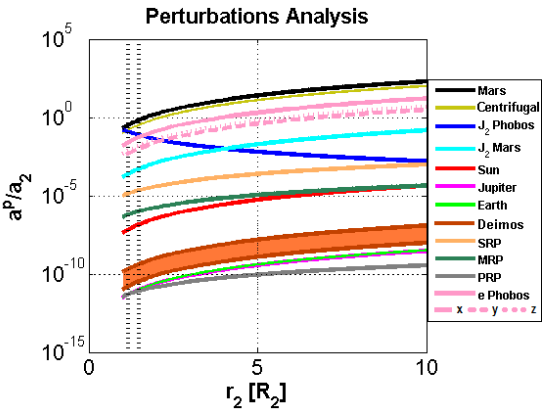

Figure 2.13: **Differential perturbations analysis inside Phobos' sphere of influence.** Vertical dotted lines indicate Phobos' major size and Hill's SOI's radius.

basic gravity respectively at 20 and 300 Phobos radii, and it is remarkable to underline that now the SRP effect overlooks the Sun's gravity up to 200 Phobos radii (but also the MRP does the same up to 10 Phobos radii).

In conclusion, *the CR3BP does not provide an accurate approximation to describe the Mars-Phobos system's dynamics*: **the gravity harmonics and the orbital eccentricity of Phobos are the main orbital perturbations in proximity of the moon**. **Outside its Hill's SOI boundary the eccentricity becomes the dominant term, with Mars' J_2 being the second most influential**. The consideration of the Sun's gravity is needed only for the design of the interplanetary transfer trajectory arriving and leaving the Phobos' orbit. In chapter 3, both the gravity harmonics and eccentricity will be incorporated into the modeling of the relative dynamics near Phobos, to derive an improved model where computing the LPOs about the Martian moon.

2.5 Radiation Environment

Space is an environment very different and distant from the normal perception that people have living on the Earth's surface. Vacuum is definitely the most peculiar effect we associate to spacecraft and space missions. It is indeed the focal point of the space environment, but its effects cover different physical aspects. First of all, the resulting absence of atmosphere (at exception of other planetary environments) produces mechanical and chemical implications, which is to be responsible for the lack of external pressure and for the outgassing phenomenon of some materials. These aspects involve the spacecraft's structure and subsystems design, as well as the human crew's physiological and biological effects (called human factors). In particular, the

last topic is connected with a broad range of ergonomics and internal environment aspects. Second of all, there is a thermodynamical implication, which is that the only heat propagation mechanism in space is the radiation. The effects are the extreme temperature interval a spacecraft could be subject to in conditions of light/shadow, but also to the threatful ionizing part[6] of the radiation emitted by the Sun, which is not shielded by the atmosphere and the magnetic field as it happens here on the Earth's surface. In particular, hazardous radiation is currently considered the most challenging engineering aspect, the showstopper as called in [79], in designing a safe manned mission in deep space. Thus, in this section the analysis of the radiation environment around Phobos is conducted, to quantify the sources and levels of radiation that a crewed spacecraft can be subjected to. This will be used in the performance analysis of the orbits around Phobos that are computed in this thesis.

2.5.1 The Space Radiation Environment

The purpose of this section is to introduce the reader to the space radiation environment [80, 81]. The main source of radiation in the Solar System is our "central heating plant" the Sun. It is worth noting that everything known about its constitution and operating principles come from long range observations. For obvious reasons, probably we will never be able to understand its most intimate aspects with studies on the field. The Sun's activity is variable, and follows a 11-years cycle, where we have a maximum and minimum of its variegated emission. This is constituted by gradual radiative and particle production and by impulsive particle events. The first emission is the well-known Solar electromagnetic radiation, whose spectrum could be divided into two zones: the high wavelength rays (radio and microwaves, IR, visible and near UV) constitute the non-ionizing part; the low wavelength rays (far UV, X and γ) constitute the ionizing part. It is well-known that the ozone layer counteracts such low wavelength rays and protects life on the Earth's surface. This source is not important for crewed spacecraft because the electromagnetic waves are easily shielded by the spacecraft's structure. The second gradual emission of the Sun is made of low-energy charged particles[7]. They are mainly protons and electrons, and they constitute a plasma flow, called the solar wind. The solar wind propagates until about $100\,AU$, like a bubble in the Milky Way, named as the Heliosphere, where our Solar System is completely included. The interaction of the solar wind with the magnetic field of a planet produces the so-called Magnetosphere. This is a region where the charged particles remain trapped by

[6] A radiation is said to be ionizing when its interaction with matter releases hazardous energy that changes the electronic or even nuclear configuration of its atoms, which could be able to produce serious damage in the chemical constitution of cells in organic tissues (and so also in the DNA present in their nucleus). Non-ionizing radiation produces instead only vibration and oscillations in the atoms, which is it increases its temperature (in case of extreme conditions, this would be tackled by the thermal subsystem design of the spacecraft).

[7] In similarity with the radiative production, made by the spectrum of electromagnetic rays, a charged particle is usually called cosmic ray.

Table 2.3: **Permissible exposure limits for radiation of astronauts.** Recommended thresholds for the Ef.D. for an entire career exposure interval [82]. The threshold indicated for one year is $0.5Sv$.

Age at exposure	Male	Female
25	$1.5Sv$	$1.0Sv$
35	$2.5Sv$	$1.75Sv$
45	$3.2Sv$	$2.5Sv$
55	$4.0Sv$	$3.0Sv$

the magnetic field lines[8]. The Earth's Magnetosphere is made by two doughnut zones called the Van Allen radiation belts[9]. The particles accumulated on the radiation belts are threatful for a spacecraft, but since they have low-energy, in outer space the solar wind becomes not important for crewed spacecraft because the particles are easily shielded by the spacecraft's structure. Despite the radiation belts are hazardous when crossed, they provide the natural shield that protects life on the Earth's surface, satellites in LEO, and in particular the crew of the ISS, from outer space radiation. Finally, the third kind of Solar emission is made of high-energy charged particles, and they constitute the hazardous ionizing part of the Solar radiation in deep space for the organic tissues, because they have too much energy to be completely stopped by the spacecraft's structure. This emission is collectively called Solar Energetic Particle Events (SEPEs), since their particles are the products of sunspots, solar flares, and coronal mass ejections.

In addition to the Sun, there is a second type of radiation in the Solar System: the Galactic Cosmic Rays (GCRs). These are gradual high-energy charged particles that originate from the interstellar space. The interaction of the GCRs with the solar wind then originates other minor sources of cosmic rays. In particular, since the source of the GCRs is not variable in time, but the reflecting capability of the Heliosphere depends on the Sun's activity, the GCRs are stronger at a minimum of the Solar cycle, and milder at a Solar maximum.

Finally, no other direct sources of threatening radiation are present in the Solar System, because all the other celestial bodies produce only IR electromagnetic emission. But a spacecraft flying in proximity of any planet or minor body is also subjected to an increased amount of solar and interstellar cosmic rays, constituted by the reflection of the rays impacting the celestial body. This is quantified by its albedo coefficient, which depends from the optical properties of the body's surface or atmosphere.

[8]The existence of this effect was first theorized by Prof. Van Allen, and only discovered by chance by the first US satellite (Explorer I, 1958).

[9]Apart from a small amount of heavy ions, the closer belt is made of protons and electrons, while the farther belt is made only of electrons). In particular, due to the Earth's magnetic field irregularities at low altitudes, the inner Van Allen belt has a threatful downward spike which is the famous South Atlantic Anomaly that LEO's spacecraft must avoid.

Table 2.4: **SPENVIS analysis of the Mars' orbital radiation environment.** Outcomes from eMEREM tool: Phobos' orbital altitude, epochs from 2010 to 2030.

Dosimetry Rate for Radiation	Ef.D.	Am.D.Eq.
SEPEs p	$125\mu Sv/h$ $3.0mSv/d$ $1.1Sv/y$	$834\mu Sv/h$ $20.0mSv/h$ $7.3Sv/y$
GCRs p & α	$90\mu Sv/h$ $2.2mSv/d$ $0.8Sv/y$	$19\mu Sv/h$ $0.5mSv/h$ $0.2Sv/y$
Total	$215\mu Sv/h$ $5.2mSv/d$ $1.9Sv/y$	$853\mu Sv/h$ $20.5mSv/h$ $7.5Sv/y$

2.5.2 Dosimetry

This section presents how the effect of the radiation environment is quantified in relation to human factors [83, 84]. Dedicated effects on electric, electromagnetic and electronic equipment (upsets, burn-outs, latch-ups) are not considered in this analysis of the radiation environment around Phobos, but they are essential for any spacecraft [81]. In addition, the spacecraft's structure is obviously a necessary shield for the crew and the payload. This will not be considered in this thesis, because it is part of the dedicated structural design. The objective is to quantify the natural and "gross" effect of the space radiation that a particular orbit around Phobos is subjected to.

The hazards for a manned spacecraft come from the ionizing radiation: its effect is to deposit its energy in the material that it impacts. The primary physical unit of dosimetry of radiation is the Absorbed Dose (Ab.D.), which is the amount of energy that a specific radiation deposits in $1kg$ of a specific material's mass (IS unit is the Grey, Gy). Thus, the Ab.D. depends from the radiation type and material. For human factors, new dosimetry measures are introduced: the physical quantity is the same, but a distinction is made, which is to consider as IS unit for these measures the Sievert, Sv. First, the Ab.D. is weighted trough all the kinds of the impacting radiation's composition: the resulting measure is called Equivalent Dose (Eq.D.). Next, the Eq.D. is weighted trough all the kinds of tissue for a common human body's composition: the resulting measure is called Effective Dose (Ef.D). An alternative approach is to relate the Eq.D. to a reference organic body (called the ICRU sphere), and the resulting measure is called Ambient Dose Equivalent (Am.D.Eq.).

Finally, to evaluate the radiation environment for a space mission, the operative dosimetry value is compared with the estimated allowable dose amount for astronauts. This is based on the recommendations of the National Council for Radiological Protection (NCRP) and it is currently used by both NASA and ESA. From Table 2.3 we see

that this depends on age, gender, and length of the mission.

2.5.3 Radiation Analysis around Phobos

The purpose of this section is to compute an approximate figure for the radiation environment in Phobos' orbit, in order to compare it with the allowable amount for a human crew.

Since Mars' magnetic field is very weak, no trapped particles (and related shielding) constitute the radiation environment for a mission following the orbit of Phobos, which is similar to a deep space environment at the Sun-Mars distance, constituted by two main sources: the protons from SEPEs, and the protons and alpha particles from GCRs [85]. The spectral distribution of the two cosmic rays is very different. GCRs are characterized by a larger energy, instead SEPEs are important due to their higher fluence[10]. GCRs, due to their origin, are isotropically distributed in the Solar System, their activity follows an inverse Solar cycle, and their reference is the ISO 15390 model. The reference model used for the SEPEs is the ESP-PSYCHIC. When a Solar event occurs, these cosmic rays are constituted by both an isotropic and directional part, and the latter depends from the dynamics of the Heliosphere.

For applications to future manned missions to Phobos' orbital environment, an estimation analysis is conducted with the open-source SPENVIS program [86] and its dedicated model for Mars MEREM. This was developed by an European research centers' network with the ESA TEC-SEE section [87, 88, 89]. To derive an approximated figure of the gross effect of the radiation environment (without any shielding effect of the spacecraft structure) to human factors, the Ef.D. is considered.

Table 2.4 summarizes the gross radiation hazards for a mission in Phobos' orbit from 2010 to 2030. The result obtained is Ef.D.= $1.9Sv/y$, $1.1Sv/y$ from SEPEs protons and $0.8Sv/y$ from GCRs protons and alpha particles. This should now be compared with the thresholds of Table 2.3. Considering the case of a 35-year old astronaut, the figure derived from the analysis, for a Martian orbital segment of one year without any structural shielding, falls inside the range 1.75-2.5Sv that indicates the maximum amount of radiation dose that such human crew could be allowed to absorb throughout the entire mission. Thus, the development of a strong shielding strategy for crewed missions to Phobos is required [85].

An interesting idea that has recently gained attention, is that a manned spacecraft, during a Martian orbital mission segment, could exploit Phobos as a passive radiation shield: *staying in its shadowing wake would theoretically counteract the gross Ef.D. of the directional part of the SEPEs, while simply remaining close to the moon will block any incoming isotropic particles (remaining SEPEs and GCRs) as much as its bulk covers the sky.* Following this idea, in this thesis possible orbits to be used also for passive shielding purposes about Phobos are investigated. However, some additional

[10] In thermodynamics, the flow is distinguished into two appropriate measures: the fluence is the density of incoming particles on the unit area; the flux is the fluence rate over time.

albedo effects (of the GCRs neutrons) could be significant, while covering the field of view of the Sun has not been proved to be relevant, as the scattering effect of the particles along the Heliosphere's lines of field is still a current topic of research [90]. Instead, the bulk's occultation is a well-known and suitable strategy [19].

2.6 Lighting Conditions

The purpose of this section is to identify the lighting conditions around Phobos. In particular a spacecraft requires sunlight for the electrical power generation from the solar arrays, and the solar flux decreases with the square of the distance from the Sun. This means that at Phobos, the intensity of the solar rays is between 1.9 (perihelion) and 2.8 (aphelion) times weaker than on Earth orbit, and larger solar arrays would be needed to produce the same amount of power for the payload. However, the spacecraft must also consider the thermal constraints of its subsystems. For this reason, the thermal control subsystem is designed in function of the lighting conditions of the mission to maintain each component within its operative temperature range. In particular, some missions could require the spacecraft to spend a significant time in shadow. Following this, the analysis of this section will quantify the shadowing opportunities about Phobos, that could exploit the wake of the moon as a natural shield against the directional solar radiation.

2.6.1 The Sun-Mars-Phobos R4BP

The derivation of the lighting condition is a purely geometrical analysis. Since the interest is for the positions in Phobos' neighborhood, the analysis is conducted in the Hill's frame of its orbit around Mars. The kinematics must now consider also the motion of the Sun in this frame, using a restricted four-body model to evaluate the FOV of the Sun over time for points around Phobos. Usually two simplified models are used for the R4BP analysis, assuming that all the three massive bodies rotate in couples of circular and co-planar orbits. It should be remarked that this approximation is not coherent, since the resulting 3B motion is not a solution of the Newton's equations of motion [91]. The simplified circular-co-planar models are the Concentric Circular Model (CCM), where two smaller bodies revolve around the massive one (like the situation of two planets in the Solar System, or two natural satellites around their central planet), and the Bicircular Model (BCM), where one body revolves around another in cascade (like the chain Sun-planet-moon). The BCM is obviously the case of the Sun-Mars-Phobos R4BP, but here two problems arise: first, the Mars' heliocentric orbit is the second most elliptic among the Solar System's planets; second, Phobos' orbit is equatorial, which is the resulting orbital plane is inclined with respect to its ecliptic plane by Mars' axial tilt $\theta_M = 25.19°$. These situations are not critical because this analysis does not require an integration of the dynamics, and the motions of Mars

around the Sun, and of Phobos around Mars, are retained from the classical 2B dynamics using the ephemeris of the two bodies at the current epoch of Table 2.1.

The motion of Mars in Phobos' Hill's frame is trivial and was already introduced in section 2.4.2. In order to describe the motion of the Sun around Phobos, a coordinates' transformation is introduced in Eq.2.53-2.54, between the inertial (which is the Sun ecliptic frame at J2000.0) and the relative (which is the adimensional 3B frame) reference frames. In these equations, $\mathbf{v}$ is a general position vector, and the symbols S,P,M identify the bodies of the general Sun-Planet-Moon chain. Thus, the four angles $\Omega_\oplus$, $i_\oplus$, $\omega_\oplus$, $\nu_{\oplus,0}$ are the Keplerian orbital elements of the body $\oplus$, as presented in Table 2.1, with $\nu_\oplus(t)$ and the position $\mathbf{r}(t)$ between the couples calculated from the 2B dynamics' solution. The orbital elements of a moon are defined in the planet's BCE, while the parameters of a planet are expressed in the heliocentric ecliptic frame $SO_E\gamma$. Eq.2.53-2.54 make use of attitude matrices $\mathbf{A}$ to define the rotation between different frames, that are generally constituted by multiple successive rotations $\mathbf{A}_n(\alpha)$ around the n-th coordinate's axis by the angle α. The notation here is simplified with the classical matrix used in the 2B dynamics, which is the chain $\mathbf{A}_3(\omega+\nu)\mathbf{A}_1(i)\mathbf{A}_3(\Omega)$, expressing $\mathbf{A}$ as a function of the respective angles. Finally, to perform the coordinates' transformation, the orientation of a body's spin axis must be taken into account. For every Solar System's planet or satellite, it is defined the right ascension $\alpha_{NP_\oplus}$ and declination $\delta_{NP_\oplus}$ of its North Pole [70]. From them, the North Pole's inclination is $i_{NP_\oplus} = \frac{\pi}{2} - \delta_{NP_\oplus}$, and the Node of reference's location is $\Omega_{N_\oplus} = \frac{\pi}{2} + \alpha_{NP_\oplus}$; for the Earth, the axial tilt $\theta_E = 23.44°$ is directly the North Pole's inclination.

$$\begin{aligned}\mathbf{v}_{SO_E\gamma} =& \mathbf{A}^{PE_E\gamma}_{PO_E\gamma}(\theta_E)\Big(\mathbf{A}^{PE_E\gamma}_{PE_PN_P}(\Omega_{N_P}, i_{NP_P})\Big)^T\Big(\mathbf{A}^{PE_PN_P}_{PH_M}(\Omega_M, i_M, \omega_M, \nu_M(t))\Big)^T \\ & \Big(\mathbf{v}_{3B} - \begin{bmatrix}-\mu\\0\\0\end{bmatrix}\Big) + \Big(\mathbf{A}^{SO_E\gamma}_{SH_P}(\Omega_P, i_P, \omega_P, \nu_P(t))\Big)^T\begin{bmatrix}r^S_P(t)\\0\\0\end{bmatrix}\end{aligned} \tag{2.53}$$

$$\begin{aligned}\mathbf{v}_{3B} =& \begin{bmatrix}-\mu\\0\\0\end{bmatrix} + \frac{1}{r^P_M(t)}\mathbf{A}^{PE_PN_P}_{PH_M}(\Omega_M, i_M, \omega_M, \nu_M(t))\mathbf{A}^{PE_E\gamma}_{PE_PN_P}(\Omega_{N_P}, i_{NP_P}) \\ & \Big(\mathbf{A}^{PE_E\gamma}_{PO_E\gamma}(\theta_E)\Big)^T\Big(\mathbf{v}_{SO_E\gamma} - \Big(\mathbf{A}^{SO_E\gamma}_{SH_P}(\Omega_P, i_P, \omega_P, \nu_P(t))\Big)^T\begin{bmatrix}r^S_P(t)\\0\\0\end{bmatrix}\Big)\end{aligned} \tag{2.54}$$

The position of the Sun in the 3B frame is obtained from Eq.2.54 along time and using the trivial inertial position of the Sun, which is the origin of the starting frame. The resulting Sun's adimensionalized position vector in the 3B frame rotates clockwise with an angular velocity equal to the difference between Phobos' and Mars' revolution rates (dominated by the first), with a fixed declination in the range $[-\theta_M, \theta_M]$ according to the seasonal phase of Mars. In particular, seasons of Phobos correspond chronologically with the ones of Mars, so they are referred in this thesis without any distinction. For

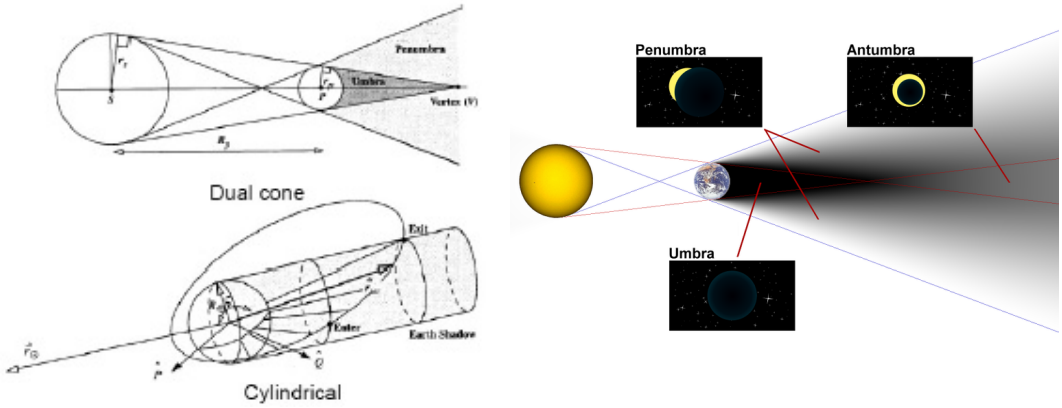

Figure 2.14: **Eclipse models.** [Vallado, Wikipedia]

simplicity, the seasons of Mars are assumed to span in between the planet's solstices and equinoxes, in the same way as they are named for the Northern Hemisphere of the Earth. Also a Martian month is consider to be 1/12 of the Martian year.

2.6.2 Eclipse Modeling

The analysis of the shadowing effects in this system is undertaken using eclipse modeling, which is to derive the zones of light and shadow produced by a shadowing central body $\oplus$ when illuminated by a radiating body $\odot$. The lighting condition is described by a scalar light function field $L_{\odot,\oplus}$. It ranges from 0 to 1 to express the ratio of incident light with respect to the complete light case. Intuitively, the shadow function S is the 1-complement of L. The most accurate eclipse model is the dual-cone model of Fig.2.14, which is able to discriminate positions of complete light ($L = 1$), complete shadow ($L = 0$, also known as umbra) inside a conic wake (the first cone), and penumbra ($L \in (0, 1)$, the second cone)[11]. When the positions of interest are very close to $\oplus$ and when there is a great difference between the two bodies' dimensions, the analysis could be simplified to a cylindric model, see Fig.2.14. This because the two cones' generatrices are close to each other for practical analysis: the penumbra zones in between them vanish, and the generatrices are practically horizontal so the shadowing wake in the region is cylindrical. The resulting positions are only in complete light or shadow.

Both the two eclipse models are axial-symmetric along the conjunction line between radiating and shadowing body, when their shape is both approximated with their mean sphere. Thus the light functions are expressed in the half-plane whose reference axis is such conjunction line. Eq.2.55 presents the light function of the cylindrical model for a generic point P. Eq.2.56-2.58 present the algorithm to compute the light function of the conic model: first the position of interest P is queried to be inside one of the cones

[11] The continuation of the cone of umbra is a subset of the cone of penumbra, specifically known as antumbra.

of umbra and penumbra, and then the percentage of incident light is determined if the position is in penumbra.

$$\begin{cases} \beta_u = \frac{\pi}{2} \\ \beta_\oplus(P) = \arccos\left(\hat{\mathbf{r}}_P^\oplus \hat{\mathbf{r}}_\oplus^\odot\right) \end{cases} \Rightarrow \begin{cases} \beta_\oplus \geq \beta_u \rightarrow L_{\odot\oplus}(P) = 1 \\ \beta_\oplus < \beta_u \rightarrow \begin{cases} \sin\beta_\oplus \geq \frac{R_\oplus}{\|\mathbf{r}_P^\oplus\|} \rightarrow L_{\odot\oplus}(P) = 1 \\ \sin\beta_\oplus < \frac{R_\oplus}{\|\mathbf{r}_P^\oplus\|} \rightarrow L_{\odot\oplus}(P) = 0 \end{cases} \end{cases} \tag{2.55}$$

$$\begin{cases} \beta_u = \arccos\frac{R_\odot - R_\oplus}{\|\mathbf{r}_\oplus^\odot\|} \\ \beta_p = \arccos\frac{R_\odot + R_\oplus}{\|\mathbf{r}_\oplus^\odot\|} \\ \gamma_{Vu} = \frac{\pi}{2} - \beta_u \\ \gamma_{Vp} = \frac{\pi}{2} - \beta_p \end{cases} \begin{cases} \mathbf{r}_{Vu}^\oplus = \frac{R_\oplus}{R_\odot - R_\oplus}\mathbf{r}_\oplus^\odot \\ \mathbf{r}_{Vp}^\oplus = -\frac{R_\oplus}{R_\odot + R_\oplus}\mathbf{r}_\oplus^\odot \\ \mathbf{r}_{Vu}^\odot = \frac{R_\odot}{R_\odot - R_\oplus}\mathbf{r}_\oplus^\odot \\ \mathbf{r}_{Vp}^\odot = \frac{R_\odot}{R_\odot + R_\oplus}\mathbf{r}_\oplus^\odot \end{cases} \tag{2.56}$$

$$\begin{cases} \beta_{Vup} = \frac{\pi}{2} + \frac{\beta_u}{2} - \frac{\beta_p}{2} \\ \left\|\mathbf{r}_{Vup}^\oplus\right\| = \frac{R_\oplus}{\sin\left(\frac{\beta_u}{2} + \frac{\beta_p}{2}\right)} \end{cases} \begin{cases} \beta_\oplus(P) = \arccos\left(\hat{\mathbf{r}}_P^\oplus \hat{\mathbf{r}}_\oplus^\odot\right) \\ \beta_{Vu}(P) = \arccos\left(\hat{\mathbf{r}}_P^{Vu} \hat{\mathbf{r}}_{Vu}^\odot\right) \\ \beta_{Vp}(P) = \arccos\left(\hat{\mathbf{r}}_P^{Vp} \hat{\mathbf{r}}_{Vp}^\odot\right) \end{cases}$$

$$\begin{cases} \beta_\oplus \geq \pi - \beta_p \rightarrow L_{\odot\oplus}(P) = 1 \\ \beta_\oplus < \pi - \beta_p \rightarrow \begin{cases} \beta_{Vp} \geq \gamma_{Vp} \rightarrow L_{\odot\oplus}(P) = 1 \\ \beta_{Vp} < \gamma_{Vp} \rightarrow \begin{cases} \beta_\oplus \geq \beta_u \rightarrow L_{\odot\oplus}(P) = p \\ \beta_\oplus < \beta_u \rightarrow \begin{cases} \beta_{Vp} \leq \pi - \gamma_{Vu} \rightarrow L_{\odot\oplus}(P) = p \\ \beta_{Vp} > \pi - \gamma_{Vu} \rightarrow L_{\odot\oplus}(P) = 0 \end{cases} \end{cases} \end{cases} \end{cases} \tag{2.57}$$

$$\begin{cases} \delta_\oplus(P) = \arcsin\left(\hat{\mathbf{r}}_P^\oplus\right) \\ \delta_\odot(P) = \arcsin\left(\hat{\mathbf{r}}_P^\odot\right) \\ \alpha_\oplus(P) = \arcsin\left(\frac{R_\oplus}{\|\mathbf{r}_P^\oplus\|}\right) \\ \alpha_\odot(P) = \arcsin\left(\frac{R_\odot}{\|\mathbf{r}_P^\odot\|}\right) \end{cases} \begin{cases} \Delta\delta = |\delta_\oplus - \delta_\odot| \\ \theta_\oplus = \arccos\left(\frac{{\alpha_\oplus}^2 - {\alpha_\odot}^2 + \Delta\delta^2}{2\alpha_\oplus \Delta\delta}\right) \\ \theta_\odot = \arccos\left(\frac{{\alpha_\odot}^2 - {\alpha_\oplus}^2 + \Delta\delta^2}{2\alpha_\odot \Delta\delta}\right) \end{cases}$$

$$L_{\odot\oplus}(P) = p \Rightarrow \begin{cases} \Delta\delta > |\alpha_\odot - \alpha_\oplus| \rightarrow L_{\odot\oplus}(P) = 1 - \frac{\frac{1}{2}{\alpha_\odot}^2(2\theta_\odot - \sin 2\theta_\odot) + \frac{1}{2}{\alpha_\oplus}^2(2\theta_\oplus - \sin 2\theta_\oplus)}{{\alpha_\odot}^2} \\ \Delta\delta \leq |\alpha_\odot - \alpha_\oplus| \rightarrow L_{\odot\oplus}(P) = 1 - \frac{{\alpha_\oplus}^2}{{\alpha_\odot}^2}\,(antumbra) \end{cases} \tag{2.58}$$

2.6.3 Sun-Mars Eclipses

The approach used is to analyze the shadowing effect of each couple of bodies. The first case is the Sun-Mars couple. Here the interest is to determine the value of L at the Phobos' location. Using the dual-cone model the location of the two cones' vertexes is approximately of 118 3B length units (always the Mars-Phobos semi-major axis). This value is definitely large if compared to Phobos' location. Fig.2.15 shows the generatrices of the umbra cone (due to the ellipticity of Phobos and Mars' orbits, the fixed length normalization results in Mars' and Phobos' radii to be variable over the Mars' seasonal phase). The inclination of the generatrices varies over the Martian

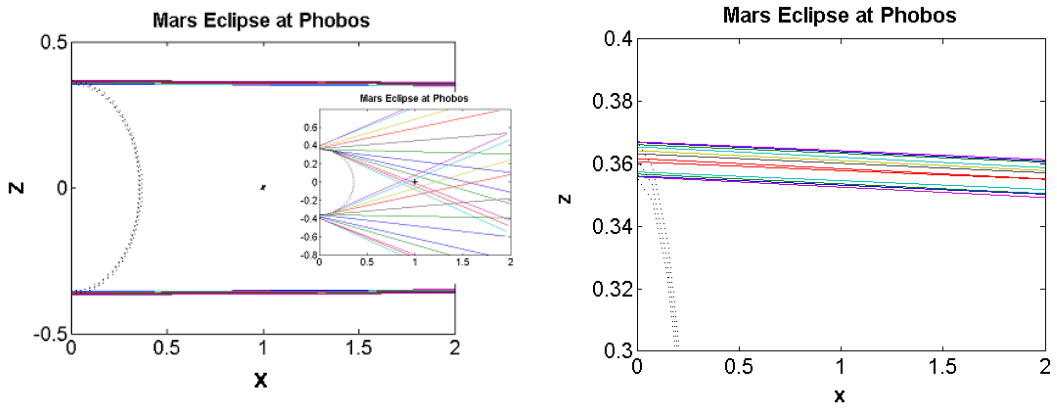

Figure 2.15: **Sun-Mars eclipse at Phobos.** Dual-cone model. Relative size of the cone with respect to Phobos taken first from equinoctial case at left, then actual seasonal variations in the adimensional model highlighted.

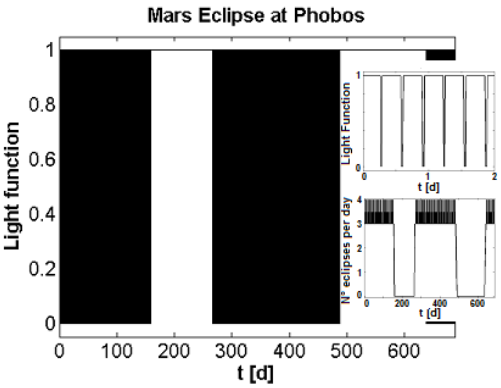

Figure 2.16: **Sun-Mars eclipse at Phobos.** Cylindric model. Light function, highlight of daily variation and number of eclipses per terrestrial day.

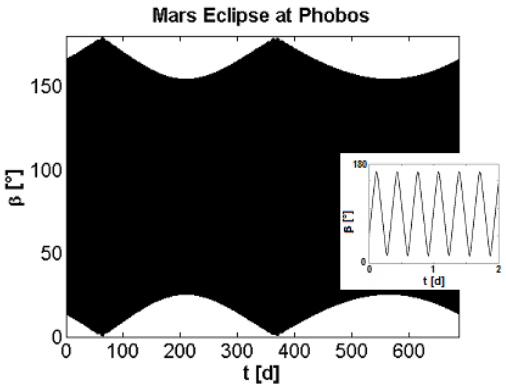

Figure 2.17: **Sun-Mars eclipse at Phobos.** Cylindric model. Lighting angle, highlight of daily variation.

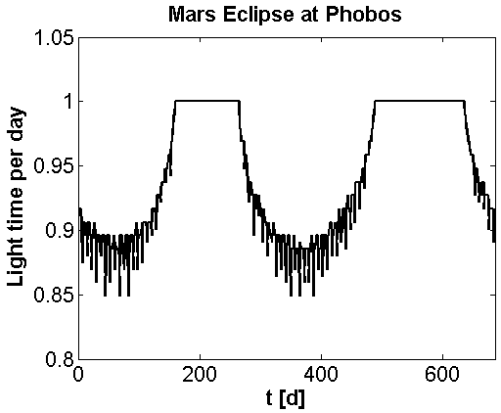

Figure 2.18: **Sun-Mars eclipse at Phobos.** Phobos' eclipse times per terrestrial day.

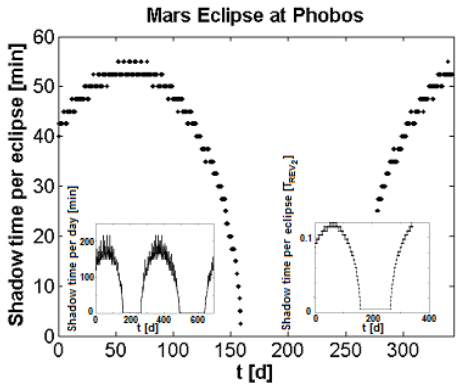

Figure 2.19: **Sun-Mars eclipse at Phobos.** Phobos' eclipse times per Phobos' day, highlight of aggregated time per day and fraction with respect to Phobos' period.

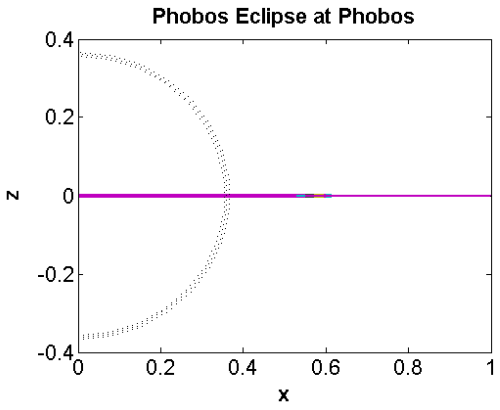

Figure 2.20: **Sun-Phobos eclipse.** Dual-cone model. Relative size of the cone with respect to the Phobos' orbital distance.

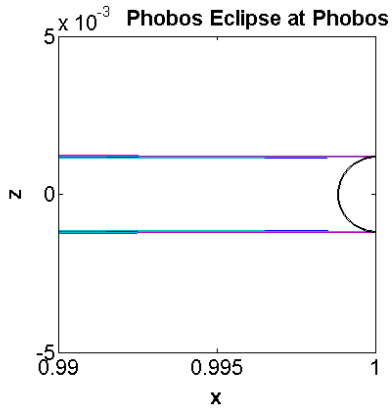

Figure 2.21: **Sun-Phobos eclipse.** Dual-cone model. Relative size of the cone inside the Phobos' neighborhood.

year from zero at the equinoxes to $\pm\theta_M$ at the solstices. Thus, Phobos' SOI is just a near and small domain in the Mars' shadowing wake. Therefore the analysis of the Sun-Mars eclipse is undertaken with the cylindric model.

The results over a full Martian year are summarized in Fig.2.16-2.19. The simulation starts from the epoch value indicated in Table 2.1, when Mars is close to its descending node, and moving towards its perihelion: since Martian summer happens at aphelion, this means that the start is during fall. The β angle of Phobos is related to the position of Phobos with respect to Mars' ecliptic plane, and it has a small-period variation due to the fast revolution of Phobos, and a long-period variation due to Mars' revolution. Amplitude of the oscillation is larger at Mars' equinoxes and smaller at Mars' solstices. The resulting light function oscillates three times a day from 1 to 0, until the inclination of the Sun with respect to the 3B orbital plane is high enough such that Mars' shadow cone does not enclose Phobos any longer, see Fig.2.15. This happens during Mars' winter and summer, when the light function becomes 1 and Phobos is constantly in light, without Martian eclipses. It is worth to remark that due to Mars' high eccentricity, seasons are unequal, with the Northern hemisphere of Mars and Phobos experiencing a summer longer than that occurring in the South. Summarizing, Phobos' daily value of the Sun-Mars light function during equinoxes is 88%, resulting in a maximum eclipse time of $54min$ (12% of Phobos' daytime). Summer's total light period is about 164 days (3 Martian months), and in the winter this is about 110 days (2 months). Middle seasons at Phobos are both about 200 days.

2.6.4 Sun-Phobos Eclipses

The second case is the shadowing effect provided by the Sun-Phobos couple, which is the most interesting. For this preliminary analysis, the mean spherical shape of Phobos is considered, since the direction of the axis of the umbra cone is not significantly affected by the real shape. Instead, the shape of the shadow wake differs from a cone

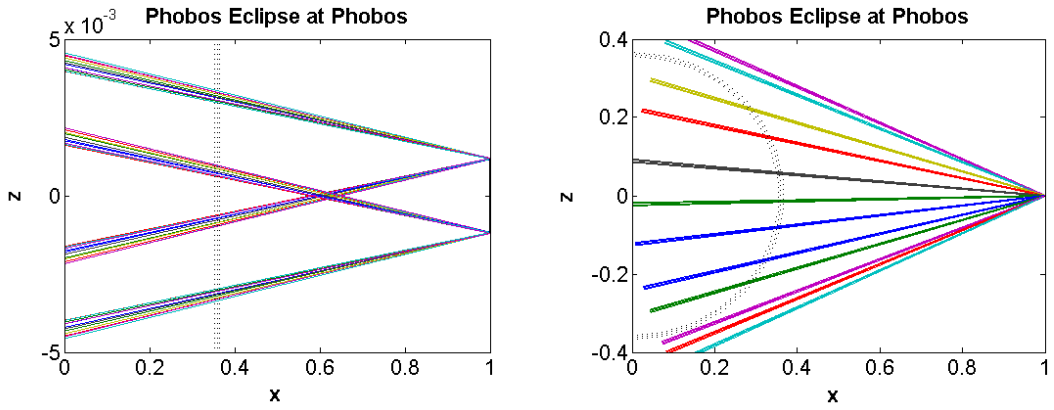

Figure 2.22: **Sun-Phobos eclipse.** Dual-cone model, seasonal variation. At left, size comparison assuming the Sun in perfect opposition to Mars. At right, real orientation of the cones.

as long as the distance from Phobos decreases. However, while orbiting the moon the accumulated differences become milder due to averaging effect. Considering an ellipsoidal approximation of Phobos' shape, the shadow wake is thinner than the one obtained with a mean spherical model, from the 3% during solstices to the 9% during equinoxes.

Using the conic model, Fig.2.20-2.23 highlight the relative size of the umbra and penumbra cones, again with their seasonal variations, orienting the Sun opposite to Mars with respect to Phobos. The location of the two cones' vertexes is placed at a distance of 327 Phobos' radii. This distance is the 39% of the Phobos' orbital distance, thus the conic model should be used for mission segments out of 10 times the Phobos' SOI boundary, but the size of Phobos' shadow is also very narrow (at Mars surface, its maximum radius in antumbra is 3 Phobos' radii), as we see in Fig.2.22-2.23. Therefore, the cylindric approximation is suitable in proximity of Phobos to model the Sun-Phobos eclipses. At the SOI's boundary the errors are less than 1%, while at 10 Phobos' radii distance, the deflection of the real shadow cones is between 2% and 6% (considering seasonal variations). Finally, at 100 Phobos' radii distance (one tenth of Phobos' orbital distance) the error is between 25% and 33%.

Unlike the Sun-Mars L_1, the Sun-Phobos L_2 is a time-variant 3D field. The mean integral value $\bar{L}_2$ along one Phobos' revolution period, for a given distance to Phobos, is minimum on the surface of motion where the conjunction line between the anti-Sun and Phobos revolves, shortly becoming 1 in points out of the surface: such minimum value rapidly increases with the distance from Phobos. This is shown in Fig.2.24: from $\bar{L} = 50\%$ at the body's surface, $\bar{L} = 78\%$ at the SOI's boundary, $\bar{L} = 83\%$ at 2 Phobos' radii.

2.6.5 Mars-Phobos Eclipses

The last shadowing case is the Mars-Phobos couple. Since the radiation of Mars (without the albedo) is inside the IR spectra, such eclipse analysis is neglected because it

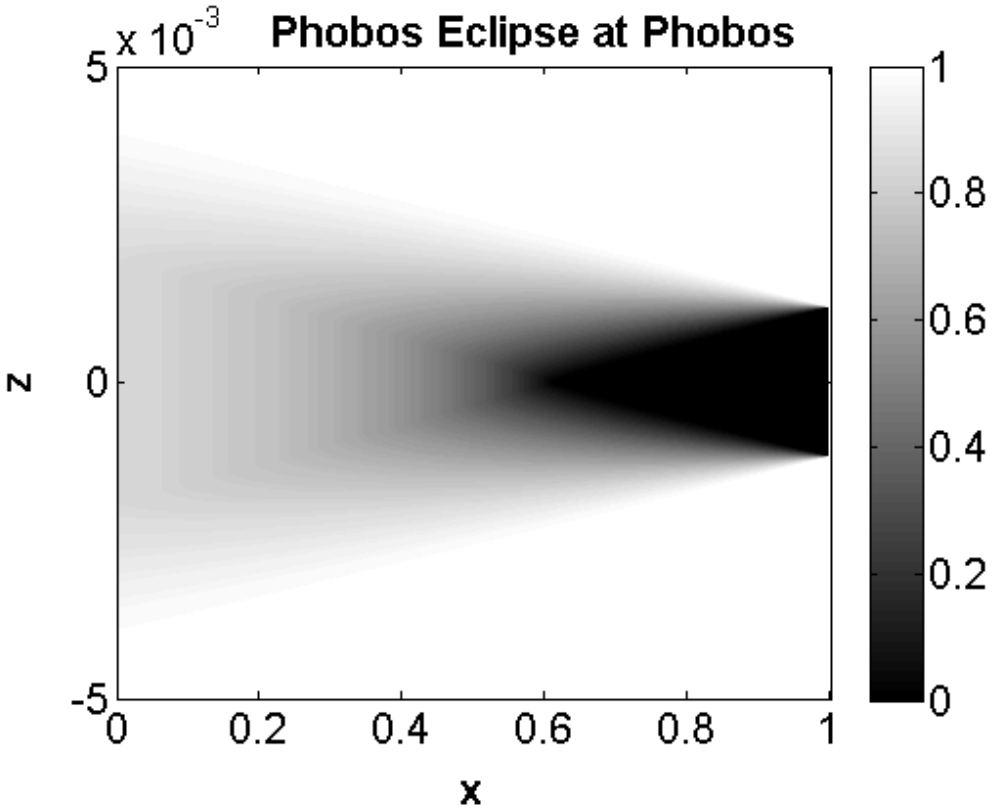

Figure 2.23: **Sun-Phobos eclipse.** Dual-cone model. Light function.

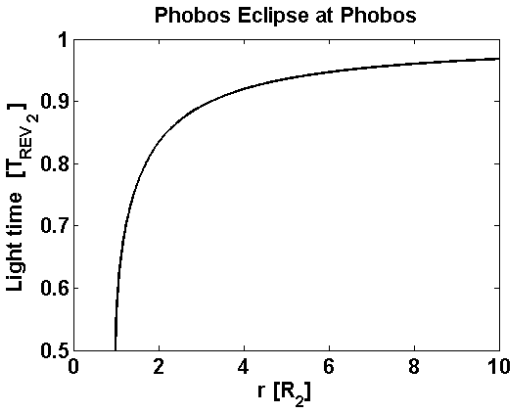

Figure 2.24: **Sun-Phobos eclipse at Phobos.** Mean light function versus distance from Phobos on the anti-Sun surface of motion, from Eq.2.61.

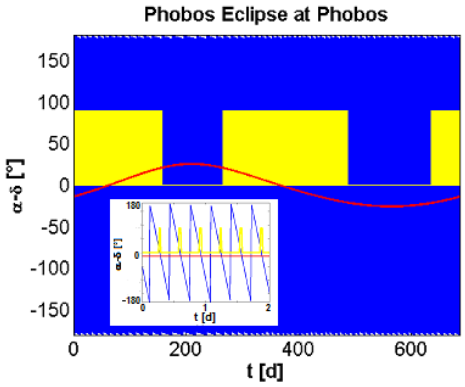

Figure 2.25: **Sun-Mars-Phobos eclipse at Phobos.** Anti-Sun location (declination in red, right ascension in blue) and Mars shadow function at Phobos in yellow, with local magnification.

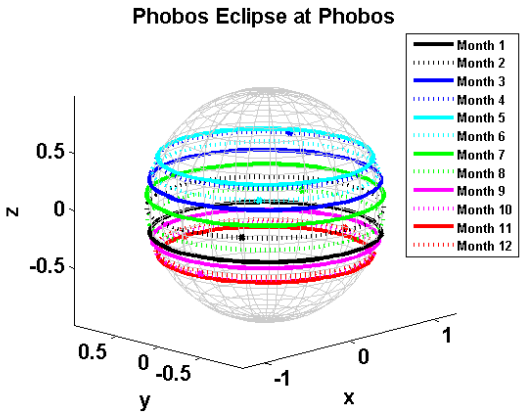

Figure 2.26: **Sun-Mars-Phobos eclipse at Phobos.** Anti-Sun daily orbit in spherical coordinates around Phobos over the Martian year. Martian eclipses during equinoctial seasons occur when the anti-Sun is on the positive side of the x-axis of the Hill's frame.

brings little variation to the lighting conditions (from Fig.2.13, MRP flux at Phobos is two orders of magnitude lower than SRP one). It is only worth to note that the analysis of this case must be undertaken with the dual-cone model, because the location of the two cones' vertexes is 2.77 Phobos' radii, so just outside the SOI of the moon.

2.6.6 Sun-Mars-Phobos Eclipses

The conclusion of the analysis of the lighting conditions is now obtained combining the previous single couples into a system of three massive bodies of a R4BP, focusing the analysis in Phobos' neighborhood. The Sun-Mars L_1 is simply a scalar value along the Martian year, while the Sun-Phobos L_2 field must now consider the real dynamics of the Sun, which is moving in the 3B frame of reference, as discussed in section 2.6.1. Actually the analysis considers the direction of the anti-Sun $\odot'$ because it is more immediate to relate it with the position of the shadowing wake of Phobos. Fig.2.25 shows that the declination of the anti-Sun is periodic along one Martian year simulation, close to Mars' axial tilt during summer and winter. Instead the right ascension, which is the azimuthal phase, varies with the revolution phase of Phobos. The outcome is highlighted in Fig.2.26, that presents a complete orbit of the anti-Sun, for every season. The cylindrical shadowing wake of Phobos revolves clockwise around its spin axis with the period of Phobos, and varies its inclination with the season $\theta_{\odot'} \in [-\theta_M, \theta_M]$ (when the anti-Sun is in the Northern hemisphere, we are in winter). Besides, Phobos' realm is in complete shadow when a Martian eclipse occurs, which is when the anti-Sun is close to the positive direction of the Hill's x-axis frame, enduring from a maximum at the equinoxes to zero during summer and winter.

The procedure used to compute the light function of the 4B model in proximity of Phobos follows two steps. The first step is to compute the Sun-Phobos mean integral

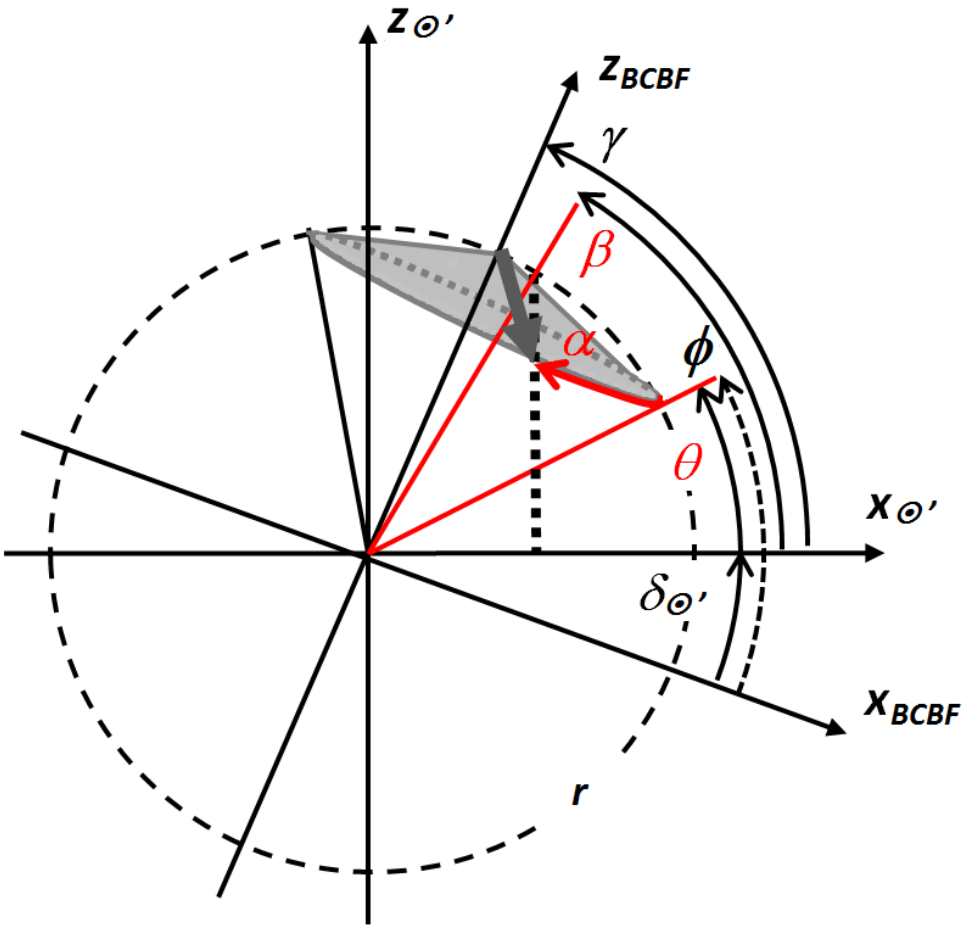

Figure 2.27: **Sun-Mars-Phobos eclipse at Phobos.** Reference frames and angles for the analysis.

field $\bar{L}_2$ over one Phobos' revolution for different seasons. The approach taken could be generalized in such a way. An axial-symmetric functional (the Sun-Phobos light function) is defined in the half-plane along the two bodies' conjunction line. This reference plane spins around a given direction (the Phobos' spin axis), which is generally tilted from the two bodies' conjunction line. For any point in a frame where the attitude of the shadowing body (Phobos) is fixed, the aim is to find the mean integral value of the functional, experienced at the point's position over one revolution of the radiating body (the Sun). In particular, the tilt angle is considered fixed during one rotation, and the value of this parameter represents the season over the Phobos' year. The mean integral value of the function will be defined in the Phobos' BCBF frame[12] and Fig.2.27 provides the reference frames and variables for this analysis. In this 2D graph, the plane corresponds to the one where the light function domain is fixed. Thus, the position of the Sun is fixed and the direction of the anti-Sun is the reference x-axis. The second frame in the graph is Phobos' BCBF frame, whose vertical axis is misaligned from the previous frame by the current anti-Sun declination $\delta_{\odot'}$. This frame is not fixed, so let imagine it rotates along its spin z-axis. Thus, a fixed point of the BCBF frame, with distance r and declination ϕ, results in a circular path around its spin axis, that goes out of the plane of the graph. This is visualized in the graph as the baseline spanned by the 3D gray cone. But since the functional is axial-symmetric, the profile of the light function that the point encounters over time could be evaluated on the plane, finding geometrically the points[13] where the light function value is the same encountered by the rotating point. This approach avoids a 3D integration over time by doing a 2D integration along one angular coordinate, which requires far less computational cost. In particular if this is performed in polar coordinates, the 2D integral is uncoupled, and the integration becomes simply 1D, and also symmetrical along the spin axis.

The general solution is presented in Eq.2.59. For convenience, $\gamma = \frac{\pi}{2} - \delta_{\odot'}$ is used in place of the anti-Sun declination, and $\theta = \phi - \delta_{\odot'}$ is used in place of the BCBF declination. For a given γ (the seasonal tilt), and for every radial distance r in the BCBF frame, each θ provides a 1D set of angles $\beta(\alpha)$[14], where $\alpha = n_{ROT}t$ is simply the spin phase of Phobos. These angles β, together with r, constitute the 1D domain in polar coordinates that represents a trajectory in the fixed reference plane of the light function of Fig.2.27. The light function profile in these equivalent points is the same encountered by the rotating point in (r,ϕ) of the BCBF frame. Thus, the cylindrical light function is evaluated in $(r,\beta(t))$ from Eq.2.55, and the respective mean integral value $\bar{L}$ is computed. In addition, for the particular case of a cylindrical light function, the analytical solution of the integration could be derived, and it is expressed in Eq.2.60. In the singular cases of this formula, the light function encountered by the rotating point is constant, so the mean value is simply the initial one.

[12] Recall from section 2.1 that Phobos' attitude is approximately fixed in its Hill's frame.

[13] These equivalent points are not the projection on the plane of the real trajectory.

[14] This is the law of the cosines for a particular spherical triangle created along the unit sphere's surface.

$$\begin{cases} \cos\beta = \cos(\gamma-\theta)\cos\gamma + \sin(\gamma-\theta)\sin\gamma\cos\alpha \\ \overline{L}_{\odot\oplus}(r,\theta,\delta_{\odot'}) = \frac{1}{2\pi}\int_0^{2\pi} L_{\odot\oplus}(r,\beta(\theta,\alpha))\,d\alpha \end{cases} \tag{2.59}$$

$$\begin{aligned} \overline{L}_{\odot\oplus}(r,\theta,\delta_{\odot'}) =& 1 - \frac{1}{\pi}\Bigg|\mathrm{Re}\left\{\arccos\left\{\frac{\cos\left(\arcsin\left(\frac{R_\oplus}{r}\right)\right)}{\sin(\gamma-\theta)\sin\gamma} - \frac{1}{\tan(\gamma-\theta)\tan\gamma}\right\}\right\} \\ & - \mathrm{Re}\left\{\arccos\left\{\frac{1}{\sin(\gamma-\theta)\sin\gamma} - \frac{1}{\tan(\gamma-\theta)\tan\gamma}\right\}\right\}\Bigg| \end{aligned} \tag{2.60}$$

Following Eq.2.61 provides the analytical solution for the zero-tilt equinoctial case, which actually could be proved to be a very good approximation also for medium-small declination angles, apart for regions very close to the surface of the shadowing body (in particular inside the two cones obtained by the projection of the Polar Circles).

$$\overline{L}_{\odot\oplus}(r,\phi) = 1 - \frac{1}{\pi}\arcsin\left\{\frac{R_\oplus\cos\left(\arcsin\left(\frac{r\sin|\phi|}{R_\oplus}\right)\right)}{r\cos|\phi|}\right\} \tag{2.61}$$

Further averaging the daily $\bar{L}_2$ along the seasons of the Martian year would be then straightforward.

Before undertaking this operation, the second step in the procedure is to extend the Sun-Phobos daily $\bar{L}_2$ to take into consideration the correction due to the Sun-Mars $\bar{L}_1$ at the current day previously derived in Fig.2.16, to obtain the aimed Sun-Mars-Phobos mean 3D light field $\bar{L}_{12}$ that models a coupled 3B eclipse. This is far from an easy operation, and in the general case the mean value of the combined light function of two shadowing bodies is unrelated to the mean values of the two single shadowing bodies. Fortunately, in our case, several simplifications are available: both 2B light fields are cylindrical, their shadowing wakes have very different dimensions around Phobos, the characteristic times of the Sun-Mars and Mars-Phobos revolution are very different, and the rotation of Phobos is synchronous. This yields the instantaneous combined L_{12} around Phobos to be the logical conjunction $\wedge$ of the two single instantaneous light functions, which results in their product: $L_{12} = L_1 \wedge L_2 = L_1 L_2$. This allows to compute the sought mean integral field $\bar{L}_{12}$ over one Phobos' revolution with only the information of the two single daily values $\bar{L}_1$ and $\bar{L}_2$, with the deal of introducing a further variable ψ, which is the right ascension with respect to Phobos of the point analyzed. This is described in Eq.2.62. $\bar{L}_2$ is axially symmetric along the spin axis, being the same for points with same ϕ: they have the same profile $L_2(t)$, but shifted along time for different ψ. Therefore the integral of the product $L_1 L_2$ produces a different $\bar{L}_{12}$, expressed by the correction term $\Delta t/T$ which is the percentage of time in one Phobos' revolution period T such that L_1 is in shadow and L_2 is in light. This correction is function of the right ascension, and acts on the 2D Sun-Phobos mean light field to provide a 3D Sun-Mars-Phobos mean light field. This functional is symmetric

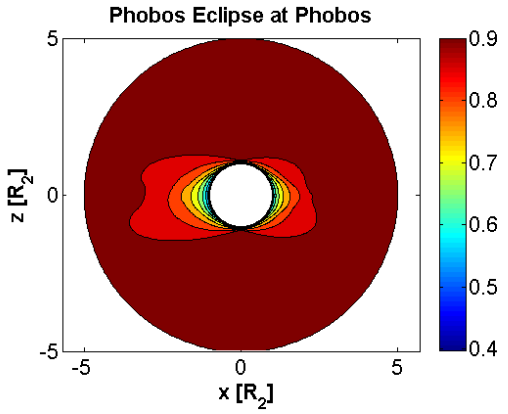

Figure 2.28: **Sun-Mars-Phobos eclipse at Phobos.** Light function, year averaging.

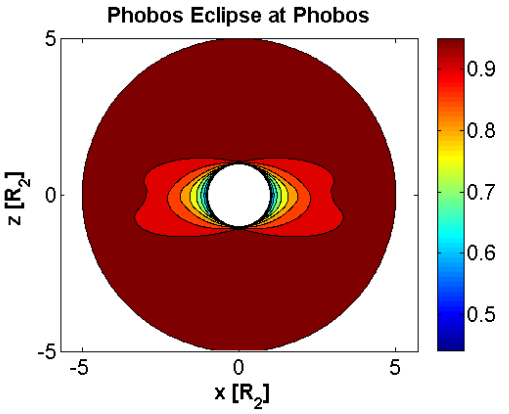

Figure 2.29: **Sun-Mars-Phobos eclipse at Phobos.** Light function, year averaging, without Sun-Mars eclipse correction.

with respect to the x-z plane of the Hill's frame, and season dependent. Eq.2.63 shows the procedure to derive the value of this correction term, which is a crescent function with respect to the right ascension. This confirms the physics: points along the x-axis' positive direction (and close to the moon) experience the Sun-Mars eclipses mostly when the Sun-Phobos eclipse already occurs, while points between Mars and Phobos have distinct eclipses because the Sun have to be on opposite parts of the sky, and so the correction is always the maximum, which is the value of the Sun-Mars basic mean integral value. Values in quadrature become closer to the maximum as far as the radial distance increases. This is presented in Eq.2.64.

$$\begin{cases} cylindric: \overline{L}_{\odot\oplus}(r,\theta,\delta_{\odot'}) = \frac{1}{T_{REV_{\oplus}}} \int_0^{T_{REV_{\oplus}}} L_{\odot\oplus}(r,\theta,\psi,\delta_{\odot'},t)\,dt,\ \forall\psi \\ double-cylindric: \overline{L}_{\odot\oplus_1\oplus_2}(r,\theta,\psi,\delta_{\odot'}) = \frac{1}{T_{REV_{\oplus_2}}} \int_0^{T_{REV_{\oplus_2}}} L_{\odot\oplus_1}(r,\theta,\psi,\delta_{\odot'},t)\, L_{\odot\oplus_2}(r,\theta,\psi,\delta_{\odot'},t)\,dt \\ Mars-Phobos: \overline{L}_{\odot\oplus_1\oplus_2}(r,\theta,\psi,\delta_{\odot'}) = \dfrac{1}{T_{REV_{\oplus_2}}} \displaystyle\int_0^{T_{REV_{\oplus_2}}} L_{\odot\oplus_1}(\delta_{\odot'},t)\, L_{\odot\oplus_2}(r,\theta,\psi,\delta_{\odot'},t)\,dt \\ \qquad\qquad = \overline{L}_{\odot\oplus_2}(r,\theta,\delta_{\odot'}) - \dfrac{\Delta t_{L_{\odot\oplus_1}=0\wedge L_{\odot\oplus_2}=1}}{T_{REV_{\oplus_2}}} \left(\overline{L}_{\odot\oplus_1}, \overline{L}_{\odot\oplus_2}, \psi\right) \end{cases} \tag{2.62}$$

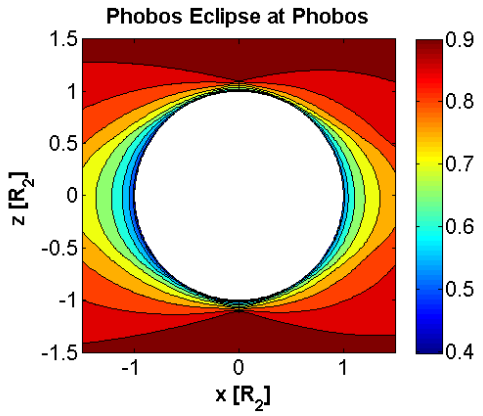

Figure 2.30: **Sun-Mars-Phobos eclipse at Phobos.** Light function, year averaging, magnification inside Phobos' SOI.

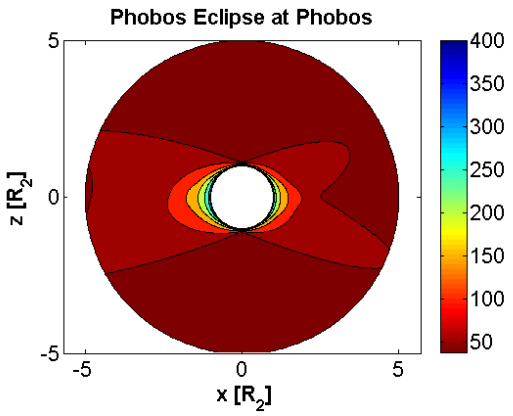

Figure 2.31: **Sun-Mars-Phobos eclipse at Phobos.** Shadows days, aggregated from light function over year.

$$
\begin{cases}
f = 0.5 - 0.5\psi/\pi,\ \psi \in [0,\pi] \\
\alpha = \overline{S}_{\odot\oplus_1} = 1 - \overline{L}_{\odot\oplus_1} \\
\beta = \overline{S}_{\odot\oplus_2} = 1 - \overline{L}_{\odot\oplus_2}
\end{cases}
\begin{cases}
y_1 = 0.5 - \alpha/2 \\
y_2 = 0.5 + \alpha/2
\end{cases}
\begin{cases}
\xi_1 = f - \beta/2 \\
\xi_2 = f + \beta/2
\end{cases}
$$

$$
\begin{cases}
\xi_1 \geq 0 \rightarrow \begin{cases}
x_1 = \xi_1, x_2 = \xi_2 \\
\begin{cases}
x_2 \geq y_1 \rightarrow \Delta t_{L_{\odot\oplus_1}=0 \wedge L_{\odot\oplus_2}=1}/T_{REV_{\oplus_2}} = \alpha - (\min(x_2,y_2) - \max(x_1,y_1)) \\
x_2 < y_1 \rightarrow \Delta t_{L_{\odot\oplus_1}=0 \wedge L_{\odot\oplus_2}=1}/T_{REV_{\oplus_2}} = \alpha
\end{cases}
\end{cases} \\
\xi_1 < 0 \rightarrow \begin{cases}
\xi_2 \geq 0 \rightarrow \begin{cases}
x_1 = \xi_2, x_2 = \xi_1 + 1 \\
\begin{cases}
x_2 \geq y_1 \rightarrow \Delta t_{L_{\odot\oplus_1}=0 \wedge L_{\odot\oplus_2}=1}/T_{REV_{\oplus_2}} = \min(x_2,y_2) - \max(x_1,y_1) \\
x_2 < y_1 \rightarrow \Delta t_{L_{\odot\oplus_1}=0 \wedge L_{\odot\oplus_2}=1}/T_{REV_{\oplus_2}} = 0
\end{cases}
\end{cases} \\
\xi_2 < 0 \rightarrow \begin{cases}
x_1 = \xi_1 + 1, x_2 = \xi_2 + 1 \\
\begin{cases}
x_1 \geq y_2 \rightarrow \Delta t_{L_{\odot\oplus_1}=0 \wedge L_{\odot\oplus_2}=1}/T_{REV_{\oplus_2}} = \alpha \\
x_1 < y_2 \rightarrow \Delta t_{L_{\odot\oplus_1}=0 \wedge L_{\odot\oplus_2}=1}/T_{REV_{\oplus_2}} = \alpha - (\min(x_2,y_2) - \max(x_1,y_1))
\end{cases}
\end{cases}
\end{cases}
\end{cases}
\tag{2.63}
$$

$$
\begin{cases}
\min\limits_{\psi} \bar{L}_{\oplus_1\oplus_2} : \dfrac{\Delta t_{L_{\odot\oplus_1}=0 \wedge L_{\odot\oplus_2}=1}}{T_{REV_{\oplus_2}}} \left(\overline{S}_{\odot\oplus_1}, \overline{S}_{\odot\oplus_2}, \psi = \pi\right) = \min\left(\overline{S}_{\odot\oplus_1}, 1 - \overline{S}_{\odot\oplus_2}\right) \\
\max\limits_{\psi} \bar{L}_{\oplus_1\oplus_2} : \dfrac{\Delta t_{L_{\odot\oplus_1}=0 \wedge L_{\odot\oplus_2}=1}}{T_{REV_{\oplus_2}}} \left(\overline{S}_{\odot\oplus_1}, \overline{S}_{\odot\oplus_2}, \psi = 0\right) = \max\left(0, \overline{S}_{\odot\oplus_1} - \overline{S}_{\odot\oplus_2}\right) \\
\overline{L}_{\odot\oplus_1\oplus_2}\left(r = R_{\oplus_2}, \theta, \psi = \frac{\pi}{2}, \delta_{\odot'}\right) = \overline{L}_{\odot\oplus_1}\overline{L}_{\odot\oplus_2}
\end{cases}
\tag{2.64}
$$

In summary, the results of the combined shadowing effects could be shown onto the x-z plane of Phobos' Hill's frame, presenting the extreme outcomes for the 0° and 180° cases of the right ascension. To interpret the results showed through Fig.2.28-2.40 we should distinguish seasonal and yearly averaging. The mean light function inside the space spanned by the rotating seasonal wake is not so different from the approximation of Fig.2.24, apart for altitudes very close to the surface of Phobos. The seasonal tilt inclines the shadow wake, so complete light and one cone of complete shadow appear in the Phobos' polar regions. The cone's maximum altitude, encountered over the North

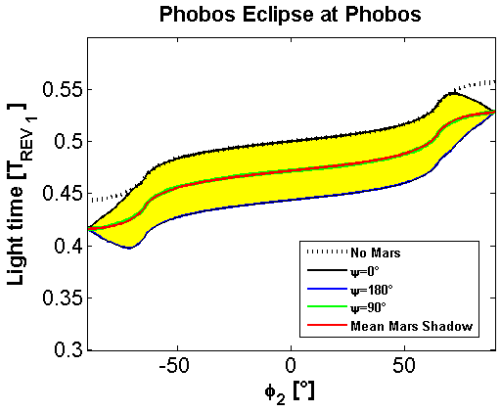

Figure 2.32: **Sun-Mars-Phobos eclipse at Phobos.** Light function at Phobos' surface, year averaging. Mean Mars shadow line is obtained as product of the two light functions. Filled area shows right ascension dependency, whose upper/lower border is for points in superior/inferior conjunction positions, and central line is for points in quadrature.

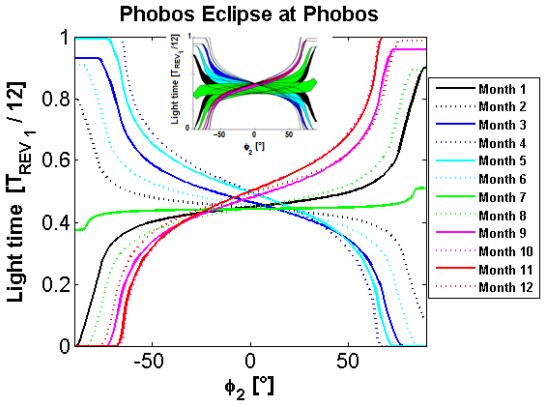

Figure 2.33: **Sun-Mars-Phobos eclipse at Phobos.** Light function at Phobos' surface, month averaging, mean Mars shadow lines. Real right ascension-dependant areas are highlighted. Winter solstice between 4th and 5th month, summer solstice between 10th and 11th month, fall equinox between 1st and 2nd month, spring equinox during 7th month.

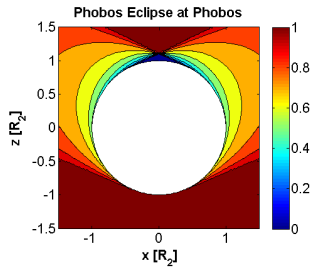

Figure 2.34: **Sun-Mars-Phobos eclipse at Phobos.** Light function during winter season (4th month).

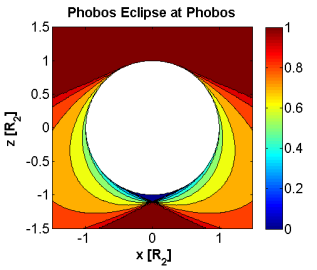

Figure 2.35: **Sun-Mars-Phobos eclipse at Phobos.** Light function during summer season (10th month).

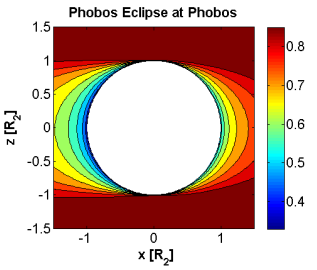

Figure 2.36: **Sun-Mars-Phobos eclipse at Phobos.** Light function during spring season (7th month).

Pole in winter and over the South Pole in summer, using a mean ellipsoidal model for Phobos' shape, is of $1.4km$. Instead during spring and fall, no complete shadow zones are present, and the minimal daily $\bar{L}$ at the day of equinoxes is 38% along the sub-Mars meridian onto the surface of the moon (this without considering its orography and morphology). Considering now the annual $\bar{L}$, yearly averaging drastically increases the lighting conditions. Due to Mars' eccentricity, Southern regions experience more shadow time than the upper counterpart; due to the Martian eclipses, points in-between Mars and Phobos and close to the moon experience more shadow time per annum.

In conclusion, this analysis provides the lighting conditions for a spacecraft orbiting Phobos. The shadowing threats or opportunities are limited, and a fixed observation point in the 3B frame could experience relevant reduction of the FOV of the Sun for long-period station-keeping only if it is inside the SOI and onto the equatorial plane,

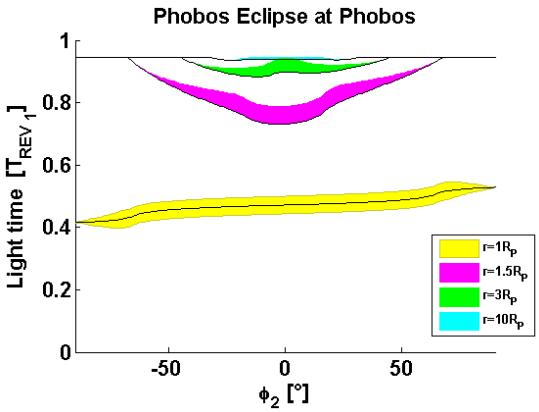

Figure 2.37: **Sun-Mars-Phobos eclipse at Phobos.** Light function at Phobos, year averaging, right ascension dependency (black lines are for $\psi = 90°$).

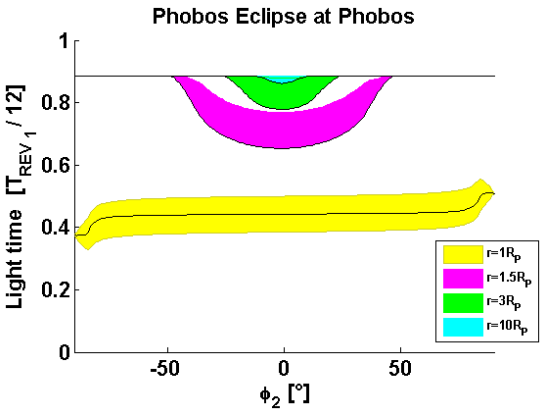

Figure 2.38: **Sun-Mars-Phobos eclipse at Phobos.** Light function at Phobos during spring season (7th month), right ascension dependency (black lines are for $\psi = 90°$).

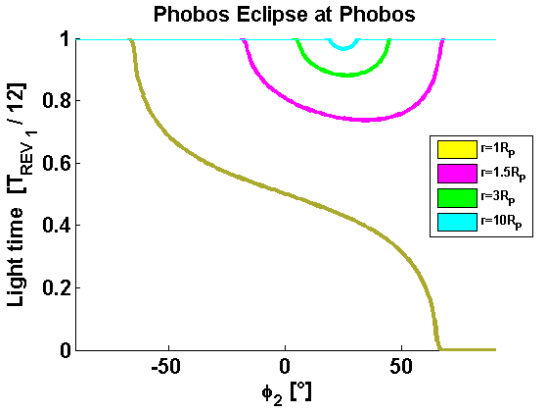

Figure 2.39: **Sun-Mars-Phobos eclipse at Phobos.** Light function at Phobos during winter season (4th month), right ascension dependency null.

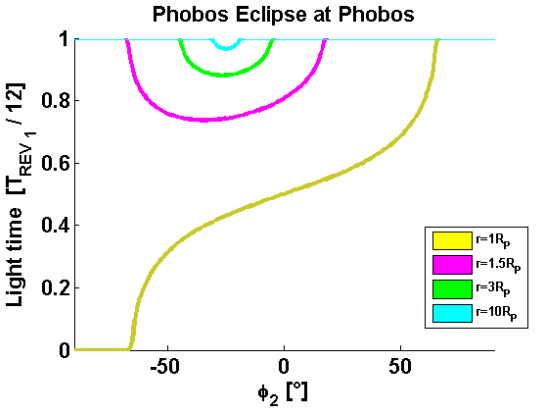

Figure 2.40: **Sun-Mars-Phobos eclipse at Phobos.** Light function at Phobos during summer season (10th month), right ascension dependency null.

and pointing Mars. Instead, a shorter period could provide continuous shadowing opportunities for points over the poles during the solstice seasons, in particular inside the Southern polar cone during summer. For middle seasons the minimum of the light field moves towards lower latitudes, and relevant reduction of the Sun's FOV is obtained only very close to the surface. Therefore during equinoctial or long observation periods, the lighting conditions around Phobos are close to experience continuous light, up to 88% due to the unavoidable Martian eclipses. Required shadowing exploitation could be obtained only using orbits that track the daily anti-Sun path, such a vertical-displaced circular orbit around the spin axis.

Finally, recall that the shadowing requirements entail a difficult trade-off with the electrical and power subsystem of the spacecraft, due to the need of energy from the solar arrays. However, possible ideas to explore could be to design more challenging mission architectures. For example, a formation flying configuration with a chief manned mothership always flying mostly in shadow, and one deputy (or more), maybe a light solar sail, able to do the opposite, and reflect the sunlight towards a solar collector on the mothership. This idea, despite quite far-out, is actually helped by the little length-scale of the Phobos' SOI, making the relative distances shorter and so the relative pointing requirements more easier to fulfill. However, the same objective could be also obtained with one (or more) ground stations on Phobos acting as the aimed reflector. Finally, another solution offered by the small length-scale of the Phobos' SOI is to keep the architecture single, but make it bigger, in order to have zones of the same spacecraft with different values of the light function, to be dedicated to human dwelling or electrical power generation. In this case, the critical subsystem becomes the structure and configuration design of the large and flexible spacecraft.

2.7 Sky Occultation

The purpose of this section is to investigate the possible exploitation of Phobos as a natural shield against the isotropic cosmic rays, which in section 2.5, for the case of the Phobos' orbital environment, they were found to be the SEPEs and GCRs. The idea is that the fluence of the incoming radiation on a spacecraft is lowered proportionally to the filling fraction in the sky of the apparent size of the body's bulk, as seen by the spacecraft's location. In astronomy, when a body is totally or partially hidden by the bulk of another one that passes between it and the observer, we speak about occultations or transits. Since in this case the hidden body is the total background sky, in this thesis this action is referred to as sky occultation.

A point-like observer sees an object with an apparent shape that corresponds to the area that it covers on a sphere centered on the observer, and radius equal to their distance. In 3D geometry, the area subtends the 2D solid angle Ω on the unit sphere, whose IS unit is the steradian sr, and the total spherical surface has $\Omega = 4\pi sr$. For a generic body bounded by the surface S and placed in position $\mathbf{r}$ from the observer,

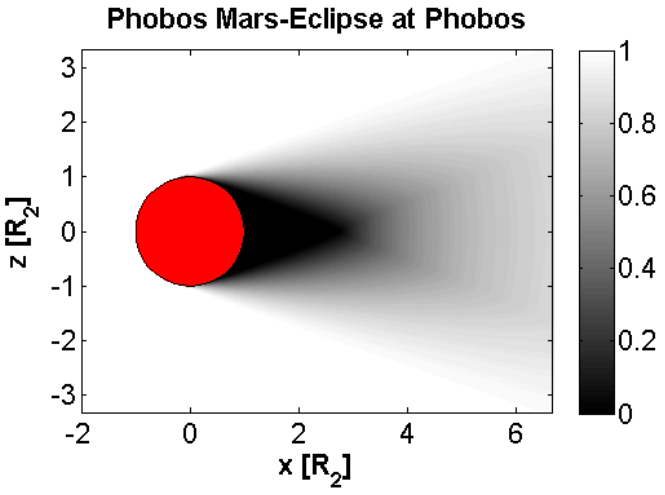

Figure 2.41: **Mars-Phobos eclipse around Phobos.** Light function field around Phobos in the radial-vertical plane of the Hill's frame of Phobos' circular orbit.

$$\Omega_S(\mathbf{r}) = \iint_S d\Omega = \iint_S \sin\vartheta d\vartheta d\phi = \int\int_{0,0}^{2\pi,\pi} M_S(\vartheta,\phi,\mathbf{r}) \sin\vartheta d\vartheta d\phi \tag{2.65}$$

M is the mask function of the body, which is a binary function of the polar and azimuthal spherical coordinates ϑ and ϕ centered on the observer, whose value is 1 or 0 if the related direction from the observer intersects or not the body. Thus, the iso-surface at the level $M = 1$ represents the apparent shape of the body on the unit sphere. The ratio with $4\pi sr$ represents the filling fraction of the body with respect to the background.

The occulting bodies in our case are Mars and Phobos, while the Sun is neglected because is very small as seen from Phobos. The approach is similar to the one undertaken for the lighting conditions in section 2.6, defining an occultation function field $O_\oplus$ which represents the bulk/sky filling fraction of the occulting body $\oplus$.

$$O_\oplus(\mathbf{r}) = \frac{\Omega_\oplus(\mathbf{r})}{4\pi} \tag{2.66}$$

This analysis is easier than the computation of the lighting conditions because in the 3B frame of the CR3BP Mars and Phobos are fixed, and their O does not depend on time. Also for a first analysis, the mean spherical shape is used for the two bodies, of radius R. In this case, the occulting body fills a spherical cap on the unit sphere, with apparent angular radius α, and O is spherically-symmetric.

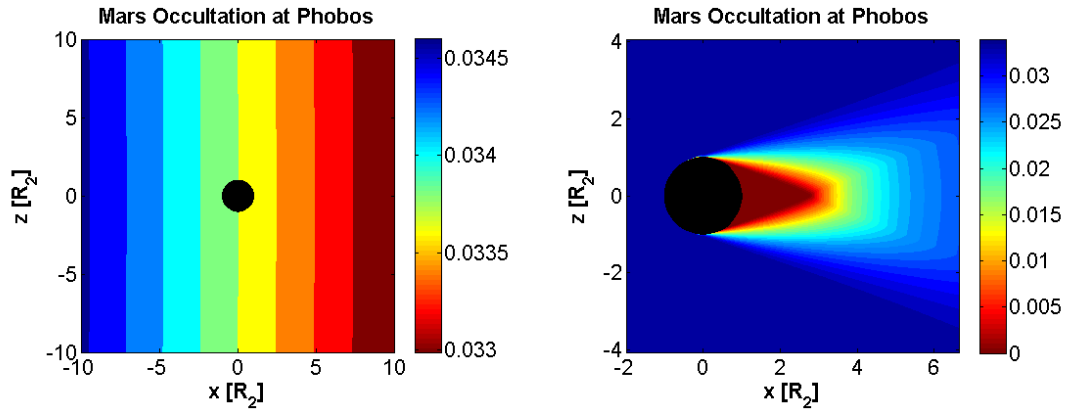

Figure 2.42: **Sky occultation by Mars' bulk around Phobos.** Occultation field around Phobos in the radial-vertical plane of the Phobos' Hill's frame. Second plot shows the real scaling effect of the Mars occultation field in Eq.2.68 considering the Mars-Phobos light function of Fig.2.41.

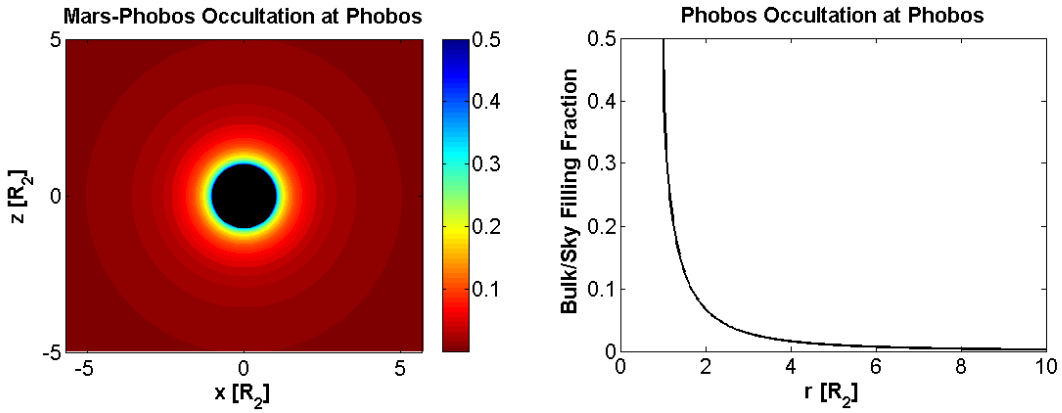

Figure 2.43: **Sky occultation by Phobos' bulk around Phobos.** Occultation field around Phobos in the radial-vertical plane of the Phobos' Hill's frame.

$$\begin{aligned} S(\varphi,\psi) = \mathbf{r} + R\begin{bmatrix}\cos\psi\cos\varphi\\ \sin\psi\cos\varphi\\ \sin\varphi\end{bmatrix} \Rightarrow \alpha_S(\mathbf{r}) = \arcsin\frac{R}{\|\mathbf{r}\|} \\ \rightarrow \Omega_S(\mathbf{r}) = 2\pi\left(1-\cos\alpha_S(\mathbf{r})\right) \rightarrow O_S(\mathbf{r}) = \frac{1-\cos\alpha_S(\mathbf{r})}{2} \end{aligned} \tag{2.67}$$

First the occultation of Mars is considered, evaluating the Mars' occulting function at the Phobos' location, since the region of interest is a small domain. The result is approximately $O_1 = 3.4\%$ and it is shown in Fig.2.42, where the relative error from this mean value at 10 Phobos' radii is 2%. The effect of the orbital eccentricity is also negligible, with a maximum relative error of 3%.

Second the occultation of Phobos is considered. Its occulting field depends only from the radial distance from the body. This function starts from $O_2 = 50\%$ on the spherical surface (astronauts staying inside of a deep crater would we shielded also

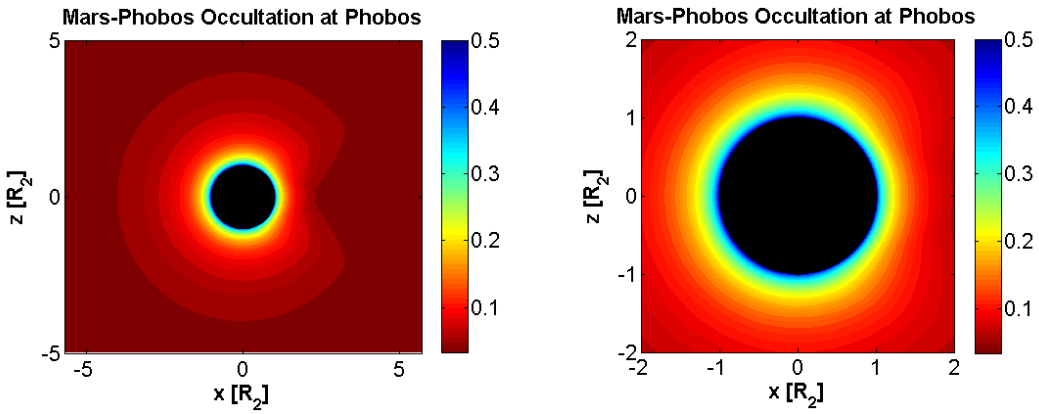

Figure 2.44: **Sky occultation by Mars' and Phobos' bulks around Phobos.** Occultation field around Phobos in the radial-vertical plane of the Phobos' Hill's frame.

laterally by the mountain ridge[15]), and then decreases rapidly: $O_2 = 13\%$ at the SOI's boundary, $O_2 = 7\%$ at 2 Phobos' radii, as shown in Fig.2.43.

The conclusion of the analysis of the sky occultation is obtained combining the previous single effects. This requires to discriminate if the apparent shapes of the two bodies' bulks intersect, and how much they overlap. Such axially-symmetric 3D field corresponds to the light function of the Mars-Phobos couple $L_{1,2}$ that was avoided to be computed in the previous lighting conditions analysis of section 2.6.5, but it is needed here. In particular, recall that this light function must be computed with the accurate dual-cone model, since due to the proximity of Mars, the shadow cone's vertex of Phobos is located only at 2.77 Phobos' radii in the anti-Mars direction, therefore its inclination inside the SOI is not negligible, as it is reported in Fig.2.41. The resulting 2B combined occultation function is

$$O_{\oplus_1,\oplus_2}(\mathbf{r}) = O_{\oplus_1}(\mathbf{r}) + L_{\oplus_1,\oplus_2}(\mathbf{r})\, O_{\oplus_2}(\mathbf{r}) \tag{2.68}$$

and it is shown is Fig.2.44.

This analysis highlighted that a significative reduction of the isotropic SEPEs and GCRs by using the bulk of Phobos to occult part of the celestial sphere is obtained inside the SOI of the moon. Besides, points on the Mars' side and over the poles experience an additional but small reduction due to the occultation of Mars. Points and orbits that remain inside the Phobos' SOI are therefore suitable to enhance the radiation protection of the spacecraft by exploiting Phobos' bulk as a passive radiation shield.

[15] As mentioned in section 1.2, the Stickney crater is one of the most sheltered places in the Solar System: Mars' bulk and Phobos' surface would naturally shield astronauts from up to 90% of the cosmic rays.

Chapter 3

Extension of the Model of the Orbital Dynamics around Phobos including its Inhomogeneous Gravity Field and Orbital Eccentricity

Following the results obtained in section 2.4, that determined the significant perturbations acting on the Mars-Phobos CR3BP, this chapter extends the model of the relative orbital dynamics around Phobos to include the main orbital perturbations. This model will be used in chapter 4 to compute the natural LPOs in a more realistic dynamical system describing the motion in the vicinity of Phobos. Section 3.1 describes how the complete gravity field of a general inhomogeneous body is modeled, and in particular presents the methodology of the gravity harmonics. In this framework, the modeling of the real complex shape is also addressed with the shape harmonics in section 3.2. These techniques will be used in section 3.3 to derive the orbital dynamics of the Mars-Phobos CR3BP-GH, which takes into account the highly inhomogeneous gravity field of the second massive body. Finally, this model is extended in section 3.4 to the Mars-Phobos ER3BP-GH, which includes also the effect of the eccentricity of the orbit of Phobos around Mars.

3.1 Modeling of the complete Gravity Field

When the altitude of the spacecraft's orbit is low over the celestial body, the point-mass approximation of the Keplerian gravity attraction of Eq.2.3 is not suitable any longer. The real distribution of the central body's mass must be considered to derive the expression of the gravitational acceleration acting on the spacecraft [92, 93].

The modeling of the external gravity field of convex bodies has been first investigated by Legendre. The gravity potential expressed in the body's BCBF frame is a conservative field, and therefore satisfies Laplace's equation. The general homogeneous solution, at a given distance from the body's barycenter, is a linear combination of normal modes in spherical coordinates. This set represents a convenient orthogonal basis and the eigenfunctions are called spherical harmonics: they are the equivalent to the Fourier series on the 2D sphere's surface. Following this, define the transformation from Cartesian to spherical coordinates as $[r;\vartheta;\psi] = \mathbf{T}_{TSE}([x;y;z])$, which are described by radial distance r, co-latitude ϑ from the body's North Pole, and East-longitude ψ with respect to the body's Prime Meridian, while ϕ is the latitude. The related physical basis ($\hat{\mathbf{e}}_r$,$\hat{\mathbf{e}}_\vartheta$,$\hat{\mathbf{e}}_\psi$) defines the local TSE frame.

The methodology of the spherical harmonics has been applied in the description of the gravitational potential $u_{G_\oplus}$ of an inhomogeneous body, as a function of the position in the body's BCBF frame. This field is expressed by the series expansion of spherical harmonics, which are called **gravity harmonics** (GHs) [92, 93]. This is presented in Eq.3.1, where $R_\oplus$ is a reference radius, for example the equivalent-volume radius of the body.

$$\begin{cases} u_{G_\oplus}(\mathbf{q}) = u_{G_\oplus}(r,\vartheta,\psi) = \frac{Gm_\oplus}{R_\oplus}\sum\limits_{n=0}^{\infty}\left(\frac{R_\oplus}{r}\right)^{n+1}\sum\limits_{m=0}^{n} C_n^m(\psi)\,P_n^m(\cos\vartheta) \\ C_n^m(\psi) = C_{n,m}\cos m\psi + S_{n,m}\sin m\psi = J_{n,m}\cos m(\psi-\lambda_{n,m}) \end{cases} \tag{3.1}$$

$$\begin{cases} P_n(x) = \frac{1}{2^n n!}\frac{d^n}{d^n x}\left(x^2-1\right)^n \\ P_n^m(x) = \left(1-x^2\right)^{\frac{m}{2}}\frac{d^m}{d^m x}P_n(x) \end{cases} \tag{3.2}$$

The double expansion of spherical harmonics is conducted with degree n and order m, using the Legendre associated polynomials P_n^m. These are functions of the co-latitude, and are derived, using Ferrer's formula, from the single-degree Legendre polynomials P_n, expressed by Rodrigues' formula. From the definition of the spherical harmonics by separation of variables, in Eq.3.1 the Legendre polynomials are scaled with a power-inverse function of the distance, and with a harmonic function of the longitude. The first depends on the degree, while the latter depends on the order, and contains the two coefficients C and S (or the related magnitude J and phase λ), which are the Stokes coefficients pair for each n-m spherical harmonic. They are the "physical inputs" needed for the computation of the series expansion of GHs, and are derived with a Fourier analysis of appropriate measurements. The series are truncated at the maximum degree and order N and M of the GHs' coefficients, given that convergence of the series is achieved with an acceptable error for the case in study. It is worth nothing that the analytical synthesis with the GHs is dependent on various kinds of normalization that MUST be in accordance with the choice made to normalize the related Legendre associated polynomials. Basically, one can find the Stokes coefficients un-normalized (which means that they are in accordance to the classical definition of the polynomials

provided in Eq.3.2) or normalized, that for the geodesy field's tradition means that the global integral on a reference sphere's surface is set to be unity. Besides, one should also consider an additional normalization, which arises from the evaluation of the Legendre polynomials with a recursive algorithm, since this is far computationally cheaper than analytically writing the expression of all the polynomials up to degree-order (N,M)[1].

The spherical harmonics consist of three distinct parts. They are inversely proportional to the distance from the barycenter, with an n-power law. The $m = 0$ case is characterized by only latitude-dependency, and the related harmonics are called zonal[2]. The $n = m$ case is characterized by only longitude-dependency, and the related harmonics are called sectorial. The other harmonics, dependent on both angular coordinates, are called tesseral. The first term $J_{0,0} = 1$ provides the basic spherical term corresponding to the Newtonian gravity potential given in section 2.2, therefore all the other terms constitute the perturbation of the GHs. In particular, first-degree harmonics are zero for barycentric frames, while the five second-degree Stokes coefficients are directly related to the body's principal moments of inertia: $C_{2,1}, S_{2,1}$ and $S_{2,2}$ are each one related to one mixed moment, while $C_{2,0}$ and $C_{2,2}$ are related to the principal moments. Note that this mismatch (5 coefficients, 6 moments) is given by the principle of irresolution of the reverse gravity problem [94]. Anyway, thanks to the trace of the inertia matrix (which is invariant), it is possible to numerically derive all the moments from the coefficients. The potential truncated to the second-degree is called quadrupole representation, and consists in the useful approximation of the central body as an ellipsoid (MacCullagh's formula).

The only requirement of this general mathematical methodology is that the field developed in series, in this case the gravity potential, could be described by a single-valued function in spherical coordinates of the body's BCBF frame. This is the case for celestial bodies with a simple shape. In contrast, complex shaped asteroids do not satisfy this requirement and the description of their gravity field must be conducted with numerical techniques. This requires an appropriate discrete distribution of tetrahedrons to model their surface and derive the related gravity field [95]. In addition, since the gravity harmonics have been chosen because they are the fundamental basis for the solution of the Laplace's equation, they are valid to describe only the external gravity field of the body. In particular, due to its definition in spherical coordinates, the domain of application is restricted to the space outward of a reference sphere, called the Brillouin's sphere. Its radius is defined as the minimum distance such that the related sphere circumscribes the body's figure[3]. For the same reason spherical harmonics are defined as eigenfunctions of Laplace's equation, elliptical harmonics could be used to describe a conservative field as well [96]. The related elliptical GHs are valid outside

[1]The total number of Legendre associated polynomials up to degree N is $\frac{(N+1)(N+2)}{2}$.

[2]For historical reason, the magnitude of the zonal harmonics is defined as the negative part of their C Stokes coefficient, while S is null.

[3]The reference radius used in Eq.3.1 is not related in principle to correspond to this reference sphere's radius.

a reference ellipsoid that circumscribes the body, therefore they can be used to model the exterior gravity field of oblate bodies.

3.1.1 Gravity Acceleration

The gravitational acceleration in the TSE frame is obtained through the spherical gradient $\nabla_{TSE} = [\frac{\partial}{\partial r}; \frac{1}{r}\frac{\partial}{\partial \vartheta}; \frac{1}{r sin\vartheta}\frac{\partial}{\partial \psi}]$ of the gravity potential expressed with the series of GHs of Eq.3.1.

$$\mathbf{a}_{\mathbf{G},TSE} = \begin{cases} -\frac{Gm_\oplus}{R_\oplus^2}\sum_{n=0}^{\infty}(n+1)\left(\frac{R_\oplus}{r}\right)^{n+2}\sum_{m=0}^{n}\left[C_{n,m}\cos m\psi + S_{n,m}\sin m\psi\right]P_n^m(\cos\vartheta) \\ \frac{Gm_\oplus}{R_\oplus^2}\sum_{n=0}^{\infty}\left(\frac{R_\oplus}{r}\right)^{n+2}\sum_{m=0}^{n}\left[C_{n,m}\cos m\psi + S_{n,m}\sin m\psi\right]\frac{d}{d\vartheta}P_n^m(\cos\vartheta) \\ \frac{Gm_\oplus}{R_\oplus^2}\sum_{n=0}^{\infty}\left(\frac{R_\oplus}{r}\right)^{n+2}\sum_{m=0}^{n} m\left[-C_{n,m}\sin m\psi + S_{n,m}\cos m\psi\right]\frac{1}{\sin\vartheta}P_n^m(\cos\vartheta) \end{cases} \tag{3.3}$$

The components are then rotated in the body's BCBF frame through the local attitude matrix of the spherical coordinates transformation, presented in Eq.3.4.

$$\mathbf{A}_{TSE}^{BCBF}(\mathbf{q}) = \mathbf{A}_{TSE}^{BCBF}(\phi,\psi) = \mathbf{A}_1\left(-\frac{\pi}{2}\right)\mathbf{A}_2(-\phi)\,\mathbf{A}_3(\psi) = \mathbf{A}_3(-\phi)\,\mathbf{A}_1\left(-\frac{\pi}{2}\right)\mathbf{A}_3(\psi) \tag{3.4}$$

Zero-degree term constitutes the fundamental term $\mathbf{a}_{\mathbf{G},\oplus}$ of Eq.2.3 used in orbital mechanics, while harmonics from $n = 2$ in barycentric frames are referred to as the net gravitational perturbation $\mathbf{a}_{\mathbf{G}}^{\mathbf{p}}$.

It is evident that this classical formulation of the spherical harmonics, when used to describe the gravitational acceleration, is singular at the Poles. However, this singularity is not embedded in the series expansion definition, but is due to the expression of the derivatives in a spherical coordinate system. Some authors have provided in the past appropriate solutions, such as the adoption of a non-minimal coordinate system in [97], as well as alternative methods [98]. However, in this thesis the need of polar orbits is never encountered, so the singularity at the Poles is treated simply considering its numerical limit at the machine tolerance.

3.1.2 Gravity Hessian

For the applications considered in the following chapters of this thesis, the Hessian matrix of the gravity potential is required. This is obtained through the spherical Hessian $\mathbf{H}_{TSE}$, then rotated and counter-rotated through $\mathbf{A}_{TSE}^{BCBF}$. The Hessian in spherical coordinates[4] is not easy to find in the literature, so it has been derived using the Hessian definition for a general curvilinear coordinates basis, that makes use of the metric matrix $\boldsymbol{g}$ and the Christoffels' symbols Γ of the coordinates transformation [99][5],

[4] Which could be seen also as the gradient of a vector, elegantly named covariant derivative.

[5] The analytical expressions of Γ for the case of spherical coordinates are not completely correct in [99].

in this case $\mathbf{T}_{TSE}$. The general procedure is summarized in the following equations. $\mathbf{T}$ represents the general coordinates' transformation from the frame F1 to the frame F2, defined by the set of coordinates x_j and z_j respectively. The metric matrix and its dual form are defined by the Jacobian of the transformation $\mathbf{J}$.

$$\begin{aligned} F1\left(\{x\}_{j=1}^{N}\right) \underset{\mathbf{T^{-1}}}{\overset{\mathbf{T}}{\rightleftarrows}} F2\left(\{z\}_{j=1}^{N}\right) \Rightarrow \begin{cases} \mathbf{g} = \mathbf{J}_{\mathbf{T^{-1}}}^{T}\mathbf{J}_{\mathbf{T^{-1}}} \\ \mathbf{g^D} = \mathbf{J_T}\mathbf{J}_{\mathbf{T}}^{T} \end{cases} \\ \Rightarrow g_{j,k} = \frac{1}{g_{j,k}^{D}} = \sum_{c=1}^{N} \frac{\partial x_c}{\partial z_j}\frac{\partial x_c}{\partial z_k} \end{aligned} \tag{3.5}$$

The physical basis $\hat{\mathbf{e}}$ is the normal basis of each frame, where each versor is associated to one coordinate, while the natural basis is described by the Jacobian, thus is not normal. The gradient operator of the new curvilinear metric is expressed in the original physical basis by the following expression.

$$\nabla_{F2} = \sum_{j=1}^{N} \hat{\mathbf{e}}_{F1,x_j}\left(\frac{1}{\sqrt{g_{j,j}}}\frac{\partial}{\partial z_j}\right) \tag{3.6}$$

The Hessian operator of the new metric corresponds to the above gradient, when applied to a vector whose components are defined in the new metric. Thus, by the chain rule, in addition to the matrix of the second derivatives, a second term shows up to take into account the gradient of the new curvilinear basis. This is expressed by the matrices of the Christoffels' symbols of the transformation.

$$\mathbf{H}_{F2} = \sum_{j=1,k=1}^{N,N} \hat{\mathbf{e}}_{F1,x_j}\hat{\mathbf{e}}_{F1,x_k}^{T}\frac{1}{\sqrt{g_{j,j}}\sqrt{g_{k,k}}}\left(\frac{\partial^2}{\partial z_k \partial z_j} + \sum_{i=1}^{N}\Gamma_{j,k}^{i}\frac{\partial}{\partial z_i}\right) \tag{3.7}$$

$$\Gamma_{r,s}^{j} = \sum_{b=1}^{N}\frac{\partial x_b}{\partial z_r}\frac{\partial^2 z_j}{\partial z_s \partial x_b} = \sum_{b=1}^{N} -\frac{\partial z_j}{\partial x_b}\frac{\partial^2 x_b}{\partial z_s \partial z_r} \tag{3.8}$$

These operators are now presented for the case of spherical coordinates.

$$\mathbf{g}_{TSE} = \begin{bmatrix} 1 & 0 & 0 \\ 0 & r^2 & 0 \\ 0 & 0 & r^2\sin^2\vartheta \end{bmatrix} \tag{3.9}$$

$$\begin{cases} \boldsymbol{\Gamma}^r = \begin{bmatrix} 0 & 0 & 0 \\ 0 & r & 0 \\ 0 & 0 & r\sin^2\vartheta \end{bmatrix} \\ \boldsymbol{\Gamma}^\vartheta = \begin{bmatrix} 0 & -\frac{1}{r} & 0 \\ -\frac{1}{r} & 0 & 0 \\ 0 & 0 & \cos\vartheta\sin\vartheta \end{bmatrix} \\ \boldsymbol{\Gamma}^\psi = \begin{bmatrix} 0 & 0 & -\frac{1}{r} \\ 0 & 0 & -\cot\vartheta \\ -\frac{1}{r} & -\cot\vartheta & 0 \end{bmatrix} \end{cases} \tag{3.10}$$

$$\mathbf{H}_{TSE} = \begin{bmatrix} \frac{\partial^2}{\partial r^2} & \frac{\partial}{\partial r}\left(\frac{1}{r}\frac{\partial}{\partial\vartheta}\right) & \frac{\partial}{\partial r}\left(\frac{1}{r\sin\vartheta}\frac{\partial}{\partial\psi}\right) \\ \frac{\partial}{\partial r}\left(\frac{1}{r}\frac{\partial}{\partial\vartheta}\right) & \frac{1}{r^2}\frac{\partial^2}{\partial\vartheta^2}+\frac{1}{r}\frac{\partial}{\partial r} & \frac{1}{r}\frac{\partial}{\partial\vartheta}\left(\frac{1}{r\sin\vartheta}\frac{\partial}{\partial\psi}\right) \\ \frac{\partial}{\partial r}\left(\frac{1}{r\sin\vartheta}\frac{\partial}{\partial\psi}\right) & \frac{1}{r}\frac{\partial}{\partial\vartheta}\left(\frac{1}{r\sin\vartheta}\frac{\partial}{\partial\psi}\right) & \frac{1}{r^2\sin^2\vartheta}\frac{\partial^2}{\partial\psi^2}+\frac{1}{r}\frac{\partial}{\partial r}+\frac{\cos\vartheta}{r^2\sin\vartheta}\frac{\partial}{\partial\vartheta} \end{bmatrix} \tag{3.11}$$

Finally, the Hessian of the GHs in the TSE frame is obtained applying 3.11 to the gravity potential of Eq.3.1.

$$\mathbf{H}_{TSE}u_{G,\oplus} = \frac{2Gm_\oplus}{R_\oplus^3}\sum_{n=0}^{\infty}\frac{1}{2}\left(\frac{R_\oplus}{r}\right)^{n+3}\begin{bmatrix} a & b & c \\ b & d & e \\ c & e & f \end{bmatrix}$$

$$\begin{cases} a = (n+1)(n+2)\sum_{m=0}^{n} C_n^m(\psi)P_n^m(\cos\vartheta) \\ b = -(n+2)\sum_{m=0}^{n} C_n^m(\psi)\frac{d}{d\vartheta}P_n^m(\cos\vartheta) \\ c = -\frac{(n+2)}{\sin\vartheta}\sum_{m=0}^{n}\frac{d}{d\psi}C_n^m(\psi)P_n^m(\cos\vartheta) \\ d = \sum_{m=0}^{n} C_n^m(\psi)\frac{d^2}{d\vartheta^2}P_n^m(\cos\vartheta) - (n+1)\sum_{m=0}^{n} C_n^m(\psi)P_n^m(\cos\vartheta) \\ e = -\frac{\cos\vartheta}{\sin^2\vartheta}\sum_{m=0}^{n}\frac{d}{d\psi}C_n^m(\psi)P_n^m(\cos\vartheta) + \frac{1}{\sin\vartheta}\sum_{m=0}^{n}\frac{d}{d\psi}C_n^m(\psi)\frac{d}{d\vartheta}P_n^m(\cos\vartheta) \\ f = \frac{1}{\sin^2\vartheta}\sum_{m=0}^{n}\frac{d^2}{d\psi^2}C_n^m(\psi)P_n^m(\cos\vartheta) - (n+1)\sum_{m=0}^{n} C_n^m(\psi)P_n^m(\cos\vartheta) + \\ \quad + \frac{\cos\vartheta}{\sin\vartheta}\sum_{m=0}^{n}\frac{d}{d\psi}C_n^m(\psi)\frac{d}{d\vartheta}P_n^m(\cos\vartheta) \end{cases} \tag{3.12}$$

3.1.3 Application to Phobos and Mars

The methodology of the GHs is the most common and easily implemented technique to model the gravity field of the Solar System's planets and moons for spacecraft orbits. Table 3.2 provides the most important GHs of Mars' gravity field, retrieved from the high-fidelity model developed from NASA's Mars Global Surveyor spacecraft. Also for the case of Phobos, the GHs have proved suitable to model its gravity field. Unlike the Earth and other bodies visited by specific space missions, gravity sensors measurements from dedicated low-altitude orbiting satellites are not available, so for the case of Phobos the GHs' coefficients have been calculated indirectly and analytically from

Table 3.1: **Coefficients for the spherical harmonics series expansion of the Phobos' gravity field.** Stokes coefficients pairs are fully-normalized, while harmonics magnitude is un-normalized. Source [94].

n,m	$C_{n,m}$	$S_{n,m}$	$J_{n,m}$	$\lambda_{n,m}$
2,0	-0.04698	-	0.1051	180°
2,1	0.00136	0.00138	0.00250	45.42°
2,2	0.02276	-0.000202	0.01469	-0.25°
3,0	0.00293	-	0.00775	0°
3,1	-0.00309	0.00181	0.00387	149.64°
3,2	-0.00847	-0.000655	0.00290	-87.79°
3,3	0.00224	-0.01392	0.00197	-26.95°
4,0	0.00762	-	0.02286	0°
4,1	0.00347	-0.000776	0.00337	-12.61°
4,2	-0.00288	-0.00112	0.000691	-79.37°
4,3	-0.0028	0.00337	0.000262	43.24°
4,4	-0.0012	-0.000622	0.0000286	-38.15°

Table 3.2: **First coefficients for the spherical harmonics series expansion of the Mars' gravity field.** Stokes coefficients pairs are fully-normalized, while harmonics magnitude is un-normalized. Source MGM1025.

n,m	$C_{n,m}$	$S_{n,m}$	$J_{n,m}$	$\lambda_{n,m}$
2,0	-0.0008745	-	0.0019555	180°
2,1	$9.459{\cdot}10^{-11}$	$-1.140{\cdot}10^{-10}$	$1.913{\cdot}10^{-10}$	-50.32°
2,2	-0.00008459	0.00004891	0.00006307	74.98°
3,0	-0.00001189	-	0.00003146	180°
4,0	0.000005123	-	0.00001537	0°

the Phobos' shape. This has been described with a homologue spherical harmonics modeling, derived from spacecraft observations. The first mission to provide Phobos' images was the Viking program [100], while recently ESA's Mars Express provided an improved set of images. It is important to remark that this indirect derivation of the GHs is obtained with the assumption of uniform density[6], which is a hypothesis not too far from reality according to scientific studies on the moons of Mars [101]. In addition, local functions are added to describe the craters of Phobos with more detail[7].

In [94], Viking observations are used to provide a model of Phobos' gravity field where the GHs are computed numerically and stated up to degree and order 4, with the most important terms summarized in Table 3.1. The dominant harmonic is J_2, which accounts for 10% of the basic term, and is 100 times the Earth's relative perturbation effect. In particular, $C_{2,1}, S_{2,1}$ and $S_{2,2}$ are very small, which is the principal axes' frame

[6]The most recent estimation of Phobos' bulk density is $1.85 g/cm^3$ [101].

[7]They consists of depth-to-diameter relationships of common craters.

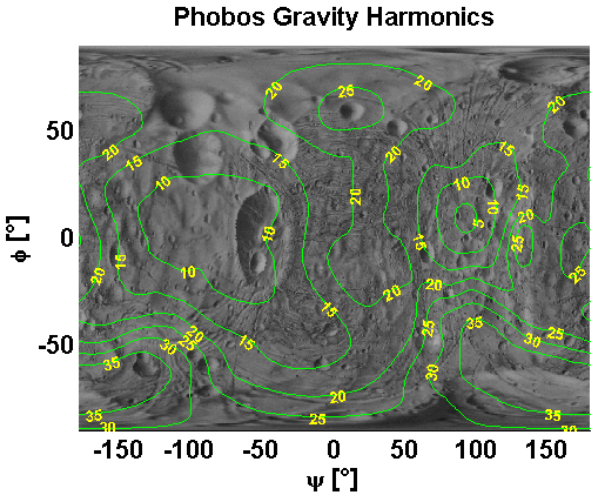

Figure 3.1: **Phobos gravity model. Contour lines over topographic map.** Magnitude of the difference of the gravity acceleration between gravity harmonics model and Keplerian point-mass model. The two fields are evaluated at $1km$ altitude over Phobos' real surface (see Fig.3.2). Difference expressed as percentage with respect to the local gravity magnitude of the Keplerian model. Spherical gravity harmonics of the model of [94] up to degree and order 4, Phobos BCBF frame. The real gravity is up to 35% higher at $1km$ altitude than that predicted by a classical model.

corresponds to the BCBF frame. It is interesting to recall that such a configuration corresponds to the stable orientation provided by the central body's gravity-gradient torque, in this case of Mars. The maximum inertia direction is aligned with the out-of-plane direction of Phobos' orbit (orbital pitch), and the minimum inertia direction is aligned with the radial direction (orbital yaw). In [102], a semi-analytical technique is used to compute the GHs of Phobos up to degree and order 6, using the same Viking's data. In [95], the tetrahedron's methodology was introduced for the first time, and applied to Phobos as a test-bed, using Viking's images. The results were compared with the GHs series expansion of [102], and the conclusion made by the author was that the two techniques produce similar results.

From this early stage [100], the model of Phobos has been further enhanced throughout the years. The delivery of Mars Express' images provided the source of data to obtain high-order shape models of Phobos [101]. In [96], the GHs of Phobos are computed up to order 20 and using a reference sphere of $14km$ radius, from the shape model of [101]. Furthermore, the same shape model is used to derive an elliptical harmonics series expansion of Phobos' gravity field, with a reference ellipsoid coincident with Phobos' mean sizes, and a tetrahedron model. The two series expansions are compared at each respective reference shape, and on the topographic surface, using the tetrahedron model's gravity as a benchmark. Outside the reference sphere, the three models are practically coincident, while between the reference sphere and ellipsoid, the elliptical GHs are preferable, but the error of the spherical GHs is only 5%. Finally, at the topographic surface of Phobos, the GHs produce large errors: up to 200% for the spherical, and up to 100% for the elliptical, both on the Southern polar zones. However,

Table 3.3: **First coefficients for the spherical harmonics series expansion of the Phobos' shape model.** Stokes coefficients pairs are fully-normalized, while harmonics magnitude is un-normalized. The mean radius of Phobos used for the shape model is $R = 10,955.8m$. Source [101].

n, m	$C_{n,m}$	$S_{n,m}$	$J_{n,m}$	$\lambda_{n,m}$
1,0	-0.0000123	-	0.0000214	180°
1,1	0.00000340	0.000000722	0.00000603	11.98°
2,0	-0.0860	-	0.192	180°
2,1	-0.00623	0.00246	0.00864	158.42°
2,2	0.0336	0.00132	0.0217	1.13°
3,0	0.0131	-	-0.0345	0°
3,1	0.0170	-0.00402	0.0188	-13.31°
3,2	-0.0186	0.000237	0.00634	89.63°
3,3	-0.00399	0.0217	0.00307	33.48°
4,0	0.00637	-	-0.0191	0°
4,1	-0.0106	0.000363	0.0101	178.04°
4,2	0.00416	-0.00421	0.0013	-22.66°
4,3	0.00836	-0.00565	0.000603	-11.36°
4,4	-0.000718	0.00333	0.0000721	25.54°

the errors at low latitudes are smaller, about 20% for the spherical GHs, and 10% for the elliptical GHs. These coefficients are not made available in [96].

Therefore, the spherical GHs technique was used to model the gravity field of Phobos in this thesis. The advantage is that the GHs are analytical functions, with far less computational cost than using a mesh of tetrahedrons, and the accuracy of the approximation could be naturally tuned by the terms of the series to be considered, unlike the tetrahedron method. It is also chosen to use the lower order GHs model of [94], while the model of [102] is used as a more accurate benchmark reference. The error between the two complete gravity fields at the SOI's boundary is of the order of a few percent of the cumulated GHs perturbation at this distance, as computed in section 3.3.6.3. The subset of methodologies developed in this paper that use Phobos' inhomogeneous gravity field will not change, and the outcomes will just depend on the series' coefficients. Fig.3.1 proves the need to use a refined model to describe the gravity field of Phobos in its proximity, by comparing the gravity provided by the gravity harmonics model of [94] with respect to the one predicted by the classical spherical model.

3.2 Modeling of the Shape

The methodology of the series expansion of spherical harmonics could be applied to analytically describe any other physical field. In particular, it could be interesting to compute the real geometrical shape of Phobos. This could be applied for graphical purposes, but in the development of this thesis the real shape of Phobos will be exploited

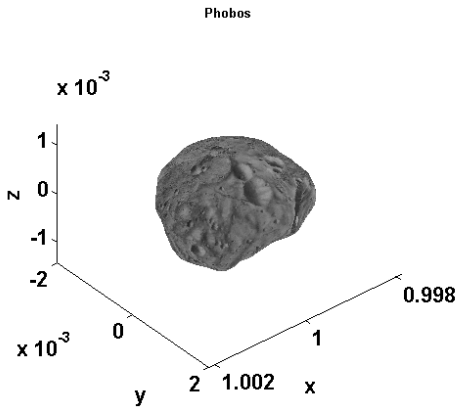

Figure 3.2: **Phobos shape model. Height.** Shape harmonics series expansions up to degree and order 17, 3B frame.

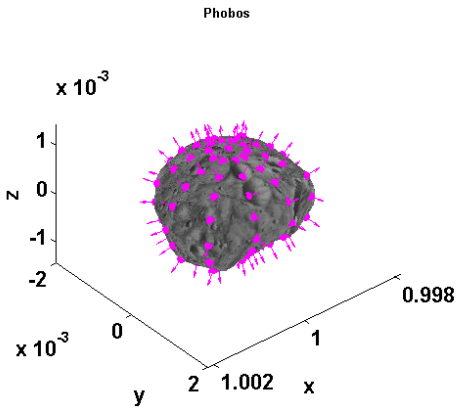

Figure 3.3: **Phobos shape model. Normal to surface.** Shape harmonics series expansions up to degree and order 17, 3B frame.

analytically in performance analyses.

The shape of a body is defined by the distance of the points on its surface from a specific point, usually its center of mass [101]. Therefore, this defines a scalar field u_R in the body's BCBF frame. The application of Eq.3.1 for a surface is simpler because the field is defined on a 2D domain, since the radial coordinate is constrained to actually be the field itself $r = u_R(\vartheta, \psi)$. The surface is expressed by the series expansion of spherical harmonics, which are called shape harmonics. This is presented in Eq.3.13, where R is the mean radius used to normalize the expression ($J_{0,0} = 1$).

$$u_R(\vartheta, \psi) = R \sum_{n=0}^{\infty} \sum_{m=0}^{n} C_n^m(\psi) P_n^m(\cos\vartheta) \tag{3.13}$$

The technique can be used under the usual requirement that the field expanded in series is a single-valued function of the spherical coordinates of the body's BCBF frame. For the particular case of the shape harmonics, a body that satisfies this constraint is called a star-like object [101]. This is a body with a globally convex surface, so without overhangs, bubbles or very complex shapes, because once defined a center no more than one point on the surface must lie along the radial axis. For example, peanut-like asteroids could not be described with this method. Despite its very large craters, in particular Stickney, Phobos does not exhibit such limits, thus a related model has been developed throughout the years. Visual images of Phobos taken from the Viking's program, the first spacecraft sent to Mars' orbit, were first used to derive the shape harmonics coefficients in [94]. Currently, with more detailed and numerous images collected from other missions sent to Mars (specifically NASA's Mars Global Surveyor and ESA's Mars Express), an updated geodesic model has been developed recently in [101] for the shape model of Phobos, using an accurate control points' network. Shape coefficients are derived in [101] up to degree and order 17 (without added local functions), and with mean fitting error on the control points' network of $40m$. The

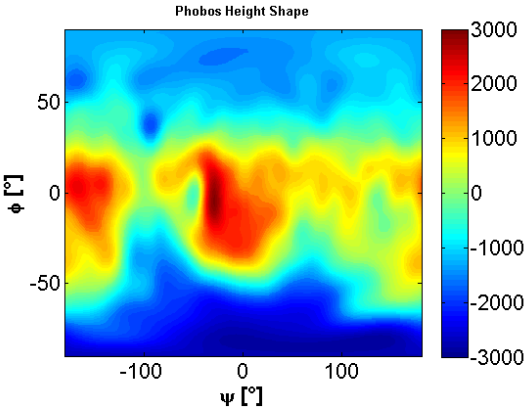

Figure 3.4: **Phobos shape model. Altitude (over the mean radius) contour map.** Shape harmonics series expansions up to degree and order 17, Phobos BCBF frame.

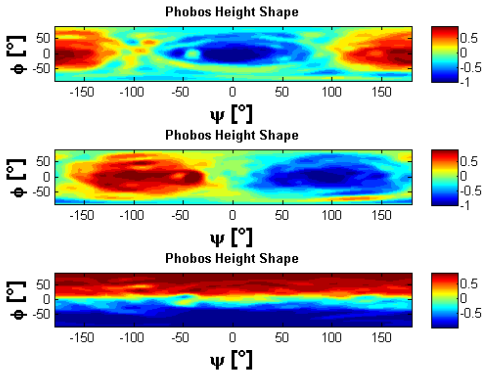

Figure 3.5: **Phobos shape model. Contour maps of the components of the normal to surface.** Shape harmonics series expansions up to degree and order 17, Phobos BCBF frame.

first shape coefficients are shown in Table 3.3, and all the set of coefficients is used in this thesis to model the surface of Phobos[8,9]. Fig.3.2 shows the resulting geometry of Phobos, where the inhomogeneous shape of this moon is evident and in particular the Stickney crater. Fig.3.4 and Fig.3.6-3.7 show the altitude maps.

The shape harmonics' coefficients could be used for calculating global physical measures of Phobos, like volume, inertia matrix, libration amplitude, and in particular, the Phobos' center of figure is displaced from its barycenter of approximately $500m$ [101]. This could be used to produce a refined model for the GHs' coefficients: this was not done in [101], and was undertaken in [96], but without reporting the coefficients. Therefore the GHs used in this thesis were chosen to be the available coefficients of [94], because the numerical calculation of them from the shape harmonics lies outside of the objectives of orbital dynamics of this research work. However, it will be proved in section 3.3.6.2 that a satisfying convergence is achieved for the purposes of this thesis.

Regarding the visualization of Phobos' shape in this thesis, to emphasize that a specific model for the gravity field or the height of Phobos is used in the analysis of the spacecraft's orbital dynamics, the shape of the moon will be shown accordingly: in particular, graphs could show Phobos either with its mean spherical, mean ellipsoidal or complete shape.

Finally, the shape harmonics' model encompasses further information in addition to the height distribution. In particular, throughout this thesis, it will be required to handle the surface's normal. In parallelism with the acceleration, which is the

[8]The cartographic map of Phobos is taken from AGI STK.

[9]The Phobos' reference frame of these coefficients is indicated in [101] to be the usual BCBF frame, but with longitudes positive towards West. Anyway, with these specifications the shape obtained by Eq.3.13 was incorrect, and the right image of Phobos is obtained with a rotation of the Prime Meridian of 180° (pointing towards the anti-Mars subpoint) and considering longitudes positive towards East in this new frame, which makes the frame simply equivalent to the Phobos' Hill's frame.

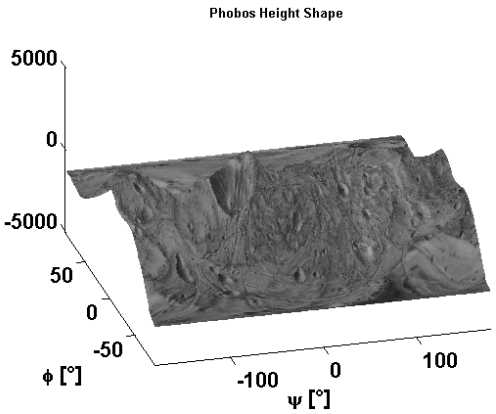

Figure 3.6: **Phobos shape model. Altitude (over the mean radius) 3D orography map (Digital Elevation Model).** Shape harmonics series expansions up to degree and order 17, Phobos BCBF frame.

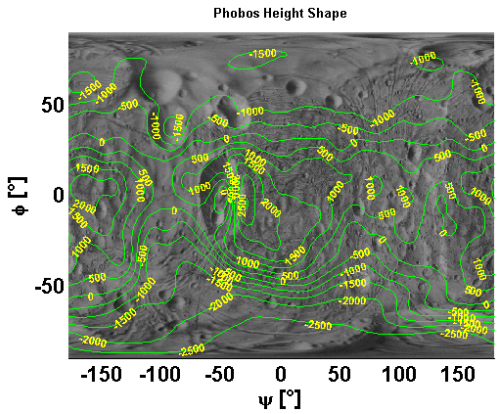

Figure 3.7: **Phobos shape model. Altitude (over the mean radius) contour lines over topographic map.** Shape harmonics series expansions up to degree and order 17, Phobos BCBF frame.

gradient (in spherical coordinates) of the gravity potential developed through spherical harmonics as shown in Eq.3.3, the components of the normal at each surface's point could be derived. To do that, the explicit function u_R is written as an implicit field f_R on the 3D domain, in order that the iso-surface at level zero corresponds to the body's figure, as shown in Eq.3.15. The outward gradient, once normalized, needs to be rotated in the Cartesian reference frame with Eq.3.4.

$$\begin{aligned}\nabla_{TSE} u_R &= \begin{bmatrix} \frac{\partial}{\partial r} \\ \frac{1}{r}\frac{\partial}{\partial \vartheta} \\ \frac{1}{r}\frac{1}{\sin\vartheta}\frac{\partial}{\partial \psi} \end{bmatrix} u_R = \\ &= \begin{cases} 0 \\ R\sum_{n=0}^{\infty}\sum_{m=0}^{n}\left[C_{n,m}\cos m\psi + S_{n,m}\sin m\psi\right]\frac{d}{d\vartheta}P_n^m(\cos\vartheta) \\ R\sum_{n=0}^{\infty}\sum_{m=0}^{n} m\left[-C_{n,m}\sin m\psi + S_{n,m}\cos m\psi\right]\frac{1}{\sin\vartheta}P_n^m(\cos\vartheta) \end{cases}\end{aligned} \tag{3.14}$$

$$\begin{cases} r = u_R(\vartheta,\psi) \Rightarrow f_R(r,\vartheta,\psi) = r - u_R(\vartheta,\psi) = 0 \\ \qquad\qquad \Rightarrow \hat{\mathbf{n}}_{OUT,TSE}(r,\vartheta,\psi) = \dfrac{\nabla_{TSE} f_R}{\|\nabla_{TSE} f_R\|} \\ \nabla_{TSE} f_R = \begin{bmatrix} 1 \\ -\frac{1}{u_R}\frac{\partial}{\partial\vartheta}u_R \\ -\frac{1}{u_R}\frac{1}{\sin\vartheta}\frac{\partial}{\partial\psi}u_R \end{bmatrix} \end{cases} \tag{3.15}$$

Fig.3.3 and Fig.3.5 show the normals' field and its maps. Obviously, also the Hessian of the shape model could be derived, and it contains the information about the curvature of the body's surface. Again, singularities at the Poles are treated as done for the GHs.

3.3 The Mars-Phobos CR3BP-GH

The purpose of this section is to extend the model of the CR3BP to include the perturbative effects of the inhomogeneous gravity field of a general celestial body. This is modeled with the GHs methodology presented in section 3.1. The GHs series expansion of both massive bodies is considered to derive a general form of this dynamical system, named CR3BP-GH.

3.3.1 Attitude Relations between Orbital and Body-Fixed Frames

The inclusion of the GHs in the 3B dynamics is a delicate operation, because the components of the gravitational acceleration are defined in the body's BCBF frame, as presented in section 3.1.1. Thus, the attitude matrix between the Hill's frame of the two massive bodies' orbit and the body-fixed frame of each body must be derived. Recall that the nomenclature used to express the frames in astrodynamics was introduced in section 2.1, and the physical variables and notation used to define the orientation of these reference frames were presented in section 2.6.1. The body's BCE frame is defined with respect to the Earth's inertial frame by the attitude matrix $\mathbf{A}_{E_\oplus N_\oplus}^{E_E\gamma}(\Omega_{N_\oplus}, i_{NP_\oplus})$. The secondary body's Hill's frame is defined with respect to the primary body's BCE frame by the attitude matrix $\mathbf{A}_{H_2}^{E_1N_1}(\Omega_2, i_2, \omega_2+\nu_2(t))$, where the true anomaly is computed from the solution of Kepler's equation. In particular, in this section numerical outcomes are obtained solving Kepler's equation, while to gain analytical insight the dynamics of the true anomaly is approximated to be uniform, which is $\nu_\oplus(t) = \nu_{0,\oplus} + n_{REV,\oplus}t$, where $n_{REV,\oplus}$ is the mean motion. This is appropriate for Phobos, whose orbit is almost circular. On the contrary Mars' eccentricity is significant, but its dynamics around the Sun is far slower than Phobos' orbital motion, thus a constant approximation of its mean motion is suitable. The body's BCBF frame is defined with respect to its BCE frame by the attitude matrix $\mathbf{A}_{BCBF_\oplus}^{E_\oplus N_\oplus} = \mathbf{A_3}\left(\Omega_{PM_\oplus}^{N_\oplus}\right)$, where the phase of the Prime Meridian (PM) with respect to the Node of reference is computed as $\Omega_{PM_\oplus}^{N_\oplus} = \Omega_{PM_\oplus,0}^{N_\oplus} + n_{ROT_\oplus}t$, and $n_{ROT_\oplus}$ is the body's spin rate. In this sense, the PM of a celestial body is taken as the longitude of a point of significant interest, like a crater [70]. For Mars, the PM's reference is the Airy-0 crater, so the corresponding angle is derived from the initial condition of 176.63° at the J2000 epoch [70]. For Phobos, the PM is taken along the sub-Mars point, since the moon is tidally-locked with Mars [69].

The resulting attitude matrices, for the primary and the secondary of the CR3BP, can now be expressed combining the appropriate successive rotations needed.

$$\begin{aligned}\mathbf{A}_{3B}^{BCBF_1} &= \mathbf{A}_{H_2}^{E_1N_1}\left(\mathbf{A}_{E_1PM_1}^{E_1N_1}\right)^T = \\ &= \mathbf{A_3}\left(n_{REV_2}t + \nu_{2,0} + \omega_2\right)\mathbf{A_1}\left(i_2\right)\mathbf{A_3}\left(\Omega_2 - \Omega_{PM_1,0}^{N_1} - n_{ROT_1}t\right)\end{aligned} \tag{3.16}$$

$$\begin{aligned}\mathbf{A}_{3B}^{BCBF_2} = \mathbf{A}_{H_2}^{E_1N_1}\mathbf{A}_{E_1N_1}^{E_E\gamma}\left(\mathbf{A}_{E_2N_2}^{E_E\gamma}\right)^T\left(\mathbf{A}_{E_2PM_2}^{E_2N_2}\right)^T = \\ =\mathbf{A_3}\left(n_{REV_2}t+\nu_{2,0}+\omega_2\right)\mathbf{A_1}\left(i_2\right)\mathbf{A_3}\left(\Omega_2\right)\mathbf{A_1}\left(i_{NP_1}\right)\cdot \\ \cdot\,\mathbf{A_3}\left(\Omega_{N_1}-\Omega_{N_2}\right)\mathbf{A_1}\left(-i_{NP_2}\right)\mathbf{A_3}\left(-\Omega_{PM_{2,0}}^{N_2}-n_{ROT_2}t\right)\end{aligned} \tag{3.17}$$

The attitude relationship between orbital and body-fixed frame is generally a function of time. It is interesting to investigate what are the conditions that allow to erase the time-dependency. The time appears twice and with opposite sign in Eq.3.16-3.17, thus the necessary condition is that the revolution and rotation rates are synchronous and coherent. However, these two terms appear on the extreme sides of the succession of elementary rotations, thus a geometrical constraint must be satisfied, which is that $\mathbf{A_1}\left(i_2\right)=\mathbf{I_3}$ for Eq.3.16, and the cluster collecting all the five central matrices of Eq.3.17 is reduced to a pure rotation along the third axis $\mathbf{A_3}\left(\Omega_2-\Omega_{N_2}\right)$. Focus now on the the conditions needed for the secondary's attitude matrix. The necessary condition $n_{REV_2}=n_{ROT_2}$ is true for Phobos, while the central core of Eq.3.17 represents the attitude matrix between the orbital and equatorial planes of the second body. The geometrical constraint is satisfied by five particular conditions, that are collected in Eq.3.18.

$$\begin{aligned}\mathbf{A}_{3B}^{BCBF_2}\neq\mathbf{A}(t)\Leftarrow&\begin{cases}i_2=0\\ i_{NP_1}=i_{NP_2}\\ \Omega_{N_1}=\Omega_{N_2}\end{cases}\vee\begin{cases}\Omega_2=0\\ i_2=i_{NP_2}-i_{NP_1}\\ \Omega_{N_1}=\Omega_{N_2}\end{cases}\vee\\ &\vee\begin{cases}i_{NP_1}=0\\ i_2=i_{NP_2}\\ \Omega_2=\Omega_{N_2}-\Omega_{N_1}\end{cases}\vee\begin{cases}i_2=0\\ i_{NP_1}=0\\ i_{NP_2}=0\end{cases}\vee\begin{cases}i_{NP_2}=0\\ i_2=-i_{NP_1}\\ \Omega_2=0\end{cases}\end{aligned} \tag{3.18}$$

The latter four mathematical conditions are rather an improbable physical occurrence, while the first condition requires that the inclination of the moon's orbit is null with respect to the central body's Equator, and that the two bodies' spin axes are aligned and coherent. This produces the secondary body's equatorial plane and its orbital plane to be coincident. As was presented in section 2.1, these physical conditions are almost satisfied by Phobos. To derive now the actual error of this approximation, the geometrical constraint is evaluated with the physical data and ephemerides of Mars and Phobos [69]. The analytical expression of the second massive body's geometrical constraint is provided below.

$$\begin{aligned}\mathbf{A}_{3B}^{BCBF_2}\neq\mathbf{A}(t)\Leftrightarrow&\sin i_2\sin\Omega_2\sin\Omega_{N_2}^{N_1}\sin i_{NP_2}+\sin i_2\cos\Omega_2\cos\Omega_{N_2}^{N_1}\cos i_{NP_1}\sin i_{NP_2}+\\ &-\sin i_2\cos\Omega_2\sin i_{NP_1}\cos i_{NP_2}+\cos i_2\cos\Omega_{N_2}^{N_1}\sin i_{NP_1}\sin i_{NP_2}+\\ &+\cos i_2\cos i_{NP_1}\cos i_{NP_2}=1\end{aligned} \tag{3.19}$$

The arccos applied to the left-hand side of Eq.3.19 yields the tilt angle θ between the equatorial and orbital planes of the second massive body. The related libration motion

in latitude is shown in Fig.3.8 for both Phobos and Deimos, and the simulation spans an epoch of interest for upcoming mission purposes to the Martian moons. It is evident that there is a significant difference between the two moons: Phobos' misalignment dynamics are considerably faster (period of 2.26 terrestrial years), while Deimos' period is almost 55 years, and the amplitude of the misalignment is nearly double for Deimos. Thus, the libration in latitude oscillates between a minimum of 0.30° and a maximum of 1.90° according to the mission's epoch, so the tilt of Phobos could be approximated to be fixed during a typical mission segment around Phobos. The libration in longitude is instead a short-period oscillation, dominated by the misalignment due to real eccentricity of the Mars-Phobos orbit, whose amplitude is 1.80° [10, 11]. In conclusion, since this angle, that represents the error taken by approximating the attitude matrix of Phobos to be fixed during an orbital period span, is relatively small, it could be approximated to be null, and the attitude matrix between the orbital and body-fixed frames of Phobos becomes time-independent,

$$\mathbf{A}_{3B}^{BCBF_2} = \mathbf{A_3}(-\Omega_{PM_2}^{R_2^1}) = \mathbf{A_3}(-\pi) \tag{3.20}$$

where the location $\Omega_{PM_2}^{R_2^1}$ of Phobos' PM (x-axis of BCBF) with respect to the Mars-Phobos radial (x-axis of 3B) is constant and formally set to $180° = \pi\ rad$ as explained previously. In particular, whereas the synchronous constraint is a common condition for the planetary systems, no simplifications would have risen if the two geometrical conditions had not been satisfied, which instead is not a very common situation in the Solar System. This approximation could be estimated to produce a residual orbital perturbation on the new Mars-Phobos CR3BP-GH of two orders of magnitude lower than the one provided by the cumulated GHs' perturbation on the CR3BP. This, together with the inaccuracy of the GHs' coefficients addressed in section 3.1.3, is a first estimation of the savings that will be provided by tracking the orbits computed in a more accurate description of the natural dynamics in the vicinity of the moon.

Eq.3.21 shows the simplification of the primary's attitude matrix for the conditions of time-independency of the secondary's attitude matrix. In this case Mars' figurative matrix is a pure rotation along the third axis too, but it is still time-dependent since the synchronous condition between the central body's rotation and the moon's revolution is a rather unique condition.

$$\mathbf{A}_{3B}^{BCBF_1} = \mathbf{A_3}\left(u_{2,0} + \Omega_2 - \Omega_{PM_1,0}^{N_1} + (n_{REV_2} - n_{ROT_1})\,(t - t_0)\right) \tag{3.21}$$

3.3.2 Apparent Effects of the Gravity Harmonics

The inclusion of the GHs is a delicate operation in the relative dynamics of the 3B problem, also because the rotating frame is set to be aligned with the Hill's frame of the two massive bodies' orbit. The inclusion of the perturbation of the GHs produces

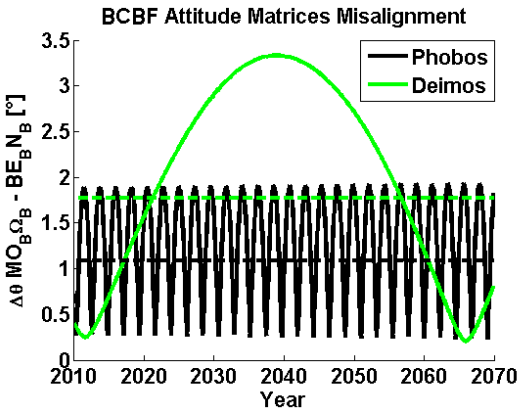

Figure 3.8: **Misalignment angle between the equatorial and orbital planes of the Martian moons.** Mean values in dotted lines.

the orbit of the two bodies to be non-Keplerian. Thus, their position with respect to their center of mass is different, and this affects the gravity field in the equations of motion. In addition, the rotation of the Hill's frame is different and not constant, and this affects the apparent acceleration's terms in the equations of motion. The analysis of non-Keplerian orbits is usually conducted with Gauss' planetary equations [103, 104], that express the derivative of the orbital elements as a function of the perturbation. The general solution could be seen as a composition of the mean orbital elements with time, and by an oscillation around them, whose spectrum could present different frequencies [103]. Thus, the mean solution is expressed by the secular derivatives of the orbital elements, and its sum with the periodic oscillation represents the osculating orbital elements that describe the non-Keplerian orbit over time.

The analytical solution is only available in terms of the mean orbital elements for the conservative GHs, which are the even zonal harmonics, while the related osculating solution is provided by semi-analytical techniques [105]. For all the other GHs, the solution can be computed only numerically, and provided explicitly as a reference signal in feed-forward to the dynamics of the perturbed-R3BP, that must be implemented in a simulator. Thus, to start gaining analytical insight, the focus is placed on describing the mean Mars-Phobos orbit under the effect of the conservative GHs, and considering at the first step the effect of Mars-J_2. The J_2 perturbation produces null secular derivatives in the orbital elements a, e, and i, while the secular derivatives of the other three angles are given below.

$$\begin{cases} \dot{\Omega}_{J_2} = -\frac{3}{2} J_2 \left(\frac{R}{p}\right)^2 n \cos i \\ \dot{\bar{\omega}}_{J_2} = 3 J_2 \left(\frac{R}{p}\right)^2 n \left(1 - \frac{5}{4}\sin^2 i\right) \\ \dot{\bar{M}}_{J_2} = n \left(1 + \frac{3}{2} J_2 \left(\frac{R}{p}\right)^2 \left(1 - \frac{3}{2}\sin^2 i\right) \sqrt{1-e^2}\right) \end{cases} \tag{3.22}$$

In particular, Eq.3.22 could be quickly probed comparing its outcomes with the difference of the related osculating ephemerides of Phobos after a day, available on the

JPL's online database. The values provided by Eq.3.22 are very close to the real ones, which indicates that Mars-J_2 secular term is the most significant perturbing effect at Phobos. Moreover, the absolute value of these derivatives is significant, which indicates that Phobos' orbit is highly non-Keplerian.

In the model of the CR3BP presented in section 2.3, the orbit of Phobos is approximated as circular, due to its small eccentricity. As discussed in section 3.3.1, the inclination of Phobos is quite small too, and for this analysis its orbit could be approximated to be equatorial. Thus, with these approximations the secular effects of the Mars-J_2 perturbation keep the geometry of the Mars-Phobos' orbit to be the same as in the CR3BP, which means that the distance of the massive bodies from their center of mass is constant, therefore not affecting the computation of their gravity field. The only effect acts on the apparent acceleration of the 3B frame, due to the change of the mean motion. However, Eq.3.22 is no longer adequate to compute the new angular motion, because it is derived from Gauss' planetary equations, which are singular for null eccentricity and inclination. There exists a non-singular version of the Gauss' planetary equations, which are stated in terms of the equinoctial orbital elements, and where the angular motion is expressed with the true longitude [104]. But also this approach is not valid for our purpose. This is because the framework of these models is represented by the osculating orbital elements, which are only a parametrization of the orbital dynamics. They express the instantaneous orbit if perturbations were not present, and cannot be used at a given time to identify the global structure of the solution like the Keplerian orbits. The case of the circular and equatorial orbit under the effect of the central body's oblateness is emblematic to recognize how the orbital dynamics are described by osculating orbital elements. The osculating solution is an equatorial ellipse, where the orbiting body is fixed at the pericenter, and the apsidal line rotates with a constant rate. This eclectic parametrization could be avoided simply writing down the equations of a circular and uniform rotation motion, deriving the constant angular velocity from the centripetal acceleration, that is now the sum of the Keplerian and the J_2 terms.

$$a_{CP} = \frac{Gm_{1-2}}{\left(r_2^1\right)^2} + \frac{Gm_{1-2}}{\left(r_2^1\right)^2}\frac{3}{2}J_{2(1)}\left(\frac{R_1}{r_2^1}\right)^2 = n^2 r_2^1 \tag{3.23}$$

The new mean motion of the Hill's frame under the central body's oblateness is expressed by means of a correction term Δ,

$$n = n_0\sqrt{1 + \frac{3}{2}J_{2(1)}\left(\frac{R_1}{r_2^1}\right)^2} = n_0\sqrt{1 + \Delta_{J_{2(1)}}} \tag{3.24}$$

where n_0 is the basic 2B mean motion. The new angular acceleration of the Hill's frame increments the apparent acceleration from the case of the CR3BP. This appears in the classical extension of the equatorial CR3BP with the central bodies' oblateness

[106, 107].

The approach could be extended to consider the Phobos-J_2 apparent effect, as well as all the other even zonal harmonics, like J_4.

$$n = n_0\sqrt{1+\Delta} = n_0\sqrt{1+\Delta_{J_{2(1)}}+\Delta_{J_{4(1)}}+\Delta_{J_{2(2)}}+\Delta_{J_{4(2)}}} \tag{3.25}$$

$$\Delta_{J_{4(1)}} = \frac{25}{8}J_{4(1)}\left(\frac{R_1}{r_2^1}\right)^4 \tag{3.26}$$

However, Mars-J_4 and Phobos-J_2 correction terms are both one thousand times smaller than the one due to Mars-J_2. Therefore, the only apparent effect of the GHs that will be considered in the Mars-Phobos system is the correction term due to Mars' oblateness. In this sense, the new centrifugal acceleration $n^2\mathbf{q}$ could be decomposed into the sum of the original one plus the correction effect $\Delta_{J_{2,(1)}}\mathbf{q}$. The latter could be seen as the sum of $\Delta_{J_{2,(1)}}\mathbf{q_2}$ and $\Delta_{J_{2,(1)}}\mathbf{r_2}$ (see Eq.2.6-2.7), which is consistent with an approach of close relative motion with respect to the secondary. But the first term is exactly equal and opposite with the Mars-J_2 gravity at Phobos. Thus, it is possible to forecast that the total effect of the Mars' oblateness, sum of the direct gravity perturbation and the apparent effect, is lower than the gross J_2 gravity term, as long as the spacecraft is close to Phobos. This is coherent with the differential analysis of the orbital perturbation undertaken in section 2.4.

3.3.3 Equations of Motion

Now that all the ingredients have been introduced and discussed separately, the Mars-Phobos CR3BP of section 2.3.3 is extended to consider the inhomogeneous gravity fields of the two massive bodies. They are modeled through the GHs methodology described in section 3.1, and introduced in the equations of motion through the attitude relations presented in section 3.3.1, together with their apparent effects addressed in section 3.3.2.

In the same way the equation of motion of the CR3BP are expressed in Eq.2.13, the emphasis is placed on the nonlinear terms in the ODEs by defining an appropriate vectorfield of the gravity of each massive body. This is decomposed into the classical Keplerian vectorfield used in Eq.2.13, and the net perturbation of the GHs starting from degree 2.

$$\mathbf{f}_{\oplus}(t,\mathbf{x}) = \mathbf{f}_{\mathbf{G}\oplus}(\mathbf{x}) + \mathbf{f}_{\mathbf{GH},\oplus}(t,\mathbf{x}) = \begin{bmatrix} \mathbf{0_{3x1}} \\ \mathbf{a_{G,\oplus}}(\mathbf{q}) \end{bmatrix} + \begin{bmatrix} \mathbf{0_{3x1}} \\ \mathbf{a_{GH,\oplus}}(t,\mathbf{q}) \end{bmatrix} \tag{3.27}$$

$$\mathbf{a_{GH},_{\oplus}}(t,\mathbf{q}) = \mathbf{A}_{3B}^{BCBF_{\oplus}}(t)\Big(\mathbf{A}_{TSE}^{BCBF_{\oplus}}(\mathbf{q})\Big)^T\nabla_{TSE}u_{G,\oplus}(\mathbf{q},n\geq 2) \tag{3.28}$$

The resulting equations of motion of the CR3BP-GH are defined in the 3B frame of the two bodies' mean circular orbit, which is now approximated also as equatorial, and

are presented in Eq.3.29.

$$\begin{aligned}\dot{\mathbf{x}} &= \mathbf{f}_{\mathbf{CR3BPGH}}(t,\mathbf{x}) = \mathbf{A}\mathbf{x} + \frac{1}{1+\Delta}\left(\mathbf{f}_1(t,\mathbf{x}) + \mathbf{f}_2(\mathbf{x})\right) = \\ &= \mathbf{A}\mathbf{x} + \frac{1}{1+\Delta}\left(\mathbf{f}_{\mathbf{G},1}(\mathbf{x}) + \mathbf{f}_{\mathbf{G},2}(\mathbf{x})\right) + \frac{1}{1+\Delta}\left(\mathbf{f}_{\mathbf{GH},1}(t,\mathbf{x}) + \mathbf{f}_{\mathbf{GH},2}(\mathbf{x})\right)\end{aligned} \tag{3.29}$$

The CR3BP-GH is expressed in non-dimensional units, with the same units of mass and length of the CR3BP, but since the time is set to correspond to the phase of Phobos around Mars, the time unit is now different to reflect the new mean motion, where the correction term Δ is given only by Mars-J_2 as discussed in section 3.3.2. The peculiarity of the Mars-Phobos system is that the secondary's gravity field in Eq.3.29 is time-invariant, since its attitude matrix is approximated to be fixed as explained in section 3.3.1. However, this Hamiltonian system is time-variant due to the fact that Mars' attitude matrix depends on time, and the specific energy of the system is not an integral of motion. The energy of the CR3BP-GH could be computed in the same way as for Eq.2.15, but expanding the gravity potential of the two bodies with the GHs series of Eq.3.1, and then scaling them down with the correction factor.

$$e = t_R(\dot{\mathbf{q}}) - u_{eff}(\mathbf{q}) = t_R - t_D - \frac{1}{1+\Delta}\left(u_{G_1} + u_{G_2}\right) \tag{3.30}$$

In the following sections, the same preliminary analysis conducted in section 2.3 for the Mars-Phobos system is undertaken using now the model of the CR3BP-GH. The approach is to study the effect of the most important GHs, introducing them separately in the series expansions, and finally consider the full CR3BP-GH.

3.3.4 Effect of J_2

The purpose of this section is to undertake the preliminary analysis of the Mars-Phobos CR3BP-GH considering the dominant GH of both massive bodies, which is J_2[10]. The resulting dynamical model is named CR3BP-J_2, and consists of the Mars-Phobos CR3BP-GH of Eq.3.29 with the Phobos-J_2, the Mars-J_2 and its apparent acceleration's correction term Δ. In this section, the analytical approach will be conducted with this complete CR3BP-J_2, and the results will be discussed adding each term in sequence.

The potential, acceleration, and Hessian, in the Cartesian coordinates of the body's BCBF frame, of the J_2 perturbation are presented in the following equations. They

[10]It should be highlighted that the summarizing figure of the perturbing effect of the GHs is given by their magnitude coefficient. However, this could depend on the normalization used, and most importantly the perturbing acceleration is a 3D field that depends on the position. Thus, the real effect of the spherical harmonic is given by the whole expression of the term used in the series expansion of Eq.3.3.

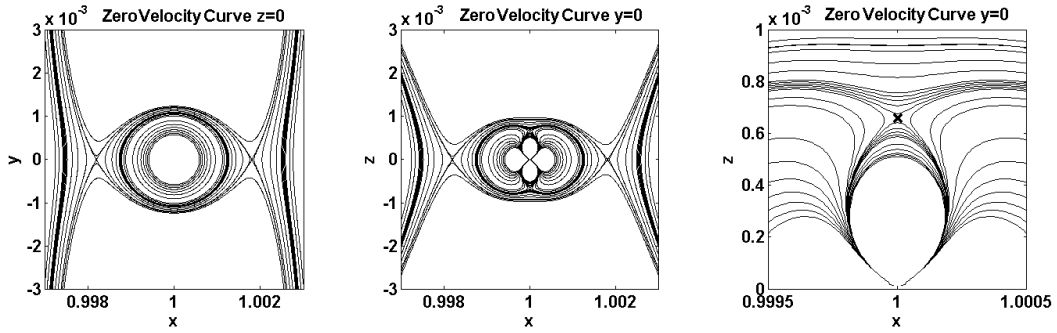

Figure 3.9: **Hill's curves in CR3BP-J_2 with Phobos-J_2.** x-y and x-z projections at different energies, with magnification around Northern additional EP.

are expressed in the non-dimensional units of the CR3BP-J_2.

$$u_{G_\oplus}^{J_{2,(\oplus)}}(\mathbf{q}_{BCBF_\oplus}) = -\frac{\mu_\oplus (R_\oplus/L)^2}{\|\mathbf{q}\|^3} J_{2,(\oplus)} \frac{1}{2}\left(3\left[\frac{q_z}{\|\mathbf{q}\|}\right]^2 - 1\right) \tag{3.31}$$

$$\mathbf{a}_{G_\oplus}^{J_{2,(\oplus)}}(\mathbf{q}_{BCBF_\oplus}) = -\frac{\mu_\oplus (R_\oplus/L)^2}{\|\mathbf{q}\|^5} J_{2,(\oplus)} \frac{3}{2} \begin{bmatrix} q_x\left(1 - 5\left[\frac{q_z}{\|\mathbf{q}\|}\right]^2\right) \\ q_y\left(1 - 5\left[\frac{q_z}{\|\mathbf{q}\|}\right]^2\right) \\ q_z\left(3 - 5\left[\frac{q_z}{\|\mathbf{q}\|}\right]^2\right) \end{bmatrix} \tag{3.32}$$

$$\mathbf{H}u_{G_\oplus}^{J_{2,(\oplus)}}(\mathbf{q}_{BCBF_\oplus}) = -\frac{\mu_\oplus (R_\oplus/L)^2}{\|\mathbf{q}\|^7} J_{2,(\oplus)} \frac{3}{2} \cdot \cdot \left\{ \begin{array}{l} 5\left(7\left[\frac{q_z}{\|\mathbf{q}\|}\right]^2 - 1\right) \begin{bmatrix} q_x \\ q_y \\ q_z \end{bmatrix} \begin{bmatrix} q_x \\ q_y \\ q_z \end{bmatrix}^T - \|\mathbf{q}\|^2 \left(5\left[\frac{q_z}{\|\mathbf{q}\|}\right]^2 - 1\right) \mathbf{I_3} + \\ -10\,(q_z) \begin{bmatrix} 0 & 0 & q_x \\ 0 & 0 & q_y \\ q_x & q_y & 2q_z \end{bmatrix} + 2\|\mathbf{q}\|^2 \begin{bmatrix} 0 & 0 & 0 \\ 0 & 0 & 0 \\ 0 & 0 & 1 \end{bmatrix} \end{array} \right\} \tag{3.33}$$

As discussed in section 3.3.3, the Martian figurative matrix in Eq.3.29 is the only term that depends on time. However, the J_2 perturbation is axially-symmetric along the z-axis, and in section 3.3.1, thanks to the orbital characteristics of Phobos, the Mars' attitude matrix was derived in Eq.3.21 to be a pure rotation along the third axis. This means that the Mars' rotation does not couple with its J_2 perturbation, and the Mars-Phobos CR3BP-J_2 is a time-invariant Hamiltonian system. The energy of the system, derived as explained in section 3.3.3, is an integral of motion, and an extended Jacobi integral c is defined through Eq.2.15.

3.3.4.1 Hill's Surfaces

The existence of an integral of motion for the Mars-Phobos CR3BP-J_2 allows an extension of the definition of the Hill's surface and the SOI also in this model. The analysis is undertaken in the same way as it was conducted in section 2.3.4 for the CR3BP,

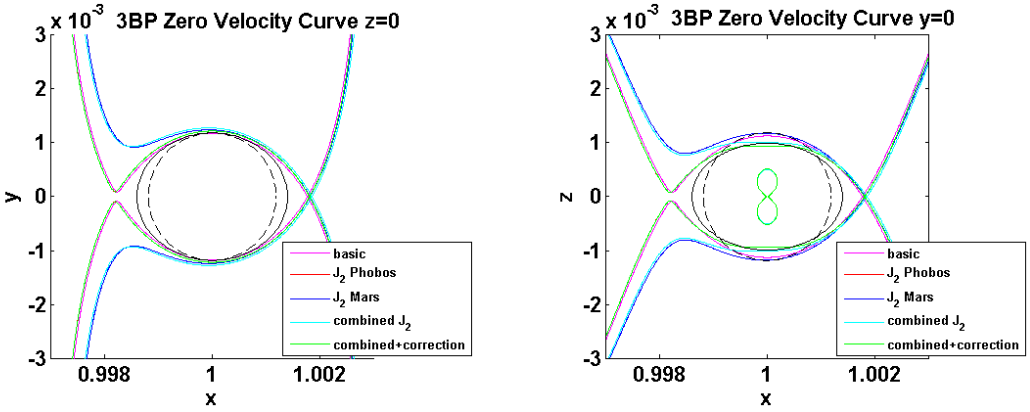

Figure 3.10: **Hill's curves at L_2 energy.** x-y and x-z projections for CR3BP and CR3BP-J_2 with only Phobos-J_2, only Mars-J_2, both terms, and finally complete case with the mean motion correction. The case of only Phobos-J_2 is indistinguishable from the final case. Energy is defined for L_2 relative to each different model. Ellipsoidal and mean sizes of Phobos.

computing the Hill's curves on the coordinates' planes. This analysis for the equatorial CR3BP with the massive bodies' oblateness has already been undertaken in [107]. Initially the effect of Phobos-J_2 is considered.

For the planar case, no important things show up, as reported in Fig.3.9. The additional J_2 potential is symmetric with respect to the own central body, just like the Keplerian potential, so the Hill's curves and their evolution on the $z = 0$ plane is the same that in the original CR3BP. It should only be reported that the collinear equilibria's energy level (which is the value of the Jacobi integral such that the curves around Phobos intersect with the ones of the Mars' and the exterior realms) is higher, and L_{1-2} are displaced farther away from Phobos. This is due to the added term in the Phobos' potential, that provides an increase of the moon's mass in the orbital plane, representing the bulge of Phobos. Therefore, this is called here the *energizing effect of the additional potential terms*.

Significant differences appear in the $y = 0$ plane (the same happens in the y-z plane). The Hill's curve is no longer a circle. Fig.3.9 shows the evolution in Phobos' realm. The effect of J_2 is paramount at low energy. The Hill's curve starts as an eight-shaped figure, whose lobes lie along the x-axis. The related Hill's surface is a doughnut. As the energy increases, the lobes increase in size, eventually intersecting in two symmetrical positions along the z-axis, and creating two internal holes below them. As the energy further increases, the internal holes implode and the Hill's surface becomes the classical ellipsoid of the CR3BP, since J_2 acts like a perturbation at the SOI's boundary.

This behavior provided by the oblateness of the massive bodies in the 3B dynamics is universal, as described in [107] for either one or both primaries. In particular, two symmetrical EPs are born for each body. These EPs are not exactly positioned along the vertical axis, but are slightly displaced towards the other body. They are L_{6-7} for Phobos, and L_{8-9} for Mars. In general, for the celestial bodies of the Solar System, these EPs are placed inside the body's figure [107].

Fig.3.10 presents the Hill's SOI of the CR3BP-J_2. The increase in Mars' potential energizes the Mars' realm, and L_{1-2} are shifted away from Mars. The increased centrifugal potential counteracts this effect, and the Hill's curves for the complete CR3BP-J_2 are indistinguishable from the ones of the case that considers only Phobos-J_2. This was expected from the consideration made in section 3.3.2, as well as the simplified analysis of the orbital perturbations in section 2.4. In particular, from Fig.3.10 we see that it is impossible to orbit around Phobos at energies lower than that of L_2.

3.3.4.2 Equilibrium Points

The natural EPs of the CR3BP-J_2 are computed in the same way as in section 2.3.5.1 for the CR3BP, as the stationary points of the new potential function.

$$
\begin{aligned}
&(1+\Delta)\begin{bmatrix} x \\ y \\ z \end{bmatrix} - \frac{(1-\mu)}{\left(\sqrt{(x+\mu)^2+y^2+z^2}\right)^3}\begin{bmatrix} x+\mu \\ y \\ z \end{bmatrix} - \frac{\mu}{\left(\sqrt{(x+\mu-1)^2+y^2+z^2}\right)^3}\begin{bmatrix} x+\mu-1 \\ y \\ z \end{bmatrix} + \\
&-\frac{\mu(R_2/L)^2}{\left(\sqrt{(x+\mu-1)^2+y^2+z^2}\right)^5} J_{2(2)} \frac{3}{2} \begin{bmatrix} (x+\mu-1)\left(1-5\left[\frac{z}{\sqrt{(x+\mu-1)^2+y^2+z^2}}\right]^2\right) \\ y\left(1-5\left[\frac{z}{\sqrt{(x+\mu-1)^2+y^2+z^2}}\right]^2\right) \\ z\left(3-5\left[\frac{z}{\sqrt{(x+\mu-1)^2+y^2+z^2}}\right]^2\right) \end{bmatrix} + \\
&-\frac{(1-\mu)(R_1/L)^2}{\left(\sqrt{(x+\mu)^2+y^2+z^2}\right)^5} J_{2(1)} \frac{3}{2} \begin{bmatrix} (x+\mu)\left(1-5\left[\frac{z}{\sqrt{(x+\mu)^2+y^2+z^2}}\right]^2\right) \\ y\left(1-5\left[\frac{z}{\sqrt{(x+\mu)^2+y^2+z^2}}\right]^2\right) \\ z\left(3-5\left[\frac{z}{\sqrt{(x+\mu)^2+y^2+z^2}}\right]^2\right) \end{bmatrix} = \begin{bmatrix} 0 \\ 0 \\ 0 \end{bmatrix}
\end{aligned}
\tag{3.34}
$$

The number of roots is now 9: the five basic equilibria, plus two additional symmetric couples above and below the two planets [107], as presented in section 3.3.4.1. The computation of these additional equilibria could not be expressed as the solution of a scalar function because they are not exactly aligned along the vertical axis. For Phobos' realm, L_{6-7} vertical position is equal to 66% of the related Phobos' mean ellipsoidal dimension, while their x-position is shifted by only $10cm$. For Mars' realm, L_{8-9} height is only 0.2% of the planet's radius. These additional equilibria created by the GHs are not practically useful because they are inside the body's figure, and they are reported here only from the mathematical point of view, to match the polynomial's degree of the stationary condition of Eq.3.34. But it should be highlighted that they are also physical meaningless, because as was stated in section 3.1, the spherical GHs are not valid inside the body's reference Brillouin's sphere. However, in terms of the global force field, the presence of these fictitious equilibria indicates that flying close to the

Polar regions (for example hovering) would be cheaper than that was predicted by a Keplerian analysis.

The focus is now placed on the basic equilibria. For the equilateral points, the shift is due only to the Mars perturbation. The new L_{4-5} shift away in both planar components with a magnitude displacement of $5m$. The analysis is more important for the collinear points L_{1-2}. They can be computed with an extended version of Euler's Eq.2.24, up to a ninth degree polynomial. The following equations show the polynomials for the two collinear cases of the CR3BP-J_2, each one with the three options: Phobos-J_2, Mars-J_2, both terms combined. For each option the apparent acceleration's correction is shown.

$$\begin{cases} \begin{array}{c} (1+\Delta)\,s^7 + (1+\Delta)\,(\mu-3)s^6 + (1+\Delta)\,(-2\mu+3)s^5 + (-\mu+\Delta\,(\mu-1))\,s^4 + \\ +2\mu s^3 - \mu\left(1+\frac{3}{2}(R_2/L)^2 J_{2(2)}\right)s^2 + 3\mu(R_2/L)^2 J_{2(2)}s - \frac{3}{2}\mu(R_2/L)^2 J_{2(2)} = 0 \end{array} \\ \begin{array}{c} (1+\Delta)\,s^7 + (1+\Delta)\,(\mu-5)s^6 + (1+\Delta)\,(-4\mu+10)s^5 + (4\mu-9+\Delta\,(6\mu-10))\,s^4 + \\ +(2\mu+3+\Delta\,(-4\mu+5))\,s^3 + \left(-6\mu+\Delta\,(\mu-1)+\frac{3}{2}\,(1-\mu)\,(R_1/L)^2 J_{2(1)}\right)s^2 + 4\mu s - \mu = 0 \end{array} \\ \begin{array}{c} (1+\Delta)\,s^9 + (1+\Delta)\,(\mu-5)s^8 + (1+\Delta)\,(-4\mu+10)s^7 + (4\mu-9+\Delta\,(6\mu-10))\,s^6 + \\ +(2\mu+3+\Delta\,(-4\mu+5))\,s^5 + \left(-6\mu+\Delta\,(\mu-1)-\frac{3}{2}(R_2/L)^2 J_{2(2)}+\frac{3}{2}\,(1-\mu)\,(R_1/L)^2 J_{2(1)}\right)s^4 + \\ +\left(4\mu+6\mu(R_2/L)^2 J_{2(2)}\right)s^3 - \left(\mu+9\mu(R_2/L)^2 J_{2(2)}\right)s^2 + 6\mu(R_2/L)^2 J_{2(2)}s - \frac{3}{2}\mu(R_2/L)^2 J_{2(2)} = 0 \end{array} \end{cases} \tag{3.35}$$

$$\begin{cases} \begin{array}{c} (1+\Delta)\,s^7 - (1+\Delta)\,(\mu-3)s^6 + (1+\Delta)\,(-2\mu+3)s^5 - (\mu+\Delta\,(\mu-1))\,s^4 + \\ -2\mu s^3 - \mu\left(1+\frac{3}{2}(R_2/L)^2 J_{2(2)}\right)s^2 - 3\mu(R_2/L)^2 J_{2(2)}s - \frac{3}{2}\mu(R_2/L)^2 J_{2(2)} = 0 \end{array} \\ \begin{array}{c} (1+\Delta)\,s^7 - (1+\Delta)\,(\mu-5)s^6 + (1+\Delta)\,(-4\mu+10)s^5 + (-6\mu+9-\Delta\,(6\mu-10))\,s^4 + \\ +(-6\mu+3+\Delta\,(-4\mu+5))\,s^3 + \left(-6\mu-\Delta\,(\mu-1)-\frac{3}{2}\,(1-\mu)\,(R_1/L)^2 J_{2(1)}\right)s^2 - 4\mu s - \mu = 0 \end{array} \\ \begin{array}{c} (1+\Delta)\,s^9 - (1+\Delta)\,(\mu-5)s^8 + (1+\Delta)\,(-4\mu+10)s^7 + (-6\mu+9-\Delta\,(6\mu-10))\,s^6 + \\ +(-6\mu+3+\Delta\,(-4\mu+5))\,s^5 + \left(-6\mu-\Delta\,(\mu-1)-\frac{3}{2}(R_2/L)^2 J_{2(2)}-\frac{3}{2}\,(1-\mu)\,(R_1/L)^2 J_{2(1)}\right)s^4 + \\ -\left(4\mu+6\mu(R_2/L)^2 J_{2(2)}\right)s^3 - \left(\mu+9\mu(R_2/L)^2 J_{2(2)}\right)s^2 - 6\mu(R_2/L)^2 J_{2(2)}s - \frac{3}{2}\mu(R_2/L)^2 J_{2(2)} = 0 \end{array} \end{cases} \tag{3.36}$$

In summary: L_1, starting from an altitude of $3,480m$ with respect to Phobos in the CR3BP, is now $365m$ farther away; L_2, starting from an altitude of $3,500m$, is now $365m$ farther away too. The difference of these value from considering or not the Mars' oblateness in the CR3BP-J_2 is of $3m$. Therefore the Phobos-J_2 perturbation provides a displacement of more than 10% of the altitude of L_{1-2}. This indicates how important it is to consider the inhomogeneous gravity field of Phobos for the calculation of the Libration points and orbits, which significantly differ from their classical solutions computed in the CR3BP.

Regarding the stability of these equilibria, the properties remain qualitatively the same: the collinear LPs are unstable, the equilateral LPs are stable, and the additional couples are unstable. In particular, L_{6-7} exhibit a center × spiral sink × spiral source phase portrait, with the couple of spirals having exactly opposite couples of eigenvalues.

3.3.4.3 Reduction of the Mars-Phobos CR3BP-GH

After the static 1D analysis of the perturbations in section 2.4, the analytical insight in section 3.3.2, and the qualitative 3D result in section 3.3.4.1, it has been also nu-

merically quantified in section 3.3.4.2 that, in the framework of the relative motion modeling around the moon, the Mars-J_2 effect is negligible inside Phobos' SOI. The next dominant Mars' GHs are $J_{2,2}$, which accounts for 0.1% of Mars-J_2 at Phobos' SOI, and J_3, which is even less. Therefore, the paramount result obtained by the preliminary analysis undertaken in this section 3.3.4, that considers only the effect of the oblateness of the two massive bodies in the CR3BP-GH, is that the complete GHs model of Mars could be disregarded from the analysis of the relative orbital dynamics around Phobos. From this point, **the Mars-Phobos CR3BP-GH** of Eq.3.29, that will be used in this thesis, **considers only the inhomogeneous gravity field of Phobos**, *without the apparent effect of its GHs*. This is presented in Eq.3.37.

$$\begin{aligned}\dot{\mathbf{x}} = \mathbf{f}_{\mathbf{CR3BPGH}}(\mathbf{x}) = \mathbf{A}\mathbf{x} + \begin{bmatrix} \mathbf{0_{3x1}} \\ \mathbf{a}_{\mathbf{G}1}(\mathbf{q}) + \mathbf{a}_{\mathbf{G}2}(\mathbf{q}) \end{bmatrix} + \begin{bmatrix} \mathbf{0_{3x1}} \\ \mathbf{A}_3(-\pi)\left(\mathbf{A}_{TSE}^{BCBF_2}(\mathbf{q})\right)^T \nabla_{TSE} u_{G,2}(\mathbf{q}, n \geq 2) \end{bmatrix} \\ = \mathbf{f}_{\mathbf{CR3BP}}(\mathbf{x}) + \mathbf{f}_{\mathbf{GH},2}(\mathbf{x})\end{aligned} \tag{3.37}$$

Thus, the time-scale of this system corresponds to the original unperturbed mean motion of the Keplerian, circular and equatorial orbit of Phobos around Mars of the CR3BP. Furthermore, this Hamiltonian system is fully autonomous in time, and the Jacobi integral of Eq.2.15 is extended with the series expansion of Phobos' GHs potential of Eq.3.1.

3.3.5 Effect of $J_{2,2}$

Consider the Phobos' GHs magnitude coefficients of Table 3.1. After J_2, which is about 10%, the other significant terms over 1% are J_4 (2%) and $J_{2,2}$ (1%). J_4 perturbation's behavior is similar to the one of J_2 (since they are even zonal harmonics), but its effect also decreases with the square of the distance if compared with J_2. The first sectorial harmonic $J_{2,2}$ has the same distance relationship as J_2, and is important in characterizing the attracting body as an ellipsoid, since it is related to the inequality of the dimensions of the body on the equatorial plane, which is commonly referred to as the triaxiality. In Table 3.1, the $J_{2,2}$ phase $\lambda_{2,2}$ is close to zero, meaning that the Phobos' BCBF frame's x-axis (and the 3B frame's x-axis too) is also the principal axis of minimum inertia.

The purpose of this section is to undertake the preliminary analysis of the Mars-Phobos CR3BP-GH, considering the effect of the triaxiality. After the paramount result obtained in section 3.3.4.3, the time-invariant dynamical model consists of the Mars-Phobos CR3BP-GH of Eq.3.37 including the Phobos-$J_{2,2}$ term, and is named CR3BP-$J_{2,2}$.

The potential, acceleration, and Hessian, in the Cartesian coordinates of the body's BCBF frame, of the $J_{2,2}$ perturbation are presented in the following equations. They

are expressed in the non-dimensional units of the CR3BP-$J_{2,2}$.

$$u_{G_\oplus}^{J_{2,2,(\oplus)}}(\mathbf{q}_{BCBF_\oplus}) = \frac{\mu_\oplus (R_\oplus/L)^2}{\|\mathbf{q}\|^3} J_{2,2,(\oplus)} 3 \left[\frac{\|\mathbf{q}\|_{x-y}}{\|\mathbf{q}\|}\right]^2 \cos 2\left(\arctan 2\left(q_y, q_x\right) - \lambda_{2,2,(\oplus)}\right) \tag{3.38}$$

$$\begin{aligned}\mathbf{a}_{G_\oplus}^{J_{2,2,(\oplus)}}(\mathbf{q}_{BCBF_\oplus}) = &- \frac{\mu_\oplus (R_\oplus/L)^2}{\|\mathbf{q}\|^5} J_{2,2,(\oplus)} 3 \cdot \\ &\cdot \begin{bmatrix} q_x \left(5\left[\frac{\|\mathbf{q}\|_{x-y}}{\|\mathbf{q}\|}\right]^2 - 2\right) \cos 2\left(\arctan 2\left(q_y, q_x\right) - \lambda_{2,2,(\oplus)}\right) + \\ - 2 q_y \sin 2\left(\arctan 2\left(q_y, q_x\right) - \lambda_{2,2,(\oplus)}\right) \\ q_y \left(5\left[\frac{\|\mathbf{q}\|_{x-y}}{\|\mathbf{q}\|}\right]^2 - 2\right) \cos 2\left(\arctan 2\left(q_y, q_x\right) - \lambda_{2,2,(\oplus)}\right) + \\ + 2 q_x \sin 2\left(\arctan 2\left(q_y, q_x\right) - \lambda_{2,2,(\oplus)}\right) \\ q_z 5\left[\frac{\|\mathbf{q}\|_{x-y}}{\|\mathbf{q}\|}\right]^2 \cos 2\left(\arctan 2\left(q_y, q_x\right) - \lambda_{2,2,(\oplus)}\right) \end{bmatrix}\end{aligned} \tag{3.39}$$

$$\begin{aligned}\mathbf{H} u_{G_\oplus}^{J_{2,2,(\oplus)}}(\mathbf{q}_{BCBF_\oplus}) = &- \frac{\mu_\oplus (R_\oplus/L)^2}{\|\mathbf{q}\|^7} J_{2,2,(\oplus)} 3 \cdot \\ &\cdot \left\{ \begin{array}{l} \left\{ \begin{array}{l} 5\left(-7\left[\frac{\|\mathbf{q}\|_{x-y}}{\|\mathbf{q}\|}\right]^2 + 2\right) \begin{bmatrix} q_x \\ q_y \\ q_z \end{bmatrix} \begin{bmatrix} q_x \\ q_y \\ q_z \end{bmatrix}^T + 10 \begin{bmatrix} q_x \\ q_y \\ 0 \end{bmatrix} \begin{bmatrix} q_x \\ q_y \\ 0 \end{bmatrix}^T \\ -10 \begin{bmatrix} 0 \\ 0 \\ q_z \end{bmatrix} \begin{bmatrix} 0 \\ 0 \\ q_z \end{bmatrix}^T + 5\|\mathbf{q}\|_{x-y}{}^2 \mathbf{I_3} - 2\|\mathbf{q}\|^2 \begin{bmatrix} 1 & 0 & 0 \\ 0 & 1 & 0 \\ 0 & 0 & 0 \end{bmatrix} \\ +4\left[\frac{\|\mathbf{q}\|}{\|\mathbf{q}\|_{x-y}}\right]^2 \begin{bmatrix} q_y{}^2 & -q_x q_y & 0 \\ -q_x q_y & q_x{}^2 & 0 \\ 0 & 0 & 0 \end{bmatrix} \end{array} \right\} \cdot \\ \cdot \cos 2\left(\arctan 2\left(q_y, q_x\right) - \lambda_{2,2,(\oplus)}\right) + \\ + \left\{ \begin{array}{l} 10 \begin{bmatrix} 2q_x q_y & q_y{}^2 - q_x{}^2 & q_y q_z \\ q_y{}^2 - q_x{}^2 & -2q_x q_y & -q_x q_z \\ q_y q_z & -q_x q_z & 0 \end{bmatrix} \\ -2\left[\frac{\|\mathbf{q}\|}{\|\mathbf{q}\|_{x-y}}\right]^2 \begin{bmatrix} 2q_x q_y & q_y{}^2 - q_x{}^2 & 0 \\ q_y{}^2 - q_x{}^2 & -2q_x q_y & 0 \\ 0 & 0 & 0 \end{bmatrix} \end{array} \right\} \cdot \\ \cdot \sin 2\left(\arctan 2\left(q_y, q_x\right) - \lambda_{2,2,(\oplus)}\right) \end{array} \right\}\end{aligned} \tag{3.40}$$

3.3.5.1 Hill's Surfaces

The analysis undertaken in this section is identical to the one conducted for the CR3BP-J_2 in section 3.3.4.1, but considering the effective potential with the triaxiality term of Phobos. The related Hill's curves on the coordinates planes show an evolution similar to the case of the CR3BP-J_2 with Phobos-J_2, but with an inverted behavior between the projections on the x-y and x-z planes. At low energies two symmetrical lobes lie along the x-axis. As the energy increases, the lobes grow in size, eventually intersecting in two symmetrical positions along the y-axis, and creating two internal holes below them. As the energy further increases, the internal holes implode and the Hill's surface eventually becomes the classical ellipsoid of the CR3BP.

Similar to the case of Phobos-J_2, the realm is energized along the x-axis, represent-

ing the maximum dimension of Phobos. Thus, L_{1-2} are displaced farther away from Phobos. Furthermore, the two additional EPs created solely by Phobos-$J_{2,2}$ GH are placed in symmetric positions along the y-axis. Again, these new equilibria L_{6-7} are internal to the figure of Phobos, positioned at around the 50% of the related dimension. All these equilibria are actually slightly displaced from the x and y-axes, since $\lambda_{2,2}$ is not exactly null.

3.3.5.2 Equilibrium Points

Approximating $\lambda_{2,2}$ to be null, the additional force field of $J_{2,2}$ remains central along the x and y directions, so the collinear EPs can be computed analytically with a scalar polynomial equation of degree 7. These two augmented Euler equations are exactly the same of the CR3BP-J_2 with Phobos' oblateness presented in Eq.3.35-3.36, substituting $3/2J_2$ with $9J_{2,2}$.

$$\begin{cases} (1+\Delta)\,s^7 + (1+\Delta)\,(\mu-3)s^6 + (1+\Delta)\,(-2\mu+3)s^5 + (-\mu+\Delta\,(\mu-1))\,s^4 + \\ +2\mu s^3 - \mu\left(1+9(R_2/L)^2 J_{2,2(2)}\right)s^2 + 18\mu(R_2/L)^2 J_{2,2(2)}s - 9\mu(R_2/L)^2 J_{2,2(2)} = 0 \\ (1+\Delta)\,s^7 - (1+\Delta)\,(\mu-3)s^6 + (1+\Delta)\,(-2\mu+3)s^5 - (\mu+\Delta\,(\mu-1))\,s^4 + \\ -2\mu s^3 - \mu\left(1+9(R_2/L)^2 J_{2,2(2)}\right)s^2 - 18\mu(R_2/L)^2 J_{2,2(2)}s - 9\mu(R_2/L)^2 J_{2,2(2)} = 0 \end{cases} \tag{3.41}$$

Therefore, the effect of $J_{2,2}$ at the Phobos' SOI's boundary is very similar and aligned to J_2. The altitude of L_{1-2} in a CR3BPH-GH with a quadrupole description of Phobos' gravity now differs by 20% of their original value in the classical CR3BP, which is very significant. The stability properties remain unchanged.

3.3.6 The CR3BP-GH with the complete Gravity Field of Phobos

This section concludes the analysis of the first extended model of the relative orbital dynamics around Phobos, by studying the Mars-Phobos system with the full CR3BP-GH of Eq.3.37, that considers the complete Phobos' GHs series expansion of Eq.3.3 with the data of Table 3.1.

3.3.6.1 Hill's Surfaces

The study of the augmented specific potential of the time-invariant Mars-Phobos full CR3BP-GH through the evolution of the Hill's surface is graphically complex because the extended model does not have any symmetry. Thus the study of the Hill's curves onto the coordinates planes is not sufficient. However, after the study of the simplified versions CR3BP-J_2 and CR3BP-$J_{2,2}$ in section 3.3.4.1-3.3.5.1, the fundamental aspects of the behavior of the GHs on the 3B dynamics are comprehended.

The first aspect is the energizing effect of the GHs on Phobos' realm, which is provided by the additional terms in the augmented potential of Phobos. The consequence is that the intersections between the realms of admissible motion around Phobos, Mars,

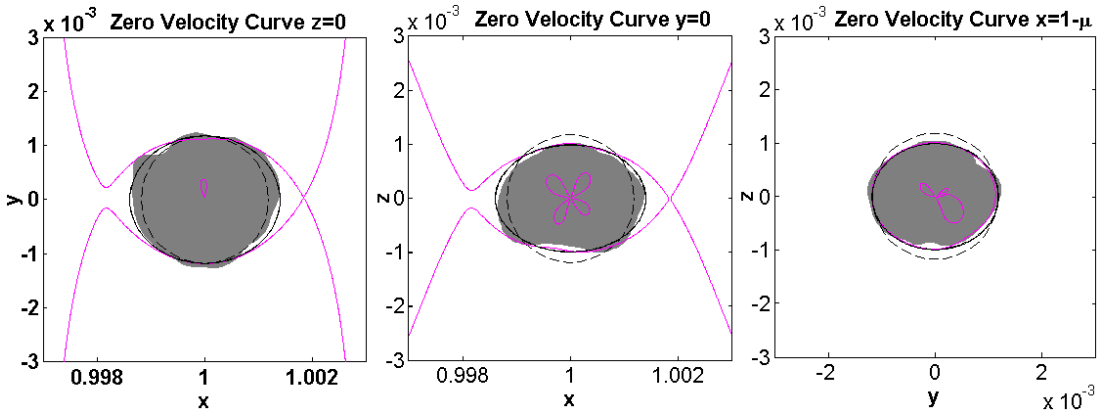

Figure 3.11: **Hill's surface in CR3BP-GH for L_2 energy.** Projections on coordinates planes. Phobos real shape, mean sphere (dashed line) and ellipsoid (plain line). Phobos' GHs model of [94].

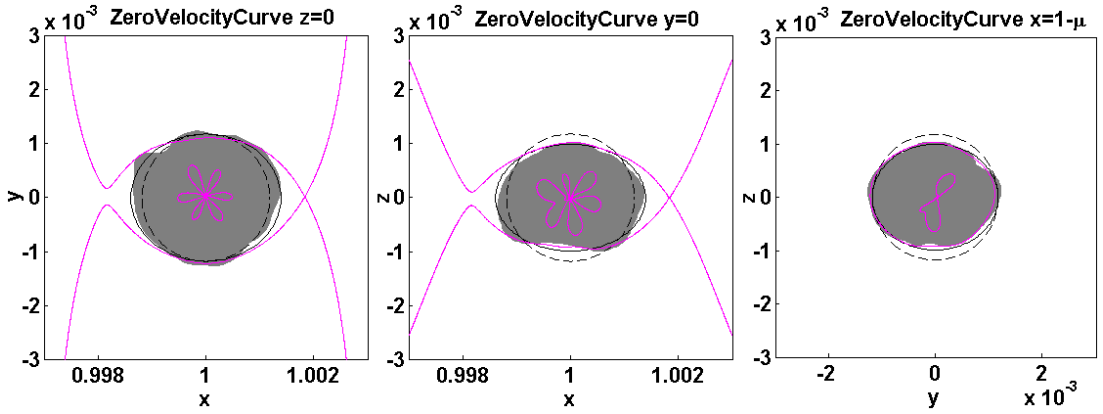

Figure 3.12: **Hill's surface in CR3BP-GH for L_2 energy.** Projections on coordinates planes. Phobos real shape, mean sphere (dashed line) and ellipsoid (plain line). Phobos' GHs model of [102].

and the whole 2B system, hold for the CR3BP-GH, but they occur farther away from Phobos. They define the position of the collinear equilibria L_{1-2}, that will be specifically addressed in section 3.3.6.2.

The second effect is the evolutionary behavior of the GHs at increasing energy. The spherical harmonics are the basis of natural modes onto the 2D sphere's surface. Thus they are 3D bubbles, and their effect on the Hill's surface is represented by a pattern of local lobes. These are evident at low energy, since the relevance of the GHs with respect to the spherical fundamental term is inversely proportional to the distance from the barycenter. This starting condition could be referred to as the "birth" of the realm. As the energy increases, the Hill's surface grows in dimension and its lobes start to collapse with each other. This evolution continues until there are no more lobes, nor residual internal holes, and the realm becomes "adult". This condition is identified by an energy such that the Hill's surface tends to the one of the classical CR3BP. The points where the lobes attach to each other are additional EPs of the model. Due to

Table 3.4: **C3BP-GH basic equilibria.** Displacement of the LPs of the CR3BP-GH from their original value in the CR3BP (Table 2.2). Absolute displacement, and relative displacement of L_{1-2} in brackets from Phobos' barycenter. The second relative value in brackets is related to the L_{1-2}'s altitude from Phobos' surface modeled with shape harmonics. Considering the Mars-J_2 oblateness, changes in x-component for L_{1-2} are of $3m$, whereas no change happens for L_3. Values for L_{4-5} are instead calculated at first with the general model.

EP	Δx	Δy	Δz
L_1	-743m (-4%,-21%)	346m (2%,10%)	-195m (-1%,-6%)
L_2	643m (4%,18%)	345m (2%,10%)	-101m (-1%,-3%)
L_3	<1m	<1m	0m
L_4	5m	-3m	0m
L_5	5m	3m	0m

Table 3.5: **C3BP-GH additional equilibria.** Location in the Phobos' BCBF frame, with related geographic coordinates and altitude from Phobos' surface modeled with shape harmonics.

EP	x	y	z	ϕ	ψ	h
L_6	4,419m	472m	5,104m	48.95°	6.09°	-3,091m
L_7	-3,349m	-1,173m	5,616m	57.71°	199.30°	-2,848m
L_8	2,116m	-951m	-5,517m	-67.19°	335.80°	-2,481m
L_9	611m	-4,766m	-5,361m	-48.13°	277.31°	-2,028m

the fact that the perturbative effects of the GHs on the Hill's surface are relevant at low energies, these EPs are usually inside the central body's figure. This is also the case of Phobos, as will be addressed in section 3.3.6.2.

Once the last additional EP is born, the "adult" realm will then intersect the Hill's surfaces of the Martian and exterior realms to provide the LPs of the CR3BP-GH. Fig.3.11-3.12 show the pattern of the Hill's surface at the energy of L_2, using the chosen GHs model of [94], and the benchmark model of [102]. Note in these figures that the Hill's surface at the energy of the LPs around Phobos is very close to its surface. This was already evident in the classical CR3BP, just considering a mean ellipsoid as reference for Phobos' shape as shown in Fig.2.6. However, *the inclusion of the GHs improves the correspondence between the two boundaries in particular in the vertical dimension.* This is evident when comparing the SOI of the two GHs models: the exterior boundaries of the Hill's curves are similar, with noticeable difference only around the Southern polar region. In this region the higher order model tends to improve the curvature to neatly follow the real shape of Phobos. This outcome could not be a coincidence. The fact that the body's shape fills entirely its SOI is considered one of the proofs of the theory of accretion which attempts to explain the origin of Phobos, as was introduced in section 1.1. The results obtained with this enhanced CR3BP-GH further suggest that the transportation of mass at low energy could be responsible for

the current shape of Phobos, in particular for the vertical dimension, where no other way of escape at low energy is available because the gateway of the invariant manifolds of the LPs is close to the orbital plane. An additional consideration on the range of dimensions of these transferred materials will be presented in section 4.4.7.

3.3.6.2 Equilibrium Points

The basic five LPs in the CR3BP-GH are still calculated by solving the stationary condition of the augmented potential function of the time-invariant model. As this enhanced system does not have any symmetry, the computation requires one to solve a coupled 3D system of nonlinear equations with Newton's method, using the values of the LPs in the original CR3BP as initial guesses. The results are presented in Table 3.4. The purpose of the analysis focuses on the collinear couple L_{1-2}. They both have moved away from Phobos, under the orbital plane, and forward with respect to Phobos along the tangential coordinate of the Hill's frame. The asymmetric displacement of L_1 and L_2 from their original values in the basic CR3BP accounts for 20% of their altitude over Phobos. This is significant because the altitude is the practical measure for space mission's applications, in contrast to the distance from the barycenter. This demonstrates how inaccurate the CR3BP would be for such applications.

Fig.3.11-3.12 show the pattern of the Hill's surface at the energy of L_2. Due to the low μ, as it was in the CR3BP, the energy difference between L_1 and L_2 is small in non-dimensional units (10^{-7}), therefore the related Hill's surfaces at the energy of L_1 and L_2, apart from the small region around each EP, are practically unchanged: they identify the boundary of the Hill's SOI of Phobos. In this sense, also considering its complete inhomogeneous gravity field, it is clearly impossible to orbit around Phobos at energies lower than the one of L_2. Regarding the stability properties, these remain qualitatively unchanged.

As discussed in section 3.3.6.1, the inclusion in the dynamics of the GHs provide additional equilibria at low energy. For the spherical harmonics model used up to fourth-degree, 4 additional EPs exist mathematically, from the solution of the stationary condition of the augmented potential. However, the employment of Newton's method to compute these EPs requires to provide a reliable initial guess for each of them. To derive the initial guess, the simple and practical procedure is to compute the iso-surfaces of the scalar field defined as the magnitude of the augmented potential's gradient[11]. This allows to visually identify "islands" where the thrust level decreases, and where an EP, which is one of the critical points where the iso-surface at null level collapses, is located in each of them. Using a position inside these four "islands" placed inside Phobos' figure, the Newton's method converges to provide the additional EPs, that have been reported in Table 3.5. Three EPs are close to the x-z plane, two above the orbital plane and symmetrical with respect to Phobos' North Pole, and one in the

[11] This corresponds to the propulsive acceleration required to hover in a fixed point of the 3B frame, and the related iso-surfaces are known as equi-thrust surfaces.

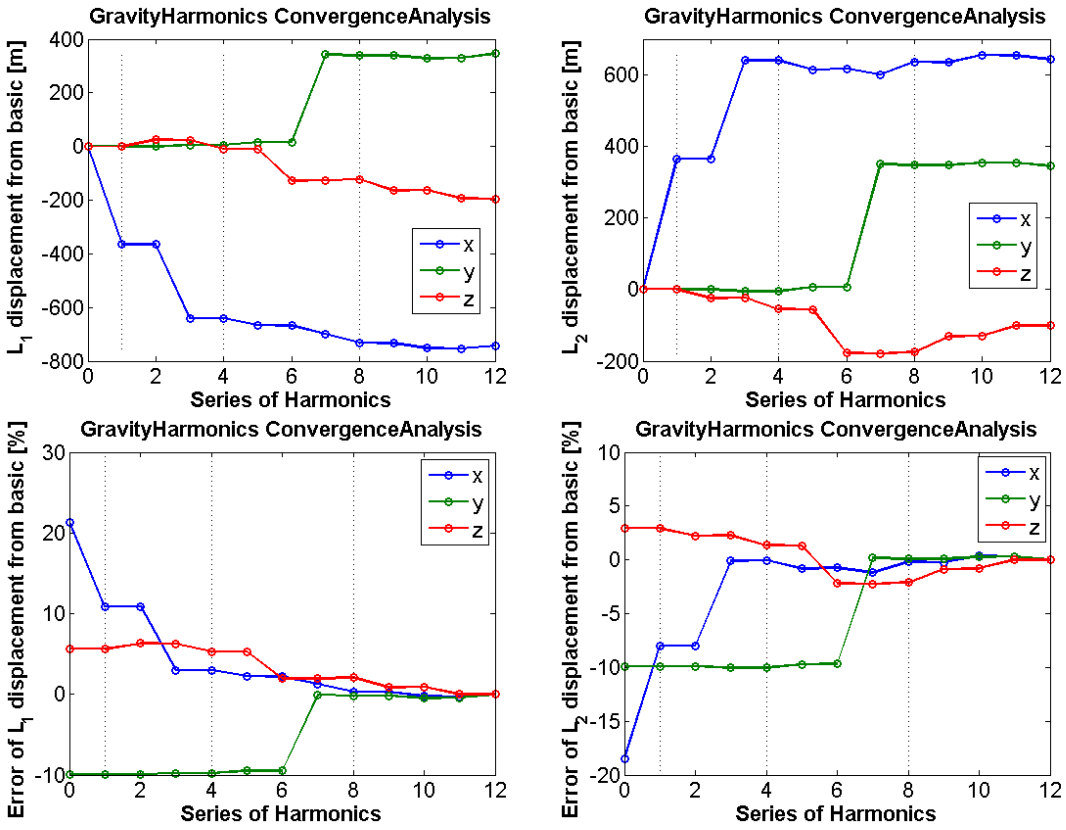

Figure 3.13: **Convergence analysis of the CR3BP-GH.** L_1 and L_2 displacement from their original value in the CR3BP. In the graphs at the bottom, the error respect to the solution with all the harmonics is normalized by the altitude over Phobos' surface. Dotted lines refer to increasing zonal harmonics degree starting from J_2. Phobos' GHs model of [94].

Southern Hemisphere; the last EP is in the South-West sector. The first two points and the last one exhibit a center × saddle × saddle phase portrait, whereas the third one is a classical center × center × saddle. The eigenvalues of the additional equilibria are on average five times stiffer than the usual values of the collinear LPs. All these additional equilibria are interior to Phobos' figure, with the outermost located $2km$ below its surface modeled with the shape harmonics. Thus, as explained in section 3.3.4.2, these additional EPs created by the GHs technique are irrelevant.

3.3.6.3 Gravity Harmonics' Convergence Analysis on the Equilibrium Points

The properties of L_{1-2} are an important summarizing figure, for the orbital behavior in proximity of the SOI's boundary, to conduct a convergence analysis on the CR3BP-GH as a function of the number of harmonics of the gravitational field of Phobos. This is done by incrementally increasing the terms of the series expansion included in the vectorfield $\mathbf{f_{GH,2}}$ of Eq.3.37.

The Phobos' GHs models available in the literature are of low-order, in our case the model used from [94] arrives just to degree four. Due to the highly-inhomogeneous shape of the moon, it would be a chance if this truncated model is already sufficient

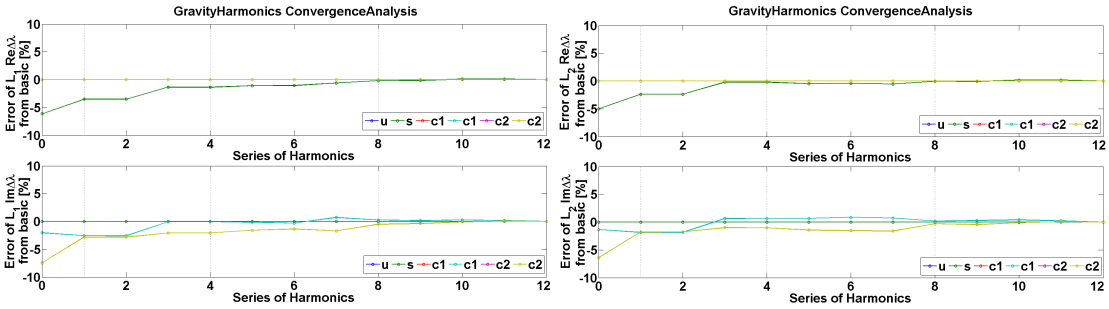

Figure 3.14: **Convergence analysis of the CR3BP-GH.** L_1 and L_2 eigenvalues deviation from their original value in the CR3BP. The error is plotted respect to the solution with all the harmonics. Dotted lines refer to increasing zonal harmonics degree starting from J_2. Phobos' GHs model of [94].

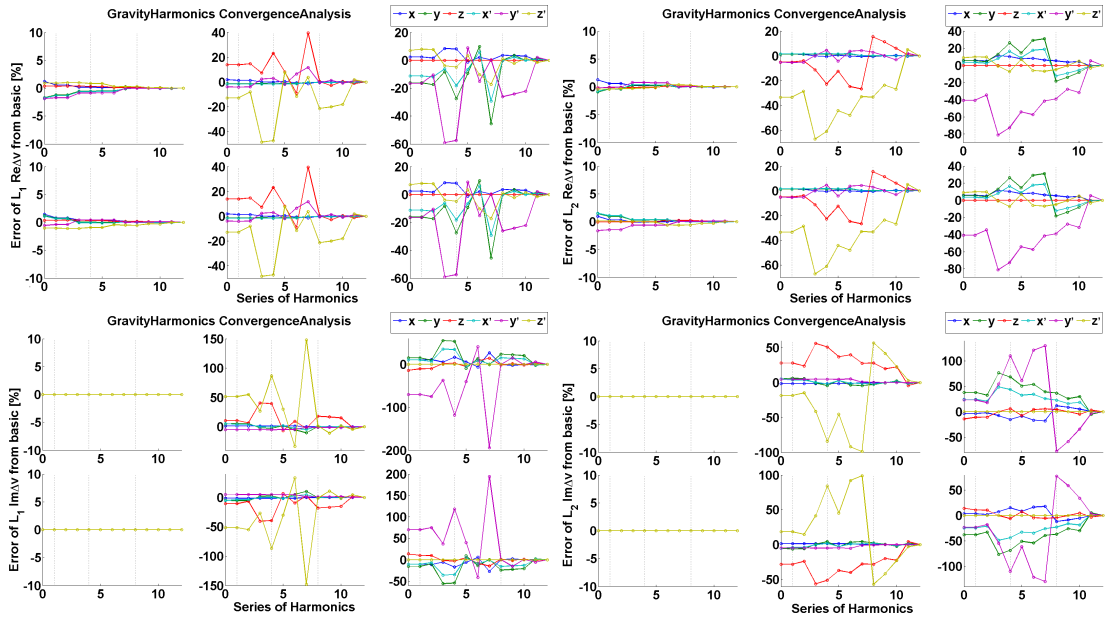

Figure 3.15: **Convergence analysis of the CR3BP-GH.** L_1 and L_2 eigenvectors' components deviation from their original value in the CR3BP. The error is plotted respect to the solution with all the harmonics. Dotted lines refer to increasing zonal harmonics degree starting from J_2. Phobos' GHs model of [94].

to provide a highly satisfying convergence value, for example under 1%. Recall that in section 3.1.3, using the benchmark model of [102], an estimation of the error of the cumulated residual GHs' perturbation at the SOI's boundary was provided: in this section this value is computed. Therefore, an initial aim of this convergence analysis is to assess if the model of [94] is at least convergent. The second aim is to derive a figure of the truncation error for the properties of the LPs. This convergence analysis is undertaken in two ways. The first option is to consider the coefficients of the model of [94], by looking at the error at degree and order 3 with respect to the property at degree and order 4. The second option is to consider the coefficients of the benchmark model of [102], by looking at the error at degree and order 4 with respect to the property at degree and order 6. If the behavior is convergent, this guarantees that the figures are

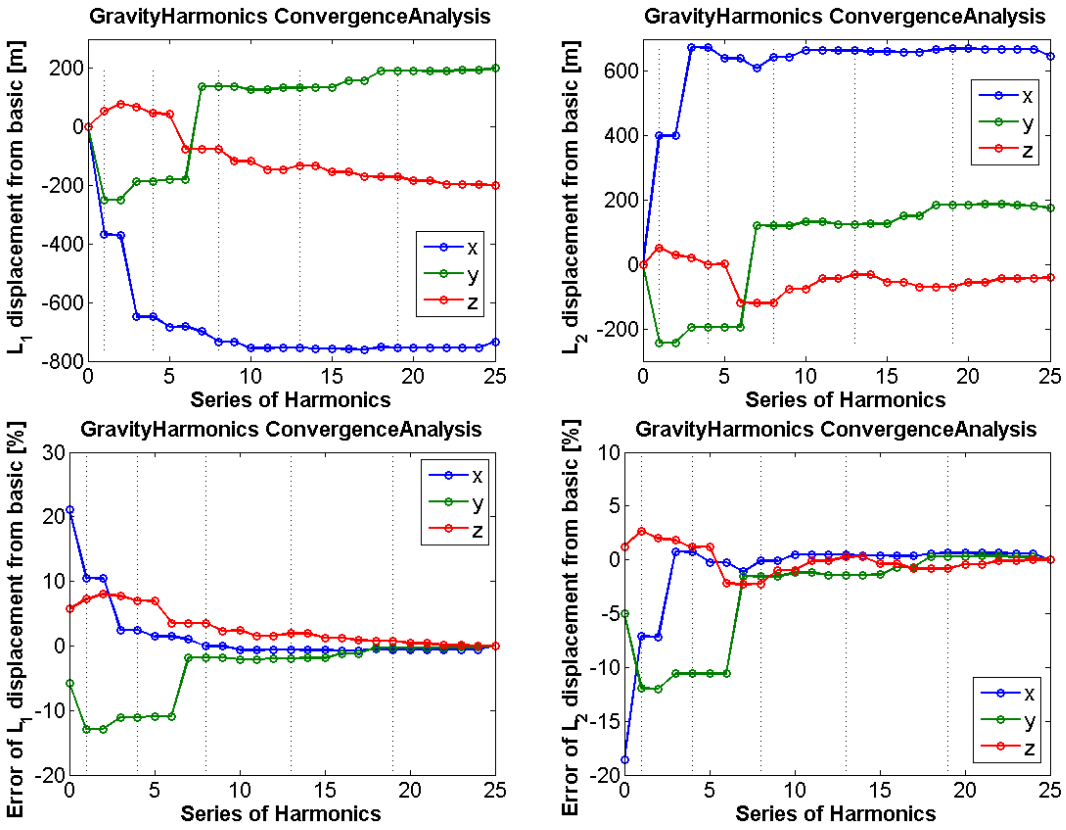

Figure 3.16: **Convergence analysis of the CR3BP-GH.** L_1 and L_2 displacement from their original value in the CR3BP. In the graphs at the bottom, the error respect to the solution with all the harmonics is normalized by the altitude over Phobos' surface. Dotted lines refer to increasing zonal harmonics degree starting from J_2. Phobos' GHs model of [102].

conservative estimations of the truncation's error.

A first overview of the convergence analysis clearly indicates that the use of a more refined model than the quadrupole is necessary. Regarding the altitude of the L_{1-2} points in Fig.3.13, the behavior is convergent, and a satisfactory solution under the 1% relative error seems to be achieved for the CR3BP-GH of degree-order 4, except for the z-components, whose error is limited by 2%. The errors of this static dynamics' indicator are even less if compared with the benchmark reference in Fig.3.16. Therefore, as reported in section 3.1.3, the error of the GHs' model used in this thesis is a few percent of the cumulated GHs' perturbation at the SOI's boundary.

Further dynamical indications are given by the eigenstructure of the LPs' manifold. The convergence analysis is extended to the computation of the eigenvalues and related eigenvectors of the two collinear EPs. Regarding the eigenvalues in Fig.3.14-3.17, for both LPs the behavior is convergent and the relative error is under 1% for every set. For the eigenvectors in Fig.3.15-3.18, the analysis is more complex. Regarding the saddle's eigenvectors, which represent the direction of the invariant manifolds, the same figure of convergence of the eigenvalues is achieved. For the eigenvectors of the two centers, the outcome depends on the components. Identifying each center manifold as the

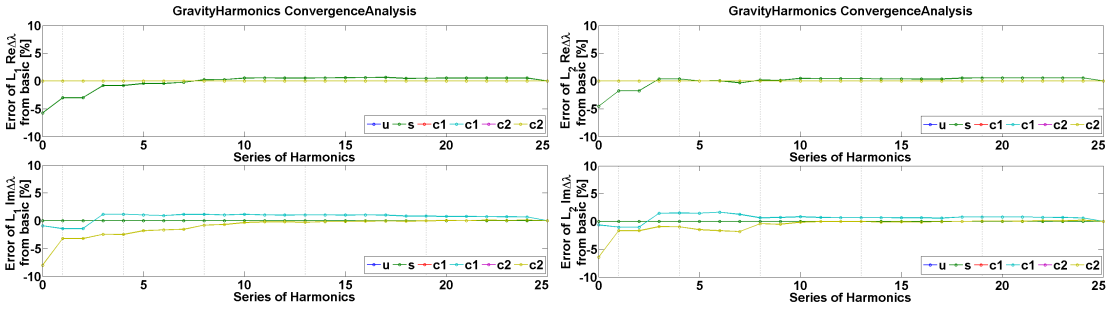

Figure 3.17: **Convergence analysis of the CR3BP-GH.** L_1 and L_2 eigenvalues deviation from their original value in the CR3BP. The error is plotted respect to the solution with all the harmonics. Dotted lines refer to increasing zonal harmonics degree starting from J_2. Phobos' GHs model of [102].

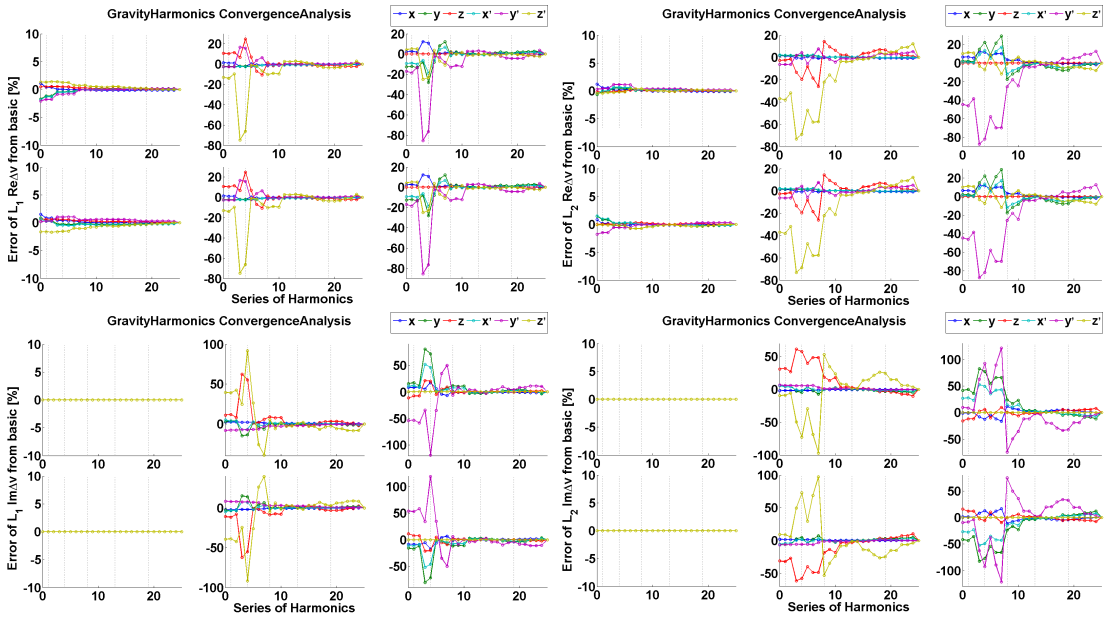

Figure 3.18: **Convergence analysis of the CR3BP-GH.** L_1 and L_2 eigenvectors' components deviation from their original value in the CR3BP. The error is plotted respect to the solution with all the harmonics. Dotted lines refer to increasing zonal harmonics degree starting from J_2. Phobos' GHs model of [102].

state-space's section around the LP where each family of periodic orbits develops, the same figure of convergence is achieved for the in-section components, while the out-of-section components are still oscillating at high amplitude, in particular over 10% for L_2. Therefore the results are accurate for the invariant manifolds and the longitudinal behavior of an invariant motion, while a more refined model is needed for the quasi-periodic motion around them.

3.4 The Mars-Phobos ER3BP-GH

In section 2.4 it was found that in addition to the irregularities of the Phobos' gravity field, a similar level of perturbation on the CR3BP, when used to describe the relative dynamics of a spacecraft in proximity of Phobos, is provided by the eccentricity of the orbit of the moon around Mars. Despite the fact that the **orbital eccentricity** $e = 0.0156$ is not particularly high, its differential modeling perturbation is significant for the motion in proximity of Phobos. This is an indirect effect of the collapse of the SOI's boundary towards the moon, because the perturbation of the eccentricity (proportional to e) is dragged towards the second massive body of the 3BP, thus the scaling of e acts on a higher gravity.

Following this, in this section the CR3BP-GH derived in section 3.3 is further extended to include the model of the elliptic orbit of the two massive bodies. The new elliptic model with the GHs of the secondary is named ER3BP-GH.

The equations of motion of the ER3BP have been already derived in section 2.4.2 when determining an acceleration figure for the elliptic perturbation on the CR3BP. Thus, recall Eq.2.44 that describes the ER3BP in the 3B frame in physical units, where the primaries' positions along the x-axis are now variable over time with the Keplerian relationships of Eq.2.44-2.45-2.49, and the 3B frame rotates with the non-uniform angular velocity and acceleration of the elliptic orbit expressed in Eq.2.46-2.47. These relationships are all functions of the true anomaly of Phobos ν, and are all proportional to e. After the approximations discussed throughout section 3.3, the Mars-Phobos ER3BP-GH can be retrieved by simply expanding the gravitational potential of Phobos with the GHs series expansion of Eq.3.1. This yields the equations of motion of the ER3BP-GH in the 3B elliptic frame and in physical units.

$$\begin{aligned}\ddot{\mathbf{q}} + \dot{\omega}_z(\nu)\mathbf{W}\mathbf{q} + 2\omega_z(\nu)\mathbf{W}\dot{\mathbf{q}} &= \mathbf{a}_{\mathbf{G},1} + \mathbf{a}_{\mathbf{G},2} - \omega_z(\nu)^2\mathbf{P}\mathbf{q} \\ &= \nabla\left(u_{G,1}\left(\mathbf{q} - \mathbf{q}_1(\nu)\right) + u_{G,2}\left(\mathbf{q} - \mathbf{q}_2(\nu)\right) - \omega_z(\nu)^2\frac{\mathbf{r}^T\mathbf{P}\mathbf{r}}{2}\right)\end{aligned} \tag{3.42}$$

In particular, the inertial position, velocity, and acceleration of Phobos with respect to Mars, in the Mars-centered Hill's frame are retrieved with the relative kinematics equations shown below.

$$\begin{cases} \mathbf{r}_2^1 = \begin{bmatrix} l(\nu) \\ 0 \\ 0 \end{bmatrix} \\ \dot{\mathbf{r}}_2^1 = \left(\frac{\partial}{\partial t} + \omega_z(\nu)\mathbf{W}\right)\mathbf{r}_2^1 = \begin{bmatrix} \dot{l}(\nu) \\ \omega_z(\nu)l(\nu) \\ 0 \end{bmatrix} \\ \ddot{\mathbf{r}}_2^1 = \left(\frac{\partial}{\partial t} + \omega_z(\nu)\mathbf{W}\right)\dot{\mathbf{r}}_2^1 = \begin{bmatrix} \ddot{l}(\nu) - \omega_z(\nu)^2 l(\nu) \\ 2\omega_z(\nu)\dot{l}(\nu) + \dot{\omega}_z(\nu)l(\nu) \\ 0 \end{bmatrix} = \begin{bmatrix} -\frac{GM}{l(\nu)^2} \\ 0 \\ 0 \end{bmatrix} \end{cases} \tag{3.43}$$

The main difference with the inclusion of the GHs is that the elliptic perturbation makes the dynamics of the ER3BP-GH non-autonomous in time, since all the terms in Eq.3.42 depend on $\nu(t)$. The dynamics of the true anomaly is given by $\dot{\nu} = \omega_z(\nu)$, and could be expressed by the solution of Kepler's equation over time. Therefore the energy of the system is not preserved, and the system is not conservative in any frame of reference [54].

3.4.1 Selection of the Reference Frame and Units

Despite the Mars-Phobos ER3BP-GH remains non-autonomous for any choice of reference coordinates, the expression of the equations of motion could be easier or more suitable for analytical and numerical analyses in a particular reference frame and with appropriate normalized units. In particular, the unit of mass is still maintained as the Mars-Phobos total mass, so the sense of μ is kept, while the choice of the units of length and time should be investigated[12]. The set of equations of motion of the ER3BP-GH with the different combinations investigated in this section are collected with more detail in appendix A.

Eq.3.42, in the 3B frame, is restated in the normalized units of the CR3BP of section 2.3.3, setting the Mars-Phobos semi-major axis as the length unit, and setting the mean anomaly M of Phobos as the normalized time. For notational convenience, the gravity potential $u_{G,\oplus}(\mathbf{r}_\oplus)$, expressed as a function of the position with respect to the body's barycenter, is accounted for both massive bodies in a single term $u_G(\mathbf{r}_1, \mathbf{r}_2)$, like in Eq.2.11. Thus, this includes the Keplerian gravity of Mars, and the extended gravity field of Phobos with the GHs.

[12]Throughout this section, normalized state is indicated with an upper bar. Derivation with respect to the normalized time is indicated with an apostrophe.

$$
\begin{cases}
\mathbf{q} = a\bar{\mathbf{q}} \\
t = \frac{1}{n}\bar{t} = \sqrt[2]{\frac{a^3}{GM}}\bar{t} = \frac{T}{2\pi}\bar{t} \rightarrow \bar{t} = M
\end{cases}
$$

$$
\begin{aligned}
\Rightarrow & \bar{\mathbf{q}}'' - 2\frac{(1+e\cos\nu)^3 e\sin\nu}{(1-e^2)^3}\mathbf{W}\bar{\mathbf{q}} + 2\frac{(1+e\cos\nu)^2}{(1-e^2)^{3/2}}\mathbf{W}\bar{\mathbf{q}}' = \\
& = \nabla\left(u_G\left(\bar{\mathbf{q}} + \mu\frac{1-e^2}{1+e\cos\nu}\begin{bmatrix}1\\0\\0\end{bmatrix}, \bar{\mathbf{q}} - (1-\mu)\frac{1-e^2}{1+e\cos\nu}\begin{bmatrix}1\\0\\0\end{bmatrix}\right) - \frac{(1+e\cos\nu)^4}{(1-e^2)^3}\frac{\bar{\mathbf{q}}^T\mathbf{P}\bar{\mathbf{q}}}{2}\right)
\end{aligned}
\tag{3.44}
$$

Using the semi-latus rectum as length unit ($\mathbf{q} = p\bar{\mathbf{q}}$) or in a related time unit ($t = \sqrt[2]{\frac{p^3}{GM}}\bar{t}$) allows the elimination of the $\left(1-e^2\right)$-terms in nonlinear (first case) and linear (second case) terms. However these are only algebraic simplifications, not significant for analytical purposes.

3.4.1.1 Time-Variant Time-Unit

The use of time-variant physical units could allow to gain analytical insight. For example, instead of the constant rate of the mean anomaly used in Eq.3.44, the time unit could be set to correspond to the true anomaly or the eccentric anomaly E of the primaries' orbit. The equations of motion with such variable time-units are shown in Eq.A.1 and Eq.A.2 respectively. They also report the post-processing relations to obtain the inertial velocities (and time).

With the eccentric anomaly, the motion is parameterized with the phase of Phobos in elliptical coordinates (from the center of the ellipse): since the orbit is elliptic, this is useful for describing Phobos' coordinates, but the equations of relative motion show no particular improvement. With the true anomaly, the motion is parameterized with the phase of Phobos from the Mars-Phobos' barycenter (the focus of the ellipse): this is more geometrically-intuitive, and Eq.A.1 shows that the Coriolis and centripetal terms are now unitary (no time-dependent coefficient). However, time-variant units introduce a further apparent term.

3.4.1.2 Time-Variant Length-Unit

The length unit is now considered as the time-variant Mars-Phobos distance. For the elliptic motion, this is called an isotropic pulsating frame, and the related equations of motion are stated in Eq.3.45-A.4 with respect to the true anomaly and eccentric anomaly respectively.

$$
\begin{cases}
\mathbf{q} = l(\nu)\bar{\mathbf{q}} \\
t = \frac{1}{\omega_z(\nu)}\bar{t} = \sqrt[2]{\frac{p^3}{GM}}\frac{1}{(1+e\cos\nu)^2}\bar{t} \rightarrow \bar{t} = \nu
\end{cases}
$$

$$
\Rightarrow \begin{cases}
\dot{\mathbf{q}} = \omega_z(\nu)l(\nu)\bar{\mathbf{q}}' + \omega_z(\nu)l'(\nu)\bar{\mathbf{q}} = an\frac{1+e\cos\nu}{\sqrt[2]{1-e^2}}\bar{\mathbf{q}}' + an\frac{e\sin\nu}{\sqrt[2]{1-e^2}}\bar{\mathbf{q}} \\
\ddot{\mathbf{q}} = \omega_z(\nu)^2\left(l(\nu)\bar{\mathbf{q}}'' + 2l(\nu)'\bar{\mathbf{q}}' + l''(\nu)\bar{\mathbf{q}}\right) + \dot{\omega}_z(\nu)\left(l(\nu)\bar{\mathbf{q}}' + l'(\nu)\bar{\mathbf{q}}\right) = \\
\quad = an^2\frac{(1+e\cos\nu)^3}{(1-e^2)^2}\bar{\mathbf{q}}'' + an^2\frac{(1+e\cos\nu)^2 e\cos\nu}{(1-e^2)^2}\bar{\mathbf{q}}'
\end{cases}
$$

$$
\begin{aligned}
&\Rightarrow \bar{\mathbf{q}}'' + 2\mathbf{W}\bar{\mathbf{q}}' = \nabla\left(\tfrac{1}{1+e\cos\nu}u_G\left(\bar{\mathbf{q}} + \mu\begin{bmatrix}1\\0\\0\end{bmatrix}, \bar{\mathbf{q}} - (1-\mu)\begin{bmatrix}1\\0\\0\end{bmatrix}\right) - \tfrac{1}{1+e\cos\nu}\tfrac{\bar{\mathbf{q}}^T\mathbf{P}\bar{\mathbf{q}}}{2} - \tfrac{e\cos\nu}{1+e\cos\nu}\tfrac{\bar{\mathbf{q}}^T(\mathbf{I}_3+\mathbf{P})\bar{\mathbf{q}}}{2}\right) \\
&\Rightarrow \bar{\mathbf{q}}'' + 2\mathbf{W}\bar{\mathbf{q}}' = \nabla\left(\tfrac{1}{1+e\cos\nu}u_G\left(\bar{\mathbf{q}} + \mu\begin{bmatrix}1\\0\\0\end{bmatrix}, \bar{\mathbf{q}} - (1-\mu)\begin{bmatrix}1\\0\\0\end{bmatrix}\right) + \tfrac{1}{1+e\cos\nu}\tfrac{\bar{\mathbf{q}}^T\bar{\mathbf{q}}}{2} - \tfrac{\bar{\mathbf{q}}^T(\mathbf{I}_3+\mathbf{P})\bar{\mathbf{q}}}{2}\right) \\
&\Rightarrow \bar{\mathbf{q}}'' + 2\mathbf{W}\bar{\mathbf{q}}' = \nabla\left(\tfrac{1}{1+e\cos\nu}u_G\left(\bar{\mathbf{q}} + \mu\begin{bmatrix}1\\0\\0\end{bmatrix}, \bar{\mathbf{q}} - (1-\mu)\begin{bmatrix}1\\0\\0\end{bmatrix}\right) - \tfrac{e\cos\nu}{1+e\cos\nu}\tfrac{\bar{\mathbf{q}}^T\bar{\mathbf{q}}}{2} - \tfrac{\bar{\mathbf{q}}^T\mathbf{P}\bar{\mathbf{q}}}{2}\right)
\end{aligned}
\tag{3.45}
$$

With the eccentric anomaly, the Euler term is discarded. With the true anomaly, more simplifications occur: Euler and additional apparent terms are discarded, Coriolis and centripetal terms are unitary, and the position of the primaries is fixed. Thus, in the planar case, only a time-scaling factor appears for the gravity terms, while in the spatial case a further time-variant apparent force is introduced. This spurious term is due to the fact that the pulsation is applied uniformly in all the directions, thus it accounts for the pulsating vertical direction. Due to their geometrical usefulness, and the fact that their expression is the simplest obtainable, the equations of motion with the combination pulsating frame - true anomaly are the most used and famous form to express the ER3BP in the literature. They were introduced in [108]. In addition, they are very powerful for analytical interpretations, because the vectorfield of the planar part corresponds to the vectorfield of the planar CR3BP with the exception of the gravitational forces which are scaled by the only time-variant term. In particular, the 3D ER3BP fully reduces to the 3D CR3BP not for $l(\nu) = a$, but in quadrature phases where $l(\nu) = p$.

It is worth to note that for some analysis, a proper averaging of the time-variant terms could be undertaken to provide their mean integral values over one orbital period. This would make the mean-ER3BP autonomous again, and is used for little eccentricity effects, which unfortunately is not the case of Phobos as explained in section 2.4.

3.4.1.3 The ER3BP-GH in Phobos' Hill's Frame

All the dynamics showcased so far are expressed in the 3B frame, which is centered on the 2B barycenter. However, for the case of Phobos, where the SOI's boundary is very close to the moon's surface, the dynamical analysis of the close orbits must be conducted with a relative motion approach. This was not a problem for the circular case, since the distance moon-barycenter is fixed, and the outcomes would differ by fixed translations in position. On the contrary, in the elliptic case the distance moon-barycenter is variable with time, and this affects the computation of both relative position and velocity over

time. It is the same requirement of formation flying: as the inter-satellite distance becomes smaller, sensitivity of relative motion's performance with absolute dynamics greatly deteriorates with time. Therefore, in a closed relative motion perspective, the dynamics of the ER3BP-GH should be expressed in Phobos' Hill's frame. This change in origin was already performed in section 2.4.2, where the differential perturbation of the eccentricity on the CR3BP is computed. Eq.2.50 describes the ER3BP in the secondary's Hill's frame in physical units. The related Phobos-centered ER3BP-GH in normalized units[13], for the fixed combination a-M is expressed in Eq.3.46, while the time-variant combination l-ν is presented in Eq.A.8.

$$
\begin{aligned}
&\begin{cases} \mathbf{q} = a\left(\bar{\bar{\mathbf{q}}} + \bar{\mathbf{q}}_2\right) \\ \bar{t} = M \end{cases} \\
&\Rightarrow \bar{\mathbf{q}}_2 = (1-\mu)\begin{bmatrix} \frac{1-e^2}{1+e\cos\nu} \\ 0 \\ 0 \end{bmatrix}, \bar{\mathbf{q}}_2' = (1-\mu)\begin{bmatrix} \frac{e\sin\nu}{\sqrt[2]{1-e^2}} \\ 0 \\ 0 \end{bmatrix}, \bar{\mathbf{q}}_2'' = (1-\mu)\begin{bmatrix} \frac{(1+e\cos\nu)^2 e\cos\nu}{(1-e^2)^2} \\ 0 \\ 0 \end{bmatrix} \\
&\Rightarrow \bar{\mathbf{a}}_{\mathbf{A},\mathbf{T}} = \frac{\dot{\omega}_z(\nu)}{n^2}\mathbf{W}\bar{\mathbf{q}}_2 + 2\frac{\omega_z(\nu)}{n}\mathbf{W}\bar{\mathbf{q}}_2' + \frac{\omega_z(\nu)^2}{n^2}\mathbf{P}\bar{\mathbf{q}}_2 + \bar{\mathbf{q}}_2'' = -\frac{\omega_z(\nu)^2}{n^2}(1-\mu)\frac{1-e^2}{(1+e\cos\nu)^2} \\
&\Rightarrow \bar{\bar{\mathbf{q}}}'' - 2\frac{(1+e\cos\nu)^3 e\sin\nu}{(1-e^2)^3}\mathbf{W}\bar{\bar{\mathbf{q}}} + 2\frac{(1+e\cos\nu)^2}{(1-e^2)^{3/2}}\mathbf{W}\bar{\bar{\mathbf{q}}}' = \\
&\quad = \nabla\left(u_G\left(\bar{\bar{\mathbf{q}}} + \frac{1-e^2}{1+e\cos\nu}\begin{bmatrix}1\\0\\0\end{bmatrix}, \bar{\bar{\mathbf{q}}}\right) - \frac{(1+e\cos\nu)^4}{(1-e^2)^3}\left(\frac{\bar{\bar{\mathbf{q}}}^T\mathbf{P}\bar{\bar{\mathbf{q}}}}{2} - (1-\mu)\frac{1-e^2}{(1+e\cos\nu)^2}\bar{\bar{x}}\right)\right)
\end{aligned}
\tag{3.46}
$$

As explained in section 2.3.6, the Hill's approximation is not considered for the Mars-Phobos system since the nonlinear effects of the 3B perturbation of Mars are rather relevant for the unstable orbits within the Phobos' SOI.

3.4.2 Equations of Motion

In section 3.4.1, the ER3BP-GH is expressed in several reference frames and units. For the close relative motion approach, the Phobos' Hill's frame of Eq.3.46-A.8 is mandatory, and this is already a difference from the classical framework of the ER3BP of [108]. The focus is now on the choice of the reference units.

Due to the necessity of including the GHs of the moon, also the classical pulsating unit of the ER3BP is avoided, as it produces different time-dependent scalings for each GH at different degree, i.e. $(1+ecos\nu)^{-n}$. Indeed, it is not desirable to have the closer massive body, in a BCBF frame, to still provide a non-conservative gravity field. Therefore, the preference here is to maintain the classical fixed length unit of the semi-major axis of the Mars-Phobos orbit.

Regarding the choice of the time unit, this is actually quite indifferent, as no particular advantages or disadvantages come out. The choice of E is not desirable for the applications of the model. The choice of ν simplifies the integration of the dynamics, as this depends directly on it, and inertial time and relative velocities could be retrieved by postprocessing. The choice of M keeps the reference with the real time, and avoids

[13] Throughout this section, normalized relative state with respect to the secondary body is indicated with a double upper bar.

post-processing of the relative state, but requires to compute $\nu(t)$.

First, the case of the fixed time unit is considered. In Eq.3.47 some intermediate variable are defined for notational convenience. This yields the generalization of the **P** and **W** matrices, defined in section 2.3.3 in the CR3BP, for a time-variant normalized angular velocity. In addition, new terms are introduced: **Y**, which corresponds to **P** but with respect to the normalized angular acceleration, and **a** which represents the normalized apparent translational acceleration of the frame.

$$\begin{cases} \mathbf{a}(\nu) = (1-\mu)\frac{(1+e\cos\nu)^2}{(1-e^2)^2}\begin{bmatrix}1\\0\\0\end{bmatrix} \\ \boldsymbol{\omega}(\nu) = \frac{(1+e\cos\nu)^2}{(1-e^2)^{3/2}}\begin{bmatrix}0\\0\\1\end{bmatrix} \rightarrow \mathbf{W}(\nu) = \boldsymbol{\omega}(\nu)\wedge \rightarrow \mathbf{P}(\nu) = \mathbf{W}(\nu)^2 \\ \dot{\boldsymbol{\omega}}(\nu) = -2\frac{(1+e\cos\nu)^3 e\sin\nu}{(1-e^2)^3}\begin{bmatrix}0\\0\\1\end{bmatrix} \rightarrow \mathbf{Y}(\nu) = \dot{\boldsymbol{\omega}}(\nu)\wedge \end{cases} \tag{3.47}$$

Eq.3.48 presents the ODEs with respect to the mean anomaly.

$$\mathbf{x} = \begin{bmatrix}\mathbf{q}\\ \dot{\mathbf{q}}\end{bmatrix} \rightarrow \dot{\mathbf{x}} = \mathbf{A}(\nu)\mathbf{x} + \begin{bmatrix}\mathbf{0_{3x1}}\\ u_{G/\mathbf{q}}(\mathbf{q},\nu) + \mathbf{a}(\nu)\end{bmatrix},\ \mathbf{A}(\nu) = \begin{bmatrix}\mathbf{0_3} & \mathbf{I_3}\\ -\mathbf{Y}(\nu) - \mathbf{P}(\nu) & -2\mathbf{W}(\nu)\end{bmatrix} \tag{3.48}$$

The reader should appreciate the similarity of Eq.3.48 with the ODEs of the CR3BP of Eq.2.13 and of the CR3BP-GH of Eq.3.37, where the linear part, given by the rotating apparent terms, is now time-variant, and the matrix **Y** and vector **a** are added to the system. Eq.3.49 shows the related effective potential of the non-autonomous Hamiltonian system, which takes into account the oscillating Keplerian gravity of the primary, the conveniently fixed complete gravity field of the secondary (and not dependent from the eccentricity), the oscillating centrifugal term, and the oscillating translational apparent term given by the opposite of the gravity of the primary at the origin of the Phobos' Hill's frame.

$$u_{eff} = u_{G,1}\left(\mathbf{q} + \frac{1-e^2}{1+e\cos\nu}\begin{bmatrix}1\\0\\0\end{bmatrix}\right) + u_{G,2}\left(\mathbf{q}\right) - \frac{(1+e\cos\nu)^4}{(1-e^2)^3}\left(\frac{\mathbf{q}^T\mathbf{P}\mathbf{q}}{2} - (1-\mu)\frac{1-e^2}{(1+e\cos\nu)^2}x\right) \tag{3.49}$$

In the same sense, the ODEs and effective potential with respect to the true anomaly are derived, and are shown in Eq.A.14-A.15. Setting the time to correspond to the true anomaly produces the normalized angular velocity to be constant, thus **W** and **P**, representing Coriolis and centrifugal terms, in these ODEs are time-invariant. However, an additional drag term due to the time-variant unit of time, and proportional to the velocity, must be taken into account, as it was addressed in Eq.A.1, and is represented by the matrix $\mathbf{Y}_I$.

It is worth noting that in these versions of the ER3BP-GH, the gravity potential of Phobos depends only on the relative position **q** in the Hill's frame, while all the other terms depend also on ν. It is easy to see that the models of Eq.3.48-A.14 reduces to the circular cases of Eq.2.13-3.37 for $e = 0$. The offset in the frame's origin is accounted by the apparent translational term **a**. This bias should be collected in the

term $-\mathbf{Pq}$ to describe the full centrifugal acceleration in the barycentric frame of the CR3BP/CR3BP-GH.

A simple way to treat non-autonomous systems [109, 110] is described in section B.1.2.4. It requires to include the time in the state space, adding a fake dynamics in the vectorfield as $\dot{t} = 1$. In this way, the system in the augmented state-space dynamics is autonomous again. This is just a trick to allow to extend the application of analytical and numerical tools of autonomous systems to time-variant ones, since the additional state dynamics is actually constrained. For this reason, the final choice of setting the time to correspond to M is made for the ER3BP-GH that will be used in this thesis. Since one phase must be appended in the state vector, using $\dot{\nu}(\bar{t}) = \frac{\omega_z(\bar{t})}{n}$ in the augmented vectorfield, instead of the trivial $\dot{\nu}(\bar{t}) = 1$, allows $\nu(M)$ to be retrieved directly from the integration of the equations of motion instead of solving Kepler's equation. This choice maintains the outcomes in fixed physical units, thus avoiding postprocessing, that would have instead been necessary in the second case.

Eq.3.50 provides the full time-invariant ODEs of the Mars-Phobos ER3BP-GH in the Phobos' Hill's frame, with the fixed physical units of the CR3BP.

$$\mathbf{x} = \begin{bmatrix} \mathbf{q} \\ \dot{\mathbf{q}} \\ \nu \end{bmatrix} \rightarrow \dot{\mathbf{x}} = \mathbf{A}(\nu)\mathbf{x} + \begin{bmatrix} \mathbf{0_{3x1}} \\ u_{G/\mathbf{q}}(\mathbf{q}, \nu) + \mathbf{a}(\nu) \\ \omega_z(\nu) \end{bmatrix}, \mathbf{A}(\nu) = \begin{bmatrix} \mathbf{0_3} & \mathbf{I_3} & \mathbf{0_{3x1}} \\ -\mathbf{Y}(\nu) - \mathbf{P}(\nu) & -2\mathbf{W}(\nu) & \mathbf{0_{3x1}} \\ \mathbf{0_{1x3}} & \mathbf{0_{1x3}} & 0 \end{bmatrix} \tag{3.50}$$

Eq.3.50 is the extended model of the relative orbital dynamics in the proximity of Phobos, including the effects of the inhomogeneous gravity field and the orbital eccentricity of the moon, that will be used in chapter 4 to compute the accurate LPOs about Phobos.

It is worth to note that appending the first-order dynamics of the true anomaly requires to add also a related momenta to derive the 8D Hamiltonian form of the ODEs of Eq.3.50. This procedure is called homogeneous formalism, and is explained in [111].

3.4.3 Hill's Surfaces

The great correspondence of terms between CR3BP and ER3BP in the 3B frame and with the classical combination of pulsating-true anomaly normalization, as highlighted in section 3.4.1, enables to see some properties of the first model as continuously transferred in the second [108, 54]. In particular, in Eq.3.45 the time-dependency is provided by a scaling factor acting equally on the terms constituting the original effective potential in the CR3BP, plus a vertical spurious term. This holds for the Mars-Phobos CR3BP-GH and ER3BP-GH in the pulsating frame of Eq.3.45.

Thus, at any frozen time, the analysis of the planar dynamics in the instantaneous elliptic problem could be conducted in the same way as it is usually done in the circular case, just considering the current length scale. For the planar ER3BP, the instantaneous effective potential is proportional to the one of the planar CR3BP, thus their

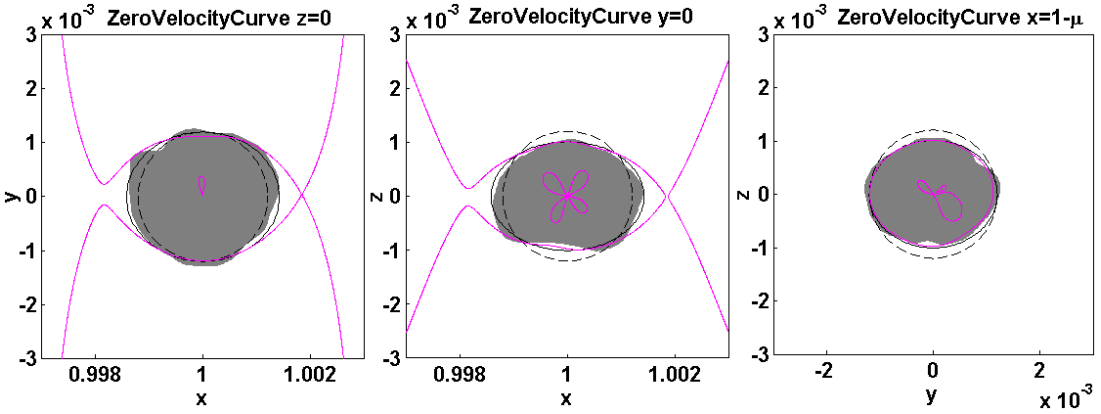

Figure 3.19: **Hill's surface in ER3BP-GH at perimars for L_2 energy.** Projections on coordinates planes. Phobos real shape, mean sphere (dashed line) and ellipsoid (plain line). Phobos' GHs model of [102].

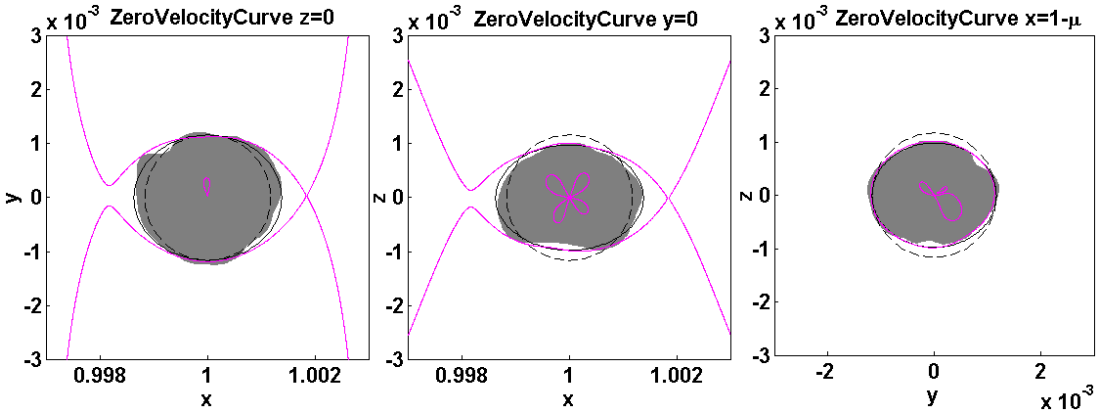

Figure 3.20: **Hill's surface in ER3BP-GH at apomars for L_2 energy.** Projections on coordinates planes. Phobos real shape, mean sphere (dashed line) and ellipsoid (plain line). Phobos' GHs model of [102].

zero-velocity curves correspond with the current normalization. Therefore, in physical units, the related Hill's surfaces move with the pulsating reference frame, and the concept of a pulsating SOI for the massive bodies has been proposed in [112] as a steady-state approximation. The mean value is the SOI of the CR3BP, and the minimum and maximum dimensions are obtained at pericenter and apocenter respectively. The vertical Hill's curves are instead not equivalent, due to the presence of the spurious term. However, this could be at first instance neglected in the spatial case, to achieve a first analytical insight.

This approach could be extended to the Mars-Phobos ER3BP-GH. However, in the CR3BP-GH, the length unit is used to normalize the reference radius in the GHs series expansion of Eq.3.1, in contrast to the normalized CR3BP where the only parameter is μ. This means that the instantaneous potential of the system is not proportionally scaled along the massive bodies' orbit. The normalized Hill's surface does not correspond at different phases of Phobos, and should therefore be recomputed within the

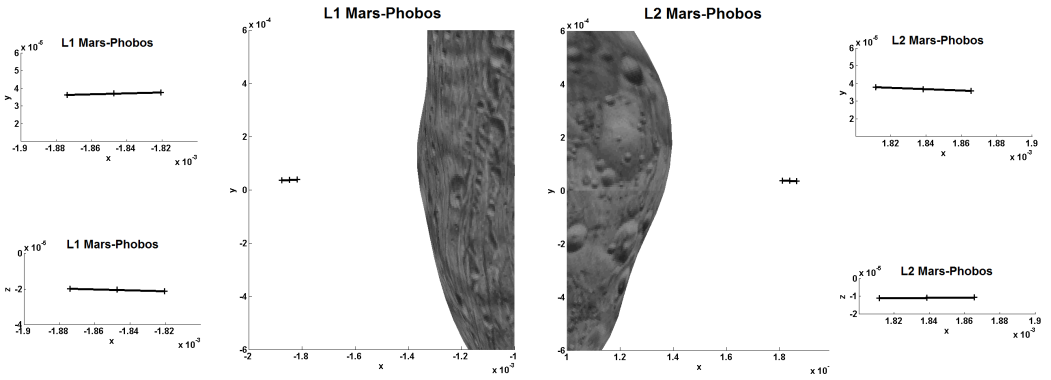

Figure 3.21: **Libration points oscillation in the Mars-Phobos ER3BP-GH.** Graphical visualization of the oscillation orbit of the libration points L_1 and L_2 of the Mars-Phobos ER3BP-GH. Crosses represent the position of them at different Phobos' phases around Mars: pericenter (closer to Phobos), apocenter (farther from Phobos), and at mean Mars-Phobos distance (central, indistinguishable from the two quadrature positions).

instantaneous normalized ER3BP-GH, before being scaled to physical units. This could be simulated considering the two extreme phases of Phobos at perimars and apomars.

The frozen Phobos' SOI at perimars and apomars is presented in Fig.3.19-3.20, while the mean SOI is the one of the CR3BP-GH shown in Fig.3.12. The length unit of these graphs is the instantaneous distance of Mars-Phobos, thus the figure of Phobos pulsates. It is evident that the Hill's curves, at the L_2 energy, at the extreme phases are similar to the mean value of the CR3BP-GH, and the main effect is only Phobos' fictitious pulsation. Thus, also the real effect of the spurious vertical term would produce similar results. Therefore the eccentricity effect does not seem to be a relevant factor for the accretion theory's validation mentioned in section 3.3.6.1.

3.4.4 Libration Points

As mentioned in section 3.4.3, the effective potentials of planar CR3BP and ER3BP in the pulsating frame are proportional over the elliptic orbit. Therefore, their planar critical points in the current length units are the same. The five EPs of the CR3BP (in the CR3BP L unit), presented in section 2.3.5.1, are all EPs of the ER3BP too (in the ER3BP pulsating L units) [108]. In the physical 3B frame they move in accordance with the pulsating frame, and become 1D periodic orbits, because their eigenvalues in the CR3BP (in normalized time-units) computed in Eq.2.29, are not integer numbers. The actual velocity of the elliptic LPs in the fixed units can be computed from the kinematics relations in Eq.3.45. Additional EPs, both in the pulsating and physical spatial ER3BP, are not possible.

This holds for the Mars-Phobos CR3BP-GH and ER3BP-GH in the pulsating frame of Eq.3.45. However, as mentioned in section 3.4.3, the presence of the GHs makes the instantaneous planar dynamics not equivalent in these two normalized systems. Thus, the LPs become elongated periodic orbits, tilted with respect to the x-axis and the x-y

plane, which are not exactly a straight line. Since the vertical component of the LPs in the Mars-Phobos CR3BP-GH is small with respect to their distance from the Phobos' barycenter, as reported in Table 3.4, the effect of the spurious vertical term could be neglected as a first analysis. Thus the instantaneous location of L_{1-2} is computed with the classical stationary condition of the instantaneous effective potential, where the reference radius for the GHs is scaled by the current Mars-Phobos distance, and the results are scaled back to physical units. These trajectories are shown in Fig.3.21. The periodic LPs of the Mars-Phobos ER3BP-GH oscillate around their location in the CR3BP-GH with an amplitude of $260m$, which is about 6% of their altitude. This could be significant due to the proximity of the Phobos' surface and the time-scale of its orbit for practical applications.

Chapter 4

Libration Point Orbits in the Mars-Phobos 3BP

The purpose of this chapter is to apply the concepts and the numerical methodologies of DST, presented in appendix B, to derive a class of natural motions of growing interest in space missions, which are the orbits around the Libration Points. The LPOs are invariant solutions of the classical CR3BP, that has been presented in section 2.3 for the case of the Mars-Phobos-spacecraft system. Following the results of the analysis of the orbital perturbations in section 2.4, the classical model of the CR3BP has been extended in chapter 3 to better describe the relative dynamics in proximity of Phobos. This first led in section 3.3 to define the CR3BP-GH, that includes the complete and inhomogeneous gravity field of the moon. The model is further extended in the ER3BP-GH defined in section 3.4, that considers the real eccentricity of the orbit of the moon. Following an iterative approach, this chapter begins in section 4.1 by computing the classical LPOs of the starting Mars-Phobos CR3BP, and then their dynamical substitutes are computed in section 4.2 in the intermediate Mars-Phobos CR3BP-GH, and in section 4.3 in the final Mars-Phobos ER3BP-GH. Section 4.4 concludes the chapter by addressing the feasibility, performance, and potential applications of these orbits for use in future missions to Phobos.

4.1 LPOs in the Mars-Phobos CR3BP

The Mars-Phobos CR3BP has been introduced in section 2.3.3 and its dynamics modeled as a system of ODEs in Eq.2.13. As explained in section B.1.3, the invariant solutions of such dynamical system are n-tori classified by their phase-space's dimension in EPs, POs, nD-QPOs. Section 4.1.1 introduces the reader to the historical advances made in the last few decades in the CR3BP. Following this, the collinear LPOs around Phobos are derived. Section 4.1.2 focuses on the EPs, and sections 4.1.3-4.1.4 address the computation of the POs and 2D-QPOs. Finally, section 4.1.5 presents the IMs of these orbits.

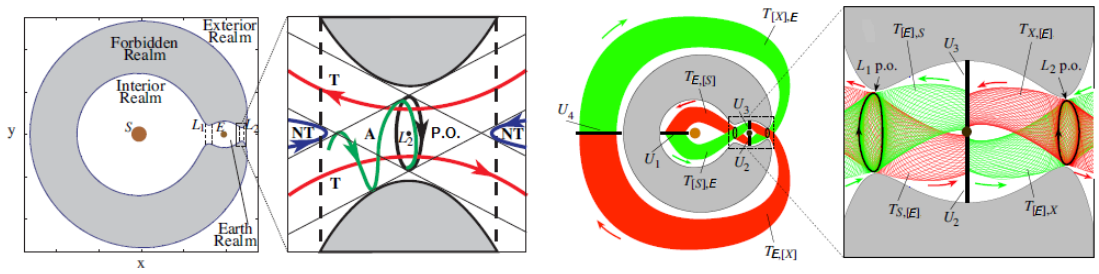

Figure 4.1: **Orbit structure of the CR3BP.** On the left, trajectories in the collinear equilibrium region of L_2. At right, invariant manifolds of the LPOs around L_1 and L_2 that identify the complete orbit structure (stable manifolds in green, unstable manifolds in red). The graphs refer to the Sun-Earth case [50], where $T_{[A,B]}$ identifies the tube from realm A to realm B, and U is a Poincaré section.

4.1.1 Global Orbit Structure of the CR3BP

The CR3BP is one of the most famous and historically investigated chaotic dynamical systems. For this reason, DST has proved essential to analyze the intimate characters and the long-term behavior of the solutions of this system [50].

In the past few decades, the tools of DST developed for the CR3BP have provided an in-depth understanding of the spacecraft's motion in this model of the orbital dynamics. In particular, the collinear EPs, L_{1-2}, have monopolized the interest in space mission design. Moser's generalization of Lyapunov's center theorem proved that the highly unstable region around them is characterized by four classes of orbits, as presented in Fig.4.1. They are the invariant tori of POs and QPOs around the LPs, named LPOs [71, 72], the asymptotic orbits of these invariant motions, called the IMs or Conley-McGehee tubes [73, 50], and the transit and non-transit orbits across the LPs. In particular, as visible in Fig.4.1, the region of space around the LPs acts as an energetic bottleneck [50]. This means that all the low-energy trajectories, that a spacecraft can use to leave or enter the SOI of the second massive body, are constrained to pass through this region.

This local orbit structure constrains the natural transitions between the two realms interfaced by L_{1-2}, which ultimately determines the global orbit structure of the CR3BP. This is obtained by the use of Poincaré maps to identify invariant sets, in combination with Symbolic Dynamics [50]. The latter allows to qualitatively analyze the general flow of the CR3BP, as shown in Fig.4.1. This is characterized by two families of symbols: the first (uncountable and finite) identifies the realm where the motion currently lies; the second (countable and infinite) identifies the number of revolutions performed within the realm. This is referred to as a Cantor set. The global orbit structure of the CR3BP is made up of four types of orbits in the secondary's realm, which can be connected globally in a chain [50]. They are stable asymptotic orbits [73], unstable asymptotic orbits [73], homoclinic/heteroclinic orbits [74, 75, 113], and non-transit/capture/oscillating orbits [50]. A dynamical system that possesses this orbit structure is said to be characterized by deterministic chaos, or is more usually referred

to as "Smale Horseshoe"-like dynamics [50]. The orbit structure around the collinear L_3 is similar to the one around L_{1-2}, whereas around the equilateral points L_4 and L_5 there is the addition of a so-called tadpole-like dynamics [50].

The study of the LPOs around the collinear EPs is the first step in the current approach of space mission analysis based on DST. Then, the identification of the IMs associated to them allows the mission designer to operate with the natural global dynamics. The LPOs have been computed extensively for the Sun-Earth and Earth-Moon systems, where the approximation of the natural dynamics using the CR3BP is an accurate one. The study of the invariant motions of these systems has proved invaluable for real space missions, such as ISEE-3/ICE (1978), WIND (1994), SOHO (1995), ACE (1997), Genesis (2001), and ARTEMIS (2010), where the LPOs and their IMs have been exploited as energy-efficient trajectories to minimize the spacecraft's fuel consumption during station-keeping and orbital transfers [50]. In particular, it has been speculated to use these LPOs to establish space hubs or gateway stations for the future exploration of the Solar System [71]. Furthermore, the exploitation of the tubes provided by the IMs allows the design of trajectories with a prescribed itinerary, coined the Solar System's "gateways" or "super-highways" [50], because they do not require any deep-space orbital maneuver along the trajectory, and so the Δv is less than the cost obtained from a patched 2B approach.

4.1.2 The LPs of the Mars-Phobos CR3BP

The identification of the EPs of the CR3BP for the case of the Mars-Phobos system constitutes the preliminary analysis of the orbital dynamics about the moon, and was performed in section 2.3.5.1. They are computed through Newton's method as explained in section B.3. The five planar LPs in the rotating 3B frame in the CR3BP are presented in Table 2.2. In this chapter, the focus will be placed on the two collinear LPs close to the second massive body, L_1 in inferior (cis) and L_2 in superior (trans) conjunction, as seen from the primary. These points are very close to Phobos, at an altitude of approximately $3.5km$, using a mean ellipsoidal model for its shape. Due to the small mass parameter of the Mars-Phobos couple, the energy difference between L_1 and L_2 is very small in non-dimensional units (10^{-8}). Therefore the location of L_{1-2} is close to the linearized approximation expressed by the Hill's SOI's radius. Furthermore, the manifolds of the two LPs are almost symmetrical, and the Hill's surfaces at the energy of L_1 and L_2, apart from the small region around each EP, are practically the same: they identify the boundary of the Hill's SOI of the body.

The stability properties of L_{1-2} have been computed in section 2.3.5.2. As further explained in sections B.3 and 4.1.1, *the orbit structure around these LPs is characterized by a 2-parameters family of invariant 2-tori and their stable and unstable IMs.* These orbits are the focus of the next sections.

4.1.3 The Lyapunov and Lissajous orbits of the Mars-Phobos CR3BP

The presence of two center manifolds around the LPs provides the origin of two continuous families of POs, which are part of one general family of 2D-QPOs. The existence of POs around the collinear LPs was proved in 1966 by Farquhar [71], and the first space mission to exploit a PO around the Sun-Earth L_1 point was NASA ISEE-3 (1978).

To derive these invariant motions, the analysis of the dynamics is undertaken in a normalized referenced frame [50], introduced in the 1980 by Richardson to have better numerical properties [114]. The normalized frame is centered on the EP of interest, and the length unit corresponds to the distance of the EP from the secondary's barycenter. This distance is identified as γ_i, where the subscript relates to L_i. This is similar to the approach of the Hill's approximation of section 2.3.6, but for the normalized frame of Richardson the scaling is given by the true position of the LP computed in the nonlinear dynamics, and not the first-order solution given by the Hill's radius. In addition, the frame is centered on the LP and not on the secondary's barycenter. The transformation of coordinates between the classical adimensional 3B frame and the normalized frame is presented in Eq.2.31. The new normalized coordinates are expressed with an upper tilde, and the position of the massive bodies along the normalized x-axis is reported.

$$\mathbf{q} = \begin{bmatrix} x = \gamma_i \tilde{x} + (1-\mu) \mp \gamma_i \\ y = \gamma_i \tilde{y} \\ z = \gamma_i \tilde{z} \end{bmatrix} = \gamma_i \tilde{\mathbf{q}} + \begin{bmatrix} 1-\mu \mp \gamma_i \\ 0 \\ 0 \end{bmatrix} \Rightarrow \begin{cases} x_1 = -\mu \leftrightarrow \tilde{x}_1 = -\frac{1 \mp \gamma_i}{\gamma_i} \\ x_2 = 1-\mu \leftrightarrow \tilde{x}_2 = \pm 1 \end{cases} \tag{4.1}$$

From above, we see that the change of coordinates provides a constant term in x, that will constitute a residual centrifugal term. The expression of the gravity forces with the new coordinates is presented below.

$$\begin{aligned} u_{/\tilde{\mathbf{q}}} = &- \frac{1}{{\gamma_i}^3} \frac{1-\mu}{\left(\sqrt[2]{\left(\tilde{x} + \frac{1 \mp \gamma_i}{\gamma_i} \right)^2 + \tilde{y}^2 + \tilde{z}^2} \right)^3} \left(\tilde{\mathbf{q}} + \begin{bmatrix} \frac{1 \mp \gamma_i}{\gamma_i} \\ 0 \\ 0 \end{bmatrix} \right) + \\ &- \frac{1}{{\gamma_i}^3} \frac{\mu}{\left(\sqrt[2]{(\tilde{x} \mp 1)^2 + \tilde{y}^2 + \tilde{z}^2} \right)^3} \left(\tilde{\mathbf{q}} + \begin{bmatrix} \mp 1 \\ 0 \\ 0 \end{bmatrix} \right) \end{aligned} \tag{4.2}$$

As discussed in section B.4, the first analytical approach for the computation of invariant motions in conducted with linearization. This yields the linearized equations of motion of the CR3BP in the normalized frame around the LPs in Eq.4.3.

$$\mathbf{x} = \begin{bmatrix} \tilde{\mathbf{q}} \\ \dot{\tilde{\mathbf{q}}} \end{bmatrix} \ , \ \dot{\mathbf{x}} = \mathbf{A}\mathbf{x} \ , \ \mathbf{A} = \begin{bmatrix} \mathbf{0_3} & \mathbf{I_3} \\ -\mathbf{P} + u_{/\tilde{\mathbf{q}}\tilde{\mathbf{q}}} & -2\mathbf{W} \end{bmatrix} \tag{4.3}$$

In particular, the linearized gravity of the primary in Eq.4.2 provides a constant term that counteracts the aforementioned residual centrifugal term originated by the change

of coordinates. The resulting system coincides with the linearized equations of motion around the LPs already derived in section 2.3.5.2, apart from the different length scale. This could be recognized by defining the Hessian matrix used in Eq.4.3 from the one for the L_{1-2} case in Eq.2.28, and using $s = \gamma_i$. The eigenvalues of these linearized dynamics are presented in Eq.2.29. Since in this framework the dynamics are uncoupled, υ is the vertical natural frequency ω_V, while ν and λ are respectively the planar natural frequency ω_P and the planar hyperbolic exponent λ_P. These quantities are linked by the following relationship.

$$\omega_P^2 = \lambda_P^2 - \omega_V^2 + 2 \tag{4.4}$$

The homogeneous solution of the mechanical system of linear ODEs of Eq.4.3 is a combination of the normal modes associated to these six eigenvalues. Reducing the analysis to the two central manifolds, the resulting general solution is a 2D-QPO characterized by a planar orbital motion around the EP, defined by the amplitude along the x-axis α and the planar frequency ω_P, and an oscillation along the out-of-plane direction, defined by the vertical amplitude β and the vertical frequency ω_V. The motion is strictly quasi-periodic because the two natural frequencies are not in an integer ratio: for the case of the Mars-Phobos system, the ratio between the two natural frequencies is close to be 1:1. Since the projections of these bounded trajectories along the coordinate planes describe Bowditch/Lissajous curves, these orbits have been named Lissajous orbits. By the orthogonality of the eigenspaces, two important extreme cases must be considered. When β is zero, the resulting planar orbit is periodic and is called the planar Lyapunov orbit. When α is zero, the resulting vertical periodic oscillation is referred to as the vertical Lyapunov orbit. The two amplitudes are related to the initial conditions, and they describe the resulting 2-parameter continuous family of Lissajous orbits around the LPs of the CR3BP of Eq.4.5.

$$\tilde{\mathbf{q}}_{QPO}(t) = \begin{bmatrix} \tilde{x} = -\alpha \cos(\omega_P t + \varphi_P) \\ \tilde{y} = K\alpha \sin(\omega_P t + \varphi_P) \\ \tilde{z} = \beta \cos(\omega_V t + \varphi_V) \end{bmatrix} , K = \frac{\omega_P^2 + 2\omega_V^2 + 1}{2\omega_P} = \frac{2\omega_P}{\omega_P^2 - \omega_V^2 + 1} , \alpha, \beta, K \geq 0 \tag{4.5}$$

In particular, each couple of planar and vertical Lyapunov orbits is connected through a continuous 1-parameter family of iso-energetic Lissajous orbits.

4.1.3.1 Computation of Lyapunov and Lissajous orbits with the Lindstedt-Poincaré method

Eq.4.5 provides the definition of the Lissajous tori only in the linearized dynamics of Eq.4.3, thus its validity is for small α-β. In addition, since the unstable eigenvalue λ_P is considerably large, the LPOs are highly unstable. Thus, the linear range of validity is further constrained, and the linear solution becomes unreliable for practical applications. To describe these orbits more accurately, the concepts of DST introduced

throughout appendix B, and the semi-analytical methodologies discussed in section B.4, have been applied to the CR3BP [50]. The methodology of the normal forms provides good qualitative results of the evolution of the orbit structure around the LPs, but these are not adequate for practical exploitation [51]. Accurate expressions of the Lissajous orbits can be provided by high-order implementations of the lp technique [115], presented in section B.4.1. This section shows how the lp technique can be applied to compute the LPOs of the general CR3BP [50, 115].

The semi-analytical techniques for the reduction to the center manifold are based on the concept that the analytical description of the dynamics is improved by considering additional nonlinear terms. For the case of the CR3BP, these are originated by the gravity of the two massive bodies. The lp technique is based on a power series approximation. Since it is inversely proportional to the norm of the position from a reference point $\mathbf{r}_0$, the Keplerian gravity potential (see section 2.2) is suitably approximated by a series expansion of Legendre polynomials[1,2] P_n.

$$\frac{1}{\|\mathbf{r}-\mathbf{r_0}\|}=\frac{1}{\|\mathbf{r_0}\|}\sum_{n=0}^{\infty}\left(\frac{\|\mathbf{r}\|}{\|\mathbf{r_0}\|}\right)^n P_n\left(\frac{\mathbf{r}^T\mathbf{r_0}}{\|\mathbf{r}\|\,\|\mathbf{r_0}\|}\right) \tag{4.6}$$

For the CR3BP, the reference point for each gravity potential is the position of the related massive body. Thus, Eq.4.6 is rewritten to describe the gravity potential of each body (at the net of their mass) of the CR3BP as a truncated power series expansion of the position's components from the reference frame's origin, introducing the coefficients of the two gravity series C_n.

$$\frac{1}{\left\|\mathbf{r}-\begin{bmatrix}A\\0\\0\end{bmatrix}\right\|}=\sum_{n=0}^{N}C_n\|\mathbf{r}\|^n P_n\left(\frac{x}{\|\mathbf{r}\|}\right) \tag{4.7}$$

Note that the product $\|\mathbf{r}\|^n P_n\left(\frac{x}{\|\mathbf{r}\|}\right)$ eliminates the denominator of P_n, thus Eq.4.7 is a polynomial in the position's components. The coefficients of this polynomial approximation of the Keplerian gravity are known in closed-form, as they follow a recursive law. The coefficients tend to zero to assure the convergence of the series at increasing order.

$$C_n=\frac{1}{|A|}\left(\frac{1}{A}\right)^n=\left(\frac{|A|}{A}\right)^n\left(\frac{1}{|A|}\right)^{n+1}\Rightarrow\begin{cases}C_{2n}=\frac{1}{|A|^{2n+1}}>0\\ C_{2n+1}=\frac{1}{A|A|^{2n+1}}\end{cases} \tag{4.8}$$

Therefore, the gravity acceleration of each body, that is required in the equations of motion, is retrieved by its definition as the gradient of the gravitational potential, which is now applied to a polynomial. For this reason, the derivative of the Legendre polynomial DP_n is introduced.

[1] They were defined by Legendre for such a specific case (see section 3.1).

[2] Recall that the definition of the Legendre polynomial was provided for their exploitation in the definition of the gravity harmonics in Eq.3.2.

$$\begin{aligned}
&\overline{\nabla}\left(\frac{1}{\left\|\mathbf{r}-[A,0,0]^T\right\|}\right)= \\
&=\sum_{n=1}^{N} C_n\|\mathbf{r}\|^{n-2}\left\{\left[nP_n\left(\frac{x}{\|\mathbf{r}\|}\right)-\left(\frac{x}{\|\mathbf{r}\|}\right)DP_n\left(\frac{x}{\|\mathbf{r}\|}\right)\right]\mathbf{r}+DP_n\left(\frac{x}{\|\mathbf{r}\|}\right)\|\mathbf{r}\|\begin{bmatrix}1\\0\\0\end{bmatrix}\right\}= \\
&=\sum_{n=1}^{N} C_n\|\mathbf{r}\|^{n-2}\mathbf{B}_n(\mathbf{r})
\end{aligned} \tag{4.9}$$

In the normalized LP-centered CR3BP presented below,

$$\mathbf{x}=\begin{bmatrix}\tilde{\mathbf{q}}\\ \dot{\tilde{\mathbf{q}}}\end{bmatrix},\ \dot{\mathbf{x}}=\mathbf{A}\mathbf{x}+\begin{bmatrix}\frac{1-\mu}{\gamma_i}\mp 1\\ 0\\ 0\end{bmatrix}+\frac{1}{{\gamma_i}^3}\begin{bmatrix}\mathbf{0_{3x1}}\\ u_{/\tilde{\mathbf{q}}}\end{bmatrix},\ \mathbf{A}=\begin{bmatrix}\mathbf{0_3} & \mathbf{I_3}\\ -\mathbf{P} & -2\mathbf{W}\end{bmatrix} \tag{4.10}$$

Eq.4.9-4.8 are used to approximate the gravity of the two massive bodies with normalized units,

$$\begin{aligned}
&\frac{1}{{\gamma_i}^3}u_{/\tilde{\mathbf{q}}}=\frac{1}{{\gamma_i}^3}\overline{\nabla}\left(\frac{1-\mu}{\left\|\tilde{\mathbf{q}}-\left[\frac{1\mp\gamma_i}{\gamma_i},0,0\right]^T\right\|}\right)+\frac{1}{{\gamma_i}^3}\overline{\nabla}\left(\frac{\mu}{\left\|\tilde{\mathbf{q}}-[\mp 1,0,0]^T\right\|}\right)= \\
&=\frac{1}{{\gamma_i}^3}\sum_{n=1}^{N} c_n\|\mathbf{r}\|^{n-2}\mathbf{B}_n(\mathbf{r})=\sum_{n=1}^{N}\bar{c}_n\|\mathbf{r}\|^{n-2}\mathbf{B}_n(\mathbf{r})
\end{aligned} \tag{4.11}$$

where the coefficients of the gravity approximation are defined by the following closed-form expression.

$$c_n={\gamma_i}^3\bar{c}_n=(1-\mu)(-1)^n\frac{{\gamma_i}^{n+1}}{(1\mp\gamma_i)^{n+1}}+\mu(\pm 1)^n \tag{4.12}$$

In particular, the first coefficients are presented below.

$$\begin{cases}
\bar{c}_1=-\frac{1-\mu}{\gamma_i}\pm 1+(1-\mu)\frac{\mp 2-\gamma_i}{(1\mp\gamma_i)^2}\pm\frac{\mu-{\gamma_i}^3}{{\gamma_i}^3}=-\frac{1-\mu}{\gamma_i}\pm 1\\
\bar{c}_2=\frac{1-\mu}{(1\mp\gamma_i)^3}+\frac{\mu}{{\gamma_i}^3}=\omega_V^2=\frac{1}{{\gamma_i}^3}u_{/\tilde{z}\tilde{z}}\\
\bar{c}_3=-(1-\mu)\frac{\gamma_i}{(1\mp\gamma_i)^4}\pm\frac{\mu}{{\gamma_i}^3}
\end{cases} \tag{4.13}$$

It is evident that, again, the linear part of the approximation allows to eliminate the residual centrifugal term of Eq.4.10 originated by the coordinates transformation. As the order is defined by the series expansion of the potential, the coefficients required for a dynamics approximated up to order n arrive to $\bar{c}_{n+1}$

The second step in the lp technique is to approximate the solution itself by a power

series expansion. With the aim of reducing it to the central manifold, the nonlinear normal modes are going to be periodic functions. Thus, the approximation used is the second one described in section B.4.1 (refer to Eq.B.47), and the presence of two natural frequencies ω,ν for a 3D orbit leads to the truncated power series in terms of the two amplitudes α,β. This requires 3 series of coefficients, a,b,c, described by $2 \times 2 = 4$ indexes. Thus, every order n requires $3 \times (n+1) \times (n+1)$ coefficients, and the total number of coefficients grows with a power square law. In addition, the key point of the lp technique is to enable the modification of the natural frequencies due to the nonlinear dynamics. Therefore also ω,ν are developed in two dedicated power series. This requires additional $2 \times (n+1)$ coefficients for every order. The analytical approximation given by the solution of the lp algorithm is the Lissajous orbit provided in Eq.4.14.

$$\begin{cases} \tilde{\mathbf{q}}_{QPO}(t) = \begin{bmatrix} \tilde{x}(t) \\ \tilde{y}(t) \\ \tilde{z}(t) \end{bmatrix} = \sum_{i+j=1}^{N} \alpha^i \beta^j \sum_{|k|=0,|m|=0}^{i,j} \begin{bmatrix} a_{ijkm} \cos\left(k\omega t + m\nu t + k\varphi_P + m\varphi_V\right) \\ b_{ijkm} \sin\left(k\omega t + m\nu t + k\varphi_P + m\varphi_V\right) \\ c_{ijkm} \cos\left(k\omega t + m\nu t + k\varphi_P + m\varphi_V\right) \end{bmatrix} \\ \begin{cases} \omega = \sum_{i+j=0}^{N} \alpha^i \beta^j \omega_{ij} \\ \nu = \sum_{i+j=0}^{N} \alpha^i \beta^j \nu_{ij} \end{cases} \end{cases} \tag{4.14}$$

The linearized Lissajous of Eq.4.5, that uses an approximation of the gravity potential up to order 2, is expressed by the following values of the coefficients up to order 1.

$$\begin{aligned} &a_{\left[\begin{smallmatrix}1000\ 0100\\1010\ 0110\\1001\ 0101\end{smallmatrix}\right]} = \left[\begin{smallmatrix}0 & 0\\1 & -\\- & 0\end{smallmatrix}\right], \; b_{\left[\begin{smallmatrix}1000\ 0100\\1010\ 0110\\1001\ 0101\end{smallmatrix}\right]} = \left[\begin{smallmatrix}0 & 0\\k & -\\- & 0\end{smallmatrix}\right], \; c_{\left[\begin{smallmatrix}1000\ 0100\\1010\ 0110\\1001\ 0101\end{smallmatrix}\right]} = \left[\begin{smallmatrix}0 & 0\\0 & -\\- & 1\end{smallmatrix}\right], \\ &\omega_{[00\ 10\ 01]} = \left[\omega_P \ 0 \ 0\right], \; \nu_{[00\ 10\ 01]} = \left[\omega_V \ 0 \ 0\right] \end{aligned} \tag{4.15}$$

The input of the lp algorithm is the linear solution, characterized by the parameters α and β, and by the related starting phases. The output of the algorithm is the set of coefficients of the analytical serial approximation of $\tilde{x}(t)$,$\tilde{y}(t)$,$\tilde{z}(t)$ up to the chosen order N, and the coefficients of the series of ω, and ν. However, the lp algorithm is ultimately a generation of reliable initial conditions $x(0)$,$y(0)$,$z(0)$ (and their related velocities) on a suitable map.

The substitution of the solution of Eq.4.14 in the dynamics approximated by the series expansion of the gravity terms of Eq.4.10-4.11, produces a series of orthogonal linear ODEs at each order, sorted by the harmonics of indexes i,j,k,m. Each of these linear ODEs is inhomogeneous, with null initial conditions, and the forcing term corresponds to the residual gravitational and apparent forces constituted by the terms of lower order of the solution. Thus, the determination of the particular integral is required to determine the coefficients at order n. The lp technique consists in the recursive solution of a linear system, whose expression is the following.

$$
\begin{cases}
\begin{bmatrix} -\left(\varpi_{km}^2+2\bar{c}_2+1\right) & -2\varpi_{km} & 0 \\ -2\varpi_{km} & -\left(\varpi_{km}^2-\bar{c}_2+1\right) & 0 \\ 0 & 0 & -\left(\varpi_{km}^2-\bar{c}_2\right) \end{bmatrix} \begin{bmatrix} a_{ijkm} \\ b_{ijkm} \\ c_{ijkm} \end{bmatrix} + \begin{bmatrix} -2(\omega_{00}+K)\delta_{1k}\delta_{0m} & 0 \\ -2(K\omega_{00}+1)\delta_{1k}\delta_{0m} & 0 \\ 0 & -2\nu_{00}\delta_{0k}\delta_{1m} \end{bmatrix} \begin{bmatrix} \omega_{i-1j} \\ \nu_{ij-1} \end{bmatrix} = \\
= \left\{ \bar{c}_n \|\mathbf{r}\|^{n-2} \mathbf{B}_n\left(\mathbf{r}\right) \right\}_{ijkm} + \\
- \begin{bmatrix} -2\sum\limits_{i+j=1}^{n-2} \omega_{ij}kb_{ijkm}+\nu_{ij}mb_{ijkm}+\sum\limits_{i+j=1}^{n-2} \omega_{ij}^2k^2a_{ijkm}+2\omega_{ij}\nu_{ij}kma_{ijkm}+\nu_{ij}^2m^2a_{ijkm} \\ 2K\sum\limits_{i+j=1}^{n-2} \omega_{ij}ka_{ijkm}+\nu_{ij}ma_{ijkm}+K\sum\limits_{i+j=1}^{n-2} \omega_{ij}^2k^2b_{ijkm}+2\omega_{ij}\nu_{ij}kmb_{ijkm}+\nu_{ij}^2m^2b_{ijkm} \\ \sum\limits_{i+j=1}^{n-2} \omega_{ij}^2k^2c_{ijkm}+2\omega_{ij}\nu_{ij}kmc_{ijkm}+\nu_{ij}^2m^2c_{ijkm} \end{bmatrix} \\
\varpi_{km} = k\omega_{00} + m\nu_{00} \\
\delta_{1k}\delta_{0m} = 1 \Rightarrow a_{ij10} = 0 \\
\delta_{0k}\delta_{1m} = 1 \Rightarrow c_{ij01} = 0
\end{cases}
\tag{4.16}
$$

When the linear system is rank-deficient, appropriate constraints on the coefficients are used, as reported above. The analytical complexity of the lp method is the determination of the forcing apparent terms on the right hand-side. Eq.4.17 provides the expression of the coefficients of the gravity term, to be used on the right hand-side of Eq.4.16, to derive all the coefficients of the solution at order-2.

$$
\begin{cases}
\bar{c}_3 \left\|\mathbf{r}\right\| \mathbf{B}_3\left(\mathbf{r}\right) = \bar{c}_3 \begin{bmatrix} \frac{3}{2}\left(2\tilde{x}^2-\tilde{y}^2-\tilde{z}^2\right) \\ -3\tilde{x}\tilde{y} \\ -3\tilde{x}\tilde{z} \end{bmatrix} = \\
= \bar{c}_3 \begin{bmatrix} \frac{3}{2}\left(2a_{1010}^2\frac{1}{2}\alpha^2\beta^0(\cos_{20}+\cos_{00})-b_{1010}^2\alpha^2\beta^0\frac{1}{2}(-\cos_{20}+\cos_{00})-c_{0101}^2\alpha^0\beta^2\frac{1}{2}(\cos_{02}+\cos_{00})^2\right) \\ -3a_{1010}b_{1010}\alpha^2\beta^0\frac{1}{2}(\sin_{20}-\sin_{00}) \\ -3a_{1010}c_{0101}\alpha^1\beta^1\frac{1}{2}(\cos_{11}+\cos_{1-1}) \end{bmatrix} \\
\left\{\bar{c}_3 \left\|\mathbf{r}\right\| \mathbf{B}_3\left(\mathbf{r}\right)\right\}_{ijkm} = \bar{c}_3 \begin{bmatrix} \frac{3}{2}a_{1010}^2-\frac{3}{4}b_{1010}^2 \\ \frac{3}{2}a_{1010}b_{1010} \\ 0 \end{bmatrix}_{2000} + \bar{c}_3 \begin{bmatrix} \frac{3}{2}a_{1010}^2+\frac{3}{4}b_{1010}^2 \\ -\frac{3}{2}a_{1010}b_{1010} \\ 0 \end{bmatrix}_{2020} + \\
+ \bar{c}_3 \begin{bmatrix} -\frac{3}{4}c_{0101}^2 \\ 0 \\ 0 \end{bmatrix}_{0200} + \bar{c}_3 \begin{bmatrix} -\frac{3}{4}c_{0101}^2 \\ 0 \\ 0 \end{bmatrix}_{0202} + \\
+ \bar{c}_3 \begin{bmatrix} 0 \\ 0 \\ -\frac{3}{2}a_{1010}c_{0101} \end{bmatrix}_{1111} + \bar{c}_3 \begin{bmatrix} 0 \\ 0 \\ -\frac{3}{2}a_{1010}c_{0101} \end{bmatrix}_{111-1}
\end{cases}
\tag{4.17}
$$

Thus, the computational burden of the lp technique required to compute 2D-QPOs in a 3D mechanical system, even with symmetries, is significant when the order required for their approximation is high. This is necessary for the case of the chaotic CR3BP, where even small errors of the approximation lead to solutions rapidly diverging in the full nonlinear dynamics.

The first use of the lp technique to produce the nonlinear LPOs in the CR3BP was made in 1980 by Richardson [114], who used an expansion up to order 3. These Lissajous orbits rapidly diverge from their approximated solution when propagated in the full CR3BP. However, this low-order solution already shows that the nonlinear vertical Lyapunov orbits are no longer a simple vertical oscillation, but they exhibit a 3D eight-shaped pattern. Following the growing appeal of the LPOs showed initially by NASA, the interest in this analytical approach paved the way in the '80s and '90s to develop increasingly high-order expansions. A team of researchers in Barcelona

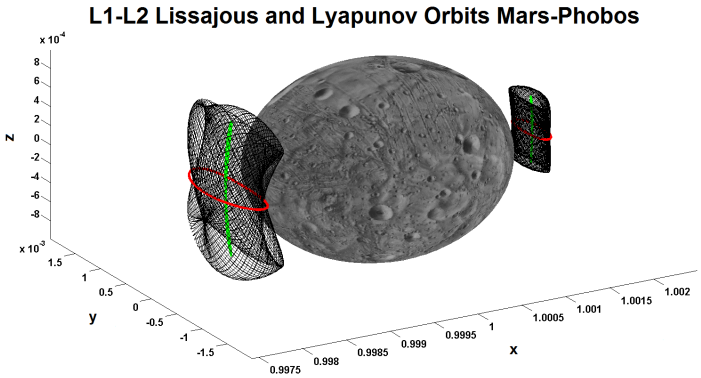

Figure 4.2: **Lissajous and Lyapunov orbits around Phobos in the CR3BP.** Examples of two planar (red) and vertical (green) Lyapunov orbits around each LP, and one iso-energetic Lissajous orbit (black) of high-width around them. The displayed LPOs around L_1 have higher energy than the LPOs displayed around L_2. The orbits are computed with the lp algorithm at the maximum order of the expansions 35, and they are inside the related practical region of convergence. Mean ellipsoidal shape of Phobos.

(Gómez, Martinez, Llibre, Masdemont, Simó, Rodríguez: usually referred to as the Barcelona group) specialized in this task. They are currently able to derive Lissajous and Lyapunov orbits in any CR3BP up to order 35 [115].

4.1.3.2 The Lyapunov and Lissajous orbits of the Mars-Phobos CR3BP

The lp technique described in section 4.1.3.1 for the computation of the LPOs has been applied for the case of the Mars-Phobos CR3BP. This means that the coefficients of the series expansion are determined with the related μ, and they have been computed up to order 35[3]. The resulting Lissajous orbits, and the related backbones of Lyapunov orbits are analytically evaluated with Eq.4.14. Fig.4.2 shows an example of these LPOs around both L_1 and L_2.

The purpose of this section is to investigate the characters of these analytical orbits, focusing on the mathematical properties of the algorithm and the engineering aspects for their practical applications.

4.1.3.2.1 Mathematical Features of the Algorithm

Convergence properties. In this section the efficiency of the lp technique is tested by deriving the properties of convergence of its solutions, which represents the fundamental mathematical feature of the algorithm. This is conducted by taking the initial condition of any orbit of the lp expansion, and simulating the flow in the full nonlinear dynamics of the CR3BP. In this case, the convergence of the algorithm refers to how much the approximated trajectory of Eq.4.14 matches the behavior in the full model of the CR3BP.

[3]This data has been provided by Prof. Josep Masdemont, through a collaboration within the AstroNet-II research network.

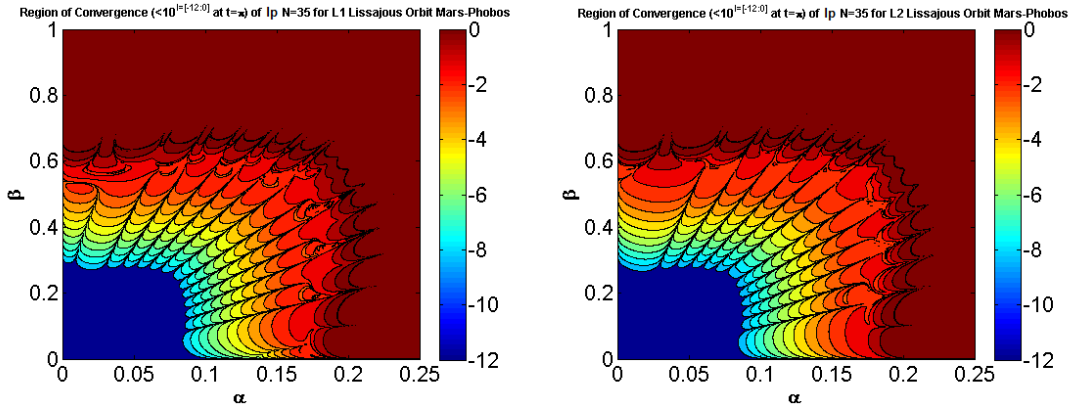

Figure 4.3: **lp region of convergence for L_1 and L_2 Lissajous orbits of the Mars-Phobos CR3BP.** Error evaluated at $t = \pi$. Order of the expansions set to 35. Initial phases set to zero.

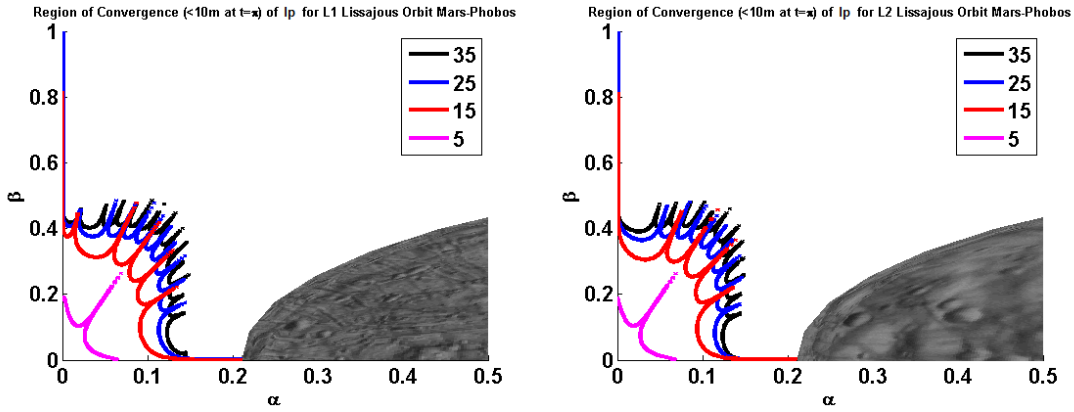

Figure 4.4: **lp region of convergence for L_1 and L_2 Lissajous orbits of the Mars-Phobos CR3BP.** Boundaries for different order of the expansion at the threshold position error of 10^{-6} adimensional units at $t = \pi$. Initial phases set to zero. Physical position and mean ellipsoidal dimensions of Phobos are represented.

The figure of the error could be expressed in two alternative ways: by fixing the propagation time and evaluating the state error between the two orbits at that instant, or by fixing the state error and evaluating the propagation time required to produce it. The first figure involves a direct calculation, and is chosen as the error's measure. The fixed propagation time is set to π (CR3BP time-units), since this is close to the natural period (both planar and vertical) of the eigenvalues of the LPs. In addition, the error is considered as the norm of only the position's components of the state's deviation from the nominal trajectory.

This error should be computed for all the 2-parameters family of Lissajous orbits: the related contours on the α-β plane constitute the region of convergence of the lp algorithm [50, 51] for the LPOs of the Mars-Phobos CR3BP. However, as introduced in section B.6.3.3.3, every n-torus is described by n phase, so is accompanied by n indeterminancies to choose its initial condition. Thus, the choice is to take, as initial condition, the point of Eq.4.14 with both null phases. The related region of convergence

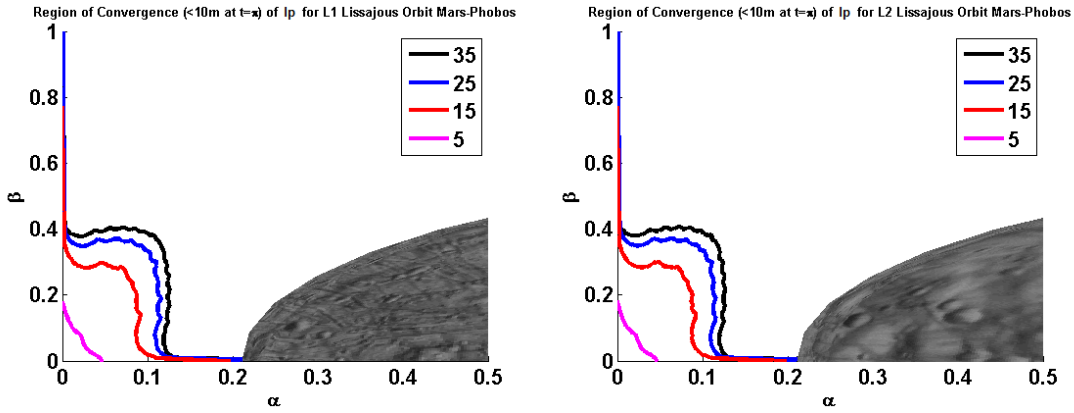

Figure 4.5: **lp practical region of convergence for L_1 and L_2 Lissajous orbits of the Mars-Phobos CR3BP.** Boundaries for different order of the expansion at the threshold position error of 10^{-6} adimensional units at $t = \pi$. Physical position and mean ellipsoidal dimensions of Phobos are represented.

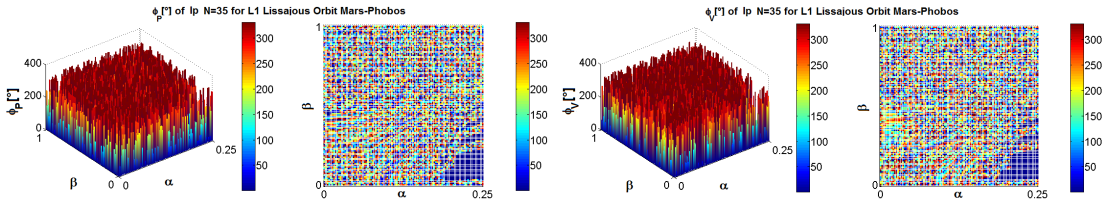

Figure 4.6: **lp practical region of convergence for L_1 Lissajous orbits of the Mars-Phobos CR3BP.** Maximizing initial planar and vertical phases.

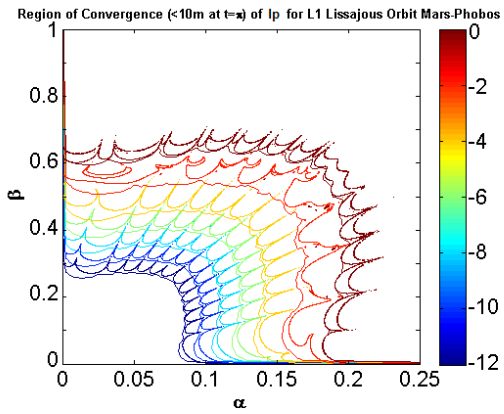

Figure 4.7: **lp region of convergence for L_1 Lissajous orbits of the Mars-Phobos CR3BP.** Comparison between the boundaries for initial starting phases null and for the practical definition, for different order of the expansion at the threshold position error of 10^{-6} adimensional units at $t = \pi$.

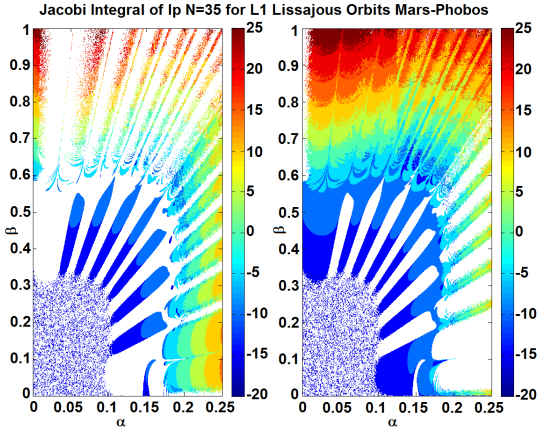

Figure 4.8: **lp region of convergence for L_1 Lissajous orbits of the Mars-Phobos CR3BP.** Error of the Jacobi integral between initial and final condition (evaluated at $t = \pi$) of the lp expansion (left graph positive error, right graph negative error; logarithmic scale). Order of the expansions set to 35. Initial phases set to zero.

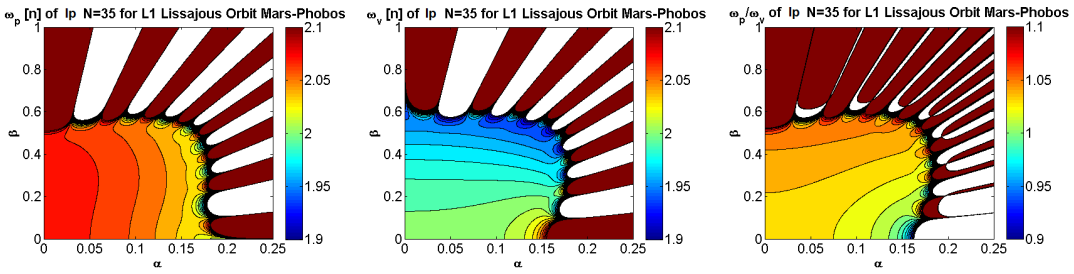

Figure 4.9: **lp region of convergence for L_1 Lissajous orbits of the Mars-Phobos CR3BP.** Planar frequency, vertical frequency, and their ratio. Order of the expansions set to 35. Initial phases set to zero.

around both LP is presented in Fig.4.3 for the LPOs computed from the lp algorithm at maximum order. The two regions are similar, and the error increases as long as the two amplitudes increase. It is worth to note that the error along the family of PO is smaller than the one of the related iso-energetic 2D-QPOs. This happens also along particular directions spreading from the EP. The closest region around the EP is characterized by a very small error (10^{-12}) after this propagation time: this area is uniform due to the presence of the machine error, as will be discussed shortly. Then the contours enlarge proportionally as the amplitudes increase, until their gradient becomes steep. However, the minimum error in this region is already very large (10^{-1}). Thus, after describing the behavior of the region of convergence, its information is reduced to its boundary. This is done by fixing a threshold for the position error, and deriving the relating iso-line. Historically, in the cases of the Sun-Earth and Earth-Moon systems, a significant threshold is considered to be 10^{-6} normalized units [51]. Thus, the same is considered for the Mars-Phobos system: due to the small length-scale's peculiarity, this results in a threshold of about $10m$[4]. The boundary of the region of convergence is suitable to be evaluated for different orders of the lp algorithm [51], as shown in Fig.4.4. Lower orders are reliable only very close to the EP, and this is particular evident for the case of the collinear region of the CR3BP, where the instability is high. The inclusion of additional nonlinear terms enlarges the region of convergence, until an asymptotic limit is reached, and incrementing the order does not provide any advantages. The reason of this behavior is not related to any analytical behavior, but is only computational. The machine error of current 16-digits computers, and in particular of the software used, is about 10^{-16}, and the accuracy of the ODEs integration is declared to be within an error 100 times higher. Thus, when the residual nonlinear terms of the dynamics approximated at high-order become smaller than this value, the latter becomes the limiting factor for the convergence, which is called here a "computational stability". Furthermore, the unstable eigenvalue of the Mars-Phobos LPs has been computed in Eq.2.29 to be about $\lambda = 2.51$[5]. For the fixed propagation time chosen, the related

[4] By comparison, the error on the Sun-Earth system is $150km$.

[5] Recall from section B.1.2.2 that a Lyapunov exponent greater than 1 is considered to indicate that the system is chaotic.

multiplier $e^{\lambda t}$ is about 2,700, and this is coherent with the asymptotic minimum error of the region of convergence discussed above.

The boundary of the region of convergence in Fig.4.4 is characterized by sharp spikes, in particular at high orders. These peaks are resonances of the lp algorithm, due to the coupling of the two frequencies ω and ν[6], which are shown in Fig.4.9. The Barcelona group analyzed this behavior in order to derive the rational numbers that express these resonances, which resulted to be characterized by a high integer denominator. These resonances are part of the algorithm, and they depend from the initial phases. For this reason, the practical region of convergence is introduced [51], and defined by the maximum error of the same torus throughout simulations for all the initial phases. The resulting plot is presented in Fig.4.5, and shows that the boundary is now smoother (see Fig.4.7 for comparison). The maximizing phases that determine this boundary are not a deterministic function of the amplitudes, as shown in Fig.4.6.

In addition, Fig.4.10-4.11 show the practical region of convergence, and its boundaries at different order, also for the second case of error figure, which is the time of permanence within a fixed position error of 10^{-6} adimensional units. Thus, this error is taken equal to the previous threshold, and the related isolines at the threshold of π in Fig.4.11 are the same as Fig.4.5. Fig.4.10 proves that the core part of the region of convergence is characterized by a "computational" time of permanence of 3 longitudinal revolutions of the Lissajous orbits. This is an important indicator, coherent with the LPOs of the Sun-Earth and Earth-Moon system, but the major different is that the small time-scale of Phobos yields this value to be just a ten of hours.

An alternative method to evaluate the efficiency of the lp algorithm is to compute the error of the Jacobi integral between initial and final conditions at a fixed propagation time of the lp solution alone, as shown in Fig.4.8. This figure does not depend on the numerical integration, and the region of convergence is naturally characterized by an error under the machine error.

In summary, the major limitation of the lp methodology is constituted by its convergence properties. The shape and size of the widest practical regional of convergence for Lissajous orbits around Phobos is coherent with the ones computed in the literature around the Earth and the Moon, in terms of normalized units [51, 50]. It is also almost rectangular, approximately measuring $(\alpha, \beta) \in [0, 0.12] \times [0, 0.40]$. At first instance, due to the collapse of the Phobos' SOI (Phobos' mean ellipsoidal surface is located at $\alpha = 0.21$), one notes that this region covers a large area of the secondary's realm, as a difference from the cases of the Earth and the Moon. The region is also larger for the POs: the boundary of the planar Lyapunov orbits is over Phobos' intersection, while the boundary of the vertical Lyapunov orbits is at $\beta = 1.25$. However, this first interpretation is misleading, since it would suggest that the set of reliable LPOs computed with the lp algorithm is larger than in the cases of the Sun-Earth and Earth-Moon

[6] Recall that the two normal frequencies are part of the nonlinear solution of the lp methodology in Eq.4.14, and they depend from α,β.

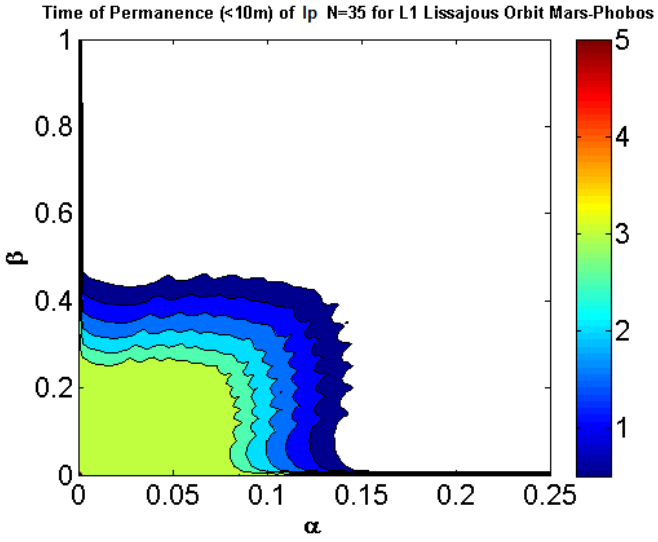

Figure 4.10: **lp time of permanence inside the practical region of convergence for L_1 Lissajous orbits of the Mars-Phobos CR3BP.** Time expressed as number of longitudinal revolutions of the Lissajous orbits. Threshold position error of 10^{-6} adimensional units.

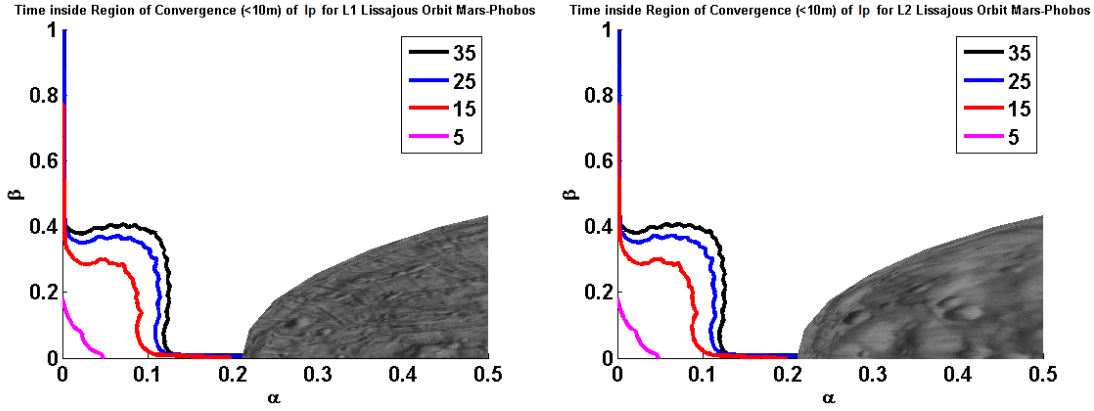

Figure 4.11: **lp time of permanence inside the practical region of convergence for L_1 and L_2 Lissajous orbits of the Mars-Phobos CR3BP.** Boundaries for different order of the expansion at the threshold $t = \pi$ to provide the position error of 10^{-6} adimensional units. Physical position and mean ellipsoidal dimensions of Phobos are represented.

systems. The gain is counteracted by the fact that the proximity to Phobos requires further and dominant forces to be included in the dynamics, as explained in section 2.4 and chapter 3. The improvement of the Phobos' LPOs computed in this section will constitute the focus of the following sections 4.2 and 4.3.

Quasi-periodic motion. An important characteristic of any PO is the related period. Fig.4.12 shows the period of the planar and vertical Lyapunov orbits, which increases with α and β. The 2D-QPOs do not have a period, and as explained in section B.6.2, they are reduced to a discrete dynamical system by iterated longitudinal returns to a transversal map. In Fig.4.12 we see that the displacement of the first-return image from the initial condition grows along the bisector's direction of the α-β plane, since these are

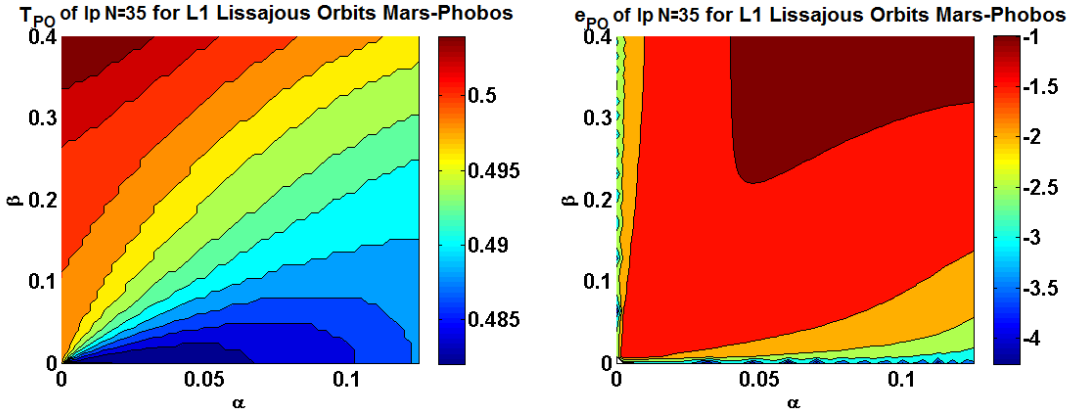

Figure 4.12: **lp periodic and quasi-periodic motion for L_1 Lyapunov and Lissajous orbits of the Mars-Phobos CR3BP.** On the left, first-return time to the transversal map where the deviation of the image after one longitudinal revolution from the initial condition is minimum. This corresponds to the period of the POs. On the right, related relative error from the initial state (logarithmic scale). Order of the expansions set to 35. Initial phases set to zero.

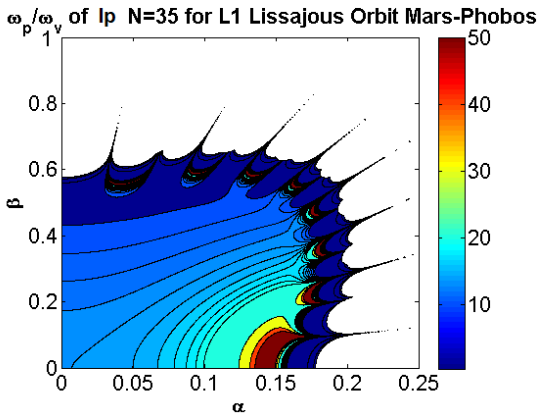

Figure 4.13: **lp region of Convergence for L_1 Lissajous orbits of the Mars-Phobos CR3BP.** Period of the first transversal revolution. Order of the expansions set to 35. Initial phases set to zero.

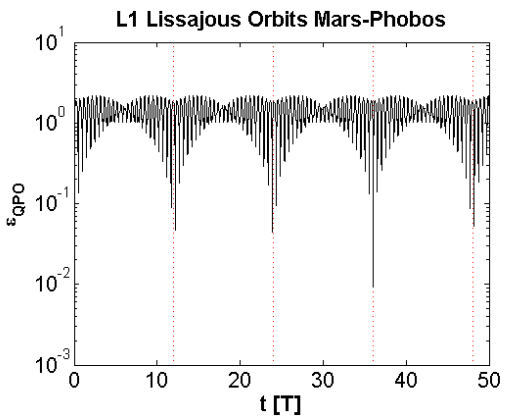

Figure 4.14: **lp quasi-periodic motion for L_1 Lissajous orbits of the Mars-Phobos CR3BP.** Relative error from the initial state (logarithmic scale) for the Lissajous orbit of $\alpha = 0.12, \beta = 0.4$. Red dotted lines indicate multiples of the period of the first transversal revolution. Order of the expansions set to 35. Initial phases set to zero.

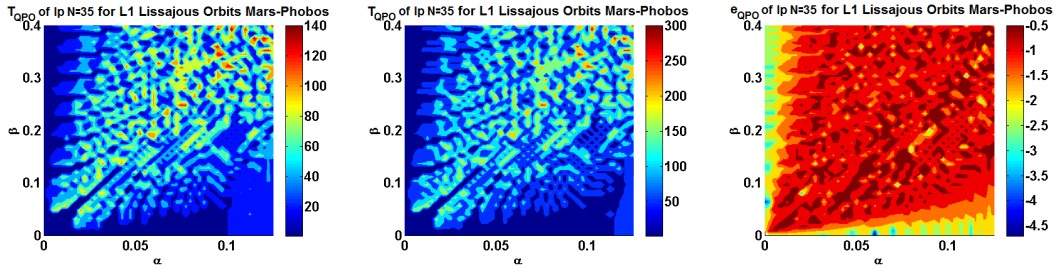

Figure 4.15: **lp quasi-periodic motion for L_1 Lissajous orbits of the Mars-Phobos CR3BP.** T_{QPO} of the Lissajous orbits in orbital units, as multiple of the related first-return time of Fig.4.14, and related error of the latter from an integer number (logarithmic scale), which shows that the two numbers are not multiple. Order of the expansions set to 35. Initial phases set to zero.

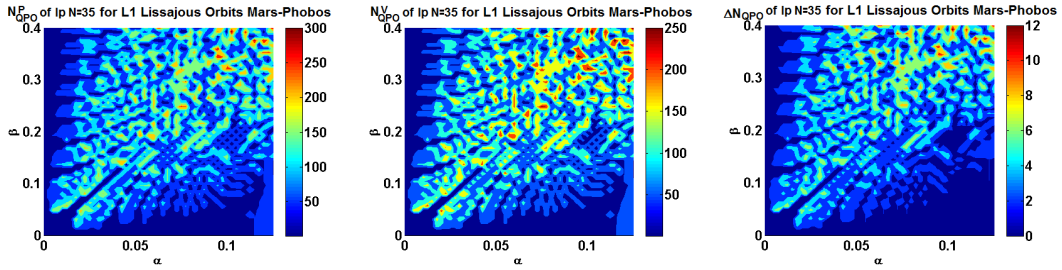

Figure 4.16: **lp quasi-periodic motion for L_1 Lissajous orbits of the Mars-Phobos CR3BP.** Planar frequency cycles, vertical frequency cycles and their gap cycles difference, associated to T_{QPO} of the Lissajous orbits. Order of the expansions set to 35. Initial phases set to zero.

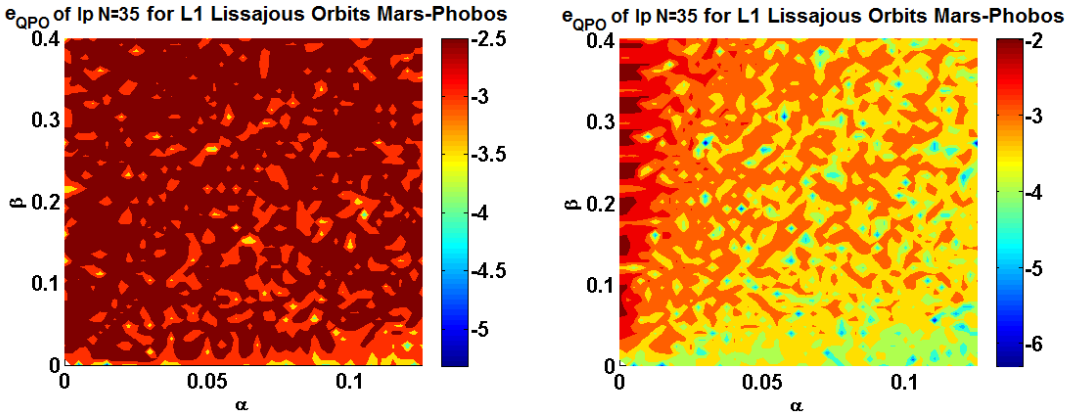

Figure 4.17: **lp quasi-periodic motion for L_1 Lissajous orbits of the Mars-Phobos CR3BP.** On the left, relative error at T_{QPO} of the Lissajous orbits from the initial state (logarithmic scale). On the right, error from an integer number of the minimum number of frequency cycles (logarithmic scale). Order of the expansions set to 35. Initial phases set to zero.

the location of the widest transversal QPOs at growing longitudinal size. As explained in section B.1.3, a characteristic feature of a 2D-QPO is the time of the first transversal revolution. This could be derived from the ratio r of the two natural frequencies, which are now made explicit by the lp method, and is shown in Fig.4.13. Since the invariant curves are covered with a discrete mapping of the rotation number, it could be possible to consider multiple laps, such that the final value is approximately close, within some tolerance, to the initial condition. This translates in the approximation of the 2D-QPO as a resonant PO with the smallest denominator. The related propagation time span is referred to as T_{QPO}. The behavior of the state trajectory deviation from the initial configuration is shown in Fig.4.14 for a sample Lissajous orbit. We see that it is characterized by a heart-shaped enveloping oscillation, which means that there are local minima repeating with time. They correspond to each transversal revolution lap. This second harmonic provides a superimposed oscillation, and the minima and its location are rigourously not periodic in general. However, this graphical approach could be useful to limit the time domain to look for T_{QPO}. This value is instead derived with an alternative approach, by finding an appropriate couple of integer numbers that fulfill r within a tolerance. As expressed in Eq.4.18, the gap ΔN between longitudinal and transversal revolutions, N_P and N_V, is incrementally increased by an integer counter, and the related N_P or N_V is derived from r. If N_P or N_V are close to an integer, T_{QPO} is identified[7]. If instead in Eq.4.18 ΔN is fixed to be one, $ceil\{N_V\}$ constitutes the period of the first transversal revolution.

$$\begin{cases} r = \frac{\omega_P}{\omega_V} > 1 \Rightarrow r = \frac{T_V}{T_P} = \frac{N_P}{N_V} = \frac{n+1}{n} = \frac{n\Delta N+\Delta N}{n\Delta N} = \frac{N_V+\Delta N}{N_V} \\ r \in \mathbb{Q}^+ \leftrightarrow n \in \mathbb{Q}^+ \wedge N_P, N_V, \Delta N \in \mathbb{N}^+ \Rightarrow T_{QPO} = N_V T_V = N_P T_P \end{cases} \tag{4.18}$$

Fig.4.15 shows T_{QPO} and Fig.4.16 presents the related N_P,N_V,ΔN for the Lissajous orbits inside the lp practical region of convergence of the Mars-Phobos system. In particular, Fig.4.17 reports the error between initial and final condition at T_{QPO}, and the error of the minimum N_P or N_V from an integer number. These errors are small for all the region ($< 10^{-2}$), and the Lissajous orbits can be practically seen as resonant periodic orbits, but with very large periods (tenths to hundreds of orbital periods). In addition, the distribution of this approximated period is stochastic, and is coherent with the density of the set of rational numbers into the set of real numbers.

4.1.3.2.2 Engineering Features of the Algorithm

This section focuses on the technical aspects, for applications in space missions around Phobos, of the LPOs derived in section 4.1.3.2 and the related lp algorithm.

Trade-off with guidance, navigation and control subsystems. The convergence properties analyzed in section 4.1.3.2.1 are addressed in terms of the boundary of the practical

[7] If $r < 1$ the two frequencies swap in the definition of longitudinal and transversal motion for the purpose of the procedure.

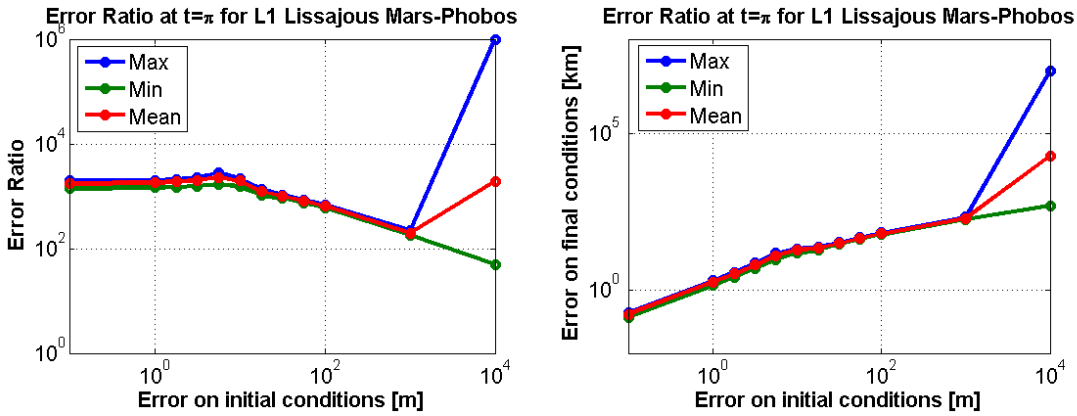

Figure 4.18: **Perturbation error's propagation inside the lp practical region of convergence for L_1 Lissajous orbits of the Mars-Phobos CR3BP.** Fixed propagation time $t = \pi$. Order of the expansions set to 35.

region of convergence, which is defined by a couple of values. They are the propagation time and the threshold on the position error. These should be chosen to be coherent with the respective measure of performance of the station-keeping control (frequency of the impulsive maneuvers) and navigation (error on estimated state) subsystem of the spacecraft. Furthermore, these values are dependent on the navigation capability (time required to achieve the orbit determination) and the guidance requirement (maximum displacement from the reference signal) of the mission. Thus, the time of permanence of the LPOs' reference signal, computed with the lp algorithm, must be larger than the navigation's processing time and smaller than the period of a maneuver. In such a propagation time, the position error's threshold of the lp solution must be larger than the navigation estimation and smaller than the guidance requirement. This trade-off is required to consider a region of convergence feasible with current technologies.

The choice of the error's threshold is conducted by simulations. The initial condition is taken from the lp algorithm, which is the guidance planner, and the related LPO constitutes the reference signal (or guidance law). Since the initial conditions are taken inside the region of convergence, to be consistent with the calculation of the propagation ratio, the reference signal is computed by the propagation of the initial condition in the CR3BP. The initial condition is then perturbed by an initial position error, which constitutes the navigation's estimation error, and is propagated in the full nonlinear dynamics, which constitute the real-world. The initial perturbation is only in position for the purpose of this analysis, assuming that the navigation's performance on the estimated velocity is coherent with the estimated position, in the sense that the first would not change significantly the trade-off. The ratio between the norms of final and initial error after the fixed propagation time π constitutes the propagation ratio. This is exactly the same procedure of computing the MLE, as presented in section B.1.2.2. The procedure undertaken is to perform a MonteCarlo simulation to derive the maximum propagation ratio. The simulations proved that the maximizing direction

is deterministic, and is constituted by the IM of the LPO at the initial point.

The simulations are performed in the same way done in section 4.1.3.2.1. The propagation ratio is derived for a sample of α-β inputs at the highest order 35, and is further maximized over the possible starting phases: this relationship has still resulted to be not deterministic. Afterwards, since the system is nonlinear, the entire session is repeated changing the norm of the initial perturbation. Finally, results are summarized in Fig.4.18 taking the maximum, minimum and mean propagation ratio for all the Lissajous orbits inside the region of convergence, as a function of the initial error. The propagation ratio is approximately constant for small deviations, where the linear approximation of the STM is worthy. This value is large, about $1,800$, and represents the Lyapunov multiplier of the LPOs, which is coherent with the analytical value at L_{1-2} mentioned in section 4.1.3.2.1. Due to the choice of the propagation time, made to approximate one longitudinal revolution, this value is also a good approximation of the Floquet multiplier of the LPOs. This shows why the orbit structure of the CR3BP is chaotic, since the LPOs have high sensitivity with respect to the initial conditions. The propagation ratio then decreases for higher deviations, but this region is not relevant for practical applications.

In summary, since the altitude of the LPs is only $3.5km$, guidance performance for LPOs should be limited to about $100m$, which would lead to lower the threshold to $0.1m$ (10^{-8} L-units). However, interplanetary orbit determination's best performance is about $1m$ (10^{-7}). Thus, no practical solution is possible, and the station-keeping should be performed at higher frequency, with an interval of the maneuvers lower than $4h$, which is already a small window for ground-processing. The demand of the GNC system is very high for the Lyapunov and Lissajous orbits around Phobos, and the need of either visual-based optical navigation or autonomous control is evident.

Trade-off with mission analysis and design. The lp algorithm, once the set of coefficients is derived up to the chosen order, takes as input the linear amplitudes α-β and delivers as output the reference signal of the LPO along time. From a mission analysis and design point of view, it is important to interface immediately with the physical dimensions of the orbit[8]. Therefore, in this perspective, an inverse relationship of the lp algorithm is needed: from the orbit required to satisfy some operations, α-β should be derived to uplink the guidance law to be tracked by the spacecraft.

Characterizing each LPO by its maximum x,y,z components, these values are computed in Fig.4.19 for the orbits inside the practical region of convergence (the starting phases are not important in defining the size of the orbit). However, we would like to invert this 3×2 relationship of outputs $\times$ inputs $[x, y, z](\alpha, \beta)$ into a 2×3 relationship $[\alpha, \beta](x, y, z)$. This is not always possible. The mismatch of the number of inputs/outputs is not a problem, since the task can be decomposed in a planar-vertical framework, and considering only one between x,y and use the constraint $x(y)$. From

[8]Recall that α-β are in γ_i-units.

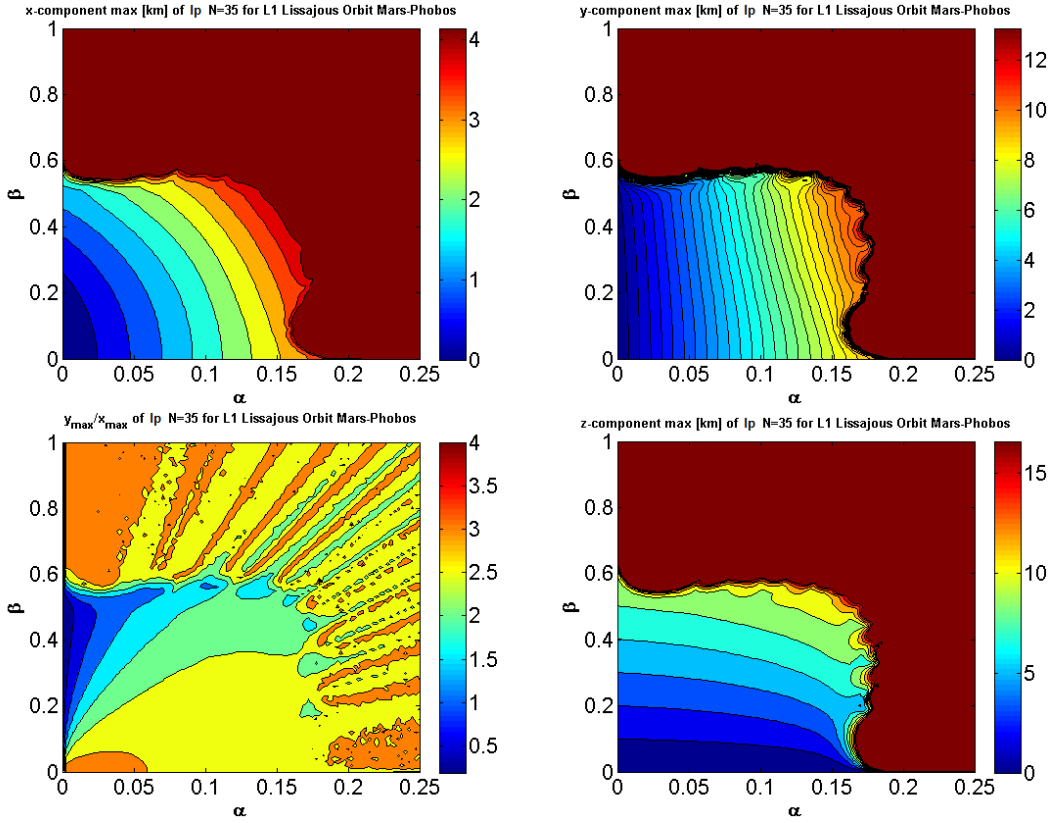

Figure 4.19: **Maximum x,y,z components and ratio y/x as a function of α,β for L_1 Lissajous orbits of the Mars-Phobos CR3BP.**

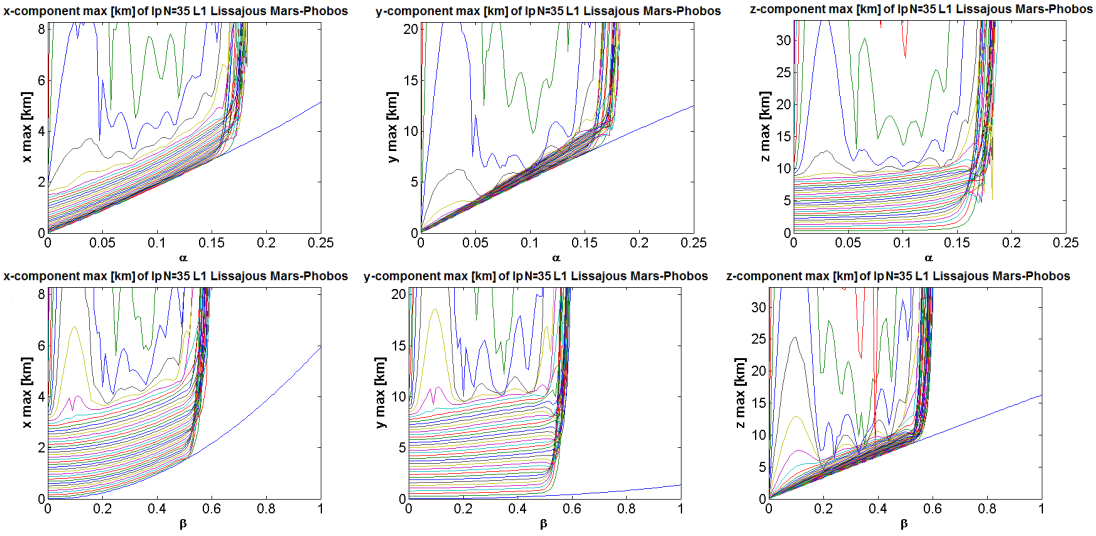

Figure 4.20: **α,β as a function of the maximum x,y,z components for L_1 Lissajous orbits of the Mars-Phobos CR3BP.** 1D approach.

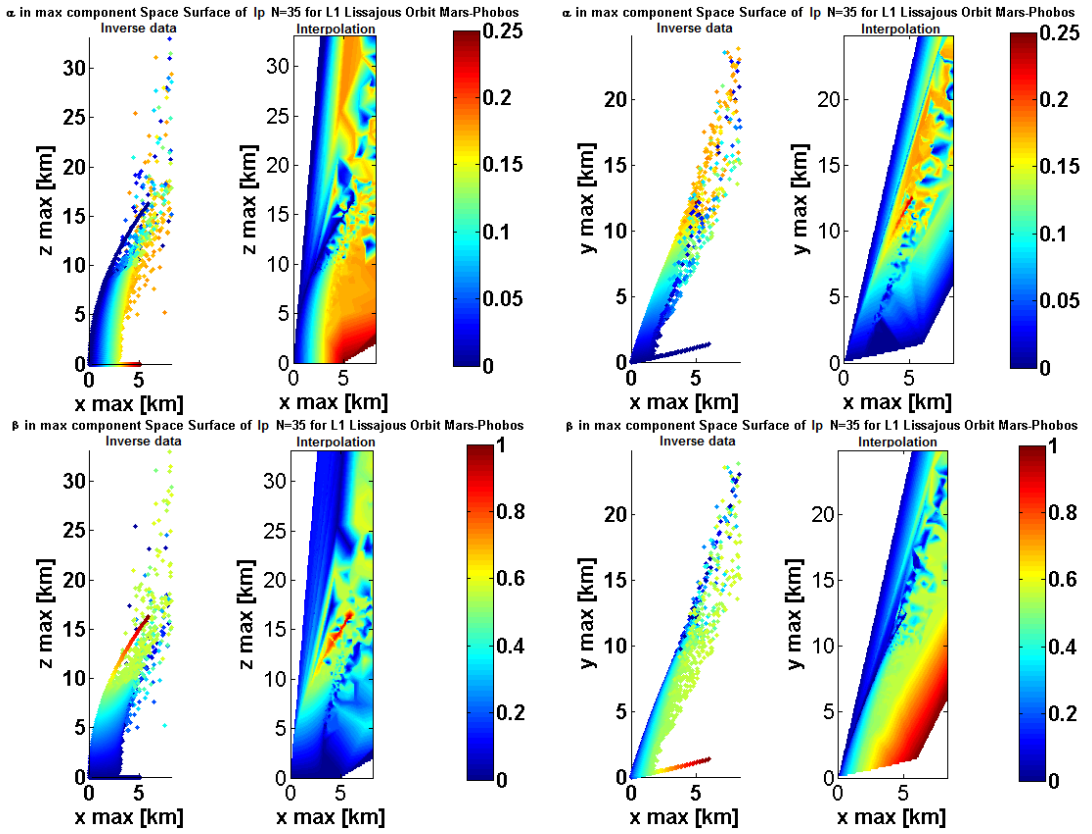

Figure 4.21: α,β **as a function of the maximum** x,y,z **components for** L_1 **Lissajous orbits of the Mars-Phobos CR3BP.** 2D approach. Comparison between the real inverse data from the lp input-output algorithm and the ones obtained with a scattered triangular interpolation.

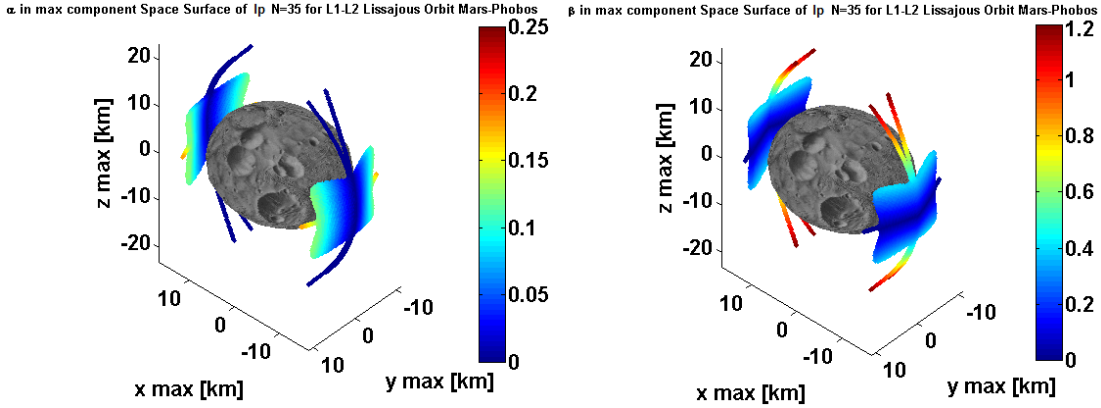

Figure 4.22: α,β **as a function of the maximum** x,y,z **components for** L_{1-2} **Lissajous orbits of the Mars-Phobos CR3BP.** 3D approach. The maximum components surfaces are restricted to the practical region of convergence at $t = \pi$ and threshold 10^{-6} adimensional units of the Lissajous orbits that do not intersect Phobos (mean ellipsoidal dimensions).

Fig.4.19, for Lissajous close to the planar Lyapunov, this ratio tends to K of the linear solution in Eq.4.5, which is about 3.21, whereas for Lissajous close to the vertical Lyapunov this ratio decreases under 1. For the classical Sun-Earth and Earth-Moon systems, y is maintained because is usually greater than x. For the Mars-Phobos system, due to the proximity of the moon, in this analysis it is better to consider instead x, thus using $y(x)$.

The approach taken is to decouple Fig.4.19, plotting the 1D relation for every output-input combination, as shown in Fig.4.20. However the task could be maintained in 2D, using the data from Fig.4.19 and interpolating with a scattered triangular algorithm. The map $[x, z](\alpha, \beta)$ is invertible inside the region of convergence, while outside of it the results of the interpolation is not valid. In particular, the smooth behavior within this region of Fig.4.19, means that it is also possible to approximate the functions with an elliptic cone $x(\alpha, \beta) = (a^2\alpha^2 + b^2\beta^2)^{1/2}$ and two inclined planes $y(\alpha, \beta) = k\alpha$, $z(\alpha, \beta) = c\beta$. The inverse functions are a hyperbolic saddle $\alpha(x, z) = (c^2x^2 - b^2z^2)^{1/2}/ac$ and two inclined planes $\beta(x, z) = z/c$, $\alpha(y, z) = y/k$. This is coherent with the behavior of the inner isolines obtained with the interpolation algorithm in Fig.4.21.

Eventually, the map $[x, y, z](\alpha, \beta)$ can be graphically inverted, which is to simply fill the 3D components space with the points sampled from Fig.4.19. The 2D region of convergence is one slice of a hyperbolic saddle in the 3D space of the max x-y-z components of the LPO. Onto this surface's domain, the 3D×2D numerical interpolation is carried out, to find the isolines of α-β. This is visualized in Fig.4.22: by picking a physical point in these two graphs, one defines the α-β values such that the lp series expansion produces a Lissajous orbit with maximum components that correspond to the coordinates of the chosen point.

Station-keeping consumption. The last important engineering implementation of the LPOs derived with the lp technique is to probe the feasibility of their unstable dynamics in terms of the station-keeping demand, required to control the spacecraft to track their path over a long period. This acts as an additional proof of the quality of the series expansion. This cost accounts for the cumulated perturbation of the residual nonlinear terms of the CR3BP, which are the ones over the order used in the lp series expansion. Thus, in addition to Fig.2.13, they constitute an additional modeling perturbation, like the eccentricity, due to the guidance law, that spills over on the control system when this is used to track such a reference signal.

Differently from the eccentricity, the modeling perturbation of the higher order nonlinear terms of the CR3BP is not derived analytically, because it would require to explicitly compute the series expansion of the model and the solution. Their perturbation, encountered along the reference LPO, can be retrieved numerically by designing a controller, and evaluating its acceleration profile. Therefore, a continuous feedback control action is considered in order to perfectly reject the nonlinear perturbations on the tracking signal. This is coherent with the analysis of the perturbations in section

2.4. In reality, impulsive control systems are the frequent choice for orbital station-keeping[9]. The control performance is summarized by the maximum tracking error, while the control consumption is given by the maximum thrust/acceleration level, and by the Δv required by the propulsion system, which is the integral of the control acceleration profile.

To derive the exact value of the perturbation of the nonlinear terms, the control action must reject it perfectly, in order to give us indirectly their measure. This is the characteristic of an optimal control algorithm to design the control law. Appendix C provides an overview of feedback optimal control theory, presenting the State-Dependent Riccati Equation (SDRE) methodology used for the case of nonlinear systems. The SDRE technique is chosen to fulfill the task to design an optimal control law that perfectly rejects the perturbation of the higher order nonlinear terms spilled over by the lp guidance law.

The state-space model of Eq.C.16 is used to design an SDRE-based control system through the procedure of Eq.C.7 to track the Lissajous and Lyapunov orbits computed by the lp algorithm. This requires an appropriate tuning of the weighting matrices and the additional weighting parameters, to obtain an optimal solution in terms of low control action[10] and state error. The simulations are carried out with a RKF78 propagator. In particular, the introduction of the control raises the stiffness of the dynamics, and a sensitivity analysis has been carried out regarding the choice of the relative tolerance of the integrator in Fig.4.23. Convergence is reached for values starting at 10^{-19}: however 10^{-18} is used for the extensive simulations session, because the computational time is still acceptable (for 1 orbital period, which is 2 longitudinal laps of the Lissajous orbits, the time required is less than $4s$), whereas with stricter tolerances a huge increase of the computational time is needed (10^{-19} requires $90s$, 10^{-20} requires $6h$, 10^{-22} requires more than $10h$). Thus, from Fig.4.23, the costs obtained with these simulations should be less than 10% cheaper than the real-life continuous case.

Fig.4.24 shows the outcomes for one simulation of the SDRE-based control system for one test case tracked Lissajous (L_1, $N = 35$, null initial phases, $\alpha = 0.05, \beta = 0.10$ which is at the center of the practical region of convergence) computed with the lp algorithm, with the SDC formulation parameters $\alpha = 1, \eta = 0$ (which means that the simplest uncoupled pseudo-linear formulation is used for the dynamics) and the SDRE weights: $Q_r = 10^{12}, Q_v = 10^6, R = 10^8$. One sees that the values of maximum thrust, position error and Δv are definitely very low.

The procedure is extended for all the L_1 Lissajous orbits of the $N = 35$ practical region of convergence, at the threshold level of $10m$ after half orbital period. An ac-

[9]Impulsive control has generally worse performances of the ones of a continuous implementation, apart from an ad-hoc choice of the frequency of the maneuvers, where the impulsive control outperforms the ones of the continuous control in terms of consumption, while in terms of tracking error the continuous implementation is always superior.

[10]A classical interplanetary spacecraft mass of $100kg$ is used as reference for the definition of the thrust profile.

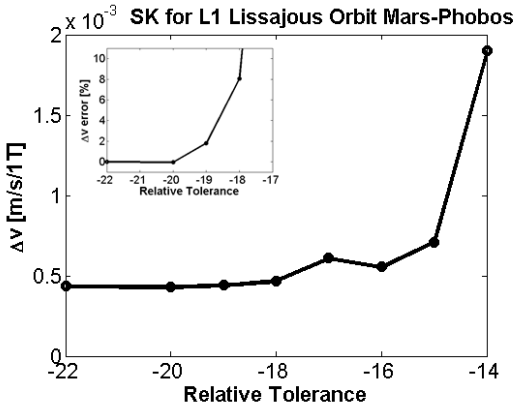

Figure 4.23: **SDRE-based station-keeping of lp tracking for L_1 Lissajous orbits.** Dependence of the Δv output from the relative tolerance (in logarithmic scale): magnification of the low tolerance cases with the percentage error from the case at minimum tolerance. Test over one longitudinal revolution of the Lissajous with $\alpha = 0.05, \beta = 0.10$ with $N = 35$. SDRE weights: $Q_r = 10^{12}, Q_v = 10^6, R = 10^8$. SDC parameters: $\alpha = 1, \eta = 0$.

curate tuning for each of these orbits is not conducted, since the focus is to derive the first-order figure of the station-keeping performances. Therefore, the same constant weights and parameters are kept all along the cases tested. The outcomes with the set of $\alpha = 1, \eta = 0$ and $Q_r = 10^{12}, Q_v = 10^6, R = 10^{9.5}$ are presented in Fig.4.25. However, a more optimal solution, shown in Fig.4.26-4.27, is obtained with the set of $\alpha = 0.25, \beta = 2.5, \eta = 0.5$ and $Q_r = 10^{12}, Q_v = 10^6, R = 10^{4.74}$. The cost of Δv is decreased considering an unbalanced weight of all the possible pseudo-linear forms of the nonlinear dynamics. The amount saved is about the 10%, which proves the efficiency of using additional DOFs for the control design, which is indeed the main advantage provided by the SDRE technique.

The performance obtained by the SDRE is compared with the one of a basic LQR based on the linearized dynamics around the EP, as a trade-off of the control cost with its simplicity. Fig.4.28 presents the outcomes obtained, which has resulted to be not particularly different from the uncoupled SDC case of SDRE-based control of Fig.4.25.

It emerged that there is an important dependence of the performance from the tracking time step used to evaluate the lp series expansion to provide the sampled guidance law. Fig.4.29-4.30 show that the Δv cost could be considerably decreased with a higher tracking frequency, which highlights again the goodness of the algorithm inside the region of convergence. Out of it, the demand for the control system design to follow a not natural tracking signal becomes expensive.

In summary, in this section the modern SDRE-based control has been applied in the CR3BP. Regarding the initial aim, this was to quantify the orbital perturbation due to the modeled tracking signal. This is provided by the plots of the maximum thrust required, which has resulted to be quite dependent from, and decreasing with, the tracking time step. Considering a frequency of 1,000 samples per Lissajous orbit, which is a time step of about $13.8s$, the control action is of the order of magnitude of

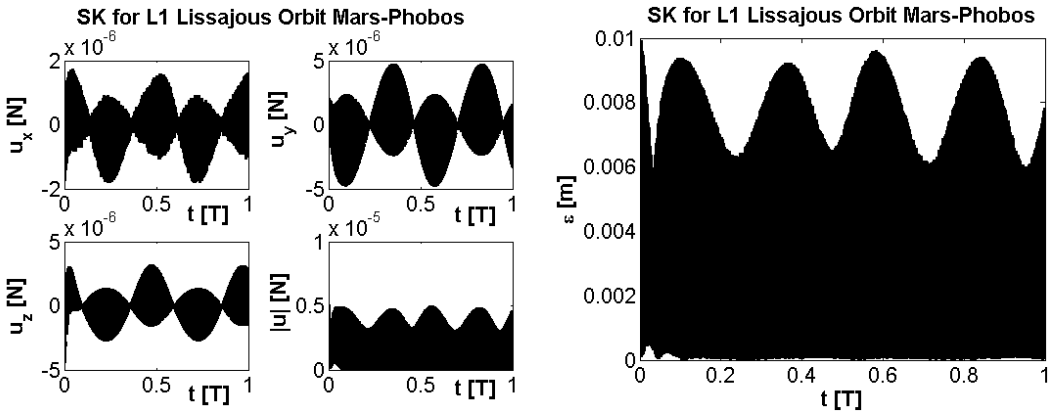

Figure 4.24: **SDRE-based station-keeping of lp tracking for L_1 Lissajous orbits.** On the right, control action required, and on the left, position error from the tracking signal. These outcomes have been obtained with a simulation at the tight tolerance of 10^{-20}. Test over one orbital period of the Lissajous with $\alpha = 0.05, \beta = 0.10$ with $N = 35$, tracked with a frequency of 1,000 samples per Lissajous orbit (resulting time step of about 13.8s). SDRE weights: $Q_r = 10^{12}, Q_v = 10^6, R = 10^8$. SDC parameters: $\alpha = 1, \eta = 0$.

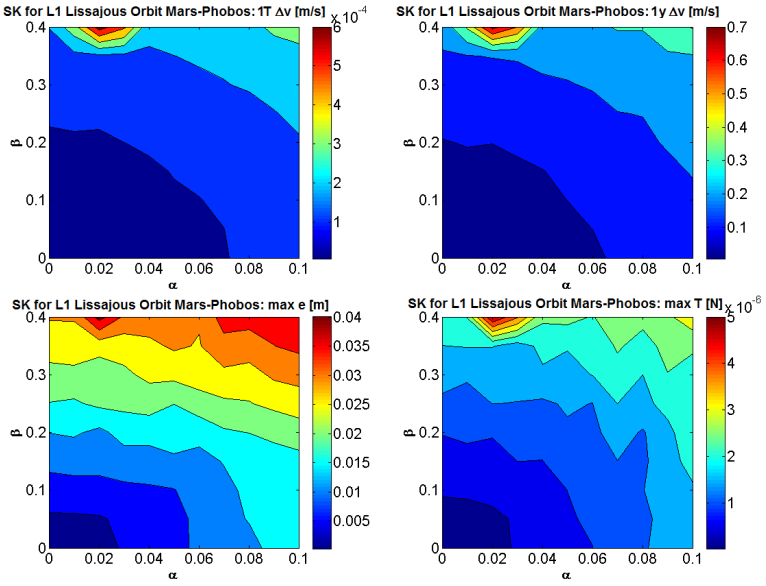

Figure 4.25: **SDRE-based station-keeping of lp tracking for L_1 Lissajous orbits.** Performances of the SDRE-based control system: Δv over one orbital period and one terrestrial year, maximum position error from target and maximum thrust required. Simulation at tolerance of 10^{-18}, over one period of the Lissajous orbits with $N = 35$ and tracked with a frequency of 1,000 samples per Lissajous orbit (resulting time step of about 13.8s). SDRE weights: $Q_r = 10^{12}, Q_v = 10^6, R = 10^{9.5}$. SDC parameters: $\alpha = 1, \eta = 0$.

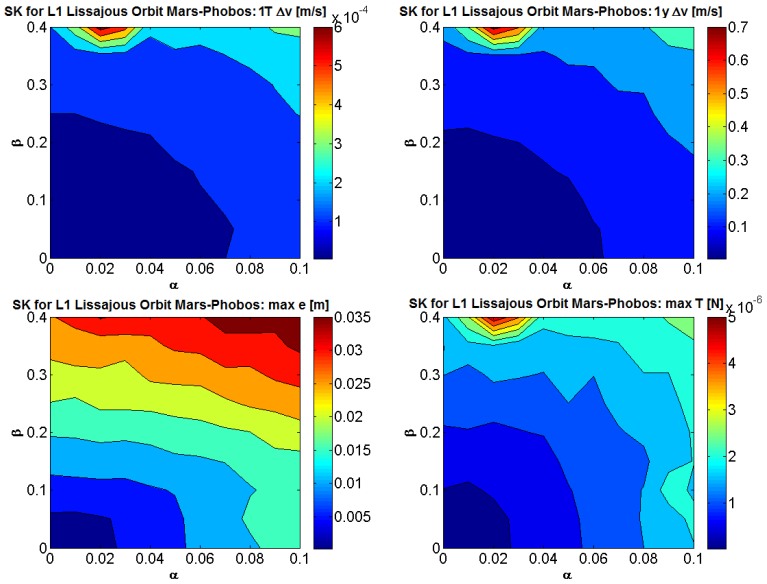

Figure 4.26: **SDRE-based station-keeping of lp tracking for L_1 Lissajous orbits.** Performances of the SDRE-based control system: Δv over one orbital period and one terrestrial year, maximum position error from target and maximum thrust required. Simulation at tolerance of 10^{-18}, over one period of the Lissajous orbits with $N = 35$ and tracked with a frequency of 1,000 samples per Lissajous orbit (resulting time step of about 13.8s). SDRE weights: $Q_r = 10^{12}, Q_v = 10^6, R = 10^{4.74}$. SDC parameters: $\alpha = 0.25, \beta = 2.5, \eta = 0.5$.

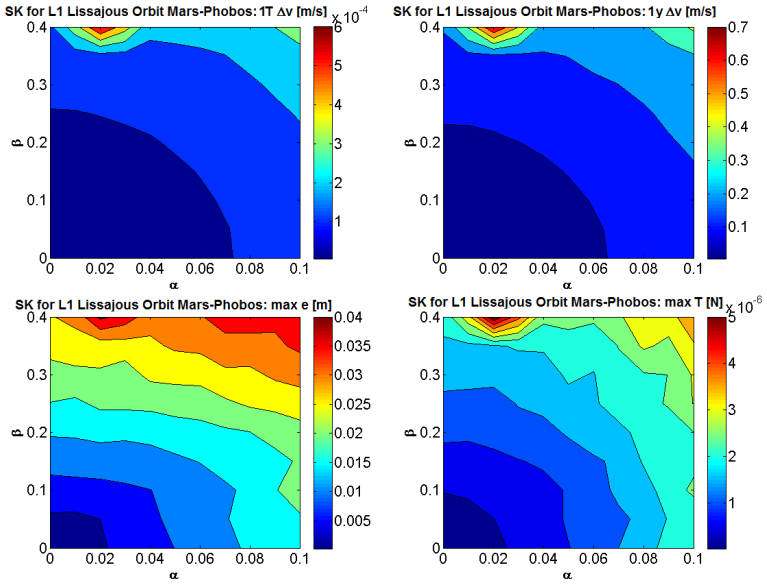

Figure 4.27: **SDRE-based station-keeping of lp tracking for L_1 Lissajous orbits.** Performances of the SDRE-based control system: Δv over one orbital period and one terrestrial year, maximum position error from target and maximum thrust required. Simulation at tolerance of 10^{-18}, over 10 periods of the Lissajous orbits with $N = 35$ and tracked with a frequency of 1,000 samples per Lissajous orbit (resulting time step of about 13.8s). SDRE weights: $Q_r = 10^{12}, Q_v = 10^6, R = 10^{4.74}$. SDC parameters: $\alpha = 0.25, \beta = 2.5, \eta = 0.5$.

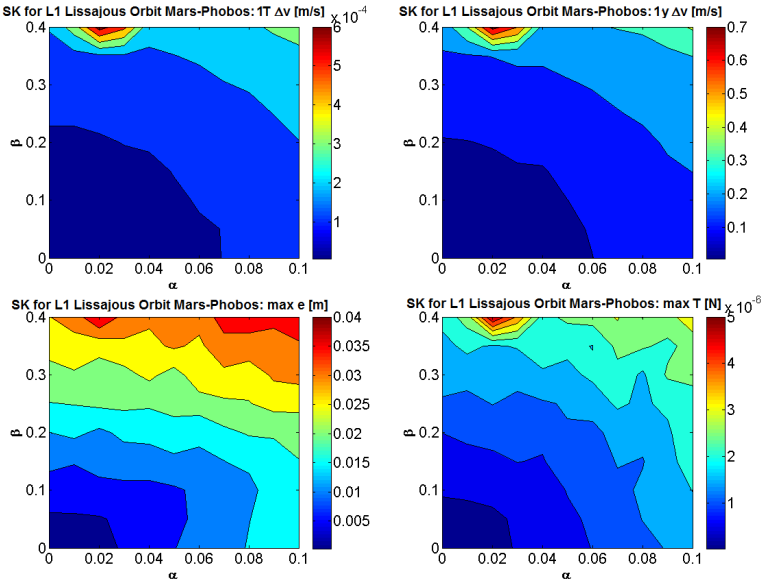

Figure 4.28: **LQR station-keeping of lp tracking for L_1 Lissajous orbits.** Performances of the LQR: Δv over one orbital period and one terrestrial year, maximum position error from target and maximum thrust required. Simulation at tolerance of 10^{-18}, over one period of the Lissajous orbits with $N = 35$ and tracked with a frequency of 1,000 samples per Lissajous orbit (resulting time step of about 13.8s). LQR weights: $Q_r = 10^{12}, Q_v = 10^6, R = 10^{9.5}$.

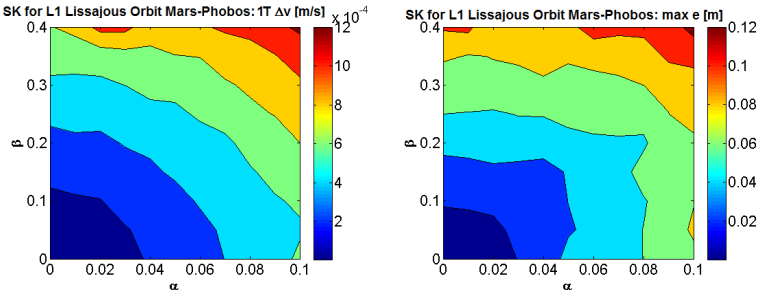

Figure 4.29: **SDRE-based station-keeping of lp tracking for L_1 Lissajous orbits.** Performances of the SDRE-based control system: Δv over one orbital period, maximum position error from target. Simulation at tolerance of 10^{-18}, over one period of the Lissajous orbits with $N = 35$ and tracked with a frequency of 500 samples per Lissajous orbit (resulting time step of about 27.6s). SDRE weights: $Q_r = 10^{12}, Q_v = 10^6, R = 10^{9.5}$. SDC parameters: $\alpha = 1, \eta = 0$.

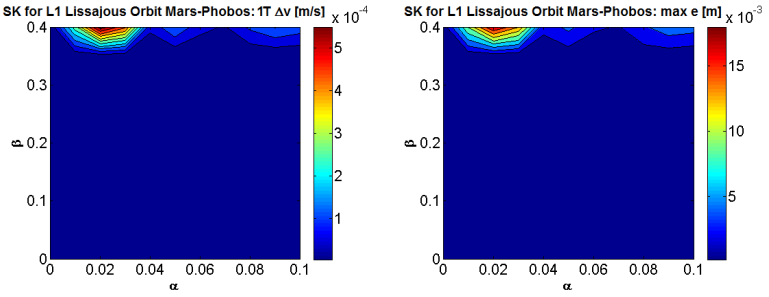

Figure 4.30: **SDRE-based station-keeping of lp tracking for L_1 Lissajous orbits.** Performances of the SDRE-based control system: Δv over one orbital period, maximum position error from target. Simulation at tolerance of 10^{-18}, over one period of the Lissajous orbits with $N = 35$ and tracked with a frequency of 10,000 samples per Lissajous orbit (resulting time step of about 1.4s). SDRE weights: $Q_r = 10^{12}, Q_v = 10^6, R = 10^{9.5}$. SDC parameters: $\alpha = 1, \eta = 0$.

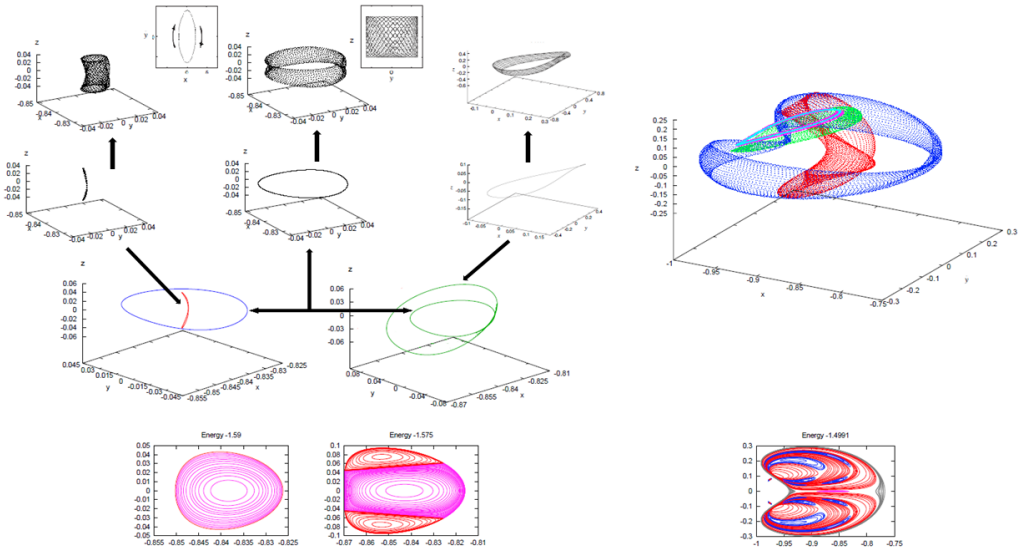

Figure 4.31: **Invariant tori in the center manifold of the collinear LPs of the CR3BP.** This picture shows the evolution of the center manifold's orbit structure as far as the energy increases from the one of the lp. The main families of POs are: vertical Lyapunov orbit, planar Lyapunov orbit and Halo orbit (here the Northern one). From each of them, additional 2D-QPOs originate: Lissajous orbits from the Lyapunov orbits, quasi-Halo orbits from the Halo orbits. On the bottom, the iso-energetic Poincaré map taken from the section at $z = 0, \dot{z} >= 0$ is shown. For higher energies, the number of bifurcations increases and the structure becomes quite complex [52].

$1\mu N$ in all the practical region of convergence of the higher order lp expansion. This is about $0.01\mu m/s^2$, 10^{-5} times the Phobos gravity at the collinear LP. Therefore, if compared with the other orbital perturbations presented in Fig.2.13, this amount is definitely lower[11] and the orbits computed with the high-order lp algorithm are accurate for practical exploitation in a continuous orbital controller. This would require a Δv for their station-keeping of only $77\mu m/s$ per orbital period, which is $8.8cm/s$ per terrestrial year. This is absolutely negligible with respect to the orbital perturbation of the gravity harmonics and orbital eccentricity of Phobos, that are required to be included in the model to derive the appropriate guidance law of the LPOs. This will be undertaken in sections 4.2-4.3.

4.1.4 The Halo orbits of the Mars-Phobos CR3BP

The Lyapunov orbits are organized in two 1-parameter families at increasing size and energy from the LPs. As their energy increases, they encounter bifurcations. The first bifurcation of the planar Lyapunov family is characterized by the 1:1 resonance of the natural frequencies (see Fig.4.9). This gives birth to two symmetrical branches (with respect to the x-y plane) of POs: they are the Northern and Southern Halo orbits

[11] The amount is of the same order of magnitude of the radiation pressures.

[50, 52]. They have been discovered by Farquhar [71], who gave them this name due to the shape of these orbits which, in the Sun-Earth system, encircle the Earth along the Sun's conjunction line. The Halo orbits are actually similar to a large Lyapunov orbit pitched along the y-axis, and softly bent in the x-z projection. However, they are no longer symmetric with respect to the orbital plane, and the sign of the max z-dimension identifies the two branches. Halo orbits have attracted the interest of space agencies for several mission applications [50].

In addition to the Halo orbits, additional bifurcations appear. The second bifurcation of the planar orbits gives birth to the two symmetrical branches (with respect to the x-axis) of the axial orbits that represent a two-lane bridge to the first bifurcation of the vertical orbits [52]. Further bifurcations provide multiplication of the orbits' period [52], and at higher energies, the structure of the possible motions becomes more complex, see Fig.4.31.

Due to the proximity of Phobos, the bifurcations of its LPOs are placed after their intersection with Phobos. The only bifurcated orbits that still exist are the Halo orbits. As we see in Fig.4.9, the ancestor planar Lyapunov is placed just ahead of the boundary of the practical region of convergence for the small-width Lissajous orbits. In this section, the computation of the Halo orbits of the Mars-Phobos CR3BP is carried out.

4.1.4.1 Computation of Halo orbits with the Lindstedt-Poincaré method

The linear solution of the ancestor planar Lyapunov orbit of the Halo family is given by locking the two natural frequencies,

$$\tilde{\mathbf{q}}_{PO}(t) = \begin{bmatrix} \tilde{x} = -\alpha \cos\left(\omega_P t + \varphi_P\right) \\ \tilde{y} = K\alpha \sin\left(\omega_P t + \varphi_P\right) \\ \tilde{z} = \beta \cos\left(\omega_P t + \varphi_V\right) \end{bmatrix} \quad , \quad \begin{cases} \alpha(\beta) \\ \varphi_V - \varphi_P = \pm\frac{\pi}{2} \end{cases} \tag{4.19}$$

which results in a constraint between the planar and vertical amplitudes to ensure that this is a 1-parameter family, and a formal relation between the two phases to ensure that this is a 1-torus. However this linear solution, which is a 1:1 resonant linear 2-torus, is isolated in the linearized CR3BP around the LP of Eq.4.3. Since the bifurcation is a nonlinear phenomena, the Halo orbits cannot be linearized, in the sense that they are not a solution of the linearized dynamics.

The Halo orbits can only be computed with higher order approximations of the dynamics, which is using the Lindstedt-Poincaré technique. The main procedure is the same showed in section 4.1.3.1 for the computation of Lyapunov orbits, but with some important modifications. The Halo orbits are the result of the combination of both center manifolds, with equal natural frequencies. Thus, to ensure that the lp technique computes 3D POs of both eigenfunctions, a constraint is needed to express the frequency locking. Due to the uncoupling of the planar and vertical dynamics in the order-1 dynamics, the vertical component of the nonlinear vectorfield is rearranged,

to force the natural vertical frequency (at first order) to be equal to the planar.

$$\begin{aligned} &\ddot{\tilde{z}} = \frac{1}{{\gamma_i}^3} u_{/\tilde{z}} = \sum_{n=1}^{N} \bar{c}_n \|\mathbf{r}\|^{n-2} \mathbf{B}_{n,z}(\mathbf{r}) = -\bar{c}_2 \tilde{z} + \sum_{n=3}^{N} \bar{c}_n \|\mathbf{r}\|^{n-2} \mathbf{B}_{n,z}(\mathbf{r}) \\ &\Rightarrow \ddot{\tilde{z}} + \omega_P^2 \tilde{z} = \Delta \tilde{z} + \sum_{n=3}^{N} \bar{c}_n \|\mathbf{r}\|^{n-2} \mathbf{B}_{n,z}(\mathbf{r}) \end{aligned} \tag{4.20}$$

This results in the introduction of a correction term Δ, and the related constraint is added as an additional power series that must be satisfied by the nonlinear terms of the dynamics. This constraint implicitly represents the constraint $\alpha(\beta)$ of Eq.4.19, while maintaining the series expansion of the solution in terms of the amplitudes of the two eigenspaces. In particular, the parameter of the family of Halo orbits is usually taken as β, since it is related to the vertical size. The coefficients of the lp expansion of the orbit are now characterized by 3 indexes.

$$\begin{cases} \tilde{\mathbf{q}}_{PO}(t) = \begin{bmatrix} \tilde{x}(t) \\ \tilde{y}(t) \\ \tilde{z}(t) \end{bmatrix} = \sum_{i+j=1}^{N} \alpha^i \beta^j \sum_{|k|=0}^{i+j} \begin{bmatrix} a_{ijk} \cos(k\omega t + k\varphi) \\ b_{ijk} \sin(k\omega t + k\varphi) \\ c_{ijk} \cos(k\omega t + k\varphi \pm \pi/2) \end{bmatrix} \\ \begin{cases} \omega = \sum_{i+j=0}^{N} \alpha^i \beta^j \omega_{ij} \\ \Delta = \omega_P^2 - \omega_V^2 = \sum_{i+j=0}^{N} \alpha^i \beta^j \Delta_{ij} = \sum_{i+j=3}^{N} \alpha^i \beta^j \Delta_{ij} + \Delta_2 \\ \Rightarrow l_1 \alpha^2 + l_2 \beta^2 + \Delta_2 + \sum_{i+j=4}^{N} \alpha^i \beta^j \Delta_{ij} = 0 \end{cases} \end{cases} \tag{4.21}$$

Due to the symmetries, the Halo orbits do not appear even at order-2, but originate at order-3. The related lowest order lp series expansion is called the Richardson's solution [114]. The related α-β relationship is defined below, where the values of the variables are taken from the Richardson's solution with the μ of interest.

$$l_1 \alpha^2 + l_2 \beta^2 + \Delta_2 = 0 \Rightarrow \beta_{\min} = 0 \leftrightarrow \alpha_{\min} = \sqrt[2]{-\frac{\Delta_2}{l_1}} \tag{4.22}$$

This allows one to analytically derive the location of the ancestor Lyapunov orbit. For the Mars-Phobos system case, the bifurcation corresponds to the normalized planar amplitude of $\alpha = 0.1372$ for L_1 and $\alpha = 0.1381$ for L_2, in accordance with Fig.4.9 and the related Lissajous expansion. This means that the minimum altitude of the smallest Halo orbits is at just $1.2km$ from the Phobos' surface. The amplitudes' constraint is graphically presented in Fig.4.32.

Regarding the region of convergence, the previous application of the lp algorithm on Lissajous and Lyapunov orbits of the Mars-Phobos system provided boundaries in nor-

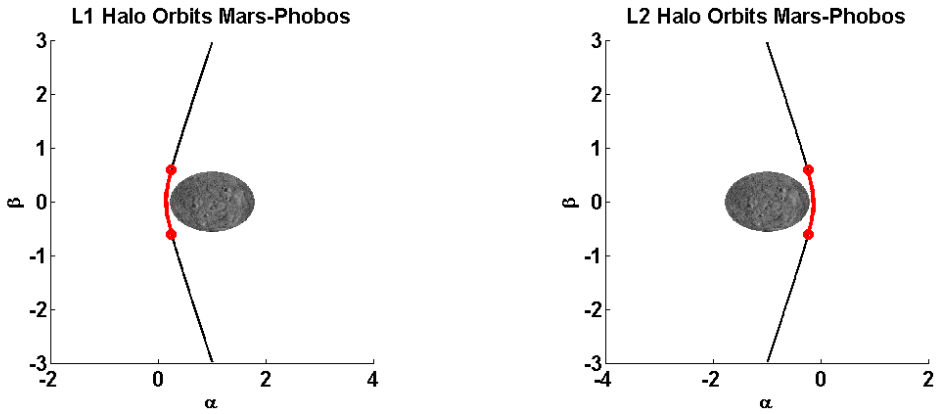

Figure 4.32: **Halo orbits around Phobos in the CR3BP.** $\alpha-\beta$ relationship for the Richardson expansions for computing Halo orbits around L_1 and L_2. Red lines indicates the theoretical practical region of convergence (fixed propagation time π, position magnitude error threshold 10^{-6} adimensional units) of the lp algorithm for order 35, assuming a normalized correspondence with the boundaries of the practical region of convergence of the Sun-Earth system. Phobos mean ellipsoidal surface.

malized units basically similar to the ones of the classical Sun-Earth system (roughly $\beta = 0.6$ [116], for the case of fixed propagation time π, at the position magnitude error threshold of 10^{-6} adimensional units). Hence, it is reasonable to imply that the same would happen for the Halo orbits too, therefore Fig.4.32 highlights also the supposed practical region of convergence of a lp series expansion up to the maximum order available from the Barcelona group. Note that, for the aforemention coupled of thresholds, the Richardson's boundary does not even exist, as we imply from Fig.4.4-4.5, where the boundary for order 5 does not reach the location of the ancestor Lyapunov orbit of the Halo families.

The increased proximity of the Halo orbits to Phobos does not motivate the use of a high-order semi-analytical expansion, due to the strong perturbation of the inhomogeneous gravity field of the moon. Thus, the Halo orbits around Phobos, in the CR3BP, will be computed in section 4.1.4.3 with a numerical technique.

4.1.4.2 Computation of Halo orbits with Differential Corrector

To obtain the Halo orbits for their preliminary analysis in the CR3BP, without deriving high precision expansions for them, a DC procedure is applied to the initial guess of the Richardson solution to consider the full nonlinear dynamics of the CR3BP.

The procedure to derive POs with DC has been presented in section B.5.3.2. Thus, with the vectorfield of the CR3BP of Eq.2.13 and the aforementioned initial guess, the single shooting DC scheme of Eq.B.75 is suitable to be included in a NC to provide the whole family of Northern and Southern Halo orbits. However, due to the symmetries of the CR3BP, the DC scheme could be wisely reduced in complexity. Thus, the Poincaré section is not the same for domain and codomain, and the objective function should expresses the symmetry condition of the state after half period, and not the

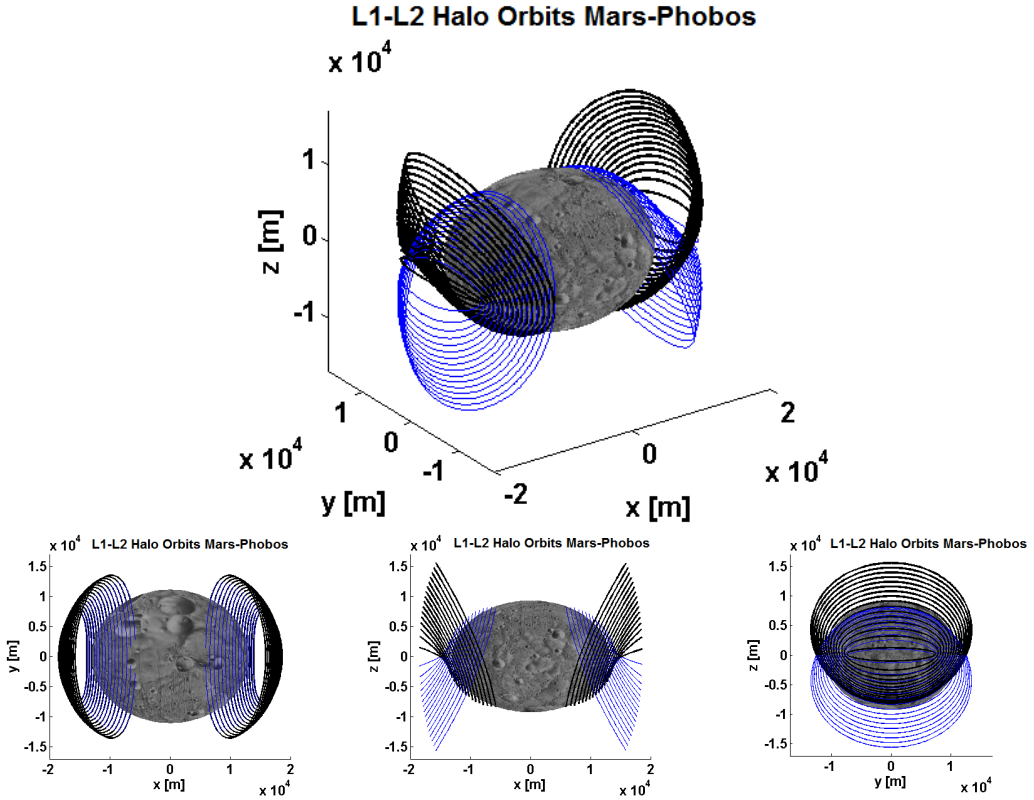

Figure 4.33: **Halo orbits around Phobos in the CR3BP.** Examples of some Northern (black) and Southern (blue) Halo orbits around L_1 and L_2, computed after a single shooting DC from the Richardson expansion, up to the first orbit that intersects the moon's mean ellipsoidal surface.

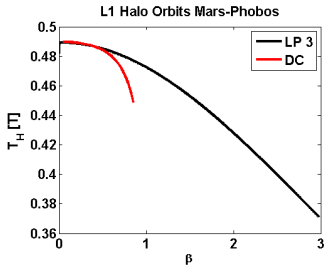

Figure 4.34: **Halo orbits around L_1 of Phobos in the CR3BP.** Characteristic curve of the period of the Halo orbits (as number of the CR3BP orbital periods), for the original Richardson expansion and after the DC.

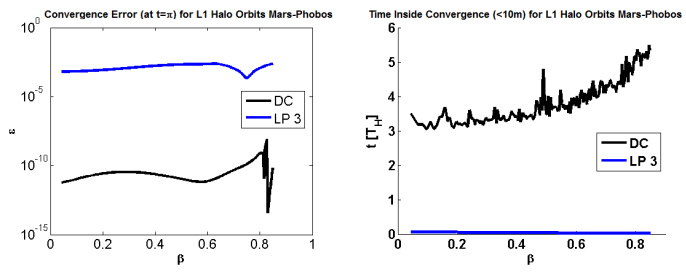

Figure 4.35: **Halo orbits around L_1 of Phobos in the CR3BP.** Region of convergence of the Richardson expansion and after the DC: position magnitude error (in adimensional units) after a fixed propagation time ($t = \pi$), and time of permanence (as number of Halo orbits) within a fixed position magnitude error (10^{-6} adimensional units).

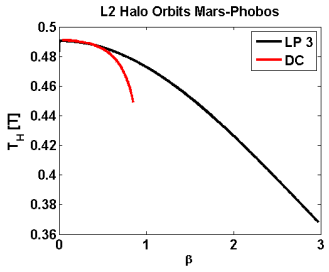

Figure 4.36: **Halo orbits around L_2 of Phobos in the CR3BP.** Characteristic curve of the period of the Halo orbits (as number of the CR3BP orbital periods), for the original Richardson expansion and after the DC.

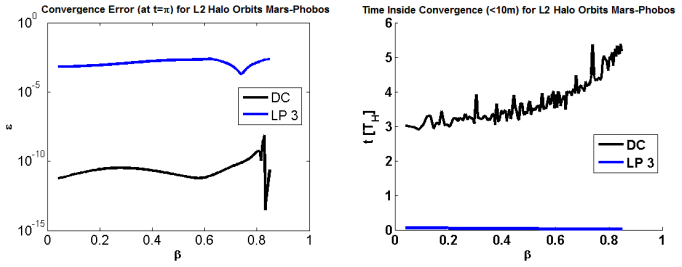

Figure 4.37: **Halo orbits around L_2 of Phobos in the CR3BP.** Region of convergence of the Richardson expansion and after the DC: position magnitude error (in adimensional units) after a fixed propagation time ($t = \pi$), and time of permanence (as number of Halo orbits) within a fixed position magnitude error (10^{-6} adimensional units).

invariant point's condition of Eq.B.64. This reduction is actually necessary, because the Richardson's solution is not an accurate initial guess: the propagation of its initial condition does not revolve around the LP but quickly diverges, so the DC will not converge if used for the whole period.

This DC scheme for Halo orbits is the same used in [72]. The initial and final surface of section to ensure symmetry is the x-z plane, $g(\mathbf{x}) = y$, with $\dot{y}$ of different sign for domain and codomain. The single shooting scheme is based on the objective function $F(x, \dot{y}) = [\dot{x}; \dot{z}]$, and is presented in Eq.4.23. Thus, the initial condition on z is maintained to be used as parameter of the NC. The byproduct of the DC step will be the half period of the Halo orbit, and the square root of its monodromy matrix.

$$\begin{cases} F(q_0, t_f) = \begin{bmatrix} \dot{x}_f \\ \dot{z}_f \end{bmatrix} = 0 \\ t_f > 0 : y_f = y(q_0, t_f) = 0 \Rightarrow \delta y_f = \begin{bmatrix} \Phi_{2,1} & \Phi_{2,5} \end{bmatrix}_{t_f, q_0} \begin{bmatrix} \delta x_0 \\ \delta \dot{y}_0 \end{bmatrix} + \dot{y}_f \delta t_f = 0 \\ \Rightarrow \delta t_f = -\dfrac{1}{\dot{y}_f} \begin{bmatrix} \Phi_{2,1} & \Phi_{2,5} \end{bmatrix}_{t_f, q_0} \begin{bmatrix} \delta x_0 \\ \delta \dot{y}_0 \end{bmatrix} \\ \delta F = \begin{bmatrix} \Phi_{4,1} & \Phi_{4,5} \\ \Phi_{6,1} & \Phi_{6,5} \end{bmatrix}_{t_f, q_0} \begin{bmatrix} \delta x_0 \\ \delta \dot{y}_0 \end{bmatrix} + \begin{bmatrix} \ddot{x}_f \\ \ddot{z}_f \end{bmatrix} \delta t_f = \\ \quad = \begin{bmatrix} \Phi_{4,1} - \frac{\ddot{x}}{\dot{y}} \Phi_{2,1} & \Phi_{4,5} - \frac{\ddot{x}}{\dot{y}} \Phi_{2,5} \\ \Phi_{6,1} - \frac{\ddot{z}}{\dot{y}} \Phi_{2,1} & \Phi_{6,5} - \frac{\ddot{z}}{\dot{y}} \Phi_{2,5} \end{bmatrix}_{t_f, q_0} \begin{bmatrix} \delta x_0 \\ \delta \dot{y}_0 \end{bmatrix} = \\ \quad = F'(q_0, t_f) \begin{bmatrix} \delta x_0 \\ \delta \dot{y}_0 \end{bmatrix} \end{cases} \tag{4.23}$$

4.1.4.3 The Halo orbits of the Mars-Phobos CR3BP

The DC of Eq.4.23, with initial guess provided by the Richardson expansion, for the case of the Mars-Phobos system, has resulted to converge up to a value of β around 0.85 for both L_1 and L_2, which is higher than the boundary of the practical region of convergence even for the maximum order 35 of the method currently available. In particular, this is already enough in our specific case, since smaller Halo orbits start to

intersect Phobos' surface: the Northern orbits intersect the Southern Hemisphere, the Southern orbits intersect the Northern Hemisphere. This happens at β 0.7682 for L_1 and 0.7687 for L_2, see Fig.4.33. Fig.4.34-4.36 show the evolution of the Halo orbits' period. The difference between the Richardson and DC outcomes is very clear.

As a difference from the semi-analytical methodology, the solution of the DC is defined in the full dynamics, and its reliability is only computational. Fig.4.35-4.37 show the convergence of the DC solution with respect to the nonlinear simulation of the CR3BP. After a fixed propagation time of π, the position error is correctly driven by the machine error. For a fixed position error of 10^{-6} adimensional units, the time of permanence is more than three revolutions, and in particular the evolution is opposite with respect to the Lissajous and Lyapunov orbits' behavior of Fig.4.11, since the time of permanence increases with the size of the Halo orbit. This is an indication coherent to the fact, as explained in [72], that for sufficiently low mass parameters, large Halo orbits around the collinear LPs could be marginally stable. The maximum Floquet stability index has resulted to decrease with β, but at the maximum β where the moon's intersection is achieved the value is still greater than 2, so no stable Halo orbits exist for the Mars-Phobos CR3BP.

4.1.5 IMs of the LPOs in the Mars-Phobos CR3BP

All the families of periodic and quasi-periodic LPOs of the Mars-Phobos system are unstable, since their Floquet stability analysis (see sections B.5.2.1-B.6.5) shows that the linearized manifolds around them are organized in a saddle $\times$ center $\times$ center structure[12]. As explained in section B.8, the presence of a saddle node implies that the LPOs are separatrices of motion: the related eigenspace contains the so-called IMs (or Conley-McGehee tubes [50, 73]), which are the trajectories that depart or approach the LPOs in an infinite time of flight. As discussed in section 4.1.1, this local behavior has paramount implications for the global orbit structure of the CR3BP. The IMs of a LPO, at the related energy, constitute the boundary of a tube in the state-space that separates the transit and non-transit trajectories to naturally enter or escape from the SOI of the second massive body. This analytical result of DST has proved invaluable to provide space mission designers with energy-efficient trajectories. They are used to minimize the fuel consumption of spacecraft for interplanetary transfer phases [50, 73], realizing prescribed itineraries throughout the Solar System RnBP by appropriately patching individual R3BPs.

The computation of the IMs' tubes has been presented for a general dynamical system in section B.8, and for each type of invariant motion, based on the dimension of its phase-space. Following this, this section presents the IMs of the periodic (Lyapunov and Halo) and quasi-periodic (Lissajous) LPOs, computed in sections 4.1.3-4.1.4, of the Mars-Phobos CR3BP. The results for all the families around both LPs are collected in

[12]The planar Lyapunov orbits, after the Halo's bifurcation, is characterized by a saddle $\times$ saddle $\times$ center manifold.

appendix D.1.

4.1.5.1 Computation of the IMs of the LPOs in the Mars-Phobos CR3BP

The unstable and stable IM of the families of POs and 2D-QPOs around Phobos has been computed with the techniques tailored for each invariant objected introduced in section B.8, for the orbits inside the respective practical region of convergence and that do not intersect Phobos. In particular, since the Lissajous orbits have been computed with a semi-analytical technique, the IMs are retained with the approach of the reduction of the 2D-QPO to a discrete dynamical system expressing the mapping of the longitudinal motion, as mentioned in section B.8.3.

The initial condition of the IMs requires the choice of an appropriate tolerance ε_W. For the CR3BP, in [117] an adimensional value of 10^{-6}, relative to the magnitude of the position's displacement, is suggested for high-precision applications, but for the Sun-Earth system also values up to 10^{-4} has resulted to be fairly accurate. Therefore, the IMs are computed in this section with a tolerance of 10^{-5}, that corresponds to about $100m$. Furthermore, every tube is made by two branches, with the outside branch exploited for transfers to and from farther mission phases, and the inside branch used for transfer within the SOI of the secondary body. Thus, since the main interest of this thesis is to model the orbital dynamics in the vicinity of Phobos, only the inside branch of the IMs is computed in this section.

Due to the collapse of the SOI, the inside branch of the unstable and stable IM of the LPOs has resulted to intersect Phobos. Thus, the globalization of the manifold is propagated in the CR3BP up to the intersection with Phobos' surface modeled with its mean ellipsoidal surface, that constitutes a kind of unusual Poincaré section's constraint. Eq.4.24 presents the expression for the radius and local normal (in the Phobos' BCBF frame) of a general ellipsoid, whose principal axes are coherent with Phobos' BCBF frame, as a function of the right ascension and declination in the BCBF frame.

$$\frac{x^2}{a^2}+\frac{y^2}{b^2}+\frac{z^2}{c^2}=1 \Rightarrow \begin{cases} r(\alpha,\delta)=1\Bigg/\sqrt[2]{\dfrac{\cos^2\alpha\cos^2\delta}{a^2}+\dfrac{\sin^2\alpha\cos^2\delta}{b^2}+\dfrac{\sin^2\delta}{c^2}}= \\ \qquad\qquad =b\Bigg/\sqrt[2]{1-\left(1-\dfrac{b^2}{a^2}\right)\cos^2\alpha\cos^2\delta-\left(1-\dfrac{b^2}{c^2}\right)\sin^2\delta} \\ \hat{\mathbf{n}}(\alpha,\delta)=\left[\begin{array}{ccc}\frac{x}{a^2} & \frac{y}{b^2} & \frac{z}{c^2}\end{array}\right]\Bigg/\sqrt[2]{\frac{x^2}{a^4}+\frac{y^2}{b^4}+\frac{z^2}{c^4}} \end{cases} \tag{4.24}$$

For an m-parameter family of invariant n-tori, the number of trajectories of the tube of IMs is organized in a (n+m)-dimensional matrix parameterized by the n phases and the m parameters. This will be the natural parametrization of the trajectories. To exploit the results in the mission design, the performances are reparameterized by the topographical map of the final condition, to represent the properties of the optimal trajectory available for each couple of angles of the spherical coordinates of the Phobos'

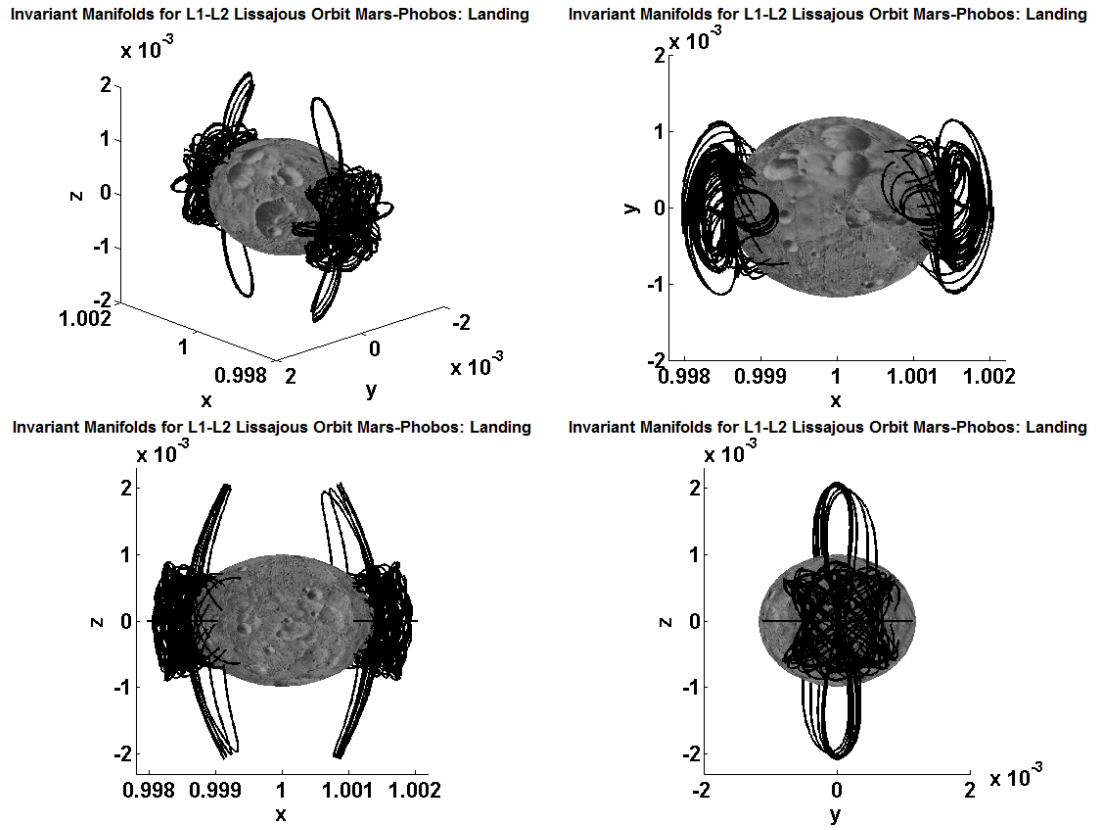

Figure 4.38: **Landing on Phobos through the Invariant Manifold of the lp L_{1-2} Lissajous orbits.** Trajectories of the inside branch of the IMs from the Lissajous and Lyapunov orbits inside the region of convergence at the max order method. Phobos mean ellipsoidal surface.

BCBF frame.

Unstable IMs. The globalization of the unstable IMs of the families of Lyapunov, Halo, and Lissajous orbits have directly intersected the mean ellipsoidal surface of Phobos for all these orbits, for both LPs. Thus, it is possible to organize the array of trajectories by the couple of longitude and latitude of the landing site, and to filter them by considering some of the most important performances at the touch-down. The outcomes considered are: the time of flight, and the properties of the final velocity, which are its total magnitude, its angle of incidence with the local horizon, and its vertical component. Since every couple of longitude and latitude can be reached by multiple trajectories, the results obtained will be further filtered by the case of minimum incidence, which is a tangential arrival.

Regarding the analysis of the results, Fig.4.40-4.44,D.1-D.4,D.5-D.8 are related respectively to the Lissajous, planar and vertical Lyapunov around L_1. Fig.D.9-D.10,D.11,D.12 are related respectively to the Lissajous, planar and vertical Lyapunov around L_2. Fig.D.13-D.16,D.16-D.17 are related respectively to the Northern and Southern Halo orbits around L_1, and Fig.D.18-D.19,D.19 are related respectively to the Northern and

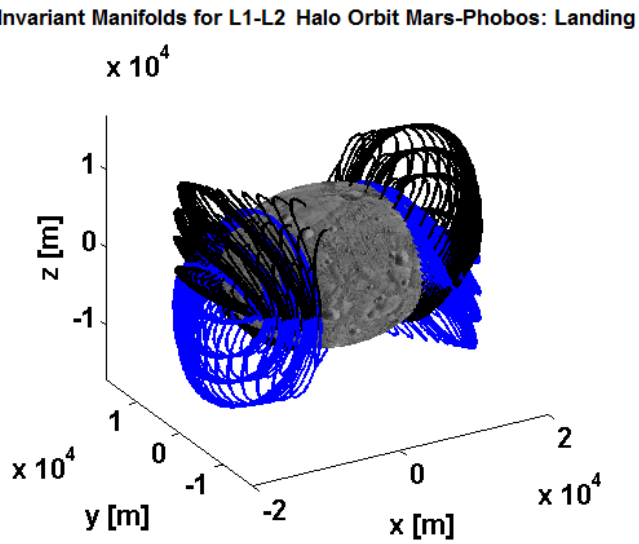

Figure 4.39: **Landing on Phobos through the Invariant Manifold of the L_{1-2} Halo orbits.** Trajectories of the inside branch of the IMs from the Northern and Southern Halo orbits computed after a DC of the Richardson expansions. Phobos mean ellipsoidal surface.

Southern Halo orbits around L_2.

Focusing on the Lissajous orbits, the global zone of possible natural landings on Phobos is a dedicated range of longitudes-latitudes centered on the LP manifold's intersection, which is slightly at East on the Equator. This zone then extends with a flat profile along the Equator for the planar Lyapunov orbits, whereas for the vertical Lyapunov orbits it has a C-like shape, extending to high latitudes, but also enabling landings at distant longitudes from the LP. Regarding the performance at the touch-down, the natural IMs enable tangential landings, with vertical velocities lower than $0.5m/s$ for high values of α-β Lissajous orbits and for a broad range of landing sites. The total magnitude of the velocity in the minimum incidence case ranges from $4 - 5.5m/s$. For the cases of large planar and vertical Lyapunov orbits, being the α or β null, performances are usually lower than the Lissajous cases. Finally, comparing the L_1-L_2 cases, outcomes are mainly identical.

Focusing on the Halo orbits, the IMs of the smallest orbits are the continuation of the ones of the widest planar Lyapunov, whose performances as mentioned above are poor. As long as β increases, the development in the out-of-plane component becomes predominant, and the performances of their IMs become very different from the Lyapunov and Lissajous orbits' families. The accessible region on Phobos from each Halo orbit has a C-shape, and the global region of landing sites spanned by an entire Halo family results to be wider than the one of the Lissajous family. In particular, higher longitudes and latitudes are reachable by the IMs of the Halo family, where tangential landings are enabled directly following the widest orbits. As a result, the total magnitude of the velocity for these landings is higher than using Lyapunov and Lissajous orbits. Due to the symmetry of the problem, performances of the Northern and Southern Halo are

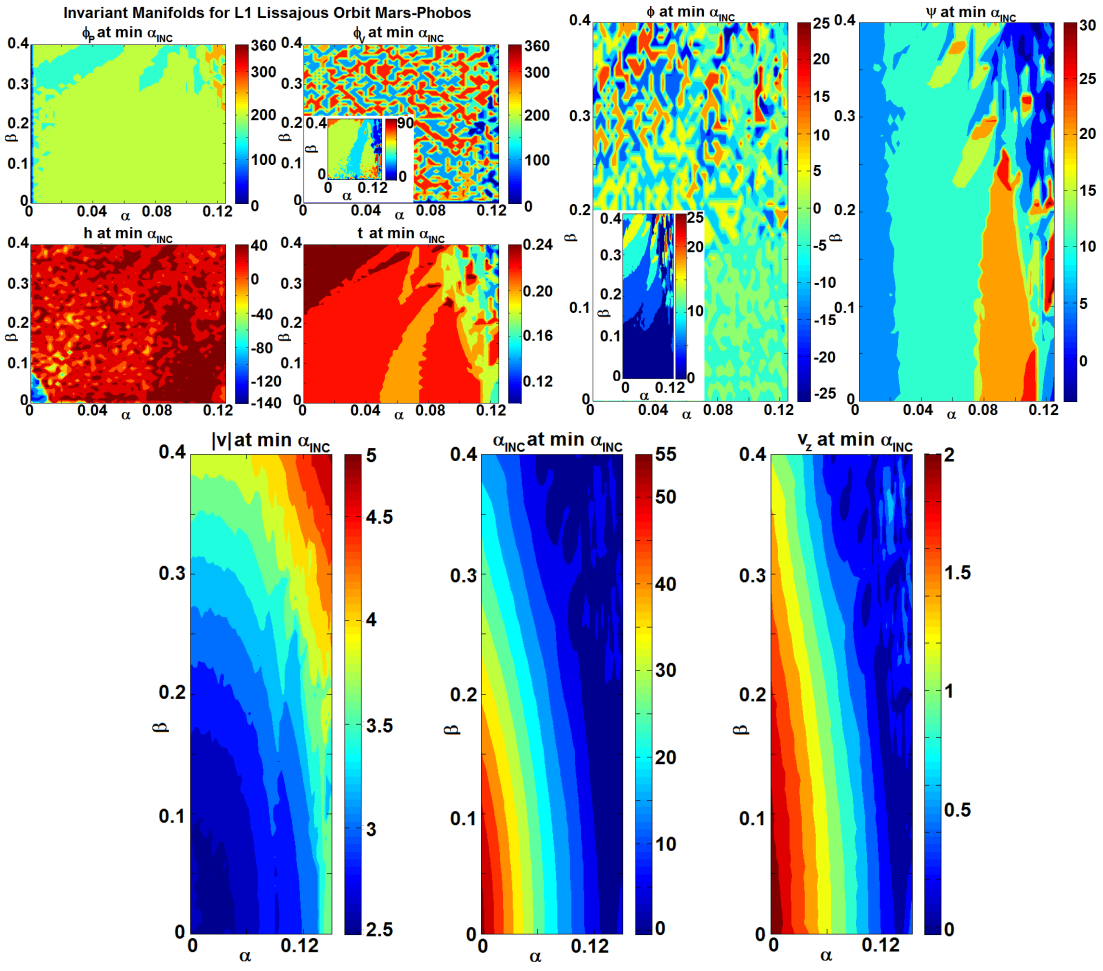

Figure 4.40: **Landing on Phobos through the Invariant Manifold of the lp L_1 Lissajous orbits.** Trajectories that provide the min incidence at the touch-down, as a function of the α and β input of the lp algorithm, for orbits inside the region of convergence at the max order method. Performances of the trajectory: initial planar and vertical phases (miniplot shows its absolute complement to 90/270°) along the departing Lissajous orbit, altitude where the integration is stopped, TOF, latitude (miniplot shows its absolute complement to 0°) and longitude of the landing site, and related velocity magnitude, angle of incidence, downward vertical velocity. Phobos mean ellipsoidal surface.

the same, with the landing sites flipped in latitude, and the trajectories in the L_1-L_2 sides are mainly identical.

Stable IMs. The globalization of the stable IMs of the families of Lyapunov, Halo, and Lissajous orbits is not necessary to be performed. Due to the symmetries of the problem, these trajectories are specular to the ones of the unstable manifold, with opposite y component and integrated backward in time. Thus, all the stable IMs depart from Phobos' surface, and this potential take-off sites are specular to the landing sites computed before with respect to the 0°/180° longitude (L_1/L_2), while the launch velocities are opposite. In this case, outcomes are more suitable to be filtered by the trajectory that depart from each couple of longitude and latitude with the minimum velocity's

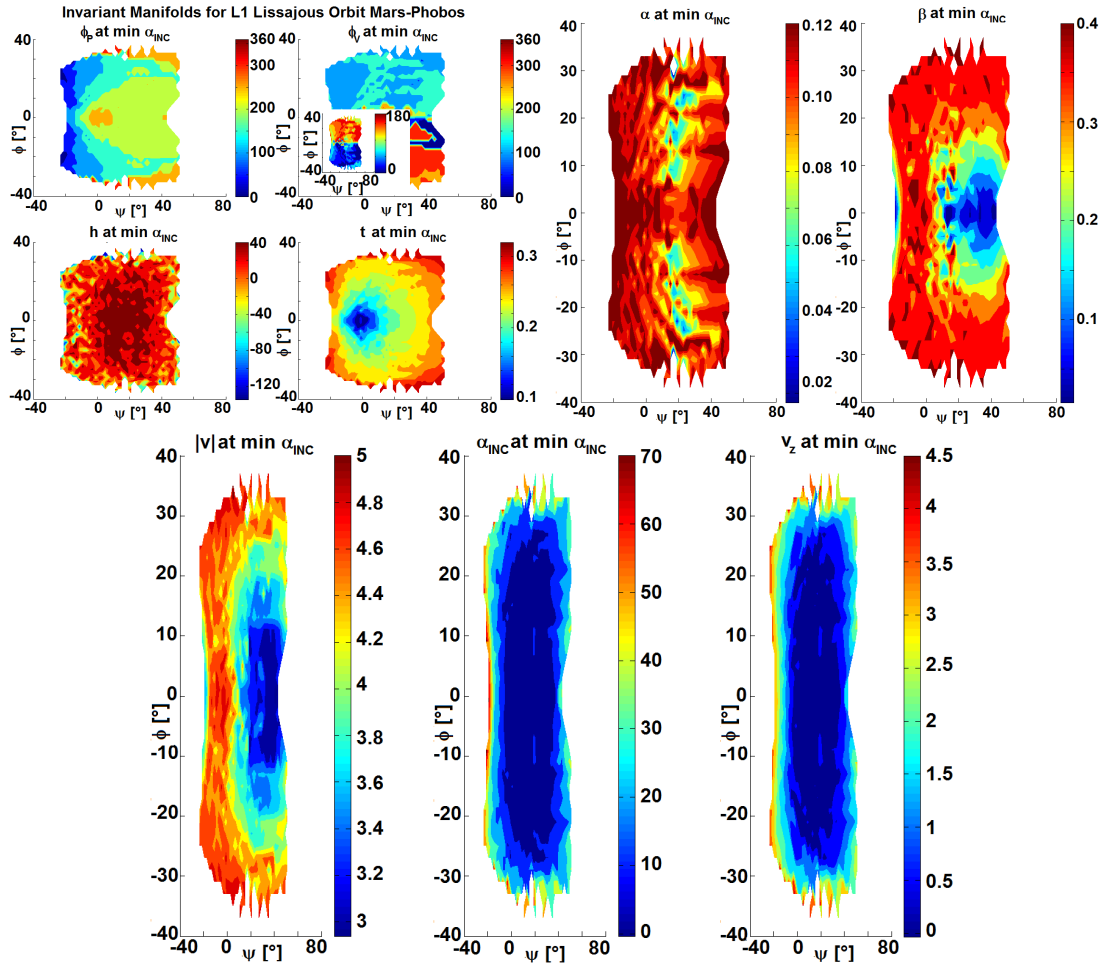

Figure 4.41: **Landing on Phobos through the Invariant Manifold of the lp L_1 Lissajous orbits.** Trajectories that provide the min incidence at the touch-down, as a function of the longitude and latitude of the landing site, for orbits inside the region of convergence at the max order method. Performances of the trajectory: initial planar and vertical phases (miniplot shows its absolute complement to 0°) along the departing Lissajous orbit, altitude where the integration is stopped, TOF, α and β input of the lp algorithm, and landing velocity magnitude, angle of incidence, downward vertical velocity. Phobos mean ellipsoidal surface.

total magnitude, that represents the escape velocity. This is reported in Fig.D.20 for the Lissajous and Lyapunov orbits around L_1, and Fig.D.21 for the Northern Halo around L_1.

In summary, the escape velocity ranges from $2.5-5m/s$ for the Lissajous and planar Lyapunov orbits, which is less than half of the Keplerian Δv computed in section 1.2. This shows how the 3B effect of Mars is important at Phobos.

In conclusion, this analysis showed that due to shrinkage of Phobos' SOI, all the inside branch of the IMs of the LPOs intersects Phobos. Therefore *no homoclinic nor heteroclinic connections* of the two LPs manifolds exist. This is a unique feature of the Mars-Phobos CR3BP, because the natural trajectories, at low energy, to transfer between the SOIs of the two primaries in the Sun-Earth and Earth-Moon systems

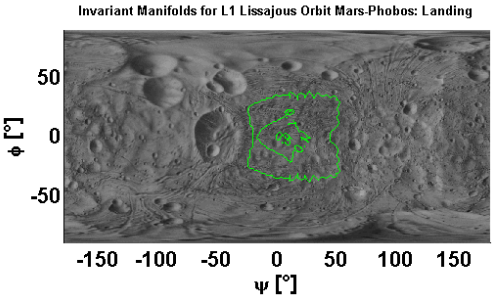

Figure 4.42: **Landing on Phobos through the Invariant Manifold of the lp L_1 Lissajous orbits.** Region of possible landing sites, for orbits inside the region of convergence at the max order method. Inner lines show subregions where the 10%, 50%, 90% levels of the cumulative distribution of the IM simulated landed (same number of trajectories from each departing orbit simulated). Phobos mean ellipsoidal surface.

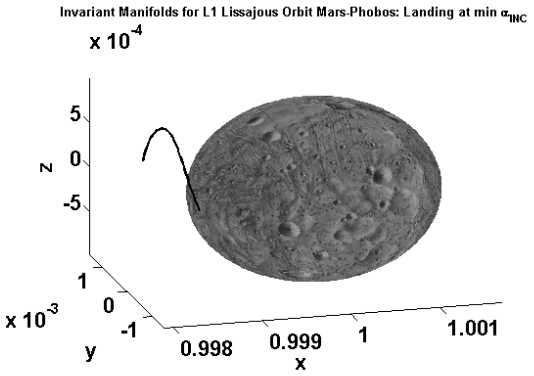

Figure 4.43: **Landing on Phobos through the Invariant Manifold of the lp L_1 Lissajous orbits.** Trajectory that provides the overall min incidence at the touch-down. Phobos mean ellipsoidal surface.

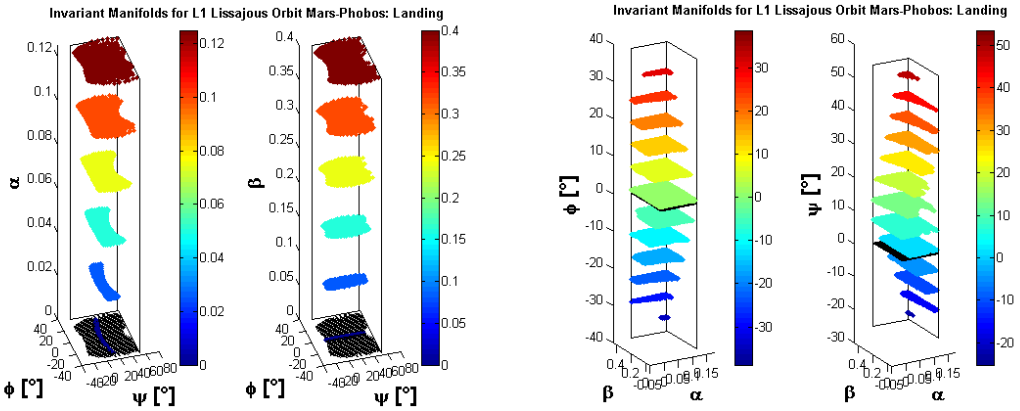

Figure 4.44: **Landing on Phobos through the Invariant Manifold of the lp L_1 Lissajous orbits.** Direct and inverse relation between the longitude and latitude of the landing site and the α and β input of the lp algorithm, for orbits inside the region of convergence at the max order method. Phobos mean ellipsoidal surface.

fly widely far from the bodies. Therefore, the IMs of the LPOs around Phobos are gateways for potential pathways, that would provide natural and efficient landing and take-off for a spacecraft to and from the cis and trans-sides of the moon.

4.2 LPOs in the Mars-Phobos CR3BP-GH

This chapter focuses on the computation of the natural orbits in close proximity of Phobos. Due to the collapsing effect of its SOI, these are the families of periodic and quasi-periodic LPOs computed in section 4.1.

In the last two decades, the orbital dynamics around highly irregular shaped bodies have been investigated in the framework of a perturbed 2B dynamics to derive EPs and orbits around them in proximity of asteroids [118, 119]. These orbits are defined in the asteroid's body-fixed frame and are not significantly influenced by the Sun's third-body perturbation [118, 48]. The manifold of the LPOs is instead defined in the Sun-asteroid orbital frame and far from the asteroid, and is not significantly influenced by the irregularities of its gravity field [49]. The two dynamical domains are therefore decoupled in the phase-space of the asteroids' orbital dynamics. In contrast, the relative dynamics around a small planetary satellite like Phobos cannot neglect any of these forces, and the CR3BP does not provide a suitable approximation to compute the LPOs of the Mars-Phobos system. This led in section 3.3 and 3.4 to define two additional dynamical models, the CR3BP-GH that encloses the modeling of the gravity field of the moon with GHs, and the ER3BP-GH that considers Phobos moving in an elliptical orbit around Mars. The idea that is presented in this section is to *use the LPOs of the CR3BP as starting solutions of a numerical continuation along the three different dynamics, computing in sequence their dynamical substitutes in the new models.* Recalling from section B.7, the notion of **dynamical substitute** was introduced in [53]. As the name suggests, a dynamical substitute is the equivalent of the classical solution of the original dynamics in a perturbed dynamical system. The dynamical substitute is an orbit that not only is a solution of the new dynamics, but also maintains in its phase-space the natural and forcing frequencies of the perturbation.

This approach was introduced in [53] in the framework of the multiple shooting, where several small and time-variant disturbances are considered to refine the reference signal of a classical LPO in the full gravitational model of the Solar System. In this sense, in [57] a multiple shooting method is used in a high-fidelity perturbation model to correct the classical LPOs of the Mars-Phobos CR3BP. This produces the resulting solutions to be only bounded for a specific time span, and they do not contain any information of the natural frequencies of the perturbations. But in our case, the effects of the GHs and eccentricity of Phobos are leading actions in the dynamics about the SOI of the moon, rather than perturbation to take into account only in the last stages of the mission design. Furthermore, the first action is stationary in the 3B frame, and the second is periodic. With the approach of [57] the performance analysis of the orbits is not suitable to be optimized in the preliminary mission design loop. In contrast, in the following sections these two forces will be treated with the classical numerical tools of DST presented in appendix B, to derive a more systematic and complete structure of the dynamical substitutes of the LPOs around Phobos.

This section presents the methodology used and the result obtained by computing the dynamical substitutes of the LPOs from the model of Eq.2.13 to the system described by Eq.3.37. The procedure undertaken is differentiated by the phase-space dimension of the invariant solutions. As the perturbation of Phobos' GHs is time-invariant in the 3B frame, the dynamical substitutes of the invariant solutions maintain the dimension

of their original phase-space in the CR3BP. Section 4.2.1 presents the EPs, section 4.2.2 focuses on the POs, and section 4.2.3 focuses on the 2D-QPOs. Finally, in section 4.2.4 the invariant manifolds of the dynamical substitutes are presented.

4.2.1 EPs in the Mars-Phobos CR3BP-GH

The identification of the dynamical substitutes of the LPs in the Mars-Phobos CR3BP-GH was performed in the framework of the preliminary analysis of this system in section 3.3.6.2. They are are computed as the roots of the vectorfield through Newton's method, as explained in section B.3.

The five LPs in the rotating 3B frame are presented in Table 3.4. Due to the energizing effect of the additional terms of the moon's gravity field, introduced in section 3.3.4.1-3.3.6.1, L_{1-2} are displaced farther away from Phobos. The asymmetric displacement from their original values in the basic CR3BP model is significant, and accounts for 20% of their altitude over Phobos. The related stability properties are maintained from their ancestor solutions in the classical system. Thus, the orbit structure around these LPs in the CR3BP-GH is characterized by a 2-parameters family of invariant 2-tori and their stable and unstable IMs. These orbits are the focus of the next sections.

4.2.2 POs in the Mars-Phobos CR3BP-GH

In this section the computation of the families of dynamical substitutes of the periodic LPOs, with the effect of the inhomogeneous gravity field of the secondary body, is addressed with the methodology of DST to identify invariant motions of section B.5.3. This approach is new in the field, thanks also to the characteristics and peculiarities that requires, and that are suitable for the case of Phobos. Some analytical works have been done considering only the J_2 effect, while the only slightly related approaches that seem to be available in the literature are: a NC with only J_2 and a special value of $J_4 = -J_2^2$ (Vinti Problem) [55], and an analysis with J_2 in the Hill's approximation of the CR3BP [56].

4.2.2.1 Linear Solution of the Dynamical Substitutes

The first step is conducted with an analytical approach, which is to compute the POs of the linearized CR3BP-GH around the nonlinear solution of L_{1-2}. The approach is identical to the one discussed in section 4.1.3, using the state $\mathbf{x}_L$ for L_{1-2} computed in Table 3.4, and extending the Hessian matrix of the potential in Eq.4.3 with the Hessian matrix of the GHs evaluated at the EP. The procedure to derive the Hessian matrix in spherical coordinates was presented in section 3.1.2: the solution for the GHs series expansion in Eq.3.12 must be rotated and counter-rotated by the combination of the local attitude matrix of Eq.3.4 and the constant matrix of Eq.3.20.

$$\begin{cases} \dot{\mathbf{x}}(t) = \mathbf{f}_{\mathbf{CR3BPGH}}(\mathbf{x}) \\ \mathbf{H}_u(\mathbf{x}_L) = u_{G_1/\mathbf{qq}}(\mathbf{x}_L) + u_{G_2/\mathbf{qq}}(\mathbf{x}_L) + u_{GH_2/\mathbf{qq}}(\mathbf{x}_L) = \mathbf{H}_{\mathbf{G}1}(\mathbf{x}_L) + \mathbf{H}_{\mathbf{G}2}(\mathbf{x}_L) + \mathbf{H}_{\mathbf{GH}2}(\mathbf{x}_L) \\ \dot{\mathbf{x}}(\mathbf{x}_L) = \mathbf{0} \rightarrow \delta\mathbf{x} = \mathbf{x} - \mathbf{x}_L \Rightarrow \delta\dot{\mathbf{x}}(t) = \mathbf{A}\delta\mathbf{x}(t), \mathbf{A} = \begin{bmatrix} \mathbf{0_3} & \mathbf{I_3} \\ -\mathbf{P} + \mathbf{H}_u(\mathbf{x}_L) & -2\mathbf{W} \end{bmatrix} \end{cases} \tag{4.25}$$

The analytical computation of the general 2-torus solution of the linearized CR3BP, which is the Lissajous orbit of Eq.4.5, was derived by the homogeneous solution of a mechanical system of uncoupled 4D+2D ODEs. For the case of the CR3BP-GH, the 3D Hessian matrix $\mathbf{H}_{\mathbf{GH}2}(\mathbf{x}_L)$ is completely coupled, and filled in all its components. Therefore a fully analytical expression is derived with the rigorous procedure of the eigenvalue problem's solution.

The first step is to compute the analytical expression of the eigenvalues of the linearized state-matrix of Eq.4.25. This is addressed in section 5.2.3.2 for the case of a general symmetrical matrix $\mathbf{H}_u$. The procedure uses the scalar invariants of $\mathbf{H}_u$ (Eq.5.12), and the expression of the three couples of eigenvalues is given by Eq.5.19, which is function of the A and C coefficients previously defined in Eq.5.12. In particular, since C is complex, the expression is the same for all the couples, differing by a rotation θ of 120° of the phasor C. The manifold of L_{1-2} is a saddle × center × center, so one couple is real (hyperbolic manifold) and describes the IMs of the LP for $\theta = 0$, and the other two are purely imaginary (elliptic manifolds). The latter are the couples of eigenvalues to be considered to compute the linearized LPOs. The linear substitute of the planar Lyapunov is the one whose eigenvalue in Eq.5.19 is rotated by $\theta = +120°$, and the linear substitute of the vertical Lyapunov is related to the rotation of $\theta = -120°$.

The second step is to compute the analytical expression of the four eigenvectors associated to the two couples of imaginary eigenvalues. Since the eigenvalues are in pair of opposite, each couples of eigenvectors are complex conjugated. This is presented in Eq.4.26. Recall that the derivation of the eigenvectors is underdetermined, so it requires to fix one component. Care must be taken to choose a component not orthogonal to the eigenspace needed. In this sense, two expressions are derived in Eq.4.26. One has the x-component set to +1, and is used for the planar Lyapunov orbit's substitute: the related eigenvector has $\delta y = 0$. The other has the $\dot{z}$-component set to +1, and is used for the vertical Lyapunov orbit's substitute: the related eigenvector has $\delta z = 0$.

$$
\begin{cases}
\theta_C = \pm\frac{\pi}{3} \Rightarrow \lambda\left(\theta_C\right) \in \mathbb{I} \Rightarrow \mathbf{v}_\lambda : \mathbf{A}\mathbf{v}_\lambda = \lambda\mathbf{v}_\lambda \\
\mathbf{v}_\lambda = \begin{bmatrix}
+1 \\
\frac{\left(H_{u3,3}-\lambda^2\right)\left(H_{u1,2}+2\lambda\right)-H_{u1,3}H_{u2,3}}{{H_{u2,3}}^2-\left(H_{u3,3}-\lambda^2\right)\left(H_{u2,2}+1-\lambda^2\right)} \\
\frac{\left(H_{u2,2}+1-\lambda^2\right)H_{u1,3}-\left(H_{u1,2}+2\lambda\right)H_{u2,3}}{{H_{u2,3}}^2-\left(H_{u3,3}-\lambda^2\right)\left(H_{u2,2}+1-\lambda^2\right)} \\
-\lambda \\
-\lambda\frac{\left(H_{u3,3}-\lambda^2\right)\left(H_{u1,2}+2\lambda\right)-H_{u1,3}H_{u2,3}}{{H_{u2,3}}^2-\left(H_{u3,3}-\lambda^2\right)\left(H_{u2,2}+1-\lambda^2\right)} \\
-\lambda\frac{\left(H_{u2,2}+1-\lambda^2\right)H_{u1,3}-\left(H_{u1,2}+2\lambda\right)H_{u2,3}}{{H_{u2,3}}^2-\left(H_{u3,3}-\lambda^2\right)\left(H_{u2,2}+1-\lambda^2\right)}
\end{bmatrix} \\
\mathbf{v}_\lambda = \begin{bmatrix}
\frac{1}{\lambda}\frac{\left(H_{u2,2}+1-\lambda^2\right)H_{u1,3}-\left(H_{u1,2}-2\lambda\right)H_{u2,3}}{\left(H_{u1,1}+1-\lambda^2\right)\left(H_{u2,2}+1-\lambda^2\right)-\left(H_{u1,2}-2\lambda\right)\left(H_{u1,2}+2\lambda\right)} \\
\frac{1}{\lambda}\frac{\left(H_{u1,1}+1-\lambda^2\right)H_{u2,3}-\left(H_{u1,2}+2\lambda\right)H_{u1,3}}{\left(H_{u1,1}+1-\lambda^2\right)\left(H_{u2,2}+1-\lambda^2\right)-\left(H_{u1,2}-2\lambda\right)\left(H_{u1,2}+2\lambda\right)} \\
-\frac{1}{\lambda} \\
-\frac{\left(H_{u2,2}+1-\lambda^2\right)H_{u1,3}-\left(H_{u1,2}-2\lambda\right)H_{u2,3}}{\left(H_{u1,1}+1-\lambda^2\right)\left(H_{u2,2}+1-\lambda^2\right)-\left(H_{u1,2}-2\lambda\right)\left(H_{u1,2}+2\lambda\right)} \\
-\frac{\left(H_{u1,1}+1-\lambda^2\right)H_{u2,3}-\left(H_{u1,2}+2\lambda\right)H_{u1,3}}{\left(H_{u1,1}+1-\lambda^2\right)\left(H_{u2,2}+1-\lambda^2\right)-\left(H_{u1,2}-2\lambda\right)\left(H_{u1,2}+2\lambda\right)} \\
+1
\end{bmatrix} \Rightarrow \hat{\mathbf{v}}_\lambda = \frac{\mathbf{v}_\lambda}{\|\mathbf{v}_\lambda\|}
\end{cases}
\tag{4.26}
$$

For better management of the problem, the eigenvectors are normalized in an eigenversor. The general homogeneous solution of the linear system of Eq.4.25 is obtained by the linear combination of the eigenversors, assembling the right-eigenversors matrix $\mathbf{V}$ and its inverse[13], and specifying the initial condition. However here the focus is to obtain a solution only with the normal modes of interest, therefore the initial condition is specified directly in the normal modes' coordinates. This leads to trivially set a common amplitude m_0 only in the two components representing the center manifold of interest.

$$
\begin{cases}
\mathbf{x}\left(t\right) = e^{\mathbf{A}(t-t_0)}\mathbf{x}_0 = \mathbf{V}_\lambda e^{\mathbf{\Lambda}(t-t_0)}\mathbf{V}_\lambda^{-1}\mathbf{x}_0 = \mathbf{V}_\lambda e^{\mathbf{\Lambda}(t-t_0)}\mathbf{m}_0 \\
\mathbf{x}\left(t_0\right) = \mathbf{x}_0
\end{cases}
\tag{4.27}
$$

The combination of the couple of conjugated eigenversors provides the linearized periodic LPO $\mathbf{x}_{PO}(t)$ around the LP in the CR3BP-GH. The combination of the couple of conjugated normal modes simplifies through Euler's formula in a linear combination of cosine and sine, whose pulsation is equal to the eigenvalue magnitude. The related coefficients could be related to the appropriate initial condition in the state space as shown in the previous equation: they are the combination of the related eigenversors.

[13]Since the LPs are isolate, the linearized state-matrix $\mathbf{A}$ is diagonizable.

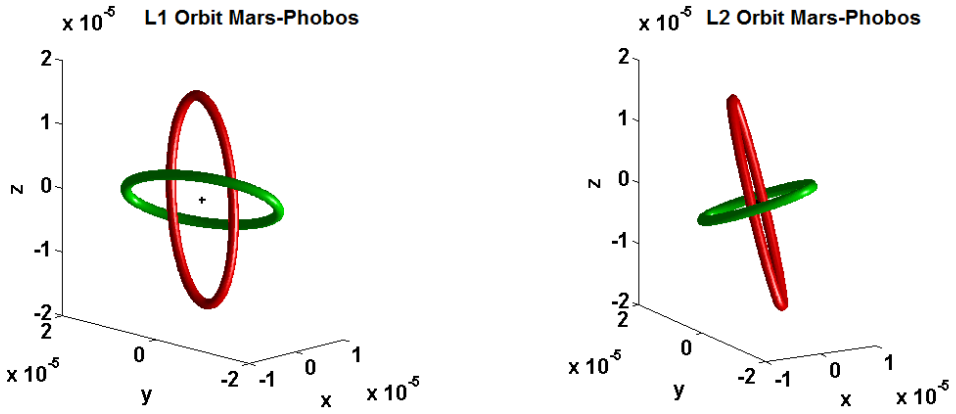

Figure 4.45: **Periodic LPOs in the Mars-Phobos CR3BP-GH.** Linear center manifold's POs around L_1 and L_2 of the Mars-Phobos CR3BP-GH. The gravity field of Phobos is considered up to 4th degree and order. The normal mode's initial condition is set to 1% of the normalized distance between secondary and LP. Origin at the LP of the CR3BP-GH.

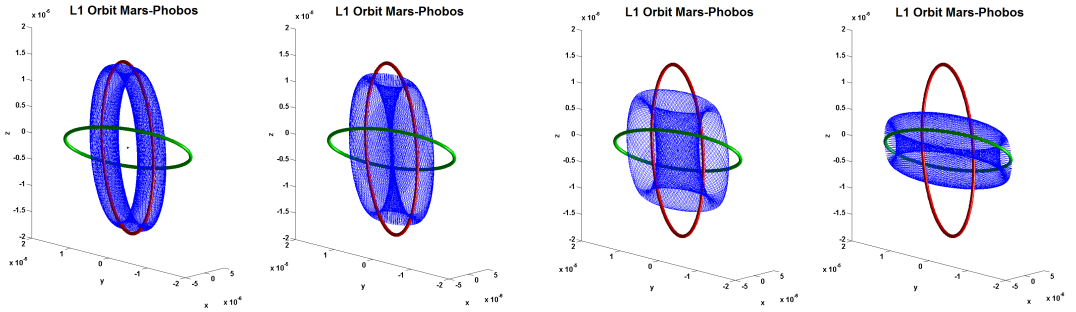

Figure 4.46: **Quasi-periodic orbits in the Mars-Phobos CR3BP-GH.** Linear center manifold's 2D-QPOs around L_1 of the Mars-Phobos CR3BP-GH. The gravity field of Phobos is considered up to 4th degree and order. The normal mode's initial condition magnitude is set to 1% of the normalized distance between secondary and LP. Origin at the LP of the CR3BP-GH.

$$
\begin{aligned}
&\theta_C = \pm\tfrac{\pi}{3} \Rightarrow \lambda\left(\theta_C\right) \in \mathbb{I} \Rightarrow \\
&\mathbf{x}_{PO}\left(t\right) = \left[\,\hat{\mathbf{v}}_{+\lambda}\ \hat{\mathbf{v}}_{-\lambda}\,\right]\begin{bmatrix} e^{\lambda(t-t_0)} \\ e^{-\lambda(t-t_0)} \end{bmatrix} m_0 = \\
&\qquad = \left[\,\mathrm{Re}\{\hat{\mathbf{v}}_\lambda\}+i\mathrm{Im}\{\hat{\mathbf{v}}_\lambda\}\ \mathrm{Re}\{\hat{\mathbf{v}}_\lambda\}-i\mathrm{Im}\{\hat{\mathbf{v}}_\lambda\}\,\right]\begin{bmatrix} e^{\lambda(t-t_0)} \\ e^{-\lambda(t-t_0)} \end{bmatrix} m_0 = \\
&\qquad = 2m_0\mathrm{Re}\left\{\hat{\mathbf{v}}_\lambda\right\}\cos\left(|\lambda|\,t+\theta_0\right) - 2m_0\mathrm{Im}\left\{\hat{\mathbf{v}}_\lambda\right\}\sin\left(|\lambda|\,t+\theta_0\right) = \\
&\qquad = \xi_0\cos\left(|\lambda|\,t+\theta_0\right) + \eta_0\sin\left(|\lambda|\,t+\theta_0\right)
\end{aligned}
\tag{4.28}
$$

This solution will be valid only for small amplitudes of the eigenvectors. Fig.4.45 shows the linear dynamical substitutes of the Lyapunov orbits around L_1 and L_2 of the CR3BP-GH for a normal mode's magnitude of 1% γ_i-normalized units. It is clearly evident the great effect of the inhomogeneous gravity field of Phobos. First of all, as a result of the new 3D-coupled linear dynamics, the substitute of the vertical Lyapunov orbit is also an ellipse like the planar Lyapunov. Second of all, the POs are considerably tilted, if compared to the orientation of their ancestors in the CR3BP, as a result of the high magnitude of the GHs. Counterintuitively, this makes the substitutes of the pla-

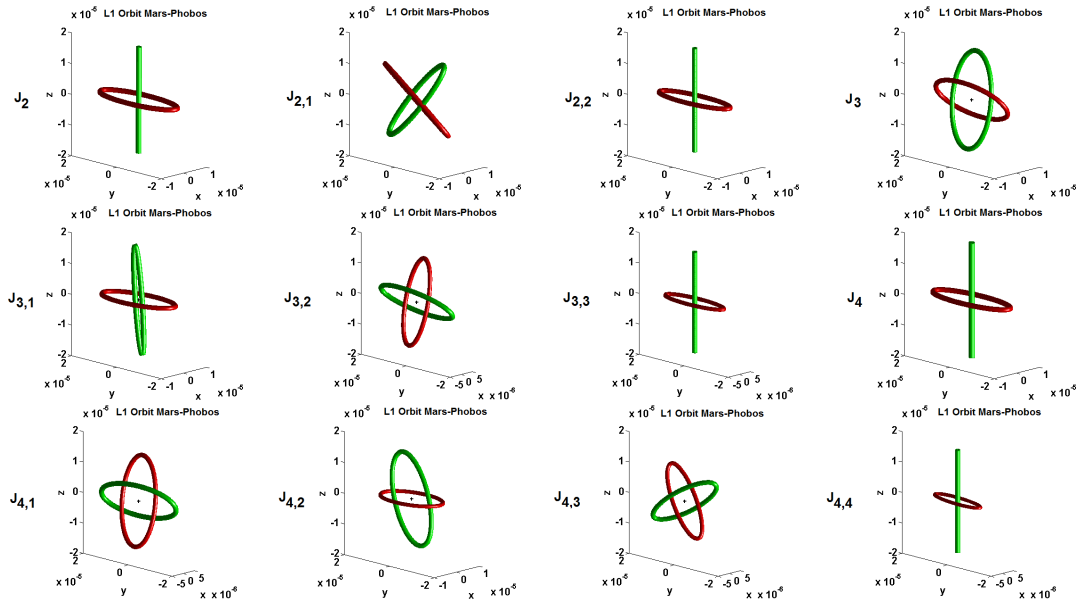

Figure 4.47: **Periodic LPOs in the Mars-Phobos CR3BP-GH.** Linear center manifold's POs around L_1 of a CR3BP-GH. The mass ratio corresponds to the one of the Mars-Phobos system; the GHs are considered individually one at a time, from J_2 up to the 4th degree and order: each spherical harmonic has the same phase of the related coefficient in the Phobos' gravity model, whereas its magnitude is considered with a constant value of 10%. The normal mode's initial condition is set to 1% of the normalized distance between secondary and EP. Origin at the LP.

nar Lyapunov orbits to be mostly vertical, and the substitutes of the vertical Lyapunov orbits to be mostly planar. Thus, the structure of the center $\times$ center manifold is no longer aligned with the coordinate axes and planes of the 3B frame. The orientation of the centers' manifolds is given by the couples of "relative inclination / ascending node's right ascension" of each family of PO. Around L_1, the substitutes of the vertical Lyapunov orbits have 46°/278°, while the substitutes of the planar Lyapunov orbits have 82°/98°. Around L_2, the firsts have 26°/43°, the seconds have 71°/223°. Interestingly, the two POs around each LP have opposite nodes, as we see also in Fig.4.45.

Combining both the normal modes of the two centers in Eq.4.27, the linear dynamical substitutes of the quasi-periodic Lissajous orbits around the POs are obtained analytically. This is shown in Fig. 4.46: the two manifolds are connected through the family of iso-energetic 2D-QPOs, in terms of the linearized Jacobi integral around the LP.

To conclude the linear analysis, it is worth to exploit the analytical expressions derived in this section to quickly study the effect of each harmonic's degree and order. This has not been done in depth: since each GH is defined by two coefficients, the phase has been kept equal to the one of Phobos' gravity model of Table 3.1. The analysis is then conducted looking to the effect of each GH independently, not cumulated: thus, the magnitude considered is the same for each GH, equal to 10%. The outcomes are showcased in Fig.4.47-4.48 for both L_1 and L_2 POs. The effect is the same and

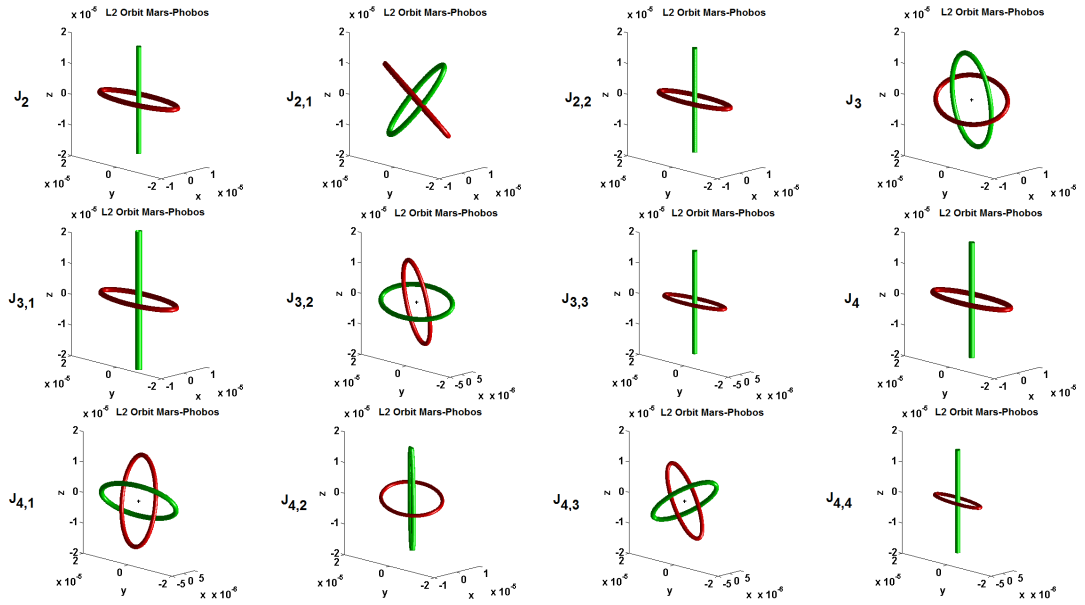

Figure 4.48: **Periodic LPOs in the Mars-Phobos CR3BP-GH.** Linear center manifold's POs around L_2 of a CR3BP-GH. The mass ratio corresponds to the one of the Mars-Phobos system; the GHs are considered individually one at a time, from J_2 up to the 4th degree and order: each spherical harmonic has the same phase of the related coefficient in the Phobos' gravity model, whereas its magnitude is considered with a constant value of 10%. The normal mode's initial condition is set to 1% of the normalized distance between secondary and EP. Origin at the LP.

specular between the two LPs. This analysis proves the condition of planar-vertical decoupling of the GHs Hessian matrix of Eq.3.12. Substitutes of planar and vertical Lyapunov orbits maintain the basic uncoupled orientation when the derivatives in the non-diagonal terms x-z and y-z of $\mathbf{H_{GH}}(\mathbf{x}_L)$ are zero. As mentioned at the beginning of this section, between $\mathbf{H_{GH}}$ and Eq.3.12 there is an attitude rotation between 3B and TSE frames, which depends on the location of $\mathbf{x}_L$. The latter depends from the GH too, and so it must be recomputed.

In summary, in Eq.3.12, the Legendre associated polynomials P_n^m are null when the EP is on the equatorial plane (or at a node of the polynomial) and $(n+m)$ is odd, whereas its derivatives are null when the EP is on the equatorial plane (or at a node of the derivative) and n is even or $n = m$. The spherical harmonic C_n^m is null in quadrature of the n-nodes of its phasor (see Eq.3.1), whereas its derivative is null on the n-nodes. Of course it is not possible to have both a trigonometric function and its derivative null at the same location. The uncoupling between planar and vertical dynamics is therefore obtained if and only if the GH only moves the EP onto the orbital plane, and if the coupling terms with the colatitude in the spherical Hessian of Eq.3.12 are null. A general situation that satisfies all these constraints is realized by an even zonal harmonic (symmetric oblateness) and a sectorial harmonic (longitude-dependent field). This because both cases have null derivative of the Legendre associated polynomial, therefore they don't move the EP along the vertical axis (second component

of Eq.3.3). The first result keeps zero the single term r-θ and the second term θ-ψ in Eq.3.12, and the second result keeps zero also the first term θ-ψ.

4.2.2.2 Computation of the Dynamical Substitutes of the Periodic LPOs in the Mars-Phobos CR3BP-GH

The linear solution of section 4.2.2.1 can be used only for very small amplitudes. To increase the validity, the extension to include higher nonlinear terms of the CR3BP-GH can be done by the use of the semi-analytical techniques exploited in the CR3BP in section 4.1.3.1. However, the inclusion of the GHs provides a complete coupling of the 3D dynamics already in the linearized case. Thus, the burden required to develop a high-order lp algorithm for the CR3BP-GH increases significantly.

The choice carried out is to use a numerical approach. The numerical methodology for the computation of POs around the LPs exploits their reduction in DST to an invariant point of a suitable iso-energetic Poincaré map, by the use of the DC scheme presented in section B.5.3.2. The first guess of the DC can well be the linear solution of the LPOs computed in section 4.2.2.1 with a small amplitude. Afterwards, NC is performed as presented in section B.5.3.2.1 to generate the two families of POs developing from the LPs of the CR3BP-GH. This would be the same approach used in section 4.1.4.2: however in that case, the initial guess was given by the Richardson's solution. This is already a nonlinear solution of small-order, and it was not accurate enough to provide a complete first-return to the Poincaré map in the full nonlinear system, so it required to exploit the symmetry condition. The CR3BP-GH is not symmetric any longer, and the Lyapunov orbits are also more unstable than the Halo orbits. Thus, the linear solution would require a very tiny amplitude to allow the convergence of the DC.

Instead of using the classical procedure, the idea is to use as initial guess the LPOs already computed in sections 4.1.3 and 4.1.4. However, using these initial guesses in the CR3BP-GH would not allow the DC to converge, because the level of perturbation of the GHs on the CR3BP is too high, and the situation appear similar to the previous case. The preference to use this alternative approach is driven by the fact that here we have available the entire families of nonlinear LPOs in a close dynamics, which is an information much more powerful than that of a couple of two linear solutions. Therefore, to make the DC to converge, NC must be used to move between the two dynamics. This is the same framework explained in [116] to perform multiple-shooting under tiny time-invariant perturbations, but this time the DC scheme will be the single-shooting of section B.5.3.1, and so the dynamical substitute will still be a PO, whose period corresponds to the nonlinear natural frequency of the CR3BP-GH.

4.2.2.2.1 NC between the dynamical models of the CR3BP and the CR3BP-GH

Unlike the classical NC used so far in the thesis, in this case the continuation acts implicitly in the dynamics, and not on an explicit characteristic of the invariant object.

The continuation parameter is, intuitively, a scaling factor σ_{GH}, from 0 to 1, to weight the GHs acceleration in the vectorfield.

$$\dot{\mathbf{x}} = \mathbf{h}\left(t, \mathbf{x}, \sigma_{GH}\right) = \mathbf{f_{CR3BP}}\left(\mathbf{x}\right) + \sigma_{GH}\mathbf{f_{GH}}\left(\mathbf{x}\right) \rightarrow \boldsymbol{\phi}_{\mathbf{h}}\left(t, \mathbf{x}, \sigma_{GH}\right) \tag{4.29}$$

The general dynamical system is now a homotopy $\mathbf{h}$ between the CR3BP and the CR3BP-GH, and its flow is dependent on σ_{GH}. Recall that the sensitivity of the flow with respect to a parameter is retrieved with the procedure explained in section B.1.2.5. The DC will now require the propagation of the augmented 7D $\times$ 7D variational systems to retrieve the STM.

$$\boldsymbol{\Phi}\left(t, \mathbf{x}_0, \sigma_{GH}\right) = \begin{bmatrix} \boldsymbol{\phi}_{h/\mathbf{x}_0} & \boldsymbol{\phi}_{h/\sigma} \\ \mathbf{0_{1x6}} & 1 \end{bmatrix} \leftrightarrow \begin{cases} \dot{\boldsymbol{\Phi}}\left(t, \mathbf{x}_0, \sigma_{GH}\right) = \begin{bmatrix} \mathbf{H_{3B}}(\mathbf{x}(t)) + \sigma_{GH}\mathbf{H_{GH}}(\mathbf{x}(t)) & \mathbf{f_{GH}}(\mathbf{x}(t)) \\ \mathbf{0_{1x6}} & 0 \end{bmatrix} \boldsymbol{\Phi}\left(t, \mathbf{x}_0, \sigma_{GH}\right) \\ \boldsymbol{\Phi}\left(0, \mathbf{x}_0, \sigma_{GH}\right) = \mathbf{I_7} \end{cases} \tag{4.30}$$

Recall from section 3.3.6 that the CR3BP-GH is still conservative and an appropriate augmented Jacobi integral is available. In the same way as their acceleration is introduced in the vectorfield, the potential of the GHs' perturbation is weighted in the general Jacobi integral of the homotopic dynamical system of Eq.4.29.

$$c\left(\mathbf{x}, \sigma_{GH}\right) = c_{3B}\left(\mathbf{x}\right) + \sigma_{GH}c_{GH}\left(\mathbf{x}\right) \tag{4.31}$$

This allows to define an appropriate iso-energetic constraint, to be used in the same DC scheme of Eq.B.75. However, the Jacobi integral is not the same in different dynamics. The most physically-related interpretation of the dynamical substitute of a LPO is an orbit with the same energy gap with respect to the LP in the coherent dynamics. Therefore the NC of the POs must embed also the computation of the current LP. This hints to continue the POs from CR3BP to CR3BP-GH in a differential way, using the relative state $\mathbf{z}$ with respect to the state of the current LP $\mathbf{x}_L$,

$$\mathbf{x}_L\left(\sigma_{GH}\right) : \mathbf{h}\left(0, \mathbf{x}_L, \sigma_{GH}\right) = \mathbf{0} \rightarrow \mathbf{z} = \mathbf{x} - \mathbf{x}_L \tag{4.32}$$

using a variant Poincaré map,

$$g(\mathbf{x}, \sigma_{GH}) = y - y_{LP}(\sigma_{GH}) \tag{4.33}$$

and with a fixed-energy constraint with respect to the energy of the LP.

$$\Delta c(\mathbf{x}, \sigma_{GH}) = c(\mathbf{x}, \sigma_{GH}) - c(\mathbf{x}_{LP}, \sigma_{GH}) \tag{4.34}$$

Since this NC scheme is rather different from the classical ones presented in appendix B, the DC scheme's step is provided explicitly in the following equations. First, one defines some index referencing: the Poincaré section is taken along the variable y, the

controlled-variables of the continuation are 4, swapping x with the Jacobi integral.

$$\begin{cases} v_M = y \rightarrow i_M = 2 \\ \mathbf{v}_X = \left[z\ \dot{x}\ \dot{y}\ \dot{z} \right] \rightarrow \mathbf{i}_X = \left[3\ 4\ 5\ 6 \right] \\ v_\sigma = \sigma \rightarrow i_\sigma = 7 \end{cases} \tag{4.35}$$

The objective function of the DC scheme is the following, where the time-return is fixed by the related map to ultimately give the period of the PO.

$$\begin{cases} \mathbf{z}_0(\sigma_{GH}) : F\left(T, \mathbf{z}_0, \sigma_{GH}\right) = \begin{bmatrix} c\left(\mathbf{z}_0 + \mathbf{x}_L, \sigma_{GH}\right) - c\left(\mathbf{x}_L, \sigma_{GH}\right) - \Delta c \\ \left\{ \boldsymbol{\phi}_h\left(T, \mathbf{z}_0 + \mathbf{x}_L, \sigma_{GH}\right) - \mathbf{z}_0 - \mathbf{x}_L \right\}_{\mathbf{i}_X} \end{bmatrix} = \mathbf{0} \\ T : g\left(T, \mathbf{z}_0, \sigma_{GH}\right) = \left\{ \boldsymbol{\phi}_h\left(T, \mathbf{z}_0 + \mathbf{x}_L, \sigma_{GH}\right) - \mathbf{z}_0 - \mathbf{x}_L \right\}_{i_M} = 0 \wedge \left\{ \mathbf{z}_0 \right\}_{i_M} = 0 \end{cases} \tag{4.36}$$

As usual, the section's variable is fixed and the time-return constraint is embedded in the derivative of the Poincaré map (see section B.5.3.2). In addition, the map depends now also on the LP, which ultimately depends on the continuation parameter σ_{GH}. This requires an additional constraint to be included in the derivative of the Poincaré map[14].

$$\begin{cases} \left\{ \delta \mathbf{z}_0 \right\}_{i_M} = 0 \\ \delta \mathbf{h}\left(0, \mathbf{x}_L, \sigma_{GH}\right) = \left[\mathbf{H_{3B}}(\mathbf{x}_L) + \sigma_{GH} \mathbf{H_{GH}}(\mathbf{x}_L)\ \mathbf{f_{GH}}(\mathbf{x}_L) \right] \begin{bmatrix} \delta \mathbf{x}_L \\ \delta \sigma_{GH} \end{bmatrix} = \mathbf{0_{6x1}} \\ \quad \rightarrow \delta \mathbf{x}_L = -\left(\mathbf{H_{3B}}\left(\mathbf{x}_L\right) + \sigma_{GH} \mathbf{H_{GH}}\left(\mathbf{x}_L\right) \right)^{-1} \mathbf{f_{GH}}\left(\mathbf{x}_L\right) \delta \sigma_{GH} \\ \delta g\left(T, \mathbf{z}_0, \sigma_{GH}\right) = \left[\left\{ \boldsymbol{\Phi}(T, \mathbf{z}_0 + \mathbf{x}_L, \sigma_{GH}) - \mathbf{I}_7 \right\}_{i_M, \mathbf{x}} \left\{ \boldsymbol{\Phi}(T, \mathbf{z}_0 + \mathbf{x}_L, \sigma_{GH}) - \mathbf{I}_7 \right\}_{i_M, \mathbf{x}} \left\{ \mathbf{h}(T, \mathbf{z}_0 + \mathbf{x}_L, \sigma_{GH}) \right\}_{i_M} \left\{ \boldsymbol{\Phi}(T, \mathbf{z}_0 + \mathbf{x}_L, \sigma_{GH}) \right\}_{i_M, \sigma} \right] \begin{bmatrix} \delta \mathbf{z}_0 \\ \delta \mathbf{x}_L \\ \delta T \\ \delta \sigma_{GH} \end{bmatrix} = 0 \\ \quad \rightarrow \delta T = -\frac{1}{\left\{ \mathbf{h}\left(T, \mathbf{z}_0 + \mathbf{x}_L, \sigma_{GH}\right) \right\}_{i_M}} \left[\left\{ \boldsymbol{\Phi}(T, \mathbf{z}_0 + \mathbf{x}_L, \sigma_{GH}) - \mathbf{I}_7 \right\}_{i_M, \mathbf{x}} \left\{ \boldsymbol{\Phi}(T, \mathbf{z}_0 + \mathbf{x}_L, \sigma_{GH}) - \mathbf{I}_7 \right\}_{i_M, \mathbf{x}} \left\{ \boldsymbol{\Phi}(T, \mathbf{z}_0 + \mathbf{x}_L, \sigma_{GH}) \right\}_{i_M, \sigma} \right] \begin{bmatrix} \delta \mathbf{z}_0 \\ \delta \mathbf{x}_L \\ \delta \sigma_{GH} \end{bmatrix} \end{cases} \tag{4.37}$$

Finally, global matrix are assembled, and the DC scheme of the NC step for computing the dynamical substitute of the periodic LPOs from CR3BP to CR3BP-GH is made by the objective function of Eq.4.36 and its Jacobian of Eq.4.39.

$$\begin{cases} g\left(\mathbf{x}\right) = c_{GH}\left(\mathbf{x}\right) \\ \mathbf{f}\left(\mathbf{x}\right) = \mathbf{f_{GH}}\left(\mathbf{x}\right) \\ \mathbf{G}\left(\mathbf{x}, \sigma_{GH}\right) = \nabla_{\mathbf{x}} c\left(\mathbf{x}, \sigma_{GH}\right) = \left[2\left\{ \left(\mathbf{f_{3B}}(\mathbf{x}) + \sigma_{GH} \mathbf{f_{GH}}(\mathbf{x}) \right)^T \right\}_{[\dot{x}\ \dot{y}\ \dot{z}]} - 2[\dot{x}\ \dot{y}\ \dot{z}] \right]_{\mathbf{X}} \\ \mathbf{J}\left(\mathbf{x}, \sigma_{GH}\right) = \left(\mathbf{H_{3B}}\left(\mathbf{x}\right) + \sigma_{GH} \mathbf{H_{GH}}\left(\mathbf{x}\right) \right) \\ \mathbf{P}\left(T, \mathbf{z}_0, \mathbf{x}_L, \sigma_{GH}\right) = \left\{ \boldsymbol{\Phi}\left(T, \mathbf{z}_0 + \mathbf{x}_L, \sigma_{GH}\right) - \mathbf{I}_7 \right\}_{\mathbf{x}, \mathbf{x}} \\ \mathbf{B}\left(T, \mathbf{z}_0, \mathbf{x}_L, \sigma_{GH}\right) = \left\{ \boldsymbol{\Phi}\left(T, \mathbf{z}_0 + \mathbf{x}_L, \sigma_{GH}\right) - \mathbf{I}_7 \right\}_{\mathbf{x}, \sigma} \end{cases} \tag{4.38}$$

[14] Recall that the Hessian at the EP is always invertible in autonomous dynamical systems with isolated EPs.

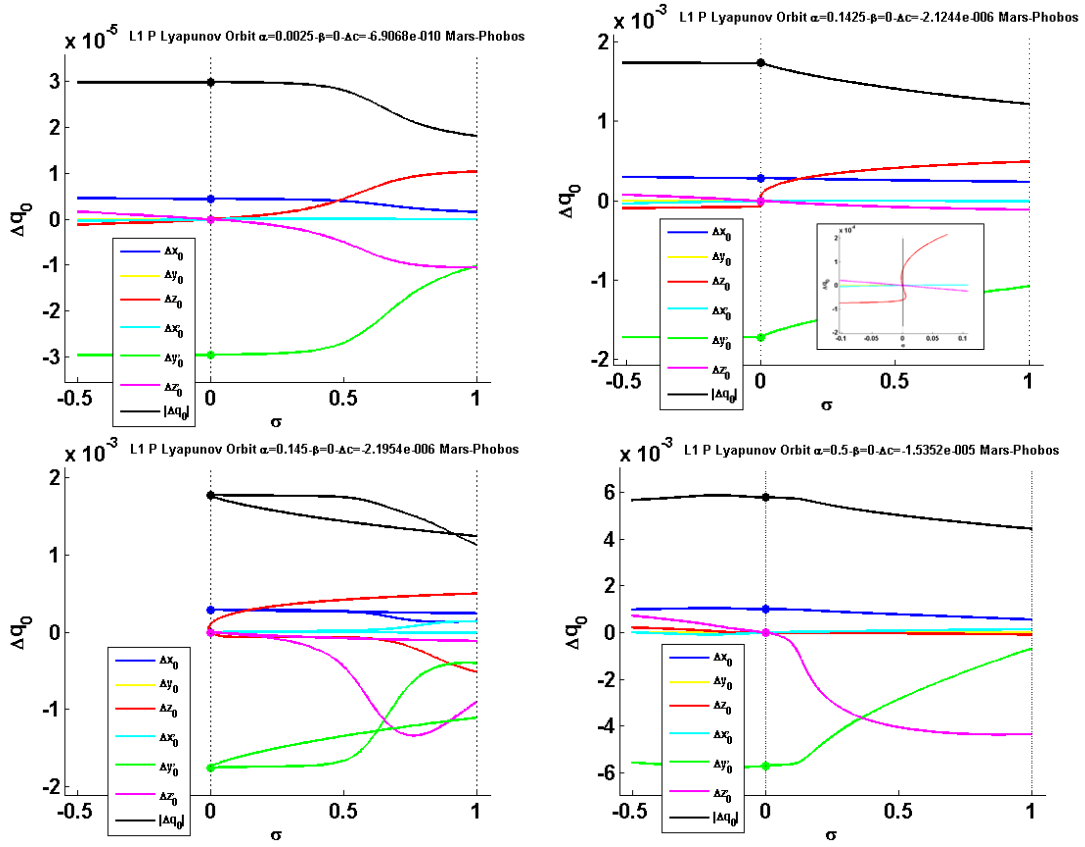

Figure 4.49: **Periodic LPOs in the Mars-Phobos CR3BP-GH.** Continuation variables' curves profile. Continuation with respect to the GHs' magnitude from CR3BP ($\sigma = 0$) to full CR3BP-GH ($\sigma = 1$). Continuation of planar Lyapunov orbits around L_1 at increasing energy.

$$
\begin{aligned}
&\delta\mathbf{H}\left(T, \mathbf{z}_0, \sigma_{GH}, \mathbf{x}_L\left(\sigma_{GH}\right)\right) = \\
&= \begin{bmatrix}
\left\{\mathbf{G}(\mathbf{z}_0+\mathbf{x}_L,\sigma_{GH})\right\}_{\mathbf{x}\setminus v_M} & \left(g\left(\mathbf{z}_0+\mathbf{x}_L\right)-g\left(\mathbf{x}_L\right)\right)+ \\
& -\left(\mathbf{G}\left(\mathbf{z}_0+\mathbf{x}_L,\sigma_{GH}\right)-\mathbf{G}\left(\mathbf{x}_L,\sigma_{GH}\right)\right)\mathbf{J}\left(\mathbf{x}_L,\sigma_{GH}\right)^{-1}\mathbf{f}\left(\mathbf{x}_L\right) \\
\left\{\begin{array}{l}\mathbf{P}\left(T,\mathbf{z}_0+\mathbf{x}_L,\sigma_{GH}\right)+ \\ -\dfrac{\left\{\mathbf{h}\left(T,\mathbf{z}_0+\mathbf{x}_L,\sigma_{GH}\right)\right\}_{\mathbf{i}_X}}{\left\{\mathbf{h}\left(T,\mathbf{z}_0+\mathbf{x}_L,\sigma_{GH}\right)\right\}_{i_M}}\cdot \\ \cdot\left\{\mathbf{P}\left(T,\mathbf{z}_0+\mathbf{x}_L,\sigma_{GH}\right)\right\}_{i_M,:}\end{array}\right\}_{\mathbf{i}_X,\mathbf{x}\setminus v_M} & \left\{\begin{array}{l}\mathbf{B}\left(T,\mathbf{z}_0+\mathbf{x}_L,\sigma_{GH}\right)+ \\ -\mathbf{P}\left(T,\mathbf{z}_0+\mathbf{x}_L,\sigma_{GH}\right)\mathbf{J}\left(\mathbf{x}_L,\sigma_{GH}\right)^{-1}\mathbf{f}\left(\mathbf{x}_L\right)+ \\ -\dfrac{\left\{\mathbf{h}\left(T,\mathbf{z}_0+\mathbf{x}_L,\sigma_{GH}\right)\right\}_{\mathbf{i}_X}}{\left\{\mathbf{h}\left(T,\mathbf{z}_0+\mathbf{x}_L,\sigma_{GH}\right)\right\}_{i_M}}\cdot \\ \cdot\left\{\begin{array}{l}\mathbf{B}\left(T,\mathbf{z}_0+\mathbf{x}_L,\sigma_{GH}\right)+ \\ -\mathbf{P}\left(T,\mathbf{z}_0+\mathbf{x}_L,\sigma_{GH}\right)\mathbf{J}\left(\mathbf{x}_L,\sigma_{GH}\right)^{-1}\mathbf{f}\left(\mathbf{x}_L\right)\end{array}\right\}_{i_M,:}\end{array}\right\}_{\mathbf{i}_X}
\end{bmatrix}\begin{bmatrix}\{\delta\mathbf{z}_0\}_{\mathbf{x}\setminus v_M} \\ \delta\sigma_{GH}\end{bmatrix} \\
&= \mathbf{H}'\left(T,\mathbf{z}_0,\sigma_{GH},\mathbf{x}_L\left(\sigma_{GH}\right)\right)\begin{bmatrix}\{\delta\mathbf{z}_0\}_{\mathbf{x}\setminus v_M} \\ \delta\sigma_{GH}\end{bmatrix}
\end{aligned}
\tag{4.39}
$$

The Jacobian is 5×6, and will become square when using the DC in the pseudo-arclength NC of Eq.B.39.

Analysis of the results. Throughout all this thesis, the terms small, medium, large are intuitively related to the range of possible LPOs existing around Phobos. Hence, they span from the small-size orbits around the LP, to the large-size orbits that intersect the moon's surface. Since the energy (from the LP) is used the parameterize the families

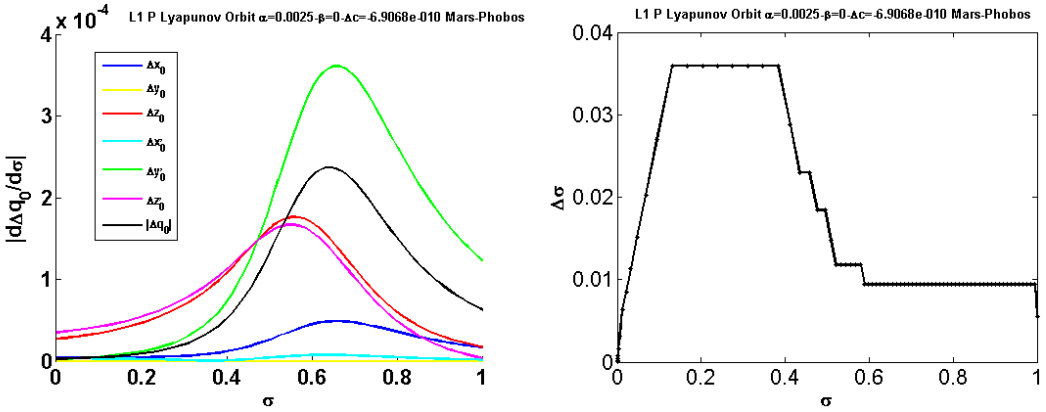

Figure 4.50: **Periodic LPOs in the Mars-Phobos CR3BP-GH.** Derivative of the continuation variables' curves profile, and continuation adaptive step profile. Continuation with respect to the GHs' magnitude from CR3BP ($\sigma = 0$) to full CR3BP-GH ($\sigma = 1$). Continuation of a small-energy planar Lyapunov orbit around L_1.

of POs, to summarize the results in the text, which are presented specifically in plots and figures, the orbits are referred to be of small, medium, large-energy[15]. This is just to quickly address the results as a trend within a family.

The DC scheme of Eq.4.39 is applied in a NC where σ_{GH} is increased from 0 to 1, using as initial guess the initial condition, on the Poincaré map, of any of the Lyapunov and Halo orbits of the CR3BP computed in section 4.1.3-4.1.4. The NC is performed for a sampling of POs for each of these four families of the CR3BP, for both LPs. The NC has resulted to be quite fast, using strict tolerances (10^{-12} for both function and step). In particular, this choice of a continuation of the differential state with respect to the current LP, has been proved to be 33% faster than continuing the absolute state, since it requires less DC iterations for a given step size.

An example of the continuation curves is shown in Fig.4.49 for the planar Lyapunov family, Fig.D.22 for the Southern Halo family, Fig.D.23 for the Northern Halo family, and Fig.D.24 for the vertical Lyapunov family. With this continuation scheme along the dynamics, the interest is only for the final solution, as intermediate dynamics have not practical exploitation. It is worth noting the presence of turning points of the continuation curve: planar Lyapunov and Northern and Southern Halo orbits of the CR3BP are linked together under the framework of the augmented state-space $[\mathbf{x}; \sigma_{GH}]$ of the vectorfield $\mathbf{h}$, when the continuation curve crosses more than once the $\sigma = 0$ axis. In such a case, the adaptive step control and the pseudo-arclength NC prove their efficiency, as shown in Fig.4.50. Therefore, with this scheme, NC should be always performed in both directions at the beginning. The NC is then stopped at the first crossing with the $\sigma = 1$ axis, and at the first one with $\sigma = -0.5$: possible bends out of these boundaries are not considered in this thesis.

[15]If another property is used to parameterize the family, the same notation applies with it. For example, the 2-parameter families of quasi-periodic orbits require to be parameterized also by the width of their invariant curves.

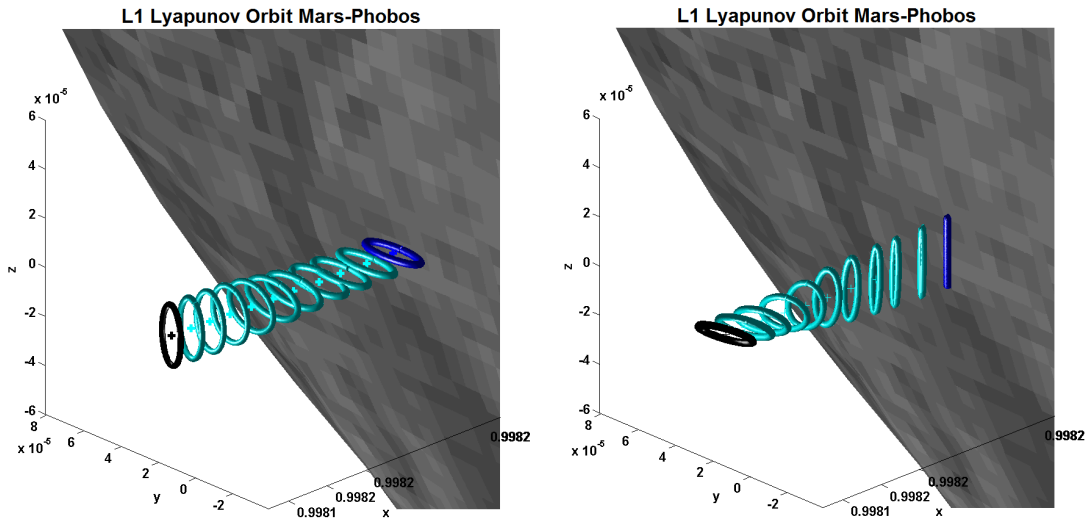

Figure 4.51: **Periodic LPOs in the Mars-Phobos CR3BP-GH.** Continuation with respect to the GHs of a small-energy planar and vertical Lyapunov orbit around L_1 of the CR3BP (blue) to their dynamical substitute in the CR3BP-GH (black) belonging to the families A and B respectively, together with the current LP.

Fig.4.51 and 4.54 show what "physically" happens: as σ_{GH} is increased from 0 to 1, the small planar and vertical Lyapunov orbits follow the corresponding LP and are highly distorted, mostly in the second half of the continuation. The results obtained with this new method are proved to be correct, because the final dynamical substitutes of these small orbits at $\sigma_{GH} = 1$ correspond to the linear solutions of the CR3BP-GH of Fig.4.45. For the discussion about the characterization of the high tilt and distortion, produced by the strong and 3D-coupled gravity field of Phobos at the LP, see related section 4.2.2.1. In particular, recall that substitutes of planar Lyapunov orbits are mostly vertical, and substitutes of vertical Lyapunov are mostly planar. It is worth to say that despite the continuation with respect to the Phobos' GHs magnitude does not provide physically-practical intermediate results, these plots for a specific case hint at some general conclusions. The set of orientation of the GHs' phasors is almost infinite in reality, but its effect is derivable from the linear eigenspace at the EP. Furthermore, the behavior of the orbits in Fig.4.51 and 4.54 can be a reference for the qualitative importance of the effect in a general case, by considering σ_{GH}, used here to scale the GHs of Phobos, to represent the ratio $\mathbf{a^P}/\mathbf{a}_2(LP)$ of a general CR3BP-GH.

Focus now on the continuation of the medium and large LPOs in Fig.4.52-4.53. After the Halo bifurcation of the CR3BP, the dynamical substitutes of the planar Lyapunov have a sudden change: they become tilted eight-shaped orbit (if seen from the y-z plane, but actually they are open orbits). By contrast, Southern Halo have the opposite behavior: their dynamical substitutes from medium-size Halo are eight-shaped orbits, while for large Halo the dynamical substitutes are similar to the ones generated by the medium-size planar Lyapunov orbits. Northern Halo orbits are connected with planar Lyapunov and Southern Halo just for medium-size orbits, and the dynamical

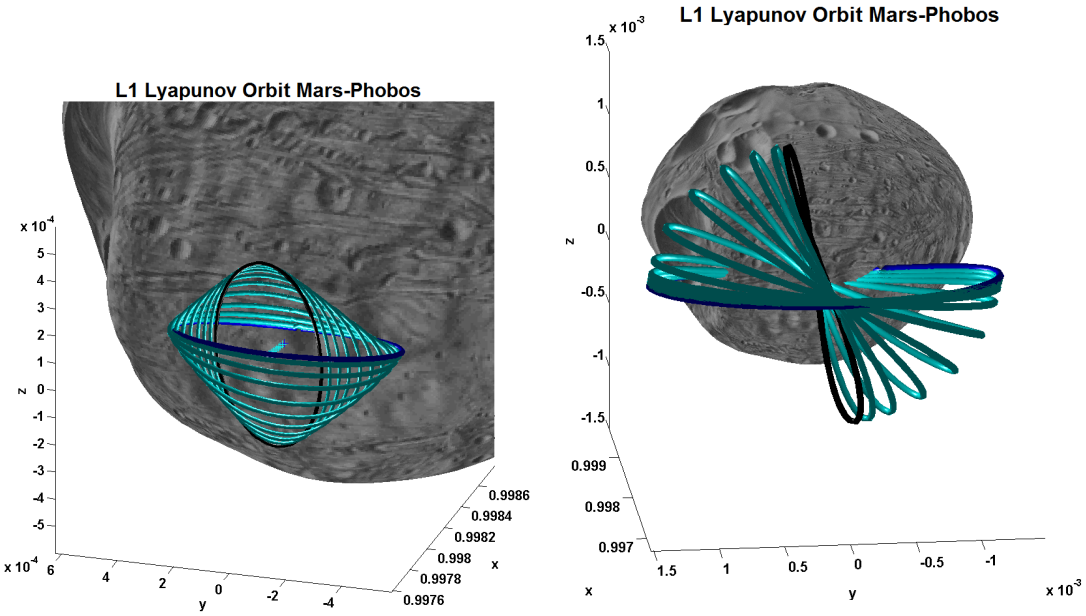

Figure 4.52: **Periodic LPOs in the Mars-Phobos CR3BP-GH.** Continuation with respect to the GHs of a medium and large-energy planar Lyapunov orbit around L_1 of the CR3BP (blue) to their dynamical substitute in the CR3BP-GH (black), together with the current LP.

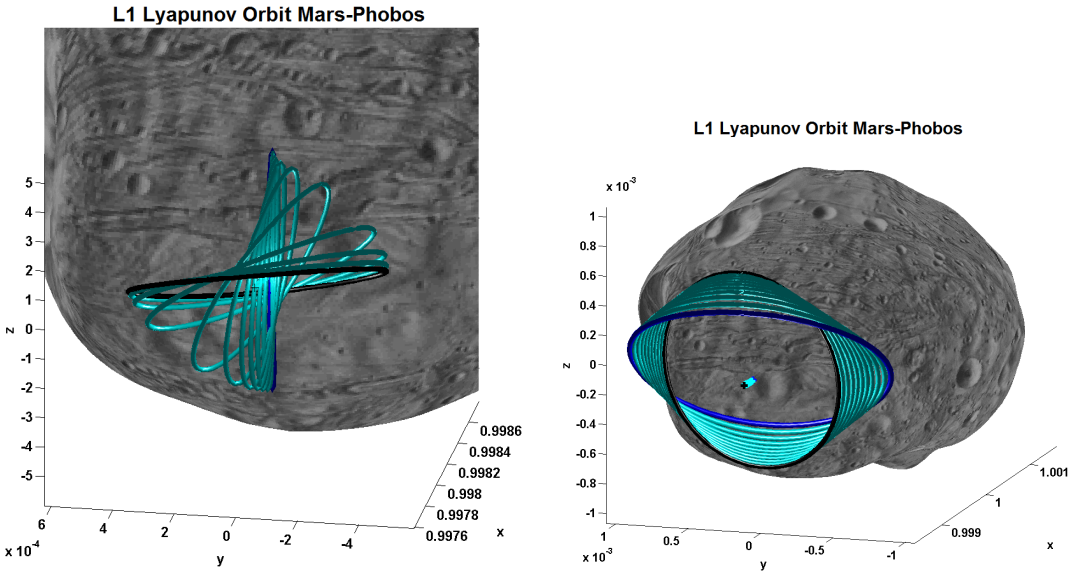

Figure 4.53: **Periodic LPOs in the Mars-Phobos CR3BP-GH.** Continuation with respect to the GHs of a large-energy vertical Lyapunov orbit and a medium-energy Northern Halo orbit around L_1 of the CR3BP (blue) to their dynamical substitute in the CR3BP-GH (black), together with the current LP.

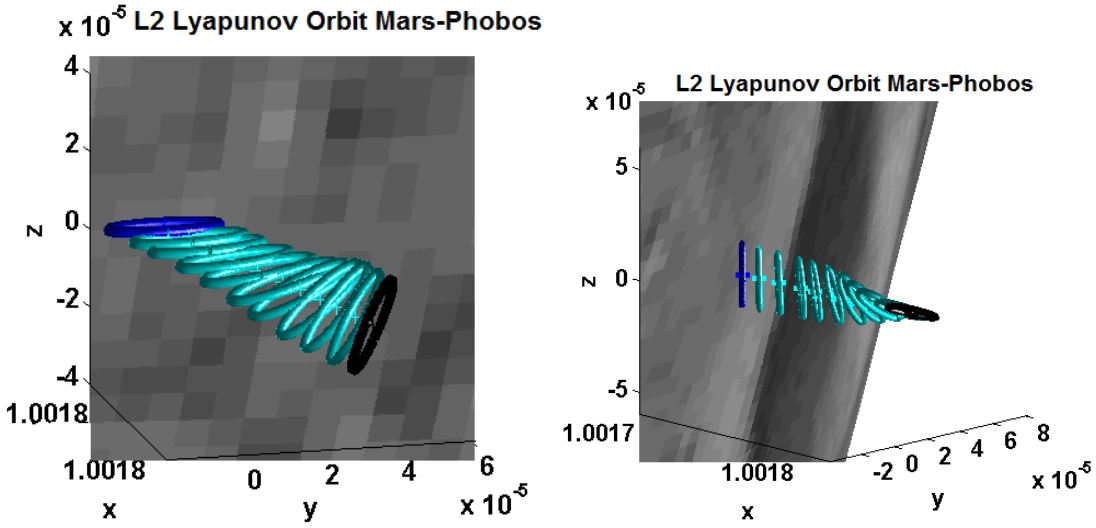

Figure 4.54: **Periodic LPOs in the Mars-Phobos CR3BP-GH.** Continuation with respect to the GHs of a small-energy planar and vertical Lyapunov orbit around L_2 of the CR3BP (blue) to their dynamical substitute in the CR3BP-GH (black), together with the current LP.

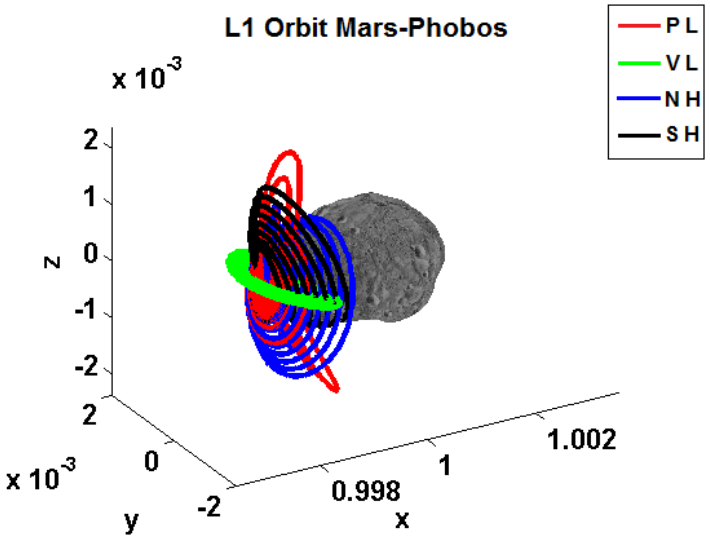

Figure 4.55: **Periodic LPOs in the Mars-Phobos CR3BP-GH.** Graphical summary of the dynamical substitutes in the CR3BP-GH obtained by continuation of the sampled POs of the families of LPOs around L_1 of the CR3BP.

substitutes of large orbits increase in size coherently. The latter behavior is exhibited by all the dynamical substitutes of the vertical Lyapunov orbits, whose inclination decreases as long as their size increases.

After performing this sampling of NCs, the related dynamical substitutes are collected together in Fig.4.55 for L_1 (NCs of the LPOs around L_2 produce similar results). This graphical analysis is necessary because, due to the continuation curves' folding, the same PO in the CR3BP can generate different dynamical substitutes, with the same energy gap with respect to the LP, in the CR3BP-GH. Therefore, it is decided to organize the dynamical substitutes by considering their shape. This gives **a new classification of the POs in the Mars-Phobos CR3BP-GH, which are grouped in the following four families**:

- **Family A**. POs generated from planar Lyapunov at low-energy, planar Lyapunov, Northern Halo and Southern Halo at medium-energy, Southern Halo at high-energy. They start like elliptic orbits mostly vertical, they end like tilted Southern Halo.
- **Family B**. POs generated from vertical Lyapunov at low-energy. They start like elliptic orbits mostly planar, they end like tilted planar Lyapunov.
- **Family C**. POs generated from planar Lyapunov, Northern Halo and Southern Halo at medium-energy, Northern Halo at high-energy. They start like large elliptic orbits mostly vertical, they end like tilted Northern Halo.
- **Family D**. POs generated from planar Lyapunov, and Southern Halo at medium-energy, planar Lyapunov at high-energy. They look like tilted vertical Lyapunov (which are the axial orbits of the CR3BP), but actually they are open orbits.

4.2.2.2.2 NC with respect to the energy in the CR3BP-GH

After obtaining the sampling of dynamical substitutes with the NC between the two dynamics, the new families of periodic LPOs are now better investigated. To refine the families of POs visually identified in Fig.4.55, one PO is taken for each of them as starting solution for a continuation with respect to the differential Jacobi integral Δc, used as a fixed constraint in the previous scheme of Eq.4.39, in the final CR3BP-GH for $\sigma_{GH} = 1$. This type of NC is pretty classic, and is already addressed in section B.5.3.2.1. Thus, the DC scheme is the same of Eq.4.39, just with a different continuation parameter. Since the latter is now explicit and limited to the iso-energetic constraint of the initial condition, and not dependent on the flow, the related column of the Jacobian is just filled in the first component. Furthermore, the STM is uncoupled and there is no need to use an augmented variational system. The starting solution of the NC is taken as the initial condition on the iso-energetic Poincaré map of the smallest-energy dynamical substitute belonging to the chosen family. The NC is stopped for a differential energy Δc such that the related PO intersects Phobos. The continuation

curves for the four families around L_1 are shown in FigD.25: clearly, as a difference from the first NC scheme, the continuation curve contains all physically meaningful POs in the Mars-Phobos CR3BP-GH.

As mentioned in section 4.2.2.2, this approach could have been used actually directly from the linear solution found at small-energy for the families A and B in section 4.2.2.1. Thus the alternative procedure by-passes the first NC, and requires only this second scheme to find a continuous curve of physically meaningful POs, on the contrary of the combination of the two schemes. However, the alternative procedure allows to compute the families A and B, but not C and D, which would require a bifurcation analysis. In this sense, continuing now one sampled PO of these families, it is found that the families C and D are actually two branches of the same global family, that is named CD, since they are connected through an ancestor orbit at the lowest energy as we see in Fig.4.60-4.58. This is proved by Fig.4.56. The curiosity would be to find the origin of this ancestor orbit. The immediate idea is to do a reverse continuation with respect to the GHs, with the same NC scheme of Eq.4.39, from $\sigma_{GH} = 1$ to the original CR3BP for $\sigma_{GH} = 0$. But as we see in Fig.4.57, the continuation curve arrives quite close to the original dynamics (where the solution appears similar to a Northern Halo), but then revolves back in a closed loop. Thus, the ancestor orbit of the family CD in the CR3BP-GH does not have a dynamical substitute in the original CR3BP at the same energy Δc.

The only possibility to track the origin of the ancestor orbit of the CD family is therefore to perform a bifurcation analysis in the CR3BP-GH. The ancestor orbit could be a bifurcation point, because its set of stability indexes suggests the presence of an additional direct parabolic manifold. Furthermore, the determinant of the DC's Jacobian is null at the ancestor orbit, as shown in Fig.4.62. The approach to conduct a bifurcation analysis is described in section B.5.3.2.1. However, a bifurcation analysis is not performed because the profile of the stability indexes of the three families in Fig.4.64 does not suggest that the family CD bifurcates from neither A nor B, even with a bridge of POs at high-energy intersecting Phobos' figure. The first singular points of these families appear after Phobos' intersection and are related to an inverse parabolic manifold. Therefore it appears that the family CD is continuous but isolated from the EP, a result strictly given by the high level of nonlinear perturbation of the inhomogeneous gravity field of Phobos, and possible under the framework of the augmented homotopic dynamical system $\mathbf{h}$ in the state-space $[\mathbf{x}; \sigma_{GH}]$ of Eq.4.29.

In summary, the strategy of two continuation schemes in cascade allowed instead to compute easily the family CD, where the first scheme finds a PO "seed" to feed the second. This is a better approach, because it exploits the fact that we already have information of the full orbit structure in a closed dynamics, the basic CR3BP.

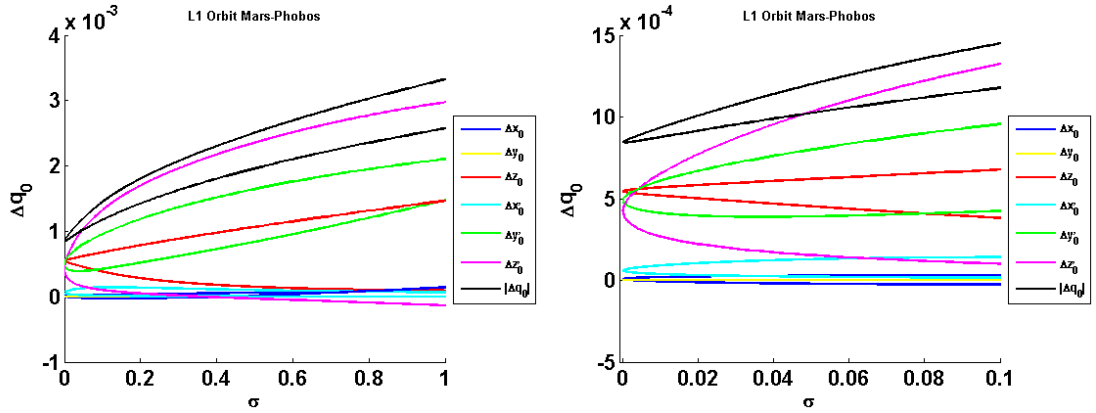

Figure 4.56: **Periodic LPOs in the Mars-Phobos CR3BP-GH.** Continuation variables' curves profile of the two branches of the family CD of POs around L_1 in the CR3BP-GH. Continuation with respect to the energy from the ancestor orbit ($\sigma = 0$) to the intersection with Phobos' surface ($\sigma = 1$). Magnification around the low-energy interval showing the connection between the two branches through the ancestor orbit.

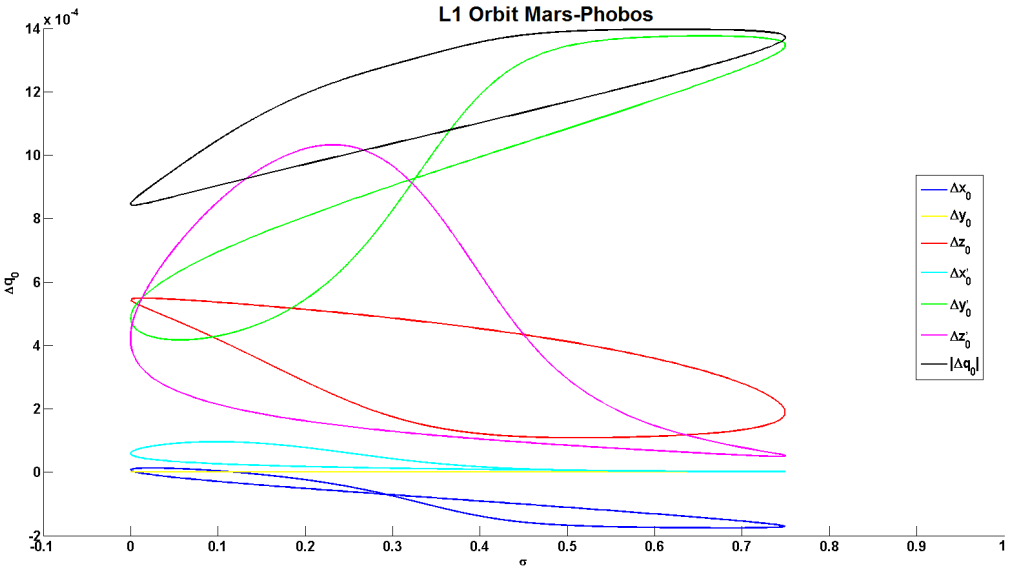

Figure 4.57: **Periodic LPOs in the Mars-Phobos CR3BP-GH.** Continuation variables' curves profile. Inverse continuation with respect to the GHs' magnitude from CR3BP-GH ($\sigma = 0$) to CR3BP ($\sigma = 1$). Continuation of the ancestor orbit of the family CD of the CR3BP-GH around L_1, showing that this orbit does not have a dynamical substitute in the original CR3BP.

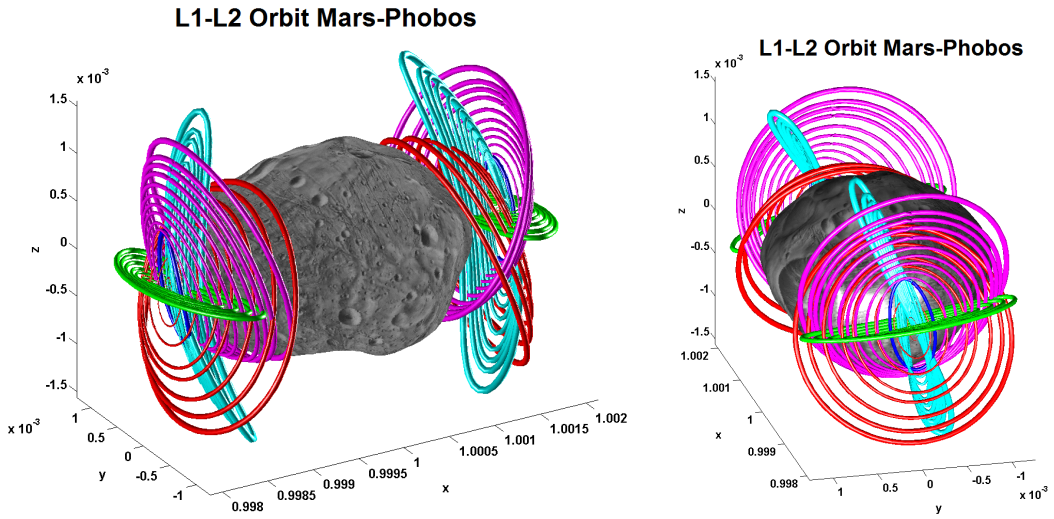

Figure 4.58: **Periodic LPOs in the Mars-Phobos CR3BP-GH.** Graphical visualization of the new A (red), B (green), C (magenta), and D (cyan) families of POs around each LP in the CR3BP-GH. The orbits are obtained by continuation with respect to the energy. Shape harmonics series expansion for Phobos' surface.

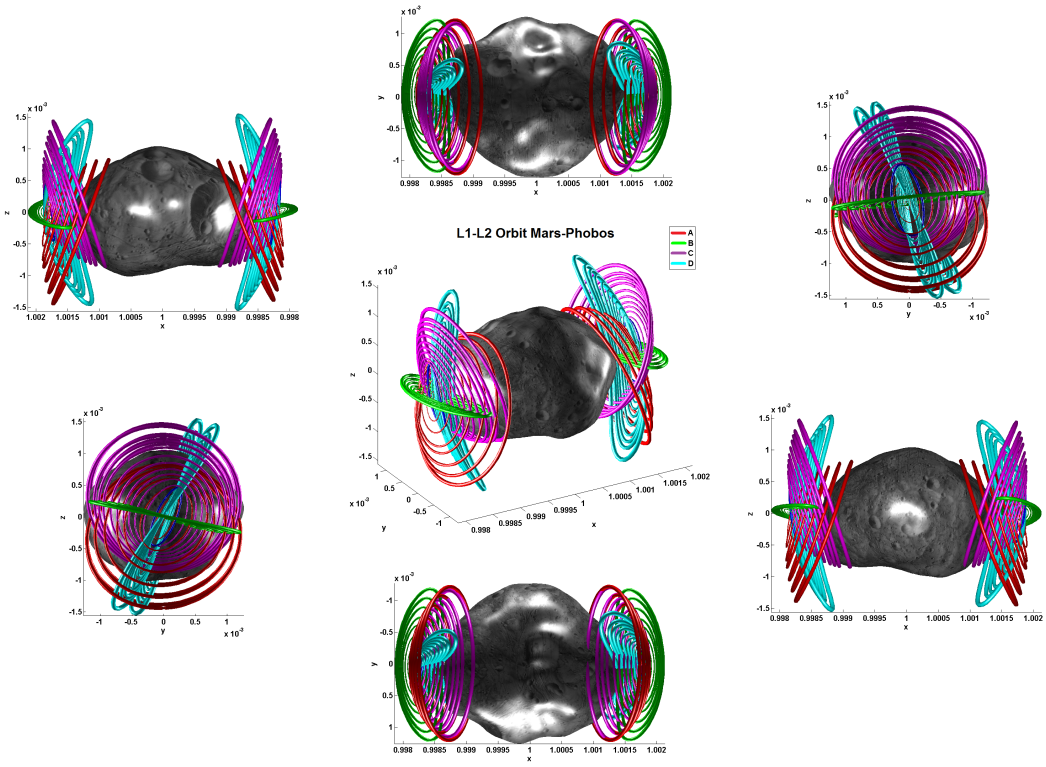

Figure 4.59: **Periodic LPOs in the Mars-Phobos CR3BP-GH.** Graphical visualization of the families of POs around each LP in the CR3BP-GH. Projections on the coordinates planes.

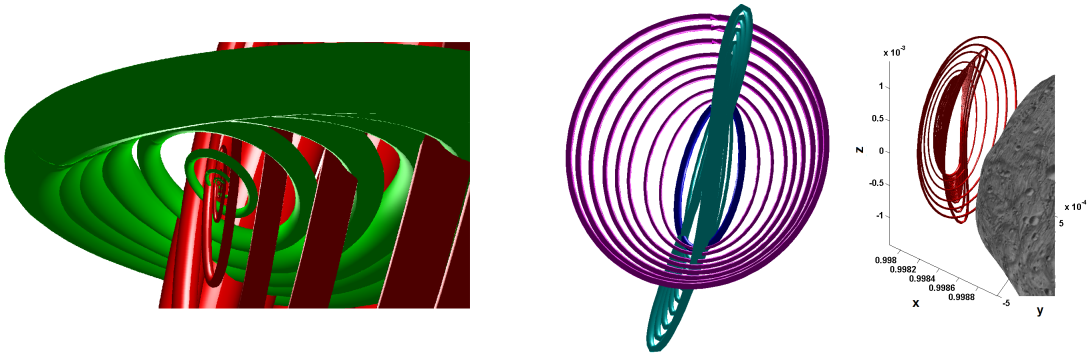

Figure 4.60: **Periodic LPOs in the Mars-Phobos CR3BP-GH.** On the left, behavior of the A and B families around L_1 at low energy. On the right, behavior of the C and D families around L_1 showing their actual connection through the ancestor orbit (in blue) as two branches of a single CD family.

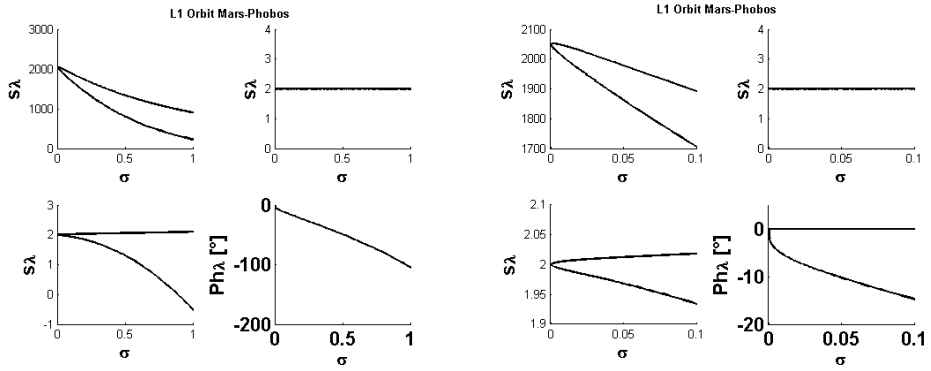

Figure 4.61: **Periodic LPOs in the Mars-Phobos CR3BP-GH.** Stability properties (the three stability indexes, with the phase of the center's eigenvalue) of the two branches of the family CD of POs around L_1 in the CR3BP-GH. Continuation with respect to the energy from the ancestor orbit ($\sigma = 0$) to the intersection with Phobos' surface ($\sigma = 1$). Magnification around the low-energy interval showing the connection between the two branches through the ancestor orbit.

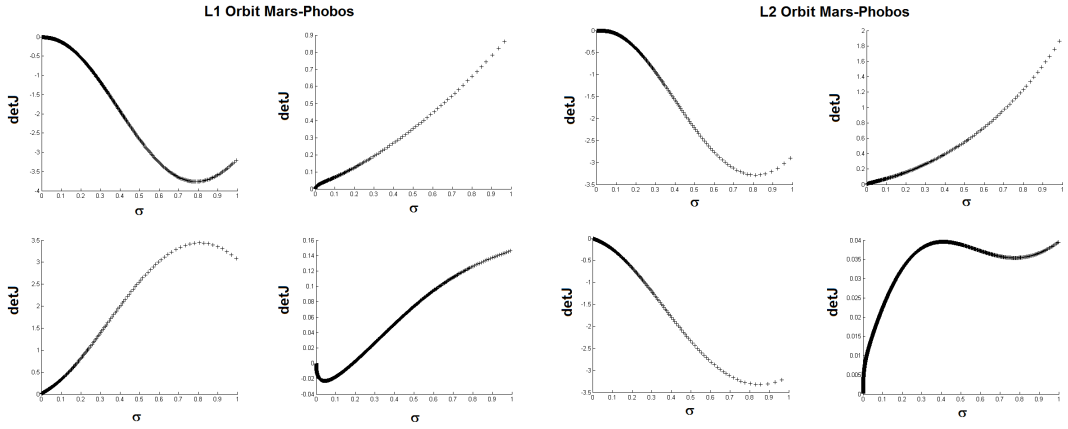

Figure 4.62: **Periodic LPOs in the Mars-Phobos CR3BP-GH.** Determinant of the DC's Jacobian of the NC with respect to the energy in the CR3BP-GH, from the EP ($\sigma = 0$) to the intersection with Phobos' surface ($\sigma = 1$), for the families of POs around L_1 and L_2 in the CR3BP-GH.

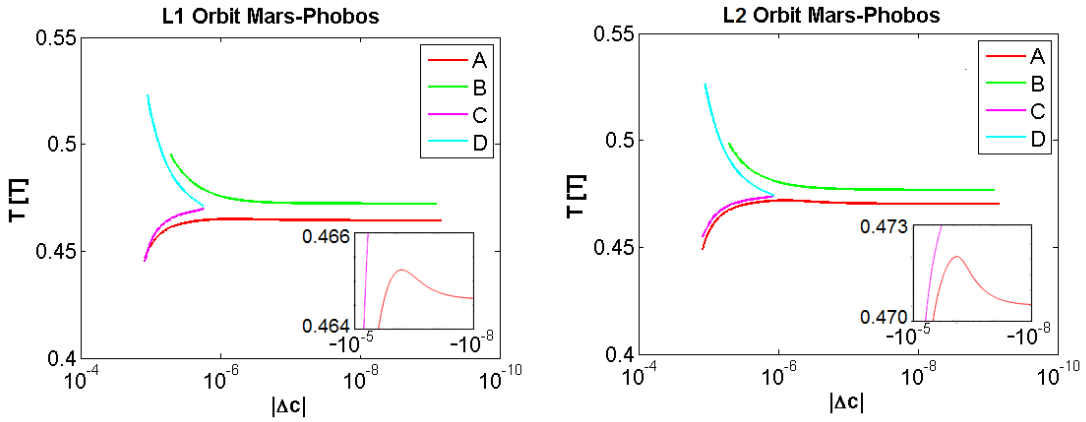

Figure 4.63: **Periodic LPOs in the Mars-Phobos CR3BP-GH.** Characteristic curves in the energy-period plane of the families of POs around L_1 and L_2 in the CR3BP-GH. Magnification of the interval at low-energy where the families A's characteristic curve is not monotonic. Energy is defined as the differential Jacobi integral with respect to the LP.

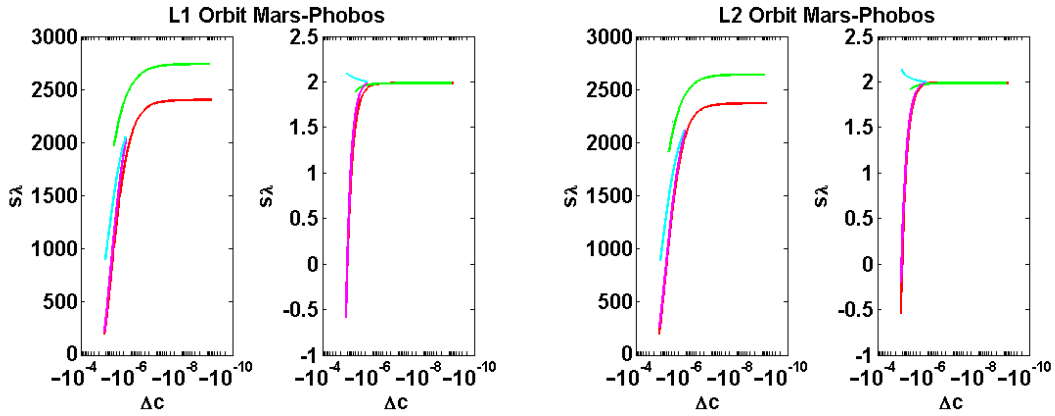

Figure 4.64: **Periodic LPOs in the Mars-Phobos CR3BP-GH.** Characteristic curves of the stability indexes of the two non-unit couples of eigenvalues of the monodromy matrix of the families of POs around L_1 and L_2 in the CR3BP-GH, parameterized by the differential Jacobi integral with respect to the LP.

4.2.2.3 The Periodic LPOs of the Mars-Phobos CR3BP-GH

The application of the two NC schemes presented in sections 4.2.2.2.1-4.2.2.2.2 allowed to obtain the dynamical substitutes of the periodic LPOs in the Mars-Phobos CR3BP-GH. These LPOs are showcased in Fig.4.58-4.59, as well as separately for each family of each LP in Fig.D.26-D.33. They are constituted by two 1-parameter families A and B originating from each LP, and by a detached 1-parameter family CD, made by two branches C and D connected by a common orbit at the lowest energy.

The low-energy orbits of the families A and B are highly distorted from their ancestor Lyapunov orbits in the CR3BP as we see in Fig.4.51 and Fig.4.60, due to the highly inhomogeneous gravity field of Phobos. Besides, the force field at the LP is no longer symmetric and highly tilted from the one of the classical CR3BP, and the structure of the saddle × center × center manifold is no longer aligned with the coordinate axes

and planes. The orientation of the centers' manifold is reported in section 4.2.2.1.

The effect of the complex gravity field of Phobos is mostly local and is therefore averaged for larger orbits, that resemble the shape of the LPOs of the classical CR3BP. The shape of larger orbits of the family A is similar to the Southern Halo, B to the planar Lyapunov, C to the Northern Halo, and D to the vertical Lyapunov. However, the tilt is still maintained, and this represents the most significant effect of the addition of the GHs of the second massive body. This information can be evaluated just from the eigenspace at the LP.

In summary, the natural LPOs that exist under the gravity field of Phobos are very different from the classical solution known in-depth under the framework of a CR3BP approximation. Thus, considering the CR3BP-GH at the very first iteration of the mission design is necessary to assess the performance against the possible mission requirements (for example surface coverage and ground-track) of feasible orbits, in terms of fuel consumption for station-keeping. This is why it became necessary to rename the families of the LPOs of Phobos.

The properties of these new families of LPOs are presented as a function of the family's parameter, which is the energy, to provide their characteristic curves. Fig.4.63 presents the period of the LPOs, which is close to the natural one of the LP. The behavior of the characteristic curve is also coherent with the one of the family of the CR3BP that looks similar to the related larger orbits in the CR3BP-GH, but a difference arises for the family A at low-energy, which is not monotonic. Fig.D.34 gives the information of minimum distance from Phobos. Fig.D.26-D.29 for L_1, and Fig.D.30-D.33 for L_2, provide the stability indexes of the monodromy matrices for each family of the new LPOs, which is finally summarized in Fig.4.64. This Floquet stability analysis shows that all the orbits are unstable. In particular, the families A and C, just like the Halo orbits, have their maximum stability index s_λ that rapidly decreases with increasing size of the orbit. The maximum stability index for the family B is less sensitive to the size. Finally, the branch D is characterized by a saddle $\times$ saddle $\times$ center manifold, therefore no QPOs exist around these POs.

4.2.2.4 Convergence Analysis of the LPOs in the CR3BP-GH

The computational demand to compute the dynamical substitutes of the LPOs in the CR3BP-GH rapidly increases when increasing the order of the GHs series. This is the aim of the guidance subsystem, that provides a reference signal that follows the natural dynamics, to be tracked by the spacecraft with less demand on the control subsystem. This is one of the trade-offs of the GNC system. Hence, it is significant to investigate the convergence of the NC procedure used to compute the dynamical substitutes of the periodic LPOs, as a function of the degree and order of the Mars-Phobos CR3BP-GH, as was done in section 3.3.6.3 for the LPs. One sample medium-energy orbit of the family A has been chosen to evaluate the cost of the different truncated models.

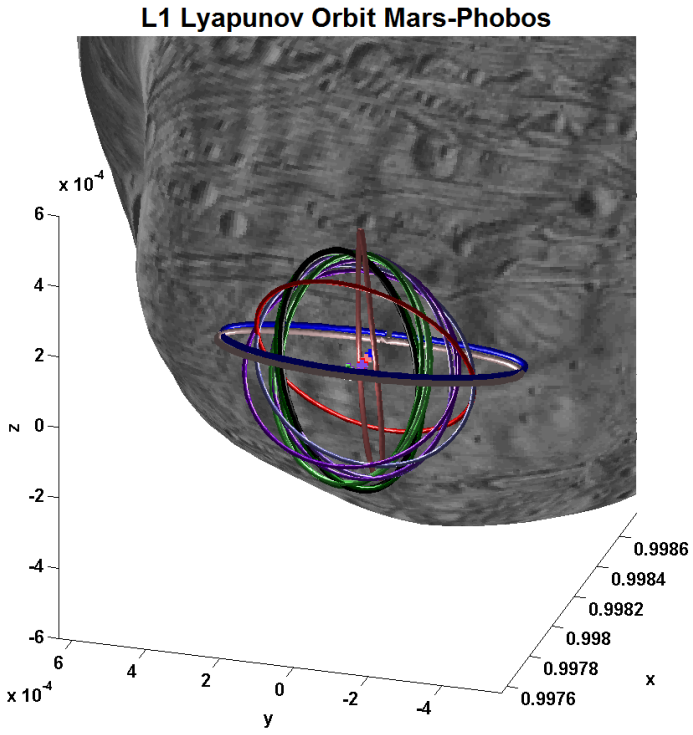

Figure 4.65: **Periodic LPOs in the Mars-Phobos CR3BP-GH.** Convergence analysis of the different dynamical substitutes of a medium-energy planar Lyapunov orbit around L_1 of the CR3BP (blue), obtained incrementally increasing the degree and order of the harmonics included in the partial CR3BP-GH (red for degree 2, purple for degree 3, green for degree 4, with color darkened by increasing order, and final orbit at fourth degree and order in black). Crosses represent the current EP.

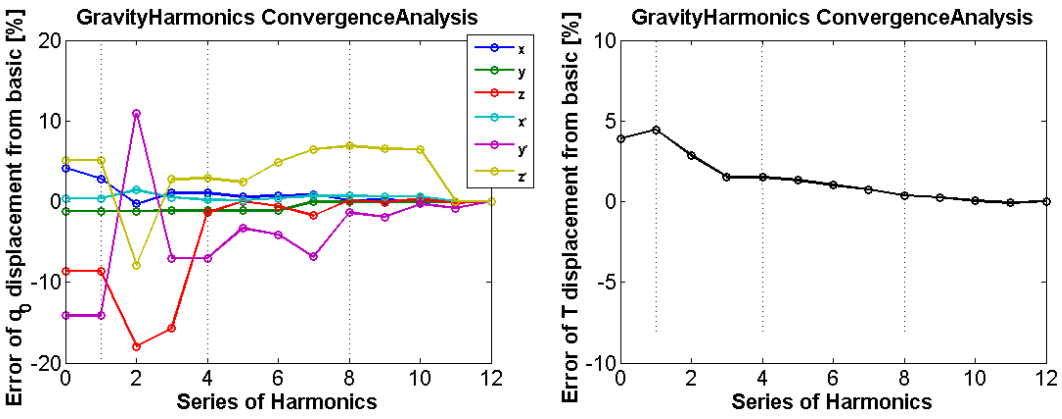

Figure 4.66: **Periodic LPOs in the Mars-Phobos CR3BP-GH.** Convergence analysis of the different dynamical substitutes in the partial CR3BP-GH of a medium-energy planar Lyapunov orbit around L_1 of the CR3BP. Percentage deviation of the initial conditions, on the chosen Poincaré map, and period. Dotted lines refer to increasing zonal harmonics degree starting from J_2.

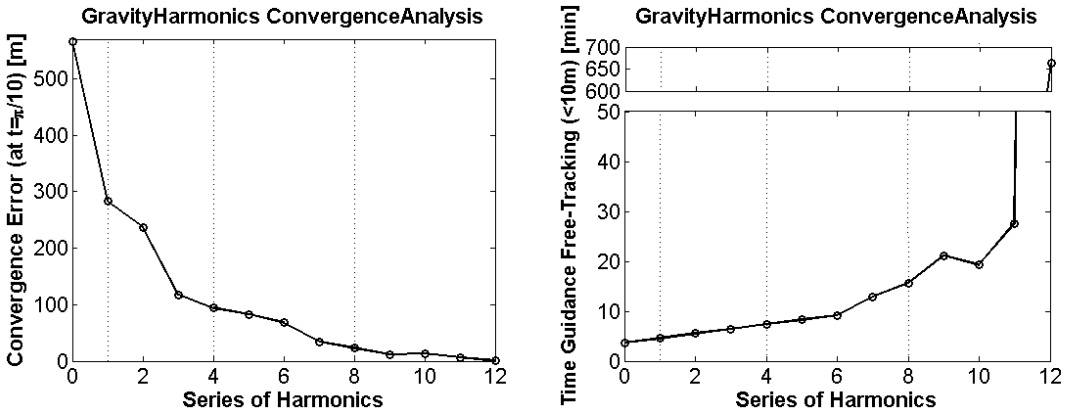

Figure 4.67: **Periodic LPOs in the Mars-Phobos CR3BP-GH.** Convergence analysis of the different dynamical substitutes in the partial CR3BP-GH of a medium-energy planar Lyapunov orbit around L_1 of the CR3BP. Simulation of the flow, from the initial condition of these solutions, in the full CR3BP-GH, and computation of the resulting deviation from their reference signal. Error of the position's magnitude after a fixed propagation time ($t = \pi/10$), and time of permanence (as number of periods) within a fixed error of position's magnitude ($10m$). Dotted lines refer to increasing zonal harmonics degree starting from J_2.

The related ancestor orbit in the CR3BP has been used as starting solution in a bundle of NCs, that provided the set of dynamical substitutes in a model with increasingly added GHs. Fig.4.65 shows the complete set of dynamical substitutes. It is clearly evident that the differences between the POs are still observable even at the last addition of a GH. This is further evident in Fig.4.66 where the static characteristics are plotted, such as the components of the initial condition. The period instead is less sensitive. Regarding the dynamical characteristics, Fig.4.68 shows that good convergence is achieved for the stable and unstable eigenvalues of the monodromy matrix, but not for the eigenvalues of the center manifold. This is confirmed also by Fig.4.69, where the eigenvectors of the latter manifold seems to have not been achieved a satisfying convergence. The IMs of the LPOs are instead reliable.

Compared to the case of the LPs in section 3.3.6.3, the outcome is that a worse convergence of 5% is achieved for both static and dynamical properties of the POs, in particular regarding the center manifold longitudinal to the PO. To have an idea of the price to pay, the set of dynamical substitutes found at each different degree and order have been simulated in the complete CR3BP-GH up to degree and order 4. This is presented in Fig.4.67. Considering the data at degree and order 3, station-keeping at a frequency of more than ten times per LPO's period (which would be about $20min$) is required to track the reference signal within $10m$.

4.2.3 2D-QPOs in the Mars-Phobos CR3BP-GH

In this section the computation of the families of dynamical substitutes of the Lissajous orbits, with the effect of the inhomogeneous gravity field of the secondary body, is addressed with the methodology of DST to identify invariant motions of section B.6.3.

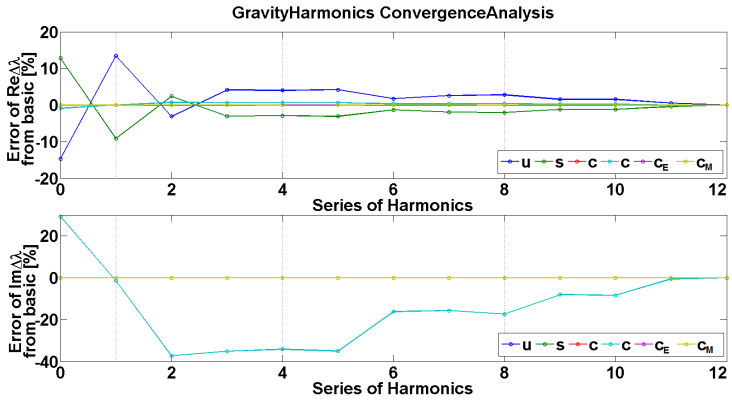

Figure 4.68: **Periodic LPOs in the Mars-Phobos CR3BP-GH.** Convergence analysis of the different dynamical substitutes in the partial CR3BP-GH of a medium-energy planar Lyapunov orbit around L_1 of the CR3BP. Percentage deviation of the eigenvalues of the derivative of the chosen Poincaré map. Dotted lines refer to increasing zonal harmonics degree starting from J_2.

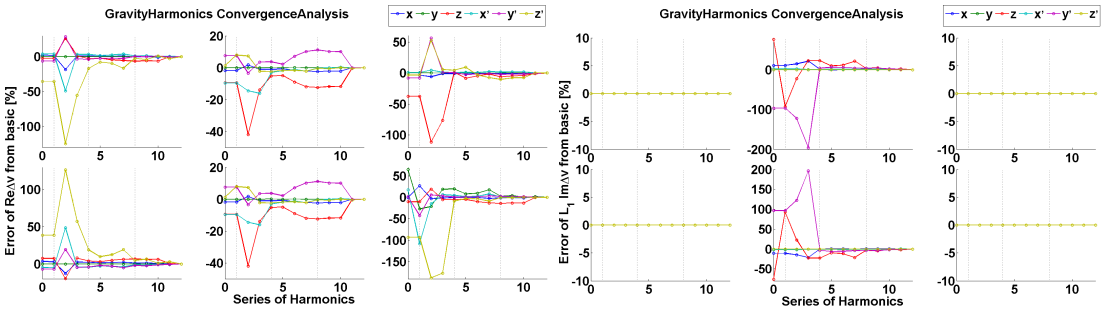

Figure 4.69: **Periodic LPOs in the Mars-Phobos CR3BP-GH.** Convergence analysis of the different dynamical substitutes in the partial CR3BP-GH of a medium-energy planar Lyapunov orbit around L_1 of the CR3BP. Percentage deviation of the eigenvectors of the derivative of the chosen Poincaré map. Dotted lines refer to increasing zonal harmonics degree starting from J_2.

The computation of the 2D-QPO around the backbone PO is provided by semi-analytical and numerical techniques. Since the periodic LPOs of the CR3BP-GH have been computed numerically, this would be the approach followed also for the Lissajous orbits around them. The numerical techniques for the computation of 2D-QPOs have been presented in section B.6.3, and they exploit their reduction in DST to an invariant closed curve of a suitable first-return map. Therefore, the approach is to use the standard techniques available in the literature, and they will be applied in this section to the periodic LPOs of the families A, B, and C computed in section 4.2.2, and for the vectorfield of the Mars-Phobos CR3BP-GH.

4.2.3.1 Computation of the Dynamical Substitutes of the Quasi-periodic LPOs in the Mars-Phobos CR3BP-GH

The Lissajous orbits around the periodic LPOs with central part of the CR3BP-GH are computed with the LMS fitting methodology presented throughout section B.6.3, that

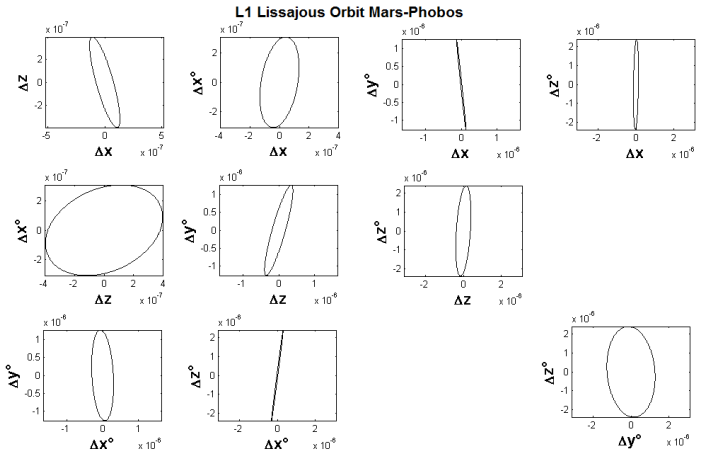

Figure 4.70: **Quasi-periodic LPOs in the Mars-Phobos CR3BP-GH.** Invariant curve's projections on the Poincaré map's coordinate planes of the linear quasi-periodic solution around a medium-energy PO of the family A around L_1 of the CR3BP-GH (at $\gamma = 4.2 \cdot 10^{-8}$, which is 10^{-3} of the maximum distance of the backbone PO from L_1). Coordinates frame in normalized units and centered on the initial condition of the PO on the chosen Poincaré map.

is based on the description of their invariant curve by Fourier analysis. In particular, it has been chosen to follow the approach used to compute the initial condition of the associated POs, thus the invariant curve is expressed on a Poincaré map, whose surface of section is $g(\mathbf{x}) = y - y_{LP}$.

The choice of the number of Fourier coefficients $2N_C + 1$ and sample points N_S, to discretize the invariant curve, depends on its morphology. A fixed ratio of 80% between the two has been used for all the orbits computed, and from 40 to 80 coefficients have been required to describe the invariant object.

Regarding the choice of the invariant curve's parametrization, in this thesis the physical parameter of [120] has been used, which is the polar anomaly ϑ between two curve's components. The choice of the latter ones is undertaken plotting the initial guess that will be used by the numerical scheme, which is the linear solution around the invariant point of the PO on the map of Eq.B.81. An example of the different projections given by the initial guess is provided in Fig.4.70.

Finally, the procedure used is the one discussed in section B.6.3.3, and the DC scheme used to compute a 2D-QPO with small-amplitude around the PO is presented in Eq.B.108. An applicative example of the procedure is given in Fig.4.71 and Fig.4.73. This is done for a sample of POs along each family of both LPs of the CR3BP-GH. As explained in section B.6.3.3.7, the DC scheme is embedded in a NC with respect to the width w of the invariant curve, to provide all the family of iso-energetic invariant tori around the sampled PO. A related applicative example of the NC is given in Fig.D.35-4.72. These tori are further sampled along their width to discretize the family of continuous 2-parameter 2D-QPOs of the Mars-Phobos CR3BP-GH. For each of them, the QPO is simulated by iterative mappings as expressed in section B.6.4, deriving its rotation number's profile. A related example is given in Fig.4.75-4.76. Using

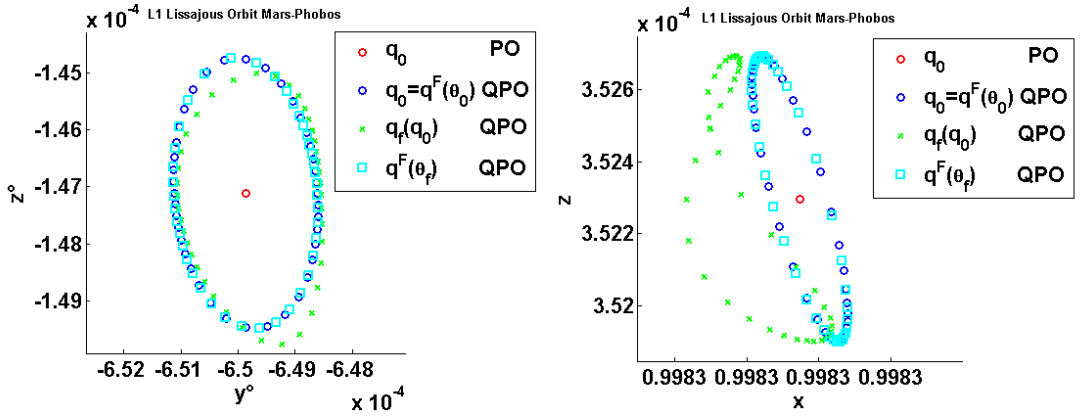

Figure 4.71: **Quasi-periodic LPOs in the Mars-Phobos CR3BP-GH.** Procedure of the DC scheme for computing a QPO around a PO of a NL dynamical system, as described in section B.6.3.3. The invariant curve on the Poincaré map around the initial condition of the backbone PO (q_0) is described as a Fourier series expansion (q^F) function of a chosen parametrization variable (θ, in this case the polar anomaly around the PO on a chosen couple of coordinates). An initial guess for the Fourier coefficients is used, and a cluster of initial conditions (q_0, function of an independent set of parameters θ_0) is obtained, to describe the initial curve. The multiple initial conditions are propagated in the NL dynamics to find their first-return condition on the Poincaré map (q_f): this cluster of points describes the first-return curve. Being the parametrization invertible, the related set of parameters (θ_f) are obtained. The Fourier series expansion is evaluated with this new set of parametrization variables: the related cluster of points is the projection of the first-return curve on the initial curve. The DC algorithm drives the two curves to correspond with each other, which is to erase the error between first-return and projected curve. When this happens, the Fourier series expansion effectively describes an invariant curve, and therefore a QPO. The graphs show two Poincaré map coordinate planes: the one whose coordinates provide the parametrization variable, and the one on the remaining position coordinates x-z (y is fixed by the chosen Poincaré map definition). Case of a medium-width QPO around a medium-energy PO of the family A around L_1 of the CR3BP-GH.

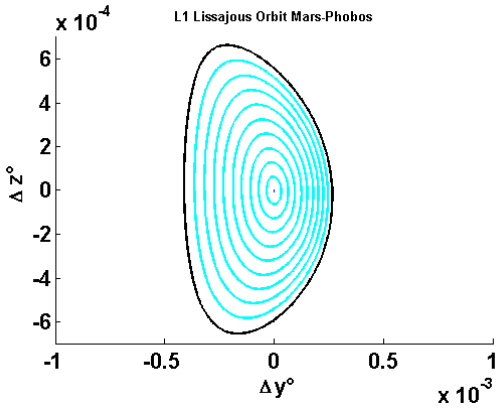

Figure 4.72: **Quasi-periodic LPOs in the Mars-Phobos CR3BP-GH.** Family of invariant curves projected on a Poincaré map coordinate plane. Continuation of QPOs around a medium-energy PO of the family A around L_1 of the CR3BP-GH.

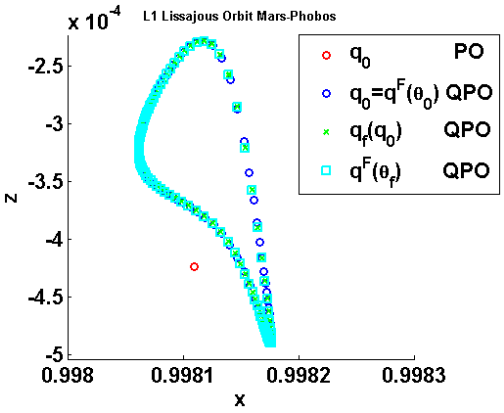

Figure 4.73: **Quasi-periodic LPOs in the Mars-Phobos CR3BP-GH.** Final iteration of the DC of a large-width QPO around a medium-energy PO of the family A around L_1 of the CR3BP-GH, showing the convergence of the first-return curve towards the projected curve on a coordinate plane.

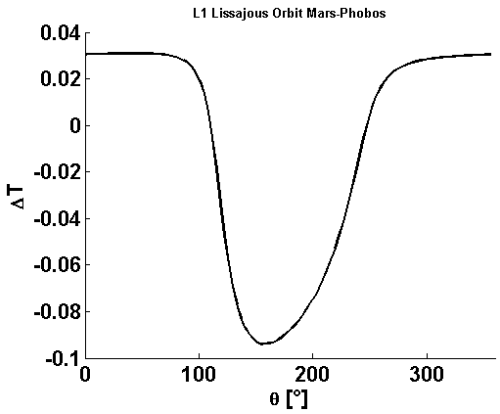

Figure 4.74: **Quasi-periodic LPOs in the Mars-Phobos CR3BP-GH.** DC of a large-width QPO around a medium-energy PO of the family A around L_1 of the CR3BP-GH. Time of first-return (difference with respect to the backbone PO's period) of the invariant curve.

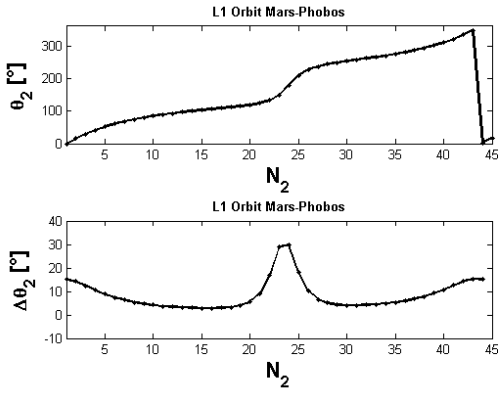

Figure 4.75: **Quasi-periodic LPOs in the Mars-Phobos CR3BP-GH.** Simulation of a large-width QPO around a medium-energy PO of the family A around L_1 of the CR3BP-GH. Invariant curve' parameter profile along time, and related rotation number's profile along time. Integration up to the time (in units of the backbone PO's period) of the first transversal revolution of the 2-torus.

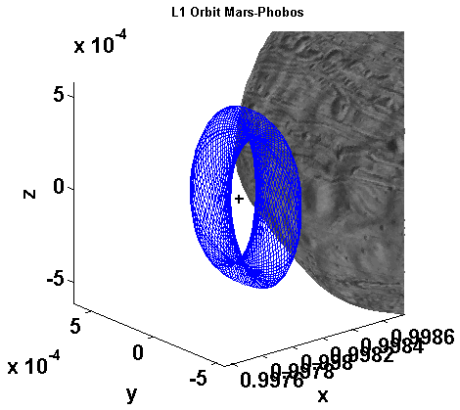

Figure 4.76: **Quasi-periodic LPOs in the Mars-Phobos CR3BP-GH.** Simulation of a large-width QPO around a medium-energy PO of the family A around L_1 of the CR3BP-GH. Trajectory integrated up to the time of the first transversal revolution of the 2-torus.

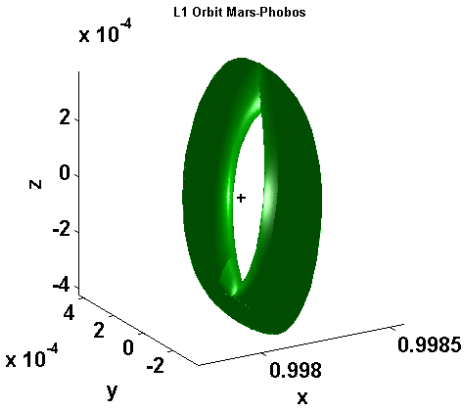

Figure 4.77: **Quasi-periodic LPOs in the Mars-Phobos CR3BP-GH.** Simulation of a large-width QPO around a medium-energy PO of the family A around L_1 of the CR3BP-GH. Surface of motion of the 2-torus.

this, the simulation is performed up to the period of the first transversal revolution. This allows one to represent the QPO as a closed surface of motion in Fig.4.77-4.81.

An example of the family of 2-tori A and B is shown in Fig.4.82, and in Fig.4.83 for the family C. The related invariant curves are represented in Fig.D.36-D.37 for L_1, and Fig.D.38-D.38 for L_2. Similarly to the CR3BP for the two Lyapunov families, the 2-tori of the families A and B of POs are connected to each other because they are part of the same 4D center manifold originating from the EP, as shown in Fig.4.82. Their invariant curves move from one PO to the iso-energetic PO of the other fam-

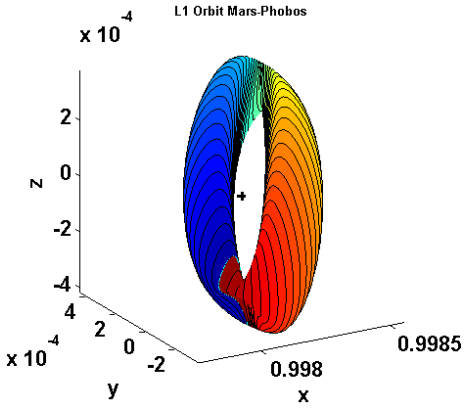

Figure 4.78: **Quasi-periodic LPOs in the Mars-Phobos CR3BP-GH.** Simulation of a large-width QPO around a medium-energy PO of the family A around L_1 of the CR3BP-GH. Surface of motion of the 2-torus parameterized by the transversal invariant curves of the stroboscopic maps around the backbone PO. Initial invariant curve displayed.

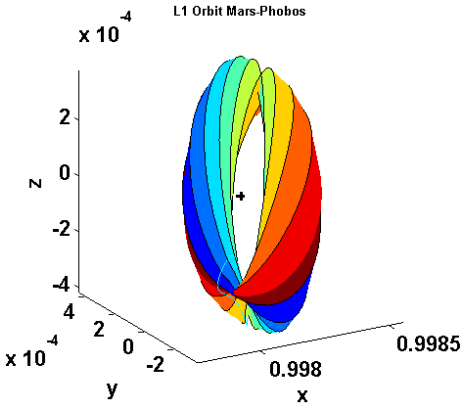

Figure 4.79: **Quasi-periodic LPOs in the Mars-Phobos CR3BP-GH.** Simulation of a large-width QPO around a medium-energy PO of the family A around L_1 of the CR3BP-GH. Surface of motion of the 2-torus parameterized by the longitudinal invariant curves of the initial Poincaré map around the backbone PO. Initial invariant curve displayed.

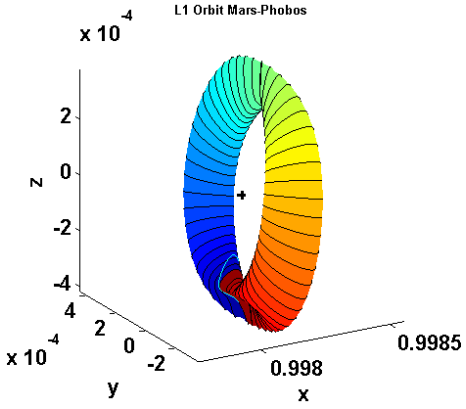

Figure 4.80: **Quasi-periodic LPOs in the Mars-Phobos CR3BP-GH.** Simulation of a large-width QPO around a medium-energy PO of the family A around L_1 of the CR3BP-GH. Surface of motion of the 2-torus parameterized by the transversal invariant curves of the tangential Poincaré maps around the backbone PO. Initial invariant curve displayed.

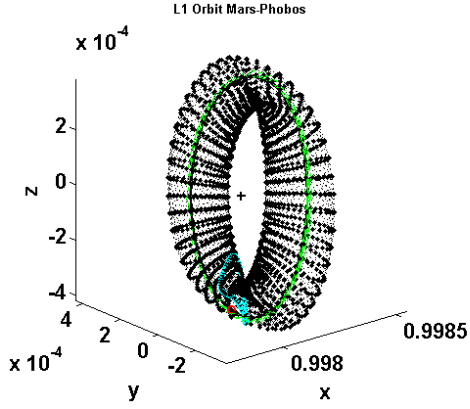

Figure 4.81: **Quasi-periodic LPOs in the Mars-Phobos CR3BP-GH.** Simulation of a large-width QPO around a medium-energy PO of the family A around L_1 of the CR3BP-GH. Surface of motion of the 2-torus parameterized by the transversal invariant curves of the tangential Poincaré maps around the backbone PO. Initial invariant curve and backbone PO (with initial conditions and velocity vectors) displayed.

ily, as shown in Fig.4.82,D.36. Thus, they constitute a single family AB of 2D-QPOs, with two branches A and B. However, as we see in Fig.D.36-D.40, it is not possible to compute the complete 2-parameter family with a single NC from one family of POs, because this process does not provide invariant curves with the requirements needed by the parametrization used. The invariant curves transit from one center point to another on the map, and the NC along the transversal families of QPOs irremediably stops, as the DC fails to converge due to a deep twisting of the invariant curve. This is discussed in section B.6.3.3, and it is the principal drawback of the invariant curve's parametrization choice of [120], and could not be avoided even by a better choice of the Poincaré section[16], due to the lack of symmetries of the CR3BP-GH as a difference from the classical CR3BP [115, 52].

As discussed in section B.6.3.3, alternative numerical schemes have been developed in the literature. In particular, with the aim of investigating the possible application of an universal parametrization, a DC scheme for computing invariant curves parameterized by the normalized arclength, has been developed in section B.6.3.3. However, despite the analytical part seems corrects, the DC scheme cannot be embedded in a NC because its Jacobian is singular at each root. In conclusion, since the missing subset of QPOs is not wide, no further implementations have been tested. This because, for the application of the quasi-periodic LPOs around Phobos, a sampling along the width for the post-processing is anyway needed, as said before. For this purpose, due to the uncontrollable stopping condition of the NC, the width of the transversal families of QPOs is normalized from 0 to 1, as a ratio with respect to its maximum value, achievable by the NC. Thus, the transversal parameter of the AB family ranges from 0 to 2, where the first half is related to the branch A, and the second corresponds to the branch B, whose parametrization is flipped from 2 to 1.

4.2.3.2 The Quasi-periodic LPOs of the Mars-Phobos CR3BP-GH

The 2D-QPOs in the Mars-Phobos CR3BP-GH have been derived with the choices of section 4.2.3.1. A summarizing example of the related 2-parameter families AB and C, around each LP, is showcased in Fig.4.84 and Fig.4.82-4.83.

The simulation of a sample of these 2D-QPOs, for each family, allows to display the period of the first transversal revolution in Fig.D.41-D.44. It is evident how the prediction of the rotation number of the linear solution is mostly appropriate for small-width invariant curves. It is worth highlighting that the time to fill the surface of the torus is very high (nearby 100 longitudinal revolutions) for small-energy LPOs, while it becomes very fast for large orbits. For these 2D-QPOs, cases of resonances with high denominator showed up, and these LPOs are actually POs with period higher than the Phobos' revolution.

[16] The plane $z = z_{LP}$ could have been more distant from the twist of the torus, but this has not been proved.

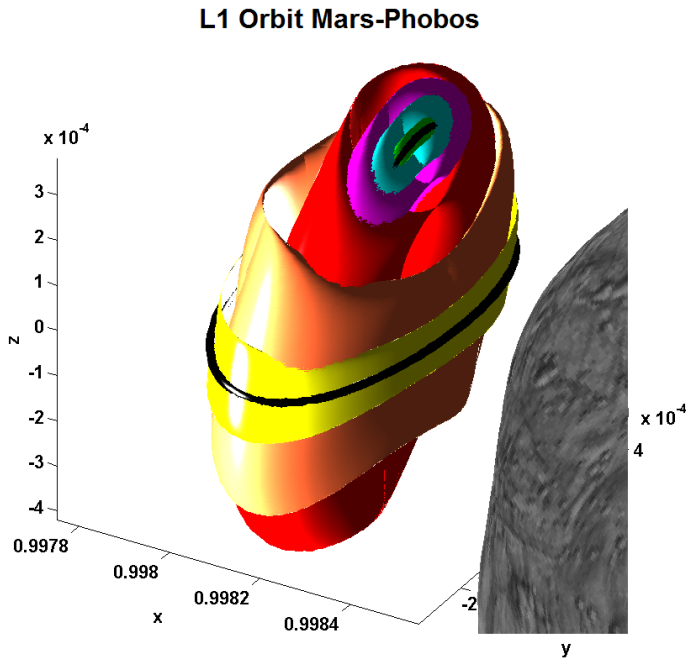

Figure 4.82: **Quasi-periodic LPOs in the Mars-Phobos CR3BP-GH.** Family of QPOs that connects the two medium iso-energetic POs of the A and B families around L_1 of the CR3BP-GH. Related two backbones POs displayed in black.

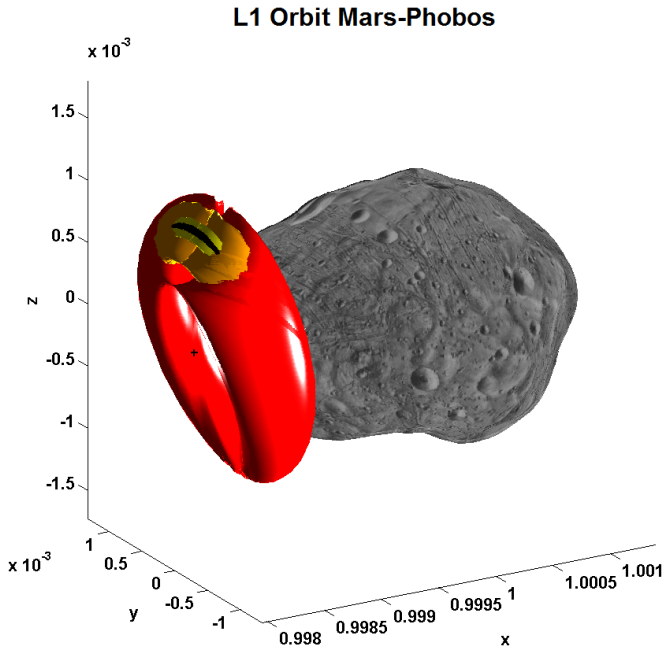

Figure 4.83: **Quasi-periodic LPOs in the Mars-Phobos CR3BP-GH.** Family of QPOs around a medium-energy PO of the C family around L_1 of the CR3BP-GH. Related backbone PO displayed.

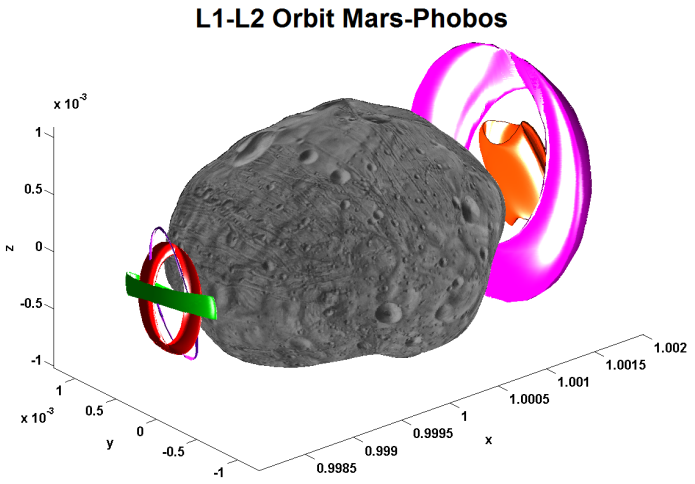

Figure 4.84: **Quasi-periodic LPOs in the Mars-Phobos CR3BP-GH.** Graphical visualization of 2-tori in the CR3BP-GH of different size and width around the LPs. Summarizing examples: three medium-size QPOs of family AB (red and green with small-width, orange with high-width) and two high-width QPOs of family C (of small and large-size). Shape harmonics series expansion for Phobos' surface.

To perform the stability analysis for the QPOs, the method of [120] is modified in section B.6.5 in order to provide a 1-1 mapping of the invariant curve in the Fourier coefficients space. This algorithm was tested by computing the quasi-periodic LPOs in the CR3BP-GH, as was done in section 4.2.3.1, and with the same invariant curve's parametrization. The application was successful and provided the same exact outcomes (same residual errors on the NC steps) of the first method employed before. However, it is not recommendable to use this method for the computation of the QPOs, because the generation of its map requires the computation of the full inverse of a large-scale left pseudo-inverse matrix with dimension $2N_C + 1$, requiring far more computational time than the previous one. However it provides, as a byproduct, a monodromy-like matrix Π for the stability analysis of the QPO. Thus this method is used afterwards, when the solution has already been derived with the first technique, to singly compute the map, and the related Π, for one 2D-QPO.

As discussed in section B.6.5, the eigenvalues for an invariant curve are organized in circles on the complex plane, and the Floquet linear stability is therefore given by their magnitude. An example of the set of eigenvalues is provided in Fig.4.85. It is evident the effect of the spurious eigenvalues introduced in section B.6.5. The stability properties of the families of 2D-QPOs are identical to the ones of the family of their backbone POs, which is a saddle $\times$ center $\times$ center structure of their manifolds.

The related eigenvectors are defined in the space of the Fourier coefficients. As discussed in section B.6.5, the problem of the spurious eigenvalues requires to identify the most accurate, amongst all multiple eigenvectors, to represent the related manifold. The selection is conducted with the norm-(1) defined in Eq.B.125. An example of the selection process is presented in Fig.4.86.

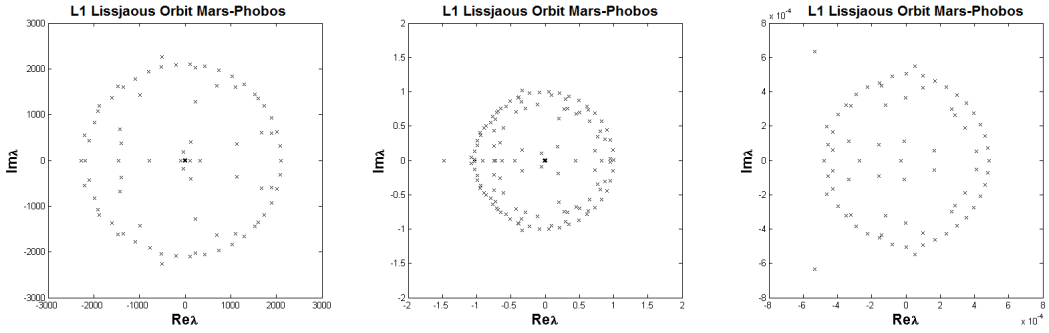

Figure 4.85: **Quasi-periodic LPOs in the Mars-Phobos CR3BP-GH.** Stability analysis. Set of eigenvalues of the invariant curve of the Poincaré map. Case of a high-width - medium-energy QPO of the family A around L_1 of the CR3BP-GH. Each of the subfigures specifically magnifies the area of the unstable, central and stable manifolds.

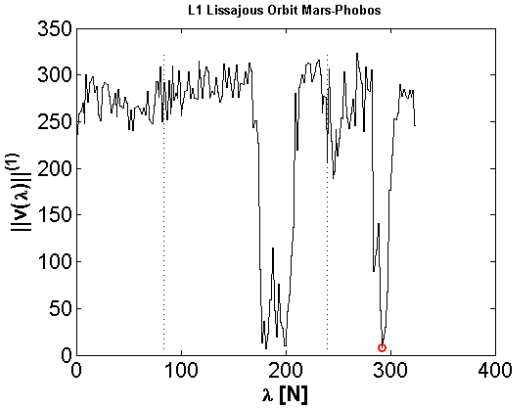

Figure 4.86: **Quasi-periodic LPOs in the Mars-Phobos CR3BP-GH.** Norm-(1) of the set of eigenvectors of the invariant curve of the Poincaré map. Case of a high-width - medium-energy QPO of the family A around L_1 of the CR3BP-GH. Dotted lines mark stable, central and unstable subset of the total eigenspace, where the eigenvectors are ordered by the related eigenvalue's magnitude. Point highlighted identifies the eigenvalue with the minimum norm-(1) of the unstable subset, that will be used for the computation of the unstable IMs.

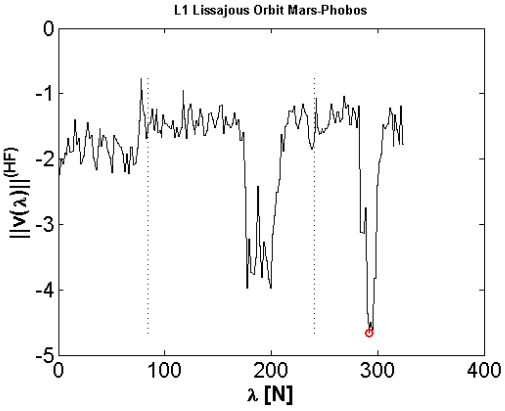

Figure 4.87: **Quasi-periodic LPOs in the Mars-Phobos CR3BP-GH.** Norm-(HF), in logarithmic scale, of the set of eigenvectors of the invariant curve of the Poincaré map. Case of a high-width - medium-energy QPO of the family A around L_1 of the CR3BP-GH. Dotted lines mark stable, central and unstable subset of the total eigenspace, where the eigenvectors are ordered by the related eigenvalue's magnitude. Point highlighted identifies the eigenvalue with the minimum norm-(1) of the unstable subset, that will be used for the computation of the unstable IMs.

4.2.4 IMs of the LPOs in the Mars-Phobos CR3BP-GH

All the families of periodic and quasi-periodic LPOs of the Mars-Phobos CR3BP-GH are unstable, therefore they are associated with stable and unstable IMs to reach and depart them. The family D of POs is characterized by a saddle × saddle × center manifold, but the second unstable Floquet multiplier is quite small (still about 2), and so the time of flight to travel around these additional four branches of hyperbolic IMs is significantly high. Therefore, the computation of these IMs is not considered in this thesis.

The computation of IMs' tubes has been addressed for a general dynamical system in section B.8 for each type of invariant motion, based on the dimension of its phase-space. Following this, this section presents the IMs of the periodic (families A, B, CD) and quasi-periodic (families AB, C) LPOs, computed in sections 4.2.2-4.2.3, of the Mars-Phobos CR3BP-GH.

4.2.4.1 Computation of the IMs of the LPOs in the Mars-Phobos CR3BP-GH

The computation and the analysis of the stable and unstable IM of the families of POs and 2D-QPOs, that do not intersect Phobos, run parallel to the one carried out in section 4.1.5 for the IMs in the CR3BP. Only the computation of the inside branch is addressed in this section, and the globalization of the manifold is propagated in the CR3BP-GH up to the intersection with Phobos' surface. Coherently with the consideration of the inhomogeneous gravity field of the moon in the orbital dynamics, the surface of Phobos is now modeled with the high-order shape harmonics of section 3.2, that constitutes a kind of complex Poincaré section's constraint. In particular, Eq.3.15 presents the formula for the normal of the surface.

Since the CR3BP-GH does not have any symmetries, the computation of the stable IM of the LPOs must be carried out specifically, as a difference from section 4.1.5, where the stable tube was symmetrical to the unstable IM with respect to x-z plane.

The globalization of the stable and unstable IMs has directly intersected Phobos for all the families of LPOs, for both LPs. Therefore, as done in section 4.1.5.1, the outcomes are presented on the topographical map of Phobos, parameterized by the couple of longitude and latitude of the landing/take-off site. The performances at the touch-down are then filtered by the case of minimum incidence for the unstable IM, which is a tangential arrival, and by the case of minimum velocity's total magnitude for the stable IM, that represents the minimum escape velocity.

IMs of the families of POs. The computation of the IMs of the POs is done exactly in the same way of the CR3BP, and they are showcased in Fig.4.88.

Fig.4.89-4.90 provide a sample of the analysis for the family A around L_1. Fig.D.45-D.46 provide the landing performances for L_1, and Fig.D.47-D.48 provide the ones for

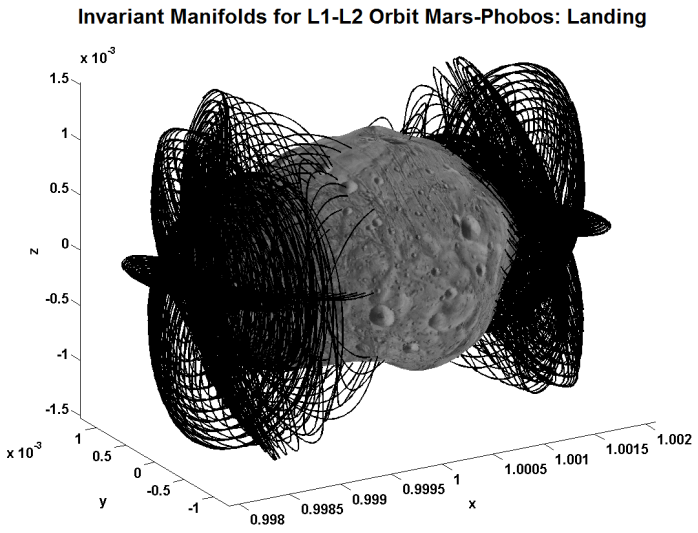

Figure 4.88: **Landing on Phobos through the Invariant Manifold of the L_{1-2} periodic LPOs of the Mars-Phobos CR3BP-GH.** Trajectories of the inside branch of the IMs from the families A, B, CD of POs. Phobos real shape.

L_2.

Fig.D.49-D.50 provide the take-off performances for L_1, and Fig.D.51-D.52 provide the ones for L_2.

Due to the significant difference in the morphology of the families of LPOs, as well as the consideration of the real inhomogeneous surface of the moon, the outcomes obtained show considerable changes in the footprint of the IMs on Phobos, with respect to the one obtained with the POs in the CR3BP. However, the range of touch-down performances is still the same, and the considerations are specular to what was discussed in section 4.1.5.1. In particular, it is still possible to arrive with very low vertical velocity, and depart with considerable less cost than the 2B Δv.

IMs of the families of 2D-QPOs. In contrast with what was done in section 4.1.5.1, where the Lissajous orbits were computed with a semi-analytical approach, the numerical technical developed in section B.6.5 allows to derive the IMs of the whole invariant object. The related procedure to compute the IMs is addressed in section B.8.3. In particular, it requires the selection of the most accurate eigenvector for each manifold, and an example of the procedure is provided in section 4.2.3. The related eigenvector acts in the Fourier coefficients space, therefore it provides a closed curve of initial conditions on the Poincaré map, for the globalization of the manifold. This requires the introduction of a further threshold ε_C, which is set to be 10^{-3} of the width of the invariant curve. An example is given in Fig.4.91. Due to the proximity of Phobos, to not invalidate the whole tube of IMs for high-width and high-energy orbits, the IMs are considered valid if the related starting point on the QPO will not intersect Phobos for a longitudinal revolution of the orbit.

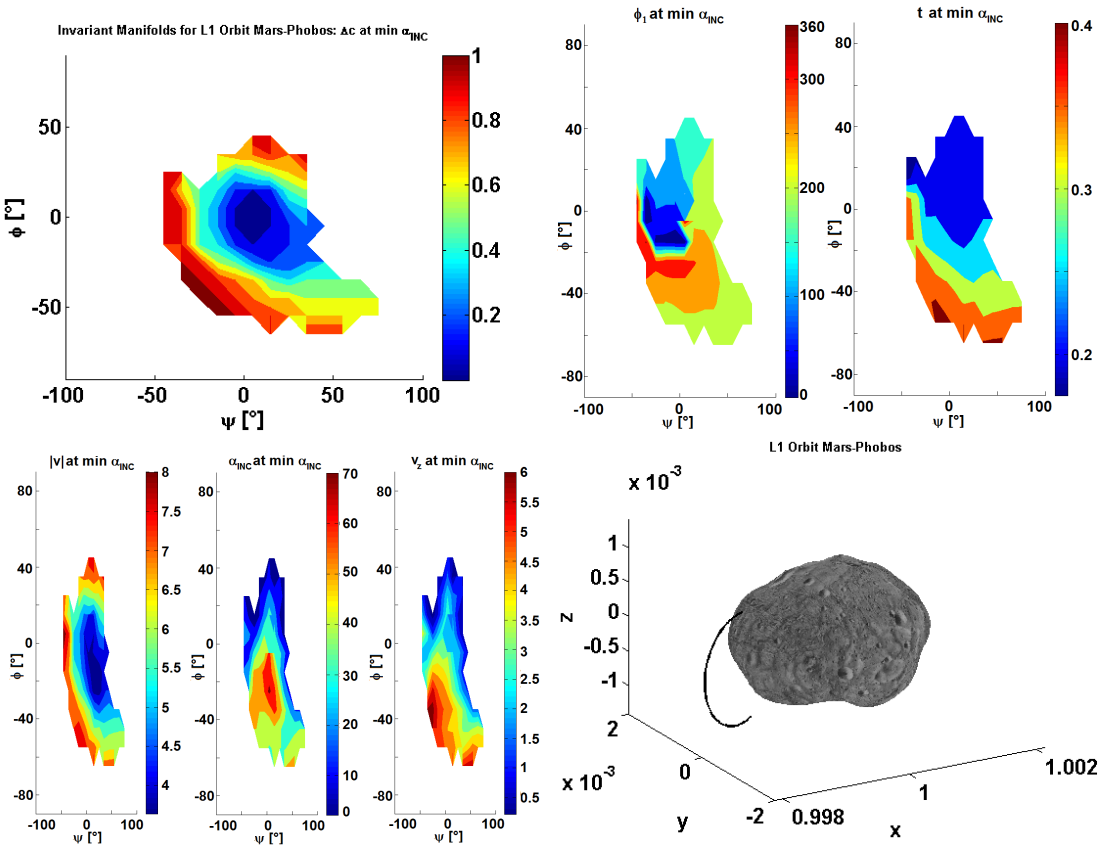

Figure 4.89: **Landing on Phobos through the Invariant Manifold of the L_1 family A of periodic LPOs of the Mars-Phobos CR3BP-GH.** Trajectories that provide the min incidence at the touch-down, as a function of the longitude and latitude of the landing site, for orbits that do not intersect Phobos' real shape. Performances of the trajectory: energy parameter of the family, initial phase along the departing orbits, TOF, and landing velocity magnitude, angle of incidence, downward vertical velocity. Trajectory that provides the overall min incidence at the touch-down.

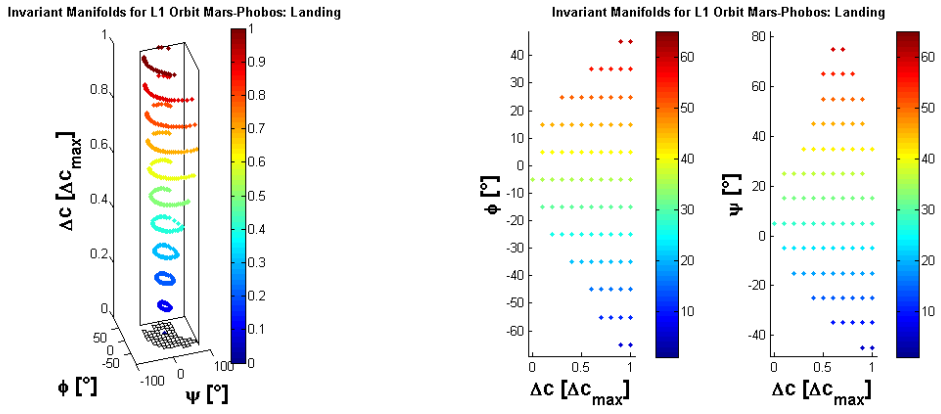

Figure 4.90: **Landing on Phobos through the Invariant Manifold of the L_1 family A of periodic LPOs of the Mars-Phobos CR3BP-GH.** Direct and inverse relation between the longitude and latitude of the landing site and the energy parameter of the family, for orbits that do not intersect Phobos' real shape.

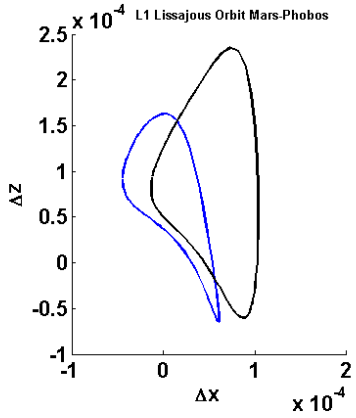

Figure 4.91: **Landing on Phobos through the Invariant Manifold of the L_1 family A of quasi-periodic LPOs of the Mars-Phobos CR3BP-GH.** Poincaré map's projection on a coordinate plane. Case of a high-width - medium-energy QPO of the family A around L_1 of the CR3BP-GH. The blue curve is the invariant curve of the QPO, and the black curve is the related set of initial condition of the inside branch of the unstable IM (for a magnified threshold ε_C =1%).

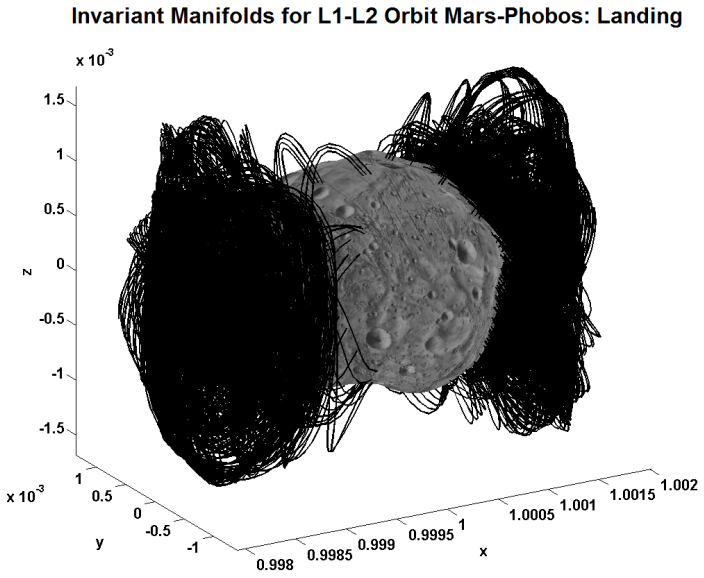

Figure 4.92: **Landing on Phobos through the Invariant Manifold of the L_{1-2} quasi-periodic LPOs of the Mars-Phobos CR3BP-GH.** Trajectories of the inside branch of the IMs from the families AB, C of QPOs. Phobos real shape.

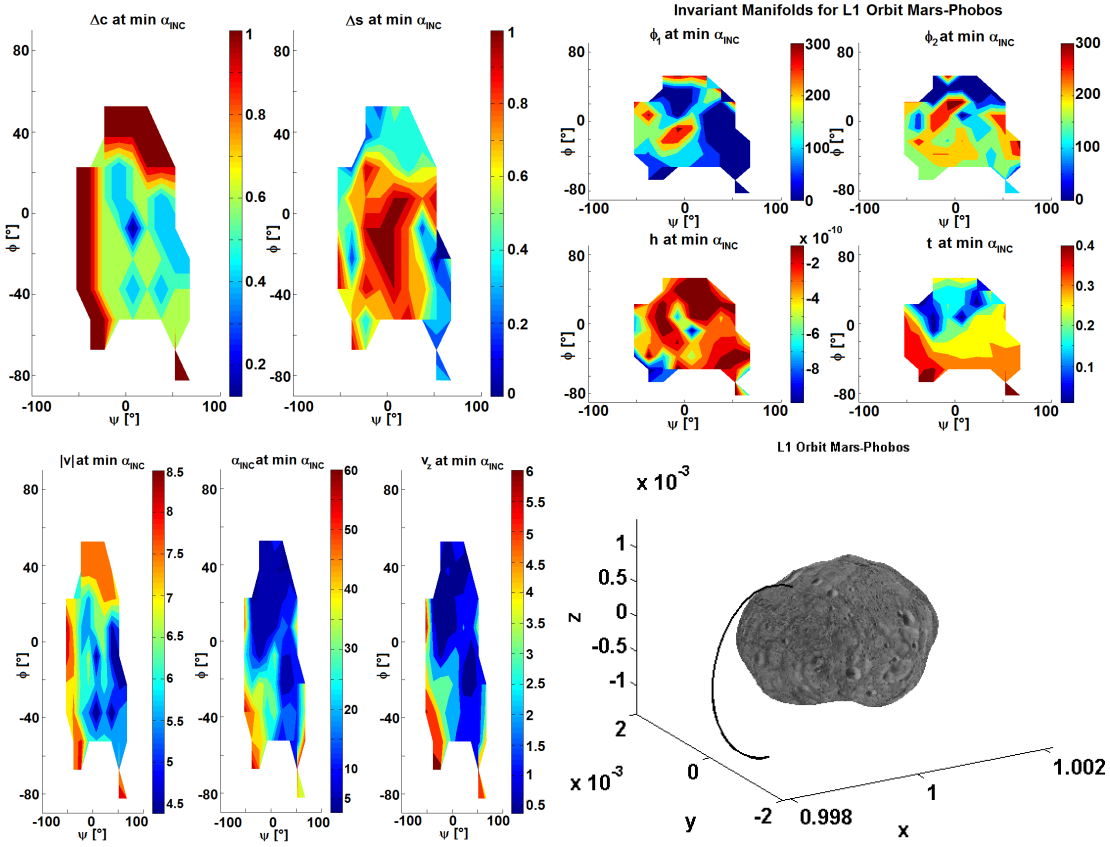

Figure 4.93: **Landing on Phobos through the Invariant Manifold of the L_1 family A of quasi-periodic LPOs of the Mars-Phobos CR3BP-GH.** Trajectories that provide the min incidence at the touch-down, as a function of the longitude and latitude of the landing site, for orbits that do not intersect Phobos' real shape. Performances of the trajectory: energy and width parameters of the family, initial longitudinal and transversal phases along the departing orbit, altitude where the integration is stopped, TOF, and landing velocity magnitude, angle of incidence, downward vertical velocity. Trajectory that provides the overall min incidence at the touch-down.

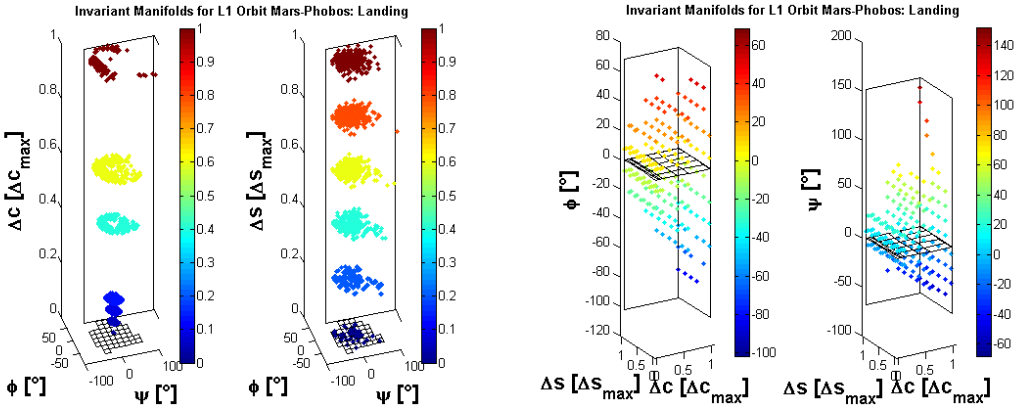

Figure 4.94: **Landing on Phobos through the Invariant Manifold of the L_1 family A of quasi-periodic LPOs of the Mars-Phobos CR3BP-GH.** Direct and inverse relation between the longitude and latitude of the landing site and the energy and width parameters of the family, for orbits that do not intersect Phobos' real shape.

The IMs of the families of 2D-QPOs in the CR3BP-GH are computed with this new approach, and they are represented in Fig.4.92.

Fig.4.93-4.94 provide a sample of the analysis for the family A around L_1. Fig.D.53-D.54 provide the landing performances for L_1, and Fig.D.55-D.56 provide the ones for L_2.

Fig.D.57-D.58 provide the take-off performances for L_1, and Fig.D.59-D.60 provide the ones for L_2.

The footprints of the IM's tubes on Phobos obtained are very different from that of the Lissajous orbits in the CR3BP. However, the range of touch-down performances is still the same, and the considerations are specular to what was discussed in section 4.1.5.1. In particular, it is still possible to arrive practically horizontal and with vertical velocities less than $0.5m/s$, and depart with escape velocities smaller than $4m/s$ in an extended region of sites. Furthermore, the large craters and grooves of Phobos are inside these natural regions, and their distribution appears to follow the boundaries of the natural IM's footprints.

In conclusion, this analysis showed that also in the more accurate CR3BP-GH, all the inside branch of the IMs of the new LPOs in this system intersects Phobos. This further demonstrates that no homoclinic nor heteroclinic connections of the two LPs manifolds exist around Phobos.

4.3 LPOs in the Mars-Phobos ER3BP-GH

Following the introduction of section 4.2, the LPOs computed in the intermediate CR3BP-GH are used as starting solutions to derive in this section their dynamical substitute in the ER3BP-GH. This model has been derived in section 3.4, to consider the real elliptic orbit of Phobos around Mars, and represents the more accurate dynamical system of the relative orbital dynamics around Phobos.

This section presents the methodology used and the results obtained by computing the dynamical substitutes of the LPOs from the model of Eq.3.37 to the system described by Eq.3.50. The ER3BP-GH is a time-variant dynamical system that can be expressed as the sum of its conservative vectorfield (the CR3BP-GH in the Hill's frame) plus a forcing term (the elliptic perturbation). It is well-known that the general solution of such ODEs consists of a homogeneous term, sum of the normal modes of the conservative part, plus a particular solution, dependent on the kind of forcing term. The elliptic perturbation on the CR3BP-GH, in Eq.3.50, is a function of ν, and it is a periodic signal at the orbital frequency of the primaries: the particular solution is a signal at the same frequency[17]. This means that the solutions of the elliptic dynamics in the phase-space have one phase constrained to follow the dynamics of $\nu(t)$, which is appended in the vectorfield and so explicitly retrievable from the integration of the

[17] In the normalized units of the ER3BP-GH, the forcing pulsation of the LPOs is unity.

equations of motion of Eq.3.50.

The dynamical substitutes of the LPOs in the Mars-Phobos ER3BP-GH will be computed with the technique of NC. The general approach used for all the LPOs is presented in section 4.3.1. The procedure undertaken is differentiated by the phase-space dimension of the invariant solutions. As the perturbation of Phobos' eccentricity is time-variant in the Phobos' Hill's frame, the NC of the LPOs of the CR3BP-GH increments by one their phase-space and produces dynamical substitutes in the ER3BP-GH that oscillate around the original orbits with a forcing period 2π.

Section 4.2.1 presents the POs of the ER3BP-GH, which consist of the dynamical substitutes of the LPs, and the resonant POs of the CR3BP-GH. Section 4.2.2 focuses on the dynamical substitutes of the POs of the CR3BP-GH, and section 4.2.3 focuses on the dynamical substitutes of the 2D-QPOs of the CR3BP-GH. Finally, in section 4.2.4 the invariant manifolds of these invariant motions are presented.

4.3.1 NC between the Dynamical Models of the CR3BP-GH and the ER3BP-GH

The vectorfield of the ER3BP-GH of Eq.3.50 is a natural homotopy with respect to the eccentricity.

$$\dot{\mathbf{x}} = \mathbf{f}_{\mathbf{ER3BPGH}}(\mathbf{x}) = \mathbf{h}(\mathbf{x}, e) \rightarrow \boldsymbol{\phi}_{\mathbf{h}}(t, \mathbf{x}, e) \tag{4.40}$$

The time-dependency that makes the problem non-autonomous is included in all the terms that depend on the true anomaly, which are all scaled by the eccentricity. In particular remark that a negative eccentricity produces a system where the flow corresponds to the one that is produced by the eccentricity's absolute value, but with a shift of π of the initial condition of ν, since $\dot{\nu} = \omega_z(\nu)$.

The dynamical substitutes of the invariant solution of the CR3BP-GH are derived with a classical numerical procedure, used in-depth in the literature for computing LPOs in the ER3BP. This is a NC between the circular and the elliptic dynamics, similar to the one undertaken in section 4.2.2, where the continuation parameter is set to be the eccentricity, which is implicitly defined in the flow of Eq.4.40 through the vectorfield.

The addition of the explicit dynamics of the true anomaly in the vectorfield of Eq.3.50 is motivated in section B.1.2.4. This trick is used in time-variant dynamical systems to retrieve the sensitivity of the flow with respect to the initial time. For this reason, the additional components of the augmented 7×7 Jacobian of the vectorfield are needed, and they are stated below.

$$\begin{cases} \mathbf{a}_{/\nu}(\nu) = -2\,(1-\mu)\,\frac{(1+e\cos\nu)e\sin\nu}{(1-e^2)^{3/2}}\begin{bmatrix}1\\0\\0\end{bmatrix} \\ \omega_{z/\nu}(\nu) = -2\frac{(1+e\cos\nu)e\sin\nu}{(1-e^2)^2} \rightarrow \mathbf{W}_{/\nu}(\nu) = -2\frac{(1+e\cos\nu)e\sin\nu}{(1-e^2)^2}\begin{bmatrix}0\\0\\1\end{bmatrix}\wedge \\ \mathbf{Y}_{/\nu}(\nu) = \left(6\frac{(1+e\cos\nu)^2e^2\sin^2\nu}{(1-e^2)^3} - 2\frac{(1+e\cos\nu)^3e\cos\nu}{(1-e^2)^3}\right)\begin{bmatrix}0\\0\\1\end{bmatrix}\wedge \\ \mathbf{P}_{/\nu}(\nu) = -4\frac{(1+e\cos\nu)^3e\sin\nu}{(1-e^2)^3}\left(\begin{bmatrix}0\\0\\1\end{bmatrix}\wedge\right)^2 \\ \mathbf{H}(\mathbf{q},\nu) = u_{G1/\mathbf{qq}}(\mathbf{q},\nu) + u_{G2/\mathbf{qq}}(\mathbf{q}) \\ \mathbf{f}_{G1/\nu}(\nu) = u_{G1/\mathbf{q}\nu}(\mathbf{q},\nu) = \frac{1-\mu}{\left\|\mathbf{q}+\frac{1-e^2}{1+e\cos\nu}\begin{bmatrix}1\\0\\0\end{bmatrix}\right\|^5}\frac{\left(1-e^2\right)e\sin\nu}{(1+e\cos\nu)^2}\begin{bmatrix}2\left(x+\frac{1-e^2}{1+e\cos\nu}\right)^2-y^2-z^2\\3\left(x+\frac{1-e^2}{1+e\cos\nu}\right)y\\3\left(x+\frac{1-e^2}{1+e\cos\nu}\right)z\end{bmatrix} \end{cases} \tag{4.41}$$

Furthermore, the sensitivity of the flow of Eq.4.40 with respect to the continuation parameter is retrieved with the procedure explained in section B.1.2.5. The derivatives of the vectorfield with respect to the eccentricity are reported below.

$$\begin{cases} \mathbf{a}_{/e}(\nu) = \left(2\,(1-\mu)\,\frac{(1+e\cos\nu)\cos\nu}{(1-e^2)^2} + 4\,(1-\mu)\,\frac{(1+e\cos\nu)^2e}{(1-e^2)^3}\right)\begin{bmatrix}1\\0\\0\end{bmatrix} \\ \omega_{z/e}(\nu) = \left(2\frac{(1+e\cos\nu)\cos\nu}{(1-e^2)^{3/2}} + 3\frac{(1+e\cos\nu)^2e}{(1-e^2)^{5/2}}\right) \\ \rightarrow \mathbf{W}_{/e}(\nu) = \left(2\frac{(1+e\cos\nu)\cos\nu}{(1-e^2)^{3/2}} + 3\frac{(1+e\cos\nu)^2e}{(1-e^2)^{5/2}}\right)\begin{bmatrix}0\\0\\1\end{bmatrix}\wedge \\ \mathbf{Y}_{/e}(\nu) = \left(-6\frac{(1+e\cos\nu)^2e\sin\nu\cos\nu}{(1-e^2)^3} - 2\frac{(1+e\cos\nu)^3\sin\nu}{(1-e^2)^3} - 12\frac{(1+e\cos\nu)^3e^2\sin\nu}{(1-e^2)^4}\right)\begin{bmatrix}0\\0\\1\end{bmatrix}\wedge \\ \mathbf{P}_{/e}(\nu) = \left(6\frac{(1+e\cos\nu)^4e}{(1-e^2)^4} + 4\frac{(1+e\cos\nu)^3\cos\nu}{(1-e^2)^3}\right)\left(\begin{bmatrix}0\\0\\1\end{bmatrix}\wedge\right)^2 \\ \mathbf{f}_{G1/e}(\nu) = u_{G1/\mathbf{q}e}(\mathbf{q},\nu) = \\ = \frac{1-\mu}{\left\|\mathbf{q}+\frac{1-e^2}{1+e\cos\nu}\begin{bmatrix}1\\0\\0\end{bmatrix}\right\|^5}\left(-2\frac{e}{1+e\cos\nu} - \frac{\left(1-e^2\right)\cos\nu}{(1+e\cos\nu)^2}\right)\begin{bmatrix}2\left(x+\frac{1-e^2}{1+e\cos\nu}\right)^2-y^2-z^2\\3\left(x+\frac{1-e^2}{1+e\cos\nu}\right)y\\3\left(x+\frac{1-e^2}{1+e\cos\nu}\right)z\end{bmatrix} \end{cases} \tag{4.42}$$

The DC will now require the propagation of the augmented 8D × 8D variational systems to retrieve the STM.

$$\boldsymbol{\Phi}\left(t,\mathbf{x}_0,e\right) = \begin{bmatrix}\boldsymbol{\phi}_{f/\mathbf{x}_0} & \boldsymbol{\phi}_{f/e}\\ \mathbf{0_{1x6}} & 1\end{bmatrix} \leftrightarrow$$
$$\begin{cases} \dot{\boldsymbol{\Phi}}\left(t,\mathbf{x}_0,e\right) = \begin{bmatrix} \mathbf{0_3} & \mathbf{I_3} & \mathbf{0_{3x1}} & \mathbf{0_{3x1}} \\ -\mathbf{Y}(\nu)-\mathbf{P}(\nu)+\mathbf{H}(\nu) & -2\mathbf{W}(\nu) & \begin{matrix}-\mathbf{Y}_{/\nu}(\nu)\mathbf{q}-\mathbf{P}_{/\nu}(\nu)\mathbf{q}-2\mathbf{W}_{/\nu}(\nu)\dot{\mathbf{q}}+\\+\mathbf{f}_{G1/\nu}(\nu)+\mathbf{a}_{/\nu}(\nu)\end{matrix} & \begin{matrix}-\mathbf{Y}_{/e}(\nu)\mathbf{q}-\mathbf{P}_{/e}(\nu)\mathbf{q}-2\mathbf{W}_{/e}(\nu)\dot{\mathbf{q}}+\\+\mathbf{f}_{G1/e}(\nu)+\mathbf{a}_{/e}(\nu)\end{matrix} \\ \mathbf{0_{1x3}} & \mathbf{0_{1x3}} & \omega_{z/\nu}(\nu) & \omega_{z/e}(\nu) \\ \mathbf{0_{1x3}} & \mathbf{0_{1x3}} & 0 & 0 \end{bmatrix}\boldsymbol{\Phi}\left(t,\mathbf{x}_0,e\right) \\ \boldsymbol{\Phi}\left(0,\mathbf{x}_0,e\right) = \mathbf{I_8} \end{cases} \tag{4.43}$$

Recall that the sensitivity of the flow with respect to the initial true anomaly can be retrieved from the general definition of the variational equations for time-variant systems presented in Eq.B.18, and applied to the ODEs of Eq.A.14, where the time is set to be ν. This is shown in Eq.4.44, for a specific case where also a stroboscopic constraint is considered.

$$\begin{cases} t_f - t_0 = \Delta t \\ \delta \Delta t = 0 \end{cases} \rightarrow \delta t_f = \delta t_0 \Rightarrow$$

$$\begin{aligned} \delta x\left(t_0 + \Delta t + \delta t_0\right) &= \Phi_f\left(t_0 + \Delta t, t_0, x_0\right) \delta x\left(t_0 + \delta t_0\right) + \\ &+ \left(f\left(t_0 + \Delta t, x\left(t_0 + \Delta t\right)\right) - \Phi_f\left(t_0 + \Delta t, t_0, x_0\right) f\left(t_0, x_0\right)\right) \delta t_0 = \\ &= \frac{\partial \phi_f}{\partial x_0}\left(t_0 + \Delta t, t_0, x_0\right) \delta x_0 + \frac{D\phi_f}{Dt_0}\left(t_0 + \Delta t, t_0, x_0\right) \delta t_0 \end{aligned} \tag{4.44}$$

This leads to the analytical formula for the sensitivity of the flow of the ER3BP-GH with respect to the initial true anomaly.

$$\mathbf{x}(\nu) = \begin{bmatrix} \mathbf{q} \\ \dot{\mathbf{q}} \end{bmatrix} \rightarrow \boldsymbol{\phi}_{f/\nu_0}\left(\nu_f, \nu_0, \mathbf{x}\right) = -\boldsymbol{\phi}_{f/\mathbf{x}_0}\left(\nu_f, \nu_0, \mathbf{x}\right) \dot{\mathbf{x}}\left(\nu_0\right) \tag{4.45}$$

As explained throughout appendix B, in time-variant dynamical systems the procedures of DST are based on the reduction of the continuous dynamics to a stroboscopic map P_T. The following sections will now present the dedicated DC scheme, which is embedded in the NC with respect of the eccentricity, for each invariant motion.

4.3.2 POs in the Mars-Phobos ER3BP-GH

Since the dynamics of the ER3BP-GH are time-variant, and the eigenvalues of the LPs of the CR3BP-GH are different from the orbital frequency of Phobos, no physical EPs exist in this non-pulsating system.

The identification of the dynamical substitutes of the LPs in the Mars-Phobos ER3BP-GH was performed in the framework of the preliminary analysis of this system in section 3.4.4. Due to the forcing perturbation of the Phobos-Mars pulsating distance, they are 1D POs, elongated along the x-axis of Phobos' Hill's frame. These trajectories are shown in Fig.3.21. Their maximum positions are computed as the EP of the ER3BP-GH expressed in pulsating units of length and time, at the extreme Phobos' phases of perimars and apomars. The periodic LPs of the Mars-Phobos ER3BP-GH oscillate around their location in the CR3BP-GH with an amplitude of $260m$, which is about 6% of their altitude. This could be significant due to the proximity of the Phobos' surface and the time-scale of its orbit for practical applications. The related stability properties are maintained from their ancestor solutions in the circular system. Thus, the orbit structure around these LPs in the ER3BP-GH is characterized by a 2-parameters family of invariant 3-tori and their stable and unstable IMs. These orbits are the focus of the next sections.

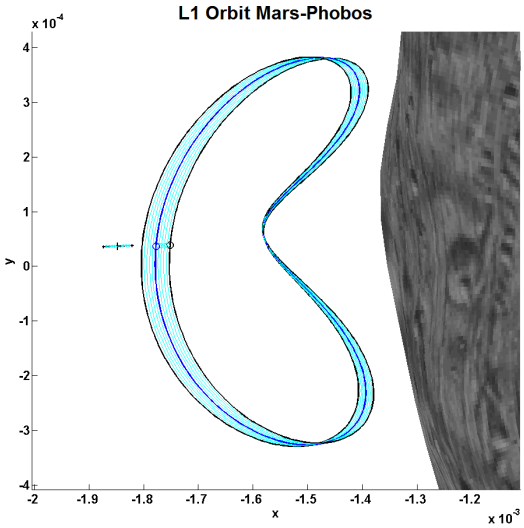

Figure 4.95: **Periodic LPOs in the Mars-Phobos ER3BP-GH.** Continuation with respect to the eccentricity from CR3BP-GH (blue) to ER3BP-GH (black) of the synchronous PO of the family D around L_1, with initial Phobos true anomaly fixed at the pericenter. Projection on the x-y plane. Points represent the initial conditions on the chosen Poincaré map, and crosses represent the current amplitudes of the oscillation of the LP.

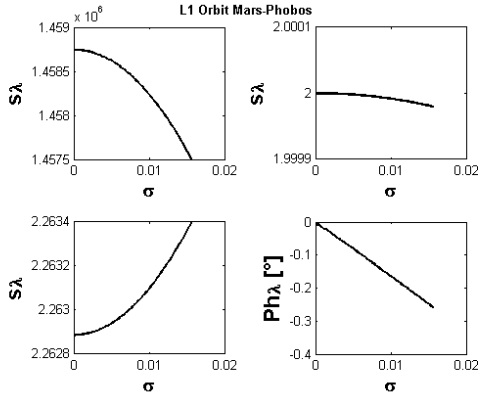

Figure 4.96: **Periodic LPOs in the Mars-Phobos ER3BP-GH.** Stability properties (stability indexes of the three couples of eigenvalues of the monodromy matrix, with the phase of the center's couple) along the NC with respect to the eccentricity from CR3BP-GH ($\sigma = 0$) to ER3BP-GH ($\sigma = e_{Phobos}$) of the synchronous PO of the family D around L_1, with initial Phobos true anomaly fixed at the pericenter.

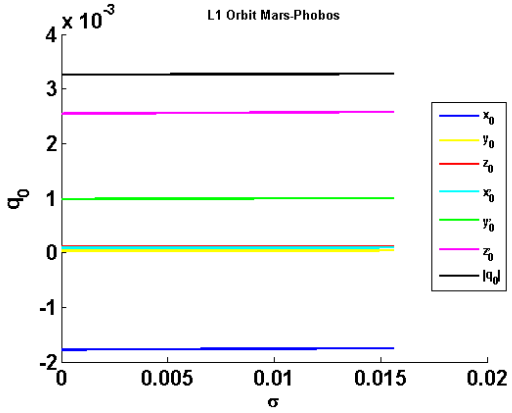

Figure 4.97: **Periodic LPOs in the Mars-Phobos ER3BP-GH.** Continuation variables' curves profile. Continuation with respect to the eccentricity from CR3BP-GH ($\sigma = 0$) to ER3BP-GH ($\sigma = e_{Phobos}$) of the synchronous PO of the family D around L_1, with initial Phobos true anomaly fixed at the pericenter.

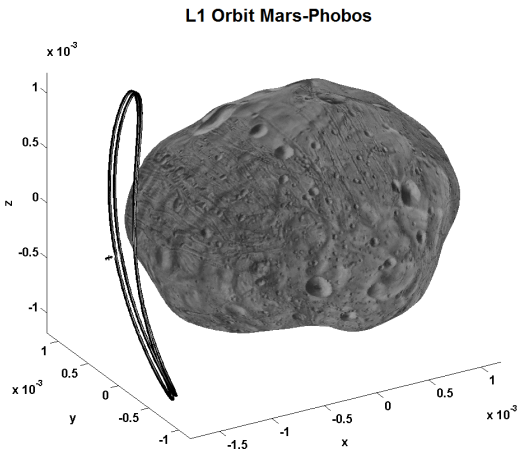

Figure 4.98: **Periodic LPOs in the Mars-Phobos ER3BP-GH.** Graphical visualization of the PO of the family D of the ER3BP-GH around L_1 with initial condition of the Phobos true anomaly at the pericenter.

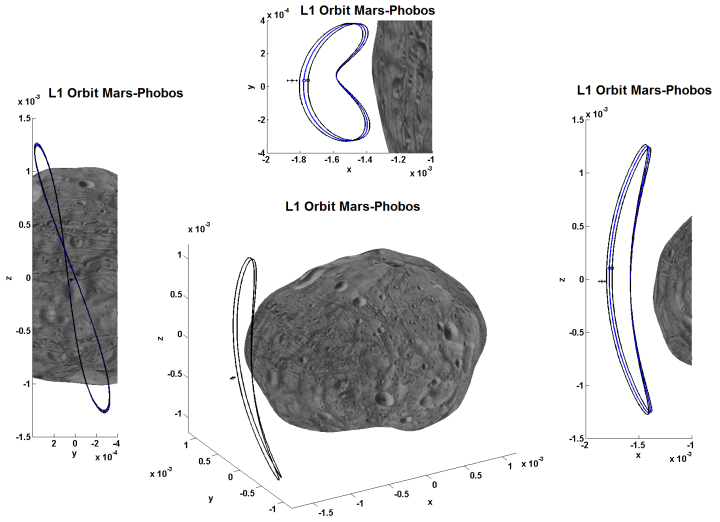

Figure 4.99: **Periodic LPOs in the Mars-Phobos ER3BP-GH.** Graphical visualization of the PO of the family D of the ER3BP-GH around L_1 with initial condition of the Phobos true anomaly at the pericenter.

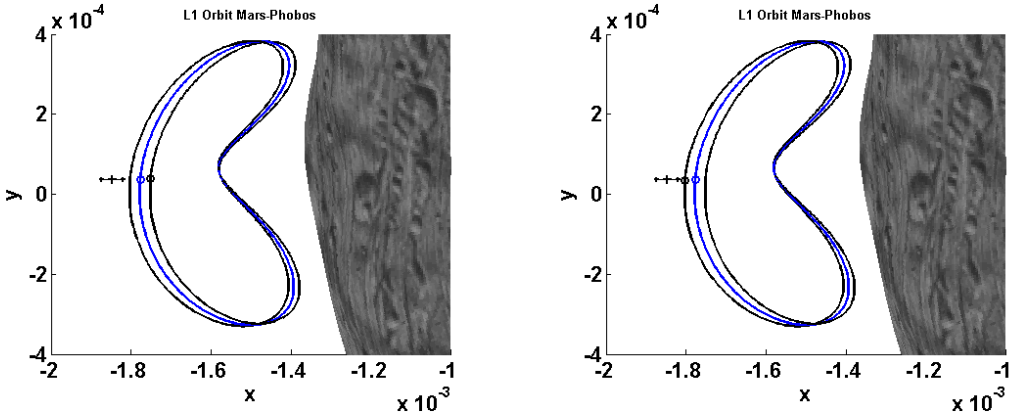

Figure 4.100: **Periodic LPOs in the Mars-Phobos ER3BP-GH.** Continuation with respect to the eccentricity from CR3BP-GH (blue) to ER3BP-GH (black) of the synchronous PO of the family D around L_1, with initial Phobos true anomaly fixed at the pericenter and at the apocenter. Projection on the x-y plane. The two orbits obtained are the same. Points represent the initial conditions on the chosen Poincaré map, and crosses represent the current amplitudes of the oscillation of the LP.

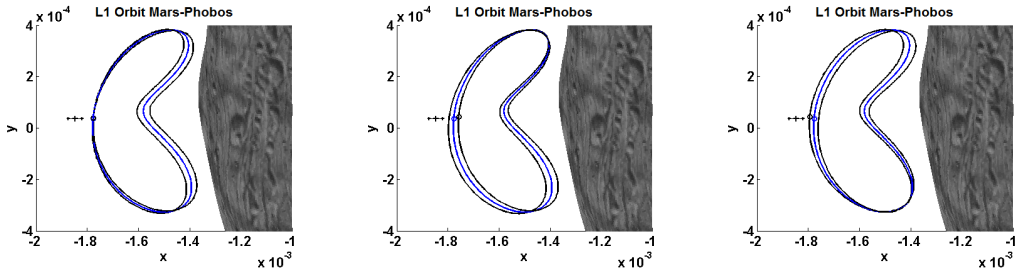

Figure 4.101: **Periodic LPOs in the Mars-Phobos ER3BP-GH.** Continuation with respect to the eccentricity from CR3BP-GH (blue) to ER3BP-GH (black) of the synchronous PO of the family D around L_1, with initial Phobos true anomaly fixed at the quadrature (90°), at 45° and at 135°. Projection on the x-y plane. Points represent the initial conditions on the chosen Poincaré map, and crosses represent the current amplitudes of the oscillation of the LP.

4.3.2.1 Resonant POs in the Mars-Phobos ER3BP-GH

Apart from the dynamical substitutes of the ancestor EPs, isolated POs in the ER3BP-GH develop when the original PO in the circular case is resonant with ν. From Eq.B.76, this happens when the natural frequency of the PO is in an integer ratio with the forcing frequency of ν, thus the related phases are coherent and the dynamical substitute maintains the phase-space's dimension of the ancestor solution in the circular dynamics. The principal interest is for resonances where the aforementioned integer ratio is characterized by a low denominator.

Therefore, the characteristic curves in Fig.4.63 of the period of the POs, for the families of the CR3BP-GH, show that the B and D families around each LP have one PO with period π, which is the usual overresonance 2:1 of the ER3BP. However, the synchronous POs of the families B slightly intersect Phobos, therefore the interest is for the remaining two synchronous POs of the families D. The dynamical substitutes of these synchronous POs in the ER3BP-GH are POs with period 2π. This gives rise to two iso-periodic families of POs in the elliptic problem, since the circular problem is a singular case for the definition of ν_0. This means that the continuation, with respect of the eccentricity, of resonant POs could be started in the circular dynamics assuming any value of ν_0 on the same stroboscopic map, and the resulting dynamical substitute in the elliptic dynamics will be a different invariant motion. Thus, ν_0 on a stroboscopic map acts as a residual parameter for the family of resonant POs.

Computation of resonant POs. The computation of these POs, with the NC of Eq.4.40, could be undertaken with the DC scheme for computing PO in a time-variant system, which is introduced in section B.5.3.2, and presented in Eq.B.72. It makes use of a stroboscopic map with propagation time 2π. This approach was first undertaken in [54], to compute dynamical substitutes of POs from CR3BP to ER3BP. The single shooting was used in [54] to compute only symmetrical dynamical substitutes, starting the continuation only at pericenter or apocenter conditions, and using the classical Poincaré section $y = 0$ (syzygy axis). This combination constitutes the strong condition to ensure symmetrical periodicity. Further works related to the search of POs in the ER3BP also used NC [121, 122, 123, 124, 125, 126, 127, 128]. A significant research was recently done in [129], where the authors computed the LPOs in the ER3BP using the semi-analytical Lindstedt-Poincaré series expansion. Considering instead other classes of orbits, that for the Mars-Phobos system are not of practical interest or do not even exist, the computation of these POs in the ER3BP have been undertaken in [130, 131, 132, 133, 134, 135]. The natural motion in the ER3BP has also been studied with the tools of Arnold's diffusion in [136, 137], and in the framework of the Lagrangian Coherent Structures in [138].

For the asymmetric ER3BP-GH, the numerical approach is considered to compute the dynamical substitutes of the synchronous POs. In particular, the fundamentals of

the classical method of [54] are used, but here not two dynamical substitutes for each synchronous PO, but the curve of initial conditions on the stroboscopic map is required. In particular, due to the overresonance, one half of this curve could be avoided, since the initial conditions at ν_0 correspond to the flows starting from the other half at $\nu_0 - \pi$ after a propagation time of π.

The approach is to use the single shooting of Eq.B.72 in the NC with respect to the eccentricity, where the sensitivity of the flow with respect to e is retrieved from the STM of Eq.4.43. In this case, ν_0 is kept fixed and chosen by the user, to compute one dynamical substitute of the family of POs in the ER3BP-GH, as explained previously.

The Jacobian of the DC scheme has resulted to be singular at the solution. Thus, the linear system at each step is solved using SVD, which is to approximate the smallest singular value to be zero [139]. This makes the DC to converge at a given step, but it penalizes the NC of the solution. However, considering also the high propagation time[18], the NC arrives to a solution at the Phobos' eccentricity whose error on the objective function's norm of Eq.B.72 is $3 \cdot 10^{-8}$ normalized units. The related position error is in the order of *cm*, which is acceptable for practical applications for two reasons. First, because navigation errors for interplanetary spacecraft are significantly higher than this value. And second, because due to the instability of the LPOs, and the residual modeling errors on the orbital perturbations, these LPOs eventually necessitate frequent station-keeping. This action would naturally include also this tracking signal's error since it represents only a small fraction of the control load required. The effect of this approximated solution could be practically evaluated in the following way. The computational time of permanence of the LPOs was derived from Fig.4.10 to be around 3.5 longitudinal revolutions, which are 1.75 orbital periods. The error on the resonant POs computed in the ER3BP-GH has resulted in a reduction of the computational time of permanence of their tracking signal to about 1.25 orbital periods. Therefore the reference signal is not too far from following a natural PO, and reliable for a whole period of the PO.

It is worth to underline that using a multiple shooting approach, in order to reduce the effect of the propagation of the machine error on this high time span, is not a solution, since the DC's Jacobian remains still singular and the approximated solution along the NC will affect also the continuity condition between subintervals.

Analysis of the results. Fig.4.95-4.99 show the NC of the pericenter orbit, and its properties, around L_1. As explained before, due to the overresonance, pericenter and apocenter POs are the same, and this is shown in Fig.4.100. Due to the vertically-

[18] As a difference from the computation of POs in the CR3BP and CR3BP-GH, where a Poincaré map was used to model the longitudinal revolution, in the ER3BP-GH the stroboscopic map is used. The related propagation time is equal to the Phobos' revolution, which is about the double of the longitudinal revolution of the LPOs. Thus, in this scheme, the effect of the machine error produces residual errors on the flow that could be estimated to be around the square of the respective error obtained by the schemes of the circular case.

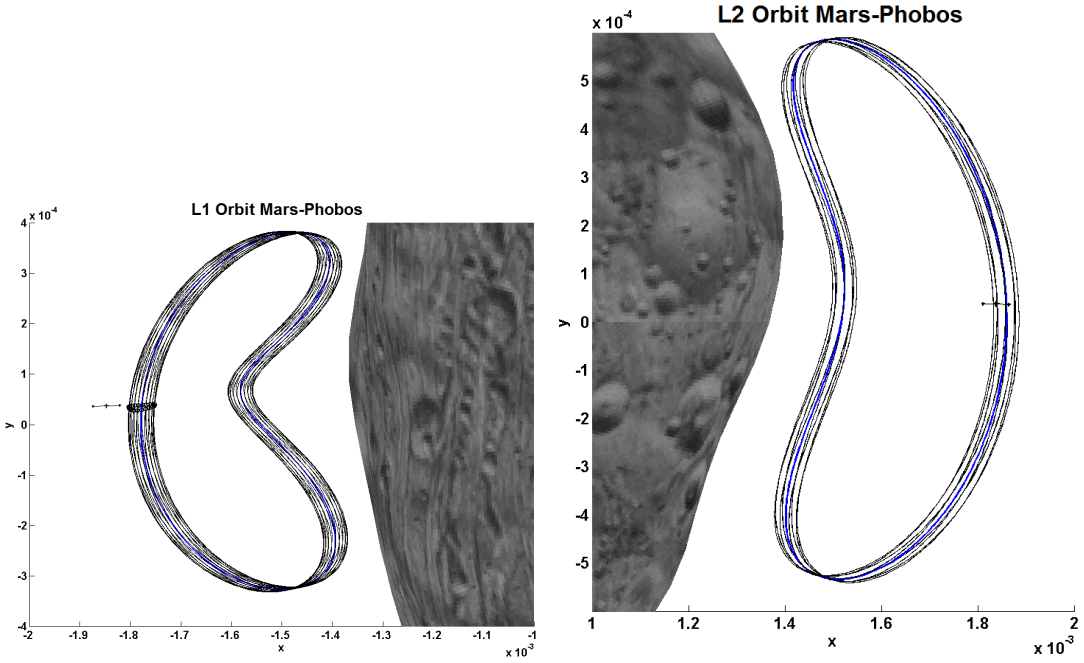

Figure 4.102: **Periodic LPOs in the Mars-Phobos ER3BP-GH.** Graphical visualization on the x-y plane of the POs of the family D around L_1 and L_2 in the ER3BP-GH. Continuation with respect to the initial Phobos true anomaly from pericenter ($\sigma = 0rad$) to apocenter ($\sigma = \pi rad$). Ancestor PO of the family D of the CR3BP-GH displayed in blue for reference. Points represent the initial conditions on the chosen Poincaré map, and crosses represent the amplitudes of the oscillation of the LP.

elongated character of the family D, these orbits are better seen on the orbital plane's projection. It is evident how the forcing perturbation produces a dynamical substitute in the ER3BP-GH that oscillates around the ancestor PO in the CR3BP-GH case, specularly along the x-axis. The magnitude of this oscillation is coherent with the one of the LP, as it could be seen in Fig.4.95. In particular, the oscillation of the pericenter/apocenter orbit exhibits a maximum amplitude at the sub-Mars point, with respect to the LP, while at the sub-Phobos point the amplitude is null.

Finally, other resonant POs of the family D around L_1 in the ER3BP-GH are computed starting the NC at different ν_0 for the initial condition of the ancestor synchronous PO. Fig.4.101 shows the orbits with ν_0 on quadrature $\frac{\pi}{2}$ (and $\frac{3\pi}{2}$) and intermediate phases $\frac{\pi}{4}$,$\frac{3\pi}{4}$ (and $\frac{5\pi}{4}$,$\frac{7\pi}{4}$). The oscillation of the PO in quadrature exhibits a maximum amplitude at the sub-Phobos point, and null at the sub-Mars point. The dynamical substitutes at the intermediate phases oscillate also along the y-axis. The phase around the LP and with respect to the x-axis, of the point that exhibits null oscillation's amplitude with respect to the ancestor orbit, is coherent with the rotation of Phobos around Mars, starting at the perimars and with double frequency.

However, it is possible to compute just the pericenter PO in the ER3BP-GH, and then perform a NC of the latter with respect to the initial true anomaly on the stroboscopic map, at the Phobos' eccentricity. Fig.4.102-4.104 show the results of this

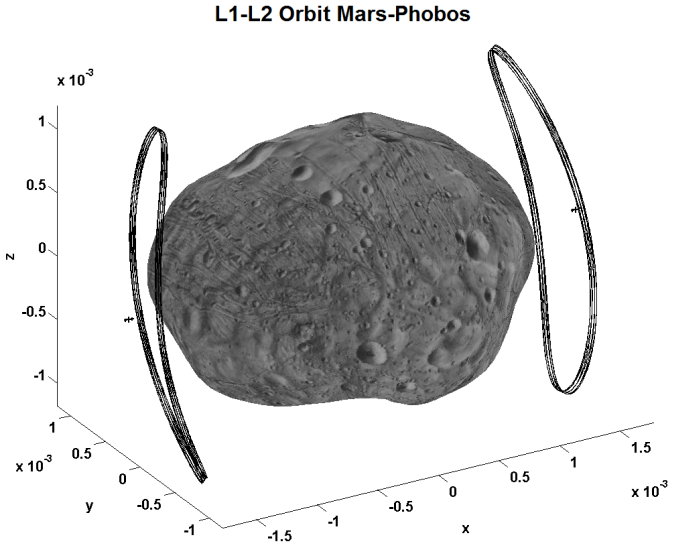

Figure 4.103: **Periodic LPOs in the Mars-Phobos ER3BP-GH.** Graphical visualization of the POs of the family D around L_1 and L_2 in the ER3BP-GH.

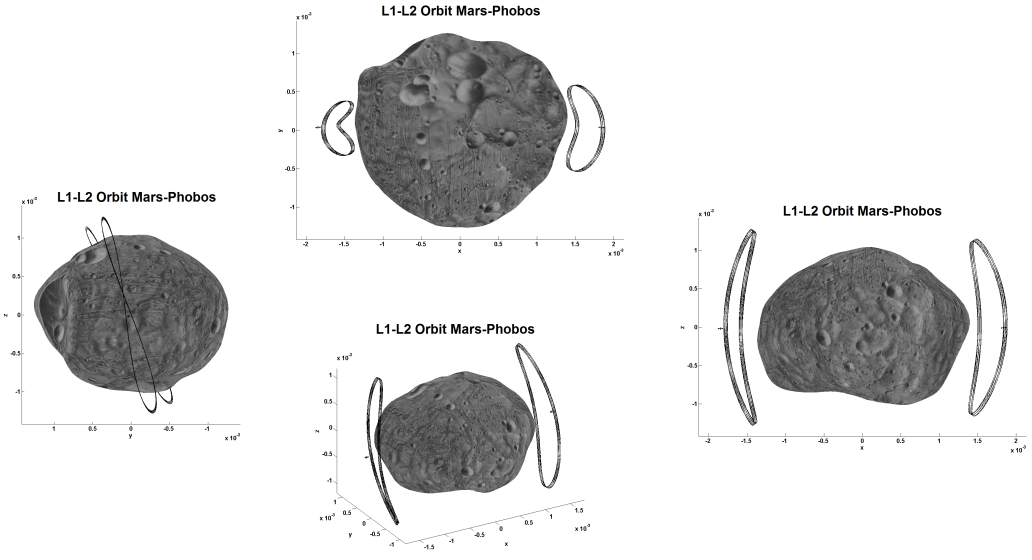

Figure 4.104: **Periodic LPOs in the Mars-Phobos ER3BP-GH.** Graphical visualization of the POs of the family D around L_1 and L_2 in the ER3BP-GH.

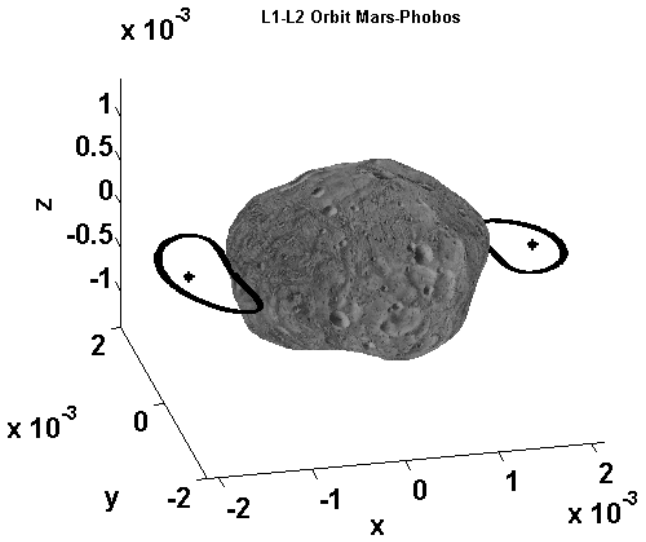

Figure 4.105: **Periodic LPOs in the Mars-Phobos ER3BP-GH.** Graphical visualization of the POs of the family B around L_1 and L_2 in the ER3BP-GH.

continuation, that yields the two families D of iso-periodic POs of the ER3BP-GHs around L_1 and L_2. These POs are large, vertically-elongated, and inclined, similar to eight-shaped orbits. Due to their shape, attitude and dimension, these POs provide good coverage of the polar regions of Phobos, without flying too close to the surface of moon.

Regarding the stability analysis of these POs, [54] provides a detailed description of the characteristics of the manifold of POs in a non-autonomous system. The STM and the monodromy matrix are still symplectic, therefore their eigenvalues are present in couples of reciprocals on the complex plane. But the absence of an integral of motion does not constrain a couple to be unity. Therefore a different manifold generates, either a center or a saddle. The stability properties for the families of POs in the Mars-Phobos ER3BP-GH are shown in Fig.D.61. The pericenter/apocenter orbits have a saddle $\times$ saddle $\times$ center manifold, whereas quadrature orbits have a saddle $\times$ saddle $\times$ saddle manifold.

In conclusion, Fig.4.105-D.63 show the iso-periodic families of dynamical substitutes of the synchronous POs of the families B around L_1 and L_2. As expected, these orbits are not exploitable as they slightly intersect (close to a tangential condition) the real surface of Phobos.

4.3.3 2D-QPOs in the Mars-Phobos ER3BP-GH

Tori with two phases are the dynamical substitutes of the POs of the CR3BP-GH in the general non-resonant case. In this section, the families of 2D-QPOs in the ER3BP-GH are derived with the numerical scheme of Eq.B.92, that computes their invariant curve as presented in section B.6.3.

4.3.3.1 Effect of the Eccentricity Perturbation on Tracking POs of the CR3BP-GH

Before computing the LPOs in the elliptic problem, in this section a simple analysis is conducted to infer what would be the effect of the eccentricity perturbation on the LPOs computed in the circular problem. This requires one to evaluate the cost of tracking in the ER3BP-GH the reference signal of the orbits computed by a guidance based on the CR3BP-GH.

This is done with the formula of the eccentricity perturbation derived in Eq.2.52. This definition was used in section 2.4 to derive a summarizing figure for the eccentricity perturbation, that was applied to fixed points in the 3B frame. Eq.2.52 is now evaluated along the reference signal of the POs computed in the CR3BP-GH, which, as usual, is translated in the Phobos' Hill's frame to maintain the same relative state of the orbit with respect to Phobos. This gives an analytical expression of the control law required to exactly compensate the eccentricity perturbation and track these orbits in the ER3BP-GH. The control acceleration's profile is then integrated along the simulation's time span to obtain the value of the Δv for one orbital period.

Since the circular dynamics is a singular case for the definition of ν_0, different scenarios come out by choosing the initial condition of the reference signal in the elliptic problem. The degrees of freedom are two: the phase along the PO to choose the initial state for the simulation, and the phase of Phobos to choose the starting epoch. This could be interesting to see the effect on the choice of ν_0 to start the NC with respect to the eccentricity discussed in sections 4.3.1-4.3.2.1 to compute the LPOs.

This brief analysis is undertaken for two cases of POs. Results are presented in Fig.4.106 for the synchronous PO of the family D around L_1, and in Fig.4.107 for one generic non-resonant PO of the family A around L_1. The control acceleration has resulted to be near the values expected in Fig.2.10. Therefore, the Δv cost is significantly high (about $5m/s$ per orbital period), and this further shows the importance of considering this perturbation in the dynamical model, used by the guidance subsystem, to obtain target signals exploitable for practical applications. Finally, the plots highlight that the effect of the choice of ν_0 to trim the reference signal provides differences in the cost, with respect to the mean value, on the same order of magnitude of the orbital eccentricity of Phobos. Thus this difference is not significant. For the case of the synchronous PO, the plot of the Δv is obviously periodic, and the minimum value is obtained starting the simulation with the spacecraft on the classical Poincaré section $y = y_{EP} \wedge \dot{y} > 0$ in perimars or apomars. This doubling of the possibilities is enabled by the overresonance, as explained in section 4.3.2.1. For the case of the general non-resonant PO, the plot is no longer periodic.

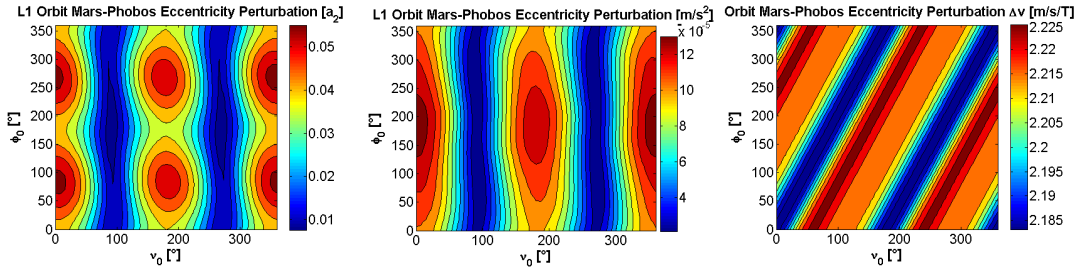

Figure 4.106: **Eccentricity perturbation on periodic LPOs of the Mars-Phobos CR3BP-GH.** Initial perturbation (in relative and absolute units) and total Δv cost for the station-keeping during one orbital period of the synchronous PO of the family D of the CR3BP-GH around L_1 in the ER3BP-GH, as a function of the Phobos' initial true anomaly and the initial longitudinal phase of the PO ($\phi_0 = 0$ on the Poincaré section $y = y_{EP} \wedge \dot{y} > 0$).

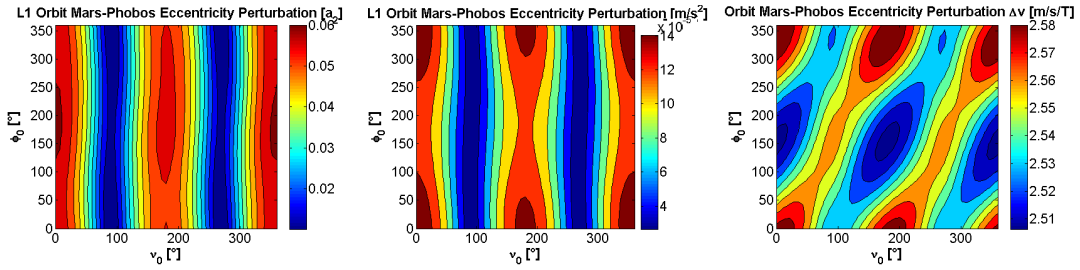

Figure 4.107: **Eccentricity perturbation on periodic LPOs of the Mars-Phobos CR3BP-GH.** Initial perturbation (in relative and absolute units) and total Δv cost for the station-keeping during one orbital period of a medium-energy PO of the family A of the CR3BP-GH around L_1 in the ER3BP-GH, as a function of the Phobos' initial true anomaly and the initial longitudinal phase of the PO ($\phi_0 = 0$ on the Poincaré section $y = y_{EP} \wedge \dot{y} > 0$).

4.3.3.2 Computation of the Dynamical Substitutes of the Periodic LPOs in the Mars-Phobos ER3BP-GH

The DC scheme of Eq.B.108 was used previously to compute families of 2-tori around a PO in the CR3BP-GH, but the procedure used in section 4.2.3.1 is adapted to consider the modifications needed for the case of a time-variant system.

The extension of the numerical methodology for the tori of autonomous systems to the case of the non-autonomous systems, is addressed in [140], where the dynamical substitutes in the ER3BP of the periodic LPOs of the CR3BP are computed. In this thesis, the original method of [120] and Eq.B.108 are used to compute the 2D-QPOs of the ER3BP-GH, extending its validity to non-autonomous cases. There are three significant differences to be considered. First, the invariant curves are now defined on a stroboscopic map, with the period fixed to the one of the original PO in the circular dynamics. Second, as discussed in sections B.6.1 and B.6.3.2, the invariant curve's parameter is fixed to be ν on the stroboscopic map, because this is a constrained phase by the time-variant eccentricity perturbation. This is the paramount difference of the methodology from the case of the 2-tori of the CR3BP-GH computed in section 4.2.3.1. In Eq.B.92, the value of the parameter at the first-return on the map is now a state's component. Therefore, the inverse parametrization is explicit and the value of ν after

one longitudinal revolution is directly retrievable by integration of the equations of motion of Eq.3.50. The third difference of the DC scheme is that the adoption of a stroboscopic map does not lock the longitudinally phase like the Poincaré section does. Therefore, the related phase's indeterminancy must be tackled as explained in section B.6.3.3.3: the choice used is to fix the mean value of the y-component of the invariant curve to be null. The transversal phase is not undetermined because the reference for ν is the pericenter.

It is worth to highlight that the Jacobian of the DC of Eq.B.108 massively simplifies for the case of a time-variant system, due to the definition of $\mathbf{T}$ (see section B.6.3.3.1). This yields the following simplification to be implemented in Eq.B.108.

$$\begin{aligned}\frac{d\theta_f}{d\mathbf{c}} &= \frac{d\theta}{d\mathbf{x}}\left(\phi_{\mathbf{f}}\left(T, C^F\left(\mathbf{c},\theta_0\right)\right)\right)\frac{d\phi_{\mathbf{f}}}{d\mathbf{x}_0}\left(T, C^F\left(\mathbf{c},\theta_0\right)\right)\begin{bmatrix}\frac{\partial C^F}{\partial \mathbf{c}}\left(\mathbf{c},\theta_0\right)\\ \frac{\partial \theta_0}{\partial \mathbf{c}}\end{bmatrix} = \\ &= \mathbf{T}\left(\phi_{\mathbf{f}}\left(T, C^F\left(\mathbf{c},\theta_0\right)\right)\right)\mathbf{P}\left(T, C^F\left(\mathbf{c},\theta_0\right)\right)\begin{bmatrix}\mathbf{E}\left(\theta_0\right)\\ \mathbf{0_{1x6(2N_C+1)}}\end{bmatrix} = \\ &= \begin{bmatrix}\mathbf{0_{1x6}} & \mathbf{\Phi}_{\nu/\nu_0}\left(\phi_{\mathbf{f}}\left(T, C^F\left(\mathbf{c},\theta_0\right)\right)\right)\end{bmatrix}\begin{bmatrix}\mathbf{E}\left(\theta_0\right)\\ \mathbf{0_{1x6(2N_C+1)}}\end{bmatrix} = \mathbf{0_{1x6(2N_C+1)}}\end{aligned} \tag{4.46}$$

NC with respect to the eccentricity. For the case of the ER3BP-GH, the stroboscopic map defined above is characterized by an isolated invariant curve, as a difference from the 2-tori of the CR3BP-GH that are embedded in a continuous 1-parameter family on an iso-energetic Poincaré or stroboscopic map. Thus, the adoption of a sizing parameter (see section B.6.3.3.4) is not necessary, because its role is played by the specific value of the eccentricity. The new DC scheme is embedded in the NC with respect to the eccentricity of section 4.3.1, where the initial solution at $e = 0$ is the invariant point on the chosen map of the PO itself, which is a singular case of invariant curve. An example of the continuation of the invariant curve up to the eccentricity of Phobos is shown in Fig.4.109.

The NC of invariant curves with respect to the eccentricity, to find the quasi-periodic dynamical substitute of a PO, has resulted to be much faster than the NC with respect to the GHs. A sample of the procedure is shown in Fig.4.108-D.65. The resulting QPO is then simulated to describe the surface of motion of the full invariant object (see section B.6.4), and this is presented in Fig.4.111-4.115 for the sample case. In particular, the simulation starts at the perimars, and Fig.4.110 shows the related rotation number's profile along time, which corresponds to the simple discrete dynamical system that describes ν every stroboscopic revolution. Due to the fact that the longitudinal motion of the LPOs is close to the 2:1 overresonance with the orbital motion of Phobos, it makes more sense to consider for the simulations the second-return stroboscopic map for the LPOs of the ER3BP-GH. Thus, Fig.4.110 and Fig.4.111-4.115 show the rotation number's profile and the surface of motion sampled at double frequency.

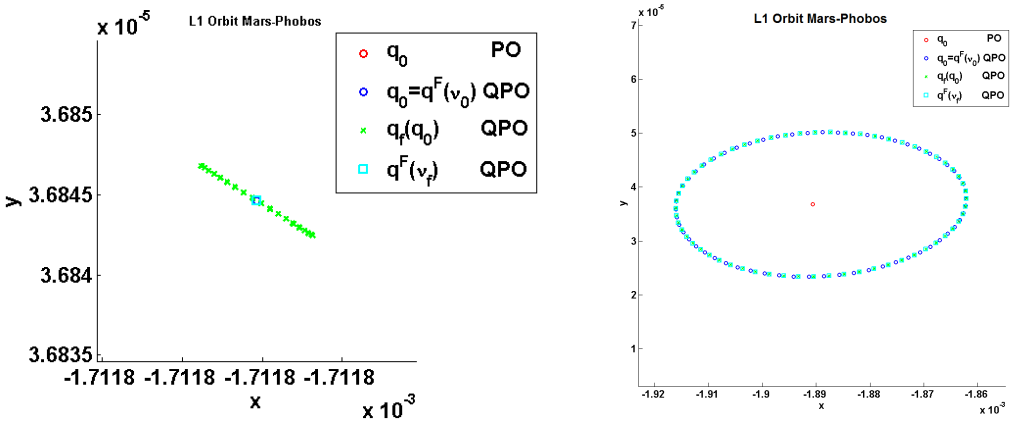

Figure 4.108: **Quasi-periodic LPOs in the Mars-Phobos ER3BP-GH.** Procedure of the DC scheme for computing the natural 2D-QPO substitute in the ER3BP-GH of a PO in the CR3BP-GH. The invariant curve on the stroboscopic map around the initial condition of the backbone PO (q_0) is described as a Fourier series expansion (q^F) function of a forced parametrization variable (ν, the Phobos true anomaly around Mars). An initial guess for the Fourier coefficients is used (which at the very beginning of the continuation, is just the PO itself, therefore a singular invariant circle coincident to the PO's initial condition point), and a cluster of initial conditions (q_0, function of the independent set of parameters ν_0) is obtained, to describe the initial curve. The multiple initial conditions are propagated in the NL dynamics to find their return condition on the stroboscopic map (q_f): this cluster of points describes the return curve. Being the parametrization explicit, the related set of parameters (ν_f) are obtained. The Fourier series expansion is evaluated with these new set of parametrization variables: the related cluster of points is the projection of the return curve on the initial curve. The aim of the DC scheme is to drive the two curves to correspond with each other, which is to erase the error between return and projected curve. When this happens, the Fourier series expansion effectively describes an invariant curve, and therefore a 2D-QPO. The graphs show the stroboscopic map projected on the x-y plane: at the initial iteration of the DC, at the beginning of the NC (which is the flow in the ER3BP-GH at small eccentricity, $e = 10^{-7}$, of the point corresponding to the PO's initial condition, for the set of ν_0), and at the final solution of the DC, at the end of the NC (eccentricity of Phobos), where the return curve converges toward the projected curve. Continuation with respect to the eccentricity from CR3BP-GH ($\sigma = 0$) to ER3BP-GH ($\sigma = e_{Phobos}$) of a medium-energy PO of the family A around L_1 of the CR3BP-GH.

NC with respect to the stroboscopic period in the ER3BP-GH. The NC presented above allows to determine a single dynamical substitute, that corresponds to the final solution at Phobos' eccentricity. In a similar way as it was undertaken in section 4.2.2.2 to compute the periodic LPOs in the CR3BP-GH, a combination of two NC schemes in cascade is now considered. Once a dynamical substitute is obtained in the ER3BP-GH, the related family can be computed using the latter as the starting solution of a NC with respect to the stroboscopic time, obtaining all the family in the ER3BP-GH with the eccentricity of Phobos. Thus, due to the absence of an integral of motion, and due to the fact that QPOs do not have a period, the parameter of the family of 2D-QPOs in the ER3BP-GH could be the period of the backbone POs, which are the ancestors of these tori in the CR3BP-GH. However, in this analysis, the chosen parameter of the families of QPOs in the ER3BP-GH is the differential Jacobi integral that param-

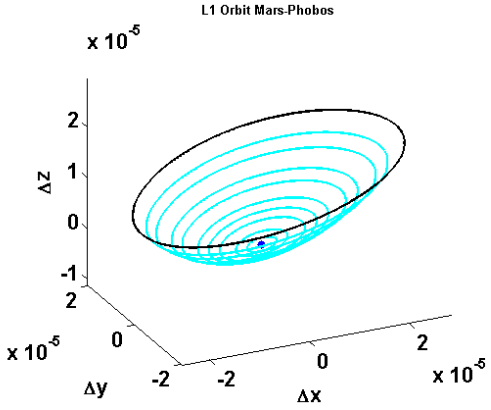

Figure 4.109: **Quasi-periodic LPOs in the Mars-Phobos ER3BP-GH.** Continuation with respect to the eccentricity from CR3BP-GH of a medium-energy PO of the family A around L_1 of the CR3BP-GH ($\sigma = 0$, blue point) to its dynamical substitute in the ER3BP-GH ($\sigma = e_{Phobos}$, black curve). Invariant curve on the stroboscopic map.

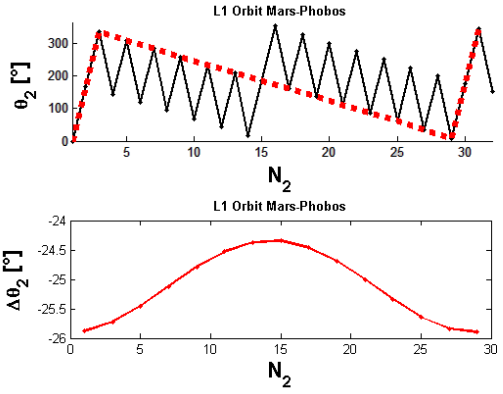

Figure 4.110: **Quasi-periodic LPOs in the Mars-Phobos ER3BP-GH.** Simulation of a medium-energy 2D-QPO of the family A around L_1 of the ER3BP-GH. Invariant curve's parameter (corresponding to Phobos true anomaly) profile along time, where the red curve highlights the profile at the second-return frequency, and related rotation number's profile along time of the second-return stroboscopic map. Integration up to the time (in stroboscopic time unit, which is the period of the backbone PO in the CR3BP-GH) of the first transversal second-return revolution of the 2-torus.

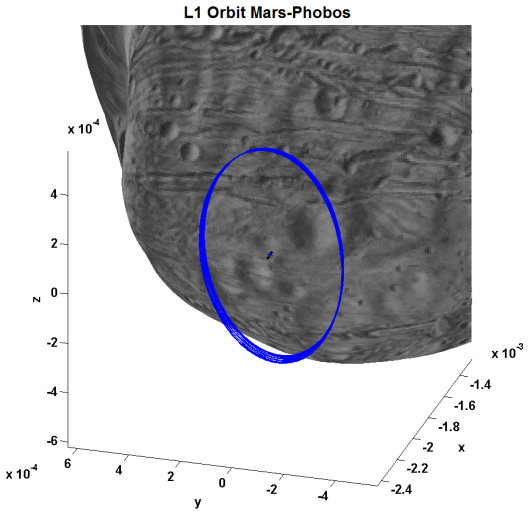

Figure 4.111: **Quasi-periodic LPOs in the Mars-Phobos ER3BP-GH.** Simulation of a medium-energy 2D-QPO of the family A around L_1 of the ER3BP-GH. Trajectory integrated up to the time of the first transversal second-return revolution of the 2-torus.

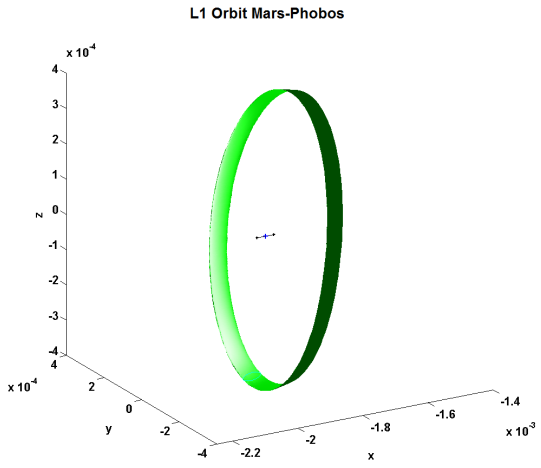

Figure 4.112: **Quasi-periodic LPOs in the Mars-Phobos ER3BP-GH.** Simulation of a medium-energy 2D-QPO of the family A around L_1 of the ER3BP-GH. Surface of motion of the 2-torus.

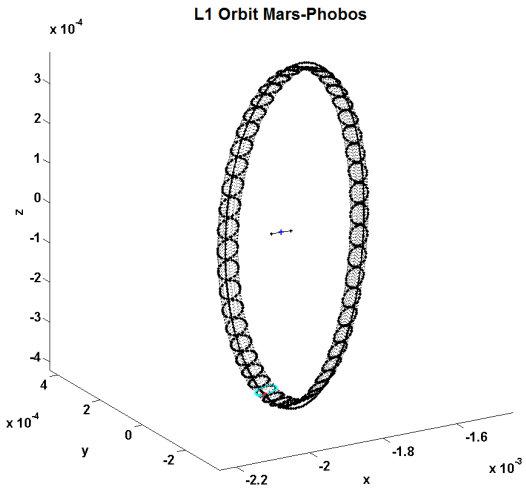

Figure 4.113: **Quasi-periodic LPOs in the Mars-Phobos ER3BP-GH.** Simulation of a medium-energy 2D-QPO of the family A around L_1 of the ER3BP-GH. Surface of motion of the 2-torus parameterized by the transversal invariant curves of the stroboscopic maps around the backbone PO of the CR3BP-GH. Initial invariant curve and backbone PO (with initial conditions) displayed.

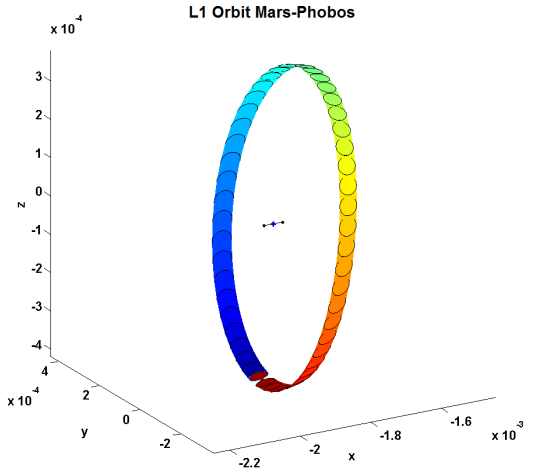

Figure 4.114: **Quasi-periodic LPOs in the Mars-Phobos ER3BP-GH.** Simulation of a medium-energy 2D-QPO of the family A around L_1 of the ER3BP-GH. Surface of motion of the 2-torus parameterized by the transversal invariant curves of the stroboscopic maps around the backbone PO of the CR3BP-GH. Initial invariant curve displayed.

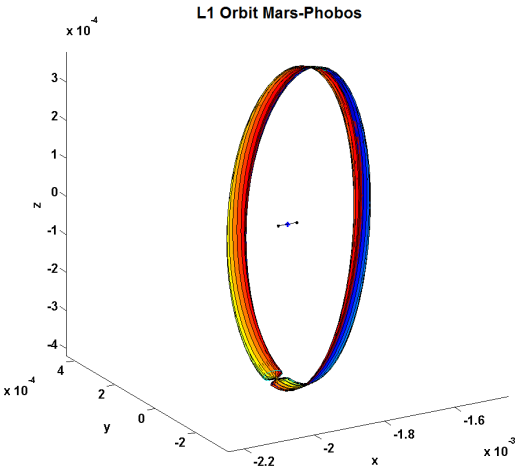

Figure 4.115: **Quasi-periodic LPOs in the Mars-Phobos ER3BP-GH.** Simulation of a medium-energy 2D-QPO of the family A around L_1 of the ER3BP-GH. Surface of motion of the 2-torus parameterized by the longitudinal invariant curves of the initial stroboscopic map around the backbone PO of the CR3BP-GH. Initial invariant curve displayed.

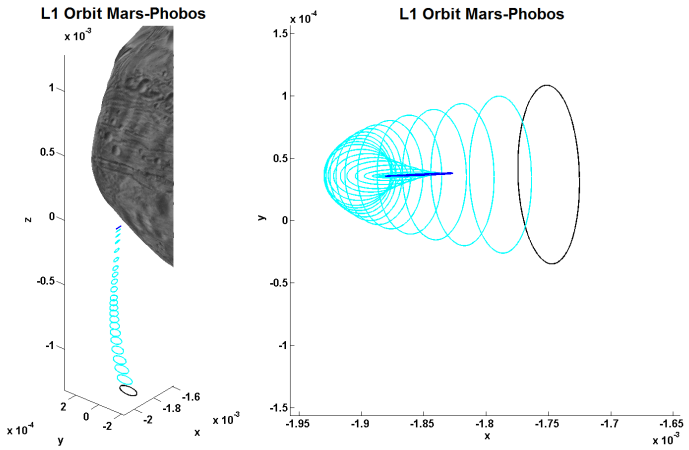

Figure 4.116: **Quasi-periodic LPOs in the Mars-Phobos ER3BP-GH.** Continuation with respect to the stroboscopic time ($\sigma = T$) from the period of a small-energy 2D-QPO (blue) to the period of the 2D-QPO intersecting Phobos' surface (black) of the family A around L_1 in the ER3BP-GH. Invariant curve on the stroboscopic map.

eterizes the families of their ancestors in the CR3BP-GH. An example of this second scheme is shown in Fig.D.66-4.116.

In particular, an unexpected *coupling between GHs and eccentricity* has been found. As a difference from the basic CR3BP (see Fig.4.12-4.34-4.36), in Fig.4.63 the characteristic curve of the family A of POs at small-energy has a local maximum. The NC of invariant curves with respect to the stroboscopic time of this family therefore has a folding, as seen in Fig.D.66. But this NC scheme hides an interesting behavior, that instead is evident undertaking the first scheme of NC, with respect to the eccentricity. Using the latter, two POs within the region of the local maxima, that have the same period, will eventually have the same invariant curve for a certain eccentricity. When this value is smaller than Phobos' eccentricity, all the original POs in the CR3BP-GH, with period larger than the one of this couple, do not have a 1-1 dynamical substitute QPO in the ER3BP-GH.

This is shown in Fig.4.119: a PO of the family A around L_1 could not be continued up to the eccentricity of Phobos because the Fourier coefficients revolve back in a closed loop, symmetrical with respect to the $e = 0$ axis. The continuation curve for all the 0-frequency Fourier coefficients intersects the $e = 0$ axis twice at different locations, while for all the other coefficients it intersects this axis at the origin. This means that there is a second PO linked within the same continuation curve, in the augmented state-space $[\mathbf{x}; e]$. Recall from section 4.3.1 that a negative eccentricity just means a shift of definition of the initial true anomaly's reference, therefore negative branches of the continuation curve are symmetrical and describe the same QPO. This peculiar behavior of the ER3BP-GH is graphically shown in Fig.4.120, where the related invariant curves are plotted. They show the connection between two POs, realized by an alter-

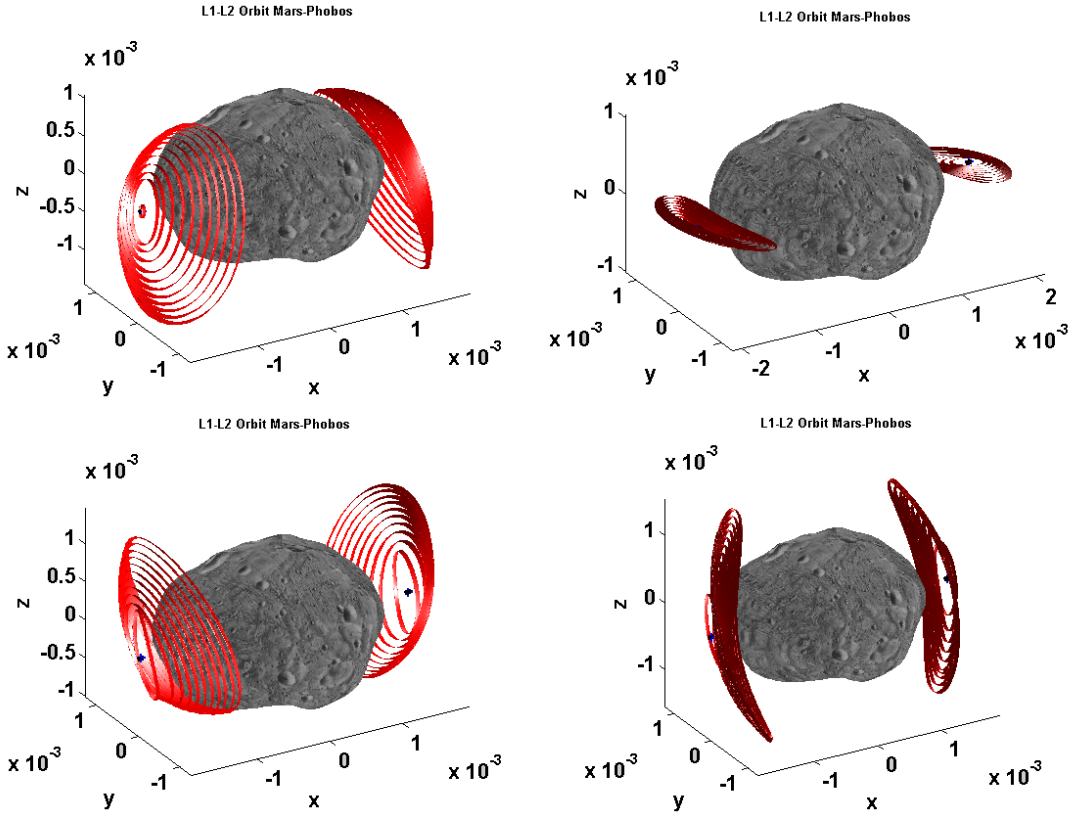

Figure 4.117: **Quasi-periodic LPOs in the Mars-Phobos ER3BP-GH.** Graphical visualization of the families of 2D-QPOs around L_1 and L_2 in the ER3BP-GH.

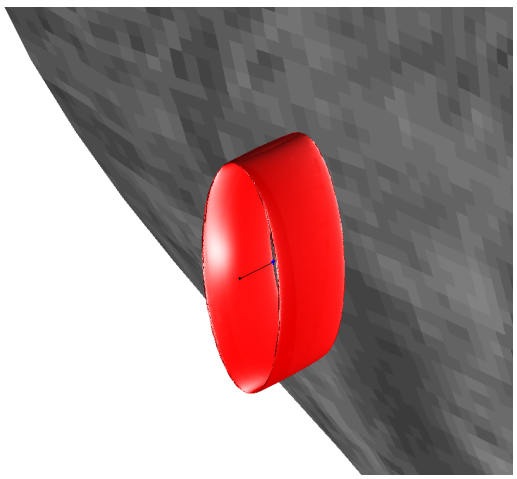

Figure 4.118: **Quasi-periodic LPOs in the Mars-Phobos ER3BP-GH.** Simulation of a small-energy 2D-QPO of the family A around L_1 of the ER3BP-GH. Surface of motion of the 2-torus.

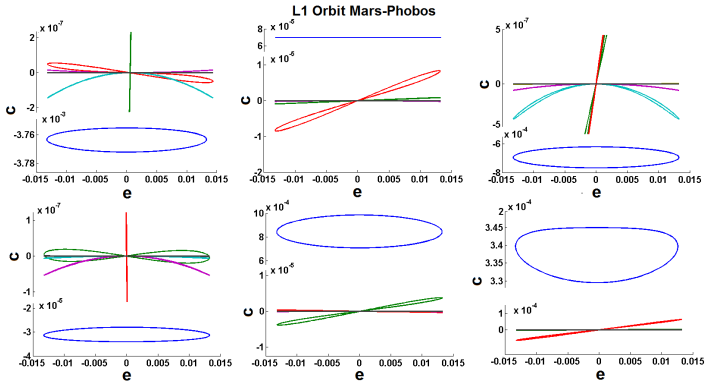

Figure 4.119: **Quasi-periodic LPOs in the Mars-Phobos ER3BP-GH.** Continuation variables' curves profile. Continuation with respect to the eccentricity from CR3BP-GH ($\sigma = 0$) to ER3BP-GH ($\sigma = e_{Phobos}$) of a small-energy PO of the family A around L_1 of the CR3BP-GH, showing that this orbit does not have a dynamical substitute in the ER3BP-GH at the eccentricity of Phobos. All the Fourier coefficients apart from the ones of 0-degree return to zero at $e = 0$, therefore this continuation actually links two POs (of the same family A, at the same period, see particular in Fig.4.63) in the globalized ER3BP-GH$(t, \nu, \mathbf{x}, e)$.

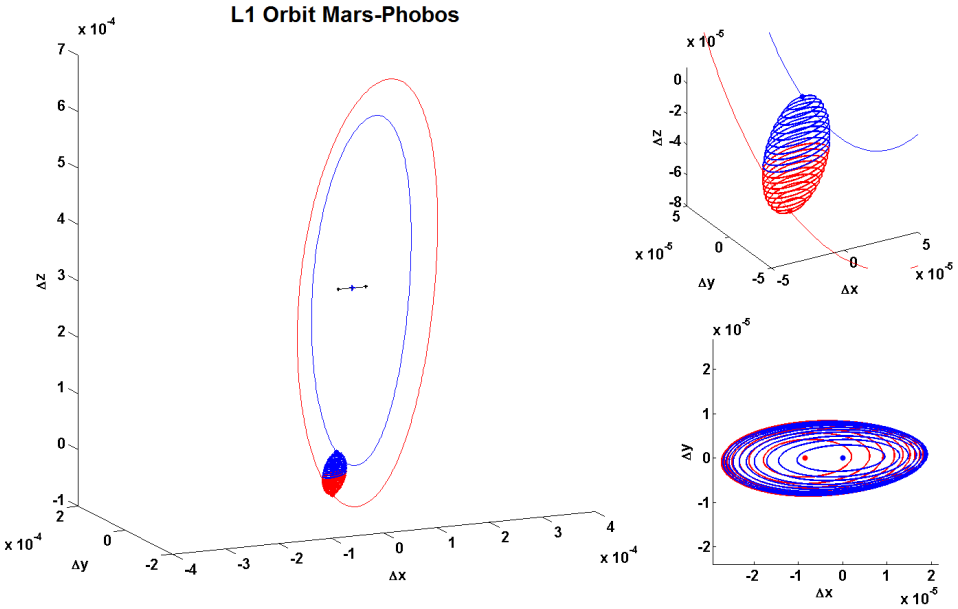

Figure 4.120: **Quasi-periodic LPOs in the Mars-Phobos ER3BP-GH.** Invariant curves of the stroboscopic map obtained by NC with respect to the eccentricity from CR3BP-GH to ER3BP-GH of a small-energy PO (blue) of the family A around L_1, showing that this orbit does not have a dynamical substitute 2D-QPO in the ER3BP-GH at the eccentricity of Phobos. This continuation links the starting PO to another one (red, of same family and period, see particular in Fig.4.63) in the globalized ER3BP-GH$(t, \nu, \mathbf{x}, e)$.

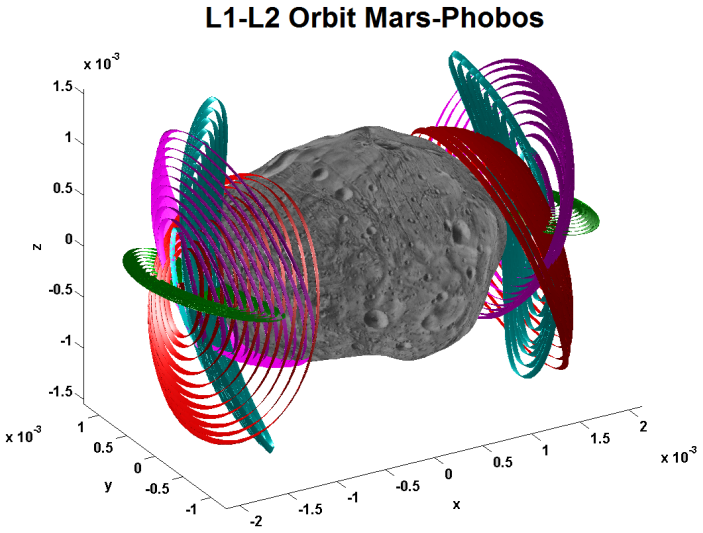

Figure 4.121: **Quasi-periodic LPOs in the Mars-Phobos ER3BP-GH.** Graphical visualization of the families of 2D-QPOs around L_1 and L_2 in the ER3BP-GH. Continuation with respect to the stroboscopic time in the ER3BP-GH. Colors are coherent with Fig.4.58.

nate shrinking of the invariant curves towards a couple of different attracting invariant points. In summary, this behavior would have not happened for the computation of LPOs between the classical CR3BP and ER3BP.

4.3.3.3 The 2D-QPOs of the Mars-Phobos ER3BP-GH

The dynamical substitutes of the POs in the ER3BP-GH are still organized in the same continuous 1-parameter families A, B, and CD, but now they consist of invariant 2-tori with one phase set to be the true anomaly of Phobos around Mars, and are showcased in Fig.4.117 and Fig.4.121-4.122. The width of their invariant curves is coherent with the LP oscillation's amplitude, as visible in Fig.4.118, where the dynamical substitute of a small-energy PO is considered. From the simulation of these QPOs, the characteristic curves of the period of the first transversal revolution on the second-return stroboscopic map are computed, and are reported in Fig.4.123.

Regarding the stability properties, the methodology of section B.6.5 is applied to undertake the Floquet stability analysis of the invariant curves of the four families of 2D-QPOs of the ER3BP-GH, around each LP. The related monodromy-like matrix shows that the stability properties are the same of the ancestor POs in the circular dynamics discussed in section 4.2.2.3, which is a saddle $\times$ center $\times$ center structure of the manifolds of the families A, B, C, and a saddle $\times$ saddle $\times$ center structure of the manifolds of the family D. An example of the set of eigenvalues is provided in Fig.4.124, where the presence of spurious eigenvalues can be seen. The selection of the most accurate eigenvector is conducted with the norm-(1) defined in Eq.B.125, and an example is provided in Fig.4.125.

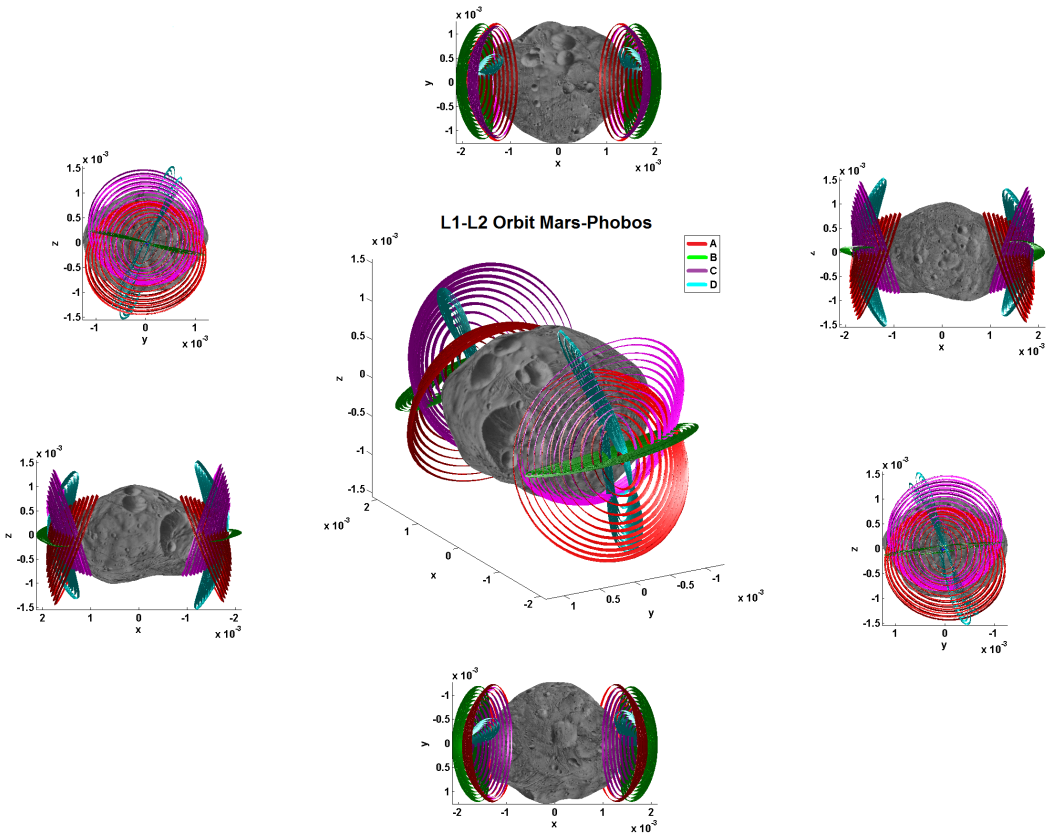

Figure 4.122: **Quasi-periodic LPOs in the Mars-Phobos ER3BP-GH.** Graphical visualization of the families of 2D-QPOs around L_1 and L_2 in the ER3BP-GH. Projections on the coordinate planes.

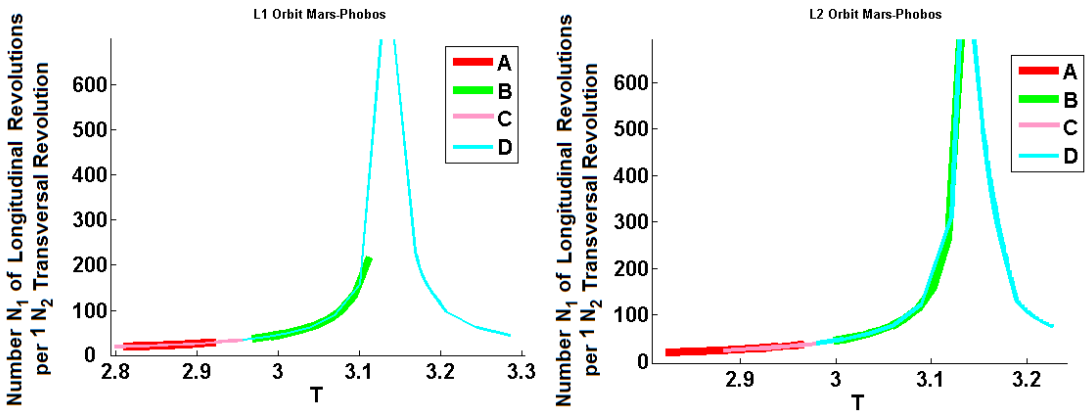

Figure 4.123: **Quasi-periodic LPOs in the Mars-Phobos ER3BP-GH.** Characteristic curves of the period of the first transversal revolution around the invariant curve on the second-return stroboscopic map of the families of 2D-QPOs around L_1 in the ER3BP-GH, parameterized by the stroboscopic period. The asymptote for the families B and D at the synchronous period $T = \pi$ corresponds to the 2:1 resonant 2D-QPOs that are actually a family of POs.

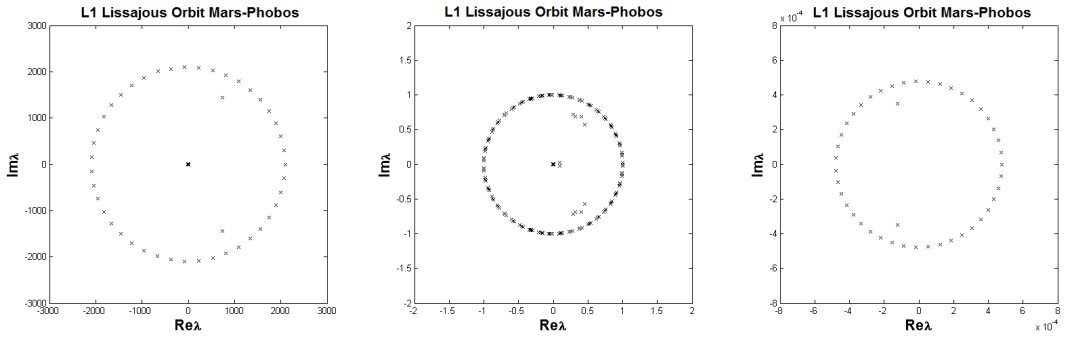

Figure 4.124: **Quasi-periodic LPOs in the Mars-Phobos ER3BP-GH.** Stability analysis. Set of eigenvalues of the invariant curve of the stroboscopic map. Case of a medium-energy 2D-QPO of the family A around L_1 of the ER3BP-GH. Each of the subfigures specifically magnifies the area of the unstable, central and stable manifolds.

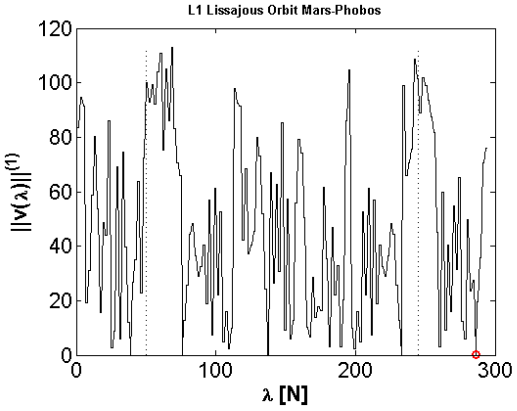

Figure 4.125: **Quasi-periodic LPOs in the Mars-Phobos ER3BP-GH.** Norm-(1) of the set of eigenvectors of the invariant curve of the stroboscopic map. Case of a medium-energy 2D-QPO of the family A around L_1 of the ER3BP-GH. Dotted lines mark stable, central and unstable subset of the total eigenspace, where the eigenvectors are ordered by the related eigenvalue's magnitude. Point highlighted identifies the eigenvalue with the minimum norm-(1) of the unstable subset, that will be used for the computation of the unstable IMs.

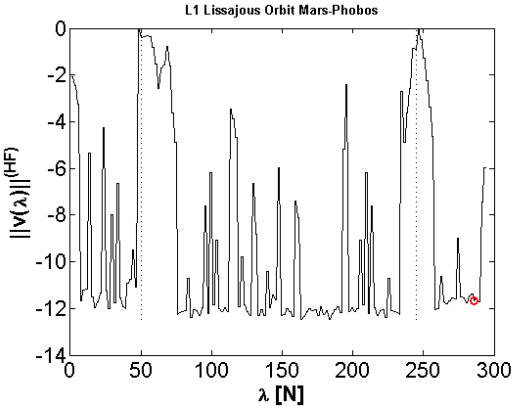

Figure 4.126: **Quasi-periodic LPOs in the Mars-Phobos ER3BP-GH.** Norm-(HF), in logarithmic scale, of the set of eigenvectors of the invariant curve of the stroboscopic map. Case of a medium-energy 2D-QPO of the family A around L_1 of the ER3BP-GH. Dotted lines mark stable, central and unstable subset of the total eigenspace, where the eigenvectors are ordered by the related eigenvalue's magnitude. Point highlighted identifies the eigenvalue with the minimum norm-(1) of the unstable subset, that will be used for the computation of the unstable IMs.

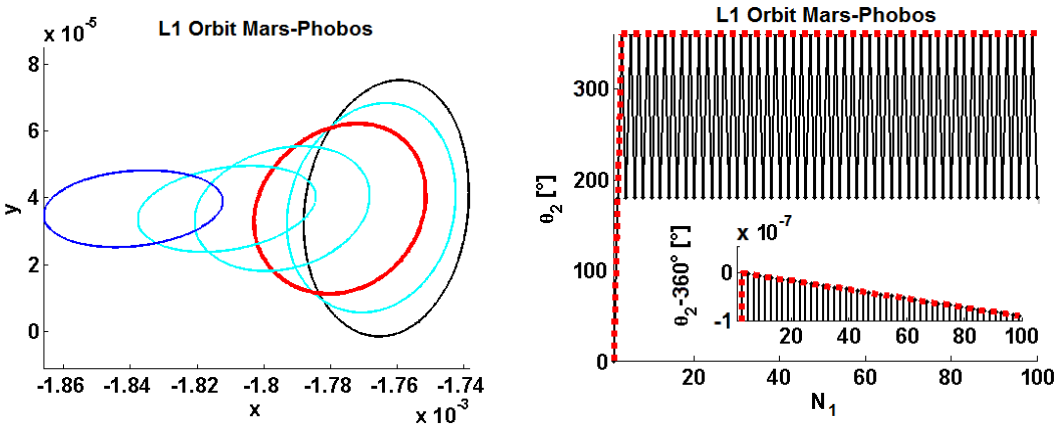

Figure 4.127: **Quasi-periodic LPOs in the Mars-Phobos ER3BP-GH.** On the left, invariant curves on the stroboscopic map of the D family around L_1, from a small-energy 2D-QPO (blue) to the 2D-QPO intersecting Phobos' surface (black). The invariant curve highlighted in red corresponds to a 2D-QPO with the resonant stroboscopic period π. On the right, the related profile of the curve's parametrization variable (corresponding to Phobos true anomaly) along iterated mappings shows that the profile at the second-return frequency (red) is flat: as the magnification highlights, the total change of the Phobos true anomaly is just 10^{-7} ° in 100 stroboscopic periods, therefore this 2D-QPO constitutes a closed family of POs in the ER3BP-GH, since every point along the curve is invariant.

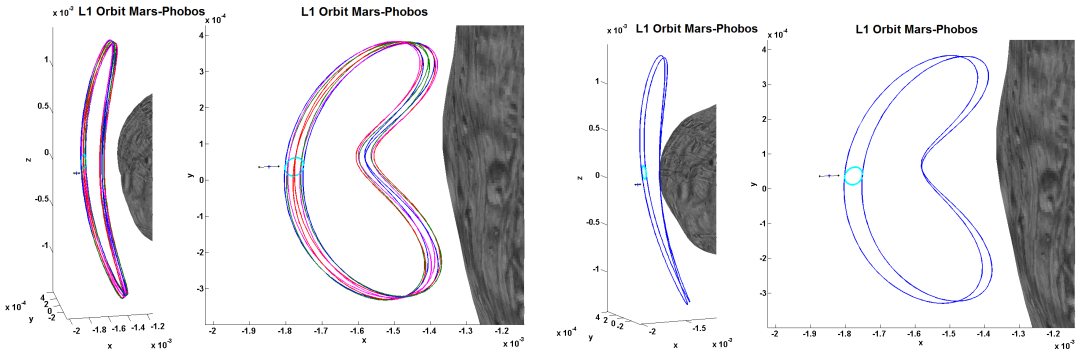

Figure 4.128: **Quasi-periodic LPOs in the Mars-Phobos ER3BP-GH.** Graphical visualization of the family of POs of the family D of the ER3BP-GH around L_1. Continuation with the DC scheme for computing the natural 2D-QPO substitute in the ER3BP-GH of the synchronous PO in the CR3BP-GH. First graph shows the POs whose starting true anomalies on the stroboscopic map are: at the pericenter, at 45°, at the first quadrature, and at 135° (the first-return points correspond to the point on the same PO at apocenter, at 225°, at the second quadrature, and at 315°). Second graph shows the PO whose starting true anomaly on the stroboscopic map is at the pericenter. Invariant curve of the stroboscopic map highlighted.

4.3.3.3.1 Resonant POs in the Mars-Phobos ER3BP-GH

In Fig.4.123, the characteristic curves of the period of the first transversal revolution on the second-return stroboscopic map show how many longitudinal revolutions are needed to achieve a full lap of the invariant curve. This number increases when the period of the ancestor PO tends to be in an integer ratio with the orbital period. In particular, we see that large 2D-QPOs of the families B and D in the ER3BP-GH are close to the resonance 2:1. The asymptote identifies the synchronous POs of the ER3BP-GH computed with the dedicated DC in section 4.3.2.1, where after two longitudinal revolutions the spacecraft will fly back at the initial condition. Thus, the invariant curve becomes a curve of invariant points, which is the family of iso-periodic POs in the ER3BP-GH of Fig.4.103-4.105. The related resonant curve is shown in Fig.4.127, together with the profile of a numerical simulation.

This algorithm for QPOs naturally embeds the *resonant cases* N:M: when the period of the ancestor PO is in an integer ratio M:N with the orbital period, the invariant curve of its dynamical substitute on a multiple-return stroboscopic map (propagation time of N times the orbital period) has a flat rotation number profile, whose value is zero, as shown in Fig.4.127. Therefore this method for QPOs is used to continue the two synchronous POs in 2:1 resonance of the families D of the CR3BP-GH. This could be done directly with the first NC scheme, continuing the synchronous PO, or retrieving the resonant invariant curve along the family D with the second NC scheme. Both approaches have been tested, and Fig.4.127 shows the resonant invariant curve. Both approaches gave the same PO that was computed with the dedicated DC scheme of section 4.3.2.1, and they suffer the same identical computational problem, as the DC's Jacobian is singular at the solution. Thus, the reference signal computed is affected by an error of *cm* scale after one orbital period. Since this has now happened with three different approaches so far, it could be recognized that the computation of a synchronous PO in the elliptic dynamics is a typical numerical problem of resonances. This name identifies the effect of small denominators that appears in the computational procedure. However, the dedicated DC scheme for QPOs is clearly superior to the dedicated one for POs of [54] used in section 4.3.2.1, because it provides not only one initial condition in the ER3BP-GH, but directly a curve of invariant points that describes the iso-periodic family of POs, as shown in Fig.4.128.

4.3.4 3D-QPOs in the Mars-Phobos ER3BP-GH

This section provides the closure of the analysis on the LPOs around Phobos in an accurate model of the orbital dynamics. This is the computation of the dynamical substitutes in the ER3BP-GH of the 2-parameters families AB and C of 2D-QPOs of the CR3BP-GH. They are tori with three phases: the longitudinal phase φ_1, the first transversal phase $\theta_1 = \varphi_2$, and the second transversal phase $\theta_2 = \varphi_3$ is constrained to be the true anomaly ν.

$$\mathbf{x}=\left[\begin{array}{c}\mathbf{q}\\ \dot{\mathbf{q}}\\ \nu\end{array}\right]\rightarrow\mathbf{x}_{3D-QPO}(t)=\phi_{\mathbf{f}}(t,0,\mathbf{x}_{0,3D-QPO}\left(\theta_1,\theta_2\right))\ ,$$

$$\forall\theta_1\in\mathrm{I}_{\theta_1}=[\theta_{1,m},\theta_{1,M}],\forall\theta_2\in\mathrm{I}_{\theta_2}=[0,2\pi]:$$

$$:\left[\begin{array}{c}\mathbf{q}_{0,3D-QPO}\left(\theta_{1,m},\theta_2\right)=\mathbf{q}_{0,3D-QPO}\left(\theta_{1,M},\theta_2\right)\\ \dot{\mathbf{q}}_{0,3D-QPO}\left(\theta_{1,m},\theta_2\right)=\dot{\mathbf{q}}_{0,3D-QPO}\left(\theta_{1,M},\theta_2\right)\end{array}\right]\wedge\left[\begin{array}{c}\mathbf{q}_{0,3D-QPO}\left(\theta_1,0\right)=\mathbf{q}_{0,3D-QPO}\left(\theta_1,2\pi\right)\\ \dot{\mathbf{q}}_{0,3D-QPO}\left(\theta_1,0\right)=\dot{\mathbf{q}}_{0,3D-QPO}\left(\theta_1,2\pi\right)\end{array}\right] \tag{4.47}$$

The set of initial conditions for such an orbit is parameterized by two phases. Therefore, a 3D-QPO is identified by an invariant 2-torus' surface S on a stroboscopic map.

$$\left\{\begin{array}{l}\mathbf{x}_{0,3D-QPO}\in\left[\begin{array}{c}S\left(\theta_1,\theta_2\right)\\ \theta_2\end{array}\right]\rightarrow P_T(\mathbf{x}_{0,3D-QPO})=\phi_{\mathbf{f}}(T,0,\mathbf{x}_{0,3D-QPO})\in\left[\begin{array}{c}S\left(\theta_1,\theta_2\right)\\ \theta_2\end{array}\right]\\ \theta_2\left(\mathbf{x}\right)=\nu\left(0\right)=\nu_{0,3D-QPO}\end{array}\right.\ ,$$

$$\forall\theta_1\in\mathrm{I}_{\theta_1}=[\theta_{1,m},\theta_{1,M}],\forall\theta_2\in\mathrm{I}_{\theta_2}=[0,2\pi]:S\left(\theta_{1,m},\theta_2\right)=S\left(\theta_{1,M},\theta_2\right)\wedge S\left(\theta_1,0\right)=S\left(\theta_1,2\pi\right) \tag{4.48}$$

4.3.4.1 Computation of the Dynamical Substitutes of the Quasi-Periodic LPOs in the Mars-Phobos ER3BP-GH

The computation of high dimensional tori was addressed in section B.6.6. The DC method for computing 2D-QPOs of section B.6.3 can be naturally extended to a phase-space with higher dimension, by using a multi-dimensional Fourier series to describe the invariant object. However, for an ER3BP this is high computationally demanding. The practical approach for high-dimensional tori is to simply treat them as bounded orbits. The related methodology is based on the tuning of the reference signal for its applications in perturbed dynamics, and is presented in section B.7.

In this section, the classical multiple shooting scheme of Eq.B.133, used for computing bounded orbits in perturbed dynamics, is exploited. Since the eccentricity of Phobos represents a strong perturbation, the DC is embedded in the NC with respect to the eccentricity of section 4.3.1, and at each intermediate dynamics it derives the closest solution that satisfies the continuity between the subintervals where the QPO's trajectory is sampled for a finite propagation time. In this sense, the subintervals are chosen as the non-uniform set of recursive return-times provided by the reduction of the ancestor 2D-QPO in the CR3BP-GH to a discrete dynamical system along the longitudinal motion, driven by the Poincaré map used to compute its invariant curve in section 4.2.3.1. Furthermore, the initial condition is taken at the origin of the ancestor invariant curve's parameter, and considering Phobos at the perimars. Finally, the time span is chosen as the period of the first transversal revolution of the ancestor 2D-QPO in the CR3BP-GH[19].

[19] As discussed in section B.7, since the last subinterval is not controlled, the time span considered is augmented by one longitudinal revolution.

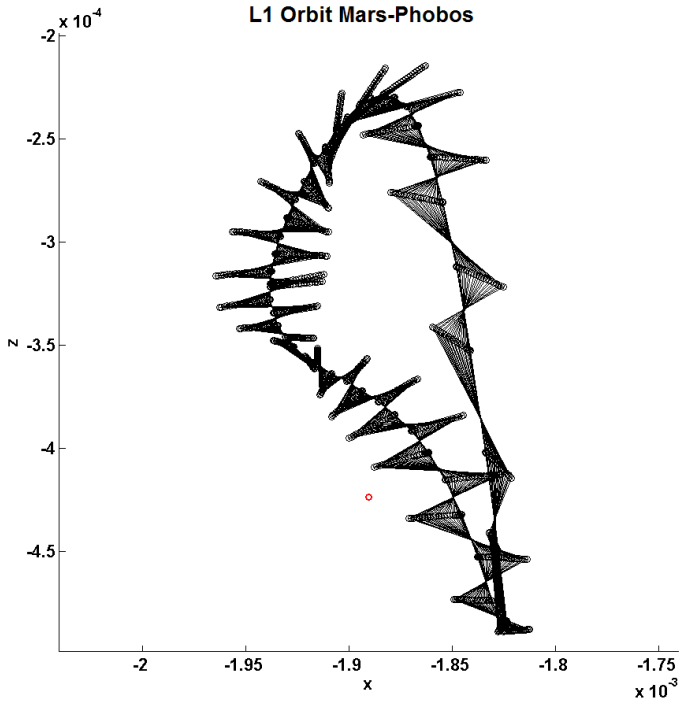

Figure 4.129: **3-tori LPOs in the Mars-Phobos ER3BP-GH.** Projection on the x-z plane of the set of initial conditions (sampling points of the multiple shooting scheme) that represent a part of the invariant surface of the 3-torus on a longitudinal map. Continuation with respect to the eccentricity from CR3BP-GH ($\sigma = 0$) to ER3BP-GH ($\sigma = e_{Phobos}$) of a large-width - medium-energy 2D-QPO of the family A around L_1, starting at the pericenter. Backbone PO of the ancestor 2D-QPO displayed.

This approach derives a practical approximation of the 3D-QPO, with any information of its invariant object S. Furthermore, the approach does not guarantee to find a bounded orbit for high perturbations, which should be the case of Phobos' eccentricity, since the solution is not a dynamical substitute. However, the orbits obtained oscillate around the ancestor 2D-QPOs with an amplitude similar to that of the LPs even for a high time span set in the DC. This is presented for a range of different 3D-QPOs in the ER3BP-GH, around their respective backbone 2D-QPO of the CR3BP-GH, in Fig.4.129-4.135. Therefore the methodology provides trajectories that describe appropriate 3-tori in the defined time span. This propagation time, in terms of integer number of longitudinal revolutions, is far longer than that of typical applications of LPOs in mission segments. Therefore, the set of initial conditions determined at the end of the NC (the sampling points) can be considered part of the invariant 2-torus of the 3D-QPO,

$$\mathbf{x}_{0,3D-QPO,s} \in \begin{bmatrix} S(\theta, \nu_0) \\ \nu_0 \end{bmatrix}, \; 1 \leq s \leq (N_{T_2} - 1) \tag{4.49}$$

and the invariant object S can be reconstructed in a discrete way with the set of initial conditions. This could be done within the same DC scheme, choosing a large time span,

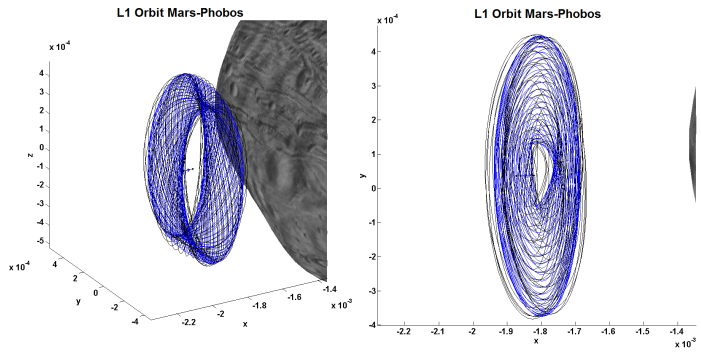

Figure 4.130: **3-tori LPOs in the Mars-Phobos ER3BP-GH.** Simulation of a large-width - medium-energy 3D-QPO of the family A around L_1 of the ER3BP-GH. Trajectory integrated up to the time of the first transversal revolution of the backbone 2D-QPO in the CR3BP-GH (blue).

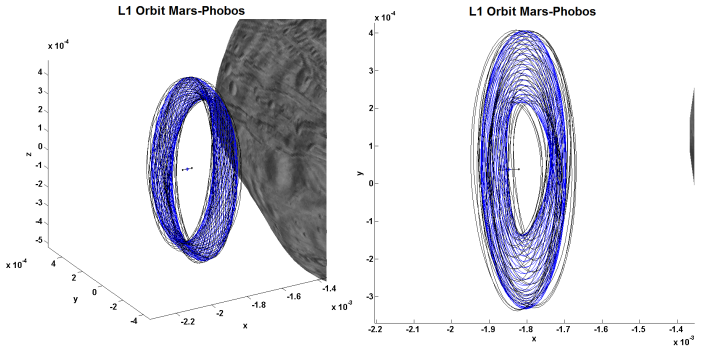

Figure 4.131: **3-tori LPOs in the Mars-Phobos ER3BP-GH.** Simulation of a medium-width - medium-energy 3D-QPO of the family A around L_1 of the ER3BP-GH. Trajectory integrated up to the time of the first transversal revolution of the backbone 2D-QPO in the CR3BP-GH (blue).

or using a shorter time but different DC schemes that start at different true anomalies. The reconstruction of the invariant 2-torus' surface is shown up to the period of the first transversal revolution of the backbone 2D-QPO in Fig.D.69 and Fig.D.70-D.72. In particular, the invariant 2-torus could be represented by its projection on a suitable surface of section, filling a bounded profile around the ancestor invariant curve, with a width corresponding to the oscillation's amplitude of the LPs.

The related period of the first transversal revolution (at double frequency) of the locked phase is retrieved by extrapolation. An example of the profile along time is presented in Fig.D.68.

4.3.4.2 The 3D-QPOs of the Mars-Phobos ER3BP-GH

A sampling of the 2D-QPOs of the CR3BP-GH has been continued with the methodology presented in section 4.3.4.1. The resulting dynamical substitutes in the ER3BP-GH are invariant 3-tori organized in the same continuous 2-parameter families AB and C, with one phase set to be the true anomaly of Phobos around Mars. They oscillate

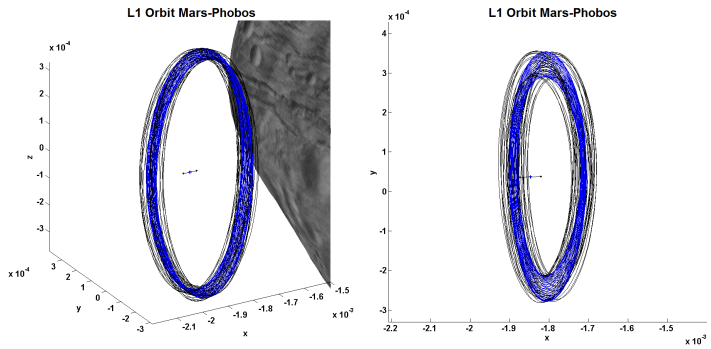

Figure 4.132: **3-tori LPOs in the Mars-Phobos ER3BP-GH.** Simulation of a small-width - medium-energy 3D-QPO of the family A around L_1 of the ER3BP-GH. Trajectory integrated up to the time of the first transversal revolution of the backbone 2D-QPO in the CR3BP-GH (blue).

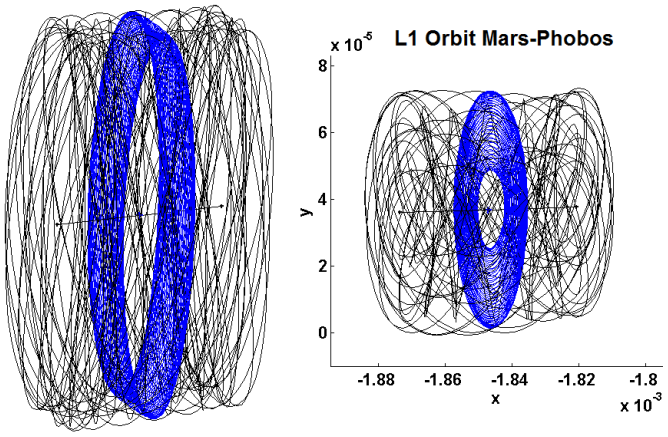

Figure 4.133: **3-tori LPOs in the Mars-Phobos ER3BP-GH.** Simulation of a large-width - small-energy 3D-QPO of the family A around L_1 of the ER3BP-GH. Trajectory integrated up to the time of the first transversal revolution of the backbone 2D-QPO in the CR3BP-GH (blue).

around their respective ancestor solutions with an amplitude similar to the one of the LPs. Fig.4.136-4.138 showcase some samples of the families of 3D-QPOs in the ER3BP-GH. This completes the manifold of LPOs in the most accurate model of the natural dynamics around the Martian moon Phobos.

From the simulation of these QPOs, the characteristic graphs of the period of the first transversal revolution are computed, and are reported in Fig.D.73-D.76 for each family, where the two parameters are taken as the ones that parameterize the backbone 2D-QPOs in the circular dynamics.

Regarding the stability properties, the Lyapunov stability analysis is undertaken from the STM of the reference signal within each subinterval, as explained in section B.6.5.

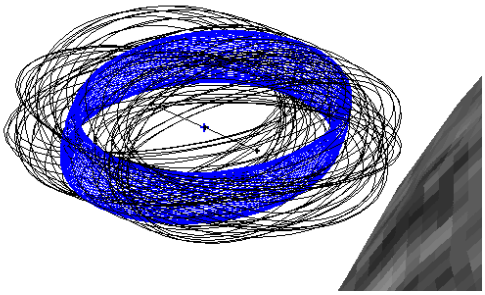

Figure 4.134: **3-tori LPOs in the Mars-Phobos ER3BP-GH.** Simulation of a small-width - small-energy 3D-QPO of the family B around L_1 of the ER3BP-GH. Trajectory integrated up to the time of the first transversal revolution of the backbone 2D-QPO in the CR3BP-GH (blue).

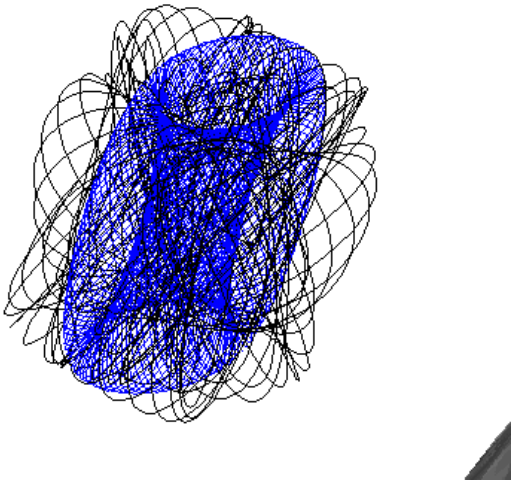

Figure 4.135: **3-tori LPOs in the Mars-Phobos ER3BP-GH.** Simulation of a large-width - small-energy 3D-QPO of the family B around L_1 of the ER3BP-GH. Trajectory integrated up to the time of the first transversal revolution of the backbone 2D-QPO in the CR3BP-GH (blue).

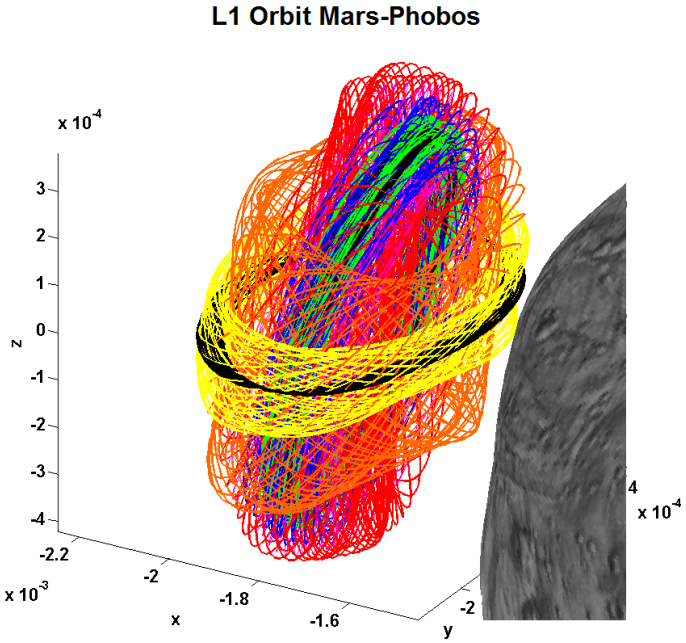

Figure 4.136: **3-tori LPOs in the Mars-Phobos ER3BP-GH.** Family of 3D-QPOs that connects the two medium iso-energetic 2D-QPOs of the families A and B around L_1 of the ER3BP-GH. Related two backbones 2D-QPOs displayed in black. Trajectory integrated up to the period of the first transversal revolution of the backbone 2D-QPO in the CR3BP-GH.

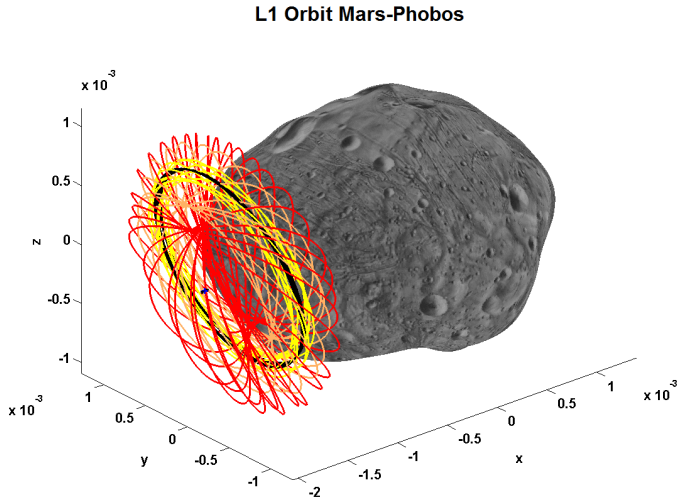

Figure 4.137: **3-tori LPOs in the Mars-Phobos ER3BP-GH.** Family of 3D-QPOs around a medium-energy 2D-QPO of the family C around L_1 of the ER3BP-GH. Related backbone 2D-QPO displayed in black. Trajectory integrated up to the period of the first transversal revolution of the backbone 2D-QPO in the CR3BP-GH.

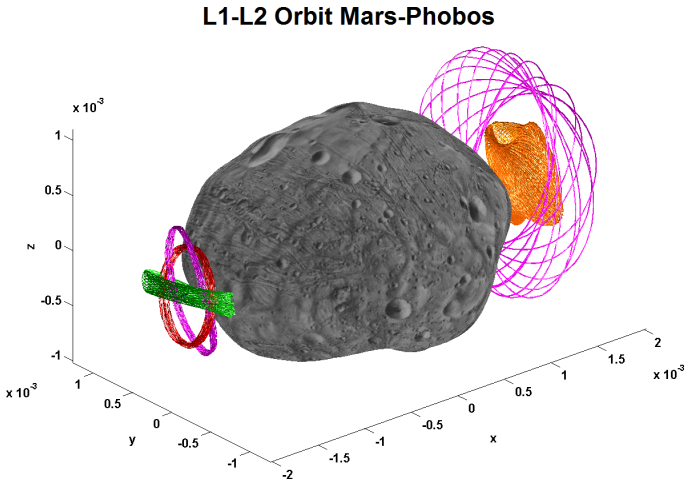

Figure 4.138: **3-tori LPOs in the Mars-Phobos ER3BP-GH.** Graphical visualization of 3-tori in the ER3BP-GH of different size and width around the LPs. Summarizing examples: three medium-size 3D-QPOs of the family AB (red and green with small-width, orange with high-width) and two high-width 3D-QPOs of the family C (of small and large-size). Trajectory integrated up to the period of the first transversal revolution of the backbone 2D-QPO in the CR3BP-GH.

4.3.5 IMs of the LPOs in the Mars-Phobos ER3BP-GH

Also in the most accurate model of the orbital dynamics in proximity of Phobos, all the families of periodic and quasi-periodic LPOs have resulted to be characterized by a dominant saddle manifold, which provides the stable and unstable IMs to reach and depart them.

The computation of the IMs' tubes has been addressed for a general dynamical system in section B.8 for each type of invariant motion, based on the dimension of its phase-space. Following this, this section presents the IMs of the resonant POs (family D), 2D-QPOs (families A, B, CD) and 3D-QPOs (families AB, C), computed in sections 4.3.2,4.3.3,4.3.4, of the LPOs of the Mars-Phobos ER3BP-GH.

4.3.5.1 Computation of the IMs of the LPOs in the Mars-Phobos ER3BP-GH

Due to the addition of a forcing term in the dynamics, the natural LPOs oscillate around their backbone in the CR3BP-GH. Therefore, the mean performances of their IMs would be equal to the ones of their ancestor orbits computed in section 4.2.4.1, but the computation of the IMs shall require the procedure dedicated for a torus of one larger dimension. The separate computation of the stable and unstable IM is carried out for the LPOs that do not intersect Phobos. Only the computation of the inside branch is addressed in this section, and the globalization of the manifold is propagated in the ER3BP-GH up to the intersection with Phobos' surface, which is modeled with the high-order shape harmonics of section 3.2.

The globalization of the stable and unstable IMs has directly intersected Phobos for all the families of LPOs, for both LPs. Therefore, as done in sections 4.1.5.1-4.2.4.1, the outcomes are presented on the topographical map of Phobos, parameterized by the couple of longitude and latitude of the landing/take-off site. The performances at the touch-down are then filtered by the case of minimum incidence for the unstable IM, which is a tangential arrival, and by the case of minimum velocity's total magnitude for the stable IM, that represents the escape velocity.

IMs of the families of resonant POs. The computation of the IMs of the two families D of iso-periodic POs is done exactly in the same way undertaken for their ancestor POs in the CR3BP-GH (Eq.B.137-B.138), just with the inclusion of the true anomaly in the monodromy matrix. The related eigenvalue is +1.

The IMs of the families of resonant POs in the ER3BP-GH are showcased in Fig.4.139.

Fig.4.140 provide a sample of the analysis for the family around L_1. Fig.D.77 provides the landing performances for L_1, and Fig.D.78 provides the ones for L_2.

Fig.D.79 provides the take-off performances for L_1, and Fig.D.80 provides the ones for L_2.

Due to the limited difference in the position and shape of the POs of each iso-periodic

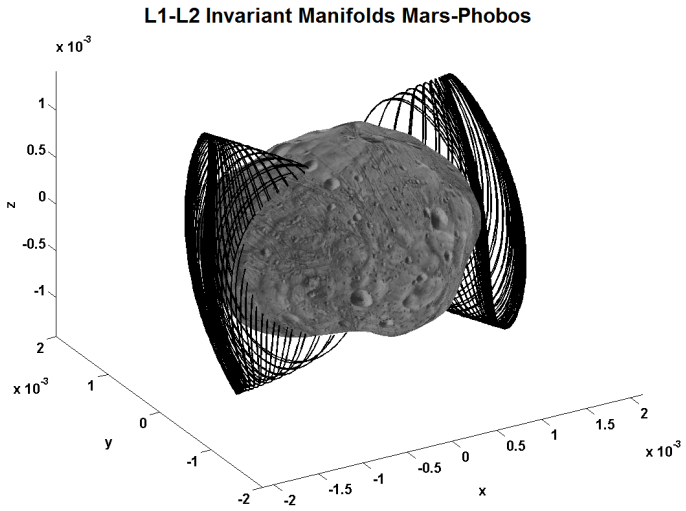

Figure 4.139: **Landing on Phobos through the Invariant Manifolds of the L_{1-2} resonant periodic LPOs of the ER3BP-GH.** Trajectories of the inside branch of the IMs from the family D of resonant POs. Phobos real shape.

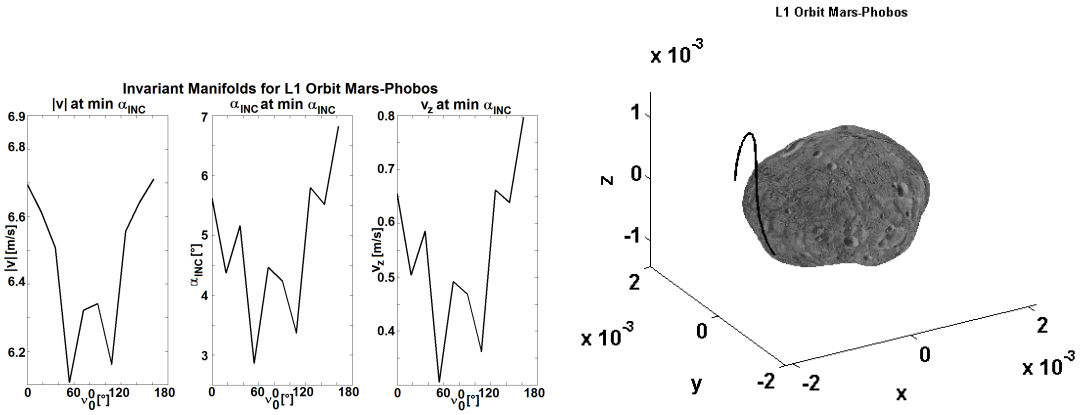

Figure 4.140: **Landing on Phobos through the Invariant Manifolds of the L_1 resonant periodic LPOs of the ER3BP-GH.** Trajectory that provides the min incidence at the touch-down, as a function of the initial Phobos true anomaly on the stroboscopic map, for orbits that do not intersect Phobos' real shape. Performances of the trajectories (velocity magnitude, angle of incidence, downward vertical velocity at the landing site), and trajectory that provides the overall min incidence at the touch-down.

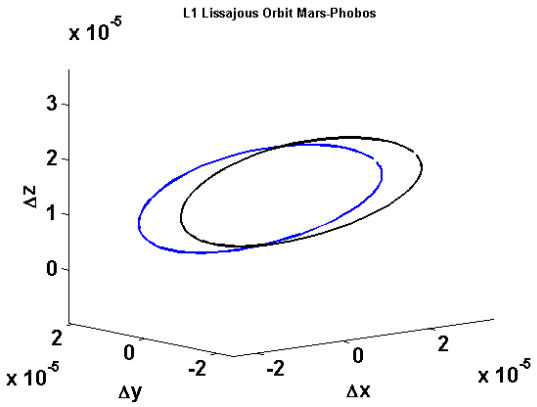

Figure 4.141: **Landing on Phobos through the Invariant Manifold of the L_1 family A of 2D-QPOs LPOs of the Mars-Phobos ER3BP-GH.** Stroboscopic map in the x-y-z space. Case of a medium-energy 2D-QPO of the family A around L_1 of the ER3BP-GH. The blue curve is the invariant curve of the 2D-QPO, and the black curve is the related set of initial condition of the inside branch of the unstable IM (for a magnified threshold ε_C =10% of the width of the 2D-QPO, which is $\gamma_i e_{Phobos}$).

family, the region of related landing or take-off site is quite narrow. However low angles of incidence are provided by them, whereas the escape velocities are medium-low. In this sense, in Fig.4.140, we see how the additional phase provided by the initial true anomaly on the stroboscopic map provides some margin to fine tune these performances.

IMs of the families of 2D-QPOs. The computation of the IMs of the 2D-QPOs is undertaken using the same procedure for the 2D-QPOs in the CR3BP-GH, where the numerical technique developed in section B.6.5 allows to derive the IMs of the whole invariant object. The related procedure to compute the IMs is addressed in section B.8.3. In particular, it requires the selection of the most accurate eigenvector for each manifold, and an example of the procedure is given in section 4.3.3. The related eigenvector provides a closed curve of initial conditions on the stroboscopic map, for the globalization of the manifold. An example is given in Fig.4.141. Since the invariant curve is parameterized by the true anomaly, the eigenvectors act only on the position and velocity coordinates to give the curve of the initial conditions at the same true anomaly, for the globalization of the manifold for each stroboscopic location. Due to the proximity of Phobos, to not invalidate the whole tube of IMs for high-energy orbits, the IMs are considered valid for slices of longitudinal revolutions that do not intersect Phobos's real shape.

The IMs of the families of 2D-QPOs in the ER3BP-GH are represented in Fig.4.142.

Fig.4.143-4.144 provide a sample of the analysis for the family A around L_1. Fig.D.81-D.82 provide the landing performances for L_1, and Fig.D.83-D.84 provide the ones for L_2.

Fig.D.85-D.86 provide the take-off performances for L_1, and Fig.D.87-D.88 provide the ones for L_2.

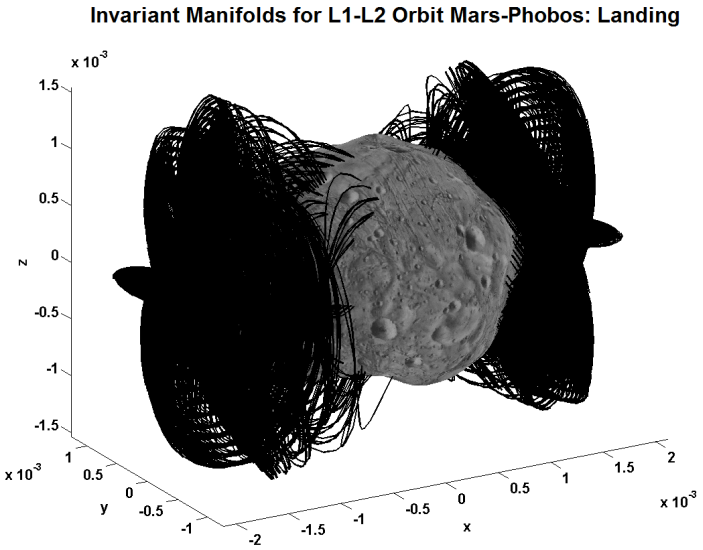

Figure 4.142: **Landing on Phobos through the Invariant Manifold of the L_{1-2} 2D-QPOs LPOs of the Mars-Phobos ER3BP-GH.** Trajectories of the inside branch of the IMs from the families A, B, CD of 2D-QPOs. Phobos real shape.

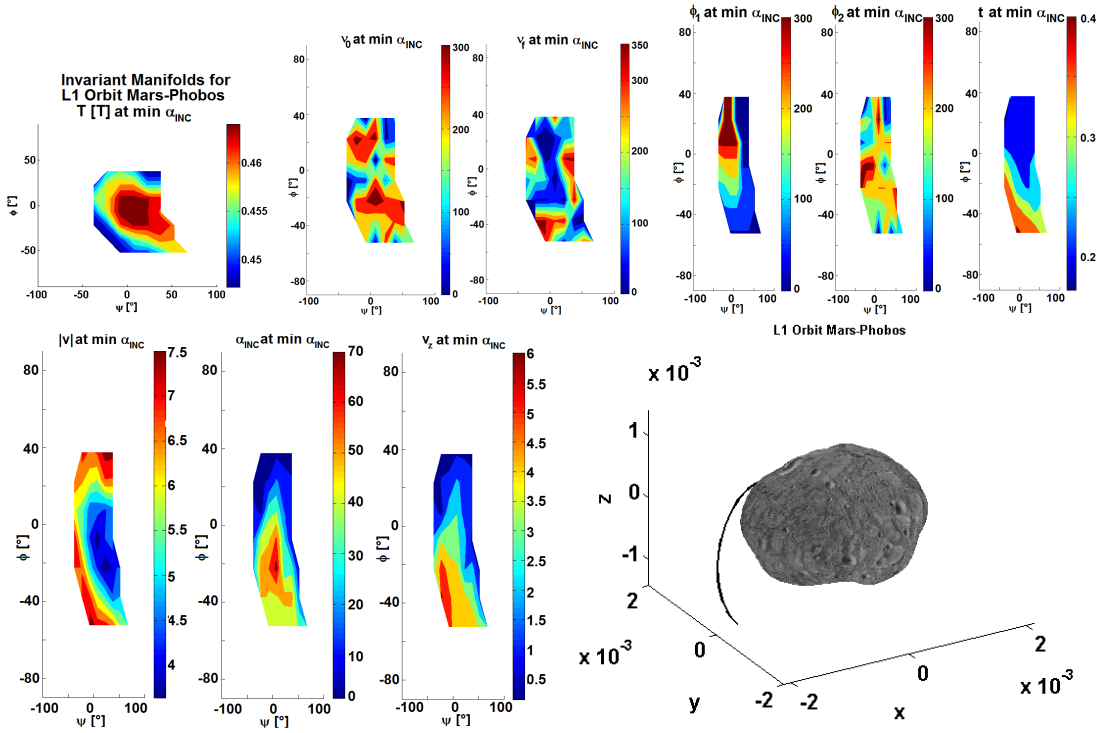

Figure 4.143: **Landing on Phobos through the Invariant Manifold of the L_1 family A of 2D-QPOs LPOs of the Mars-Phobos ER3BP-GH.** Trajectories that provide the min incidence at the touch-down, as a function of the longitude and latitude of the landing site, for orbits that do not intersect Phobos' real shape. Performances of the trajectory: stroboscopic period parameter of the family, initial and final true anomaly, initial longitudinal and transversal phases along the departing orbits, TOF, and landing velocity magnitude, angle of incidence, downward vertical velocity. Trajectory that provides the overall min incidence at the touch-down.

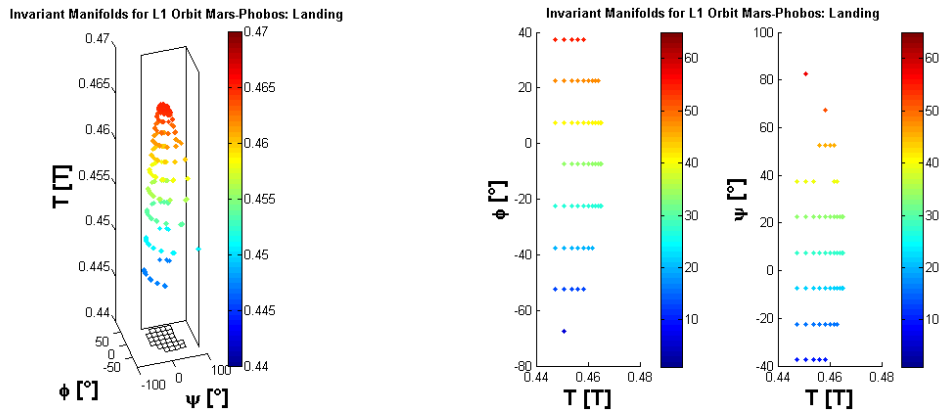

Figure 4.144: **Landing on Phobos through the Invariant Manifold of the L_1 family A of 2D-QPOs LPOs of the Mars-Phobos ER3BP-GH.** Direct and inverse relation between the longitude and latitude of the landing site and the stroboscopic period parameter of the family, for orbits that do not intersect Phobos' real shape.

The footprints of the IMs on Phobos are similar to the ones obtained with the families of POs in the CR3BP-GH, but the performances at the touch-down and launch are further optimized in the elliptic problem with the additional phase of Phobos required to identify the LPOs' initial condition.

IMs of the families of 3D-QPOs. In section 4.2.4.1, the IMs of the whole invariant object associated to the QPOs were computed from the monodromy-like matrix, provided by the numerical technique developed in section B.6.5. However, the dynamical substitutes of these LPOs in the ER3BP-GH have been approximated in section 4.3.4 with a time-limited reference signal. Therefore, the computation of the IMs of these 3D-QPOs in the ER3BP-GH is undertaken using the same procedure for the Lissajous orbits in the CR3BP in section 4.1.5, which is to calculate the manifold at each sample point from the STM associated to the related longitudinal subinterval of the reference signal (see section B.8.3). An example of the set of initial conditions (that include the true anomaly) is provided in Fig.4.145-4.146. Due to the proximity of Phobos, to not invalidate the whole tube of IMs for high-width and high-energy orbits, the IMs are considered for slices of longitudinal revolutions that do not intersect Phobos's real shape.

The IMs of the families of 3D-QPOs in the ER3BP-GH are computed with this approach, and they are represented in Fig.4.147.

Fig.4.148-4.149 provide a sample of the analysis for the family A around L_1. Fig.D.89-D.90 provide the landing performances for L_1, and Fig.D.91-D.92 provide the ones for L_2.

Fig.D.93-D.94 provide the take-off performances for L_1, and Fig.D.95-D.96 provide the ones for L_2.

The footprints of the IMs on Phobos are similar to the ones obtained with the families of 2D-QPOs in the CR3BP-GH, but the performances at the touch-down and launch

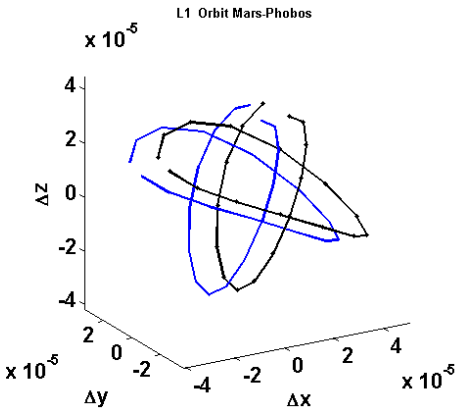

Figure 4.145: **Landing on Phobos through the Invariant Manifold of the L_1 family A of 3-tori LPOs of the Mars-Phobos ER3BP-GH.** Set of initial conditions that represent a part of the invariant surface of the 3D-QPO on a longitudinal map. Case of a small-width - medium-energy 3D-QPO of the family A around L_1 of the ER3BP-GH. The blue curve is the reduced 3D-QPO, and the black curve is the related set of initial condition of the inside branch of the unstable IM (for a threshold of 10^{-5} adimensional units). Integration up to the period of the first transversal revolution of the backbone 2D-QPO in the CR3BP-GH.

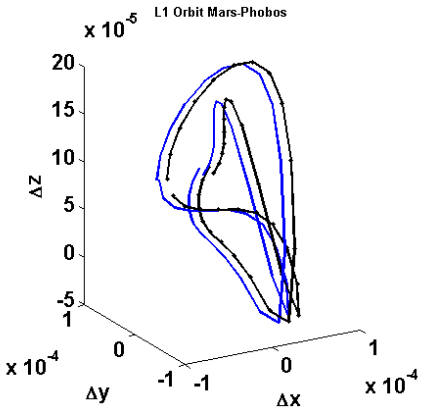

Figure 4.146: **Landing on Phobos through the Invariant Manifold of the L_1 family A of 3-tori LPOs of the Mars-Phobos ER3BP-GH.** Set of initial conditions that represent a part of the invariant surface of the 3D-QPO on a longitudinal map. Case of a large-width - medium-energy 3D-QPO of the family A around L_1 of the ER3BP-GH. The blue curve is the reduced 3D-QPO, and the black curve is the related set of initial condition of the inside branch of the unstable IM (for a threshold of 10^{-5} adimensional units). Integration up to the period of the first transversal revolution of the backbone 2D-QPO in the CR3BP-GH.

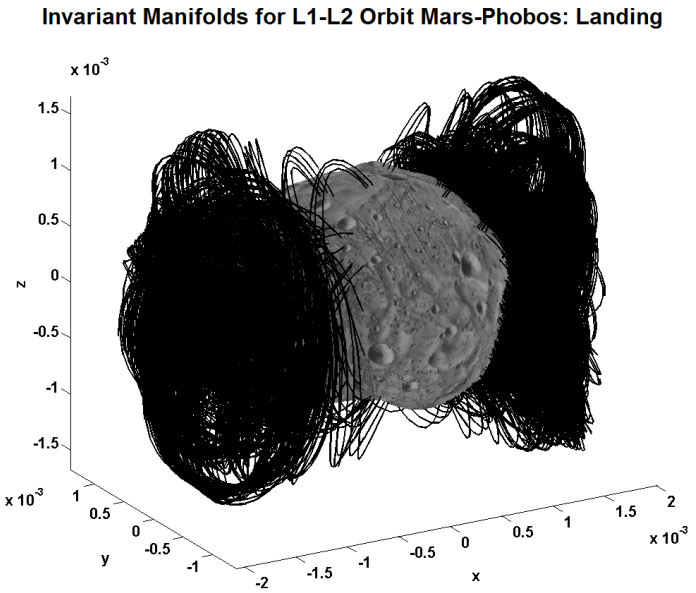

Figure 4.147: **Landing on Phobos through the Invariant Manifold of the L_{1-2} 3-tori LPOs of the Mars-Phobos ER3BP-GH.** Trajectories of the inside branch of the IMs from the families AB, C of 3D-QPOs. Phobos real shape.

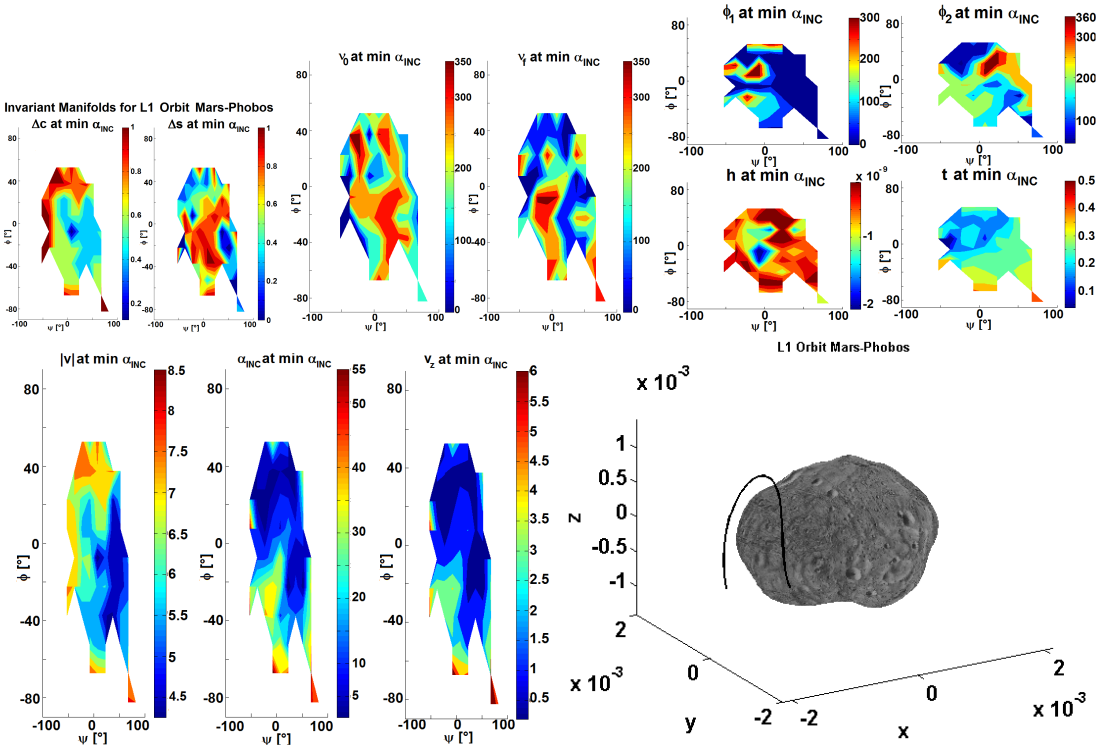

Figure 4.148: **Landing on Phobos through the Invariant Manifold of the L_1 family A of 3-tori LPOs of the Mars-Phobos ER3BP-GH.** Trajectories that provide the min incidence at the touch-down, as a function of the longitude and latitude of the landing site, for orbits that do not intersect Phobos' real shape. Performances of the trajectory: energy and width parameters of the family, initial and final true anomaly, initial longitudinal and transversal phases along the departing orbits, altitude where the integration is stopped, TOF, and landing velocity magnitude, angle of incidence, downward vertical velocity. Trajectory that provides the overall min incidence at the touch-down.

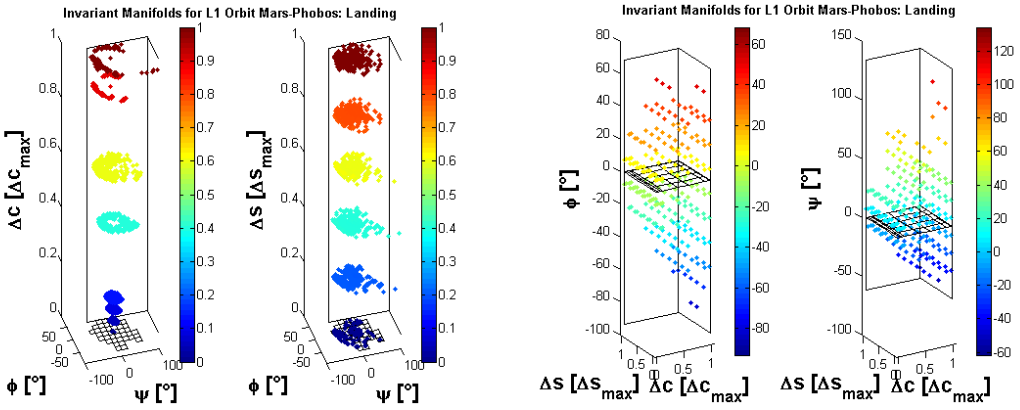

Figure 4.149: **Landing on Phobos through the Invariant Manifold of the L_1 family A of 3-tori LPOs of the Mars-Phobos ER3BP-GH.** Direct and inverse relation between the longitude and latitude of the landing site and the energy and width parameters of the family, for orbits that do not intersect Phobos' real shape.

are further optimized in the elliptic problem with the additional phase of Phobos that enlarges the phase-space of the LPOs. In particular, it is possible to arrive practically horizontal and with vertical velocities less than $0.5m/s$, and depart with escape velocities smaller than $4m/s$ in an extended region of sites. Furthermore, the large craters and grooves of Phobos are inside these natural regions, and their distribution appears to follow the boundaries of these natural footprints. In particular, despite the large bulge of Phobos on the cis and trans-side, the Stickney crater is still reachable by the IMs.

In conclusion, this analysis shows that also in the more accurate ER3BP-GH, with Phobos' eccentricity and GHs up to fourth degree and order, all the inside branch of the IMs of the new families of LPOs in this system intersects Phobos. Therefore, no homoclinic nor heteroclinic connections of the two LPs manifolds exist at all around Phobos. The IMs of the most accurate LPOs around Phobos are proposed to provide natural and efficient landing and take-off pathways for a spacecraft to and from the cis and trans-sides of the moon. This application will be discussed in detail in section 4.4.6.

4.4 Application of the LPOs around Phobos

The dynamical substitutes of the LPOs and their IMs have been computed in sections 4.2-4.3 in the more accurate models of the orbital dynamics in proximity of Phobos, the CR3BP-GH and the ER3BP-GH respectively.

In this section the performances of these orbits are evaluated. These characteristics are probed with respect to a number of potential applications that can be required in the design of a space mission to Phobos.

4.4.1 Lighting Conditions

The analysis of the lighting conditions is essential for any spacecraft, since it requires sunlight for the electrical power generation from the solar arrays. The methodologies for the assessment of the lighting conditions, and in particular the characteristics of the environment in the vicinity of Phobos, have been presented in section 2.6. In particular, recall that the lighting conditions are expressed through a light function field L, and the Sun rotates in the Phobos' Hill's frame clockwise, with an angular velocity approximately equal to Phobos' revolution rate, and a fixed declination according to the season of Mars, as expressed in Fig.2.26.

The general analysis of the lighting conditions was undertaken in section 2.6 to evaluate the instantaneous field of view of the Sun for a point around Phobos. The analysis is now conducted for the periodic LPOs of the CR3BP-GH. The choice to use the POs in the circular case is done to retain the essential information with a simplified

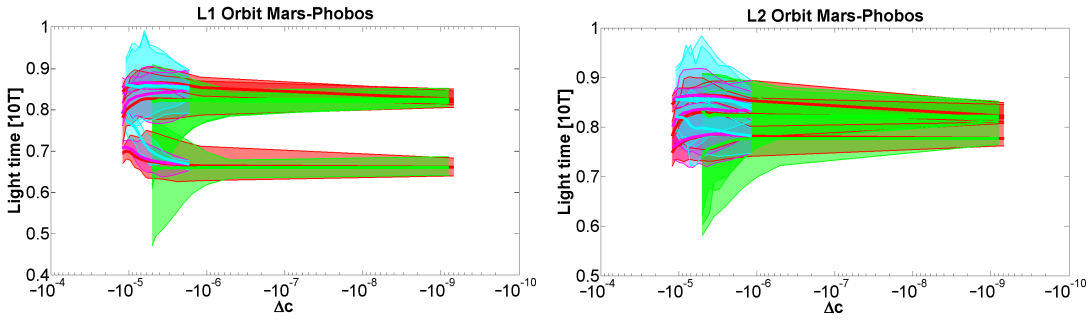

Figure 4.150: **LPOs lighting conditions.** Light function of the families of POs around L_1 and L_2 of the CR3BP-GH (parameterized by the differential Jacobi integral with respect to the LP), averaged over 10 PO periods, at the days of equinoxes (lower cluster) and solstices (upper cluster). Filled area spans values for different starting phases of the Sun (thick line is for mean values), where families' colors are coherent with Fig.4.58.

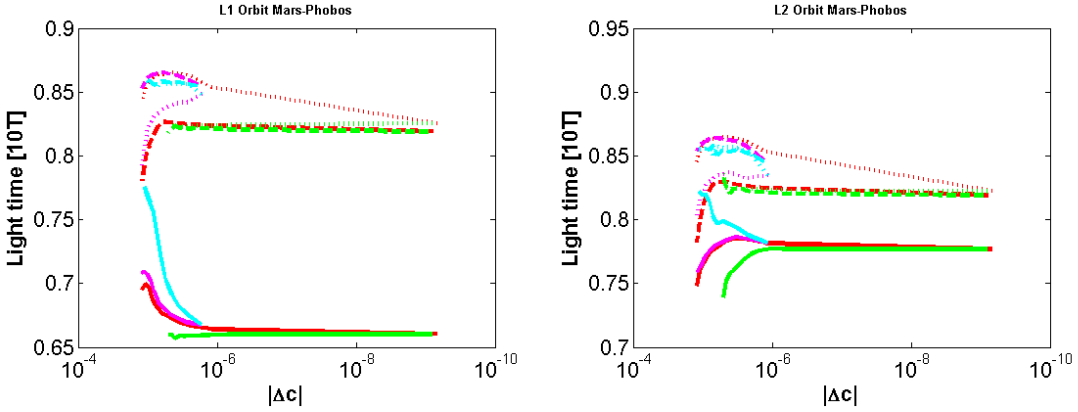

Figure 4.151: **LPOs lighting conditions.** Light function of the families of POs around L_1 and L_2 of the CR3BP-GH (parameterized by the differential Jacobi integral with respect to the LP), averaged over 10 PO periods and over the starting phases of the Sun, at the days of equinoxes (lower cluster, dashed lines for summer, dotted lines for winter) and solstices (upper cluster in plain lines).

approach. The POs of the CR3BP-GH provide the backbone of both the QPOs in the same dynamical model, and the QPOs in the ER3BP-GH. Therefore their performances are the mean value of the performances of all the respective families of LPOs in the most accurate model.

The outcomes are presented in Fig.4.150-4.151, and they consider the mean spherical shape of Phobos. Due to the additional phase of the Sun, the light function of the LPO is defined by averaging its value over 10 revolutions of the trajectory, and the results will depend on the initial condition of the Sun around Phobos. Medium-small LPOs within the families are similar to close-range hovering points on the two L_{1-2}-sides of the moon and the dependence of the Sun phase is mild (less than 5%). Such LPOs of the families A and B are more exposed to light during the solstices than the equinoxes. At the equinoxes, all large orbits of the families A, B, and C experience more lighting time on the L_1-side, while the ones of A and C on the L_2-side experience more shadowing time than their medium-size orbits. Instead both families D experience more lighting time.

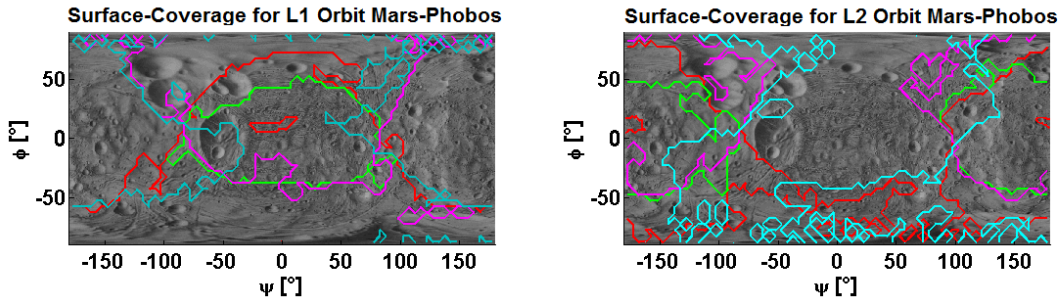

Figure 4.152: **LPOs surface coverage.** Boundaries the regions of full geometrical coverage on Phobos' surface of the largest orbits of the families of POs around L_1 and L_2 of the CR3BP-GH. Families' colors are coherent with Fig.4.58.

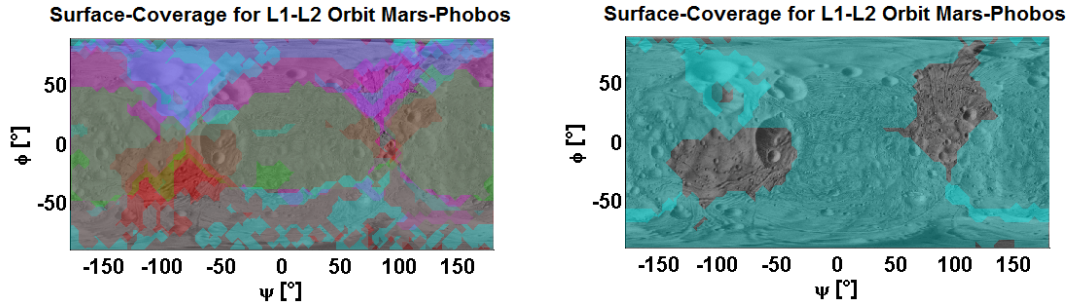

Figure 4.153: **LPOs surface coverage.** On the left, colored areas fill the regions of full geometrical coverage on Phobos' surface of the largest orbits of the families of POs around L_1 and L_2 of the CR3BP-GH. Families' colors are coherent with Fig.4.58. On the right, surface coverage of the synchronous POs of the family D around L_1 and L_2 of the ER3BP-GH.

At the solstices, more shadowing/ligthing is obtained by the family A/C in summer, and by C/A in winter, while the families B and D are not altered by the type of solstice. The light time of large LPOs, if used for short operations, can be tuned accordingly to the Sun phase along Phobos, with the families B and D allowing to increase/decrease the mean light function up to 15%.

4.4.2 Surface Coverage

One of the most important requirements for any mission is the region of the surface that the instruments can point while the spacecraft moves along the chosen orbit. This could refer to visual-instruments, for observation, or radio-instruments, for communication. Fig.4.152-4.153 collect the regions of full geometrical coverage for the larger LPOs of every family of POs in the CR3BP-GH around both LPs. Thus, these outcomes consider no technical constraints and data of the instruments, such as the minimum elevation angle on the ground, and the maximum angles of view that define the field of view of the instrument around its beam's boresight. In particular, observation of

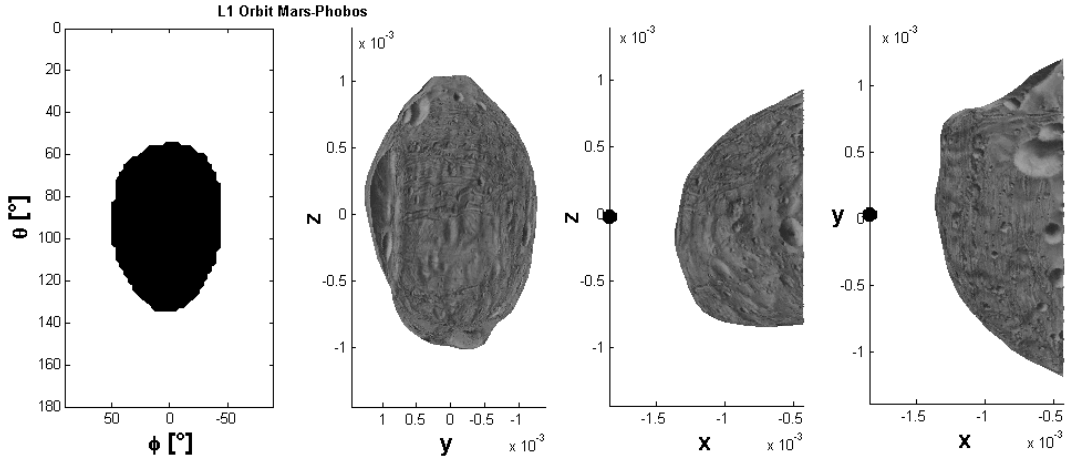

Figure 4.154: **LPOs occulting conditions.** Occultation mask function by the Phobos's bulk at L_1 of the CR3BP-GH.

celestial objects is usually conducted strictly with nadir-pointing[20], and it requires also the point observed to be in light. The outcomes are obtained using the high-order shape harmonics model for Phobos' surface.

The family B provides the least surface coverage of all the families, allowing to point only at the regions on the cis and trans-side of the moon, and covering respectively 28% and 31% of the whole surface during a full orbit. The large POs of the family D, which are vertically-elongated and inclined, allow to cover both Poles and also a significant region on the leading and trailing-side of the moon, resulting in a 45%/43% coverage ratio. The families A (47%/44%) and C (39%/39%) cover the South and North polar sides respectively, and most importantly the leading and trailing-sides. Fig.4.153 shows that the union of the areas provided by all the families covers the whole surface. In particular, a combination of a large D orbit and an A or C orbit on the other side, as well as one A and one C on each side, could fill most of the map.

Finally, Fig.4.153 shows the surface coverage of the D families of POs of the ER3BP-GH. This case is very interesting because the orbits are synchronous, and the combined surface coverage is 73% missing only two sectors on the leading and trailing-sides. A constellation, using a minimum of one spacecraft on each side, would enable a stationary communications bridge between most of the opposite sides of the moon (cis/trans, North/South, part of lead/trail) where different human crews or rovers could be displaced, as well as repeated access times to equatorial and middle latitude sites on Mars.

4.4.3 Radiation Shielding

The radiation environment in orbit of Phobos was assessed in section 2.5. Recall that the levels of radiation are close to the allowable thresholds, thus the hazard of the cosmic rays is currently considered the showstopper in designing a safe manned mission in deep

[20]In this case, the surface coverage reduces simply to the ground-track of the orbit, and the swath is usually small since the field of the camera is narrow.

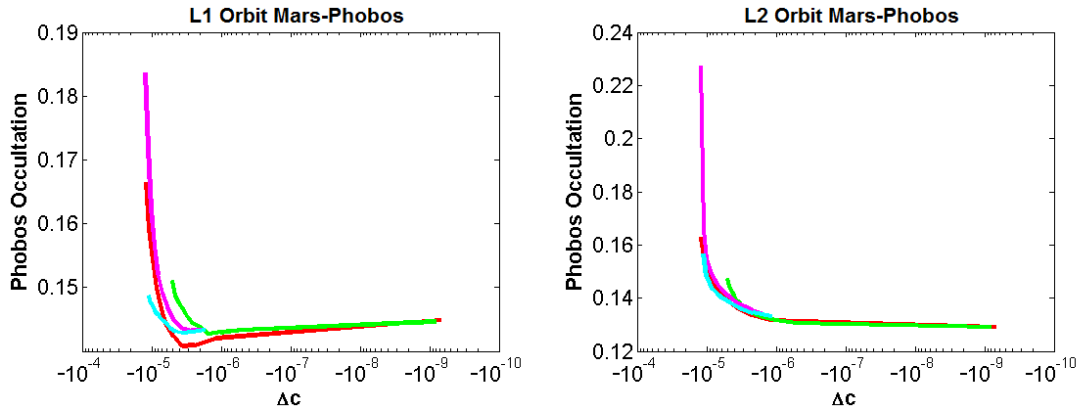

Figure 4.155: **LPOs occulting conditions.** Sky occultation function by the Phobos' bulk of the families of POs around L_1 and L_2 of the CR3BP-GH (parameterized by the differential Jacobi integral with respect to the LP), averaged over 1 PO period. Families' colors are coherent with Fig.4.58. Additional occultation by Mars' bulk will be 3.4% on the L_1-side.

space [79]. This section considers the proposed concept mentioned in section 2.7. This is the possibility that a manned spacecraft, during a Mars orbital mission segment, could exploit Phobos as a natural and passive shield against the isotropic cosmic rays. This is accounted by the occultation of the celestial sky by the bulk of Phobos. The methodologies for the assessment of the occulting conditions, and in particular the characteristics of the environment in the vicinity of Phobos, have been presented in section 2.7. In particular, recall that the occulting conditions are expressed through an occultation function field O.

The general analysis of the occulting conditions was undertaken in section 2.7 to evaluate these properties for a point around Phobos, and considering the mean sphere of Phobos. To model the occultation of Phobos' bulk with the accurate high-order shape harmonics model, the general definition of the solid angle of Eq.2.65 is needed, and the subsequent definition of the mask function M of the real Phobos' surface seen from a general point. This is highly-computational demanding, and the procedure used is the following. For the point considered, a 2D input matrix of the two spherical coordinates' angles is set up. For each input, corresponding to a ray irradiated from the observer, some waypoints are derived with a uniform step along this direction, and each of them is tested to be inside or outside the Phobos' surface modeled by the shape harmonics. In accordance to the ray intersecting or not intersecting Phobos, the mask function value on the related cell of the 2D input matrix is 1 or 0 respectively. At the end of the procedure, for the point considered, the mask function is integrated over the 2D input domain as in Eq.2.65, and the value of the occultation function is derived. An example of the mask function for L_1 is presented in Fig.4.154, whose resulting Phobos's bulk/sky ratio is about 14.5% (for L_2 it is about 13%). The analysis is now conducted for the periodic LPOs of the CR3BP-GH, where the occultation function is averaged for one period of the PO.

The outcomes are presented in Fig.4.155. Recall that Mars provides a constant

occultation of 3.4%, but this is scaled through the Mars-Phobos light function field, as displayed in Fig.2.42. Therefore, the combined occultation is a few percent greater for LPOs on the L_1-side of the moon, than on the L_2-side. The major effect is indeed given by Phobos' bulk, and due to their proximity to Phobos, the sky occultation produced by the natural LPOs is significant. Fig.4.155 shows that **larger LPOs around both L_{1-2} can provide passive radiation shielding from over 20% of the incoming isotropic cosmic rays**. Clearly, if the mission would enable the crew also to land, the reduction could be far higher, more then 50% if inside a crater and close to its deep ridge. Using Mars' bulk, to provide the same shielding factor of the natural LPOs around Phobos, would require a low Martian orbit's altitude under $850km$, while LPOs around Deimos are too distant from the body ($13.7km$) to provide relevant natural shielding.

4.4.4 Sensitivity Analysis and Tracking Performance of the LPOs

The POs of the family D in the ER3BP-GH are chosen to conduct a first-order sensitivity analysis to assess the effect of the uncertainties of the modeling parameters, navigation sensors, and the physical perturbations in tracking the reference signal of the orbit computed. The initial condition of this reference trajectory is propagated in the perturbed dynamics, and the error of the resulting flow from the reference signal is computed. Two metrics are used to assess the tracking performance: the position error from the guidance law after a prescribed propagation time, and the time of permanence such that the flow freely tracks the reference signal within a prescribed position error. Thus, two thresholds are introduced. The prescribed propagation time is set to be one tenth of the Mars-Phobos (and the PO itself) orbital period, as this is close to the reference value of $44min$ required for a transponder's signal's round-trip at the farthest Earth-Mars distance. The prescribed position error is set to be $10m$, as this is close to the value of 10^{-6} L units commonly used for the Sun-Earth and Earth-Moon systems [50].

Fig.4.156 presents the analysis for several parameters, normalized in abscissa by the sensitivity number S. For semi-major axis a, mass parameter μ, eccentricity e, GHs' coefficients, and initial condition $\mathbf{x_0}$ of relative position and velocity, S weights these uncertainties with respect to the related reference value of the ER3BP-GH. For the other actions, $1rad$ is used for the initial true anomaly ν_0, the mean motion (equal to 1/time unit) for the angular velocity ω of the BCBF frame, 1/(time unit)^2 for its angular acceleration $\dot{\omega}$, 1.80° as the maximum misalignment θ between BCBF and Hill's frames, the Phobos gravity at the SOI's boundary for the magnitude of a harmonic perturbing acceleration a^P at the orbital frequency. Furthermore, the GHs model of [102] is used as a benchmark representing a more realistic dynamical model of the spacecraft around Phobos, to relate the sensitivity of the other perturbations. This test indicates that station-keeping is required at least every $17min$ for the POs around L_1. In this

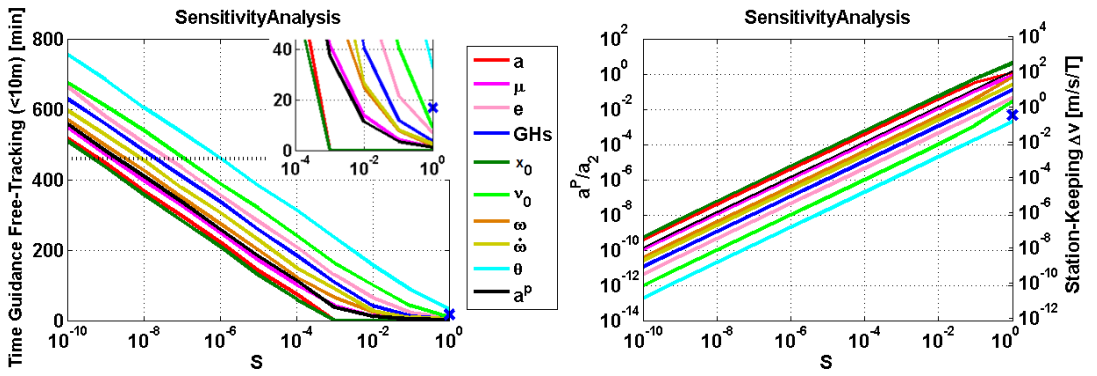

Figure 4.156: **Sensitivity and performance analysis of the LPOs in the Mars-Phobos ER3BP-GH.** The first figure shows the propagation time where the spacecraft remains within the prescribed position error of $10m$ from the reference signal of one PO of the D family around L_1 in the ER3BP-GH, when propagated in a perturbed dynamical model where the modeling parameters, navigation inaccuracies, and physical forces in the legend are weighted by the sensitivity factor S. The blue cross represents the benchmark dynamics. The horizontal dotted line is the reference of the PO period. The second figure shows the related equivalent perturbing acceleration (normalized by the Phobos gravity at L_1) that produces the same final response as a constant input in a forced undamped unstable 1D oscillator. The second ordinate axis represents the associated Δv consumption over one period.

sense, not including the GHs would have required maintenance actions at least every $4min$, while not including the eccentricity would have required station-keeping at least every $7min$. The savings on the duty cycle are 76% and 58% respectively, which highlight the importance of including these forces in the dynamical model to design orbits around Phobos.

The second conclusion arises from the comparison of the sensitivity of the perturbations. Recall that in section 3.1.3 and 3.3.1 respectively, it was estimated that in the dynamical model used the residual perturbations of both the benchmark dynamics and the frame's libration motion account for a few percent of the cumulated GHs perturbation at the SOI, which itself is of the order of 10^{-1} of the Keplerian gravity (see Fig.2.13). This first estimation is now confirmed for the LPOs computed in the ER3BP-GH, as the results of the benchmark and the maximum tilt in the first graph of Fig.4.156 fall within the ones of an additional relative perturbing acceleration a^P between 10^{-3}-10^{-2}, and an inaccuracy of μ of the same range. Inaccuracies of the semi-major axis and the relative non-dimensional state are similar, and very sensitive (inaccuracies over $6 \cdot 10^{-4}$ produce initial errors larger than the $10m$ threshold), while inaccuracies of the true anomaly and rotational rates of the frame are allowed to be higher. Summarizing, the first graph of Fig.4.156 provides the maximum inaccuracies: if the parameters are acquired within these inaccuracies, station-keeping at the frequency of the time threshold chosen will maintain the spacecraft within the deadband defined by the position threshold required. Relative inaccuracies larger than

$$3 \cdot 10^{-4} \text{ for } a,$$
$$9 \cdot 10^{-4} \text{ for } \mu,$$

$3 \cdot 10^{-2}$ for e,
$9 \cdot 10^{-3}$ for GHs' coefficients,
$2 \cdot 10^{-4}$ for $\mathbf{x}_0$,
$9 \cdot 10^{-2}$ for ν_0,
$3 \cdot 10^{-3}$ for ω,
$5 \cdot 10^{-3}$ for $\dot{\omega}$,
$6 \cdot 10^{-1}$ for θ,
$8 \cdot 10^{-4}$ for a^P,

require the control load every $44min$ to be increased, or the guidance performance of $10m$ to be relaxed. In particular, the value for ω is larger than the perturbation on the mean motion of the Hill's frame introduced by Mars J_2 (see correction term Δ in section 3.3.2), which is $2 \cdot 10^{-4}$. Therefore, this further confirms that this term could be disregarded from the model of the dynamics, as explained in section 3.3.4.3, also from the point of the view of the station-keeping cost.

It is now possible to plot these actions deriving an associated figure of perturbing acceleration, in order to universally compare the sensitivity effects with the preliminary orbital perturbations analysis in Fig.2.13. This is done with an equivalent model that considers only the unstable normal mode, which is responsible for the drift of the perturbed trajectory from the reference signal. In the 1D linear ODE $\ddot{x} - \omega_0^2 x = a^P$, the state x represents the magnitude of the position error from the reference signal, and the natural pulsation ω_0 is taken as the maximum unstable Floquet exponent of the PO (2.26 of the mean motion). The system is forced by the constant acceleration a^P, and the analytical solution is available. Thus, the equivalent constant acceleration that produces the same final response of the numerical simulation is computed for every perturbing action, and is presented in the second graph of Fig.4.156, in terms of the same ratio a^P/a_2 used in Fig.2.13. The two cases (response at prescribed propagation time and at prescribed position error) have produced a similar output, so the graph refers to the first one. For a linear approximation comparison, related Δv consumptions over one period are indicated in parallel.

In conclusion, the LPO computed in the proposed ER3BP-GH would require $0.5m/s$ per period to be tracked in the more accurate GHs and maximum-misaligned model, that constitute the main residual perturbations assuming the remaining model parameters and navigation variables are acquired within the following relative and absolute inaccuracies:

$5 \cdot 10^{-4}$ for a ($5km$),
$4 \cdot 10^{-3}$ for μ ($10^3 m^3/s^2$ for Phobos' GM and $9 \cdot 10^{10} m^3/s^2$ for Mars' GM),
10^{-1} for e ($2 \cdot 10^{-3}$),
$4 \cdot 10^{-2}$ for GHs' coefficients,
$4 \cdot 10^{-4}$ for $\mathbf{x}_0$ ($6m$ for relative position and $2 \cdot 10^{-3} m/s$ for relative velocity),
$3 \cdot 10^{-1}$ for ν_0 ($20°$),
10^{-2} for ω ($2 \cdot 10^{-6} rad/s$),

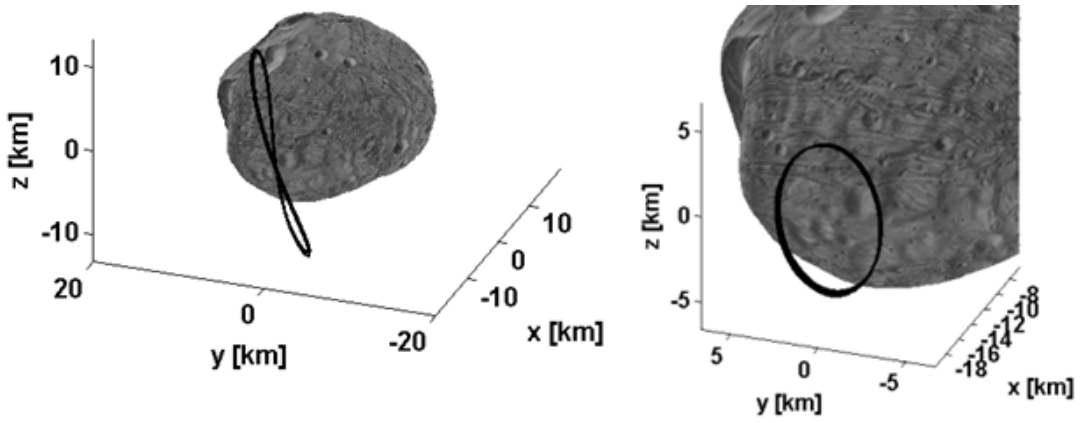

Figure 4.157: **Station-keeping of the LPOs in the Mars-Phobos ER3BP-GH.** The first and second orbit considered for the feasibility analysis on the station-keeping of the LPOs of the Mars-Phobos ER3BP-GH. The PO of the family D around L_1 starting at the perimars; the 3-torus of medium-size and medium-width of the family A around L_1.

$$2 \cdot 10^{-2} \text{ for } \dot{\omega} \ (10^{-9} rad/s^2),$$
$$3 \cdot 10^{-3} \text{ for } a^P \ (8 \cdot 10^{-6} m/s^2).$$

This represents a considerable saving from the $11 m/s$ and $3.2 m/s$ per period if, respectively, the GHs and eccentricity are not included in the dynamical model.

4.4.5 Station-keeping and GNC Requirements

The preliminary analysis, conducted in section 4.4.4, on the requirements of the GNC subsystem for the station-keeping of the LPOs computed in this thesis, is now extended in a more detailed study. This analysis consists of an assessment of the practical feasibility of the LPOs[21]. The operations and characteristics of the ESA mission Phootprint will be used as references.

The analysis is conducted in a way similar to what was done in [57], where the LPOs around Phobos have been computed with a multiple shooting of the classical LPOs in the CR3BP, and considering a high-fidelity dynamical model (GHs up to degree and order 3, SRP, further attractors). The point is not the accuracy of the model, because the final differential correction will provide a guidance law whose error on a^P is much less than the error on $\mathbf{x}_0$ (see section 4.4.4). Thus, downstream the computation of the accurate guidance signals (from ground or from board), the drivers for the station-keeping of any interplanetary spacecraft are the estimation error of the state spilt-over by the navigation (after filtering of the measurements from the sensors), and the realization error of the actuators to provide the required control action.

[21] This research was conducted during an internship in Airbus Defence & Space, Stevenage.

4.4.5.1 Objective

In [57], the station-keeping of the LPOs around Phobos is considered to be undertaken with a regular schedule of classical impulsive maneuvers. In this reference the cost is computed as $\Delta \mathrm{v}/day$, as a function of the navigation's inaccuracy of the position, and the frequency of the maneuvers. A single LPO around L_1 is considered. The inaccuracy of the velocity is kept fixed to $1mm/s$. The inaccuracy of the Δv is kept fixed to $0.5mm/s$. Due to the use of multiple shooting directly from the classical CR3BP, this orbit represents a bounded trajectory, with the reference of a vertical Lyapunov orbit.

The procedure of the work done in [57] is maintained. Two LPOs of the ER3BP-GH, both around L_1, will be tested: the first orbit is the PO of the family D starting at the perimars; the second orbit is the 3-torus of medium-size and medium-width of the family A. These orbits are visible in Fig.4.157. It is also considered a cut-off value for the Δv, equal to the inaccuracy of the velocity.

The reference [57] lacks of several details for the reproducibility of the results. Nevertheless, the orbits and the models themselves are not the same, thus it is not important to exactly reproduce the same results. In particular, the reference does not provide indication on how the inaccuracies are considered to carry on the simulations (single deterministic or multiple Monte-Carlo simulation, fixed or random errors' direction, fixed or stochastic inaccuracy, 1σ or 3σ definition of errors and results). In addition, the reference does not indicates what is the algorithm used to derive the impulsive control law, and does not provide its performances in terms of the state error from the target signal to be compared.

4.4.5.2 The Target Point Technique

Theory. The classical methodology for the SK of LPOs is the Target Point algorithm [141]. It is an optimal control technique (see section C.1) with impulsive control action Δv. It consists in the minimization of the cost functional made up of the control action and a discrete set of errors evaluated at NTP target points.

$$\begin{aligned} J &= \frac{1}{2}\boldsymbol{\Delta}\mathbf{v}^T\mathbf{R}\boldsymbol{\Delta}\mathbf{v} + \frac{1}{2}\sum_{i=1}^{NTP}\Delta\mathbf{x}(t_i)^T\mathbf{Q}_i\Delta\mathbf{x}(t_i) = \\ &= \frac{1}{2}\boldsymbol{\Delta}\mathbf{v}^T\mathbf{R}\boldsymbol{\Delta}\mathbf{v} + \frac{1}{2}\sum_{i=1}^{NTP}\Delta\mathbf{q}(t_i)^T\mathbf{Q}_i^{\mathbf{r}}\Delta\mathbf{q}(t_i) + \Delta\dot{\mathbf{q}}(t_i)^T\mathbf{Q}_i^{\mathbf{v}}\Delta\dot{\mathbf{q}}(t_i) \end{aligned} \tag{4.50}$$

The solution is obtained in closed-form exploiting the linearization of the dynamics around the reference orbit $\mathbf{x}_T$, which is by using its STM through its variational equations.

$$\Delta\mathbf{x}(t) = \mathbf{x}(t) - \mathbf{x}_T(t) = \begin{bmatrix} \Delta\mathbf{q}(t) \\ \Delta\dot{\mathbf{q}}(t) \end{bmatrix} = \boldsymbol{\Phi}(t,t_0)\Delta\mathbf{x}(t_0) = \begin{bmatrix} \boldsymbol{\Phi}^{\mathbf{r},\mathbf{r}}(t,t_0) & \boldsymbol{\Phi}^{\mathbf{r},\mathbf{v}}(t,t_0) \\ \boldsymbol{\Phi}^{\mathbf{v},\mathbf{r}}(t,t_0) & \boldsymbol{\Phi}^{\mathbf{v},\mathbf{v}}(t,t_0) \end{bmatrix} \begin{bmatrix} \Delta\mathbf{q}(t_0) \\ \Delta\dot{\mathbf{q}}(t_0) \end{bmatrix} \tag{4.51}$$

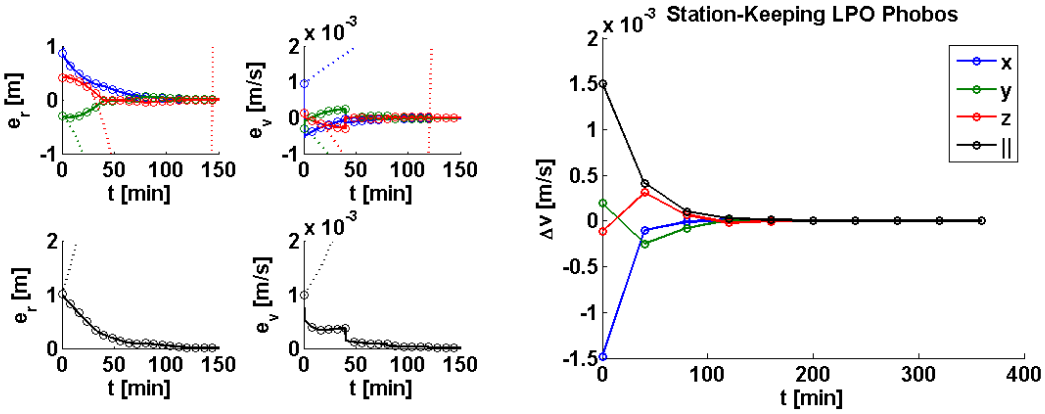

Figure 4.158: **Station-keeping of the LPOs in the Mars-Phobos ER3BP-GH.** Target Point control. Error on initial condition. State error tracking performance (uncontrolled motion in dotted lines) and control action. Orbit-1.

The control action Δv is considered to be implemented at the initial condition. This is not restrictive: it just means that the trajectory is divided in the intervals fixed by the choice of the maneuvers' frequency, and the algorithm is used to derive separately one by one Δv, using the STM of the related interval. The target points could be considered at any time within the interval: the classical choice is to define them uniformly. Hence, the initial state deviation from the guidance law, as seen by the controller, is given by the deviation of the estimated position $\mathbf{q}$ and velocity $\dot{\mathbf{q}}$, plus the explicit maneuver to be computed. This is the $\Delta\mathbf{x}(t_0)$ that should now be used in Eq.4.51, to minimize the cost functional of Eq.4.50.

$$\Delta\mathbf{x}(t_0) = \begin{bmatrix} \Delta\mathbf{q}(t_0) \\ \Delta\dot{\mathbf{q}}(t_0) + \mathbf{\Delta v} \end{bmatrix} \tag{4.52}$$

The control law is the classical feedback implementation, which is proportional to the error from the target. It is worth to remark that this error is initially due to the navigation, which will feed the controller continuously over the simulation, as well as with the realization error of the actuators.

$$\begin{aligned}
\mathbf{\Delta v} &= -\left\{\mathbf{R} + \sum_{i=1}^{NTP} \mathbf{\Phi}^{\mathbf{r},\mathbf{v}}(t_i,t_0)^T \mathbf{Q}_i^{\mathbf{r}} \mathbf{\Phi}^{\mathbf{r},\mathbf{v}}(t_i,t_0) + \mathbf{\Phi}^{\mathbf{v},\mathbf{v}}(t_i,t_0)^T \mathbf{Q}_i^{\mathbf{v}} \mathbf{\Phi}^{\mathbf{v},\mathbf{v}}(t_i,t_0)\right\}^{-1} \cdot \\
&\cdot \left\{ \sum_{i=1}^{NTP} \begin{bmatrix} \mathbf{\Phi}^{\mathbf{r},\mathbf{v}}(t_i,t_0)^T \mathbf{Q}_i^{\mathbf{r}} \mathbf{\Phi}^{\mathbf{r},\mathbf{r}}(t_i,t_0) + \mathbf{\Phi}^{\mathbf{v},\mathbf{v}}(t_i,t_0)^T \mathbf{Q}_i^{\mathbf{v}} \mathbf{\Phi}^{\mathbf{v},\mathbf{r}}(t_i,t_0) \\ \mathbf{\Phi}^{\mathbf{r},\mathbf{v}}(t_i,t_0)^T \mathbf{Q}_i^{\mathbf{r}} \mathbf{\Phi}^{\mathbf{r},\mathbf{v}}(t_i,t_0) + \mathbf{\Phi}^{\mathbf{v},\mathbf{v}}(t_i,t_0)^T \mathbf{Q}_i^{\mathbf{v}} \mathbf{\Phi}^{\mathbf{v},\mathbf{v}}(t_i,t_0) \end{bmatrix}^T \begin{bmatrix} \Delta\mathbf{q}(t_0) \\ \Delta\dot{\mathbf{q}}(t_0) \end{bmatrix} \right\} = \\
&= -\left\{\mathbf{R} + \sum_{i=1}^{NTP} \begin{bmatrix} \mathbf{\Phi}^{\mathbf{r},\mathbf{v}}(t_i,t_0) \\ \mathbf{\Phi}^{\mathbf{v},\mathbf{v}}(t_i,t_0) \end{bmatrix}^T \begin{bmatrix} \mathbf{Q}_i^{\mathbf{r}} & \mathbf{0_{3x3}} \\ \mathbf{0_{3x3}} & \mathbf{Q}_i^{\mathbf{v}} \end{bmatrix} \begin{bmatrix} \mathbf{\Phi}^{\mathbf{r},\mathbf{v}}(t_i,t_0) \\ \mathbf{\Phi}^{\mathbf{v},\mathbf{v}}(t_i,t_0) \end{bmatrix}\right\}^{-1} \cdot \\
&\cdot \left\{ \sum_{i=1}^{NTP} \begin{bmatrix} \mathbf{\Phi}^{\mathbf{r},\mathbf{v}}(t_i,t_0) \\ \mathbf{\Phi}^{\mathbf{v},\mathbf{v}}(t_i,t_0) \end{bmatrix}^T \begin{bmatrix} \mathbf{Q}_i^{\mathbf{r}} & \mathbf{0_{3x3}} \\ \mathbf{0_{3x3}} & \mathbf{Q}_i^{\mathbf{v}} \end{bmatrix} \mathbf{\Phi}(t_i,t_0) \begin{bmatrix} \Delta\mathbf{q}(t_0) \\ \Delta\dot{\mathbf{q}}(t_0) \end{bmatrix} \right\}
\end{aligned} \tag{4.53}$$

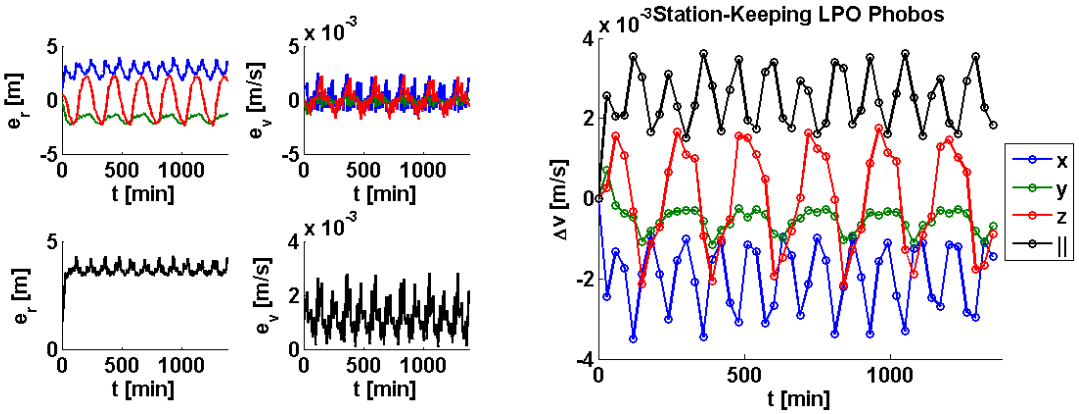

Figure 4.159: **Station-keeping of the LPOs in the Mars-Phobos ER3BP-GH.** Target Point control. Error on state estimation (along unstable manifold). State error tracking performance and control action. Orbit-1.

Table 4.1: **Station-keeping of the LPOs in the Mars-Phobos ER3BP-GH.** Target Point control. Deterministic analysis. Performance: $\Delta v/day$, state error from target. Orbits 1 and 2.

\ Frequency SK Inaccuracy Position \	0.5h	1h	1.5h	2h
0.1m	0.0755 m/s 2.89 m 1.87 mm/s	0.133 m/s 10.3 m 4.81 mm/s	0.198 m/s 19.9 m 11.5 mm/s	0.313 m/s 54.0 m 28.5 mm/s
1m	0.117 m/s 4.31 m 2.83 mm/s	0.219 m/s 12.4 m 7.88 mm/s	0.346 m/s 29.6 m 18.3 mm/s	0.494 m/s 83.5 m 41.7 mm/s
10m	0.540 m/s 20.4 m 12.9 mm/s	1.10 m/s 60.8 m 42.6 mm/s	1.84 m/s 152 m 110 mm/s	1.99 m/s 360 m 208 mm/s
100m	4.83 m/s 183 m 116 mm/s	10.3 m/s 587 m 415 mm/s	17.7 m/s 1.73 km 1.22 m/s	N/A

\ Frequency SK Inaccuracy Position \	0.5h	1h	1.5h	2h
0.1m	0.0870 m/s 2.89 m 1.52 mm/s	0.195 m/s 8.78 m 5.45 mm/s	0.400 m/s 25.2 m 18.8 mm/s	0.692 m/s 86.8 m 52.9 mm/s
1m	0.141 m/s 4.39 m 2.39 mm/s	0.321 m/s 13.8 m 9.02 mm/s	0.686 m/s 42.7 m 31.6 mm/s	1.15 m/s 146 m 77.8 mm/s
10m	0.686 m/s 20.1 m 11.6 mm/s	1.61 m/s 68.7 m 45.8 mm/s	3.72 m/s 239 m 170 mm/s	4.78 m/s 779 m 582 mm/s
100m	6.23 m/s 182 m 105 mm/s	16.0 m/s 678 m 465 mm/s	N/A	N/A

Table 4.2: **Station-keeping of the LPOs in the Mars-Phobos ER3BP-GH.** Target Point control. Worst-case analysis: deterministic analysis, apart from the first column, whose inaccuracies' direction is random. Performance: $\Delta v/day$, state error from target. Orbits 1 and 2.

\ Frequency SK Inaccuracy Position \	0.5h	1h	1.5h	2h
0.1m	0.133 m/s 2.87 m 3.06 mm/s	0.133 m/s 10.3 m 4.81 mm/s	0.198 m/s 19.9 m 11.5 mm/s	0.313 m/s 54.0 m 28.5 mm/s
1m	0.143 m/s 3.43 m 3.54 mm/s	0.219 m/s 12.4 m 7.88 mm/s	0.346 m/s 29.6 m 18.3 mm/s	0.494 m/s 83.5 m 41.7 mm/s
10m	0.881 m/s 19.2 m 17.7 mm/s	1.10 m/s 60.8 m 42.6 mm/s	1.84 m/s 152 m 110 mm/s	1.99 m/s 360 m 208 mm/s
100m	9.84 m/s 236 m 277 mm/s	10.3 m/s 587 m 415 mm/s	17.7 m/s 1.73 km 1.22 m/s	N/A

\ Frequency SK Inaccuracy Position \	0.5h	1h	1.5h	2h
0.1m	0.132 m/s 2.88 m 2.90 mm/s	0.195 m/s 8.78 m 5.45 mm/s	0.400 m/s 25.2 m 18.8 mm/s	0.692 m/s 86.8 m 52.9 mm/s
1m	0.175 m/s 4.21 m 4.35 mm/s	0.321 m/s 13.8 m 9.02 mm/s	0.686 m/s 42.7 m 31.6 mm/s	1.15 m/s 146 m 77.8 mm/s
10m	0.941 m/s 20.4 m 21.6 mm/s	1.61 m/s 68.7 m 45.8 mm/s	3.72 m/s 239 m 170 mm/s	N/A
100m	10.2 m/s 224 m 266 mm/s	16.0 m/s 678 m 465 mm/s	N/A	N/A

Application. Eq.4.53 is implemented in a controller. First, the algorithm is tested with the classical response to a deviation in the initial condition, assuming the state estimation and actuator realization are perfect. This example is provided in Fig.4.158, where the error and control action converge impulsively to zero. It is evident also what would have been the uncontrolled drift of the state.

The set of simulations are carried out for each of the two orbits, with the combination of the inaccuracies introduced in section 4.4.5.1. Due to the lack of information of the reference, as discussed in section 4.4.5.1, the first choice, also to tune the gain matrices, is to consider a deterministic analysis. DST helps in such an analysis, because it is already known that the LPOs have an unstable manifold. Thus, the direction of the navigation and actuator error is considered to be along the inside branch of the local unstable manifold of the reference orbit. This should give the worst-case scenario of the station-keeping. Regarding the magnitude of the errors, for a deterministic analysis, this is considered to be fixed to the inaccuracies provided. In reality, since the direction of the IMs is 6D, the ratio between position and velocity magnitude is constrained, but the two inaccuracies are considered independent. Thus, it is not actually guaranteed that the results are really the worst-case, nevertheless they should not be too far from it. An example of the deterministic analysis is provided in Fig.4.159, where now the error and control action are stationary. Table 4.1 provides the results of this analysis for the two orbits.

The values are of the same order of magnitude of the analysis undertaken by the JPL in [57]. In particular, the consumptions are smaller, but we do not know their error performances nor all the other features of their analysis, in particular the control algorithm and the type of analysis. The consumptions are for most of the cases less than $1m/s/day$, thus the Phobos' LPOs are feasible from the control point of view. Large inaccuracies and SK intervals are not feasible choices, and the spacecraft will crash into the moon. Some additional considerations are provided below.

- The number of target points has resulted to be not significant: it must be $NTP > 1$, but with $NTP = 2$ the better performance achieved, and this is the case that will be used in this section.

- It is not possible to go down from $0.07m/s/day$ and $2m$ error due to the other fixed inaccuracies used.

- The difference between the two orbits is coherent with the stability indicators: the respective Floquet multipliers are 1,200 and 2,100.

- The control is obtained using sub-optimal weighting matrices varied by the SK-frequency (interval T_{SK}): $\mathbf{R} = (0.01m/s)^{-2} \cdot diag\{[1,1,1]\}$, $\mathbf{Q}_i^{\mathbf{r}} = (2m)^{-2} \cdot (T_{SK}/30min)^{-4} \cdot diag\{[4,1,1]\}$, $\mathbf{Q}_i^{\mathbf{v}} = (0.01m/s)^{-2} \cdot diag\{[1,1,1]\}$. The cost could be probably improved by a margin of 10%.

Table 4.3: **Station-keeping of the LPOs in the Mars-Phobos ER3BP-GH.** Δv/*day* of the analysis of [57].

\ Frequency SK Inaccuracy Position \	0.5h	1h	1.5h	2h
0.1m	0.22	0.17	0.29	0.73
1m	0.25	0.22	0.35	1.0
10m	1.3	1.0	1.9	N/A
100m	13.8	9.8	N/A	N/A

- The consumption is calculated as the norm of the maneuver, not with separate 3-axes contributions (Δv will be larger up to 1.7 times).
- Within feasible SK performances, Δv of single maneuver ranges in $[1-500]mm/s$. Thus, with Phootprint mass of $2,000kg$, the required impulse interval ranges in $[0.1 - 50]s$ with $20N$ thrust (which is the Phootprint AOCS value), and $[2s - 17min]$ with $1N$. Thus, with a feasible and not particularly large thruster, impulsive approximation of the control action is perfectly feasible within the maneuvering interval.

However, repeating the analysis with random direction of the errors, the case at smallest SK-interval is now the worst-case scenario. Thus, Table 4.2 provides the resulting worst-case scenario for the two LPOs, just updating the first column of Table 4.1.

Table 4.3 provides the consumptions of the JPL analysis. It seems that the relative ratios inside each table are very similar. Thus the scaling between this analysis and the JPL results is about 1.7. It could be that near the same absolute values can be obtained in a stochastic analysis and interpreting the inaccuracies 1σ, or by considering the total consumption as the sum of separate 3-axes contributions.

4.4.5.3 The Floquet Mode Technique

Theory. An alternative station-keeping methodology for the LPOs is given by the Floquet Mode algorithm [142]. The technique is based on the analytical assist of DST. Since, in the linearized dynamics around the LPO, the spacecraft will drift rapidly as a result of an error along the unstable IM, the control action can be designed to specifically counteract this error with an impulse in velocity.

In the same way undertaken for the first control algorithm, the control action Δv is considered to be implemented at the initial condition of each of the intervals fixed by the choice of the maneuvers' frequency, and the algorithm exploits the STM of the related interval. The technique requires the computation of the eigenvectors of the STM at the point, on the reference LPO, isochronic with the spacecraft.

$$\mathbf{\Phi}(T,0) = \mathbf{VDU}, \mathbf{V}_{:,k} = \hat{\mathbf{e}}_k, \mathbf{D}_{k,k} = e^{\lambda_k T}, \mathbf{U} = \mathbf{V}^{-1} \tag{4.54}$$

$$\mathbf{e}_{\mathbf{F},k}(0 \leq t < T) = \mathbf{\Phi}(t,0)\hat{\mathbf{e}}_k \rightarrow \hat{\mathbf{e}}_{\mathbf{F},k}(t), \mathbf{V}_{\mathbf{F}}(t), \mathbf{U}_{\mathbf{F}}(t) \tag{4.55}$$

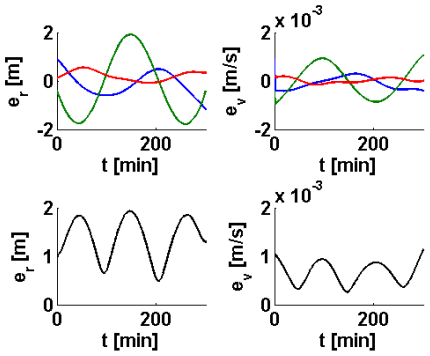

Figure 4.160: **Station-keeping of the LPOs in the Mars-Phobos ER3BP-GH.** Floquet mode control. Error on initial condition. State error tracking performance with single maneuver at beginning. Orbit-1.

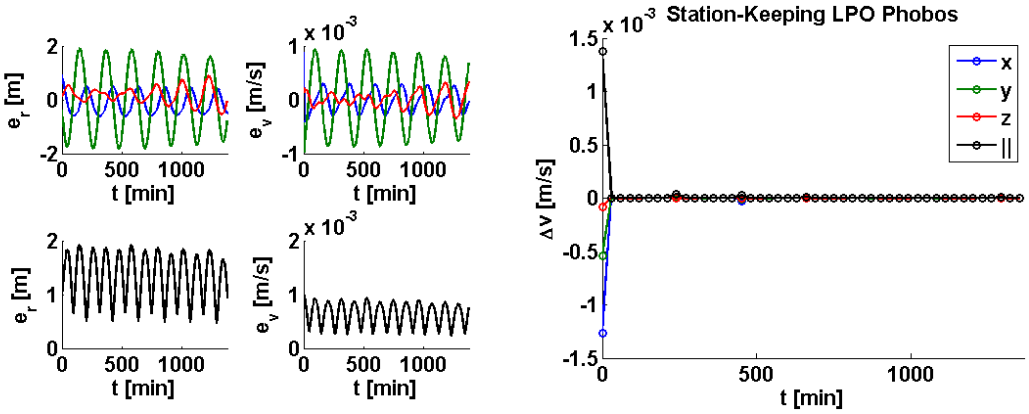

Figure 4.161: **Station-keeping of the LPOs in the Mars-Phobos ER3BP-GH.** Floquet mode control. Error on initial condition. State error tracking performance and control action. Orbit-1.

The procedure in Eq.4.54-4.55 is the same used in sections B.8.2-B.8.3, computing the manifolds at the starting point and transporting its direction through the variational equations. The resulting direction of the local manifold is represented here by the eigenversor $\hat{\mathbf{e}}_F$, which is called Floquet mode. From the set of eigenspaces W^k, the set of orthogonal projectors is derived, where each vector $\boldsymbol{\pi}$ is associated to an eigenspace.

$$\mathbf{U_F}(t)\mathbf{V_F}(t) = \mathbf{I} \rightarrow \mathbf{\Pi}(t) = \mathbf{U_F}(t)^T, \mathbf{\Pi}_{:,k}(t) = \boldsymbol{\pi}_k(t) \tag{4.56}$$

The state error is now expressed in the local frame of Floquet modes, whose components are collected in the vector $\boldsymbol{\alpha}$.

$$\Delta\mathbf{x}(t) = \mathbf{V_F}(t)\boldsymbol{\alpha}(t) \rightarrow \boldsymbol{\alpha}(t) = \mathbf{U_F}(t)\Delta\mathbf{x}(t) \tag{4.57}$$

The objective of the technique is to produce a maneuver such that the unstable component of the state error is impulsively set to zero. This requires to use the projector

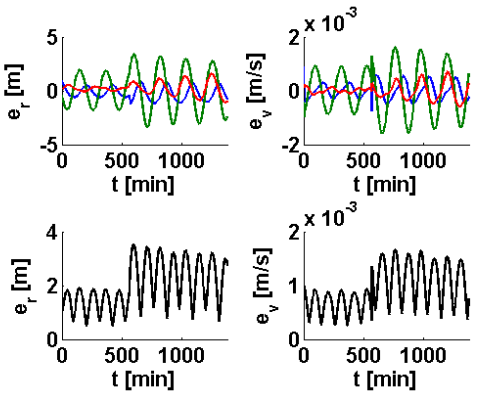

Figure 4.162: **Station-keeping of the LPOs in the Mars-Phobos ER3BP-GH.** Floquet mode control. Error on initial condition and state impulse at half simulation. State error tracking performance and control action. Orbit-1.

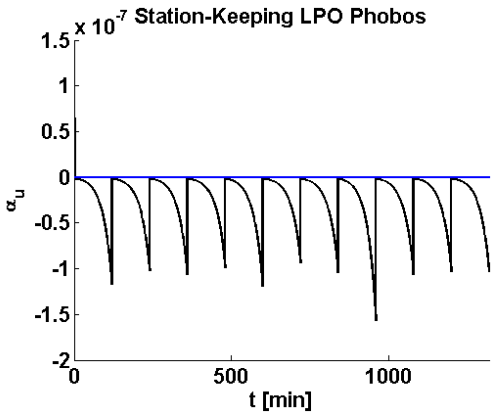

Figure 4.163: **Station-keeping of the LPOs in the Mars-Phobos ER3BP-GH.** Floquet mode control. Error on initial condition and small state impulses throughout simulation. This plot shows the state component (in normalized units) along the unstable manifold. Orbit-1.

$k = u$ of the unstable IM W^{u}[22].

$$\boldsymbol{\pi}_u(t)^T \left(\Delta\mathbf{x}(t) + \begin{bmatrix} \mathbf{0_{3x1}} \\ \boldsymbol{\Delta}\mathbf{v}(t) \end{bmatrix} \right) = \alpha_u(t) + \boldsymbol{\pi}_{u,4:6}(t)^T \boldsymbol{\Delta}\mathbf{v}(t) = 0 \tag{4.58}$$

Eq.4.58 is simple, but is underdetermined. To find Δv, the classical mathematical solution with minimum norm is also the one physically wanted, because it gives the cheaper maneuver to achieve the objective.

$$\begin{cases} \boldsymbol{\pi}_{u,4:6}(t)^T \boldsymbol{\Delta}\mathbf{v}(t) = -\alpha_u(t) \\ \min\limits_{\boldsymbol{\Delta}\mathbf{v}(t)} \|\boldsymbol{\Delta}\mathbf{v}(t)\| \end{cases} \Rightarrow \boldsymbol{\Delta}\mathbf{v}(t) = -\boldsymbol{\pi}_{u,4:6}(t) \left[\boldsymbol{\pi}_{u,4:6}(t)^T \boldsymbol{\pi}_{u,4:6}(t) \right]^{-1} \alpha_u(t) \tag{4.59}$$

Therefore, the resulting feedback control law in Eq.4.59 is simple and analytic, with no gain matrices to tune.

Application. Eq.4.59 is implemented in a controller. First, the algorithm is tested with the classical response to a deviation in the initial condition, assuming the state estimation and actuator realization are perfect. This example is provided in Fig.4.160, and the behavior appears promising. As a difference from the target point technique's

[22] The procedure works also for more than one manifold' components of $\boldsymbol{\alpha}$ to be erased. The first orbit considered in this section has two unstable manifolds. However, the second one is slightly unstable: the Floquet multiplier is only 1.6 over one orbital period. Thus the departure along this manifold, for the simulation's time span, is not significant if compared to the principal unstable manifold. The control law has been implemented also to counteract this second direction: outcomes did not change significantly, thus the classical 1-direction control law has been used also for the first orbit to produce the results shown in this section.

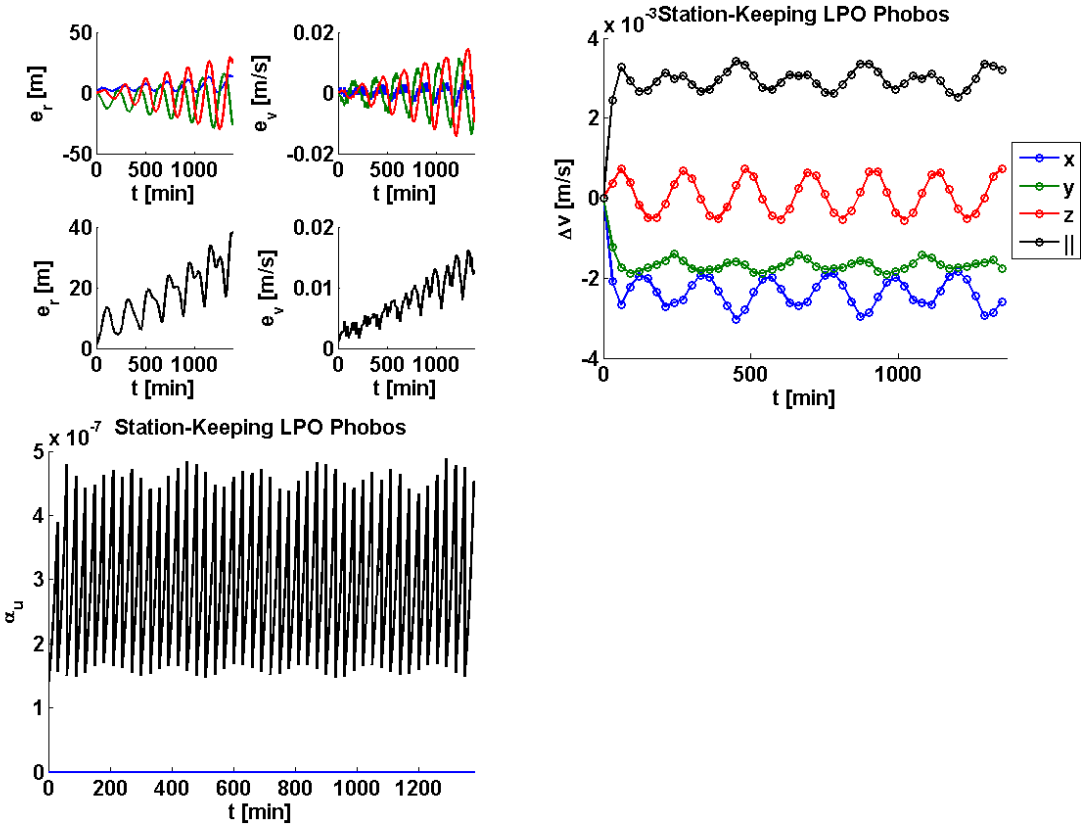

Figure 4.164: **Station-keeping of the LPOs in the Mars-Phobos ER3BP-GH.** Floquet mode control. Error on state estimation (along unstable manifold). State error tracking performance, control action, and state component along the unstable manifold. Orbit-1.

test case of Fig.4.158, where a sequence of convergently maneuvers are needed to drive the error to zero, here just the first maneuver allows the spacecraft to oscillate around the reference LPO for more than $4h$. After this time the residual error, that is always present for the inaccuracy of the control system, accumulates too much, so a maneuver must be executed. But this is a small amount, as it shown in Fig.4.161 where only the first Δv is relevant.

However the problems are made evident in Fig.4.162, where a fictitious second impulse on the state is inserted at half simulation. The spacecraft is still perfectly stabilized by the low-cost control law, but the oscillation's amplitude increases. The control law is implemented correctly, as it is shown in Fig.4.163, that presents the profile of the unstable component of the error in the Floquet coordinates $\boldsymbol{\alpha}$. In this simulation multiple fictitious impulses are inserted with a tight frequency, acting along the unstable IM. This component grows exponentially within each SK-interval, but is erased by the maneuvers computed with the algorithm.

The set of simulations are then carried out for each of the two orbits considering the navigation and actuator errors, like in section 4.4.5.2. Fig.4.164 shows an example of the completely deterministic analysis, where the inaccuracies are fixed in magnitude and direction (along the inside branch of the local unstable IM). Fig.4.165 shows an

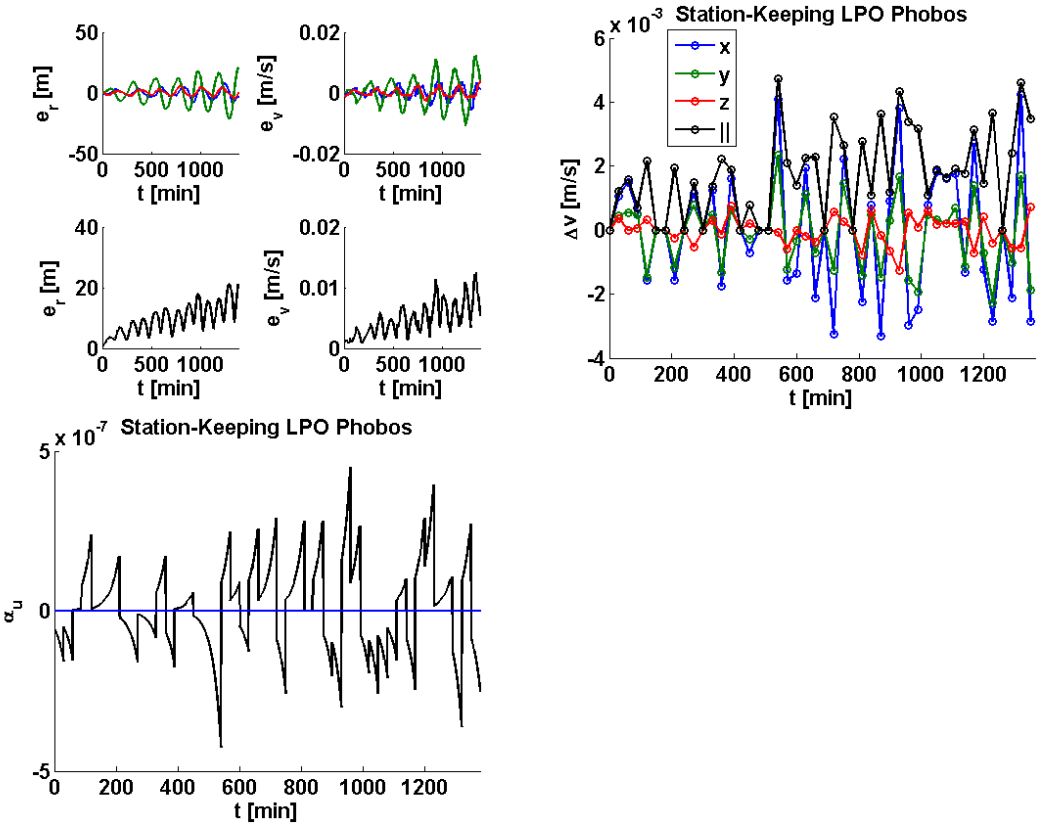

Figure 4.165: **Station-keeping of the LPOs in the Mars-Phobos ER3BP-GH.** Floquet mode control. Error on state estimation (random direction). State error tracking performance, control action, and state component along the unstable manifold. Orbit-1.

Table 4.4: **Station-keeping of the LPOs in the Mars-Phobos ER3BP-GH.** Floquet mode control. Deterministic analysis. Performance: $\Delta \mathrm{v}/day$, state error from target. Orbits 1 and 2.

\ Frequency SK Inaccuracy Position \	0.5h	1h	1.5h	2h
0.1m	0.0622m/s 70.9m 29.3mm/s	0.0872m/s 118m 49.5mm/s	0.152m/s 227m 94.2mm/s	0.253m/s 593m 235mm/s
1m	0.0903m/s 136m 56.6mm/s	0.146m/s 194m 78.7mm/s	0.255m/s 331m 136mm/s	0.422m/s 971m 380mm/s
10m	0.421m/s 635m 254mm/s	0.685m/s 1.05km 398mm/s	1.08m/s 1.49km 631mm/s	NA
100m	4.81m/s 4.27km 1.79m/s	NA	NA	NA

\ Frequency SK Inaccuracy Position \	0.5h	1h	1.5h	2h
0.1m	0.0837m/s 25.2m 10.7mm/s	0.155m/s 47.3m 21.2mm/s	0.297m/s 84.3m 44.6mm/s	0.554m/s 218m 106mm/s
1m	0.139m/s 38.3m 16.1mm/s	0.260m/s 71.4m 31.5mm/s	0.495m/s 141m 71.4mm/s	0.841m/s 325m 167mm/s
10m	0.686m/s 172m 79.1mm/s	1.23m/s 330m 163mm/s	1.85m/s 685m 333mm/s	2.18m/s 1.21km 637mm/s
100m	5.14m/s 1.49km 726mm/s	7.38m/s 2.85km 1.51m/s	NA	NA

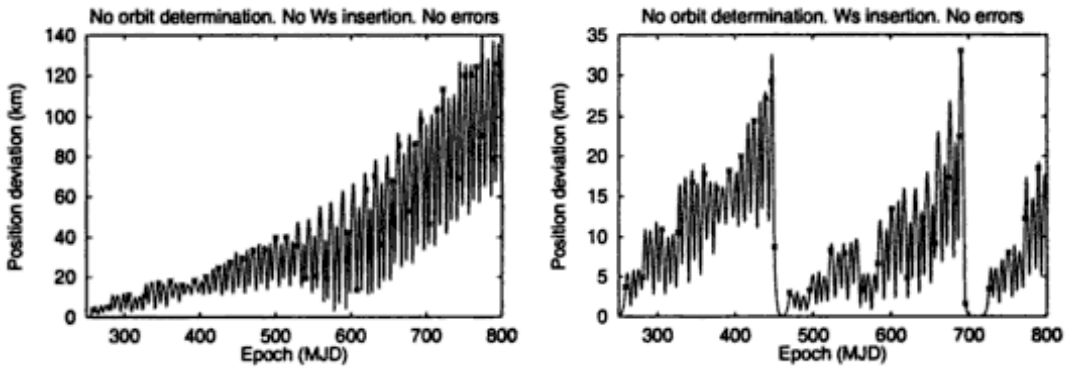

Figure 4.166: **Station-keeping of the LPOs in the Mars-Phobos ER3BP-GH.** Floquet mode control. Unstable component from system in [143]. The drift is evident. On the right, periodical maneuvers are performed to stop it.

Table 4.5: **Station-keeping of the LPOs in the Mars-Phobos ER3BP-GH.** Target Point control. Deterministic analysis. Performance: $\Delta \mathrm{v}/day$, state error from target. Orbit 1.

\ Inaccuracy Velocity Other \	0.1mm/s	1mm/s	10mm/s	100mm/s
Frequency SK 1h	0.144 m/s	0.219 m/s	0.977 m/s	8.71 m/s
Inaccuracy Position 1m	8.75 m	12.4 m	54.5 m	513 m
Inaccuracy Δv 0.5mm/s	5.41 mm/s	7.88 mm/s	34.1 mm/s	312 mm/s

Table 4.6: **Station-keeping of the LPOs in the Mars-Phobos ER3BP-GH.** Target Point control. Deterministic analysis. Performance: $\Delta \mathrm{v}/day$, state error from target. Orbit 1.

\ Inaccuracy Δv Other \	0.05mm/s	0.5mm/s	5mm/s	50mm/s
Frequency SK 1h	0.184 m/s	0.219 m/s	0.613 m/s	4.15 m/s
Inaccuracy Position 1m	10.5 m	12.4 m	57.6 m	351 m
Inacc. Velocity 1mm/s	6.64 mm/s	7.88 mm/s	37.5 mm/s	173 mm/s

example of the case where the inaccuracies' direction is random. The completely deterministic analysis has resulted now to be always the worst-case. Table 4.4 provides the results of the worst-case for the two orbits with the Floquet mode technique.

In comparison with Table 4.2, this technique requires less fuel consumption, relaxing the SK frequency. But this control law is designed to counteract departures only along the unstable direction of the orbit's manifold. The drawback of this approach is that every error introduced by the navigation on the other components of the orbit's manifold is never counteracted. It produces the resulting trajectory to become a quasi-periodic motion that jumps onto different orbits of the same family of the reference orbit. This drift accumulates every time a maneuver is executed (as a maneuver is necessary to counteract the departure on the unstable direction for a long time span). Therefore the error from the target orbit is far larger than the one obtained with the first control law, in particular for the low SK interval cases. The strength of the Floquet mode technique is that it allows to give analytical insight on the control of the instability of the LPOs, reducing the control's consumption and load. But it cannot be used as a stand-alone control law for a high time span, and periodically correction maneuvers must be undertaken to insert the spacecraft back to the stable manifold of the reference orbit, as it shown in the plot of Fig.4.166, which has been taken from the

Table 4.7: **Station-keeping of the LPOs in the Mars-Phobos ER3BP-GH.** Target Point control. Stochastic analysis. Mean performance: $\Delta v/day$, state error from target. Further row indicates 3x-standard deviation of the performance (percentage with respect to mean performance above). Orbits 1 and 2.

\ Frequency SK Other \	0.5h	1h	1.5h	2h
Inaccuracy Position 1m	0.158 m/s 5.90 m	0.116 m/s 14.5 m	0.163 m/s 41.1 m	0.436 m/s 259 m
Inacc. Velocity 1mm/s	5.52 mm/s 0.235 m/s	9.34 mm/s 0.167 m/s	23.3 mm/s 0.233 m/s	106 mm/s 0.635 m/s
Inaccuracy Δv 0.5mm/s	0.024,5 m/s (16%)	0.058,4 m/s (51%)	0.091,2 m/s (56%)	0.664 m/s (152%)
Threshold Δv 1mm/s	2.47 m (42%) 1.93 mm/s (35%) 0.034,8 m/s (15%)	8.40 m (58%) 5.79 mm/s (62%) 0.084,4 m/s (50%)	39.3 m (96%) 25.7 mm/s (110%) 0.136 m/s (58%)	551 m (213%) 211 mm/s (199%) 0.973 m/s (153%)

\ Frequency SK Other \	0.5h	1h	1.5h	2h
Inaccuracy Position 1m	0.162 m/s 6.46 m	0.119 m/s 14.5 m	0.236 m/s 49.5 m	0.517 m/s 187 m
Inacc. Velocity 1mm/s	5.91 mm/s 0.238 m/s	10.1 mm/s 0.158 m/s	35.9 mm/s 0.312 m/s	106 mm/s 0.694 m/s
Inaccuracy Δv 0.5mm/s	0.041,9 m/s (26%)	0.035,9 m/s (30%)	0.086,9 m/s (37%)	0.195 m/s (38%)
Threshold Δv 1mm/s	6.17 m (95%) 5.00 mm/s (85%) 0.058,0 m/s (24%)	15.8 m (110%) 12.2 mm/s (121%) 0.043,7 m/s (28%)	64.2 m (130%) 48.8 mm/s (136%) 0.117 m/s (37%)	167 m (89%) 107 mm/s (101%) 0.292 m/s (42%)

Table 4.8: **Station-keeping of the LPOs in the Mars-Phobos ER3BP-GH.** Target Point control. Stochastic analysis. Max performance: $\Delta v/day$, state error from target. Orbits 1 and 2.

\ Frequency SK Other \	0.5h	1h	1.5h	2h
Inaccuracy Position 1m	0.170 m/s	0.139 m/s	0.210 m/s	0.913 m/s
Inacc. Velocity 1mm/s	7.81 m	20.1 m	61.1 m	607 m
Inaccuracy Δv 0.5mm/s	6.59 mm/s	13.5 mm/s	39.4 mm/s	0.239 mm/s
Threshold Δv 1mm/s	0.250 m/s	0.199 m/s	0.301 m/s	1.33 m/s

\ Frequency SK Other \	0.5h	1h	1.5h	2h
Inaccuracy Position 1m	0.183 m/s	0.140 m/s	0.279 m/s	0.676 m/s
Inacc. Velocity 1mm/s	11.2 m	27.3 m	91.9 m	272 m
Inaccuracy Δv 0.5mm/s	9.79 mm/s	20.3 mm/s	68.9 mm/s	169 mm/s
Threshold Δv 1mm/s	0.264 m/s	0.184 m/s	0.373 m/s	0.940 m/s

technique's authors in [143].

Due to the low time-scale of the LPOs of Phobos, this second technique, even if possible and valid for particular and single SK maneuvers, is not suitable for exploitation in the further sensitivity investigation on the GNC requirements for the LPOs. The consumptions are of the same order of magnitude of the first technique, but even if they are lower, correction maneuvers would augment the cost to be further similar to the consumptions of the first technique.

4.4.5.4 Further Sensitivity Investigation

The Target Point technique is used to conduct further analyses from the one of the JPL on the feasibility of the LPOs with respect to the GNC performances. The first orbit is considered with a deterministic analysis. Table 4.5 shows the dependency on the inaccuracy of the velocity for a single central case of the previous tables, where the cut-off is now considered when Δv is less than twice the related inaccuracy. Table 4.6 shows the dependency on the inaccuracy of the Δv for a single central case of the previous tables, where the cut-off is considered as above.

This analysis probes the sensitivity of the SK from these two inaccuracies with respect to the one from the inaccuracy of the relative position. The results indicate that the sensitivity is the same for a ratio roughly of $1m : 1mm/s$ for both cases. This is useful to quickly know, from a set of inaccuracies on position, velocity, and Δv, which one is the driver for the SK performances. Regarding the effect of the Δv cut-off, this has been tested but it is of minor importance. If the cut-off is much more larger than the inaccuracy of the velocity and Δv, the practical result is the same that lowering the SK-frequency, since a maneuver will be missed.

Finally, a brief stochastic analysis is undertaken. With the same conditions and

control law of Table 4.2, where the errors are always considered with random direction, their magnitude is now varied and computed from the related inaccuracies interpreted as 1σ. The simulations have been only repeated 9 times for a 2 days span to average the outcomes. The mean performances are presented in the first row of Table 4.7. The second row reports the 3x-standard deviations, and its percentage with respect to the mean value above. The fourth row within a cell expresses the Δv evaluated from separate 3-axes contributions. The maximum values are provided in Table 4.8. As expected, either considering the inaccuracies as 3σ and taking the output's maximum value in a stochastic analysis, or considering the separate 3-axis contribution, furthers moves the results of the consumption towards the ones of the JPL. Recall that the results depend also on the type of reference orbit, and the first one is probably more stable than the one used in the JPL paper, while the second could be similar. The row of the max values with 3-axis contribution in Table 4.8 is the nearest to the respective row of the JPL values in Table 4.3. In particular it is worth to emphasize that now the consumption is not linear with the SK-frequency, but has a minimum for $1h$. This is a common result and in particular is coherent with the JPL.

It is worth to underline the growth of the performances' uncertainty with respect to the SK intervals for only the first orbit, maybe due to the low number of samples. However, for both orbits the uncertainty is more sensible for the max position-velocity than for the consumption.

4.4.5.5 Trade-off with Navigation

A survey has been conducted on the best performance of the deep-space navigation technologies. This is first to assess the precision of the state estimation (to check if is coherent with the inaccuracies used in this station-keeping analysis), and second to consider if there is a trade-off with the time required to obtain such estimation with the best precisions (to check also the coherency of the SK frequency used in this SK analysis). These performances must be considered downstream the filtering process.

Ground-based radiofrequency navigation is probably avoided for such close-range and fast-speed LPOs, because it is not precise for close relative motion and must consider also the Earth-Mars round-trip light-time (medium $24min$, max $42min$). Thus, only the bottom-right corners of the tables would be feasible for this type of navigation, but this zone is expensive, very imprecise and even unsafe for some orbits.

Therefore, optical navigation for the relative motion, and probably fully autonomous, is required for Phobos' LPOs. The techniques used are line-of-sight observations to determine the Phobos' barycenter at large distances, and landmarks navigation with NPAL camera[23] for approach and landing. The latter should be the necessary since Phobos' figure at the LPOs' altitude is far from a sphere. Optical measures are then combined with the altimeter (which is very precise, with errors less than $1m$).

[23]The required camera in [144] has $25° \times 25°$ FOV, 1024×1024 pixels, CCD.

Unfortunately specific information on optical navigation performances is not available with detail in the literature. Furthermore, such close relative motion is not usual, and space missions to asteroids and comets have different time-scales. The current Astrium documentation on Phootprint [144] has not considered LPOs, thus navigation sizing has not been probed for them. An indication could be given by the errors on the landing sequence's initial condition, which is about $5m$ and $15mm/s$ (1σ). But these values rely on ground-based navigation, thus performance are poor and time required high: $2.5h$ are speculated to be required by ESOC for final orbit determination to start the descent from hovering, but this has not been confirmed.

A study in JPL [145] investigated the performance of various filtering techniques for autonomous optical landmarks navigation. And they are tested for close relative motion ($20km$) around a small-body (Eros). The only mismatch is that the analysis is carried out with a large-view camera ($35° \times 35°$, 512×512 pixels, CCD), thus results could be at least 10 times worse. The performances achieved are mean accuracies of $200m$ (max $1km$) in relative position and $50mm/s$ (max $500mm/s$) in relative velocity. Another paper from JPL [146] suggests AutoNav would provide accuracies of $3m$ and $20mm/s$. Regarding the time, translational state's estimation is provided at incomparable rate with respect to orbital times ($1Hz$), and the simulation of JPL around Eros is conducted with an update of the image every $17min$.

A study in GMV [147] assessed GNC requirements for QSOs and hovering around Phobos. They can have precisions of $5m$ and $5mm/s$ with ground-based navigation. The impact of operational delay is assessed, but no indication is given due to the fact this is not a constraint for QSOs. Finally GMV assessed the capability of landmark optical navigation, and provides the geometrical estimation precision in terms of altitude and camera's FOV (1024×1024 pixels, CCD). For the LPOs' altitude, less than $30m$ are feasible with any wide camera, and to improve ground-based performance FOV$< 10°$ is required, reaching errors of $< 1m$ for FOV$= 2°$.

In conclusion, with an appropriate camera and current filtering techniques, autonomous optical navigation should provide precisions between [1-20]m and [0.5-5]mm/s (1σ), with maneuver frequency at least every $30min$. Radiofrequency navigation could achieve the same worse performances, but with time required of $3h$.

4.4.5.6 Conclusions

The feasibility of the Phobos' LPOs probed in this analysis should therefore be constrained to two cases.

- 1st case (orange): autonomous optical navigation: the outcomes of the station-keeping at the center-left side of the tables[24].

[24] Obviously also the right side is achievable, but it will be just indicated as inappropriate since no sensor's constraints on the time update have been risen. However, relaxation of the time could be required to allow the spacecraft to perform particular operations, for example telecommunications: if the antennas are not steerable, the spacecraft must rotate to provide the required pointing, and this

Table 4.9: **Station-keeping of the LPOs in the Mars-Phobos ER3BP-GH.** Target Point control. Conclusion after trade-off with navigation subsystem for the LPOs around Phobos. Values to be considered as order of magnitude.

\ Frequency SK Inaccuracy pos-vel-Δv\	0.5h	1h	1.5h	>2h,<3h
0.1m-0.1mm/s-0.1mm/s	NAvailab	NAavailab	NAvailab	NAvailab
1m-1mm/s-1mm/s	0.2 m/s 5 m 5 mm/s	NAappropr	NAvailab	NAvailab
10m-10mm/s-10mm/s	1 m/s 20 m 20 mm/s	Nappropr	2 m/s 200 m 200 mm/s	>5 m/s 800 m 800 mm/s or Unsafe
100m-100mm/s-100m/s	NAvailab	Navailab	Unsafe	Unsafe

- 2nd case (green): ground-based radiofrequency navigation: the bottom-right corner of the tables, which seems unfeasible for more unstable orbits (like the second orbit): if used, it requires accuracies of $10m/10mm/s$ and frequencies shorter than $2h$ ground-processing (which is at net of the light-time).

The trade-off with the navigation is therefore the driver of the feasibility study of the LPOs around Phobos, and this is summarized in Table 4.10. This could have already been hinted from the simple trade-off analysis in section 4.1.3.2.2.

Therefore Phobos' LPOs require either:

- 1st case: autonomous navigation (Δv= $[0.2 - 1]m/s/day$)
- 2nd case: optical measures to help the ground-processing to improve performance above (Δv= $[2 - 5]m/s/day$).

The advantages from the current observation scenario planned for Phootprint [144], which is a sequence of fly-by and hovering, are:

- the observation capabilities (low altitude, long time) over the sub-Mars and anti-Mars faces of Phobos (where landing site seems currently constrained for the mission's mass budget)
- the fuel consumption savings.

However, the 1st case is not allowed by ESA policy[25], and requirement for the Phootprint mission is that no autonomous absolute navigation shall be allowed. Absolute navigation refers to the estimation of the relative state of the spacecraft with respect to Phobos. Absolute navigation sensors (which is, a narrow and precise nadir-pointing NPAL camera) could be used (and should be necessary) but they must be processed on-ground. However, autonomous relative navigation is allowed. Relative navigation refers to the estimation of the relative state of the spacecraft with respect to a previous absolute measure. In particular, from Astrium documentation, UFS3 filtering allows

would stop the acquisition of the image with a fixed camera.

[25]This policy is due to the failure of the autonomous absolute navigation in the Hayabusa mission.

Table 4.10: **Station-keeping of the LPOs in the Mars-Phobos ER3BP-GH.** Target Point control. Deterministic analysis. Performance: $\Delta v/day$, state error from target. Orbits 1 and 2.

\ Frequency SK Inaccuracy pos-vel-Δv\	1.5h	2h	2.5h	3h
5m-10mm/s-1.7%	2.53 m/s 220 m 133 mm/s	3.70 m/s 626 m 321 mm/s	N/A	N/A
10m-10mm/s-1.7%	3.57 m/s 293 m 189 mm/s	5.28 m/s 784 m 387 mm/s	N/A	N/A

\ Frequency SK Inaccuracy pos-vel-Δv\	1.5h	2h	2.5h	3h
5m-10mm/s-1.7%	7.14 m/s 425 m 308 mm/s	N/A	N/A	N/A
10m-10mm/s-1.7%	11.3 m/s 675 m 493 mm/s	N/A	N/A	N/A

Table 4.11: **Station-keeping of the LPOs in the Mars-Phobos ER3BP-GH.** Lyapunov multipliers of the two orbits.

\ Frequency SK orbit\	1h	1.5h	2h	2.5h	3h
1	6.5	16	42	107	274
2	8.4	24	70	204	592

to reduce integration of velocity errors to be only 5%. Ground absolute navigation provides estimation errors (1σ) of $5m$ and $15mm/s$ (for Rosetta in $8h$, for Phootprint it is supposed to be provided in $2.5h$). Thus, this would augment the position error of $3m$ every $1h$. However, also autonomous relative navigation cannot be used for the purpose of controlling the LPOs, because the spacecraft still needs an absolute measure from ground. This again cannot be determined by propagation from ground, if the spacecraft autonomously controls itself in the same corresponding time window. Thus, the 2nd case can only be conducted totally on-ground.

Finally, the approach of the feasibility study has been conducted in parallel to JPL analysis, with fixed inaccuracies (deterministic or stochastic) for estimated state and Δv. But the latter is probably not worthy to be considered in such sense. Error of Δv depends on thrusters realization, which is indicated in Astrium documentation to be 5% as 3σ, thus 1.7% following the approach used so far. Now, the Δv of the single maneuver depends from the SK frequency. With the fixed inaccuracy of Δv used, the center of the tables is mostly coherent with the mentioned relative inaccuracy of Δv, with the upper left conservative. The problem is in the right and lower part, where Δv inaccuracy is constrained. This should be probed again and this is done focusing on the part of interest, which is the 2nd case of the trade-off with the navigation. For this purpose, deterministic analysis is used (recall this is the worst-case scenario) to compare results of Table 4.1[26].

The outcomes are presented in Table 4.10. The error of Δv worsens the performances and the limit of the minimum ground response time moves further left. The first orbit can be realized with $2h$, but in an extended time simulation this seems to be guaranteed only for $1-1.5$ days. The $1.5h$ frequency case is safe for both orbits whatever the time span is.

In conclusion, the situation is now critical for the feasibility of Phobos' LPOs:

[26]The relation with the stochastic output can be hinted by a ratio comparing the past analyses in Table 4.7-4.8.

- 1st case: not allowed by ESA
- 2nd case: time required for ground processing (and light travel) is the major driver and looks not possible.

Indeed, the Floquet multiplier of the two orbits analyzed is respectively 1,200 and 2,100, which is a Floquet exponent of 2.26 and 2.61. The related Lyapunov multipliers of the guidance real error during the maneuver interval are shown in Table 4.11. Considering that the navigation error from ground could be optimistically $5 - 10m$ (1σ), and the realization error of the control system would make the total real error double, just from this latter table it really seems unfeasible using ground-in-the-loop if this requires more than $2h$ (more stable LPOs) or $1.5h$ (more unstable LPOs), because the spacecraft in the worst-case would drift of more than $3km$ (3σ) on an orbit whose min altitude is less than $3.5km$.

In conclusion, the LPOs around Phobos are:

- not generally feasible from ground, unless using the more stable and distant from Phobos, however the required time response from ground would be at a level never done before.
- feasible with autonomous GNC with state-of-the-art optical navigation, but not allowed by ESA, however a mission landing on Phobos necessary needs the final stages of the descent to be performed autonomously.

4.4.6 Natural Landing and Take-off

The IMs of the LPOs in the Mars-Phobos ER3BP-GH have been computed in section 4.3.5. The IMs are usually exploited as the natural low-energy transfers between different bodies, exploiting the nB dynamics. Since the LPOs are close to the moon, all the inside branch of their IMs intersect Phobos. This is a **unique feature** of the Mars-Phobos 3BP, because the natural trajectories, at low energy, to transfer between the SOIs of the two primaries in the Sun-Earth and Earth-Moon systems fly widely far from the bodies. In [68], a selection of the smallest planar Lyapunov orbits whose IMs naturally intersect the smallest primary of the Sun-Earth and Earth-Moon systems, and provide whole-coverage along the body's orbital equator, has been undertaken. These orbits are very large and so require high energy relative to the one of L_{1-2}, and the analysis undertaken is 2D. The same approach could be extended considering impulsive propulsion to modify the IMs at the starting point at the LP [68] or along a smaller orbit, as well as including low-thrust continuous propulsion to modify directly the LPO. Instead in this unique case, a spacecraft could land or take-off from Phobos using the gateway of small-energy LPOs and with no need of thrust. This section summarizes the possibility offered by the IMs of the ER3BP-GH to provide natural landing and take-off trajectories to and from the 3D surface of Phobos, modeled with the high-order shape harmonics model. Examples of these tubes are shown in Fig.4.167.

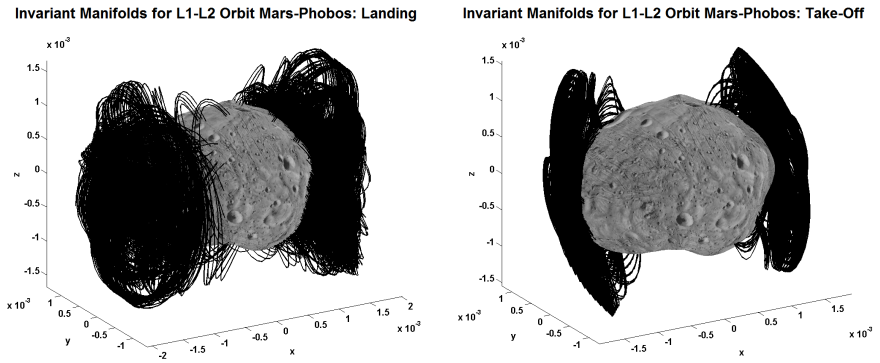

Figure 4.167: **IMs of the LPOs in the Mars-Phobos ER3BP-GH.** On the left, inside branch of the tube of unstable IMs from the families of 3-tori LPOs. On the right, inside branch of the tube of stable IMs from the families D of 2-tori LPOs.

4.4.6.1 Landing on Phobos

The landing problem. The landing phase of a space mission is usually identified with the name EDL, which stands for Entry-Descent-Landing. The outline of a general EDL segment is made up of the following phases.

- 0: initial orbit.
- 1: de-orbiting trajectory: in case phase 0 is not an open orbit captured toward the body, there will be a maneuver to produce such impacting orbit.
- 2: descent: trajectory that it is not anymore an orbital dynamics problem (the gravity field becomes mainly vertical) which is now dealt by the GNC subsystem: atmospheric drag and heating are major design drivers, landing site starts to be targeted.
- 3 effective landing: very last moments related to the touch-down and the related systems' deployment.

In particular, the examples of the traditional descent phase are presented below.

- ballistic descent strategy. For an unmanned spacecraft. The flight-path angle could be also steep for a completely uncontrolled phase 2.
- gliding descent strategy. For a manned spacecraft, where the flight-path angle is kept flat.
- skipping descent strategy. There is close-loop control of the spacecraft during phase 2, whose objective is to slow down the descent and therefore increment the range of possible landing sites.

The complete EDL schedule is used for the problem of the effective entry in a celestial body with atmosphere. For a minor body, the transition from phase 1 to phase 2

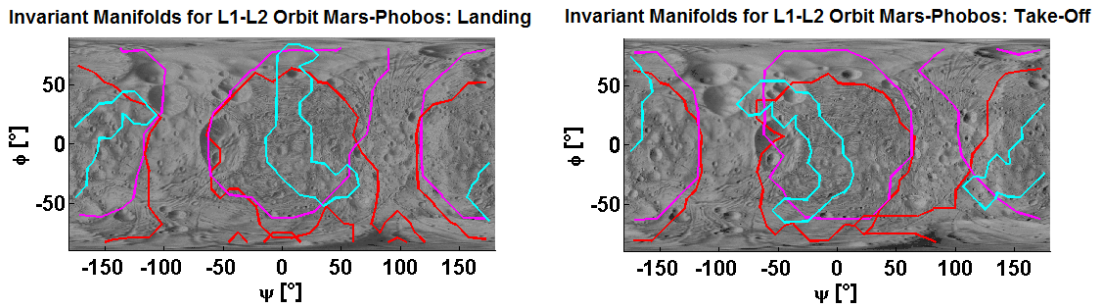

Figure 4.168: **IMs of the LPOs in the Mars-Phobos ER3BP-GH.** On the left, outer boundaries of the region of the possible landing sites through the IM of all the families of tori around both LPs. On the right, outer boundaries of the region of the possible take-off sites through the IM of all the families of tori around both LPs. Families' colors are coherent with Fig.4.58, with red associated to the global family AB.

is smoother and faster, because phase 2 is not driven by atmospheric actions. Thus, despite the closed-loop control of the GNC would be activated, phase 1 and 2 can be treated together still as an orbital mechanics problem that targets the aimed arrival site. The forced motion will incrementally increase its duty cycle as long as the altitude decreases, to assure the spacecraft is controlled in a funnel-like space around the reference landing profile.

For the case of Phobos, in this thesis the IMs are proposed as natural de-orbiting trajectories that evolve from the LPOs (that represent phase 0), since they are the asymptotic separatrices of their center manifold. Since the perturbation of the GHs grows exponentially as the proximity to Phobos increases, the globalization of the manifolds, using a low-order series expansion, produces a not very accurate approximation in the last stages of the descent and landing (and first stages of the take-off). This is a common problem for any lander, where the final maneuvers are mostly managed by the GNC subsystem to satisfy the performances required. Results in this section should therefore be considered as an estimation of these performances at the touch-down and launch, more refined than the CR3BP, to lower the load on the GNC subsystem in the real scenario. Therefore, the IM final condition is considered as an input to the final descent undertaken by the GNC subsystem. In other terms, the trajectory of the natural IMs could well be a convenient starting guess for an optimal control software that computes the profile of the forced motion.

Performances of the IMs of Phobos. The inside branch of the unstable IM of the family D of 2-tori, and of the families AB and C of 3-tori of the ER3BP-GH, has been computed in section 4.3.5.1 up to the intersection with Phobos' surface modeled with the high-order shape harmonics model.

The region of possible landing topographical sites enabled by all the families of LPOs is provided in Fig.4.168. This area is restricted to the collinear-faced sites on Phobos, due to the collapsing effect of the SOI. In particular, large tori within the families AB

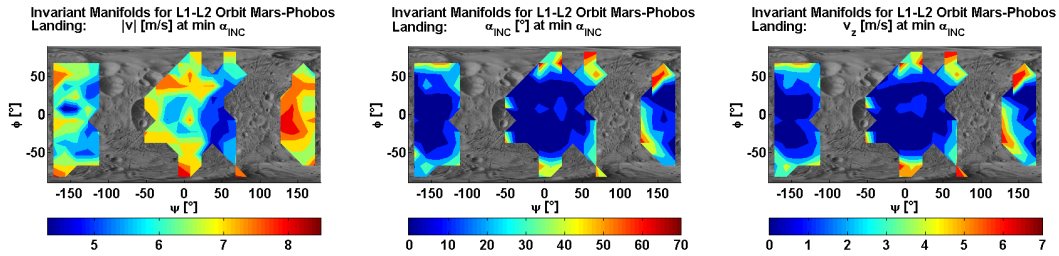

Figure 4.169: **IMs of the LPOs in the Mars-Phobos ER3BP-GH.** Performances of the trajectories that provide the minimum incidence at the touch-down from all the families of tori around both LPs, as a function of the longitude and latitude of the landing site on Phobos surface modeled through shape harmonics series expansion: landing velocity magnitude, angle of incidence, downward vertical velocity.

and C can extend the region in both longitude and latitude, while the POs and the QPOs of the branch D are more restricted. Also the region of the big crater Stickney is accessible with both stable and unstable IMs of large QPOs of the families AB and C.

The selection of the optimal landing trajectory, for a given landing site, could be driven by several considerations. Apart from arrival site and time of flight, the performances are given by the velocity at the touch-down: total magnitude, angle of incidence and vertical component. The desired trajectory would minimize the longitudinal control as well as yield a soft landing.

Minimizing the incidence (tangential landing) and the vertical component has the same effect, as presented in Fig.4.169-4.170. Minimizing the vertical component is useful for minimizing the impact on the ground. The GNC will then be required to brake the spacecraft horizontally to verticalize the final stages of the descent, starting from a small vertical velocity and so facilitating the shock absorbtion at touch-down. In particular an indicative figure for the shock force could be derived from the law of conservation of momentum, considering a time interval for the impulse of $0.1s$ (inversely proportional to the rigidity of the absorbtion structure). Therefore, numerically the shock force in terrestrial g is approximately equal to the vertical velocity in m/s. Thus, it is possible to land naturally with a tangential path, which is arrive with vertical velocities even less than $0.1m/s$. The total velocity instead ranges in $3-8m/s$.

Instead, minimizing the velocity magnitude provides the outcomes of Fig.4.171. An extended area is reachable with a total velocity of $3-5m/s$, with incidence $30-60°$, and vertical component $2-3m/s$.

Finally, a classical landing would aim to arrive perpendicular to the local slope. This should also be required by the autonomous navigation tracking of the landing site. Thus, maximizing the incidence provides the outcomes of Fig.4.172. An extended area is reachable with incidence of $60-90°$, total velocity $3.5-5m/s$, and vertical $3-5m/s$.

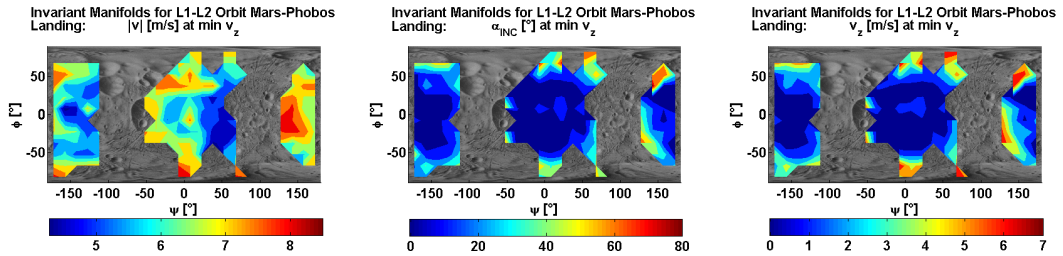

Figure 4.170: **IMs of the LPOs in the Mars-Phobos ER3BP-GH.** Performances of the trajectories that provide the minimum vertical velocity at the touch-down from all the families of tori around both LPs, as a function of the longitude and latitude of the landing site on Phobos surface modeled through shape harmonics series expansion: landing velocity magnitude, angle of incidence, downward vertical velocity.

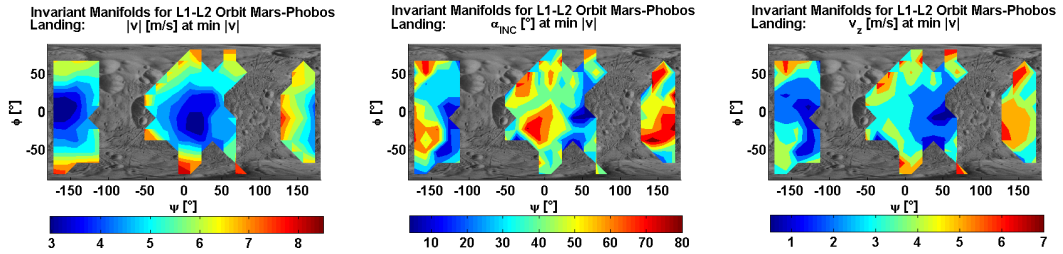

Figure 4.171: **IMs of the LPOs in the Mars-Phobos ER3BP-GH.** Performances of the trajectories that provide the minimum velocity magnitude at the touch-down from all the families of tori around both LPs, as a function of the longitude and latitude of the landing site on Phobos surface modeled through shape harmonics series expansion: landing velocity magnitude, angle of incidence, downward vertical velocity.

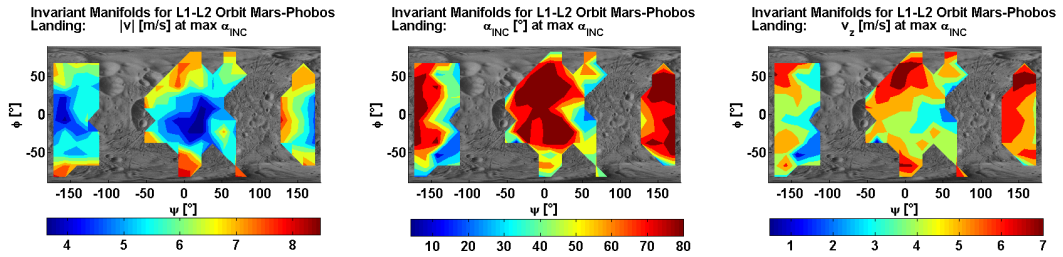

Figure 4.172: **IMs of the LPOs in the Mars-Phobos ER3BP-GH.** Performances of the trajectories that provide the maximum incidence at the touch-down from all the families of tori around both LPs, as a function of the longitude and latitude of the landing site on Phobos surface modeled through shape harmonics series expansion: landing velocity magnitude, angle of incidence, downward vertical velocity.

4.4.6.2 Take-off from Phobos

The inside branch of the stable IM of the family D of 2-tori, and of the families AB and C of 3-tori of the ER3BP-GH, has been computed in section 4.3.5.1 up to the intersection with Phobos' surface modeled with the high-order shape harmonics model.

The region of possible take-off topographical sites enabled by all the families of LPOs is provided in Fig.4.168. The considerations are specular to what has been said for the landing in section 4.4.6.1.

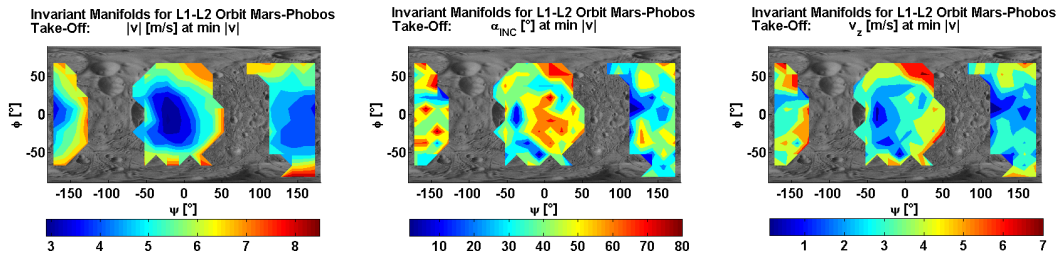

Figure 4.173: **IMs of the LPOs in the Mars-Phobos ER3BP-GH.** Performances of the trajectories that provide the minimum velocity magnitude at the launch from all the families of tori around both LPs, as a function of the longitude and latitude of the departure site on Phobos surface modeled through shape harmonics series expansion: landing velocity magnitude, angle of incidence, upward vertical velocity.

The selection of the optimal take-off trajectory, for a given departure site, is simpler than the landing. The driver is to minimize the escape velocity (total magnitude). The results are provided in Fig.4.173. An extended area allows to depart with an escape velocity between $3.5 - 5m/s$.

In conclusion, the IMs of the LPOs of Phobos provide **highly efficient natural trajectories that are able to land tangentially, facilitating a soft controlled touch-down, and depart with a very small escape velocity, less than 30% of the 2B Δv value, for an extended region of topographical collinear-faced sites on Phobos**. These trajectories have the potential to be exploited for future sample-and-return missions to this moon, where free-fall is required to avoid contamination of the sample's soil by the exhaust plume of the thrusters or rockets' nozzle.

4.4.7 Extension of the LPOs and IMs to Model Natural Impacts on the Surface and the Dust Dynamics around Phobos

The LPOs and IMs presented in this chapter have been applied to model the motion of a spacecraft about Phobos. According to the analysis of the orbital perturbations in section 2.4, SRP is not significant if the spacecraft does not use solar sails. SRP becomes important also in the well-known photo-gravitational 3BP for the orbital dynamics of dust grains around the secondary body, because the perturbation a^P is inversely proportional to the grain radius, as was discussed about Eq.2.43. This is very important for an asteroid, where the SRP could be higher than the Sun 3B perturbation, and affect even a spacecraft. The ratio $a^P/a_\odot$ with the full Solar gravity magnitude $a_\odot$ is known as the lightness number λ. An analysis on the order of magnitude of the physical characteristics leads to an interesting outcome for the Mars-Phobos system.

The objective here is to *study the transition from a classical CR3BP to a photo-gravitational CR3BP*. This means to identify the conditions that make the SRP a significant force in the modeling of the dynamics around a body of the Solar System. The transition between the two models is weighted referring λ to the second massive

body gravity, which is a^P/a_2. The dust grain is modeled as a sphere as in Eq.2.43, with common physical values[27]. Thus λ, for a given couple of primaries in the Solar System, is now a function of the grain radius and the distance from the secondary. Assuming a threshold $\lambda = 1\%$ to identify when the SRP becomes relevant enough to be included in the modeling of the dynamics, the transition grain radius is computed as a function of the distance from the secondary r_2. This is summarized in Eq.4.60.

$$r_{grain} = \frac{\frac{3}{4\rho_{grain}} \frac{1}{c_{light}} q_{\odot,ref} \left(\frac{d_{ref}}{\|\mathbf{r}^{\odot}\|} \right)^2 \left[(1 - c_{rs}) + 2 \left(c_{rs} + \frac{1}{3} c_{rd} \right) \right]}{\lambda_{ref} a_2 \left(\mathbf{r}_2 \right)} \tag{4.60}$$

This radius does not change order of magnitude inside the SOI of Phobos, due to its small altitude over the body. Its value is quite low: $20\mu m$ at the Hill's radius, and $9\mu m$ on the mean surface[28]. As a difference, if Phobos had been an asteroid orbiting the Sun at the Sun-Mars distance, its gravity field at the LPs would have been 10,000 times lower, so the equivalent dust grain radius that requires the transition to a photo-gravitational problem has risen to $20cm$.

Therefore, **the LPOs and IMs of the ER3BP-GH** obtained in this chapter, that do not consider the SRP, in addition to common spacecraft, **also provide a good approximation for the natural motion of dust grains down to** $10^{-5}m$ **scale**. This is definitely a broad range considering the common distribution of minor bodies' regolith ($m - 0.01nm$). So for Phobos, only very small dust grains require the photo-gravitational model to be used. This means that *the IMs of the ER3BP-GH could be the trajectories followed by a large dimensional range of meteoroids that have impacted Phobos, as well as clusters of regolith that left its surface*[29]. In this sense, Fig.4.168 highlights that the medium-small craters are densely accumulated on the two collinear sides where the IMs of the LPOs impact or leave the moon, and their boundaries link neatly together all the larger craters, in particular Stickney and the craters on the Northern sub-Mars sector. With the help of the map in Fig.1 of [15], it is immediately noticeable that most of the characteristic grooves of Phobos run parallel to the boundary of the regions of landing and take-off sites computed. In particular, recall that only the IMs of the practical LPOs that do not intersect Phobos were considered in this chapter, but larger orbits (which refer to higher energy transferred material) provide additional impact trajectories themselves. Their footprint will correspond to the pattern of the remaining grooves, since they both develop farther concentrically on the L_1 and L_2-sides of the moon.

The study of the transition between CR3BP and photo-gravitational CR3BP through Eq.4.60 is extended for all the major couples of primaries of the Solar System. The transition grain radius is reported in Fig.4.174, and is evaluated at the

[27] Specular and diffusive reflectance coefficients both set to 5%, and density to $3,000 kg/m^3$.

[28] For Deimos, these values are respectively $0.25mm$ and $20\mu m$.

[29] A study of the impacts provided by the transit trajectories in the Earth-Moon system is undertaken in [148].

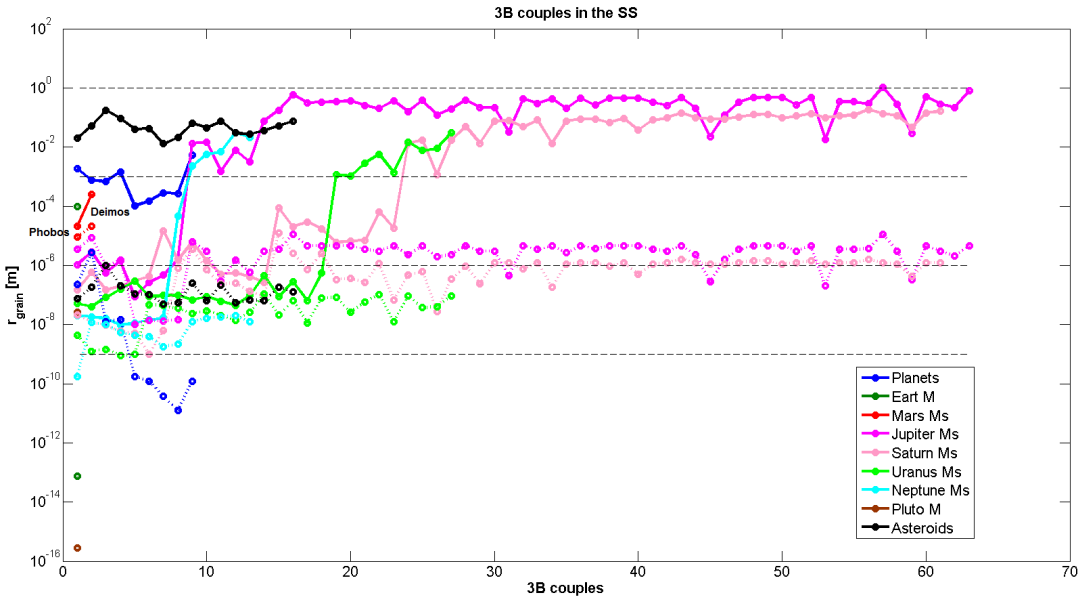

Figure 4.174: **Transition from CR3BP to photo-gravitational CR3BP of the 3B couples in the Solar System.** Equivalent dust grain radius to obtain a lightness number of 1% relative to the second massive body's gravity reference. Plain lines correspond to a reference at the related Hill's radius, dotted lines correspond to a reference at the secondary body's mean radius. Major moon and asteroids are considered.

extreme boundaries of each secondary's SOI, which is at its Hill's radius and at its mean radius[30]. Asteroids, planets and small moons of the outer planets have the highest values of the dust radius at the Hill's sphere boundary, because the size of the SOI is large: dust around L_{1-2} of these systems in the range of $m - mm$ must be modeled with a photo-gravitational problem. In contrast, the transition grain radius massively decreases at decreasing distance from the secondary, and only around small bodies the dust grains can compete with the body gravity and float in space. The difference between the two extreme locations reduces when the SOI is comparable with the secondary body's dimension, which are the few peculiar cases that have already been highlighted in section 2.3.4. In this sense, it is remarkable that the two Martian moons have the highest values of transition grain radius on the mean surface among the bodies considered in all the Solar System. This means that Phobos and Deimos could experience rings of dust clouds of micrometer scale around them [17] and some authors theorize that dust dynamics on the surface is responsible for the origin of the grooves of Phobos [14, 15, 18]. Following this, it is possible to propose the idea that the footprint of IMs and large LPOs could have originated in the past the craters and the grooves of Phobos, and that current dust clouds of grain dimension over $20\mu m$ could correspond to the LPOs presented in this thesis.

[30] For secondary bodies with an atmosphere, the transition grain radius at the surface is not valid due to the effect of the drag perturbation.

Chapter 5

Artificial Orbits with Low-Thrust in the Mars-Phobos 3BP

This chapter investigates the opportunity provided by the inclusion of a propulsive acceleration in the analysis of the orbital dynamics of a spacecraft around Phobos. This additional acceleration term in Eq.2.1 is considered to be continuous and with low-thrust. Thus, it is usually provided by a solar electric propulsion system (SEP). The related orbits are referred to as artificial, because they are not possible naturally.

The inclusion of low-thrust is first analyzed in this chapter with the case of a constant acceleration profile. This allows to derive artificial equilibria, such as artificial equilibrium points and vertical-displaced circular orbits, that will be presented respectively in section 5.2 and section 5.3. Furthermore, the possibility of hovering around the artificial equilibria is considered in section 5.4, by realizing artificial Libration Point Orbits. In conclusion, the case of artificial Martian Formation Flying with respect to Phobos is discussed in section 5.5.

5.1 Rationale of Low-Thrust Artificial Orbits around Phobos

The two peculiarities of the Mars-Phobos system introduced in section 2.3.2 lead to an important perspective, that will be recurrently used in this and in the following chapter. As a result of the combination of Phobos' low gravity and the collapse of its SOI, the gravity pull of Phobos is still small ([$1mm/s^2$-$50\mu m/s^2$]) at the distances used in common interplanetary spacecraft operations ([10-100]km altitude). This could be inferred also from the analysis of the orbital perturbations of section 2.4. Thus, in the inertial frame centered on Mars and out of Phobos' SOI, the natural trajectories are similar to slightly perturbed Keplerian orbits around Mars, close to Phobos' orbit. Original Keplerian orbits would be exactly tracked artificially by compensation of Phobos' gravity, which could be feasible with a low-thrust propulsion system even for large spacecraft. The reduction to a Keplerian perspective, in the framework of the relative

motion, implies that the mission design at such distances could be undertaken using the same approach of Formation Flying (FF). This means that the osculating orbit of the secondary body of the R3BP (in our case Phobos) could be considered as a chief spacecraft orbiting the primary (in our case Mars), that the third body, which is the deputy spacecraft in FF (but in our case is the only spacecraft), follows in proximity.

The analysis of artificial trajectories is undertaken adding the propulsive acceleration $\mathbf{a_P}$ of Eq.2.1 to the equation of the relative dynamics around Phobos. In particular, the propulsive acceleration for an artificially maintained orbit requires to be continuous in time. Thus, to use an artificial orbit for an extended range of time, without consuming a lot of propellant, low-thrust is required. Recall that the SEP Hall/ion thrusters operate roughly in the medium range of $0.01mN$-$0.1N$, new generation FEEP and colloid thrusters provide low-thrust down to $1\mu N$ scale, and electrothermal propulsion (resistojets and arcjets) supplies the higher ranges up to $1N$. Over this value, classical chemical propulsion is required, which could make use of cold gas, liquid, or solid propellant. It is worth to recall that, to derive the type of thruster or rocket, the level of propulsive acceleration required by the artificial orbit must be scaled accordingly to the mass of the spacecraft. In this sense, the range to be considered lies from $100kg$ for a medium-size interplanetary satellite, to 100 times larger for a big manned module.

5.2 Hovering Points around Phobos

A simple trajectory for a mission around Phobos is provided by maintaining a fixed position with respect to its BCBF frame, which is referred to as *body-fixed hovering*. With the FF perspective, hovering around Phobos is analogous to a Trailing/Leading configuration [149].

5.2.1 Equations of Motion

The analysis of the body-fixed[1] hovering is undertaken by adding a constant $\mathbf{a_P}$ to the equations of motion of the Mars-Phobos CR3BP of Eq.2.13, which will be referred to as CR3BP-CA,

$$\begin{cases} \dot{\mathbf{x}} = \mathbf{f_{CR3BP-CA}}(\mathbf{x}) = \mathbf{f_{CR3BP}}(\mathbf{x}) + \mathbf{f_{CA}} = \mathbf{A}\mathbf{x} + \begin{bmatrix} \mathbf{0_{3x1}} \\ \nabla u(\mathbf{q}) \end{bmatrix} + \begin{bmatrix} \mathbf{0_{3x1}} \\ \mathbf{a_P} \end{bmatrix} \\ \mathbf{a_P} = |\mathbf{a_P}|\, \hat{\mathbf{n}}_{\mathbf{a_P}} \end{cases} \tag{5.1}$$

where $\hat{\mathbf{n}}_{\mathbf{a_P}}$ represents the fixed direction of the thrust applied. Recall that to provide a constant acceleration, the thrust required would slightly decrease along the time by the effect of the spacecraft's fuel consumption. However, for SEP and small thrusters, the specific impulse is 10 times greater than the one of chemical propulsion, so the

[1] Recall from section 3.3.1 that Phobos' BCBF frame and 3B frame are approximated to be aligned with each other.

propellant burned is just a tiny amount even for very long time spans.

The CR3BP-CA is a conservative dynamical system. It is characterized by a new effective potential, which is the one of the CR3BP of Eq.2.15 augmented by the linear potential of the constant acceleration vectorfield $\mathbf{f_{CA}}$ (where C_{CA} represents a free-defined constant).

$$\begin{cases} u_{eff,CR3BP-CA} = u_{eff,CR3BP} + u_{CA} \\ u_{CA}(\mathbf{q}) = |\mathbf{a_P}|\, \mathbf{q}^T \hat{\mathbf{n}}_{\mathbf{a_P}} + C_{CA} \end{cases} \tag{5.2}$$

5.2.2 Artificial Equilibrium Points around Phobos

The aim of hovering at a point is to counteract the natural acceleration of the CR3BP, sum of apparent and gravity acceleration of primary and secondary (see Eq.2.1).

$$\mathbf{a_P} = \mathbf{a_A} - \mathbf{a_G} \tag{5.3}$$

A hovering point can be viewed as an *artificial equilibrium point* (AEP) of the augmented potential of the CR3BP-CA of Eq.5.2, and it is computed from the related stationary condition [150, 151].

$$u_{eff,CR3BP-CA/\mathbf{q}} = \nabla u - \mathbf{P}\mathbf{q} + \mathbf{a_P} = \mathbf{0} \tag{5.4}$$

Thus, the addition of the thrust displaces the natural LPs, and their artificial dynamical substitutes in the CR3BP-CA are AEPs. To investigate the capability of the propulsion system, the direction of the thrust is not important, so the approach is to solve the underdetermined magnitude constraint of Eq.5.4.

$$\begin{cases} \|\nabla u - \mathbf{P}\mathbf{q}\| = \|\mathbf{a_P}\| \\ \hat{\mathbf{n}}_{\mathbf{a_P}}(\mathbf{q}) = \frac{\nabla u - \mathbf{P}\mathbf{q}}{\|\nabla u - \mathbf{P}\mathbf{q}\|} \end{cases} \tag{5.5}$$

This leads to compute a set of infinite AEPs, which are the iso-surfaces of the first of Eq.5.5 at the level $\|\mathbf{a_P}\|$ of the propulsion system. The direction required to push is found explicitly a posteriori with the second of Eq.5.5. The set of AEPs lies around each natural LP of the CR3BP, as it is displayed in Fig.5.1, that focuses on the L_1 planar region for a low thrust level. Fig.5.1 shows also the direction of the thrust required: note that to displace the LP along the y (and z) axis, the spacecraft should push coherently along the same direction, while the direction of the thrust is opposite from the displacement's direction of the LP along the x-axis. Fig.5.2 shows the pattern of AEPs for a 100 times upper thrust level. The set of AEPs is an ellipse with the major axis along the y direction, whereas for heavy propulsion systems the pattern is distorted to a bean/tadpole shape. For AEPs displaced in the out-of-plane direction, x-z evolution is similar to the x-y projection.

In summary, the procedure to find the hovering points corresponds to the computation of the iso-surfaces of the propulsive acceleration, which are called *equi-thrust*

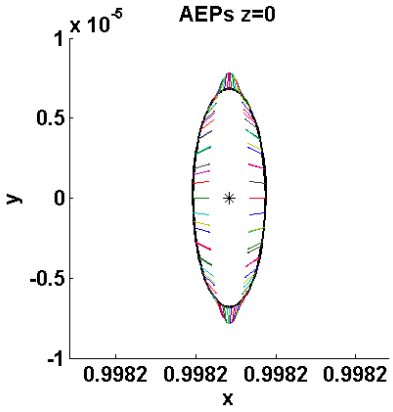

Figure 5.1: **AEPs around Phobos.** Iso-line for the propulsive acceleration magnitude of $10\mu m/s^2$ around L_1. The arrows show the direction of the thrust required. The semi-major axes of the 3D iso-surface are: $23m$-$64m$-$48m$.

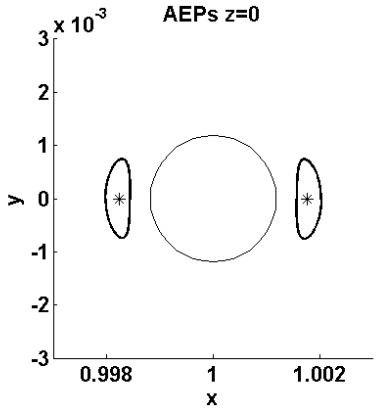

Figure 5.2: **AEPs around Phobos.** Iso-line for the propulsive acceleration magnitude of $1mm/s^2$ around L_{1-2}. Phobos mean sphere.

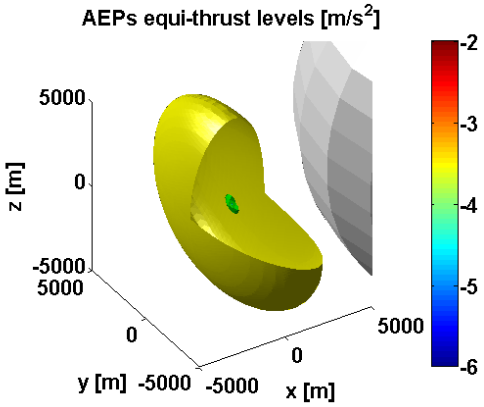

Figure 5.3: **AEPs around Phobos.** Iso-surfaces slices of propulsive acceleration magnitude (logarithmic scale) around L_1. Phobos mean sphere.

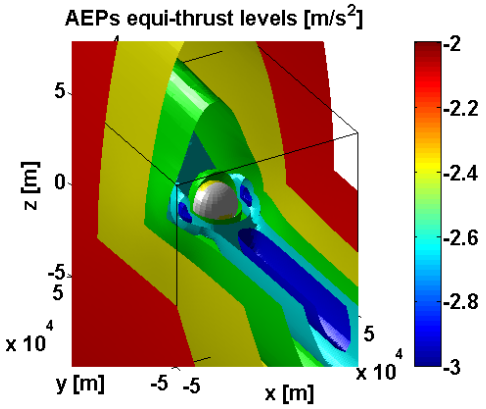

Figure 5.4: **AEPs around Phobos.** Iso-surfaces slices of propulsive acceleration magnitude (logarithmic scale). Phobos mean sphere.

surfaces. This is summarized in Fig.5.3-5.4 for the case of Phobos, which is represented with its mean spherical shape. As the magnitude of the propulsion grows, AEPs are farther displaced away from the five natural equilibrium points of the CR3BP. Despite their proximity to Phobos, the thrust level required to establish an AEP displacing L_{1-2} is very demanding: $1mm/s^2$ is required for $1km$ along x. Instead, displacing the equilateral LPs L_{4-5} is very economic and effective: in Fig.5.4, they are clearly visible the two isthmuses arriving close to Phobos along the y-axis, still with very small values of thrust ($1mm/s^2$). These two isthmuses finally connect with the tadpoles around L_{1-2}, establishing a ring-like equi-thrust surface around Phobos, that lies on the orbital plane. This ring will eventually enclose Phobos, thus establishing AEPs over polar regions requires high-thrust levels ($5mm/s^2$).

5.2.3 Stability of the AEPs

The next step in the hovering analysis is to look for the stability of the AEPs [150, 151]. The procedure is to analyze the linearized system of Eq.5.1 for each AEP, thus for every position around Phobos. This leads to infinite CR3BP-CA, where the constant $\mathbf{a_P}$ is different to satisfy Eq.5.3. But since this term is constant for each case, the Jacobian of the vectorfield $\mathbf{f_{CA}}$ is null, and the infinite number of linearized CR3BP-CA share the same structure of the linearized CR3BP of Eq.2.26. In particular, the 3D Hessian matrix $\mathbf{H}_u = u_{/\mathbf{qq}}$ of the gravity potential is the same of Eq.2.27. The only difference is that the latter must be now evaluated at the current AEP. The linearized stability analysis requires to compute the eigenvalues of the 6D linearized state-matrix of Eq.2.26, and for AEPs not aligned along the coordinate axes, the 3D Hessian matrix of the potential $\mathbf{H}_u(\mathbf{q}_{AEP})$ is no longer diagonal, but full and symmetrical.

The computation of the eigenvalues of the linearized CR3BP in all the position domain is undertaken first for the planar case, and then for the spatial case. Section 5.2.3.3 discusses the validity of these results in a nonlinear stability analysis.

5.2.3.1 Planar case

The analysis of the stability of the hovering positions is first conducted on the orbital plane of the Mars-Phobos system, which is where all the natural EPs lie. For the 6D $\times$ 6D Jacobian of Eq.2.26 with a general symmetrical Hessian $\mathbf{H}_u$, evaluated for a point on the orbital plane, the characteristics polynomial of the linearized system is the following,

$$\left(\lambda^2 + g(\mathbf{q})\right)\left(\lambda^4 + \left(2 - Tr\{\mathbf{H}_u\}_{x-y}\right)\lambda^2 + \det\left\{\mathbf{P} - \mathbf{H}_u\right\}_{x-y}\right) = \mathbf{0} \tag{5.6}$$

where the subscript x-y is used to indicate that only the 2×2 block of the x-y components of the related matrix must be taken into account, and $g(\mathbf{q})$ is the same of Eq.2.27. The first couple of eigenvalues $\lambda^2 = -g(\mathbf{q})$ is related to the linear stability along the out-of-plane direction for AEPs on the orbital plane, in the same way it holds for the natural LPs of Eq.2.29. This couple is stable for all the planar domain, and this is important to check because otherwise any further analysis would have been meaningless. The expression for the other two couples of eigenvalues is the following.

$$\lambda^2 = \left(\frac{1}{2}Tr\{\mathbf{H}_u\}_{x-y} - 1\right) \pm \sqrt{\left(\frac{1}{2}Tr\{\mathbf{H}_u\}_{x-y} - 1\right)^2 - \det\left\{\mathbf{P} - \mathbf{H}_u\right\}_{x-y}} < 0 \tag{5.7}$$

To assure that the two couples of planar eigenvalues are both imaginary, three constraints must be satisfied.

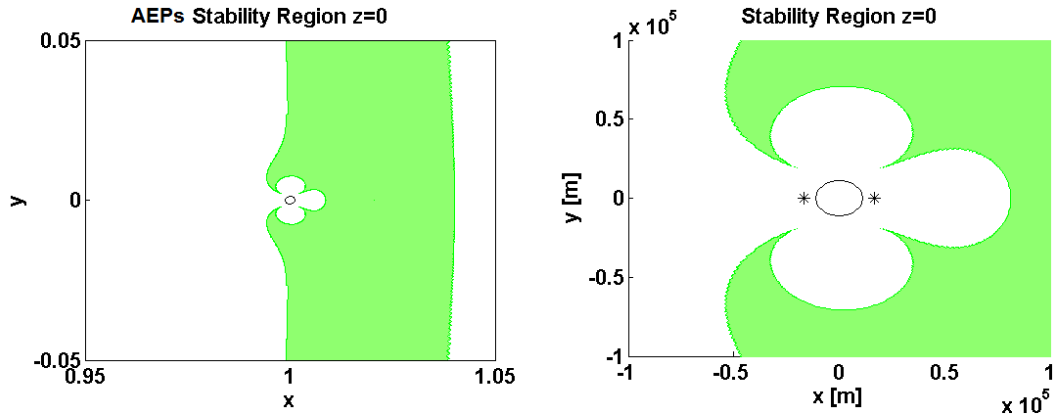

Figure 5.5: **AEPs around Phobos.** Stability region in the orbital plane of the Mars-Phobos CR3BP. L_{1-2} displayed. Phobos mean sphere.

$$\begin{cases} \frac{1}{2}Tr\{\mathbf{H}_u\}_{x-y} - 1 \leq 0 \Rightarrow 2 - g(\mathbf{q}) \geq 0 \\ \left(\frac{1}{2}Tr\{\mathbf{H}_u\}_{x-y} - 1\right)^2 - \det\{\mathbf{P} - \mathbf{H}_u\}_{x-y} \geq 0 \Rightarrow \left(\frac{1}{2}g(\mathbf{q}) - 1\right)^2 - \det\{\mathbf{P} - \mathbf{H}_u\}_{x-y} \geq 0 \\ \sqrt{\left(\frac{1}{2}Tr\{\mathbf{H}_u\}_{x-y} - 1\right)^2 - \det\{\mathbf{P} - \mathbf{H}_u\}_{x-y}} < \left|\frac{1}{2}Tr\{\mathbf{H}_u\}_{x-y} - 1\right| \Rightarrow \det\{\mathbf{P} - \mathbf{H}_u\}_{x-y} > 0 \end{cases} \tag{5.8}$$

By changing the variables from x and y to the couple of distance range from the two massive bodies of Eq.2.7, one obtains a set of three equations suitable to be computed with polar coordinates centered on the second massive body (see Eq.5.10).

$$\begin{cases} 2|\mathbf{r_1}|^3|\mathbf{r_2}|^3 - m_1|\mathbf{r_2}|^3 - m_2|\mathbf{r_1}|^3 \geq 0 \\ \frac{9}{4}{m_1}^2|\mathbf{r_2}|^6 + \frac{9}{4}{m_2}^2|\mathbf{r_1}|^6 - 2m_1|\mathbf{r_1}|^3|\mathbf{r_2}|^6 - 2m_2|\mathbf{r_1}|^6|\mathbf{r_2}|^3 + \frac{9}{2}m_1m_2|\mathbf{r_1}|^3|\mathbf{r_2}|^3 + \\ -9m_1m_2\,|\mathbf{r_1}|\,|\mathbf{r_2}|\,{y_e}^2 \geq 0 \\ |\mathbf{r_1}|^6|\mathbf{r_2}|^6 - 2{m_1}^2|\mathbf{r_2}|^6 - 2{m_2}^2|\mathbf{r_1}|^6 + m_1|\mathbf{r_1}|^3|\mathbf{r_2}|^6 + m_2|\mathbf{r_1}|^6|\mathbf{r_2}|^3 + \\ -4m_1m_2|\mathbf{r_1}|^3|\mathbf{r_2}|^3 + 9m_1m_2\,|\mathbf{r_1}|\,|\mathbf{r_2}|\,{y_e}^2 > 0 \end{cases} \tag{5.9}$$

$$\begin{cases} |\mathbf{r_1}|^2 = |\mathbf{r_2}|^2 + 2\,|\mathbf{r_2}|\cos\vartheta + 1 \\ y_e = |\mathbf{r_2}|\sin\vartheta \end{cases} \tag{5.10}$$

The stability region is the intersection of the regions bounded by these curves. The planar stability region in the orbital plane of the Mars-Phobos system is a thin corona extending along the Mars-Phobos orbital distance, that comprises the equilateral LPs and cuts off the three collinear LPs. In proximity of the secondary body, the inner stability region boundary is distorted to represent a three-leaf clover. The two curves representing the root and the central petal are related to the third equation of Eq.5.9, the curve of the flower head is related to the first equation, and the curves of the other two petals are related to the second equation. The graph is presented in Fig.5.5, and corresponds with the result obtained in a previous study of the AEPs in the Mars-Phobos CR3BP [60].

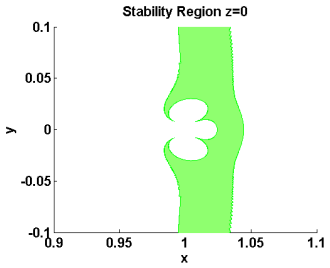

Figure 5.6: **Stability region of AEPs in the orbital plane of the CR3BP, for $\mu = 10^{-6}$.**

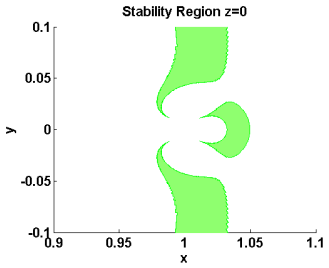

Figure 5.7: **Stability region of AEPs in the orbital plane of the Sun-Earth system.**

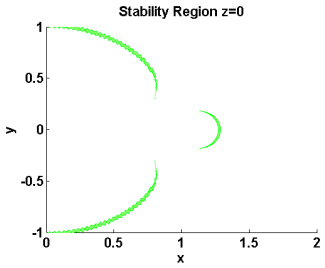

Figure 5.8: **Stability region of AEPs in the orbital plane of the Earth-Moon system.**

5.2.3.1.1 Applications

If we compare the stability region with the equi-thrust curves of Fig.5.4 on the orbital plane, it can be seen that the planar stability boundary is not too far from Phobos, starting from $25km$ (in the petal-head connection border, requiring $1.9mm/s^2$), $71km$ (on the tip of the top and down leaves, $0.4mm/s^2$) or $81km$ (along the x-axis, $12mm/s^2$) and arriving to $400km$ (along the x-axis, where the outer boundary lies).

Therefore six attractive positions for medium distance observation of Phobos are identified: four minimum-distance AEPs, and two minimum-control AEPs. It is remarkable that these positions are all obtained by the displacement of the equilateral LPs, and are affordable by current light electric thrusters. Farther trailing/leading orbits around Mars provide attractive cheap, stable, in-light fixed positions with respect to Phobos at long distances from the moon. All the AEPs available with a low-thrust level are not stable near the collinear LPs, and AEPs closer to Phobos, used to maximize the shadowing time and the sky occultation ratio, or perform short dedicated operations, are feasible only with heavy or multiple thrusters, and must take into consideration in the model also the complete inhomogeneous gravity of Phobos: this increases the precision, frequency and computational load of the GNC subsystem.

5.2.3.1.2 Relation to other CR3BPs

As a reference, Fig.5.6-5.8 show also the planar stability region evolution for increasing value of the mass parameter. The first graph shows the region for the value $\mu = 10^{-6}$, which is significant because for higher values the region of stability loses the three-leaf clover's pattern. The following graphs show the orbital plane's stability region for two important cases: the Sun-Earth system and the Earth-Moon system. In the first case, the top and down leaves collapse to the outer curve and the stability region is now made by three detached domains[2]. In the second case, the detachment is far more evident. These are the same results obtained in [63].

[2]This refers to the space in proximity of the second body, whereas globally the domains are now two: a big C-shaped opened thin foil, and a smaller one rotated on the opposite side.

5.2.3.2 3D case

In this section the procedure to derive the stability region of the AEPs in any CR3BP is extended to the spatial case, extending the analysis of the planar case undertaken in [63].

The 3D Hessian matrix of the potential $\mathbf{H}_u$ is now fully filled in all its components. However, due to the fact that it is symmetric, and the resulting 6D linear state-matrix still maintains a sparse structure, it is possible to derive a condensed analytical expression of the three couples of opposite eigenvalues in terms of the three scalar invariants of the Hessian matrix I_1, I_2, and I_3. It is worth to note that the procedure presented in this section could be applied to derive the stability region of any mechanical system that describes a relative dynamics in an uniformly rotating frame, and driven by position-dependent forces. The characteristic polynomial of the 6D linear state-matrix is the following.

$$\lambda^6 + (-I_1 + 2)\,\lambda^4 + (I_2 + I_1 + 1 - H_{u3,3})\,\lambda^2 + \left(-I_3 - I_2 + H_{u1,1}H_{u2,2} - H_{u1,2}^2 - H_{u3,3}\right) = 0 \tag{5.11}$$

One introduces some coefficients to simplify the notation. They are derived from the scalar invariants: A, B and D are strictly real scalars by definition, instead C could be complex.

$$\begin{cases} A = \frac{I_1 - 2}{3} \\ B = \frac{I_2 + I_1 + 1 - H_{u3,3}}{3} - A^2 \\ C = \sqrt[3]{\sqrt[2]{D^2 + B^3} + D} \\ D = \frac{I_3 + I_2 - H_{u1,1}H_{u2,2} + H_{u1,2}^2 + H_{u3,3}}{2} - 3\frac{AB}{2} - \frac{A^3}{2} = \frac{C^6 - B^3}{2C^3} \end{cases} \tag{5.12}$$

The characteristic polynomial is now expressed in the following way.

$$\lambda^6 - 3A\lambda^4 + 3\left(B + A^2\right)\lambda^2 - 2\left(D + 3\frac{AB}{2} + \frac{A^3}{2}\right) = 0 \tag{5.13}$$

Mathematical manipulations make possible to eventually simplify the above expression. The new form of the characteristic polynomial is constituted by two factors of second and fourth degree, and the latter shows again a bi-quadratic structure.

$$\left(\lambda^2 - \left(A - \frac{B}{C} + C\right)\right)\left(\lambda^4 - 2\left(A + \frac{B}{2C} - \frac{C}{2}\right)\lambda^2 + \left(A^2 + \frac{B^2}{C^2} + C^2 + \frac{AB}{C} - AC + B\right)\right) = 0 \tag{5.14}$$

This implies that the expression of the eigenvalues of the CR3BP-CA is analytically defined.

$$\lambda = \begin{cases} \pm\sqrt{A - \frac{B}{C} + C} \\ \pm\sqrt{\left(A + \frac{B}{2C} - \frac{C}{2}\right) - \sqrt{\left(A + \frac{B}{2C} - \frac{C}{2}\right)^2 - \left(A^2 + \frac{B^2}{C^2} + C^2 + \frac{AB}{C} - AC + B\right)}} \\ \pm\sqrt{\left(A + \frac{B}{2C} - \frac{C}{2}\right) + \sqrt{\left(A + \frac{B}{2C} - \frac{C}{2}\right)^2 - \left(A^2 + \frac{B^2}{C^2} + C^2 + \frac{AB}{C} - AC + B\right)}} \end{cases} \tag{5.15}$$

The inner square root of the last two couples of eigenvalues of Eq.5.15 can be further simplified, giving an imaginary term to the expressions.

$$\lambda = \begin{cases} \pm\sqrt{A - \frac{B}{C} + C} \\ \pm\sqrt{\left(A + \frac{B}{2C} - \frac{C}{2}\right) - \frac{\sqrt{3}}{2}\left(\frac{B}{C} + C\right)i} \\ \pm\sqrt{\left(A + \frac{B}{2C} - \frac{C}{2}\right) + \frac{\sqrt{3}}{2}\left(\frac{B}{C} + C\right)i} \end{cases} \tag{5.16}$$

Recall that A, B, and D are strictly real scalars. The linear Lyapunov marginal stability for the AEP requires all the eigenvalues to be purely imaginary, which is their squares to be real and negative. From Eq.5.16, C MUST be a complex number, with real and imaginary part both not null, to assure that the three squares are real and satisfy this first necessary condition for stability. With the notation used to represent phasors, Eq.5.16 could be rewritten in a convenient symmetrical form in the complex field, as presented in Eq.5.17.

$$\lambda = \begin{cases} \pm\sqrt{A + \frac{B}{C}e^{\pi i} + Ce^{0i}} \\ \pm\sqrt{A + \frac{B}{C}e^{-\frac{1}{3}\pi i} + Ce^{-\frac{2}{3}\pi i}} \\ \pm\sqrt{A + \frac{B}{C}e^{\frac{1}{3}\pi i} + Ce^{\frac{2}{3}\pi i}} \end{cases} \tag{5.17}$$

Using the phasor's notation also for C, which is $C = |C|e^{\theta_C}$, it is straightforward to impose the first necessary condition for stability, which is that each of the three arguments' imaginary parts shall be null. This happens for different pairs of opposite phases for each eigenvalue, but also for one shared and simple relationship between B and C. This is the necessary condition for real eigenvalues.

$$\lambda^2 \in \mathbb{R} \Rightarrow \begin{cases} \theta_C = 0 \vee \theta_C = \pi \vee B = -|C|^2 \\ \theta_C = \frac{2}{3}\pi \vee \theta_C = -\frac{1}{3}\pi \vee B = -|C|^2 \\ \theta_C = -\frac{2}{3}\pi \vee \theta_C = \frac{1}{3}\pi \vee B = -|C|^2 \end{cases} \tag{5.18}$$

Using this necessary condition, Eq.5.17 could be rewritten in a compact way where the six solutions derive from the same definitions of C as a cubic root of Eq.5.12.

$$\lambda = \pm\sqrt{A + 2\,|C|\cos\left(\theta_C + \theta\right)},\ \theta = 0, \pm 2\pi/3 \tag{5.19}$$

The stability constraint consists of one simple inequality, which considers the algebraic root of C with maximum real part (there is at least one that is strictly positive-definite). The 3D stability region of the hovering points in the CR3BP is described by the following two constraints.

$$\begin{cases} B = -|C|^2 \\ A + 2\text{maxRe}\left\{C\right\} < 0 \end{cases} \tag{5.20}$$

For the Mars-Phobos CR3BP, the 3D stability region of the hovering points in Fig.5.9 is made by three realms: one central ring, and two symmetric halves of hyperbolic coronas placed at very high out-of-plane altitudes. More interesting, as presented in Fig.5.10-5.11, the inner surface of the ring is distorted in proximity to the second massive body to a kind of double nose, leaving outside the body's SOI. The footprint on the orbital plane of these surfaces corresponds to the boundaries of the planar stability region computed in section 5.2.3.1.

5.2.3.2.1 Hill's approximation of the CR3BP

The 3D stability analysis of the hovering is undertaken also with the Hill's approximation of the CR3BP introduced in section 2.3.6. The system of equations for the planar stability is presented in Eq.5.21, while for the 3D case the procedure requires the Hessian in Eq.5.22.

$$\begin{cases} |\bar{\mathbf{q}}|^3 - 3 \geq 0 \\ \frac{1}{4}|\bar{\mathbf{q}}|^6 + \frac{15}{2}|\bar{\mathbf{q}}|^3 - 27\,|\bar{\mathbf{q}}|\,\bar{y}^2 + \frac{81}{4} \geq 0 \\ -9|\bar{\mathbf{q}}|^3 + 27\,|\bar{\mathbf{q}}|\,\bar{y}^2 - 18 > 0 \end{cases} \tag{5.21}$$

$$\mathbf{H}_u(\bar{\mathbf{q}}) = -\mathbf{A_{H1}} - \frac{3}{\|\bar{\mathbf{q}}\|^3}\mathbf{I_3} + \frac{9}{\|\bar{\mathbf{q}}\|^5}\bar{\mathbf{q}}\bar{\mathbf{q}}^T \tag{5.22}$$

Fig.5.12-5.13 highlight the great difference in the stability region, which shows that the Hill's approximation is definitely not worthy for the analysis of the medium-large distance hovering points.

5.2.3.2.2 Applications

The 3D stability analysis probed that it is possible to have also stable AEPs above the poles of Phobos. However, their distances are much greater then the ones of the planar case, ranging from $250km$ to $1400km$. Therefore, considering also the high-thrust required to hover at these positions found in section 5.2.2, no significant positions for applications to mission segments around Phobos are identified. Thus, the major information for the stability of the hovering around Phobos is provided by the planar stability analysis of section 5.2.3.1.

5.2.3.2.3 Relation to other CR3BPs

As a reference, the 3D stability region in proximity of the secondary's realm is computed

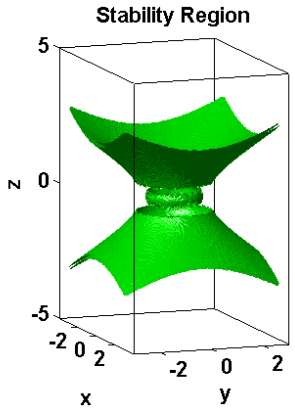

Figure 5.9: **AEPs around Phobos.** 3D stability region in the Mars-Phobos CR3BP. Global view of the boundaries.

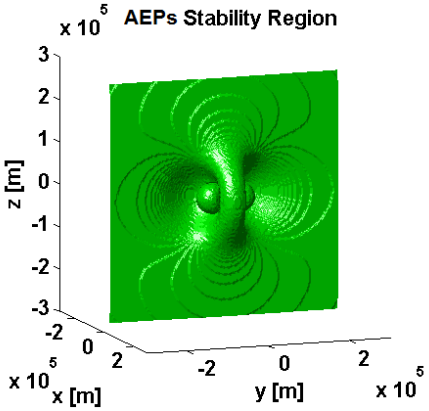

Figure 5.10: **AEPs around Phobos.** 3D stability region in the Mars-Phobos CR3BP. Inner boundary near Phobos.

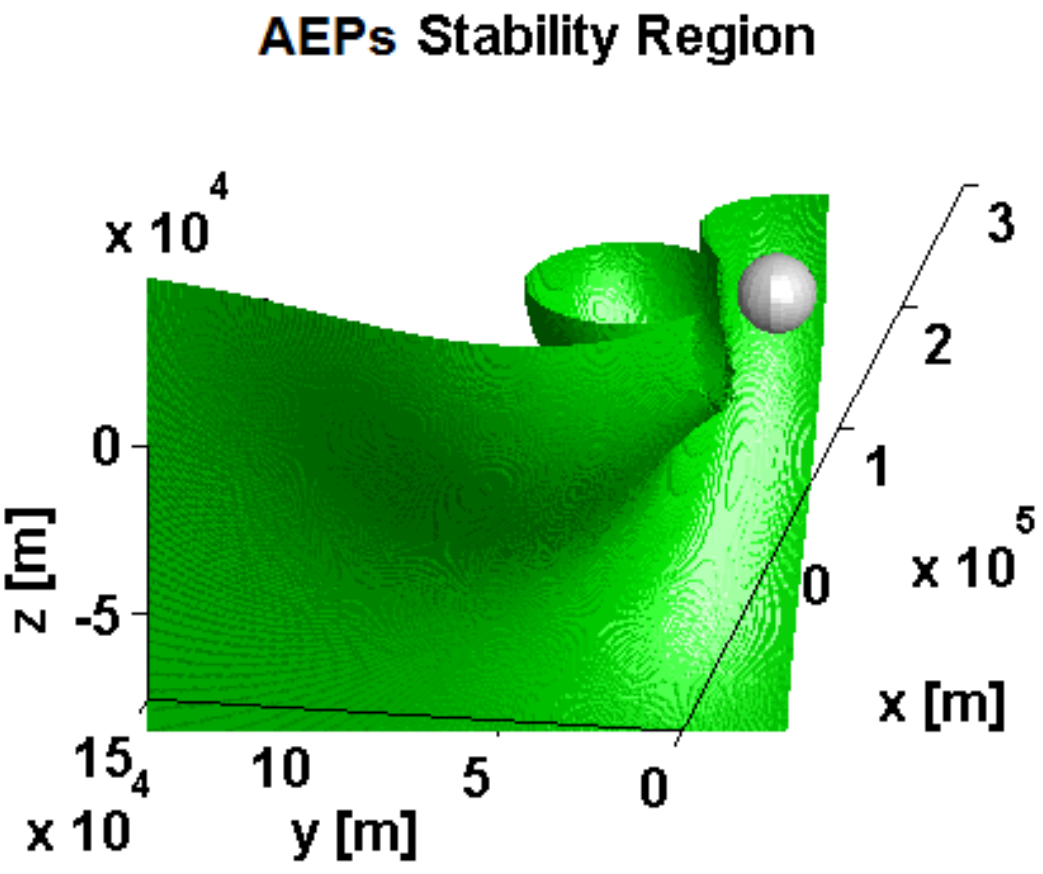

Figure 5.11: **AEPs around Phobos.** 3D stability region in the Mars-Phobos CR3BP. One half of the lower hemisphere of the inner boundary near Phobos, represented with its mean sphere.

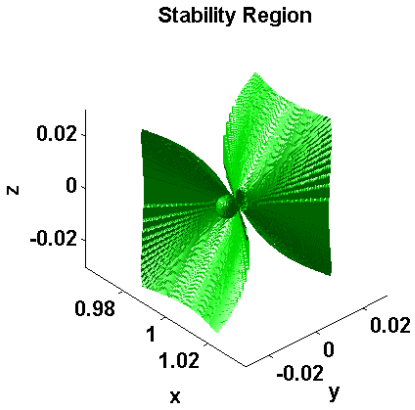

Figure 5.12: **AEPs around Phobos.** 3D Stability region in the Mars-Phobos Hill's approximation of the CR3BP.

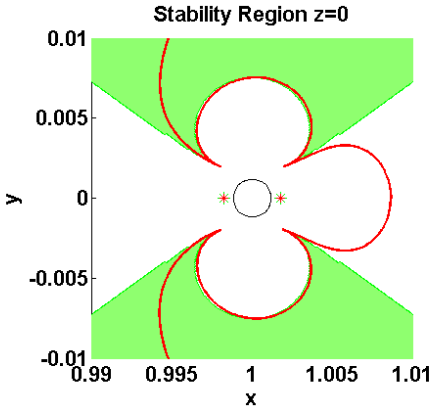

Figure 5.13: **AEPs around Phobos.** Stability region in the orbital plane of the Mars-Phobos Hill's approximation of the CR3BP. Red line represents the boundary of the planar stability region of the CR3BP. L_{1-2} displayed. Phobos mean sphere.

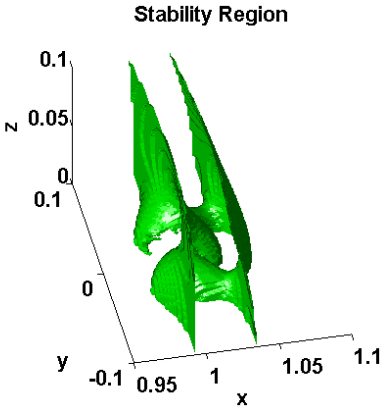

Figure 5.14: **Stability region of AEPs of the Sun-Earth system.**

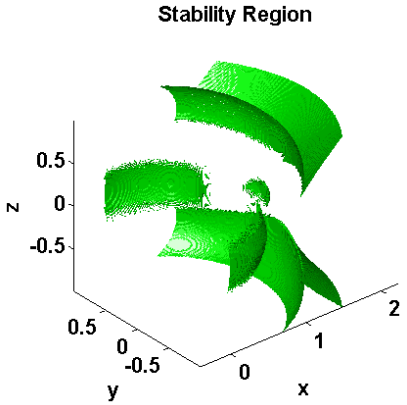

Figure 5.15: **Stability region of AEPs of the Earth-Moon system.**

also for the cases of the Sun-Earth and Earth-Moon systems. While for the planar case the topology of the two systems is basically the same as found in section 5.2.3.1.2, their 3D shapes show a basic difference. For low values of the mass parameter (Sun-Earth case), the collapse of the outer surface towards the inner one is not complete, which is the central ring is still one-piece as shown in Fig.5.14. It was only its projection on the orbital plane that is detached as seen in Fig.5.7. At high values of μ (Earth-Moon case), the detachment is fully complete also in the 3D space as shown in Fig.5.15, and this means that no stable AEPs exist perpendicularly to the Moon.

5.2.3.3 Nonlinear Analysis

The procedure presented in sections 5.2.3.1-5.2.3.2 provides the linearized stability region, which for the case of marginal stability encountered by the AEPs does not assure stability in the original CR3BP-CA.

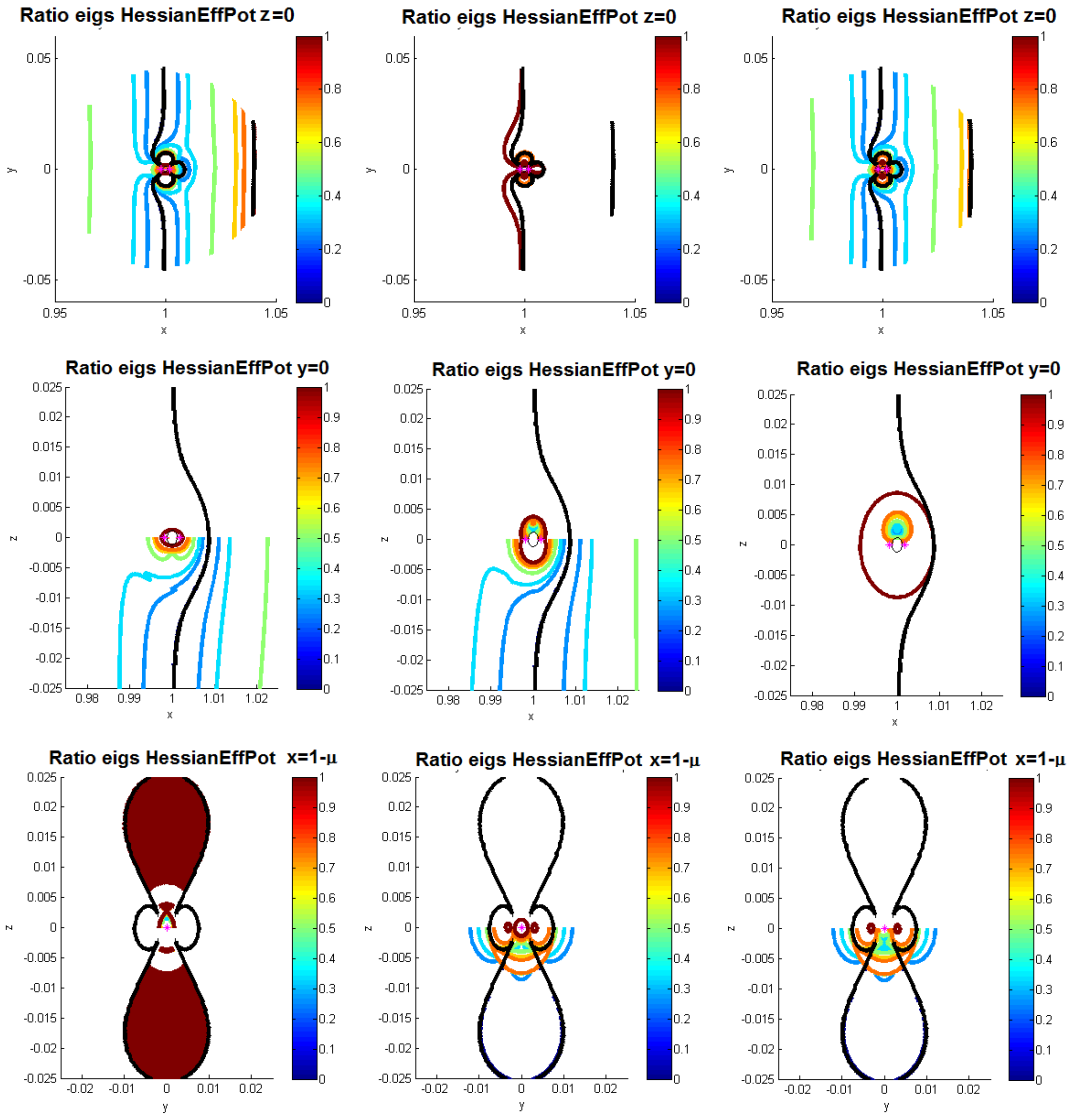

Figure 5.16: **AEPs around Phobos.** NL stability region of the Mars-Phobos CR3BP. Projections on the coordinate planes, of the resonance surfaces that identify NL instability. For the x-z and y-z projections, due to the symmetry, each half-plane shows the contours for one of the two reciprocal ratios $N : M$ and $M : N$. Linear stability region's boundaries plotted in black line.

The case of marginally stable EPs in nonlinear systems has already been studied in the past [152, 153, 154], and requires to extend the analysis to higher order terms, and to apply the two conditions of the **Arnold's stability theorem (KAM theory)**: the non-resonance condition and the reversibility condition. This has been done to demonstrate the nonlinear behavior around the stable equilateral EPs of the CR3BP [152, 153, 154]. Recall from section 2.3.5.1 that their position in the normalized CR3BP is fixed, therefore this analysis was conducted to probe their nonlinear stability through different values of μ. The results obtained show that the linearized stability describes also the nonlinear behavior apart from single cases of μ that do not satisfy the planar

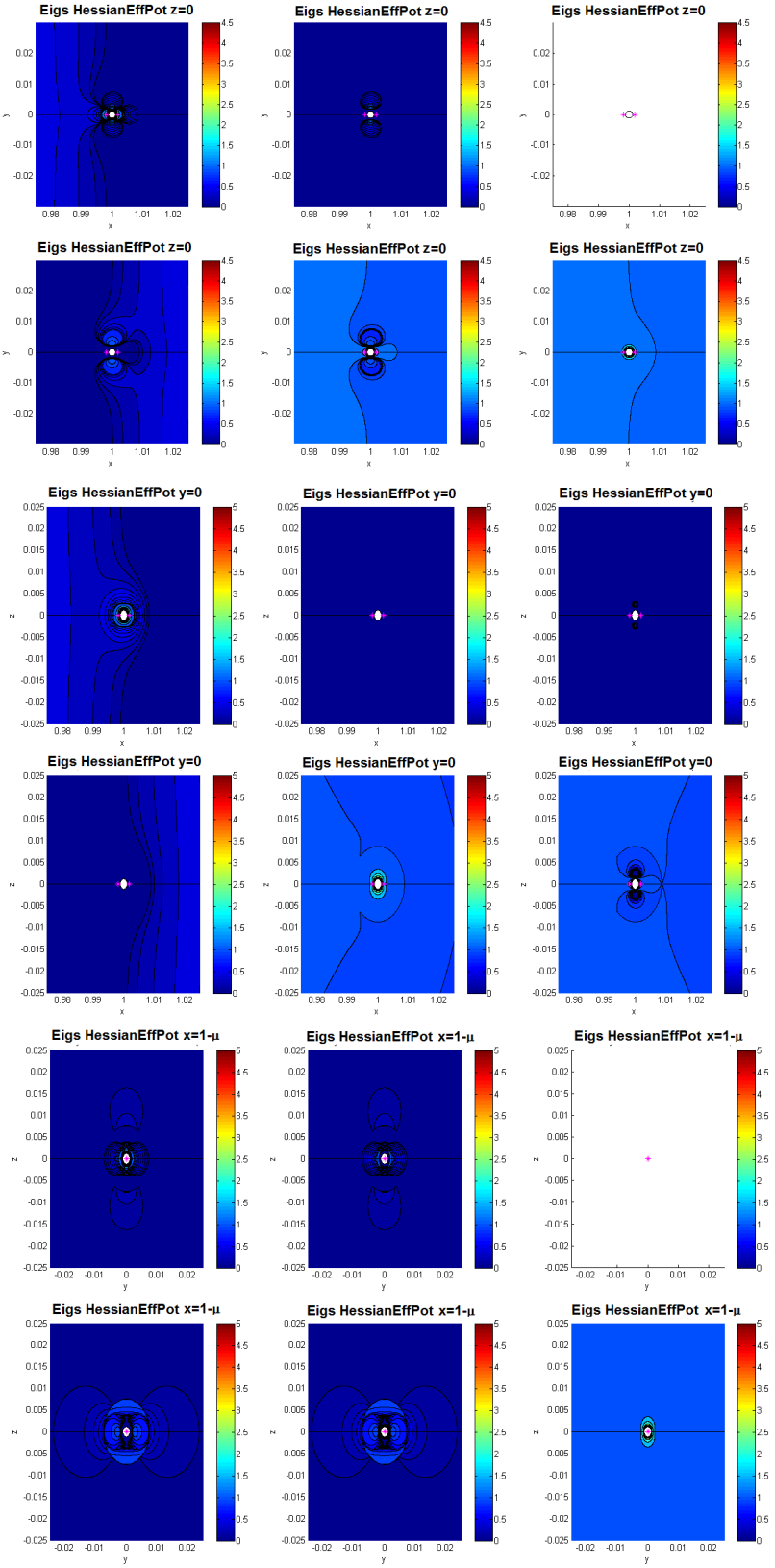

Figure 5.17: **AEPs around Phobos.** Real and imaginary parts of the eigenvalues of the Mars-Phobos CR3BP-CA on the coordinate planes.

non-resonance condition. Thus, these cases constitute a zero-measure set (single points in the 1D set of possible values of μ).

For the case of the CR3BP-CA and the related AEPs, the scenario changes because μ is fixed, and the EPs vary (2D or 3D), but the approach remains the same and consists of the evaluation of the two constraints mentioned before. The first is to check the resonance conditions between the eigenvalues of the linearized system at the AEP of Eq.5.1 [63]. The second is to expand the Hamiltonian of the system to higher order terms (up to the 4th) to check the reversibility condition, by using a suitable canonical set of variables, which is the Birkhhoff normal form [63, 150]. This procedure is presented in [63], but the outcomes are only inferred to effectively behave in the same way of the aforementioned classical case of L_{4-5} in the μ-dependent CR3BP. The result is that all the linearly-derived marginally stable AEPs are also nonlinear stable apart from those lying on two families of curves (in the planar case) or surfaces (in the 3D case) where the planar couple of eigenvalues are in 2:1 and 3:1 resonance. In particular, in [63] such results are only inferred by comparison with the equilateral EPs and not tested, while the 1:1 resonance and the resonances 4:1, 5:1, and 3:2, which are related also to the vertical dynamics, and the reversibility condition, are not checked at all.

However the summarizing point is that the AEPs of the linearized stability region are also stable in the full nonlinear dynamics apart from singular cases that lie on co-1D domains of the stability region, where resonance effects are present.

Fig.5.16 presents the families of curves that satisfy the resonance conditions of the eigenvalues of the AEPs[3] on the orbital plane of the Mars-Phobos system. They can be compared with the curves displayed for a similar case of CR3BP-CA in [63], which is for $\mu = 1.1 \cdot 10^{-9}$ of the Jupiter-Amalthea system. Fig.5.16 extends these curves also to their homologue surfaces' projections on the other 3D coordinate planes. The analysis of the planar case could be undertaken straightforward because the dynamics are decoupled. It is interesting to note in Fig.5.17, how the resonance ratio of the two planar eigenvalues (stable/unstable) moves along three directions from 0 to 1:1, from the right leaf to the outer boundary, and from the inner boundary to the top/down leaves. This is because the unstable eigenvalue correspondingly goes from 1 to purely imaginary[4].

The stability analysis undertaken so far has been conducted with the classical analytical approach. However, a straightforward implementation is to test the linearized stability region of the AEPs in the Mars-Phobos system, by running a set of simulations in the real nonlinear system. The approach is the same used in section 4.1.3.2.2 for LPOs, which is to derive the propagation ratio of a displacement error in the initial condition after a fixed propagation time. Each hovering point in the associated CR3BP-CA is perturbed in position by $1m$ along all the directions. If the resulting

[3]Only the part of the curves in the linearized stable regions are to be considered.

[4]The unstable region inside the top/down leaves is characterized by a planar manifold made by a couple of spirals.

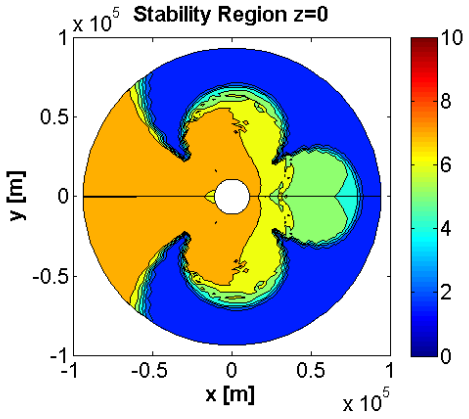

Figure 5.18: **AEPs around Phobos.** NL simulations of AEPs on the orbital plane of the Mars-Phobos CR3BP. Max displacement (logarithmic scale) after 10 orbital periods with initial position error of $1m$. Phobos mean sphere.

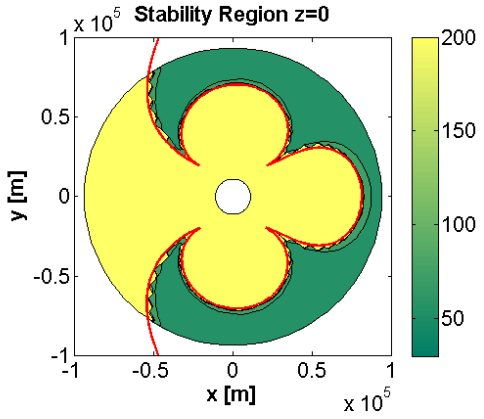

Figure 5.19: **AEPs around Phobos.** NL simulations of AEPs on the orbital plane of the Mars-Phobos CR3BP. Max displacement after 10 orbital periods with initial position error of $1m$. Linear stability region's boundary is reported in red line. Phobos mean sphere.

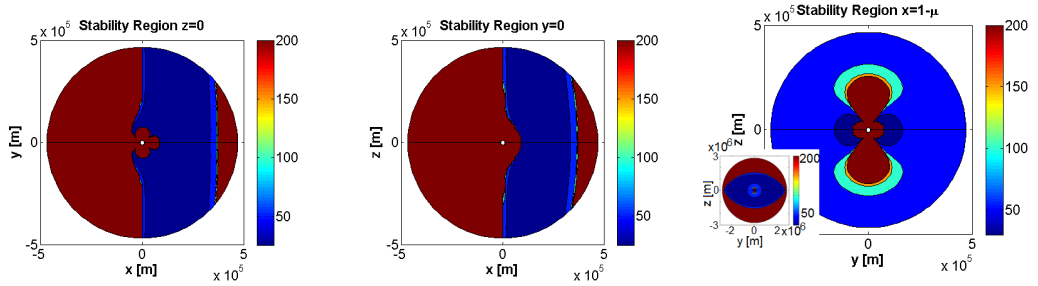

Figure 5.20: **AEPs around Phobos.** NL simulations of AEPs of the Mars-Phobos CR3BP. Max displacement after 10 orbital periods with initial position error of $1m$. Phobos mean sphere.

motion, for every case, is bounded around the reference position, the AEP is stable, and the maximum ratio gives the normalized amplitude of this oscillation. This is a physical measure to quantify the nonlinear stability, in contrast to the linearized case where the stability region is plotted from the satisfaction of disequalities.

Unstable AEPs obviously diverge immediately, so their is no stable boundary, and the final value of the simulation is meaningless. Stable AEPs oscillate periodically, and that has been demonstrated for a long simulation time. After this behavior is proved, a shorter final time has been taken to run the set of all simulations, which is for 10 orbital periods.

Results are presented in Fig.5.18-5.20 for the planar and 3D cases. The divergence ratio at the boundary of the linear stability region is roughly of 200. Here the gradient is sharp, because inside the boundaries the solution is periodic, outside is divergent. The amplitude ratio of stable hovering points, close to the clover's boundaries, is about 30.

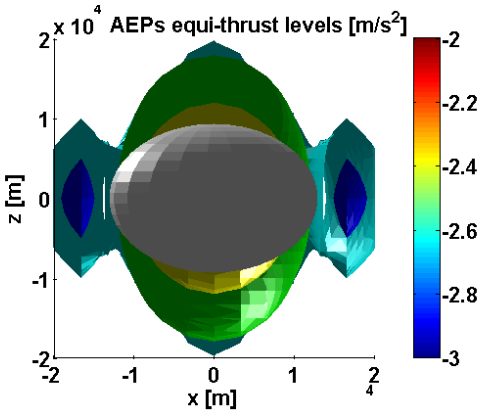

Figure 5.21: **AEPs around Phobos.** Equi-thrust surfaces for the CR3BP (logarithmic scale). x-z projection. Phobos mean ellipsoid.

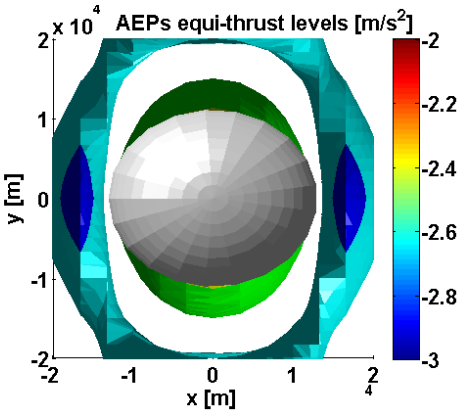

Figure 5.22: **AEPs around Phobos.** Equi-thrust surfaces for the CR3BP (logarithmic scale). x-y projection. Phobos mean ellipsoid.

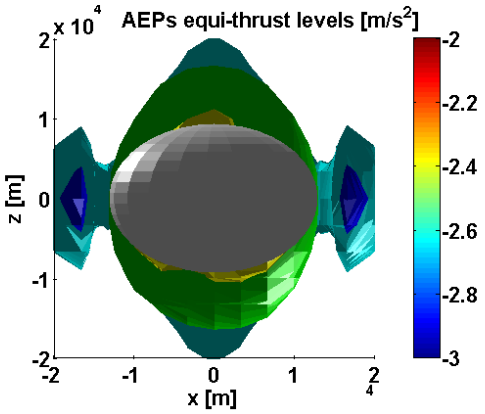

Figure 5.23: **AEPs around Phobos.** Equi-thrust surfaces for the CR3BP-GH (logarithmic scale). x-z projection. Phobos mean ellipsoid.

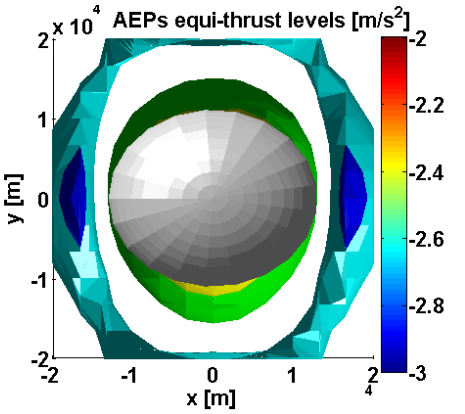

Figure 5.24: **AEPs around Phobos.** Equi-thrust surfaces for the CR3BP-GH (logarithmic scale). x-y projection. Phobos mean ellipsoid.

5.2.4 AEPs in More Accurate Models of the Mars-Phobos Orbital Dynamics

The computation of body-fixed hovering points is a trivial task since it requires only to compute the level of thrust required to compensate all the apparent and physical forces that constitute the relative acceleration in Eq.2.1. The analysis has been undertaken in the Mars-Phobos CR3BP. The consideration of a more accurate description of the dynamics depends from the distance from Phobos, which is now no longer limited to the tiny SOI. Thus, the selection of the additional forces to be considered requires the perusal of Fig.2.12-2.13. However, due to the fact that all the forces must be compensated, the additional perturbations do not change the results significantly.

In particular, the most destabilizing effect is Mars-J_2 at great distances from Phobos, which needs to be appropriately counteracted. The greatest perturbation is the

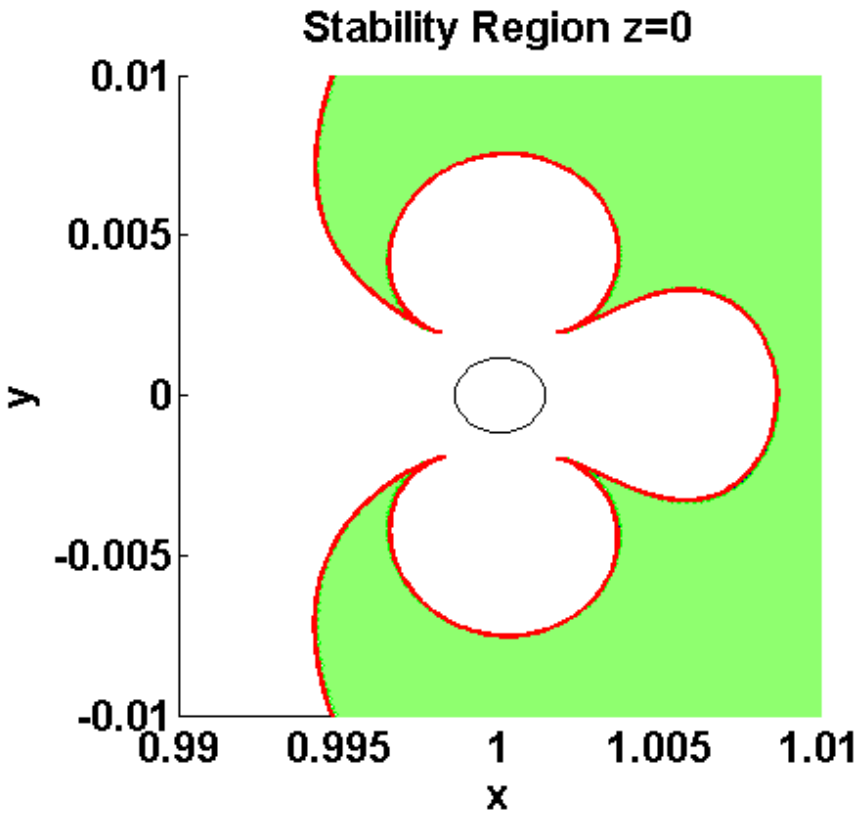

Figure 5.25: **AEPs around Phobos.** Stability region on the orbital plane of the Mars-Phobos CR3BP-GH. Red line represents the boundary of the CR3BP. Phobos mean ellipsoid.

eccentricity, already outside of the SOI. In this case, direct compensation[5] is inappropriate, because expensive, and a trailing/leading configuration can be achieved with an appropriate synchronous Keplerian orbit around Mars: the resulting relative motion is an oscillation and not a body-fixed hovering point. However, at such distances the field of view of Phobos would not be significantly influenced by this motion.

For close distances, the relevant perturbation is given by the GHs of Phobos. Their effect is negligible on the stability of the AEPs, because the boundaries of the stability region lie far from Phobos, as visible in Fig.5.25. However, the highly-inhomogeneous gravity field of Phobos is necessary to be compensated for close-range hovering. The equi-thrust surface in the Mars-Phobos CR3BP-GH of Fig.5.23-5.24 show that, with respect to the CR3BP of Fig.5.21-5.22, savings seem to occur hovering in the Southern Hemisphere, and in proximity of the two additional internal EPs of the Northern Hemisphere (see section 3.3.6.2).

[5]When using the classical form of the ER3BP in Eq.3.45, the addition of a constant acceleration in the pulsating frame would physically become a variable acceleration profile in the physical-units frame, by scaling of a term $l(\nu)\omega^2 = |\mathbf{a_G}(\nu)|(1 + ecos\nu)$, where $\mathbf{a_G}$ is the instantaneous gravity between the two massive bodies. On the contrary, a physically constant acceleration is scaled by the inverse of the previous term in the classical ER3BP. Finally, if the aim would be to reproduce the same effect of a constant acceleration in the CR3BP, the physical acceleration shall have a profile proportional to $|\mathbf{a_G}(\nu)|$.

5.3 Vertical-Displaced Circular Orbits around Phobos

The AEPs computed in section 5.2 are a fixed solution in the rotating frame of the CR3BP. It is possible to further generalize the concept, which is to model the dynamics in a generic uniformly rotating frame, and find the related AEPs. In our case, this new rotating frame is called R, and is centered on Phobos. The related constant angular velocity of the frame $\boldsymbol{\omega}_R$ is defined with respect to Phobos' BCBF frame. Hence, in the usual 3B and Phobos' Hill's frame, this artificial solution results in a circular orbit, with chosen period and height, around a reference axis of Phobos.

This section focuses on a particular set of these AEPs, where the reference axis of the R frame is Phobos' vertical axis (z-axis of 3B, Hill's, and BCBF frame). The resulting trajectory is a Vertical-Displaced Circular Orbit (VDCO), as represented in Fig.5.26. Furthermore, ω_R is fixed to be opposite to the Phobos' revolution n. The reason for such a choice is to realize an inertial-fixed hovering, in a time frame[6] that a mission segment around Phobos could make use of continuous thrust. An orbit that revolves around Phobos provides the spacecraft with an extended ground-track for observation of its surface at different longitudes. Furthermore, recall from Fig.2.26 that the orbit of the Sun around Phobos is a retrograde VDCO with the period of Phobos' revolution too, where the height of the orbit varies through the Martian seasons in a range of declinations $[-\theta_M, \theta_M]$. Therefore, an inertial-hovering realizes a Sun-Synchronous (SS) seasonal orbit, whose β-angle performance (expressing the mean time in light) is set by the choice of the initial phase along the VDCO with respect to the Sun. In particular, for continuous shadowing ($\beta = 0$) the spacecraft tracks the position of the anti-Sun (whose declination and phase are opposite to the ones of the Sun) moving clockwise around Phobos: as introduced in section 2.5, such a configuration would allow the spacecraft to be shielded from the directional part of the SEPEs[7].

5.3.1 VDCOs in the Phobos R2BP

The approach followed in this section is to start from the 2B dynamics around Phobos, described not in the usual inertial frame of the central body like in the Keplerian problem, but in the rotating frame R. These dynamics are named R2BP-R.

5.3.1.1 Equations of Motion

The equations of motion of the generic R2BP-R, for a generic rotation's pole O_R and time-variant angular velocity $\boldsymbol{\omega}_R$, with respect to the reference frame, named I, centered

[6] It it not an exact inertial-hovering, because the center of Phobos' revolution, which is the Mars-Phobos' barycenter, rotates around the Sun too. However, due to the large difference between the two characteristic times, the motion defined in such sense, for the time span of tens of Phobos' revolutions, is with good approximation inertially-fixed.

[7] For this objective, the spacecraft would need not to be exactly in phase with the Sun, but to take into account the travel time of the cosmic ray from the Sun to Mars, as well as the dynamics of Heliosphere, whose lines of field are not radial.

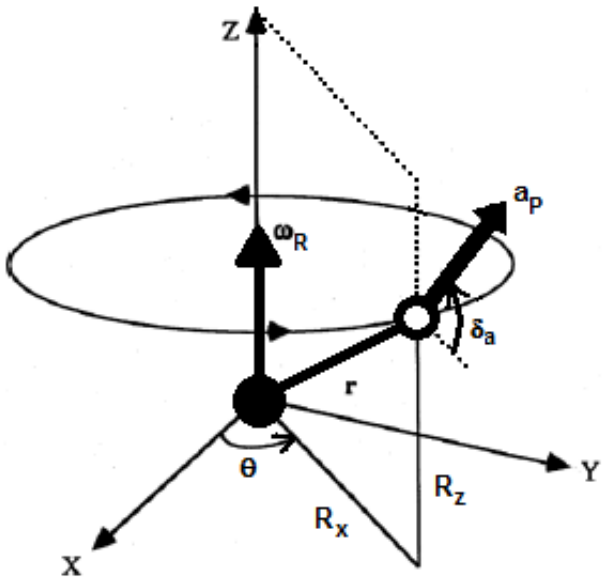

Figure 5.26: **Vertical-Displaced Circular Orbits.** Reference model for the description of the dynamics.

on the central body, are expressed in Eq.5.23. The direction of $\boldsymbol{\omega}_R$ is given by its spherical coordinates α_R, ϕ_R, and the initial phase of the spacecraft in the R frame is $\theta_{R,0}$.

$$\begin{cases} \mathbf{a} = -\frac{GM}{\|\mathbf{q}+\mathbf{A}_R^I\mathbf{q}_O\|^3}\left(\mathbf{q}+\mathbf{A}_R^I\mathbf{q}_O\right) - \boldsymbol{\omega}_R \wedge \boldsymbol{\omega}_R \wedge \mathbf{q} - \dot{\boldsymbol{\omega}}_R \wedge \mathbf{q} - 2\boldsymbol{\omega}_R \wedge \dot{\mathbf{q}} \\ \boldsymbol{\omega}_R = \omega_R \begin{bmatrix} \cos\alpha_R \cos\phi_R \\ \sin\alpha_R \cos\phi_R \\ \sin\phi_R \end{bmatrix} \\ \mathbf{A}_R^I = \mathbf{A}_3(\int_0^t \omega_R dt + \theta_{R,0})\mathbf{A}_2(\frac{\pi}{2} - \phi_R)\mathbf{A}_3(\alpha_R) \end{cases} \tag{5.23}$$

In particular, any offset of the rotation's pole position $\mathbf{q}_O$ perpendicular to the angular velocity produces a time-variant term. This section focuses on SS-VDCOs, therefore the above dynamics is simplified with the choices discussed in section 5.3, and an example is represented in Fig.5.26. This yields the ODEs of the R2BP-R associated to a general VDCO, where $\mathbf{W}$ and $\mathbf{P}$ are defined like in section 2.3.3 but now with respect to the constant $\boldsymbol{\omega}_R$. For a SS-VDCO, $\omega_R = -n = -\sqrt{\frac{GM_{1-2}}{a_2^3}}$, and $\mathbf{W}$ and $\mathbf{P}$ are opposite to the ones of the CR3BP.

$$\begin{cases} \mathbf{x} = \begin{bmatrix} \mathbf{q} \\ \dot{\mathbf{q}} \end{bmatrix}, \dot{\mathbf{x}} = \mathbf{A}\mathbf{x} + \begin{bmatrix} \mathbf{0_{3x1}} \\ -\frac{GM}{\|\mathbf{q}\|^3}\mathbf{q} \end{bmatrix}, \mathbf{A} = \begin{bmatrix} \mathbf{0_3} & \mathbf{I_3} \\ -\mathbf{P}_R & -2\mathbf{W}_R \end{bmatrix} \\ \boldsymbol{\omega}_R = \omega_R \hat{\mathbf{z}} \\ \mathbf{A}_R^I = \mathbf{A}_3(\omega_R t + \theta_{R,0}) \end{cases} \tag{5.24}$$

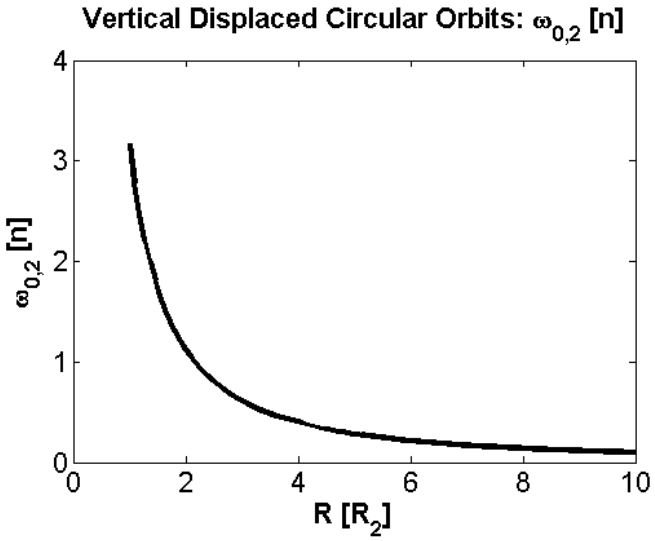

Figure 5.27: **2B SS-VDCOs around Phobos.** Value of $\omega_{0,2}$ as a function of R_R in n units.

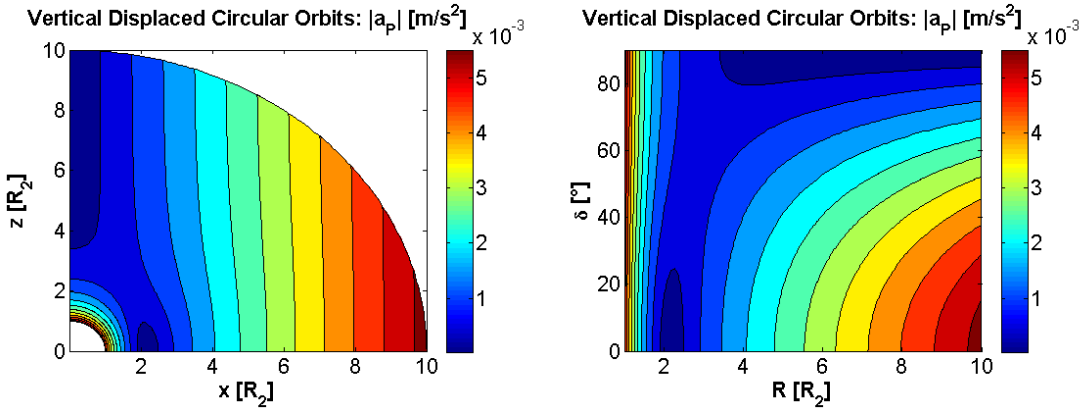

Figure 5.28: **2B SS-VDCOs around Phobos.** Propulsive acceleration's magnitude in the x-z and R-δ planes of the SS-R frame.

The model is axially symmetric around the vertical axis, therefore the analysis is reduced to a 2D mechanical system, defined either in the positive x-z plane of the R frame, or in the polar counterpart R-δ.

$$\mathbf{q} = \begin{bmatrix} R_x \\ 0 \\ R_z \end{bmatrix} = R_R \begin{bmatrix} \cos\delta_R \\ 0 \\ \sin\delta_R \end{bmatrix} \tag{5.25}$$

5.3.1.2 SS-VDCOs around Phobos

The SS-VDCOs are AEPs of the model of Eq.5.24 maintained by a constant acceleration in the R frame's components from Eq.5.3. To simplify the notation, define the distant-dependent quantity $\omega_{0,ID}$, where ID is referred to the central body (Phobos ID=2 to

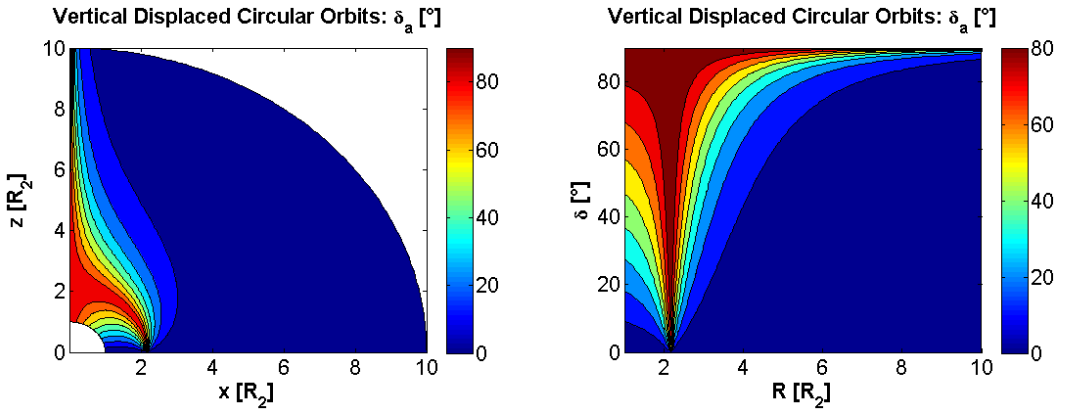

Figure 5.29: **2B SS-VDCOs around Phobos.** Propulsive acceleration's yaw angle in the x-z and R-δ planes of the SS-R frame.

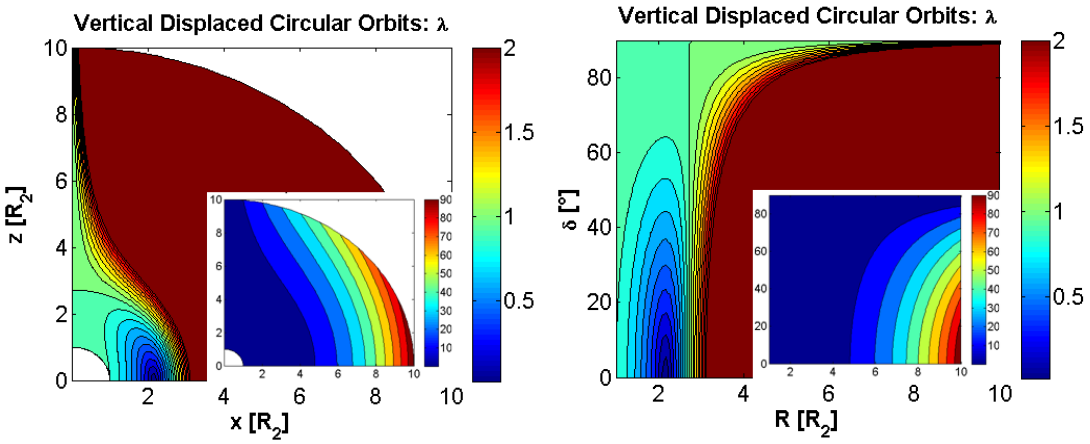

Figure 5.30: **2B SS-VDCOs around Phobos.** Ratio λ between the control and gravity acceleration's magnitudes in the x-z and R-δ planes of the SS-R frame.

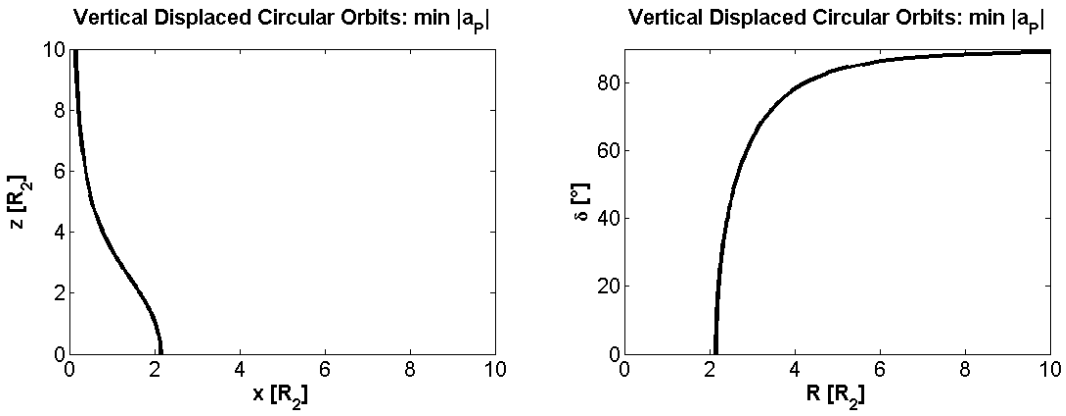

Figure 5.31: **2B SS-VDCOs around Phobos.** Referring to Fig.5.28, this curve identifies, for every vertical height, the minimum control AEP in the x-z and R-δ planes of the SS-R frame.

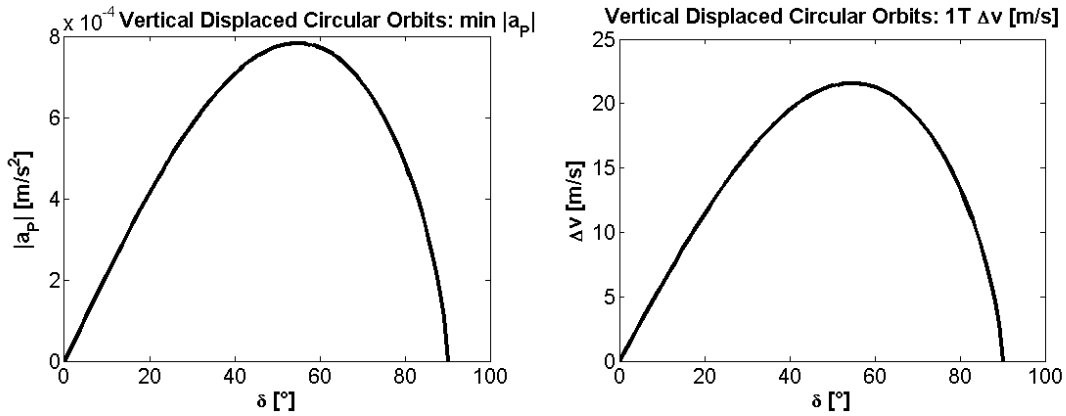

Figure 5.32: **2B SS-VDCOs around Phobos.** Propulsive acceleration's level and Δv (for one VDCO period), for every vertical height, of the minimum control AEPs in the x-z and R-δ planes of the SS-R frame.

remain coherent with the 3BP), and this quantity is plotted in Fig.5.27.

$$\mathbf{a_P} = \left(\mathbf{P}_R + \frac{GM_2}{\|\mathbf{q}_{AEP}\|^3} \right) \mathbf{q}_{AEP} = \begin{bmatrix} (\omega_{0,2}^2 - \omega_R^2) R_x \\ 0 \\ \omega_{0,2}^2 R_z \end{bmatrix} \tag{5.26}$$

In case of complete shadowing applications, the declination of the AEP must be equal to the seasonal anti-Sun declination, therefore the domain of interest is $0 \leq \delta \leq \theta_M$, or $0 \leq z \leq x\tan\theta_M$. The propulsive acceleration's magnitude and direction, which is defined by the yaw angle δ_a (as represented in Fig.5.26), are the following.

$$\begin{cases} \|\mathbf{a_P}\| = \sqrt[2]{\left(\omega_{0,2}^2 - \omega_R^2\right)^2 R_x^2 + \omega_{0,2}^4 R_z^2} \\ \delta_a = \arcsin\left(\frac{\omega_{0,2}^2 R_z}{\|\mathbf{a_P}\|}\right) \end{cases} \tag{5.27}$$

In [64], a broad analysis of the various classes of displaced circular orbits was undertaken looking to solar sailing applications. All the possible VDCOs lie in a $[R_x, R_z, \omega_R] = \mathbb{R}_0^{+3}$ domain, or $[R_R, \delta_R, \omega_R] = \mathbb{R}_0^{+2} \times [0, \pi/2]$ domain. In [64], the following classification is used for VDCOs:

- Type I: $\omega_R = \omega_{0,ID}(R_x, R_z)$. Every AEP in the x-z plane defines a VDCO with a different angular velocity, which is a different R frame. If $R_z = 0$ the resulting equatorial orbits are Keplerian (no control action required).
- Type II: $\omega_R = \omega_{0,ID}(R_x, R_z = 0)$. Every AEP with the same R_x component in the x-z plane defines VDCOs with the same angular velocity, which are associated to the same R frame. These orbits are synchronous with Keplerian equatorial orbits with radius R_x.
- Type III: ω_R is a free parameter. Every AEP point in the x-z plane defines a VDCO with the same angular velocity, so the R frame is unique.

The SS-VDCOs that are considered in this section belong to the type III orbits of [64], which have fixed period, synchronous with the Sun around Phobos. The VDCOs are usually highly non-Keplerian orbits: in our case $\mathbf{a_P}$ is not given by a solar sail, but from a propulsive system and so requires propellant's consumption.

The procedure is the same followed in section 5.2 for the hovering, computing the consumption and the linear Lyapunov stability region. From Eq.5.27, the equi-thrust curves are presented in Fig.5.28, while the yaw angle is plotted in Fig.5.29. In particular, Fig.5.30 shows the ratio between control and natural gravity acceleration: this number is called λ in [64], and used to rate if the VDCO is considered lowly or highly non-Keplerian. It is evident in Fig.5.28 the presence of one natural equilibrium point, that corresponds to the Keplerian equatorial and circular orbit with a SS period. This is achieved at the distance of $\tilde{R} = 2.16$ Phobos radii (mean altitude of $11.8km$), and no other local minima of the thrust level are present.

Focusing on possible shadowing exploitations throughout the Martian year, it is worth to evaluate the minimum of the propulsive acceleration's magnitude for a seasonal height. This could be done analytically looking for the minimum of Eq.5.27 with respect to R_R. This is obtained for the following value.

$$R_R|_{\min\|\mathbf{a_P}\|}(\delta_R) = \sqrt[3]{\frac{GM}{\omega_R^2}} \sqrt[3]{\frac{4}{\cos^2\delta_R} \frac{1}{1+\sqrt[2]{1+\frac{8}{\cos^2\delta_R}}}} \tag{5.28}$$

The related curve that describes the minimum control SS-VDCOs in the R frame is plotted in Fig.5.31, starting from the natural EP. Fig.5.32 provides the control action's level and consumption along this curve: the zero minimum is achieved at the natural EP and asymptotically for a pole-sitter hovering at infinite distance from Phobos. The reader can see that the intermediate values are very demanding.

However, shadowing is provided not only by strictly pointing towards the anti-Sun, but remaining just inside the eclipse wake: using a mean ellipsoidal model for Phobos' shape, a SS equatorial circular orbit with radius less than 2.04 Phobos mean radii provides continuous shadow for all the Martian year.

5.3.1.3 Stability Analysis

The linear stability analysis of the SS-VDCOs in the Phobos R2BP-R is undertaken similarly to that described in the hovering case of section 5.2.3. Since the control action is constant, the structure of the linearized R2BP-R is unique for every SS-VDCO, where the Hessian of the Phobos' gravity in the R frame's coordinates is expressed in Eq.5.29 and should be evaluated for every AEP.

$$u_{G,2/\mathbf{qq}}(\mathbf{q}_{AEP}) = -\omega_{0,2}^2 \begin{bmatrix} 1-3\cos^2\delta_R & 0 & -3\cos\delta_R\sin\delta_R \\ 0 & 1 & 0 \\ -3\cos\delta_R\sin\delta_R & 0 & 1-3\sin^2\delta_R \end{bmatrix} \tag{5.29}$$

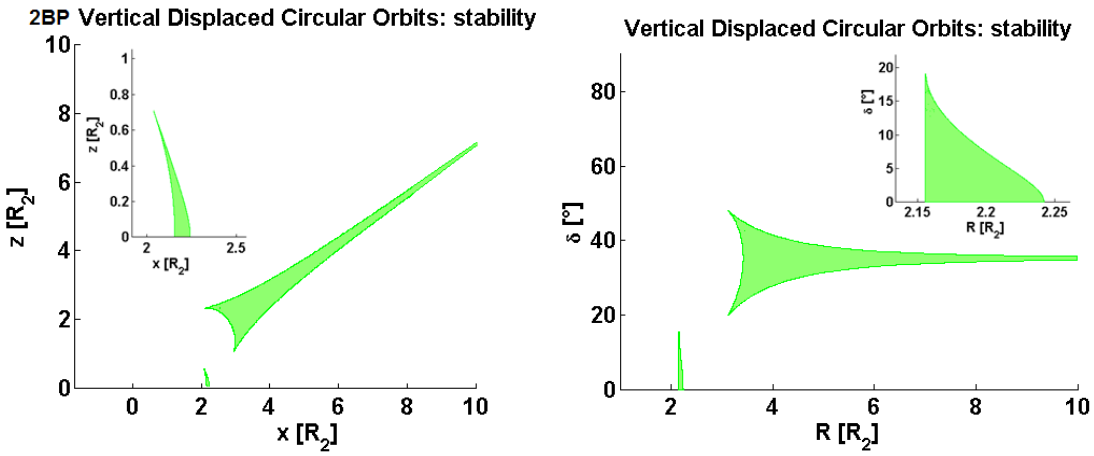

Figure 5.33: **2B SS-VDCOs around Phobos.** Linearized stability region of the AEPs in the x-z and R-δ planes of the SS-R frame. Magnification of the inner section.

The computation of the eigenvalues of the linearized 4D state-matrix can be undertaken with the general 6D procedure illustrated in section 5.2.3.2. In particular, the planar case, in this axially symmetric framework, reduces to the 1D x-axis of the R frame. The planar stability region can be derived analytically. The eigenvalues are the following,

$$\lambda(R_R, \delta_R = 0) = \begin{cases} \pm i\omega_{0,2} \\ \pm\sqrt[2]{GM_2}\sqrt[2]{\frac{1}{2}\frac{1}{R_R^3} - \frac{1}{\tilde{R}_R^3} + \sqrt[2]{\frac{9}{2}\frac{1}{R_R^6} - 2\frac{1}{R_R^3}\frac{1}{\tilde{R}_R^3}}} \\ \pm\sqrt[2]{GM_2}\sqrt[2]{\frac{1}{2}\frac{1}{R_R^3} - \frac{1}{\tilde{R}_R^3} - \sqrt[2]{\frac{9}{2}\frac{1}{R_R^6} - 2\frac{1}{R_R^3}\frac{1}{\tilde{R}_R^3}}} \end{cases} \tag{5.30}$$

and the stability region is presented in Eq.5.31, where the distances are normalized with respect to the previously mentioned Keplerian SS-VDCO's radius $\tilde{R}_R$.

$$\lambda^2(R_R, \delta_R = 0) < 0 \Leftrightarrow \tilde{R}_R < R_R < \frac{\sqrt[3]{9}}{2}\tilde{R}_R \tag{5.31}$$

Equatorial SS-VDCOs outermost the Keplerian solution, and up to 2.24 Phobos radii (12.8km of mean altitude), are linearly stable in the 2B dynamics.

Fig.5.33 highlights the linear stability region of the 3D case in the axially symmetric plane of the R frame. The three realms of the linear stability region are similar to the ones of the 3D stability region for AEPs of the CR3BP-CA in Fig.5.9, swapping the Mars-Phobos barycenter and Phobos with Phobos and the Keplerian equilibria, and without the distortion of a second massive body like in Fig.5.10. The inner section in Fig.5.33 is very narrow and reaches declinations up to 20°, but is also close to the overall minimum control area of Fig.5.28. The second section is useful for higher heights, but requires large distances from Phobos: it asymptotically tends to a declination around 35.26°, where the thrust required is very high, as the reader can see in Fig.5.28.

5.3.2 SS-VDCOs in the Mars-Phobos CR3BP

This section looks to the solution of VDCOs around Phobos in the framework of the CR3BP, which is under the influence also of the Mars' gravity. The relative dynamics are still described in the rotating frame R centered on Phobos, which rotates with constant $\omega_R = -n$ along the z-axis of the 3B and Hill's frame. These dynamics are named CR3BP-R.

5.3.2.1 Equations of Motion

The equations of motion of the Mars-Phobos CR3BP-R are obtained from the Phobos R2BP-R of Eq.5.24 adding the time-variant gravity of Mars, and its apparent translational acceleration on the R frame's origin. These terms have already been introduced when describing the dynamics of the CR3BP in Phobos' Hill's frame in Eq.2.51. The differences are two. First of all, these two terms must be expressed in the R frame's components. The reference frame I, used in the framework of the R2BP-R in section 5.3.1, becomes now the Phobos' Hill's frame H. Thus, the attitude matrix between R and I frames is retrieved from Eq.5.23, and the time-variant position of Mars in the R frame is provided below.

$$\begin{cases} \mathbf{q}_{1,3B} = -a\hat{\mathbf{x}} \\ \mathbf{A}_R^H = \mathbf{A}_3\left(\omega_R t + \theta_0\right) \end{cases} \Rightarrow \mathbf{q}_{1,R} = \begin{bmatrix} -a\cos(\omega_R t + \theta_0) \\ a\sin(\omega_R t + \theta_0) \\ 0 \end{bmatrix} \tag{5.32}$$

The sum of Mars' gravity and apparent effect represents the so-called Mars 3B perturbation. This is the term, upon expression in the R frame's components, to be added in the Phobos R2BP-R of Eq.5.24, and is presented below.

$$\begin{cases} \mathbf{a}_{3B,R} = -\frac{GM_1}{\left\|\mathbf{q}-\mathbf{q}_{1,R}\right\|^3}\left(\mathbf{q}-\mathbf{q}_{1,R}\right) - \frac{G(M_1+M_2)}{a^3}\left(1-\mu\right)\mathbf{q}_{1,R} = -\omega_{0,1}^2\left(\mathbf{q}-\mathbf{q}_{1,R}\right) - \bar{\omega}_{0,1}^2\mathbf{q}_{1,R} \\ \lim\limits_{\mathbf{q}\to\mathbf{0}} \mathbf{a}_{3B,H} = -\frac{GM_1}{a^3}\mathbf{A_{H1}}\mathbf{q}_H \Rightarrow \mathbf{a}_{3B,R} \simeq -\frac{GM_1}{a^3}\mathbf{A}_R^H\mathbf{A_{H1}}\left(\mathbf{A}_R^H\right)^T\mathbf{q} = -\bar{\omega}_{0,1}^2\mathbf{A_{H1-R}}\mathbf{q} \\ \mathbf{A_{H1-R}} = \begin{bmatrix} 1-3\cos^2(\omega_R t) & 3\cos(\omega_R t)\sin(\omega_R t) & 0 \\ 3\cos(\omega_R t)\sin(\omega_R t) & 1-3\sin^2(\omega_R t) & 0 \\ 0 & 0 & 1 \end{bmatrix} \end{cases} \tag{5.33}$$

The second equation represents the Hill's linearized approximation, already presented in Eq.2.33 in the Hill's frame components, which is now expressed in the R frame's components. The relative error of the linearized approximation up to 10 Phobos radii is of 10^{-4}. This expression could be useful for a first-order analytical insight into the computation of the SS-VDCOs that will be undertaken in this section. In this sense, the initial phase of the VDCO θ_0 is now taken as zero, since the time-variant analysis will refer to a full revolution of the VDCO.

The second difference is the correction of the angular velocity in the apparent rotational acceleration's terms of Eq.2.2, because ω_R is now defined with respect to the H frame, which is not inertial but rotates with angular velocity $+n$. As expected from

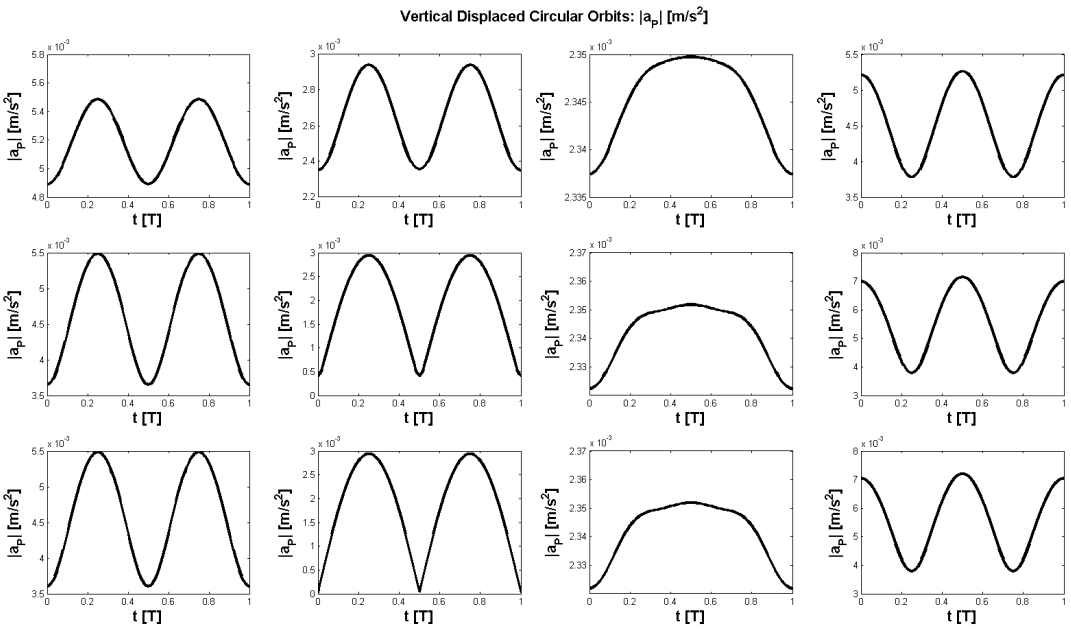

Figure 5.34: **3B SS-VDCOs around Phobos.** Propulsive acceleration magnitude's profile over time, for some AEPs ($R_R = 1.09, 1.72, 2.71, 6.31 R_2$ from left to right, $\delta_R = 0, 8.1, 53.1°$ from the bottom to the top).

section 5.3, in the framework of the 3B dynamics $\boldsymbol{\omega}_R = \mathbf{0}$[8], and *for a short-term analysis with respect to the Martian year, the R frame is approximately inertial and its AEPs represent an inertial hovering*, dragged along the Mars-Phobos orbit.

The equations of motion of the Mars-Phobos CR3BP-R, in a short-term SS rotating frame, are expressed in Eq.5.34. The second set of ODEs represents the Hill's approximation.

$$\begin{cases} \mathbf{x} = \begin{bmatrix} \mathbf{q} \\ \dot{\mathbf{q}} \end{bmatrix}, \dot{\mathbf{x}} = \mathbf{A}\mathbf{x} + \begin{bmatrix} \mathbf{0_{3x1}} \\ -\frac{GM}{\|\mathbf{q}\|^3}\mathbf{q} \end{bmatrix} + \begin{bmatrix} \mathbf{0_{3x1}} \\ -\omega_{0,1}^2 (\mathbf{q} - \mathbf{q}_{1,R}) - \bar{\omega}_{0,1}^2 \mathbf{q}_{1,R} \end{bmatrix}, \mathbf{A} = \begin{bmatrix} \mathbf{0_3} & \mathbf{I_3} \\ \mathbf{0_3} & \mathbf{0_3} \end{bmatrix} \\ \mathbf{x} = \begin{bmatrix} \mathbf{q} \\ \dot{\mathbf{q}} \end{bmatrix}, \dot{\mathbf{x}} = \mathbf{A}\mathbf{x}, \mathbf{A} = \begin{bmatrix} \mathbf{0_3} & \mathbf{I_3} \\ -\omega_{0,2}^2 \mathbf{I_3} - \bar{\omega}_{0,1}^2 \mathbf{A_{H1-R}} + & \mathbf{0_3} \end{bmatrix} \end{cases} \tag{5.34}$$

The system is no longer axially symmetric due to the Mars' offset, but the VDCOs are periodic, so the analysis could still be conducted in the positive x-z plane of the R frame, or in the polar counterpart R-δ.

5.3.2.2 SS-VDCOs around Phobos

The SS-VDCOs are AEPs of the model of Eq.5.34 maintained by a time-variant acceleration in the R frame's components from Eq.5.3. The propulsive acceleration is a feedforward profile over time in all the three directions, thus requires the yaw and pitch angles δ_a-α_a.

[8] To be precise, the Sun-Mars revolution rate disregarded from this analysis is 2,000 times smaller than the Mars-Phobos revolution rate n.

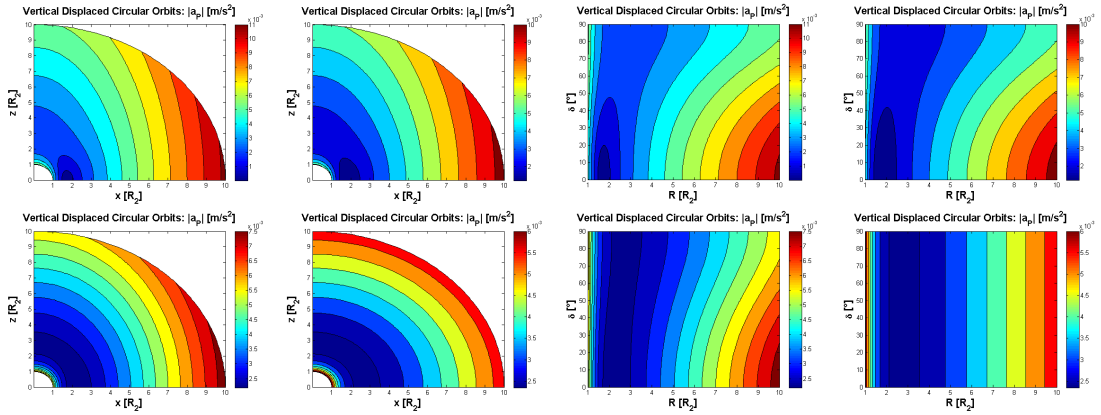

Figure 5.35: **3B SS-VDCOs around Phobos.** Propulsive acceleration's magnitude in the x-z and R-δ planes of the SS-R frame, for phases of $0, 25.2, 57.6, 90°$.

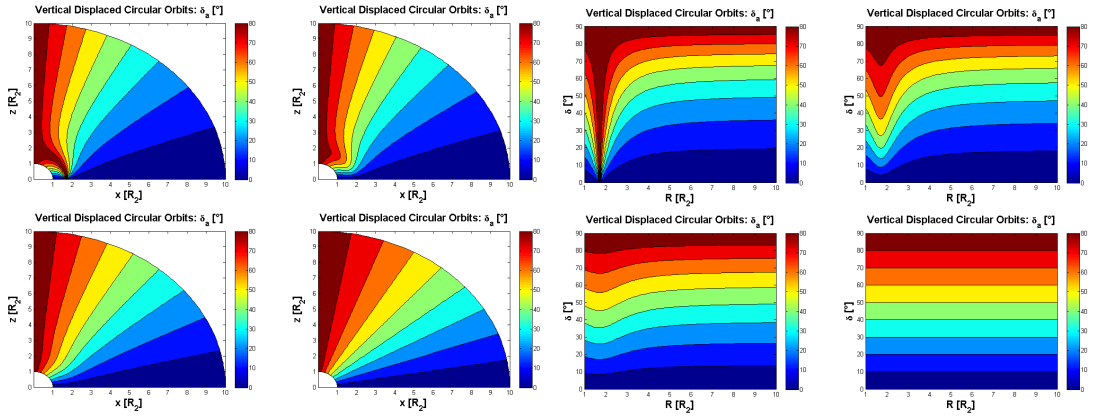

Figure 5.36: **3B SS-VDCOs around Phobos.** Propulsive acceleration's yaw angle in the x-z and R-δ planes of the SS-R frame, for phases of $0, 25.2, 57.6, 90°$.

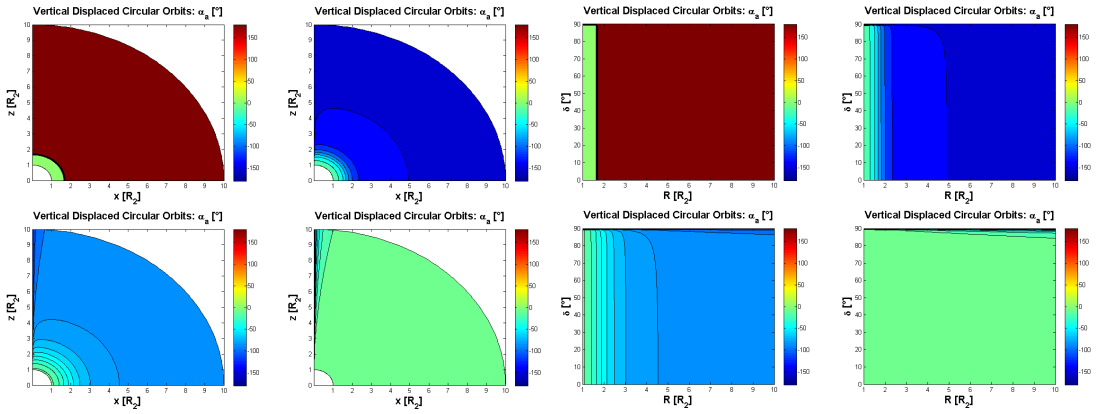

Figure 5.37: **3B SS-VDCOs around Phobos.** Propulsive acceleration's pitch angle in the x-z and R-δ planes of the SS-R frame, for phases of $0, 25.2, 57.6, 90°$ (angle is opposite every quarter).

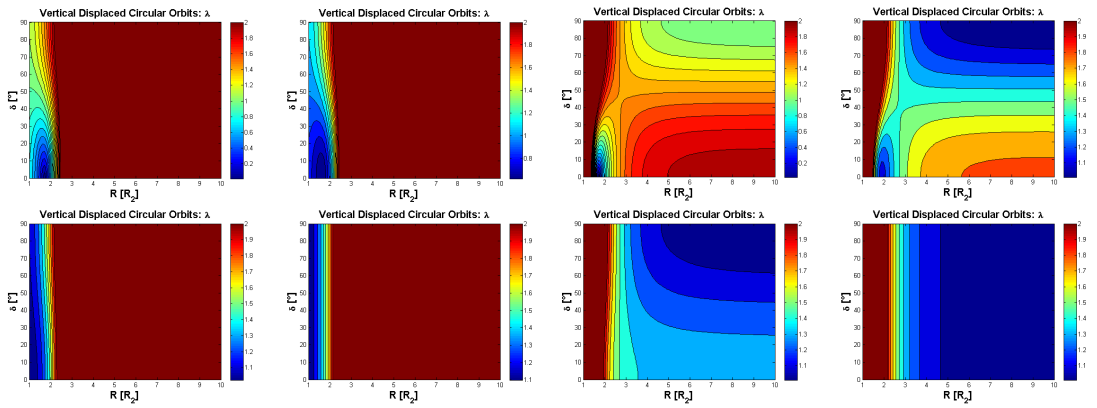

Figure 5.38: **3B SS-VDCOs around Phobos.** Ratio λ between the control and gravity acceleration's magnitudes (on the left with respect of Phobos gravity, on the right with respect to the mean Mars 3B perturbation) in the R-δ plane of the SS-R frame, for phases of $0, 25.2, 57.6, 90°$.

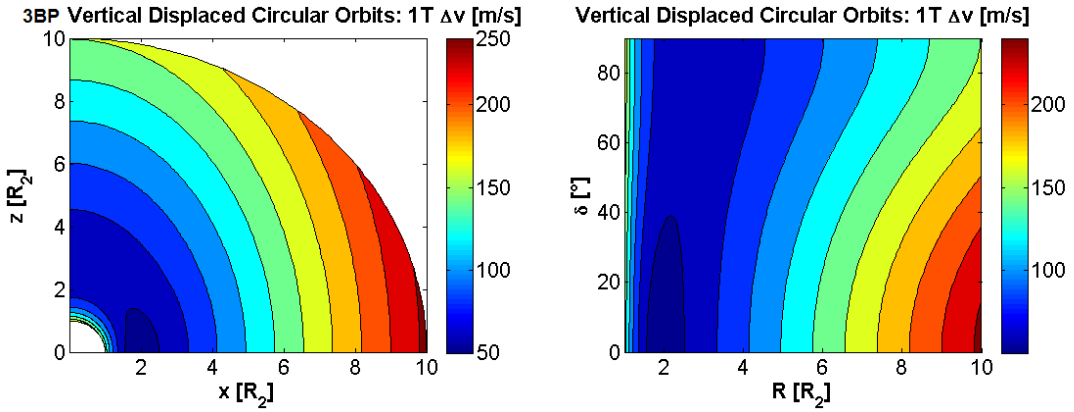

Figure 5.39: **3B SS-VDCOs around Phobos.** Δv (for one VDCO period) of the AEPs in the x-z and R-δ planes of the SS-R frame.

$$\begin{cases} \mathbf{a_P} = \omega_{0,2}^2 \mathbf{q}_{AEP} + \omega_{0,1}^2 \left(\mathbf{q}_{AEP} - \mathbf{q}_{1,R}\right) + \bar{\omega}_{0,1}^2 \mathbf{q}_{1,R} \\ \mathbf{a_P} = \left(\omega_{0,2}^2 \mathbf{I_3} + \bar{\omega}_{0,1}^2 \mathbf{A_{H1-R}}\right) \mathbf{q}_{AEP} = \begin{bmatrix} \left[\omega_{0,2}^2 - \left(3\cos^2\left(\omega_R t\right) - 1\right) \bar{\omega}_{0,1}^2\right] R_x \\ 9\cos\left(\omega_R t\right) \sin\left(\omega_R t\right) \bar{\omega}_{0,1}^2 R_x \\ \left(\omega_{0,2}^2 + \bar{\omega}_{0,1}^2\right) R_z \end{bmatrix} \end{cases} \tag{5.35}$$

The required propulsive acceleration is periodic, with half the period of the Phobos' revolution. The constant terms are due to counteract Phobos' gravity, while the periodic terms have null tangential component both in conjunction and quadrature phases of the spacecraft as seen from Mars, and the maximum effect is in the intermediate phases. Their radial component oscillates along a non-null mean value, and the amplitude is maximum in conjunction, minimum in quadrature, and null at phases $\pm 54.74°, \pm 125.26°$.

Eq.5.35 is now evaluated to derive the consumption of the inertial hovering in the CR3BP. Fig.5.34 presents the thrust magnitude's profile for a few SS-VDCOs. It is

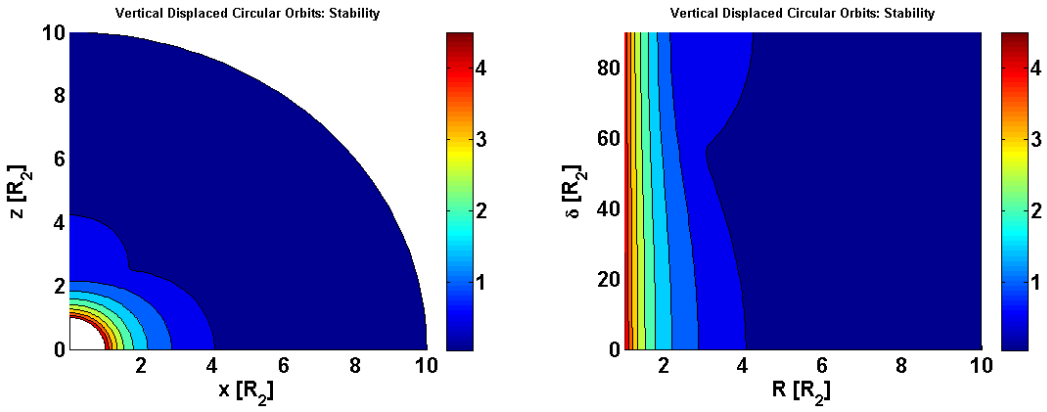

Figure 5.40: **3B SS-VDCOs around Phobos.** Linear stability analysis: Floquet exponents of the AEPs in the x-z and R-δ planes of the SS-R frame.

evident that there is a transition in the profile with increasing distance from Phobos. Fig.5.35-5.37 present the values of the propulsive acceleration's magnitude and angles for a few Phobos phases, and Fig.5.38 plots the value of the λ ratio, defined both with respect to Phobos gravity and Mars 3B perturbation. When the spacecraft is in inferior conjunction (phase 0), as seen from Mars, there is an instantaneous natural EP close to the previous SS Keplerian orbit in the R2BP, now located at 1.71 Phobos radii. Recall that in the CR3BP-R there is no more an apparent rotational acceleration, thus the Phobos' gravity cannot be counteracted by a centrifugal force[9], like in the R2BP-R, but its role is played by the Mars 3B perturbation. At phase 0 the two actions are opposite, and this explains the existence of the instantaneous equilibria on the orbital plane. However, at increasing phases a thrust in the y-component (and so a pitch angle) is required, and no instantaneous natural EPs are available. This is deducible from the linearized form in Eq.5.35. In summary, inertial hovering in the CR3BP cannot be provided naturally, and the focus is to look to minimum control SS-VDCOs in these Mars-Phobos 3B dynamics.

In summary, the maximum level of the propulsive acceleration profile determines the thruster's choice. From Fig.5.35, the maximum thrust level for a $100kg$ spacecraft at small-medium distances from Phobos would be less than $1N$, so the maintenance of a SS-VDCO around Phobos for a larger spacecraft requires rockets. Fig.5.39 shows the Δv consumption over one period of the inertial hovering at Phobos. The minimum cost still happens in a region close to 2 Phobos radii, up to the maximum Sun's declination at the solstices, but this is large (Δv= $50m/s$) making the demand for the propulsion system very high for more than one Phobos period. In comparison to the R2BP dynamics in Fig.5.32, the costs of the SS-VDCOs in the CR3BP have meanly grown of about 5-10 times.

[9]The neglected centrifugal force of the Sun-Mars orbit is too small to counteract Phobos gravity.

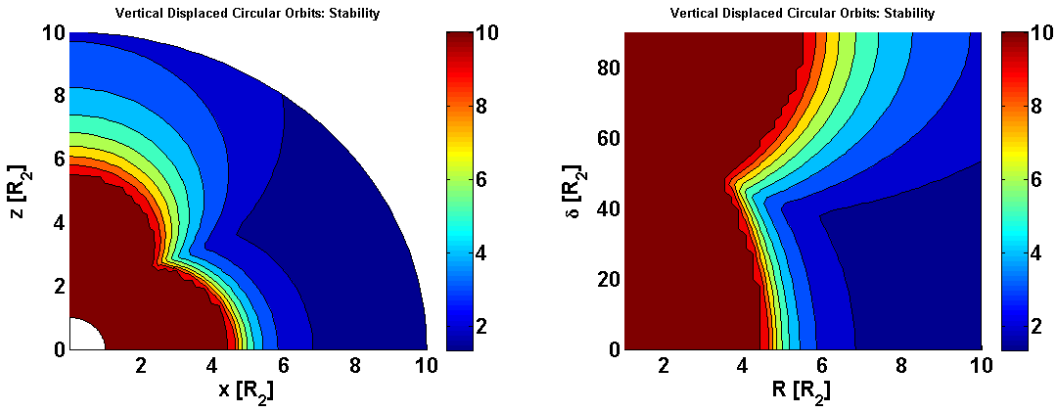

Figure 5.41: **3B SS-VDCOs around Phobos.** Linear stability analysis: Floquet multipliers (cut-off at 10 for greater values) of the AEPs in the x-z and R-δ planes of the SS-R frame.

5.3.2.3 Stability Analysis

The linear stability analysis of the SS-VDCOs in the Mars-Phobos CR3BP-R can be undertaken like in the body-fixed hovering case, with the general procedure illustrated in section 5.2.3.2. The difference with respect to the body-fixed hovering is that the 3D stiffness submatrix, of the 6D linearized state-matrix, does not have the matrix $\mathbf{P}$, and the trace of this matrix $\omega_{0,2}^2 + \omega_{0,1}^2$ will be always positive. This means that the set of eigenvalues will always be unstable. This has been proved with the classical Floquet linear stability analysis for periodic orbits in dynamical systems illustrated in section B.5.1.1, by computing the eigenvalues of the monodromy matrix of the SS-VDCOs. Fig.5.40 shows the Floquet exponents, that can be compared with the eigenvalues of the body-fixed hovering positions, and Fig.5.41 shows the Floquet multipliers of the inertial hovering positions. All the close-range SS-VDCOs are highly unstable, and this is a structural property of all the orbits in proximity of the secondary's SOI in the chaotic dynamics of the CR3BP. Their instability lowers at increasing size of the SS-VDCOs, but recall that the consumption in Fig.5.35 massively increases with the distance from Phobos, since the 2B-like dynamics is not valid out of its SOI.

5.3.3 Applications

Following the idea of exploiting the shadow of Phobos to protect a spacecraft from the directional solar radiation during the station-keeping at the Mars-Phobos orbital distance, this section has analyzed the most simple orbits around Phobos to track the anti-Sun motion, which are the SS-VDCOs. In particular, these orbits turn out to be a classical inertial hovering. This analysis is complementary to the one of section 5.2, and concludes the analysis of this classical spacecraft configuration for the case of Phobos in this thesis.

Inertial hovering is usually exploited to enable occultation-free communications with the Earth, and in this case also provides advantages in terms of surface coverage of

Phobos. However, the first aim is not valid any longer for any planetary satellite. In addition, for the case of Phobos, due to the strong influence of the Mars 3B perturbation, the SS-VDCOs require significant fuel consumption, which is infeasible over one period (Δv$> 50m/s$).

As a comparison, the natural SS equatorial and circular orbit around Mars is located at 461 Mars radii, out of its SOI, and is therefore unworthy for missions to Mars. Instead the cost of artificially maintain the Keplerian SS circular orbit around Deimos, which is located at 5 mean radii ($24.0km$ of mean altitude), has resulted to be of $16m/s$ per period, and it requires 10 times lighter thrusters than for Phobos.

5.4 Artificial Libration Point Orbits around Phobos

The body-fixed hovering points investigated in section 5.2 are the dynamical substitutes of the LPs of the Mars-Phobos CR3BP in the CR3BP-CA defined in Eq.5.1 (and the CR3BP-GH-CA analyzed in section 5.2.4). Therefore, in a way analogous to the natural dynamics, artificial LPOs (ALPOs) exist around these AEPs with the same propulsion level [59].

The natural LPOs of the ER3BP-GH around Phobos, computed in section 4.3, are investigated in this section in the framework of the addition of a constant acceleration, and focusing on the artificial LPOs around the displaced L_{1-2}. Recall from chapter 4, where the dynamical substitutes of classical LPOs have been computed first in the CR3BP-GH and then in ER3BP-GH, that the effects of the GHs and the eccentricity act in a different way. The first is responsible for the change in position, shape and orientation of the LPOs, and the second causes the motion to oscillate around them. For the same reason explained in section 4.4, where the performances of the dynamical substitutes of the LPOs are presented, in this section to undertake an immediate analysis of the advantages and opportunities provided by the low-thrust propulsion, only the periodic ALPOs are derived as dynamical substitutes of the families of periodic LPOs of the CR3BP-GH.

The dynamical substitutes are computed numerically by the NC technique (see section B.2.2) as presented in section 5.4.1. Section 5.4.2 presents the periodic ALPOs of the Mars-Phobos CR3BP-GH, and section 5.4.4 provides the related artificial IMs (AIMs).

5.4.1 Numerical Continuation with respect to the Propulsive Acceleration's Level

The CR3BP-CA has been presented in Eq.5.1 to derive the related AEPs for a fixed propulsive acceleration $\mathbf{a_P}$, by adding the constant vectorfield $\mathbf{f}_{CA}$ to the equations of motion of the CR3BP. The same procedure is required to derive the ODEs of the Mars-Phobos CR3BP-GH-CA, used in section 5.2.4 to derive the related AEPs. The

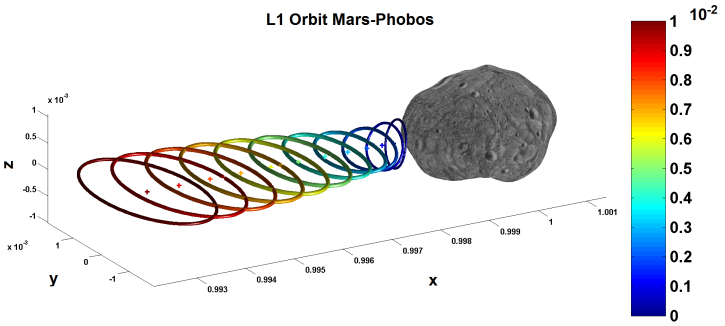

Figure 5.42: **Periodic artificial LPOs in the Mars-Phobos CR3BP-GH.** Continuation with respect to the constant acceleration magnitude (m/s^2) with direction $+\hat{\mathbf{x}}$ of a medium energy PO of the family A around L_1 of the CR3BP-GH. Crosses represent the current EP. Phobos real shape.

vectorfield of the CR3BP-GH-CA is a natural homotopic dynamical system, parameterized by the propulsion level. Thus, quite intuitively, the dynamical substitutes of the solutions of the CR3BP-GH are computed by NC schemes where the continuation parameter σ_{CA} is set to be the propulsive acceleration's constant magnitude[10]. This NC provides an entire family of dynamical substitutes physically worthy, parameterized by the propulsion level, for each invariant motion in the CR3BP-GH. The direction of the thrust is fixed for a given homotopic CR3BP-GH-CA, and for this reason one defines a constant vectorfield $\mathbf{f_n} = [\mathbf{0_{3x1}}; \hat{\mathbf{n}}_{\mathbf{aP}}]$.

$$\dot{\mathbf{x}} = \mathbf{h}\left(t, \mathbf{x}, \sigma_{CA}\right) = \mathbf{f_{CR3BP-GH}}\left(\mathbf{x}\right) + \mathbf{f}_{CA} = \mathbf{f_{CR3BP-GH}}\left(\mathbf{x}\right) + \sigma_{CA}\mathbf{f_n} \rightarrow \boldsymbol{\phi}_{\mathbf{h}}\left(t, \mathbf{x}, \sigma_{CA}\right) \tag{5.36}$$

The definitions of the related augmented variational dynamical system and STM are the following.

$$\Phi\left(t, \mathbf{x}_0, \sigma_{CA}\right) = \begin{bmatrix} \phi_{h/\mathbf{x}_0} & \phi_{h/\sigma} \\ \mathbf{0_{1x6}} & 1 \end{bmatrix} \leftrightarrow \begin{cases} \dot{\Phi}\left(t, \mathbf{x}_0, \sigma_{CA}\right) = \begin{bmatrix} \mathbf{H_{3BGH}}\left(\mathbf{x}(t)\right) & \mathbf{f_n} \\ \mathbf{0_{1x6}} & 0 \end{bmatrix} \Phi\left(t, \mathbf{x}_0, \sigma_{CA}\right) \\ \Phi\left(0, \mathbf{x}_0, \sigma_{CA}\right) = \mathbf{I_7} \end{cases} \tag{5.37}$$

The effect of the Phobos' GHs in the 3B dynamics is stationary as discussed in section 3.3, and the potential u_{CA} of the constant propulsive acceleration is presented in Eq.5.2. These yield the augmented Jacobi integral of the conservative CR3BP-GH-CA below.

$$\begin{aligned} c_{CR3BP-GH-CA}\left(\mathbf{x}, \sigma_{CA}\right) &= c_{CR3BP-GH}\left(\mathbf{x}\right) + c_{CA}\left(\mathbf{x}, \sigma_{CA}\right) = \\ &= c_{CR3BP-GH}\left(\mathbf{x}\right) + \sigma_{CA} 2\mathbf{q}^T \hat{\mathbf{n}}_{\mathbf{aP}} \end{aligned} \tag{5.38}$$

[10] Recall that σ_{CA} is defined in normalized units.

5.4.2 Periodic Libration Point Orbits through Body-Fixed Hovering in the Mars-Phobos CR3BP-GH

In this section the NC of the invariant solutions between CR3BP-GH and CR3BP-GH-CA is undertaken increasing the constant acceleration's magnitude. The procedure maintains the phase-space's dimension of the solutions. The NC is undertaken with the same differential approach used for computing the dynamical substitutes of the POs from CR3BP to CR3BP-GH in section 4.2.2.2.1. This means that the differential initial condition with respect to the current AEP is continued on the variant Poincaré map $g(\mathbf{x}, \sigma_{CA}) = y - y_{LP}(\sigma_{CA}) = 0$, and the dynamical substitutes are defined as the orbits with the same augmented Jacobi integral's gap with respect to the hovering point in different dynamics. The DC scheme is exactly the same from Eq.4.35 to Eq.4.39, just using the new homotopic dynamics of Eq.5.36, the STM from Eq.5.37, and the Jacobi integral of Eq.5.38 to compute the matrices of Eq.4.38. In particular, now $g(\mathbf{x}) = 2\mathbf{q}^T\hat{\mathbf{n}}_{\mathbf{ap}}$, $\mathbf{f} = \mathbf{f_n}$, and $\mathbf{J}(\mathbf{x}) = \mathbf{H_{3B}}(\mathbf{x}) + \mathbf{H_{GH}}(\mathbf{x})$, to yield the DC scheme of Eq.4.39.

The difference with respect to the continuation in section 4.2.2.2.1 is that the dimension of the parameters of the problem is now higher, since it depends also on the orientation of the thrust vector. Therefore, in this section the analysis is undertaken with six NCs, computing the ALPOs with thrust directions along all coordinated axes $\pm\hat{\mathbf{x}}$, $\pm\hat{\mathbf{y}}$, and $\pm\hat{\mathbf{z}}$.

After obtaining a dynamical substitute in the CR3BP-GH-CA, the related family of periodic LPOs at the same propulsive level and direction, can be refined through a second NC in cascade, where the continuation parameter is taken as the Jacobi integral of Eq.5.38, used as fixed constraint in the first scheme, as explained in section 4.2.2.2.2.

Analysis of the results. The NC of the periodic LPOs with respect to the propulsive acceleration's magnitude, from the dynamical model of the CR3BP-GH to the one of the CR3BP-GH-CA, has resulted to be fast up to medium-small propulsion levels, as we see in Fig.5.43-5.44. For high-thrust, the NC becomes slow due to the presence of strong nonlinear effects (turning points of the continuation curve) that require to decrease the integration step.

Fig.5.42 shows an example of the NC with respect to the propulsive acceleration's magnitude of a medium-energy PO of the family A around L_1. The NC is conducted up to high-thrust directed along the $+x$-axis. Fig.5.43-5.46 show the related profile of the NC and the properties of the curve of ALPOs. Fig.5.47-5.48 show the artificial dynamical substitutes of the small-energy periodic LPOs of the families A and B along all the coordinate axes' directions.

Fig.5.49-5.51 show the resulting families of POs in the Mars-Phobos CR3BP-GH-CA, along all the thrusting coordinate directions. Due to the high dimension of the problem, a precise nomenclature of the families of LPOs at different thrust level has not

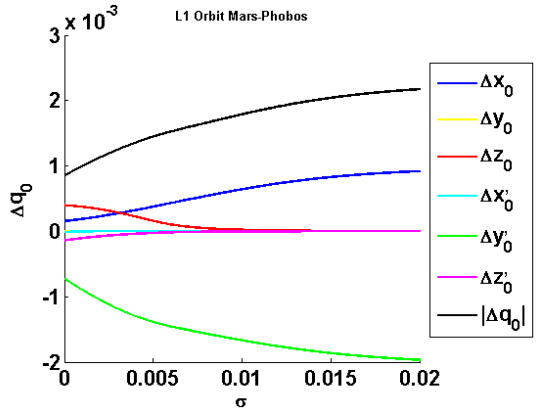

Figure 5.43: **Periodic artificial LPOs in the Mars-Phobos CR3BP-GH.** Continuation variables' curves profile. Continuation with respect to the constant acceleration magnitude with direction $+\hat{\mathbf{x}}$ from CR3BP-GH ($\sigma = 0$) to $0.01 m/s^2$. Continuation of a medium energy PO of the family A around L_1 of the CR3BP-GH.

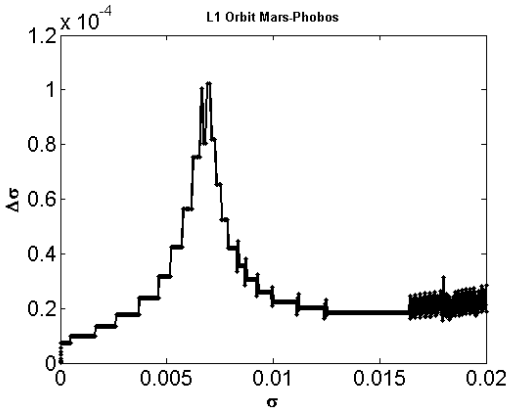

Figure 5.44: **Periodic artificial LPOs in the Mars-Phobos CR3BP-GH.** Continuation adaptive step's profile. Continuation with respect to the constant acceleration magnitude with direction $+\hat{\mathbf{x}}$ from CR3BP-GH ($\sigma = 0$) to $0.01 m/s^2$. Continuation of a medium energy PO of the family A around L_1 of the CR3BP-GH.

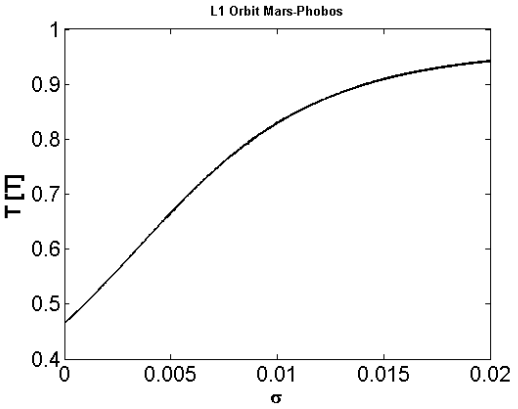

Figure 5.45: **Periodic artificial LPOs in the Mars-Phobos CR3BP-GH.** Profile of the period. Continuation with respect to the constant acceleration magnitude with direction $+\hat{\mathbf{x}}$ from CR3BP-GH ($\sigma = 0$) to $0.01 m/s^2$. Continuation of a medium energy PO of the family A around L_1 of the CR3BP-GH.

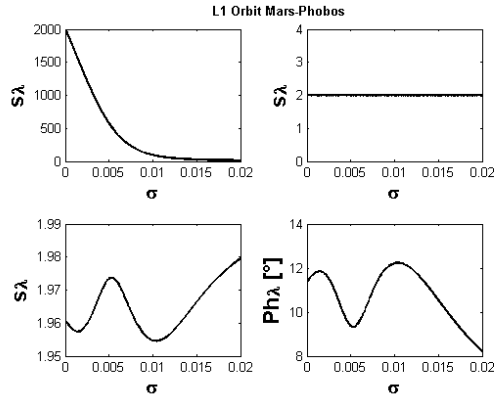

Figure 5.46: **Periodic artificial LPOs in the Mars-Phobos CR3BP-GH.** Profile of the stability properties (stability indexes of the three couples of eigenvalues of the monodromy matrix, with the phase of the center's couple). Continuation with respect to the constant acceleration magnitude with direction $+\hat{\mathbf{x}}$ from CR3BP-GH ($\sigma = 0$) to $0.01 m/s^2$. Continuation of a medium energy PO of the family A around L_1 of the CR3BP-GH.

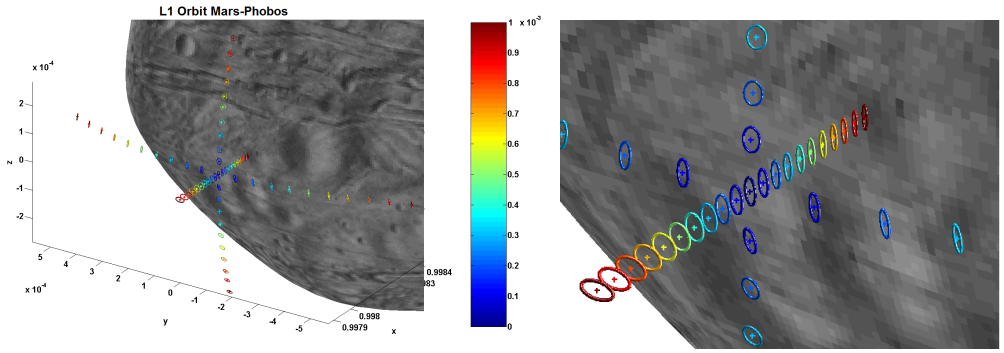

Figure 5.47: **Periodic artificial LPOs in the Mars-Phobos CR3BP-GH.** Continuation with respect to the constant acceleration magnitude (m/s^2) along all coordinate axes directions, of a small energy PO of the family A around L_1 of the CR3BP-GH. Crosses represent the current EP. Phobos real shape.

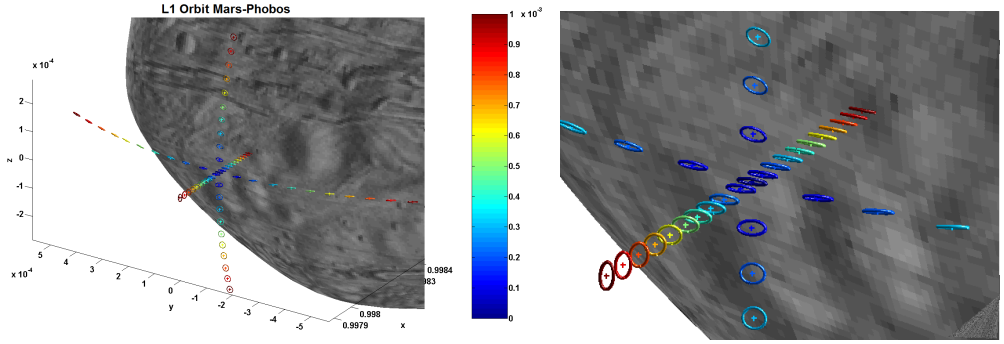

Figure 5.48: **Periodic artificial LPOs in the Mars-Phobos CR3BP-GH.** Continuation with respect to the constant acceleration magnitude (m/s^2) along all coordinate axes directions, of a small energy PO of the family B around L_1 of the CR3BP-GH. Crosses represent the current EP. Phobos real shape.

been addressed. In this sense, the analysis of the families of ALPOs is the following.

- Thrusting away from Phobos moves the LPOs closer to the moon, without great changes in the shape and orientation of larger orbits even with high thrust, apart from the larger POs of the family D that become more vertically aligned.
- On the contrary, thrusting towards Phobos moves the orbits farther from the moon, and as the thrust level increases the effect of the GHs rapidly decreases and the LPOs tend to become similar to the families of the classical CR3BP.

The effect of the thrust along the other two coordinate axes is more complicated: the manifold moves accordingly to the thrust direction, with the displacement of the artificial LP moving in accordance to the equi-thrust surfaces computed before in Fig.5.4.

- Thrust in tangential direction maintains the shape of families B and C, while the families D are similar to vertical Lyapunov orbits, and the families A are highly distorted.
- High thrust in the vertical direction greatly modifies the manifold, since only two families of POs are now present, because the bifurcation is moved at high-energy

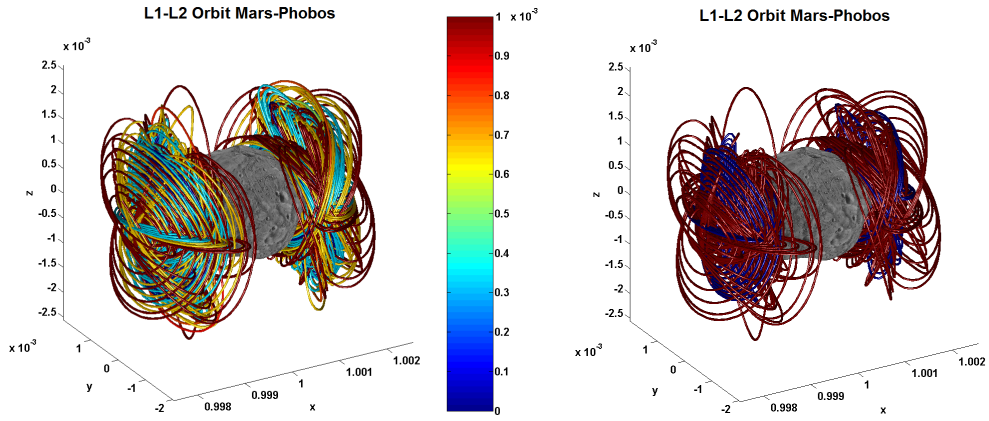

Figure 5.49: **Periodic artificial LPOs in the Mars-Phobos CR3BP-GH.** Summary of the POs (brown) obtained by displacement of the four families of POs around each LP of the CR3BP-GH (blue) with constant acceleration (m/s^2) along all coordinate axes directions. Phobos real shape.

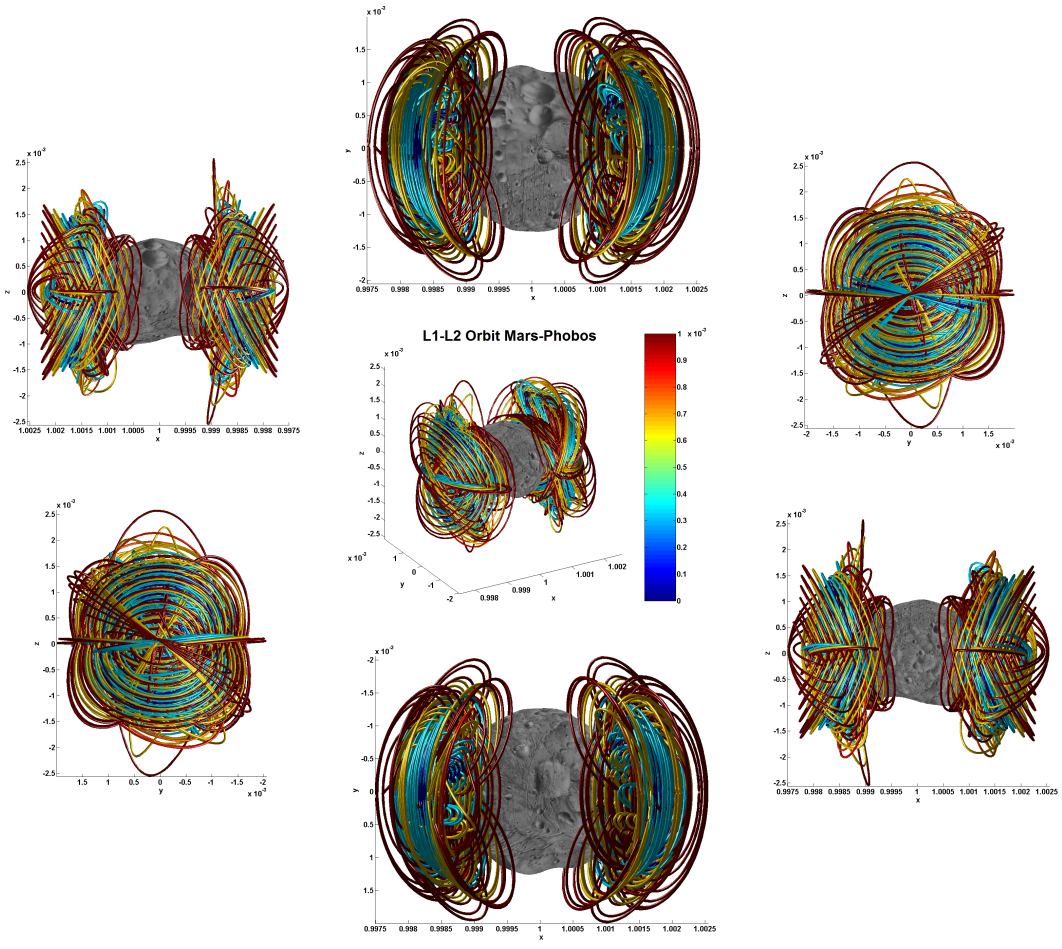

Figure 5.50: **Periodic artificial LPOs in the Mars-Phobos CR3BP-GH.** Summary of the POs (brown) obtained by displacement of the four families of POs around each LP of the CR3BP-GH (blue) with constant acceleration (m/s^2) along all coordinate axes directions. Phobos real shape.

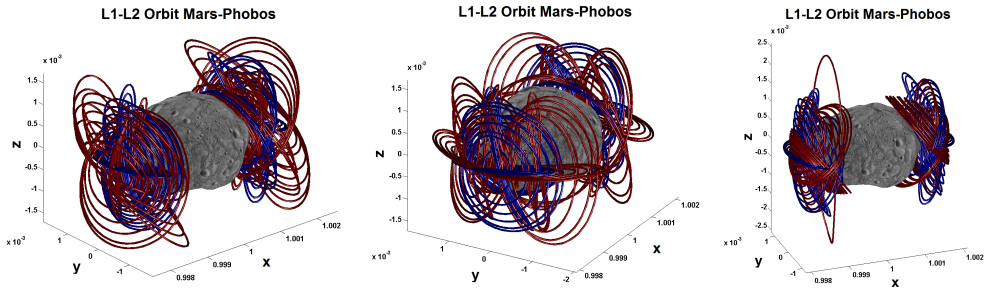

Figure 5.51: **Periodic artificial LPOs in the Mars-Phobos CR3BP-GH.** Summary of the POs (brown) obtained by displacement of the four families of POs around each LP of the CR3BP-GH (blue) with constant acceleration ($1 m/s^2$) along all coordinate axes directions (on the left directions $\pm\hat{\mathbf{x}}$, in the center directions $\pm\hat{\mathbf{y}}$, on the right directions $\pm\hat{\mathbf{z}}$). Phobos real shape.

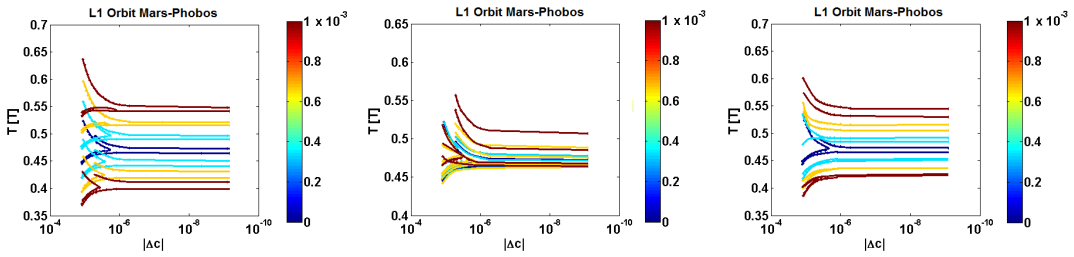

Figure 5.52: **Periodic artificial LPOs in the Mars-Phobos CR3BP-GH.** Characteristic curves of the period of the four families of POs around L_1 in the CR3BP-GH-CA, parameterized by the differential Jacobi integral with respect to the current LP. Constant acceleration magnitude (m/s^2) along all coordinate axes directions (on left directions $\pm\hat{\mathbf{x}}$, in the center directions $\pm\hat{\mathbf{y}}$, on the right directions $\pm\hat{\mathbf{z}}$).

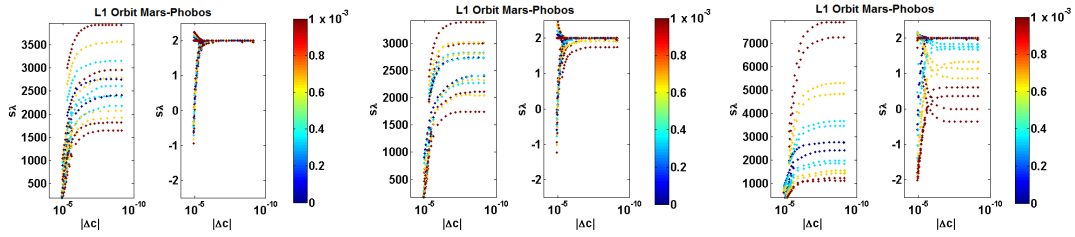

Figure 5.53: **Periodic artificial LPOs in the Mars-Phobos CR3BP-GH.** Stability properties (stability indexes of the two non-unit couples of eigenvalues of the monodromy matrix) of the four families of POs around L_1 in the CR3BP-GH-CA, parameterized by the differential Jacobi integral with respect to the current LP. Constant acceleration magnitude (m/s^2) along all coordinate axes directions (on left directions $\pm\hat{\mathbf{x}}$, in the center directions $\pm\hat{\mathbf{y}}$, on the right directions $\pm\hat{\mathbf{z}}$).

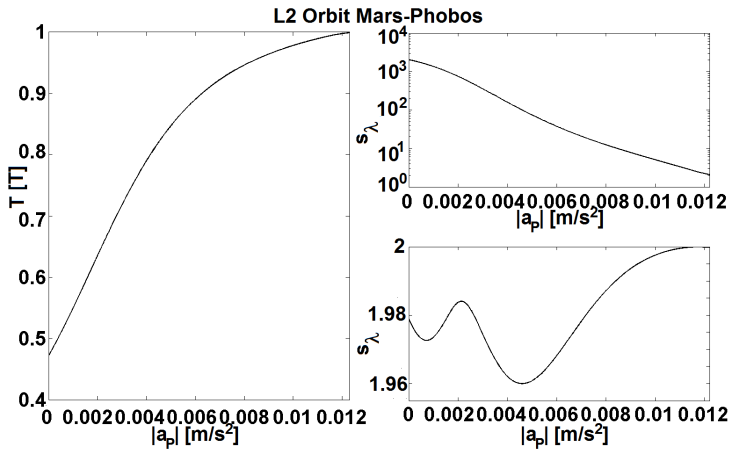

Figure 5.54: **Periodic artificial LPOs in the Mars-Phobos CR3BP-GH.** Example of one natural medium-size periodic LPO of the family A around L_2 modified by different levels of constant acceleration magnitude along the direction $-\hat{\mathbf{x}}$: period and stability properties (stability indexes of the two non-unit couples of eigenvalues of the monodromy matrix).

levels. The first family is similar to the Halo orbits (Southern for $+\hat{\mathbf{z}}$), and the LPOs of the second family are distorted and perfectly lie on the y-z plane, as we see in Fig.5.49-5.51.

5.4.3 Applications

The addition of a constant acceleration around Phobos has revealed some interesting mission opportunities.

Fig.5.52 provides the characteristics curves of the period of the ALPOs. As visible also from Fig.5.45 and Fig.5.54, the NC at a fixed differential energy makes the period of the POs to be very sensitive to the NC. In particular, since the dimension of the manifold of the LPOs is constrained due to the proximity of Phobos, the range of periods of the natural LPOs is limited (see Fig.4.63), and the addition of constant low-thrust allows cheap artificial LPOs to be obtained with period equal to the 2:1 orbital overresonance of Phobos around Mars. This means that they remain periodic also in the elliptical real scenario, which could be an advantage for designing the insertion maneuvers between the mission segments interfacing with such ALPOs.

Fig.5.53 provides the characteristics curves of the stability properties of the ALPOs. Thrusting away from Phobos makes all the POs more unstable, while thrusting towards Phobos lowers the max Floquet stability index[11]. Thrust in the tangential direction makes the dynamical substitutes of the families A and C more stable, and the ones of the families B and D more unstable. Vertical thrust makes the families A and B respectively more stable and unstable, while the family C is more stable with a negative displacement, and both stability indexes of the families D are lowered. In particular this family eventually retains a central part.

[11]The second stability index of the family D becomes more unstable.

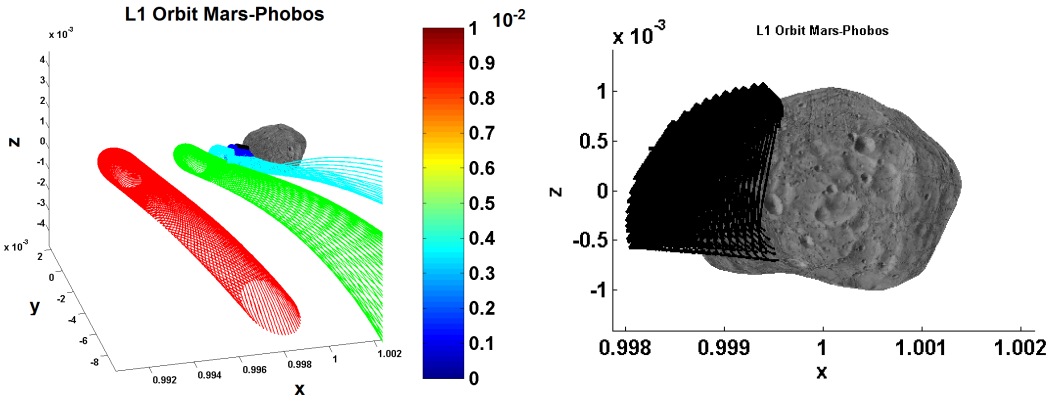

Figure 5.55: **Landing on Phobos through the Invariant Manifold of the family A of periodic artificial LPOs around L_1 of the Mars-Phobos CR3BP-GH.** On the left, trajectories of the inside branch of the unstable IMs of a medium energy PO of the family A around L_1 of the CR3BP-GH-CA, modified by different levels of constant acceleration magnitude (m/s^2) along $+\hat{\mathbf{x}}$ (propagation time of 2 PO periods). On the right, trajectories of the inside branch of the POs of the family A around L_1 of the CR3BP-GH-CA, at a constant acceleration magnitude of $1mm/s^2$ along $+\hat{\mathbf{z}}$. Phobos real shape.

Therefore, with the addition of this simple thrust profile, despite the LPOs remain unstable, it is remarkable to underline that the Floquet stability index could be massively lowered with the thrust required to displace the LP far from Phobos. This has a great impact on the frequency demand for the GNC subsystem, reducing the duty cycle up to the 25% for ALPOs displaced at an altitude over $60km$ from Phobos along the Mars-Phobos radial direction. In particular in Fig.5.54, the trans-Phobos ALPOs over the $70km$ altitude boundary of the Lyapunov stability region of the AEPs (the tip of the right leaf of Fig.5.5) become Floquet stable, while stable ALPOs along the y-axis are obtained displacing the equilateral LPs.

Finally, displacing LPOs away from the natural SOI, in addition to reducing instability, it has other important advantages. Indeed, all the problems of the dynamical modeling of the relative motion in proximity of this moon are related to the collapse of the realm of attraction of Phobos, therefore the manifold of LPOs is already too close in comparison to common interplanetary spacecraft operations. Therefore, pushing inward Phobos with a simple constant propulsion profile artificially enlarges the Phobos' SOI, and there is a great advantage not only for mission operations constraints and lighting condition requirements, but in particular for the computational load of tracking these orbits: the effect of Phobos' gravity field quickly lowers with the distance, so the convergence of the solution of the LPOs (and so its reliability) will be obtained with a far lower order of the truncated GHs model to be used in the NC.

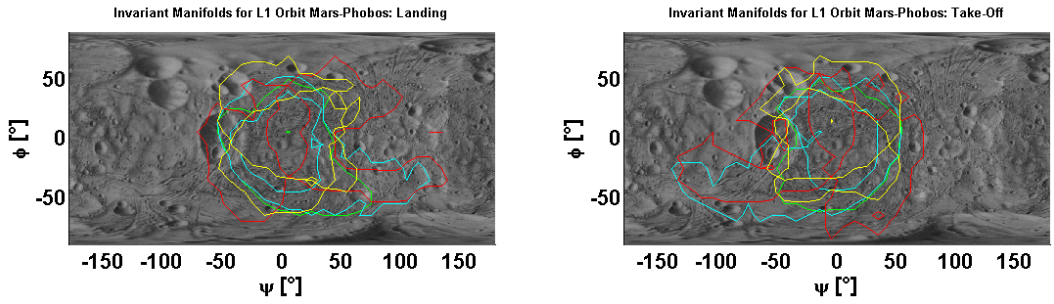

Figure 5.56: **Landing/Take-Off to/from Phobos through the Invariant Manifold of the L_1 family A of periodic artificial LPOs of the Mars-Phobos CR3BP-GH.** Region of possible landing/take-off sites, for orbits that do not intersect Phobos' real shape, through the IM of the family A of POs around L_1 of the CR3BP-GH-CA. Constant acceleration magnitude of $1mm/s^2$ along all coordinate axes directions (green line for CR3BP-GH, cyan for directions $\pm\hat{\mathbf{x}}$, red for directions $\pm\hat{\mathbf{y}}$, yellow for directions $\pm\hat{\mathbf{z}}$). Phobos real shape.

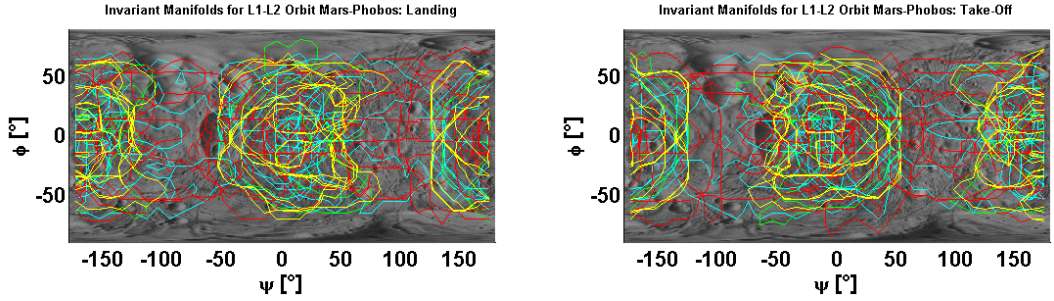

Figure 5.57: **Landing/Take-Off to/from Phobos through the Invariant Manifold of the L_{1-2} families of periodic artificial LPOs of the Mars-Phobos CR3BP-GH.** Region of possible landing/take-off sites, for orbits that do not intersect Phobos' real shape, through the IM of all the families of POs around L_{1-2} of the CR3BP-GH-CA. Constant acceleration magnitude of $1mm/s^2$ along all coordinate axes directions (green line for CR3BP-GH, cyan for directions $\pm\hat{\mathbf{x}}$, red for directions $\pm\hat{\mathbf{y}}$, yellow for directions $\pm\hat{\mathbf{z}}$). Phobos real shape.

5.4.4 Invariant Manifolds of the Periodic Libration Point Orbits of the Mars-Phobos CR3BP-GH with Constant Acceleration

The IMs of the artificial periodic LPOs have been computed in this section with the procedure explained in section B.8.2. These trajectories require the same constant acceleration maintained by the propulsion system to leave and approach the ALPO.

The analysis of the AIMs has revealed that this simple control law, directed along an appropriate fixed direction, allows to enlarge the region of landing and take-off sites to cover all the longitude range. This is realized mostly with thrust along $\pm\hat{\mathbf{y}}$, but also inward Phobos. Also the limit of the latitudes can be raised with thrust along $\pm\hat{\mathbf{z}}$, to become closer to the polar zones, that could be enclosed when considering also the

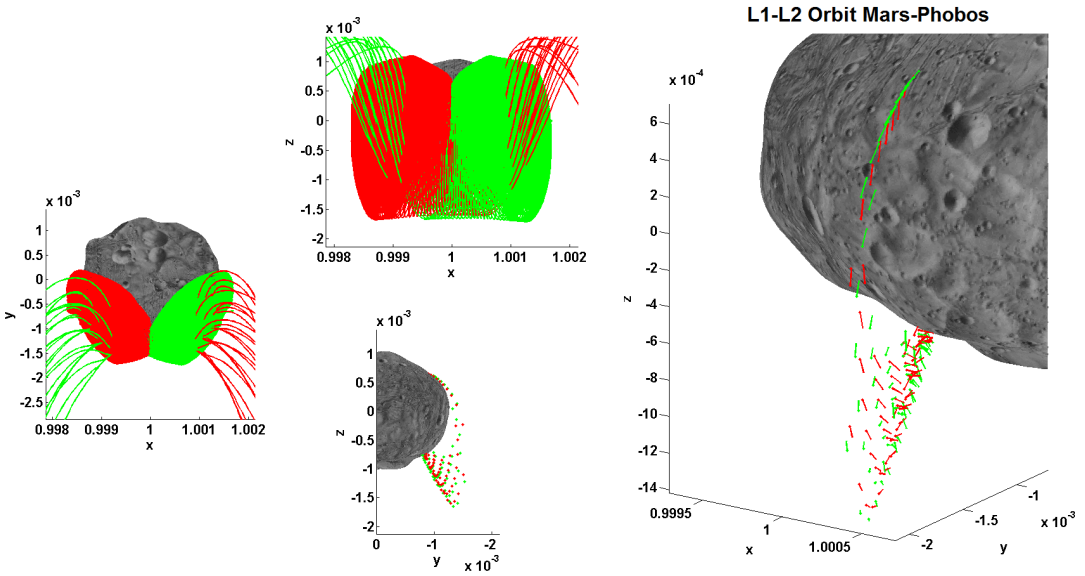

Figure 5.58: **Heteroclinic connections around Phobos through the Invariant Manifold of the L_{1-2} families of periodic artificial LPOs of the Mars-Phobos CR3BP-GH.** Trajectories from the POs of the family A around L_1 (red) and trajectories to the POs of the family A around L_2 (green) of the CR3BP-GH-CA, at constant acceleration magnitude of $1mm/s^2$ along $-\hat{\mathbf{y}}$, up to their intersection with Phobos or with the Poincaré section $x = 1-\mu$. Particular of the final conditions on the Poincaré section. Phobos real shape.

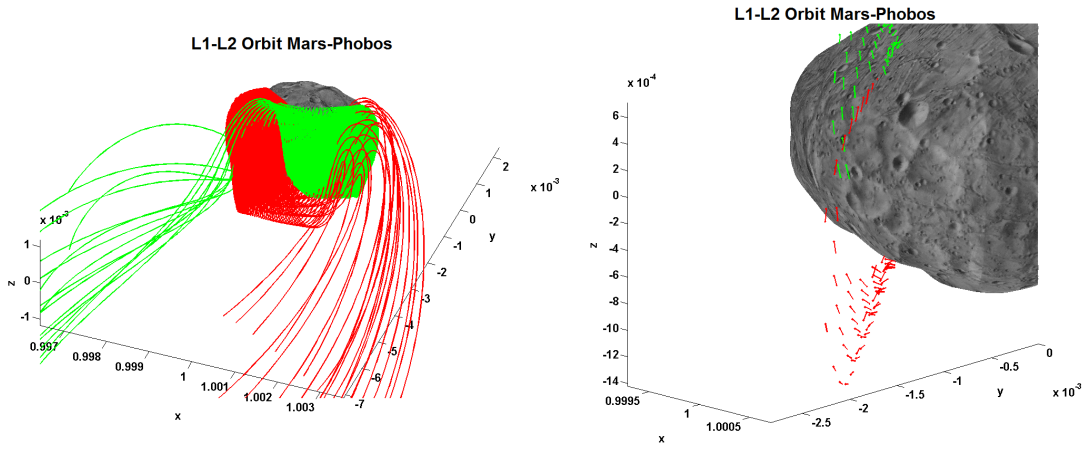

Figure 5.59: **Heteroclinic connections around Phobos through the Invariant Manifold of the L_{1-2} families of periodic artificial LPOs of the Mars-Phobos CR3BP-GH.** Trajectories from the POs of the family A around L_1 (red) and trajectories to the POs of the family C around L_2 (green) of the CR3BP-GH-CA, at constant acceleration magnitude of $1mm/s^2$ along $-\hat{\mathbf{y}}$, up to their intersection with Phobos or with the Poincaré section $x = 1-\mu$. Particular of the final conditions on the Poincaré section. Phobos real shape.

families of artificial QPOs. This is presented in Fig.5.55-5.57, and Fig.D.97-D.100.

The displacement of the LPOs away from Phobos (families B and D, only with high-thrust) and along the tangential axis (families C and D, only with high-thrust) enables artificial heteroclinic connections between two manifolds that were not possible with the natural dynamics. These trajectories could be exploited for fast orbital displacements around the two sides of Phobos for close-range mission segments. However, Fig.5.58-5.59 display just an example, and the identification of possible heteroclinic connections, that requires to tune the matching of the interfacing condition of two stable and unstable manifolds, of two orbits at same energy, of families around two different LPs, has not been undertaken. In particular, this could be obtained further artificially, which is by introducing also an impulsive maneuver to match slightly different velocities on a suitable Poincaré map.

5.5 Martian Formation Flying to Orbit around Phobos

Following the perspective introduced in section 5.1 of flying in formation with Phobos, in section 5.2 the most simple trajectory was analyzed, which is a fixed hovering in the orbital and figurative frame of Phobos. In this section, the analysis of more refined trajectories is conducted, which is the use of the classical relative orbits of FF missions. The artificial realization of these guidance laws requires the continuous compensation of Phobos' gravity, thus either high distances or short time windows are required for these orbits to limit the fuel consumption. Throughout this section, the model used to compute the reference signal of the relative state with respect to Phobos' Hill's frame, could be directly stated as a Martian 2B FF (see section 6.1.1), assuming the presence at minimum of a thrust profile that counteracts the 3B gravity of Phobos.

The orbits analyzed in this section are in a crossover between the artificial orbits that characterize all this chapter, and the natural dynamical substitutes of 2B FF in the 3B dynamics, the Quasi-Satellite orbits, that will be presented in the next dedicated chapter 6. In particular, this section will refer to some of the topics of natural FF that are presented in more detail in chapter 6. Furthermore, the analysis of the artificial FF orbits undertaken in this chapter is related to their possible implementation in the ESA mission Phootprint, in place of the QSOs[12]. A detailed outline of the phases and constraints of this mission is reported in section 6.4.1.

5.5.1 Artificial J_2-invariant FF around Phobos

In the pre-phase A assessment study in [144] of Phootprint, the mission analysis is conducted. For the operative and observation phase, the artificial FF around Phobos is probed. This requires the continuous compensation of Phobos' gravity. The thrust required by the liquid propulsion system is deemed feasible with the current spacecraft

[12]This research was conducted during an internship in Airbus Defence & Space, Stevenage.

mass, and the inevitable problem is the cumulated time for the Δv.

The artificial guidance laws investigated, for the relative orbits in Phobos' Hill's and BCBF frame, are the Keplerian epicycles[13]. These periodic orbits are introduced in detail in section 6.1.1.1, and an example is provided in Fig.6.1. The required operative orbit for Phootprint shall provide global observation, with nadir-pointing, of Phobos to characterize at least the 50% of its surface (with a goal of 100%), with a resolution of meters and a local Solar elevation angle between [30°-60°], and within a limit of 200 days.

The second problem is the fact that these Keplerian relative orbits are tidally-locked with Phobos' BCBF frame, as it is explained in section 6.1.1.1, and so would be their ground-track on the moon's surface. This is the same situation of geosynchronous orbits. Hence, orbital maneuvers must be performed to change the formation periodically. This is a second cost in the Δv budget in addition to the first, already high due to Phobos' compensation. Therefore, these artificial solutions, which are analytically simple since they are periodic guidance signals, have been disregarded, in favor of realizing the operative orbit with a Quasi-Satellite orbit. This class of orbits is analyzed in chapter 6: their motion is quasi-periodic and complicated to be described analytically, but they have the advantage to be natural, mostly stable, and to provide a fast complete coverage of Phobos' surface.

However, the conclusion drawn lacks of a consideration: from the analysis of the orbital perturbations conducted in section 2.4, Mars J_2 is another player at large distances from Phobos. The differential J_2 perturbation is a famous destabilizing effect for FF. But there are particular solutions: the J_2-invariant formations [155], which are presented in section 6.3.2. These naturally perturbed quasi-periodic orbits have the property of maintaining the Keplerian epicycle, but they have an additional natural frequency. This is a precession on the orbital plane, which makes the epicycle to naturally rotate. Hence, they work exactly like a Quasi-Satellite orbit, enabling a global coverage of the moon's surface. In particular, they are highly inclined, allowing observations of high latitudes of Phobos, up to 75° on the cis/trans-side, and 60° on the leading/trailing-side. However, section 6.3.2 explains that the solution of these orbits is obtained at first-order. Thus, J_2-invariant formations eventually will drift away along the transversal direction θ for high propagation time, and for a high J_2 [155].

An example of the J_2-invariant formations around Phobos, which will require the implicit compensation of the moon's gravity, is provided in Fig.6.13. The formation rotates but it will take 1,305 periods = 417 days to complete a full precession revolution. This is too long both for the mission's time constraint and for the implicit Δv due to Phobos' gravity.

[13]Please note that in this section, formations will be referred with the 1:2 size of their nominal epicycle on the orbital plane.

5.5.2 Artificial-J_2 J_2-invariant FF around Phobos

In section 5.5.1, the precession rate of the artificial J_2-invariant FF, under the natural oblateness of Mars, is equal to the secular derivative of ω, and is linear with the J_2 magnitude. The idea pursued in this section is that, since the natural J_2 effect is an analytically known thrust profile that makes an epicycle's line of nodes to rotate, to increase the precession rate we can just artificially amplify its effect. This will be a second thrust and related Δv cost to add to the compensation of Phobos' gravity. The point is that even if there is a second Δv, the decrease of the time required for the full coverage, provided by this idea, will lower the first Δv. These new reference orbits are named artificial-J_2 J_2-invariant FF. Their computation is immediate, since they are the same of section 5.5.1 in the dynamics where Mars J_2 is a free parameter. The objective of this section is to quantify the new thrust required, and to evaluate the observation capabilities of these solutions.

5.5.2.1 Model of the Dynamics, Guidance, and Control

In this section, the thrust required to reproduce a relative motion of the artificial-J_2 dynamics, in the natural Mars-J_2 dynamics, is derived. The nomenclature used in this section is the following. ρ is the relative position in Phobos' Hill's frame, which is used to define the orbit, while x is the absolute position (thus for the spacecraft is a function of ρ). The angular velocity of the Hill's frame is ω. The Mars Newtonian gravity is a^G, the Mars J_2 gravity is a^{J_2}, and the Phobos gravity is a^g. The apparent acceleration is a^A, and the propulsive acceleration is t. The subscripts refer to Phobos (P), spacecraft (S), and target (T).

Eq.5.39 provides the equations of motion of the relative orbital dynamics with J_2 in Phobos' Hill's frame[14]. The relative motion comes from the apparent acceleration and the differential terms.

$$\ddot{\rho} = -a^A(\omega, \dot{\omega}, \rho, \dot{\rho}) + \left(a_S^G(\rho, x_P) - a_P^G(x_P)\right) + \left(a_S^{J_2}(\rho, x_P) - a_P^{J_2}(x_P)\right) + a^g(\rho) + t \quad (5.39)$$

In our case, Phobos' gravity is always compensated, so $t = -a^g$ in these dynamics.

Now we need a target model with an amplified $K \times J_2$.

$$\ddot{\rho} = -a^A(\omega, \dot{\omega}, \rho, \dot{\rho}) + \left(a_S^G(\rho, x_P) - a_P^G(x_P)\right) + \left(a_S^{KJ_2}(\rho, x_P) - a_P^{KJ_2}(x_P)\right) \quad (5.40)$$

In this model, the J_2-invariant solution is the target solution ρ_T. The aim is to maintain the same relative motion in the real dynamics. To make ρ_T a solution in the real dynamics with $1 \times J_2$, there is the need to provide an additional thrust (recall we already have to account for a $t = -a^g$).

[14] Recall from section 3.3.2 that the Hill's frame is not Keplerian but osculating with J_2.

$$\ddot{\rho}_T = -a^A(\omega, \dot{\omega}, \rho_T, \dot{\rho}_T) + \left(a_S^G(\rho_T, x_P) - a_P^G(x_P)\right) + \left(a_S^{J_2}(\rho_T, x_P) - a_P^{J_2}(x_P)\right) + a^g(\rho_T) + t \tag{5.41}$$

The thrust will be the difference between the acceleration in target and real dynamics, evaluated for the target solution.

$$\begin{aligned} t = &- a^g(\rho_T) + \\ &+ \left[-a^A(\omega_T, \dot{\omega}_T, \rho_T, \dot{\rho}_T) + a^A(\omega, \dot{\omega}, \rho_T, \dot{\rho}_T)\right] + \\ &+ \left[\left(a_S^G(\rho_T, x_{P,T}) - a_P^G(x_{P,T})\right) - \left(a_S^G(\rho_T, x_P) - a_P^G(x_P)\right)\right] + \\ &+ \left[\left(a_S^{KJ_2}(\rho_T, x_{P,T}) - a_P^{KJ_2}(x_{P,T})\right) - \left(a_S^{J_2}(\rho_T, x_P) - a_P^{J_2}(x_P)\right)\right] \end{aligned} \tag{5.42}$$

Thus, in the analytical thrust profile of Eq.5.42 there are residual differential terms not only for J_2, but also for Mars' gravity and apparent acceleration, because in the two models Phobos moves in different orbits, $x_P \neq x_{P,T}$, and also for its Hill's frame rotation ($\omega \neq \omega_T$). To gain more insight, the thrust definition is rearranged, changing the last term and introducing the "physical" $(K-1)$ differential J_2 effect that we want to provide. The other three terms are "modeling" perturbations of the reference signal.

$$\begin{aligned} t = &- a^g(\rho_T) + (K-1)\left(a_S^{J_2}(\rho_T, x_P) - a_P^{J_2}(x_P)\right) + \\ &+ \left[-a^A(\omega_T, \dot{\omega}_T, \rho_T, \dot{\rho}_T) + a^A(\omega, \dot{\omega}, \rho_T, \dot{\rho}_T)\right] + \\ &+ \left[\left(a_S^G(\rho_T, x_{P,T}) - a_P^G(x_{P,T})\right) - \left(a_S^G(\rho_T, x_P) - a_P^G(x_P)\right)\right] + \\ &+ \left[\left(a_S^{KJ_2}(\rho_T, x_{P,T}) - a_P^{KJ_2}(x_{P,T})\right) - K\left(a_S^{J_2}(\rho_T, x_P) - a_P^{J_2}(x_P)\right)\right] \end{aligned} \tag{5.43}$$

5.5.2.2 Reference Orbit

The first step is to validate the target solution, which is a J_2-invariant formation around Phobos with amplified J_2. A sample orbit used throughout this section is a $50x100km$ formation with $10 \times J2$. This is visible in Fig.5.60.

The nadir-pointing geometrical observation capabilities are presented in Fig.5.61. In this section, Phobos is always considered with its mean sphere. The sample orbit is able to cover Phobos' surface in a reasonable time of 131 periods = 41 days. High latitudes are obtained as mentioned previously, and with different ranges. The vertical dimension of the formation is roughly 3.6 times the minimum dimension, thus the range at high latitudes is higher than the limit of $150km$ suggested for the observation phase in [144].

Compared with the solution shown previously in Fig.6.13 at $1 \times J_2$, a problem seems to arise. The nonlinear effects neglected in the algorithm to compute the J_2-invariant

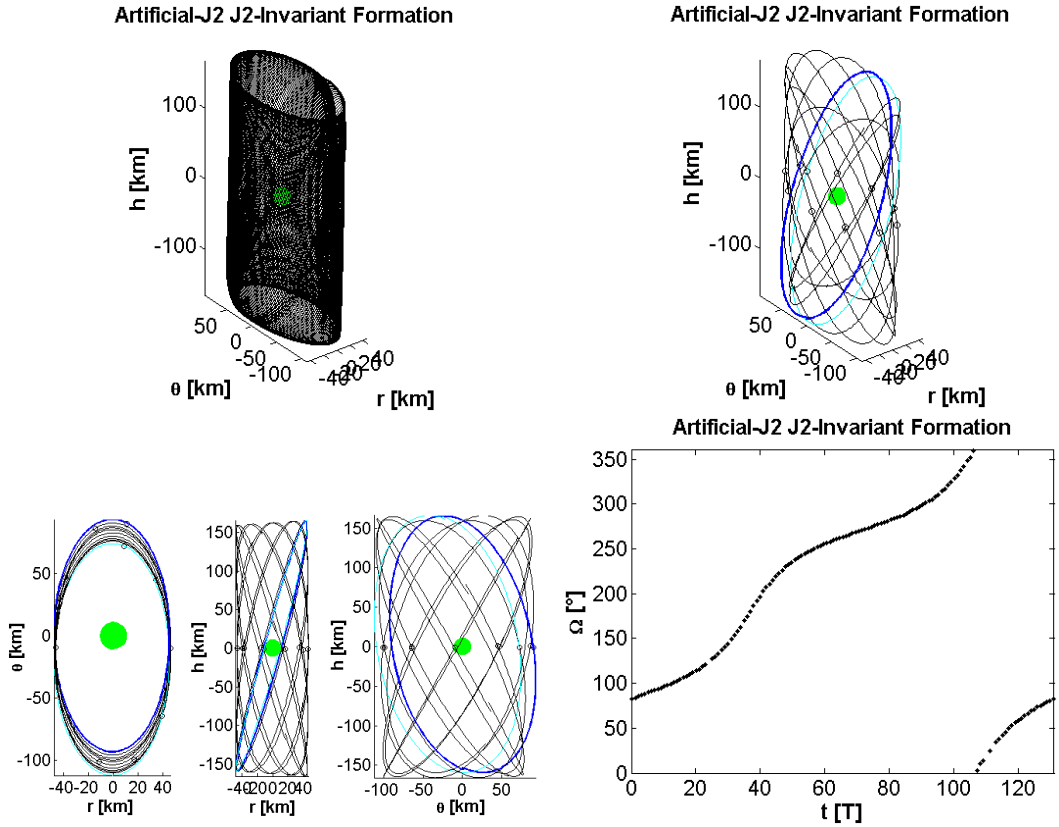

Figure 5.60: **Artificial-J_2 J_2-invariant FF around Phobos.** $10\times J_2$-invariant $50x100km$ formation around Phobos. The simulation covers 131 periods to achieve one precession revolution of the relative line of nodes. On the top, full orbit and sampled orbit with frequency 1:10. Black circles identify the relative ascending node. Starting/final epicycle in blue/cyan. Phobos mean sphere in green. On the bottom, projections on the coordinate planes, and discrete profile of the right ascension of the relative ascending node of the orbit.

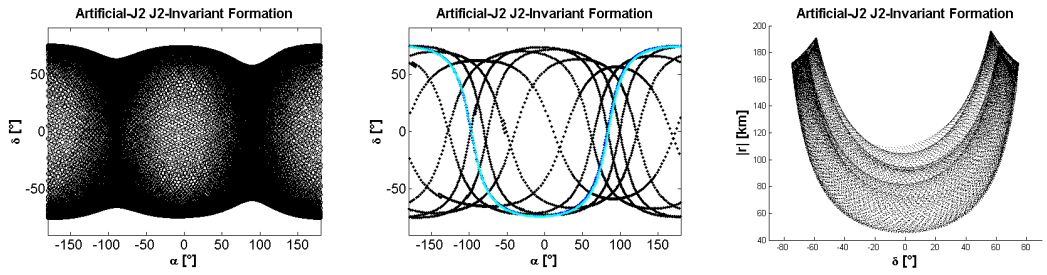

Figure 5.61: **Artificial-J_2 J_2-invariant FF around Phobos.** $10\times J_2$-invariant 50x100km formation around Phobos, simulated for 1 precession revolution. On the left, ground-track (nadir points) on mean spherical Phobos (right ascension considered as longitude, declination considered as latitude) for the full orbit, sampled 1:10 orbit. On the right, range distance envelope.

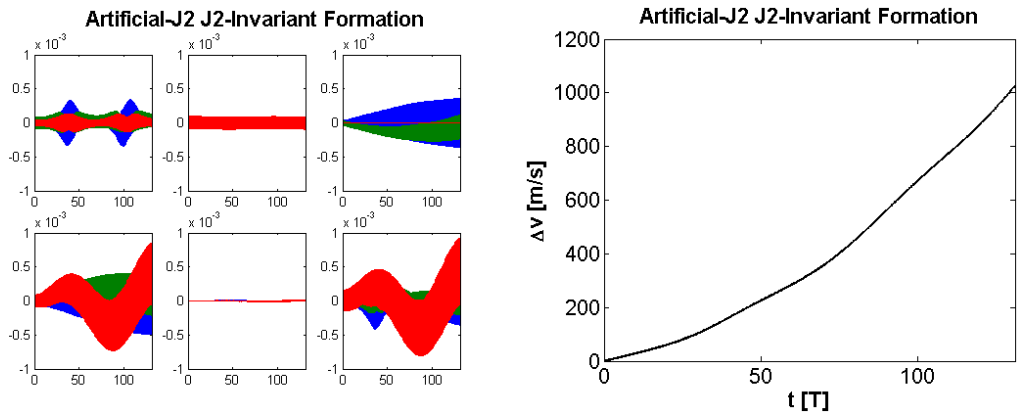

Figure 5.62: **Artificial-J_2 J_2-invariant FF around Phobos.** $10\times J_2$-invariant $50x100km$ formation around Phobos, simulated for 1 precession revolution. On the left, propulsive acceleration profile. The thrust components are expressed in Phobos $1\times J_2$-osculating Hill's frame: r blue, θ green, h red. The first five thrust windows are related to each of the terms of the Eq.5.43, and the last window shows their resultant. On the right, cumulated Δv over time in orbital periods.

formation[15] start to be evident with $10\times J_2$ and 131 periods. The final epicycle has a drift of $20km$ along $-\theta$. This affects slightly range and maximum latitude of the nadir on the leading/trailing sides in opposite ways, as visible in Fig.5.60-5.61.

5.5.2.3 Control Consumption

The thrust required to maintain the sample formation is evaluated with the analytical formula of Eq.5.43. Then, this is integrated to yield the Δv consumption over one full precession revolution. The results are represented in Fig.5.62.

The conclusions derived are two. First of all, the "modeling" thrust terms are divergent, in particular the one of the Mars' gravity, but also the one of the apparent term, while the amplitude of the $K\times J_2$ term is far lower. This divergence is explained by the fact that the target derived is drifting away as explained previously in section 5.5.2.2. However, this does not affect the derivation of the major conclusion looked for at this stage. The "physical" $(K-1)\times J_2$ term and the "modeling" Mars' gravity term are of the same order of magnitude of Phobos' gravity, and they definitely do not offer a lucky compensation between each other[16]. Thus the cost of maintaining the artificial $10xJ_2$-invariant sample formation is roughly 2-3 times the cost of compensating only Phobos' gravity. The latter is $215m/s$ for our simulation of 41 days ($5.3m/s/day$) and for a Phootprint mass of $2,000kg$ requires maximum $0.7N$ with the natural continuous profile in feedforward. If we neglect the evident amplification of the cumulated Δv profile due to the target's drift, taking the double of the middle period's value, this

[15]The algorithm is presented in section 6.3.2. In particular, in this section the NL system of Eq.6.10 is solved with all the terms, and not like in the approximated version of Eq.6.9.

[16]It is worth to note that the r-θ components of Mars and apparent forces do well compensate each other. The major component remains the vertical component of the differential Mars' gravity between the two models.

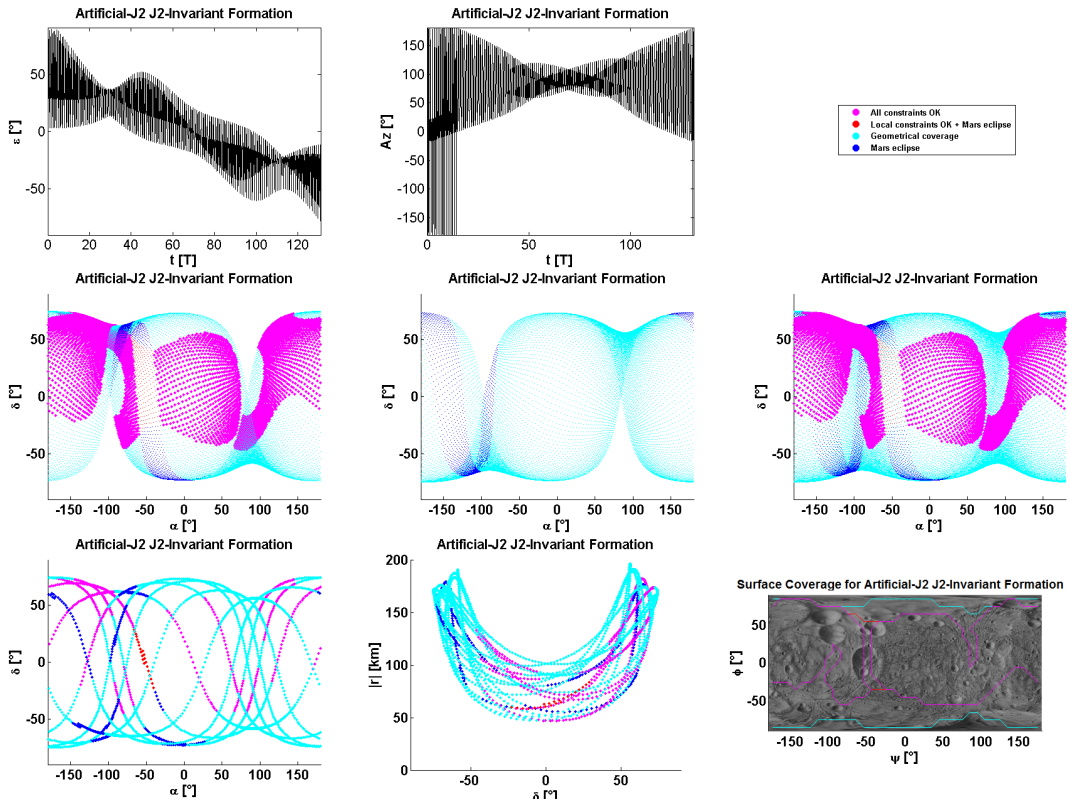

Figure 5.63: **Artificial-J_2 J_2-invariant FF around Phobos.** $10\times J_2$-invariant $50x100km$ formation around Phobos, simulated for 1 precession revolution. Start at local noon, mid-summer. On the top, elevation and azimuth angles of the nadir point. The following graphs represent the related surface coverage, which is represented by a sample of nadir points, whose color is discriminated in the legend by the illumination conditions. The three graphs in the center, starting from the left, are related to the first half of the orbit, the second half, and the full orbit. The following graphs on the bottom are related to the full orbit sampled 1:10, with the related range envelope. The final graph is the cumulated area, that represents the surface coverage, for observation under the illumination constraints, of the orbit, by discretization with boxes of 10°-10°.

provides an estimation without drift of $652m/s$ in 41 days, and a maximum thrust lower than $1.5N$. The cost is greater than the one that should be required by a sequence of QSOs[17], and the Phootprint mass budget is already close to an acceptable limit [144].

5.5.2.4 Applications

The ground-track capabilities of the sample formation have been highlighted in Fig.5.61, and they are greatly satisfying: nadir points cover 97% of the surface in just 41 days. However, as mentioned in section 5.5.1, for Phootprint there is a technical requirement given by ESA that actually drives the observation phase: the observation is viable only if the local elevation angle ϵ is between $+30°$ and $+60°$[18].

Thus the lighting conditions on the surface must be considered, and this analysis has

[17] In [144], the analysis of the QSOs suggests a sequence of 7 maneuvers of $\tilde{1}$0-20m/s, for a total of 60-80m/s. A more detailed analysis provides a figure of $18-40m/s$ for >55 days.

[18] This technical constraint can be considered as a Phobos' constrained eclipse.

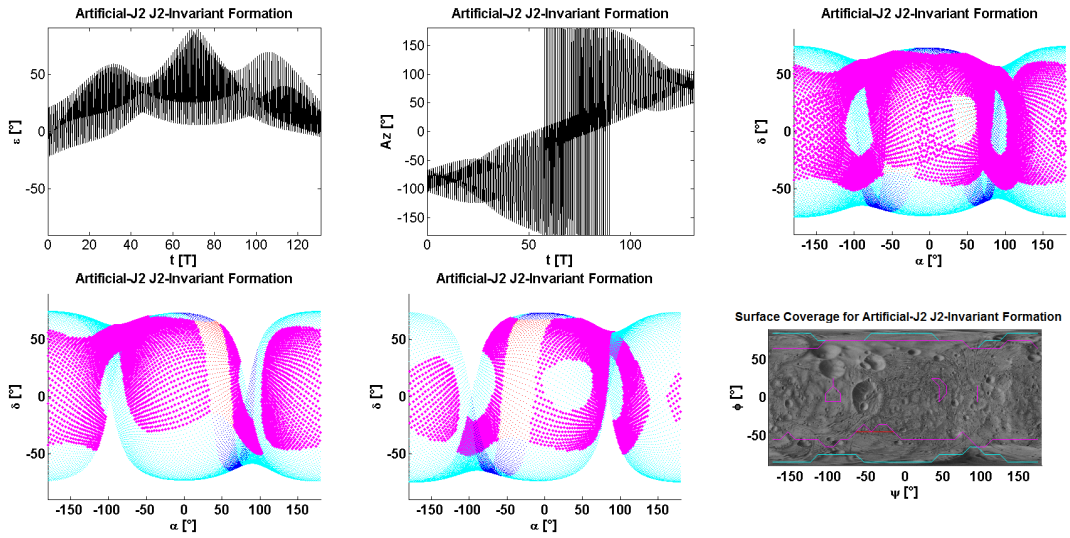

Figure 5.64: **Artificial-J_2 J_2-invariant FF around Phobos.** $10\times J_2$-invariant $50x100km$ formation around Phobos, simulated for 1 precession revolution. Start at local dawn, mid-summer. On the top, elevation and azimuth angles of the nadir point. Following graphs, from left to right, represent the surface coverage of the full orbit, the first half, and the second half. The final graph is the cumulated area, that represents the surface coverage, for observation under the illumination constraints, of the orbit, by discretization with boxes of 10°-10°.

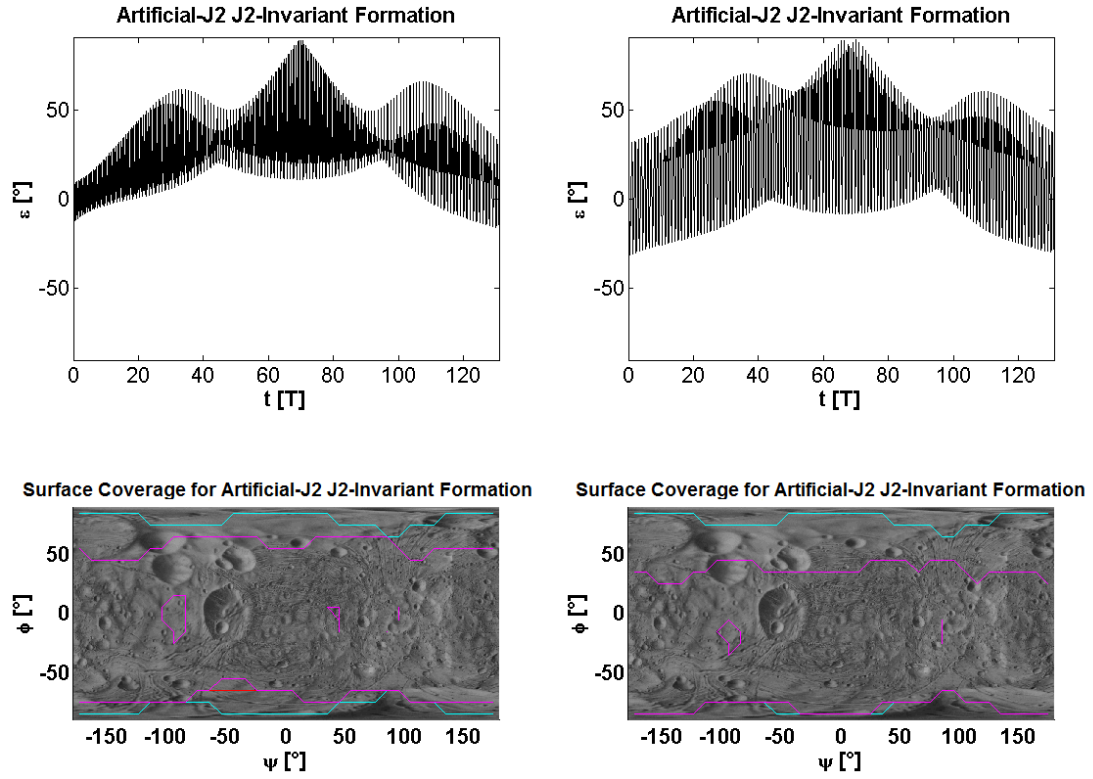

Figure 5.65: **Artificial-J_2 J_2-invariant FF around Phobos.** $10\times J_2$-invariant $50x100km$ formation around Phobos, simulated for 1 precession revolution. Start at local dawn, and, on the left, at fall equinox and, on the right, at winter solstice. On the top, elevation angle of the nadir point. On the bottom, surface coverage for observation under the illumination constraints, of the orbit, by discretization with boxes of 10°-10°.

already been conducted in section 2.6. In particular, recall that the Sun, as represented in Fig.2.26, follows a VDCO around Phobos' BCBF frame, with the period of Phobos revolution and the height depending on the Martian season. Thus, there are two phases to consider: the initial heliocentric anomaly of Mars, and the initial angle of the Sun in Phobos' Hill's frame. But this is actually a post-processing analysis, because the kinematics of the Sun do not significantly affect the orbital dynamics around Phobos (see Fig.2.13). The target orbit remains the same, and the two phases are varied to evaluate the lighting conditions encountered by the ground-track of the orbit during the simulation. In particular, the objectives are to calculate the local elevation angle of the nadir points of Fig.5.61, which measures if a Phobos' eclipse occurs, and to calculate if a Martian eclipse occurs. In this analysis, Phobos is approximated with its mean sphere.

The first attempt is to set the start of target orbit, where Phobos is at perimars and the spacecraft is on the cis-side, to be at local noon. Furthermore, the season is taken at a Solar longitude[19] of 145°. Thus, this is middle summer approaching fall equinox. In [144] an interval 145°-175° is specified for the QSO phase.

Fig.5.63 shows that the nadir points are in daylight for exactly half of the orbit simulated, so this $10 \times J_2$ enhanced precession is nearly resonant with the Sun. Since we are still in summer, high latitudes are observable at high range. The illumination conditions are satisfied for 65% of the surface, reduced to 61% for the Martian eclipses (in particular they happen when the spacecraft is over the Stickney crater). This figure of coverage is derived considering a homogeneous discretization of the surface in longitude-latitude with boxes of 10°-10°. In this sense, the FOV of the instruments (Narrow Angle Camera) in [144] is designed to be a 16° square at $100km$. Thus the swath span from the nadir point is 8°. Therefore, for the sample formation, 10° is conservative for high latitudes, where the swath becomes $> 12°$, and optimistic for lower latitudes, where the swath becomes $> 4°$.

From these results, the consideration is to wisely change the Solar phase. Starting at local dawn would maximize the coverage in the time window chosen, because the observation is enabled during all the single precession revolution. This is shown in Fig.5.64. Now the sample orbit covers 79% of the surface with the illumination constraints. The Martian eclipses always affect the cis-side observability during equinoctial seasons. A second swath on Stickney helps to increase its observability.

Another simulation is ran at the fall equinox and the winter solstice, whose results are represented in Fig.5.65. Starting at fall enhances the Southern observability, covering 81% of the surface with the illumination constraints, and Stickney is fully observable. Starting at winter allows to get rid of the Martian eclipses, and covers practically the South pole, but the global coverage is reduced to 72%. However this could be achieved also with a shorter period, like half a precession revolution, lowering the consumption.

[19] The Solar longitude's reference is 0° at the spring equinox.

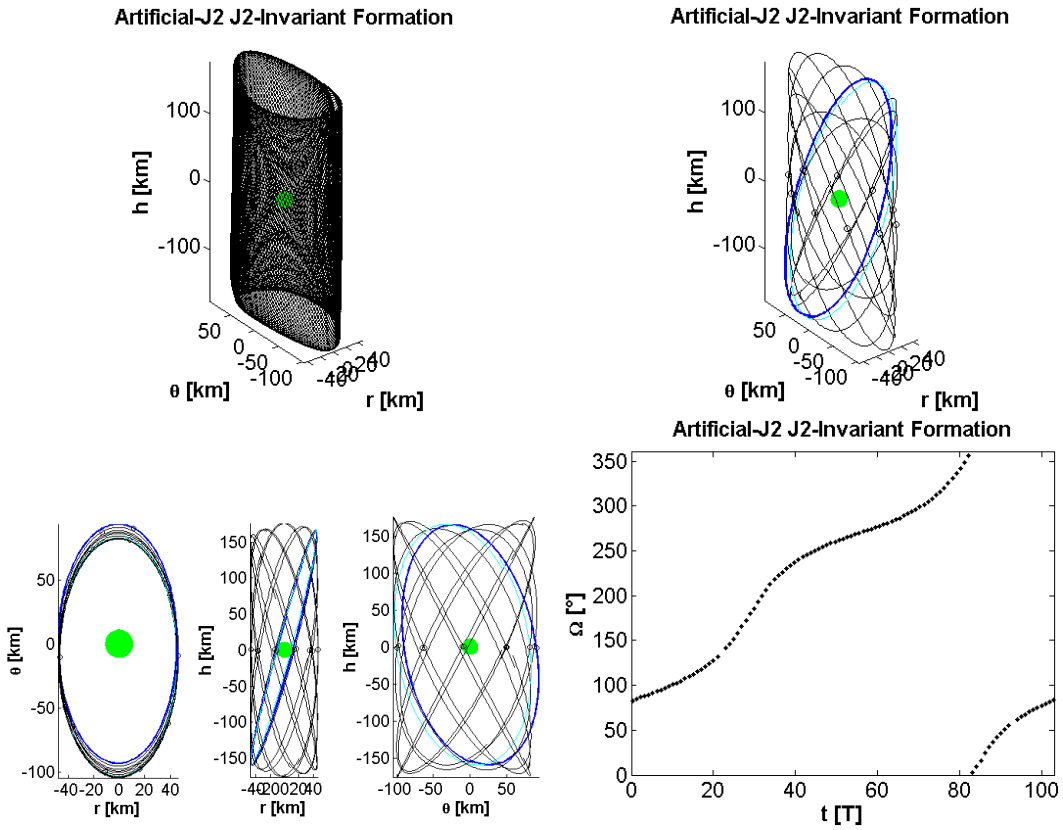

Figure 5.66: **Artificial-J_2 J_2-invariant hybrid FF around Phobos.** Hybrid $10\times J_2$-invariant $50x100km$ formation around Phobos with $r\theta$ compensation. The simulation covers 103 periods to achieve one precession revolution of the relative line of nodes. On the top, full orbit and sampled orbit with frequency 1:10. Black circles identify the relative ascending node. Starting/final epicycle in blue/cyan. Phobos mean sphere in green. On the bottom, projections on the coordinate planes, and discrete profile of the right ascension of the relative ascending node of the orbit.

5.5.2.5 Hybrid Realization

In [144] the analysis of the FF by compensation of Phobos' gravity is conducted in the linearized Clohessy-Wiltshire model. It is suggested that since the instability for 3D QSOs, in the 3B dynamics, develops in the transversal dynamics (see section 6.3.3), the compensation of Phobos' gravity could be reduced only to such direction of the Phobos' Hill's frame. The resulting orbit could be named either hybrid-artificial QSO or hybrid-artificial FF, since it is a crossover between the artificial FF investigated in this section, and the natural QSOs addressed in chapter 6.

This hint makes sense and has been tested with the sample $10 \times J_2$-invariant formation. However after half precession revolution, this hybrid-artificial QSO drifts away. The reason could be again due to the nonlinear terms, since the hint is based on the linearized FF. All the other combinations of partial compensation have been tested (which are: r,h,$r\theta$,rh,θh) but none of them worked alone. In addition, also all the six permutations have been tested considering the components in the spacecraft's Hill's frame. It happened that actually compensating $r\theta$ in this reference frame (so just not

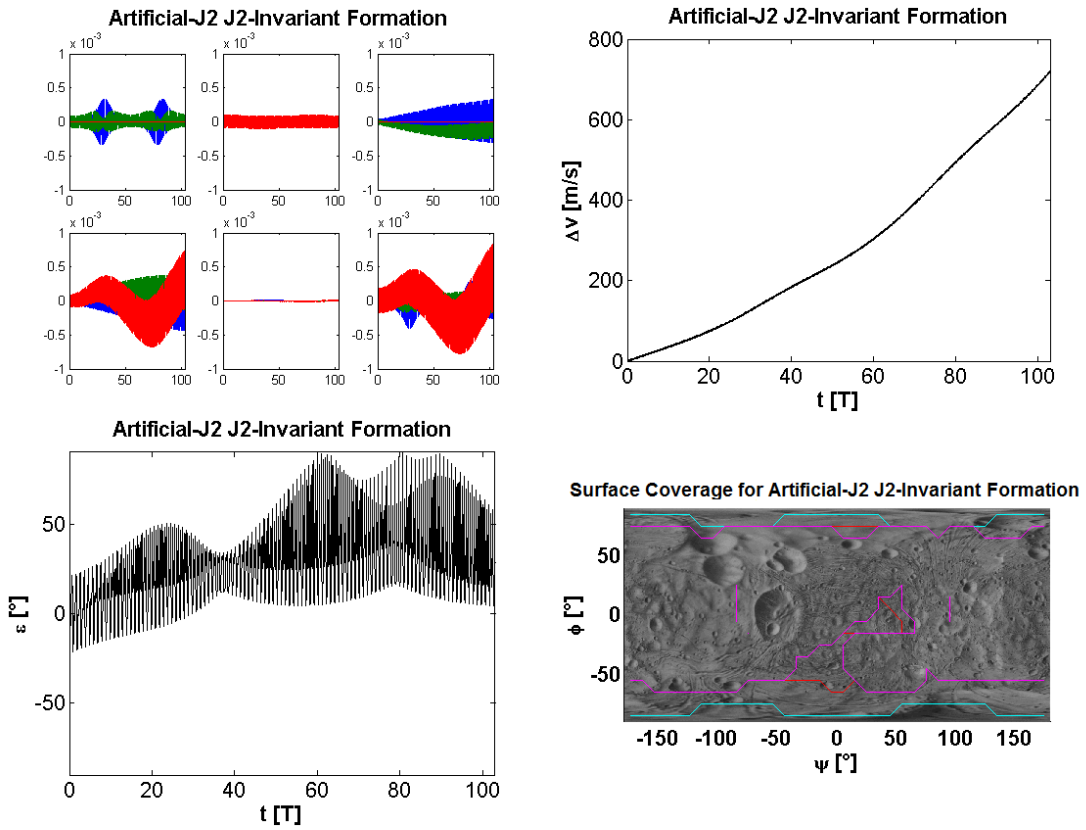

Figure 5.67: **Artificial-J_2 J_2-invariant hybrid FF around Phobos.** Hybrid $10\times J_2$-invariant $50x100km$ formation around Phobos with $r\theta$ compensation. On the top, propulsive acceleration profile and cumulated Δv over time in orbital periods. On the bottom, simulation for 1 precession revolution, with start at local dawn, mid-summer. Related elevation angle of the nadir point, and surface coverage for observation under the illumination constraints, of the orbit, by discretization with boxes of 10°-10°.

compensating the vertical component h) still provides a classical J_2-invariant motion.

The artificial-J_2 J_2-invariant $(r\theta)$-hybrid realization of the sample formation is shown in Fig.5.66. In particular, the θ-drift due to the nonlinear terms is now erased, and the epicycle oscillates in the Phobos' Hill's frame θ-direction with an amplitude of $10km$, just like a QSO. Second of all, the inclusion of a partial component of Phobos' gravity in the equations of motion of Eq.5.39[20] naturally speeds up the precession of the epicycle, just like the QSOs. Hence, a shorter period, by 21%, is now required by the sample formation to achieve a full precession lap.

From the consumption point of view, this solution offers a slightly cheaper cost since one component of Phobos' gravity is not compensated. As visible in Fig.5.67, despite the θ-drift is erased, the leftover θ-oscillation is still responsible for an increase of the "modeling" thrust terms. The main advantage is the reduced period. With the same consideration made in section 5.5.2.3, it could be estimated that without this oscillation

[20]The component to be considered in Eq.5.39 is the projection on the three components r,θ,h of Phobos' Hill's frame, of the Phobos' gravity acting on the spacecraft along the vertical component h of the spacecraft's Hill's frame.

Table 5.1: **Artificial-J_2 J_2-invariant FF around Phobos.** Consumption and surface coverage for observation under the illuminations constraints, for artificial-($K \times J_2$) J_2-invariant formations of different size, simulated for 1 precession revolution, and start at local dawn, in summer.

$K \times J_2 \backslash$ QSO	$25x50km$	$50x100km$	$100x200km$
5	$1649m/s$ 83%	$1304m/s$ 81%	$1375m/s$ 77%
10	$830m/s$ 80%	$652m/s$ 79%	$925m/s$ 78%
100	$308m/s$ 34%	$472m/s$ 35%	$833m/s$ 31%

the Δv for one revolution would be $500m/s$.

From the observability point of view, Fig.5.67 proves that the smaller period does not allow to achieve the same coverage of the previous fully artificial formation. However, the reduction is mild: the orbit covers 77% of the surface with the illumination constraints, and Stickney.

5.5.2.6 Extension to other Configurations

Finally, from the sample $10\times J_2$-invariant formation, the test matrix is slightly enlarged. The cases considered are simply: an amplification K of 5, 10, 100 for $J2$, and a nominal epicycle of $25x50$, $50x100$, $100x200$. Actually the epicycle with the J_2-invariant algorithm of Eq.6.10 is selected by the Δi, which is 0.5°, 1.0°, 1.5°: this produces a smaller epicycle for $100\times J_2$. This leads to eight additional cases, all analyzed without taking into account the hybrid option mentioned in section 5.5.2.5. For the observability analysis, the start is at local dawn, and mid-summer. Simulations are conducted for a single precession revolution. Table 5.1 summarizes the consumption and observation features.

Increasing/lowering J_2 lowers/increases the precession's period, but also increases/lowers the "modeling" terms and the "physical" J_2 term of the required thrust in Eq.5.43. The first effect dominates the second in terms of consumption, but highly decreases the observation's capability since the spacecraft quickly loses the reference of the Sun above its track, and the swath of the wider ground-track is not thick enough to cover this loss. Hence, the optimum of this observability/consumption trade-off is for middle amplification of J_2.

Increasing/lowering the size of the formation lowers/increases the Phobos' gravity compensation, but increases/lowers all the other terms in Eq.5.43. The two effects cancel each other out both in terms of consumption and observation. Hence, the optimum of this trade-off is for middle-size formations for small-middle amplification of J_2, while for a higher J_2 smaller formations are favorable.

Summarizing, the trade-off for the artificial FF around Phobos is very difficult and

is particularly constrained by the observability conditions required by the instruments' guidelines and ESA requirements. With the results provided in Table 5.1, a $20\times J_2$-invariant formation $40x80km$ was additionally tested. It requires $418m/s$ in 21 days to achieve a coverage of 77%. Considering the hybrid implementation, the value lowers to $367m/s$ (with thrust less than $2N$) in 16 days to achieve a coverage of 78%.

The results obtained with the small matrix of sample cases are enough to draw a summarizing conclusion of the investigation of the idea presented at the beginning of this section 5.5.2. The natural J_2-invariant FF has an interesting geometry for application in the observation of Phobos, but it is too slow to perform a full precession revolution, thus the cost for the compensation of Phobos' gravity surges. The artificial J_2 amplification with an analytical profile over time has been tested in this section. The major constraint is given by the local observation requirements, that, like for a QSO, increase the time required to obtain a satisfying surface coverage. To achieve that in an acceptable time, a summarizing cost figure lies on the order of $600m/s$, which for this preliminary analysis should be considered with a margin of $\pm 50\%$. Optimization is possible, in particular regarding the acceptable coverage amount and the appropriate choice of the epoch on the area of interest. Different seasons do not offer a great difference in total coverage, but observation close to solstices is necessary for a hemisphere's high latitudes. Instead, specific longitudes on low latitudes require the time of Phobos' day to be tuned. Considering a hybrid implementation, an optimum could exist in the order of $300m/s$ for small epicycles and medium-large amplification of J_2.

It is worth noting that interplanetary orbits with continuous thrust, even if low, are not appreciated for the risk associated with their maintenance. In particular, with the mass of Phootprint, the thrust level of these orbits would be also over the maximum limit for SEP. And these orbits, due to their high relative inclination, are also unstable as will be discussed in section 6.3.3.

In conclusion, the orbits analyzed in this section are not recommended for practical applications, due to the availability at lower cost of the QSOs. The only idea given by this analysis, that could be evaluated in the future, is that artificial amplification of J_2 has been considered with the J_2 analytical definition to speed up the precession of the epicycle. This is easy to implement, but it probably produces a waste of propellant: in fact, only the secular effect of J_2 is of interest, and could be used in place of multiple maneuvers in a QSO.

Chapter 6

Quasi-Satellite Orbits around Phobos

Starting from section 2.3.2, the collapse of the SOI of Phobos has become the driver that constrains the design of the orbits in the proximity of the moon. As a result of this unique condition, both the classical R2BP and CR3BP do not provide an accurate approximation to describe the spacecraft's dynamics in the vicinity of Phobos. However, this situation enables also new solutions and perspectives. The contraction of the SOI indirectly drags the manifold of distant orbits much closer to the second massive body than they would be in classical systems studied with the model of the CR3BP. This chapter focuses on the last class of natural orbits that can be used in future missions to Phobos. Section 6.1 introduces the new framework of the dynamics under the perspective of a Martian Formation Flying in Phobos' orbit, and presents the orbits analyzed in this chapter, the Quasi-Satellite Orbits[1]. The QSOs around Phobos are computed in section 6.2, and their stability analysis is conducted in section 6.3. Finally, section 6.4 presents applications for this class of orbits in the framework of a proposed mission to Phobos.

6.1 Formation Flying

As the distance of the spacecraft to the second massive body decreases, the differential gravity of the primary in the Hill's frame decreases significantly relative to the secondary's Keplerian gravity. In this case, the dynamics can be simplified to a R2BP around the second massive body[2]. This holds in the reverse sense, and the gravity of the secondary's rapidly decreases outside of its SOI with respect to the differential gravity of the primary. In this case, the relative dynamics around the secondary is expressed by a R2BP around the primary in the Hill's frame. This coincides with the framework used in Formation Flying (FF), where the osculating orbit of the secondary body, in

[1]This research was conducted during an internship in Thales Alenia Space, Toulouse.
[2]Eventually including additional perturbations due to the second massive body.

our case Phobos, could be considered as a chief spacecraft orbiting Mars, that the third body, which is the actual spacecraft, follows in proximity. This section presents the extension of the Formation Flying's dynamics and their natural orbits to the case of a 3B dynamics, when the reference point is not a spacecraft but a massive body.

6.1.1 Formation Flying Dynamics

FF is a classical case of relative orbital dynamics. In particular, the first FF mission Landsat7 was launched quite recently in 1999, but the interest in such a type of mission configuration has exponentially grown from then, because it enables mission objectives that would be not achievable with the practical size limitation of a single spacecraft, in particular for laser interferometric observations. Nevertheless, FF missions have only flown in Earth orbit. Therefore, the case of Keplerian FF, where the orbital dynamics is given by the R2BP, represents the main field where the research on FF is applied to [149].

The model of the Keplerian FF describes the orbital dynamics of the deputy spacecraft in the Hill's frame of the chief spacecraft. Thus, since the reference frame is the same, the equations of motion of the Keplerian FF correspond to the ones of the ER3BP of Eq.2.50 and ER3BP-GH of Eq.3.50, by erasing the gravity of the second massive body, and by considering $\mu = 0$ for the expression of the primary's gravity in Eq.2.5 and its location with respect to the barycenter in Eq.2.6. In particular, the classical form found in the literature uses physical units, and highlights the primary's gravity terms and the apparent translational acceleration of the frame of Eq.2.50-3.50 in an explicit differential term of the primary's gravity between deputy and chief [149].

The invariant solutions of these dynamics are the well-known Keplerian orbits. However, their relative dynamics require the rotation through the time-variant attitude matrix $A(\Omega, i, \omega, \nu(t))$ (see section 2.6.1), where ν should be solved through Kepler's equation. This operation yields a long analytical expression to express the position of the deputy spacecraft in the Hill's frame of the chief spacecraft.

Simplified analyses are required. The Clohessy-Wiltshire equations consider a circular orbit for the chief, thus they correspond to Eq.2.51 without the secondary, which is the CR3BP centered on the latter. This simplification yields an autonomous system. The addition of the usual Hill's linearization of Eq.2.35 provides the Hill's equations, which correspond to Eq.2.34 without the secondary[3]. This further simplification yields a linear time-invariant dynamical system.

The linearized Keplerian FF equations of motion provide different analytical solutions, in terms of different kinds of state parametrizations. A collection of these solutions is given in [156]. In particular, since the FF motion is the "difference" between two Keplerian orbits, its general solution will depend on two phases. The relative orbit will be periodic if and only if the two orbits of the chief and the deputy are synchronous

[3]Eq.A.11-A.12 are the TV Hill's equation in time or true anomaly, which are the linearization of the Keplerian FF dynamics in a general elliptical orbit.

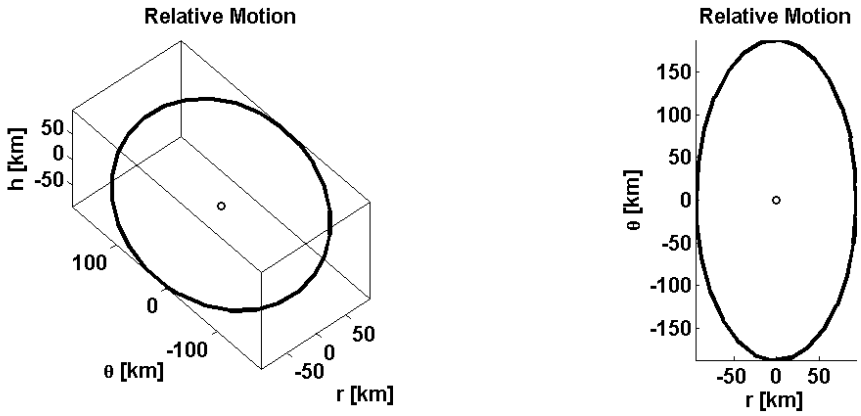

Figure 6.1: **Epicycle in the Hill's frame of the primary body.** 3D and planar view of the epicycle around the secondary body (represented as the point at the origin).

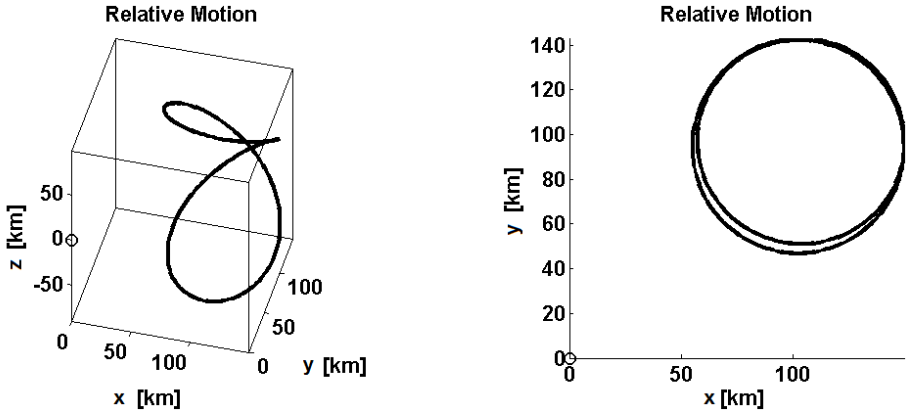

Figure 6.2: **Epicycle in the inertial frame.** 3D and planar view of the epicycle around the secondary body (represented as the point at the origin).

(1:1 resonance). From Kepler's laws, this implies that the two semi-major axes are the same.

6.1.1.1 Epicycle

A classical periodic solution of the linear Keplerian FF is the epicycle. Its general analytical expression is provided in [149]. The epicycle for the case of chief's slightly eccentric orbits (as is the case of Phobos) is a retrograde elliptical orbit centered on the chief. This results in an *artificial satellite of the secondary body, but due only to the gravity attraction of the primary*[4], as visible in Fig.6.1.

The epicycle is usually described by the difference of the orbital elements (OEs) of the deputy with respect to the ones of the chief. The shape of the epicycle on the orbital plane is an ellipse too, whose maximum and minimum axes are in a fixed ratio 2:1. The maximum axis lies always along the tangential Hill's θ-axis of the chief orbit. The amplitude of the orbit's planar axes is proportional to a difference in eccentricity. A

[4] A natural example of epicycle is provided by the Near Earth Objects, which are asteroids orbiting the Sun at the Earth's distance, and could be seen as distant satellites of the Earth.

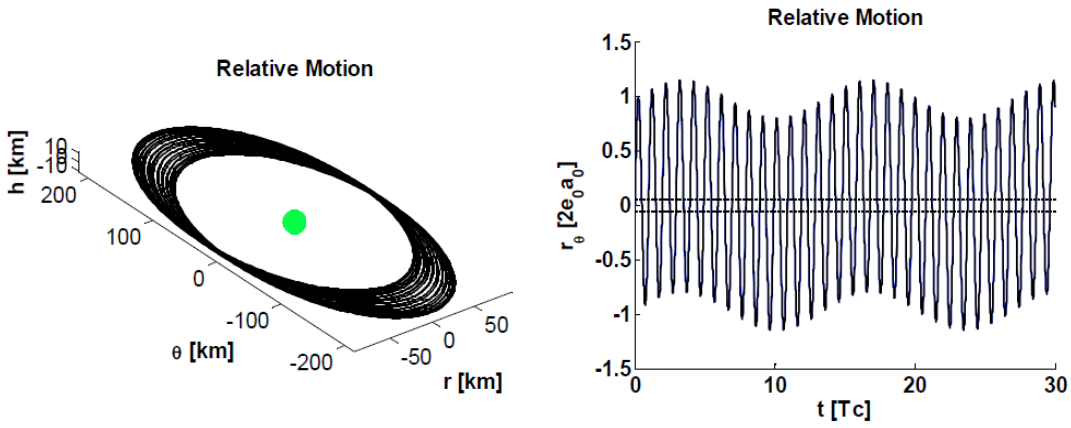

Figure 6.3: **2D QSO in the Hill's frame of the primary body.** On the left, the QSO around the secondary body (represented as the Phobos' mean sphere at the origin). On the right, distance from Phobos along the θ-axis, with the normalized units indicated (1 unit of distance corresponds to the original Keplerian epicycle's max θ-component). The plot in black is obtained with a ER3BP, and is indistinguishable from the plot in blue, which is obtained with an equivalent CR3BP (where the chief orbit is circular with radius equal to the semi-major axis, and the difference in the orbital elements between deputy and chief is maintained consistently).

difference in inclination, or right ascension of ascent node, inclines the epicycle, and the relative motion is 3D. However, on the orbital plane the projection of the 3D epicycle remains a 2:1 ellipse. In particular, in the linearized dynamics of FF, the 3D motion allows to realize a 3D circular epicycle: this configuration is called cartwheel formation. As mentioned in section 6.1.1, the difference in semi-major axis between the two inertial orbits is zero: a small error provokes a secular departure of the relative motion along the Hill's θ-axis.

Recall that such an ellipse is defined in the rotating Hill's frame. The third body NEVER rotates around the chief in the inertial frame, centered on the chief. This is shown in Fig.6.2 where the third body remains at one side. *Due to the spinning rotation of the secondary body*, that for the case of Phobos is synchronous with the Hill's frame rotation, *the third body rotates in the BCBF frame of the secondary in 1:1 resonance*. This is not always the case, and the relative orbit in the BCBF frame will be a quasi-periodic rotation around the chief, if the BCBF frame spins faster than its revolution, or a quasi-periodic hovering, if the spin rate is lower.

6.1.2 Quasi-Satellite Orbit

The QSO is the motion of the epicycle when the chief is not a spacecraft but a second massive body. Thus the QSO is the solution of the 3B dynamics, either the CR3BP of Eq.2.51, or the ER3BP of Eq.2.50. In a precise way, *the QSO is the dynamical substitute of the epicycle in the R3BP*.

The addition of the gravity field of the chief provides the dynamical substitutes with two additional natural frequencies. Thus a 3D QSOs in the ER3BP is a torus with three phases. A QSO can be decomposed in a sequence of epicycles along subintervals

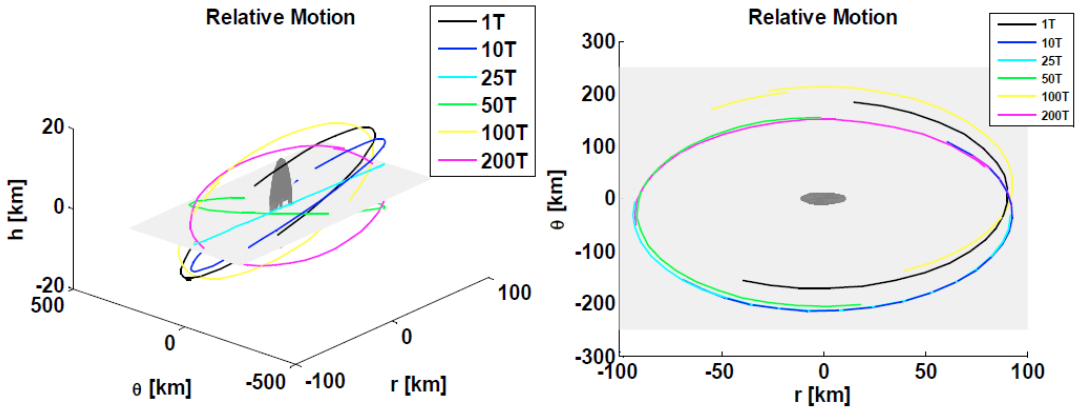

Figure 6.4: **3D QSO in the Hill's frame of the primary body.** 3D and planar view of the sub-epicycles of the QSO around the secondary body (represented as the Phobos' mean sphere at the origin). The length scale of the three axes is not uniform to show the 3D behavior of the QSO's precession rotation of the relative line of nodes. This is highlighted introducing the intersection with the orbital plane in light grey. The planar view allows to see also the typical oscillation along the Hill's θ-axis, which is preserved in the 3D motion.

coincident with the chief's orbital revolutions. A QSO is a QPO characterized by an oscillation of the whole epicycle along the y-axis of the 3B frame, as shown in Fig.6.3. This tangential oscillation can be described by an amplitude and a period. In addition, 3D sub-epicycles experience a secular precession of their relative line-of-nodes, as presented in Fig.6.4. The shape and size of the planar projection of the sub-epicycles remain the same. The period of this precession rotation grows as far as the size of the sub-epicycles increases, until their relative line-of-nodes becomes fixed in the Hill's frame. This asymptotic behavior at great distances is the 1:1 resonance, since the gravity of the chief becomes negligible: larger QSOs tend to a Keplerian epicycle.

The QSOs constitute a family of QPOs coined by various names in the literature: Quasi-Satellite, Quasi-Synchronous, Distant Satellite, Distant Retrograde orbits. They were first investigated long time ago by no other than Hill. In particular, planar QSOs are the quasi-periodic solution around the Strömgren's f class[5] of periodic orbits of Hill's approximation of the planar CR3BP, as indicated in the seminal papers of Hénon [157, 158]. QSOs are more generally considered as one of three kinds of co-orbital configurations in a CR3BP with 1:1 resonance[6] together with Tadpole and Horseshoe orbits: in [67] it is shown that unstable QSOs evolve from and to Horseshoe orbits, which are linked together.

6.2 QSOs around Phobos

As explained in section 6.1, the QSOs are QPOs around the primary body that fall outside the SOI of the second massive body of a 3BP. The peculiar case of a small

[5] According to Matukuma's classification, this is named the a class.
[6] This is the motion of the Near Earth Objects and the Trojan asteroids.

planetary satellite like Phobos is therefore suitable for the exploitation of these orbits because of the collapse of its SOI, which indirectly drags the manifold of these orbits closer to the body. In this section the computation of the QSOs around Phobos is undertaken.

6.2.1 Equations of Motion

The QSOs are solutions of the 3B dynamics, and are studied in the framework of a CR3BP since the seminal work of [157, 158]. However this approach requires approximations to be made, first of all the reduction to a circular orbit for the secondary body. Additional simplifications usually taken are the linearization and the planar analysis.

The analysis of the QSOs around Phobos in this section is conducted with the approach of a long-range Martian FF. The starting model is given by the Keplerian dynamics around Mars, parameterized by the classical Keplerian orbital elements, for both Phobos and the spacecraft, thus without any of the aforementioned simplifications. These 2B dynamics are then improved to a perturbed 2B model, named P-R2BP. The equations of motion of the P-R2BP in terms of the Keplerian OEs are the Gauss' Planetary Equations [104], as presented in Eq.6.1.

$$\begin{bmatrix} \dot{a} \\ \dot{e} \\ \dot{\Omega} \\ \dot{i} \\ \dot{\omega} \\ \dot{M}-n \end{bmatrix} = \begin{bmatrix} \frac{2a^2e}{h}\sin\nu & \frac{2a^2p}{hr} & 0 \\ \frac{p}{h}\sin\nu & \frac{\left(1-e^2\right)\left(ap-r^2\right)}{her} & 0 \\ 0 & 0 & \frac{r}{h}\frac{\sin u}{\sin i} \\ 0 & 0 & \frac{r}{h}\cos u \\ -\frac{p}{he}\cos\nu & \frac{(p+r)}{he}\sin\nu & -\frac{r}{h}\frac{\sin u}{\tan i} \\ \frac{\sqrt[2]{1-e^2}}{he}\left(p\cos\nu-2re\right) & -\frac{\sqrt[2]{1-e^2}(p+r)}{he}\sin\nu & 0 \end{bmatrix} \begin{bmatrix} a_r^p \\ a_\theta^p \\ a_h^p \end{bmatrix} \tag{6.1}$$

The trajectory of the OEs in the R2BP is stationary, apart from M which is linear with the time. In the P-R2BP, the forcing term $\mathbf{a^P}$ is introduced, and represents the perturbing acceleration. Using the OEs as state variables is convenient when the perturbation is mild, because it keeps the reference with a Keplerian-like description of the dynamics. In addition, Gauss' equations are convenient because they are expressed with respect to the chief's Hill's frame's components of $\mathbf{a^P}$, which is the same frame where the relative orbital dynamics of FF is expressed.

Since Phobos' orbit is nearly circular and equatorial, it is advised to use an alternative form of the P-R2BP. This is because the Gauss' planetary equations are singular in case of null eccentricity or inclination. In this situation, the equinoctial OEs are used: the transformation between the two state's sets is provided below.

$$
\begin{cases}
P_1 = e\sin(\Omega+\omega) \\
P_2 = e\cos(\Omega+\omega) \\
Q_1 = \tan\frac{i}{2}\sin\Omega \\
Q_2 = \tan\frac{i}{2}\cos\Omega \\
l = \Omega+\omega+M = K + P_1\cos K - P_2\sin K \\
L = \Omega+\omega+\nu = \arctan\frac{\left(a+b-aP_2^2\right)\sin K + aP_1P_2\cos K - (a+b)P_1}{\left(a+b-aP_1^2\right)\cos K + aP_1P_2\sin K - (a+b)P_2} \\
K = \Omega+\omega+E = \Omega+\omega+2\arctan\left(\sqrt[2]{\frac{1-e}{1+e}}\tan\frac{L-\Omega-\omega}{2}\right) \\
r = \frac{p}{1+P_1\sin L+P_2\cos L} = a\left(1-P_1\sin K - P_2\cos K\right)
\end{cases}
\Leftrightarrow
\begin{cases}
e = \sqrt[2]{P_1^2+P_2^2} \\
\Omega = \arctan 2\left\{Q_1, Q_2\right\} \\
i = 2\arctan\sqrt[2]{Q_1^2+Q_2^2} \\
\omega = \arctan 2\left\{P_1, P_2\right\} - \arctan 2\left\{Q_1, Q_2\right\} \\
M = l - \arctan 2\left\{P_1, P_2\right\} = E - e\sin E \\
\nu = L - \arctan 2\left\{P_1, P_2\right\} = 2\arctan\left(\sqrt[2]{\frac{1+e}{1-e}}\tan\frac{E}{2}\right) \\
E = K - \arctan 2\left\{P_1, P_2\right\} = 2\arctan\left(\sqrt[2]{\frac{1-e}{1+e}}\tan\frac{\nu}{2}\right) \\
r = \frac{p}{1+e\cos\nu} = a\left(1-e\cos E\right)
\end{cases}
\tag{6.2}
$$

The equinoctial Gauss' planetary equations are expressed in Eq.6.3.

$$
\begin{bmatrix} \dot{a} \\ \dot{P}_1 \\ \dot{P}_2 \\ \dot{Q}_1 \\ \dot{Q}_2 \\ \dot{l}-n \end{bmatrix} =
\begin{bmatrix}
-\frac{2a^2}{h}\left(P_1\cos L - P_2\sin L\right) & \frac{2a^2p}{hr} & 0 \\
-\frac{p}{h}\cos L & \frac{1}{h}\left(rP_1+(p+r)\sin L\right) & -\frac{rP_2}{h}\left(Q_1\cos L - Q_2\sin L\right) \\
\frac{p}{h}\sin L & \frac{1}{h}\left(rP_2+(p+r)\cos L\right) & \frac{rP_1}{h}\left(Q_1\cos L - Q_2\sin L\right) \\
0 & 0 & \frac{r\left(1+Q_1^2+Q_2^2\right)}{2h}\sin L \\
0 & 0 & \frac{r\left(1+Q_1^2+Q_2^2\right)}{2h}\cos L \\
-\frac{1}{h}\left(\frac{ap}{a+b}\left(P_1\sin L + P_2\cos L\right)+\frac{2br}{a}\right) & -\frac{a(p+r)}{h(a+b)}\left(P_1\cos L - P_2\sin L\right) & -\frac{r}{h}\left(Q_1\cos L - Q_2\sin L\right)
\end{bmatrix}
\begin{bmatrix} a_r^p \\ a_\theta^p \\ a_h^p \end{bmatrix}
\tag{6.3}
$$

To compute the QSOs around Phobos, the ER3BP is retained using as forcing action the 3B gravity perturbation of Phobos in the osculating Hill's frame centered on the moon. By postprocessing, Eq.6.2 is used to retrieve the trajectory in Keplerian OEs, which leads to the inertial state of the spacecraft around Mars. Assuming Phobos to follow its mean Keplerian orbit, the inertial state is trivially known a priori. Thus, the relative kinematics of section 3.4 are used to compute the relative trajectory of the spacecraft with respect to Phobos in its Hill's frame.

The P-R2BP is suitable to include additional orbital perturbations. From the analysis of perturbations conducted in section 2.4, for the range of QSOs' distance from Phobos, the major effects are due to the eccentricity (already embedded in the model of Eq.6.3) and the Mars J_2 GH. In particular, as a difference from the R3BP, in the P-R2BP the orbital perturbations not due to Phobos are no longer expressed in differential terms but directly in absolute terms, because the state of the dynamical model is inertial. The differential action on the relative motion appears by computing a priori the osculating

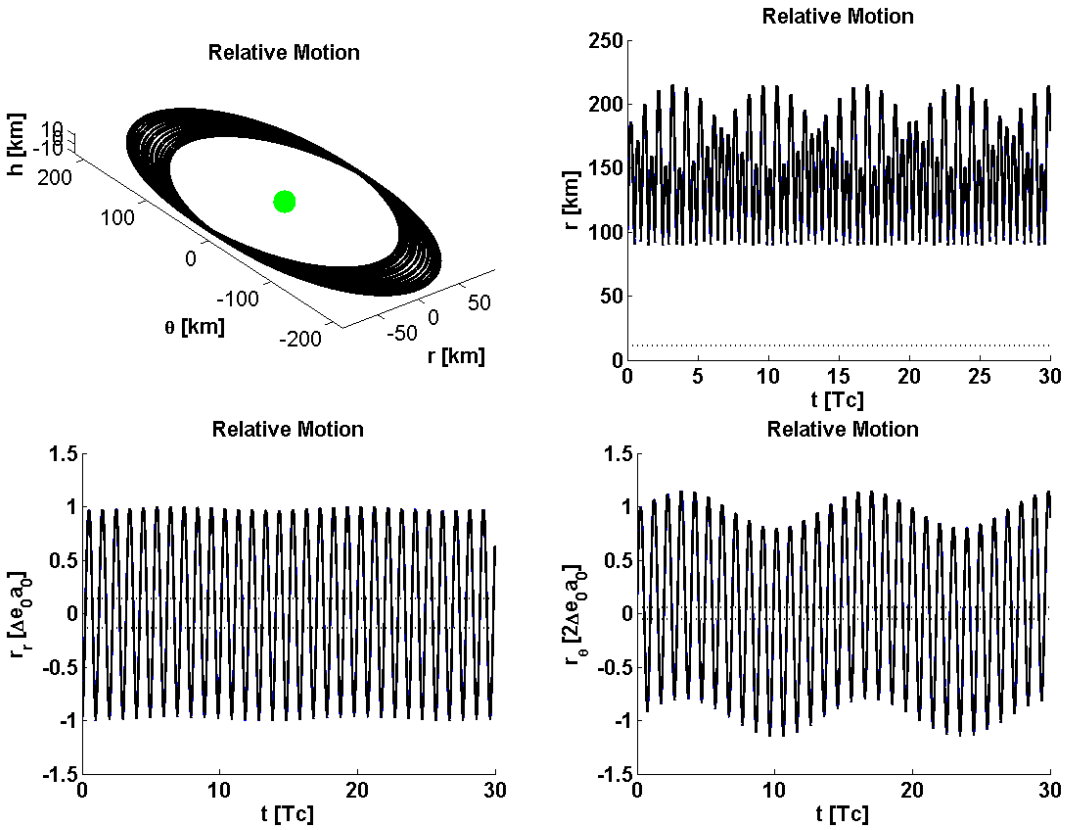

Figure 6.5: **QSOs around Phobos.** Phobos orbit circular and equatorial, without Mars J_2. $\Delta e = 0.01$, $\Delta i = 0$. Orbit and plots in black line of the relative distance's magnitude, radial and transversal component. The plots coincide with the blue lines that are related to the CR3BP. Dotted lines indicate the reference distance of Phobos' mean radius.

motion[7] of Phobos and the angular velocity of its Hill's frame, with a dedicated P-R2BP under the effect of the same perturbation. Thus, Eq.6.3 is now required to propagate both the absolute state of the spacecraft and Phobos, since the osculating motion of the latter is no longer known analytically a priori.

In this sense, recall that when defining an initial condition using mean OEs for the spacecraft and Phobos, and starting with true anomalies in accordance with the 2B dynamics, it produces different orbits. The same orbit is obtained with osculating OEs in accordance to the perturbation, but their analytical expression is only available for particular cases, like J_2 [105]. However, such an analytical expression is not available for the 3B perturbation. The effect of the choice of the initial true anomaly on the QSOs will be addressed in the next section.

6.2.2 The QSOs around Phobos

The QSOs around Phobos are simulated with the ODEs of Eq.6.3 and using the ephemerides of Phobos from Table 2.1. The initial condition is taken from the an-

[7] With the terminology of control theory, this is a feedforward signal for the dynamics of the spacecraft.

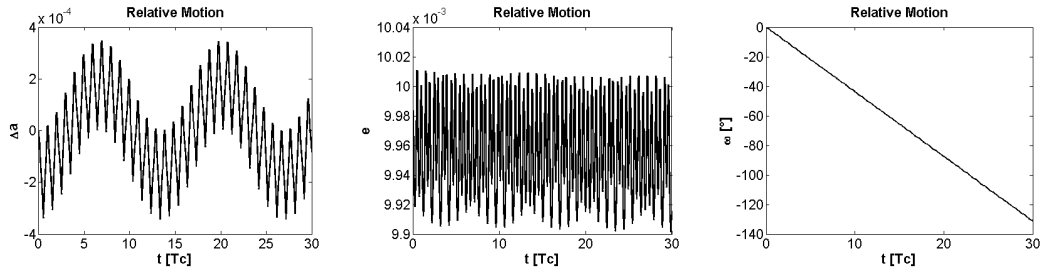

Figure 6.6: **QSOs around Phobos.** Phobos orbit circular and equatorial, without Mars J_2. $\Delta e = 0.01$, $\Delta i = 0$. Orbital elements.

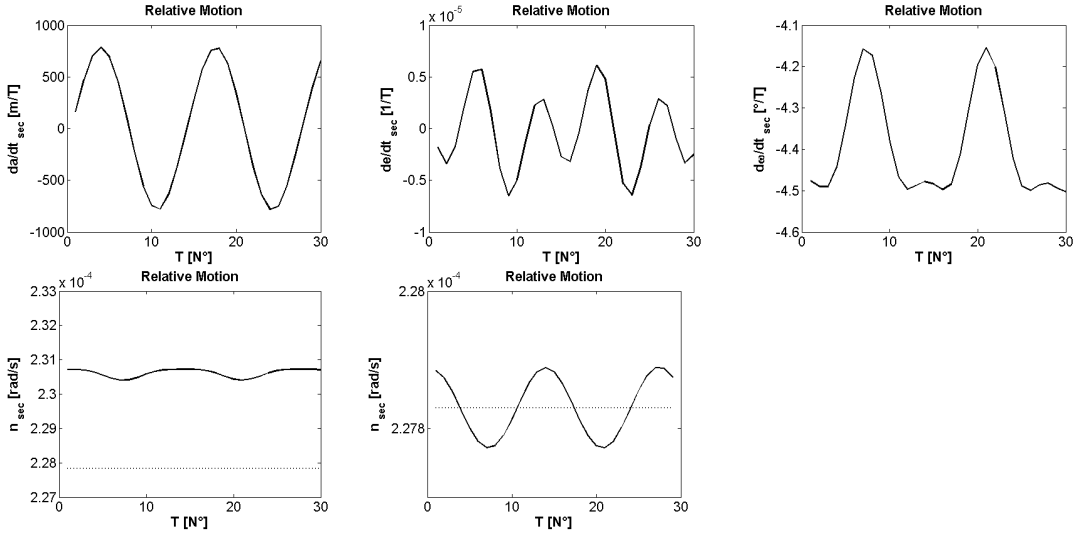

Figure 6.7: **QSOs around Phobos.** Phobos orbit circular and equatorial, without Mars J_2. $\Delta e = 0.01$, $\Delta i = 0$. Secular derivative of the orbital elements, taken every orbital period. The last two graphs correspond to the mean motion, respectively considered as the derivative of the mean anomaly and the mean longitude, where the dotted line is the reference of the original 2B value.

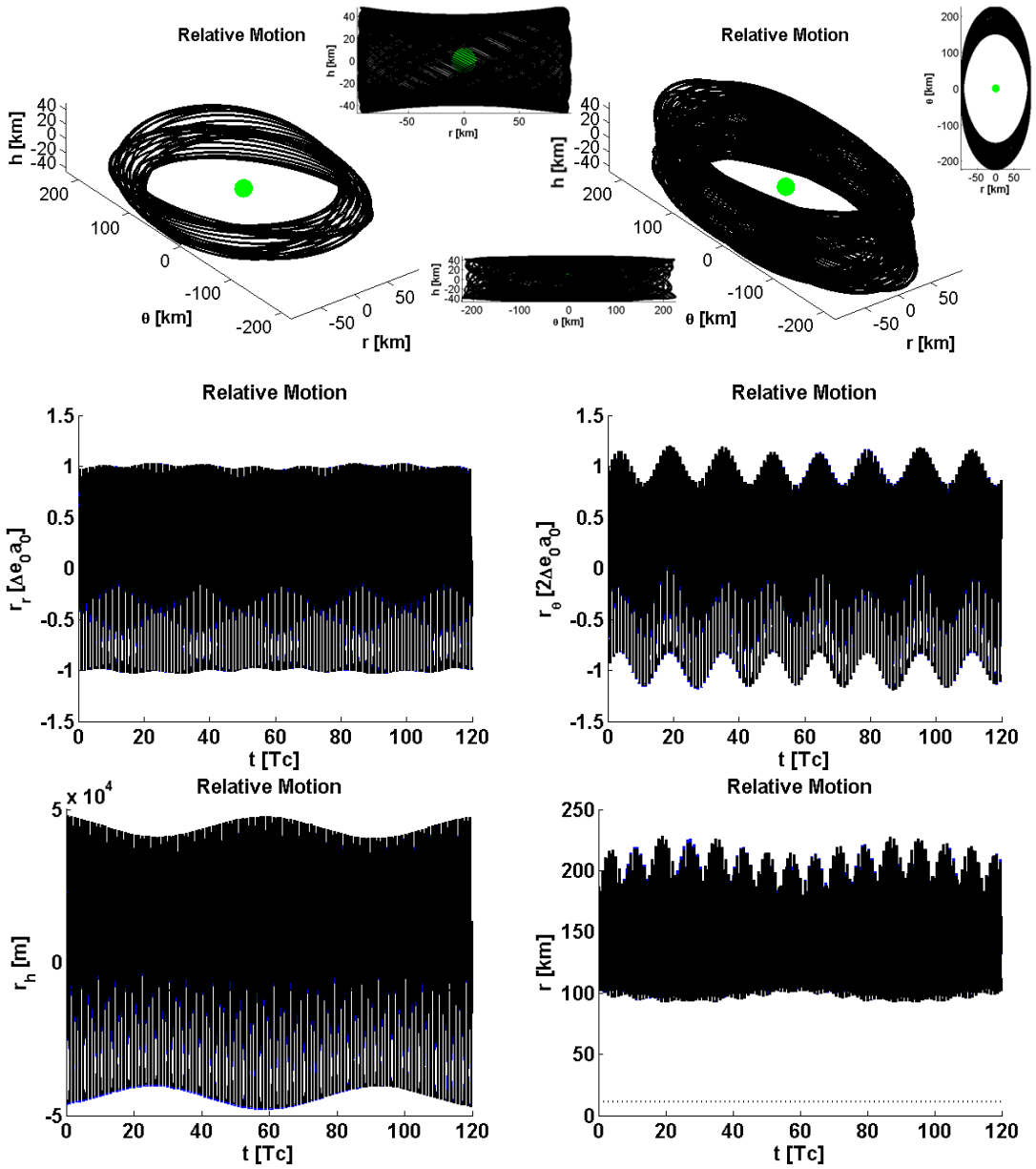

Figure 6.8: **QSOs around Phobos.** Phobos Keplerian orbit, without Mars J_2. $\Delta e = 0.01$, $\Delta i = 0.005 rad$. Orbit after 30 and 120 orbital periods, with projections on the coordinate planes. Plots in black line of the relative distance's magnitude, radial, transversal and vertical component. The plots overlap with the blue lines that are related to the equivalent CR3BP. Dotted lines indicate the reference distance of Phobos' mean radius.

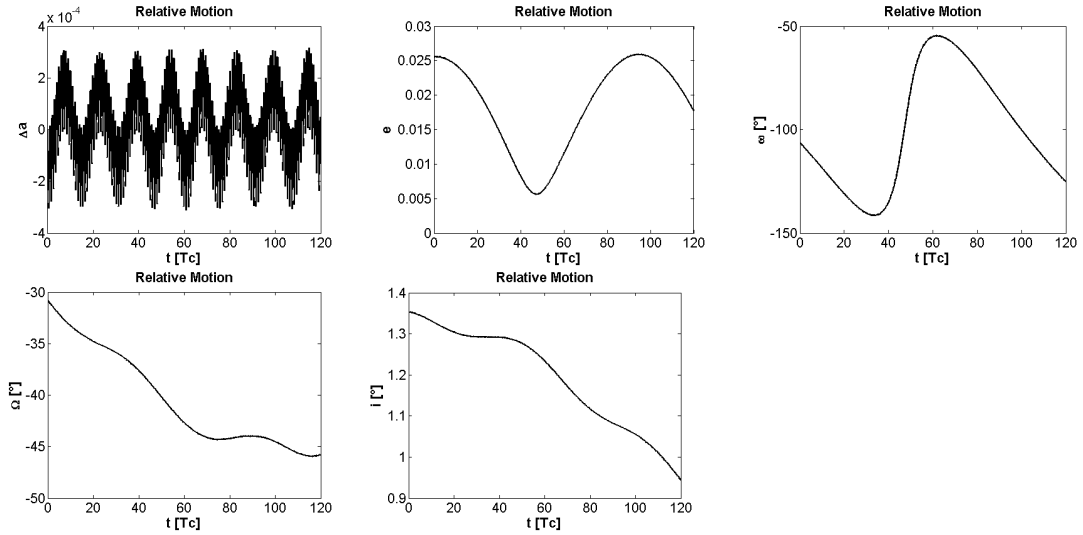

Figure 6.9: **QSOs around Phobos.** Phobos Keplerian orbit, without Mars J_2. $\Delta e = 0.01$, $\Delta i = 0.005 rad$. Orbital elements.

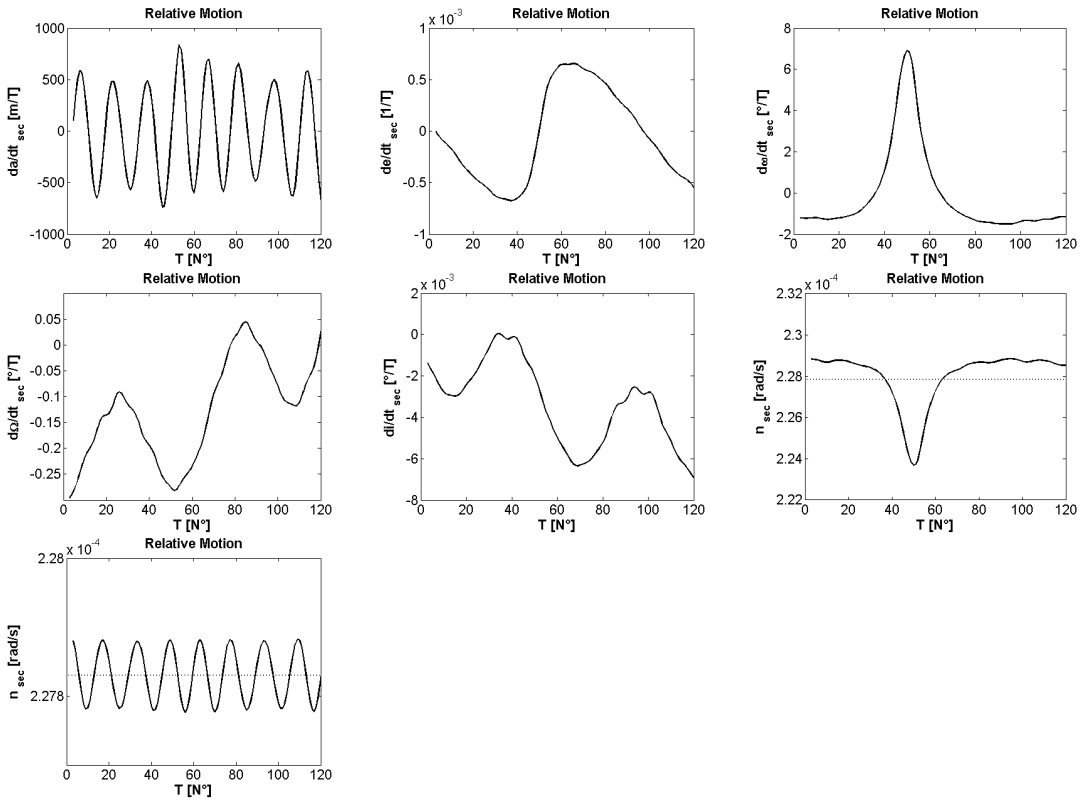

Figure 6.10: **QSOs around Phobos.** Phobos Keplerian orbit, without Mars J_2. $\Delta e = 0.01$, $\Delta i = 0.005 rad$. Secular derivative of the orbital elements, taken every orbital period. The last two graphs correspond to the mean motion, respectively considered as the derivative of the mean anomaly and the mean longitude, where the dotted line is the reference of the original 2B value.

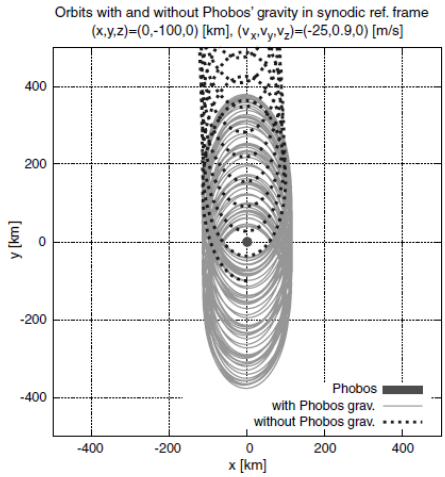

Figure 6.11: **Epicycle instability.** This image is taken from [61], to show the evolution of the epicycle, with and without Phobos gravity, in a high-fidelity simulator with all the differential perturbations.

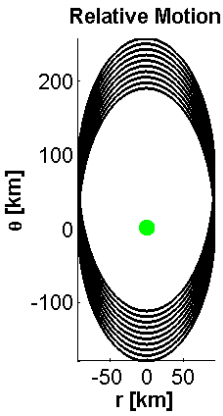

Figure 6.12: **Epicycle instability.** This image shows the evolution of the epicycle without Phobos gravity, when the differential Mars J_2 perturbation is introduced in the relative P-R2BP, where the osculating orbit of Phobos is the chief reference.

cestor epicycle, considering both Phobos and the spacecraft at perimars. The epicycle is defined by a difference in eccentricity and inclination. Thus, the QSOs around Phobos are suitable to be parameterized by the couple Δe-Δi of its mean ancestor epicycle. This gives also an indication of the r,θ,h-amplitudes of the spacecraft from Phobos, still in the 2B reference. The actual minimum and maximum amplitudes are retrieved a posteriori.

The first step is to compute a reference 2D QSO in the CR3BP, which is $\Delta e \neq 0$. This is visible in Fig.6.5, while Fig.6.6-6.7 provide the orbital elements evolution and their secular derivatives. This configuration produces the θ-oscillation of the epicycle, as discussed in section 6.1.2. In particular, such behavior is characterized by the only not null secular derivative, which is the one of the argument of pericenter. The inclusion of the eccentricity in Fig.E.1-E.3 for a 2D QSO in the ER3BP does not change significantly the effects, as well as the inclusion of the inclination. Finally, the case of a 3D QSO in the complete Keplerian Phobos' orbit is provided in Fig.6.8-6.10, which is $\Delta i \neq 0$. This configuration enables the precession rotation of the epicycle, as discussed in section 6.1.2. In terms of Keplerian OEs, the 3D QSO has short-period (rotation around Phobos along the epicycle) and medium-period (tangential motion of the epicycle) oscillations for semi-major axis, eccentricity and argument of pericenter, while the inclination and right ascension experience a long-period oscillation (precession of the epicycle). In particular, the argument of pericenter seems to be the one affecting mostly the mean motion evaluated as the secular derivative of M over one M-period, whereas the secular derivative of l over one l-period remains a perfect sinusoid along the original 2B value.

As mentioned in section 6.2.1, the Mars J_2 action should be considered in the P-R2BP

to model the QSOs around Phobos. Differential perturbations in FF always destabilize the relative motion, since they introduce secular derivatives in the OEs. This is shown in Fig.6.11. For the case of a 3BP, the gravity of the secondary is responsible to stabilize the motion, by means of the θ-oscillation.

The addition of Mars' J_2 perturbation, without Phobos gravity, is highlighted in Fig.6.12, where the epicycle departs along the Hill's θ-axis. The QSOs are now investigated with the same schedule done before, including eccentricity, inclination of Phobos, and Δe, Δi. The outcomes are reported in Fig.E.4-E.15, and they are similar to the previous ones. The differential Mars J_2 adds a shorter-amplitude and shorter-period oscillation to the 3D QSO, which is now a 4-torus. This has no great effects on the secular derivatives and mostly acts in shifting the l-derivative mean motion. Therefore, at the distances of a typical observation segment, the stability effect of Phobos' gravity dominates the dynamics of the QSOs.

Finally, recall from section 6.2.1 that the absence of an analytical expression of the 3B perturbation does not give knowledge of the dynamics of the natural phases. In this sense, it is worth to report that starting with the spacecraft in perimars and inferior conjunction, and starting in Mars-Phobos quadrature and phase in accordance on the same epicycle, it produces very different QSOs with the latter having a far lower amplitude of the θ-axis oscillation.

6.3 Stability Analysis

The QSOs around Phobos have been computed in section 6.2 by numerical simulation in the P-R2BP, using the initial condition of the original epicycle in the R2BP. The description of the initial condition by OEs can be immediately related to a previous mission segment, where the spacecraft follows an orbit around Mars. The use of the initial condition of the original epicycle is possible because the QSOs are stable orbits, as an effect of the θ-oscillation produced by the gravity pull of the second massive body. However, these simulations do not provide any analytical description of the motion, nor any numerical representation of the invariant object. The use of the methods of DST of section B.6.6 would be highly computational demanding, since the 3D QSOs are 3-tori, eventually 4-tori when Mars' oblateness is considered too. In particular, the latter is the major source of instability of the relative motion around Phobos, as seen in section 6.2.2.

From the computation of the sample of QSOs in section 6.2.2, it was clearly inferred that Phobos stabilizing effect is predominant with respect to the instability brought by the differential Mars J_2 perturbation. The point is to find the range of QSOs' distances where Phobos' gravity effects are predominant, without making the spacecraft to fall towards the moon. In this section, the stability analysis of the QSOs around Phobos is addressed.

6.3.1 Semi-analytical Approach

To compare the effects of the two disturbances, Phobos 3B perturbation and differential Mars J_2 perturbation, the first approach is to follow a classical semi-analytical procedure used in the framework of the P-R2BP. This is the computation of the secular derivatives of the OEs by the effect of the related perturbation in the Gauss' planetary equations of Eq.6.3. This will also help to characterize the two motions of the QSO, the θ-oscillation and the 3D precession rotation.

Such a procedure is already available for J_2. It consists in the analytical computation of the mean integral value $\bar{u}$ of the potential u_{a^P} of the perturbation $\mathbf{a^P}$, by means of the mean OEs. This is shown below for the case of J_2.

$$\begin{cases} u_{J_2} = -\frac{GM}{\|\mathbf{r}\|} J_2 \left(\frac{R}{\|\mathbf{r}\|}\right)^2 \frac{1}{2}\left(3\cos^2\vartheta - 1\right) = -\frac{GMR^2J_2}{2a^3(1-e^2)^3}\left(1+e\cos\nu\right)^3\left(3\sin^2\left(\omega+\nu\right)\sin^2 i - 1\right) \\ \bar{u}_{J_2} = \dfrac{1}{2\pi}\displaystyle\int_0^{2\pi} u_{J_2} dM = \dfrac{1}{2\pi}\int_0^{2\pi} u_{J_2} n \dfrac{\|\mathbf{r}\|^2}{h} d\nu = \\ \quad = -\dfrac{1}{2\pi}\dfrac{n^2R^2J_2}{2(1-e^2)^{3/2}}\displaystyle\int_0^{2\pi}\left(1+e\cos\nu\right)\left(3\sin^2\left(\omega+\nu\right)\sin^2 i - 1\right) d\nu = \\ \quad = \dfrac{n^2R^2J_2}{4(1-e^2)^{3/2}}\left(2 - 3\sin^2 i\right) \end{cases} \tag{6.4}$$

The Gauss' planetary equations of Eq.6.1 can be written in terms of the forcing action expressed through the gradient of its potential with respect to the OEs. This is called the Lagrange's form of the planetary equations [104], which is $\frac{dOE}{dt}\left(\frac{du_{a^P}}{dOE}\right)$. Thus, by using the derivatives of the mean integral value of Eq.6.4, it yields analytically the secular derivatives of the OEs, which are $\frac{d\overline{OE}}{dt}$. For the case of J_2, in a mean orbit with not null eccentricity and inclination, the only not null secular derivatives are the ones of Ω, ω, and M. These secular derivatives were already presented in Eq.3.22.

The aim is to undertake the same procedure for the 3B perturbation of Phobos. The rationale will then be to combine the secular motions due to the two perturbations, to describe the QSO at the first-order approximation, assuming also that the coupling effects are negligible.

$$\left.\frac{d\overline{OE}}{dt}\right|_{J_2+3B} = \left.\frac{d\overline{OE}}{dt}\right|_{J_2} + \left.\frac{d\overline{OE}}{dt}\right|_{3B} + \left.\frac{d\overline{OE}}{dt}\right|_{J_2-3B,coupl} \approx \left.\frac{d\overline{OE}}{dt}\right|_{J_2} + \left.\frac{d\overline{OE}}{dt}\right|_{3B} \tag{6.5}$$

The effect of the 3B perturbation is made by the direct and the apparent term, as shown in the first of Eq.6.6, where the indexes 1,2,3 are now assigned in the framework of the P-R2BP[8], and they refer respectively to the primary (Mars), the spacecraft, and the secondary (Phobos). The ratio of the two terms corresponds to the square of the two distances magnitude used in Eq.6.6. For distances up to $100km$ from Phobos, the apparent term is 10^{-4} times the direct one. Thus, the 3B perturbation for this procedure is reduced to only the direct gravity of the moon. This yields the integral

[8]The indexes 2 and 3 are swapped with respect to the R3BP.

required to express the mean integral value of the 3B perturbation in a P-R2BP, where to simplify the notation, from now on Phobos and the spacecraft are referred to as the chief (c) and the deputy (d) reference.

$$\begin{cases} u_{3B} = -\frac{GM_{23}}{\left\|\mathbf{r}_2^3\right\|} - \frac{GM_3}{\left\|\mathbf{r}_3^1\right\|}\frac{\left(\mathbf{r}_2^1\right)^T\mathbf{r}_3^1}{\left\|\mathbf{r}_3^1\right\|^2} \approx -\frac{GM_3}{\left\|\mathbf{r}_2^3\right\|} \\ \bar{u}_{3B} = \frac{1}{2\pi}\int_0^{2\pi} u_{3B}dM_d = \frac{1}{2\pi}\int_0^{2\pi} -\frac{GM_c}{\left\|\mathbf{r}_d^c\right\|}\frac{\left(1-e_c^2\right)^{3/2}}{\left(1+e_d\cos\nu_d\right)^2}d\nu_d \end{cases} \tag{6.6}$$

The integral in Eq.6.6 requires the expression of the relative distance between the spacecraft and Phobos. This is presented in Eq.6.7, and requires the use of the attitude matrices between the Hill's frame of chief and deputy with respect to the inertial reference.

$$\begin{aligned} &\mathbf{r}_{d,H_c}^c = \mathbf{A}_{H_c}^I\left(\mathbf{A}_{H_d}^I\right)^T\mathbf{r}_{d,H_d}^1 - \mathbf{r}_{c,H_c}^1 = \\ &= \begin{bmatrix} \left\{\begin{array}{c} \cos u_d\left[\sin\Omega_d\left(\cos u_c\sin\Omega_c + \sin u_c\cos i_c\cos\Omega_c\right) + \cos\Omega_d\left(\cos u_c\cos\Omega_c - \sin u_c\cos i_c\sin\Omega_c\right)\right] + \\ -\sin u_d\left(\cos u_d\left[\sin\Omega_d\left(\cos u_c\cos\Omega_c - \sin u_c\cos i_c\sin\Omega_c\right) - \cos\Omega_d\left(\cos u_c\sin\Omega_c + \sin u_c\cos i_c\cos\Omega_c\right)\right] - \sin u_c\sin i_c\sin u_d\right) \end{array}\right\} \\ \left\{\begin{array}{c} -\cos u_d\left[\sin\Omega_d\left(\sin u_c\sin\Omega_c - \cos u_c\cos i_c\cos\Omega_c\right) + \cos\Omega_d\left(\sin u_c\cos\Omega_c + \cos u_c\cos i_c\sin\Omega_c\right)\right] + \\ +\sin u_d\left(\cos u_d\left[\sin\Omega_d\left(\sin u_c\cos\Omega_c + \cos u_c\cos i_c\sin\Omega_c\right) - \cos\Omega_d\left(\sin u_c\sin\Omega_c - \cos u_c\cos i_c\cos\Omega_c\right)\right] + \cos u_c\sin i_c\sin u_d\right) \end{array}\right\} \\ \left\{\sin u_d\left(\cos i_c\sin u_d - \sin i_c\cos\Omega_c\cos\Omega_d\cos u_d\right) - \cos u_d\sin i_c\left(\cos\Omega_c\sin\Omega_d - \sin\Omega_c\cos\Omega_d\right)\right\} \end{bmatrix}\cdot \\ &\cdot\frac{a_d\left(1-e_d^2\right)}{1+e_d\cos\nu_d} - \frac{a_c\left(1-e_c^2\right)}{1+e_c\cos\nu_c}\begin{bmatrix}1\\0\\0\end{bmatrix} \end{aligned} \tag{6.7}$$

As anticipated in section 6.1, the attitude matrices are time-variant and Eq.6.7 becomes very tedious. Furthermore, the magnitude of Eq.6.7 is required, and this shall go to the denominator of the function inside the integral of Eq.6.6. Therefore, no analytical expression is possible.

A second possibility is to linearize from the beginning the ODEs of the relative R2BP, without the perturbation. The solution of the relative orbit is presented in [156] in terms of the difference of OEs between deputy and chief. For Phobos, the case of a circular non-equatorial orbit is considered. This requires to use as OEs a, i, Ω, the argument of true latitude λ, and the equinoctial parameters S and C[9]. The solution of the linearized Keplerian FF is presented in Eq.6.8, as a function of the initial or current difference of osculating OEs.

[9] C and S are the same of P_1 and P_2 defined in Eq.6.2, when considering only the argument of pericenter ω and not the longitude of pericenter u.

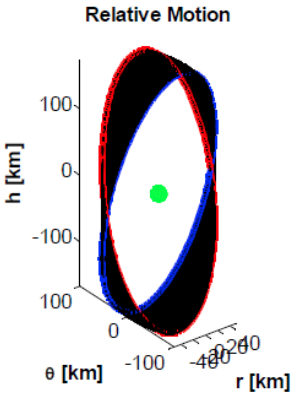

Figure 6.13: J_2**-invariant FF around Phobos.** Relative orbit without Phobos gravity. 3D and planar views. Propagation time of 200 orbital periods (about 2 months): first orbit in blue line, last orbit in red line.

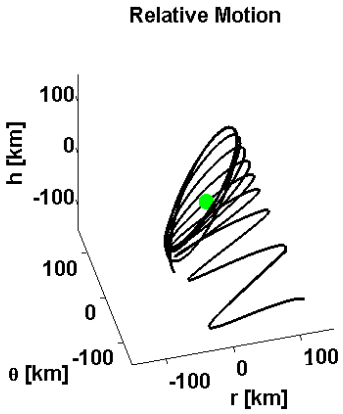

Figure 6.14: J_2**-invariant FF around Phobos.** Relative orbit with Phobos gravity. Same initial condition of Fig.6.13.

$$\bar{u}_{3B} = \frac{1}{2\pi}\int_0^{2\pi} u_{3B} d\lambda_d = \frac{1}{2\pi}\int_0^{2\pi} -\frac{GM_c}{\|\mathbf{r}_d^c\|} d\lambda_d$$

$$\begin{cases} \mathbf{r}_{d,H_c}^c(t,\lambda,OE_0) = \begin{bmatrix} \Delta a_0 - a_c\Delta C_0\cos\lambda - a_c\Delta S_0\sin\lambda \\ 2a_c\Delta C_0\sin\lambda - 2a_c\Delta S_0\cos\lambda + a_c\Delta\lambda_0 - a_c\cos i_c\Delta\Omega_0 - \frac{3}{2}n_c\Delta a_0\,(t-t_0) \\ a_c\Delta i_0\sin\lambda - a_c\sin i_c\Delta\Omega_0\cos\lambda \end{bmatrix} = \\ = \begin{bmatrix} 1 & -a_c\cos\lambda & -a_c\sin\lambda & 0 & 0 & 0 \\ -\frac{3}{2}n_c\,(t-t_0) & 2a_c\sin\lambda & -2a_c\cos\lambda & -a_c\cos i_c & 0 & a_c \\ 0 & 0 & 0 & -a_c\sin i_c\cos\lambda & a_c\sin\lambda & 0 \end{bmatrix} \begin{bmatrix} \Delta a_0 \\ \Delta C_0 \\ \Delta S_0 \\ \Delta\Omega_0 \\ \Delta i_0 \\ \Delta\lambda_0 \end{bmatrix} \\ \mathbf{r}_{d,H_c}^c(OE(t)) = \begin{bmatrix} \Delta a - a_c\Delta C\cos\lambda - a_c\Delta S\sin\lambda \\ 2a_c\Delta C\sin\lambda - 2a_c\Delta S\cos\lambda + a_c\Delta\lambda - a_c\cos i_c\Delta\Omega \\ a_c\Delta i\sin\lambda - a_c\sin i_c\Delta\Omega\cos\lambda \end{bmatrix} = \\ = \begin{bmatrix} 1 & -a_c\cos\lambda & -a_c\sin\lambda & 0 & 0 & 0 \\ 0 & 2a_c\sin\lambda & -2a_c\cos\lambda & -a_c\cos i_c & 0 & a_c \\ 0 & 0 & 0 & -a_c\sin i_c\cos\lambda & a_c\sin\lambda & 0 \end{bmatrix} \begin{bmatrix} \Delta a \\ \Delta C \\ \Delta S \\ \Delta\Omega \\ \Delta i \\ \Delta\lambda \end{bmatrix} \end{cases} \tag{6.8}$$

However, the problem leads to the same conclusion of the first approach. The magnitude of the orbit of Eq.6.8 shall go to the denominator of the function inside the updated integral of the first of Eq.6.8. The latter is not solvable analytically.

In summary, the problem of the secular description of the 3B perturbation has already been considered in the past, and it could not be expressed in a closed-form, but it requires to be undertaken numerically.

6.3.2 Combined Semi-analytical-Numerical Approach

Following the result of section 6.3.1, the approach in this section is to consider the well-known analytical secular solution of the relative motion with oblateness, and then add the gravity of Phobos numerically.

The differential J_2 perturbation is always destabilizing, apart from peculiar configurations that disable the departure of the epicycle. These no-drift solutions are known as J_2-invariant FF [155, 156]. The procedure to derive such orbits consists in the linearization of the secular derivatives due to J_2 in Eq.3.22, with respect to the difference of the remaining mean OEs. This yields three equations to be matched to zero, forcing the secular derivatives of the OEs to be the same for both spacecraft. This is presented in Eq.6.9, where a common simplification is made, which is to neglige the derivative of the J_2 effect with respect to $\Delta a_{0,M}$, since these terms are too large in comparison to the others in each constraint of Eq.6.9. The derivatives neglected are proportional to the ratio between Keplerian and J_2 gravity, thus this assumption is worthy for the cases of Earth and Mars.

$$\left.\frac{d\overline{OE}}{dt}\right|_{J_2} = 0 \Rightarrow \begin{cases} \bar{\dot{\Omega}} = 0 \\ \bar{\dot{\omega}} = 0 \\ \bar{\dot{M}} = 0 \end{cases} \Rightarrow$$

$$\Rightarrow \begin{cases} \frac{4e_c}{1-e_c^2}\cos i_c \Delta e_{0,M} - \sin i_c \Delta i_{0,M} = 0 \\ \frac{4e_c}{1-e_c^2}\left(1-5\cos^2 i_c\right)\Delta e_{0,M} + 5\sin 2i_c \Delta i_{0,M} = 0 \\ \Delta a_{0,M} + 3a_c\left(\frac{R}{p_c}\right)^2 J_2 \frac{e_c}{\sqrt[2]{1-e_c^2}}\left(1-3\cos^2 i_c\right)\Delta e_{0,M} + \frac{3}{2}a_c\left(\frac{R}{p_c}\right)^2 J_2 \sqrt[2]{1-e_c^2}\sin 2i_c \Delta i_{0,M} = 0 \end{cases} \tag{6.9}$$

The system of Eq.6.9 is homogeneous, therefore the solution is classically obtained erasing only the secular derivative of Ω and $\lambda = \omega + M$, and one between a difference of mean eccentricity or inclination becomes a free parameter. This yields a family of J_2-invariant orbits. This solution is reported in Eq.6.10.

$$\left.\frac{d\overline{OE}}{dt}\right|_{J_2} = 0 \Rightarrow \begin{cases} \bar{\dot{\Omega}} = 0 \\ \bar{\dot{\lambda}} = \bar{\dot{\omega}} + \bar{\dot{M}} = 0 \end{cases} \Rightarrow$$

$$\Rightarrow \begin{cases} \Delta e_{0,M} = \frac{1-e_c^2}{4e_c}\tan i_c \Delta i_{0,M} \\ \Delta a_{0,M} = -\frac{1}{2}a_c\left(\frac{R}{p_c}\right)^2 J_2 \tan i_c \left[\left(1+\frac{3}{2}\sqrt[2]{1-e_c^2}\right) + \cos^2 i_c\left(5+\frac{21}{2}\sqrt[2]{1-e_c^2}\right)\right]\Delta i_{0,M} \end{cases} \tag{6.10}$$

The resulting solution is made up of the mean Δa and Δe, as a function of the mean Δi and the remaining OEs. This couple of six mean OEs are transformed in osculating OEs. This transformation is known analytically for the case of J_2 [105]. The resulting couple of six osculating OEs is the set of initial conditions of Phobos and the spacecraft for the J_2-R2BP of Eq.6.3. Recall that Phobos gravity is still not considered yet. An example of J_2-invariant FF with Phobos is reported in Fig.6.13. As a difference from Fig.6.12 the epicycle does not drift any longer along the θ-axis. In fact, its planar projection is fixed. However, a J_2-invariant FF is not a fixed PO like the original epicycle, but only a

2-torus. This is the only possible reduction of the phase-space of the invariant relative solutions due to the introduction of J_2. This result is understandable from the fact that Eq.6.10 does not solve Eq.6.9, but only a wise combination of its constraints. A J_2-invariant FF is a 3D 2D-QPO, whose additional natural phase describes the precession of the relative line of nodes. For the case of a Phobos, as a difference from a FF between two spacecraft, the J_2-invariant FF is actually a better solution than an epicycle. This is because the Hill's frame of the orbit is fixed with respect to Phobos' BCBF frame. Thus, the precession enables to avoid the 1:1 resonance of a PO, providing global observation of the surface of the moon.

The second step is to introduce Phobos gravity numerically, in the P-R2BP with the initial condition of the J_2-invariant FF. The idea was that, since Phobos has a stabilizing effect, the domain of ΔOEs derived for stable relative orbits would be enlarged. This has resulted to be a wrong prediction, as visible in the example of Fig.6.14. No original J_2-invariant FF is stable in the ER3BP, and the QSO departs along the Hill's θ-axis. This behavior is related to the fact that, for the case of Phobos, the J_2-invariant FF provided by Eq.6.10 requires a difference in inclination higher than the difference in eccentricity ($\Delta i/\Delta e = 3.4$), so the resulting relative orbit is highly inclined[10]. This will be addressed in the following section.

6.3.3 Numerical Approach

The dynamical analysis of the QSOs requires the derivation of the secular derivatives of the 3B perturbation in the P-R2BP, in a similar way to the case of J_2. But the solution of the mean integral value of the 3B perturbation could not be undertaken analytically. The integral of Eq.6.6 is solved numerically in [67], and used to address the physical interpretation of the stability analysis of the QSOs. These results were applied to the case of the asteroid's orbits, which are QSOs around other planets. In particular, the integral of Eq.6.6 is required also to derive the secular motion of the precession of the 3D QSOs. By describing the secular mean longitude between the second massive body and the spacecraft, the stability conditions of the QSOs found in [67] are two.

- Any 2D QSO large enough that the oscillation amplitude of the epicycle does not make it fall towards the secondary body (minimum distance of the epicycle) is always stable.

- For any 3D QSO the secular precession will rotate the epicycle with the relative line-of-nodes towards the Hill's r-axis (relative nodes in conjunction with the two central bodies). Such attitude becomes unstable as far as the inclination of the QSO increases, therefore the QSO leaves the body neighborhood and becomes a Horseshoe orbit. This 3D stability condition of the QSOs requires the difference in inclination (in radians) to be smaller than the difference in eccentricity.

[10] Each J_2-invariant formation around Phobos has max declination of 75° on the cis/trans-side, and 60° on the leading/trailing-side.

The second condition is coherent with the results of section 6.3.2. The condition of the J_2-invariant FF is the opposite, thus the Phobos gravity will make the resulting QSO unstable every time the precession rotates the sub-epicycle in such an attitude. This mechanism is clearly visible in Fig.6.14.

In addition, a linear Floquet stability analysis of the QSOs, that fulfil the above stability conditions, in the CR3BP has highlighted the high stability of them [61]. Thus, for the range of distance from Phobos, the constraints of the 3B effect of [67] are the drivers of the stability analysis of the QSOs in the Mars-Phobos system.

In [62], a different approach is considered and consists in the linearized dynamical analysis, in the ER3BP, of the epicycles of the R2BP. Furthermore, the analysis is applied to the Mars-Phobos case. First of all, the linearized description of the QSOs is coherent with the nonlinear simulations, describing both the θ-oscillation and precession rotation, in particular their periods. In addition, there is a relationship that bounds the mean motion of the sub-epicycles with the mean motion of the secondary body around the primary: the natural period of the sub-epicycles increases for decreasing distance from the second massive body, as expected from section 6.1.2. Second of all, the linearized stability conditions are consistent with the physical interpretation given by [67], and also more precise. They are the following.

- The expression of the minimum distance, above which the planar QSO is stable, is provided. For Phobos, this is $29.4km$ ($\Delta e = 0.00315$).
- The 3D stability condition, that bounds the admissible difference in inclination to the difference in eccentricity below which the inclined QSO is stable, is $\Delta i/\Delta e < 96\%$.

Similar numerical outcomes were obtained for the stability analysis of QSOs around Jupiter's moon Europa [65].

In particular, it appears that the minimum distance corresponds to a peculiar condition presented by Hénon in [158] on the stability of the planar QPOs around the f family of POs of the Hill's approximation of the planar CR3BP[11]. As far as the dimension of the QPOs increases, the stability is influenced by the 1:3 and 1:4 resonances with the families of multiple-revolution direct satellite orbits, where the QPO motion is disabled. Thus, these intersections, visualized in [158] through a Poincaré map $y = 0$, are stability conditions. In [158], a summarizing graph shows the range of the initial conditions, on the velocity components, that provide a quasi-periodic motion as a function of the initial x position on the Poincaré section. The last intersection, at the resonance 1:4, is encountered by an epicycle of minimum distance equal to $1.2\sqrt[3]{\mu}$ of the orbital semi-major axis. After that, the QPO remains bounded even at infinite distance (within the Hill's approximation). This value for the Mars-Phobos system leads

[11] In [157], five classes of periodic solutions (for the case of a single revolution around the secondary body), have been obtained: they are the LPOs, the retrograde satellite orbits, the direct satellite orbits and their specular couples of asymmetric bifurcated orbits.

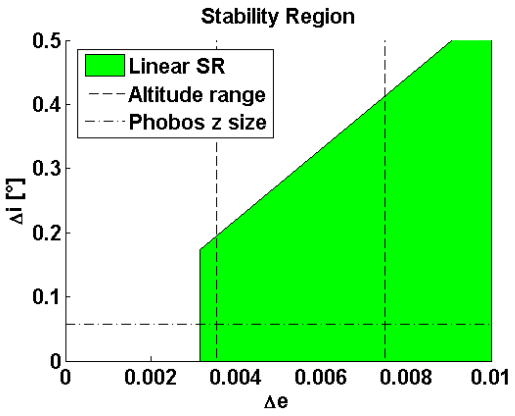

Figure 6.15: **Linear stability region of QSOs around Phobos.** Initial conditions on osculating OEs around Mars for the spacecraft and Phobos: positive differences in eccentricity and inclination.

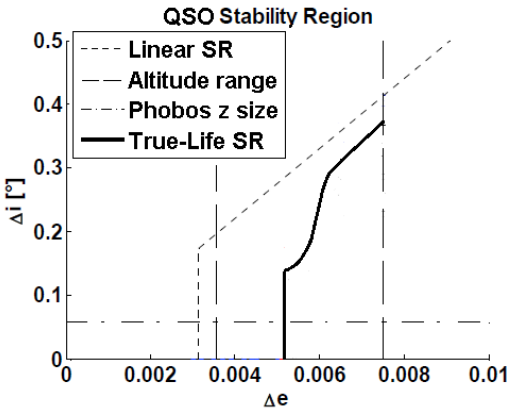

Figure 6.16: **Nonlinear stability region of QSOs around Phobos.** High-fidelity 1 year simulations, defined by initial conditions on osculating OEs around Mars for the spacecraft and Phobos: positive differences in eccentricity and inclination, starting at perimars epoch.

to a distance of $28.7km$, which is so close to the value obtained above in the linearized ER3BP. Thus, the QSOs are the natural invariant motions around the Strömgren's f class of orbits of the 3BP, after the 1:4 resonance.

In addition, [158] found a significantly different sensitivity of the stability of the QPO between the two velocity components, with the radial one (with respect to the primary) being far less critical at pericenter and apocenter. Regarding the sensitivity at different phases, a set of simulations is carried out considering the other most interesting points, which are the two quadrature positions. The outcomes have resulted to be the same, with the range of radial velocity smaller than the one of the tangential velocity. The reason could be because an increase in tangential velocity increases the semi-major axis. As explained in section 6.1.1, the semi-major axis is the critical parameter for a FF, because it is directly related to the mean motion of the two spacecraft, thus determines whether the relative motion will be invariant or rapidly drifting away along the θ-axis. This means that the accuracy required by the GNC subsystem for the insertion maneuver to the QSO is less critical in Mars-Phobos and Phobos-spacecraft common quadrature configurations, where the epicycle has only radial velocity on the orbital plane and the amplitude of the tangential oscillation is the smallest using mean OEs.

6.3.4 Simulations

After the procedure undertaken throughout section 6.3 to investigate the stability analysis of the QSOs, it emerged that Phobos' perturbation is not analytically able to be approximated in terms of OEs. Moreover it is not able to be passively combined with Mars J_2 secular motion, because it has a different natural frequency and also a dominating effect, which is expensive to counteract actively for a long period, as investigated

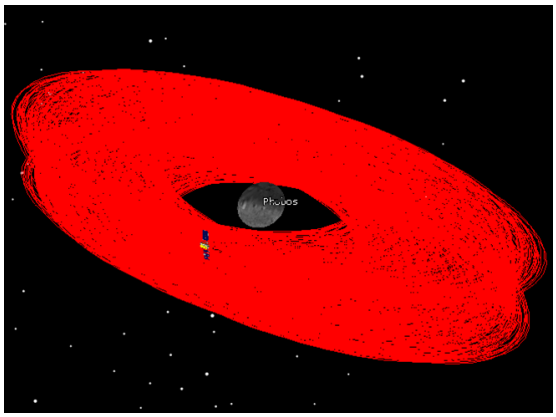

Figure 6.17: **QSO around Phobos.** Example of a 3D stable QSO in the Phobos Hill's frame for 1 year propagation.

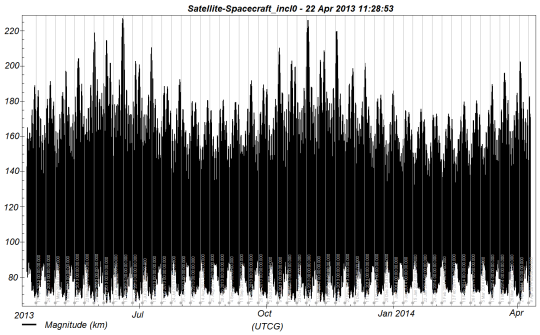

Figure 6.18: **QSO around Phobos.** Example of a 3D stable QSO in the Phobos Hill's frame for 1 year propagation. Distance's magnitude from Phobos.

in section 5.5. However, this compensation is not an efficient choice because the Phobos' gravity mostly has a stabilizing effect, and the linear stability requirements of section 6.3.3 are a reliable approximation of the range of stable QSOs in the perturbed dynamics.

Therefore, the linearized stability analysis of the QSOs is already provided in the literature, in particular for the case of Phobos. In this section, the nonlinear stability of the QSOs around Phobos is probed with numerical simulations. In [61], the stability has been tested scanning the state-space in relative position and velocity with a high-fidelity simulator. In this chapter, the stability analysis of the QSOs has been undertaken in the framework of the relative P-R2BP, which is suited to interface with a previous orbital segment around Mars. Thus, the approach followed is to use the linear stability region of [62] as a first guess in order to limit the boundary of the state-space in terms of osculating OEs where conduct the nonlinear simulations. The linearized stability region of the QSOs around Phobos is a trapezoid in the plane Δe-Δi, as shown in Fig.6.15. In particular, the minimum distance is smaller than the minimum altitude required by observation missions, which is considered to be $20km$ ($\Delta e = 0.00355$), while the required maximum altitude, which is considered to be $60km$ ($\Delta e = 0.00750$), is definitely inside the range of distances such that Phobos gravity is still predominant with respect to the differential Mars J_2 perturbation. In addition, the boundary of the maximum inclination at these distances provides a vertical amplitude of the QSOs much higher than Phobos' vertical size ($\Delta i = 0.001rad = 0.06°$), therefore 3D QSOs close to this boundary are unlikely to be used in a typical mission to Phobos. This practical range of QSOs is inside the linear stability region.

These range of distances, together with the limit of inclinations provided by the linear stability region in Fig.6.15, is used to simulate the QSOs. This has been undertaken with the STK software, considering the default ephemerides of Phobos, starting at 10 April 2013 08:35:30UTCG (perimars), and the additional perturbations of the Mars

GHs up to 15th degree/order, the Phobos GHs up to 4th degree/order, the Sun and SRP perturbations. The set of initial conditions is limited to positive Δe-Δi, while all the other initial conditions' differences in osculating OEs at the perimars are null. The QSOs are simulated up to one year of propagation time. A QSO is considered stable when it does not drift away by the end of the simulation. This is very reliable and not too much restricting because the strong nonlinearity of the 3B dynamics change drastically the motion when crossing the stability region's boundaries (as proved with the AEPs in section 5.2). Furthermore, the time allocated to a single QSO segment in a typical mission should be lower: ESA Phootprint will use a QSO from 6 to 9 months.

An example of a stable QSO is provided in Fig.6.17. The resulting true-life stability region boundary is presented in Fig.6.16. The observations are the followings.

- The minimum distance requirement is significantly higher than the linear one.
- In the smallest stable range of Δe, the 3D stability boundary is smaller than the linear one.
- For higher eccentricity, such boundary asymptotically reaches the linear one.

Furthermore, the starting Δe of the epicycle does not define trivially the minimum distance from Phobos of the QSO for the smallest range of eccentricities, as visible from Fig.6.18: the planar QSO at minimum stable Δe has a minimum altitude of $25km$. Regarding the dependence of the stability region from initial phase of Phobos, the second part of [62] is devoted to nonlinear stability simulations using Fast Lyapunov Indicators, where the dependence on the initial true anomaly is conducted. The outcomes shows that results at perimars and apomars are similar, whereas a quadrature phase has a smaller linear stability region. This counteracts what it is stated and suggested in [61], where the sensibility to initial conditions on the velocity is favorable along the Hill's θ-axis.

It is worth noting that despite the range of interest, for exploitation in missions to Phobos, of Δe-Δi in the nonlinear stability region is not compromised from their stable range in the linear approximation, the key point becomes the accuracy of the control system to insert precisely the spacecraft in the chosen QSO.

6.4 Applications

The stability of this class of orbits, combined with the collapse of the SOI and the synchronous rotation, makes the QSOs attractive solutions to orbit Phobos. In this section the main features of the QSOs are investigated, in the framework of their exploitation in the proposed sample-and-return ESA mission Phootprint.

6.4.1 Reference Guidelines for ESA Phootprint

At the time this research was carried out, preliminary studies of the Mars Moon Sample and Return were undertaken by CDF at ESTEC (MAGs [66]), and the renamed mission Phootprint was entering in Phase 0/A. The mission outline has a significant heritage of the two previous Russian missions to Phobos discussed in section 1.2, which is:

- the Earth/Mars transfer (around 2024)
- an observation orbit, which is a Trailing FF, for measuring the moon's state (orbital elements) and parameters (gravity parameter and inhomogeneous gravity field)
- the operative orbit around Phobos, which is a QSO, used to observe the surface thoroughly and identify the landing site where obtaining a sample of the soil
- landing
- sampling
- take-off
- return back to Earth.

Regarding the preliminary guidelines in [66], the Earth-Mars transfer is designed to bring the spacecraft in a Mars orbit, which is then changed to reach Phobos' inclination and altitude. This is the observation orbit required for measuring Phobos' state evolution (position and velocity) and mass parameters: this is necessary because Phobos is a very small body flying very close to Mars, therefore its gravity field and orbital elements should be validated (recall that the orbit of Phobos is not Keplerian, in particular due to Mars' oblateness) prior to the approaching segments. This observation orbit is a trailing configuration with a distance of $500km$ from Phobos.

Once the measurements are taken, the spacecraft is inserted in a closer observation orbit around Phobos. This is realized with a QSO, that will be used for a very long time (6-9 months), and required to remain stable during the solar conjunctions that would black out the communications to the Earth for approximately 1 month. The mission does not use SEP, and requires the spacecraft to maximize the lighting conditions.

Preliminary studies were also undertaken for the previous Russian missions, and in particular [159] focuses on the QSO determination. Regarding Phootprint, research studies at ESOC have been conducted in [61, 160, 78]. A preliminary study of orbits around Phobos, including QSOs, has been conducted by JPL in [57].

6.4.2 Time of Coverage

From a sample of QSOs simulated in section 6.3.4, the period of the secular precession for 3D QSOs is computed. This natural motion of the 3B dynamics is useful for observation purposes because it allows to overcome the 1:1 resonance of the sub-epicycles

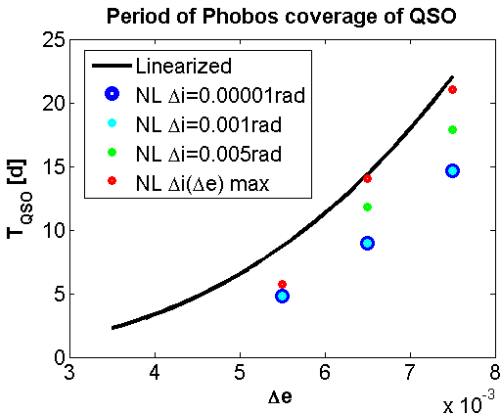

Figure 6.19: **Surface coverage of the 3D QSOs around Phobos.** Period of precession of the relative line-of-nodes that indicates the minimum time for a complete Phobos' surface coverage of the QSOs. Linearized solution as a function of Δe and outcomes from the NL simulations with different values of Δi.

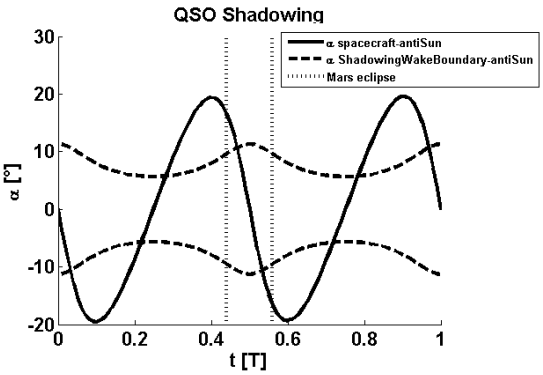

Figure 6.20: **Lighting conditions of the QSOs around Phobos.** Example of the lighting conditions for a Keplerian epicycle at 50-110km distance range, remaining in the Mars and Phobos shadowing wakes for 34% of the time.

and provide a complete coverage of the surface of Phobos. Every 360° that this motion is completed, the sub-epicycles has swathed the r-h and θ-h planes around Phobos, as we see in Fig.E.12 and Fig.6.17.

Fig.6.19 presents this time for the QSOs of the stability region, and compare it with the linearized solution from [62]. The latter is a function of Δe^3, and has resulted to be close to the results of the nonlinear simulations for the 3D QSOs near to the stability boundary $\Delta i(\Delta e)$ in Fig.6.16 and for high eccentricities. In contrast, the linearization is not accurate for smaller QSOs. In summary, the QSO is not resonant with Phobos, and all the range of stable 3D QSOs of interest provide a fast coverage of the moon, which is the main objective of this mission segment in Phootprint. Obviously to verify if the complete coverage of Phobos' surface is possible, and subsequently derive the required Δi of the 3D QSO, the knowledge of the technical data (FOV, elevation from ground) of the optical instruments to be used in the mission is required. These requirements have been considered in section 5.5.2.

6.4.3 Lighting Conditions

The analysis undertaken in this section provided a region of QSOs that are naturally stable with a high-fidelity perturbed model, potentially for a whole long-period mission scenario. Their distances from Phobos are suitable for observation, and the exploitation of the natural precession motion provides a fast complete coverage of the surface of the moon. Considering the results of the analysis of the lighting conditions around Phobos conducted in section 2.6, such a fast precession, combined with the exploitation of these orbits for long periods, allows a spacecraft to remain mostly in light.

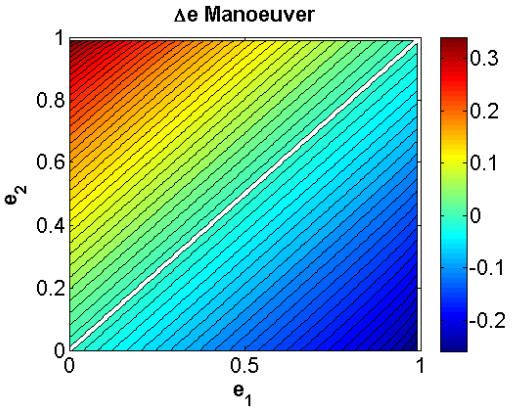

Figure 6.21: **Maneuver for change of eccentricity.** Δv relative gain by performing the maneuver at the apocenter versus at the pericenter.

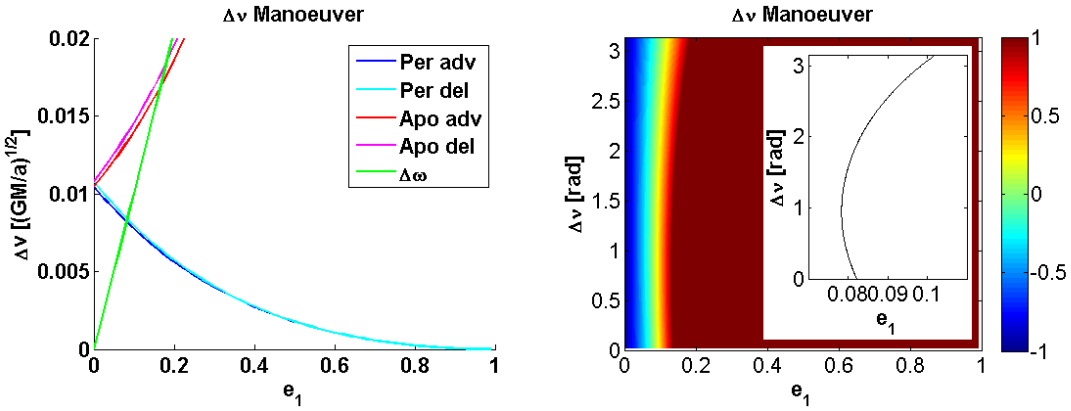

Figure 6.22: **Phasing maneuver.** On the left, comparison of the adimensional Δv for a single lap phasing ($\Delta\nu = 0.1rad$) at pericenter/apocenter in leading/trailing configuration, and related ω-phasing. On the right, Δv relative gain by performing the ω-phasing versus the cheapest ν-phasing (single lap, trailing, at the pericenter) for different $\Delta\nu$. Magnification of the break-even front.

In contrast, QSOs can be controlled to maintain a 1:1 resonance with Phobos' BCBF frame: this would provide constant lighting conditions, ranging from continuous light (during solstices) to continuous shadow (during equinoxes), controlling the β-angle thermal condition desired, by fine tuning the initial phase of the spacecraft along the epicycle with respect to the VDCO of the Sun around Phobos (see Fig.2.26). An example in Fig.6.20 shows that a planar epicycle in the middle of the stability region, during an equinoctial season, could remain in shadow from the field of view of the Sun for the 34% of the time.

6.4.4 Insertion Maneuver

Another important measure of the trade-off that could be used in the mission design, to select the optimal QSO inside the stable domain, is the Δv of the insertion maneuver. This is undertaken in this section by considering a previous mission segment realized by

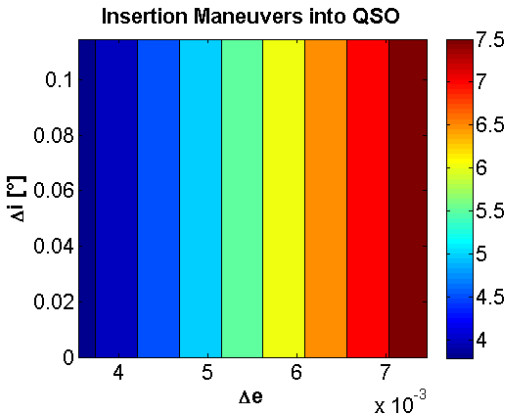

Figure 6.23: **Insertion maneuver to QSO around Phobos.** Δv $[m/s]$ cost for Δe.

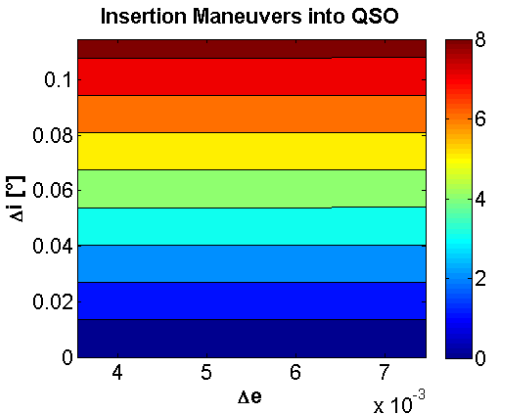

Figure 6.24: **Insertion maneuver to QSO around Phobos.** Δv $[m/s]$ cost for Δi.

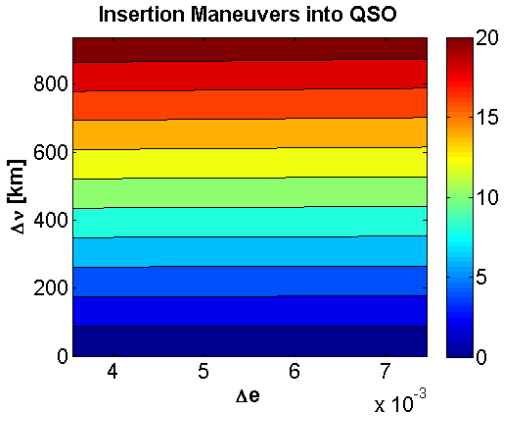

Figure 6.25: **Insertion maneuver to QSO around Phobos.** Δv $[m/s]$ cost for $\Delta\nu$, 1 lap phasing from trailing configuration.

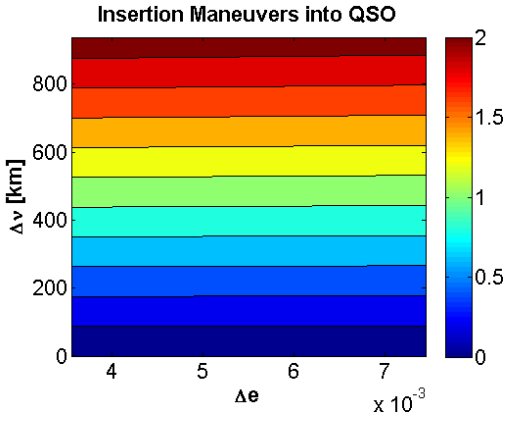

Figure 6.26: **Insertion maneuver to QSO around Phobos.** Δv $[m/s]$ cost for $\Delta\nu$, 10 laps phasing from trailing configuration.

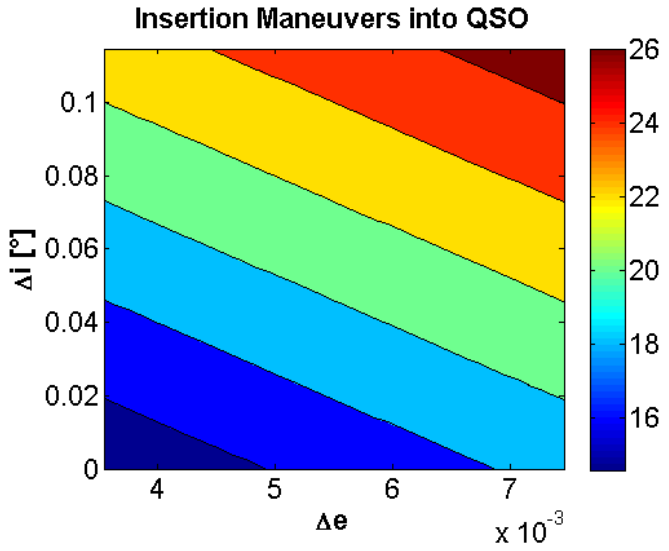

Figure 6.27: **Insertion maneuver to QSO around Phobos.** Δv $[m/s]$ total cost with 1 lap phasing from $500km$-trailing configuration.

a Martian trailing orbit, which is a body-fixed hovering point analyzed in section 5.2. The range of phases considered is $\Delta\nu = [0°, -6°]$ from Phobos, that corresponds to a distance 0-1000km. Since the starting OEs are the same of Phobos, apart from ν, the differences of eccentricity and inclination of the QSO with respect to the trailing orbit are directly the ones with respect to Phobos, used to express the stability region. The difference in anomaly/longitude with respect to the trailing orbit is the same between the latter and Phobos. In this section the Δv budget is computed to provide, with the cheapest strategy of impulsive maneuvers, the initial conditions of the QSO Δe, Δi, and to erase the initial phasing $\Delta\nu$.

The impulsive maneuvers required to achieve these single differences are analyzed separately. The subscripts indicate whether the maneuver is performed at the pericenter (P) or apocenter (A), the initial (1) and final orbit (2), the transfer orbit (T) between the two impulses, the leading (a) or trailing (d) phasing configuration. The superscripts indicate the condition before (-) and after (+) the burn.

- Change of eccentricity: a double impulse at pericenter/apocenter, keeping constant the semi-major axis.

$$\begin{aligned}
&\Delta v_{\Delta e,P/A} = \left|v_1^+ - v_1^-\right|_{P/A} + \left|v_2^+ - v_2^-\right|_{A/P} = \\
&= \left|\sqrt[2]{\frac{GM}{p_T}}\left(1 \pm e_T\right) - \sqrt[2]{\frac{GM}{p_1}}\left(1 \pm e_1\right)\right| + \left|\sqrt[2]{\frac{GM}{p_2}}\left(1 \mp e_2\right) - \sqrt[2]{\frac{GM}{p_T}}\left(1 \mp e_T\right)\right| = \\
&= \sqrt[2]{\frac{GM}{a}}\left\{\left|\sqrt[2]{\frac{1 \pm e_2}{1 \mp e_1}\frac{2}{2 \pm \Delta e}} - \sqrt[2]{\frac{1 \pm e_1}{1 \mp e_1}}\right| + \left|\sqrt[2]{\frac{1 \mp e_2}{1 \pm e_2}} - \sqrt[2]{\frac{1 \mp e_1}{1 \pm e_2}\frac{2}{2 \pm \Delta e}}\right|\right\}
\end{aligned} \tag{6.11}$$

- Change of inclination: a single impulse performed at the ascending/descending node, which does not change Ω.

$$\left\{\begin{array}{l}
\Delta v_{\Delta i,\Delta\Omega,\nu} = \Delta v_\theta = 2v_\theta \sin\frac{\alpha}{2} \\
\left\{\begin{array}{l}
\cos\alpha = \cos i_1 \cos i_2 + \sin i_1 \sin i_2 \cos\Delta\Omega \\
\frac{\sin(\omega_1+\nu)}{\sin i_2} = \frac{\sin(\omega_2+\nu)}{\sin i_1}
\end{array}\right.
\end{array}\right. \Rightarrow \left\{\begin{array}{l}
\Delta v_{\Delta i} = 2\sqrt[2]{\frac{GM}{p}}\left(1 + e\cos\omega\right)\sin\frac{\Delta i}{2} \\
\alpha = \Delta i \\
\Delta\Omega = 0 \\
u_1 = u_2 = 0
\end{array}\right. \tag{6.12}$$

- Change of true anomaly: a two impulses phasing.

$$\begin{aligned}
&\Delta v_{\Delta\nu,P/A,N,a/d} = \sum_i^N 2\left|v_{P/A}^+ - v_{P/A}^-\right|_{\Delta\nu_i} = \\
&= 2\sqrt[2]{\frac{GM}{a}}\left|\sqrt[2]{\frac{2}{1 \mp e} - \frac{1}{\left(1 \pm |_{a/d}\frac{|\Delta M(\Delta\nu,e)|}{2\pi N}\right)^{\frac{2}{3}}}} - \sqrt[2]{\frac{1 \pm e}{1 \mp e}}\right|
\end{aligned} \tag{6.13}$$

A preliminary sensitivity analysis on the free parameters of these maneuvers provides the following indications.

- The eccentricity maneuver is cheaper at the pericenter for increasing the eccentricity (see Fig.6.21), which is the case considered in the computation of the stability region of the QSOs.

- The inclination maneuver is minimum on the orbital plane, but the cost also decreases with the distance from the central body. For the case of Phobos, the ascending node is at $\nu = 106°$, and the inclination and eccentricity of the orbit are small. Therefore, it should be preferable to perform this maneuver still at the ascending node. With this choice, the maneuver is cheaper with high eccentricity: the minimum is for $e = -cos(\nu_\Omega) = 0.27$.

- The phasing maneuver is always cheaper at the pericenter, for high eccentricity, in the leading configuration (see Fig.6.22). However, the demand for the mission outline is a trailing configuration, and the difference between the two cases is negligible (about 2%). In addition, the cost could be lowered quite linearly performing multiple laps.

- Note that for elliptic orbits, the phasing could be achieved also keeping the same anomaly, but changing the line of apses, which is a change of the argument of pericenter ω.

$$\begin{cases} \Delta v_{\Delta\omega,\Delta\nu} = \Delta v_r = 2\sqrt[2]{\frac{GM}{p}}e\left|\sin\frac{\Delta\omega}{2}\right| \\ \begin{cases} \Delta\nu = \Delta\omega \\ \nu^- = \begin{cases} \frac{\Delta\omega}{2} \ , \ \nu^- \geq \Delta\omega \\ \frac{\Delta\omega}{2} + \pi \ , \ \nu^- < \Delta\omega \end{cases} \end{cases} \end{cases} \tag{6.14}$$

  The advantage of this maneuver is that the relative position's direction is fixed in the Hill's frame, in case of Keplerian motion. However, this alternative phasing strategy is usually far more expensive than the usual phasing in anomaly, apart from very small eccentricities: for the case of Phobos, this happens for $e < 0.081$, comparing it with the case of single lap phasing in anomaly (see Fig.6.22).

In conclusion, since the last two maneuvers are cheaper for high eccentricity, the best sequence of maneuvers chosen is:

- eccentricity maneuver at the perimars;

- inclination maneuver at the ascending node;

- anomaly phasing at the perimars.

The outcomes of the Δv cost are provided separately, for the range of difference of eccentricity and inclination inside the stability region. The first maneuver is presented in Fig.6.23, and clearly is independent from the second. The second maneuver is

presented in Fig.6.24, and is dominated by the Δi. Finally, the anomaly phasing is considered for the single lap case in Fig.6.25, but its cost is easy to be controlled, to lower the total Δv budget, by adding more laps, as presented in Fig.6.26. This is appealing also for the fact that the Phobos' orbit around Mars has a short period ($7h39min$). Recall that also a single phasing in ω is possible and cheaper that the single phasing in ν at the eccentricity of Phobos. The cost of the phasing maneuver is approximately independent from the inclination, therefore it is plotted has a function of eccentricity and anomaly. The latter has been transformed in the mean distance spacecraft-Phobos.

In conclusion, Fig.6.27 provides the total cost for the insertion maneuver to the QSOs inside the high-fidelity stability region. Since Δe and Δi are small the cost range for their related maneuvers is moderate (5-7.5m/s and 0-8m/s), and so it is the cost of the phasing (0-20m/s), which could be lowered for distant body-fixed AEPs linearly, by performing multiple laps. The drawback is the accuracy of the GNC subsystem to insert precisely the spacecraft in this small range of initial conditions.

Chapter 7

Conclusions

This chapter concludes the thesis by summarizing the results of the analyses undertaken to address the objectives set in section 1.3.

7.1 Outcomes of the Research

This thesis has analyzed several kinds of orbits around the Martian moon Phobos, each one defined and investigated in the light of the characterization features introduced in section 1.3. The design of a future space mission to Phobos requires multiple objectives and constraints to be satisfied. In this sense, the outcomes of the analysis carried out in this thesis are collected in Table 7.1, where each orbit has a number of potential applications and their performance can be assessed against the requirements of each mission segment. For this task, the analysis of the physical and orbital environment around Phobos conducted in chapter 2 is indispensable.

Trailing/Leading orbits around Mars are the most simple orbits to observe Phobos, and they have been analyzed in section 5.2. The orbits that start from $25km$ distance from Phobos are attractive configurations for body-fixed hovering, because they are *cheap and affordable by SEP even for heavy human modules*, they are *stable* to perturbations, and they are *mostly in full light*. They are *the best orbits to start to approach Phobos' SOI*, however their ground-track on the moon is stationary and constrained. Other distant configurations or **close-range AEPs** require either high-thrust or high station-keeping cost for hovering in Phobos' BCBF frame over long-time: they can be used only for *short and dedicated operations of small unmanned spacecraft*.

The preliminary analysis of the orbital dynamics around Phobos conducted in section 2.3 pointed the attention to **the collapse of the realm of attraction of the moon towards its surface**. As a result of this situation, natural Keplerian orbits with respect to Phobos are infeasible to orbit around the moon. Section 5.3 investigated the artificial realization of these orbits, and focusing on the case of hovering in the inertial frame around Phobos, which would provide a spacecraft stationary lighting conditions during a Martian season. Due to the pull of Mars these **SS-VDCOs** require continuous

Table 7.1: **Summary of orbits around Phobos.** First driver within a row is the altitude range (-). For IMs, (/) distinguishes the branch direction. Propulsive thrust range is indicated considering a 100/10,000kg spacecraft mass.

Orbit	Altitude Range	Reference Signal Computation	Dynamical Model	Orbital Propulsion	Maintanance Strategy			Surface Coverage	Lighting Conditions	Potential Mission Applications
					Control action	Guidance error	Navigation accuracy			
AEP	0-4.5km x 0m/s	relative fixed position, accurate gravity field model	C3B-GH	0.5/50-0/0N (150-0m/s/T) constant acceleration	unstable: SK 3-3m/s/T every 7-7min	10-10m 0.05-0.05m/s	1-1m 0.001-0.001m/s	stationary ground-track cis/trans-Phobos region	solstices: 50-80% equinoxes: 40-70% (cis), 50-80% (trans)	dedicated proximity operations, radiation shield (53-13%)
	0-4.5km y 0m/s	relative fixed position, accurate gravity field model	C3B-GH	0.5/50-0.3/30N (150-100m/s/T) constant acceleration	unstable: SK 0.6-0.6m/s/T every 14-15min	10-10m 0.02-0.02m/s	1-1m 0.001-0.001m/s	stationary ground-track lead/trail-Phobos region	solstices: 50-80% equinoxes: 45-75%	dedicated proximity operations, radiation shield (50-16%)
	0-4.5km z 0m/s	relative fixed position, accurate gravity field model	C3B-GH	1/100-0.4/40N (300-120m/s/T) constant acceleration	unstable: SK 0.9-0.9m/s/T every 11-12min	10-10m 0.03-0.02m/s	1-1m 0.001-0.001m/s	stationary ground-track North/South pole-Phobos region	S/W solstice: North/South light, South/North shadow under 1.4km then light, equinoxes: 88%	dedicated proximity ops, complete lighting/shadowing, radiation shield (58-20%)
	4.5-70km x 0m/s	relative fixed position	C3B	0/0-1.5/150N (0-400m/s/T) constant acceleration	unstable: SK 6-20m/s/T every 15-9min	100-100m 0.2-0.5m/s	10-10m 0.01-0.01m/s	stationary ground-track cis/trans-Phobos region	solstices: light equinoxes: 88%	short close observation
	4.5-60km y 0m/s	relative fixed position	C3B	0.3/30-0.04/4N (100-12m/s/T) constant acceleration	unstable: SK 3-3m/s/T every 20-21min	100-100m 0.2-0.2m/s	10-10m 0.01-0.01m/s	stationary ground-track lead/trail-Phobos region	solstices: light equinoxes: 88%	long close observation
	4.5-250km z 0m/s	relative fixed position	C3B	0.4/40-1.5/150N (120-400m/s/T) constant acceleration	unstable: SK 3-20m/s/T every 20-9min	100-100m 0.2-0.5m/s	10-10m 0.01-0.01m/s	stationary ground-track North/South pole-Phobos region	solstices: light equinoxes: 88%	short close observation
	70-400km x 0m/s	relative periodic orbit - cis/trans-Mars orbit	E3B - 2B(Mars)	1.5/150-6/600N (420-2000m/s/T) feedforward profile	stable	1-10km 0.5-2m/s	0.1-1km 0.01-1m/s	stationary ground-track cis/trans-Phobos region	solstices: light equinoxes: 88%	short stand-by, measurements, observation, comm-relay
	60-500km υ 0m/s	relative periodic orbit - lead/trail-Mars orbit	C3B - 2B(Mars)	0.04/4-0.0004/0.04N (12-0.12m/s/T) feedforward profile	stable	0.1-10km 0.05-2m/s	0.01-1km 0.01-0.1m/s	stationary ground-track lead/trail-Phobos region	solstices: light equinoxes: 88%	long stand-by, measurements (acquisition of Phobos orbit and GM), comm-relay
	250-1400km z 0m/s	North/South-Mars orbit	2B(Mars)	1.5/150-8/800N (420-2500m/s/T) feedforward profile	stable	10-50km 2-10m/s	1-10km 0.1-1m/s	stationary ground-track North/South pole-Phobos region	solstices: light equinoxes: 88%	short stand-by, measurements, observation, comm-relay
VDCO	0-10km 2-7m/s	relative circular equatorial orbit daily Sun-synch	2B(Phobos)	0.5/50-0.3/30N (100-50m/s/T) feedforward profile	unstable: SK 30-6m/s/T every 7-15min	100-100m 0.5-0.2m/s	10-10m 0.01-0.01m/s	equatorial swath	fixed, controllable (solstices: 0-100%, equinoxes: 0-88%)	fixed light/shadow conditions (directional solar radiation protection), comm-relay
	10-100km 7-30m/s	relative circular orbit at height 0-0/10-50km daily Sun-synch	2B(Phobos)	0.3/30-1.5/150N (50-250m/s/T) feedforward profile	unstable: SK 6-30m/s/T every 38-21min	1-1km 1-1.5m/s	100-100m 0.1-0.1m/s	hemispheric sector	fixed, controllable (solstices: 0-100%, equinoxes: 0-88%)	fixed light/shadow conditions (directional solar rad protection), hemisphere comm-relay
$L_{1,2}$-LPO	0-10km 0-8m/s	relative periodic (2:1) or quasi-periodic orbit, high-computational techniques, accurate gravity field model	E3B-GH	not required	unstable: SK 0.15-0.05m/s/T every 20-32min	10-10m 0.02-0.01m/s	1-1m 0.001-0.001m/s	stationary ground-track on wide Phobos region	solstices: 100-60% equinoxes: 80-50% (cis), 88-60% (trans)	short close observation, approaching manoeuvers comm-bridges, radiation shield (23-13%)
	0-80km 0-20m/s	relative periodic (N:M) or quasi-periodic orbit, high-computational techniques, accurate-lighter gravity field model	E3B-GH - E3B	0/0-1.5/150N (0-400m/s/T) constant acceleration	unstable: SK 0.15-0.2m/s/T every 19-68min	10-100m 0.02-0.05m/s	1-10m 0.001-0.01m/s	stationary ground-track on dedicated region of whole Phobos surface	solstices: 100-60% equinoxes: 88-50%	short dedicated ops, radiation shield (35-3%) - short standby, measurements (Phobos gravity field), comm-relay
IM-LPO	0-10km / 0-500km 0-15m/s / 0-60m/s	relative trajectory from LPO / Mars orbit 0.5-2h / 10-20h	E3B-GH	not required	SK 0.02m/s every 20min / 3m/s every 70min	10m / 1km 0.02m/s / 0.5m/s	1m / 100m 0.001m/s / 0.1m/s	landing site cis/trans-Phobos region / stationary ground-track lead/trail-Phobos region	controllable by epoch 0-100% / solstices: light, equinoxes: 88%	natural performanced soft landing (from 0.5g) / approach to Phobos or insertion manoeuveur to LPO
	0-10km / 0-500km 0-15m/s / 0-60m/s	relative trajectory from take-off site / LPO 0.5-2h / 10-20h	E3B-GH	not required	SK 0.02m/s every 20 min / 3m/s every 70min	10m / 1km 0.02m/s / 0.5m/s	1m / 100m 0.001m/s / 0.1m/s	take-off site cis/trans-Phobos region / stationary ground-track lead/trail-Phobos region	controllable by epoch 0-100% / solstices: light, equinoxes: 88%	natural performanced cheap take-off (from 3m/s) to LPO / escape from Phobos
	0-20km / 0-500km 0-25m/s / 0-60m/s	relative trajectory from LPO / Mars orbit 0.1-3h / 8-20h	E3B-GH - E3B	0/0-0.1/10N (0-10m/s / 0-100m/s) constant acceleration	SK 0.02-0.05m/s every 20 min / 2-3m/s every 70min	10m / 1km 0.02m/s / 0.5m/s	1m / 100m 0.001m/s / 0.1m/s	landing site on dedicated region of whole Phobos surface (apart near poles) / stationary ground-track lead/trail-Phobos region	controllable by epoch 0-100% / solstices: light, equinoxes: 88%	performanced soft landing (from 0.5g) / approach to Phobos or insertion manoeuveur to LPO
	0-20km / 0-500km 0-25m/s / 0-60m/s	relative trajectory from take-off site / LPO 0.1-3h / 8-20h	E3B-GH - E3B	0/0-0.1/10N (0-10m/s / 0-100m/s) constant acceleration	SK 0.02-0.05m/s every 20min / 2-3m/s every 70min	10m / 1km 0.02m/s / 0.5m/s	1m / 100m 0.001m/s / 0.1m/s	take-off site on dedicated region of whole Phobos surface (apart near poles) / stationary ground-track lead/trail-Phobos region	controllable by epoch 0-100% / solstices: light, equinoxes: 88%	performanced cheap take-off (from 3m/s) to LPO / escape from Phobos
	20-500km / 20-500km 0-60m/s / 0-60m/s	relative trajectory from LPO, take-off site / Mars orbit, LPO, take-off site 3-13h / 5-15h	E3B-GH / E3B	0.1/10-1/100N (10-500m/s / 50-600m/s) constant acceleration	SK 0.1-0.5m/s every 20min / 1-2m/s every 70min	10m / 1km 0.02m/s / 0.5m/s	1m / 100m 0.001m/s / 0.1m/s	dedicated ground-track / stationary ground-track lead-trail-Phobos region	controllable by epoch 0-100% / solstices: light, equinoxes: 88%	transfer manoeuver around Phobos / approach/escape to/from Phobos or insertion manoeuver to LPO
QSO	25-200km 8-50m/s	relative quasi-periodic orbit, high-fidelity simulations	2B(Mars)-P	not required	naturally stable without SK	10-100m 0.01-0.1m/s	10-100m 0.01-0.1m/s	complete in 5-25days	solstices: light equinoxes: 88%	parking orbits (repairs, refuelling), measu- rements (Phobos gravity field), complete fast mapping and frequent access comms
	40-100km 10-25m/s	relative quasi-periodic orbit, high-fidelity simulations	2B(Mars)-P	if required by β-angle control system	naturally stable without SK	10-100m 0.01-0.1m/s	10-100m 0.01-0.1m/s	stationary swath	adjustable by dedicated control system	long stand-by, comm-relay, control of lighting conditions (directional solar radiation protection)

propulsion, and they are *too expensive* even for few revolutions, and also unstable.

The collapse of the Phobos' SOI allows to use Keplerian orbits with respect to Mars to orbit around its moon at feasible distance. The realization of classical relative orbits by artificially **flying in formation with Phobos** has been investigated in section 5.5. The level of thrust required to compensate Phobos' gravity is affordable by SEP, but these orbits are resonant with the Phobos' BCBF frame, thus they require an *additional schedule of frequent maneuvers to provide a full coverage for observation* of the surface of the moon. Chapter 6 focused on the natural equivalents of these orbits under the effect of the gravity of Phobos, which are the **QSOs**. These orbits are *the best solution for a precursor unmanned mission to Phobos*. They are both *natural orbits with no need of propulsion, and stable up to very long time with no need of station-keeping*, and so they can be used as *parking orbits* with distance starting from $25km$ from Phobos. In particular, closer 3D QSOs provide a *fast complete coverage to map the surface of Phobos and identify the landing site*, and they are mostly in light. 2D QSOs during equinoctial seasons are suitable to be controlled to provide nearly Sun-synchronous orbits around Phobos, enabling constant and adjustable lighting conditions: in particular, lighting condition scheduling could be important for a first-generation manned spacecraft while orbiting Mars. The long-time stability of the QSOs around Phobos could be exploited as an *orbital repository* to send, in advance, unmanned propulsion modules, fuel stockpiles, and provisions, to remain parked in *a secure low altitude Martian orbit without orbital maintenance costs and with short-period phasing maneuvers to dock the modules*. To allow the first human expeditions to visit Mars and return to the Earth, the spacecraft could make scheduled pit-stops at this orbital garage on Phobos' orbit.

A final class of interesting orbits to consider to fly in proximity of Phobos are the invariant motions around the collinear LPs, L_1 and L_2, of the Mars-Phobos system. In this sense, the analysis of the natural dynamics inside Phobos' realm of attraction has resulted to be the main focus of this thesis. In the first part of chapter 4, the classical families of **periodic and quasi-periodic LPOs** in the basic CR3BP have been computed for the case of the Mars-Phobos system. This has been undertaken by using well-known methodologies of dynamical systems theory, that are presented in appendix B. The LPOs are well-known exploitable solutions for orbiting about the smaller primary and they provide energy-efficient trajectories for interplanetary transfers of spacecraft through their IMs. However they are highly unstable, and station-keeping is required. For the Mars-Phobos system, the small SOI makes *the altitude of the LPs to be very close to Phobos*' irregular surface. In this situation, section 2.4 proved that *the basic dynamical approximation provided by the CR3BP falls short, and in particular two differential orbital perturbations* become relevant in describing the natural relative motion around this moon. They are shown to be its *highly inhomogeneous gravity field* and its *orbital eccentricity*.

For this reason, in chapter 3 an improved system of the relative dynamics in proximity of Phobos, named ER3BP-GH, has been derived, upgrading the Mars-Phobos ER3BP

with the real gravity field of the moon, modeled with a gravity harmonics series expansion. The second part of chapter 4 is devoted to the computation of the **dynamical substitutes of the LPOs** in these enhanced dynamics, through numerical continuation techniques that maintain the phase-space of the perturbations. In particular, whereas the time-dependent eccentricity effect has already been studied throughout the years, no deep analysis has been undertaken to consider the additional GHs of the secondary body in the computation of the dynamical substitutes of the LPOs. The Mars-Phobos-spacecraft system is particulary suitable for two reasons: firstly because their perturbation is significant due to the collapse of the collinear region, and then because the additional physical and orbital characteristics make this system so unique to preserve the time-invariance of the Hamiltonian model. In this sense, *the effect of the gravity harmonics produces families of periodic and quasi-periodic orbits highly distorted and tilted from the classical case.*

These natural motions have revealed some potential opportunities for future missions to Phobos. The LPOs are very close to the moon's surface, therefore they are *similar to close-range points* but with an *extended ground-track and range of lighting conditions*, and the Phobos' bulk occultation of the sky could provide relevant *passive shielding from the cosmic rays radiation.* Despite their instability, the LPOs are *natural motion* and so will require no propulsion and *low station-keeping cost* to provide: close-range *observation of Phobos*, mission segments to *directly interface with landing and take-off phases*, proximity *parking orbits* for mothership modules to remotely command lighter probes deployed on the surface, and *communication bridges* to manage robotic scouts on Mars and Phobos. However, they require the *high accuracy of an optical navigation subsystem*, and *high load on the guidance subsystem*, whose reference signal must be computed with advanced analytical and numerical techniques of dynamical systems theory that need *the acquisition of a high-fidelity gravity field of the moon.* In this sense, the accuracies required for the modeling parameters of the ER3BP-GH have been assessed against the GNC requirements, to track a spacecraft along the reference signal of the new orbits computed in the improved dynamical model. A preliminary estimation proved that such LPOs **considerably lower the control load and enhance the fuel savings between one and two orders of magnitude with respect to tracking the classical LPOs of the CR3BP, enabling feasible station-keeping by exploiting the natural dynamics around Phobos**. Another useful application is to exploit the **IMs** of these new LPOs as landing or take-off gateways to and from the surface of Phobos. In this thesis it was demonstrated that there exist *natural trajectories for a specific range of longitude-latitude sites able to facilitate a soft controlled landing, and depart with very low escape velocity injections*, less than the 2B Δv value. The optimization of these performances to select the best trajectory at a given location on Phobos will be paramount for *sample-and-return missions* (where soil contamination avoidance is necessary) as well as *first manned explorations of this moon.*

Finally, the addition of a simple propulsive law, to obtain **artificial LPOs with**

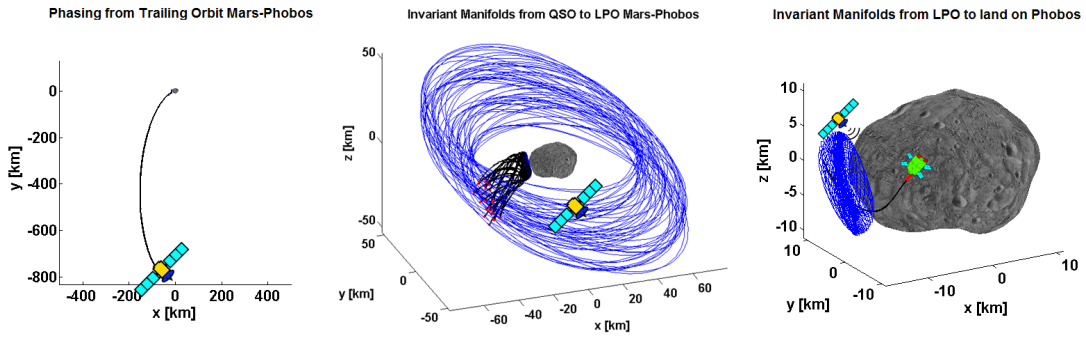

Figure 7.1: **Mission scenario at Phobos.** From the left to the right. The starting mission segment is a trailing orbit of the spacecraft in Phobos orbit. A phasing maneuver inserts the spacecraft into a Quasi-Satellite orbit around Phobos. The spacecraft then moves along the outward tube of the stable invariant manifold associated to the targeted Libration point orbit. The lander is deployed along the inward tube of the unstable invariant manifold, braking with a retro-maneuver in the last segment of the descent, to touch-down on the chosen site on Phobos, while the mothership remotely controls it on the Libration point orbit.

constant acceleration, has been investigated in section 5.4. This implementation offers some advantages when using these LPOs for short-phases: *the surface coverage and landing/take-off targeting could be extended to the whole surface of Phobos*, *the instability of the orbits could be lowered*, and the computation of the orbits themselves could be simplified to *maintain them periodic* also in the true elliptic dynamics, and to *lower the accuracy of the model of the gravity field of the moon* to be taken into account. In particular, artificial heteroclinic connections would now exist for fast orbital *fly-bys* around two opposite sides of Phobos.

7.2 Proposed Mission Scenario at Phobos

In summary, an outline for a potential future space mission to Phobos is proposed and presented in Fig.7.1.

- The starting mission segment is a trailing orbit around Mars, with a phasing of 0.4-1.2° from Phobos. This preliminary orbit is used to track the real position of Phobos and to acquire its gravity parameter.
- A phasing maneuver is carried out to reach a QSO at an intermediate distance from Phobos. This operative orbit is used to measure the real gravity field and to map the surface of the moon.
- The spacecraft moves along the tube of the artificial invariant manifolds displaced away from the moon with a constant acceleration along the x-axis. This solution allows the guidance signal, required to track the LPOs and its invariant manifold, to be less affected in its numerical computation by the GHs perturbations. This trajectory can be used to move the spacecraft to a closer LPO for a dedicated

close-range operation, or to directly reach with a probe the desired landing site on Phobos.

- In the case of a sample-and-return mission, the spacecraft moves in reverse choosing the trajectory inside the tube of the IMs that provides the minimum escape velocity from its landing site. This is used to reach a mothership that has been parked on a closer LPO or in the starting QSO, to remotely command the smaller probe.

7.3 Future Work

Based on the results of this research, presented in section 7.1, the contributions of this thesis are addressed in section 1.4. Moreover, the following extensions of the work are recommended.

The dynamical substitutes of the LPOs have been computed in an improved model of the relative orbital dynamics around Phobos. The Phobos' GHs and orbital eccentricity significantly affect the position and morphology of these orbits, thus they must be considered in the preliminary mission design to account for the natural ground-track and distance envelope provided by the natural LPOs. Station-keeping is then necessary to maintain these invariant motions, and the inclusion of these strong actions is invaluable to lower the demand of the control system. The impact on such guidance laws by additional physical perturbations, modeling inaccuracies, navigation and control errors, have been considered and assessed. In particular, the navigation and the fidelity of the gravity model of Phobos are the main drivers to make these orbits feasible in the real-world.

Due to the two peculiarities of the Mars-Phobos couple introduced in section 2.3.2, the LPOs of Phobos require autonomous absolute navigation, and subsequently autonomous control. Vision-based navigation and estimation algorithms have emerged in the last decade, and this technological capability should be further assessed and flight-proven in readiness. The case of the anticipated missions to Phobos is an appealing opportunity to foster such complementary research.

The inhomogeneous gravity field of Phobos, considered in the analytical model for the computation of the LPOs, has been described with the classical methodology of the spherical GHs. In particular, only a low-order model was freely available at the start of this research. The convergence of the solution of the LPOs with respect to the order of the truncated series is critical due to the instability of these orbits. The first suggestion for future work is to derive a higher order model with the most up-to-date data on Phobos' shape, provided by the recent spacecraft sent to Mars' orbit. With this model, the same algorithms presented in this thesis could be applied to derive more accurate dynamical substitutes, and compared with the ones identified in this thesis. However, a specific geodesic analysis of Phobos' gravity has been carried out in [96],

using high-order spherical GHs, elliptical GHs, tetrahedrons. The first technique is deemed accurate for a distance from Phobos' barycenter greater than $14km$, but provides significant errors on the surface of the moon. In this thesis, it has resulted that the effect of the GHs is to provide high distorsion and tilt on the smallest LPOs around the LPs, while the shape of larger orbits remains similar to their ancestor solutions in the classical CR3BP, and their tilt remains consistent with the orientation showed at the LP. This behavior becomes clear if one considers that, even if larger orbits require the spacecraft to fly for a considerable time closer to Phobos, where the GHs' effect is greater[1], than in the case of a smaller orbit, the effect of the high-order GHs is local. Hence, on a large orbit, the resulting average of the perturbation is less significant than its effect on a smaller orbit, where the disturbance is more stationary. The LPs are located outermost the $14km$ threshold, thus small LPOs are successfully described with spherical GHs according to [96], and their reliability depends only on the truncated order. Subsequently, the orientation of the large LPOs should be coherent with the modeling error at the LP, while their global shape should be poorly affected by the local error of the GHs in proximity of Phobos' surface. These predictions, estimated from the results obtained in this thesis, are the objectives of a research proposal based on the computation of the LPOs in an ER3BP where the gravity field of Phobos is described with a high-order model of tetrahedrons.

The IMs of the natural LPOs have been proposed as trajectories to land or take-off to and from Phobos, which is an unique opportunity in the Solar System. However, control assistance would be essential to meet all the requirements of a precise and safe landing. Hence, the natural solution of the IMs could represent a reliable initial guess in an optimizer, used in a research task whose objective is to design the maneuver to land on Phobos for a specific mission.

In this thesis, low-thrust implementation has been considered with simple control laws, such as a constant acceleration or the compensation of time-variant profile of the differential gravity forces. This is undertaken to investigate the potential of using such propulsion technologies. More sophisticated profiles or motion planners should be probed, based on all the classes of orbits existing in the natural dynamics around Phobos that have been studied in this thesis.

In this thesis, QSOs around Phobos have been briefly investigated. Following the deep qualitative knowledge of these orbits in the literature, in particular their stability, in contrast to the complex analytical description of these invariant motions, the QSOs have been probed with simulations. Since these orbits represent the best solution to naturally orbit around Phobos, analytical and numerical computation of the QSOs in this system should be required in the following years to efficiently boost the mission design of the anticipated missions to this Martian moon.

[1]Note that for this reason, large LPOs are highly improbable to be used as operative orbits, for the risk of collision during the innermost section. They can be used only in closed-loop descent maneuvers, thus the counteraction of the perturbations is already accounted since the motion is forced.

In conclusion, the research undertaken in this thesis, whose focus is to model the motion of a spacecraft about Phobos, led to a suitable description also of the natural motion of meteoroids and dust grains down to the $10\mu m$ scale. Three extensions of research are proposed. First, the new natural dynamics upgraded with the inhomogeneous gravity field of Phobos provide further evidence to support the formation of Phobos by Mars' ejecta accretion. Second, the natural LPOs and IMs could support the evidence for the formation of the craters and grooves distribution on the moon. Furthermore, they can also model the dynamics of the clouds of dust thought to exist near Phobos.

Appendix A

Equations of Motion of the ER3BP in different Reference Frames and Units

A.1 Time-Variant Time-Unit

Instead of the constant rate of the mean anomaly used in Eq.3.44, the time unit could be set to correspond to the true anomaly or the eccentric anomaly E of the primaries' orbit. The equations of motion with such variable[1] time-units are shown in Eq.A.1 and Eq.A.2 respectively. They also report the post-processing relations to obtain the inertial velocities (and time).

$$
\begin{aligned}
&\begin{cases} \mathbf{q} = a\bar{\mathbf{q}} \\ t = \frac{1}{\omega_z(\nu)}\bar{t} = \sqrt[2]{\frac{p^3}{GM}}\frac{1}{(1+e\cos\nu)^2}\bar{t} \rightarrow \bar{t} = \nu \rightarrow \frac{d^2}{dt^2} = \omega_z(\nu)^2\frac{d^2}{d\bar{t}^2} + \dot{\omega}_z(\nu)\frac{d}{d\bar{t}} \end{cases} \\
\Rightarrow &\begin{cases} \dot{\mathbf{q}} = an\frac{(1+e\cos\nu)^2}{(1-e^2)^{3/2}}\bar{\mathbf{q}}' \\ \ddot{\mathbf{q}} = an^2\frac{(1+e\cos\nu)^4}{(1-e^2)^3}\bar{\mathbf{q}}'' - 2an^2\frac{(1+e\cos\nu)^3 e\sin\nu}{(1-e^2)^3}\bar{\mathbf{q}}' \end{cases} \\
\Rightarrow &\bar{\mathbf{q}}'' - 2\frac{e\sin\nu}{1+e\cos\nu}\bar{\mathbf{q}}' - 2\frac{e\sin\nu}{1+e\cos\nu}\mathbf{W}\bar{\mathbf{q}} + 2\mathbf{W}\bar{\mathbf{q}}' = \\
&\quad = \nabla\left(\frac{\left(1-e^2\right)^3}{\left(1+e\cos\nu\right)^4}u_G\left(\bar{\mathbf{q}} + \mu\frac{1-e^2}{1+e\cos\nu}\begin{bmatrix}1\\0\\0\end{bmatrix}, \bar{\mathbf{q}} - (1-\mu)\frac{1-e^2}{1+e\cos\nu}\begin{bmatrix}1\\0\\0\end{bmatrix}\right) - \frac{\bar{\mathbf{q}}^T\mathbf{P}\bar{\mathbf{q}}}{2}\right)
\end{aligned}
\tag{A.1}
$$

$$
\begin{aligned}
&\begin{cases} \mathbf{q} = a\bar{\mathbf{q}} \\ t = \frac{1}{n}\frac{1-e^2}{1+e\cos\nu}\bar{t} \rightarrow \bar{t} = E \end{cases} \Rightarrow \begin{cases} \frac{d}{d\nu} = \frac{\sqrt[2]{1-e^2}}{1+e\cos\nu}\frac{d}{dE} = \frac{1-e\cos E}{\sqrt[2]{1-e^2}}\frac{d}{dE} \\ \frac{d^2}{d\nu^2} = \frac{(1-e\cos E)^2}{1-e^2}\frac{d^2}{dE^2} + \frac{(1-e\cos E)e\sin E}{1-e^2}\frac{d}{dE} \end{cases} \\
\Rightarrow &\bar{\mathbf{q}}'' - \frac{e\sin E}{1-e\cos E}\bar{\mathbf{q}}' - 2\frac{\sqrt[2]{1-e^2}e\sin E}{(1-e\cos E)^2}\mathbf{W}\bar{\mathbf{q}} + 2\frac{\sqrt[2]{1-e^2}}{1-e\cos E}\mathbf{W}\bar{\mathbf{q}}' = \\
&\quad = \nabla\left((1-e\cos E)^2 u_G\left(\bar{\mathbf{q}} + \mu(1-e\cos E)\begin{bmatrix}1\\0\\0\end{bmatrix}, \bar{\mathbf{q}} - (1-\mu)(1-e\cos E)\begin{bmatrix}1\\0\\0\end{bmatrix}\right) - \frac{1-e^2}{(1-e\cos E)^2}\frac{\bar{\mathbf{q}}^T\mathbf{P}\bar{\mathbf{q}}}{2}\right)
\end{aligned}
\tag{A.2}
$$

[1] Throughout this section, normalized state is indicated with an upper bar. Derivation with respect to the normalized time is indicated with an apostrophe.

$$\begin{cases} \cos\nu = \frac{\cos E - e}{1 - e\cos E} \\ \sin\nu = \frac{\sqrt[2]{1-e^2}\sin E}{1-e\cos E} \end{cases} \wedge \begin{cases} \cos E = \frac{\cos\nu - e}{1+e\cos\nu} \\ \sin E = \frac{\sqrt[2]{1-e^2}\sin\nu}{1+e\cos\nu} \end{cases} \tag{A.3}$$

A.2 Time-Variant Length-Unit

The length unit is now considered as the time-variant Mars-Phobos distance. For the elliptic motion, this is called an isotropic pulsating frame, and the related equations of motion are stated in Eq.3.45-A.4 with respect to the true anomaly and eccentric anomaly respectively.

$$\begin{cases} \mathbf{q} = l(\nu)\bar{\mathbf{q}} \\ t = \frac{1}{n}\frac{1-e^2}{1+e\cos\nu}\bar{t} \rightarrow \bar{t} = E \end{cases} \Rightarrow \begin{cases} \frac{d}{d\nu} = \frac{\sqrt[2]{1-e^2}}{1+e\cos\nu}\frac{d}{dE} = \frac{1-e\cos E}{\sqrt[2]{1-e^2}}\frac{d}{dE} \\ \frac{d^2}{d\nu^2} = \frac{(1-e\cos E)^2}{1-e^2}\frac{d^2}{dE^2} + \frac{(1-e\cos E)e\sin E}{1-e^2}\frac{d}{dE} \end{cases}$$
$$\Rightarrow \bar{\mathbf{q}}'' + \frac{e\sin E}{1-e\cos E}\bar{\mathbf{q}}' + 2\frac{\sqrt[2]{1-e^2}}{1-e\cos E}\mathbf{W}\bar{\mathbf{q}}' =$$
$$= \nabla\left(\frac{1}{1-e\cos E}u_G\left(\bar{\mathbf{q}} + \mu\left(1-e\cos E\right)\begin{bmatrix}1\\0\\0\end{bmatrix}, \bar{\mathbf{q}} - (1-\mu)\left(1-e\cos E\right)\begin{bmatrix}1\\0\\0\end{bmatrix}\right) - \frac{1}{1-e\cos E}\frac{\bar{\mathbf{q}}^T\mathbf{P}\bar{\mathbf{q}}}{2} + \frac{e^2-e\cos E}{\left(1-e\cos E\right)^2}\frac{\bar{\mathbf{q}}^T\left(\mathbf{I}_3+\mathbf{P}\right)\bar{\mathbf{q}}}{2}\right)$$
$$\Rightarrow \bar{\mathbf{q}}'' + \frac{e\sin E}{1-e\cos E}\bar{\mathbf{q}}' + 2\frac{\sqrt[2]{1-e^2}}{1-e\cos E}\mathbf{W}\bar{\mathbf{q}}' =$$
$$= \nabla\left(\frac{1}{1-e\cos E}u_G\left(\bar{\mathbf{q}} + \mu\left(1-e\cos E\right)\begin{bmatrix}1\\0\\0\end{bmatrix}, \bar{\mathbf{q}} - (1-\mu)\left(1-e\cos E\right)\begin{bmatrix}1\\0\\0\end{bmatrix}\right) + \frac{1}{1-e\cos E}\frac{\bar{\mathbf{q}}^T\bar{\mathbf{q}}}{2} - \frac{1-e^2}{\left(1-e\cos E\right)^2}\frac{\bar{\mathbf{q}}^T\left(\mathbf{I}_3+\mathbf{P}\right)\bar{\mathbf{q}}}{2}\right)$$
$$\Rightarrow \bar{\mathbf{q}}'' + \frac{e\sin E}{1-e\cos E}\bar{\mathbf{q}}' + 2\frac{\sqrt[2]{1-e^2}}{1-e\cos E}\mathbf{W}\bar{\mathbf{q}}' =$$
$$= \nabla\left(\frac{1}{1-e\cos E}u_G\left(\bar{\mathbf{q}} + \mu\left(1-e\cos E\right)\begin{bmatrix}1\\0\\0\end{bmatrix}, \bar{\mathbf{q}} - (1-\mu)\left(1-e\cos E\right)\begin{bmatrix}1\\0\\0\end{bmatrix}\right) + \frac{e^2-e\cos E}{\left(1-e\cos E\right)^2}\frac{\bar{\mathbf{q}}^T\bar{\mathbf{q}}}{2} - \frac{1-e^2}{\left(1-e\cos E\right)^2}\frac{\bar{\mathbf{q}}^T\mathbf{P}\bar{\mathbf{q}}}{2}\right) \tag{A.4}$$

Eq.A.5-A.6 report the expression of the ER3BP for the combinations a-M and l-ν in Hamiltonian form. In particular, Hamiltonian function and derivatives are fully intended in the related units used. For a Hamiltonian approach to the ER3BP see [161].

$$\begin{cases} \mathbf{q} = a\bar{\mathbf{q}} \\ t = \frac{1}{n}\bar{t} \rightarrow \bar{t} = M \end{cases}$$
$$\Rightarrow \begin{cases} \bar{\mathbf{p}} = \bar{\mathbf{q}}' + \frac{\omega_z(\nu)}{n}\mathbf{W}\bar{\mathbf{q}} \\ \bar{h} = \frac{1}{2}\bar{\mathbf{p}}^T\bar{\mathbf{p}} - \frac{\omega_z(\nu)}{n}\bar{\mathbf{p}}^T\mathbf{W}\bar{\mathbf{q}} - u_G\left(\bar{\mathbf{q}} + \mu\frac{1-e^2}{1+e\cos\nu}\begin{bmatrix}1\\0\\0\end{bmatrix}, \bar{\mathbf{q}} - (1-\mu)\frac{1-e^2}{1+e\cos\nu}\begin{bmatrix}1\\0\\0\end{bmatrix}\right) \end{cases}$$
$$\Rightarrow \begin{cases} \bar{\mathbf{q}}' = \bar{\mathbf{p}} - \frac{\omega_z(\nu)}{n}\mathbf{W}\bar{\mathbf{q}} \\ \bar{\mathbf{p}}' = -\frac{\omega_z(\nu)}{n}\mathbf{W}\bar{\mathbf{p}} + \nabla u_G\left(\bar{\mathbf{q}} + \mu\frac{1-e^2}{1+e\cos\nu}\begin{bmatrix}1\\0\\0\end{bmatrix}, \bar{\mathbf{q}} - (1-\mu)\frac{1-e^2}{1+e\cos\nu}\begin{bmatrix}1\\0\\0\end{bmatrix}\right) \\ \bar{h}' = -\frac{\dot{\omega}_z(\nu)}{n^2}\bar{\mathbf{p}}^T\mathbf{W}\bar{\mathbf{q}} \end{cases} \tag{A.5}$$

$$\begin{cases} \mathbf{q} = l(\nu)\bar{\mathbf{q}} \\ t = \frac{1}{\omega_z(\nu)}\bar{t} \rightarrow \bar{t} = \nu \end{cases}$$
$$\Rightarrow \begin{cases} \bar{\mathbf{p}} = \bar{\mathbf{q}}' + \left(\mathbf{W} + \frac{f_e{}'(\nu)}{f_e(\nu)}\mathbf{I}_3\right)\bar{\mathbf{q}} \\ \bar{h} = \frac{1}{2}\bar{\mathbf{p}}^T\bar{\mathbf{p}} - \bar{\mathbf{p}}^T\left(\mathbf{W} + \frac{f_e{}'(\nu)}{f_e(\nu)}\mathbf{I}_3\right)\bar{\mathbf{q}} - f_e(\nu)u_G\left(\bar{\mathbf{q}} + \mu\left(1-e^2\right)f_e(\nu)\begin{bmatrix}1\\0\\0\end{bmatrix}, \bar{\mathbf{q}} - (1-\mu)\left(1-e^2\right)f_e(\nu)\begin{bmatrix}1\\0\\0\end{bmatrix}\right) \end{cases}$$
$$\Rightarrow \begin{cases} \bar{\mathbf{q}}' = \bar{\mathbf{p}} - \left(\mathbf{W} + \frac{f_e{}'(\nu)}{f_e(\nu)}\mathbf{I}_3\right)\bar{\mathbf{q}} \\ \bar{\mathbf{p}}' = -\left(\mathbf{W} - \frac{f_e{}'(\nu)}{f_e(\nu)}\mathbf{I}_3\right)\bar{\mathbf{p}} + f_e(\nu)\nabla u_G\left(\bar{\mathbf{q}} + \mu\left(1-e^2\right)f_e(\nu)\begin{bmatrix}1\\0\\0\end{bmatrix}, \bar{\mathbf{q}} - (1-\mu)\left(1-e^2\right)f_e(\nu)\begin{bmatrix}1\\0\\0\end{bmatrix}\right) \\ \bar{h}' = -\bar{\mathbf{p}}^T\left(\frac{f_e{}''(\nu)}{f_e(\nu)} - \frac{f_e{}'(\nu)^2}{f_e(\nu)^2}\right)\bar{\mathbf{q}} - f_e{}'(\nu)u_G\left(\bar{\mathbf{q}} + \mu\left(1-e^2\right)f_e(\nu)\begin{bmatrix}1\\0\\0\end{bmatrix}, \bar{\mathbf{q}} - (1-\mu)\left(1-e^2\right)f_e(\nu)\begin{bmatrix}1\\0\\0\end{bmatrix}\right) \end{cases} \tag{A.6}$$

$$\begin{cases} f_e(\nu) = \frac{1}{1+e\cos\nu} \rightarrow \frac{\omega_z(\nu)}{n} = \frac{1}{(1-e^2)^{3/2}}\frac{1}{f_e(\nu)^2} \\ {f_e}'(\nu) = \frac{e\sin\nu}{(1+e\cos\nu)^2} \rightarrow \frac{\dot{\omega}_z(\nu)}{\omega_z(\nu)^2} = \frac{{\omega_z}'(\nu)}{\omega_z(\nu)} = -2\frac{{f_e}'(\nu)}{f_e(\nu)} \\ {f_e}''(\nu) = 2\frac{e^2\sin^2\nu}{(1+e\cos\nu)^3} + \frac{e\cos\nu}{(1+e\cos\nu)^2} \end{cases} \tag{A.7}$$

A.3 The ER3BP in Phobos' Hill's Frame

Eq.2.50 describes the ER3BP in the secondary's Hill's frame in physical units. The related Phobos-centered ER3BP in normalized units[2], for the fixed combination a-M is expressed in Eq.3.46, while the time-variant combination l-ν is presented in Eq.A.8.

$$\begin{cases} \mathbf{q} = l(\nu)\left(\bar{\bar{\mathbf{q}}} + \bar{\mathbf{q}}_2\right) \\ \bar{t} = \nu \end{cases}$$
$$\Rightarrow \bar{\mathbf{q}}_2 = (1-\mu)\begin{bmatrix}1\\0\\0\end{bmatrix}, \bar{\mathbf{q}}_2' = \begin{bmatrix}0\\0\\0\end{bmatrix}, \bar{\mathbf{q}}_2'' = \begin{bmatrix}0\\0\\0\end{bmatrix}$$
$$\Rightarrow \bar{\mathbf{a}}_{\mathbf{A},\mathbf{T}} = 2\mathbf{W}\bar{\mathbf{q}}_2' + \frac{1}{1+e\cos\nu}\mathbf{P}\bar{\mathbf{q}}_2 + \frac{1}{l(\nu)\omega_z(\nu)^2}\bar{\mathbf{q}}_2'' = -(1-\mu)\frac{1}{1+e\cos\nu}$$
$$\Rightarrow \bar{\bar{\mathbf{q}}}'' + 2\mathbf{W}\bar{\bar{\mathbf{q}}}' = \nabla\left(\frac{1}{1+e\cos\nu}u_G\left(\bar{\bar{\mathbf{q}}} + \begin{bmatrix}1\\0\\0\end{bmatrix}, \bar{\bar{\mathbf{q}}}\right) - \frac{1}{1+e\cos\nu}\frac{\bar{\bar{\mathbf{q}}}^T\mathbf{P}\bar{\bar{\mathbf{q}}}}{2} - \frac{e\cos\nu}{1+e\cos\nu}\frac{\bar{\bar{\mathbf{q}}}^T(\mathbf{I}_3+\mathbf{P})\bar{\bar{\mathbf{q}}}}{2} + (1-\mu)\frac{1}{1+e\cos\nu}\bar{\bar{x}}\right)$$
$$\Rightarrow \bar{\bar{\mathbf{q}}}'' + 2\mathbf{W}\bar{\bar{\mathbf{q}}}' = \nabla\left(\frac{1}{1+e\cos\nu}u_G\left(\bar{\bar{\mathbf{q}}} + \begin{bmatrix}1\\0\\0\end{bmatrix}, \bar{\bar{\mathbf{q}}}\right) + \frac{1}{1+e\cos\nu}\frac{\bar{\bar{\mathbf{q}}}^T\bar{\bar{\mathbf{q}}}}{2} - \frac{\bar{\bar{\mathbf{q}}}^T(\mathbf{I}_3+\mathbf{P})\bar{\bar{\mathbf{q}}}}{2} + (1-\mu)\frac{1}{1+e\cos\nu}\bar{\bar{x}}\right)$$
$$\Rightarrow \bar{\bar{\mathbf{q}}}'' + 2\mathbf{W}\bar{\bar{\mathbf{q}}}' = \nabla\left(\frac{1}{1+e\cos\nu}u_G\left(\bar{\bar{\mathbf{q}}} + \begin{bmatrix}1\\0\\0\end{bmatrix}, \bar{\bar{\mathbf{q}}}\right) - \frac{e\cos\nu}{1+e\cos\nu}\frac{\bar{\bar{\mathbf{q}}}^T\bar{\bar{\mathbf{q}}}}{2} - \frac{\bar{\bar{\mathbf{q}}}^T\mathbf{P}\bar{\bar{\mathbf{q}}}}{2} + (1-\mu)\frac{1}{1+e\cos\nu}\bar{\bar{x}}\right) \tag{A.8}$$

Related Hamiltonian forms are presented in Eq.A.9-A.10.

$$\begin{cases} \mathbf{q} = a\left(\bar{\bar{\mathbf{q}}} + \bar{\mathbf{q}}_2\right) \\ \bar{t} = M \end{cases}$$
$$\Rightarrow \begin{cases} \bar{\mathbf{p}} = \bar{\bar{\mathbf{q}}}' + \frac{\omega_z(\nu)}{n}\mathbf{W}\bar{\bar{\mathbf{q}}} + (1-\mu)\frac{1}{\sqrt[2]{1-e^2}}\begin{bmatrix}e\sin\nu\\1+e\cos\nu\\0\end{bmatrix} \\ \bar{h} = \frac{1}{2}\bar{\mathbf{p}}^T\bar{\mathbf{p}} - \frac{\omega_z(\nu)}{n}\bar{\mathbf{p}}^T\mathbf{W}\bar{\bar{\mathbf{q}}} - (1-\mu)\frac{1}{\sqrt[2]{1-e^2}}\bar{\mathbf{p}}^T\begin{bmatrix}e\sin\nu\\1+e\cos\nu\\0\end{bmatrix} - u_G\left(\bar{\bar{\mathbf{q}}} + \frac{1-e^2}{1+e\cos\nu}\begin{bmatrix}1\\0\\0\end{bmatrix}, \bar{\bar{\mathbf{q}}}\right) \end{cases}$$
$$\Rightarrow \begin{cases} \bar{\mathbf{q}}' = \bar{\mathbf{p}} - \frac{\omega_z(\nu)}{n}\mathbf{W}\bar{\bar{\mathbf{q}}} - (1-\mu)\frac{1}{\sqrt[2]{1-e^2}}\begin{bmatrix}e\sin\nu\\1+e\cos\nu\\0\end{bmatrix} \\ \bar{\mathbf{p}}' = -\frac{\omega_z(\nu)}{n}\mathbf{W}\bar{\mathbf{p}} + \nabla u_G\left(\bar{\bar{\mathbf{q}}} + \frac{1-e^2}{1+e\cos\nu}\begin{bmatrix}1\\0\\0\end{bmatrix}, \bar{\bar{\mathbf{q}}}\right) \\ \bar{h}' = -\frac{\dot{\omega}_z(\nu)}{n^2}\bar{\mathbf{p}}^T\mathbf{W}\bar{\bar{\mathbf{q}}} - (1-\mu)\frac{(1+e\cos\nu)^2}{(1-e^2)^2}\bar{\mathbf{p}}^T\begin{bmatrix}e\cos\nu\\-e\sin\nu\\0\end{bmatrix} \end{cases} \tag{A.9}$$

$$\begin{cases} \mathbf{q} = l(\nu)\left(\bar{\bar{\mathbf{q}}} + \bar{\mathbf{q}}_2\right) \\ \bar{t} = \nu \end{cases}$$
$$\Rightarrow \begin{cases} \bar{\mathbf{p}} = \bar{\bar{\mathbf{q}}}' + \left(\mathbf{W} + \frac{{f_e}'(\nu)}{f_e(\nu)}\mathbf{I}_3\right)\bar{\bar{\mathbf{q}}} + (1-\mu)\begin{bmatrix}\frac{{f_e}'(\nu)}{f_e(\nu)}\\1\\0\end{bmatrix} \\ \bar{h} = \frac{1}{2}\bar{\mathbf{p}}^T\bar{\mathbf{p}} - \bar{\mathbf{p}}^T\left(\mathbf{W} + \frac{{f_e}'(\nu)}{f_e(\nu)}\mathbf{I}_3\right)\bar{\bar{\mathbf{q}}} - (1-\mu)\bar{\mathbf{p}}^T\begin{bmatrix}\frac{{f_e}'(\nu)}{f_e(\nu)}\\1\\0\end{bmatrix} - f_e(\nu)u_G\left(\bar{\bar{\mathbf{q}}} + \left(1-e^2\right)f_e(\nu)\begin{bmatrix}1\\0\\0\end{bmatrix}, \bar{\bar{\mathbf{q}}}\right) \end{cases}$$
$$\Rightarrow \begin{cases} \bar{\bar{\mathbf{q}}}' = \bar{\mathbf{p}} - \left(\mathbf{W} + \frac{{f_e}'(\nu)}{f_e(\nu)}\mathbf{I}_3\right)\bar{\bar{\mathbf{q}}} - (1-\mu)\begin{bmatrix}\frac{{f_e}'(\nu)}{f_e(\nu)}\\1\\0\end{bmatrix} \\ \bar{\mathbf{p}}' = -\left(\mathbf{W} - \frac{{f_e}'(\nu)}{f_e(\nu)}\mathbf{I}_3\right)\bar{\mathbf{p}} + f_e(\nu)\nabla u_G\left(\bar{\bar{\mathbf{q}}} + \left(1-e^2\right)f_e(\nu)\begin{bmatrix}1\\0\\0\end{bmatrix}, \bar{\bar{\mathbf{q}}}\right) \\ \bar{h}' = -\bar{\mathbf{p}}^T\left(\frac{{f_e}''(\nu)}{f_e(\nu)} - \frac{{f_e}'(\nu)^2}{f_e(\nu)^2}\right)\bar{\bar{\mathbf{q}}} - (1-\mu)\bar{\mathbf{p}}^T\begin{bmatrix}\frac{{f_e}''(\nu)}{f_e(\nu)} - \frac{{f_e}'(\nu)^2}{f_e(\nu)^2}\\0\\0\end{bmatrix} - {f_e}'(\nu)u_G\left(\bar{\bar{\mathbf{q}}} + \left(1-e^2\right)f_e(\nu)\begin{bmatrix}1\\0\\0\end{bmatrix}, \bar{\bar{\mathbf{q}}}\right) \end{cases} \tag{A.10}$$

Finally, Hill's approximation of the ER3BP could be applied for the two combination

[2]Throughout this section, normalized relative state with respect to the secondary body is indicated with a double upper bar.

cases, as shown in Eq.A.11-A.12.

$$\begin{cases} \mathbf{q} = a\left(\bar{\bar{\mathbf{q}}} + \bar{\mathbf{q}}_2\right) \\ \bar{t} = M \end{cases}$$
$$\Rightarrow \lim_{\mu\to 0} \nabla \left(u_{G1}\left(\bar{\bar{\mathbf{q}}} + \frac{1-e^2}{1+e\cos\nu}\begin{bmatrix}1\\0\\0\end{bmatrix}\right) - \frac{(1+e\cos\nu)^4}{(1-e^2)^3}\left(\frac{\bar{\bar{\mathbf{q}}}^T\mathbf{P}\bar{\bar{\mathbf{q}}}}{2} - (1-\mu)\frac{1-e^2}{(1+e\cos\nu)^2}\bar{\bar{x}}\right)\right) =$$
$$= \nabla\left(-\frac{(1+e\cos\nu)^3}{(1-e^2)^3}\frac{\bar{\bar{\mathbf{q}}}^T\left((1+e\cos\nu)\mathbf{P}+\mathbf{A_{H1}}\right)\bar{\bar{\mathbf{q}}}}{2}\right)$$
$$\Rightarrow \bar{\bar{\mathbf{q}}}'' - 2\frac{(1+e\cos\nu)^3 e\sin\nu}{(1-e^2)^3}\mathbf{W}\bar{\bar{\mathbf{q}}} + 2\frac{(1+e\cos\nu)^2}{(1-e^2)^{3/2}}\mathbf{W}\bar{\bar{\mathbf{q}}}' = \nabla\left(-\frac{(1+e\cos\nu)^3}{(1-e^2)^3}\frac{\bar{\bar{\mathbf{q}}}^T((1+e\cos\nu)\mathbf{P}+\mathbf{A_{H1}})\bar{\bar{\mathbf{q}}}}{2} + u_{G2}\left(\bar{\bar{\mathbf{q}}}\right)\right) \tag{A.11}$$

$$\begin{cases} \mathbf{q} = l(\nu)\left(\bar{\bar{\mathbf{q}}} + \bar{\mathbf{q}}_2\right) \\ \bar{t} = \nu \end{cases}$$
$$\Rightarrow \lim_{\mu\to 0} \nabla \left(\begin{array}{l} \frac{1}{1+e\cos\nu} u_{G1}\left(\bar{\bar{\mathbf{q}}} + \begin{bmatrix}1\\0\\0\end{bmatrix}\right) - \frac{1}{1+e\cos\nu}\frac{\bar{\bar{\mathbf{q}}}^T\mathbf{P}\bar{\bar{\mathbf{q}}}}{2} + \\ -\frac{e\cos\nu}{1+e\cos\nu}\frac{\bar{\bar{\mathbf{q}}}^T\left(\mathbf{I}_3+\mathbf{P}\right)\bar{\bar{\mathbf{q}}}}{2} + (1-\mu)\frac{1}{1+e\cos\nu}\bar{\bar{x}} \end{array}\right) =$$
$$= \nabla\left(-\frac{1}{1+e\cos\nu}\frac{\bar{\bar{\mathbf{q}}}^T\left(\mathbf{P}+\mathbf{A_{H1}}\right)\bar{\bar{\mathbf{q}}}}{2} - \frac{e\cos\nu}{1+e\cos\nu}\frac{\bar{\bar{\mathbf{q}}}^T\left(\mathbf{I}_3+\mathbf{P}\right)\bar{\bar{\mathbf{q}}}}{2}\right)$$
$$\Rightarrow \bar{\bar{\mathbf{q}}}'' + 2\mathbf{W}\bar{\bar{\mathbf{q}}}' = \nabla\left(-\frac{1}{1+e\cos\nu}\frac{\bar{\bar{\mathbf{q}}}^T(\mathbf{P}+\mathbf{A_{H1}})\bar{\bar{\mathbf{q}}}}{2} - \frac{e\cos\nu}{1+e\cos\nu}\frac{\bar{\bar{\mathbf{q}}}^T(\mathbf{I}_3+\mathbf{P})\bar{\bar{\mathbf{q}}}}{2} + \frac{1}{1+e\cos\nu}u_{G2}\left(\bar{\bar{\mathbf{q}}}\right)\right)$$
$$\Rightarrow \bar{\bar{\mathbf{q}}}'' + 2\mathbf{W}\bar{\bar{\mathbf{q}}}' = \nabla\left(\frac{1}{1+e\cos\nu}\frac{\bar{\bar{\mathbf{q}}}^T(\mathbf{I}_3-\mathbf{A_{H1}})\bar{\bar{\mathbf{q}}}}{2} - \frac{\bar{\bar{\mathbf{q}}}^T(\mathbf{I}_3+\mathbf{P})\bar{\bar{\mathbf{q}}}}{2} + \frac{1}{1+e\cos\nu}u_{G2}\left(\bar{\bar{\mathbf{q}}}\right)\right)$$
$$\Rightarrow \bar{\bar{\mathbf{q}}}'' + 2\mathbf{W}\bar{\bar{\mathbf{q}}}' = \nabla\left(-\frac{1}{1+e\cos\nu}\frac{\bar{\bar{\mathbf{q}}}^T(e\cos\nu\mathbf{I}_3+\mathbf{A_{H1}})\bar{\bar{\mathbf{q}}}}{2} - \frac{\bar{\bar{\mathbf{q}}}^T\mathbf{P}\bar{\bar{\mathbf{q}}}}{2} + \frac{1}{1+e\cos\nu}u_{G2}\left(\bar{\bar{\mathbf{q}}}\right)\right) \tag{A.12}$$

A.4 Equations of Motion

First, the case of the fixed time unit is considered. Eq.3.48 presents the ODEs of the Mars-Phobos ER3BP-GH in Phobos' Hill's frame, with the length unit set to be the semi-major axis, and with respect to the mean anomaly.

In the same sense, the ODEs and effective potential with respect to the true anomaly are derived, and are shown in Eq.A.14-A.15.

$$\begin{cases} \mathbf{a}(\nu) = (1-\mu)\frac{1-e^2}{(1+e\cos\nu)^2}\begin{bmatrix}1\\0\\0\end{bmatrix} \\ \boldsymbol{\omega} = \begin{bmatrix}0\\0\\1\end{bmatrix} \rightarrow \mathbf{W} = \boldsymbol{\omega}\wedge \rightarrow \mathbf{P} = \mathbf{W}^2 \\ \dot{\boldsymbol{\omega}}(\nu) = -2\frac{e\sin\nu}{1+e\cos\nu}\begin{bmatrix}0\\0\\1\end{bmatrix} \rightarrow \mathbf{Y}_I(\nu) = -2\frac{e\sin\nu}{1+e\cos\nu}\mathbf{I_3},\ \mathbf{Y}(\nu) = \dot{\boldsymbol{\omega}}(\nu)\wedge \\ w_f(\nu) = \frac{\left(1-e^2\right)^3}{(1+e\cos\nu)^4} \end{cases} \tag{A.13}$$

$$\mathbf{x} = \begin{bmatrix}\mathbf{q}\\ \dot{\mathbf{q}}\end{bmatrix} \rightarrow \dot{\mathbf{x}} = \mathbf{A}(\nu)\mathbf{x} + \begin{bmatrix}\mathbf{0_{3x1}}\\ w_f(\nu)u_{G/\mathbf{q}}(\mathbf{q},\nu) + \mathbf{a}(\nu)\end{bmatrix},\ \mathbf{A}(\nu) = \begin{bmatrix}\mathbf{0_3} & \mathbf{I_3}\\ -\mathbf{Y}(\nu) - \mathbf{P} & -2\mathbf{W} - \mathbf{Y}_I(\nu)\end{bmatrix} \tag{A.14}$$

$$u_{eff} = \frac{\left(1-e^2\right)^3}{(1+e\cos\nu)^4}u_{G,1}\left(\mathbf{q} + \frac{1-e^2}{1+e\cos\nu}\begin{bmatrix}1\\0\\0\end{bmatrix}\right) + \frac{\left(1-e^2\right)^3}{(1+e\cos\nu)^4}u_{G,2}\left(\mathbf{q}\right) - \left(\frac{\mathbf{q}^T\mathbf{P}\mathbf{q}}{2} - (1-\mu)\frac{1-e^2}{(1+e\cos\nu)^2}x\right) \tag{A.15}$$

Appendix B

Methods of Dynamical Systems Theory to compute Invariant Objects and their Invariant Manifolds

This thesis investigates the equilibrium, periodic and quasi-periodic solutions of the Mars-Phobos-spacecraft system for their use as potential station-keeping orbits around the moon in future missions. This chapter is a review of the methodologies required in the thesis to compute these invariant motions, that will be presented for the case of a general dynamical system. Section B.1 introduces the reader to the concepts of the theory of dynamical systems that are used in this thesis, and section B.2 recalls the numerical techniques to solve nonlinear parametric equations. Following this, the solutions of a general dynamical system are computed with the methodologies of dynamical systems theory. Section B.3 focuses on the equilibrium points. Section B.4 presents the analytical and semi-analytical techniques to compute invariant objects, while the numerical methodologies to compute them are illustrated in sections B.5-B.6-B.7, that focus respectively from periodic orbits to high-dimensional forced quasi-periodic orbits. Finally, the computation of the invariant manifolds of these solutions is addressed in section B.8.

B.1 Fundamentals of Dynamical Systems

In the broad mathematical field of deterministic processes, consider in Eq.B.1 a general-defined nonlinear and time-variant (NL and TV) continuous-time dynamical system. This is a system of first-order ordinary differential equations (ODEs) with respect to the time t, described by the state vector $x \in \mathbb{R}^n$, its initial condition x_0 at t_0, and its

time-derivative f called a vectorfield[1].

$$\begin{cases} \dot{x}(t) = f(t,x) \\ x(t_0) = x_0 \end{cases} \Leftrightarrow \phi_f(t, t_0, x_0) : x(t_0) \rightarrow x(t) \tag{B.1}$$

The solution of this system is the trajectory $x(t)$ in the state-space with respect to time. In other words, each continuous dynamical system is linked to a 1-1 map[2] called flow ϕ that associates the initial state to the trajectory at a prescribed point in time. Thus, the trajectory (or orbit[3]) is the flow map of the vectorfield for a specific initial condition. The resulting integral solution of the dynamical system is reported in Eq.B.2, where we see that the differential relationships between x and $\dot{x}$ are the same between f and ϕ.

$$\begin{cases} x(t) = \phi_f(t, t_0, x_0) = x_0 + \int_{t_0}^{t} f dt \\ \dot{x}(t) = \dot{\phi}_f = f(t,x) \end{cases} \Leftrightarrow \begin{cases} dx = \dot{x} dt \\ d\phi_f = f dt \end{cases} \Leftrightarrow \begin{cases} dx = d\phi_f \\ d\dot{x} = df \end{cases} \tag{B.2}$$

B.1.1 Particular cases

B.1.1.1 Autonomous Dynamical Systems

In the case of time-invariant (TI) dynamical systems, the vectorfield does not depend explicitly on the time, therefore the flow depends only on the propagation time span $\Delta t = t - t_0$.

$$\begin{cases} \dot{x}(t) = f(x) \\ x(0) = x_0 \end{cases} \Leftrightarrow \phi_f(\Delta t, x_0) : x(0) \rightarrow x(\Delta t) \tag{B.3}$$

B.1.1.2 Mechanical Systems

The information provided in this section is valid for any general deterministic and continuous dynamical system. However this thesis focuses on orbital dynamics: the equations of motion of a mechanical system, where $\mathbf{q}$ is the position in the chosen reference frame, are ruled by a system of n second-order ODEs $\ddot{\mathbf{q}}(t) = \mathbf{d}(t, \mathbf{q}, \dot{\mathbf{q}})$. Thus, the dynamics are brought to a $2n$ system of first-order ODEs to derive a related vectorfield in compliance to Eq.B.1. In particular, Lagrangian and Hamiltonian[4] descriptions could be used to express the additional n state's components, as done in Eq.2.13 and Eq.2.18 for the case of the CR3BP. The dynamical models presented in chapter 3 are

[1] The vectorfield is time-continuous and Lipschitz in x.

[2] A general-defined map is indicated as $P : x \rightarrow P(x)$. In particular, a general-defined discrete-time dynamical system is described by an order-1 recurrence equation, which is a map $P : x_{k+1} = P(k, x_k)$, with initial condition x_0 at $k = 0$.

[3] In mathematical terms: the trajectory is the graph of the flow along time, and the orbit is the image of the flow along time.

[4] A Hamiltonian system is completely described by a scalar function, the Hamiltonian, which could be either TI or TV. In the first case, the Hamiltonian is an integral of motion preserved by the vectorfield through its flow. For physical TI dynamical systems, the Hamiltonian corresponds to the energy of the system. For mechanical systems, the Hamiltonian corresponds to the inertial mechanical energy, made up of kinetic and potential terms, as presented in Eq.2.15.

all stated in the Lagrangian form, which will be solely used in the analysis undertaken in this section and in chapters 4-5-6.

Note that the same physical problem could be described by dynamical systems with different vectorfields, by expressing the dynamics in different reference frames, state variables, or time. This is useful sometimes to simplify the equations of motion.

B.1.2 Sensitivity of Dynamical Systems

Two important quantities that are frequently used in this thesis are now defined. A represents the pointwise derivative of the vectorfield with respect to the state, usually called the Jacobian of the dynamical system, which also represents its pointwise linearized state-matrix. Φ represents the pointwise derivative of the flow map with respect to the initial state, which is the state transition matrix (STM).

$$\begin{cases} \left.\frac{\partial f}{\partial x}\right|_{t,x} = A_f(t,x) \\ \left.\frac{\partial \phi_f}{\partial x_0}\right|_{t,t_0} = \Phi_f(t,t_0) \end{cases} \tag{B.4}$$

With these first-order derivatives (generally $n \times n$ matrices), the variational form of the vectorfield and its associated flow map can be expressed.

$$\begin{cases} \delta f = A_f \delta x \\ \delta \phi_f = \Phi_f \delta x_0 \end{cases} \tag{B.5}$$

Using Eq.B.2, the above relations lead to the variational equations for the dynamical system and its associated solution. They express a linear sensitivity of the time-derivative with respect to the state, and of the trajectory with respect to the initial conditions.

$$\delta \dot{x} = A_f \delta x \Leftrightarrow \delta x = \Phi_f \delta x_0 \tag{B.6}$$

We see that in the linearized environment the two sensitivities can be straightforward related.

$$\delta \dot{x} = A_f \Phi_f \delta x_0 \Leftrightarrow \delta \dot{x} = \dot{\Phi}_f \delta x_0 \tag{B.7}$$

This leads in Eq.B.8 to a dynamical relationship between the two quantities defined in Eq.B.4. The STM components obey to a specific TV dynamical system (called in this thesis the variational system) where the state-matrix is constituted by the components of the pointwise state-matrix of the original dynamical system. The initial conditions of the variational system are easily obtained in Eq.B.8 evaluating the STM at the initial time: the relation between the state and the initial state is trivially an identity.

$$\begin{cases} \dot{\Phi}_f(t,t_0) = A_f(t,x)\Phi_f(t,t_0) \\ \delta x(t_0) = \Phi_f(t_0,t_0)\delta x_0 \rightarrow \Phi_f(t_0,t_0) = I \end{cases} \tag{B.8}$$

In summary, for the starting general dynamical system of Eq.B.1, the pointwise linearization along the trajectory is associated with the variational system of Eq.B.8. The solution of this system is the STM, and represents a measure of the sensitivity of the trajectory of the dynamical system from the initial condition $\delta x(t) = \Phi_f(t, t_0)\delta x_0$. This approximation holds for little variations from the reference trajectory. It is important to underline the pointwise character of the variational dynamical system: to be solved, the elements of its TV state-matrix must be defined, but they depend on the Jacobian of the system evaluated along the trajectory. This means that if, as usual, the analytical form of the solution is not available, the variational system of ODEs must be numerically integrated alongside the principal system of ODEs. For a n-dimensional state, this leads to solve a $n + n^2$ system of ODEs.

B.1.2.1 Sensitivity and Stability of Linear Systems

For a linear TI dynamical system, the variational equations of Eq.B.6 and the variational system of Eq.B.8 express the exact sensitivity. In this situation, the pointwise state-matrix A is constant, whereas the STM has the simple matrix-exponential form presented in Eq.B.9[5]. Thus, the STM is constituted by n decaying/growing terms along time, represented by exponential functions of the spectrum of eigenvalues λ of A, linearly combined through its eigenvectors v[6].

$$\dot{x}(t) = Ax(t) \rightarrow x(\Delta t) = \phi(\Delta t, x_0) = e^{A\Delta t}x_0 \rightarrow \Phi(\Delta t) = e^{A\Delta t} = V_A e^{\Lambda_A \Delta t} V_A^{-1} \quad \text{(B.9)}$$

This analytical expression of the behavior around the flow of linear systems allows the determination of the stability of the trajectory. The most common notion of stability is due to Lyapunov, who provided the following classification[7] based on the spectrum of A.

- Asymptotically stable, if all the eigenvalues have real part strictly negative (the system is dissipative).
- Unstable, if at least one eigenvalue has real part strictly positive (the system is unstable).
- Marginally/neutrally stable, if all the eigenvalues have real part negative or null, at least one of them has null real part, and all the eigenvalues with null real part are complete[8] (the system is conservative).

[5] Eq.B.9 refers to a diagonalizable matrix A. If A is defective, the matrix-exponential should be evaluated with a series expansion.

[6] As usual, the eigenvalues $\lambda = eig\{A\}$ are assembled in the diagonal matrix Λ, and the corresponding right eigenvectors are sorted in the columns of the matrix V.

[7] This classification is tailored for a continuous dynamical system, where the linearized stability properties are defined by the sign of the real part of the eigenvalues of the Jacobian of its vectorfield, whereas for a discrete dynamical system the same stability properties refer to the magnitude of the eigenvalues of the Jacobian of its map, and are defined by comparing this value with respect to 1.

[8] If the eigenvalues are not complete, A is defective.

The associated phase portraits of the orbit are:

- An attractor: a sink node or inward spiral.
- A repellor: a source node or outward spiral if the remaining eigenvalues have real part positive too, or a real or complex hyperbolic saddle node if the remaining set has at least one eigenvalue with negative real part.
- A neutral point: an isolated node (which represents a limit invariant object, such as a fixed point, a limit cycle, or generally a limit torus) or center. In addition, the multiplicity of the eigenvalue with null real part indicates the phase-space dimension of this invariant solution, as will be explained in section B.1.3.

B.1.2.2 Sensitivity and Stability of Nonlinear Systems

For a NL dynamical system, the linearized variational equations are still useful to describe the behavior of the real dynamics. This approximation fails as long as the perturbation δx_0 becomes too large, or the time span grows.

In parallelism with the linear behavior, Lyapunov proposed a direct method for the analysis of the dynamical properties of a general dynamical system. This uses the spectrum of the STM within the propagation interval, whose elements $\mu = eig\{\Phi\}$ are called Lyapunov multipliers. The set of Lyapunov exponents λ is derived from the STM with the relation of the linear case of Eq.B.9.

$$\dot{x}(t) = f(t,x) \rightarrow \lambda(t,t_0,x_0) = \frac{1}{t-t_0}\ln\left(eig\left\{\Phi_f(t,t_0)\right\}\right) = \frac{1}{t-t_0}\ln\mu(t,t_0,x_0) \quad \text{(B.10)}$$

Thus the Lyapunov exponents are associated to a specific trajectory, as a difference from the linear case, where the spectrum is a structural property for the system. Furthermore, the resulting spectrum of λ is a function of the initial conditions and the propagation time. Therefore, a summarizing figure is given considering the behavior at the infinite-horizon of the spectrum. Since the components of the STM grow exponentially with the time, the solution of the eigenvalue problem for a long simulation span is impracticable. Thus, the maximum Lyapunov exponent (MLE) of the orbit $x(t)$ is computed directly from the divergence ratio between perturbed and reference orbit.

$$\dot{x}(t) = f(t,x) \rightarrow MLE(t_0,x_0) = \lim_{t\to\infty}\frac{1}{t-t_0}\ln\frac{||\delta x(t)||}{||\delta x_0||} \quad \text{(B.11)}$$

To neglect the dependence of the MLE from the direction of δx_0, the Euclidian norm of the right Cauchy-Green tensor $\Phi^T\Phi$ is considered for a finite-time span. The Lyapunov exponents, associated to the eigenvalues in Eq.B.12, are called finite-time Lyapunov exponents (FTLEs) [138].

$$\dot{x}(t) = f(t,x) \rightarrow FTLE(t,t_0,||x_0||) = eig\left\{\frac{1}{t-t_0}\ln\left(\Phi_f(t,t_0)^T\Phi_f(t,t_0)\right)^{\frac{1}{2}}\right\} = \\ = \ln\left(eig\left\{\left(\Phi_f(t,t_0)^T\Phi_f(t,t_0)\right)^{\frac{1}{2(t-t_0)}}\right\}\right) \tag{B.12}$$

Like for the linear case, the set of the Lyapunov exponents (or directly the multipliers) could be used to determine the stability of the trajectory. The extension of the Lyapunov stability to the NL systems provides the following classification, based on the spectrum of Lyapunov exponents.

- Asymptotically stable, if all the exponents have real part strictly negative.
- Unstable, if at least one exponent has real part strictly positive.
- If the linearized system is marginally stable, additional analysis on higher derivatives must be undertaken to describe the region of stability in the original NL system.

The stability rules show that for NL dynamical systems, the focus is on the maximum real part of the spectrum of Lyapunov exponents. This explains the use of the maximum FTLE as the Fast Lyapunov Indicator (FLI) of the orbit.

- A negative FLI indicates asymptotic stability of the trajectory (attracting object).
- A positive FLI indicates instability of the trajectory (repelling object).
- A null FLI indicates possible marginal/neutral stability of the trajectory in the proximity of the trajectory (neutral object).

In particular, the Lyapunov exponents are used as a measure of chaoticity of the dynamical system. It is commonly accepted that, when the FLI is greater than 1, the region around the unstable orbit is defined to be chaotic. This means that even minimum perturbed trajectories are highly divergent from the reference orbits.

This analysis is paramount also for the structural stability analysis of the dynamical system, which is to define whether its stability properties (the Lyapunov exponents) change as a function of some parameters of the vectorfield. When there is a sudden qualitative change, the term bifurcation is used.

B.1.2.3 Propagation Time

From Eq.B.2, the linear sensitivity of the flow with respect to the propagation time is given by the vectorfield itself.

$$\left.\frac{\partial\phi_f}{\partial t}\right|_{t,t_0} = f\left(t, x\left(t\right)\right) \tag{B.13}$$

B.1.2.4 Non-Autonomous Dynamical Systems

The general TV case corresponds to a dynamical system where a forcing action, explicitly dependent on time, is embedded in the vectorfield. This situation is usually treated in dynamical systems theory with the mathematical trick of appending the time in the state vector [109, 110], and so the vectorfield is augmented by the trivial dynamics of the time with respect to itself $\dot{t} = 1$. This allows to retrieve the sensitivity of the original flow with respect to the initial time from the additional column of the $(n+1) \times (n+1)$ STM, which is now the solution of the augmented variational system.

$$f(t,x) \rightarrow \begin{cases} y(t) = \begin{bmatrix} x(t) \\ t \end{bmatrix} \\ \dot{y}(t) = d(t,y) = \begin{bmatrix} f(t,x) \\ 1 \end{bmatrix} \end{cases} \Leftrightarrow \begin{cases} \Phi_d(t,t_0) = \begin{bmatrix} \Phi_f(t,t_0) & \left.\frac{\partial \phi_f}{\partial t_0}\right|_{t,t_0} \\ 0 & 1 \end{bmatrix} \\ \dot{\Phi}_d(t,t_0) = \begin{bmatrix} A_f(t,x) & \left.\frac{\partial f}{\partial t}\right|_{t,x} \\ 0 & 0 \end{bmatrix} \Phi_d(t,t_0) \end{cases} \tag{B.14}$$

Due to the structure of the augmented variational system, the sensitivity of the flow with respect to the initial time in non-conservative systems can be analytically retrieved in an alternative way, without augmenting the ODEs. This could be derived expanding the variational equations of Eq.B.6 to consider also the final time variation along the flow, whose sensitivity is given by Eq.B.13.

$$\delta\phi_f(t_f + \delta t_f, t_0, x_0 + \delta x_0) = \Phi_f(t_f, t_0, x_0)\,\delta x_0 + f(t_f, \phi_f(t_f, t_0, x_0))\,\delta t_f \tag{B.15}$$

Eq.B.15 is rearranged to isolate the variation only with respect to the initial state, and evaluated at the initial and final time.

$$\begin{cases} \delta x(t_f) = \delta\phi_f(t_f, t_0, x_0 + \delta x_0) = \Phi_f(t_f, t_0, x_0)\,\delta x_0 = \\ \qquad\qquad = \delta\phi_f(t_f + \delta t_f, t_0, x_0 + \delta x_0) - f(t_f, \phi_f(t_f, t_0, x_0))\,\delta t_f \\ \delta x(t_0) = \delta\phi_f(t_0, t_0, x_0 + \delta x_0) = \delta x_0 = \\ \qquad\qquad = \delta\phi_f(t_0 + \delta t_0, t_0, x_0 + \delta x_0) - f(t_0, \phi_f(t_0, t_0, x_0))\,\delta t_0 \end{cases} \tag{B.16}$$

To simplify the notation, the variations of the flow, with respect to the initial conditions, is written as a function of only the final time.

$$\begin{cases} \delta x(t_f + \delta t_f) = \delta\phi_f(t_f + \delta t_f, t_0, x_0 + \delta x_0) \\ \delta x(t_0 + \delta t_0) = \delta\phi_f(t_0 + \delta t_0, t_0, x_0 + \delta x_0) \end{cases} \tag{B.17}$$

The two conditions in Eq.B.16 can be combined to yield the explicit formula for the derivative of the flow with respect to the initial time, which corresponds to the last column of the augmented STM of Eq.B.14. Eq.B.18 is the most general form of the variational equations of the flow map of a TV dynamical system: in the linearized dynamics along the reference orbit, it bounds the final state condition to the initial

state condition when the initial time changes.

$$\begin{aligned}\delta x\left(t_f+\delta t_f\right)&=\Phi_f\left(t_f,t_0,x_0\right)\delta x\left(t_0+\delta t_0\right)-\Phi_f\left(t_f,t_0,x_0\right)f\left(t_0,x_0\right)\delta t_0+f\left(t_f,x\left(t_f\right)\right)\delta t_f=\\&=\left.\frac{\partial\phi_f}{\partial x_0}\right|_{t_f,t_0,x_0}\delta x\left(t_0+\delta t_0\right)+\left.\frac{\partial\phi_f}{\partial t_0}\right|_{t_f,t_0,x_0}\delta t_0+\left.\frac{\partial\phi_f}{\partial t}\right|_{t_f,t_0,x_0}\delta t_f\end{aligned}\tag{B.18}$$

This procedure is also shown in [162], when used to conduct a numerical approach to compute LPOs in the ER3BP similar to the two-levels differential corrector used for the Lissajous orbits in [163].

B.1.2.5 Parametric Dynamical Systems

The strategy presented in section B.1.2.4 is also widely used to compute the linear sensitivity of the flow with respect to a parameter σ of the dynamical system. In this case the parameter itself is appended in the state vector and the vectorfield is augmented by its fake dynamics $\dot{\sigma}=0$, with the additional column of the related STM providing the sensitivity.

$$f\left(t,x,\sigma\right)\rightarrow\begin{cases}y\left(t\right)=\left[\begin{smallmatrix}x(t)\\\sigma\end{smallmatrix}\right]\\\dot{y}\left(t\right)=d\left(t,y\right)=\left[\begin{smallmatrix}f(t,x,\sigma)\\0\end{smallmatrix}\right]\end{cases}\Leftrightarrow\begin{cases}\Phi_d\left(t,t_0\right)=\left[\begin{smallmatrix}\Phi_f\left(t,t_0,\sigma\right)&\left.\frac{\partial\phi_f}{\partial\sigma}\right|_{t,t_0,\sigma}\\0&1\end{smallmatrix}\right]\\\dot{\Phi}_d\left(t,t_0\right)=\left[\begin{smallmatrix}A_f\left(t,x,\sigma\right)&\left.\frac{\partial f}{\partial\sigma}\right|_{t,x,\sigma}\\0&0\end{smallmatrix}\right]\Phi_d\left(t,t_0\right)\end{cases}\tag{B.19}$$

B.1.3 Solution of Dynamical Systems

The trajectory along a finite-time span, as any other function, could be developed in a Fourier synthesis along a continuous frequency spectrum of harmonic functions. This allows classical solutions, such as equilibrium points (EPs) and periodic orbits (POs), to be characterized by a singular harmonic spectrum at zero or one frequency. Quasi-periodic orbits (QPOs) are their extension to a general discrete spectrum, from one frequency up to potentially infinite terms to reach the general solution synthesis transition from Fourier series to inverse Fourier transform. For this reason, EPs, POs, and QPOs constitute the invariant solutions of a dynamical system, because they are preserved by the vectorfield for any time span. The identification of these orbits is the most important step in the analysis of the dynamics.

The invariant motions can be expressed as dependent on a discrete number of phases φ, rather than time, each one with the appropriate harmonic frequency ω. Mathematically speaking [164], an invariant object is a n-torus, where n is the dimension of the phase-space ($n=0$ for EPs, $n=1$ for POs, and $n\geq 2$ for nD-QPOs). This is expressed by Eq.B.20, where the n-torus' flow ν of a vectorfield u is stated in the phase-space, and the ODEs with respect to the phases assume a form known as the invariance equation.

$$\begin{cases} \dot{x}(t) = f(t,x) \\ x_{QPO}(t) = \phi_f(t, t_0, x_{0,QPO}) \end{cases} \rightarrow \begin{cases} \frac{\partial x}{\partial \boldsymbol{\varphi}} \boldsymbol{\omega} = u(\boldsymbol{\varphi}, x) \\ x_{QPO}(\boldsymbol{\varphi}) = \nu_u(\boldsymbol{\varphi}, \boldsymbol{\varphi}_0, x_{0,QPO}) \end{cases} , \boldsymbol{\varphi} = \boldsymbol{\varphi}_0 + \boldsymbol{\omega}\,(t - t_0) \in \mathbb{R}^n \tag{B.20}$$

$$\mathbf{k}^T \boldsymbol{\omega} \neq 0,\ \forall \mathbf{k} \in \mathbb{Z}_0^n \tag{B.21}$$

The condition given by Eq.B.21 represents the non-resonance constraint of the frequency-space, which is just a case that lowers the torus' phase-space dimension.

Thus, for a torus described in the phase-space domain, original flow maps on time must be stated in the coordinate phases. This is straightforward because each phase is associated with a harmonic, thus its dynamics is driven by a constant frequency. Each phase shift of the flow map after a given time interval is called rotation number ρ. With the condition of Eq.B.21, the sum of harmonics at different and not resonant pulsations will never be periodic, therefore the propagation of a $(n \geq 2)$-torus is usually done by iterated flow mappings, realizing a time-discrete dynamical system, where each phase increases by the respective rotation number. Since the phases are periodic, the QPO can be seen along these multiple-time axes as a motion along multiple circles, where each phase runs with different angular velocities[9]. Therefore they perform each revolution at different periods T. Usually one phase is fixed by the map iteration, and this is called the longitudinal motion, while all the other phases describe the transversal motion. For them, the periods of the first transversal revolution are defined as the number of map's iterations N_T needed by the related transversal phase to perform at least one loop. This is summarized in Eq.B.22 for an iterated flow map P_{T_1} with constant propagation time set to the period of the first phase. Note that these are not real periods, since the QPO is not resonant, they are just related to the first crossing of the 2π span. If two frequencies are resonant, this number of iterations will fit their ratio r (which is rational, when Eq.B.21 is not satisfied), and the dimension of the torus lowers to consider only the related phase with lowest synchronous pulsation.

$$\begin{cases} \mathbf{T}: T_i = P_{\tau_i}(x_{0,QPO}) = \dfrac{2\pi}{\omega_i} \rightarrow \boldsymbol{\rho} = \boldsymbol{\omega} T_1 = \begin{bmatrix} 2\pi \\ \left\{2\pi \frac{\omega_i}{\omega_1}\right\}_{i=2}^n \end{bmatrix} = \begin{bmatrix} 2\pi \\ \{2\pi r_i\}_{i=2}^n \end{bmatrix} \\ \quad \rightarrow P_{T_1}(x_{0,QPO}) = \nu_u(\boldsymbol{\varphi}_0 + \boldsymbol{\rho}, \boldsymbol{\varphi}_0, x_{0,QPO}) = \nu_u\left(\begin{bmatrix} \varphi_{0,1} \\ \{\varphi_{0,i} + 2\pi r_i\}_{i=2}^n \end{bmatrix}, \begin{bmatrix} \varphi_{0,1} \\ \{\varphi_{0,i}\}_{i=2}^n \end{bmatrix}, x_{0,QPO}\right) \\ \boldsymbol{\rho} = [\{\rho_i\}_{i=1}^n] \wedge \boldsymbol{\rho}_0 = \mathbf{0} \rightarrow \rho_{i,k} = \mathrm{mod}\,\{\rho_i, (-\pi, \pi]\} = const \\ \quad \Rightarrow N_{T_i} : \left|\sum_{k=1}^{N_{T_i}} \rho_{i,k}\right| = N_{T_i}\,|\rho_i| \geq 2\pi \Rightarrow T_i \leq \sum_{k=1}^{N_{T_i}} T_1 = N_{T_i} T_1 \end{cases} \tag{B.22}$$

[9] It is like not having a single reference time, but different asynchronous clocks.

B.1.3.1 Non-Autonomous Dynamical Systems

The case of TV dynamical systems is characterized by forced phases $\tilde{\varphi}$, where their dynamics are constrained: their frequencies $\tilde{\omega}$ correspond to the spectrum of the forcing action. This turns out to be an advantage [164], because their solutions are explicitly retrievable from integration of the related equations of motion $\dot{\tilde{\varphi}} = \tilde{\omega}$. Eq.B.23 provides the generalization of the expression for the orbit of a n-torus of Eq.B.20 to take into account also constrained phases. This is done appending their forced dynamics in the vectorfield as discussed in section B.1.2.4.

$$\mathbf{x} = \begin{bmatrix} x \\ \tilde{\varphi} \end{bmatrix} \wedge \boldsymbol{\varphi} = \begin{bmatrix} \varphi \\ \tilde{\varphi} \end{bmatrix} = \boldsymbol{\varphi}_0 + \int \boldsymbol{\omega} dt = \begin{bmatrix} \varphi_0 \\ \tilde{\varphi}_0 \end{bmatrix} + \begin{bmatrix} \omega t \\ \int \tilde{\omega} dt \end{bmatrix}, \varphi \in \mathbb{R}^{n-C}, \tilde{\varphi} \in \mathbb{R}^{C}$$
$$\rightarrow \begin{cases} \begin{cases} \dot{x}(\boldsymbol{\varphi}(t)) = u(\boldsymbol{\varphi}(t), \mathbf{x}) \\ \dot{\tilde{\varphi}} = \tilde{\omega} \end{cases} \\ \begin{cases} x_{QPO}(\boldsymbol{\varphi}(t)) = \nu_u(\boldsymbol{\varphi}(t), \boldsymbol{\varphi}_0, x_{0,QPO}) \\ \tilde{\varphi}_{QPO}(t) = \tilde{\varphi}_{0,QPO} + \int \tilde{\omega} dt \end{cases} \end{cases} \Rightarrow \begin{cases} \begin{cases} \frac{\partial x}{\partial \boldsymbol{\varphi}} \boldsymbol{\omega} = u(\boldsymbol{\varphi}, \mathbf{x}) \\ \frac{\partial \tilde{\varphi}}{\partial \boldsymbol{\varphi}} \boldsymbol{\omega} = \tilde{\omega} \end{cases} \\ \begin{cases} x_{QPO}(\boldsymbol{\varphi}) = \nu_u(\boldsymbol{\varphi}, \boldsymbol{\varphi}_0, x_{0,QPO}) \\ \tilde{\varphi}_{QPO}(\boldsymbol{\varphi}) = \tilde{\varphi} \end{cases} \end{cases} \tag{B.23}$$

B.1.4 Dynamical Systems Theory

When applied in mathematical problems and engineering applications, every physical law is represented by a system of differential (or recursive) equations, which are solved and investigated with analytical or numerical techniques. This is also the case of Newtonian mechanics, and in particular for the orbital mechanics of a particles system. When a global analytical solution is not available for the problem under study, numerical methods must be employed. However, considering that the dynamical model is always an approximation of the real perturbed dynamics (see Eq.2.1), mathematical analysis could still be used to qualitative understand the global dynamics of the flow, which is its main property for the long-term behavior. This is indicated as the global structure of the system of dynamical equations. Its investigation is one of the subjects of applied mathematics, and is called Dynamical Systems Theory (DST). DST found immediate application to nonlinear systems, which are usually characterized by chaotic dynamics: the case of the CR3BP was a paramount milestone [50].

The theorems and tools of DST are presented throughout this chapter, and are applied in chapters 4-5-6 of the thesis to compute the invariant motions in the models of the Mars-Phobos system derived in chapter 3.

B.2 Solution of Nonlinear Equations

The purpose of this section is to present the classical methodology for the solution of the systems of nonlinear algebraic equations. These techniques are used throughout this thesis, and constitute the basis of the numerical methods of DST used to compute invariant motions, that will be discussed in sections B.3, B.5, B.6, and B.7.

B.2.1 Newton's Method

The computation of the zero x_0 of a general NL system of equations $F(x) = 0$ is done with the well-known Newton's method [50]. This consists in the application of the variational equation of the function F

$$\delta F = A_F(x)\delta x \tag{B.24}$$

in the neighborhood of the sought solution U_{x_0}, thus using an initial guess $x_{0,0}$ for x_0. Newton's method assumes a linearized approximation of the function in U_{x_0}, which allows to derive the root. In particular, Newton's method requires the knowledge of the Jacobian A of the function F.

$$x_{0,0} \in U_{x_0} : F(x_0) = 0 \Rightarrow x_0 = x_{0,0} - A_F(x_{0,0})^{-1} F(x_{0,0}) \tag{B.25}$$

Therefore, Eq.B.25 is exactly true only if the analyzed function is linear. However, the variational form is still powerful for a general NL function, because it guarantees the convergence of the solution when applied iteratively $x_{0,j} \to x_0$, evaluating F and A_F at the intermediate root $x_{0,j}$.

$$\begin{aligned} &x_{0,0} \in U_{x_0} : F(x_0) = 0 \Rightarrow \\ &\Rightarrow x_0 = \lim_{j\to\infty} x_{0,j} = \lim_{j\to\infty} \left\{ x_{0,j-1} - A_F(x_{0,j-1})^{-1} F(x_{0,j-1}) \right\} : \begin{cases} ||F(x_{0,j})|| < \varepsilon_F \\ ||x_{0,j} - x_{0,j-1}|| < \varepsilon_x \end{cases} \end{aligned} \tag{B.26}$$

In Eq.B.26, ε_F and ε_x represent the chosen tolerance on function and step respectively. To achieve the convergence of the procedure, it is worth to remark the satisfaction of one requirement, which is that the initial guess must be close enough to the unknown zero. This is to assure that the local slope of the NL function attracts towards the aimed zero, and not another root or any critical point. When this requirement is satisfied, the convergence to the zero is quadratic, unless the aimed solution is a critical point, which lowers the order of convergence to be linear with the iteration step.

In particular, Newton's method is still the best powerful tool at the basis of the methods used to solve the optimization problems, which is the minimization/maximization of a general NL functional $V(x)$. Since in this case the sought solution is a stationary point of the functional, the problem translates in the computation of the zero of the functional's derivative. Thus Newton's method is applied using the gradient $V'(x)$ in place of $F(x)$, and using the Hessian $V''(x)$ in place of $A_F(x)$ in Eq.B.26. The optimizers based on this approach are called gradient methods. They are massively used for local optimization, when the initial guess is close to the minima/maxima of interest. The determination of a suitable initial guess in large scale or multi-objective problems (multiple parameters constituting x) is far more difficult, and is called global

Figure B.1: **Numerical continuation.** Sketch of some different continuation curves of the root x_0 of a function dependent from a parameter σ [165].

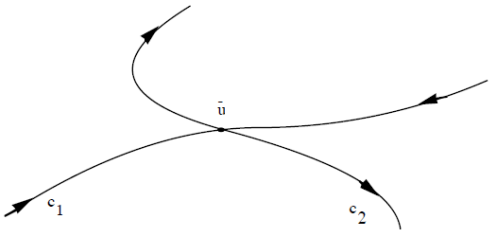

Figure B.2: **Numerical continuation.** Bifurcation of the continuation curve in two branches [165].

optimization: genetic algorithms are used for this task.

B.2.2 Numerical Continuation

The basic idea of the numerical continuation (NC) technique is given by considering two slightly different functions $F(x)$ and $G(x)$ on a set U_x. It is immediate to assemble a transformation from F to G through an added parameter σ that acts in a linear combination's fashion, weighting the two functions from 0 to 1.

$$x \in U_x : F(x) \approx G(x) \Rightarrow \begin{cases} H(x,\sigma) = (1-\sigma)F(x) + \sigma G(x) = H(y) \\ y = \left[\begin{smallmatrix} x \\ \sigma \end{smallmatrix}\right] \end{cases} \leftrightarrow \begin{cases} H(x,0) = F(x) \\ H(x,1) = G(x) \end{cases} \tag{B.27}$$

The resulting function H, dependent now also on the parameter (σ is named the continuation parameter), is called a convex homotopy. Another trivial way to introduce the global function H is using σ to directly weight a perturbation function D on F: this is called a general homotopy.

$$G(x) = F(x) + D(x) \Rightarrow H(y) = H(x,\sigma) = F(x) + \sigma D(x) \tag{B.28}$$

Now suppose that F is an "easy" function to be solved analytically or numerically, or generally a function where a root x_0 is available. A Newton's method could use it as a first guess to numerically compute the root of H for σ small. This is shown in Eq.B.29, where $\oplus_{/\odot}$ represents the Jacobian of $\oplus$ with the partial derivatives with respect to $\odot$.

$$\begin{aligned} & x_0 \in U_x : F(x_0) = 0 \rightarrow y_0(\sigma) = \left[\begin{smallmatrix} x_0(\sigma) \\ \sigma \end{smallmatrix}\right] : H(y_0(0)) = 0 \Rightarrow \\ & \Rightarrow \begin{cases} y_0(\sigma) \in U_{y_0(\sigma+\Delta\sigma)} : H\left(y_0(\sigma+\Delta\sigma)\right) = 0 \\ \delta H = \left((1-(\sigma+\Delta\sigma))A_F + (\sigma+\Delta\sigma)A_G\right)\delta x = \left(A_F + (\sigma+\Delta\sigma)A_D\right)\delta x \\ \quad\quad = H_{/x}\left(x_0(\sigma), \sigma+\Delta\sigma\right)\delta x \end{cases} \end{aligned} \tag{B.29}$$

The motivation is to find a root of G, when Newton's method would not converge using as initial guess the root of F, because the level of perturbation between the two functions is too high. Therefore intuitively, we can increment the parameter slowly, solving Newton's methods by iteratively using, as an initial guess, the solution found at the previous step, until the solution for the desired value of the parameter is obtained.

$$
\begin{aligned}
&x_0(\sigma) : H(y_0(\sigma)) = 0 \Rightarrow \\
&\Rightarrow y_0(\sigma) = \lim_{\sigma_k \to \sigma} y_0(\sigma_k) : \begin{cases} \sigma_k = \sigma_{k-1} + \Delta\sigma_k \\ y_0(\sigma_{k-1}) \in U_{y_0(\sigma_k)} : H\left(y_0(\sigma_k)\right) = 0 \\ \delta H = \left((1-\sigma_k)A_F + \sigma_k A_G\right)\delta x = \left(A_F + \sigma_k A_D\right)\delta x \\ \qquad = H_{/x}\left(x_0(\sigma_{k-1}), \sigma_k\right)\delta x \end{cases}
\end{aligned}
\tag{B.30}
$$

Eq.B.30 is in fact the NC method, which is the adaptation of Newton's method of section B.2.1 to compute the solutions of a parametric system of NL algebraic equations. In this case, it can be interesting not only to calculate the final solution (the root at the final function G), but to find its value as a function of the parameter weighting the perturbation. The global solution is therefore a curve of roots $x_0(\sigma)$ (see Fig.B.1). The NC could be stated as an iterated Newton's method along the discretized solution curve,

$$
\begin{cases} C(y) = \begin{bmatrix} H(y) \\ S(y) \end{bmatrix} = 0 \\ \delta C = \begin{bmatrix} H_{/x} & H_{/\sigma} \\ S_{/x} & S_{/\sigma} \end{bmatrix} \begin{bmatrix} \delta x \\ \delta\sigma \end{bmatrix} = A_C(y)\delta y \end{cases}
\tag{B.31}
$$

and Eq.B.31 shows the general step appending σ and adding the function S. The choice of S completes the Newton's method scheme treating the continuation parameter as part of a global fictitious vector of variables y, and defines the type of NC. In this sense, when the NL effects of the added terms are high, different implementations are needed to efficiently continue the solution, and this will be addressed now.

B.2.2.1 Components of a Numerical Continuation Code

The NC is characterized by four ingredients to be implemented in a computational code.

B.2.2.1.1 Objective function

The first ingredient is given by the function $H(y) = H(x, \sigma)$ used in the Newton's method scheme of Eq.B.31.

B.2.2.1.2 Predictor for the initial guess

The second ingredient regards the initial guess used throughout the iteration steps. Using the solution computed at the previous step was the first idea, but an improvement

of the Newton's method step's convergence is given by better estimating the solution at the future step. This allows the solution curve to be integrated with a larger step's size. This is done with a dedicated Predictor-Corrector algorithm: the corrector is the first ingredient of the NC, the predictor is an interpolation algorithm of the solution curve up to the previous step, that extrapolates a value for the current step trough a step-dependent direction vector v.

$$y_0(\sigma_k) = y_0(\sigma_{k-1}) + v_y(\sigma_{k-1}) = y_0^P\left(\{x_0(\sigma_i)\}_{i=0}^{k-1}, \{\Delta\sigma_i\}_{i=1}^{k}\right) : H\left(y_0(\sigma_i)\right) = 0, \forall 0 \leq i \leq k-1 \tag{B.32}$$

In case the predictor is absent, as stated above we use the previous solution. This is a predictor of order-0 where v only updates the continuation parameter.

$$y_0(\sigma_k) = \begin{bmatrix} x_0(\sigma_{k-1}) \\ \sigma_k \end{bmatrix} : H(y_0(\sigma_{k-1})) = 0 \tag{B.33}$$

Usually, a solution of order-1, that uses the finite differences up to the first derivative to approximate the curve, is sufficient to improve the corrector's convergence. Higher order extrapolations are not necessary, unless the case in study suggests a particular curve's evolution.

$$y_0^P = y_0(\sigma_{k-1}) + v_y(\sigma_{k-1}) = y_0(\sigma_{k-1}) + \Delta y_{0,k-1} = 2y_0(\sigma_{k-1}) - y_0(\sigma_{k-2}) \tag{B.34}$$

The best value of the vector v is the actual derivative of the curve at the current location, instead of approximating it by finite differences. By definition, if we see the curve as an isoline of the global function H in the augmented space defined by y, the tangent space of the curve is the kernel's direction of the linearized $H(y)$. Regarding the direction's way, assuming that the continuation step is not large, it should be maintained consistency with the previous step, as indicated in Eq.B.35. Therefore, the computation of the kernel is the best predictor, and it requires the expression of the derivative of the global function with respect to the continuation parameter $H_{/\sigma}$.

$$v_y(\sigma_{k-1}) \in \ker\left\{\left[\, H_{/x}(y_0(\sigma_{k-1}))\ H_{/\sigma}(y_0(\sigma_{k-1}))\,\right]\right\} \wedge v_y(\sigma_{k-1})^T v_y(\sigma_{k-2}) > 0 \tag{B.35}$$

B.2.2.1.3 Continuation curve's parametrization

The third ingredient is the parametrization of the continuation curve, and is the most important because it drives the choice of the function S in the general definition of the NC in Eq.B.31. Using the continuation parameter was the first idea, because it physically relates the solution x with the perturbation level σ: indeed $x(\sigma)$ is called the natural parametrization of the continuation curve. In this case, we fix every time a value of the continuation parameter and we find the solution for exactly that value: this is expressed by the following choice of the step function S of the NC.

$$\begin{cases} C(y) = \begin{bmatrix} H(y) \\ \sigma - \sigma^T \end{bmatrix} = 0 \\ \delta C = \begin{bmatrix} H_{/x} & H_{/\sigma} \\ 0 & 1 \end{bmatrix} \begin{bmatrix} \delta x \\ \delta\sigma \end{bmatrix} = A_C(y)\delta y \end{cases} \tag{B.36}$$

Thus, this augmented Newton's method is just fictitious, because S is uncoupled, and the Newton's method solves a correction only on the solution variables δx. Referring to Fig.B.1, the Newton's method corrects the predicted solution, at a value of σ, moving vertically to find the point on the curve at this fixed σ. But when the nonlinear effects are high, as it can be seen in the same figure, the continuation curve folds[10]. In this case, with the natural parametrization, when the predictor moves the initial guess ahead of the σ where the turning point is located, the Newton's method of Eq.B.36 will irremediably fail, because there is any solution moving vertically (in the neighborhood of the initial guess). Smaller steps would just reach the vertical asymptote slower. The solution is obtained considering the continuation curve in the global space of y, and parameterizing the curve with its arclength s. This parametrization is called *pseudo-arclength* because the NC step γ of the arclength s is evaluated by finite differences.

$$y_0(s) = \begin{bmatrix} x_0(s) \\ \sigma(s) \end{bmatrix} \tag{B.37}$$

$$ds = \gamma = \sqrt[2]{dx_0{}^2 + d\sigma^2} \tag{B.38}$$

Therefore S is the constraint required to maintain the arclength's step in the predicted direction. Eq.B.39 summarizes the Newton's method scheme's step of the pseudo-arclength NC, which was introduced by Keller [166, 165, 167].

$$\begin{cases} C(y) = \begin{bmatrix} H(y) \\ \hat{v}_y^T \Delta y - \gamma \end{bmatrix} = 0 \\ \delta C = \begin{bmatrix} H_{/x} & H_{/\sigma} \\ \frac{v_x{}^T}{\|v_y\|} & \frac{v_\sigma}{\|v_y\|} \end{bmatrix} \begin{bmatrix} \delta x \\ \delta\sigma \end{bmatrix} = A_C(y)\delta y \end{cases} , \Delta y = y(\sigma_k) - y(\sigma_{k-1}) \tag{B.39}$$

This NC enables corrections in both solution δx and parameter $\delta\sigma$, so the Newton's method can move from the initial guess along any direction in the global x-σ plane, overcoming any possible turning point. Recall that this NC, as well as the predictor through the kernel of Eq.B.35, requires the partial derivative with respect to the continuation parameter $H_{/\sigma}$.

Using the pseudo-arclength NC, there is no control on the continuation parameter's value, therefore the stopping condition of the NC must be added in the code [116]. This is realized with a linear approximation of the predicted x when the predicted value of the parameter overcomes the target value. Following this, the Newton's method at the

[10] It could be even possible that, for strong perturbations, the continuation curve never arrives to the desired final σ.

desired final step is performed with the natural parametrization's scheme of Eq.B.36.

$$\sigma^P > \sigma^T \Rightarrow \gamma_k = \frac{\sigma^T - \sigma_{k-1}}{\frac{v_\sigma(s_{k-1})}{\|v_y(s_{k-1})\|}} \Rightarrow y_0^P = y_0(s_{k-1}) + \gamma_k \hat{v}_y(s_{k-1}) = \begin{bmatrix} x_0(s_{k-1}) + \gamma_k \frac{v_x(s_{k-1})}{\|v_y(s_{k-1})\|} \\ \sigma^T \end{bmatrix} \tag{B.40}$$

B.2.2.1.4 Integration step

The fourth and last ingredient is the strategy for the variable step control. Using a constant step, whether it is for the natural or the arclength parametrization, not only slows down the NC but could also halt it when the curve has narrow bends (which is there is a high slope at least in one component of x). The step size is made explicit in the predicted direction vector v,

$$y_0^P = \begin{bmatrix} x_0^P \\ \sigma^P \end{bmatrix} = y_0(s_{k-1}) + v_y(s_{k-1}) = y_0(s_{k-1}) + \gamma_k \hat{v}_y(s_{k-1}) \tag{B.41}$$

and an adaptive algorithm is required to update the value of γ along the NC. This algorithm is based on the convergence properties of the Newton's method performed at the last step of the NC. Ideally, one wants to keep constant the number of iterations n of each Newton's method along all the NC, therefore a simple proportional control law is the following [116].

$$\gamma_k = \gamma_{k-1} \frac{n_{des}}{n_{k-1}} \tag{B.42}$$

The choice of the desired number of iterations is delicate. A low number of Newton's method iterations provides high accuracy and fidelity of the NC, but it results in small steps and so long computation time to finish the NC. On the opposite, a high number of Newton's method iterations would provide larger steps and so speed up the NC, but this increases the possibility that the predicted solution would fall outside of the radius of attraction of the solution, and the Newton's method will not converge.

Additional step's updating laws have been used in the literature, for example based on the determinant of the Newton's method matrix [168, 165].

B.2.2.2 Implementation

The NC will be intensively used in chapter 4 in different algorithms. All of these schemes use a backbone code for the continuation. First, an initial guess must be available, usually a linear solution or one of order-0 obtained from a simpler problem. Then, the NC starts with a very tiny value of the continuation parameter (less than 10^{-6} with respect to the desired final value). The NC is a while-loop controlled by the stopping condition, and is constituted by:

- the predictor algorithm to provide the initial guess along the NC's steps,
- the Newton's method algorithm for each step,

- the computation of the kernel (in case the predictor is based on it),
- the saving of the data structure with possible intermediate post-processing.

The Newton's method algorithm is constituted by:

- the scaling of the direction vector of the predictor with the current step size,
- a selection between pseudo-arclength and natural scheme (always used at the final step) provides the core of the Newton's method, where at each iteration the evaluation of $H(x, \sigma)$, its derivatives, and the solution of the linear system are performed.

The Newton's method is incorporated in an inner while-loop that controls the variable step: if the Newton's method performances are satisfying (numbers of iterations, needed to converge to the required function and step tolerances, less than a maximum number, like 10) the loop ends and the new step size is evaluated from Eq.B.42; if instead the convergence is not been reached, the loop restarts decimating the step size.

Since the nonlinear effects of the perturbations treated in this thesis are significant, to overcome possible turning points in the continuation curve the NC is implemented with the pseudo-arclength algorithm of section B.2.2.1.3. To enhance the convergence of the Newton's method and speed up the continuation, a predictor is used, and is given either by the kernel of the linearized H or by its first-order finite differences. For the last ingredient, the adaptive step strategy based on the control of the number of Newton's method iterations, presented in section B.2.2.1.4, is used.

B.2.2.3 Bifurcations

The NC, apart from turning points, could encounter non-regular solutions. These are points on the continuation curve that have singular Newton's method matrix, so its kernel has dimension greater than 1. This means that there are multiple directions where proceed with the continuation, like a crossroad. This situation is a bifurcation of the solution, which means that the continuation curve breaks in two (or more) branches, like in Fig.B.2. This situation is paramount in the analysis of parametric systems. Identification of bifurcations is a major issue for the application of NC [168, 167, 165], since if not carefully treated the continuation could be captured in any of the region of attraction of one of the branches. The selection of the branch of interest is important and not usually trivial, since it depends from the case in study.

B.3 Computation of Equilibrium Points

The first step in the determination of the invariant solutions of a dynamical system is to identify equilibria, from which proceed to find periodic orbits and quasi-periodic orbits.

Definition. EPs are 0-tori identified as fixed flows, roots of the vectorfield such that

$$x_{EP}(t) = x_{EP} \Leftrightarrow f(t, x_{EP}) = 0, \forall t \tag{B.43}$$

In particular, for the case of a TI mechanical system, since the velocity components of the state vector are zero, EPs are directly the stationary points of the potential function of the system.

Computation. Therefore, the computation of the EPs of a NL dynamical system is performed using Newton's method, as described in section B.2.1, where the function F is taken as the vectorfield [116]. In particular, the Jacobian used in Newton's method corresponds to the linear state-matrix A_f defined in Eq.B.4, at the point of the current iteration. In case of a TI mechanical system, this corresponds to the Hessian matrix of the potential.

Stability and manifolds. The EPs are fundamental solutions of a dynamical system: in the usual case where $A_f(x_{EP})$ is full-rank, the EP is isolated. Once identified, the study of the linear behavior around the EPs is very important in DST. In section B.1.2.1, the behavior around the general flow of a linear system was addressed. The information is entirely provided by $A_f(x_{EP})$: its spectrum of eigenvalues defines the Lyapunov stability property of the EP.

The extension of this procedure to provide the linearized behavior in a NL dynamical system was presented in section B.1.2.2. In particular, for mechanical systems, eigenvalues are present in couples with the same absolute value, therefore the possible linearized manifolds around an EP can have the phase portrait of: saddle (unstable), center (marginally/neutrally stable, which could be singular if the EP is not isolated), spiral (asymptotically stable or unstable).

For TI linear dynamical systems, the *Lyapunov's center theorem* demonstrates that for every center around an EP, there is a continuous 1-parameter family of POs, parameterized by the energy [50]. *Moser's theorem* proved that this result is valid also for nonlinear systems [77, 169]. Therefore, in autonomous dynamical systems, POs are not isolated but organized in families, and they develop with growing energy from an EP.

The identification of the EPs and the dynamical analysis of the orbit structure in their neighborhood is a basic operation, and is performed in section 2.3.5 in the CR3BP, for the preliminary analysis of the Mars-Phobos system, where the EPs are the five planar LPs. Furthermore, the analysis is undertaken in section 3.3.6.2 for the improved model of the CR3BP-GH.

B.4 Analytical and Semi-analytical Techniques for Solution of Nonlinear Differential Equations

The purpose of this section is to provide an overview of the most used strategies to develop closed-form approximated solutions for nonlinear ODEs.

The most simple but still useful approach to approximate a nonlinear problem is by linearization. This because every infinitesimal application is intrinsically linear, and its closed-form solution, even if valid in this framework, still holds qualitative meaning and practical properties in the real nonlinear scenario. In the case of a NL dynamical system of Eq.B.1, the linearization of the vectorfield is undertaken around a given flow. Thus, the new state of the linearized dynamics is the variation $\delta x(t)$ from the trajectory $x(t)$. This leads exactly to the variational equations of Eq.B.6, whose TV state-matrix is the Jacobian of the vectorfield, and whose solution is given by the STM of the trajectory in Eq.B.9. At the start of the analysis of a dynamical system, the first solutions to be computed are the EPs, as presented in section B.3. Thus, in TI systems, the linear dynamics around them is fully described by a TI state-matrix, the analytical solution is given by Eq.B.9, and the linear behavior is represented by the associated manifolds, as explained in section B.1.2.1. They describe the global orbit structure around the EP, thus they approximate the local behavior in the original nonlinear system, after Moser's theorem [50]. This information is paramount to identify the existence of families of invariant motions (elliptic manifold), such as POs and QPOs, which are provided by the normal modes of the imaginary eigenvalues of $A_f(x_{EP})$. The eigenspace of the spectrum with non-null real part (hyperbolic manifold) identifies the invariant manifolds of the EPs.

Once the invariant motions and manifolds have been identified, their linear solution could be improved with a straightforward analytical approach, which is to include additional terms of the Taylor series' approximation of the nonlinear terms in the dynamics. Several methodologies are used in this sense. Scientists baffle by playing a little with the absence of a borderline in the terminology, that defines a mathematical method to be analytical, semi-analytical, semi-numerical, and numerical. In substance, as stated before, these techniques requires an analytical approximation, which could be pushed from low to high order. As long as the order increases, the computational load (high dimensions for the solution's expression, CPU's time and storage of the huge set of coefficients) requires numerical capabilities, such as the use of symbolic manipulators and parallel computers.

The focus of these methodologies is the computation of the invariant motions around an equilibria, thus they are globally indicated as techniques for the *reduction to the central manifold* [50].

An example of the lower order cases consists in the method of the normal forms [169]. The method requires to approximate the Hamiltonian of the system by a series expansion, erasing the hyperbolic part. This approach has been applied in the CR3BP

in [51] and is useful for qualitative investigation of the center manifold.

An example of the upper order methodology is the differential algebra [170], also called jet transport. The approach requires to approximate the nonlinear terms of the dynamics with very high-order Taylor series. The point of this work is that the entire computer programming is re-written in polynomial algebra. Once this is done, any general dynamical system can be solved by polynomial approximation. Care must be taken to check that the dynamical analysis is undertaken inside the domain of convergence of the series. In particular, this methodology is useful for parametric analyses.

Finally, the basis of the most used technique to compute invariant objects in NL dynamical systems is presented below with more detail. This methodology has been used in the framework of the CR3BP and applied in preliminary space missions' design up to high-order [115, 51].

B.4.1 The Lindstedt-Poincaré Method

The lp technique has been applied in several fields, from low to high order. Despite the technique is dependent on the NL problem under study, and different choices are available to implement it, the main points required by the technique are few and systematic. The aim of this section is to provide a general summary of the basis of the methodology [50].

The lp technique starts with the decomposition of the full dynamics[11] in a dominant linear part plus additional nonlinear terms (where ε represents some parameters of the nonlinear dynamics). In Eq.B.44 the case of a first-order TI ODE is taken as a reference[12].

$$\begin{cases} \dot{x} + ax + f_{NL}(x, \varepsilon) = 0 \ , \ \varepsilon, \alpha \to 0 \\ x(0) = \alpha \end{cases} \tag{B.44}$$

The lp technique is based on an approximation by power series expansions [50]. Thus, the nonlinear dynamics should be conducted to an appropriate form to apply the method: the nonlinear part is fully determined by a power series in terms of x, with coefficients ε.

$$f_{NL}(x, \epsilon) = \sum_{n=2}^{N} \varepsilon_n x^n \tag{B.45}$$

Following this, the solution x itself is approximated by a power series expansion, in terms of either ε or α: but this time the coefficients $x_n(t)$ are unknown. Alternatively the coefficients can be expressed to represent directly the solution wanted, which are the normal modes of the center manifold, and the unknown terms reduce to TI coefficients $c_{n,r}$ [51, 50].

[11] Remember that the dynamics is expressed in a frame centered on the EP.

[12] The spectrum of a must have an elliptic part for the existence of invariant motions.

$$x(t) = \sum_{n=0}^{N} \varepsilon^n x_n(t) = x_0(t) + \sum_{n=1}^{N} \varepsilon^n x_n(t) \tag{B.46}$$

$$x(t) = \sum_{n=0}^{N} \alpha^n \sum_{|r|=0}^{n} c_{n,r} e^{\sum_m ir(\omega_m t + \phi_m)} = x_0(t) + \sum_{n=1}^{N} \alpha^n \sum_{|r|=0}^{n} c_{n,r} e^{\sum_m ir(\omega_m t + \phi_m)} \tag{B.47}$$

In both cases, the first-order terms of the solution are known as they are the linear homogeneous solution. Thus, the initial condition is accounted by the linear part of the solution, while the remaining coefficients will be the solution with homogeneous initial conditions but dependent on the nonlinear dynamics, like a forcing term.

$$x_0(t) = x_L(t) \leftrightarrow \begin{cases} \dot{x}_0 + a x_0 = 0 \\ x_0(0) = x(0) = x_0 \rightarrow x_{n\geq 1}(0) = 0 \end{cases} \tag{B.48}$$

Substituting back the approximated solution in the dynamical equations, the result of the solution's series in terms of ε or α is a system of $N \times n$ recursive differential equations (n being the dimension of the original dynamical system, N being the order of nonlinear terms considered in the expansion) to be satisfied. We see that each term x_n is the solution of a non-homogeneous ODE, where the forcing term is constituted by solution's terms of lower order.

$$\begin{aligned} \dot{x}_n + a x_n &= -f_{NL}(\left\{\varepsilon^j x_j\right\}_{j<n}, \varepsilon) \\ &= -f_{NL}\left(\left\{\alpha^j \sum_{|r|=0}^{j} c_{j,r} e^{\sum_m ir(\omega_m t + \phi_m)}\right\}_{j<n}, \varepsilon\right) \end{aligned} \tag{B.49}$$

The power series in the right-hand side will recursively bring forward the original linear solution. This constitutes a resonant forcing term, and all the non-homogeneous ODEs have a particular integral with a term proportional to t. Thus, each solution's term for $n \geq 1$ will be made up of periodic and secular terms.

$$x_n(t) = f(t, a, \varepsilon, \alpha, x_{j<n}/c_{j<n,r}) + g(t, a, \varepsilon, \alpha, x_{j<n}/c_{j<n,r})t \tag{B.50}$$

To obtain an invariant motion, the aim is to erase all these secular terms. This is obtained with the key point of the lp methodology. It assumes that the nonlinear dynamics changes the natural frequencies of the linear system. Thus, a change of the time variable is introduced, again described by a power series expansion, similar to the one of the solution.

$$\tau = \nu(\varepsilon)t \rightarrow \frac{d}{dt} = \nu(\varepsilon)\frac{d}{d\tau} \tag{B.51}$$

$$\nu^{-1}(\varepsilon) = \sum_{n=0}^{N} \varepsilon^n \upsilon_n = 1 + \sum_{n=1}^{N} \varepsilon^n \upsilon_n \tag{B.52}$$

For the second choice of the solution's series, where the natural frequencies of the center manifold were explicit, these are modified directly and the time kept original, where the first-order term is the frequency in the linear system.

$$\omega_m(\alpha) = \sum_{n=0}^{N} \alpha^n \omega_{m,n} = \omega_{m,0} + \sum_{n=1}^{N} \alpha^n \omega_{m,n} \tag{B.53}$$

Repeating the procedure, now the secular terms of the analytical solution are functions of the additional time/frequency series' coefficients. It is worth to note that now the left-hand size of the n-recursive ODE contains also lower order terms, residuals from the linear part of the dynamics, that should be shifted on the right-hand side as additional forcing terms.

$$\begin{aligned} x' + \nu^{-1}\left(ax + f_{NL}(x,\varepsilon)\right) &= 0 \\ x' + \omega_m\left(ax + f_{NL}(x,\varepsilon)\right) &= 0 \end{aligned} \tag{B.54}$$

$$\begin{aligned} \dot{x}_n + ax_n &= -f_{NL}(\left\{\varepsilon^j x_j\right\}_{j<n}, \varepsilon) - \left\{\varepsilon^j \upsilon_j a x_j\right\}_{j<n} \\ &= -f_{NL}\left(\left\{\alpha^j \sum_{|r|=0}^{j} c_{j,r} e^{\sum_m ir(\omega_m t + \phi_m)}\right\}_{j<n}, \varepsilon\right) - \left\{\alpha^j \omega_{m,j} a x_j\right\}_{j<n} \end{aligned} \tag{B.55}$$

Therefore, the additional coefficients are chosen to erase the secular terms and make the solution a torus for the approximated dynamics up to order N.

$$\begin{aligned} &x_n(t) = f(t, a, \varepsilon, \alpha, x_{j<n}/c_{j<n,r}, \upsilon_{j<n}/\omega_{m,j<n}) + g(t, a, \varepsilon, \alpha, x_{j<n}/c_{j<n,r}, \upsilon_{j<n}/\omega_{m,j<n})t \\ &\rightarrow \upsilon_j/\omega_{m,j} : g_n = 0 \end{aligned} \tag{B.56}$$

The lp method involves successive adjustments of frequencies to avoid secular terms and allows one to obtain approximate invariant solutions [50]. It considers the reality that in nonlinear systems also the frequencies are dependent from the initial conditions, and change accordingly to the size of the orbit.

The lp technique and the semi-analytical methods are very powerful generators of initial conditions for highly NL systems. However their performances depend on two conditions: a high enough order of the series, and good stability properties of the manifold around the EP. In particular, if the second requirement is not satisfied by the dynamical system, it is possible that even very high-order expansions do not have a very extended region of convergence [50, 51], whose boundary represents the size, from the EP, of the tori computed by the method, that is reliable also in the full nonlinear dynamics. Sometimes, when the instability of the EP's manifold is very high, even the machine error is a limiting factor in the numerical simulation of the full nonlinear dynamics. This means that even improving the order of the series not only increases the computation effort, but also does not provide any gain in terms of computational performance of the solution simulated in the full dynamics. In these cases, numerical

methodologies must be applied to provide reliable solutions for practical applications, where low-order analytical solutions are used as starting guesses [50]. Such techniques will be the focus of the next sections.

B.5 Numerical Techniques for Computation of Periodic Orbits

A paramount property of any dynamical system is the existence of POs. This section presents to the reader the notions of DST used to define a PO and its properties. Following this, the section shows how these concepts are applied to numerically compute these invariant motions.

B.5.1 Definition

A periodic orbit for the general dynamical system of Eq.B.1 is the 1-torus defined in Eq.B.57.

$$x_{PO}(t_0+T) = x_{PO}(t_0)\ ,\ \forall t_0 \rightarrow \begin{cases} x_{PO}(t) = \phi_f(t, t_0, x_{0,PO}) \\ M = \Phi_f(T+t_0, t_0) \end{cases} \tag{B.57}$$

T is the associated period, as the minimum time interval within the solution repeats exactly. In addition, the STM evaluated after one revolution is called the monodromy matrix M of the PO.

B.5.1.1 Linearized Behavior, Stability, and Floquet Theory

The monodromy matrix has important features in the analysis of POs. These characters represent the Floquet theory [50].

The monodromy matrix represents the linear behavior after one revolution of the PO. The Floquet theorem states that the STM of a PO is composed by the product of a T-periodic matrix, representing the linearized behavior around the PO within the period, and an exponential matrix, representing the linear variation after an integer number of revolutions [50]. Thus, the STM after an integer N number of periods is simply the N-power of the monodromy matrix: this means that the linear sensitivity of the initial conditions propagates with a power law each revolution. This is a discrete TI and linear dynamical system, where M is the state matrix.

The Floquet theory is the analogue of the linearized Lyapunov approach to NL system, but is tailored to a periodic flow. Thanks to the Floquet theorem, the analysis of the linearized behavior is decoupled in iterated mappings for every full revolution, and periodic relationships along the internal motion within a period. Thus, the stability properties of the PO are formulated in the framework of the discrete dynamical systems (see sections B.1.2.1-B.1.2.1) and are completely determined by the monodromy

matrix. The eigenvalues of the monodromy matrix are called the Floquet multipliers λ_M, and in parallelism with the linearized Lyapunov exponents for a general flow, the Floquet exponents are defined in the same fashion for the case of a PO.

For the case of Hamiltonian systems, the STM and the monodromy matrix are symplectic. Therefore the Floquet multipliers show up always with their inverse and conjugate counterparts (with the same multiplicity), and the determinant of M is unit. Following this, the stability properties of the POs of $2n$-dimensional Hamiltonian systems are represented by the n Floquet stability indexes s_λ, which are the sum of the related couple of Floquet multipliers. Thus, for the aforementioned character, this brings to the following definition.

$$s_\lambda = \lambda_M + \frac{1}{\lambda_M} \tag{B.58}$$

The Floquet stability indexes are actually a measure proportional to the instability of the PO. This brings to express the linear and linearized Lyapunov stability classification of sections B.1.2.1-B.1.2.2 in terms of the spectrum of Floquet indexes. The related phase portraits are the following.

- $s_\lambda \in \mathbb{R}, |s_\lambda| > 2$: hyperbolic manifold (a saddle, constituting a couple of attracting and repelling objects).
- $s_\lambda \in \mathbb{R}, |s_\lambda| \leq 2$: elliptic manifold (a center, constituting one or two neutral objects).
- $s_\lambda \in \mathbb{C} \backslash \mathbb{R}$: complex hyperbolic manifold (two opposite spirals, constituting a couple of attracting and repelling objects).

Thus, the hyperbolic manifolds are unstable and their eigenspace identifies the invariant manifolds of the PO, while the elliptic manifold is stable and its eigenspace provides a continuous 1-parameter family of invariant 2-tori developing at growing size around the PO, as an extension of Lyapunov's center theorem to POs, and also TV systems. In particular, if $s_\lambda = \pm 2$, the center is singular. This is a parabolic manifold, that provides a second continuous 1-parameter family of POs, and the PO under study is at the crossroad of the four branches. This situation is a bifurcation, because the two intersecting families swap one of their phase portraits through the "customs' gate" of the parabolic manifold. This is particularly important when the trade involves a saddle and a center. The inverse parabolic manifold, which is $s_\lambda = -2$, provides the second family of POs to have double the period of the first family (this is called a bifurcation by period-multiplication).

If the Hamiltonian system is also conservative, the existence of one integral of motion (the energy) constrains a couple of the Floquet spectrum to be unit, which is a direct parabolic manifold ($s_\lambda = +2$). The related eigenvectors are one directed along the vectorfield (parallel to the flow's manifold), and the other directed along the gradient

of the energy. Since they are not coincident, the second eigenspace identifies another manifold of POs, as discussed above. This is indeed the proof of Lyapunov's center theorem, and the Moser's generalization, presented in section B.3 to highlight that, in TI dynamical systems, POs are organized in continuous families parameterized by the energy. The POs are the periodic normal modes of the linearized system, as discussed in section B.4. In particular, the energy is directly proportional to the amplitude of these eigenfunctions, thus the energy is tout-court equivalent to the size of the orbit in the neighborhood of the equilibria.

B.5.2 Approach of Dynamical Systems Theory

The approach used in DST for the definition of a PO is to *reduce the original continuous dynamical system to an appropriate map function of the same state*, $P : x \to P(x)$ [50, 116]. In case of TV dynamical systems, the flow map for a propagation time equal to the period of the PO is used, which is called stroboscopic map P_T.

$$P_T(x) = \phi_f(T + t_0, t_0, x) \tag{B.59}$$

For TI dynamical systems, the approach is due to Poincaré, and consists of the following procedure [50, 116].

- First, define a surface of section (or event) of the state-space Γ, called Poincaré section, which represents a co-1D hypersurface of the state domain (not parallel to the flow). Thus, the Poincaré section is defined by an appropriate constraint $g(x) = 0$, enclosing also the crossing direction of the surface. Usually the section's constraint consists in fixing one state's component v_M, of index i_M, such that $g(x) = v_M - \bar{v}_M = x_{i_M} - \bar{x}_{i_M} = 0$. Remember that the focus is on a subdomain U around an EP of the autonomous system.

$$\Gamma = \left\{ x \in U : g(x) = 0 \wedge (f(t,x) \wedge \nabla g(x)) = 0 \wedge f(t,x)^T \nabla g(x) \gtrless 0 \right\} \tag{B.60}$$

- Then, define a time-return map $P_{\tau,\Gamma}$, that gives the minimum time when the flow, starting from Γ, returns to the surface itself.

$$P_{\tau,\Gamma}(x) = \{\min t \geq t_0 : \phi_f(t, t_0, x) \in \Gamma, x \in U\} \tag{B.61}$$

- Finally, a second map, named the first-return map (also called the Poincaré map) $P_{\phi(\tau),\Gamma}$, associates to the initial state on Γ the final state at the first return.

$$P_{\phi_f(\tau),\Gamma}(x) = \phi_f(P_{\tau,\Gamma}(x), t_0, x) \tag{B.62}$$

Therefore, a PO is identified as the equilibrium fixed point of a stroboscopic map (for TV systems)

$$P_T(x_{0,PO}) = x_{0,PO} \tag{B.63}$$

or of a first-return map (for TI systems, where the time-return map gives the period of the PO).

$$x_{0,PO} \in \Gamma \rightarrow P_{\tau,\Gamma}(x_{0,PO}) = T + t_0 \rightarrow P_{\phi_f(\tau),\Gamma}(x_{0,PO}) = x_{0,PO} \tag{B.64}$$

In particular, this strategy could already provide a graphical method to look for POs. A subset of the state-space could be taken as initial conditions of the aforementioned maps, thus propagated in time. The images are plotted to visually identify the existence of an invariant point (TV systems), or a family of invariant points (TI systems). In case of autonomous systems, these graphs are shortly called a Poincaré map tout-court. Of course, this approach is qualitative and mostly applicable for low-dimensional dynamical systems.

B.5.2.1 Linearized Behavior and Stability of a Poincaré Map

With the approach of DST, the stability analysis of the POs is undertaken in the framework of the discrete dynamical system of the iterated stroboscopic or Poincaré map. For TV systems, no differences are born with respect to the continuous case: the derivative of the stroboscopic map is the STM after one revolution, which is the monodromy matrix. For TI systems, the derivative of the first-return map is a material derivative[13], since the flow depends also on the time-return map [52, 116]. This is presented in Eq.B.65: the total derivative is composed by the STM (the monodromy matrix), the vectorfield (see section B.1.2.3), and the derivative of the time-return map. The latter is obtainable from the differential identity expressing that the directional derivative of the Poincaré section's constraint is null onto the section itself.

$$\begin{cases} \frac{D}{Dx}P_{\phi_f(\tau),\Gamma} = \frac{\partial \phi_f}{\partial x_0} + \frac{\partial \phi_f}{\partial P_{\tau,\Gamma}}\frac{\partial}{\partial x}P_{\tau,\Gamma} = \Phi_f(P_{\tau,\Gamma}, t_0) + f(P_{\tau,\Gamma}, P_{\phi_f(\tau),\Gamma})\frac{\partial}{\partial x}P_{\tau,\Gamma} \\ \nabla_\Gamma g = 0 \rightarrow \dfrac{\partial g}{\partial P_{\phi_f(\tau),\Gamma}}\dfrac{D}{Dx}P_{\phi_f(\tau),\Gamma} = \nabla g(P_{\phi_f(\tau),\Gamma})\dfrac{D}{Dx}P_{\phi_f(\tau),\Gamma} = 0 \rightarrow \\ \qquad \rightarrow \dfrac{\partial}{\partial x}P_{\tau,\Gamma} = -\Big[\nabla g(P_{\phi_f(\tau),\Gamma}) f(P_{\tau,\Gamma}, P_{\phi_f(\tau),\Gamma})\Big]^{-1} \nabla g(P_{\phi_f(\tau),\Gamma})\Phi_f(P_{\tau,\Gamma}, t_0) \end{cases} \tag{B.65}$$

$$\begin{aligned} & t : g\left(\mathbf{x}\left(t\right)\right) = \left\{\mathbf{x}\right\}_{i_M} - \left\{\mathbf{x}_{PO}\right\}_{i_M} = 0 \Rightarrow \delta t\left(\delta\mathbf{x}\right) \Rightarrow \\ & \delta\mathbf{x}_f = \left(\mathbf{I} - \frac{\mathbf{f}\left(P_{\tau,\Gamma}(\mathbf{x}_0), \phi_f\right)\nabla g\left(\phi_f\right)}{\nabla g\left(\phi_f\right)\mathbf{f}\left(P_{\tau,\Gamma}(\mathbf{x}_0), \phi_f\right)}\right)\Phi\left(P_{\tau,\Gamma}(\mathbf{x}_0)\right)\delta\mathbf{x}_0 = \\ & = \left(\mathbf{I} - \Psi_g\left(P_{\tau,\Gamma}(\mathbf{x}_0), \phi_f\left(P_{\tau,\Gamma}(\mathbf{x}_0), \mathbf{x}_0\right)\right)\right)\Phi\left(P_{\tau,\Gamma}(\mathbf{x}_0)\right)\delta\mathbf{x}_0 = \frac{dP_g}{d\mathbf{x}_0}\left(P_{\tau,\Gamma}(\mathbf{x}_0), \mathbf{x}_0\right)\delta\mathbf{x}_0 \end{aligned} \tag{B.66}$$

[13] A material derivative is also called substantial derivative, or Lagrangian derivative, or total derivative.

The resulting total derivative is shown in Eq.B.66, where the classical Poincaré section's constraint consists of the single state's component v_M, of index i_M. However the constraint is also valid on the initial condition.

$$\begin{aligned}
&\mathbf{x}: g\left(t,\mathbf{x}\right)=\left\{\mathbf{x}_0\right\}_{i_M}-\left\{\mathbf{x}_{PO}\right\}_{i_M}=0\Rightarrow\left\{\delta\mathbf{x}\right\}_{i_M}\left(\left\{\delta\mathbf{x}\right\}_{i_X\setminus i_M}\right)\Rightarrow\\
&\Rightarrow\delta\mathbf{x}\left(\mathbf{x}\right)=\left(\mathbf{I}-\frac{\left\{\mathbf{I}\right\}_{:,i_M}\left\{\mathbf{I}\right\}_{i_M,:}}{1}\right)\delta\mathbf{x}\left(\mathbf{x}\right)=\left(\mathbf{I}-\boldsymbol{\Psi}_{g_M}\left(\mathbf{x}\right)\right)\delta\mathbf{x}\left(\mathbf{x}\right)
\end{aligned}\tag{B.67}$$

Therefore, the appropriate derivative of the Poincaré map is the following.

$$\begin{cases}
\frac{dP_{\phi_f(\tau),\Gamma}}{d\mathbf{x}_0}\left(P_{\tau,\Gamma}(\mathbf{x}_0),\mathbf{x}_0\right)=\left(\mathbf{I}-\Psi_g\left(P_{\tau,\Gamma}(\mathbf{x}_0),\phi_f\left(P_{\tau,\Gamma}(\mathbf{x}_0),\mathbf{x}_0\right)\right)\right)\Phi\left(P_{\tau,\Gamma}(\mathbf{x}_0)\right)\left(\mathbf{I}-\Psi_{g_M}\left(\mathbf{x}_0\right)\right)\\
\mathbf{P_0}=\left\{\mathbf{I}\right\}_{:,\mathbf{x}\setminus v_M}\Rightarrow\\
\left\{\delta\mathbf{x}_f\right\}_{\mathbf{x}\setminus v_M}=\mathbf{P_0}^T\left(\mathbf{I}-\Psi_g\left(P_{\tau,\Gamma}(\mathbf{x}_0),\phi_f\right)\right)\Phi\left(P_{\tau,\Gamma}(\mathbf{x}_0)\right)\left(\mathbf{I}-\Psi_{g_M}\left(\mathbf{x}_0\right)\right)\mathbf{P_0}\{\delta\mathbf{x}_0\}_{\mathbf{x}\setminus v_M}=\\
\qquad=\left\{\frac{dP_{\phi_f(\tau),\Gamma}}{d\mathbf{x}_0}\left(P_{\tau,\Gamma}(\mathbf{x}_0),\mathbf{x}_0\right)\right\}_{\mathbf{x}\setminus v_M,\mathbf{x}\setminus v_M}\{\delta\mathbf{x}_0\}_{\mathbf{x}\setminus v_M}
\end{cases}\tag{B.68}$$

The result is simply the original monodromy matrix of the PO removed from the eigenspace of its flow's manifold. Thus, the relevant stability properties are coincident with the starting monodromy matrix. In [171, 172], a linear stability parameter is introduced and corresponds to half of the trace of the total derivative matrix.

The same procedure of Eq.B.66 can be undertaken by further constraining the Poincaré section to also be at fixed energy $c(x)=\bar{c}$. Also, the constraint locks another state's component v_E, of index i_E.

$$\begin{aligned}
&\mathbf{x}: g_E\left(\mathbf{x}\right)=c\left(\mathbf{x}\right)-\bar{c}=0\Rightarrow\left\{\delta\mathbf{x}\right\}_{i_E}\left(\left\{\delta\mathbf{x}\right\}_{i_X\setminus i_E}\right)\Rightarrow\\
&\delta\mathbf{x}\left(\mathbf{x}\right)=\left(\mathbf{I_6}-\frac{\left\{\mathbf{I_6}\right\}_{:,i_E}\nabla g_E\left(\mathbf{x}\right)}{\left\{\nabla g_E\left(\mathbf{x}\right)\right\}_{i_E}}\right)\delta\mathbf{x}\left(\mathbf{x}\right)=\\
&=\left(\mathbf{I_6}-\boldsymbol{\Psi}_{g_E}\left(\mathbf{x}\right)\right)\delta\mathbf{x}\left(\mathbf{x}\right)=\frac{dP_{\phi_f(\tau),\Gamma,E}}{d\mathbf{x}_0}\left(P_{\tau,\Gamma}(\mathbf{x}_0),\mathbf{x}_0\right)\delta\mathbf{x}_0
\end{aligned}\tag{B.69}$$

$$\begin{cases}
\frac{dP_{\phi_f(\tau),\Gamma,E}}{d\mathbf{x}_0}\left(P_{\tau,\Gamma}(\mathbf{x}_0),\mathbf{x}_0\right)=\\
=\left(\mathbf{I_6}-\Psi_g\left(t_fP_{\tau,\Gamma}(\mathbf{x}_0),\phi_{\mathbf{f}}\left(t_fP_{\tau,\Gamma}(\mathbf{x}_0),\mathbf{x}_0\right)\right)\right)\Phi\left(t_fP_{\tau,\Gamma}(\mathbf{x}_0),\mathbf{x}_0\right)\left(\mathbf{I_6}-\Psi_{g_M}\left(\mathbf{x}_0\right)-\Psi_{g_E}\left(\mathbf{x}_0\right)\right)\\
\mathbf{P_0}=\left\{\mathbf{I_6}\right\}_{:,\mathbf{x}\setminus[\,v_M\ v_E\,]}\Rightarrow\\
\left\{\delta\mathbf{x}_f\right\}_{\mathbf{x}\setminus[\,v_M\ v_E\,]}=\\
=\mathbf{P_0}^T\left(\mathbf{I_6}-\Psi_g\left(t_fP_{\tau,\Gamma}(\mathbf{x}_0),\phi_{\mathbf{f}}\right)\right)\Phi\left(t_fP_{\tau,\Gamma}(\mathbf{x}_0),\mathbf{x}_0\right)\left(\mathbf{I_6}-\Psi_{g_M}\left(\mathbf{x}_0\right)-\Psi_{g_E}\left(\mathbf{x}_0\right)\right)\mathbf{P_0}\{\delta\mathbf{x}_0\}_{\mathbf{x}\setminus[\,v_M\ v_E\,]}=\\
=\left\{\frac{dP_{\phi_f(\tau),\Gamma,E}}{d\mathbf{x}_0}\left(P_{\tau,\Gamma}(\mathbf{x}_0),\mathbf{x}_0\right)\right\}_{\mathbf{x}\setminus[\,v_M\ v_E\,],\mathbf{x}\setminus[\,v_M\ v_E\,]}\{\delta\mathbf{x}_0\}_{\mathbf{x}\setminus[\,v_M\ v_E\,]}
\end{cases}\tag{B.70}$$

The resulting total derivative in Eq.B.70 is removed also from the eigenspace of the PO's family. The resulting map $P_{\phi_f(\tau),\Gamma,E}$ is called iso-energetic Poincaré map, and contains isolated POs, which are called limit cycles.

B.5.3 Numerical Computation

A trivial case of POs is when the TV dynamical system is forced by a periodic action. In this case, POs are simply the particular solutions of the ODEs. In some Hamiltonian systems, it could be possible to perform a change of state's components, to express the vectorfield in a frame synchronous and isotropic with the forcing action. If the resulting potential of the system is simply scaled by a time-dependent term, the transformed system has EPs, that can be computed as discussed in section B.3. These instantaneous EPs move synchronously with the forced frame in the original dynamics.

The Lyapunov center's theorem (and the Moser's generalization) is the analytical backbone for the identification of families of POs in a conservative dynamical system. Therefore the computation of POs starts from the identification of the EPs and then different methodologies could be exploited. In section B.4, the analytical and semi-analytical methodologies to compute invariant motions were addressed. To overcome their limitations for practical applications, they are coupled with numerical techniques, where low-order analytical solutions are used as starting guesses. The numerical techniques used in DST are based on the differential corrector, that will be introduced below.

B.5.3.1 Differential Corrector

When the objective function $F(x)$ of the Newton's method is not fully algebraic, but contains the solution $x(t)$ of a NL dynamical system $f(t, x)$, we speak about differential corrector (DC) [173]. The DC is the numerical technique most widely used in DST [50]. A DC scheme is essentially a Newton's method used to fine tune the initial condition x_0 to obtain an accurate orbit $x(t) = \phi(t, t_0, x_0)$ that satisfies the objective function $F(x_0) = 0$.

There are several examples for the exploitation of a DC, which is essential because the analytical solution of a NL dynamical system is usually not available. It could be required to compute a desired trajectory that passes through a point at a specific time[14], or a set of them at prescribed times. Usually the DC is exploited when we want to find an orbit $x(t)$ that preserves some qualities of (or is simply close to) a reference trajectory $\bar{x}(t)$, where the latter is the solution of a close dynamical system $\bar{f}(t, x)$. This second dynamical system is either an approximated model of the real perturbed dynamics (see section 2.2) or a simpler model to compute a solution (like the linearized dynamics).

For the application of Newton's method in Eq.B.26, the derivative of the objective function around the trajectory is needed. This involves the derivative of the flow of the dynamical system with respect to the initial condition. Thus, any DC scheme requires the computation of the STM defined in section B.1. This means that at every iteration,

[14] When the time t is not fixed, but is implicitly defined by $G(t, x(t)) = 0$, we call this condition an event. This is a constraint to be appended in the augmented objective function $\left[\begin{smallmatrix} F \\ G \end{smallmatrix}\right] = 0$.

the DC scheme consists in the numerical integration of the dynamical system of Eq.B.1 and its associated variational system of Eq.B.8.

For this reason the DC is often called shooting method, and referred to as *single shooting* for the case when only one trajectory is propagated at each iteration, and the objective function refers to a condition at a single time/event. When instead the objective function collects conditions at different times, or when the time span required for a single final condition is too large[15], the DC is called *multiple shooting*. In this case, the trajectory is divided in N smaller subintervals, requiring N independent trajectories to be propagated and increasing the order of the linear system (which now is multiplied N times) at each iteration of Newton's method. This technique was initially used for the numerical solution of boundary-value problems [173].

In summary, the DC is a numerical technique used in DST for the solution of NL-TV dynamical systems. It requires a suitable initial guess for the trajectory, which is usually provided by low-order analytical or semi-analytical methods applied to the system in study [50]. This alliance matches the advantages of both approaches and provides reliable solutions with acceptable computational effort. In particular, when the dynamical model is only an approximation of the real dynamics, even a high-order semi-analytical solution must undergo a differential correction afterwards, for practical applications [116].

B.5.3.2 Computation of Periodic Orbits with Differential Corrector

The DC can be applied for the computation of a PO of a dynamical system, by using the definition of the PO as an invariant point of a stroboscopic map (TV systems) or of a Poincaré map (TI systems). This is a basic single shooting implementation where the point to be determined represents the initial condition of the PO [116, 52].

$$F(x_0) = P_{(\cdot)}(x_0) - x_0 = 0 \tag{B.71}$$

The first guess of the DC could be retrieved as the initial condition of a small-size PO in the linear or low-order approximation of the dynamics.

The Jacobian of the objective function requires the derivative of the map expressed in section B.5.2.1. For TV system, the initial time t_0 is usually kept fixed, and the DC's scheme is the following, where define $\mathbf{P}\left(T, t_0, \mathbf{x}_0\right) = \frac{\partial \mathbf{x}_f}{\partial \mathbf{x}_0}\left(T + t_0, t_0, \mathbf{x}_0\right) - \mathbf{I} = \mathbf{\Phi_f}\left(\mathbf{T} + \mathbf{t_0}, \mathbf{t_0}, \mathbf{x_0}\right) - \mathbf{I}$.

$$\begin{cases} F\left(t_0, \mathbf{x}_0\right) = \phi_f\left(T + t_0, t_0, \mathbf{x}_0\right) - \mathbf{x}_0 = 0 \\ \delta F\left(t_0, \mathbf{x}_0\right) = \left[\, \mathbf{P}(T, t_0, \mathbf{x}_0) \,\right] \left[\, \delta \mathbf{x}_0 \,\right] \end{cases} \tag{B.72}$$

[15] Recall that the DC and the STM are based on a linearized approximation of the dynamics around the reference orbit. In particular the Newton's method iteration requires the solution of the linear system of Eq.B.26, and the STM for unstable orbits and long propagation time becomes ill-conditioned.

Alternatively, one state's component v_M, of index i_M, could be kept fixed. The related column in the derivative's matrix of Eq.B.72 is taken out and a new column is filled with the sensitivity of the flow with respect to the initial time $\mathbf{P}_t\left(T,t_0,\mathbf{x}_0\right) = \frac{\partial \mathbf{x}_f}{\partial t_0}\left(T+t_0,t_0,\mathbf{x}_0\right)$ of Eq.B.14, which now must be corrected at each iteration as a δt_0 inserted in the variations' vector.

$$\begin{cases} F\left(t_0,\mathbf{x}_0\right) = \left\{\phi_f\left(T+t_0,t_0,\mathbf{x}_0\right) - \mathbf{x}_0\right\}_{i_X \setminus i_M} = 0 \\ \delta F\left(t_0,\mathbf{x}_0\right) = \left[\, \{\mathbf{P}(T,t_0,\mathbf{x}_0)\}_{:,i_X \setminus i_M} \; \mathbf{P}_t(T,t_0,\mathbf{x}_0) \,\right] \begin{bmatrix} \{\delta \mathbf{x}_0\}_{i_X \setminus i_M} \\ \delta t_0 \end{bmatrix} \end{cases} \tag{B.73}$$

For TI systems, the Poincaré map requires the satisfaction of the section's constraint on the initial and return condition, $g(x_0) = 0$ and $g(P_{\phi_f(\tau),\Gamma}(x_0)) = 0$. Considering as usual the constraint on the single state's component v_M, of index i_M, the first condition was used in Eq.B.67, and the second in Eq.B.66, to define the total derivative of the Poincaré map in Eq.B.68, which bounds the correction of the propagation time to satisfy the Poincaré return event: $\delta T(\delta t_0, \delta x_0)$. Define from Eq.B.68 $\mathbf{P}\left(P_{\tau,\Gamma}(\mathbf{x}_0),\mathbf{x}_0\right) = \left\{\frac{dP_{\phi_f(\tau),\Gamma}}{d\mathbf{x}_0}\left(P_{\tau,\Gamma}(\mathbf{x}_0),\mathbf{x}_0\right) - \mathbf{I}\right\}_{\mathbf{x}\setminus v_M, \mathbf{x}\setminus v_M}$, to consider only the coordinates of interest. In conclusion, the DC's scheme is the following.

$$\begin{cases} F\left(t_0,\mathbf{x}_0\right) = \left\{\phi_f\left(P_{\tau,\Gamma}(\mathbf{x}_0),\mathbf{x}_0\right) - \mathbf{x}_0\right\}_{i_X \setminus i_M} = 0 \\ \delta F\left(\mathbf{x}_0\right) = \left[\, \mathbf{P}_{(P_{\tau,\Gamma}(\mathbf{x}_0),\mathbf{x}_0)} \,\right] \left[\, \{\delta \mathbf{x}_0\}_{i_X \setminus i_M} \,\right] \end{cases} \tag{B.74}$$

However this DC scheme is not useful because the derivative matrix is singular at the solution. Indeed, the STM would eventually converge to the monodromy matrix of the PO, which carries the unit eigenvalue of the manifold of the PO's family, while the eigenspace of the other unit eigenvalue is taken out by the total derivative of the Poincaré map in Eq.B.66-B.68. To make the solution isolated, the iso-energetic Poincaré map of Eq.B.69 is needed, whose derivative is provided in Eq.B.70. From that, one defines $\mathbf{P}\left(P_{\tau,\Gamma}(\mathbf{x}_0),\mathbf{x}_0\right) = \left\{\frac{dP_{\phi_f(\tau),\Gamma,E}}{d\mathbf{x}_0}\left(P_{\tau,\Gamma}(\mathbf{x}_0),\mathbf{x}_0\right) - \mathbf{I}\right\}_{\mathbf{x}\setminus[\,v_M\;\,v_E\,],\mathbf{x}\setminus[\,v_M\;\,v_E\,]}$. In conclusion, the DC's scheme is the following.

$$\begin{cases} F\left(t_0,\mathbf{x}_0\right) = \left\{\phi_f\left(P_{\tau,\Gamma}(\mathbf{x}_0),\mathbf{x}_0\right) - \mathbf{x}_0\right\}_{\mathbf{x}\setminus[\,v_M\;\,v_E\,]} = 0 \\ \delta F\left(\mathbf{x}_0\right) = \left[\, \mathbf{P}_{(P_{\tau,\Gamma}(\mathbf{x}_0),\mathbf{x}_0)} \,\right] \left[\, \{\delta \mathbf{x}_0\}_{\mathbf{x}\setminus[\,v_M\;\,v_E\,]} \,\right] \end{cases} \tag{B.75}$$

Alternatively, one component of the objective function could have been replaced by the iso-energetic constraint $g_E(x) = 0$ itself, keeping the same dimension of the variations' vector. Other constraints could have been possible though, to bound some properties of the initial guess to be maintained in the final solution (this should be in accordance to the nature of the problem analyzed). Finally, sometime the existence of symmetries in the problem allows to change the objective function, considering the flow at a previous symmetrical event [50]: this is necessary to reduce the propagation of the single shooting, lowering the unstable departure of the perturbed flow, which ultimately allows to

use initial guesses at lower order.

As a byproduct of the DC, the propagation time and the STM at the final convergent iteration of the DC will provide T and M of the PO.

B.5.3.2.1 Computation of Families of Periodic Orbits with Numerical Continuation

In conclusion, as discussed in section B.5.1.1, for autonomous dynamical systems the POs are organized in continuous families of one parameter. This is usually the energy of the orbit, but could also be taken as the period or a representative amplitude for the size, such as one state's component. Once one small-energy PO is identified with the DC of Eq.B.75, its initial condition provides the starting point of a NC, whose procedure is presented in section B.2.2. The technique iterates the DC scheme of Eq.B.74 to compute the curve of initial conditions on the Poincaré section, providing the whole family of POs [52]. The continuation parameter σ is chosen as one of the possible parameters p of the family mentioned early. The objective function of the NC is the one of the DC scheme of Eq.B.75, where one component of $F(\mathbf{x}_0)$ is replaced by the parameter's constraint $p - \sigma = 0$.

The NC is integrated to reach the PO of interest, for example the one of a particular size. It is worth to note that out of the neighborhood of the EP, the NC of large-amplitude POs usually encounters nonlinear effects, such as turning points of the continuation curve, which means that the size of the orbit could now decrease/increase for increasing/decreasing energy. In particular, as mentioned in section B.2.2.3, the NC could encounter bifurcations, that represent the birth of another family of POs. As discussed in section B.5.1.1, the bifurcation is a parabolic manifold, due to the fact that the PO at the crossroad of the four branches has one Floquet index $s_\lambda = \pm 2$. Thus, for the case of POs, the stability indexes identify the bifurcations during NC [52]. This is a paramount result of DST, because the couple of parabolic eigenvectors of the monodromy matrix provide the tangent space of the two continuation curves, and so they are used to select which branch the NC is driven through.

B.6 Numerical Techniques for Computation of Quasi-Periodic Orbits

This section presents to the reader the notions of DST used to define a 2D-QPO and its properties. Following this, the section shows how these concepts are applied to numerically compute these invariant motions.

B.6.1 Definition

For the general dynamical system of Eq.B.1, Eq.B.20 provides the most general way to mathematically define a nD-QPO, which is the sum of a discrete number n of harmonics,

by expressing the flow as n-torus, function of the n phases. After section B.5 presented the methodology of DST used to identify POs, this section will now focus on the next step for the analysis of the invariant motions of a dynamical system, which is the identification of 2D-QPOs.

A 2-D QPO is the 2-torus defined in Eq.B.76.

$$\begin{aligned} &x_{QPO}(t) = \phi_f(t, t_0, x_{0,QPO}) \rightarrow x_{QPO}(\varphi_1, \varphi_2) = \nu_u(\varphi_1, \varphi_2, \varphi_{1,0}, \varphi_{2,0}, x_{0,QPO}) \\ &\varphi_1 = \varphi_{1,0} + \omega_1 (t - t_0) \ , \ \varphi_2 = \varphi_{2,0} + \omega_2 (t - t_0) \\ &\frac{\omega_2}{\omega_1} \notin \mathbb{Z} \end{aligned} \tag{B.76}$$

As discussed in section B.1.3, the flow of a torus is usually decomposed in longitudinal and transversal motion, choosing a reference longitudinal phase φ_1. The stroboscopic map of the transversal phase φ_2 for a stroboscopic time equal to the longitudinal revolution $T_1 = \frac{2\pi}{\omega_1}$ easily provides the fixed rotation number $\rho = 2\pi\frac{\omega_2}{\omega_1}$, which indicates how many longitudinal revolutions $N_{T_1} = ceil\left\{\frac{2\pi}{\rho}\right\}$ are needed to perform a full transversal revolution [164].

The expression of the toroidal flow was updated in Eq.B.23 to consider the forced phases in the general case of TV systems. Thus, for a 2D-QPO in a TV system, the transversal phase is naturally taken as the forced phase $\tilde{\varphi}_2$. As discussed in section B.1.3.1, the constrained phases are actually computed by the explicit integration of the equations of motion. On the opposite, for a n-torus in a TI system, the n phases are all equivalent to be chosen as the longitudinal phase. Their pulsation ω is a natural frequency of the solution, thus their dynamics is implicit in the equations of motion [164].

Following this approach, the 2-torus of Eq.B.76 can expressed as a function of time, by reducing its flow, as well as the related linearized behavior and Floquet stability, to the longitudinal motion.

$$x_{QPO}(t) = \phi_f(t, t_0, x_{0,QPO}(\varphi_2)) \ , \ \forall \varphi_2 \in [0, 2\pi) \tag{B.77}$$

This requires that the initial condition of the 2D-QPO is parameterized by the starting phase along the transversal motion. However, the parameterized flow of Eq.B.77 is not an invariant motion, because N_{T_1} is not an integer. This produces the bounded trajectory to become a surface of motion, that fills for infinite time the surface of a torus in the state-space (since the trajectory is parameterized by two phases). The filling is not continuous in the transversal phase, since the rotation number evolution is a discrete dynamical system given by an iterated mapping. Following this, the linearized behavior of a 2D-QPO is usually analyzed in subintervals, representing a single longitudinal revolution, and the stability analysis is conducted with the related bundles of STMs.

B.6.2 Approach of Dynamical Systems Theory

The definition of a 2D-QPO in DST follows the approach used for POs in section B.5.2, which is to reduce the original continuous dynamical system to a map [116, 52]. In particular, this is a stroboscopic map for TV systems, or either a Poincaré or stroboscopic map for TI systems [140]. The Poincaré section and the stroboscopic period are chosen to lock one phase, which is the longitudinal phase φ_1 of Eq.B.76. Thus for a stroboscopic map, the stroboscopic period is T_1, and the map produces fixed rotation numbers shifts of the transversal phase, as discussed in section B.6.1. For a Poincaré map, the time-return map of Eq.B.61 is variable, thus the rotation number ρ_2 depends on the initial transversal phase φ_2, but apart from this, the procedure is basically the same of Eq.B.22.

$$\begin{cases} t_f = P_{\tau,\Gamma}\left(x_{0,QPO}\right) \rightarrow \boldsymbol{\rho}\left(x_{0,QPO}\right) = \boldsymbol{\omega} t_f = P_{\rho(\tau),\Gamma}(x_{0,QPO}) \\ \rightarrow P_{\phi_f(\tau),\Gamma}(x_{0,QPO}) = \nu_u\left(\boldsymbol{\varphi}_0 + P_{\rho(\tau),\Gamma}(x_{0,QPO}), \boldsymbol{\varphi}_0, x_{0,QPO}\right) \\ \boldsymbol{\rho} = [\{\rho_i\}_{i=1}^{n}] \wedge \boldsymbol{\rho}_0 = \mathbf{0} \rightarrow \rho_{i,k} = \mathrm{mod}\left\{P_{\rho(\tau),\Gamma}\left(x_{QPO}\left(\boldsymbol{\varphi}_0 + \sum_{m=1}^{k-1}\rho_{i,m}\right)\right), (-\pi,\pi]\right\} \\ \Rightarrow N_{T_i} : \left|\sum_{k=1}^{N_{T_i}}\rho_{i,k}\right| \geq 2\pi \Rightarrow T_i = \sum_{k=1}^{N_{T_i}} P_{\tau,\Gamma}\left(x_{QPO}\left(\varphi_0 + \sum_{m=1}^{k-1}\rho_{i,m}\right)\right) \end{cases} \tag{B.78}$$

The chosen map is now applied to the decomposed 2D-QPO of Eq.B.77, where the initial conditions are parameterized by the transversal phase. This results to be a mapping from one closed curve to another. Generalize the curve of initial conditions $x_{0,QPO}\left(\varphi_2\right)$ on the chosen map to a curve $C(\theta)$, where the curvilinear coordinate is $\theta \in \mathrm{I}_\theta = [\theta_m, \theta_M) : C\left(\theta_m\right) = C\left(\theta_M\right)$. Therefore, a 2D-QPO is identified as the invariant curve of a stroboscopic map

$$x_{0,QPO} \in C\left(\theta\right) \Leftrightarrow P_T(x_{0,QPO}) = \phi_f(T + t_0, t_0, x_{0,QPO}) \in C\left(\theta\right) \ , \forall \theta \in \mathrm{I}_\theta \tag{B.79}$$

or of a first-return map (for TI systems, where the time-return map provides the rotation number from Eq.B.78).

$$x_{0,QPO} \in C\left(\theta\right) \in \Gamma \Leftrightarrow P_{\phi_f(\tau),\Gamma}(x_{0,QPO}) = \phi_f(P_{\tau,\Gamma}(x_{0,QPO}), t_0, x_{0,QPO}) \in C\left(\theta\right) \ , \forall \theta \in \mathrm{I}_\theta \tag{B.80}$$

The selection of the Poincaré section is subjected to the same constraint of the case of a PO in section B.5.2, which is that the flow, in this case of the full invariant curve, must not be tangent to the surface of section.

Therefore, the invariant condition of the torus' motion is expressed in terms not of a point, but of a curve, which is a continuous object, and the whole 2D-QPO has been reduced in DST to a discrete dynamical system, and not a single map like for the case of a PO. Following this, the linearized behavior of a 2D-QPO is analyzed on the subintervals sampled by the chosen map, and so is reduced within each step of

the discrete dynamical system that represents the 2-torus, and the stability analysis is conducted with the related bundles of STMs [116].

The invariant curve's condition of Eq.B.79-B.80 could be probed by analyzing the linear solution around a PO, and focusing on the elliptic manifold. As discussed in sections B.5.1.1 and B.5.2.1, if this is present, the PO's monodromy matrix (or the derivative of the Poincaré map used to compute the initial condition of the PO) has a couple of conjugated eigenvalues on the unit complex circle. If we define a curve $C(\theta)$ by a linear combination of their eigenvectors with a circle of radius γ, centered around the invariant point identified by the initial condition of the PO,

$$x_{0,PO}, \exists \pm \lambda_{\frac{DP_{(\cdot)}}{Dx_0}(x_0)} = e^{i\rho} \in \mathbb{C} \Rightarrow C(\theta) = x_{0,PO} + \gamma \left(\mathrm{Re}\left\{\hat{\mathbf{v}}_\lambda\right\} \cos\theta - \mathrm{Im}\left\{\hat{\mathbf{v}}_\lambda\right\} \sin\theta \right) \tag{B.81}$$

and compute its image though the linearized flow map around the PO, which is given by the variational equations of Eq.B.6 using the monodromy matrix,

$$\begin{cases} M\left(\mathrm{Re}\left\{\hat{\mathbf{v}}_\lambda\right\} + i\mathrm{Im}\left\{\hat{\mathbf{v}}_\lambda\right\}\right) = (\cos\rho + i\sin\rho)\left(\mathrm{Re}\left\{\hat{\mathbf{v}}_\lambda\right\} + i\mathrm{Im}\left\{\hat{\mathbf{v}}_\lambda\right\}\right) = \\ \qquad = \left(\cos\rho\mathrm{Re}\left\{\hat{\mathbf{v}}_\lambda\right\} - \sin\rho\mathrm{Im}\left\{\hat{\mathbf{v}}_\lambda\right\}\right) + i\left(\sin\rho\mathrm{Re}\left\{\hat{\mathbf{v}}_\lambda\right\} + \cos\rho\mathrm{Im}\left\{\hat{\mathbf{v}}_\lambda\right\}\right) \\ M\left(\mathrm{Re}\left\{\hat{\mathbf{v}}_\lambda\right\} - i\mathrm{Im}\left\{\hat{\mathbf{v}}_\lambda\right\}\right) = (\cos\rho - i\sin\rho)\left(\mathrm{Re}\left\{\hat{\mathbf{v}}_\lambda\right\} - i\mathrm{Im}\left\{\hat{\mathbf{v}}_\lambda\right\}\right) = \\ \qquad = \left(\cos\rho\mathrm{Re}\left\{\hat{\mathbf{v}}_\lambda\right\} - \sin\rho\mathrm{Im}\left\{\hat{\mathbf{v}}_\lambda\right\}\right) - i\left(\sin\rho\mathrm{Re}\left\{\hat{\mathbf{v}}_\lambda\right\} + \cos\rho\mathrm{Im}\left\{\hat{\mathbf{v}}_\lambda\right\}\right) \end{cases}$$
$$\Rightarrow \begin{cases} M\mathrm{Re}\left\{\hat{\mathbf{v}}_\lambda\right\} = \cos\rho\mathrm{Re}\left\{\hat{\mathbf{v}}_\lambda\right\} - \sin\rho\mathrm{Im}\left\{\hat{\mathbf{v}}_\lambda\right\} \\ M\mathrm{Im}\left\{\hat{\mathbf{v}}_\lambda\right\} = \sin\rho\mathrm{Re}\left\{\hat{\mathbf{v}}_\lambda\right\} + \cos\rho\mathrm{Im}\left\{\hat{\mathbf{v}}_\lambda\right\} \end{cases} \tag{B.82}$$

$$\begin{aligned} M\left(C(\theta) - x_{0,PO}\right) &= \gamma\left(\left(\cos\theta\cos\rho - \sin\theta\sin\rho\right)\mathrm{Re}\left\{\hat{\mathbf{v}}_\lambda\right\} - \left(\cos\theta\sin\rho + \sin\theta\cos\rho\right)\mathrm{Im}\left\{\hat{\mathbf{v}}_\lambda\right\}\right) = \\ &= \gamma\left(\mathrm{Re}\left\{\hat{\mathbf{v}}_\lambda\right\}\cos(\theta+\rho) - \mathrm{Im}\left\{\hat{\mathbf{v}}_\lambda\right\}\sin(\theta+\rho)\right) = C(\theta+\rho) - x_{0,PO} \\ \Rightarrow P_{(\cdot)}\left(C(\theta)\right) &\simeq x_{0,PO} + M\left(C(\theta) - x_{0,PO}\right) = C(\theta+\rho) \ \ , \forall\theta \in \mathrm{I}_\theta \end{aligned} \tag{B.83}$$

we see that any variation in the initial conditions, that belongs to this curve, produces a variation in the final condition that still belongs to the curve itself [52]. The image has shifted along the invariant curve, and the shift of the curve's parameter is the rotation number. Indeed the invariant curve represents the solution of a discrete dynamical system, and is not filled continuously. We see that in this linearized dynamics, the rotation number is fixed along the invariant curve, and corresponds to the elliptic eigenvalue's phase. It is also independent from the invariant curve's size γ, which is not a radius but just a width's reference. Thus, Eq.B.81 represents a continuous 1-parameter family of invariant curves that develops around a PO, which represents the backbone of the 2-torus. This is indeed the proof of the extension of Lyapunov's center theorem, and the related Moser's generalization, to POs in TV dynamical systems, that was presented in section B.5.1.1, where the family's parameter could now be naturally stated as the invariant curve's width. Thus, the 2D-QPOs are the periodic normal modes of the linearized system around the PO, and their invariant curves are the periodic normal modes of the chosen map.

For the case of TI dynamical systems, since the elliptic eigenspace used to define the

linearized invariant curve of Eq.B.81 is orthogonal to the parabolic eigenspace where the energy varies, the paramount result is that the continuous 1-parameter family of invariant curves is iso-energetic with the PO. Thus, the family is uniquely identified on the iso-energetic Poincaré map of the PO of Eq.B.69. Furthermore, POs are part of the center manifold of an EP, and so in autonomous dynamical systems 2D-QPOs are organized in continuous 2-parameter families developing from an EP with two center manifolds, and are the combination of the normal modes of their related eigenspaces, as discussed in section B.4.

In the case of any NL dynamical system, the rotation number is not fixed along the invariant curve any longer. Thus the profile along the invariant curve must be determined to completely characterize the dynamics of the full 2-torus. Recall from section B.6.1 that for TV systems, the invariant curve parameter is the constrained phase, thus the rotation number profile is explicit from the dynamics of the forcing action. On the contrary, in TI dynamical systems, the invariant curve's parameter could be taken as any appropriate variable, because the torus' frequencies are all natural. Therefore, the rotation number profile is implicit, and it must be retrieved by the mapping of the invariant curve's equation $C(\theta)$.

Furthermore, for any NL dynamical system, the rotation number profile is also not maintained along the family of invariant curves. Thus, also the period of the first transversal revolution (see Eq.B.22 and Eq.B.78), obtained from the rotation number profile, is also not maintained. Due to its relevant dynamical meaning, such variable (or similarly the associated mean rotation number of the invariant curve) could be used as parameter of the 1-parameter family of invariant curves around a PO, in place of the width [52].

Finally, it is worth to remember that using the graphical approach mentioned in section B.5.2, the family of invariant curves can be visually identified on a Poincaré map for low-order dynamical systems.

B.6.3 Numerical Computation

The analytical and semi-analytical techniques for the computation of QPOs are parallel to the ones for computing POs, since the reduction to the center manifold could be naturally extended to more than one eigenspace (see section B.4.1) [51, 50]. To overcome their limitations for practical applications, they are coupled with numerical techniques, where low-order analytical solutions are used as starting guesses. Following the extension of Lyapunov center's theorem (and the Moser's generalization), the numerical computation of 2D-QPOs starts from the identification of the POs with an elliptic manifold, and then different methodologies could be exploited. These schemes are based on the DC presented in section B.5.3.1, that will be combined with NC.

The first kind of numerical technique to compute 2-tori in NL dynamical systems such as the CR3BP was used in [163]. The 2D-QPO is reduced to the discrete dynami-

cal system, and the method is a two-levels DC of a trajectory limited on a defined time span. Therefore this method does not provide any insights of the invariant curve, nor identify the full 2-torus.

In the last two decades, the concepts of DST introduced in section B.6.2 have been applied to fully identify a 2-torus, by the related invariance condition of Eq.B.79-B.80. Different numerical schemes have been developed, but they are all based on a common approach, which is the Fourier analysis.

Fourier analysis. Recall that, for a scalar and P-periodic function $f(x)$ of the scalar variable x, its Fourier approximation f^F is a truncated series of harmonics

$$f^F(x) = \sum_{n=-N}^{N} c_n e^{i\frac{2\pi}{P}nx} = \frac{a_0}{2} + \sum_{n=1}^{N} a_n \cos\left(\tfrac{2\pi}{P}nx\right) + b_n \sin\left(\tfrac{2\pi}{P}nx\right) = \frac{a_0}{2} + \sum_{n=1}^{N} A_n \cos\left(\tfrac{2\pi}{P}nx - \theta_n\right) \tag{B.84}$$

where the Fourier coefficients (a_0, a_n, b_n in the real form, and c_n in the complex form, truncated at degree N) are retrieved by the discrete Fourier transform.

$$\begin{cases} a_n = \frac{2}{P}\int_{x_0}^{x_0+P} f(x)\cos\left(\frac{2\pi}{P}nx\right)dx = a_{-n} \\ b_n = \frac{2}{P}\int_{x_0}^{x_0+P} f(x)\sin\left(\frac{2\pi}{P}nx\right)dx = -b_{-n} \end{cases} \leftrightarrow \begin{cases} A_n = \sqrt[2]{a_n^2 + b_n^2} \\ \theta_n = atan2\left(b_n, a_n\right) \end{cases}$$
$$\leftrightarrow c_n = \frac{1}{P}\int_{x_0}^{x_0+P} f(x)e^{-i\frac{2\pi}{P}nx}dx = \frac{1}{2}\left(a_n - ib_n\right) \tag{B.85}$$

B.6.3.1 Invariant Curve Description

The common approach of the numerical techniques for computing 2D-QPOs is the approximation of the invariant curve by a truncated Fourier series C^F, at degree N_C, function of the chosen invariant curve's parameter θ (generally of period P),

$$\begin{aligned} C^F(\mathbf{c},\theta) - \mathbf{x}_{PO} &= \frac{\mathbf{a}_0}{2} + \sum_{n=1}^{N_C} \mathbf{a}_n \cos(n\theta) + \mathbf{b}_n \sin(n\theta) = \\ &= \left[\mathbf{a}_0 \ \{\mathbf{a}_n \ \mathbf{b}_n\}_{n=1}^{N_C}\right] \begin{bmatrix} \frac{1}{2} \\ \left\{\begin{matrix}\cos(n\theta)\\ \sin(n\theta)\end{matrix}\right\}_{n=1}^{N_C} \end{bmatrix} = \mathbf{C}\mathbf{e}(\theta) = \\ &= \begin{bmatrix} \ddots & \ddots & \\ \mathbf{0_{1x(2N_C+1)}} & \mathbf{e}(\theta)^T & \mathbf{0_{1x(2N_C+1)}} \\ & \ddots & \ddots \end{bmatrix} \begin{bmatrix} \vdots \\ a_0 \\ \left\{\begin{matrix}a_n\\ b_n\end{matrix}\right\}_{n=1}^{N_C} \\ \vdots \end{bmatrix} = \mathbf{E}(\theta)\,\mathbf{c} \end{aligned} \tag{B.86}$$

where the Fourier coefficients a_0, a_n, b_n are included in the global vector of coefficients $\mathbf{c}$, and they are $2N_C + 1$ for each coordinate variable. In Eq.B.86 the real form of the Fourier series' coefficients is used, but the truncated approximation could be well used also with the complex form [140]. However, the real form simplifies the algebra and also avoids possible computational problems (related to the machine error) that would arise when using complex numbers.

Remember from section B.6.2 that the invariant curve could be defined in either a stroboscopic or a Poincaré iso-energetic map. In the second case, appropriate for TI systems, the coordinate variables of the curve needed to be considered are two less with respect to the total state's dimension. Thus, the components v_M and v_E, of index i_M and i_E, are not included in the discrete approximation of Eq.B.86 for both C^F and $\mathbf{c}$, due to the related constraints $g(\mathbf{x})$ and $g_E(\mathbf{x})$ on the map (see Eq.B.66,B.67,B.69).

B.6.3.2 Invariant Curve's Parameter

As discussed in section B.6.2, for the case of TV systems, the curve's parameter is taken as the constrained phase, due to the fact the its dynamics and the resultant rotation number's profile along the invariant curve is explicit [140]. Instead for any TI system, the curve parametrization could be absolutely general. This selection could result delicate for two reasons, and is one of the main difference among the range of numerical techniques used in the literature to compute 2D-QPOs. The first reason is that, for the numerical algorithm that will be discussed shortly, the curve parametrization must be invertible. The second reason will be better considered in the proceedings of this section, and it involves the convergence and burden of the DC scheme.

A first idea is to use as parameter of $C^F(\mathbf{c},\theta)$ the same general transversal phase φ_2 used till now to define the 2-torus in Eq.B.76, which is a general variable but without any meaning, and also implicit, since the transversal frequency of the torus is natural [52]. The problem is that without any explicit definition for φ_2, there is no availability of the required inverse law $\theta(\mathbf{x}) : \mathbf{x} = C^F(\mathbf{c},\theta), \forall \mathbf{x} \in C^F(\mathbf{c},\theta)$. The inverse relationship is required in the numerical algorithm that will be presented shortly to compute the rotation number, whose profile $\rho(\varphi_2)$ is implicit. Thus, if this parametrization is chosen, the rotation number's profile must be considered as an additional unknown. This brings to use another Fourier series $\rho^F(\mathbf{c},\varphi_2)$ to approximate it, enlarging the global vector of coefficients $\mathbf{c}$ to include also the ones of these series [52].

Another simple approach is used in [120], which is to consider a physical meaning for the curve's parameter. This is taken as the polar coordinate ϑ between two coordinates of the stroboscopic or iso-energetic Poincaré surface of section. Eq.B.87 provides the trivial definition of ϑ, which constitutes the inverse parametrization of the invariant curve.

$$\begin{cases} \mathbf{v}_C = [\, v_{C1} \; v_{C2} \,] \rightarrow \mathbf{i}_C = [\, i_{C1} \; i_{C2} \,] \\ \vartheta(\mathbf{x}) = atan2\left(\{\mathbf{x} - \mathbf{x}_{PO}\}_{i_{C1}}, \{\mathbf{x} - \mathbf{x}_{PO}\}_{i_{C2}} \right) \\ \begin{cases} \{\mathbf{x}\}_{i_{C1}} = \mathbf{x}_{PO} + r(\mathbf{x}) \cos\vartheta \\ \{\mathbf{x}\}_{i_{C2}} = \mathbf{x}_{PO} + r(\mathbf{x}) \sin\vartheta \end{cases} \end{cases} \leftrightarrow \forall\theta, \exists!\vartheta\,(C(\theta)) \tag{B.87}$$

The two parameter's section's coordinates are v_{C_1} and v_{C_2}, with indexes i_{C_1} and i_{C_2}, and the parameter's section's center is naturally taken as the PO's invariant point on the chosen map, since it is the backbone of the 2D-QPO. However, the choice of the

section's coordinates and center is not free, because they must ensure the invertibility of the parametrization along the curve, which is C must be a function of ϑ. In particular, this approach does not allow the computation of tori whose invariant curve is complex, such as a concave invariant curve, or an invariant curve with intersections [120]. In addition, the choice of the section's coordinates is also related to the burden of the algorithm. The projection of C onto the planes of the possible section's coordinates could be of any shape. Thus, the two coordinates for the polar parametrization must ensure the projection onto the related plane to be the more circular as possible. This allows the resulting function $C^F(\mathbf{c},\vartheta)$, with respect to the chosen ϑ, to have the lowest gradients as possible, and so less harmonics (lower N_C, lower dimension of the unknown $\mathbf{c}$) are required to approximate the invariant curve with Eq.B.86. Unfortunately, this is not known at the beginning, since C is unknown. However, the linear solution of Eq.B.81 could help to give some indication for small-width tori.

In particular, with this curve parametrization, in Eq.B.87 we recognize that the two section's coordinates along the curve are defined by the polar coordinates r-ϑ. But ϑ is the independent variable, so the two curve's components are only function of r. Therefore, the physical meaning of this parametrization allows to further decrease of one component the dimension of the unknown curve, using a single Fourier series for $r^F(\vartheta) = \{C^F(\mathbf{c},\vartheta)\}_r$ [120]. In summary, the approximation of Eq.B.86 could be extended only to the relevant components $[r,\mathbf{v}_X]$. $\mathbf{v}_X$ consists of the remaining state's components after the exclusion of v_{C_1},v_{C_2}, and v_M,v_E in case an iso-energetic Poincaré map is considered. This is a net reduction of 1 or 3 components in the dimension of the unknown $\mathbf{c}$, which will be retrieved by postprocessing.

$$
\begin{aligned}
&\left\{C^F\left(\mathbf{c},\vartheta\right)-\mathbf{x}_{PO}\right\}_{[r,\mathbf{v}_X]} = \frac{\mathbf{a}_0}{2}+\sum_{n=1}^{N_C}\mathbf{a}_n\cos\left(n\vartheta\right)+\mathbf{b}_n\sin\left(n\vartheta\right) = \\
&= \left[\left\{\,\mathbf{a}_0\;\left\{\,\mathbf{a}_n\;\;\mathbf{b}_n\,\right\}_{n=1}^{N_C}\,\right\}_{[r,\mathbf{v}_X]}\right]\left[\left\{\begin{array}{c}\frac{1}{2}\\ \left\{\begin{array}{c}\cos(n\vartheta)\\ \sin(n\vartheta)\end{array}\right\}_{n=1}^{N_C}\end{array}\right\}_{[r,\mathbf{v}_X]}\right] = \mathbf{C}\mathbf{e}\left(\vartheta\right) = \\
&= \left[\left\{\begin{array}{ccccc}\ddots & \ddots & \ddots & \ddots & \ddots\\ \ddots & \mathbf{0_{1x(2N_C+1)}} & \mathbf{e}(\vartheta)^T & \mathbf{0_{1x(2N_C+1)}} & \ddots\\ \ddots & \ddots & \ddots & \ddots & \ddots\end{array}\right\}_{[r,\mathbf{v}_X]}\right]\left[\left\{\begin{array}{c}\mathbf{a}_0\\ \left\{\begin{array}{c}\mathbf{a}_n\\ \mathbf{b}_n\end{array}\right\}_{n=1}^{N_C}\end{array}\right\}_{[r,\mathbf{v}_X]}\right] = \mathbf{E}\left(\vartheta\right)\mathbf{c}
\end{aligned}
\tag{B.88}
$$

Finally, other options for the curve parametrization can be used. A possible interesting choice is the universal parametrization of a curve, where the parameter is taken as the normalized arclength. This would make possible to describe any invariant curve by Fourier series, with the lowest number of Fourier coefficients, and also avoid to include the Fourier series of the rotation number profile in the algorithm. This option was suggested in [120] backreferencing a research work that did so in [174]. Unfortunately, the latter is based on the computation of invariant curves on a 2D map with the same,

now trivial, polar parametrization, and just at the conclusions the paper states that "complex cases" would require the normalized arclength. The paper concludes stating that despite the universality of the approach, the authors do not advise its use, due to the complexity of the numerical resolution of the DC scheme. This parametrization is now derived in this thesis, and the related DC scheme will be presented in the appropriate section. This scheme will be tested in chapter 4 for the computation of LPOs.

The parametrization of the Fourier series through the normalized arclength of the invariant closed curve should be defined in the following way, where the arclength s is normalized to l using the closed curve length L_C.

$$\begin{cases} \left\{C^F\left(\mathbf{c},l\right)-\mathbf{x}_{p.o.}\right\}_{\mathbf{v}_X}=\mathbf{E}\left(l\right)\mathbf{c}=\left[\begin{Bmatrix} \ddots & \ddots & \ddots & \ddots & \ddots \\ \ddots & \mathbf{0_{1\times(2N_C+1)}} & \mathbf{e}^{(l,1)^T} & \mathbf{0_{1\times(2N_C+1)}} & \ddots \\ \ddots & \ddots & \ddots & \ddots & \ddots \end{Bmatrix}_{\mathbf{v}_X}\right]\left[\left\{\mathbf{c}\right\}_{\mathbf{v}_X}\right] \\ ds=\sqrt[2]{\sum_{\mathbf{v}_X} d\left\{C^F\left(\mathbf{c},s\right)-\mathbf{x}_{p.o.}\right\}_{v_X}^2}\Rightarrow\begin{cases} L_C=\oint_C ds \\ l=\frac{\int_0^s ds}{L_C} \end{cases} \end{cases}, \\ l\in \mathrm{I}_l=[0,1]:C^F\left(\mathbf{c},0\right)=C^F\left(\mathbf{c},1\right) \tag{B.89}$$

Thus the curve's parameter now ranges from 0 to 1, so the Fourier series approximation of Eq.B.86 use $P=1$, and this is made explicit from seek of clearness in Eq.B.89. Now the invertible law must be derived, which is the definition of $l(\mathbf{x})$ from a general point $\mathbf{x}$. The idea is to define the parameter l that provides the closest point to $\mathbf{x}$ on the curve $C(l)$. From this we can understand the true potentiality of this parametrization because it measures the total distance of the error from a curve, and does not perform a projection on a subspace like the section's plane where the polar anomaly ϑ is defined. Of course if the point lies on the curve, the distance point-curve is zero.

$$l\left(\mathbf{x}\right):\left\|C^F\left(\mathbf{c},l\right)-\mathbf{x}\right\|=0\leftrightarrow\mathbf{x}\in C\left(l\right) \tag{B.90}$$

This hints at the use of the above distance curve-point to derive the invertible law, where the curve is expressed with the Fourier series of Eq.B.89. This is done introducing the function D, which is actually the half square of the distance, because the properties are the same than using the distance, and this function will simplify the algebra. Therefore, the problem is the minimization of the functional D, which is to find the zero of the function F_D, the derivative of D. Thus, the invertible law is not explicit, but requires a Newton's solver.

$$
\begin{aligned}
&\forall \mathbf{x}, D\left(l,\mathbf{c},\mathbf{x}\right)=\tfrac{1}{2}\left\|C^{F}\left(\mathbf{c},l\right)-\mathbf{x}\right\|^{2}=\tfrac{1}{2}\sum_{\mathbf{v}_X}\left(\mathbf{e}(l,1)^{T}\{\mathbf{c}\}_{v_X}+\{\mathbf{x}_{p.o.}\}_{v_X}-\{\mathbf{x}\}_{v_X}\right)^{2}\\
&\rightarrow F_{D}\left(l,\mathbf{c},\mathbf{x}\right)=\tfrac{\partial D}{\partial l}\left(l,\mathbf{c},\mathbf{x}\right)=\sum_{\mathbf{v}_X}\left(\mathbf{e}(l,1)^{T}\{\mathbf{c}\}_{v_X}+\{\mathbf{x}_{p.o.}\}_{v_X}-\{\mathbf{x}\}_{v_X}\right)\mathbf{e}'(l,1)^{T}\{\mathbf{c}\}_{v_X}\\
&l\left(\mathbf{x}\right):D\left(l,\mathbf{c},\mathbf{x}\right)=\min_{y\in[0,1]}\left\{D\left(y,\mathbf{c},\mathbf{x}\right)\right\}\Rightarrow\\
&\Rightarrow\begin{cases}
l\left(\mathbf{x}\right):F_{D}\left(l,\mathbf{c},\mathbf{x}\right)=\mathbf{e}'(l,1)^{T}\left(\left(\sum_{\mathbf{v}_X}\{\mathbf{c}\}_{v_X}\{\mathbf{c}^{T}\}_{v_X}\right)\mathbf{e}\left(l,1\right)-\sum_{\mathbf{v}_X}\{\mathbf{c}\}_{v_X}\left(\{\mathbf{x}\}_{v_X}-\{\mathbf{x}_{p.o.}\}_{v_X}\right)\right)=0\\
\delta F_{D}=\dfrac{\partial F_{D}}{\partial l}\left(l,\mathbf{c},\mathbf{x}\right)\delta l=\dfrac{\partial^{2}D}{\partial l^{2}}\left(l,\mathbf{c},\mathbf{x}\right)\delta l=\\
\quad=\left[\begin{array}{l}\mathbf{e}''(l,1)^{T}\left(\left(\sum_{\mathbf{v}_X}\{\mathbf{c}\}_{v_X}\{\mathbf{c}^{T}\}_{v_X}\right)\mathbf{e}\left(l,1\right)-\sum_{\mathbf{v}_X}\{\mathbf{c}\}_{v_X}\left(\{\mathbf{x}\}_{v_X}-\{\mathbf{x}_{p.o.}\}_{v_X}\right)\right)+\\+\mathbf{e}'(l,1)^{T}\left(\sum_{\mathbf{v}_X}\{\mathbf{c}\}_{v_X}\{\mathbf{c}^{T}\}_{v_X}\right)\mathbf{e}'\left(l,1\right)\end{array}\right]\delta l=\\
\quad=F_{D}{}'\left(l,\mathbf{c},\mathbf{x}\right)\delta l
\end{cases}
\end{aligned}
\tag{B.91}
$$

B.6.3.3 Computation of 2D-QPOs with Differential Corrector

After the definition of the invariant curve with a truncated Fourier series in section B.6.3.1, and the selection of its parametrization in section B.6.3.2, in this section the DC scheme to compute 2D-QPOs is presented.

B.6.3.3.1 Invariance Condition

The identification of a 2-torus has been reduced in section B.6.2 to the computation of its invariant curve on a chosen map, defined by the invariance condition of Eq.B.79-B.80. This is quite different from the case of a PO of section B.5.3.2, because the solution is not a point but a continuous object. For this reason, the numerical techniques for computing 2-tori are all based on the approximation of the invariant curve by Fourier series, as discussed in section B.6.3.1, reducing the solution to a set of Fourier coefficients $\mathbf{c}$. These coefficients should be derived in order to satisfy the invariance condition. Thus, the strategy is to discretize the invariant curve in N_S sample points, by a set of initial parameters θ_0. In particular, this section considers as baseline the case of the polar parametrization ϑ for the invariant curve showed in section B.6.3.2.

The algorithmic scheme is presented in Eq.B.92, for the general case of a Poincaré or stroboscopic map $P_{(\cdot)}$.

$$
\begin{cases}
F(\mathbf{c})=P_{(\cdot)}(x_0)-C^{F}\left(\mathbf{c},\vartheta_f\right)=0\\
x_0=C^{F}\left(\mathbf{c},\vartheta_0\right) & ,\ \forall\vartheta_0\in[0,2\pi)\\
\vartheta_f=\vartheta\left(P_{(\cdot)}(x_0)\right)
\end{cases}
\tag{B.92}
$$

The procedure is the following [120].

- We have a set of initial conditions x_0, evaluating the Fourier series at the initial curve parameters.

- For each of them, the image by the chosen map is computed. This constitutes the set of final conditions of the map.
- As the parametrization law is invertible, we can find the set of parameters function of the final conditions, which are going to be the final curve parameters ϑ_f. In the case the implicit transversal phase φ_2 is taken as curve's parameter, the image of the final curve parameter is retrieved from the approximated rotation number's profile: $\varphi_{2,f} = \varphi_{2,0} + \rho^F(\mathbf{c}, \varphi_{2,0})$.

If the curve is invariant, the same Fourier series evaluated this time at the final curve parameters must correspond to the final conditions. This represents the objective function F of the DC scheme, that will tune the set of Fourier coefficients until convergence. This will be summarized in section B.6.3.3.6.

Regarding the initial parameters θ_0, an uniform sampling is the common choice, despite is not mandatory. An uniform spacing allows to control the description of the curve just by the number of harmonics N_C, whereas using a non-uniform spacing, without knowing the properties of the solution, is risky because it can lower the efficacy of the Fourier analysis.

To DC requires the derivative of the objective function. To calculate the derivatives of the invariant curve's condition, related matrices are derived, where $\mathbf{P}$ represents the derivative of the chosen map,

$$\begin{cases} \mathbf{P}\left(t_f, \mathbf{x}_0\right) = \dfrac{dP_{(\cdot)}}{d\mathbf{x}_0}\left(t_f, \phi_{\mathbf{f}}\left(t_f, \mathbf{x}_0\right)\right) \\ \quad \rightarrow \mathbf{P}_r\left(t, \mathbf{x}_0\right) = \dfrac{dr}{d\mathbf{x}_0}\left(t_f, \phi_{\mathbf{f}}\left(t_f, \mathbf{x}_0\right)\right) = \left[\cos\vartheta_f\left(t_f,\mathbf{x}_0\right)\ \sin\vartheta_f\left(t_f,\mathbf{x}_0\right)\right]\left[\left\{\mathbf{P}\left(t, \mathbf{x}_0\right)\right\}_{\mathbf{i}_C,:}\right] \\ \mathbf{d}\left(\vartheta\right) = \frac{d\mathbf{e}}{d\vartheta}\left(\vartheta\right) = \left[\begin{matrix}0\\ \left\{\begin{matrix}-n\sin(n\vartheta)\\ n\cos(n\vartheta)\end{matrix}\right\}_{n=1}^{N_C}\end{matrix}\right] \\ \rightarrow \mathbf{D}\left(\mathbf{c}, \vartheta\right) = \frac{\partial C^F}{\partial \vartheta}\left(\mathbf{c}, \vartheta\right) = \left[\left\{\begin{matrix}\ddots & \ddots & \ddots & \ddots & \ddots \\ \ddots & \mathbf{0_{1x(2N_C+1)}} & \mathbf{d}(\vartheta)^T & \mathbf{0_{1x(2N_C+1)}} & \ddots \\ \ddots & \ddots & \ddots & \ddots & \ddots\end{matrix}\right\}_{[r,\mathbf{v}_X]}\right]\mathbf{c} \\ \mathbf{T}\left(\mathbf{x}\right) = \frac{d\vartheta}{d\mathbf{x}}\left(\mathbf{x}\right) \Rightarrow \left\{\mathbf{T}\left(\vartheta\right)\right\}_{\mathbf{i}_C} = \left[-\frac{\sin\vartheta(\mathbf{x})}{r(\mathbf{x})}\ \ \frac{\cos\vartheta(\mathbf{x})}{r(\mathbf{x})}\right] \end{cases} \tag{B.93}$$

and assembled in related global matrices that consider all the sampling points.

$$
\boldsymbol{\vartheta}_0 = \left[\{\vartheta_{0,s}\}_{s=1}^{N_S}\right] \Rightarrow \begin{cases} \mathbf{X}_0(\mathbf{c},\boldsymbol{\vartheta}_0) = \left[\{\mathbf{x}_{0,s}\}_{s=1}^{N_S}\right] = \left[\left\{C^F(\mathbf{c},\vartheta_{0,s})\right\}_{s=1}^{N_S}\right] \\ \qquad\qquad = C^F(\mathbf{c},\boldsymbol{\vartheta}_0) = \{\mathbf{x}_{p.o.}\}_{s=1}^{N_S} + \mathbf{E}^C(\boldsymbol{\vartheta}_0)\,\mathbf{c} \\ \mathbf{X}_f(\mathbf{X}_0) = \left[\{\mathbf{x}_{f,s}\}_{s=1}^{N_S}\right] = \left[\{\phi_{\mathbf{f}}(t_f(\mathbf{x}_{0,s}),\mathbf{x}_{0,s})\}_{s=1}^{N_S}\right] \\ \boldsymbol{\vartheta}_f(\mathbf{X}_f) = \left[\{\vartheta(\mathbf{x}_{f,s})\}_{s=1}^{N_S}\right] \wedge \mathbf{r}_f(\mathbf{X}_f) = \left[\{r(\mathbf{x}_{f,s})\}_{s=1}^{N_S}\right] \end{cases}
$$

$$
\Rightarrow \begin{cases} \mathbf{E}^C(\boldsymbol{\vartheta}) = \frac{\partial C^F}{\partial \mathbf{c}}(\boldsymbol{\vartheta}) = \left[\left\{ \begin{array}{c} \vdots \\ \mathbf{E}(\vartheta_s) \\ \vdots \end{array} \right\}_{s=1}^{N_S}\right] \\ \mathbf{P}^C(\mathbf{X}_0) = \frac{d\mathbf{X}_f}{d\mathbf{X}_0}(\mathbf{X}_0) = \left[\left\{ \begin{array}{ccccc} \ddots & \ddots & \ddots & \ddots & \ddots \\ \ddots & \mathbf{0_6} & \mathbf{P}\left(t_f(\mathbf{x}_{0,s}),\mathbf{x}_{0,s}\right) & \mathbf{0_6} & \ddots \\ \ddots & \ddots & \ddots & \ddots & \ddots \end{array} \right\}_{s=1}^{N_S}\right] \\ \mathbf{P}_r^C(\mathbf{X}_0) = \frac{d\mathbf{r}_f}{d\mathbf{X}_0}(\mathbf{X}_0) = \left[\left\{ \begin{array}{ccccc} \ddots & \ddots & \ddots & \ddots & \ddots \\ \ddots & \mathbf{0_{1x6}} & \mathbf{P}_r\left(t_f(\mathbf{x}_{0,s}),\mathbf{x}_{0,s}\right) & \mathbf{0_{1x6}} & \ddots \\ \ddots & \ddots & \ddots & \ddots & \ddots \end{array} \right\}_{s=1}^{N_S}\right] \\ \mathbf{D}^C(\mathbf{c},\boldsymbol{\vartheta}) = \frac{\partial C^F}{\partial \boldsymbol{\vartheta}}(\mathbf{c},\boldsymbol{\vartheta}) = \left[\left\{ \begin{array}{ccccc} \ddots & \ddots & \ddots & \ddots & \ddots \\ \ddots & \mathbf{0_{6x1}} & \mathbf{D}(\mathbf{c},\vartheta_s) & \mathbf{0_{6x1}} & \ddots \\ \ddots & \ddots & \ddots & \ddots & \ddots \end{array} \right\}_{s=1}^{N_S}\right] \\ \mathbf{T}^C(\mathbf{X}) = \frac{d\vartheta}{d\mathbf{X}}(\mathbf{X}) = \left[\left\{ \begin{array}{ccccc} \ddots & \ddots & \ddots & \ddots & \ddots \\ \ddots & \mathbf{0_{1x6}} & \mathbf{T}(\vartheta_s) & \mathbf{0_{1x6}} & \ddots \\ \ddots & \ddots & \ddots & \ddots & \ddots \end{array} \right\}_{s=1}^{N_S}\right] \end{cases}
\tag{B.94}
$$

It is worth noting the presence of the matrices $\mathbf{T}$, expressing the derivatives of the curve's parameter, in this case the polar anomaly. In the case the implicit transversal phase φ_2 is taken as the curve's parameter, this will require the derivatives of the approximated rotation number's profile, as introduced previously, that will introduce further matrices of partial derivatives. In the case of the universal parametrization of Eq.B.89, the procedure requires to derive the derivatives of the solution of a Newton's method of Eq.B.91: they are expressed in Eq.B.95-B.96.

$$
\begin{cases} \frac{\partial F_D}{\partial \mathbf{x}}(l,\mathbf{c}) = -\left[\left\{\mathbf{e}'(l,1)^T\{\mathbf{c}\}_{v_X}\right\}_{\mathbf{v}_X}\right] = -(\mathbf{E}'(l)\,\mathbf{c})^T = -\left(\frac{\partial C^F}{\partial l}(l,\mathbf{c})\right)^T \\ \frac{\partial F_D}{\partial \mathbf{c}}(l,\mathbf{c},\mathbf{x}) = \left[\left\{\{\mathbf{c}^T\}_{v_X}\left(\mathbf{e}'(l,1)\,\mathbf{e}(l,1)^T + \mathbf{e}(l,1)\,\mathbf{e}'(,1l)^T\right)\right\}_{\mathbf{v}_X}\right] - \left[\left\{\mathbf{e}'(l,1)^T\{\mathbf{x}\}_{v_X}\right\}_{\mathbf{v}_X}\right] \end{cases}
\tag{B.95}
$$

$$
\begin{cases} l_f = l(\phi_{\mathbf{f}}(t_f,0,\mathbf{x}_0)) : F_D(l_f,\mathbf{c},\phi_{\mathbf{f}}(t_f,0,\mathbf{x}_0)) = 0 \\ \delta F_D = \frac{\partial F_D}{\partial l}(l,\mathbf{c},\mathbf{x})\,\delta l \\ \delta l_f = -\left(\frac{\partial F_D}{\partial l}(l_f,\mathbf{c},\phi_{\mathbf{f}}(t_f,0,\mathbf{x}_0))\right)^{-1}\frac{\partial F_D}{\partial \mathbf{x}}(l_f,\mathbf{c})\,\delta\phi_{\mathbf{f}} + \\ \qquad -\left(\frac{\partial F_D}{\partial l}(l_f,\mathbf{c},\phi_{\mathbf{f}}(t_f,0,\mathbf{x}_0))\right)^{-1}\frac{\partial F_D}{\partial \mathbf{c}}(l,\mathbf{c},\phi_{\mathbf{f}}(t_f,0,\mathbf{x}_0))\,\delta\mathbf{c} \end{cases}
\tag{B.96}
$$

The related global matrices that consider all the sampling points of this DC scheme are showed below, where $\mathbf{\Phi}_l$,$\mathbf{\Phi}_x$,$\mathbf{\Phi}_c$ are the required matrices of partial derivatives in place of only $\mathbf{T}$.

$$\begin{aligned}
&\mathbf{l}_0 = \left[\{l_{0,s}\}_{s=1}^{N_S}\right] \Rightarrow \mathbf{X}_0\left(\mathbf{c},\mathbf{l}_0\right) = \left[\{\mathbf{x}_{0,s}\}_{s=1}^{N_S}\right] = \left[\left\{C^F\left(\mathbf{c},l_{0,s}\right)\right\}_{s=1}^{N_S}\right] = C^F\left(\mathbf{c},\mathbf{l}_0\right) \\
&\Rightarrow \mathbf{X}_f\left(\mathbf{X}_0\right) \rightarrow \mathbf{l_f}\left(\mathbf{X}_f\right) \\
&\Rightarrow \mathbf{E}^C\left(\mathbf{l}\right), \mathbf{P}^C\left(\mathbf{X}_0\right), \mathbf{D}^C\left(\mathbf{c},\mathbf{l}\right) \\
&\begin{cases}
\mathbf{\Phi}_l\left(\mathbf{l},\mathbf{c},\mathbf{X}\right) = \frac{\partial \mathbf{F_D}}{\partial \mathbf{l}}\left(\mathbf{l},\mathbf{c},\mathbf{X}\right) = \left[\left\{\begin{matrix} \ddots & \ddots & & \ddots & \ddots & \ddots \\ \ddots & 0 & \frac{\partial F_D}{\partial l}(l_s,\mathbf{c},\mathbf{x}_s) & 0 & \ddots & \\ \ddots & \ddots & & \ddots & \ddots & \ddots \end{matrix}\right\}_{s=1}^{N_S}\right] \\
\mathbf{\Phi}_x\left(\mathbf{l},\mathbf{c}\right) = \frac{\partial \mathbf{F_D}}{\partial \mathbf{x}}\left(\mathbf{l},\mathbf{c}\right) = \left[\left\{\begin{matrix} \ddots & \ddots & & \ddots & \ddots & \ddots \\ \ddots & 0 & \frac{\partial F_D}{\partial \mathbf{x}}(l_s,\mathbf{c}) & 0 & \ddots & \\ \ddots & \ddots & & \ddots & \ddots & \ddots \end{matrix}\right\}_{s=1}^{N_S}\right] \\
\mathbf{\Phi}_c\left(\mathbf{l},\mathbf{c},\mathbf{X}\right) = \frac{\partial \mathbf{F_D}}{\partial \mathbf{c}}\left(\mathbf{l},\mathbf{c},\mathbf{X}\right) = \left[\left\{\begin{matrix} \vdots \\ \frac{\partial F_D}{\partial \mathbf{c}}(l_s,\mathbf{c},\mathbf{x}_s) \\ \vdots \end{matrix}\right\}_{s=1}^{N_S}\right]
\end{cases}
\end{aligned} \tag{B.97}$$

Finally, recall that in the case of TV systems, the invariant curve's parameter on the stroboscopic map is set to be the constrained phase, which is appended in the state vector with the trick presented in section B.1.2.4. Thus, in this case, the matrix $\mathbf{T}$ is trivially a sparse matrix with a 1 in the component corresponding to the appended variable in the state vector.

B.6.3.3.2 Initial Guess

The DC requires a first guess for the Fourier coefficients. To compute a small-width 2D-QPOs around a PO, the linearized invariant curve of Eq.B.81 could be used. It is important to remark that Eq.B.81 is parameterized by the circle's anomaly for the linear combination of the eigenvectors. Thus this is by far not the curve's parameter that one wants to use[16], unless in the case of using the implicit transversal phase. Therefore, the linear solution must be reparameterized before proceeding.

To not lose precision on the initial guess, the numerical reparametrization requires one to evaluate Eq.B.81 with a higher sampling than the chosen N_S (100 times). Then, the respective values of the wanted parameters are derived: they would not come out sorted from θ_m to θ_M, so they must be rearranged. Now that the sampling is defined with respect to the correct parameter, it is non-uniform though: an interpolation must be performed (this is why the oversampling was required) to obtain the N_S initial conditions with respect to the correct parametrization.

The linear solution is fed to the DC through its Fourier coefficients. The uniform sampling of the initial guess is needed to use the discrete Fourier transform of Eq.B.85.

[16] This is a misleading error in [120].

It must be underlined that this is the only occasion when a Fourier transform is performed in all the DC scheme: afterwards, the algorithm requires only the Fourier series evaluations of Eq.B.84. Of course, Eq.B.85 is implemented with classical FFT algorithm, which provides the complex form of the Fourier coefficients up to the $N_S/2$ harmonic[17]. Real form is then derived with Eq.B.85, and coefficients up to the N_C harmonic are taken as the initial guess of the DC scheme.

B.6.3.3.3 Indeterminancies of the Torus

An invariant solution, which is a n-torus, is described by n phases, thus it implicitly has N indeterminancies [52].

Using a Poincaré map to reduce the invariant curve locks the initial condition of the longitudinal phase. If a stroboscopic map is used, an additional constraint is needed in the DC scheme, which is to lock one curve's component to have its 0-frequency Fourier coefficient null [52]. This means we are mocking a Poincaré condition on only the related mean value.

For the constraint on the initial condition of any transversal phase (considering as usual the single case of a 2D-QPO), the procedure is more complicated. Using the polar parametrization of the invariant curve naturally locks ϑ_0, because that is defined by the chosen axis of v_{C_1}. For the other parameterizations, a mere mathematical choice is to find the component of the initial guessed curve, whose couple of 1-frequency Fourier coefficients has the maximum norm. Following this, one should impose to be null the coefficient of this couple with the smallest absolute value [52].

B.6.3.3.4 Sizing Parameter of the Invariant Curve

In section B.5.1.1 and in Eq.B.81 it is shown that if a PO constitutes the backbone of a 2D-QPO, the related invariant curve is embedded in a continuous 1-parameter families of growing size from the invariant point of the PO. This is a very common situation, excluded only by the majority of dynamical systems forced by non-periodic actions, where the QPOs are isolated (they are called limit tori).

If an invariant curve is not isolated, an additional constraint is needed for the DC scheme, to compute a single 2D-QPO within the family. As mentioned above, the natural choice for the parameter of a family of QPOs is the size of the invariant curve. A simple idea to express this size would be to use an upper value of the curve along one coordinate, but this is not straightforward to implement analytically in the DC's derivative. A better choice is the area of the invariant curve projected onto a coordinate plane. This is coherent with the polar anomaly parametrization, and should be used in that case [120]. In particular, this is straightforward in Fourier analysis, because the area of any closed curve in polar coordinates is a function of the radius, whose Fourier coefficients constitute the set of variables of the DC scheme. The area A of any closed curve in polar coordinates is the following.

[17] It should be recognized that this is the condition of the Nyquist-Shannon sampling theorem.

$$A_C = \oint_C dx_{i_{C1}} dx_{i_{C2}} = \frac{1}{2}\int_0^{2\pi} r(\vartheta)^2 d\vartheta \tag{B.98}$$

Recalling the discrete version of the Parseval's theorem for two functions developed in Fourier series,

$$\begin{aligned}\frac{1}{P}\int_0^P f(x)g(x)^* dx &= \sum_{n=-N}^{N} c_{f,n} c_{g,n}^* \\ &= \frac{1}{4}\left(a_{f,0}a_{g,0}\right) + \frac{1}{2}\sum_{n=1}^{N}\left(a_{f,n}a_{g,n} + b_{f,n}b_{g,n}\right) + i\left(a_{f,n}b_{g,n} - b_{f,n}a_{g,n}\right)\end{aligned} \tag{B.99}$$

for the particular case of the square of a function developed in Fourier series Eq.B.99 becomes the Parseval's identity.

$$\frac{1}{P}\int_0^P f(x)^2 dx = \sum_{n=-N}^{N} |c_{f,n}|^2 = \frac{1}{4}a_{f,0}^2 + \frac{1}{2}\sum_{n=1}^{N}\left(a_{f,n}^2 + b_{f,n}^2\right) = \frac{1}{4}A_{f,0}^2 + \frac{1}{2}\sum_{n=1}^{N} A_{f,n}^2 \tag{B.100}$$

Therefore, applying Eq.B.100, Eq.B.98 becomes a convenient function of the Fourier coefficients of the radius of the closed curve.

$$\begin{aligned}A_C(\mathbf{c}) &= \frac{\pi}{2}\left(\frac{1}{2}a_0^2 + \sum_{n=1}^{N_C}\left(a_n^2 + b_n^2\right)\right)_r = \frac{\pi}{2}\left[\left\{\begin{matrix}\frac{1}{2}\mathbf{a}_0 \\ \left\{\begin{matrix}\mathbf{a}_n \\ \mathbf{b}_n\end{matrix}\right\}_{n=1}^{N_C}\end{matrix}\right\}_r\right]^T \left[\left\{\begin{matrix}\mathbf{a}_0 \\ \left\{\begin{matrix}\mathbf{a}_n \\ \mathbf{b}_n\end{matrix}\right\}_{n=1}^{N_C}\end{matrix}\right\}_r\right] = \mathbf{A}(\mathbf{c})\,\mathbf{c} \\ \{\mathbf{A}(\mathbf{c})\}_r &= \frac{\pi}{2}\left[\left\{\begin{matrix}\frac{1}{2}\mathbf{a}_0 \\ \left\{\begin{matrix}\mathbf{a}_n \\ \mathbf{b}_n\end{matrix}\right\}_{n=1}^{N_C}\end{matrix}\right\}_r\right]^T \Rightarrow w_C(\mathbf{c}) = \sqrt[2]{A_C(\mathbf{c})}\end{aligned} \tag{B.101}$$

To maintain the same units of the state $\mathbf{x}$, in Eq.B.101 the square root of the approximated area is defined as the width w of the invariant curve, to represent the parameter of the family of 2D-QPOs. Therefore, the constraint to be added in the objective function of the DC scheme is trivially to fix a target value for the width. This is presented in Eq.B.102, together with the derivative of this constraint.

$$\begin{cases} w_C(\mathbf{c}) - w_C^T = 0 \\ \mathbf{W}(\mathbf{c}) = \frac{dw_C}{d\mathbf{c}}(\mathbf{c}) = \frac{1}{2}\frac{1}{w_C}\frac{dA_C}{d\mathbf{c}}(\mathbf{c}) = \frac{1}{2}\frac{1}{w_C}\mathbf{A}(\mathbf{c}) \Rightarrow \{\mathbf{W}(\mathbf{c})\}_r = \frac{1}{2}\frac{1}{w_C}\{\mathbf{A}(\mathbf{c})\}_r \end{cases} \tag{B.102}$$

For the case of the universal parametrization of Eq.B.89, the natural choice is to use as sizing parameter of the family of 2D-QPOs the total arclength L of the invariant curve. This is computed by finite differences over the current sampling. Eq.B.103-B.104 present its definition and its derivatives with forward finite differences, Eq.B.105-B.106 with central finite differences.

$$\begin{cases} L_C\left(\mathbf{X}_0\left(\mathbf{c},\mathbf{l}_0\right)\right) = \sum\limits_{s=1}^{N_S-1} \Delta L_s\left(\mathbf{X}_0\left(\mathbf{c},\mathbf{l}_0\right)\right) + \Delta L_{N_S}\left(\mathbf{X}_0\left(\mathbf{c},\mathbf{l}_0\right)\right) \\ \Delta L_s\left(\mathbf{X}_0\left(\mathbf{c},\mathbf{l}_0\right)\right) = \sqrt[2]{\sum\limits_{\mathbf{v}_X} \Delta s^2_{v_X,s}\left(\mathbf{X}_0\left(\mathbf{c},\mathbf{l}_0\right)\right)} = \sqrt[2]{\sum\limits_{\mathbf{v}_X} \left\{\mathbf{x}_{0,s+1}\left(\mathbf{c}\right) - \mathbf{x}_{0,s}\left(\mathbf{c}\right)\right\}^2_{v_X}} \\ \Delta L_{N_S}\left(\mathbf{c},\mathbf{l}_0\right) = \sqrt[2]{\sum\limits_{\mathbf{v}_X} \Delta s^2_{v_X,N_S}\left(\mathbf{X}_0\left(\mathbf{c},\mathbf{l}_0\right)\right)} = \sqrt[2]{\sum\limits_{\mathbf{v}_X} \left\{\mathbf{x}_{0,1}\left(\mathbf{c}\right) - \mathbf{x}_{0,N_S}\left(\mathbf{c}\right)\right\}^2_{v_X}} \end{cases} \tag{B.103}$$

$$\begin{cases} L_C\left(\mathbf{X}_0\left(\mathbf{c},\mathbf{l}_0\right)\right) - L_C^T = 0 \\ \mathbf{S}\left(\mathbf{X}_0\right) = \frac{dL_C}{d\mathbf{X}}\left(\mathbf{X}_0\left(\mathbf{c},\mathbf{l}_0\right)\right) = \left[\left\{\mathbf{s}_s\left(\mathbf{X}_0\left(\mathbf{c},\mathbf{l}_0\right)\right)\right\}_{s=1}^{N_S}\right] \Rightarrow \mathbf{s}_s\left(\mathbf{X}_0\left(\mathbf{c},\mathbf{l}_0\right)\right) = \left[\left\{\xi_{v_X,s}\left(\mathbf{X}_0\left(\mathbf{c},\mathbf{l}_0\right)\right)\right\}_{\mathbf{v}_X}\right] \\ \Rightarrow \xi_{v_X,s}\left(\mathbf{X}_0\left(\mathbf{c},\mathbf{l}_0\right)\right) = \frac{\Delta s_{v_X,s-1}(\mathbf{X}_0(\mathbf{c},\mathbf{l}_0))}{\Delta L_{s-1}(\mathbf{X}_0(\mathbf{c},\mathbf{l}_0))} - \frac{\Delta s_{v_X,s}(\mathbf{X}_0(\mathbf{c},\mathbf{l}_0))}{\Delta L_s(\mathbf{X}_0(\mathbf{c},\mathbf{l}_0))} \\ \xi_{v_X,1}\left(\mathbf{X}_0\left(\mathbf{c},\mathbf{l}_0\right)\right) = \frac{\Delta s_{v_X,N_S}(\mathbf{X}_0(\mathbf{c},\mathbf{l}_0))}{\Delta L_{N_S}(\mathbf{X}_0(\mathbf{c},\mathbf{l}_0))} - \frac{\Delta s_{v_X,1}(\mathbf{X}_0(\mathbf{c},\mathbf{l}_0))}{\Delta L_1(\mathbf{X}_0(\mathbf{c},\mathbf{l}_0))} \end{cases} \tag{B.104}$$

$$\begin{cases} L_C\left(\mathbf{X}_0\left(\mathbf{c},\mathbf{l}_0\right)\right) = \Delta L_1\left(\mathbf{X}_0\left(\mathbf{c},\mathbf{l}_0\right)\right) + \sum\limits_{s=2}^{N_S-1} \Delta L_s\left(\mathbf{X}_0\left(\mathbf{c},\mathbf{l}_0\right)\right) + \Delta L_{N_S}\left(\mathbf{X}_0\left(\mathbf{c},\mathbf{l}_0\right)\right) \\ \Delta L_s\left(\mathbf{X}_0\left(\mathbf{c},\mathbf{l}_0\right)\right) = \sqrt[2]{\sum\limits_{\mathbf{v}_X} \Delta s^2_{v_X,s}\left(\mathbf{X}_0\left(\mathbf{c},\mathbf{l}_0\right)\right)} = \sqrt[2]{\sum\limits_{\mathbf{v}_X} \left\{\frac{\mathbf{x}_{0,s+1}(\mathbf{c}) - \mathbf{x}_{0,s-1}(\mathbf{c})}{2}\right\}^2_{v_X}} \\ \Delta L_1\left(\mathbf{X}_0\left(\mathbf{c},\mathbf{l}_0\right)\right) = \sqrt[2]{\sum\limits_{\mathbf{v}_X} \Delta s^2_{v_X,1}\left(\mathbf{X}_0\left(\mathbf{c},\mathbf{l}_0\right)\right)} = \sqrt[2]{\sum\limits_{\mathbf{v}_X} \left\{\frac{\mathbf{x}_{0,2}(\mathbf{c}) - \mathbf{x}_{0,N_S}(\mathbf{c})}{2}\right\}^2_{v_X}} \\ \Delta L_{N_S}\left(\mathbf{X}_0\left(\mathbf{c},\mathbf{l}_0\right)\right) = \sqrt[2]{\sum\limits_{\mathbf{v}_X} \Delta s^2_{v_X,N_S}\left(\mathbf{X}_0\left(\mathbf{c},\mathbf{l}_0\right)\right)} = \sqrt[2]{\sum\limits_{\mathbf{v}_X} \left\{\frac{\mathbf{x}_{0,1}(\mathbf{c}) - \mathbf{x}_{0,N_S-1}(\mathbf{c})}{2}\right\}^2_{v_X}} \end{cases} \tag{B.105}$$

$$\begin{cases} L_C\left(\mathbf{X}_0\left(\mathbf{c},\mathbf{l}_0\right)\right) - L_C^T = 0 \\ \mathbf{S}\left(\mathbf{X}_0\right) = \frac{dL_C}{d\mathbf{X}}\left(\mathbf{X}_0\left(\mathbf{c},\mathbf{l}_0\right)\right) = \left[\left\{\mathbf{s}_s\left(\mathbf{X}_0\left(\mathbf{c},\mathbf{l}_0\right)\right)\right\}_{s=1}^{N_S}\right] \Rightarrow \mathbf{s}_s\left(\mathbf{X}_0\left(\mathbf{c},\mathbf{l}_0\right)\right) = \left[\left\{\xi_{v_X,s}\left(\mathbf{X}_0\left(\mathbf{c},\mathbf{l}_0\right)\right)\right\}_{\mathbf{v}_X}\right] \\ \xi_{v_X,s}\left(\mathbf{X}_0\left(\mathbf{c},\mathbf{l}_0\right)\right) = \frac{\Delta s_{v_X,s-1}(\mathbf{X}_0(\mathbf{c},\mathbf{l}_0))}{2\Delta L_{s-1}(\mathbf{X}_0(\mathbf{c},\mathbf{l}_0))} - \frac{\Delta s_{v_X,s+1}(\mathbf{X}_0(\mathbf{c},\mathbf{l}_0))}{2\Delta L_{s+1}(\mathbf{X}_0(\mathbf{c},\mathbf{l}_0))} \\ \xi_{v_X,1}\left(\mathbf{X}_0\left(\mathbf{c},\mathbf{l}_0\right)\right) = \frac{\Delta s_{v_X,N_S}(\mathbf{X}_0(\mathbf{c},\mathbf{l}_0))}{2\Delta L_{N_S}(\mathbf{X}_0(\mathbf{c},\mathbf{l}_0))} - \frac{\Delta s_{v_X,2}(\mathbf{X}_0(\mathbf{c},\mathbf{l}_0))}{2\Delta L_2(\mathbf{X}_0(\mathbf{c},\mathbf{l}_0))} \\ \xi_{v_X,N_S}\left(\mathbf{X}_0\left(\mathbf{c},\mathbf{l}_0\right)\right) = \frac{\Delta s_{v_X,N_S-1}(\mathbf{X}_0(\mathbf{c},\mathbf{l}_0))}{2\Delta L_{N_S-1}(\mathbf{X}_0(\mathbf{c},\mathbf{l}_0))} - \frac{\Delta s_{v_X,1}(\mathbf{X}_0(\mathbf{c},\mathbf{l}_0))}{2\Delta L_1(\mathbf{X}_0(\mathbf{c},\mathbf{l}_0))} \end{cases} \tag{B.106}$$

Finally, in the case the implicit transversal phase φ_2 is taken as the curve's parameter, no natural choices arise for the selection of the sizing parameter. However, in section B.6.2 it was noted that for a general NL dynamical system, the rotation number is not fixed along the invariant curve, and its profile is not maintained along the family, so the mean rotation number along the invariant curve can be taken as the curve's parameter in this case [52].

B.6.3.3.5 Note on Iso-energetic Poincaré Map

In case of an iso-energetic Poincaré map, the iso-energetic constraint $g_E(\mathbf{x}) = c_{PO}$ can be taken out from the map, whose derivative returns the one of Eq.B.68, and the Fourier coefficients must be derived for an additional state's component. In this case, as done in [120], the iso-energetic constraint should be added in the objective function of the DC scheme. The related partial derivatives and global matrices are derived for the inclusion in the Jacobian.

$$\begin{cases} c\left(\mathbf{x}_0\left(\mathbf{c},\vartheta_0\right)\right)-c_{PO}=0\Rightarrow\mathbf{C}\left(\mathbf{X}\right)=\left[\left\{c\left(\mathbf{x}_s\right)\right\}_{s=1}^{N_S}\right] \\ \mathbf{g}\left(\mathbf{x}\right)=\frac{dc}{d\mathbf{x}}\left(\mathbf{x}\right)=\left[\begin{array}{cc}2\left\{\mathbf{f}(\mathbf{x})^T\right\}_{[\dot{x}\ \dot{y}\ \dot{z}]} & -2[\dot{x}\ \dot{y}\ \dot{z}]\end{array}\right] \\ \Rightarrow\mathbf{G}\left(\mathbf{X}\right)=\frac{d\mathbf{C}}{d\mathbf{X}}\left(\mathbf{X}\right)=\left[\left\{\begin{array}{ccccc}\ddots & \ddots & \ddots & \ddots & \ddots \\ \ddots & \mathbf{0_{1x6}} & \mathbf{g}(\mathbf{x}_s) & \mathbf{0_{1x6}} & \ddots \\ \ddots & \ddots & \ddots & \ddots & \ddots\end{array}\right\}^{N_S}_{s=1}\right] \end{cases} \tag{B.107}$$

B.6.3.3.6 Differential Corrector Scheme

Following the concepts introduced throughout section B.6.3, the DC for the computation of 2D-QPOs could be synthesized in a N_S-multiple shooting scheme, whose objective function and Jacobian are expressed in Eq.B.108.

$$\begin{cases} F\left(\mathbf{c},w_C^T,\vartheta_0\right)=\left[\begin{array}{c}\left[\left\{\mathbf{X}_f(\mathbf{X}_0(\mathbf{c},\vartheta_0))\right\}_{[r\ \mathbf{x}\backslash[v_M\ \mathbf{v}_C]]}\right]-\underbrace{\left[\left\{C^F(\mathbf{c},\vartheta_f(\mathbf{X}_f(\mathbf{X}_0(\mathbf{c},\vartheta_0))))\right\}_{[r\ \mathbf{x}\backslash[v_M\ \mathbf{v}_C]]}\right]}_{w_C(\mathbf{c})-w_C^T} \\ \left[\left\{\mathbf{0}\right\}_{s=1,[r\ \mathbf{x}\backslash[v_M\ \mathbf{v}_C]]}^{N_S}\right]\end{array}\right] \\ \delta F\left(\mathbf{c},w_C^T,\vartheta_0\right)= \\ =\left[\begin{array}{cc}\frac{d\mathbf{X}_f}{d\mathbf{X}_0}\left(\mathbf{X}_0\left(\mathbf{c},\vartheta_0\right)\right)\frac{\partial C^F}{\partial\mathbf{c}}\left(\vartheta_0\right)-\frac{\partial C^F}{\partial\mathbf{c}}\left(\vartheta_f\left(\mathbf{X}_f\left(\mathbf{X}_0\left(\mathbf{c},\vartheta_0\right)\right)\right)\right)+ & \\ -\frac{\partial C^F}{\partial\vartheta}\left(\mathbf{c},\vartheta_f\left(\mathbf{X}_f\left(\mathbf{X}_0\left(\mathbf{c},\vartheta_0\right)\right)\right)\right)\underbrace{\frac{d\vartheta}{d\mathbf{X}}\left(\mathbf{X}_f\left(\mathbf{X}_0\left(\mathbf{c},\vartheta_0\right)\right)\right)}_{\frac{dw_C}{d\mathbf{c}}(\mathbf{c})}\frac{d\mathbf{X}_f}{d\mathbf{X}_0}\left(\mathbf{X}_0\left(\mathbf{c},\vartheta_0\right)\right)\frac{\partial C^F}{\partial\mathbf{c}}\left(\vartheta_0\right) & \begin{array}{c}\left[\left\{\mathbf{0}\right\}_{s=1}^{N_S}\right] \\ -1\end{array}\end{array}\right]\left[\begin{array}{c}\delta\mathbf{c} \\ \delta w_C^T\end{array}\right]= \\ =\left[\begin{array}{cc}\left\{\mathbf{P}^C\left(\mathbf{X}_0\right)\right\}_{[r\ \mathbf{x}\backslash[v_M\ \mathbf{v}_C]],\mathbf{x}\backslash[v_M]}\left\{\mathbf{E}^C\left(\vartheta_0\right)\right\}_{\mathbf{x}\backslash[v_M],:}-\left\{\mathbf{E}^C\left(\vartheta_f\right)\right\}_{[r\ \mathbf{x}\backslash[v_M\ \mathbf{v}_C]],:}+ & \\ -\left\{\mathbf{D}^C\left(\mathbf{c},\vartheta_f\right)\right\}_{[r\ \mathbf{x}\backslash[v_M\ \mathbf{v}_C]],:}\underbrace{\left\{\mathbf{T}^C\left(\mathbf{X}_f\right)\right\}_{:,\mathbf{x}\backslash v_M}\left\{\mathbf{P}^C\left(\mathbf{X}_0\right)\right\}_{\mathbf{x}\backslash v_M,\mathbf{x}\backslash[v_M]}}_{\mathbf{W}(\mathbf{c})}\left\{\mathbf{E}^C\left(\vartheta_0\right)\right\}_{\mathbf{x}\backslash[v_M],:} & \begin{array}{c}\left[\left\{\mathbf{0}\right\}_{s=1}^{N_S}\right] \\ -1\end{array}\end{array}\right]\left[\begin{array}{c}\delta\mathbf{c} \\ \delta w_C^T\end{array}\right]= \\ =F'\left(\mathbf{c},w_C^T,\vartheta_0\right)\left[\begin{array}{c}\delta\mathbf{c} \\ \delta w_C^T\end{array}\right] \end{cases} \tag{B.108}$$

Furthermore, the scheme is a *LMS fitting*, that drives the image of the curve to coincide with the initial curve, by fine tuning its Fourier coefficients, and evaluating the error at sample locations. For this reason, the number of samples MUST be greater than the number of Fourier coefficients for each component[18]. Therefore, just like a polynomial regression, the linear system of Eq.B.108 is overdetermined and is solved with the left pseudo-inverse of the Jacobian matrix, that minimizes the norm of the residual.

$$\begin{cases} Ax=b+r, A\in\mathbb{R}^{N\times M}, N>M \\ \min\limits_x\left\{\frac{1}{2}r^Tr\right\} \end{cases}\Rightarrow x=\left(A^TA\right)^{-1}A^Tb=A_{LPSI}b \tag{B.109}$$

Regarding the tolerances of the Newton's method, with respect to the values used for the DC of the POs, they should be increased to account for the global multiple shooting dimension, therefore they are scaled by a factor $\sqrt[2]{N_S}$.

Note that in the presence of highly NL systems, which is the case of QPOs with a high Floquet multiplier, as well as to increase the reliability of the initial conditions for practical applications, the convergence of the multiple shooting scheme could be compromised. In this cases, one full revolution of the longitudinal phase is too long. The

[18] This paramount information is not given, as well as the definition of a LMS implementation, in [120].

solution implemented in [120] is to take multiple sections and related intermaps along the longitudinal motion, and so compute in the same DC scheme multiple invariant curves.

Eq.B.108 shows the DC scheme for the baseline case of the polar anomaly parametrization. In the case the implicit transversal phase φ_2 is taken as the curve's parameter, the appropriate changes on the derivatives of the rotation number's profile, the increased Fourier coefficients required for its approximation, and the appropriate sizing parameter must be considered. For the case of the universal parametrization of Eq.B.89, the related DC scheme is shown in Eq.B.110.

$$
\begin{cases}
F\left(\mathbf{c}, L_C^T, \mathbf{l}_0\right) = \begin{bmatrix} \left[\left\{\mathbf{X}_f(\mathbf{X}_0(\mathbf{c},\mathbf{l}_0))\right\}_{[r\ \mathbf{x}\backslash[v_M\ \mathbf{v}_C]]}\right] - \left[\left\{C^F(\mathbf{c},\mathbf{l}_f(\mathbf{X}_f(\mathbf{X}_0(\mathbf{c},\mathbf{l}_0))))\right\}_{[r\ \mathbf{x}\backslash[v_M\ \mathbf{v}_C]]}\right] \\ L_C(\mathbf{X}_0(\mathbf{c},\mathbf{l}_0)) - L_C^T \end{bmatrix} = \begin{bmatrix} \left[\{\mathbf{0}\}_{s=1,[r\ \mathbf{x}\backslash[v_M\ \mathbf{v}_C]]}^{N_S}\right] \\ 0 \end{bmatrix} \\
\delta F\left(\mathbf{c}, L_C^T, \mathbf{l}_0\right) = \\
= \begin{bmatrix} \frac{d\mathbf{X}_f}{d\mathbf{X}_0}\left(\mathbf{X}_0\left(\mathbf{c},\mathbf{l}_0\right)\right)\frac{\partial C^F}{\partial \mathbf{c}}\left(\mathbf{l}_0\right) - \frac{\partial C^F}{\partial \mathbf{c}}\left(\mathbf{l}_f\left(\mathbf{X}_f\left(\mathbf{X}_0\left(\mathbf{c},\mathbf{l}_0\right)\right)\right)\right) + \\ -\frac{\partial C^F}{\partial \mathbf{l}}\left(\mathbf{c},\mathbf{l}_f\left(\mathbf{X}_f\left(\mathbf{X}_0\left(\mathbf{c},\mathbf{l}_0\right)\right)\right)\right)\left(\frac{\partial \mathbf{F_D}}{\partial \mathbf{l}}\left(\mathbf{l}_f\left(\mathbf{X}_f\left(\mathbf{X}_0\left(\mathbf{c},\mathbf{l}_0\right)\right)\right),\mathbf{c},\mathbf{X}_f\left(\mathbf{X}_0\left(\mathbf{c},\mathbf{l}_0\right)\right)\right)\right)^{-1}\cdot \\ \cdot\frac{\partial \mathbf{F_D}}{\partial \mathbf{X}}\left(\mathbf{l}_f\left(\mathbf{X}_f\left(\mathbf{X}_0\left(\mathbf{c},\mathbf{l}_0\right)\right)\right),\mathbf{c}\right)\frac{d\mathbf{X}_f}{d\mathbf{X}_0}\left(\mathbf{X}_0\left(\mathbf{c},\mathbf{l}_0\right)\right)\frac{\partial C^F}{\partial \mathbf{c}}\left(\mathbf{l}_0\right) + \\ -\frac{\partial C^F}{\partial \mathbf{l}}\left(\mathbf{c},\mathbf{l}_f\left(\mathbf{X}_f\left(\mathbf{X}_0\left(\mathbf{c},\mathbf{l}_0\right)\right)\right)\right)\left(\frac{\partial \mathbf{F_D}}{\partial \mathbf{l}}\left(\mathbf{l}_f\left(\mathbf{X}_f\left(\mathbf{X}_0\left(\mathbf{c},\mathbf{l}_0\right)\right)\right),\mathbf{c},\mathbf{X}_f\left(\mathbf{X}_0\left(\mathbf{c},\mathbf{l}_0\right)\right)\right)\right)^{-1}\cdot \\ \cdot\frac{\partial \mathbf{F_D}}{\partial \mathbf{c}}\left(\mathbf{l}_f\left(\mathbf{X}_f\left(\mathbf{X}_0\left(\mathbf{c},\mathbf{l}_0\right)\right)\right),\mathbf{c},\mathbf{X}_f\left(\mathbf{X}_0\left(\mathbf{c},\mathbf{l}_0\right)\right)\right) \\ \frac{dL_C}{d\mathbf{X}}(\mathbf{X}_0(\mathbf{c},\mathbf{l}_0))\frac{\partial C^F}{\partial \mathbf{c}}(\mathbf{l}_0) \end{bmatrix}_{\left[\{\mathbf{0}\}_{s=1}^{N_S}\right]}^{-1} \begin{bmatrix} \delta\mathbf{c} \\ \delta L_C^T \end{bmatrix} = \\
= \begin{bmatrix} \left\{\mathbf{P}^C\left(\mathbf{X}_0\right)\right\}_{[r\ \mathbf{x}\backslash[v_M\ \mathbf{v}_C]],\mathbf{x}\backslash[v_M]}\left\{\mathbf{E}^C\left(\mathbf{l}_0\right)\right\}_{\mathbf{x}\backslash[v_M],:} - \left\{\mathbf{E}^C\left(\mathbf{l}_f\right)\right\}_{[r\ \mathbf{x}\backslash[v_M\ \mathbf{v}_C]],:} + \\ -\left\{\mathbf{D}^C\left(\mathbf{c},\mathbf{l}_f\right)\right\}_{[r\ \mathbf{x}\backslash[v_M\ \mathbf{v}_C]],:}\boldsymbol{\Phi}_l(\mathbf{l}_f,\mathbf{c},\mathbf{X}_f)^{-1}\{\boldsymbol{\Phi}_x\left(\mathbf{l}_f,\mathbf{c},\right)\}_{:,\mathbf{x}\backslash v_M}\cdot \\ \cdot\left\{\mathbf{P}^C\left(\mathbf{X}_0\right)\right\}_{\mathbf{x}\backslash v_M,\mathbf{x}\backslash[v_M]}\left\{\mathbf{E}^C\left(\mathbf{l}_0\right)\right\}_{\mathbf{x}\backslash[v_M],:} + \\ -\left\{\mathbf{D}^C\left(\mathbf{c},\mathbf{l}_f\right)\right\}_{[r\ \mathbf{x}\backslash[v_M\ \mathbf{v}_C]],:}\boldsymbol{\Phi}_l(\mathbf{l}_f,\mathbf{c},\mathbf{X}_f)^{-1}\boldsymbol{\Phi}_c\left(\mathbf{l}_f,\mathbf{c},\mathbf{X}_f\right) \\ \{\mathbf{S}(\mathbf{c})\}_{\mathbf{x}\backslash v_M}\left\{\mathbf{E}^C(\mathbf{l}_0)\right\}_{\mathbf{x}\backslash v_M,:} \end{bmatrix}_{\left[\{\mathbf{0}\}_{s=1}^{N_S}\right]}^{-1} \begin{bmatrix} \delta\mathbf{c} \\ \delta L_C^T \end{bmatrix} = \\
= F'\left(\mathbf{c}, L_C^T, \mathbf{l}_0\right)\begin{bmatrix} \delta\mathbf{c} \\ \delta L_C^T \end{bmatrix}
\end{cases}
\tag{B.110}
$$

Recalling that any references are available in the literature for this universal scheme, the analytical part seems correct, but the DC is not convergent. Analysis shows that this happens because the Jacobian becomes singular at the root. Eq.B.111 shows that the images of the initial conditions are a solution of the Fourier series at the return parameters. With this equivalence the partial derivatives simplify, and in particular $\partial F_D/\partial\phi_f$ becomes opposite to the local tangent of the curve. This produces a cascade of simplifications in the DC matrix which becomes an orthogonal projector with respect to the curve, and orthogonal projectors are singular matrices.

$$
\begin{aligned}
&\phi_{\mathbf{f}}\left(t_f,0,\mathbf{x}_0\right)=C^F\left(\mathbf{c},l_f\right)\\
&\Rightarrow\begin{cases}
D\left(l_f,\mathbf{c},\phi_{\mathbf{f}}\left(t_f,0,\mathbf{x}_0\right)\right)=0\\
F_D\left(l_f,\mathbf{c},\phi_{\mathbf{f}}\left(t_f,0,\mathbf{x}_0\right)\right)=0\\
\frac{\partial F_D}{\partial l}\left(l_f,\mathbf{c},\phi_{\mathbf{f}}\left(t_f,0,\mathbf{x}_0\right)\right)=\sum\limits_{\mathbf{v}_X}\left(\mathbf{e}'(l,1)^T\{\mathbf{c}\}_{v_X}\right)^2=\left\|\frac{\partial C^F}{\partial l}\left(\mathbf{c},l_f\right)\right\|^2\\
\frac{\partial F_D}{\partial \mathbf{x}}\left(l_f,\mathbf{c}\right)=-\left(\frac{\partial C^F}{\partial l}\left(\mathbf{c},l_f\right)\right)^T\\
\frac{\partial F_D}{\partial \mathbf{c}}\left(l_f,\mathbf{c},\phi_{\mathbf{f}}\left(t_f,0,\mathbf{x}_0\right)\right)=\left[\left\{\mathbf{e}(l_f,1)^T\mathbf{e}'(l_f,1)^T\{\mathbf{c}\}_{v_X}\right\}_{\mathbf{v}_X}\right]=\left(\frac{\partial C^F}{\partial l}\left(\mathbf{c},l_f\right)\right)^T\mathbf{E}\left(l_f\right)
\end{cases}\\
&\Rightarrow\begin{cases}
\frac{\partial C^F}{\partial l}\left(\mathbf{c},l_f\right)\left(-\frac{\partial F_D}{\partial l}\left(l_f,\mathbf{c},\phi_{\mathbf{f}}\left(t_f,\mathbf{x}_0\right)\right)\right)^{-1}\frac{\partial F_D}{\partial \mathbf{x}}\left(l_f,\mathbf{c}\right)=\mathbf{P}_{//\frac{\partial C^F}{\partial l}(\mathbf{c},l_f)}\\
\frac{\partial C^F}{\partial l}\left(\mathbf{c},l_f\right)\left(-\frac{\partial F_D}{\partial l}\left(l_f,\mathbf{c},\phi_{\mathbf{f}}\left(t_f,\mathbf{x}_0\right)\right)\right)^{-1}\frac{\partial F_D}{\partial \mathbf{c}}\left(l_f,\mathbf{c},\phi_{\mathbf{f}}\left(t_f,\mathbf{x}_0\right)\right)=-\mathbf{P}_{//\frac{\partial C^F}{\partial l}(\mathbf{c},l_f)}\mathbf{E}\left(l_f\right)
\end{cases}\\
&\Rightarrow\frac{dF(\mathbf{c})}{d\mathbf{c}}=\frac{d\phi_{\mathbf{f}}}{d\mathbf{x}_0}\left(t_f,\mathbf{x}_0\right)\frac{\partial C^F}{\partial \mathbf{c}}\left(l_0\right)-\frac{\partial C^F}{\partial \mathbf{c}}\left(l_f\right)+\\
&-\frac{\partial C^F}{\partial l}\left(\mathbf{c},l_f\right)\left(-\frac{\partial F_D}{\partial l}\left(l_f,\mathbf{c},\phi_{\mathbf{f}}\left(t_f,\mathbf{x}_0\right)\right)\right)^{-1}\frac{\partial F_D}{\partial \mathbf{x}}\left(l_f,\mathbf{c}\right)\frac{d\phi_{\mathbf{f}}}{d\mathbf{x}_0}\left(t_f,\mathbf{x}_0\right)\frac{\partial C^F}{\partial \mathbf{c}}\left(\mathbf{c},l_f\right)+\\
&-\frac{\partial C^F}{\partial l}\left(\mathbf{c},l_f\right)\left(-\frac{\partial F_D}{\partial l}\left(l_f,\mathbf{c},\phi_{\mathbf{f}}\left(t_f,\mathbf{x}_0\right)\right)\right)^{-1}\frac{\partial F_D}{\partial \mathbf{c}}\left(l_f,\mathbf{c},\phi_{\mathbf{f}}\left(t_f,\mathbf{x}_0\right)\right)=\\
&=\left(\mathbf{I}-\mathbf{P}_{//\frac{\partial C^F}{\partial l}(\mathbf{c},l_f)}\right)\left(\frac{d\phi_{\mathbf{f}}}{d\mathbf{x}_0}\left(t_f,\mathbf{x}_0\right)\frac{\partial C^F}{\partial \mathbf{c}}\left(l_0\right)-\frac{\partial C^F}{\partial \mathbf{c}}\left(l_f\right)\right)=\mathbf{P}_{\perp\frac{\partial C^F}{\partial l}(\mathbf{c},l_f)}\left(\mathbf{\Phi}_f\left(t_f,\mathbf{x}_0\right)\mathbf{E}\left(l_0\right)-\mathbf{E}\left(l_f\right)\right)
\end{aligned}
\tag{B.111}
$$

There are some numerical treatments for this situation. They consist in either erasing the smallest singular values [139], or using the Levenberg-Marquardt algorithm. These choices fully work, but they penalize the DC scheme's solution when embedded in a NC, as will be discussed in section B.6.3.3.7. Therefore no solution has been found to this problem.

B.6.3.3.7 Computation of Families of 2D-QPOs with Numerical Continuation

In conclusion, as discussed in section B.6.3.3.4, in the usual case that the invariant curves are organized in a continuous 1-parameter family on the chosen map, the sizing parameter has been introduced to lock the computation of the DC scheme of Eq.B.108 to one small-width invariant curve around the backbone PO, assuming that the initial guess was taken as the linearized solution. Once such small-width 2D-QPO is computed, the Fourier coefficients of its invariant curve provide the starting point of a NC. The technique iterates the DC scheme to compute the family of invariant curves on the chosen map [52]. The continuation parameter σ is chosen as the target value of the possible sizing parameters of the family mentioned in section B.6.3.3.4. The objective function of the NC is already the one of the DC scheme of Eq.B.108, with the continuation's constraint acting on the last component of $F\left(\mathbf{c},\sigma,\boldsymbol{\vartheta}_0\right)$. Again, the continuation is solved in the LMS sense.

The NC is integrated until the 2D-QPO of interest, for example the one of a particular size. Note that out of the neighborhood of the PO, the NC of large-amplitude invariant curves usually encounters nonlinear effects, such as turning points and bifurcations of the continuation curve. In particular, the NC when a Poincaré map is used for the reduction of the QPO, in highly NL systems eventually produces large bendings

and twists in the torus' surface, and the Poincaré section becomes parallel to the flow in some points of the invariant curve. This would make the NC to fail: the remedy used in [52] is to have variable Poincaré maps during the NC. In addition, the initial choice of the curve's parameter shows its practical weaknesses in highly NL systems. Simple methods like the polar anomaly parametrization certainly fail in such conditions, because large invariant curves would locally shrink, give birth to concavities, and most importantly not be centered any longer on the PO. If such large-width tori are required, more robust parameterizations and algorithms must be used: unfortunately not the universal parametrization, but definitely the methodology with the implicit transversal phase and the inclusion of the rotation number's profile in the solution. A general paper regarding the continuation of invariant tori is [175].

B.6.4 Simulation

Once the Fourier coefficients are computed with the methodology of section B.6.3, and the related invariant curve is retrieved, it is possible to simulate the 2D-QPO. This is done with the approach of DST of section B.6.2, where the torus' flow is reduced to a discrete dynamical system, by numerically integrating through iterative mappings. The invariant curve is treated as a set of initial conditions on the chosen map. But for unstable QPOs the machine error does not allow simulations of a single initial condition for an extended time span. However, the convergence of the DC guarantees that the first-return flow of these points lies on the same curve, within the tolerance error's threshold. Thus, the initial conditions within the discrete dynamical system are retrieved interpolating the intermediate initial condition along the invariant curve, using the inverse law of the curve parametrization.

Since the orbit is a QPO, we will fill the invariant curve following the discrete steps of the rotation's number profile, which now can be plotted along time. Thus, the image will never come back to the first initial condition, unless in the case of resonances with high-denominator from Eq.B.21, condition that actually is easily encountered.

Therefore, the simulation of the 2D-QPO produces a bounded trajectory, with the final time span of user's free-choice. A physical and graphical request could be to arrive at the period of the first transversal revolution of the invariant curve, in order to fill the surface of a 2-torus (however this is graphically affected when the rotation number is large, as well as at the occurrence of a resonance). This time is not explicitly available and is computed within the simulation of the QPO, plotting the rotation number's profile along time. This is an important information as it could be used as parameter of the family of QPOs as mentioned in section B.6.3.3.4. In conclusion the 2D-QPO is represented as a surface of motion, and this graphical torus could be parameterized by multiple transversal or longitudinal invariant curves along the backbone PO. They can be located at stroboscopic subintervals or Poincaré subsections. In particular, an interesting section's constraint for such objective is the perpendicularity of the backbone

PO's flow: $g(\mathbf{x}) = \dot{\mathbf{q}}_{PO}^{T}(\mathbf{q} - \mathbf{q}_{PO})$).

B.6.5 Linearized Behavior and Stability Analysis

As a difference from the definition of a PO in DST, the reduction of a 2D-QPO to a discrete dynamical system does not provide any global stability information of the invariant object. In particular the numerical computation does not provide a linearized description of the manifold associated to the whole torus. This because the invariance condition is formulated in the state-space, while the invariant curve is described by Fourier coefficients. This means that the linearized behavior and the related manifolds must be decomposed along the sampled longitudinal revolutions of the 2D-QPOs, considering the STM along each of these subintervals [116], since there is not a single monodromy matrix like for the PO.

An idea to have more global insight of the linearized behavior around a 2-torus is to implement a numerical method for the determination of the invariant curve in a way that resembles the invariance condition of POs, and so reducing the 2D-QPO to a single map, not a discrete dynamical system. This is similar to [176, 177, 140], where the rotation number's profile is used: however in this thesis a different approach is used, that does not make use of this requirement. The idea lies in the fact that the continuous invariant curve is approximated with a truncated Fourier series expansion. One should now think to the starting curve as globally defined by this set of coefficients, not by a set of sampled points. The global image of the curve is another curve: this second curve could be defined as well by another set of Fourier coefficients $\mathbf{c}_f$. Thus this is a map from a set of Fourier coefficients to another, at the same truncated degree.

$$\begin{aligned} &P_{(\cdot),\theta}(\mathbf{c}_0) = \mathbf{c}_f \in \mathbb{R}^{n(2N_C+1)} : C^F\left(\mathbf{c}_f, \theta\left(P_{(\cdot)}\left(C^F(\mathbf{c}_0, \theta_s)\right)\right)\right) = P_{(\cdot)}\left(C^F(\mathbf{c}_0, \theta_s)\right), \\ &\forall \theta_s \in [\theta_m, \theta_M), \left[\{\theta_s\}_{s=1}^{N_S}\right] = \boldsymbol{\theta} \end{aligned} \tag{B.112}$$

If the curve is invariant under the chosen map $P_{(\cdot)}$, the initial Fourier coefficients $\mathbf{c}_0$ are a fixed point of the map. $P_{(\cdot),\theta}$.

$$P_{(\cdot)}\left(C^F(\mathbf{c}, \theta)\right) = C^F(\mathbf{c}, \theta) \ , \forall \theta \Leftrightarrow \begin{cases} P_{(\cdot),\theta}(\mathbf{c}) = \mathbf{c} \\ \Pi = \frac{D}{D\mathbf{c}} P_{(\cdot),\theta}(\mathbf{c}) \end{cases} \tag{B.113}$$

Thus the map of Eq.B.112 must be implemented. The first part of the algorithm is exactly the same of the methods of section B.6.3, which is to perform multiple shooting of the sampling of initial conditions along the starting curve $C^F(\mathbf{c}_0, \theta)$, and derive the related set of final conditions. But now the set of final conditions is used to compute the Fourier coefficients of the final curve $C^F(\mathbf{c}_f, \theta)$. This requires to use the discrete Fourier transform.

$$\begin{aligned}
&\left\{P_{(\cdot),\theta}\left(\mathbf{c}\right)\right\}_{v_X,n} = \\
&= \begin{bmatrix} \frac{2}{P}\int_{\theta\left(P_{(\cdot)}\left(C^F(\mathbf{c},\theta_m)\right)\right)}^{\theta\left(P_{(\cdot)}\left(C^F(\mathbf{c},\theta_M)\right)\right)} \left\{P_{(\cdot)}\left(C^F\left(\mathbf{c},\theta\right)\right)\right\}_{v_X}\left(\theta_f\right)\cos\left(\frac{2\pi}{P}n\theta_f\right)d\theta_f \\ \frac{2}{P}\int_{\theta\left(P_{(\cdot)}\left(C^F(\mathbf{c},\theta_m)\right)\right)}^{\theta\left(P_{(\cdot)}\left(C^F(\mathbf{c},\theta_M)\right)\right)} \left\{P_{(\cdot)}\left(C^F\left(\mathbf{c},\theta\right)\right)\right\}_{v_X}\left(\theta_f\right)\sin\left(\frac{2\pi}{P}n\theta_f\right)d\theta_f \end{bmatrix}
\end{aligned} \tag{B.114}$$

Unfortunately FFT requires an uniform sampling of the data (the flows) over the independent variable (the return parameters). Despite the initial set of parameters is uniform because that is the independent variable, the set of the return parameters is not uniform any longer because the rotation number's profile is not flat for a NL system. Therefore it is not possible to exploit the orthogonality conditions of cosine and sine to solve numerically the above integrals with an appropriate quadrature sum. In case of non-uniform sampling, discrete Fourier transform is solved in the LMS sense. This is shown in the following equation, for a general vector of N_S sampled data $\mathbf{x}$[19] described by truncated Fourier series collected in the vector $\mathbf{e}$, with parameter ϑ of period P.

$$\begin{aligned}
x\left(\theta\right) = \mathbf{e}(\theta,P)^T\mathbf{c} \Rightarrow &\begin{cases} \boldsymbol{\theta} = \left[\left\{\theta_s\right\}_{s=1}^{N_S}\right] \\ \mathbf{x} = \left[\left\{x\left(\theta_s\right)\right\}_{s=1}^{N_S}\right] \\ \mathbf{M}\left(\boldsymbol{\theta}\right) = \left[\left\{\mathbf{e}(\theta_s,P)^T\right\}_{s=1}^{N_S}\right] \end{cases} \Rightarrow \\
\Rightarrow &\begin{cases} \mathbf{x} = \mathbf{M}\left(\boldsymbol{\theta}\right)\mathbf{c} \\ \mathbf{c} = \left(\mathbf{M}(\boldsymbol{\theta})^T\mathbf{M}\left(\boldsymbol{\theta}\right)\right)^{-1}\mathbf{M}(\boldsymbol{\theta})^T\mathbf{x} = \mathbf{V}\left(\boldsymbol{\theta}\right)\mathbf{x} = \left[\left\{\mathbf{v}\left(\theta_s\right)\right\}_{s=1}^{N_S}\right]\mathbf{x} \end{cases}
\end{aligned} \tag{B.115}$$

The multiplication by the left pseudo-inverse matrix $\mathbf{V}$ of $\mathbf{M}$ is analytically written down in its components, to define the mapping of Eq.B.112. This is reported in Eq.B.116, assembling a global matrix for each state's component ($\mathbf{M}$ is the same for every state's component).

[19] Attention: this is a vector of N_S samples of one state's component, not the state vector for one sample.

$$\begin{cases} \left[\left\{\phi_{\mathbf{f}}\left(t_f\left(\theta_{0,s}\right), C^F\left(\mathbf{c},\theta_{0,s}\right)\right) - \mathbf{x}_{p.o.}\right\}_{s=1,\mathbf{v}_X}^{N_S}\right] = \mathbf{E}^C\left(\left\{\theta\left(\phi_{\mathbf{f}}\left(t_f\left(\theta_{0,s}\right), C^F\left(\mathbf{c},\theta_{0,s}\right)\right)\right)\right\}_{s=1}^{N_S}\right)\mathbf{c} \rightarrow \\ \rightarrow \left[\left\{\phi_{\mathbf{f}}\left(t_f\left(\theta_{0,s}\right), C^F\left(\mathbf{c},\theta_{0,s}\right)\right) - \mathbf{x}_{p.o.}\right\}_{s=1,v_X}^{N_S}\right] = \mathbf{M}\left(\left\{\theta\left(\phi_{\mathbf{f}}\left(t_f\left(\theta_{0,s}\right), C^F\left(\mathbf{c},\theta_{0,s}\right)\right)\right)\right\}_{s=1}^{N_S}\right)\{\mathbf{c}\}_{v_X} \\ P_{(\cdot),\boldsymbol{\theta}_0}\left(\mathbf{c}\right) = \left[\left\{ \cdots \left\{ \begin{pmatrix} \ddots & \ddots & \ddots & \ddots & \ddots \\ \ddots & \ddots & \ddots & \ddots & \ddots \\ \ddots & \ddots & \mathbf{v}\left(\theta\left(\phi_{\mathbf{f}}\left(t_f(\theta_{0,s}), C^F(\mathbf{c},\theta_{0,s})\right)\right)\right) & \ddots & \ddots \\ \ddots & \ddots & \ddots & \ddots & \ddots \\ \ddots & \ddots & \ddots & \ddots & \ddots \end{pmatrix}_{\mathbf{v}_X} \cdots \right\}_{\mathbf{0}_{(\mathbf{2N_C+1})\mathbf{x1}}}^{\mathbf{0}_{(\mathbf{2N_C+1})\mathbf{x1}}} \right\}_{s=1}^{N_S}\right] \cdot \\ \qquad \cdot \left[\left\{\phi_{\mathbf{f}}\left(t_f\left(\theta_{0,s}\right), C^F\left(\mathbf{c},\theta_{0,s}\right)\right) - \mathbf{x}_{p.o.}\right\}_{s=1,\mathbf{v}_X}^{N_S}\right] = \\ \qquad = \mathbf{V}^C\left(\boldsymbol{\theta}_f\left(\mathbf{X}_f\left(\mathbf{X}_0\left(\mathbf{c},\boldsymbol{\theta}_0\right)\right)\right)\right)\mathbf{X}_f\left(\mathbf{X}_0\left(\mathbf{c},\boldsymbol{\theta}_0\right)\right) \end{cases} \tag{B.116}$$

The DC scheme in Eq.B.117 is very simple, just like the case of a PO. In particular the Jacobian includes a square monodromy-like matrix Π that acts in the Fourier coefficients space.

$$\begin{cases} F\left(\mathbf{c},\boldsymbol{\theta}_0\right) = P_{(\cdot),\boldsymbol{\theta}_0}\left(\mathbf{c}\right) - \mathbf{c} = \mathbf{0} \\ \delta F\left(\mathbf{c},\boldsymbol{\theta}_0\right) = \left[\frac{D}{D\mathbf{c}} P_{(\cdot),\boldsymbol{\theta}_0}\left(\mathbf{c}\right) - \mathbf{I}_{\mathbf{6(2N_C+1)}}\right]\delta\mathbf{c} = \left[\Pi - \mathbf{I}_{\mathbf{6(2N_C+1)}}\right]\delta\mathbf{c} = \frac{\partial F}{\partial \mathbf{c}}\left(\mathbf{c},\boldsymbol{\theta}_0\right)\delta\mathbf{c} \end{cases} \tag{B.117}$$

The DC scheme is simple but the complexity has been transferred to the implementation of the map itself, because the same LMS fitting is embedded inside it. Indeed the burden is due to the computation of the monodromy matrix, which will require the derivative of a large-scale left pseudo-inverse matrix $\mathbf{V}$.

$$\begin{aligned} \Pi = & \left(\begin{array}{l} \frac{\partial P_{(\cdot),\boldsymbol{\theta}_0}}{\partial \phi_{\mathbf{f}}}\left(\boldsymbol{\theta}\left(\phi_{\mathbf{f}}\left(t_f\left(\boldsymbol{\theta}_0\right), C^F\left(\mathbf{c},\boldsymbol{\theta}_0\right)\right)\right)\right) + \\ + \frac{\partial P_{(\cdot),\boldsymbol{\theta}_0}}{\partial \boldsymbol{\theta}}\left(\boldsymbol{\theta}\left(\phi_{\mathbf{f}}\left(t_f\left(\boldsymbol{\theta}_0\right), C^F\left(\mathbf{c},\boldsymbol{\theta}_0\right)\right)\right), \phi_{\mathbf{f}}\left(t_f\left(\boldsymbol{\theta}_0\right), C^F\left(\mathbf{c},\boldsymbol{\theta}_0\right)\right)\right)\frac{d\boldsymbol{\theta}}{d\mathbf{X}}\left(\phi_{\mathbf{f}}\left(t_f\left(\boldsymbol{\theta}_0\right), C^F\left(\mathbf{c},\boldsymbol{\theta}_0\right)\right)\right) \end{array} \right) \cdot \\ & \cdot \frac{d\phi_{\mathbf{f}}}{d\mathbf{x}_0}\left(t_f\left(\boldsymbol{\theta}_0\right), C^F\left(\mathbf{c},\boldsymbol{\theta}_0\right)\right)\frac{\partial C^F}{\partial \mathbf{c}}\left(\boldsymbol{\theta}_0\right) = \\ = & \left(\begin{array}{l} \frac{\partial P_{(\cdot),\boldsymbol{\theta}_0}}{\partial \mathbf{X}_f}\left(\boldsymbol{\theta}_f\left(\mathbf{X}_f\left(\mathbf{X}_0\left(\mathbf{c},\boldsymbol{\theta}_0\right)\right)\right)\right) + \\ + \frac{\partial P_{(\cdot),\boldsymbol{\theta}_0}}{\partial \boldsymbol{\theta}}\left(\boldsymbol{\theta}_f\left(\mathbf{X}_f\left(\mathbf{X}_0\left(\mathbf{c},\boldsymbol{\theta}_0\right)\right)\right), \mathbf{X}_f\left(\mathbf{X}_0\left(\mathbf{c},\boldsymbol{\theta}_0\right)\right)\right)\frac{d\boldsymbol{\theta}}{d\mathbf{X}}\left(\mathbf{X}_f\left(\mathbf{X}_0\left(\mathbf{c},\boldsymbol{\theta}_0\right)\right)\right) \end{array} \right) \frac{d\mathbf{X}_f}{d\mathbf{X}_0}\left(\mathbf{X}_0\left(\mathbf{c},\boldsymbol{\theta}_0\right)\right)\frac{\partial C^F}{\partial \mathbf{c}}\left(\boldsymbol{\theta}_0\right) \end{aligned} \tag{B.118}$$

The definition of $\mathbf{V}$ contains the inverse of a A^TA matrix inside, where A is the rectangular $\mathbf{M}$. We will need its derivative with respect to a parameter, as it is $A(x)$. First one derives the general rule for the derivative of the inverse of a matrix (where the scalar case is proofed).

$$\mathbf{A}(x)\mathbf{A}^{-1}(x) = \mathbf{I} \rightarrow \mathbf{A}^{-1}(x)' = -\mathbf{A}^{-1}(x)\mathbf{A}(x)'\mathbf{A}^{-1}(x) \tag{B.119}$$

Now we can exploit it in the chain rule for the case A^TA.

$$\begin{aligned}
&\tfrac{d}{dx}\left(\left(\mathbf{A}(x)^T\mathbf{A}(x)\right)^{-1}\mathbf{A}(x)^T\right) = \tfrac{d}{dx}\left(\left(\mathbf{A}(x)^T\mathbf{A}(x)\right)^{-1}\right)\mathbf{A}(x)^T + \left(\mathbf{A}(x)^T\mathbf{A}(x)\right)^{-1}\tfrac{d\mathbf{A}(x)^T}{dx} = \\
&= -\left(\mathbf{A}(x)^T\mathbf{A}(x)\right)^{-1}\left(\tfrac{d}{dx}\left(\mathbf{A}(x)^T\mathbf{A}(x)\right)\right)\left(\mathbf{A}(x)^T\mathbf{A}(x)\right)^{-1}\mathbf{A}(x)^T + \left(\mathbf{A}(x)^T\mathbf{A}(x)\right)^{-1}\tfrac{d\mathbf{A}(x)^T}{dx} = \\
&= -\left(\mathbf{A}(x)^T\mathbf{A}(x)\right)^{-1}\tfrac{d\mathbf{A}(x)^T}{dx}\mathbf{A}(x)\left(\mathbf{A}(x)^T\mathbf{A}(x)\right)^{-1}\mathbf{A}(x)^T + \\
&-\left(\mathbf{A}(x)^T\mathbf{A}(x)\right)^{-1}\mathbf{A}(x)^T\tfrac{d\mathbf{A}(x)}{dx}\left(\mathbf{A}(x)^T\mathbf{A}(x)\right)^{-1}\mathbf{A}(x)^T + \left(\mathbf{A}(x)^T\mathbf{A}(x)\right)^{-1}\tfrac{d\mathbf{A}(x)^T}{dx}
\end{aligned} \tag{B.120}$$

The derivatives required in Eq.B.118 are the following: the first is immediate, the second requires an algorithm to be performed for every coordinate variable. They both require the complete left pseudo-inverse $\mathbf{V}$, and so this approach requires to invert a large-scale matrix $\mathbf{M}^T\mathbf{M}$ with dimension $(2N_C+1)\times(2N_C+1)$.

$$\begin{cases}
\frac{\partial P_{(\cdot),\boldsymbol{\theta}_0}}{\partial \mathbf{X}_f}\left(\boldsymbol{\theta}_f\right) = \mathbf{V}^C\left(\boldsymbol{\theta}_f\right) \\
\frac{\partial P_{(\cdot),\boldsymbol{\theta}_0}}{\partial \boldsymbol{\theta}}\left(\boldsymbol{\theta}_f, \mathbf{X}_f\right) = \mathbf{W}^C\left(\boldsymbol{\theta}_f, \mathbf{X}_f\right) = \frac{\partial\left(\mathbf{V}^C(\boldsymbol{\theta})\mathbf{X}_f\right)}{\partial\boldsymbol{\theta}}\left(\boldsymbol{\theta}_f\right) = \left[\left\{\begin{array}{c}\vdots\\ \left\{\cdots\ \mathbf{y}_s\left(\boldsymbol{\theta}_f, \{\mathbf{X}_f\}_{v_X}\right)\ \cdots\right\}_{s=1}^{N_S}\\ \vdots\end{array}\right\}_{\mathbf{v}_X}\right]
\end{cases} \tag{B.121}$$

$$\begin{cases}
\mathbf{y}_s\left(\boldsymbol{\theta}_f, \{\mathbf{X}_f\}_{v_X}\right) = \frac{\partial\mathbf{V}(\boldsymbol{\theta})}{\partial\theta_s}\left(\boldsymbol{\theta}_f\right)\{\mathbf{X}_f\}_{v_X} \\
\begin{cases}
\{\mathbf{M}'(\boldsymbol{\theta})\}_s : \{\{\mathbf{M}'(\boldsymbol{\theta})\}_s\}_{s,:} = \mathbf{e}'(\theta_s, P)^T \\
\mathbf{K}(\boldsymbol{\theta}) = \mathbf{M}(\boldsymbol{\theta})^T\mathbf{M}(\boldsymbol{\theta}) \\
\frac{\partial\mathbf{V}(\boldsymbol{\theta})}{\partial\theta_s}(\boldsymbol{\theta}) = -\mathbf{K}^{-1}(\boldsymbol{\theta})\left(\left(\{\mathbf{M}'(\boldsymbol{\theta})\}_s{}^T\mathbf{M}(\boldsymbol{\theta}) + \mathbf{M}(\boldsymbol{\theta})^T\{\mathbf{M}'(\boldsymbol{\theta})\}_s\right)\mathbf{K}^{-1}(\boldsymbol{\theta})\,\mathbf{M}(\boldsymbol{\theta})^T - \{\mathbf{M}'(\boldsymbol{\theta})\}_s{}^T\right)
\end{cases}
\end{cases} \tag{B.122}$$

In conclusion the monodromy matrix is the following.

$$\Pi = \mathbf{V}^C\left(\boldsymbol{\theta}_f\right)\mathbf{P}^C\left(\mathbf{X}_0\right)\mathbf{E}^C\left(\boldsymbol{\theta}_0\right) + \mathbf{W}^C\left(\boldsymbol{\theta}_f, \mathbf{X}_f\right)\mathbf{T}^C\left(\mathbf{X}_f\right)\mathbf{P}^C\left(\mathbf{X}_0\right)\mathbf{E}^C\left(\boldsymbol{\theta}_0\right) \tag{B.123}$$

This numerical method to compute an invariant curve requires far more computational time than the ones of section B.6.3, due to the aforementioned computation of the full inverse of a large-scale matrix (which is the solution of $2N_C+1$ different linear systems). However it provides as byproduct a monodromy matrix for the stability analysis of the invariant curve, avoiding so an approximation of the manifolds from a decomposition in several STMs.

The square monodromy matrix has dimension proportional to the number of Fourier coefficients. This is a result of the truncation, and provides a large number of eigenfunctions, as a difference from the physical state-space in the case of a continuous dynamical system.

$$\Pi \in \mathbb{R}^{(N_X(2N_C+1))\times(N_X(2N_C+1))} \Rightarrow \left\{\left(\lambda_\Pi, \hat{v}_{\Pi,\lambda}\right)_i\right\}_{i=1}^{N_X(2N_C+1)}, \lambda_\Pi \in \mathbb{C}, \hat{v}_{\Pi,\lambda} \in \mathbb{C}^{N_X(2N_C+1)} \tag{B.124}$$

For a map, the eigenvalues for an invariant curve are organized in circles on the complex plane [176, 177]. Since they are related to a map, the Floquet linear stability is given by their magnitude. The number of circles corresponds to the physical manifolds, thus

is equal to the state's dimension. The multiplication of the same information to a large number of values is an outcome of using the Fourier series. In reality, the eigenset is made by continuous complex circle entities, like the invariant curve is a single continuous entity in the state's components. Thus, the multiplication of the same information is actually a downsizing due to the discretization. In particular, if the truncation of the series if poor, there could be additional low-density filled circles, so a number of circles higher than expected. This is of course a poor implementation, similar to the aliasing effect described by the Nyquist-Shannon sampling theorem's condition, that folds back the missed harmonics on the discrete spectrum.

However, the organization in circles is usually not perfect. This result is called the problem of the spurious eigenvalues, and it is due only to computational problems, as explained in [178, 176, 177]. Large-scale matrices, when solved with the power method algorithms, produce inaccuracies. This has a major impact in the selection of which, amongst the multiple eigenvectors, one should use to represent the single information of each physical manifold.

In summary, the answer is to choose as representative eigenvector the more accurate computed from the power method. As explained in [176], some special norms are used to evaluate the inaccuracy of the multiple eigenvectors. In particular, the concept is to penalize the eigenmodes with high frequencies.

The suggested norm-(p) of a vector, characterized by an indexing map k of its components, is expressed in Eq.B.125, where the indexing map is the frequency of the Fourier series expansion which sorts the components of the Fourier coefficients space.

$$\mathbf{v} = \left[\{v_i\}_{i=1}^{N}\right] \in \mathbb{C}^N, k(i) \in \mathbb{Z}, p \in \mathbb{N} \rightarrow \|\mathbf{v}\|_{(p)} = \sum_{i=1}^{N} |v_i| \, |k(i)|^p \tag{B.125}$$

$$\mathbf{c} = \left[\left\{ \begin{matrix} \mathbf{a}_0 \\ \left\{ \begin{matrix} \mathbf{a}_n \\ \mathbf{b}_n \end{matrix} \right\}_{n=1}^{N_C} \end{matrix} \right\}_{[r,\mathbf{v}_X]}\right] = \left[\{\{\mathbf{c}_{v_X,n}\}\}_{n=0,\mathbf{v}_X}^{N_C}\right] \rightarrow k(\mathbf{c}_{v_X,n}) = n \tag{B.126}$$

Also another norm-(HF) could be used, but this is more exploited as a fast post-processing index of the inaccuracy error.

$$\mathbf{v} = \left[\{v_i\}_{i=1}^{N}\right] \in \mathbb{C}^N, k(i) \in \mathbb{Z} \rightarrow \|\mathbf{v}\|_{(HF)} = \sum_{\substack{i=1 \\ |k(i)|>N_{HF}}}^{N} |v_i| \tag{B.127}$$

In conclusion, the norm-(1) is suggested as reliable measure of accuracy. It is computed for all the eigenvectors, and the eigenversor of the eigenset of interest with the least norm-(1) is chosen to represent the manifold. Now the eigenversor acts in the Fourier coefficients space. Therefore it produces a closed curve that represents the linear approximation of the manifold of the continuous invariant curve of reference.

B.6.6 Extension to High-Dimensional Tori

This whole section B.6 focused on the lower dimensional case of QPOs, which are 2-tori. Now it is briefly addressed the general case of a nD-QPO of Eq.B.20 and Eq.B.23, focusing on the numerical techniques, since the analytical and semi-analytical methodologies can simply consider the reduction to additional center manifolds [51, 50], further extending the Lyapunov's center theorem and the Moser's generalization (see section B.4.1).

The approach of DST does not change, and the nD-QPO is reduced to a discrete dynamical system defined by an appropriate map. As mentioned in section B.6.2, this provides a decomposition of the flow in a single longitudinal motion, and a transversal motion provided in the general case by the remaining $n-1$ phases $\varphi_{2:n}$. This is $\mathbf{x}_{nD-QPO}(t) = \phi_{\mathbf{f}}(t, t_0, \mathbf{x}_{0,nD-QPO}(\varphi_2, ..., \varphi_n))$. Thus, the initial conditions on the map are parameterized by all the transversal phases. This means that in DST the determination of a n-torus, which is a nD surface of motion, is reduced to the identification of the invariant closed $(n-1)$-torus S of a map $P_{(\cdot)}$.

$$\begin{aligned}
&\mathbf{x}_{0,QPO} \in S(\theta_1, ..., \theta_{n-1}) \rightarrow P_{(\cdot)}(\mathbf{x}_{0,QPO}) \in S(\theta_1, ..., \theta_{n-1}) \ , \\
&\forall \theta_i \in \mathrm{I}_{\theta_i} = [\theta_{i,m}, \theta_{i,M}] : \forall \theta_j \in \mathrm{I}_{\theta_j}, j \neq i, S(\theta_j, ..., \theta_{i,m}, ..., \theta_j) = S(\theta_j, ..., \theta_{i,M}, ..., \theta_j)
\end{aligned} \tag{B.128}$$

The computation of such invariant object can be undertaken with the same numerical techniques introduced in section B.6.3, which are naturally extendable to higher phase-space dimensions by the use of the general nD Fourier series [140], here reported for the 2D case.

$$\begin{aligned}
f^F(x_1, x_2) &= \sum_{n_2=-N_2}^{N_2} \sum_{n_1=-N_1}^{N_1} c_{n_1,n_2} e^{i\frac{2\pi}{P_1} n_1 x_1} e^{i\frac{2\pi}{P_2} n_2 x_2} \\
&= \frac{a_{0,0}}{2} + \sum_{n_2=1}^{N_2} \sum_{n_1=1}^{N_1} a_{n_1,n_2} \cos\left(\frac{2\pi}{P_1} n_1 x_1 + \frac{2\pi}{P_2} n_2 x_2\right) + b_{n_1,n_2} \sin\left(\frac{2\pi}{P_1} n_1 x_1 + \frac{2\pi}{P_2} n_2 x_2\right) \\
&= \frac{a_{0,0}}{2} + \sum_{n_2=1}^{N_2} \sum_{n_1=1}^{N_1} A_{n_1,n_2} \cos\left(\frac{2\pi}{P_1} n_1 x_1 + \frac{2\pi}{P_2} n_2 x_2 - \theta_{n_1,n_2}\right)
\end{aligned} \tag{B.129}$$

The resulting numerical approximation of the invariant 2-torus of a 3-torus' longitudinal mapping, around a PO, is shown below.

$$\left\{S^F\left(\mathbf{c},\theta_1,\theta_2\right)-\mathbf{x}_{PO}\right\}_{\mathbf{X}}=\frac{\mathbf{a}_{0,0}}{2}+\sum_{n_2=1}^{N_{C2}}\sum_{n_1=1}^{N_{C1}}\mathbf{a}_{n_1,n_2}\cos\left(\frac{2\pi}{P_1}n_1\theta_1+n_2\theta_2\right)+\mathbf{b}_{n_1,n_2}\sin\left(\frac{2\pi}{P_1}n_1\theta_1+n_2\theta_2\right)=$$
$$=\left[\left\{\mathbf{a}_{0,0}\ \left\{\mathbf{a}_{n_1,n_2}\ \mathbf{b}_{n_1,n_2}\right\}_{n_1=1,n_2=1}^{N_{C1},N_{C2}}\right\}_{\mathbf{X}}\right]\left[\left\{\left\{\begin{matrix}\cos\left(\frac{2\pi}{P_1}n_1\theta_1+n_2\theta_2\right)\\ \sin\left(\frac{2\pi}{P_1}n_1\theta_1+n_2\theta_2\right)\end{matrix}\right\}_{n_1=1,n_2=1}^{N_{C1},N_{C2}}\right\}_{[r,\mathbf{v}_X]}^{\frac{1}{2}}\right]=\mathbf{C}\mathbf{e}\left(\theta_1,\theta_2\right)$$
$$=\left[\left\{\begin{matrix}\ddots & \ddots & \ddots & \ddots & \ddots\\ \ddots & \mathbf{0}_{\mathbf{1x(4N_{C1}N_{C2}+1)}} & \mathbf{e}(\theta_1,\theta_2)^T & \mathbf{0}_{\mathbf{1x(4N_{C1}N_{C2}+1)}} & \ddots\\ \ddots & \ddots & \ddots & \ddots & \ddots\end{matrix}\right\}_{\mathbf{X}}\right]\left[\left\{\left\{\begin{matrix}\mathbf{a}_{0,0}\\ \mathbf{a}_{n_1,n_2}\\ \mathbf{b}_{n_1,n_2}\end{matrix}\right\}_{n_1=1,n_2=1}^{N_{C1},N_{C2}}\right\}_{\mathbf{X}}\right]=\mathbf{E}\left(\theta_1,\theta_2\right)\mathbf{c} \tag{B.130}$$

However, the problem becomes merely computational, similar to require a high-order expansion for a semi-analytical technique in highly NL systems. In this case, the dimension of the problem rises considerably, and the number of Fourier coefficients, which was already $dim\{\mathbf{x}\}\times(N_C+1)$, grows exponentially with the phase-space dimension of the invariant object. This is particular significant in terms of the solution of the linear system of the Newton's method, which will require numerical techniques for large-scale problems. This will penalize the solution when the DC scheme, as usual, is embedded in a NC. Apparently in the literature the computation of such dynamical objects is not common. The practical approach for high-dimensional tori is to simply treat them as bounded orbits. This will be the aim of the next section B.7.

B.7 Computation of Orbits for application in Perturbed Dynamics

As discussed in section B.6.6, high-dimensional tori in multi-state NL systems are quite cumbersome to be fully defined by an invariant closed object. Moreover, having more than one transversal phase means that the flow fills a volume of motion, and the motion practically appears in mechanical systems as a bounded trajectory in space. Some authors refer to them as chaotic motions, in the sense that the practical utility of these orbits is reduced to their permanence in a particular region for a specific time span, with a known amplitude of motion. The initial conditions must be accurately tuned for this trajectory in the time window required, but there is no interest in the knowledge of the full range of initial conditions on a map. The example is the case when a simpler invariant object, like an EP, a PO, and a 2D-QPO, is fully determined in a dynamical model, to study and optimize their performance that will be assessed against the engineering requirements. But the dynamical model is only an approximation of the real-world dynamics (see Eq.2.1), so it is not worthwhile to increase the complexity of the solution when its performances will be similar to its reference backbone, while the same effect will be eventually provided by the perturbations.

The perturbations are neglected in the dynamical system because they are small forces compared to the leading actions of the dynamics, whose modeling could be

also affected by inaccuracies in the knowledge of their parameters, which introduces a stochastic analysis of their effects. In addition, they can also behave stochasticly in time. However, when a perturbation is deterministic, it is usually time-dependent. This is a forcing action, and as mentioned in section B.1.3.1, in relation to its harmonics content, it will increase the phase-space of the solution by a number of constrained phases, thus leading to a torus around a backbone orbit. Therefore, as discussed above, the case of high-dimensional tori is practically reduced to the necessary task of the determination of the bounded trajectory around a reference orbit in a realistic, perturbed, dynamics [53].

The aim is to find an accurate reference signal $\mathbf{x}(t)$, for the required time span T, in the dynamical system enlarged by the TV disturbances. This reference signal is also expected to be close to the original reference orbit, selected and computed in the unperturbed model. The numerical procedure is a multiple shooting scheme [116]. The original orbit is sampled in N_T subintervals, that could well be non-uniform (for example the 2D-QPO reduced to a discrete dynamical system). The time subintervals will remain fixed. The solution is obtained finding an orbit in the perturbed dynamics that satisfies the continuity between these subintervals, and using the original orbit as initial guess. This is summarized below,

$$\begin{aligned} &\mathbf{T} = \left[\{t\}_{s=1}^{N_T+1}\right] \rightarrow \\ &\rightarrow \mathbf{x}(\mathbf{T}) = \left[\{\mathbf{x}_{0,s}\}_{s=1}^{N_T+1}\right] = \mathbf{X}_0 \Rightarrow \\ &\Rightarrow \mathbf{x}(t) : \mathbf{x}(t_{s+1}) = \phi_{\mathbf{f}}\left(t_{s+1}, t_s, \mathbf{x}_{0,s}\right) = \mathbf{x}_{0,s+1} \ , \\ &\forall 1 \leq s \leq (N_T - 1) \end{aligned} \tag{B.131}$$

and global matrices are defined to bring the continuity conditions of Eq.B.131 in the objective function of the DC scheme of Eq.B.133.

$$
\left\{
\begin{array}{l}
\mathbf{X_f} = \left[\left\{ \mathbf{x}_{f,s} \right\}_{s=1}^{N_T+1} \right] = \left[\left\{ \phi_{\mathbf{f}} \left(t_{s+1}, t_s, \mathbf{x}_{0,s} \right) \right\}_{s=1}^{N_T+1} \right] \\
\left\{
\begin{array}{l}
\mathbf{P} \left(t_f, t_0, \mathbf{x}_0 \right) = \frac{d\phi_{\mathbf{f}}}{d\mathbf{x}_0} \left(t_f, \phi_{\mathbf{f}} \left(t_f, t_0, \mathbf{x}_0 \right) \right) = \left\{ \mathbf{\Phi} \left(t_f, t_0, \mathbf{x}_0 \right) \right\}_{\mathbf{x},\mathbf{x}} \\
\mathbf{B}_e \left(t_f, t_0, \mathbf{x}_0 \right) = \frac{d\phi_{\mathbf{f}}}{de} \left(t_f, \phi_{\mathbf{f}} \left(t_f, t_0, \mathbf{x}_0 \right) \right) = \left\{ \mathbf{\Phi} \left(t_f, \mathbf{x}_0 \right) \right\}_{\mathbf{x},e}
\end{array}
\right.
\end{array}
\right. \Rightarrow
$$

$$
\Rightarrow \left\{
\begin{array}{l}
\mathbf{P}^C \left(\mathbf{T}, \mathbf{X}_0 \right) = \frac{d\mathbf{X}_f}{d\mathbf{X}_0} \left(\mathbf{T}, \mathbf{X}_0 \right) = \left[\left\{ \begin{array}{ccccc} \ddots & \ddots & \ddots & \ddots & \ddots \\ \ddots & \mathbf{0_{7x7}} & \mathbf{P}(t_{s+1},t_s,\mathbf{x}_{0,s}) & \mathbf{0_{7x7}} & \ddots \\ \ddots & \ddots & \ddots & \ddots & \ddots \end{array} \right\}_{s=1}^{N_T-1} \right] \\
\mathbf{B}_e^C \left(\mathbf{T}, \mathbf{X}_0 \right) = \frac{d\mathbf{X}_f}{de} \left(\mathbf{T}, \mathbf{X}_0 \right) = \left[\left\{ \begin{array}{c} \vdots \\ \mathbf{B}_e(t_{s+1},t_s,\mathbf{x}_{0,s}) \\ \vdots \end{array} \right\}_{s=1}^{N_T-1} \right] \\
\mathbf{I}^C = \frac{d\mathbf{X}_0}{d\mathbf{X}_0} \left(\mathbf{T}, \mathbf{X}_0 \right) = \left[\left\{ \begin{array}{ccccc} \ddots & \ddots & \ddots & \ddots & \ddots \\ \ddots & \mathbf{0_7} & \mathbf{0_7} & \mathbf{I_7} & \ddots \\ \ddots & \ddots & \ddots & \ddots & \ddots \end{array} \right\}_{s=1}^{N_T-1} \right]
\end{array}
\right. \tag{B.132}
$$

$$
\left\{
\begin{array}{l}
F \left(\mathbf{X}_0, \mathbf{T}, N_T, e \right) = \left[\left[\left\{ \mathbf{x}_{f,s} \right\}_{s=1}^{N_T-1} \right] - \left[\left\{ \mathbf{x}_{0,s} \right\}_{s=2}^{N_T} \right] \right] = \left[\left\{ \mathbf{0_{7x1}} \right\}_{s=1}^{N_T-1} \right] \\
\delta F \left(\mathbf{X}_0, \mathbf{T}, N_T, e \right) = \\
= \left[\begin{array}{l} \frac{d\mathbf{X}_f}{d\mathbf{X}_0} \left(\left\{ t_{0,s} \right\}_{s=2}^{N_T}, \left\{ t_{0,s} \right\}_{s=1}^{N_T-1}, \left\{ \mathbf{x}_{0,s} \right\}_{s=1}^{N_T-1} \right) + \\ - \frac{d\mathbf{X}_0}{d\mathbf{X}_0} \left(\left\{ t_{0,s} \right\}_{s=2}^{N_T}, \left\{ t_{0,s} \right\}_{s=2}^{N_T}, \left\{ \mathbf{x}_{0,s} \right\}_{s=2}^{N_T} \right) \end{array} \right. \left. \begin{array}{l} \\ \frac{d\mathbf{X}_f}{de} \left(\left\{ t_{0,s} \right\}_{s=2}^{N_T}, \left\{ t_{0,s} \right\}_{s=1}^{N_T-1}, \left\{ \mathbf{x}_{0,s} \right\}_{s=1}^{N_T-1} \right) \end{array} \right] \left[\begin{array}{c} \left\{ \delta \mathbf{X}_0 \right\}_{s=1}^{N_T-1} \\ \delta e \end{array} \right] = \\
= \left[\mathbf{P}^C(\mathbf{T},\mathbf{X}_0) - \mathbf{I}^C \ \mathbf{B}_e^C(\mathbf{T},\mathbf{X}_0) \right] \left[\begin{array}{c} \left\{ \delta \mathbf{X}_0 \right\}_{s=1}^{N_T-1} \\ \delta e \end{array} \right] = F' \left(\mathbf{X}_0, \mathbf{T}, N_T, e \right) \left[\begin{array}{c} \left\{ \delta \mathbf{X}_0 \right\}_{s=1}^{N_T-1} \\ \delta e \end{array} \right]
\end{array}
\right. \tag{B.133}
$$

In the above DC scheme, the vectorfield $\mathbf{f}$ is now associated to the perturbed dynamical system. Furthermore, the parameter e is introduced (there could be more than one if necessary), to weight the perturbations between the new and the original dynamics [53]. This means that the real-world vectorfield should be written as a homotopy $\mathbf{f}(t, \mathbf{x}, e)$ between the two models: recall that the sensitivity of the flow with respect to a parameter of the dynamics, required in Eq.B.133, is computed with the procedure explained in section B.1.2.5. This could be necessary if the level of perturbation is too high to allow the DC scheme, without e, to converge. In this case, the multiple shooting of Eq.B.133 is embedded in a NC where the continuation parameter is e. The bounded solution obtained is called a dynamical substitute of the original one in the new dynamics [53, 179].

The DC is used to satisfy only the continuity of the state between the subintervals. Therefore for $N_T + 1$ sampling points, only the first N_T are the controlling points to be tuned by the DC of Eq.B.133. This means that only the continuity conditions of the inner $N_T - 1$ states are included in the objective function of Eq.B.133. The last N_T-th subinterval is uncontrolled and the flow drifts away from the original orbit in unstable systems[20]. Therefore, the resulting linear system of the DC is n times

[20] This is not a problem, as the time span is free of choice by the user, and could be simply enlarged.

underdetermined, n being the dimension of the state. If the rank of the Jacobian is not deeply compromised, multiple solutions are available. The dynamical substitute is chosen as the one that minimizes some scaled Euclidian norm, thus the system is solved with the related right pseudo-inverse matrix of the Jacobian.

$$\begin{cases} Ax = b, A \in \mathbb{R}^{N \times M}, N < M \\ \min\limits_{x} \left\{ \frac{1}{2} x^T W x \right\}, W = C^T C > 0 \end{cases} \Rightarrow x = W^{-1} A^T \left(A W^{-1} A^T \right)^{-1} b = C^{-1} \left(A C^{-1} \right)_{RPSI} b \tag{B.134}$$

If the sampling points are considered to be of the same importance, the classical flat-weighted Euclidian norm is used, and the dynamical substitute is indeed the closest flow to the original orbit in the real-world dynamics [116]. This is the reference signal to be used for practical applications.

Note that if the level of perturbations is too high, the NC would converge but there is no guarantee that the dynamical substitute is close, in the mere practical sense, to the aimed orbit any longer, since a long continuation will drift away the solution. This happens because the DC scheme looks only to satisfy the continuity of the subintervals, and the closeness of the whole orbit is only minimized by the right pseudo-inverse's algorithm. Thus, this multiple shooting is useful at the last stage to fine tune the reference orbit for practical applications. The method is not recommended to simplify the analysis of relevant TV perturbations, that should actually be included as leading actions in the TV dynamical system, to identify appropriate invariant motions of Eq.B.23.

B.8 Computation of Invariant Manifolds

An object is named invariant with respect to a transformation, when it remains unchanged to such operation. This is the case of the invariant motions of a dynamical system presented in section B.1.3, which are n-tori. They describe a closed set of states, whose flow remains inside the set for any propagation time. The DC schemes used in DST apply their invariance condition on a map to identify the reduced invariant object used for their definition.

The linearized behavior around the invariant object is described by the STM, as discussed in sections B.3, B.5.1.1, B.6.1, and in particular, the behavior around the reduced invariant object is described by a monodromy matrix, as discussed in sections B.5.2.1, B.6.5. It is well-known that in linear algebra, the eigenvectors span an invariant set with respect to the application. Thus the eigenspaces of the monodromy matrix constitute the invariant manifolds associated to the invariant object, in the linearized approximation [50].

These manifolds have been classified in section B.5.1.1 in parabolic, elliptic, and hyperbolic. The parabolic manifold spans the flow of the n-torus itself, and the family of n-tori where it is embedded. The elliptic manifold spans the families of $(n+1)$-tori

around it. Finally the hyperbolic manifold spans the trajectories to reach it or depart from it. In particular, the real hyperbolic manifolds are the asymptotic trajectories to reach and depart the n-torus, because the time required to approach or escape the invariant object is infinity [50]. In contrast, the complex hyperbolic manifolds are traveled in a finite time, because they are damped. With an abuse of notation, the real hyperbolic manifolds associated to an invariant object are referred to as simply the invariant manifolds (IMs) [73, 50]. Thus, for the phase portrait of a saddle, there are two kinds of IMs W: the IM to reach the orbit (s) and the one to leave it (u), and each of them has two branches. W^s is the linear span of the stable eigenvectors along the orbit, W^u is the linear span of the unstable eigenvectors along the orbits. The two branches are simply distinct by the sign of the versor ($\pm$).

The linear eigenspace is only a local approximation of the IMs. To derive the complete tube of asymptotic trajectories in the nonlinear system, for each of the branches available, the numerical procedure is known as the globalization of the manifold [116]. It consists in using the linear IMs in proximity of the invariant object as initial condition, to integrate the flow in the nonlinear dynamics. Care must be taken to select the magnitude of the displacement of the initial condition along the eigenvector [117]. This should be small enough to make the linearized approximation of the manifold around the orbit worthy. But it must not be too small, because the real hyperbolic manifolds are asymptotic trajectories. When the initial condition, chosen along the IM, approaches the reference orbit, the time required to approach or escape such an orbit grows[21]. The integration is backward in time for the stable branches, and forward in time for the unstable branches. The globalization is usually stopped for all the flows at an appropriate Poincaré section for a dedicated exploitation[22]. For example different trajectories can be patched to realize prescribed itineraries in the full state domain of the nonlinear dynamical system [50], exploiting the existence of different isolated families of n-tori. These are called heteroclinic connections [75]. Alternatively, a stable and an unstable manifold of the same invariant object, or of the same family, can be connected through a common point at large distance from the orbits. This is possible because the eigenspaces are orthogonal only in the linear approximation. These are called homoclinic connections [74]. In particular, the patching can be perfect, or defecting in some state's components[23]. In the second case, to realize the connection, a control action must be performed. This is for example the case of a mechanical system, where the paramount condition is to have the same position, while the velocity can be adjusted with a maneuver. Patching trajectories in high-dimensional systems is usu-

[21] When practical applications are needed, the chosen trajectory of the IM is computed with an accurate simulation, deriving the location of the point where a very light perturbation is performed to insert or escape the orbit. The key point is that indeed this action is energetically not demanding: the IMs are called energy-efficient transfer trajectories.

[22] It is worth to note that since the invariant object has closure, its image under a Poincaré map is always closed too. If a TI energy exists for the system in study, points inside/outside the Poincaré map are at lower/higher energy than the energy of the invariant motion of reference.

[23] One component is always fixed by the Poincaré section's constraint.

ally complicated, and the presence of integrals of motion allows to lower the analysis. A sequence of different connections and intermediate flows along invariant objects, is called a dynamical chain [50].

Finally, note that apart from the numerical technique presented in this section, the analytical and semi-analytical methodologies discussed in section B.4 to compute invariant motions can be extended in the same way to consider the reduction to hyperbolic manifolds instead of the centers [170].

B.8.1 Computation of Invariant Manifolds of Equilibrium Points

In the trivial case of an equilibria, as discussed in section B.3, the IMs are the eigenspace spanned by the saddle eigenvectors of the linearized state-matrix A at its location.

$$\begin{cases} W^{u\pm} = span_{\pm}\left\{\hat{v}_{A,\max\lambda_A}(x_{EP})\right\} \\ W^{s\pm} = span_{\pm}\left\{\hat{v}_{A,\min\lambda_A}(x_{EP})\right\} \end{cases}, \forall t_0 \tag{B.135}$$

Thus the globalization of the manifold is applied to four points to derive the four asymptotic trajectories.

$$\begin{cases} x_{W^{u/s\pm}}(t) = \phi_f(t, t_0, x_{0,W^{u/s\pm}}) \\ x_{0,W^{u/s\pm}} = x_{EP} + \varepsilon_W W^{u/s\pm}(x_0) \\ W^{u/s\pm}(x_0) = \pm\hat{v}_{A,u/s}(x_{EP}) \end{cases} \tag{B.136}$$

As discussed in section B.8, ε_W represents the threshold to trigger the initial condition of the IM. For a mechanical system, the threshold is expressed in term of the norm of the resulting displacement in only the position's components [117].

B.8.2 Computation of Invariant Manifolds of Periodic Orbits

As discussed in section B.5.1.1, the IMs of a PO are the eigenspace spanned by the hyperbolic eigenvectors of the monodromy matrix M. Recall that the monodromy matrix is defined on the map where the PO is reduced to an invariant point. The stability property is unique for the whole PO, but the related eigenvectors span the IMs only at that location, just like the case of an EP.

$$\begin{cases} W^{u\pm} = span_{\pm}\left(\hat{v}_{M,\max\lambda_M}(x_{PO}(t))\right) \\ W^{s\pm} = span_{\pm}\left(\hat{v}_{M,\min\lambda_M}(x_{PO}(t))\right) \end{cases}, \forall t \in [t_0, T + t_0) \tag{B.137}$$

The procedure can be well iterated for a sampling of points along the PO, but this means solving multiple eigenvalue problems, and is not smart. Due to the linearized approximation, the IMs for the whole PO are retrieved by using the variational equation of Eq.B.6, thus transporting the initial condition for the IM on the chosen map through all the longitudinal phases with the local STM. Be aware that this would simply produce the same single IM, so the displacement must be considered in its direction, and the

threshold ε_W must be applied consistently [116]. Now the globalization of the manifold is applied to all the sampled points along the PO, to derive the tube of each of the four asymptotic branches.

$$\begin{cases} x_{W^{u/s\pm}}(t) = \phi_f(t, t_{0,W}, x_{0,W^{u/s\pm}}(t_{0,W})) \\ x_{0,W^{u/s\pm}}(t_{0,W}) = x_0(t_{0,W}) + \varepsilon_W W^{u/s\pm}(x_0(t_{0,W})) \\ x_0(t_{0,W}) = x_{PO}(t_{0,W}) = \phi_f(t_{0,W}, t_0, x_{PO}(t_0)) \\ W^{u/s\pm}(x_0(t_{0,W})) = \pm\hat{v}_{M,u/s}(x(t_{0,W})) = \Phi_f(t_{0,W}, t_0)\, W^{u/s\pm}(x_{PO}(t_0)) = \\ \qquad\qquad = \pm\Phi_f(t_{0,W}, t_0)\, \hat{v}_{M,u/s}(x_{PO}(t_0)) \end{cases},$$

$$\forall t_{0,W} \in [t_0, T + t_0)$$

(B.138)

B.8.3 Computation of Invariant Manifolds of Quasi-Periodic Orbits

As discussed in section B.6.1, the analysis of a general n-tori is reduced to a discrete dynamical system along the related longitudinal motion, thus the linearized behavior is described by means of the STMs among these subintervals. The related IMs can be computed exactly as for the case of a PO, by applying Eq.B.137-B.138 in each subinterval, and considering the appropriate STM in place of M [116].

However, for the case of a 2D-QPO, section B.6.5 presented an implementation of the classical numerical techniques for the computation of an invariant curve, that uses a mapping in the Fourier coefficients space. This approach provides a monodromy-like matrix Π. The related hyperbolic eigenspace gives the IMs of the invariant curve in the Fourier coefficients space, thus provides a curve on the chosen map for each branch [140]. In particular, in section B.6.1 the selection of the most accurate eigenvector for each manifold was undertaken to tackle the problem of the spurious eigenvalues, which makes use of the norm-(1) defined in Eq.B.125. Thus the IMs associated to the invariant curve are the following.

$$\begin{cases} W^{u\pm} = span_{\pm}\left(\hat{v}_{\Pi,\max\lambda_\Pi}(x(t))\right) : \left\|\hat{v}_{\Pi,\max\lambda_\Pi}(x(t))\right\|_{(1)} = \min\limits_{|\lambda_\Pi|>\varepsilon_\lambda}\left\{\left\|\hat{v}_{\Pi,\lambda_\Pi}(x(t))\right\|_{(1)}\right\} \\ W^{s\pm} = span_{\pm}\left(\hat{v}_{\Pi,\min\lambda_\Pi}(x(t))\right) : \left\|\hat{v}_{\Pi,\min\lambda_\Pi}(x(t))\right\|_{(1)} = \min\limits_{|\lambda_\Pi|<\varepsilon_\lambda^{-1}}\left\{\left\|\hat{v}_{\Pi,\lambda_\Pi}(x(t))\right\|_{(1)}\right\} \end{cases},$$

$$\forall t \in [0, t_f(\theta))$$

(B.139)

The fact that the eigenvectors act in the Fourier coefficients space requires to introduce a further threshold ε_C to preliminary displace the whole curve of initial conditions on the chosen map. However, all the initial conditions will be scaled downstream appropriately to the required ε_W. After this, the globalization of the manifold is performed similarly to the case of a PO, as well as the case of a general QPO, decomposing the procedure in the set of longitudinal motions parameterized by the transversal phase θ. The difference is that with this procedure the starting IM on the map is globally defined, because it is

the hyperbolic curve associated to the invariant object and computed as a whole, and is not taken from the sample of points derived independently from a bundle of STMs. The result is the filled tube of the four asymptotic branches.

$$\begin{cases} x_{W^{u/s\pm}}(t) = \phi_f(t, t_{0,W}, x_{0,W^{u/s\pm}}(t_{0,W})) \\ x_{0,W^{u/s\pm}}(t_{0,W}) = x_0(t_{0,W}) + \varepsilon_W W^{u/s\pm}(x_0(t_{0,W}), \theta) \\ x_0(t_{0,W}) = x_{QPO}(t_{0,W}) = \phi_f(t_{0,W}, t_0, x_{0,QPO}(\theta)) \\ W^{u/s\pm}(x_0(t_{0,W}), \theta) = \Phi_f\left(t_{0,W}, t_0(\theta)\right) W^{u/s\pm}(x_0(t_0), \theta) \\ W^{u/s\pm}(x_0(t_0), \theta) = C^F\left(\mathbf{c} + \varepsilon_C \hat{v}_{\Pi,u/s}(x_0(t_0), \theta), \theta\right) - C^F\left(\mathbf{c}, \theta\right) \end{cases}, \tag{B.140}$$

$$\forall t_{0,W} \in \left[t_0(\theta), t_f\left(\theta\right)\right), \forall \theta \in I_\theta$$

Appendix C

Time-Continuous Optimal Control in the CR3BP

C.1 Fundamentals of Optimal Control

Optimal Control Theory is a methodology first developed by the work of Pontryagin [180] and Bellman [181, 182]. Classical linear optimal control is a design technique for linear systems describable in the well-known analytical form provided below,

$$\begin{cases} \dot{\mathbf{x}} = \mathbf{A}\mathbf{x} + \mathbf{B}\mathbf{u} \\ \mathbf{z} = \mathbf{C}\mathbf{x} + \mathbf{D}\mathbf{u} \end{cases} \tag{C.1}$$

where the ODEs represent the system dynamics of state x under the effect of the control actions u, while the algebraic equation defines the performance outputs z, and all the matrices are constant. In order to control the system dynamics, a simple control law could be a proportional feedback with respect to the state error, between the target state and the real state.

$$\mathbf{u} = \mathbf{K}\mathbf{e} = \mathbf{K}\left(\mathbf{x_T} - \mathbf{x}\right) \tag{C.2}$$

Linear optimal control is undertaken by the definition of a cost quadratic functional J, that takes care of all the project requirements [180]. Here, the case of infinite-horizon (IH, $t_{fin} = \infty$) control is taken, which is to drive the system to zero state error. The aim is so to find the controller gain matrix solution K that minimizes the cost functional. The solution depends on the state and control weight matrices Q and R (and in case of coupling between x and u in the definition of z, also N), that are independent variables chosen by the designer in order to achieve, with the prescribed control law, the best performances' compromise among the project requirements.

$$J = \frac{1}{2}\int_0^\infty \begin{bmatrix} \mathbf{x} \\ \mathbf{u} \end{bmatrix}^T \begin{bmatrix} \mathbf{Q} & \mathbf{N} \\ \mathbf{N}^T & \mathbf{R} \end{bmatrix} \begin{bmatrix} \mathbf{x} \\ \mathbf{u} \end{bmatrix} dt \tag{C.3}$$

From the variational principle, which is the minimization of the cost functional under the system dynamics and control law constraints, a Hamiltonian system between state and co-state is expressed by the reduced matrices $\bar{A}$,$\bar{R}$,$\bar{Q}$.

$$\begin{cases} \bar{\mathbf{A}} = \mathbf{A} - \mathbf{B}\mathbf{R}^{-1}\mathbf{N}^T \\ \bar{\mathbf{Q}} = \mathbf{Q} - \mathbf{N}\mathbf{R}^{-1}\mathbf{N}^T \\ \bar{\mathbf{R}} = \mathbf{B}\mathbf{R}^{-1}\mathbf{B}^T \end{cases} \tag{C.4}$$

The minimization brings to two necessary conditions: one is the definition of the wanted gain matrix as a function of the so-called sensitivity matrix P,

$$\mathbf{K} = \mathbf{R}^{-1}\left(\mathbf{N} + \mathbf{B}^T\mathbf{P}\right) \tag{C.5}$$

and the other is named the Hamilton-Jacobi-Bellman equation (HJB) and provides the solution for P through a differential Riccati equation. This equation, strictly nonlinear, can be solved with various numerical methods: due to IH assumption, the dynamical part is removed and the NL Riccati equation is only algebraic (ARE).

$$\dot{\mathbf{P}} + \bar{\mathbf{A}}^T\mathbf{P} + \mathbf{P}\bar{\mathbf{A}} - \mathbf{P}\bar{\mathbf{R}}\mathbf{P} + \bar{\mathbf{Q}} = \mathbf{0} \tag{C.6}$$

The above analytical procedure allows to derive the optimal Linear Quadratic Regulator (LQR) of the linear system dynamics, that would reject the perturbations. Unfortunately, for a NL system like the CR3BP this is not guaranteed. The problem of NL control techniques is that an unified analytical theory cannot be provided. A number of NL control techniques for state-model systems have been developed so far, and are very sensitive to the case in study, and could not warrant the optimality of the solution. For example, the simplest approach for our task is to use an LQR based on the linearized system dynamics around an EP, which is a PID controller whose gains must be tuned appropriately.

C.2 State-Dependent Riccati Equation control

In the second half of the '90s [183, 184], a new nonlinear control methodology, based on a systematic procedure and so applicable to all NL systems was presented. This technique is known as SDRE, because the control gain matrix is obtained from the solution of the State-Dependent Riccati Equation. This equation has the same exact structure obtained from the LQR, but the matrices are treated as state dependent. The procedure consists of *transforming the NL system dynamics* (with control affinity) *in an identical pseudo-linear form.* This parametrization is called State-Dependent Coefficient (SDC) form. So the SDC system, at a given state, can be controlled with an Algebraic Riccati Equation solution, to give the gain matrix K, in order to optimize the associate state-control energetic cost functional, where the weight matrices Q-R

can also be expressed in an SDC form.

$$\begin{cases} \dot{\mathbf{x}} = \mathbf{A}(\mathbf{x})\mathbf{x} + \mathbf{B}(\mathbf{x})\mathbf{u} \\ J = \frac{1}{2}\int_0^\infty \begin{bmatrix} \mathbf{x} \\ \mathbf{u} \end{bmatrix}^T \begin{bmatrix} \mathbf{Q}(\mathbf{x}) & \mathbf{N}(\mathbf{x}) \\ \mathbf{N}^T(\mathbf{x}) & \mathbf{R}(\mathbf{x}) \end{bmatrix} \begin{bmatrix} \mathbf{x} \\ \mathbf{u} \end{bmatrix} dt \\ \mathbf{K}(\mathbf{x}) = \mathbf{R}^{-1}(\mathbf{x}) \left(\mathbf{N}(\mathbf{x}) + \mathbf{B}^T(\mathbf{x})\mathbf{P}(\mathbf{x})\right) \\ \dot{\mathbf{P}}(\mathbf{x}) + \bar{\mathbf{A}}^T(\mathbf{x})\mathbf{P}(\mathbf{x}) + \mathbf{P}(\mathbf{x})\bar{\mathbf{A}}(\mathbf{x}) - \mathbf{P}(\mathbf{x})\bar{\mathbf{R}}(\mathbf{x})\mathbf{P}(\mathbf{x}) + \bar{\mathbf{Q}}(\mathbf{x}) = \mathbf{0} \end{cases} \tag{C.7}$$

Advantages of SDRE technique are evident: this is a systematic methodology, close to the well-known linear optimal regulator's procedures, and so it could be applied to every NL system, and also the SDC form provides new opportunities to improve the control system performances. On the other hand, the procedure does still not provide an analytical solution, and the numerical solution could be proved to be sub-optimal and asymptotically stable only close to the origin. However, NL SDRE-based control, in fact, has been successfully used in a various number of engineering fields so far: spacecraft control, autonomous pilots for missiles and aircrafts, process control, robots, biomedical devices (artificial pancreas), Maglev trains.

The main feature of the SDRE technique is rewriting in a SDC form the system dynamics. The SDC form of the matrices has the main effect of introducing additional terms in the HJB equation. This part tends to zero as the state does too, and so its contribution in the full HJB is usually smaller than the remaining part, which is still the classical HJB of the LQR. Thus, the approach is to neglect it, as a necessary condition for optimality. The HJB reduces to only the SDRE, that is solved at each time step to give the pointwise stabilizing control action along the state trajectory. It can be proved that this is always verified for the single-order NL system, but not in the multi-order case. The reason is *the multiplicity of SDC parametrizations, which is an intrinsic peculiarity of the multiple-state NL systems.* The resulting SDRE-based control is so sub-optimal, in the sense that using for the solution only the SDRE, the resulting controlled state trajectories tend to optimal ones in proximity of the equilibrium state. To prove the existence of infinite SDC parameterizations for multiple-order nonlinear systems, it is sufficient to show that two different SDC forms exist for the same vectorfield: infinite cases are derived from a simple linear combination of the two, constituting a parameterized hyperplane as shown below.

$$\mathbf{A}_1(\mathbf{x})\mathbf{x} = \mathbf{A}_2(\mathbf{x})\mathbf{x} \Rightarrow \mathbf{A}_{1-2}(\mathbf{x}, \alpha_{1-2}) = \alpha_{1-2}\mathbf{A}_1(\mathbf{x}) + (1 - \alpha_{1-2})\,\mathbf{A}_2(\mathbf{x}) \tag{C.8}$$

The additional parameter α can also be state-dependent, realizing an indexed family of hyperplanes. Generalizing to the existence of k different independent SDC forms, the global hyperplane can be stated with $k-1$ additional parameters. In conclusion, the existence of multiple pseudo-linear SDC forms for the same NL system is intrinsically related to the impossibility to find an unique analytical solution of the complete HJB equation. But the real strength of the SDRE technique is to turn the previous analytical

brake in own favor, because the vectorfield in the SDC form results to be parameterized by a set of additional degrees of freedom. This allows to enhance the capability of the control remaining in the framework of the SDRE formulation, improving the optimality or other classical properties of the system (controllability, observability), in order to overcome practical problems. The second source of improved control design through the SDRE application derives from the possibility of using state-dependent weight matrices, realizing the same concepts of gain-scheduling intrinsically within the optimal controller algorithm. The third source of enhancement comes from the easy way to treat additional state-constraints through SDRE methodology intrinsically in the optimal control formulation.

The highest demand for the SDRE-based control is indeed the computational cost for the pointwise solution of the SDRE itself. The best way would be to do that continuously at each time step, but that can be wasteful and so various techniques have been implemented to enable an SDRE solution's timing [149, 185, 186], either on-line and off-line. The computational cost of the SDRE methodology on high-order systems is pricey among common nonlinear techniques, and that was the major obstacle to its diffusion. With the information technology development of the '00s, SDRE technique has widespread emerged for the applied control design in all the engineering branches.

C.3 Application of SDRE control to track LPOs in the CR3BP

The nonlinearities in the CR3BP of Eq.2.13 come from the two bodies' gravity terms. Eq.C.7 shows how the basic 2B gravity acceleration can be arranged in a pseudo-linear form[1].

$$\mathbf{a_G} = -\frac{GM}{\|\mathbf{r}\|^3}\mathbf{r} = -\frac{GM}{\left(x^2+y^2+z^2\right)^{3/2}}\begin{bmatrix} x \\ y \\ z \end{bmatrix} = -\frac{GM}{\|\mathbf{r}\|^3}\mathbf{I_3}\begin{bmatrix} x \\ y \\ z \end{bmatrix} = \mathbf{A}_{G,SDRE}\left(\mathbf{r}\right)\begin{bmatrix} x \\ y \\ z \end{bmatrix} \quad \text{(C.9)}$$

However, the above is the simplest, but not unique, SDC form. When generally this happens, despite the diagonal pseudo-linear form is easier, it is recommended to try to enable cross-dependencies of the state, which is to find some mathematical manipulations to fill up all the terms of the SDC state matrix. For the 2B gravity, this is carried out by dividing and multiplying by the square of the distance magnitude. The additional x^2,y^2,z^2 at the numerator can be shuffled with the state vector components x,y,z to provide up to seven different pseudo-linear forms, as shown in Eq.C.10. These seven SDC forms are weighted in the vectorfield through the introduction of a set of additional parameters α. The resulting SDC state-matrix, when multiplied by the position vector, provides the exact expression of the 2B gravity acceleration vector, without any approximation and for any value of the additional parameters. These parameters

[1] It is worth to underline the difference between SDC and linearization: the pseudo-linear state matrix is not the Hessian of the Keplerian gravity potential.

are additional DOFs, which allow to weight the formulation of the dynamics itself in order to obtain the solution most tailored to our aims.

$$\begin{cases} \mathbf{a_G} = -\dfrac{GM}{(x^2+y^2+z^2)^{3/2}}\begin{bmatrix}x\\y\\z\end{bmatrix} = -\dfrac{GM}{\|\mathbf{r}\|^5}\left(\|\mathbf{r}\|^2\mathbf{I_3}\begin{bmatrix}x\\y\\z\end{bmatrix}\right) = \\ \quad = -\dfrac{GM}{\|\mathbf{r}\|^5}\left\{\alpha_{i,j}r_j^2\delta_{i,j}\right\}_{i,j}\begin{bmatrix}x\\y\\z\end{bmatrix} - \dfrac{GM}{\|\mathbf{r}\|^5}\left\{(1-\alpha_{i,j})\,r_ir_j\right\}_{i,j}\begin{bmatrix}x\\y\\z\end{bmatrix} = \mathbf{A}_{G,SDRE}(\mathbf{r},\boldsymbol{\alpha})\begin{bmatrix}x\\y\\z\end{bmatrix} \\ \mathbf{A}_{G,SDRE}(\mathbf{r},\boldsymbol{\alpha}) = -\frac{GM}{\|\mathbf{r}\|^5}\begin{bmatrix} x^2+\alpha_{12}y^2+\alpha_{13}z^2 & (1-\alpha_{12})xy & (1-\alpha_{13})xz \\ (1-\alpha_{21})xy & \alpha_{21}x^2+y^2+\alpha_{23}z^2 & (1-\alpha_{23})yz \\ (1-\alpha_{31})xz & (1-\alpha_{32})yz & \alpha_{31}x^2+\alpha_{32}y^2+z^2 \end{bmatrix} \end{cases} \tag{C.10}$$

The gravity of each body is now expressed in the CR3BP framework. The only difference is that the barycenter of the central body is not at the origin of the frame, but there is an offset along the x-axis component, of distance a. With the same procedure, the SDC form turns out with a bias term.

$$\begin{aligned} \mathbf{a_G} = -\frac{GM}{\|\mathbf{r}\|^3}\mathbf{r} = -\frac{GM}{\left((x+a)^2+y^2+z^2\right)^{3/2}}\begin{bmatrix}x+a\\y\\z\end{bmatrix} = \\ = -\frac{GM}{\|\mathbf{r}\|^5}\begin{bmatrix} (x+a)^2+\alpha_{12}y^2+\alpha_{13}z^2 & (1-\alpha_{12})(x+a)y & (1-\alpha_{13})(x+a)z \\ (1-\alpha_{21})(x+a)y & \alpha_{21}(x+a)^2+y^2+\alpha_{23}z^2 & (1-\alpha_{23})yz \\ (1-\alpha_{31})(x+a)z & (1-\alpha_{32})yz & \alpha_{31}(x+a)^2+\alpha_{32}y^2+z^2 \end{bmatrix}\begin{bmatrix}x\\y\\z\end{bmatrix} + \\ -\frac{GM}{\|\mathbf{r}\|^5}\begin{bmatrix} (x+a)^2+\alpha_{12}y^2+\alpha_{13}z^2 \\ (1-\alpha_{21})(x+a)y \\ (1-\alpha_{31})(x+a)z \end{bmatrix}a \end{aligned} \tag{C.11}$$

This happens frequently with NL systems. A common technique to treat biases, as suggested by [183, 184], is to add an artificial stable state s in the SDC formulation, so include the biases inside the SDC state-matrix. This is shown in Eq.C.12 and requires three things. The simple, artificial, and uncoupled dynamics of s are determined by an eigenvalue, whose value must be chosen to be far more slower than the natural ones of the system. The s state is fictitious and so its value will always be set to one. For the two previous reasons, the additional state is not controllable: this is not a problem in the optimal control formulation because the state weight matrix must be at least semi-positive defined. This means that optimal control works also with uncontrollable but already stable dynamics.

$$\begin{cases} \dot{s} = -\lambda_s s \ , \ \lambda_s > 0 \\ s = 1 \Rightarrow Q_{ss} = 0 \end{cases} \tag{C.12}$$

$$\begin{aligned} &\begin{bmatrix} (x+a)^2+\alpha_{12}y^2+\alpha_{13}z^2 \\ (1-\alpha_{21})(x+a)y \\ (1-\alpha_{31})(x+a)z \end{bmatrix}a = \begin{bmatrix} (1-\eta_1)a\left[(x+a)^2+\alpha_{12}y^2+\alpha_{13}z^2\right] \\ (1-\eta_2)(1-\alpha_{21})a(x+a)y \\ (1-\eta_3)(1-\alpha_{31})a(x+a)z \end{bmatrix} + \\ &+\begin{bmatrix} \eta_1 a(x+2a) & \eta_1\alpha_{12}ay & \eta_1\alpha_{13}az \\ \eta_2\beta_{12}(1-\alpha_{21})ay & \eta_2(1-\alpha_{21})\left[(1-\beta_{12})ax+a^2\right] & 0 \\ \eta_3\beta_{13}(1-\alpha_{31})az & 0 & \eta_3(1-\alpha_{31})\left[(1-\beta_{13})ax+a^2\right] \end{bmatrix}\begin{bmatrix}x\\y\\z\end{bmatrix} + \begin{bmatrix}\eta_1 a^3\\0\\0\end{bmatrix} \end{aligned} \tag{C.13}$$

In addition, two other sets of parameters have been introduced in Eq.C.13 to weight an acceptable number of pseudo-linear forms to fill up the SDC state matrix. There are two β parameters that come out within the bias terms, and three η parameters to weight the bias itself. Therefore, with three sets of 11 weighting parameters, the SDC form of the CR3BP is made by 84 different pseudo-linear forms for each of the two gravity terms. The resulting SDC state matrix is reported in Eq.C.14 for one general body of mass parameter GM and x-axis' offset of a, in Eq.C.15 for the pseudo-linear complete CR3BP's gravity term definition, and in Eq.C.16 within the resulting SDC form of the CR3BP that is going to be used for the SDRE-based controller.

$$
\begin{cases}
\mathbf{a_G} = -\frac{GM}{\left((x+a)^2+y^2+z^2\right)^{3/2}} \begin{bmatrix} x+a \\ y \\ z \end{bmatrix} = \mathbf{A}_{G,SDRE}(\mathbf{r},\boldsymbol{\alpha},\boldsymbol{\beta},\boldsymbol{\eta}) \begin{bmatrix} x \\ y \\ z \\ s \end{bmatrix} \\
\mathbf{A}_{G,SDRE}(\mathbf{r},\boldsymbol{\alpha},\boldsymbol{\beta},\boldsymbol{\eta}) = -\frac{GM}{\|\mathbf{r}\|^5} \begin{bmatrix} a & b & c & d \\ e & f & g & h \\ i & j & k & l \end{bmatrix} \\
\quad \begin{cases}
a = (x+a)^2 + \eta_1 a\,(x+2a) + \alpha_{12} y^2 + \alpha_{13} z^2 \\
b = \left[(1-\alpha_{12})\,x + (1-(1-\eta_1)\,\alpha_{12})\,a\right] y \\
c = \left[(1-\alpha_{13})\,x + (1-(1-\eta_1)\,\alpha_{13})\,a\right] z \\
d = \eta_1 a^3 + (1-\eta_1)\,a\left[(x+a)^2 + \alpha_{12} y^2 + \alpha_{13} z^2\right] \\
e = (1-\alpha_{21})\left[x + (1+\eta_2\beta_{12})\,a\right] y \\
f = \alpha_{21} x^2 + \left[(2-\eta_2\,(1-\beta_{12}))\,\alpha_{21} + \eta_2\,(1-\beta_{12})\right] ax + y^2 + \alpha_{23} z^2 + (\eta_2 + (1-\eta_2)\,\alpha_{21})\,a^2 \\
g = (1-\alpha_{23})\,yz \\
h = (1-\eta_2)\,(1-\alpha_{21})\,a\,(x+a)\,y \\
i = (1-\alpha_{31})\left[x + (1+\eta_3\beta_{13})\,a\right] z \\
j = (1-\alpha_{32})\,yz \\
k = \alpha_{31} x^2 + \left[(2-\eta_3\,(1-\beta_{13}))\,\alpha_{31} + \eta_3\,(1-\beta_{13})\right] ax + \alpha_{32} y^2 + z^2 + (\eta_3 + (1-\eta_3)\,\alpha_{31})\,a^2 \\
l = (1-\eta_3)\,(1-\alpha_{31})\,a\,(x+a)\,z
\end{cases}
\end{cases}
\tag{C.14}
$$

$$
\begin{aligned}
\mathbf{a_G},_{3BP} &= -\frac{1-\mu}{\left((x+\mu)^2+y^2+z^2\right)^{3/2}} \begin{bmatrix} x+\mu \\ y \\ z \end{bmatrix} - \frac{\mu}{\left((x+\mu-1)^2+y^2+z^2\right)^{3/2}} \begin{bmatrix} x+\mu-1 \\ y \\ z \end{bmatrix} = \\
&= \mathbf{A}_{G1,SDRE}(\mathbf{q},\boldsymbol{\alpha}^1,\boldsymbol{\beta}^1,\boldsymbol{\eta}^1, GM=1-\mu, a=\mu) \begin{bmatrix} \mathbf{q} \\ s_1 \end{bmatrix} + \\
&+ \mathbf{A}_{G2,SDRE}(\mathbf{q},\boldsymbol{\alpha}^2,\boldsymbol{\beta}^2,\boldsymbol{\eta}^2, GM=\mu, a=\mu-1) \begin{bmatrix} \mathbf{q} \\ s_2 \end{bmatrix} = \\
&= \begin{bmatrix} \left\{\mathbf{A}_{G1,SDRE}\right\}_{1:3,1:3} + \left\{\mathbf{A}_{G2,SDRE}\right\}_{1:3,1:3} & \left\{\mathbf{A}_{G1,SDRE}\right\}_{1:3,4} & \left\{\mathbf{A}_{G2,SDRE}\right\}_{1:3,4} \end{bmatrix} = \\
&= \mathbf{A}_{G3BP,SDRE}(\mathbf{q},\boldsymbol{\alpha}^1,\boldsymbol{\beta}^1,\boldsymbol{\eta}^1,\boldsymbol{\alpha}^2,\boldsymbol{\beta}^2,\boldsymbol{\eta}^2) \begin{bmatrix} \mathbf{q} \\ s_1 \\ s_2 \end{bmatrix}
\end{aligned}
\tag{C.15}
$$

$$
\mathbf{x} = \begin{bmatrix} \mathbf{q} \\ \dot{\mathbf{q}} \\ s_1 \\ s_2 \end{bmatrix} \;,\; \dot{\mathbf{x}} = \mathbf{A}\mathbf{x}_\mathbf{L} + \mathbf{B}\mathbf{u} \;,\; \mathbf{B} = \mathbf{I_3} \;,
$$

$$
\mathrm{A} = \begin{bmatrix} \mathbf{0_3} & \mathbf{I_3} & \mathbf{0_{3x2}} \\ -\mathbf{P} + \left\{\mathbf{A}_{G3BP,SDRE}(\mathbf{q},\boldsymbol{\alpha}^1,\boldsymbol{\beta}^1,\boldsymbol{\eta}^1,\boldsymbol{\alpha}^2,\boldsymbol{\beta}^2,\boldsymbol{\eta}^2)\right\}_{1:3,1:3} & -2\mathbf{W} & \left\{\mathbf{A}_{G3BP,SDRE}(\mathbf{q},\boldsymbol{\alpha}^1,\boldsymbol{\beta}^1,\boldsymbol{\eta}^1,\boldsymbol{\alpha}^2,\boldsymbol{\beta}^2,\boldsymbol{\eta}^2)\right\}_{1:3,4:5} \\ \mathbf{0_{3x2}} & \mathbf{0_{3x2}} & -\lambda_s \mathbf{I}_2 \end{bmatrix}
\tag{C.16}
$$

One can prove that the original basic diagonal structure of EqC.10 is obtainable with $\alpha = 1$ $(\forall\beta)$, $\eta = 0$. Usually, the suggestion is to use balanced value of the weighting parameters, which is 0.5. Also the suggestion is to choose values inside the $[0, 1]$ interval, in order to avoid "negative" weighting of the formulation. In section 4.1.3.2.2, the square eigenvalue of the two additional stable states is set to be 0.001, which is acceptably slower than the eigenvalues of the natural system of Eq.2.29. Smaller values do not improve the results, on the contrary make the matrices to become ill-conditioned.

Appendix D

Libration Point Orbits and Invariant Manifolds of the Mars-Phobos 3BP

D.1 Invariant Manifolds of the LPOs of the Mars-Phobos CR3BP

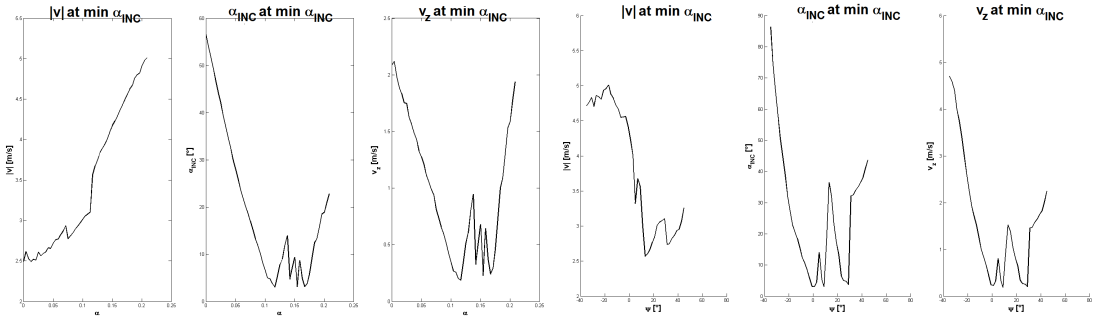

Figure D.1: **Landing on Phobos through the Invariant Manifold of the lp L_1 Planar Lyapunov orbits.** Trajectories that provide the min incidence at the touch-down, as a function of the α input of the lp algorithm or the longitude of the landing site, for orbits inside the region of convergence at the max order method. Performances of the trajectory: landing velocity magnitude, angle of incidence, downward vertical velocity. Phobos mean ellipsoidal surface.

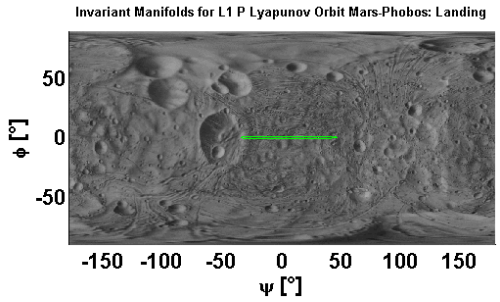

Figure D.2: **Landing on Phobos through the Invariant Manifold of the lp L_1 Planar Lyapunov orbits.** Region of possible landing sites, for orbits inside the region of convergence at the max order method. Phobos mean ellipsoidal surface.

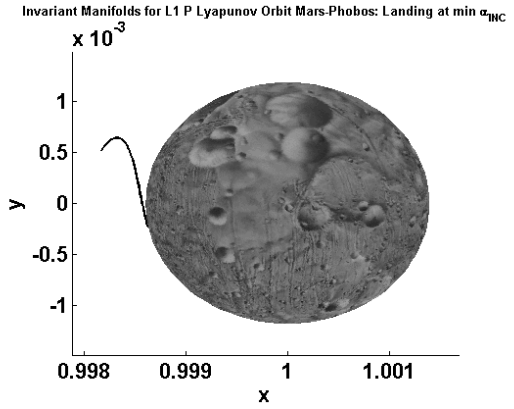

Figure D.3: **Landing on Phobos through the Invariant Manifold of the lp L_1 Planar Lyapunov orbits.** Trajectory that provides the overall min incidence at the touch-down. Phobos mean elipsoidal surface.

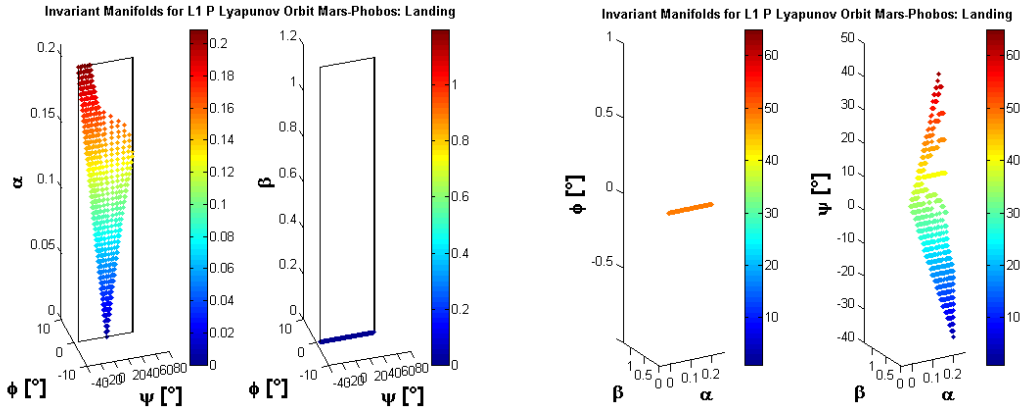

Figure D.4: **Landing on Phobos through the Invariant Manifold of the lp L_1 Planar Lyapunov orbits.** Direct and inverse relation between the longitude and latitude of the landing site and the α and β input of the lp algorithm, for orbits inside the region of convergence at the max order method. Phobos mean ellipsoidal surface.

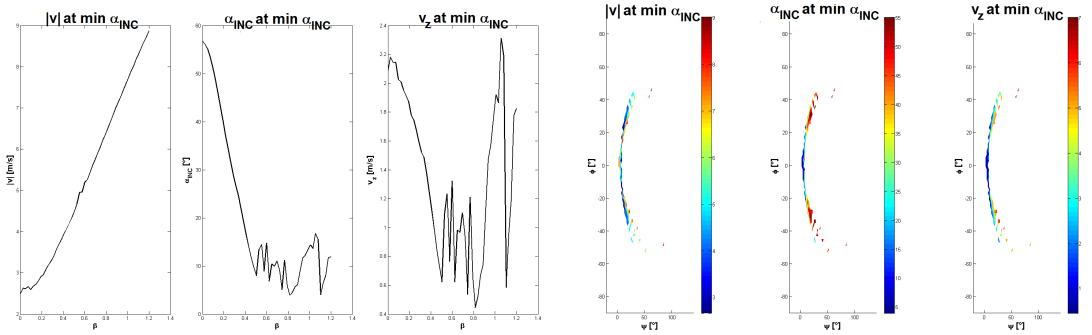

Figure D.5: **Landing on Phobos through the Invariant Manifold of the lp L_1 Vertical Lyapunov orbits.** Trajectories that provide the min incidence at the touch-down, as a function of the β input of the lp algorithm or the longitude and latitude of the landing site, for orbits inside the region of convergence at the max order method. Performances of the trajectory: landing velocity magnitude, angle of incidence, downward vertical velocity. Phobos mean ellipsoidal surface.

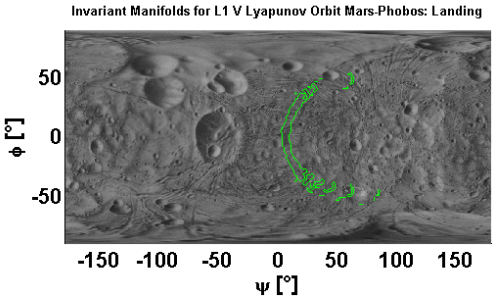

Figure D.6: **Landing on Phobos through the Invariant Manifold of the lp L_1 Vertical Lyapunov orbits.** Region of possible landing sites, for orbits inside the region of convergence at the max order method. Phobos mean ellipsoidal surface.

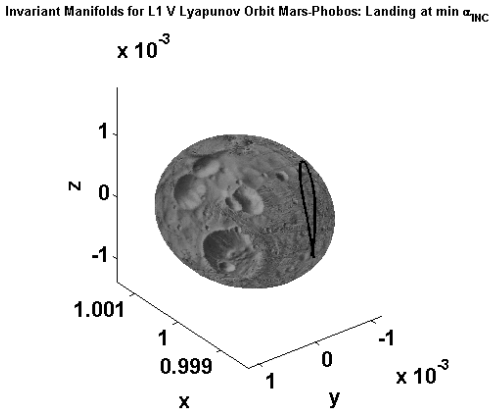

Figure D.7: **Landing on Phobos through the Invariant Manifold of the lp L_1 Vertical Lyapunov orbits.** Trajectory that provides the overall min incidence at the touch-down. Phobos mean ellipsoidal surface.

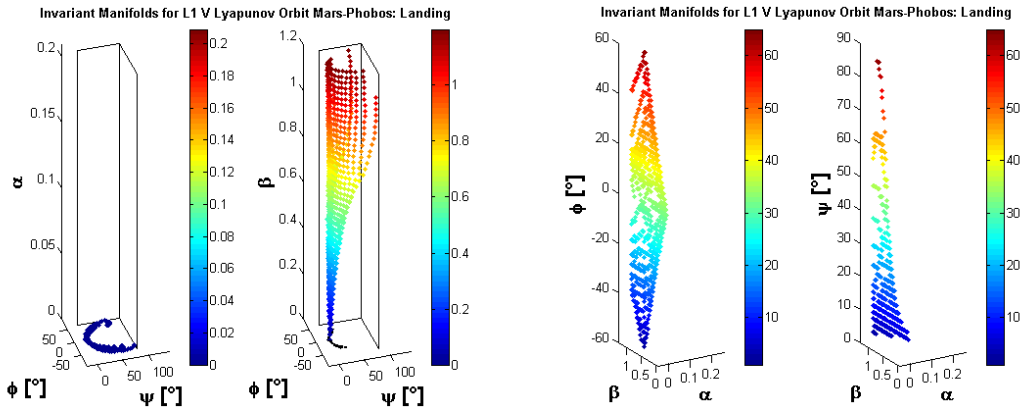

Figure D.8: **Landing on Phobos through the Invariant Manifold of the lp L_1 Vertical Lyapunov orbits.** Direct and inverse relation between the longitude and latitude of the landing site and the α and β input of the lp algorithm, for orbits inside the region of convergence at the max order method. Phobos mean ellipsoidal surface.

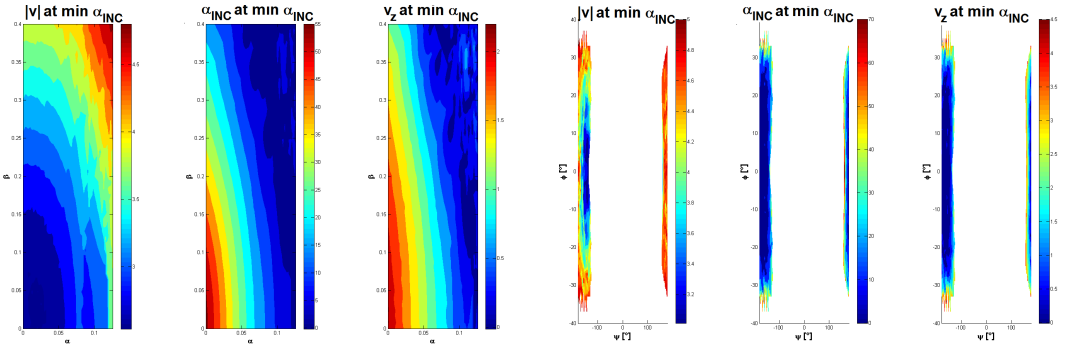

Figure D.9: **Landing on Phobos through the Invariant Manifold of the lp L_2 Lissajous orbits.** Trajectories that provide the min incidence at the touch-down, as a function of the α and β input of the lp algorithm or the longitude and latitude of the landing site, for orbits inside the region of convergence at the max order method. Performances of the trajectory: landing velocity magnitude, angle of incidence, downward vertical velocity. Phobos mean ellipsoidal surface.

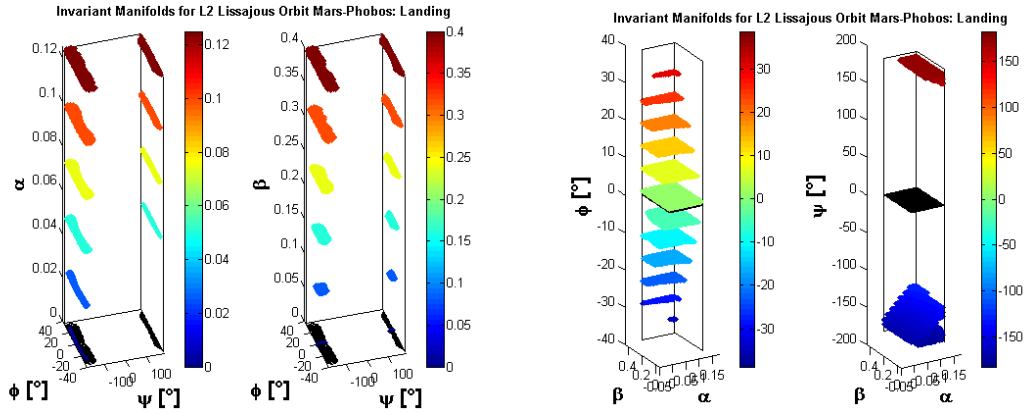

Figure D.10: **Landing on Phobos through the Invariant Manifold of the lp L_2 Lissajous orbits.** Direct and inverse relation between the longitude and latitude of the landing site and the α and β input of the lp algorithm, for orbits inside the region of convergence at the max order method. Phobos mean ellipsoidal surface.

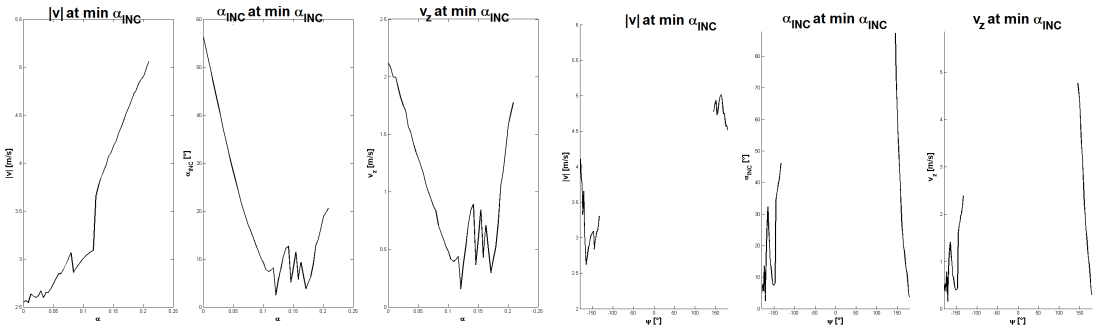

Figure D.11: **Landing on Phobos through the Invariant Manifold of the lp L_2 Planar Lyapunov orbits.** Trajectories that provide the min incidence at the touch-down, as a function of the α input of the lp algorithm or the longitude of the landing site, for orbits inside the region of convergence at the max order method. Performances of the trajectory: landing velocity magnitude, angle of incidence, downward vertical velocity. Phobos mean ellipsoidal surface.

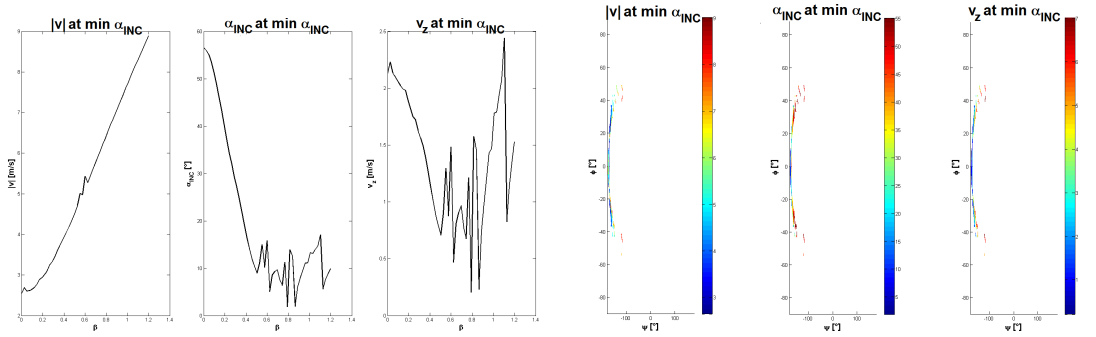

Figure D.12: **Landing on Phobos through the Invariant Manifold of the lp L_2 Vertical Lyapunov orbits.** Trajectories that provide the min incidence at the touch-down, as a function of the β input of the lp algorithm or the longitude and latitude of the landing site, for orbits inside the region of convergence at the max order method. Performances of the trajectory: landing velocity magnitude, angle of incidence, downward vertical velocity. Phobos mean ellipsoidal surface.

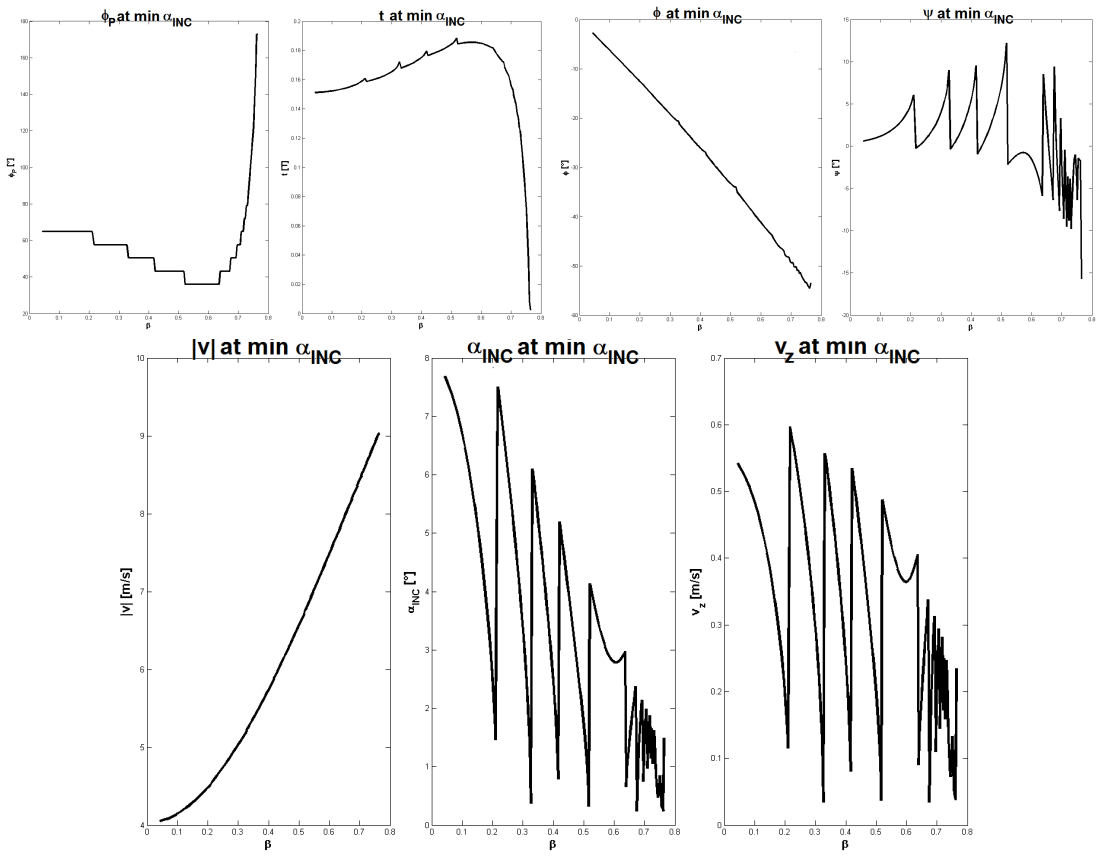

Figure D.13: **Landing on Phobos through the Invariant Manifold of the L_1 Northern Halo orbits.** Trajectories that provide the min incidence at the touch-down, as a function of the β input of the lp algorithm, for DC orbits that do not intersect Phobos mean ellipsoidal surface. Performances of the trajectory: initial planar phase along the departing Halo orbit, TOF, latitude and longitude of the landing site, and related velocity magnitude, angle of incidence, downward vertical velocity. Phobos mean ellipsoidal surface.

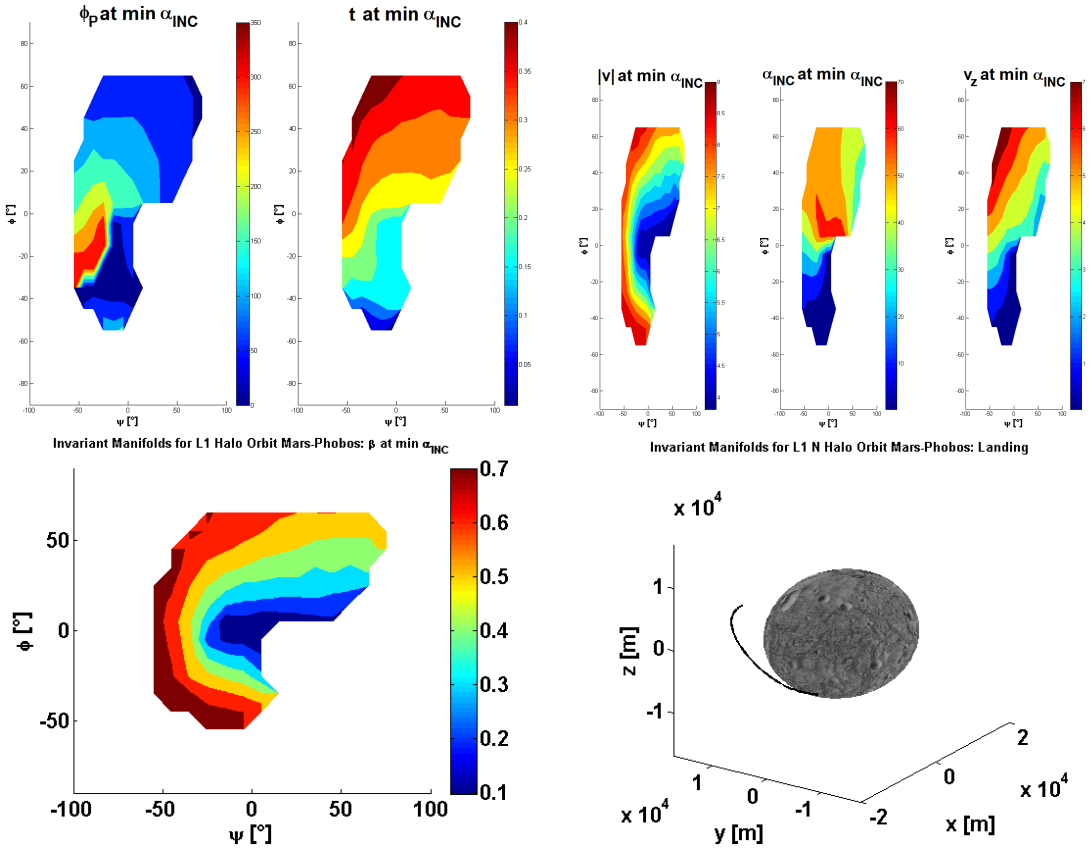

Figure D.14: **Landing on Phobos through the Invariant Manifold of the L_1 Northern Halo orbits.** Trajectories that provide the min incidence at the touch-down, as a function of the longitude and latitude of the landing site, for DC orbits that do not intersect Phobos mean ellipsoidal surface. Performances of the trajectory: initial planar phase along the departing Halo orbit, TOF, β input of the lp algorithm, and landing velocity magnitude, angle of incidence, downward vertical velocity. Trajectory that provides the overall min incidence at the touch-down. Phobos mean ellipsoidal surface.

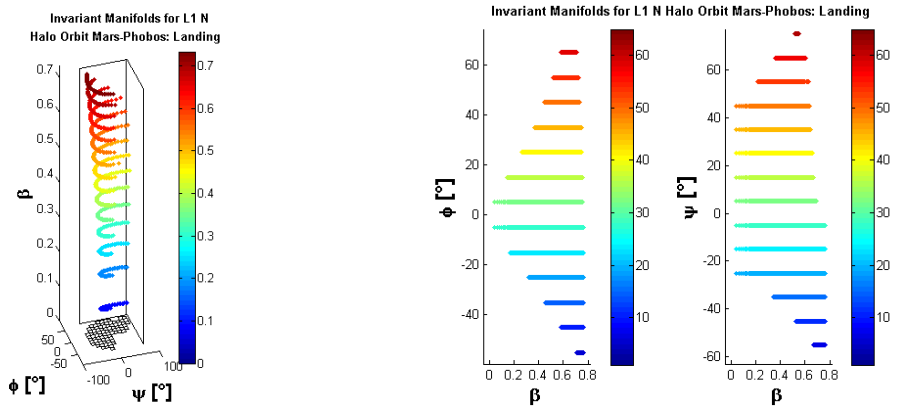

Figure D.15: **Landing on Phobos through the Invariant Manifold of the L_1 Northern Halo orbits.** Direct and inverse relation between the longitude and latitude of the landing site and the β input of the lp algorithm, for DC orbits that do not intersect Phobos mean ellipsoidal surface. Phobos mean ellipsoidal surface.

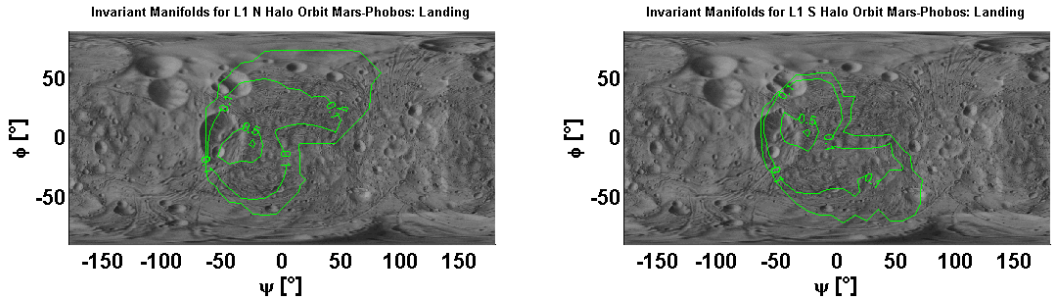

Figure D.16: **Landing on Phobos through the Invariant Manifold of the L_1 Northern and Southern Halo orbits.** Region of possible landing sites, for DC orbits that do not intersect Phobos mean ellipsoidal surface. Inner lines show subregions where the 10%, 50%, 90% levels of the cumulative distribution of the IM simulated landed (same number of trajectories from each departing orbit simulated). Phobos mean ellipsoidal surface.

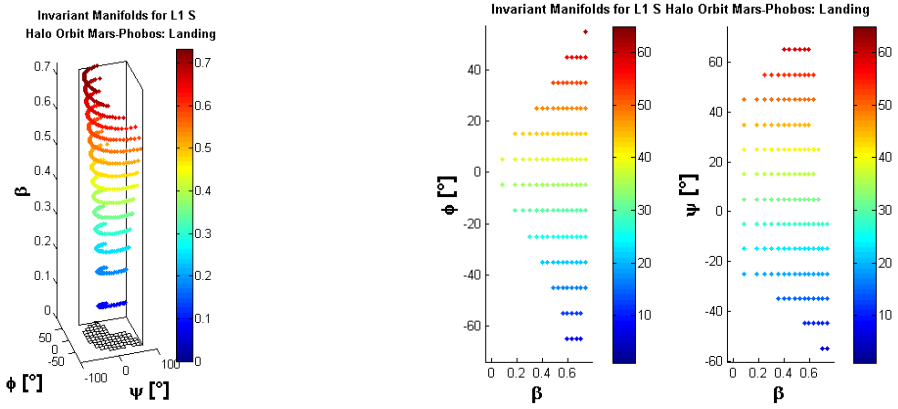

Figure D.17: **Landing on Phobos through the Invariant Manifold of the L_1 Southern Halo orbits.** Direct and inverse relation between the longitude and latitude of the landing site and the β input of the lp algorithm, for DC orbits that do not intersect Phobos mean ellipsoidal surface. Phobos mean ellipsoidal surface.

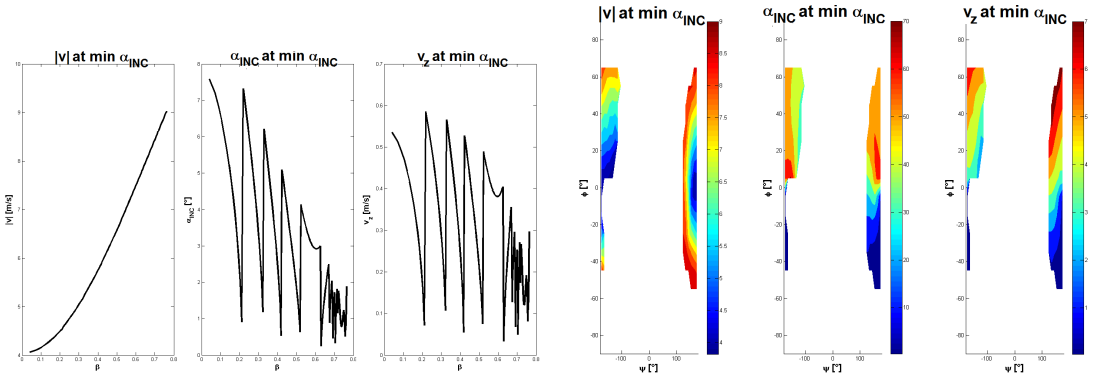

Figure D.18: **Landing on Phobos through the Invariant Manifold of the lp L_2 Northern Halo orbits.** Trajectories that provide the min incidence at the touch-down, as a function of the β input of the lp algorithm or the longitude and latitude of the landing site, for DC orbits that do not intersect Phobos mean ellipsoidal surface. Performances of the trajectory: landing velocity magnitude, angle of incidence, downward vertical velocity. Phobos mean ellipsoidal surface.

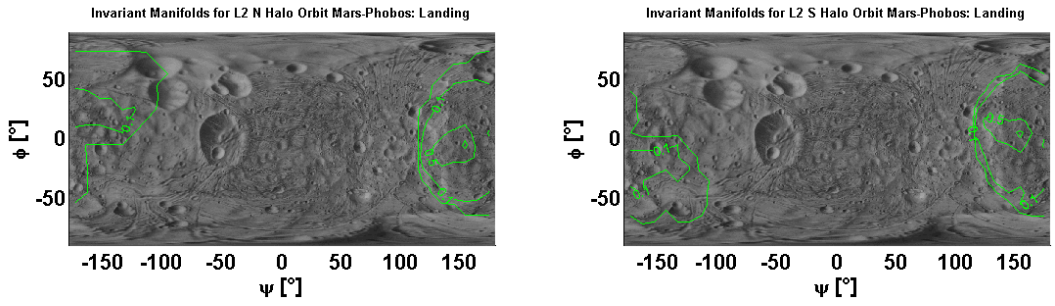

Figure D.19: **Landing on Phobos through the Invariant Manifold of the L_2 Northern and Southern Halo orbits.** Region of possible landing sites, for DC orbits that do not intersect Phobos mean ellipsoidal surface. Inner lines show subregions where the 10%, 50%, 90% levels of the cumulative distribution of the IM simulated landed (same number of trajectories from each departing orbit simulated). Phobos mean ellipsoidal surface.

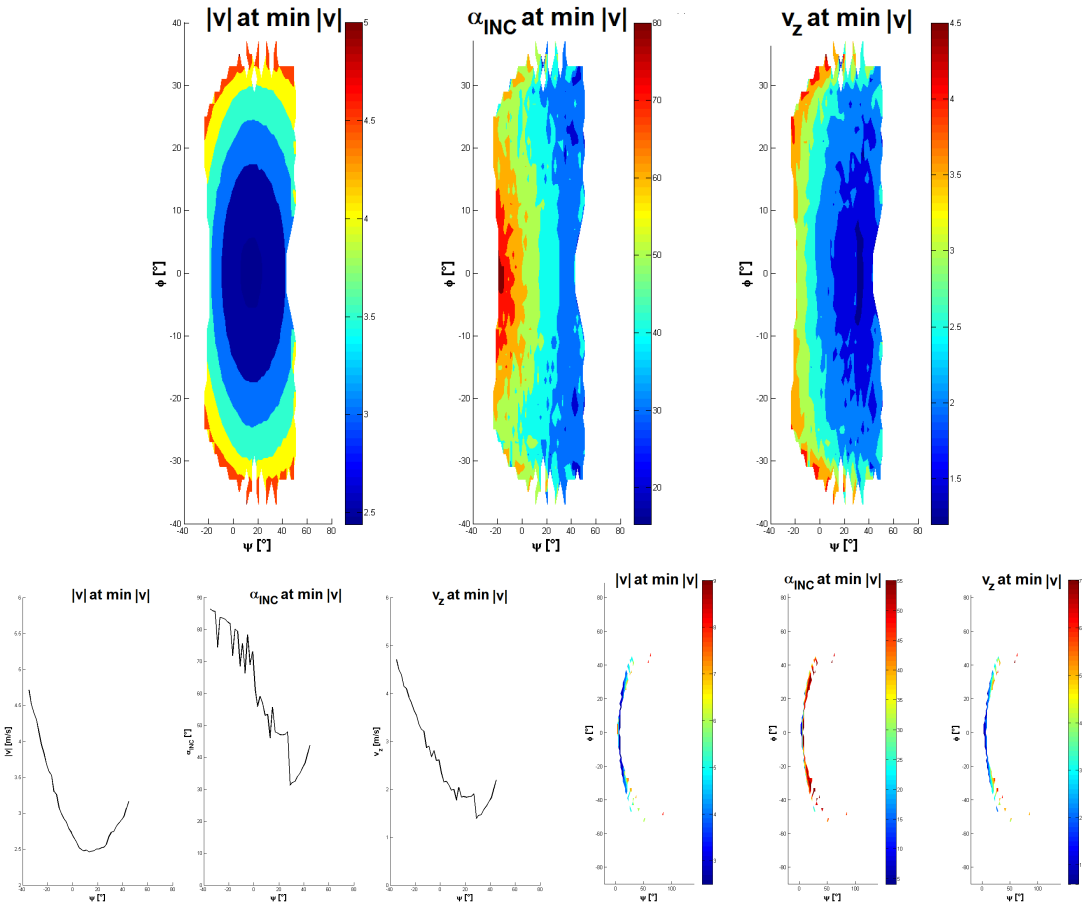

Figure D.20: **Landing on Phobos through the Invariant Manifold of the lp L_1 Lissajous and Planar and Vertical Lyapunov orbits.** Trajectories that provide the min velocity total magnitude at the touch-down, as a function of the longitude and latitude of the landing site, for orbits inside the region of convergence at the max order method. Performances of the trajectory: landing velocity magnitude, angle of incidence, downward vertical velocity. Phobos mean ellipsoidal surface.

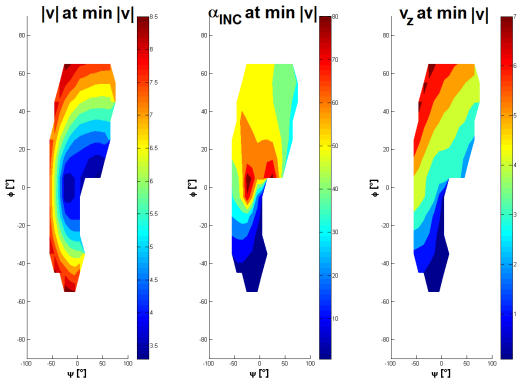

Figure D.21: **Landing on Phobos through the Invariant Manifold of the L_1 Northern Halo orbits.** Trajectories that provide the min velocity total magnitude at the touch-down, as a function of the longitude and latitude of the landing site, for DC orbits that do not intersect Phobos mean ellipsoidal surface. Performances of the trajectory: landing velocity magnitude, angle of incidence, downward vertical velocity. Phobos mean ellipsoidal surface.

D.2 LPOs of the Mars-Phobos CR3BP-GH

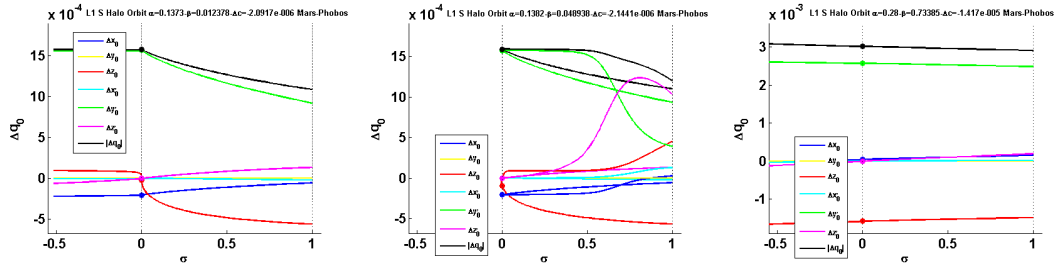

Figure D.22: **Periodic LPOs in the Mars-Phobos CR3BP-GH.** Continuation variables' curves profile. Continuation with respect to the GHs' magnitude from CR3BP ($\sigma = 0$) to full CR3BP-GH ($\sigma = 1$). Continuation of Southern Halo orbits around L_1 at increasing energy.

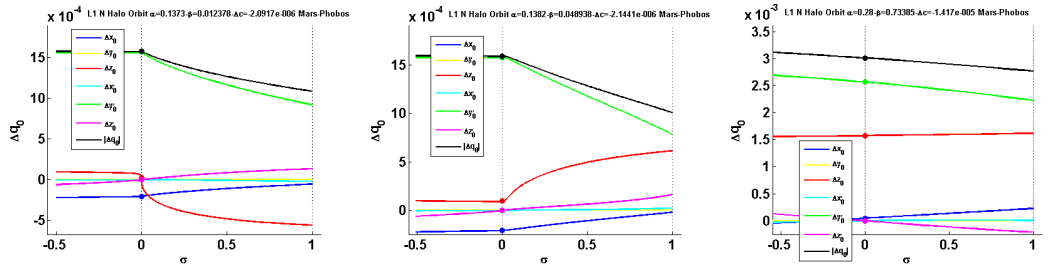

Figure D.23: **Periodic LPOs in the Mars-Phobos CR3BP-GH.** Continuation variables' curves profile. Continuation with respect to the GHs' magnitude from CR3BP ($\sigma = 0$) to full CR3BP-GH ($\sigma = 1$). Continuation of Northern Halo orbits around L_1 at increasing energy.

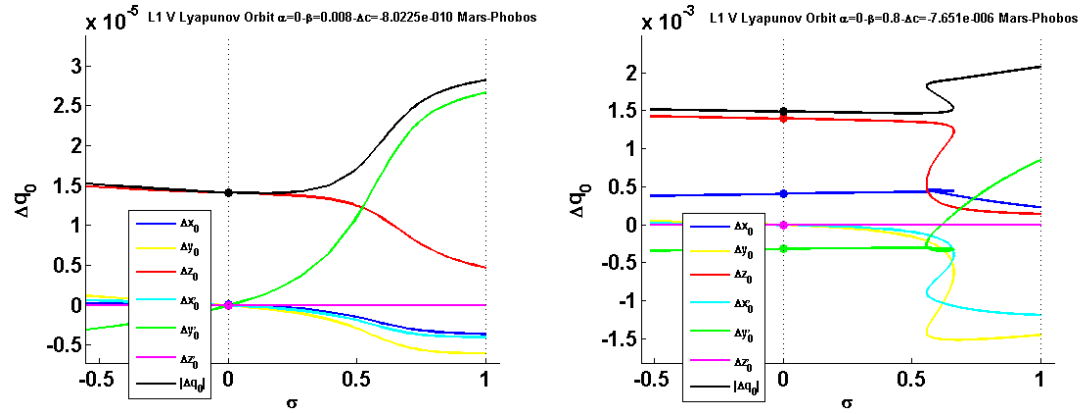

Figure D.24: **Periodic LPOs in the Mars-Phobos CR3BP-GH.** Continuation variables' curves profile. Continuation with respect to the GHs' magnitude from CR3BP ($\sigma = 0$) to full CR3BP-GH ($\sigma = 1$). Continuation of vertical Lyapunov orbits around L_1 at increasing energy.

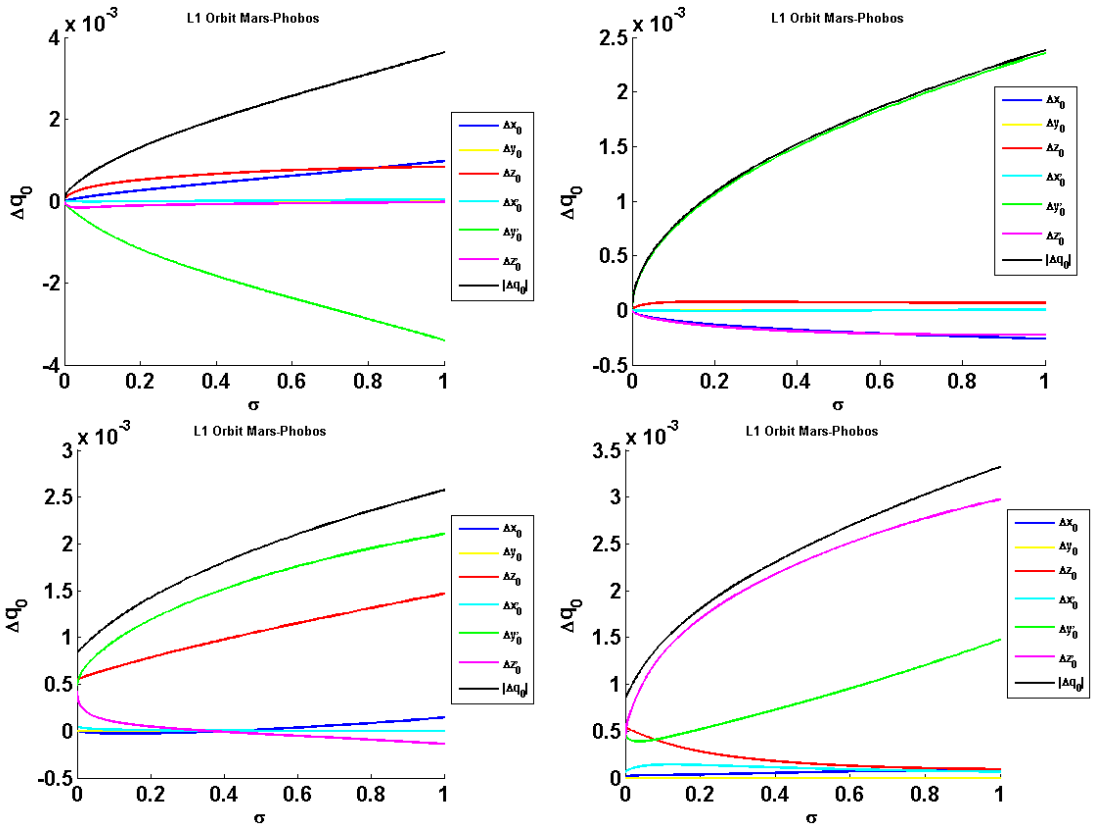

Figure D.25: **Periodic LPOs in the Mars-Phobos CR3BP-GH.** Continuation variables' curves profile for each family of POs around L_1 in the CR3BP-GH. Continuation with respect to the energy from L_1 ($\sigma = 0$) to the intersection with Phobos' surface ($\sigma = 1$).

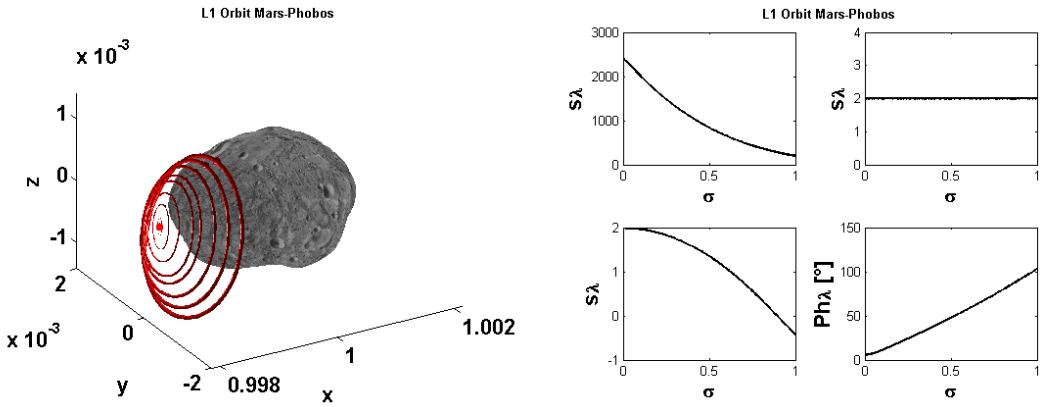

Figure D.26: **Periodic LPOs in the Mars-Phobos CR3BP-GH.** Graphical visualization and stability properties (the three stability indexes, with the phase of the center's eigenvalue) of the family A of POs around L_1 in the CR3BP-GH. Continuation with respect to the energy from L_1 ($\sigma = 0$) to the intersection with Phobos' surface ($\sigma = 1$).

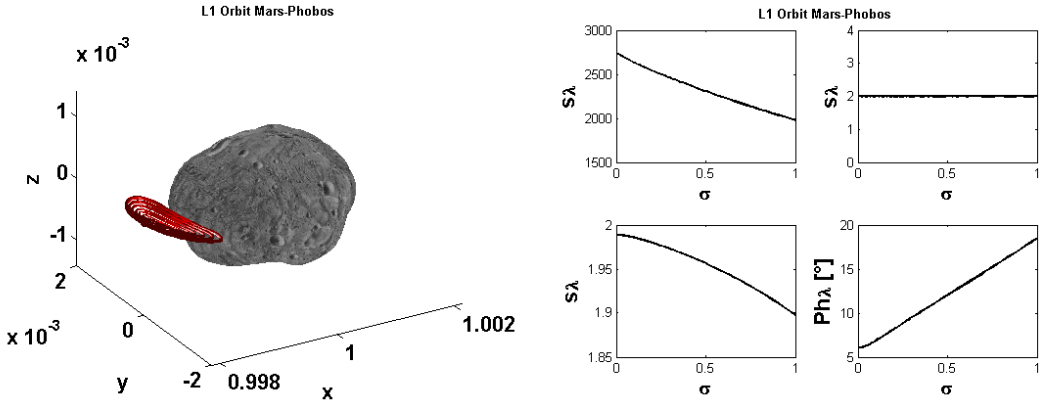

Figure D.27: **Periodic LPOs in the Mars-Phobos CR3BP-GH.** Graphical visualization and stability properties (the three stability indexes, with the phase of the center's eigenvalue) of the family B of POs around L_1 in the CR3BP-GH. Continuation with respect to the energy from L_1 ($\sigma = 0$) to the intersection with Phobos' surface ($\sigma = 1$).

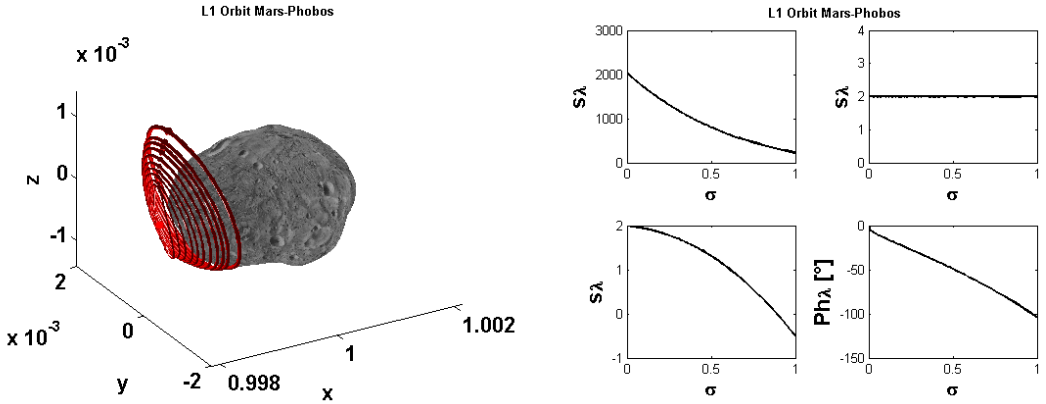

Figure D.28: **Periodic LPOs in the Mars-Phobos CR3BP-GH.** Graphical visualization and stability properties (the three stability indexes, with the phase of the center's eigenvalue) of the family C of POs around L_1 in the CR3BP-GH. Continuation with respect to the energy from L_1 ($\sigma = 0$) to the intersection with Phobos' surface ($\sigma = 1$).

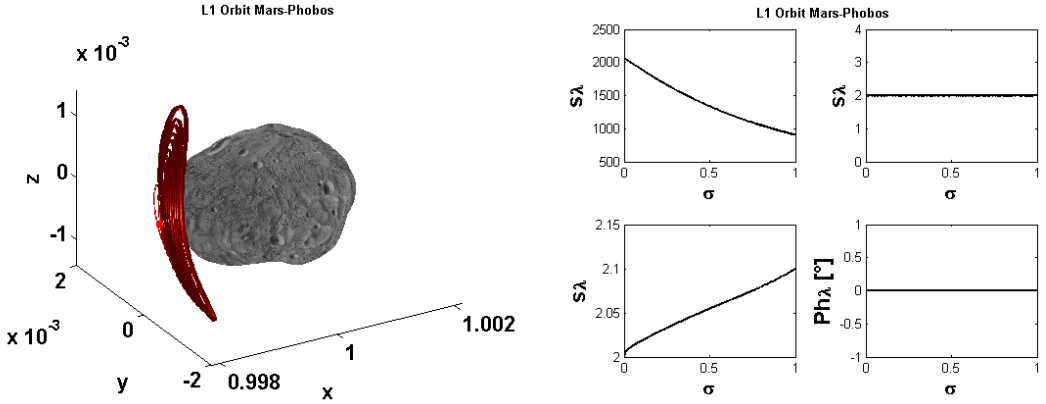

Figure D.29: **Periodic LPOs in the Mars-Phobos CR3BP-GH.** Graphical visualization and stability properties (the three stability indexes, with the phase of the center's eigenvalue) of the family D of POs around L_1 in the CR3BP-GH. Continuation with respect to the energy from L_1 ($\sigma = 0$) to the intersection with Phobos' surface ($\sigma = 1$).

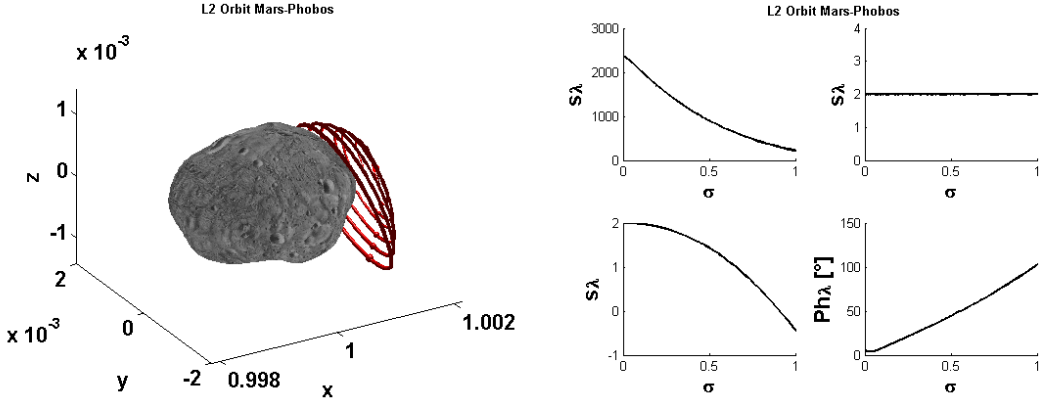

Figure D.30: **Periodic LPOs in the Mars-Phobos CR3BP-GH.** Graphical visualization and stability properties (the three stability indexes, with the phase of the center's eigenvalue) of the family A of POs around L_2 in the CR3BP-GH. Continuation with respect to the energy from L_2 ($\sigma = 0$) to the intersection with Phobos' surface ($\sigma = 1$).

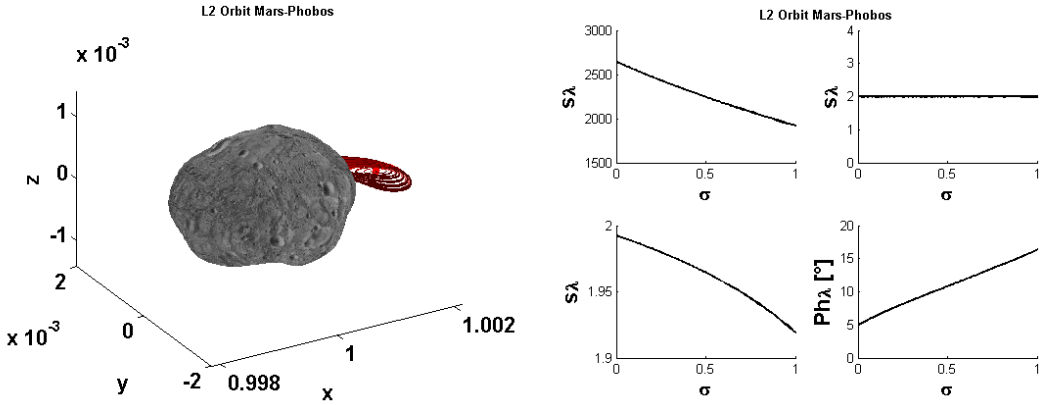

Figure D.31: **Periodic LPOs in the Mars-Phobos CR3BP-GH.** Graphical visualization and stability properties (the three stability indexes, with the phase of the center's eigenvalue) of the family B of POs around L_2 in the CR3BP-GH. Continuation with respect to the energy from L_2 ($\sigma = 0$) to the intersection with Phobos' surface ($\sigma = 1$).

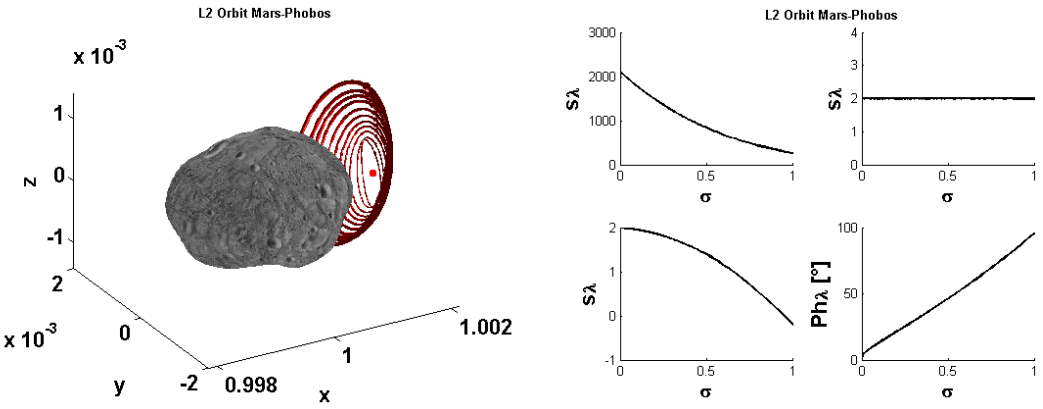

Figure D.32: **Periodic LPOs in the Mars-Phobos CR3BP-GH.** Graphical visualization and stability properties (the three stability indexes, with the phase of the center's eigenvalue) of the family C of POs around L_2 in the CR3BP-GH. Continuation with respect to the energy from L_2 ($\sigma = 0$) to the intersection with Phobos' surface ($\sigma = 1$).

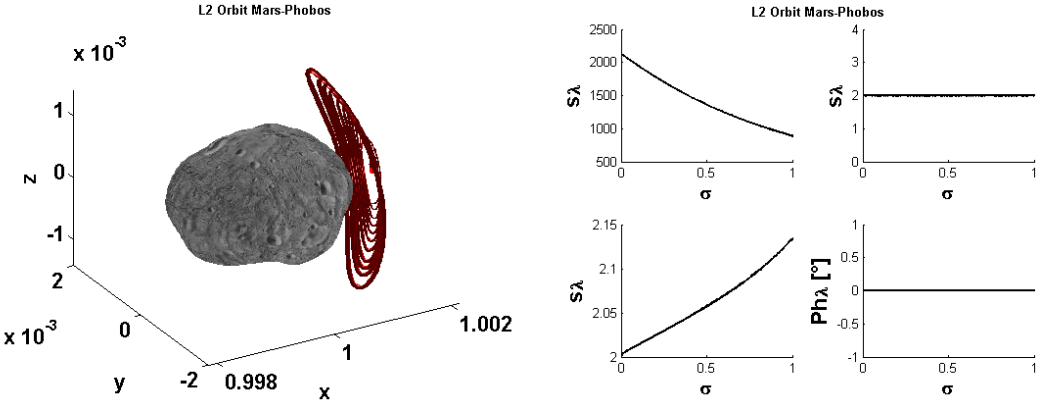

Figure D.33: **Periodic LPOs in the Mars-Phobos CR3BP-GH.** Graphical visualization and stability properties (the three stability indexes, with the phase of the center's eigenvalue) of the family D of POs around L_2 in the CR3BP-GH. Continuation with respect to the energy from L_2 ($\sigma = 0$) to the intersection with Phobos' surface ($\sigma = 1$).

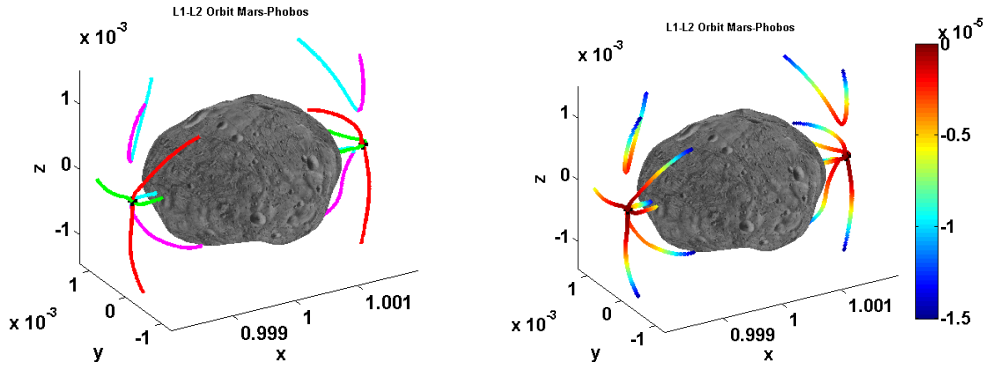

Figure D.34: **Periodic LPOs in the Mars-Phobos CR3BP-GH.** Characteristic curves of the families of POs around L_1 and L_2 in the CR3BP-GH, highlighting the position where the PO has the extreme distances from Phobos (the two branches showed for each family represent one the maximum and one the minimum distance). First picture identifies the family each curve belongs to, second picture shows the parametrization of the family's curve by the energy, defined as the differential Jacobi integral with respect to the LP.

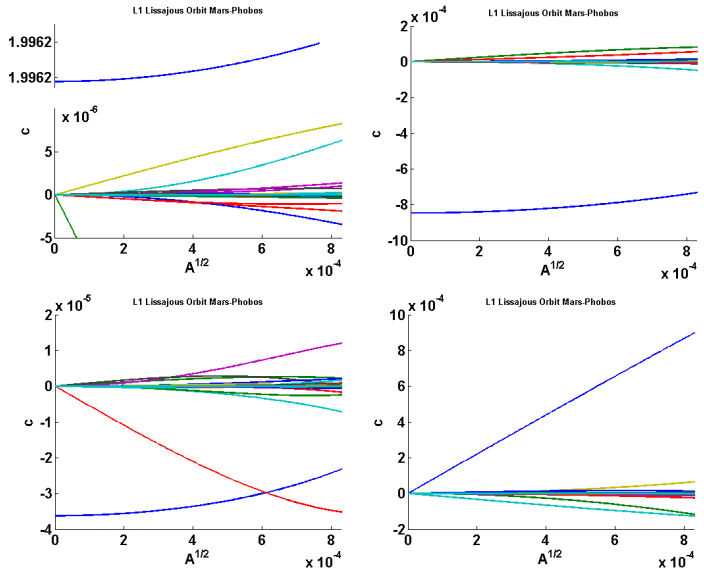

Figure D.35: **Quasi-periodic LPOs in the Mars-Phobos CR3BP-GH.** Continuation variables' curves profile, for the three curve's coordinates and the radial distance of the remaining two (case of polar anomaly parametrization). Continuation of QPOs around a medium-energy PO of the family A around L_1 of the CR3BP-GH, with respect to the area of the invariant curve on the plane that defines the parametrization of the invariant curve.

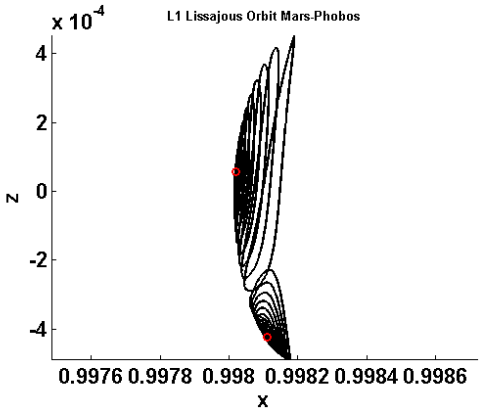

Figure D.36: **Quasi-periodic LPOs in the Mars-Phobos CR3BP-GH.** Family of invariant curves projected on a Poincaré map coordinate plane, connecting the two medium iso-energetic POs of the A and B families around L_1 of the CR3BP-GH.

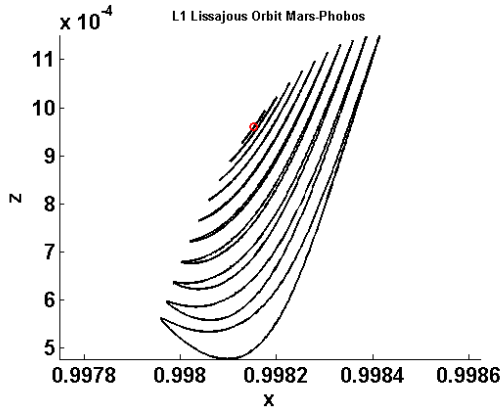

Figure D.37: **Quasi-periodic LPOs in the Mars-Phobos CR3BP-GH.** Family of invariant curves projected on a Poincaré map coordinate plane, around a medium-energy PO of the C family around L_1 of the CR3BP-GH.

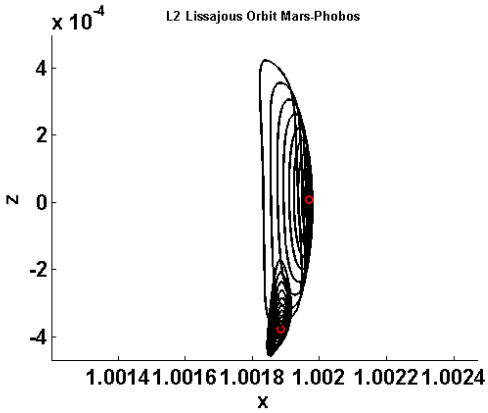

Figure D.38: **Quasi-periodic LPOs in the Mars-Phobos CR3BP-GH.** Family of invariant curves projected on a Poincaré map coordinate plane, connecting the two medium iso-energetic POs of the A and B families around L_2 of the CR3BP-GH.

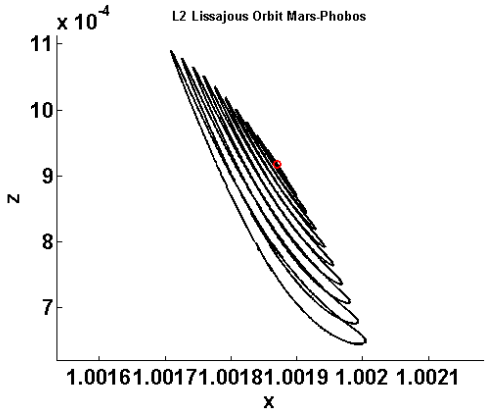

Figure D.39: **Quasi-periodic LPOs in the Mars-Phobos CR3BP-GH.** Family of invariant curves projected on a Poincaré map coordinate plane, around a medium-energy PO of the C family around L_2 of the CR3BP-GH.

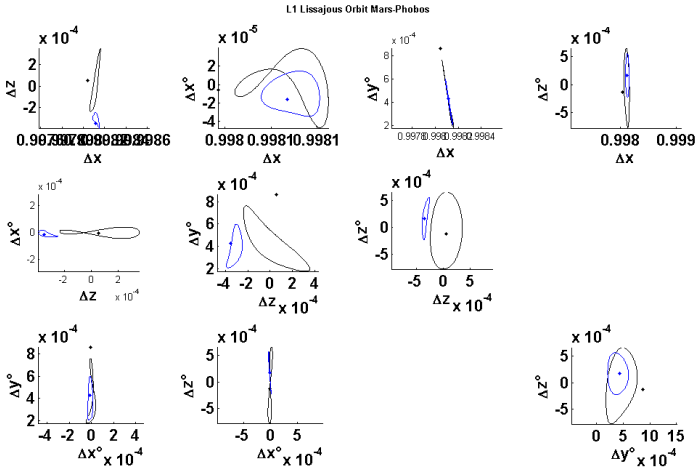

Figure D.40: **Quasi-periodic LPOs in the Mars-Phobos CR3BP-GH.** Projections on the coordinate planes of the invariant curve of the larger-width QPO around each of the two medium iso-energetic POs of the A and B family around L_1 of the CR3BP-GH, obtained by NC and using the polar anomaly parametrization.

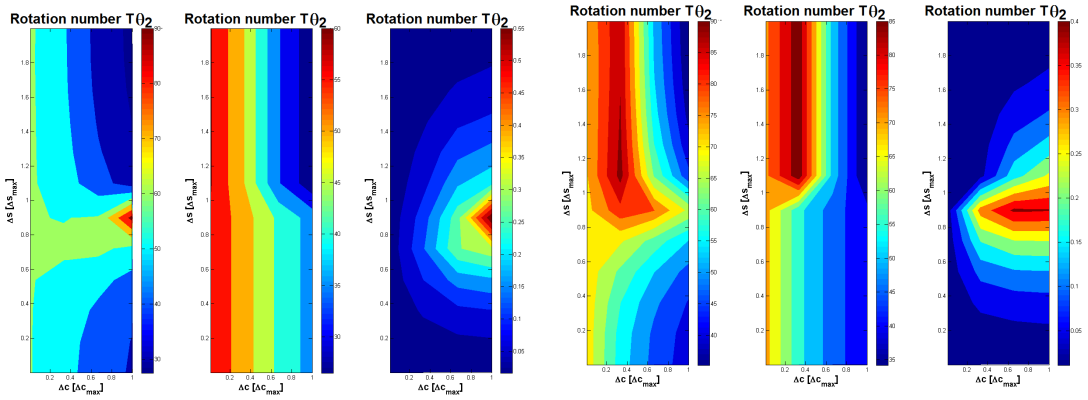

Figure D.41: **Quasi-periodic LPOs in the Mars-Phobos CR3BP-GH.** Period of the first transversal revolution of the 2-tori of the family AB around L_1 and L_2 of the CR3BP-GH. Values from the nonlinear and linear analysis, and related percentage error. The QPOs are parameterized by the CR3BP-GH's differential Jacobi integral and the width around the backbone PO, and they are normalized by their maximum values. The normalization of the width is conducted separately for the two A and B branches, then joined together reversing the parametrization of the B family, which is now defined in the interval from 2 to 1.

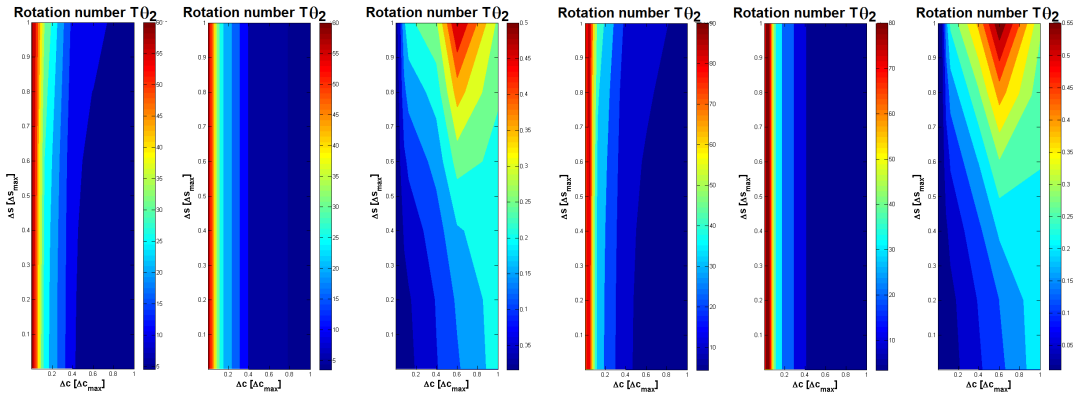

Figure D.42: **Quasi-periodic LPOs in the Mars-Phobos CR3BP-GH.** Period of the first transversal revolution of the 2-tori of the family A around L_1 and L_2 of the CR3BP-GH. Values from the nonlinear and linear analysis, and related percentage error.

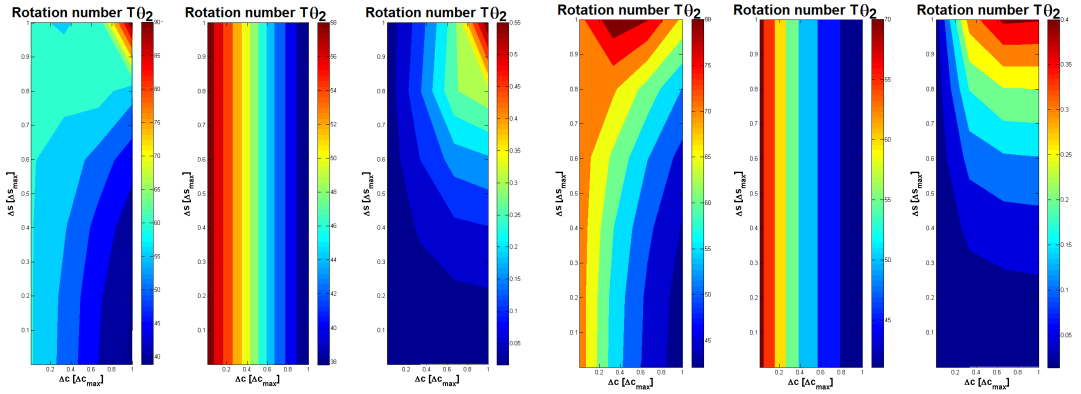

Figure D.43: **Quasi-periodic LPOs in the Mars-Phobos CR3BP-GH.** Period of the first transversal revolution of the 2-tori of the family B around L_1 and L_2 of the CR3BP-GH. Values from the nonlinear and linear analysis, and related percentage error.

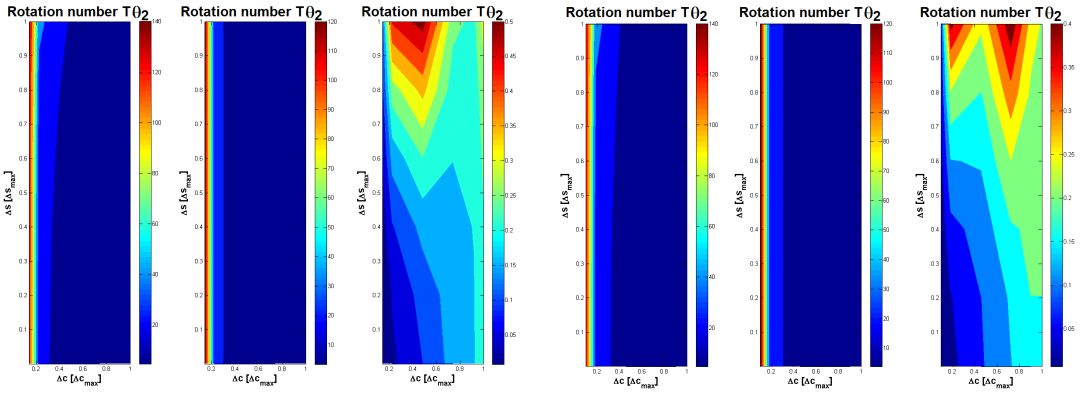

Figure D.44: **Quasi-periodic LPOs in the Mars-Phobos CR3BP-GH.** Period of the first transversal revolution of the 2-tori of the family C around L_1 and L_2 of the CR3BP-GH. Values from the nonlinear and linear analysis, and related percentage error.

D.3 Invariant Manifolds of the LPOs of the Mars-Phobos CR3BP-GH

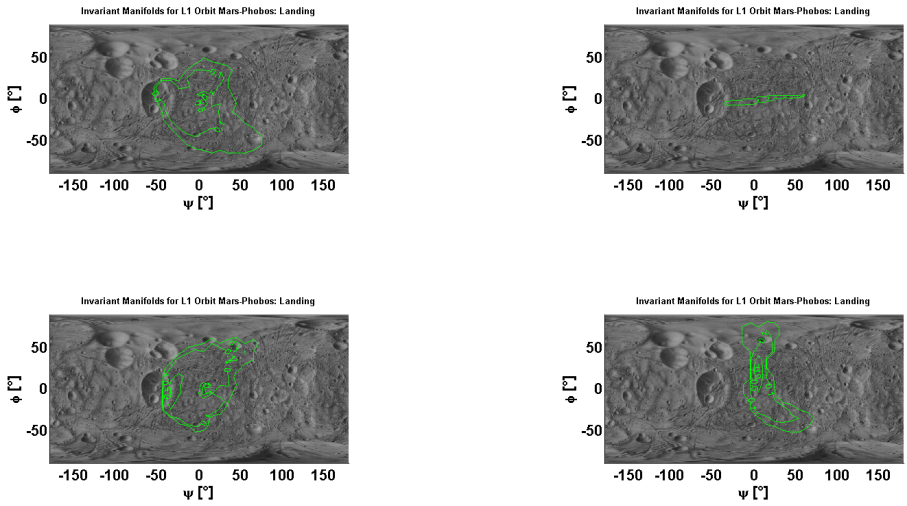

Figure D.45: **Landing on Phobos through the Invariant Manifold of the L_1 families of periodic LPOs of the Mars-Phobos CR3BP-GH.** Region of possible landing sites, for orbits that do not intersect Phobos' real shape. Inner lines show subregions where the 10%, 50%, 90% levels of the cumulative distribution of the IM simulated landed (same number of trajectories from each departing orbit simulated). Phobos real shape.

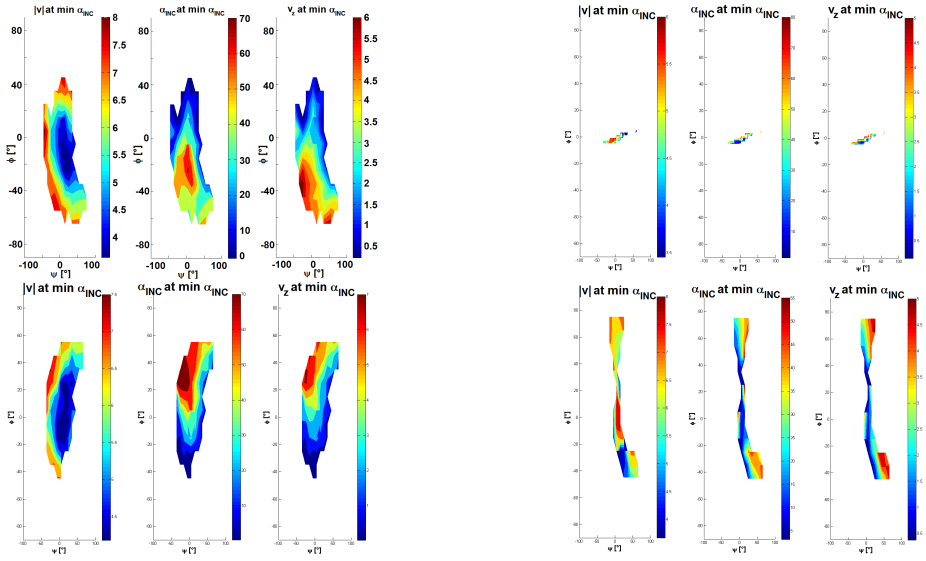

Figure D.46: **Landing on Phobos through the Invariant Manifold of the L_1 families of periodic LPOs of the Mars-Phobos CR3BP-GH.** Trajectories that provide the min incidence at the touch-down, as a function of the longitude and latitude of the landing site, for orbits that do not intersect Phobos' real shape. Performances of the trajectory: landing velocity magnitude, angle of incidence, downward vertical velocity. Phobos real shape.

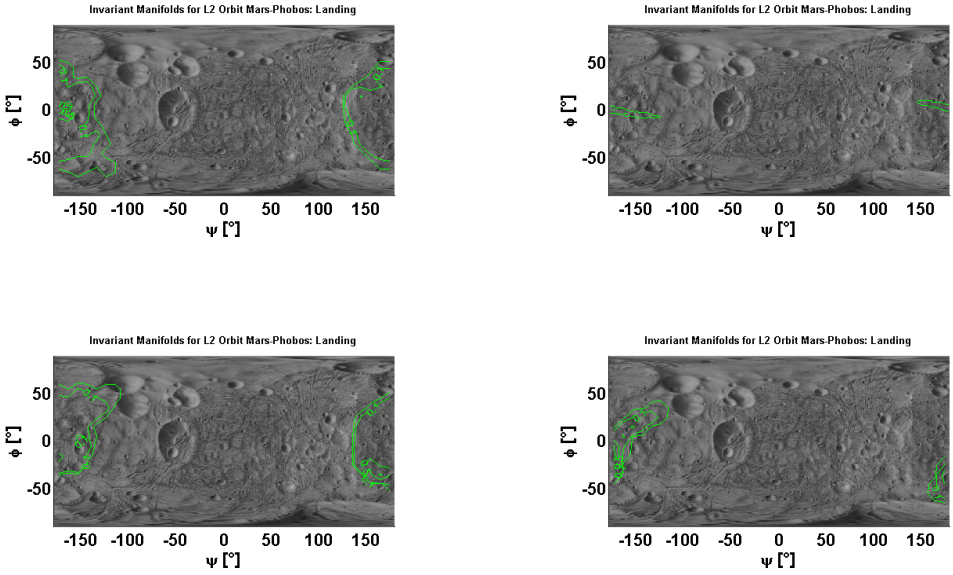

Figure D.47: **Landing on Phobos through the Invariant Manifold of the L_2 families of periodic LPOs of the Mars-Phobos CR3BP-GH.** Region of possible landing sites, for orbits that do not intersect Phobos' real shape. Inner lines show subregions where the 10%, 50%, 90% levels of the cumulative distribution of the IM simulated landed (same number of trajectories from each departing orbit simulated). Phobos real shape.

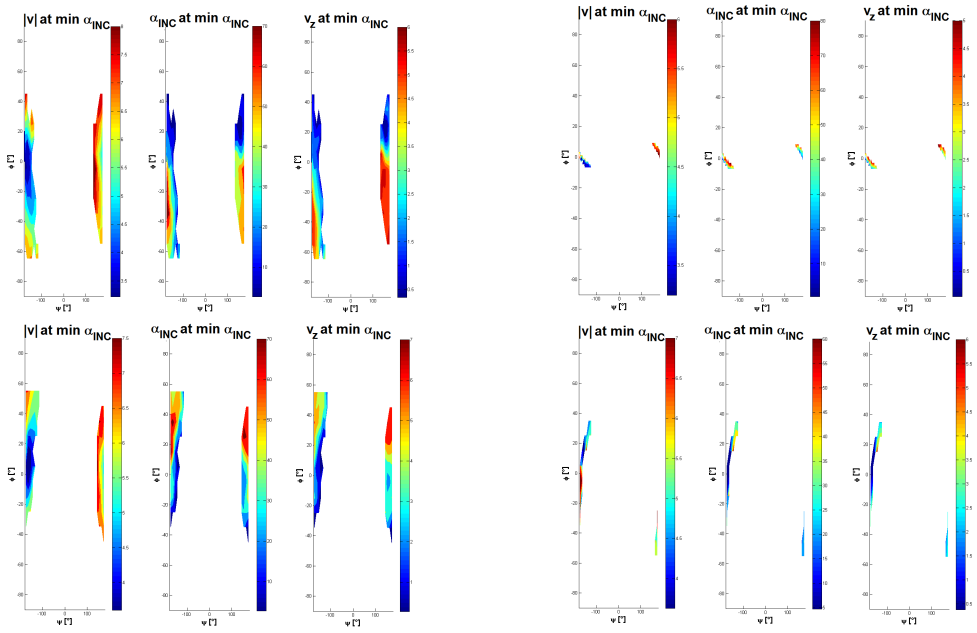

Figure D.48: **Landing on Phobos through the Invariant Manifold of the L_2 families of periodic LPOs of the Mars-Phobos CR3BP-GH.** Trajectories that provide the min incidence at the touch-down, as a function of the longitude and latitude of the landing site, for orbits that do not intersect Phobos' real shape. Performances of the trajectory: landing velocity magnitude, angle of incidence, downward vertical velocity. Phobos real shape.

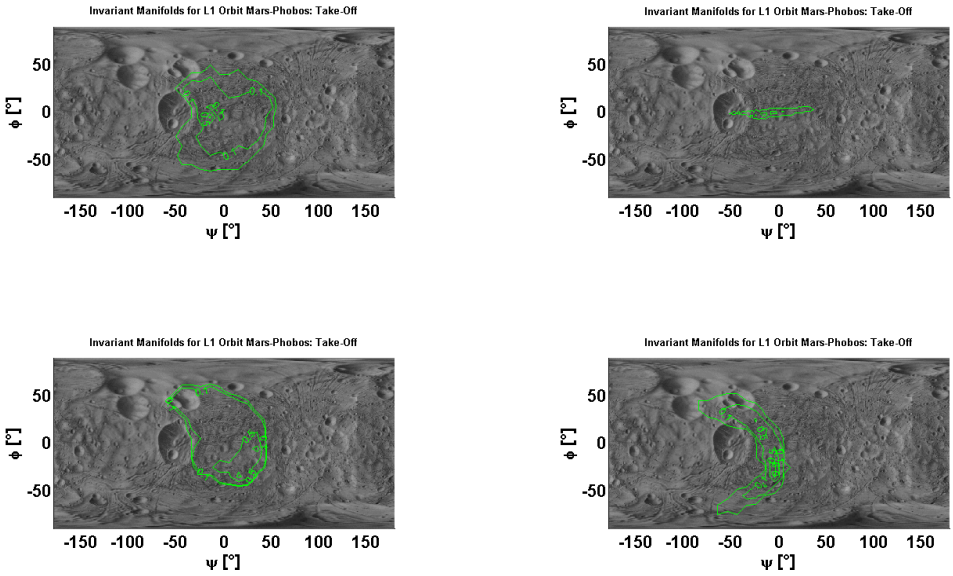

Figure D.49: **Take-off from Phobos through the Invariant Manifold of the L_1 families of periodic LPOs of the Mars-Phobos CR3BP-GH.** Region of possible departure sites, for orbits that do not intersect Phobos' real shape. Inner lines show subregions where the 10%, 50%, 90% levels of the cumulative distribution of the IM simulated departed (same number of trajectories from each departing orbit simulated). Phobos real shape.

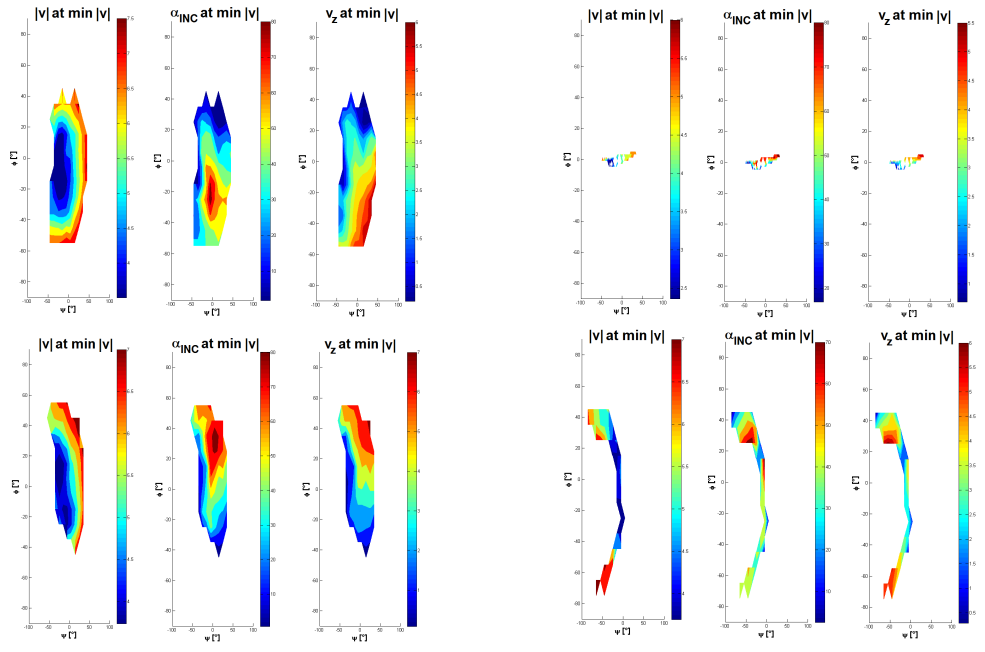

Figure D.50: **Take-off from Phobos through the Invariant Manifold of the L_1 families of periodic LPOs of the Mars-Phobos CR3BP-GH.** Trajectories that provide the min velocity total magnitude at the launch, as a function of the longitude and latitude of the departure site, for orbits that do not intersect Phobos' real shape. Performances of the trajectory: departure velocity magnitude, angle of incidence, upward vertical velocity. Phobos real shape.

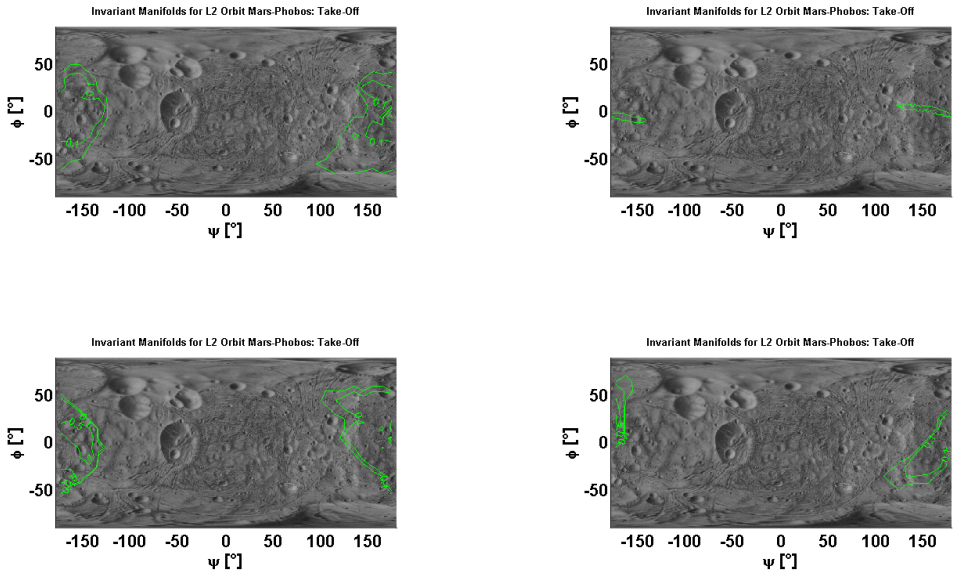

Figure D.51: **Take-off from Phobos through the Invariant Manifold of the L_2 families of periodic LPOs of the Mars-Phobos CR3BP-GH.** Region of possible departure sites, for orbits that do not intersect Phobos' real shape. Inner lines show subregions where the 10%, 50%, 90% levels of the cumulative distribution of the IM simulated departed (same number of trajectories from each departing orbit simulated). Phobos real shape.

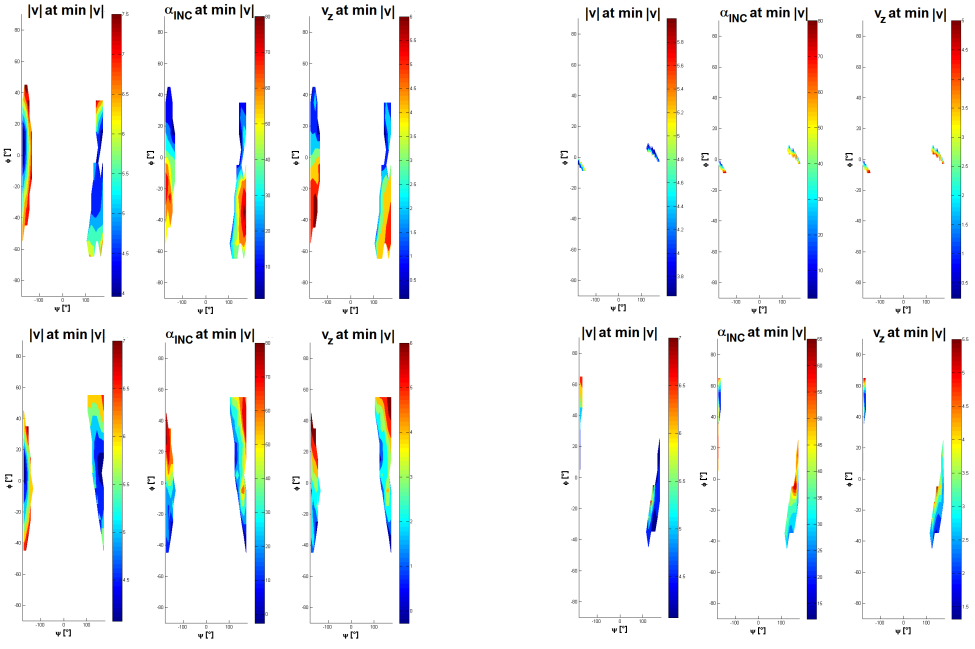

Figure D.52: **Take-off from Phobos through the Invariant Manifold of the L_2 families of periodic LPOs of the Mars-Phobos CR3BP-GH.** Trajectories that provide the min velocity total magnitude at the launch, as a function of the longitude and latitude of the departure site, for orbits that do not intersect Phobos' real shape. Performances of the trajectory: departure velocity magnitude, angle of incidence, upward vertical velocity. Phobos real shape.

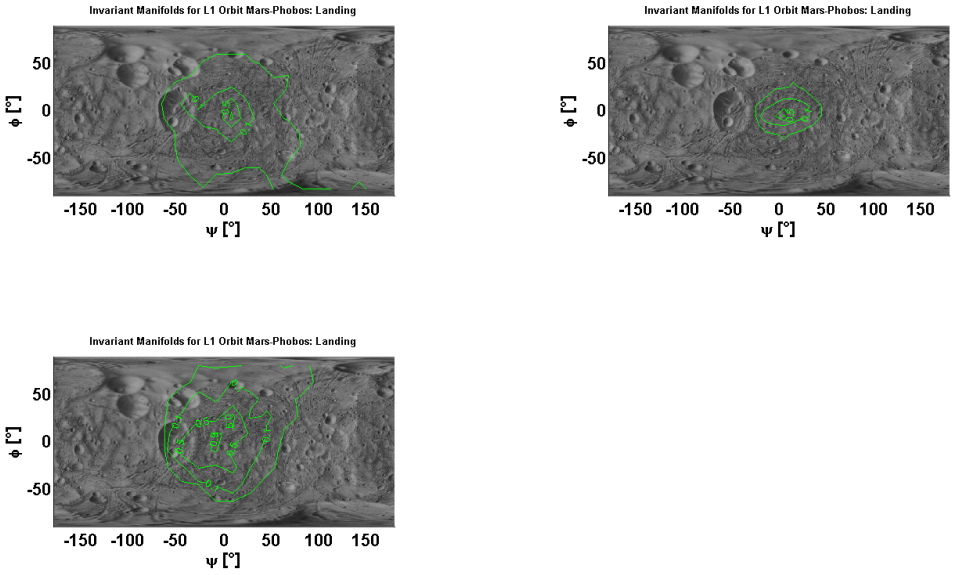

Figure D.53: **Landing on Phobos through the Invariant Manifold of the L_1 families of quasi-periodic LPOs of the Mars-Phobos CR3BP-GH.** Region of possible landing sites, for orbits that do not intersect Phobos' real shape. Inner lines show subregions where the 10%, 50%, 90% levels of the cumulative distribution of the IM simulated landed (same number of trajectories from each departing orbit simulated). Phobos real shape.

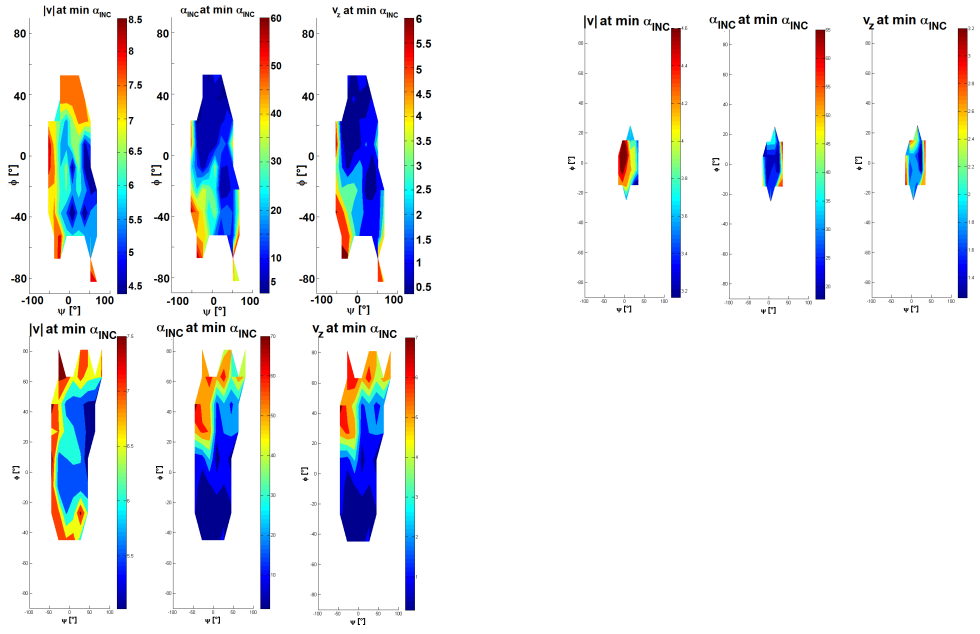

Figure D.54: **Landing on Phobos through the Invariant Manifold of the L_1 families of quasi-periodic LPOs of the Mars-Phobos CR3BP-GH.** Trajectories that provide the min incidence at the touch-down, as a function of the longitude and latitude of the landing site, for orbits that do not intersect Phobos' real shape. Performances of the trajectory: landing velocity magnitude, angle of incidence, downward vertical velocity. Phobos real shape.

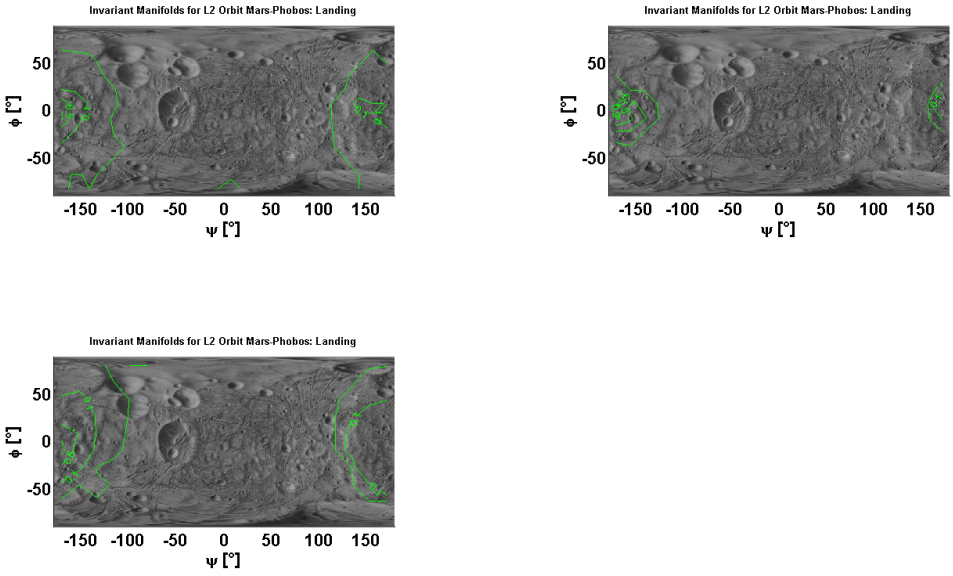

Figure D.55: **Landing on Phobos through the Invariant Manifold of the L_2 families of quasi-periodic LPOs of the Mars-Phobos CR3BP-GH.** Region of possible landing sites, for orbits that do not intersect Phobos' real shape. Inner lines show subregions where the 10%, 50%, 90% levels of the cumulative distribution of the IM simulated landed (same number of trajectories from each departing orbit simulated). Phobos real shape.

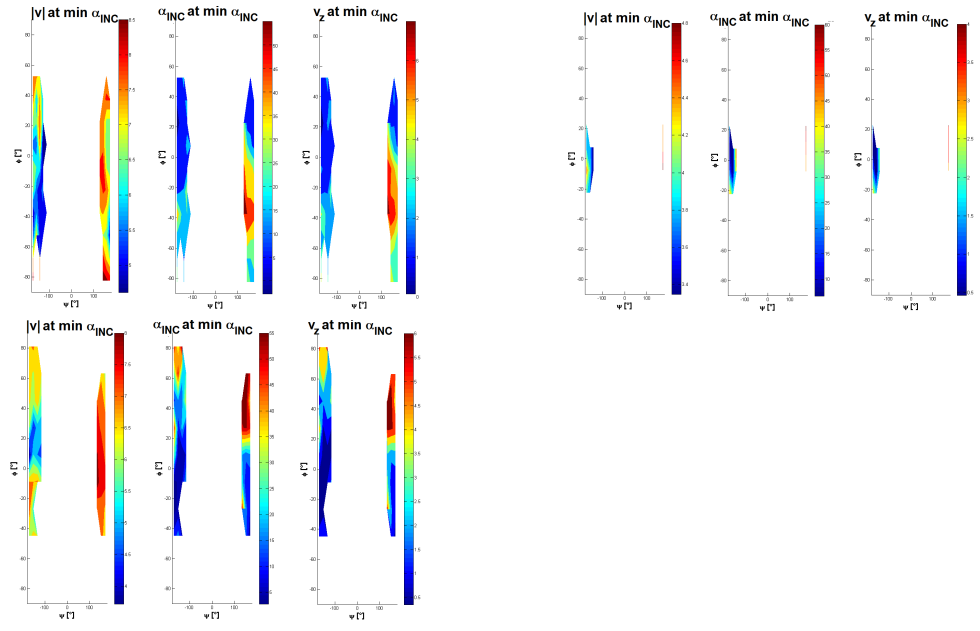

Figure D.56: **Landing on Phobos through the Invariant Manifold of the L_2 families of quasi-periodic LPOs of the Mars-Phobos CR3BP-GH.** Trajectories that provide the min incidence at the touch-down, as a function of the longitude and latitude of the landing site, for orbits that do not intersect Phobos' real shape. Performances of the trajectory: landing velocity magnitude, angle of incidence, downward vertical velocity. Phobos real shape.

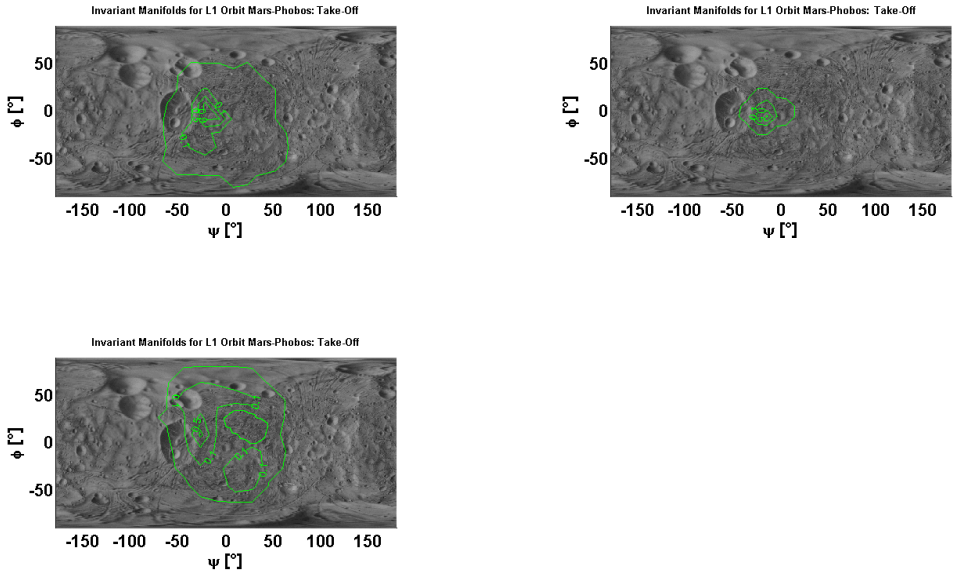

Figure D.57: **Take-off from Phobos through the Invariant Manifold of the L_1 families of quasi-periodic LPOs of the Mars-Phobos CR3BP-GH.** Region of possible departure sites, for orbits that do not intersect Phobos' real shape. Inner lines show subregions where the 10%, 50%, 90% levels of the cumulative distribution of the IM simulated departed (same number of trajectories from each departing orbit simulated). Phobos real shape.

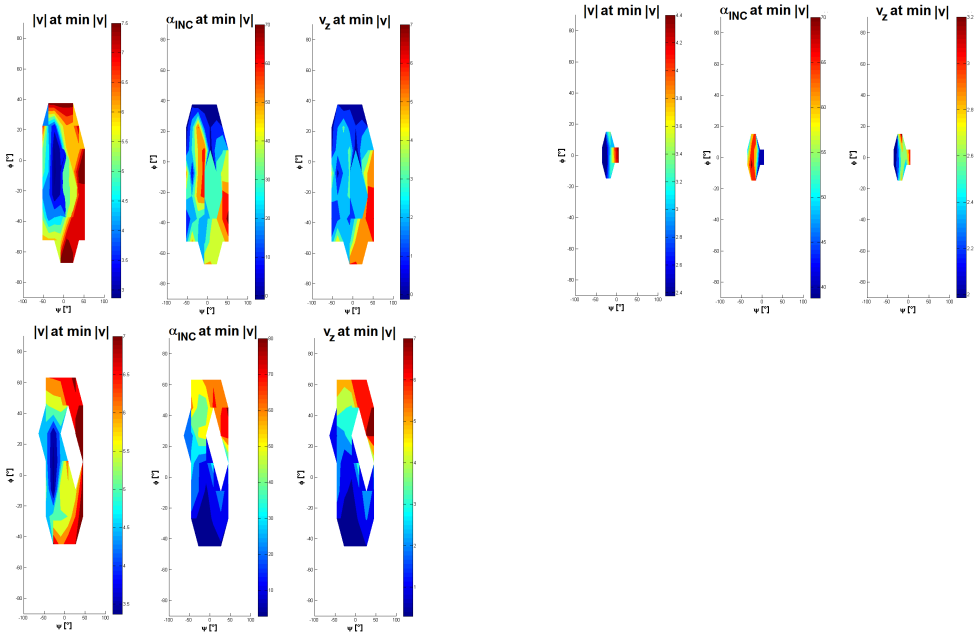

Figure D.58: **Take-off from Phobos through the Invariant Manifold of the L_1 families of quasi-periodic LPOs of the Mars-Phobos CR3BP-GH.** Trajectories that provide the min velocity total magnitude at the launch, as a function of the longitude and latitude of the departure site, for orbits that do not intersect Phobos' real shape. Performances of the trajectory: departure velocity magnitude, angle of incidence, upward vertical velocity. Phobos real shape.

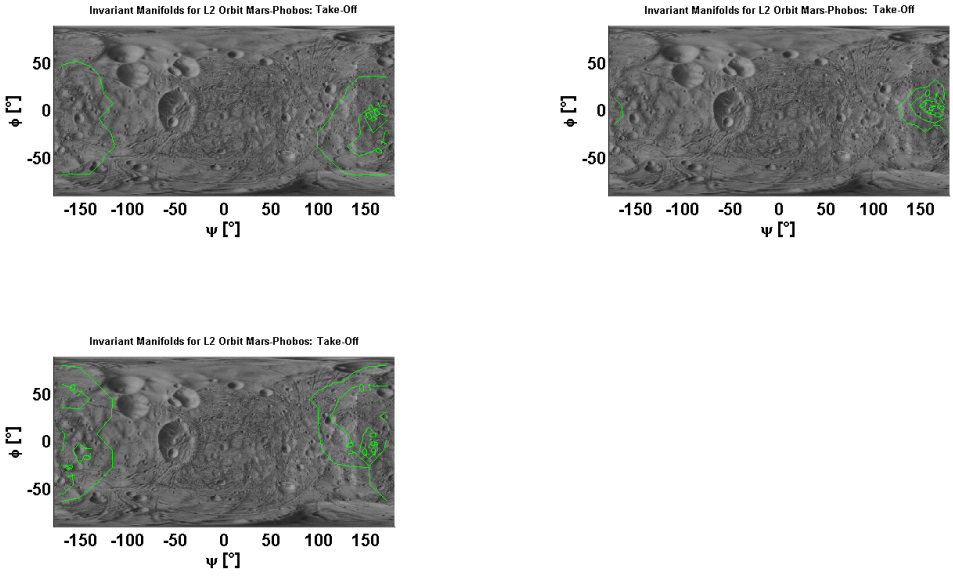

Figure D.59: **Take-off from Phobos through the Invariant Manifold of the L_2 families of quasi-periodic LPOs of the Mars-Phobos CR3BP-GH.** Region of possible departure sites, for orbits that do not intersect Phobos' real shape. Inner lines show subregions where the 10%, 50%, 90% levels of the cumulative distribution of the IM simulated departed (same number of trajectories from each departing orbit simulated). Phobos real shape.

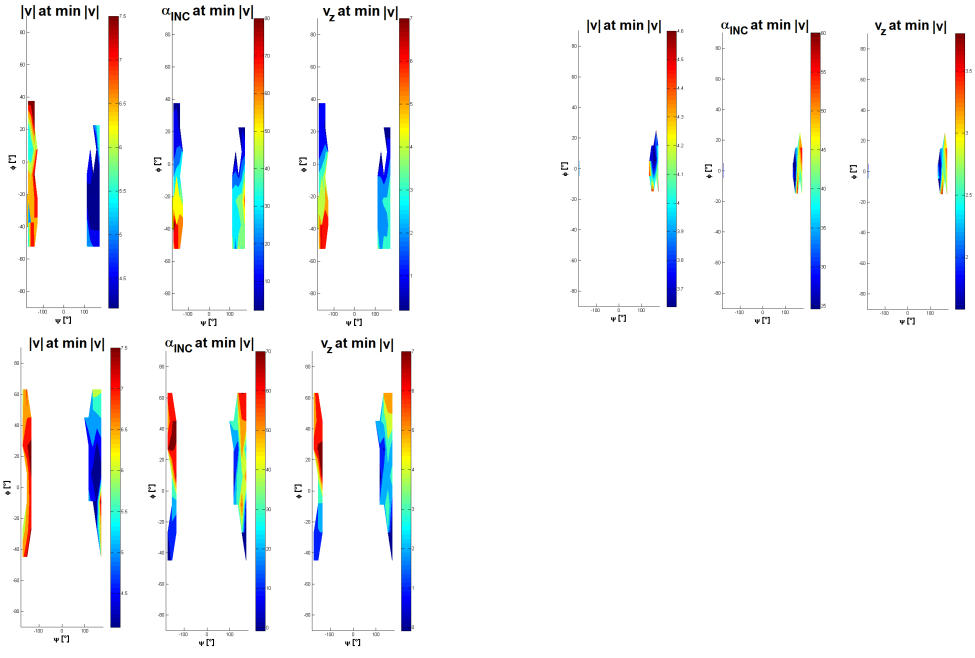

Figure D.60: **Take-off from Phobos through the Invariant Manifold of the L_2 families of quasi-periodic LPOs of the Mars-Phobos CR3BP-GH.** Trajectories that provide the min velocity total magnitude at the launch, as a function of the longitude and latitude of the departure site, for orbits that do not intersect Phobos' real shape. Performances of the trajectory: departure velocity magnitude, angle of incidence, upward vertical velocity. Phobos real shape.

D.4 LPOs of the Mars-Phobos ER3BP-GH

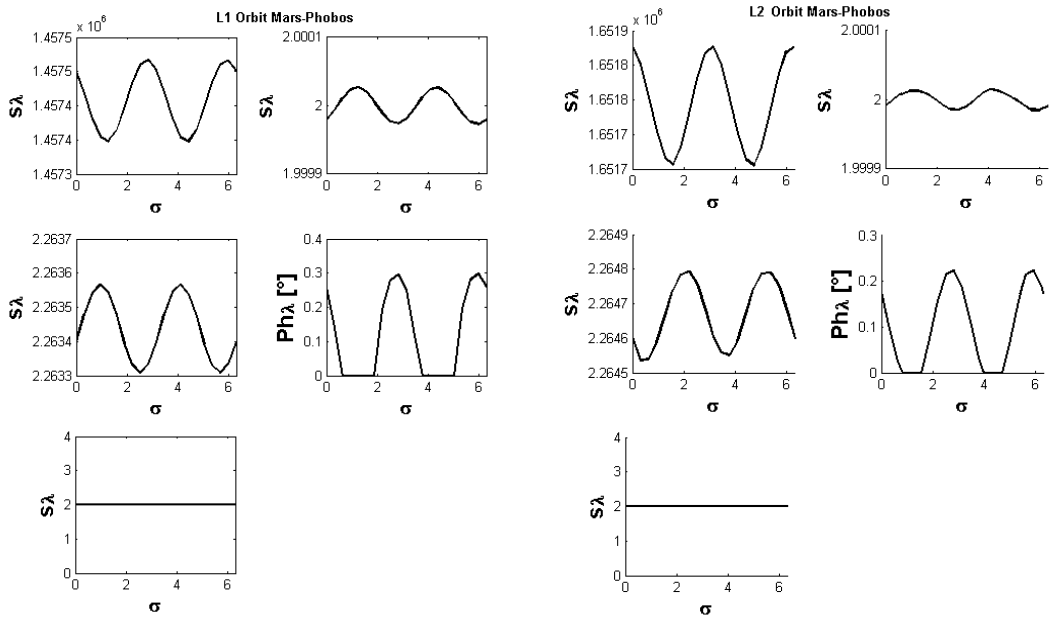

Figure D.61: **Periodic LPOs in the Mars-Phobos ER3BP-GH.** Stability properties (stability indexes of the three couples of eigenvalues, plus the additional anomaly's eigenvalue, of the monodromy matrix, with the phase of the complex couple) of the POs of the family D around L_1 and L_2 in the ER3BP-GH. Continuation with respect to the initial Phobos true anomaly from pericenter ($\sigma = 0rad$) to apocenter ($\sigma = \pi rad$).

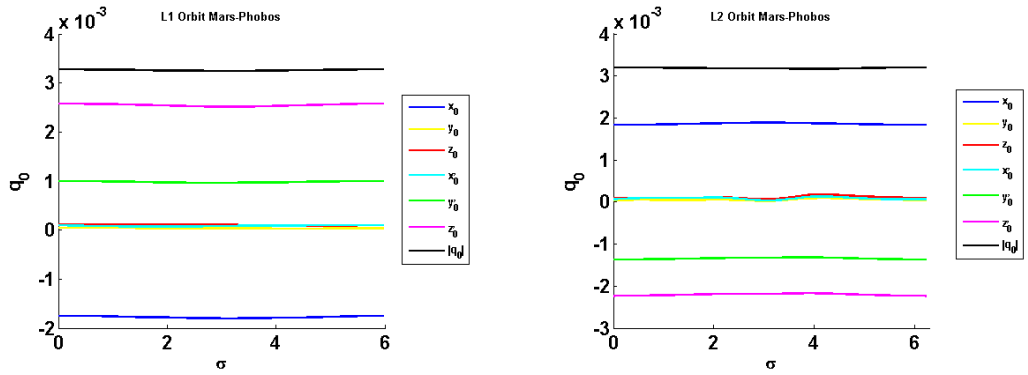

Figure D.62: **Periodic LPOs in the Mars-Phobos ER3BP-GH.** Continuation variables' curves profile. Continuation with respect to the initial Phobos true anomaly from pericenter ($\sigma = 0rad$) to apocenter ($\sigma = \pi rad$) of the PO of the family D around L_1 and L_2 in the ER3BP-GH.

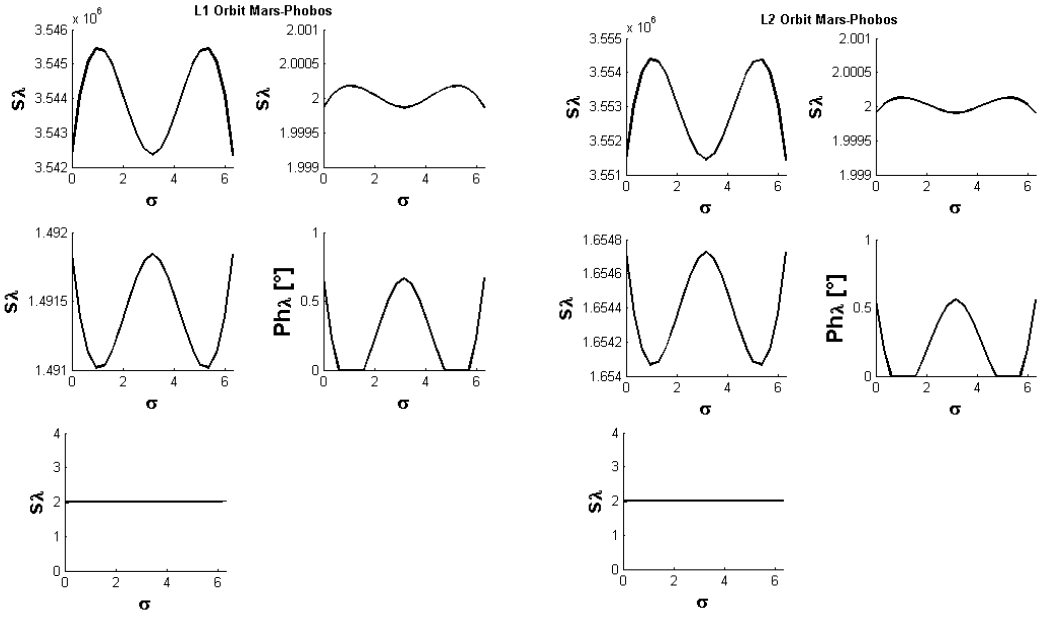

Figure D.63: **Periodic LPOs in the Mars-Phobos ER3BP-GH.** Stability properties (stability indexes of the three couples of eigenvalues, plus the additional anomaly's eigenvalue, of the monodromy matrix, with the phase of the complex couple) of the POs of the family B around L_1 and L_2 in the ER3BP-GH. Continuation with respect to the initial Phobos true anomaly from pericenter ($\sigma = 0rad$) to apocenter ($\sigma = \pi rad$).

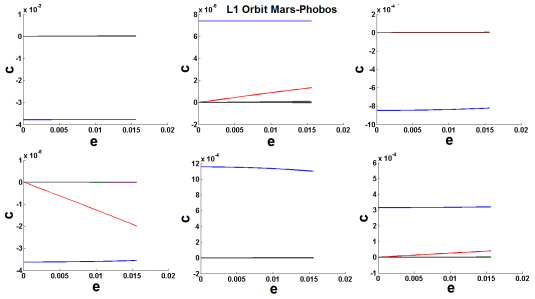

Figure D.64: **Quasi-periodic LPOs in the Mars-Phobos ER3BP-GH.** Continuation variables' curves profile. Continuation with respect to the eccentricity from CR3BP-GH ($\sigma = 0$) to ER3BP-GH ($\sigma = e_{Phobos}$) of a medium-energy PO of the family A around L_1 of the CR3BP-GH.

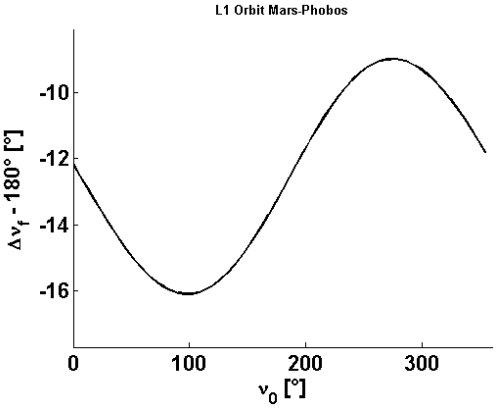

Figure D.65: **Quasi-periodic LPOs in the Mars-Phobos ER3BP-GH.** Continuation with respect to the eccentricity from CR3BP-GH to ER3BP-GH of a medium-energy PO of the family A around L_1 of the CR3BP-GH. Rotation number's profile of the true anomaly (difference with respect to 180°).

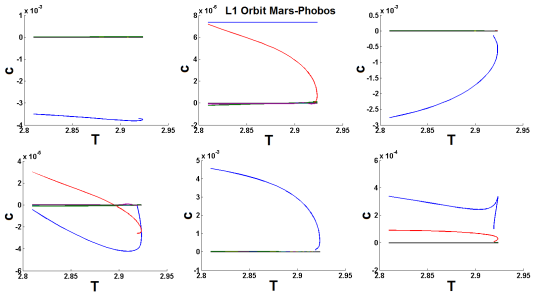

Figure D.66: **Quasi-periodic LPOs in the Mars-Phobos ER3BP-GH.** Continuation variables curves' profile. Continuation with respect to the stroboscopic time ($\sigma = T$) from the period of a small-energy 2D-QPO to the period of the 2D-QPO intersecting Phobos' surface of the family A around L_1 in the ER3BP-GH.

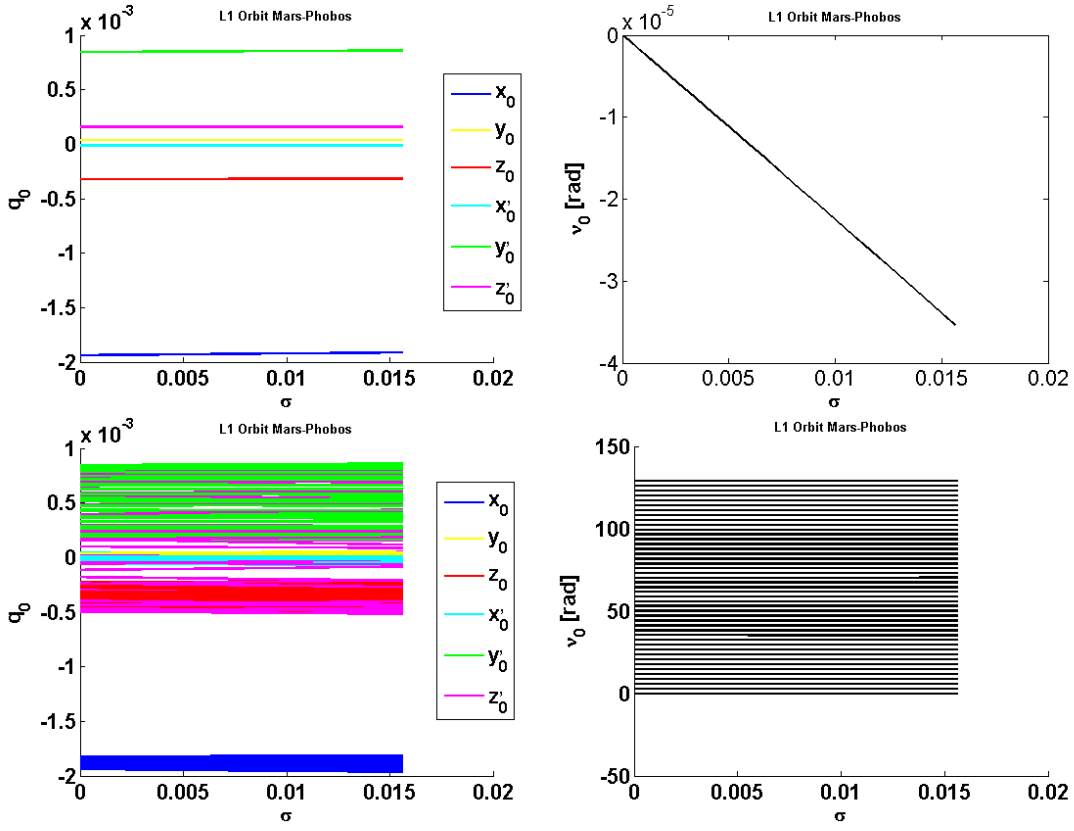

Figure D.67: **3-tori LPOs in the Mars-Phobos ER3BP-GH.** Continuation variables' curves profile: upper graphs are the coordinates and true anomaly of the first initial condition, lower graphs are the coordinates and true anomaly of all the set of sampling points of the multiple shooting scheme. Continuation with respect to the eccentricity from CR3BP-GH ($\sigma = 0$) to ER3BP-GH ($\sigma = e_{Phobos}$) of a large-width - medium-energy 2D-QPO of the family A around L_1, starting at the pericenter.

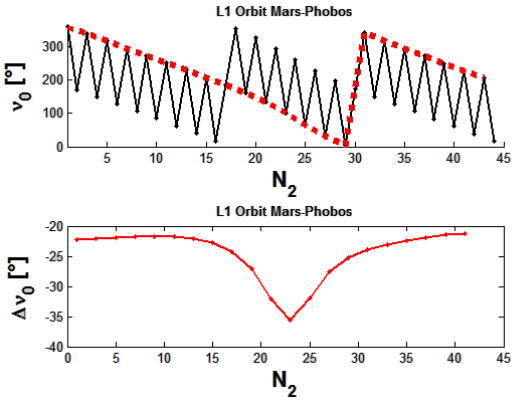

Figure D.68: **3-tori LPOs in the Mars-Phobos ER3BP-GH.** Simulation of a large-width - medium-energy 3D-QPO of the family A around L_1 of the ER3BP-GH. Phobos true anomaly's profile, where the red curve highlights the profile at the double-frequency, and related rotation number's profile along time at double-frequency. Integration up to the period of the first transversal revolution of the backbone 2D-QPO in the CR3BP-GH.

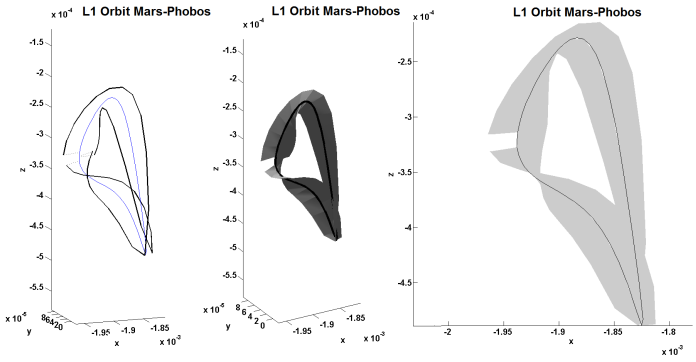

Figure D.69: **3-tori LPOs in the Mars-Phobos ER3BP-GH.** Simulation of a large-width - medium-energy 3D-QPO of the family A around L_1 of the ER3BP-GH. Graphical visualization of the set of initial conditions that represent a part of the invariant surface on a longitudinal map. The first graph shows the two boundaries, that represent the set of the initial conditions (sampling points of the multiple shooting scheme) collected at double-frequency. Invariant curve of the backbone 2D-QPO displayed. The second graph shows also the surface on the x-y-z plane filled within the two boundaries. The third graph shows the projection on the x-z plane. Integration up to the period of the first transversal revolution of the backbone 2D-QPO in the CR3BP-GH.

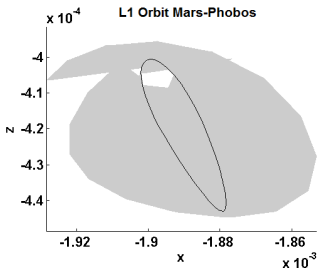

Figure D.70: **3-tori LPOs in the Mars-Phobos ER3BP-GH.** Simulation of a large-width - small-energy 3D-QPO of the family A around L_1 of the ER3BP-GH. Graphical visualization of the set of initial conditions that represent a part of the invariant surface on a longitudinal map. Area on the x-z plane filled within the two boundaries, that represent the set of the initial conditions (sampling points of the multiple shooting scheme) collected at double-frequency. Invariant curve of the backbone 2D-QPO displayed. Integration up to the period of the first transversal revolution of the backbone 2D-QPO in the CR3BP-GH.

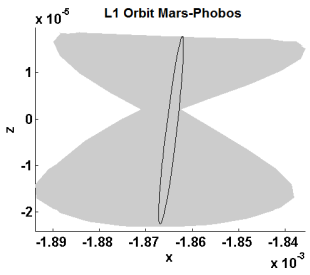

Figure D.71: **3-tori LPOs in the Mars-Phobos ER3BP-GH.** Simulation of a large-width - small-energy 3D-QPO of the family B around L_1 of the ER3BP-GH. Graphical visualization of the set of initial conditions that represent a part of the invariant surface on a longitudinal map. Area on the x-z plane filled within the two boundaries, that represent the set of the initial conditions (sampling points of the multiple shooting scheme) collected at double-frequency. Invariant curve of the backbone 2D-QPO displayed. Integration up to the period of the first transversal revolution of the backbone 2D-QPO in the CR3BP-GH.

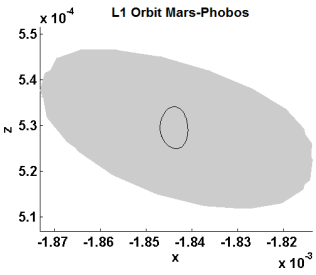

Figure D.72: **3-tori LPOs in the Mars-Phobos ER3BP-GH.** Simulation of a large-width - small-energy 3D-QPO of the family C around L_1 of the ER3BP-GH. Graphical visualization of the set of initial conditions that represent a part of the invariant surface on a longitudinal map. Area on the x-z plane filled within the two boundaries, that represent the set of the initial conditions (sampling points of the multiple shooting scheme) collected at double-frequency. Invariant curve of the backbone 2D-QPO displayed. Integration up to the period of the first transversal revolution of the backbone 2D-QPO in the CR3BP-GH.

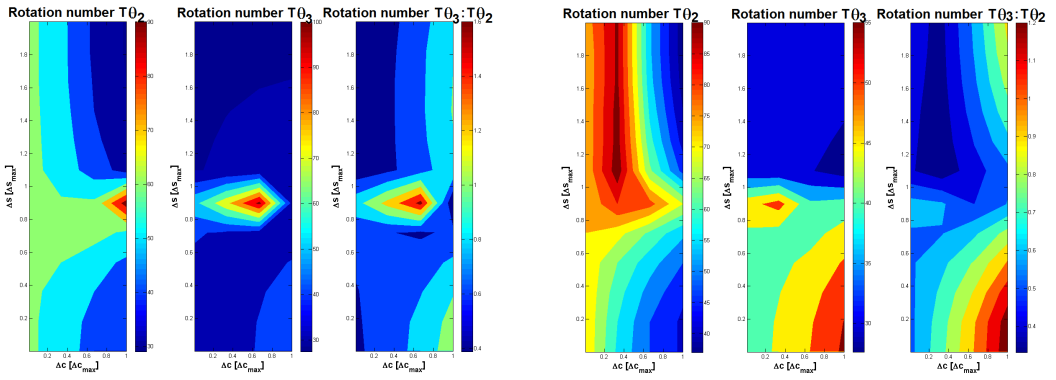

Figure D.73: **3D-Tori in the Mars-Phobos ER3BP-GH.** Period of the first revolution of the third and second phases (see Eq.4.48) of the 3-tori of the AB family around L_1 and L_2 of the ER3BP-GH. The second graph is taken from the backbone 2D-QPO in the CR3BP-GH (Fig.D.41). The third graph is the ratio between the periods of the two transversal phases. The 3D-QPOs are parameterized in the same way as their backbone 2D-QPO in the CR3BP-GH.

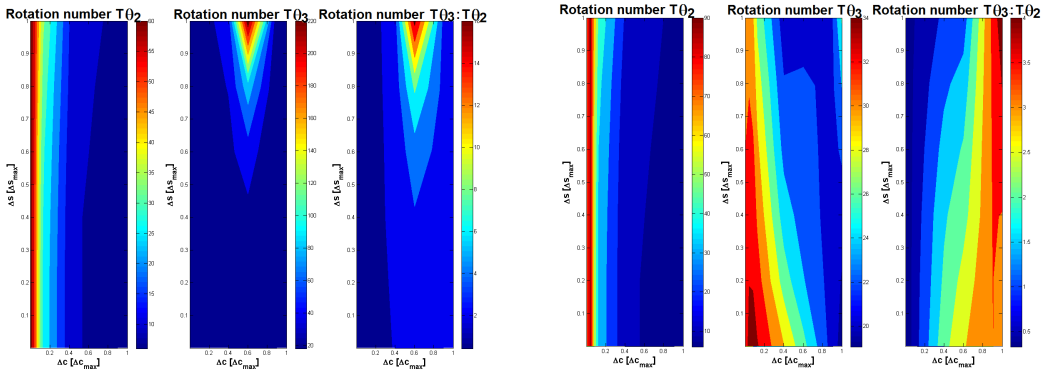

Figure D.74: **3-tori LPOs in the Mars-Phobos ER3BP-GH.** Period of the first revolution of the third and second phases (see Eq.4.48) of the 3-tori of the A family around L_1 and L_2 of the ER3BP-GH. The second graph is taken from the backbone 2D-QPO in the CR3BP-GH (Fig.D.42). The third graph is the ratio between the periods of the two transversal phases. The 3D-QPOs are parameterized in the same way as their backbone 2D-QPO in the CR3BP-GH.

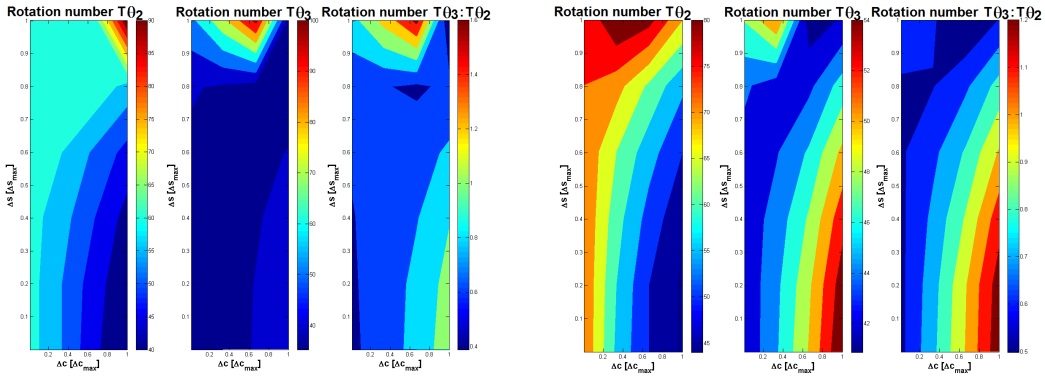

Figure D.75: **3-tori LPOs in the Mars-Phobos ER3BP-GH.** Period of the first revolution of the third and second phases (see Eq.4.48) of the 3-tori of the B family around L_1 and L_2 of the ER3BP-GH. The second graph is taken from the backbone 2D-QPO in the CR3BP-GH (Fig.D.43). The third graph is the ratio between the periods of the two transversal phases. The 3D-QPOs are parameterized in the same way as their backbone 2D-QPO in the CR3BP-GH.

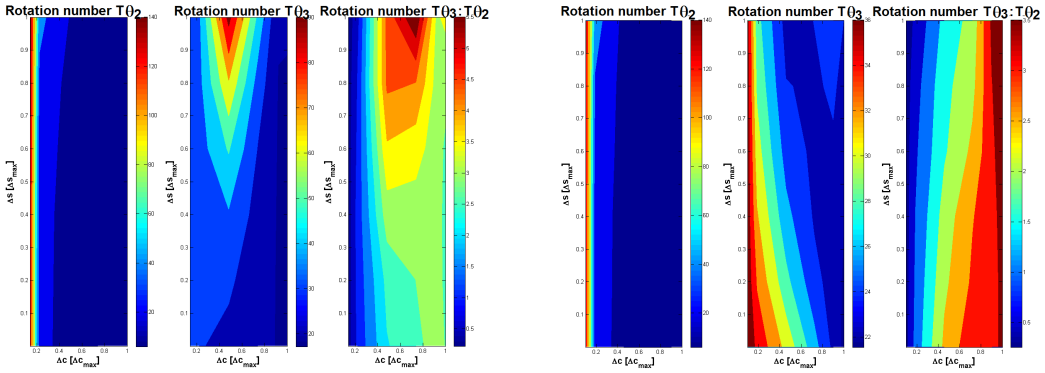

Figure D.76: **3-tori LPOs in the Mars-Phobos ER3BP-GH.** Period of the first revolution of the third and second phases (see Eq.4.48) of the 3-tori of the C family around L_1 and L_2 of the ER3BP-GH. The second graph is taken from the backbone 2D-QPO in the CR3BP-GH (Fig.D.44). The third graph is the ratio between the periods of the two transversal phases. The 3D-QPOs are parameterized in the same way as their backbone 2D-QPO in the CR3BP-GH.

D.5 Invariant Manifolds of the LPOs of the Mars-Phobos ER3BP-GH

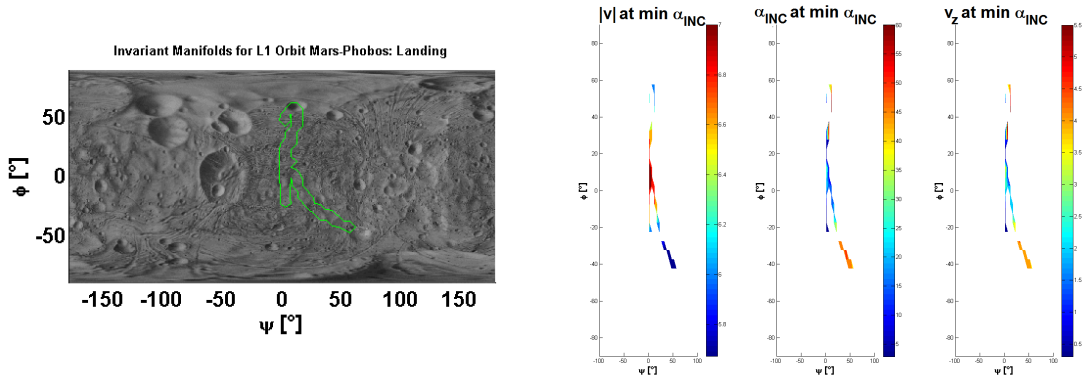

Figure D.77: **Landing on Phobos through the Invariant Manifolds of the L_1 resonant periodic LPOs of the ER3BP-GH.** Region of possible landing sites, for orbits that do not intersect Phobos' real shape. Trajectories that provide the min incidence at the touch-down, as a function of the longitude and latitude of the landing site. Performances of the trajectory: landing velocity magnitude, angle of incidence, downward vertical velocity. Phobos real shape.

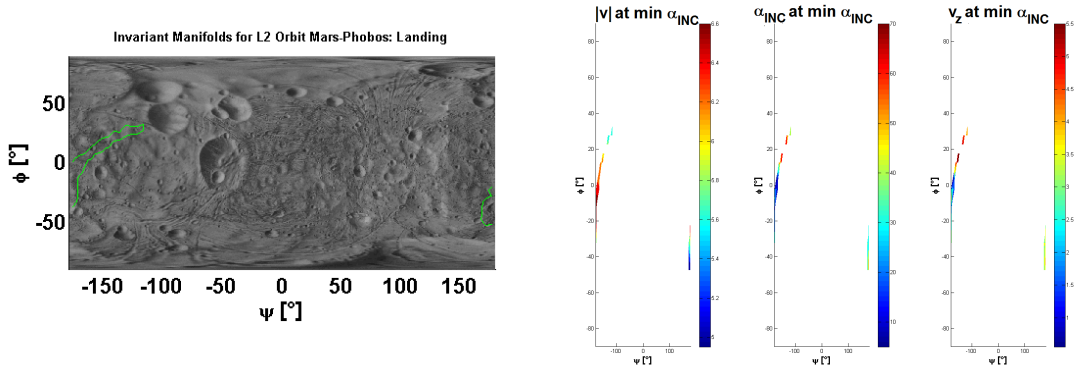

Figure D.78: **Landing on Phobos through the Invariant Manifolds of the L_2 resonant periodic LPOs of the ER3BP-GH.** Region of possible landing sites, for orbits that do not intersect Phobos' real shape. Trajectories that provide the min incidence at the touch-down, as a function of the longitude and latitude of the landing site. Performances of the trajectory: landing velocity magnitude, angle of incidence, downward vertical velocity. Phobos real shape.

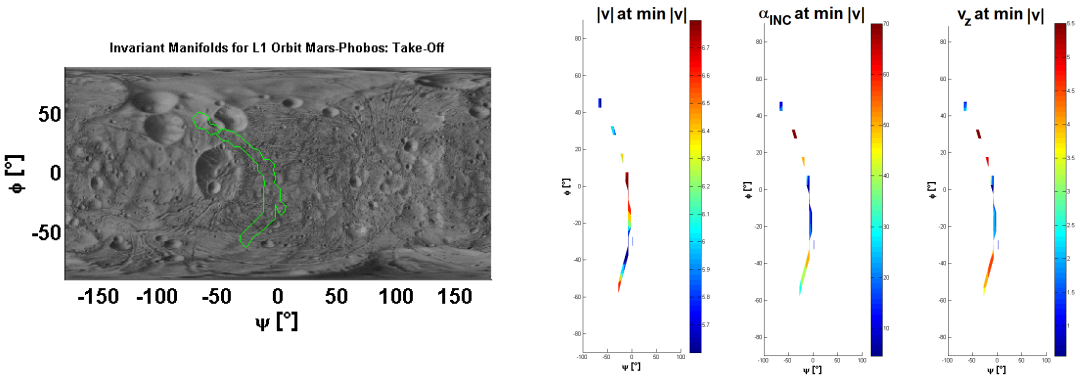

Figure D.79: **Take-off from Phobos through the Invariant Manifolds of the L_1 resonant periodic LPOs of the ER3BP-GH.** Region of possible departure sites, for orbits that do not intersect Phobos' real shape. Trajectories that provide the min velocity total magnitude at the launch, as a function of the longitude and latitude of the departure site. Performances of the trajectory: landing velocity magnitude, angle of incidence, upward vertical velocity. Phobos real shape.

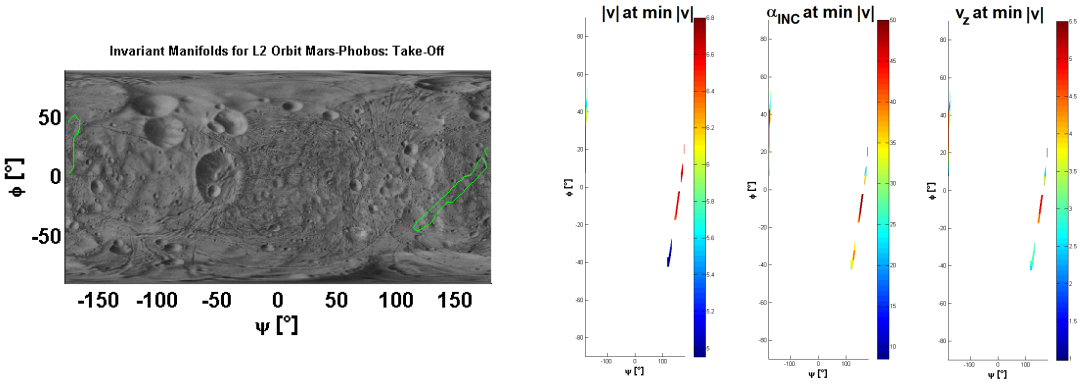

Figure D.80: **Take-off from Phobos through the Invariant Manifolds of the L_2 resonant periodic LPOs of the ER3BP-GH.** Region of possible departure sites, for orbits that do not intersect Phobos' real shape. Trajectories that provide the min velocity total magnitude at the launch, as a function of the longitude and latitude of the departure site. Performances of the trajectory: landing velocity magnitude, angle of incidence, upward vertical velocity. Phobos real shape.

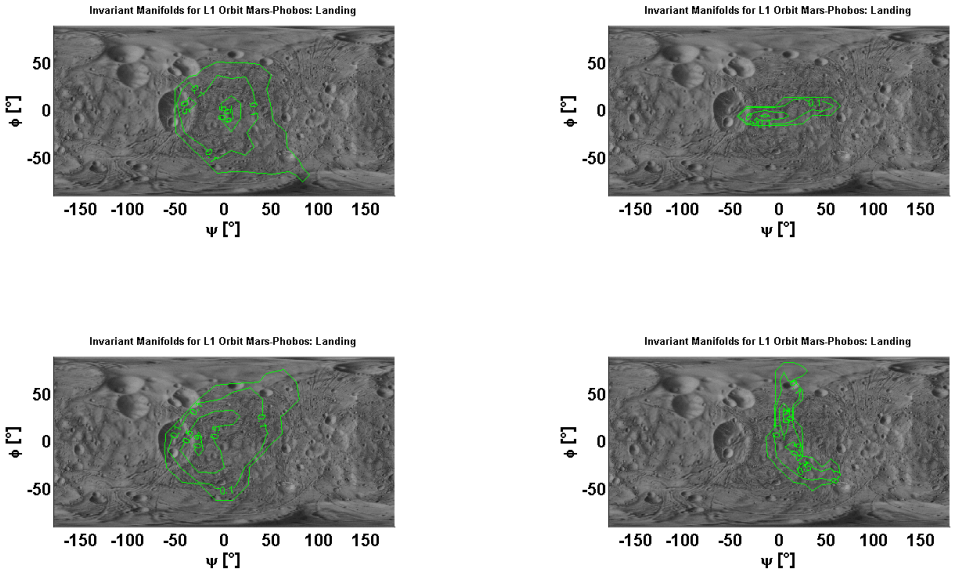

Figure D.81: **Landing on Phobos through the Invariant Manifold of the L_1 families of 2D-QPOs LPOs of the Mars-Phobos ER3BP-GH.** Region of possible landing sites, for orbits that do not intersect Phobos' real shape. Inner lines show subregions where the 10%, 50%, 90% levels of the cumulative distribution of the IM simulated landed (same number of trajectories from each departing orbit simulated). Phobos real shape.

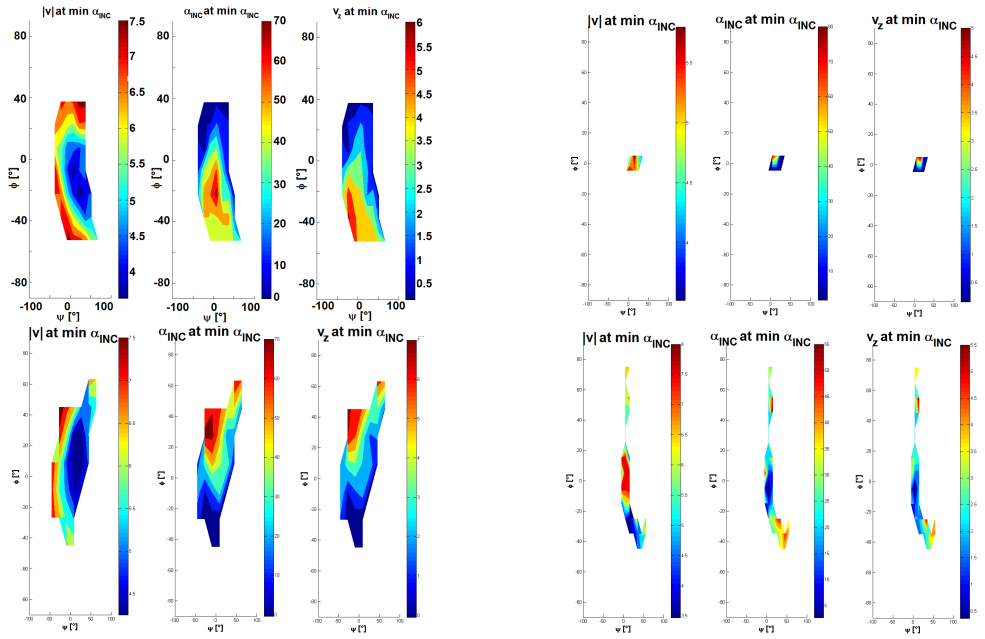

Figure D.82: **Landing on Phobos through the Invariant Manifold of the L_1 families of 2D-QPOs LPOs of the Mars-Phobos ER3BP-GH.** Trajectories that provide the min incidence at the touch-down, as a function of the longitude and latitude of the landing site, for orbits that do not intersect Phobos' real shape. Performances of the trajectory: landing velocity magnitude, angle of incidence, downward vertical velocity. Phobos real shape.

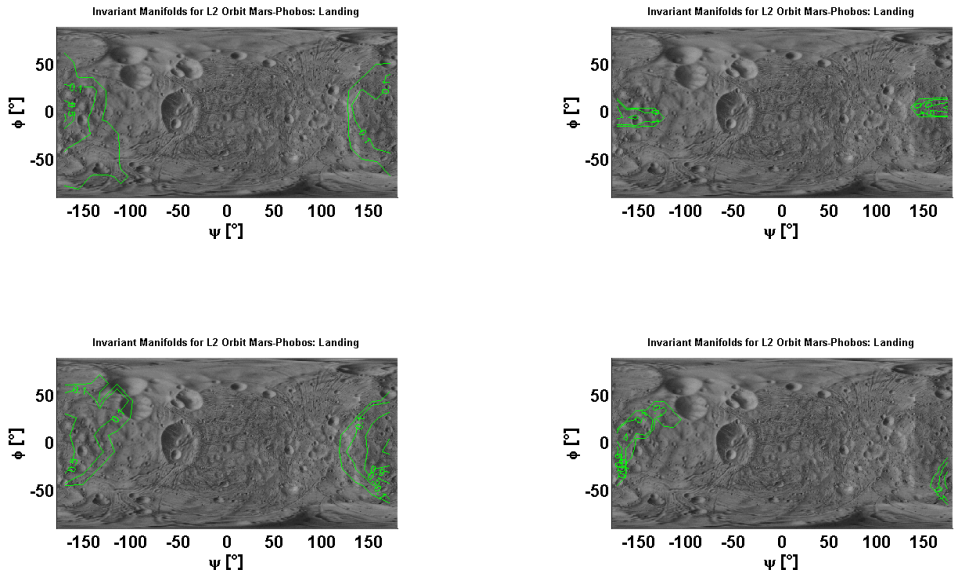

Figure D.83: **Landing on Phobos through the Invariant Manifold of the L_2 families of 2D-QPOs LPOs of the Mars-Phobos ER3BP-GH.** Region of possible landing sites, for orbits that do not intersect Phobos' real shape. Inner lines show subregions where the 10%, 50%, 90% levels of the cumulative distribution of the IM simulated landed (same number of trajectories from each departing orbit simulated). Phobos real shape.

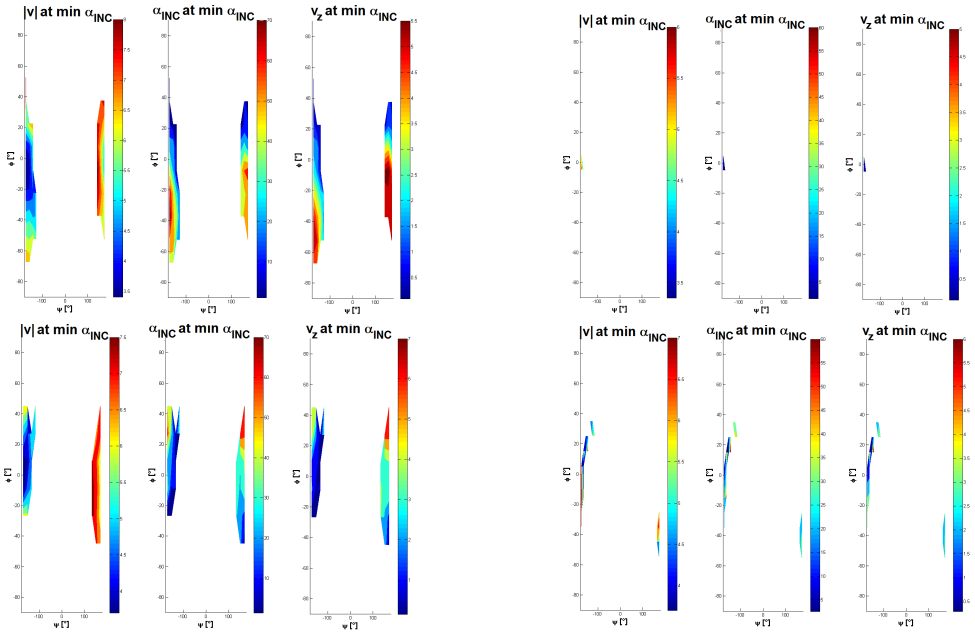

Figure D.84: **Landing on Phobos through the Invariant Manifold of the L_2 families of 2D-QPOs LPOs of the Mars-Phobos ER3BP-GH.** Trajectories that provide the min incidence at the touch-down, as a function of the longitude and latitude of the landing site, for orbits that do not intersect Phobos' real shape. Performances of the trajectory: landing velocity magnitude, angle of incidence, downward vertical velocity. Phobos real shape.

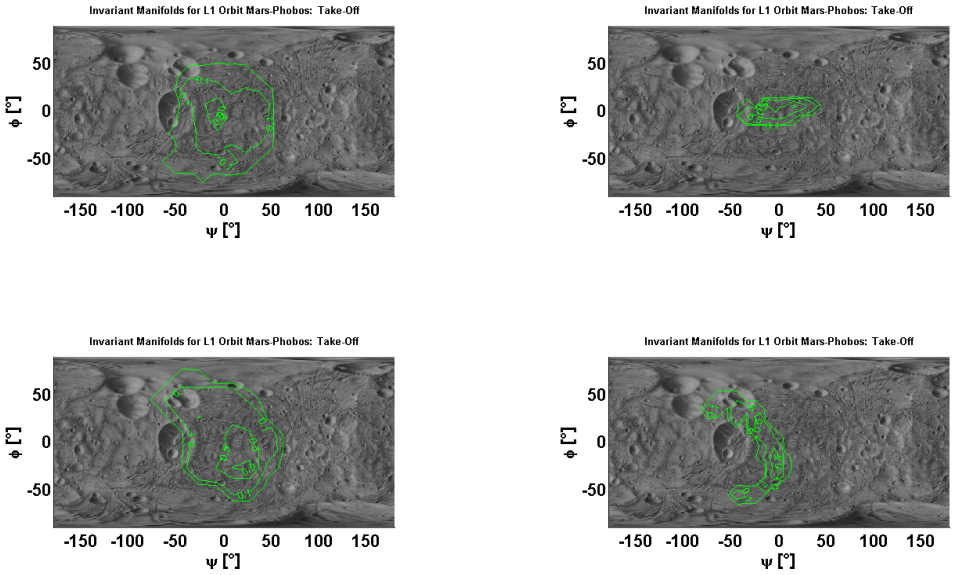

Figure D.85: **Take-off from Phobos through the Invariant Manifold of the L_1 families of 2D-QPOs LPOs of the Mars-Phobos ER3BP-GH.** Region of possible departure sites, for orbits that do not intersect Phobos' real shape. Inner lines show subregions where the 10%, 50%, 90% levels of the cumulative distribution of the IM simulated departed (same number of trajectories from each departing orbit simulated). Phobos real shape.

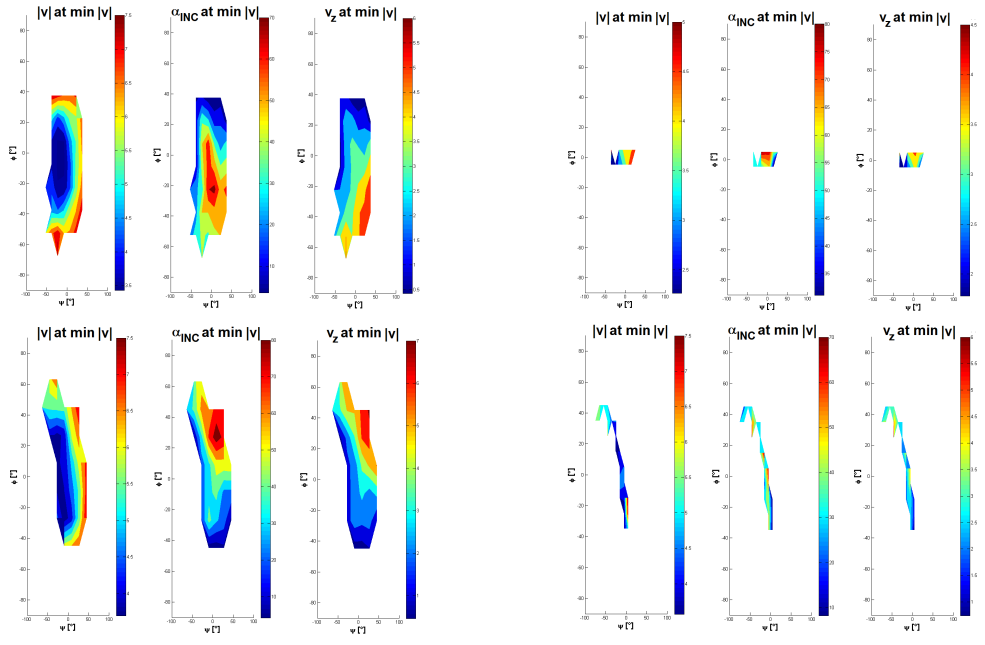

Figure D.86: **Take-off from Phobos through the Invariant Manifold of the L_1 families of 2D-QPOs LPOs of the Mars-Phobos ER3BP-GH.** Trajectories that provide the min velocity total magnitude at the launch, as a function of the longitude and latitude of the departure site, for orbits that do not intersect Phobos' real shape. Performances of the trajectory: departure velocity magnitude, angle of incidence, upward vertical velocity. Phobos real shape.

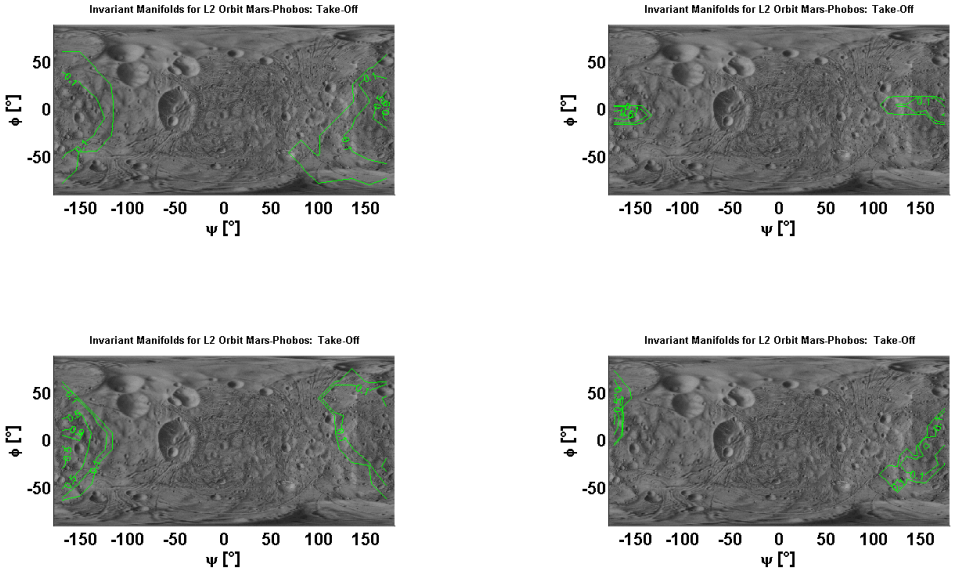

Figure D.87: **Take-off from Phobos through the Invariant Manifold of the L_2 families of 2D-QPOs LPOs of the Mars-Phobos ER3BP-GH.** Region of possible departure sites, for orbits that do not intersect Phobos' real shape. Inner lines show subregions where the 10%, 50%, 90% levels of the cumulative distribution of the IM simulated departed (same number of trajectories from each departing orbit simulated). Phobos real shape.

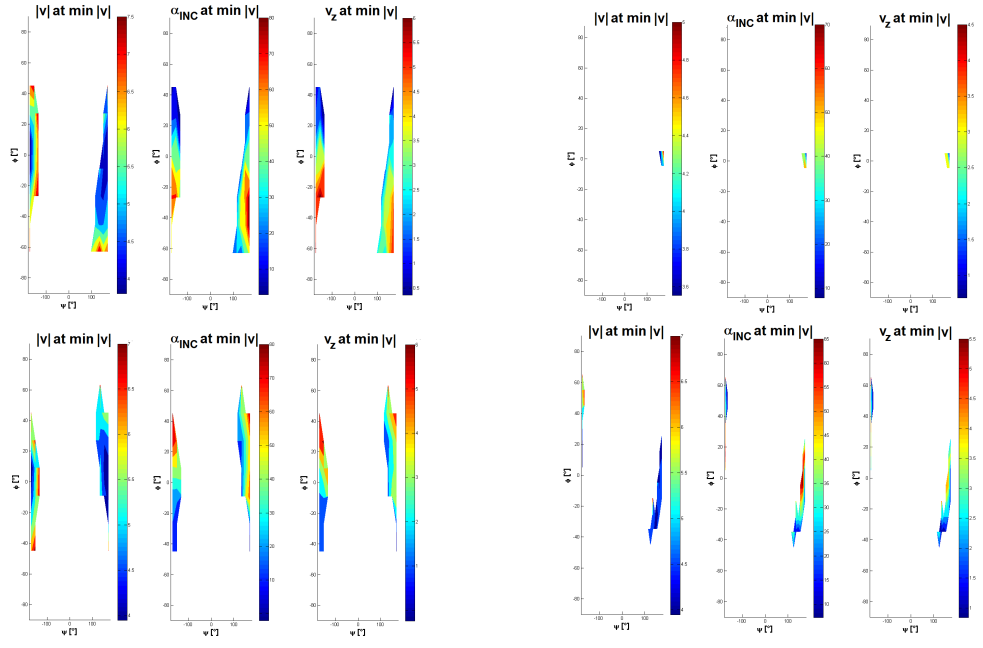

Figure D.88: **Take-off from Phobos through the Invariant Manifold of the L_2 families of 2D-QPOs LPOs of the Mars-Phobos ER3BP-GH.** Trajectories that provide the min velocity total magnitude at the launch, as a function of the longitude and latitude of the departure site, for orbits that do not intersect Phobos' real shape. Performances of the trajectory: departure velocity magnitude, angle of incidence, upward vertical velocity. Phobos real shape.

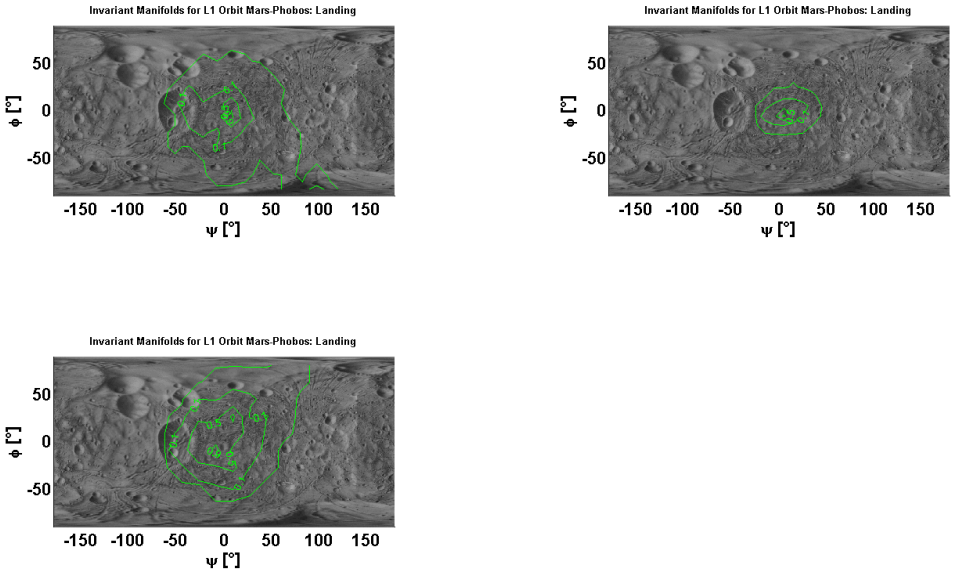

Figure D.89: **Landing on Phobos through the Invariant Manifold of the L_1 families of 3-tori LPOs of the Mars-Phobos ER3BP-GH.** Region of possible landing sites, for orbits that do not intersect Phobos' real shape. Inner lines show subregions where the 10%, 50%, 90% levels of the cumulative distribution of the IM simulated landed (same number of trajectories from each departing orbit simulated). Phobos real shape.

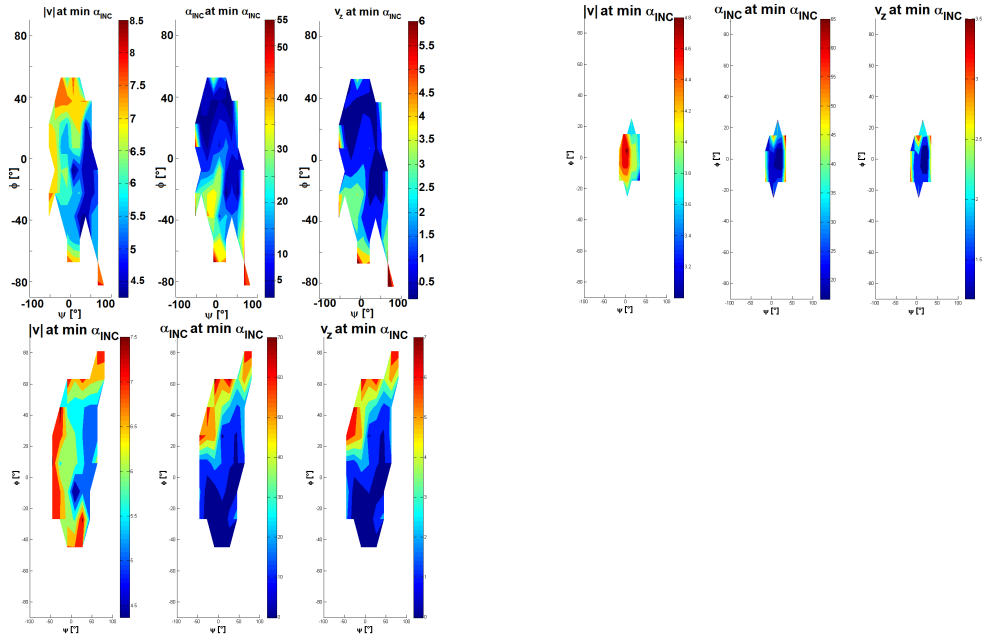

Figure D.90: **Landing on Phobos through the Invariant Manifold of the L_1 families of 3-tori LPOs of the Mars-Phobos ER3BP-GH.** Trajectories that provide the min incidence at the touch-down, as a function of the longitude and latitude of the landing site, for orbits that do not intersect Phobos' real shape. Performances of the trajectory: landing velocity magnitude, angle of incidence, downward vertical velocity. Phobos real shape.

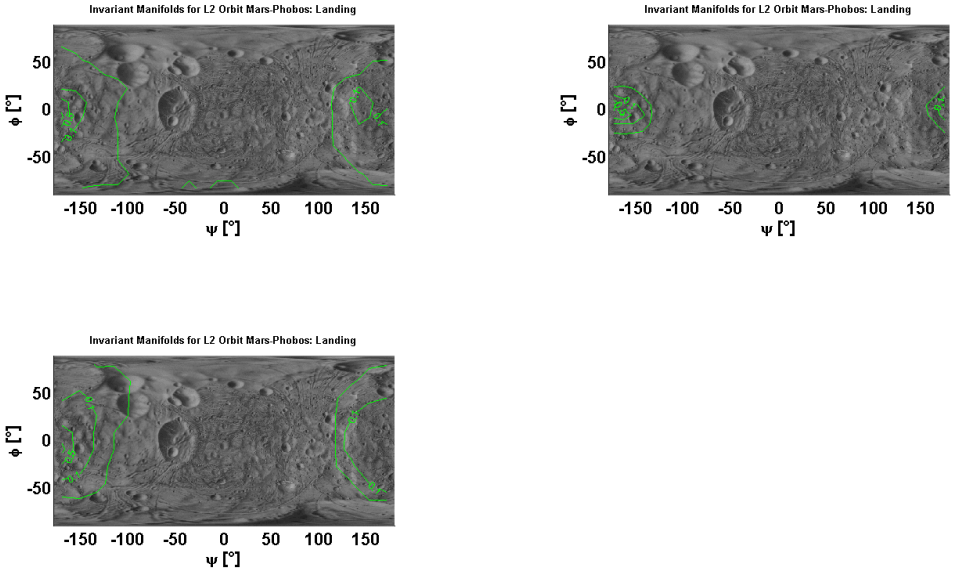

Figure D.91: **Landing on Phobos through the Invariant Manifold of the L_2 families of 3-tori LPOs of the Mars-Phobos ER3BP-GH.** Region of possible landing sites, for orbits that do not intersect Phobos' real shape. Inner lines show subregions where the 10%, 50%, 90% levels of the cumulative distribution of the IM simulated landed (same number of trajectories from each departing orbit simulated). Phobos real shape.

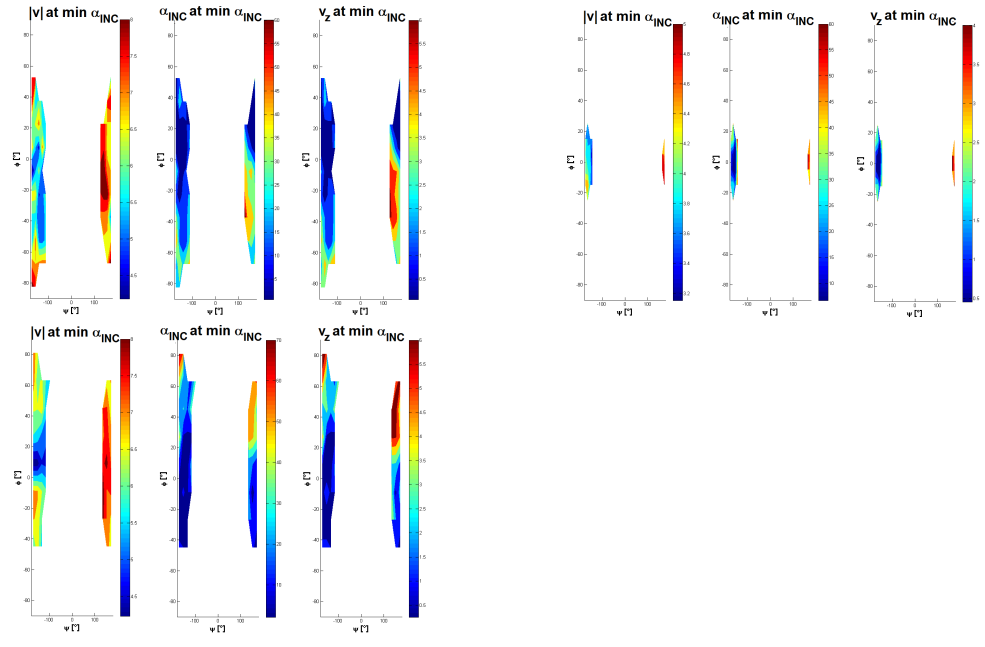

Figure D.92: **Landing on Phobos through the Invariant Manifold of the L_2 families of 3-tori LPOs of the Mars-Phobos ER3BP-GH.** Trajectories that provide the min incidence at the touch-down, as a function of the longitude and latitude of the landing site, for orbits that do not intersect Phobos' real shape. Performances of the trajectory: landing velocity magnitude, angle of incidence, downward vertical velocity. Phobos real shape.

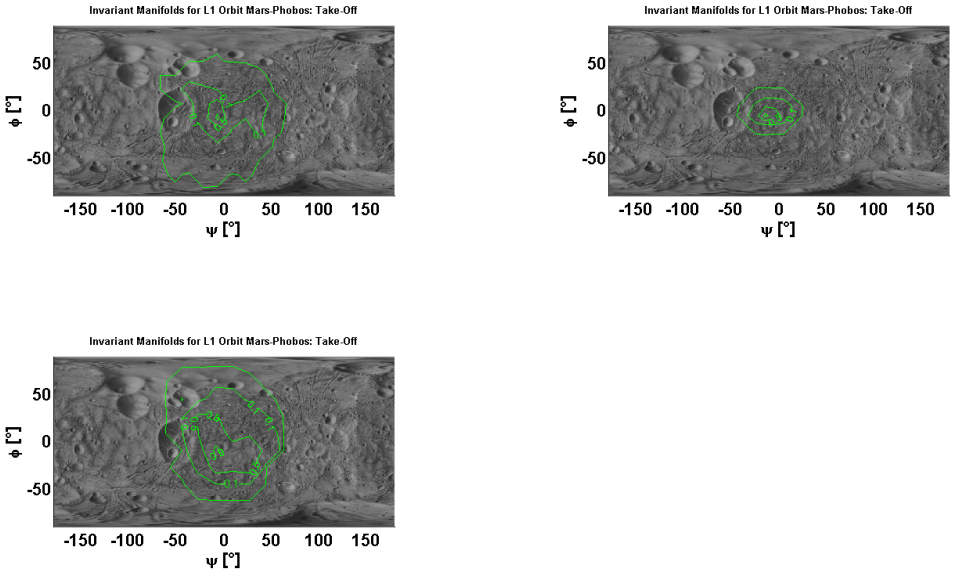

Figure D.93: **Take-off from Phobos through the Invariant Manifold of the L_1 families of 3-tori LPOs of the Mars-Phobos ER3BP-GH.** Region of possible departure sites, for orbits that do not intersect Phobos' real shape. Inner lines show subregions where the 10%, 50%, 90% levels of the cumulative distribution of the IM simulated departed (same number of trajectories from each departing orbit simulated). Phobos real shape.

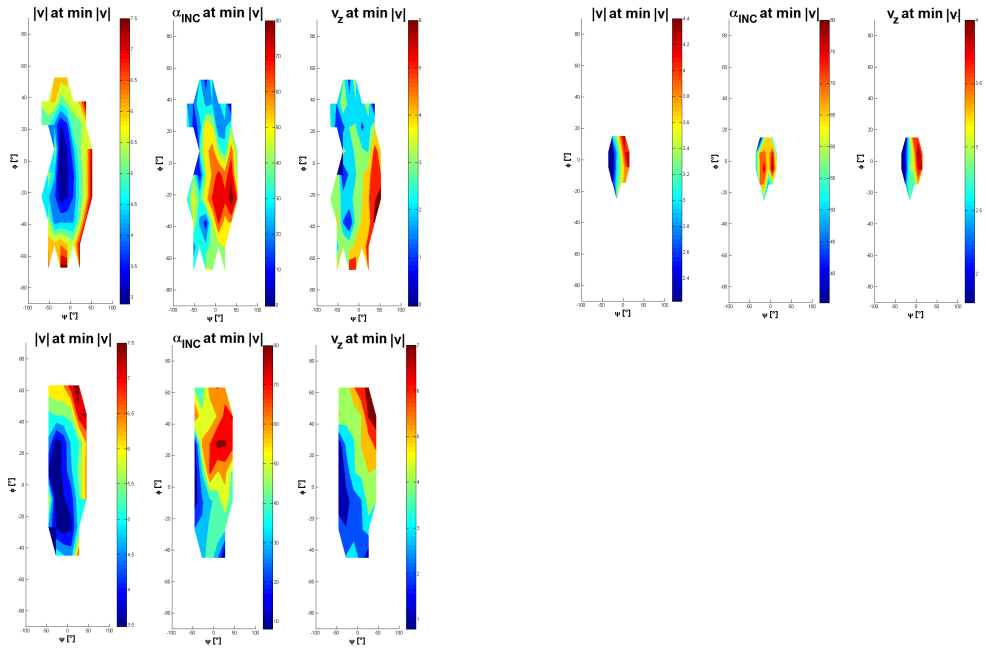

Figure D.94: **Take-off from Phobos through the Invariant Manifold of the L_1 families of 3-tori LPOs of the Mars-Phobos ER3BP-GH.** Trajectories that provide the min velocity total magnitude at the launch, as a function of the longitude and latitude of the departure site, for orbits that do not intersect Phobos' real shape. Performances of the trajectory: departure velocity magnitude, angle of incidence, upward vertical velocity. Phobos real shape.

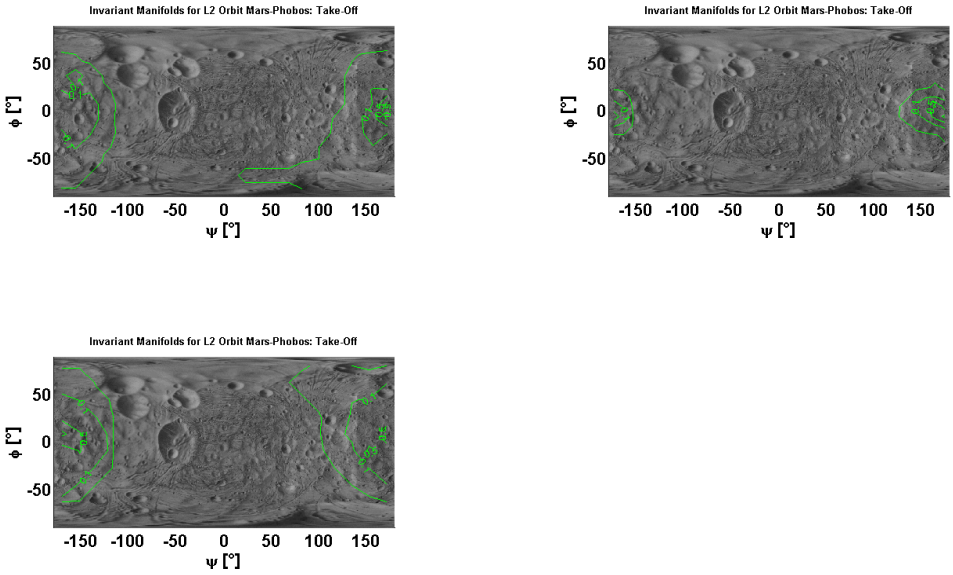

Figure D.95: **Take-off from Phobos through the Invariant Manifold of the L_2 families of 3-tori LPOs of the Mars-Phobos ER3BP-GH.** Region of possible departure sites, for orbits that do not intersect Phobos' real shape. Inner lines show subregions where the 10%, 50%, 90% levels of the cumulative distribution of the IM simulated departed (same number of trajectories from each departing orbit simulated). Phobos real shape.

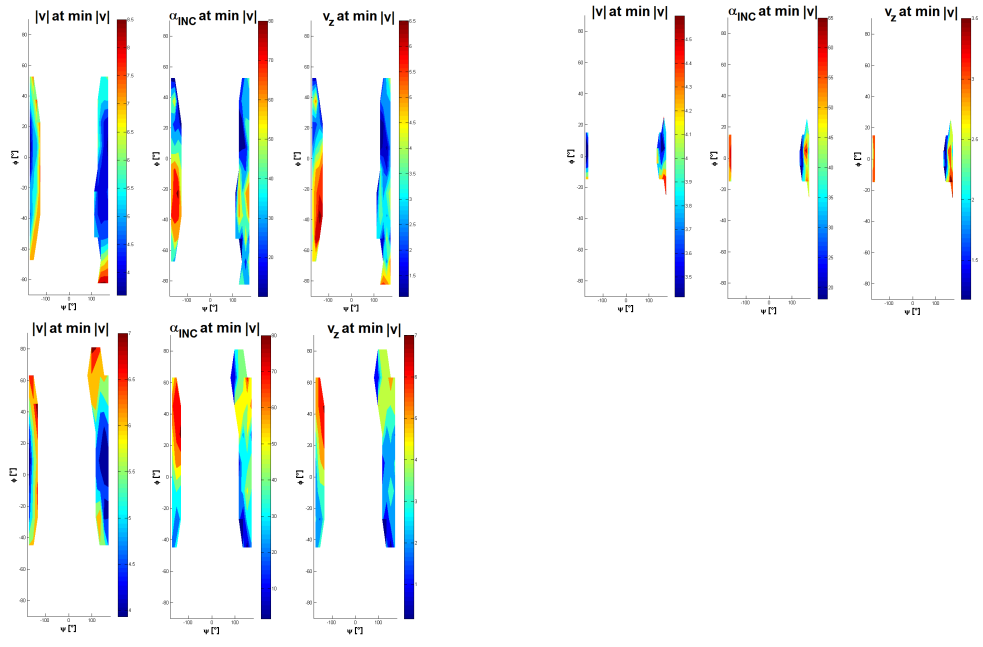

Figure D.96: **Take-off from Phobos through the Invariant Manifold of the L_2 families of 3-tori LPOs of the Mars-Phobos ER3BP-GH.** Trajectories that provide the min velocity total magnitude at the launch, as a function of the longitude and latitude of the departure site, for orbits that do not intersect Phobos' real shape. Performances of the trajectory: departure velocity magnitude, angle of incidence, upward vertical velocity. Phobos real shape.

D.6 Invariant Manifolds of the ALPOs of the Mars-Phobos CR3BP-GH

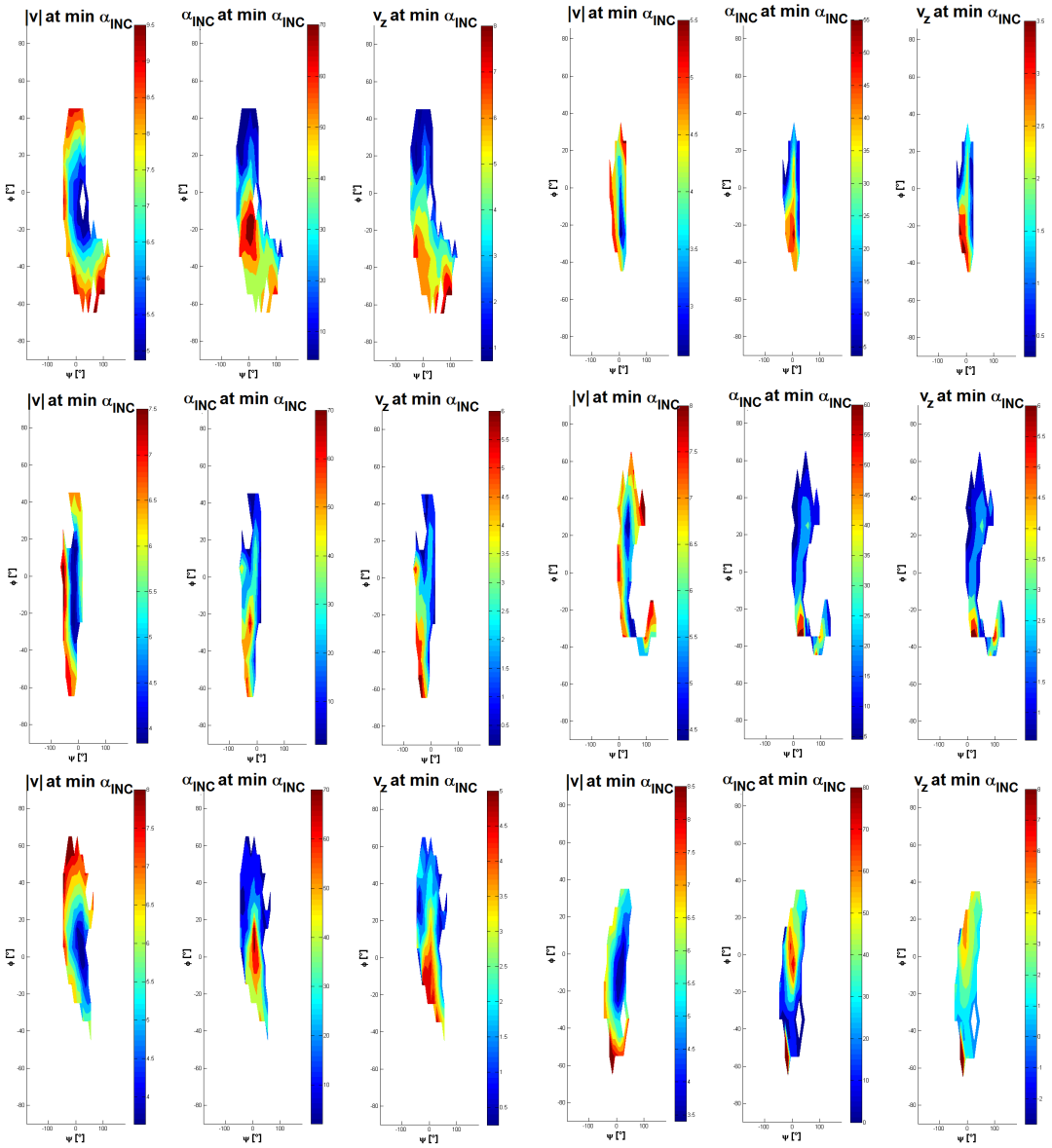

Figure D.97: **Landing on Phobos through the Invariant Manifold of the family A of L_1 periodic artificial LPOs of the Mars-Phobos CR3BP-GH.** Trajectories that provide the min incidence at the touch-down, as a function of the longitude and latitude of the landing site, for orbits that do not intersect Phobos' real shape. Performances of the trajectory: landing velocity magnitude, angle of incidence, downward vertical velocity. Constant acceleration magnitude of $1mm/s^2$ along all coordinate axes directions (on the left/right directions $+/-$, on the top directions $\pm\hat{\mathbf{x}}$, in the center directions $\pm\hat{\mathbf{y}}$, on the bottom directions $\pm\hat{\mathbf{z}}$). Phobos real shape.

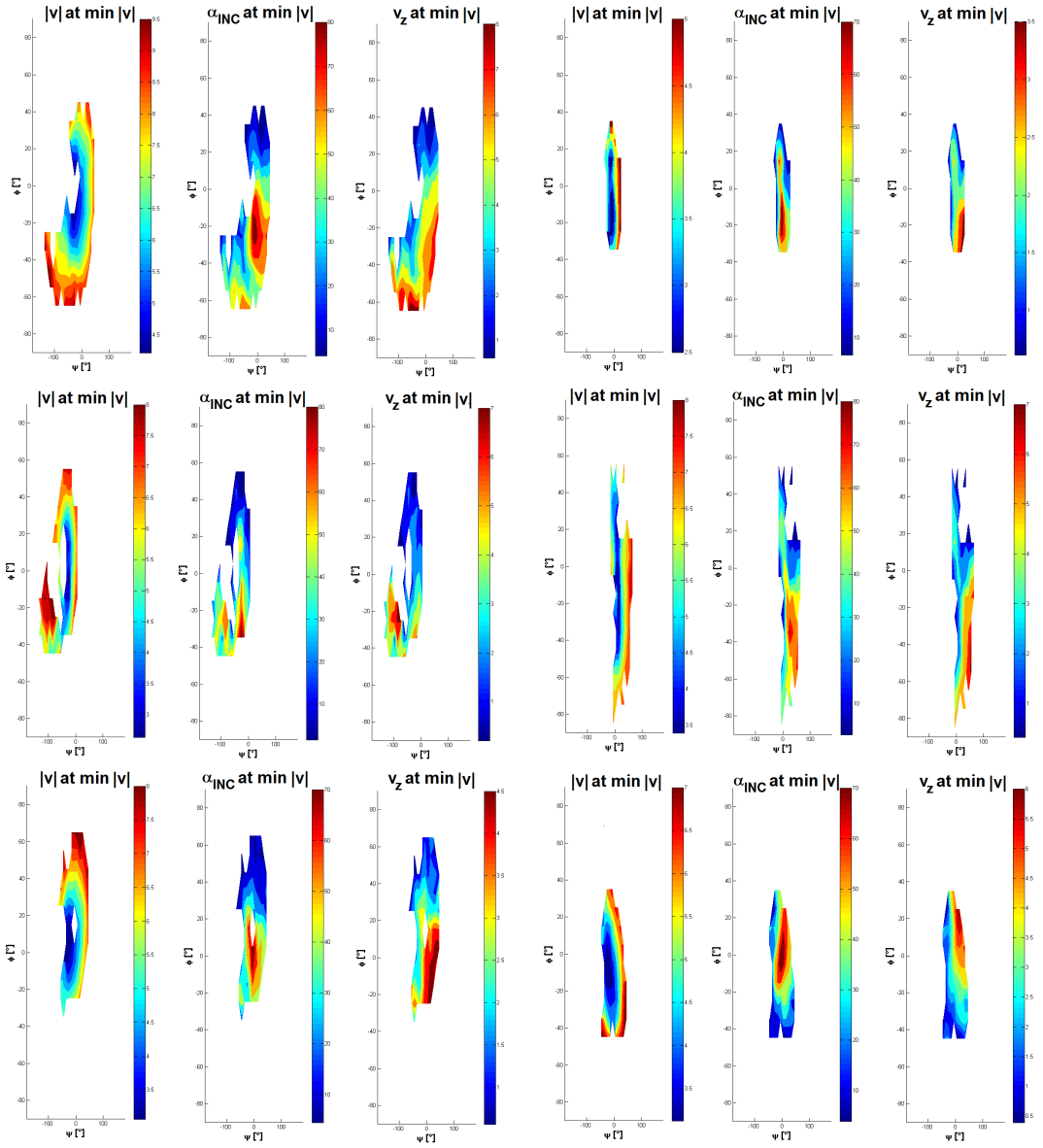

Figure D.98: **Take-Off from Phobos through the Invariant Manifold of the L_1 family A of periodic artificial LPOs of the Mars-Phobos CR3BP-GH.** Trajectories that provide the min velocity total magnitude at the launch, as a function of the longitude and latitude of the departure site, for orbits that do not intersect Phobos' real shape. Performances of the trajectory: departure velocity magnitude, angle of incidence, upward vertical velocity. Constant acceleration magnitude of $1mm/s^2$ along all coordinate axes directions (on the left/right directions $+/-$, on the top directions $\pm\hat{\mathbf{x}}$, in the center directions $\pm\hat{\mathbf{y}}$, on the bottom directions $\pm\hat{\mathbf{z}}$). Phobos real shape.

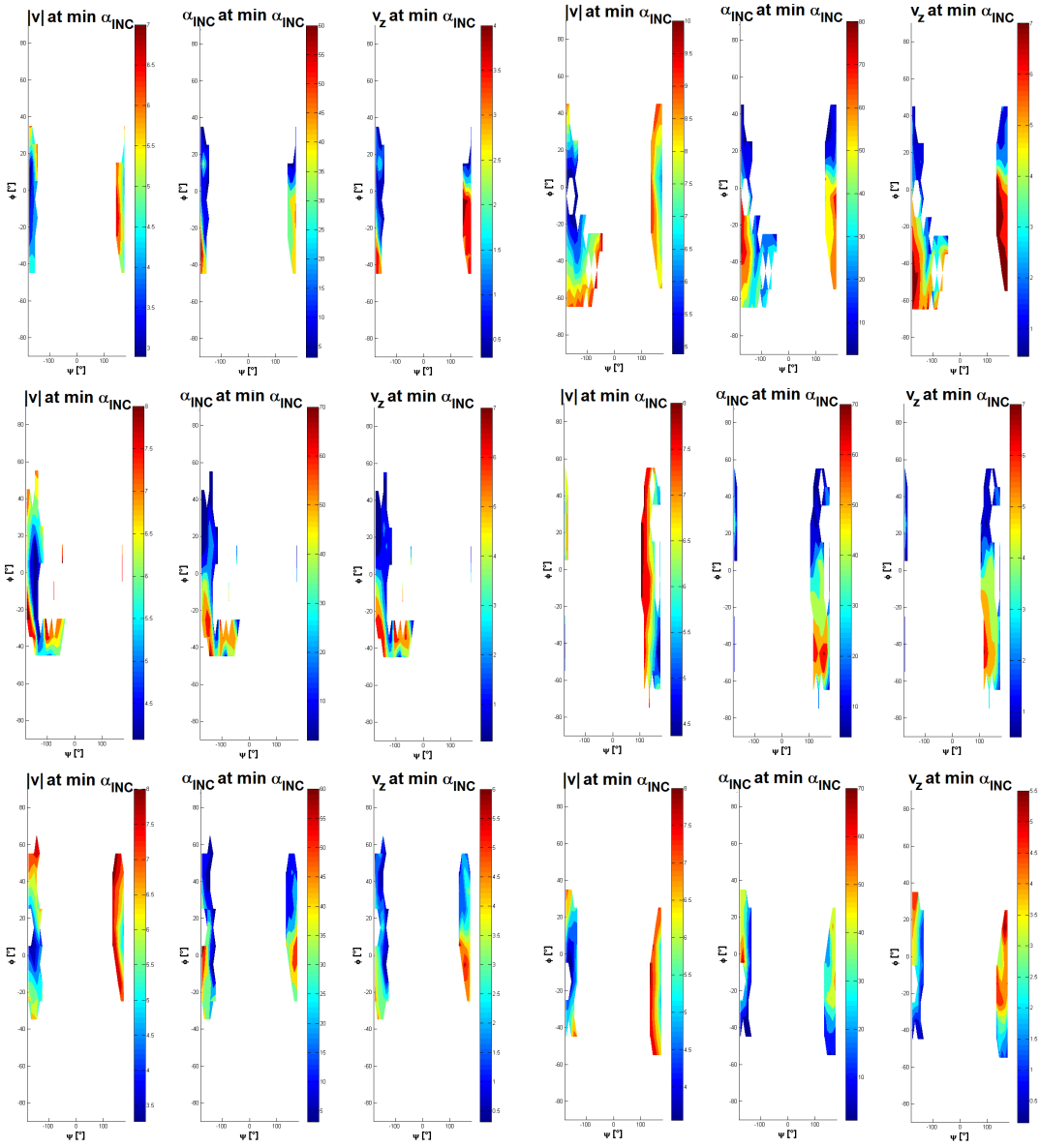

Figure D.99: **Landing on Phobos through the Invariant Manifold of the family A of L_2 periodic artificial LPOs of the Mars-Phobos CR3BP-GH.** Trajectories that provide the min incidence at the touch-down, as a function of the longitude and latitude of the landing site, for orbits that do not intersect Phobos' real shape. Performances of the trajectory: landing velocity magnitude, angle of incidence, downward vertical velocity. Constant acceleration magnitude of $1mm/s^2$ along all coordinate axes directions (on the left/right directions $+/-$, on the top directions $\pm\hat{\mathbf{x}}$, in the center directions $\pm\hat{\mathbf{y}}$, on the bottom directions $\pm\hat{\mathbf{z}}$). Phobos real shape.

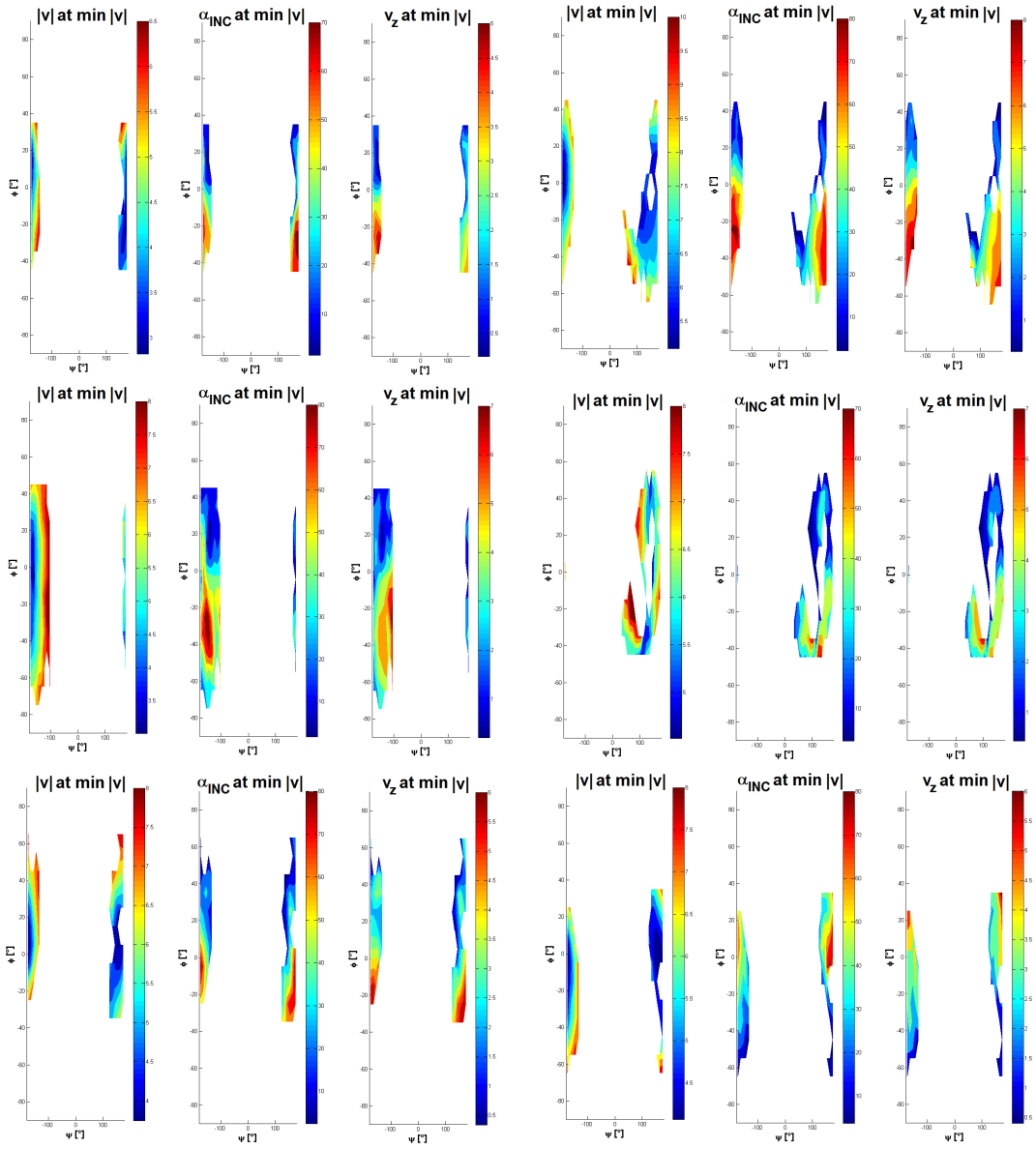

Figure D.100: **Take-Off from Phobos through the Invariant Manifold of the L_2 family A of periodic artificial LPOs of the Mars-Phobos CR3BP-GH.** Trajectories that provide the min velocity total magnitude at the launch, as a function of the longitude and latitude of the departure site, for orbits that do not intersect Phobos' real shape. Performances of the trajectory: departure velocity magnitude, angle of incidence, upward vertical velocity. Constant acceleration magnitude of $1mm/s^2$ along all coordinate axes directions (on the left/right directions $+/-$, on the top directions $\pm\hat{\mathbf{x}}$, in the center directions $\pm\hat{\mathbf{y}}$, on the bottom directions $\pm\hat{\mathbf{z}}$). Phobos real shape.

Appendix E

Quasi-Satellite Orbits of the Mars-Phobos 3BP

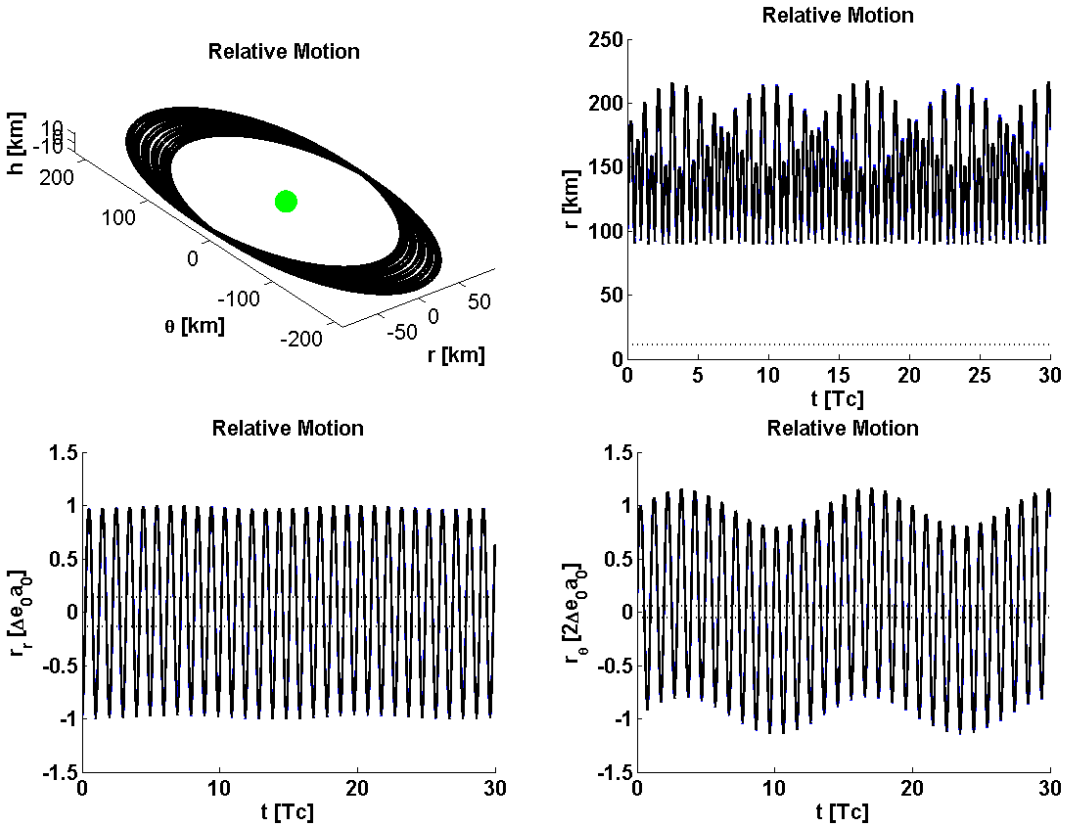

Figure E.1: **QSOs around Phobos.** Phobos orbit equatorial, without Mars J_2. $\Delta e = 0.01$, $\Delta i = 0$. Orbit and plots in black line of the relative distance's magnitude, radial and transversal component. The plots overlap with the blue lines that are related to the equivalent CR3BP. Dotted lines indicate the reference distance of Phobos' mean radius.

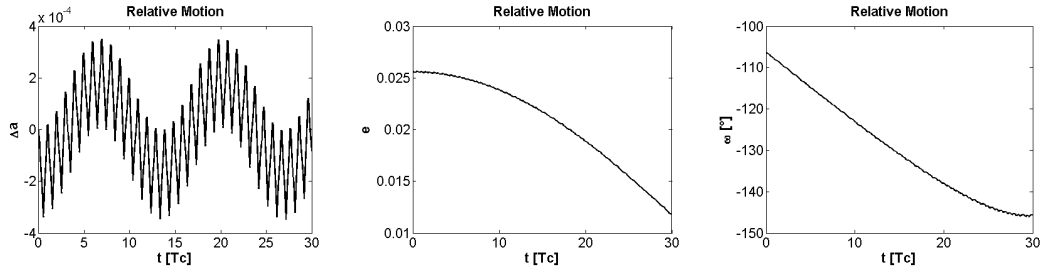

Figure E.2: **QSOs around Phobos.** Phobos orbit equatorial, without Mars J_2. $\Delta e = 0.01$, $\Delta i = 0$. Orbital elements.

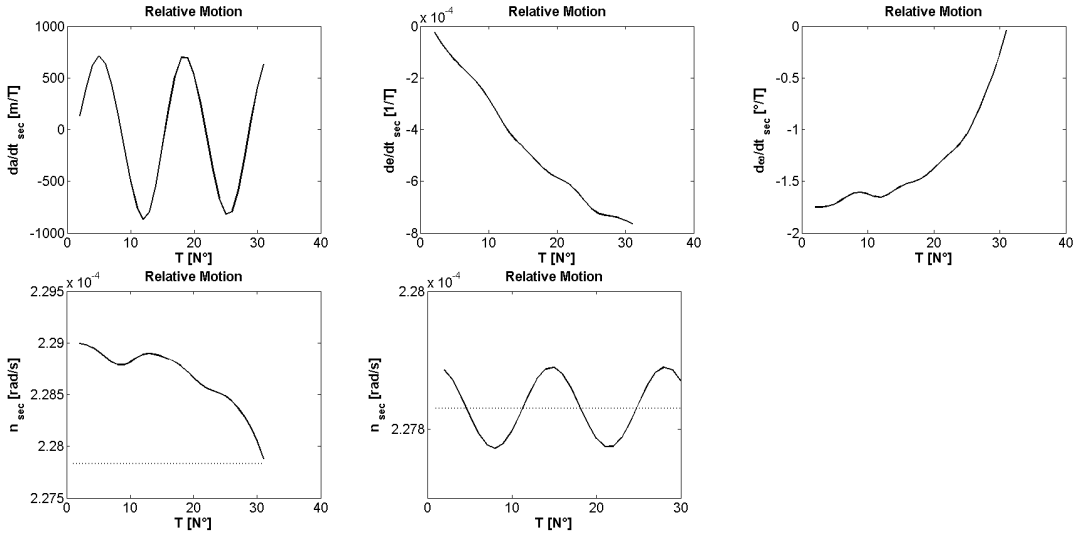

Figure E.3: **QSOs around Phobos.** Phobos orbit equatorial, without Mars J_2. $\Delta e = 0.01$, $\Delta i = 0$. Secular derivative of the orbital elements, taken every orbital period. The last two graphs correspond to the mean motion, respectively considered as the derivative of the mean anomaly and the mean longitude, where the dotted line is the reference of the original 2B value.

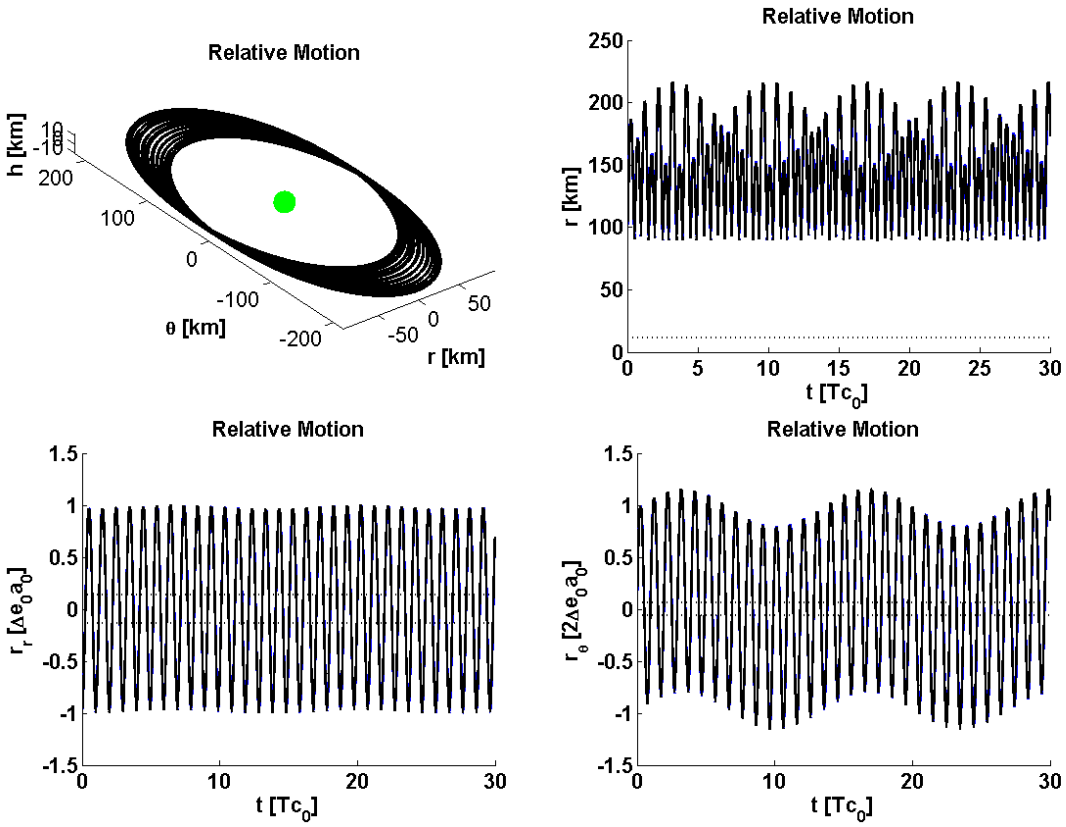

Figure E.4: **QSOs around Phobos.** Phobos orbit circular and equatorial, with Mars J_2. $\Delta e = 0.01$, $\Delta i = 0$. Orbit and plots in black line of the relative distance's magnitude, radial and transversal component. The plots do not overlap with the blue lines that are related to the mean CR3BP. Dotted lines indicate the reference distance of Phobos' mean radius.

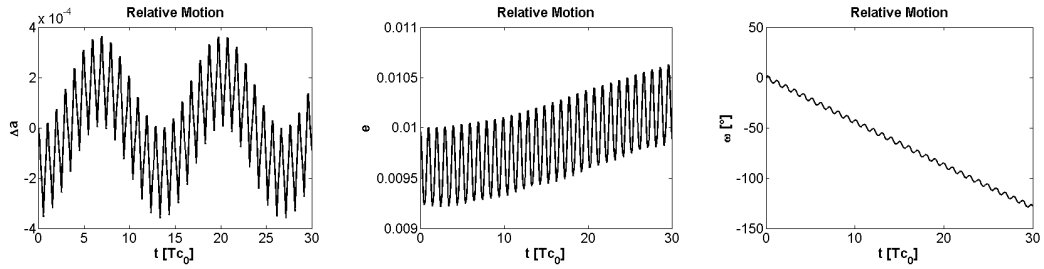

Figure E.5: **QSOs around Phobos.** Phobos orbit circular and equatorial, with Mars J_2. $\Delta e = 0.01$, $\Delta i = 0$. Orbital elements.

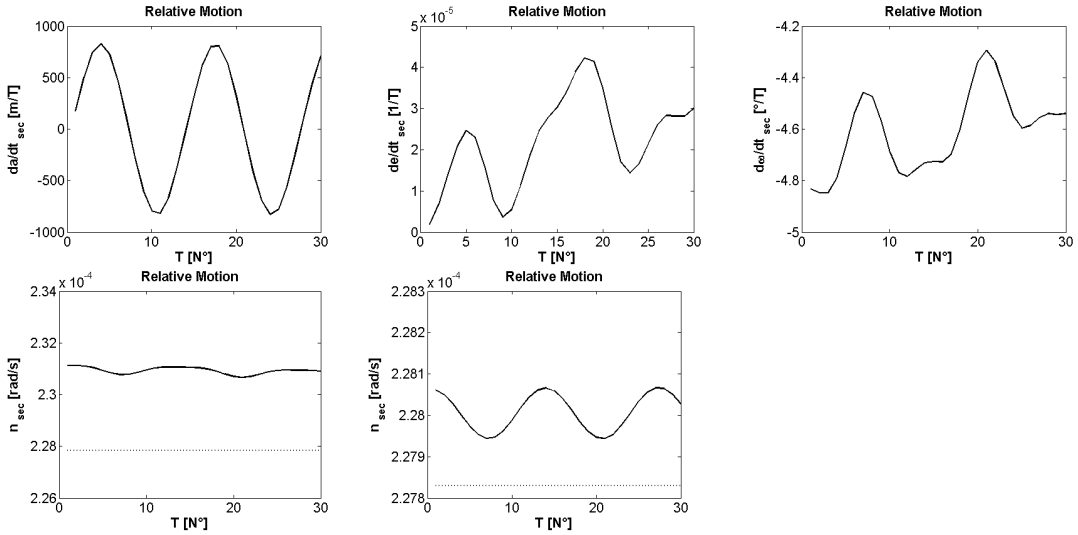

Figure E.6: **QSOs around Phobos.** Phobos orbit circular and equatorial, with Mars J_2. $\Delta e = 0.01$, $\Delta i = 0$. Secular derivative of the orbital elements, taken every orbital period. The last two graphs correspond to the mean motion, respectively considered as the derivative of the mean anomaly and the mean longitude, where the dotted line is the reference of the original 2B value.

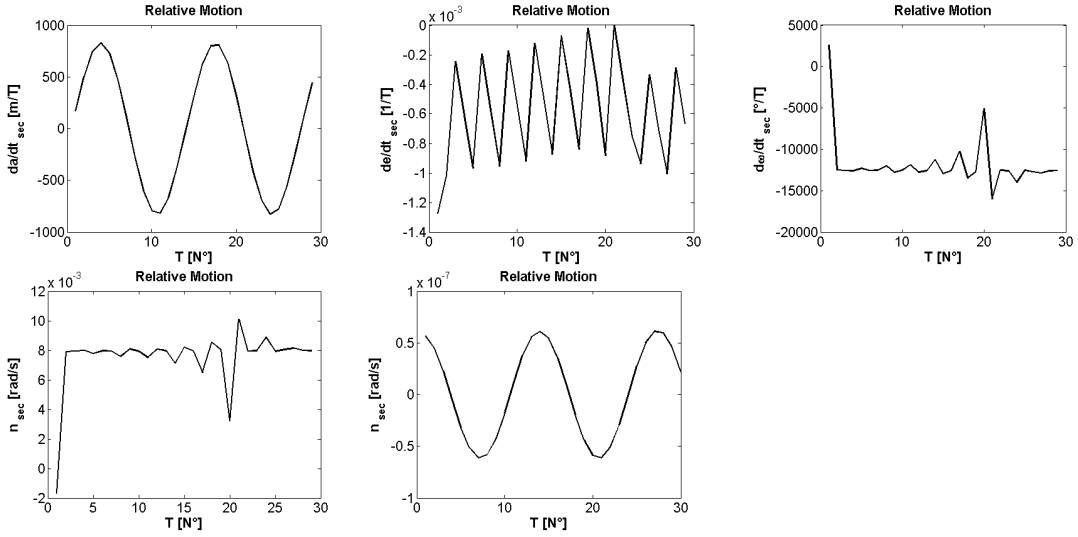

Figure E.7: **QSOs around Phobos.** Phobos orbit circular and equatorial, with Mars J_2. $\Delta e = 0.01$, $\Delta i = 0$. Difference between the spacecraft and Phobos' secular derivatives of the orbital elements, taken every orbital period. The last two graphs correspond to the difference of the mean motions, respectively considered as the derivative of the mean anomaly and the mean longitude, where the dotted line is the reference of the original 2B value.

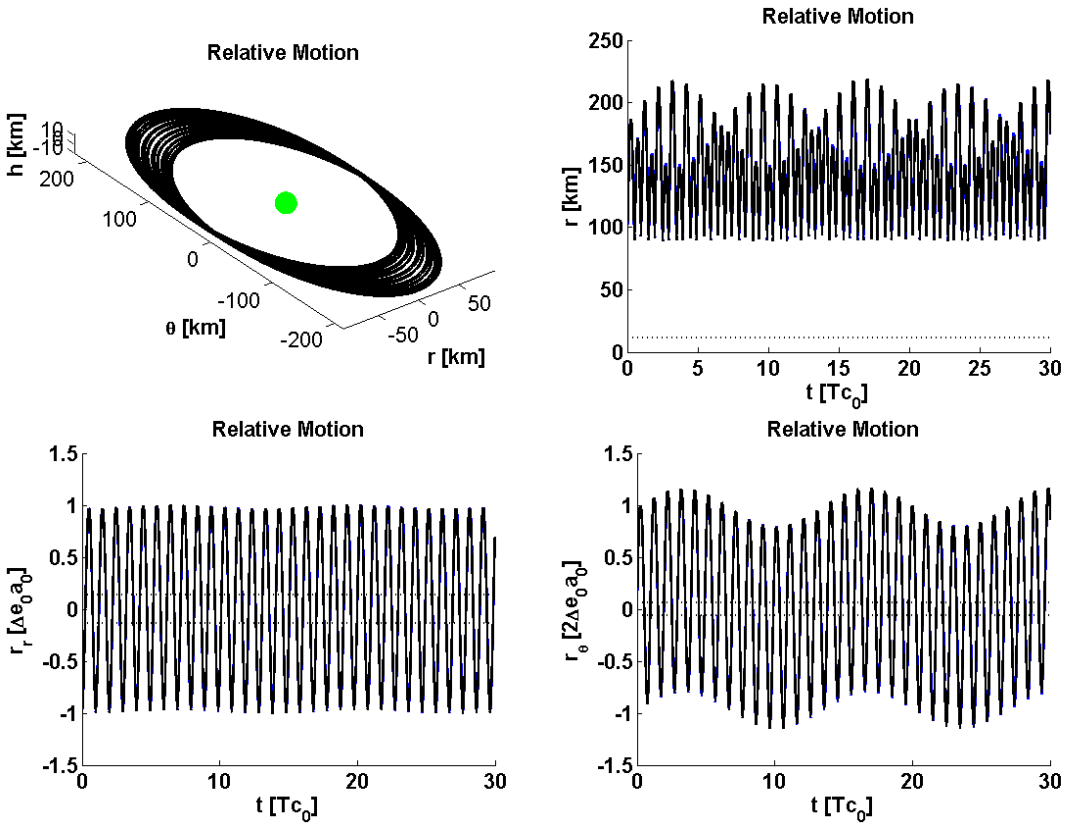

Figure E.8: **QSOs around Phobos.** Phobos orbit equatorial, with Mars J_2. $\Delta e = 0.01$, $\Delta i = 0$. Orbit and plots in black line of the relative distance's magnitude, radial and transversal component. The plots do not overlap with the blue lines that are related to the equivalent mean CR3BP. Dotted lines indicate the reference distance of Phobos' mean radius.

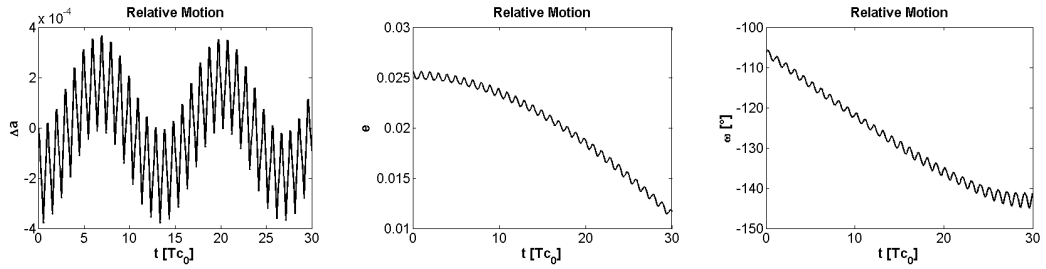

Figure E.9: **QSOs around Phobos.** Phobos orbit equatorial, with Mars J_2. $\Delta e = 0.01$, $\Delta i = 0$. Orbital elements.

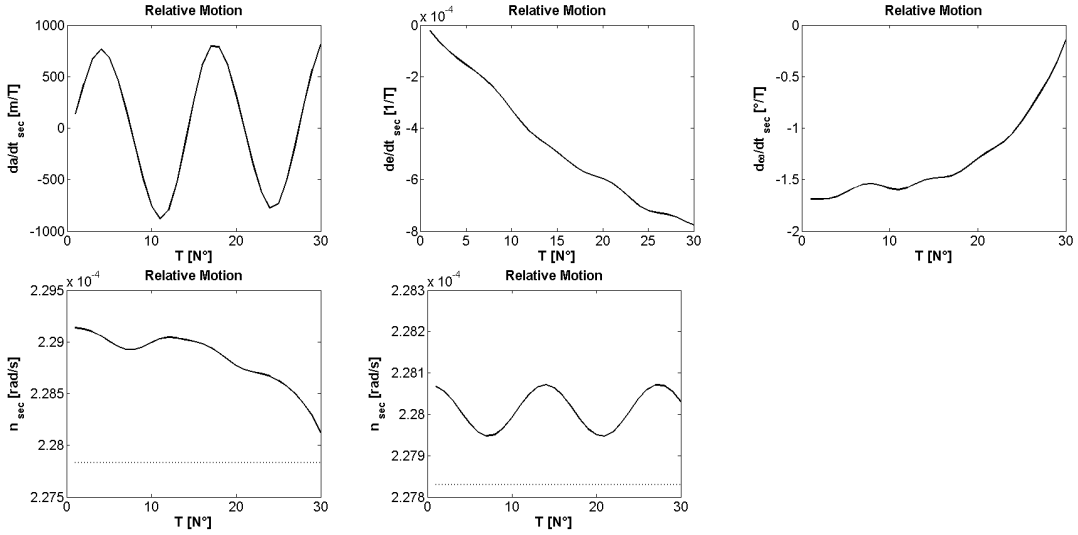

Figure E.10: **QSOs around Phobos.** Phobos orbit equatorial, with Mars J_2. $\Delta e = 0.01$, $\Delta i = 0$. Secular derivative of the orbital elements, taken every orbital period. The last two graphs correspond to the mean motion, respectively considered as the derivative of the mean anomaly and the mean longitude, where the dotted line is the reference of the original 2B value.

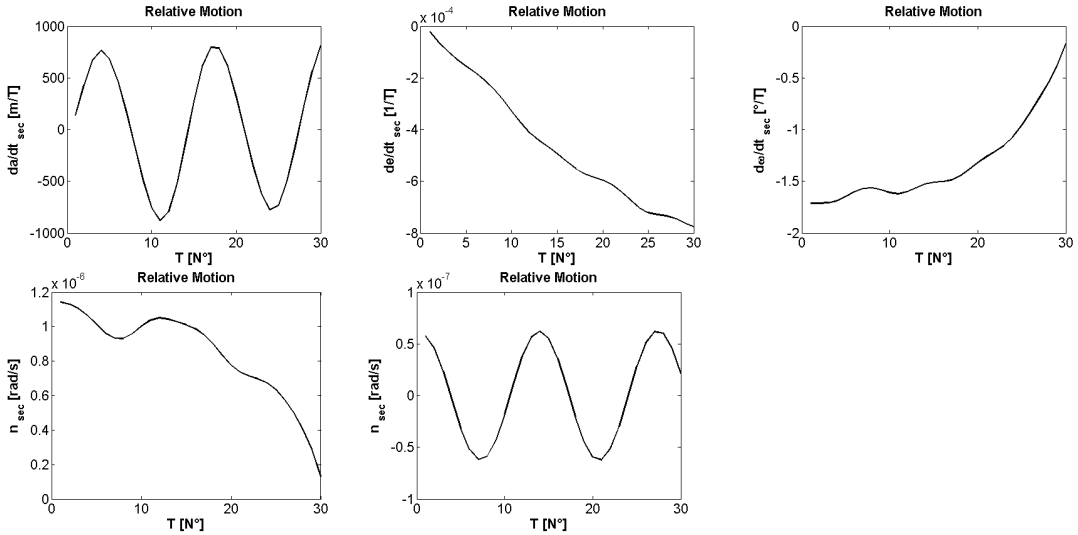

Figure E.11: **QSOs around Phobos.** Phobos orbit equatorial, with Mars J_2. $\Delta e = 0.01$, $\Delta i = 0$. Difference between the spacecraft and Phobos' secular derivatives of the orbital elements, taken every orbital period. The last two graphs correspond to the difference of the mean motions, respectively considered as the derivative of the mean anomaly and the mean longitude, where the dotted line is the reference of the original 2B value.

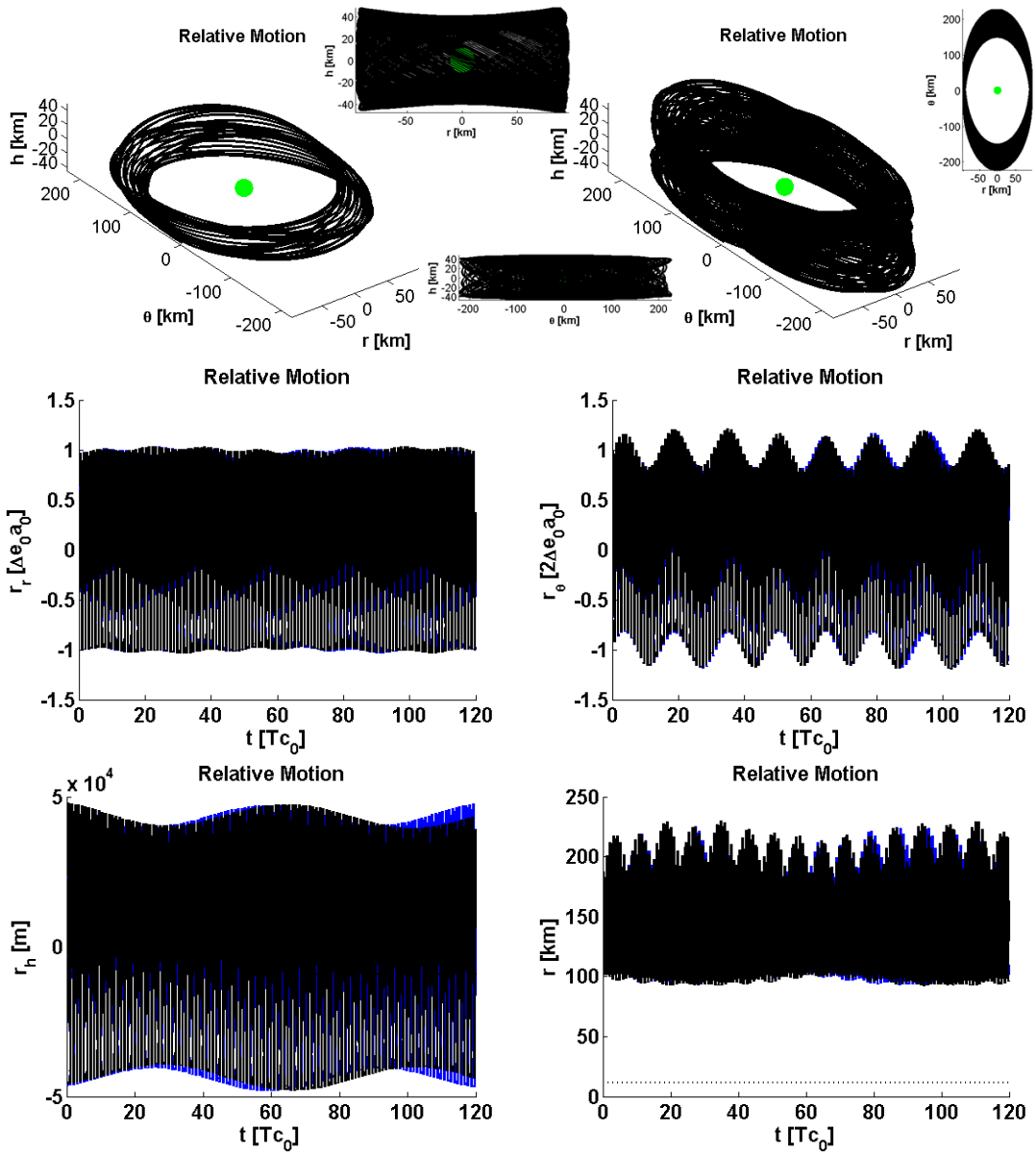

Figure E.12: **QSOs around Phobos.** Phobos real orbit, with Mars J_2. $\Delta e = 0.01$, $\Delta i = 0.005 rad$. Orbit after 30 and 120 orbital periods, with projections on the coordinate planes. Plots in black line of the relative distance's magnitude, radial, transversal and vertical component. The plots do not overlap with the blue lines that are related to the equivalent mean CR3BP. Dotted lines indicate the reference distance of Phobos' mean radius.

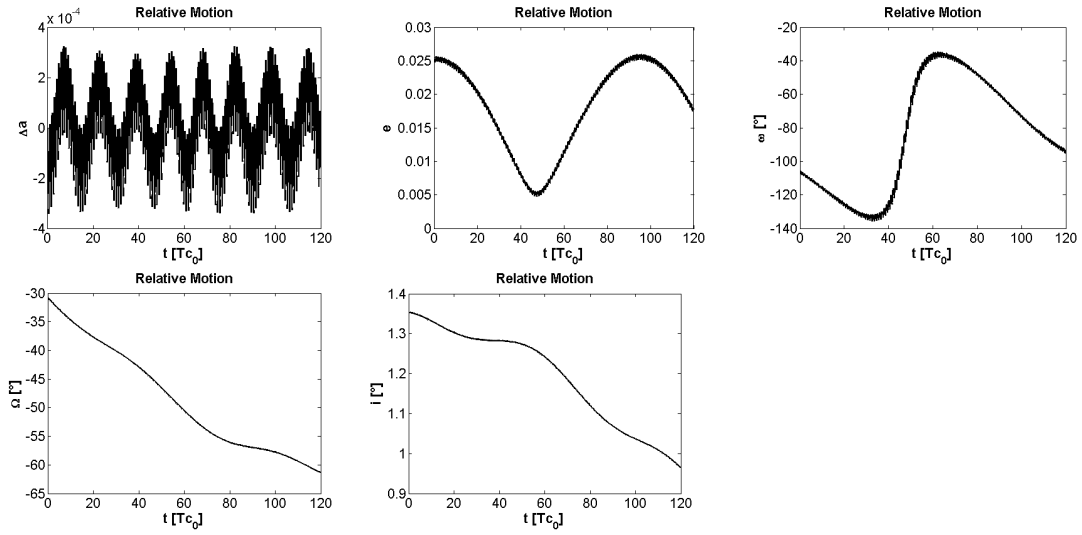

Figure E.13: **QSOs around Phobos.** Phobos real orbit, with Mars J_2. $\Delta e = 0.01$, $\Delta i = 0.005 rad$. Orbital elements.

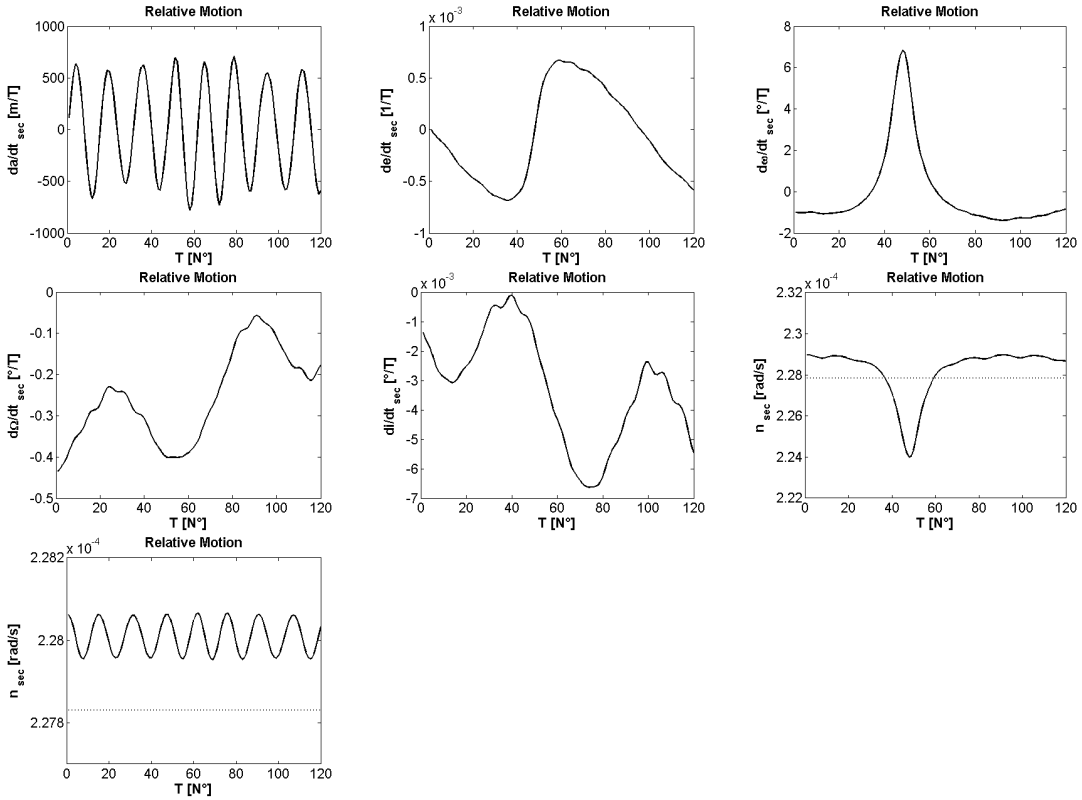

Figure E.14: **QSOs around Phobos.** Phobos real orbit, with Mars J_2. $\Delta e = 0.01$, $\Delta i = 0.005 rad$. Secular derivative of the orbital elements, taken every orbital period. The last two graphs correspond to the mean motion, respectively considered as the derivative of the mean anomaly and the mean longitude, where the dotted line is the reference of the original 2B value.

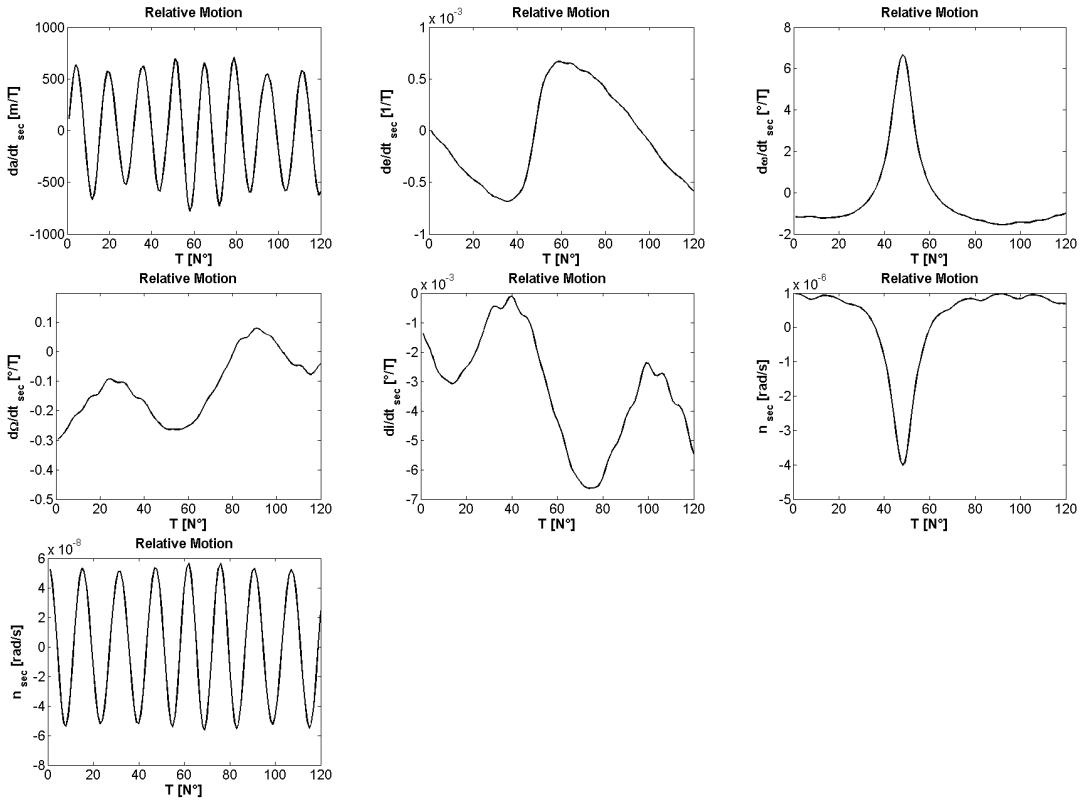

Figure E.15: **QSOs around Phobos.** Phobos real orbit, with Mars J_2. $\Delta e = 0.01$, $\Delta i = 0.005 rad$. Difference between the spacecraft and Phobos' secular derivatives of the orbital elements, taken every orbital period. The last two graphs correspond to the difference of the mean motions, respectively considered as the derivative of the mean anomaly and the mean longitude, where the dotted line is the reference of the original 2B value.

Appendix F

Libration Point Orbits around Deimos

In this chapter a preliminary analysis of the orbital dynamics around the Martian moon **Deimos** is conducted, using the same approach followed in this thesis for Phobos.

The physical and orbital characteristics of Deimos are collected in Table 2.1. It is evident that Deimos has half the size and double the distance from Mars with respect to Phobos. This significantly differentiates the SOI of the two moons for practical applications. The Hill's SOI of Deimos has radius $21.471km$ and its maximum altitude over Deimos' surface (mean ellipsoid) is $13.671km$. Recall that the maximum width of the shell between the Hill's SOI and Phobos' surface is instead of only $3.5km$. Hence, *the volume of the region of influence of Deimos, where a spacecraft can fly, is significantly larger than the case of Phobos, and this space is more distant in average from the surface of the body, which is also smaller.*

The following step is to evaluate the orbital perturbations in the vicinity of Deimos. The gravity field of Deimos is described in [187] with a GHs series expansions up to degree and order four, and this reference provides also the shape harmonics to model the surface of the moon up to degree and order six. In particular, J_2 is the dominant GH, and its value is approximately the same than the one of Phobos. One notes that the eccentricity of Deimos is only 1% of the one of Phobos. The results are presented in Fig.F.1, with the same approach described in section 2.4 (a_2 now refers to the magnitude of Deimos' Keplerian gravity). As said above, since the Deimos' SOI spans a range of altitudes much larger than the case of Phobos, the relative weight of the perturbation of the inhomogeneous gravity field of Deimos over the main forces of the CR3BP is only the 20% of what happens with Phobos. The effect of the eccentricity of the Mars-Deimos' orbit is also less significant, consistently with the ratio of the two eccentricity values. Compared with the case of Phobos, there is a significant decrease also on the Mars' J_2 differential perturbation, and a slight increase (as a relative ratio a^P/a_2) in the Sun's 4B effect and SRP, consistently with the larger extension of the SOI. However, these effects remain still small perturbations of the relative motion.

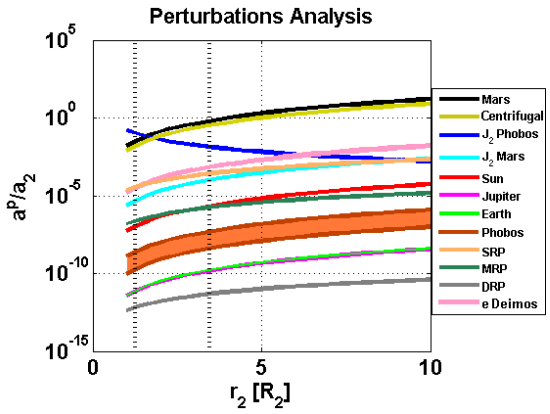

Figure F.1: **Differential perturbations analysis inside Deimos' sphere of influence.** Vertical dotted lines indicate Deimos' major size and Hill's SOI's radius.

Thus, the main result of this preliminary analysis is that, as a paramount difference from the case of Phobos, **the CR3BP is a reliable model for the preliminary analysis of the relative orbital dynamics around Deimos**.

Regarding the exploitation of the natural **LPOs** around Deimos, only the effect of the Deimos' gravity harmonics should be probed to be considered or not in the model of the dynamics. In particular, Deimos is tidally locked like Phobos, thus the model of the CR3BP-GH of Eq.3.37 can be used also for this moon. From the first-order 20% figure, of the difference between the relative weight of the GHs in the two cases estimated before, it could be forecasted that the LPOs of the CR3BP would not be significantly influenced.

The LPs in the Mars-Deimos CR3BP are positioned at an altitude over Deimos of $13.664km$ (L_1) and $13.678km$ (L_2). The LPs in the CR3BP-GH with the GHs of Deimos are positioned at an altitude of $13.911km$ (L_1) and $13.956km$ (L_2), and they are displaced in the y-z components by $[-23m, -25m]$ (L_1) and $[-20m, -42m]$ (L_2). Thus, the position of the two LPs in the more accurate dynamics is displaced for a total of $246m$ (L_1) and $279m$ (L_2), and this is consistent with the first-order forecast.

To probe the effect of the GHs on the LPOs, it is straightforward to do that by computing the behavior of small LPOs. Their linear solution is computed like in section 4.2.2.1, and is shown in Fig.F.2. The effect of the inhomogeneous gravity field of Deimos is difficult to be appreciated, because it produces only a very small tilt if compared with the case of Phobos in Fig.4.45, where the LPOs are also highly distorted and so completely different families develop. Thus, the GHs of Deimos do not change the families of the LPOs, that remain *the classical families of the CR3BP*: planar and vertical Lyapunov, Northern and Southern Halo, right and left axials. Moreover, the eccentricity effect introduces an oscillation on the LPOs of only $4m$. This is not significant because is of the same order of magnitude (more likely inferior) than the estimation error of the navigation system.

Finally, the periodic LPOs around Deimos can be computed with the classical method-

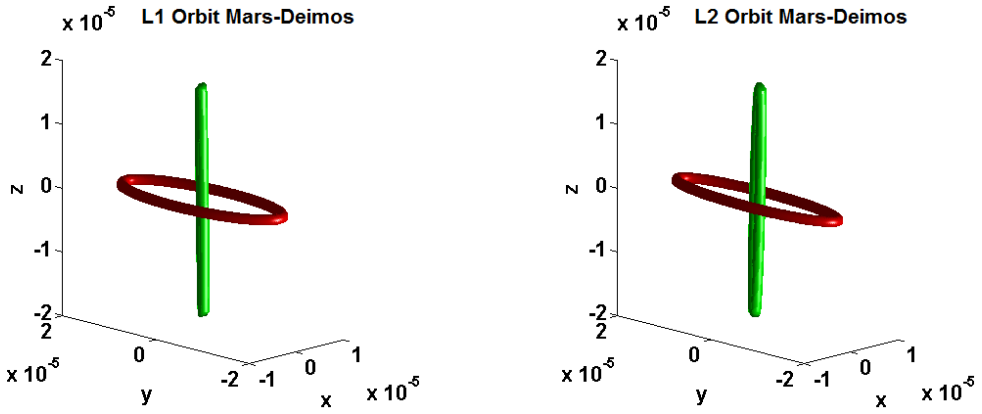

Figure F.2: **Periodic LPOs in the Mars-Deimos CR3BP-GH.** Linear center manifold's POs around L_1 and L_2 of the Mars-Deimos CR3BP-GH. The normal mode's initial condition is set to 1% of the normalized distance between secondary and LP. Origin at the LP of the CR3BP-GH.

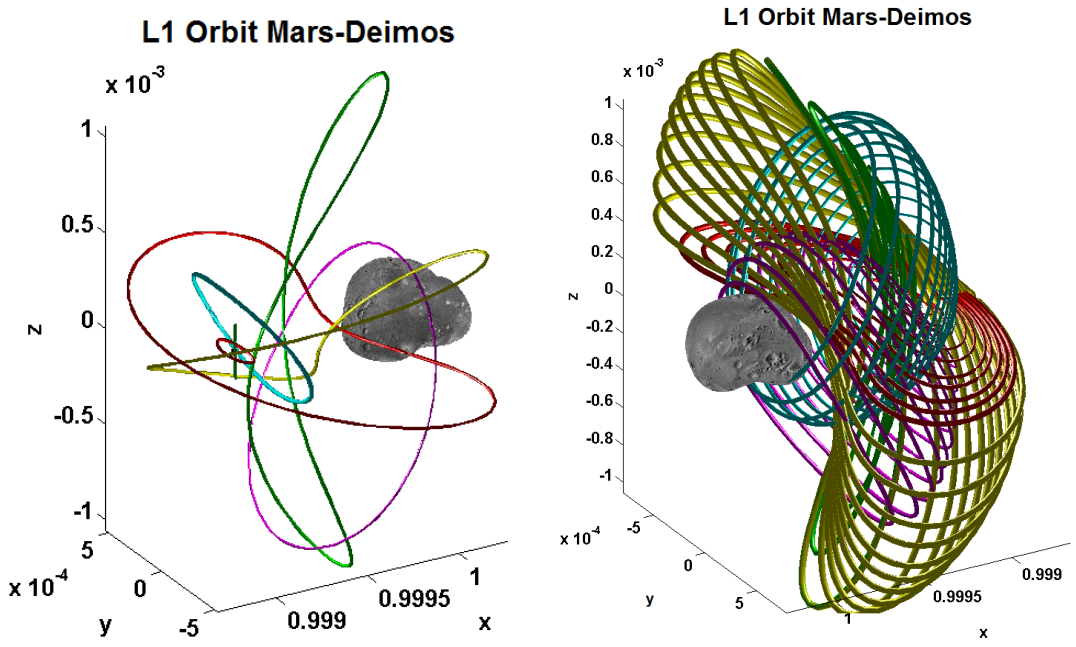

Figure F.3: **Periodic LPOs in the Mars-Deimos CR3BP-GH.** Graphical visualization of the planar Lyapunov (red), vertical Lyapunov (green), Northern Halo (cyan), Southern Halo (magenta), and right axial (yellow) families of POs around L_1 in the CR3BP-GH. Shape harmonics series expansion for Deimos' surface.

ologies tailored for the CR3BP. Nevertheless, in this chapter the model of the CR3BP-GH is used to compute the LPOs, following the techniques developed in this thesis for the case of Phobos (see section 4.2.2). In particular, the numerical approach is chosen, focusing on the LPOs around L_1. Due to the smaller μ with respect to the one of Phobos, the two collinear manifolds are approximately symmetric. The linear solutions of Fig.F.2, that represent the planar and vertical Lyapunov orbits at small-energy, are used as starting guesses for a NC with respect to the energy. It is worth to note that

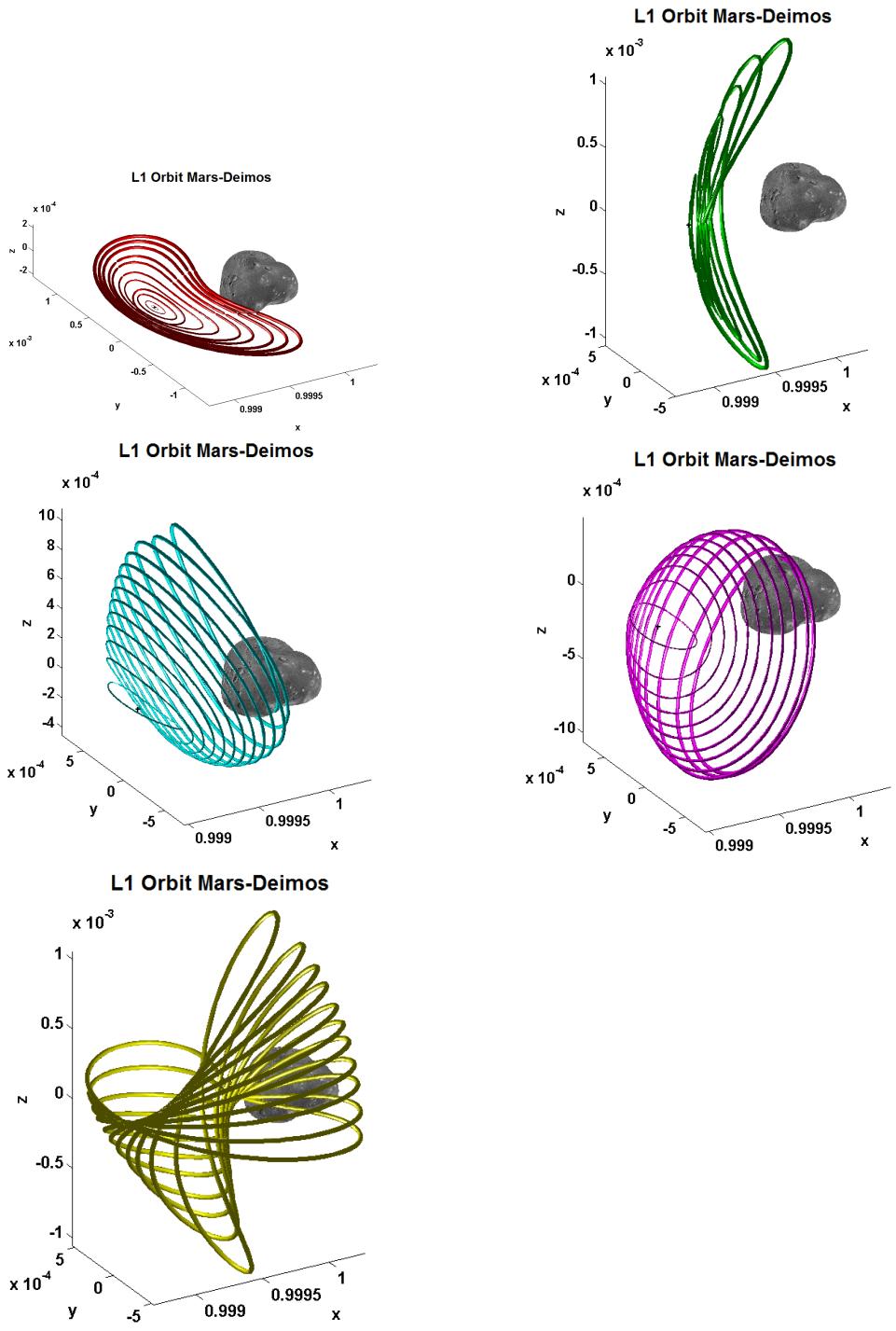

Figure F.4: **Periodic LPOs in the Mars-Deimos CR3BP-GH.** Graphical visualization of the planar Lyapunov (red), vertical Lyapunov (green), Northern Halo (cyan), Southern Halo (magenta), and right axial (yellow) families of POs around L_1 in the CR3BP-GH. Shape harmonics series expansion for Deimos' surface.

a smaller μ anticipates the bifurcations, that tend to develop closer to the LP (in normalized units). The CR3BP-GH is not symmetric, therefore the bifurcation diagram of the families of LPOs does not correspond to the classical scheme of the CR3BP.

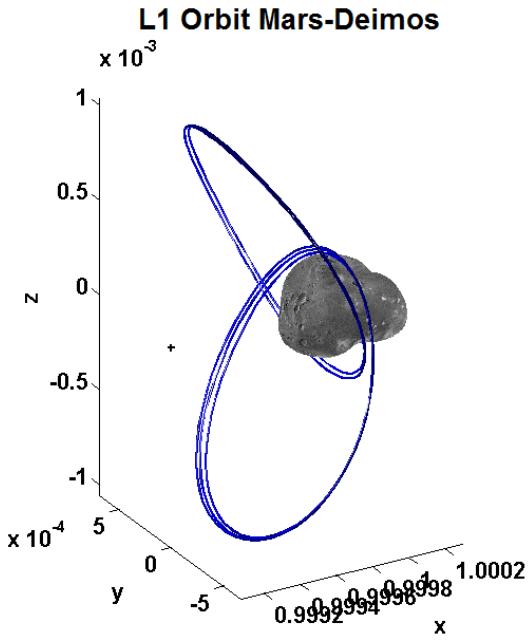

Figure F.5: **Periodic LPOs in the Mars-Deimos CR3BP-GH.** Examples of stable Halo orbits: two Northern Halo and three Southern Halo around L_1 in the CR3BP-GH.

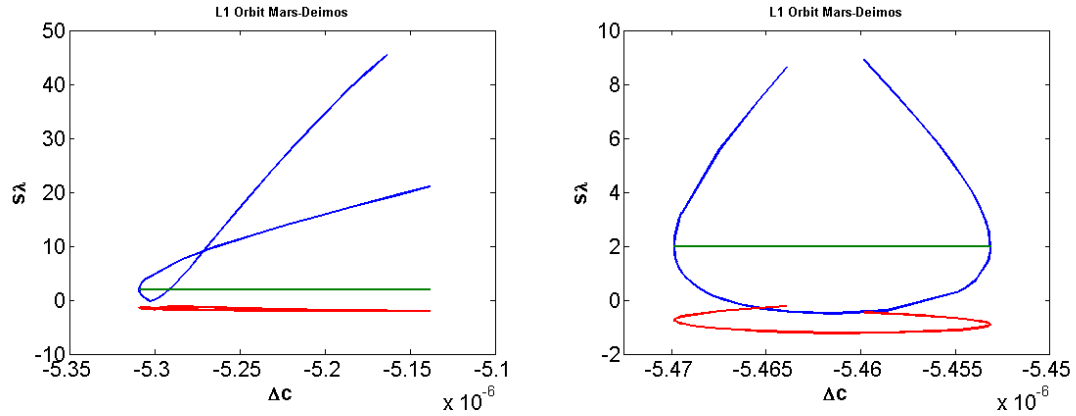

Figure F.6: **Periodic LPOs in the Mars-Deimos CR3BP-GH.** Characteristic curves of the three stability indexes of the families of Northern (on the left) and Southern (on the right) Halo orbits around L_1 in the CR3BP-GH, parameterized by the differential Jacobi integral with respect to the LP. Focus on the region of stable orbits, where the stability indexes are in $[-2, 2]$.

However, the effect of the GHs on the morphology of the orbits is not significant as proved before, so there is no need to rename the families of LPOs like in the case of Phobos. Fig.F.3 provides a sample of the periodic LPOs around L_1: a medium and large planar Lyapunov (red), a medium and large vertical Lyapunov (green), a small Northern Halo (cyan), a large Southern Halo (magenta), a medium right axial (yellow). Fig.F.3-F.4 provide a summary of all the families. One notes that large vertical Lyapunov and large Halo orbits can provide a ground-track over the poles. In particular, due to the fact that the ancestor Lyapunov of the Halo branches has moved closer to the LP, and the altitude of the SOI over Deimos' surface is much larger than it happens

for Phobos, a paramount result is obtained: **large Halo orbits around Deimos are marginally stable**. This is proved in Fig.F.6, where the Floquet stability indexes are represented. These stable Halo orbits are visualized in Fig.F.5. The range of this subset is constrained with respect to the whole family: for the Northern Halo orbit its spans orbits in a range of $738m$, for the Southern Halo orbits $1,614km$. Moreover, these large stable orbits are close to Deimos, and the largest stable Halo orbits of the Southern branch intersect Deimos' surface.

The inside branch of the invariant manifolds of the large LPOs will intersect Deimos' surface, and can be used for natural landing and take-off, like in the case of Phobos (see section 4.4.6). In contrast, the largest volume available inside the SOI of Deimos should allow the existence of homoclinic and heteroclinic connections between the two LPs, revolving around the moon.

In conclusion, Deimos' orbital dynamics are far more classic than Phobos, and mission planning could be undertaken with the classical CR3BP.

Bibliography

[1] P. Lee. Phobos and Deimos update. In *7th SBAG Meeting*, Pasadena, July 10-11 2012.

[2] P. Rosenblatt. The origin of the Martian moons revisited. *The Astronomy and Astrophysics Review*, 19(44), 2011.

[3] P. Lee. Mission to Phobos and Deimos: Exploring the moons of Mars. `www.youtube.com/watch?v=4S7M-Wt61Hk`, June 3 2014. [Online].

[4] J. F. Bell, F. Fanale, and D. P. Cruikshank. Chemical and physical properties of the Martian satellites. In *Resources of Near-Earth Space*, Space Science Series, pages 887–901. The University of Arizona Press, 1993.

[5] M. Pajola, M. Lazzarin, C. M. Dalle Ore, D. P. Cruikshank, T. L. Roush, S. Magrin, I. Bertini, F. La Forgia, and C. Barbieri. Phobos as a D-Type captured asteroid, spectral modeling from 0.25 to 4.0 μm. *The Astrophysical Journal*, 777 (2), 2013.

[6] P. Lee and K. Lorber. Phobos and Deimos: Planetary protection knowledge gaps for human missions. In *Workshop on Planetary Protection Knowledge Gaps for Human Extraterrestrial Missions*, NASA Ames Research Center, March 24-26 2015.

[7] R. A. Craddock. Are Phobos and Deimos the result of a giant impact? *Icarus*, 211(2):1150–1161, 2011.

[8] P. Rosenblatt and C. Charnoz. On the formation of the Martian moons from a circum-mars accretion disk. In *46th ESA ESLAB Symposium: Formation and Evolution of Moons*, Noordwijk, June 25-28 2012.

[9] E. K. Gardner. Evidence of life on Mars could come from Martian moon. `www.purdue.edu/newsroom/general/2012/120628T-MeloshHowellPhobos.html`, June 28 2012. [Online].

[10] R. A. Jacobson. The orbits and masses of the Martian satellites and the libration of Phobos. *The Astronomical Journal*, 139(2):668–679, 2010.

[11] N. Borderies and C. F. Yoder. Phobos' gravity field and its influence on its orbit and physical librations. *Astronomy and Astrophysics*, 233:235–251, 1990.

[12] A. P. Yefremov. Relativistic warning to space missions aimed to reach Phobos. *International Journal of Astronomy and Astrophysics*, 1:200–203, 2011.

[13] B. K. Sharma. Theoretical formulation of the Phobos, moon of Mars, rate of altitudinal loss. arXiv(0805.1454), 2008. [e-prints].

[14] K. R. Ramsley and J. W. Head III. Mars imapct ejecta in the regolith of Phobos: Bulk concentration and distribution. *Planetary and Space Science*, 87:115–129, 2013.

[15] K. R. Ramsley and J. W. Head III. The origin of Phobos grooves from ejecta launched from impact craters on Mars: Test of the hypothesis. *Planetary and Space Science*, 75:69–95, 2013.

[16] L. Chappaz, H. J. Melosh, M. Vaquero, and K. C. Howell. Transfer of impact material from the surface of Mars to Phobos and Deimos. In *22nd AAS/AIAA Space Flight Mechanics Meeting*, Charleston, January 29 - February 2 2012.

[17] A. V. Krikov, L. L. Sokolov, and V. V. Dikarev. Dynamics of Mars-orbiting dust: Effects of light pressure and planetary oblateness. *Celestial Mechanics and DynamicaI Astronomy*, 63:313–339, 1996.

[18] A. J. Dombard, O. S. Barnouin, L. M. Prockter, and P. C. Thomas. Boulders and ponds on the asteroid 433 Eros. *Icarus*, 210(2):713–721, 2010.

[19] J. B. Hopkins and W. D. Pratt. Comparison of Deimos and Phobos as destinations for human exploration, and identification of preferred landing sites. In *AIAA Space 2011 Conference & Exposition*, Long Beach, September 27-29 2011.

[20] S. F. Singer. The PhD proposal: A manned mission to Phobos and Deimos. In *The case for Mars Conference*, Boulder, April 29 - May 2 1981.

[21] B. O'Leary. Rationales for early human missions to Phobos and Deimos. In *Lunar Bases and Space Activities of the 21st Century*, Houston, 1985.

[22] T. H. Sweetser. Phobos first! the right focus for NASA's vision. In *Concepts and Approaches for Mars Exploration Workshop*, Houston, June 12-14 2012.

[23] P. Troutman. The evolvable Mars campaign: The moons of Mars as a destination. In *11th NASA Small Body Assessment Group Meeting*, Washington, July 29-31 2014.

[24] P. Abell, J. Antoll, B. Barbee, D. Beaty, D. Bass, J. Castillo-Rogez, D. Coan, T. Colaprete, K. Daugherty, B. Drake, K. Earle, L. Graham, M. Hembree, S. Hoffman, S. Jefferies, R. Lewis, M. Lupisella, D. Mazanek, and D. Reeves. Considerations for designing a human mission to the Martian Moons. In *2013 Space Challenge*, California Institute of Technology, March 25-29 2013.

[25] R. Walker. To explore Mars with likes of occulus rift and virtuix omni: From Mars capture orbit, Phobos or Deimos. `www.science20.com/robert_inventor/to_explore_mars_with_likes_of_occulus_rift_virtuix_omni_from_mars_capture_orbit_phobos_or_deimos-155974`, June 6 2015. [Online].

[26] M. McCaughrean. *ESA's Report to the 39th COSPAR Meeting*. ESA Communications, Noordwijck, 2012.

[27] M. Pavone, J. Castillo-Rogez, J. A. Hoffman, and I. A. D. Nesnas. Spacecraft-rover hybrids for the exploration of small solar system bodies. Final report NASA NIAC Phase-I study, September 30 2012.

[28] R. Staehle and L. Friedman. Interplanetary cubesats to the Moon and beyond. In *1st International Workshop on LunarCubes*, Palo Alto, November 13 2012.

[29] J. Sommerer. Technical and programmatic prospects for human space exploration 2015-2030. In *65th International Astronautical Congress*, Toronto, September 29 - October 3 2014.

[30] J. E. Brandenburg. Mars-Phobos: A Mars mission architecture with Mars-Moon synergy. *Journal of Space Exploration*, 2012.

[31] ESA Media Relations Office. N°37-2012: European ministers decide to invest in space to boost Europes competitiveness and growth. `www.esa.int`. [Online].

[32] J. L. Vago and M. Coradini. ExoMars: Mars exploration program. In *Concepts and Approaches for Mars Exploration Workshop*, Houston, June 12-14 2012.

[33] D. Koschny. Phootprint: An ESA mission study. In *Concepts and Approaches for Mars Exploration Workshop*, Houston, June 12-14 2012.

[34] F. Mura, A. Ferri, M. A. Perino, P. Rideau, R. Gelmi, F. Cacciatore, D. Rebuffat, and J. Larranaga. Phootprint. In *65th International Astronautical Congress*, Toronto, September 29 - October 3 2014.

[35] S. L. Murchie, D. T. Britt, and C. M. Pieters. The value of Phobos sample return. *Planetary and Space Science*, 102:176–182, 2014.

[36] B. Dodson. NASA investigates sending CubeSats to Phobos and back. `http://www.gizmag.com/cubesats-phobos-nasa/22037`, April 3 2012. [Online].

[37] P. Abell, D. Beaty, D. Bass, J. Castillo-Rogez, T. Colaprete, S. Hoffman, R. Lewis, and D. Mazanek. Instruments needed for a human exploration mission of Phobos and Deimos. In *International Workshop on Instrumentation for Planetary Missions*, NASA Goddard Space Flight Center, October 2012.

[38] H. W. Price, R. C. Woolley, N. J. Strange, and J. D. Baker. Human missions to Mars orbit, Phobos, and Mars surface using 100-kWe-class solar electric propulsion. In *AIAA Space 2014 Conference*, San Diego, August 4-7 2014.

[39] A. Rivkin. NEO-Phobos-Deimos strategic knowledge gaps: Special action team final report. In *NASA SBAG Meeting*, November 28 2012.

[40] P. Lee, M. Bicay, A. Colaprete, R. Elphic, A. Genova, B. Hine, M. Horanyi, B. Jaroux, D. Korsmeyer, B. S. Lewis, and S. P. Worden. Phobos And Deimos & Mars Environment (PADME): A LADEE-derived mission to explore Mars's moons and the Martian orbital environment. In *45th Lunar and Planetary Science Conference*, The Woodlands, March 17-21 2014.

[41] M. Pandika. Stanford researchers develop acrobatic space rovers to explore moons and asteroids. `news.stanford.edu/news/2012/december/rover-mars-phobos-122812.html`, December 28 2012. [Online].

[42] B. Dorminey. Phobos as first pit stop in manned Mars exploration. `http://www.forbes.com/sites/brucedorminey/2013/06/26/phobos-as-potential-first-pit-stop-in-human-mission-to-mars`, June 26 2013. [Online].

[43] M. Pavone, J. Castillo-Rogez, J. A. Hoffman, I. A. D. Nesnas, and N. J. Strange. Spacecraft-rover hybrids for the exploration of small solar system bodies. In *IEEE Aerospace Conference*, Big Sky, March 2-9 2013.

[44] J. J. Lang, J. D. Baker, J. C. Castillo-Rogez, T. P. McElrath, J. S. Piacentine, and J. S. Snyder. Phobos exploration using two small SEP spacecraft. In *Global Space Exploration Conference*, Washington, May 22-24 2012.

[45] N. Bosanac, V. Dang, A. Diaz, F. Ebersohn, A. Fraeman, A. Gibbings, S. Gonzalez, T. Maddox, C. Nie, J. Qi, J. Rankin, T. Rebelo, N. Sweet, G. Taylor, N. Tie, and G. Valentino. Technology Advancing Phobos Exploration and Return. Caltech Space Challenge. Team Explorer report, March 29 2013.

[46] A. Kumar, A. R. Dahir, A. A. Williams, A. R. Chadwick, B. N. Hassan, C. P. Thomas, E. Nathanson, J. Kolmas, J. B. Price, K. M. Schlottke, M. Tanner, O. J. Igbinosun, P. Nizenkov, S. A. Hall, S. Krishnamoorthy, and S. Do. Asaph-1. Caltech Space Challenge. Team Voyager report, March 29 2013.

[47] P. Lee. 1st international conference on the exploration of Phobos and Deimos: Summary and recommendations. In *1st International Conference on the Exploration of Phobos and Deimos: The Science, Robotic Reconnaissance, and Human Exploration of the Two Moons of Mars*, NASA Ames Research Center, November 5-7 2007.

[48] Y. Ni, H. Baoyin, and J. Li. Orbit dynamics in the vicinity of asteroids with solar perturbation. In *65th International Astronautical Congress*, Toronto, September 29 - October 3 2014.

[49] E. I. Abouelmagd and M. A. Sharaf. The motion around the libration points in the restricted three-body problem with the effect of radiation and oblateness. *Astrophysics and Space Science*, 344(2):321–332, 2013.

[50] W. S. Koon, M. W. Lo, J. E. Marsden, and S. D. Ross. *Dynamical Systems, the Three-Body Problem and Space Mission Design.* Springer-Verlag, New York City, 2011.

[51] J. J. Masdemont. High order expansions of invariant manifolds of libration point orbits with applications to mission design. *Dynamical Systems: An International Journal*, 20(1):59–113, 2004.

[52] G. Gómez and J. M. Mondelo. The dynamics around the collinear equilibrium points of the restricted three-body problem. *Physica D*, 157(4):283–321, 2001.

[53] G. Gómez, J. J. Masdemont, and J. M. Mondelo. The dynamical substitutes of the libration points for simplified Solar System models. In *Libration Point Orbits and Applications*, Aiguablava, June 10-14 2002.

[54] R. Broucke. Stability of periodic orbits in the elliptic restricted three-body problem. *AIAA Journal*, 7(6):1003–1009, 1969.

[55] M. Lara. On numerical continuation of families of periodic orbits in a parametric potential. *Mechanics Research Communications*, 23(3):291–298, 1996.

[56] M. Lara. Three-body dynamics around the smaller primary: Application to the design of science orbits. *Journal of Aerospace Engineering, Sciences and Applications*, 2(1):53–65, 2010.

[57] M. S. Wallace, J. S. Parker, N. J. Strange, and D. Grebow. Orbital operations for Phobos and Deimos exploration. In *AIAA-AAS Astrodynamics Specialist Conference*, Minneapolis, August 13-16 2012.

[58] M. Ceccaroni and J. Biggs. Low thrust propulsion in a coplanar circular restricted four-body problem. *Celestial Mechanics and Dynamical Astronomy*, 112(2):191–219, 2012.

[59] M. Morimoto, H. Yamakawa, and K. Uesugi. Periodic orbits with low thrust propulsion in the restricted three-body problem. *Journal of Guidance, Control, and Dynamics*, 29(5):1131–1139, 2006.

[60] C. Bombardelli. Stable artificial equilibrium points in the Mars-Phobos system. In *1st IAA-AAS Conference on Dynamics and Control of Space Systems*, Porto, March 19-21 2012.

[61] P. J. S. Gil and J. Schwartz. Simulations of Quasi-Satellite orbits around Phobos. *Journal of Guidance, Control and Dynamics*, 33(3):901–914, 2010.

[62] F. da Silva Pais Cabral. On the stability of Quasi-Satellite orbits in the elliptic restricted three-body problem. Master's thesis, Universidade Técnica de Lisboa, 2011.

[63] C. Bombardelli and J. Peláez. On the stability of artificial equilibrium points in the circular restricted three-body problem. *Celestial Mechanics and Dynamical Astronomy*, 109:13–26, 2011.

[64] R. J. McKay, M. Macdonald, J. D. Biggs, and C. McInnes. Survey of highly non-keplerian orbits with low-thrust propulsion. *Journal of Guidance, Control and Dynamics*, 34(3):645–666, 2011.

[65] T. Lam and G. J. Whiffen. Exploration of Distant Retrograde orbits around Europa. In *15th AAS-AIAA Space Flight Mechanics Conference*, Copper Mountain, January 23-27 2005.

[66] ESA/ESTEC. Mission analysis guidelines for Martian moon sample return. Final report, 2012.

[67] S. Mikkola, K. Innanen, P. Wiegert, M. Connors, and R. Brasser. Stability limits for the Quasi-Satellite orbit. *Monthly Notices of the Royal Astronomical Society*, 369:15–24, 2006.

[68] H. Baoyin and C. R. McInnes. Trajectories to and from the Lagrange points and the primary body surfaces. *Journal of Guidance, Control, and Dynamics*, 29(4): 998–1003, 2006.

[69] T. C. Duxbury and J. D. Callahan. Pole and Prime Meridian expressions for Phobos and Deimos. *The Astronomical Journal*, 86(11):1722–1727, 1981.

[70] A. R. Conrad. The 2009 report of the IAU working group on cartographic coordinates and rotational elements. *Celestial Mechanics and Dynamical Astronomy, Special Report*, 2010.

[71] R. W. Farquhar. *The Control and Use of Libration-Point Satellite*. PhD thesis, Stanford University, 1968.

[72] K. C. Howell. Three-dimensional, periodic, 'Halo' orbits. *Celestial Mechanics*, 32 (53):53–71, 1984.

[73] C. C. Conley. Low energy transit orbits in the restricted three-body problem. *SIAM Journal of Applied Mathematics*, 16:732–746, 1969.

[74] R. McGehee. *Some Homoclinic Orbits for the Restricted Three-Body Problem*. PhD thesis, University of Wisconsin, 1969.

[75] W. S. Koon, M. W. Lo, J. E. Marsden, and S. D. Ross. Heteroclinic connections between periodic orbits and resonance transitions in celestial mechanics. *Chaos*, 10:427–469, 2000.

[76] J. Llibre, R. Martinez, and C. Simó. Transversality of the invariant manifolds associated to the Lyapunov family of periodic orbits near L2 in the restricted three-body problem. *Journal of Differential Equations*, 58:104–156, 1985.

[77] J. Moser. On the generalisation of a theorem of Lyapunov. *Communications on Pure and Applied Mathematics*, 11:257–271, 1985.

[78] P. J. S. Gil. QSO: Current state of the art and mission analysis results for a class of Phobos observation and access orbits. In *3rd International Workshop on Spaceflight Dynamics and Control*, Covilhã, October 9 2007.

[79] G. Genta, A. Dupas, and J. M. Salotti. IAA study group on global human Mars system missions exploration. In *65th International Astronautical Congress*, Toronto, September 29 - October 3 2014.

[80] J. Sabino. Radiation environment and effects in human spaceflight: A lunar mission. Master's thesis, Universidade Técnica de Lisboa, 2012.

[81] A. Keating. *Mars Radiation Environment and Effects on EEE Components*. PhD thesis, Universidade Técnica de Lisboa, 2008.

[82] G. Reitz. Biological effects of space radiation. In *ESA Space Weather Workshop*, 1998.

[83] Committee on the Evaluation of Radiation Shielding for Space Exploration, Aeronautics and Space Engineering Board, and National Research Council. *Managing Radiation Risk in the New Era of Exploration*. National Academies Press, Washington, 2008.

[84] F. A. Cucinotta, M. H. Y. Kim, and L. J. Chappell. Space radiation cancer risk projections and uncertainties. NASA report, 2012.

[85] R. Turner. Radiation risks and challenges associated with human missions to Phobos-Deimos. In *2013 Space Challenge*, California Institute of Technology, March 25-29 2013.

[86] Belgisch Instituut voor Ruimte-Aëronomie (BIRA-IASB) and ESA/ESTEC TEC-SEE Section. SPENVIS: The space environment information system. `www.spenvis.oma.be/intro.php`. [Online].

[87] P. Gonçalves, A. Keating, S. Valente, P. Truscott, F. Lei, L. Desorgher, D. Heynderickx, N. Crosby, H. de Witt, G. Degreef, P. Nieminenk, and G. Santin. MarsREM: The Mars Energetic Radiation Environment Models. In *31st International Cosmic Ray Conference*, Łódź, July 7-15 2009.

[88] S. McKenna-Lawlor, P. Gonçalves, A. Keating, G. Reitz, and D. Matthiä. Overview of energetic particle hazards during prospective manned missions to Mars. *Planetary and Space Science*, 63(64):123–132, 2012.

[89] S. McKenna-Lawlor, P. Gonçalves, A. Keating, B. Morgado, D. Heynderickx, P. Nieminen, G. Santin, P. Truscott, F. Lei, B. Foing, and J. Balaz. Characterization of the particle radiation environment at three potential landing sites on Mars. *Icarus*, 218:723–734, 2012.

[90] C. Pei. *Solar Energetic Particle Transport in the Heliosphere.* PhD thesis, University of Arizona, 2007.

[91] M. A. Andreu. *The Quasi-Bicircular Problem.* PhD thesis, Universitat de Barcelona, 1998.

[92] W. M. Kaula. *Theory of Satellite Geodesy.* Blaisdell, Waltham, 1966.

[93] W. M. Kaula. Geophysical implications of satellite determination of the Earth gravitational field. *Space Science Revolution*, 7:769–794, 1967.

[94] B. F. Chao and D. P. Rubincam. The gravitational field of Phobos. *Geophysical Research Letters*, 16(8):859–862, 1989.

[95] R. A. Werner. The gravitational potential of a homogeneous polyhedron or don't cut corners. *Celestial Mechanics and Dynamical Astronomy*, 59:253–278, 1994.

[96] X. Hu. A comparison of ellipsoidal and spherical harmonics for gravitational field modeling of non-spherical bodies. Master's thesis, Ohio State University, June 2012.

[97] S. Pines. Uniform representation of the gravitational potential and its derivatives. *AIAA Journal*, 11(11):1508–1511, 1973.

[98] B. A. Jones, G. H. Born, and G. Beylkin. Orbit determination with the cubed-sphere gravity model. *Journal of Spacecraft and Rockets*, 49(1), 2012.

[99] R. M. Brannon. *Curvilinear Analysis in an Euclidian Space. University of New Mexico Supplemental Book Draft.* University of New Mexico, Albuquerque, 2004.

[100] R. J. Turner. A model of Phobos. *Icarus*, 33:116–140, 1978.

[101] K. Willner. *The Martian Moon Phobos. A Geodetic Analysis of its Motion, Orientation, Shape, and Physical Parameters*. PhD thesis, Technische Universität Berlin, 2009.

[102] Z. Martinec, K. Pěč, and M. Burša. The Phobos gravitational field modeled on the basis of its topography. *Earth, Moon, and Planets*, 45:219–235, 1989.

[103] V. A. Chobotov. *Orbital Mechanics*. American Institute of Aeronautics and Astronautics Inc., Renston, 2002.

[104] R. H. Battin. *An Introduction to the Mathematics and Methods of Astrodynamics*. American Institute of Aeronautics and Astronautics Inc., Renston, 1999.

[105] Y. Kozai. The motion of a close Earth satellite. *Astronomical Journal*, 64:367, 1959.

[106] J. A. Arredondo, J. Guo, C. Stoica, and C. Tamayo. On the restricted three-body problem with oblate primaries. *Astrophysics and Space Science*, 341(2):315–322, 2012.

[107] C. N. Douskos and V. V. Markellos. Out-of-plane equilibrium points in the restricted three-body problem with oblateness. *Astronomy and Astrophysics*, 446:357–360, 2006.

[108] V. Szebehely. *Theory of Orbits: The Restricted Problem of Three Bodies*. Academic Press, New York City, 1967.

[109] P. A. Ramamoorthy. *The Classical Approach to Time-Variable Non-Autonomous Linear and Nonlinear Systems. Nonlinear and Adaptive (Intelligent) Systems Modeling, Design and Control: a Building Block Approach, Nonlinear and Self-Learning Dynamics*. University of Cincinnati, Cincinnati, 2003.

[110] M. R. Roussel. *Nonautonomous Systems. Nonlinear Dynamics*. University of Lethbridge, Lethbridge, 2005.

[111] E. L. Stiefel and G. Scheifele. *Linear and Regular Celestial Mechanics: Perturbed Two-Body Motion, Numerical Methods, Canonical Theory*. Springer, New York City, 1971.

[112] S. Campagnola, M. Lo, and P. Newton. Subregion of motion and elliptic halo orbits in the elliptic restricted three-body problem. In *8th AIAA/AAS Space Flight Mechanics Meeting*, Glaveston, 2008 January 27-31.

[113] J. M. Mondelo, M. Ollé, P. A. de Sousa-Silva, and M. O. Terra. Families of heteroclinic connections between quasi-periodic libration point trajectories. In

65th International Astronautical Congress, Toronto, September 29 - October 3 2014.

[114] D. L. Richardson. Analytic construction of periodic orbits about the collinear points. *Celestial Mechanics*, 22:241–253, 1980.

[115] G. Gómez, J.J. Masdemont, and C. Simó. Lissajous orbits around Halo orbits. *Advances in Astronautical Sciences*, 95:117–134, 1997.

[116] J. J Masdemont and J. M. Mondelo. Notes for the numerical and analytical techniques lectures. In *Advanced Topics in Astrodynamics Summer Course*, Barcelona, 2004.

[117] G. Gómez, A. Jorba, J. J. Masdemont, and C. Simó. Study refinement of semi-analytical Halo orbit theory. final report ESOC contract, 1991.

[118] Y. Yu and H. Baoyin. Orbital dynamics in the vicinity of asteroid 216 Kleopatra. *The Astronomical Journal*, 143(62), 2012.

[119] Y. Yu and H. Baoyin. Generating families of 3D periodic orbits about asteroids. *Monthly Notices of the Royal Astronomical Society*, 427:872–881, 2012.

[120] E. Kolemen, N. J. Kasdin, and P. Gurfil. Multiple Poincaré sections method for finding the quasiperiodic orbits of the restricted three-body problem. *Celestial Mechanics and Dynamical Astronomy*, 112:47–74, 2012.

[121] J. Kribbel and R. Dvorak. Stability of periodic resonance-orbits in the elliptic restricted three-body problem. *Celestial Mechanics*, 43:391–398, 1995.

[122] J. Llibre and D. G. Saari. Periodic orbits for the planar newtonian three-body problem coming from the elliptic restricted three-body problem. *Transactions of the American Mathematical Society*, 347(8), 1995.

[123] J. D. Hadjidemetriou. The stability of periodic orbits in the three-body problem. *Celestial Mechanics*, 12:255–276, 1975.

[124] E. Sarris. Families of symmetric-periodic orbits in the 3D elliptic restricted three-body problem. *Astrophysics and Space Science*, 162:107–122, 1989.

[125] M. Ollé and J. R. Pacha. The 3D elliptic restricted three-body problem. Periodic orbits which bifurcates from limiting restricted problems. *Astrodynamics and Astrophysics*, 1999.

[126] J. F. Palacián, P. Yanguas, S. Fernández, and M. A. Nicotra. Searching for periodic orbits of the spatial elliptic restricted three-body problem by double averaging. *Physica D*, 213:15–24, 2006.

[127] J. M. Cors, C. Pinyol, and J. Soler. Periodic solutions in the spatial elliptic restricted three-body problem. *Physica D*, 154:195–206, 2001.

[128] G. Macris, G. A. Katsiaris, and C. L. Goudas. Doubly-symmetric motions in the elliptic problem. *Astrophysics and Space Science*, 33:333–340, 1975.

[129] X. Y. Hou and L. Liu. On motions around the collinear libration points in the elliptic restricted three-body problem. *Monthly Notices of the Royal Astronomical Society*, 415:3552–3560, 2011.

[130] R. Broucke. Periodic collision orbits in the elliptic restricted three-body problem. *Celestial Mechanics*, 3:461–477, 1971.

[131] G. Gómez and M. Ollé. A note on the elliptic restricted three-body problem. *Celestial Mechanics*, 39:33–55, 1986.

[132] G. Gómez and M. Ollé. Second-species solutions in the circular and elliptic restricted three-body problem. I Existence and asymptotic approximation. *Celestial Mechanics and Dynamical Astronomy*, 52:107–146, 1991.

[133] G. Gómez and M. Ollé. Second-species solutions in the circular and elliptic restricted three-body problem. II Numerical explorations. *Celestial Mechanics and Dynamical Astronomy*, 52:147–166, 1991.

[134] I. A. Robin. Bifurcatios of plane with 3D periodic orbits in the elliptic restricted problem. *Celestial Mechanics and Dynamical Astronomy*, 23:97–106, 1981.

[135] I. A. Robin and V. V. Markellos. Numerical determination of 3D periodic orbits generated from vertical self-resonant satellite orbits. *Celestial Mechanics*, 21: 395–434, 1980.

[136] Z. Xia. Arnold diffusion in the elliptic restricted three-body problem. *Journal of Dynamics and Differential Equations*, 5(2):219–240, 1993.

[137] M. J. Capinski and P. Zgliczynski. Transition tori in the planar elliptic restricted three-body problem. *Nonlinearity*, 2009.

[138] E. Gawlik. Lagrangian coherent structures in the elliptic restricted three-body problem. SURF 2007 final report, 2007.

[139] R. J. Hanson and C. L. Lawson. Extension and applications of the Householder algorithm for solving linear least squares problems. *Mathematics of Computation*, 23(108):787–812, 1969.

[140] Z. Olikara and D. J. Scheeres. Numerical methods for computing quasi-periodic orbits and their stability in the restricted three-body problem. In *1st IAA-AAS Conference on Dynamics and Control of Space Systems*, Porto, March 19-21 2012.

[141] K. C. Howell and H. J. Pernicka. Numerical determination of Lissajous trajectories in the restricted three-body problem. *Celestial Mechanics*, 41:107–124, 1988.

[142] C. Simó, G. Gómez, J. Llibre, and R. Martinez. Station keeping of a quasiperiodic Halo orbit using invariant manifolds. In *2nd International Symposium on Spacecraft Flight Dynamics*, pages 65–70, Darmstadt, October 20-23 1986.

[143] G. Gómez, K. C. Howell, J. J. Masdemont, and C. Simó. Station keeping strategies for translunar libration point orbits. In *AAS/AIAA Astrodynamics Specialist Conference*, Monterey, February 9-11 1998.

[144] C. Warren. Phootprint pre-phase A assessment study, September 2014.

[145] C. Olson, R. P. Russell, and J. R. Carpenter. Small body optical navigation using the additive divided difference sigma point filter. In *24th AAS/AIAA Spaceflight Mechanics Meeting*, Santa Fe, January 26-30 2014.

[146] S. Bhaskaran. Autonomous navigation for deep space missions. In *SpaceOps 2012 Conference*, Stockholm, June 11-15 2012.

[147] F. Cacciatore and J. Martin. Mission analysis and trajectory GNC for Phobos proximity phase of Phootprint mission. In *2nd IAA-AAS Conference on Dynamics and Control of Space Systems*, Roma, March 24-26 2014.

[148] E. M. Alessi, G. Gómez, and J. J. Masdemont. A motivating exploration on lunar craters and low-energy dynamics in the Earth-Moon system. *Celestial Mechanics and DynamicaI Astronomy*, 107:187–207, 2010.

[149] M. Zamaro. Coupled orbital and attitude SDRE control system for spacecraft formation flying. Master's thesis, Politecnico di Milano, April 2011.

[150] M. Ceccaroni and J. D. Biggs. Low-thrust propulsion in coplanar circular restricted four-body problem. *Celestial Mechanics and Dynamical Astronomy*, 112 (2):191–219, 2012.

[151] M. Ceccaroni and J. D. Biggs. Nonlinearly stable equilibria in the Sun-Jupiter-Trojan four-body problem. In *62nd International Astronautical Congress*, Cape Town, October 3-7 2011.

[152] A. M. Leontovich. On the stability of the Lagrange periodic solutions of the restricted three-body problem. *Doklady Mathematics*, 3:425–428, 1962. in Russian.

[153] A. Deprit and A. Deprit-Bartholome. Stability of the triangular lagrangian points. *Astronomical Journal*, 72(2):173–179, 1967.

[154] A. Markeev. Stability of the triangular lagrangian solutions of the restricted three-body problem in the three-dimensional circular case. *Soviet Astronomy*, 15 (4):682–686, 1972.

[155] H. Schaub and K. T. Alfriend. J2 invariant relative orbits for spacecraft formations. *Celestial Mechanics and Dynamical Astronomy*, 79(2):77–95, 2001.

[156] J. Fontdecaba i Baig. *Dynamics of Formation Flying: Applications to Earth and Universe Observation.* PhD thesis, Observatoire de Paris, Ecole Doctorale Astronomie et Astrophyisique d'Île de France, 2008.

[157] M. Hénon. Numerical exploration of the restricted problem V. Hill's case: Periodic orbits and their stability. *Astronomy and Astrophysics*, 1:223–238, 1969.

[158] M. Hénon. Numerical exploration of the restricted problem VI. Hill's case: Non-periodic orbits. *Astronomy and Astrophysics*, 9:24–36, 1970.

[159] M. L. Lidov and M. A. Vashkovyak. On quasi-satellite orbits in the elliptic restricted three-body problem. *Astronomy Letters*, 20(5):676–690, 1994. Translated from *Pisma v Astronomičeskji Žurnal* (1994), 20(10), 781-795.

[160] P. J. S. Gil. QSO: Preliminary mission analysis for Phobos observation and access orbits. In *Simpósio Espaço "50 anos do* 1^o *Voo Espacial Tripulado"*, Lisboa, April 12 2011.

[161] J. Llibre and C. Pinol. On the elliptic restricted three-body problem. *Celestial Mechanics and Dynamical Astronomy*, 48(4):319–345, 1990.

[162] B. Mahajan. Libration point orbits near small bodies in the elliptic restricted three-body problem. Master's thesis, Missouri University of Science and Technology, 2013.

[163] K. C. Howell and H. J. Pernicka. Numerical determination of Lissajous trajectories in the restricted three-body problem. *Celestial Mechanics*, 41:107–124, 1988.

[164] Z. Olikara. Computation of quasi-periodic tori in the circular restricted three body problem. Master's thesis, Purdue University, 2010.

[165] E. L. Allgower and K. Georg. *Introduction to Numerical Continuation Methods.* Classics in Applied Mathematics, 45. SIAM, Philadelphia, 2003.

[166] H. B. Keller. *Numerical Solution of Bifurcation and Nonlinear Eigenvalue Problems. Applications of Bifurcation Theory.* Academic Press, New York City, 1977.

[167] D. Puigjaner. Continuation method: Theory, 2011. Advanced Course on New Trends in Applied Bifurcation Analysis, Castro Urdiales.

[168] T. Wagenknecht and J. Sieber. Numerical continuation of bifurcations. an introduction, part 1, 2005. London Dynamical Systems Group Graduate School, University of Bristol.

[169] B. Rink and T. Tuwankotta. Stability in hamiltonian systems: Applications to the restricted three-body problem, 2003.

[170] P. Di Lizia, F. Bernelli, and M. Berz. High order integration and sensitivity analysis of multibody systems using differential algebra. In *19th Congress of the Italian Association of Aeronautics and Astronautics*, Forlí, 2007.

[171] M. Hénon. Exploration numérique du probléme restreint I. Masses égales, orbites périodiques [Numerical exploration of the restricted problem I. Equal masses, periodic orbits]. *Annales d'Astrophysique*, 28:499, 1965.

[172] M. Hénon. Exploration numérique du probléme restreint II. Masses égales, stabilité des orbites périodiques [Numerical exploration of the restricted problem II. Equal masses, stability of periodic orbits]. *Annales d'Astrophysique*, 28:992, 1965.

[173] J. Stoer and R. Bulirsch. *Introduction to Numerical Analysis*. Springer-Verlag, New York City, 1983.

[174] I. G. Kevrekidis, R. Aris, L. D. Schmidt, and S. Pelikan. The numerical computation of invariant circles of maps. *Physica D*, 16:243–251, 1985.

[175] F. Shilder, H. M. Osinga, and W. Vogt. Continuation of quasi-periodic invariant tori. *SIAM Journal on Applied Dynamical Systems*, 4(3), 2004.

[176] A. Jorba. Numerical computation of the normal behavior of invariant curves of n-dimensional maps. *Nonlinearity*, 14:943–976, 2001.

[177] A. Jorba and E. Olmedo. On the computation of reducible invariant tori in a parallel computer. *SIAM Journal of Applied Dynamical Systems*, 8(4):1382–1404, 2009.

[178] R. A. Adomaitis. The trouble with spurious eigenvalues. *International Journal of Bifurcation and Chaos*, 17(4):1375–1381, 2007.

[179] X. Y. Hou and L. Liu. On quasi-periodic motion around the collinear libration points in the real Earth-Moon system. *Celestial Mechanics and Dynamical Astronomy*, 110:71–98, 2011.

[180] L. S. Pontryagin. *The Mathematical Theory of Optimal Processes*. Classics of Soviet Mathematics. Gordon and Breach Science Publishers, Montreux, 1986. R. V. Gamkrelidze, Trans. Original work published 1961.

[181] R. E. Bellman. Dynamic programming and a new formalism in the calculus of variations. *Proceedings from The National Academy of Sciences of the United States of America*, 40(4):231–235, 1954.

[182] R. E. Bellman and S. E. Dreyfus. An application of dynamic programming to the determination of optimal satellite trajectories. *Journal of the British Interplanetary Society*, 17:78–83, 1959.

[183] J. R. Cloutier, C. N. D'Souza, and C. P. Mracek. Nonlinear regulation and nonlinear H_∞ control via the state-dependent Riccati equation technique: part 1. Theory. In *1st International Conference on Nonlinear Problems in Aviation and Aerospace*, Daytona Beach, 1996.

[184] J. R. Cloutier, C. N. D'Souza, and C. P. Mracek. Nonlinear regulation and nonlinear H_∞ control via the state-dependent Riccati equation technique: part 2. Examples. In *1st International Conference on Nonlinear Problems in Aviation and Aerospace*, Daytona Beach, 1996.

[185] M. Massari and M. Zamaro. Application of SDRE technique to orbital and attitude control of spacecraft formation flying. *Acta Astronautica*, 94:409–420, 2014.

[186] M. Massari and M. Zamaro. Application of SDRE technique to orbital and attitude control of spacecraft formation flying. *Advances in the Astronautical Sciences. Proceedings from the 1st IAA-AAS Conference on Dynamics and Control of Space Systems*, 145:1323–1342, 2012.

[187] B. F. Chao, D. P. Rubincam, and P. C. Thomas. The gravitational field of Deimos. *Icarus*, 114:63–67, 1995.